Rubin Wang
Fanji Gu
Enhua Shen
Editors

Advances in Cognitive Neurodynamics

Proceedings of the International Conference on Cognitive Neurodynamics - 2007

Springer

Advances in Cognitive Neurodynamics

Rubin Wang · Fanji Gu · Enhua Shen
Editors

Advances in Cognitive Neurodynamics

Proceedings of the International Conference on Cognitive Neurodynamics - 2007

This conference was supported by the National Natural Science Foundation of China (Grant No. 10710301053)

Springer

Editors

Prof. Rubin Wang
East China University of Science and Technology
The Institute for Cognitive Neurodynamics
130 Meilong Road
200237 Shanghai
People's Republic of China

Enhua Shen
East China University of Science and Technology
The Institute for Cognitive Neurodynamics
130 Meilong Road
200237 Shanghai
People's Republic of China

Dr. Fanji Gu
East China University of Science and Technology
The Institute for Cognitive Neurodynamics
130 Meilong Road
200237 Shanghai
People's Republic of China

ISBN 978-1-4020-8386-0 e-ISBN 978-1-4020-8387-7

Library of Congress Control Number: 2008928127

Printed on acid-free paper

9 8 7 6 5 4 3 2 1

springer.com

This page intentionally left blank

Preface

Fifty years ago, enthused by successes in creating digital computers and the DNA model of heredity, scientists were confident that solutions to the problems of understanding biological intelligence and creating machine intelligence were within their grasp. Progress at first seemed rapid. Giant 'brains' that filled air-conditioned rooms were shrunk into briefcases. The speed of computation doubled every two years.

What these advances revealed is not the solutions but the difficulties of the problems. We are like the geographers who 'discovered' America, not as a collection of islands but as continents seen only at shores and demanding exploration. We are astounded less by the magnitude of our discoveries about how brains cogitate than by the enormity of the tasks we have undertaken, to explain and replicate the higher functions of brains.

Five decades of brain research have led to the emergence of a new field, which spans the entire range of brain cognition from quantum fields to social interactions, and which is combined by the conceptions of nonlinear neurodynamics operating simultaneously at and across all levels. A new breed of scientists has emerged, schooled in multiple academic disciplines, comfortable in working with data from different levels, and conversant with the mathematical tools that are essential to cross boundaries.

Cognition in its essence is dynamic and multilayered, and pursuit of new clues inevitably leads from one layer to the next, both reductive and holistic. Something more is needed to track these clues than the collaboration of experts. It is the self-education of scientists in each field to journeyman competence in adjacent fields. Thus, a new scientific branch focused on these topics, cognitive neurodynamics has been emerged and intrigued scientists and engineers working in various fields.

An international journal "Cognitive Neurodynamics" edited by us was published early this year by Springer, which may be the first one totally dedicated to this important new branch and provide a forum for scientists and engineers, including neuroscientists, neuropsychologists, cognitive scientists, physicists, mathematicians, IT engineers, and many other experts to publish their results and exchanges their ideas and views.

Although there were special sessions with the title of "Neurodynamics" in many conferences, however, there were very few international meetings focusing all its themes on cognitive neurodynamics, maybe except for a series of Tamagawa

Dynamic Brain Forums organized by the Japanese "Gang of Five" on nonlinear dynamics in the past decade. We are very glad now that the 1st International Conference on Cognitive Neurodynamics was held in Shanghai, China Nov. 17–21, which is sponsored and organized by East China University of Science & Technology, Shanghai Society for Biophysics, the journal "Cognitive Neurodynamics", and cosponsored by The National Natural Science Foundation of China (NSFC), Shanghai Association for Science & Technology, Beijing University of Aeronautics and Astronautics, Beijing University of Technology, Brain Science Center of Tamagawa University, Brain Science Research Center of KAIST, CAS-MPG Partner Institute for Computational Biology (PICB), Chinese Society for Neuroscience (CSN), Chinese Society of Theoretical and Applied Mechanics (CSTAM), IEEE Singapore Computational Intelligence Chapter, International Neural Network Society (INNS), Japanese Neural Network Society (JNNS), Nanjing University Aeronautics and Astronautics, Research Center for Brain Science of Fudan University, RIKEN Brain Science Institute (BSI), Shanghai Jiaotong University, Shanghai Society for Nonlinear Science (SSNS), Shanghai University, Tongji University, Xi'an Jiaotong University, Zhejiang University. We are also very glad that the conference has warmly welcomed by the scientists and engineers working in this field. We have 10 plenary talks given by the leading scientists in this field and 14 mini-symposia organized by some of them and other outstanding experts. In addition, we have other 8 special sessions and one poster session. The topics of the contributions almost cover all the fields of cognitive neurodynamics, from micro-, meso- to macroscopic cognitive neurodyanmics, their applications and some related topics. Within our knowledge, this conference is the biggest one wholly dedicated to this topic up to now. It's also our great pleasure to notice the high quality of the contributions, which come from about 30 countries and areas all over the world. We hope the readers will also enjoy and be inspired by the papers in this book.

We hope this is only the first step to create a forum for the scientists and engineers working in the field to show their latest progress, to exchange their ideas and views, and discuss the perspective of this fast growing interdisciplinary area. We hope this book is only the 1st volume of a book series on cognitive neurodynamics.

We would like to express our sincere gratitude to all the sponsors and the contributors, this book could not be published without their supports.

Rubin Wang
Fanji Gu
Enhua Shen

Contents

This page intentionally left blank

ICCN 2007 Organization

Sponsored and Organized by

East China University of Science and Technology, China
Shanghai Society for Biophysics (SSB)
Editorial Board of "Cognitive Neurodynamics" published by Springer

Co-sponsored by

The National Natural Science Foundation of China (NSFC)
Shanghai Association for Science & Technology
Beijing University of Aeronautics and Astronautics, China
Beijing University of Technology, China
Brain Science Center, Tamagawa University, Japan
Brain Science Research Center, KAIST, Korea
CAS-MPG Partner Institute for Computational Biology (PICB)
Chinese Society for Neuroscience (CSN)
Chinese Society of Theoretical and Applied Mechanics (CSTAM)
IEEE Singapore Computational Intelligence Chapter, Singapore
International Neural Network Society (INNS)
Japanese Neural Network Society (JNNS), Japan
Nanjing University Aeronautics and Astronautics, China
Research Center for Brain Science, Fudan University, China
RIKEN Brain Science Institute (BSI), Japan
Shanghai Society for Nonlinear Science (SSNS)
Shanghai University, China
Tongji University, China
Xi'an Jiaotong University, China
Zhejiang University, China

Honorary Chairs

Amari, Shun-ichi, RIKEN Brain Science Institute (BSI), Japan
Freeman, Walter J., University of California, Berkeley, USA
Grossberg, Stephen, Boston University, USA
Haken, Hermann, University of Stuttgart, Germany
Richmond, Barry J., NIMH/NIH/DHHS, USA
Sokoloff, Louis, National Institutes of Health (NIH), USA

General Chair

Wang, Rubin, East China University of Science and Technology, China

General Co-Chairs

Hu, Haiyan, Nanjing University Aeronautics and Astronautics, China
Lu, Qishao, Beijing University Aeronautics and Astronautics, China
Sandner, Guy, University Louis Pasteur, France
Taylor, John, King's College, UK

International Advisory Committee

Chairs

Aihara, Kazuyuki	Tokyo University	Japan
Duch, Wlodzislaw	Nicolaus Copernicus University	Poland
Guo, Aike	Chinese Academy of Sciences	P. R. China
Kötter, Rolf	Radboud University Nijmegen	Netherlands
Schöner, Gregor	Ruhr-Universität Bochum	Germany
Wang, Deliang	The Ohio State University	U.S.A
Usui, Shiro	RIKEN Brain Science Institute (BSI)	Japan

Members

Borisyuk, Roman	Institute of Mathematical Problems in Biology of the Russian Academy of Sciences and the University of Plymouth	UK
Dress, Andreas	CAS-MPG Partner Institute for Computational Biology (PICB), China	Germany
Érdi, Peter	Kalamazoo College, KFKI Research Institute for Particle and Nuclear of the Hungarian, Academy of Sciences	Hungary
Hayashi, Hatsuo	Kyushu Institute of Technology	Japan
Hertz, John	NORDITA	Denmark
Hojjat Adeli	The Ohio State University	USA
Jose C. Principe	University of Florida	USA
Kopell, Nancy J.	Boston University	USA
Kamel, Mohamed	University of Waterloo	Canada
Kaski, Samuel	Helsinki University of Technology	Finland
König, Peter	University Osnabrück	Germany
Li, Chaoyi	Shanghai Institutes of Biological Sciences, Chinese Academy of Sciences	P. R. China
Maass, Wolfgang	Technische Universität Graz	Austria
Olds, James L.	George Mason University	USA

OKADA, Masato	University of Tokyo	Japan
Rabinovich, Mikhail I.	UCSD	USA
Shou, Tiande	Fudan University	P. R. China
Siegel, Ralph Mitchell	Rutgers University	USA
Sporns, Olaf	Indiana University	USA
Tang, Xiaowei	Zhejiang University	P. R. China
Teich, Malvin Carl	Boston University	USA
Trappenberg, Thomas	Dalhousie University	Canada
Tsuda, Ichiro	Hokkaido University	Japan
Tsukada, Minoru	Tamagawa University	Japan
van Leeuwen, Cees	RIKEN Brain Science Institute (BSI)	Japan
Ventriglia, Francesco	Institute of Cybernetics of CNR	Italy
Wang, Xingyu	East China University of Science and Technology	P. R. China
Wermter, Stefan	University of Sunderland	UK
Yamaguchi, Yoko	RIKEN Brain Science Institute (BSI)	Japan
Yang, Fusheng	Tsinghua University	P. R. China
Zhu, Weiqiu	Zhejiang University	P. R. China

Program Committee

Chairs

Gu, Fanji	Shanghai Society for Biophysics Fudan University	P. R. China
Lee, Soo-Young	BSRC, KAIST	Korea
Liljenström, Hans	Swedish University of Agricultural Sciences	Sweden
Nara, Shigetoshi	Okayama University	Japan
Rapp, Paul E	Drexel University College of Medicine	USA
Wang, Lipo	Nanyang Technological University	Singapore

Members

Aertsen, Ad	Albert-Ludwigs Universitat Freiburg	Germany
Andras, Peter	University of Newcastle	UK
Andrew Laung	City University of Hong Kong	Hong Kong
Brette, Romain	Ecole Normale Supérieure, Paris	France
Cao, Jianting	Sitama Institute of Technology	Japan
Cao, Jinde	Southeast University	P. R. China
Chen, Liqun	Shanghai University	P. R. China
Del Moral Hernandez, Emilio	University of Sao Paulo	Brazil
Denham, Mike	University of Plymouth	UK
Depireux, Didier	University of Maryland	USA
Ding, Mingzhou	University of Florida	USA
Egan, Gary	University of Melbourne	Australia
Erwin, Harry	University of Sunderland	UK
Feldman, Jerry	ICSI, University of California at Berkeley	USA
Fellous, Jean-Marc	Duke University	USA
Franceschini, Nicolas	CNRS/Univ. de la Méditerranée	France
Fujii, Hiroshi	Kyoto Sangyo University	Japan
Gao, Shangkai	Tsinghua University	P. R. China

Giese, Martin	University Clinic Tübingen	Germany
Goldfarb, Lev	University of New Brunswick	Canada
Graham, Lyle J.	Laboratory of Neurophysics and Physiology, CNRS	France
Gu, Xingsheng	East China University of Science and Technology	P. R. China
Han, Seung Kee	Chungbuk National University	Korea
Han, Shihui	Peking University	P. R. China
Hellgren Kotaleski, Jeanette	Royal Institute of Technology	Sweden
Hillyard, Steven A.	University of California San Diego	USA
Hofmann, Ulrich G.	University of Lübeck	Germany
Jiang, Tianzi	Institute of Automation, Chinese Academy of Sciences	P. R. China
Kashimori, Yoshiki	University of Electro-Communications	Japan
Kay, Leslie M.	University of Chicago	USA
Kendall, Graham	University of Nottingham	UK
Kozma, Robert	The University of Memphis	USA
Lappe, Markus	Westfälische Wilhelms University	Germany
Lee, Vincent C S	Monash University	Australia
Li, Guang	Zhejiang University	P. R. China
Li, Lei	Hosei University	Japan
Liang, Hualou	University of Texas	USA
Liang, Peiji	Shanghai Jiaotong University	P. R. China
Matsuoka, Kiyotoshi	Kyushu Institute of Technology	Japan
Neskovic, Pedja	Brown University	USA
Ogmen, Haluk	University of Houston	USA
Redman, Steve	Australian National University	Australia
Safronov, Boris V.	IBMC	Portugal
Sato, Shunsuke	Aino University	Japan
Shao, Zhiqing	East China University of Science and Technology	P. R. China
Shi, Hongbo	East China University of Science and Technology	P. R. China
Szeto Kwok Yip	Hong Kong University of Science and Technology	Hong Kong
T. Chow	City University of Hong Kong	Hong Kong
van Ooyen, Arjen	Vrije Universiteit	Netherlands
van Pelt, Jaap	Netherlands Institute for Neurosciences	Netherlands
Wang, Bin	Fudan University	P. R. China
Wright, James	Auckland University	New Zealand
Xu, Jian	Tongji University	P. R. China
Xu, Jianxue	Xi'an Jiaotong University	P. R. China
Yang, Yufang	Institute of Psychology, Chinese Academy of Sciences	P. R. China

Young, Eric D.	Johns Hopkins University	USA
Zhang, Wei	Beijing University of Technology	P. R. China
Zhang, Liqing	Shanghai Jiaotong University	P. R. China
Zhang, Yi	University of Electronic Science and Technology of China	P. R. China

This page intentionally left blank

Mini-Symposium Organizers

MS – 1. Models of Mental Disorders

Hans Liljenström,	Swedish University of Agricultural Sciences	Sweden
James Wright,	Auckland University	New Zealand

MS – 2. Cognitive Machines

John Taylor,	King's College	UK

MS – 3. Visual cortex: Information processing and dynamics

Tiande Shou,	Fudan University	P.R China
Anna W Roe,	Vanderbilt University	USA

MS – 4. K-sets: Theory and Applications

Guang Li,	Zhejiang University	P.R China
Robert Kozma,	The University of Memphis	USA

MS – 5. Advanced Signal Processing Techniques for Brain Data Analysis

Jianting Cao,	Sitama Institute of Technology	Japan
Danilo Mandic,	Department of Electrical and Electronic Engineering, Imperial College	UK

Tomasz Rutkowski,	Brain Science Institute RIKEN	Japan
Toshihisa Tanaka,	Tokyo University of Agriculture and Technology	Japan

MS – 6. Neuroinformatics

Shiro Usui,	Brain Science Institute (BSI)	Japan

MS – 7. Dynamics in learning and memory

Yoko Yamaguchi,	Brain Science Institute (BSI)	Japan
Minoru Tsukada,	Tamagawa University	Japan

MS – 8. Cognitive Computational Modeling of Human Language Processing

Heui-Seok Lim,	Hanshin University	Korea

MS – 9. Translational Cognitive Neuroimaging

Gary Egan,	University of Melbourne	Australia

MS – 10. Brain Networks: From Anatomy to Dynamics

Tianzi Jiang,	Institute of Automation, Chinese Academy of Sciences	P.R. China

MS – 12. Dynamics of Firing Patterns and Synchronization in Neuronal Systems

Qishao Lu,	Beijing University of Aeronautics and Astronautics	P.R. China

MS – 13. Central nervous system synchronization

Paul E. Rapp,	Drexel University, College of Medicine	USA

MS – 14. Cognitive Neurodynamics of Attention: Bottom-Up and Top-Down

Soo-young Lee,	Korea Advanced Institute of Science and Technology	Korea
Minho Lee,	Kyungpook National University	Korea

MS – 15. Structure Formation through Interaction

Andreas Dress,	CAS-MPG Partner Institute for Computational Biology (PICB) Shanghai Institutes for Biological Sciences (SIBS) Chinese Academy of Sciences (CAS),	Germany

Proceeding Chair

Shen, Enhua	East China University of Science and Technology	P.R.China

Finance Chair

Shi, Yongde	Shanghai Society for Biophysics	P.R.China

Secretary

Qian, Zhiqin	East China University of Science and Technology	P.R.China

This page intentionally left blank

Reviewers

Adeli,	Hojjat
Aertsen,	Ad
Aihara,	Kazuyuki
Amari,	Shun-ichi
Andras,	Peter
Andrew,	Laung
Borisyuk,	Roman
Brette,	Romain
Cao,	Jianting
Cao,	Jinde
Chen,	Liqun
Chen,	Zhe
Cheng,	Feiyan
Chow,	T.
Del Moral Hernandez,	Emilio
Denham,	Mike
Depireux,	Didier
Ding,	Mingzhou
Dress,	Andreas
Duch,	Wlodzislaw
Egan,	Gary
Érdi,	Peter
Erwin,	Harry
Feldman,	Jerry
Fellous,	Jean-Marc
Franceschini,	Nicolas
Freeman,	Walter J.
Fujii,	Hiroshi
Gao,	Shangkai
Giese,	Martin
Goldfarb,	Lev
Graham,	Lyle J.
Grossberg,	Stephen

Gu,	Fanji
Gu,	Huaguang
Gu,	Xingsheng
Guo,	Aike
Haken,	Hermann
Han,	Seung Kee
Han,	Shihui
Hayashi,	Hatsuo
Hellgren,	Kotaleski Jeanette
Hertz,	John
Hillyard,	Steven A.
Hofmann,	Ulrich G.
Hu,	Haiyan
Jiang,	Tianzi
Jiao,	Xianfa
Kamel,	Mohamed
Kashimori,	Yoshiki
Kaski,	Samuel
Kay,	Leslie M.
Kendall,	Graham
König,	Peter
Kopell,	Nancy J.
Kötter,	Rolf
Kozma,	Robert
Lanyon,	Linda
Lappe,	Markus
Lee,	Soo-Young
Lee,	Vincent C. S.
Li,	Chaoyi
Li,	Guang
Li,	Lei
Liang,	Hualou
Liang,	Peiji
Liljenström,	Hans
Liu,	Shenquan
Lu,	Huiming
Lu,	Qishao
Maass,	Wolfgang
Matsuoka,	Kiyotoshi
Nara,	Shigetoshi
Neskovic,	Pedja
Ogmen,	Haluk
Okada,	Masato
Olds,	James L.
Omlor,	Lars

Principe,	Jose C.
Rabinovich,	Mikhail I.
Rapp,	Paul E.
Redman,	Steve
Richmond,	Barry J.
Rutkowski,	Tomasz
Safronov,	Boris V.
Sandner,	Guy
Sato,	Shunsuke
Schöner,	Gregor
Shao,	Zhiqing
Shen,	Enhua
Shi,	Hongbo
Shou,	Tiande
Siegel,	Ralph Mitchell
Sokoloff,	Louis
Sporns,	Olaf
Szeto,	Kwok Yip
Tanaka,	Toshihisa
Tang,	Akaysha
Tang,	Xiaowei
Taylor,	John
Teich,	Malvin Carl
Trappenberg,	Thomas
Tsuda,	Ichiro
Tsukada,	Minoru
Usui,	Shiro
van Leeuwen,	Cees
van Ooyen,	Arjen
van Pelt,	Jaap
Ventriglia,	Francesco
Vialatte,	Francois
Wang,	Bin
Wang,	Deliang
Wang,	Lipo
Wang,	Rubin
Wang,	Xingyu
Washizawa,	Yoshikazu
Wermter,	Stefan
Wohrer,	Adrien
Wright,	James
Xu,	Jian
Xu,	Jianxue
Yamaguchi,	Yoko
Yang,	Fusheng

Yang, Yufang
Young, Eric D.
Yu, Hongjie
Zhang, Liqing
Zhang, Wei
Zhang, Yi

This page intentionally left blank

Part I
Microscopic Cognitive Neurodynamics

Chapter 1
Dynamic Interaction Networks and Global Ontology-Based Modelling of Brain Dynamics

Nikola Kasabov and Lubica Benuskova

Abstract With the advancements of bioinformatics and brain research technologies more and more data becomes available tracing the activity of genes, neurons, neural networks and brain areas over time. How can such data be used to create dynamic models that capture dynamic interactions at a particular functional level and across levels over time? The paper addresses these questions through dynamic interaction network (DIN) modelling: first, at a genetic level, a Gene Regulatory Network (GRN) model can be created from a time series gene expression data; second, at a cognitive level, a DIN can be created from a time series of data (e.g. LFP/EEG data) related to perceptual or cognitive functions; and third, a DIN model can be developed for cross-level dynamic interactions, e.g. between GRN and brain signals measured as LFP/EEG. We conclude with introducing brain-gene ontology integrated environment for representing and modelling brain-gene dynamic relations.

Keywords Dynamic interaction networks · gene regulatory networks · neuroinformatics · brain-gene ontology · gene expression data · EEG

Introduction

The brain is a dynamic information processing system that evolves its structure and functionality in time through information processing at different levels (Table 1.1), i.e. quantum-, molecular (genetic)-, single neuron-, ensemble of neurons-, cognitive-, and evolutionary. These states can change, and evolve under certain conditions.

N. Kasabov
Knowledge Engineering and Discovery Research Institute, Auckland University of Technology, 585 Great South Rd, Penrose, 1135 Auckland, New Zealand
e-mail: nkasabov@aut.ac.nz

R. Wang et al. (eds.), *Advances in Cognitive Neurodynamics*,

Table 1.1 Functional levels and processes in the brain

Level	Process
6^{th}-level	Evolutionary (population/generation) processes
5^{th}-level	Cognitive processes
4^{th}-level	System information processing (neural ensembles)
3^{rd}-level	Information processing in a cell (neuron)
2^{nd}-level	Molecular information processing (genes, proteins)
1^{st}-level	Quantum information processing

General Framework

Focusing on levels 2–5 from Table 1.1, a future state of a molecule M' or a group of molecules (e.g. genes, proteins) is represented as a function of its current state M and external signals E_m:

$$M' = F_m\ (M, F_m) \tag{1.1}$$

A future state N' of a neuron, or an ensemble of neurons, is represented as a function of its current state N, the state of the molecules M (e.g. genes) and external signals E_n:

$$N' = F_n\ (N,\ M,\ E_n) \tag{1.2}$$

A future cognitive state C' of the brain is represented as a function of its current state C, the neuronal – N, and the molecular – M state and the external stimuli E_c:

$$C' = F_c\ (C, N, M, E_c) \tag{1.3}$$

The above set of equations (or algorithms) is a general one and in different cases it can be implemented differently as introduced and described in [1].

DIN and GRN Models

DINs represent a generalization of GRN models used to model the expression of many biological genes over time. A node $N_j(t)$ in the model represents an object's (e.g. a gene $G_j(t)$) activation (expression) at a particular time t and the weighted arcs W_{ij} represent the degree of interaction between the objects (e.g. genes G_i and G_j) (for $i = 1,\ 2, \ldots,\ n$) at two consecutive time moments t and $(t + 1)$. In order to evaluate $N_j(t + 1)$ a function $F_j\ (N_i,\ W_{ij};\ i = 1,\ 2, \ldots,\ n)$ is used.

The DIN (GRN in the example above) is created through an optimization procedure that optimizes the connection weight matrix $\mathbf{W}$ and the functions F_j $(j = 1,\ 2, \ldots,\ n)$ to match a time course data of gene expressions. To define the

connection weight matrix **W** from a time series data of all objects (e.g. genes) different learning and optimization methods can be used as already illustrated on GRNinference:

- Kalman filters [2, 3] (a Matlab SW GNetXP available free from www.kedri.info);
- Neural networks and evolving connectionist systems (ECOS) [4, 5]. In this case an ECOS is trained on [input, output] vectors of the activation values of the genes at the time (t) and $(t + 1)$ e.g. $[\mathbf{G}(t),\ \mathbf{G}(t + 1)]$.
- Evolutionary computation, and more specifically – genetic algorithms, where a population of GRN is evolved over generations to optimize a fitness function measuring the model generated time series vs. the real time series data as in [6].

DIN of Brain Signal Transition Rules from EEG Time Series

We formulate a general brain signal transition rule in the following general form:

$$\begin{aligned}&\text{IF} < \text{certain stimulus is present} > \text{and} < \text{the current state of the brain is C}(t) >\\ &\text{THEN} < \text{the next state of the brain is C}(t + \Delta t) >\end{aligned} \tag{1.4}$$

We assume, that a state of activity of the brain at a moment t is represented by an EEG channel vector $C(t)$, each channel $c_i(t)$ representing the activity of an area of the brain at the moment t. An DIN is incrementally trained (evolved) from a time series of EEG channel vectors $C(t_0),\ C(t_1),\ C(t_2), \ldots$, representing the values of the channels. If ECOS neural network modeling technique is used, consecutive vectors $C(t)$ and $C(t + \Delta t)$ are used as input and output vectors respectively in an ECOS model [7, 8]. After training of an ECOS on the data, brain signal transitional rules are extracted. Each rule represents a transition between a current and a next state of the brain measured via EEG signals at the channels. All rules together form a DIN representation of the transitional processes when a stimulus is presented. By modifying a threshold for rule extraction, one can extract in an incremental way stronger, or weaker patterns of transitions. Using a specialized ECOS model called Dynamic Evolving Neuro-Fuzzy Inference Systems (DENFIS) [9] more elaborate types of transitional rules can be extracted, e.g. where the cluster for which the value of the variable c_i is defined is a fuzzy cluster represented through Gaussian membership functions. Rules may change with the addition of new data, thus making it possible to identify stable versus dynamic parts of the transitional brain areas.

DIN and Computational NeuroGenetic Models (CNGM)

Genetic studies show that human EEG has a strong genetic basis [10]. Therefore we use DIN as part of computational neurogenetic models (CNGM) to model the dependency of neural electrical activity upon internal gene interactions in order to account for the spectral differences in the LFP in different brain conditions [11].

The hierarchical model of LFP generation introduced in [12, 13] has the following components: neuronal genes and their expression levels; protein expression levels; interactions between genes; receptor and ion channels related functions; generation of electric signals in neurons; and generation of a local field potential (LFP). Each neuron within a spiking neural network (SNN) is represented as an internal DIN model – an abstract GRN. Genes are related to neuronal parameters like excitation and inhibition and thus their expression levels determine the value of these parameters. For simplicity we assume all GRN to be the same. We can optimize the GRN interactions **W** to match the DIN output with the real signal. The found CNGM that incorporates significant gene interactions constitutes the main result for further experimental testing. Through the obtained model, it should be theoretically possible to simulate the effect of gene knockouts on the brain activity.

Conclusion

Capturing the so far available data, information and knowledge about all levels of the functioning of the brain in one global repository and using it to develop complex multi-model systems is an ultimate goal that cannot yet be achieved. A step towards this goal is to create an open source, multiple-access evolving ontology. So far, a prototype brain-gene ontology (BGO) of about 500 genes has been developed [14].

Acknowledgments Supported by KEDRI (http://www.kedri.info), AUT and the FRST grant AUTX02001 (2002–2007). We would like to thank the PhD students V. Jain and S. G. Wysoski for their contributions to BGO and CNGM, respectively.

References

1. Benuskova, L., Kasabov, N.: Computational Neurogenetic Modeling. Springer, New York (2007)
2. Chan, Z., Kasabov, N., Collins, L.: A Two-Stage Methodology for Gene Regulatory Network Extraction from Time-Course Gene Expression Data. Expert Systems with Applications: An International Journal 30 (2006) 59–63
3. Chan, Z. S. H., Collins, L., Kasabov, N. K.: Bayesian Learning of Sparse Gene Regulatory Networks. Biosystems 87 (2007) 299–306
4. Kasabov, N., Dimitrov, D.: A Method for Gene Regulatory Network Modelling with the Use of Evolving Connectionist Systems. In: ICONIP. IEEE Press, Singapore (2002)
5. Kasabov, N., Chan, S. H., Jain, V., Igor, S., Dimiter, D.: Computational Modeling of Gene Regulatory Networks. In: Bajic, V. B., Wee, T. T. (eds.): Information Processing and Living Systems. World Scientific (2005) 673–686
6. Benuskova, L., Jain, V., Wysoski, S. G., Kasabov, N.: Computational neurogenetic modelling: a pathway to new discoveries in genetic neuroscience. Intl. J. Neural Systems 16 (2006) 215–227
7. Kasabov, N. K.: Evolving Connectionist Systems. Methods and Applications in Bioinformatics, Brain Study and Intelligent Machines. Springer-Verlag, London (2003)
8. Kasabov, N.: Evolving Connectionist Systems. The Knowledge Engineering Approach. Springer, New York (2007)

9. Kasabov, N., Song, Q.: DENFIS: Dynamic, Evolving Neural-Fuzzy Inference Systems and its Application for Time-Series Prediction. IEEE Trans. Fuzzy Systems 10 (2002) 144–154
10. Buzsaki, G., Draguhn, A.: Neuronal Oscillations in Cortical Networks. Science 304 (2004) 1926–1930
11. Villa, A. E. P., Asai, Y., Tetko, I. V., Pardo, B., Celio, M. R., Schwaller, B.: Cross-Channel Coupling of Neuronal Activity in Parvalbumin-Deficient Mice Susceptible to Epileptic Seizures. Epilepsia 46 (2005) 359
12. Kasabov, N., Benuskova, L.: Computational Neurogenetics. Journal of Computational and Theoretical Nanoscience 1 (2004) 47–61
13. Kasabov, N., Benuskova, L., Wysoski, S. G.: Biologically Plausible Computational Neurogenetic Models: Modeling the Interaction between Genes, Neurons and Neural Networks. Journal of Computational and Theoretical Nanoscience 2 (2005) 569–573
14. Kasabov, N., Jain, V., Gottgtroy, P. C. M., Benuskova, L., Joseph, F.: Brain Gene Ontology and Simulation System (BGOS) for a Better Understanding of the Brain. Cybernetics and Systems 38 (2007) 495–508

Chapter 2
The Cauchy Problem for Spiking Neuron Models

Romain Brette

Abstract I consider spiking neuron models defined by a differential equation and a reset – i.e., neuron models of the integrate-and-fire type. I address the question of the existence and uniqueness of a solution on R for a given initial condition. It turns out that the reset introduces a countable and ordered set of backward solutions for a given initial condition. I discuss the implications of these mathematical results in terms of neural coding and spike timing precision.

Spiking Neuron Models

Integrate-and-fire models are defined by a differential equation governing the dynamics of the membrane potential x:

$$\frac{dx}{dt} = f(x,t) \tag{2.1}$$

and a reset: when $x(t)$ reaches a threshold x_t, then a spike is produced and $x(\cdot)$ is instantaneously reset to x_r. Up to a change of variables, one can set $x_t = 1$ and $x_r = 0$. We assume that the differential equation (without reset) admits a flow on R. I previously showed that two particular classes of spiking models have especially interesting properties [1]:

– *leaky models*, such that $\frac{\partial f}{\partial x} \leq \alpha < 0$;
– *reflecting models*, such that $f(0,t) \geq 0$ for all t.

Standard integrate-and-fire models are leaky (and $\frac{\partial f}{\partial x} = g/C$, where g is total conductance and C is the membrane capacitance), the quadratic model is reflecting. In particular, these models have a unique firing rate (independent of initial condition). An important mathematical object for these models is the *spike map* φ, which is defined such that a spike train produced by the model is the orbit of

R. Brette
Equipe Odyssée (INRIA/ENS/ENPC), Département d'Informatique, Ecole Normale Supérieure, 45, rue d'Ulm, F-75230 Paris Cedex 05, France
e-mail: brette@di.ens.fr

R. Wang et al. (eds.), *Advances in Cognitive Neurodynamics*,

the first spike time under φ. More precisely, $\varphi(t)$ is the minimal $s \geq t$ such that the forward solution starting at $(t, 0)$ reaches 1 at time s. For leaky and reflecting models, the spike map is (strictly) increasing on its range but often discontinuous.

Even though Eq. (2.1) defines a flow, the spiking dynamical system only admits a semi-flow because of the resets. The question of existence and uniqueness of solutions on R for a given initial condition (the Cauchy problem) is not only of mathematical interest, but it also has important implications in terms of neural coding. Indeed, consider that Eq. (2.1) reflects the synaptic integration of a number of input spike trains, which are then encoded in an output spike train via the reset mechanism. The set of possible output spike trains in response to the given input spike trains corresponds to the set of solutions defined on R. In section 'The Cauchy Problem', I describe the structure of backward spiking trajectories. In section 'Implication for Neural coding', I argue that the set of meaningful solutions on R is in general not very large and I conjecture that for random realizations of input spike trains, the spiking dynamical system actually defines a single-valued function *input spike trains* $\mapsto$ *output spike train*.

The Cauchy Problem

Let us consider the set $\mathcal{S}$ of solutions $x(\cdot)$ of the spiking dynamical system defined on R, i.e., the set of piecewise differentiable functions $x(\cdot)$ such that $x(t^+) = 0$ whenever $x(t) = 1$, and which satisfy the differential equation (1) everywhere else. We examine the solutions $x(\cdot) \in \mathcal{S}$ that satisfy a given initial condition $x(t_0) = x_0$. By construction, there is a single solution on $[t_0, +\infty[$, which we shall call the *forward solution*. However, a backward solution on $]-\infty, t_0]$ does not necessarily exist. For example, consider the (continuous) solution $u(\cdot)$ to equation (1) such that $u(t_0) = x_0$; if there is an $s < t_0$ such that $u(s) = 1$ and $u(t) > 0$ on $[s, t_0]$, then clearly there can be no backward solution, and thus no solution on R. The following theorem makes this remark more precise:

Theorem 1 (Existence). *Let (t_0, x_0) be an initial condition ($x_0 < 1$) and let $u(\cdot)$ be the (non-spiking) solution to equation (1) such that $u(t_0) = x_0$. There is a solution to the spiking dynamical system on R with initial condition (t_0, x_0) if and only if $u(t) < 1$ for all $t < t_0$.*

Theorem 1 holds for any one-dimensional model (even non leaky and non reflecting).

When a backward solution exists, it is in general not unique. A construction of a set of backward solutions is sketched in Fig. 2.1: every time a backward trajectory reaches 0, it can split between a continuous and a spiking trajectory.

The following theorem makes this statement more precise:

Theorem 2 (Structure of solutions on R). *Assume the model is leaky or reflecting. Let (t_0, x_0) be an initial condition ($x_0 < 1$). There is a countable set of solutions to the spiking dynamical system on R satisfying the initial condition. Let $N \in N \cup \{\infty\}$ be the number of solutions. There is a decreasing sequence of spike times $s_{N-1} <$*

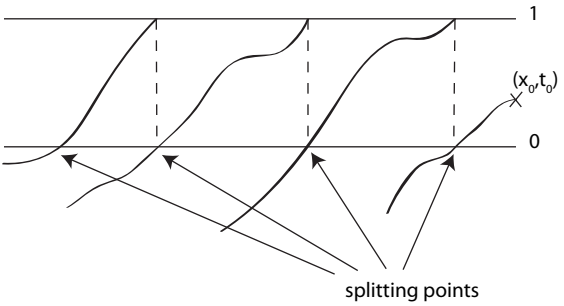

Fig. 2.1 Backward trajectories split at reset

$\ldots < s_2 < s_1 \leq t_0$ such that the spike times of every backward solution corresponds to a subset of that sequence of the form $s_k < \ldots < s_1$.

The integer N is called the degree of the initial condition (t_0, x_0), and the solution with $N - 1$ spikes is called the maximal solution.

Note that a solution to a spiking dynamical system is uniquely defined by its set of spike times.

The following proposition characterizes the bounded solutions, which can be thought of as the only realistic solutions (since physiologically, the membrane potential is constrained by the reversal potentials of ions):

Proposition 1 (Bounded solutions). *We assume the model is leaky and f is bounded. Then a solution is bounded if and only if it has infinite degree (infinitely many spikes on R^-), unless the model is silent before some time t_0 (i.e., no solution on R can spike before t_0).*

Thus, for a given Eq. (2.1), i.e., for a given set of inputs, the set of solutions with infinite degree defines the possible outputs of the neuron model.

Implications for Neural Coding

Our interest for solutions on R can be rephrased as follows. Since an integrate-and-fire model transforms input spike trains into an output spike train through a dynamic state variable, its output for a given set of inputs depends on its state at some point (the initial condition). However, we have seen that not all states are possible if we consider that the neuron has a past; only initial conditions with an infinite degree lead to bounded solutions on R, which constrains the possible outputs of the model.

What is the set Ω of times t such that there is a bounded solution spiking at time t? In terms of the spike map φ defined in section 'Spiking Neuron Models', and since a bounded solution has infinitely many spikes on R^- (except for silent models), it can be written simply as:

$$\Omega = \bigcap_n \varphi^n(R)$$

This is the intersection of a decreasing sequence of sets. When φ is continuous, we simply have $\Omega = R$, i.e., any spike time is admissible. However this is not a physiologically plausible situation for cortical neurons. Indeed, spikes of cortical neurons in vivo are known to be triggered by fast fluctuations of the synaptic current, the average of which is far from threshold [2]. In terms of spiking models, this fact means that most of the time $f(1,t) < 0$ (outward current at threshold), and we know that $\varphi(R) \subset \{t \in R | f(1,t) \geq 0\}$ [1]. Thus, $\varphi(R)$ is already a small set, which suggests that Ω is much smaller. In a previous paper [3], I showed that such a construction generally leaves only a finite number of solutions for periodic inputs, and seems to leave a single solution for aperiodic inputs (realizations of noise), although this latter fact is still lacking a rigorous proof.

Thus, I conjecture that a spiking model defined by Eq. 2.1, where f is determined by a given realization of random inputs, has a single solution on R, which determines its unique output to the given inputs. In this way, spiking neuron models encode their inputs into specific sequences of precisely timed spikes. This conjecture is consistent with the experimental finding that cortical neuron respond reliably to time-varying currents injected in vitro at the soma [4].

References

1. Brette, R.: Dynamics of one-dimensional spiking neuron models. J. Math. Biol. **48** (2004) 38–56.
2. Destexhe, A., Rudolph, M., Paré, D.: The high-conductance state of neocortical neurons in vivo. Nat. Rev. Neurosci. **4** (2003) 739–751.
3. Brette, R., Guigon, E.: Reliability of spike timing is a general property of spiking model neurons. Neural Comp. **15** (2003) 279–308.
4. Mainen, Z.F., Sejnowski, T.J.: Reliability of spike timing in neocortical neurons. Science **268** (1995) 1503–1506.

Chapter 3
On the Dynamics of Spectro-Temporal Tuning in Auditory Cortex

Didier A. Depireux, Heather D. Dobbins and Barak Shechter

Abstract We have previously characterized the steady state tuning of auditory cortical cells with a linear model called the spectro-temporal receptive field. It describes the steady-state tuning of cells with respect to the spectro-temporal envelope of a stable sound. On the other hand, speech and other natural sounds have spectro-temporal features that change dramatically over milliseconds. We explore the time evolution of spectro-temporal tuning in primary auditory cortex following a transient in spectro-temporal content and study how cortical cells stabilize to their asymptotic tuning following presentation of a new sound of given spectro-temporal content.

Dynamics of the Tuning to Spectro-Temporal Features

The question addressed in this work is: What is the time-evolution of neural tuning to spectro-temporal features during the presentation of a complex sound? Neurons in primary auditory cortex (AI) can be characterized by their steady-state response to ongoing broadband sounds with well defined spectro-temporal content. We have previously used auditory gratings, sometimes called ripples [1, 2], to describe the response of AI neurons and predict their response to new sounds, using an essentially linear model called the spectro-temporal receptive field (STRF). In general terms, the cortical response to the presentation of a spectro-temporally rich sound is made up of two components: part of the response is to the level or the change in level (level transient) and part of the response is to the spectro-temporal content or change in spectro-temporal content (feature transient). Our goal is to understand how and on what time scales a cortical neuron reaches its steady-state tuning. We use sounds with a constant mean level, and study the responses near feature transients with a well-defined spectro-temporal envelope emerging from flat spectral noise. One advantage of our stimuli is that the sound is derived from an analytically defined

D.A. Depireux
Department of Anatomy and Neurobiology, University of Maryland, 20 Penn St - S251, Baltimore MD 21201, USA
e-mail: ddepi001@umaryland.edu

R. Wang et al. (eds.), *Advances in Cognitive Neurodynamics*,

spectro-temporal envelope, allowing for feature transients to exist independent of level transients, something difficult to control when using natural sounds.

Reference [3] detailed some important properties of STRFs in cortex: in particular the "separability" of the STRF can be modeled as arising from the existence of two populations of cells earlier in the auditory pathway, called lagged and non-lagged cells [4]. If the observed cortical separability arises from lagged and non-lagged cells (and we have since found there exist two such populations in the inferior colliculus), it implies that the tuning of a cortical cell should evolve in time: upon new spectro-temporal content, the non-lagged cells will provide the early input to the cortical cells, and therefore, the initial tuning. At longer lags in the presence of an unchanging spectro-temporal content, lagged cells will provide an additional, delayed excitatory input and modify the input to cortical cells as provided by thalamic cells.

Methods

We recorded from 183 single units from awake ferrets implanted with a chronic 12-moveable-electrode system as described in [5]. Steady-state STRFs were measured with Temporally Orthogonal Ripple Combinations (TORC) [1, 6]. Briefly, the TORC stimuli are the sum of periodic auditory gratings each having a spectro-temporal profile modulated sinusoidally in spectrum and in time. Each of the gratings comprising a TORC has the same spectral density and depth, but differs in angular frequency. In the TORC stimulus, the amplitude $S(x,t)$ of each tone of frequency f, with $x = \log_2(f/f_0)$ and f_0 the lower edge of the spectrum, is then adjusted as

$$S(x,t) = L[1 + \Delta A \cdot \Sigma_i \ \cos(2 * \pi * (\Omega \cdot x + w_i \cdot t) + \phi_i)]$$

L is the overall intensity base of the stimulus and ϕ_i are the starting phases of each of the component gratings in the TORC.

Stimulus Set for Transient Tuning and Analysis

To measure the dynamics of tuning, we use the broadband transient grating stimuli illustrated in Fig. 3.1. A typical spectro-temporal envelope is flat with the exception of eight 50 ms intervals (transients) of modulation randomly distributed throughout the stimulus. Each 50 ms transient is effectively an auditory grating with specific spectral density, angular frequency and starting phase. In a given waveform, the eight transients have the same density and angular frequency, but random starting phases. A 3-ms ramp is applied to the onset and offset of the transient envelope. Effectively, except for the randomness of the phase, the transients corresponds to switching ΔA from 0 to 1 for 50 ms intervals in the equation above.

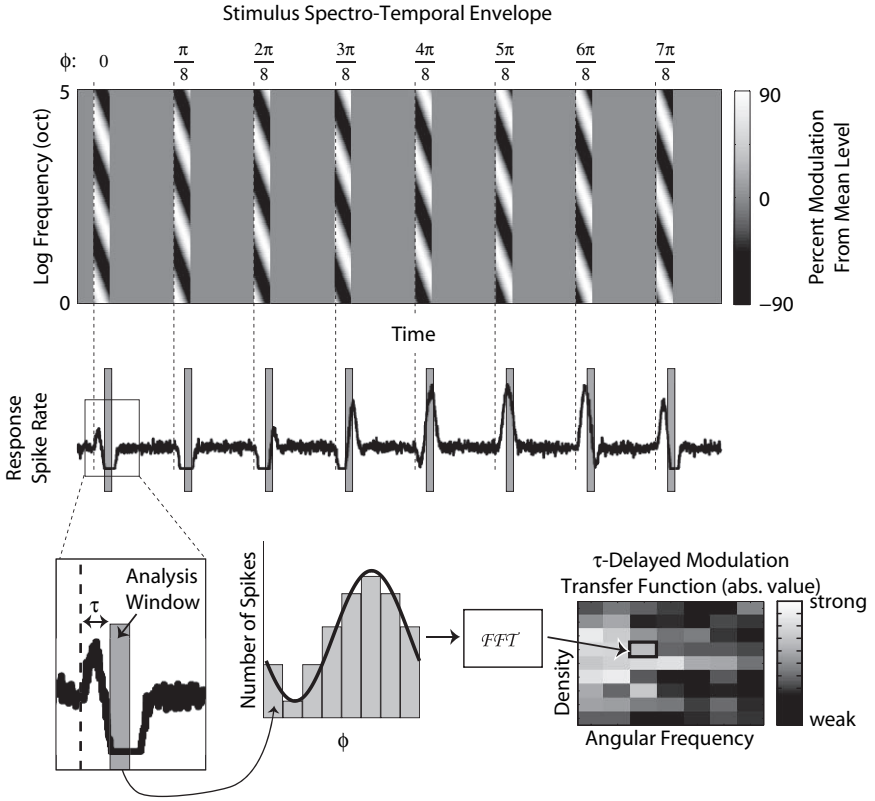

Fig. 3.1 (Top) Spectro-temporal envelope of a transient grating. The stimulus has a flat envelope with eight 50 ms transient gratings. Each transient has the same density (Ω) and angular frequency (w), but a random phase (ϕ). (Middle) Response of a neuron. We compute a tMTF for each lag τ after the transient onsets by computing the average spiking rate in a window (gray box) of duration $(8 \cdot w)^{-1}$ s for each starting phase. (Bottom) Spiking rates evoked by each phase of the modulation are Fourier transformed and the amplitude and phase of the first harmonic extracted. This provides a tMTF for each lag τ msec for each (Ω, w) pair

We compute a lag-dependent or transient modulation transfer function (tMTF) for a set of lags τ after the onset of feature transients (Fig. 3.1). We compute the average spiking rate starting at τ ms after each of the eight transients' onsets. We compensate for the phase shift in the stimulus due to the time elapsed post-transient onset to the center of the window. We combine the rates obtained for each of the eight phases and calculate the Fourier transform. The phase-locking and lag of the response with respect to the feature transient at τ ms after its onset is extracted by taking the amplitude and phase, respectively, of the first component in the transform. This is effectively the modulation of the neural response as a function of the initial phase of the transient and of the lag. We obtain a tMTF as a function of lag post-transient onset.

Once we obtain a set of tMTFs, we can analyze how the tMTF evolves into the steady-state MTF, as measured here by the TORC stimuli. Several parameters have been developed to characterize steady-state STRFs and can be directly adapted to the present situation [1]. Because of space constraints, here we will only consider the asymmetry of the spectral aspect (α_s) and temporal aspect (α_t) of the transfer functions around $\Omega = 0$ and $w = 0$, respectively (see [1]). Together, these two indices afford another way of analyzing the time-dependent build-up of direction selectivity towards the steady state, by quantifying how asymmetric the transfer functions are with respect to down-moving versus up-moving components of the

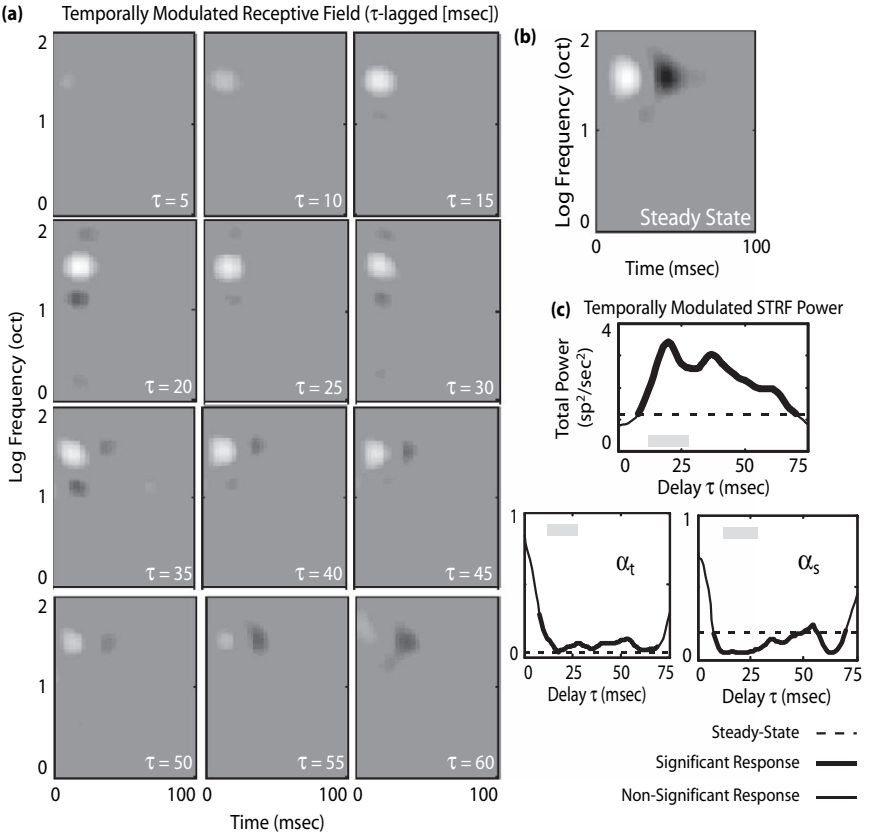

Fig. 3.2 (a) Lag-dependent STRFs. Each frame shown is a reverse correlation with the transient grating stimuli, using the method depicted in Fig. 3.1. The analysis window used for each frame is started at τ ms post-transient onset. The lag-dependent STRF shows sideband inhibitory regions at intermediate lags (from 20 to 40 ms), but these regions are not seen with the steady-state TORC method onset. (b) The steady state STRF obtained through reverse correlation with TORC stimuli. (c) The total power in the transient modulation transfer functions plotted as a function of lag post-transient onset. This value is used to determine whether there is a sufficient phase-locking response to the transient gratings

spectro-temporal envelope. Values near 0 correspond to symmetric transfer functions, whereas values near 1 correspond to asymmetry of the corresponding aspect of the transfer function. We have previously shown that steady state STRFs in AI of the ferret are by and large temporally symmetric ($\alpha_t = 0$) [7]. Since most cells in cortex show quadrant separability in the steady-state [1] and a large percentage of cells had an initially separable transient receptive field, we expected α_s to have a low value for small lags τ. Given the low steady-state value of α_t, the temporal progression of α_s would determine the degree of separability, and thus indirectly, the cell's direction selectivity. Most cells (61%) exhibited this type of behavior, where α_s was initially low and then climbed to a non-zero steady-state value (see Fig. 3.2).

The onset of a spectro-temporal feature should produce a low α_s that indicates spectral symmetry, since the spectrum of sounds is almost instantaneously represented in the cochlea using a unique and complex time-frequency representation. Spectral asymmetry should therefore take a certain integration time before direction selectivity, measured by α_s as a function of lag, could be manifest.

Conclusions: Are Transient Sounds Coded Differently from Unchanging Sounds?

We look at dynamics of tuning: how does one go from only spectral information (at the beginning of a complex sound) to the full steady state tuning to spectro-temporal content? Altogether, our findings show that the linear STRF model should be complemented by including a lag-dependence, so that when the spectro-temporal content of a sound is unchanging or slowly changing, the linear STRF is appropriate, but near a transient such as seen in running speech, cortical neurons are better described as an adaptive filter.

References

1. Depireux DA, Simon JZ, Klein DJ, and Shamma SA: Spectro-temporal response field characterization with dynamic ripples in ferret AI. J. Neurophys. **85** (2001) 1220–1234.
2. Shechter B, and Depireux DA: Response adaptation to broadband sounds in primary auditory cortex of the awake ferret. Hear Res. **221** (2006) 91–103.
3. Simon JZ, Depireux DA, Klein DJ, Fritz JB, and Shamma SA: Temporal symmetry in primary auditory cortex: implications for cortical connectivity. Neural Comput. **19** (2007) 583–638.
4. Saul AB, and Humphrey AL: Spatial and temporal response properties of lagged and nonlagged cells in cat lateral geniculate nucleus. J. Neurophys. **64** (1990) 206–224.
5. Dobbins HD, Marvit P, Ji Y, and Depireux DA: A chronic multi-electrode implant for recording in an awake ferret cortex. J. Neurosci. Methods. **161** (2007) 101–111.
6. Klein DJ, Depireux DA, Simon JZ, and Shamma SA: Robust spectrotemporal reverse correlation for the auditory system: optimizing stimulus design. J. Comput. Neurosci. **9** (2000) 85–111.
7. Simon H: Adaptive Filter Theory, Prentice Hall, 2002, ISBN 0-13-048434-2.

Chapter 4
A European Collaboration on Cerebellar LTD and Pattern Recognition

Erik De Schutter and Volker Steuber

Abstract We review the main results of a study on how the effects of cerebellar long-term depression are reflected in Purkinje cell spiking. An initial modeling study produced surprising results: when actual spike trains were simulated it was predicted that synaptic depression resulted in an increase of the spiking output. Subsequent collaboration with another team led to the confirmation of the main results using patch clamp recordings in *in vitro* cerebellar slices, which suggested additional modeling. A third team provided supporting data from *in vivo* cerebellar recordings. This group effort provides useful insights into ethical and professional issues concerning collaborations between modelers and experimentalists in neuroscience.

Introduction

During 1999 a modeling study was started by Dr. V. Steuber at the Laboratory of Theoretical Neurobiology of the University of Antwerp, Belgium, which eventually led to the publication of an extensive paper in a high profile journal [1]. The present paper reviews the main results of this study but also focuses on the historical process that led to 8 years between start of the initial work and final publication.

The Initial Modeling Study

Dr. V. Steuber started working in Antwerp end of 1999, supported by a fellowship from the Human Frontier Science Program. He wanted to combine an interest in cerebellar learning by Purkinje cells, which had been the topic of his PhD thesis, with the more detailed compartmental modeling in which the Antwerp group has a lot of expertise. We decided to study the consequences of cerebellar long-term

E. De Schutter
Computational Neuroscience Unit, Okinawa Institute of Science and Technology, Onna, Okinawa 904-0411, Japan
e-mail: erik@oist.jp

R. Wang et al. (eds.), *Advances in Cognitive Neurodynamics*,

depression (LTD) of parallel fiber (PF) synapses [2] on Purkinje cell output, in the form of simple spike trains, from a pattern recognition perspective. PF synaptic plasticity is supposed to be the substrate of cerebellar motor learning and it is generally assumed that LTD leads to decreased Purkinje cell output [2].

To make this modeling study possible within acceptable run times we decided to simulate the recognition of PF activity patterns in a previously constructed complex Purkinje cell model [3] in two steps. In the first step, binary input patterns were generated and stored in a corresponding artificial neural network. The resulting vector of synaptic strengths was then transferred to the Purkinje cell model. The responses of this model to both learned and novel patterns were compared and the pattern recognition capabilities of the system were measured as a signal (response to learned pattern) to noise (response to novel patterns) ratio for different features of the spike train. Detailed procedures can be found in [1].

This work led already in 2000 to a very surprising conclusion. In the presence of simulated in vivo simple spike firing, the only criterion that could be used to distinguish the responses to learned patterns was the length of the simple spike pause that followed the presentation of a PF pattern. Contrary to the classic view, learned patterns elicited shorter pauses and resulted therefore in an increased Purkinje cell output. These results raised doubts concerning one of the predictions of classic theories of cerebellar learning.

Preliminary results of this work were presented at scientific meetings in 2000 and a subset of the results, describing the effect of cerebellar LTD on somatic excitatory postsynaptic potentials and their dependence on pattern number and size was published as a conference proceeding [4]. A first manuscript describing the modeling results was submitted to the journal *Neuron* end of 2002, but returned without review as the editor did not consider a modeling study without experimental verification of sufficient general interest. It was subsequently submitted to two other journals, where it was sent out for review but not accepted because of similar concerns from the reviewers.

Experimental Verification

Early in 2004 we decided that it would be better to delay publication and get experimental verification of the data. In the meantime, Dr. Steuber had moved to a second postdoc position at University College London (UCL). Research groups led by Dr. Häusser and Dr. Silver at UCL are specialized in patch clamp recording from *in vitro* cerebellar slices. Together with the team in Antwerp and several other teams in Europe they received funding from the European Commission to study computation and plasticity in the cerebellar system and it was therefore relatively easy to start a collaboration. Dr. W. Mittmann, then a PhD student in Dr. Häusser's lab, started the first experiments in spring 2004. These confirmed that there was a positive relation between the strength of a PF stimulus and the length of the pause in the simple spike firing, a crucial prediction of the model. This work was done with inhibition blocked to ensure that the pause was not caused by inhibition. Unfortunately it took

quite some time to confirm these initial results. One factor was the sensitivity to the experimental condition. While it was easy to reproduce the effect using attached-cell mode it was much more variable under the more standard whole-cell mode condition, presumably because of wash-out [1]. In addition, these experiments were a side project for the student who was at the same time performing several other studies.

So it took more than a year before the experimental work was completed. By that time it also included experiments demonstrating that induction of LTD of the PFs, using a standard protocol, had the predicted effect on the pause [1], making the experimental verification much stronger. With additional authors involved it took quite a bit of time to revise the manuscript and it was not until May 2006 that the manuscript was resubmitted to *Neuron*. Fortunately it was now sent out for review and the reviewers were quite positive, but insisted on additional work. First they wanted proof that the effects could also be demonstrated in the presence of normal inhibition of Purkinje cells, which required additional modeling and experiments [1]. Second, they wanted evidence that the effect was also present *in vivo*. Such data were not available to the research labs involved. However, an additional partner of the European consortium, Dr. De Zeeuw, did have *in vivo* data and an analysis showed that, as predicted, there were longer pauses in Purkinje cell spike trains from transgenic mice lacking LTD [1]. A final revised paper was submitted in February 2007 and published 2 months later.

Lessons Learned

A number of useful conclusions can be drawn from this experience. The good news is that modelers and experimentalists can work together productively and that this can result in exciting findings and high impact papers. It is also a success story for the European funding system, which brings together strong scientific teams from different countries in joint projects [5]. But it took a lot of attention to detail, several visits to each other's laboratories and extensive phone calls to make it all work.

In hindsight it has become clear that it was worthwhile to take the longer route and wait for experimental verification as opposed to publish just the modeling results in a lower impact journal. But this was not so evident initially. First, doing so entailed a risk for the postdoc, who spent almost 2 years on the modeling study. If the experimental work had not confirmed the modeling predictions, but instead contradicted them, it would have been ethically impossible to publish the work. So in some aspects waiting was a gamble, or a question of belief in the strength of our modeling approach. Moreover, because of the multiple partners involved, who all had also other ongoing projects, it took considerable time to accomplish the requested complete experimental verification. This could have had a negative impact on the career of the postdoc and students involved. In fact, Dr. Steuber had moved on to an independent academic position before the paper got published.

Acknowledgments This research was supported by a HFSP fellowship to V.S. and EU QLRT-2000-02256 to E.D.S.

References

1. Steuber, V., Mittmann, W., Hoebeek, F.E., Silver, R.A., De Zeeuw, C.I., Häusser, M., De Schutter, E.: Cerebellar LTD and Pattern Recognition by Purkinje Cells. Neuron 54 (2007) 121–136
2. Ito, M.: Cerebellar long-term depression: Characterization, signal transduction, and functional roles. Physiol. Rev. 81 (2001) 1143–1195
3. De Schutter, E., Bower, J.M.: An active membrane model of the cerebellar Purkinje cell. I. Simulation of current clamps in slice. J. Neurophysiol. 71 (1994) 375–400
4. Steuber, V., De Schutter, E.: Long-term depression and recognition of parallel fibre patterns in a multi-compartmental model of a cerebellar Purkinje cell. Neurocomput. 38 (2001) 383–388
5. Shin, S.-L, Hoebeek, F.E., Schonewille, M., De Zeeuw, C.I., Aertsen, A., De Schutter E.: Regular temporal patterns in cerebellar Purkinje cell simple spike trains. PLoS One 2 (2007) e485

Chapter 5
The Role of Layer 6 Feedback Cells in the Primary Visual Cortex

Wei Wang

Abstract The abiding challenge in vision is to unravel the role of the extensive feedback systems that parallel the ascending feed-forward pathways. Feed-forward projections in the cerebral cortex, which transmit bottom-up information away from sensory receptors, are matched by feedback projections that can transmit top-down signals. The role of layer 6 feedback cells in visual processing is of particular appealing for those cells in the visual cortex sit in a crucial place in the circuitry involved in the early processing of the visual input in higher mammals such as cats and primates [1, 2, 3]. They make connections that straddle both the relay of information from retinal afferents to LGN cells and the transfer of information from LGN cells to layer 4 of the visual cortex. In simple numerical terms the connections from layer 6 cells to LGN and layer 4 of the visual cortex greatly exceed the contribution from the axons carrying the ascending input [4, 5, 6, 7, 8]. This suggests that layer 6 cells play a special role in controlling the access of the visual input to the cortex. The question is what is this role?

It is hard to get direct evidence for this issue but recently we have developed a method to get insight into the functional role of layer 6 feedback cells. Basically with a very small, focal iontophoretic application of GABAb antagonist CGP to layer 6 simple cells, we made simultaneously recording both a group of relay cells in LGN with multi electrode array and the visual responses of layer 6 cells [9]. With this experimental approach we are able to manipulate the visual responses of feedback cells and isolate the effects of such a change on LGN cells in a controlled fashion. We observed that focal enhancement of the gain of visual responses in the layer 6 of primary visual cortex can switch the transmission mode of cells in the visual thalamus in either direction between tonic and burst patterns [3, 10]. This refreshes the view that the two firing modes reflect mechanisms tuned to separate tasks in visual processing [11]. Specifically we speculate that a focus of enhanced visual responses in the visual cortex provides a "feedback searchlight" [12].

W. Wang
Faculty of Life Science, University of Manchester, Manchester M60 1QD
e-mail: wang.wei@manchester.ac.uk

R. Wang et al. (eds.), *Advances in Cognitive Neurodynamics*,

Since the classical work of Hubel and Wiesel, it has been recognized that the orientation and the on- and off-zones of receptive fields of layer 4 simple cells in the visual cortex are linked to the spatial alignment and properties of the cells in the visual thalamus that relay the retinal input [13]. Whether or not the feedback from layer 6 to the LGN is organised in a reciprocal way? For the first time we presented evidence showing that the orientation and the on- and off-zones of receptive fields of layer 6 simple cells in cat visual cortex that provide feedback to the thalamus are similarly linked to the alignment and properties of the receptive fields of the thalamic cells they contact. However, the pattern of influence linked to on- and off-zones is phase-reversed [2, 3]. This has important functional implications and underlines the importance of the way by which the functional connectivity in relation to orientation and spatial phase seems to be conserved and coordinated in the bidirectional interactions between visual cortex and LGN.

We further examined the precision of the firing patterns of simultaneously recorded cell pairs in the A laminae of the LGN to moving stimuli with and without feedback. We have quantified the precision in the synchronization by plotting tuning curves from the synchronized spikes as we vary the orientation of the drifting contour in small steps, which serve to create a varying delay in the timing of the arrival of the contour over one receptive field with respect to the other. We constructed orientation tuning curves from the central 5 msecs in the raw cross-correlograms of the outputs of pairs of LGN cells and this revealed much sharper tuning with feedback [14]. Our data show a remarkable difference in the precision of the responses of LGN cells with and without corticofugal feedback. This documents an emergent temporal precision for moving stimuli from the operation of the cortico-geniculate-geniculo-cortical circuit as a whole. The significance of these data for cortical function suggests the precision in stimulus linked firing in the LGN appears as an emergent factor from the cortico-thalamic interaction [15, 16, 17].

By lifting the focal gain of layer 6 cells visually driven responses in a controlled fashion, we also revealed that most affected thalamus cells with the corticofugal elicited excitation or inhibition were located retinotopic relevant to the extraction of the orientation of contours in their parent cells. Furthermore, the enhanced visually driven feedback restructured the receptive field spatial profiles of those thalamic cells and caused its spatial focus shifting [9]. These results highly indicate that the dynamic and specific positive influences of feedback rather than generic roles contributed to the visual system to adapt rapidly to constantly changing scenes of visual environment. This is relevant to our understanding of not only the functional organization of the visual system but also other sensory systems with the same circuitry, concerning fundamental brain mechanisms and how the brain acquires, processes and stores information.

References

1. Sillito AM, Cudeiro J and Jones HE (2006). Always returning: feedback and sensory processing in visual cortex and thalamus. Trends Neurosci. 29: 307–316.
2. Wang W, Jones HE, Andolina IM, Salt TE, Sillito AM (2004). Functional alignment of feedback effects from visual cortex to LGN. Society for Neuroscience Abstracts: 409.11.

3. Wang W, Jones HE, Andolina IM, Salt TE, Sillito AM (2006). Functional alignment of feedback effects from visual cortex to thalamus. Nature Neurosci. Oct; 9(10): 1330–6.
4. Ahmed B, Anderson JC, Douglas RJ, Martin KAC, Nelson JC (1994). Poly neuronal innervations of spiny stellate neurons in cat visual cortex. *J Comp Neurol* 341, 39–49
5. Erisir A, et al. (1997). Relative numbers of cortical and brainstem inputs to the lateral geniculate nucleus. PNAS, 1517–1520.
6. Van Horn SC, Erişir A and Sherman SM (2000). Relative distribution of synapses in the A-laminae of the lateral geniculate nucleus of the cat. *J Comp Neurol* Jan 24, 416 (4): 509–20.
7. Murphy PC, Duckett SG & Sillito AM (1999). Feedback connections to the lateral geniculate nucleus and cortical response properties. Science 286, 1552–1554.
8. Murphy PC and Sillito AM (1996). Functional morphology of the feedback pathway from area 17 of the cat visual cortex to the lateral geniculate nucleus. *J Neurosci* Feb 1, 16(3): 1180–92.
9. Wang W, Jones HE, Andolina IM, Salt TE, Sillito AM (2000). Influence of enhanced feedback from V1 on visual responses in the LGN. Society for Neurosci Abstracts 162.9.
10. Wang W, Jones HE, Andolina IM, Salt TE, Sillito AM (2001). Focal activation of feedback from V1 to LGN shifts cell firing patterns between bursting and tonic modes. Society for Neurosci Abstracts 27: 723.3.
11. Sherman SM (2001). Tonic and burst firing: dual modes of thalamocortical relay. Trends Neurosci. 24, 122–126.
12. Crick F (1984). Function of the Thalamic Reticular Complex: The Searchlight Hypothesis. PNAS vol. 81, no. 14: 4586–4590.
13. Hubel DH & Wiesel TN (1962). Receptive fields, binocular interaction and functional architecture in the cat's visual cortex. J. Physiol. (Lond.) 160, 106–154.
14. Andolina IM, Jones HE, Wang W and Silito AM (2007). Cortico-thalamic Feedback Enhances Stimulus Response Precision in the Visual System. PNAS Jan 30, vol. 104, no. 5: 1685–16901.
15. Sillito AM, Jones HE, Gerstein GL & West DC (1994). Feature-linked synchronization of thalamic relay cell firing induced by feedback from the visual cortex. Nature 369, 479–482.
16. Cudeiro J & Sillito AM (1996). Spatial frequency tuning of orientation-discontinuity-sensitive corticofugal feedback to the cat lateral geniculate nucleus. J. Physiol. (Lond.) 490, 481–492.
17. Wörgötter, F. et al. (1998). The influence of corticofugal feedback on the temporal structure of visual responses of cat thalamic relay cells. J. Physiol. 509, 797–815.

Chapter 6
What Language is Spoken Here? Conversations Between Neurons in Primate Visual Cortex

Vivien A. Casagrande, Xin Chen and Walter J. Jermakowicz

Abstract In this review we summarize results of our recent studies examining the role of spike timing between cells across early primate visual areas. Using methods that allowed us to examine spike timing between both pairs and larger groups of neurons we provide evidence that spike timing may be an important mechanism for propagating feed forward signals between the primary, secondary and tertiary cortical visual areas and that the propagation of this form of local cooperativity in the network is supported by oscillatory activity in the gamma frequency range.

Keywords Synchrony · coding · vision · primate · oscillations

Perception requires that we transform physical energy, such as patterns of photons for vision, into an interpretable pattern of neural impulses, or spikes. Patterns of sensory spikes must ultimately be transmitted through the different regions of our brains to muscles in order to result in measurable behavior. The question of how the nervous system codes information in the form of spikes to represent our sensory world is still not fully resolved. Traditionally, experts have assumed that firing rate codes information. But firing rate for individual cells can vary across features, making it difficult to understand how complex objects such as faces can be represented. This coding problem is compounded as one considers that more than 30 distinct visual areas appear to specialize in coding different feature attributes of objects in primates.

One highly controversial hypothesis suggests that cells cooperate by synchronizing spikes to represent features in a dynamic way in local networks [1, 2, 3, 4]. We recently examined this hypothesis by determining the degree to which small networks of neurons in primate visual cortex can synchronize their conversations to represent simple visual features, and testing how well this code is transmitted between visual areas. We had two primary questions: (1) Is neuronal gain more dependent on spike firing rate or synchrony? (2) How efficiently are changes in firing rate and synchrony propagated between the early cortical visual areas?

V.A. Casagrande
Departments of & Developmental Biology, Psychology, Ophthalmology & Visual Sciences Vanderbilt Medical School, Nashville, TN 37215, USA
e-mail: vivien.casagrande@vanderbilt.edu

R. Wang et al. (eds.), *Advances in Cognitive Neurodynamics*,

We used a 100-electrode array (Cyberkinetics, Neurotechnology Inc.) to simultaneously record single-cell activity in primary visual cortex (V1) and the second and third visual areas (V2 and V3) in the bush baby, a prosimian primate. In this species area V1 sends it main projection to area V2 but also connects to V3 and area V2 sends it main projection to V3. All experiments were done in accordance with guidelines set by the American Physiological Society and Vanderbilt University's Animal Care and Use Committee under an approved protocol.

Bush babies were anesthetized with propofol and N2O and paralyzed with pancuronium bromide. The dura was exposed and removed, and the 100-electrode array was pneumatically inserted into layers 2/3 of V1, V2 and V3 as determined using stereotaxic coordinates. Receptive fields (RFs) of each electrode were manually mapped with a light bar. The placement of the array was later confirmed by removing the array, fixing the brain in 2% formaldehyde, flattening the cortex, cutting tangential sections and staining for cytochrome oxidase (CO) to reveal CO blobs in V1. The V1-V2 border was defined based on the presence of CO blobs in V1. The V2-V3 border was delineated based on large changes in average receptive field (RF) sizes (V3 RFs are significantly larger than those in V1 or V2). In addition to these criteria we used known differences in mean spatial and temporal frequency preference to further confirm the location of each electrode.

Stimuli were presented on a Monitronix monitor with a 120-Hz refresh rate. Full-screen drifting sine-wave gratings (0.5 cyc/deg) varying in orientation (0–170°, 10° intervals) were presented at 60% contrast. Only cells whose firing rates exceeded 4 sps/s and whose responses to the preferred orientations exceeded the responses to nonpreferred orientations by a factor of two were included in our analysis. To test how well changes in either firing rate or synchrony were propagated between visual areas 200 2 s trials of 30 drifting sine-wave grating stimuli varying in orientation (0–170°), spatial frequency (0.2–1.2 cyc/deg) and temporal frequency (0.5–10.0 Hz) were presented. Spike sorting was used to isolate the most robust units and remove noise and artifacts on each channel [5].

Two different methods were used to correlate spike times. The first method, described earlier [6, 7] was the Joint Peristimulus Time Histogram (JPSTH) Method. To distinguish changes in effective connectivity from changes caused by the covariation of firing rates, we subtracted the cross-product of PSTHs from the raw JPSTH and divided by the standard deviation of the PSTH predictor. We quantified the magnitude of spike synchrony as the percentage of maximum possible effective connectivity, ranging from −100% to 100%. All cross-correlation histograms (CCHs) computed with this method between cells with similar orientation tuning (within 10°) and firing rate above 4 sps/s were used for subsequent analyses.

The second method we developed [8, 9] specifically for quantitative comparison of the propagation of changes in firing rate and synchrony between larger neuron groups in spatially segregated visual areas. Method 1 only allowed us to examine correlations between pairs of neurons. For both methods we selected groups of neurons with similar orientation preferences and overlapping receptive fields in the three visual areas. We then calculated two different peristimulus time histograms (PSTHs) for each group, one representing raw spikes (firing rate) and one representing coincident spikes (synchrony). The latter was corrected using a

standard shift predictor. We correlated these PSTHs for the different cells groups at all time lags, see also [7, 9]. If, for example, firing rate is better propagated between areas V1-V2 than changes in synchrony, the firing rate PSTHs should be more correlated at the 4–6 ms time lag than the synchrony PSTHs.

To examine the relationships of firing rate and synchrony to neuronal gain, we correlated these response properties with neuronal driving efficacy. We quantified driving efficacy by computing cross correlation histograms (CCHs) between neurons in different visual areas with similar orientation preferences and overlapping RFs. The majority of the CCHs (89%) had correlation peaks at 4–6 ms. This peak in the CCH was used as the value to define driving efficacy. The synchrony between neurons in one visual area was highly correlated (0.66) with how well these same neurons drove spikes in target area neurons. In contrast, firing rate correlated poorly with downstream driving efficacy (0.06). These *in vivo* data are the first to support recent simulation studies that show that neuronal gain is better predicted by input synchrony than input firing rate [10].

Our original correlation method, described above, was used to compare propagation of synchrony and firing rate through both feedforward and feedback pathways between V1-V2, V2-V3 and V1-V3. In every case, changes in synchrony correlated better than firing rate at time lags representative of the axonal conduction delays between visual areas, suggesting that coincident spikes provide a more efficient means of communication between early cortical visual areas. The results were consistent even when correlations were made across more than two cells using method 2. Interestingly, synchronous spikes among all cell groups within visual areas occurred in conjunction with oscillations in the mid-gamma band (65–80 Hz) range. In addition, the JPSTH method demonstrated that oscillations at this same frequency also occurred between neurons in different visual areas that preferred the same orientation and whose RFs overlapped.

Our findings suggest that neuronal conversations in the form of synchronous responses may be a fundamental mechanism used to propagate visual information between early visual areas. Neurons are highly sensitive to input spike synchrony. Synchrony increases the probability of generating precisely timed action potentials in the target, leading to the efficient propagation of synchronous responses through the hierarchy to higher order visual areas in a manner that oscillations could support. As suggested previously [1, 2, 3, 4], the oscillations could increase the probability of spike-timing precision among functionally related groups of neurons.

Acknowledgments We are very grateful to AB Bonds, Ilya Khaytin, Gopathy Purushothaman, Zhiyi Zhou and Melanie Bernard for advice and help with these experiments. Support contributed by: EY01778 (VAC), EY08126 (AB Bonds) and core grants HD 15052 and EY014860-03.

References

1. Jermakowicz, W.J., Casagrande, V.A.: Neuronal Networks a Century After Cajal in A Century of Neuroscience Discovery: Reflecting on the 1906 Nobel Prizes to Golgi and Cajal in Brain Research Reviews (L. Swanson, ed.), Elsevier, in press. (2007).

2. Shadlen, M.N., Movshon, J.A.: Synchrony unbound: a critical evaluation of the temporal binding hypothesis. Neuron 24 (1999) 67–25.
3. Singer, W., Gray, C.M. Visual feature integration and the temporal correlation hypothesis. Annu. Rev. Neurosci. 18 (1995) 555–586.3.
4. Usrey, W.M., Reid, R.C.: Synchronous activity in the visual system. Annu. Rev. Physiol. 61 (1999) 435–456.
5. Samonds, J.M., Zhou, Z., Bernard, M.R., Bonds, A.B.: Synchronous activity in cat visual cortex encodes collinear and cocircular contours. J. Neurophysiol. 95 (2006) 2602–2616.
6. Aertsen, A.M., Gerstein, G.L., Habib, M.K., Palm, G.: Dynamics of neuronal firing correlation: modulation of "effective connectivity". J. Neurophysiol. 61 (1989) 900–917.
7. Jermakowicz, W.J., Chen, X., Khaytin, I., Zhou, Z., Bernard, M., Bonds, A.B., Casagrande, V.A.: Is local neuronal synchrony better at discriminating stimulus spatial frequency in primary visual cortex (V1) than firing rate? Society for Neuroscience (2006) Program No. 734.12/J14.
8. Jermakowicz, W.J., Chen, X., Purushothaman, G., Khaytin, I., Madison, C., Bonds, A.B., Casagrande, V.A.: Synchronous spikes are readily propagated between the early cortical visual areas. Submitted (2007).
9. Jermakowicz, W.J., Chen, X., Khaytin, I., Zhou, Z., Bernard, M., Bonds, A.B., Casagrande, V.A.: Is synchrony a reasonable coding strategy for visual areas beyond V1 in primates? J. Vision 7 (2007) 325.
10. Azouz R.: Dynamic spatiotemporal synaptic integration in cortical neurons: neuronal gain, revisited. J. Neurophysiol. 94 (2005) 2785–2796.

Chapter 7
On the Emergence of Orientation Biases in V1

Mehdil and Nouri Shirazi

Abstract Though the site of the emergence of orientation biases in the primary visual cortex (V1) is still debated, it seems that the consensus is converging on the idea originally suggested by Hubel and Wiesel in early 1960's; the idea that the convergence of spatially-arranged geniculate inputs on single cortical cells is the source of orientation biases in V1. But, is the Hubel–Wiesel type of geniculocortical connectivity is the only choice V1 has to generate orientation biases?

Introduction

Intracellular recordings [1] provided strong evidence that the excitatory centers of the RFs of the studied orientation-selective simple cells were nearly circular. In addition, experimental studies based on blocking the cortical GABAergic inhibition by intracortical administration of bicuculline [2] demonstrated that the orientation selectivity of the studied simple cells were reversibly abolished to a degree that their RFs became virtually circular, or that even in some cases, the cells' original orientation preferences were reversibly changed. These pieces of experimental evidence, firstly, imply the existence of non-thalamic source of orientation biases in the responses of cortical cells, and secondly indicate that the convergence of spatially-arranged non-oriented geniculate inputs is by no means the only possible mechanism that enables V1 to generate orientation biases.

Research Goal

The main goal is to construct a spiking neuromorphic model in order to demonstrate how foveal V1's neural circuitry could generate orientation biases from non-oriented thalamic inputs without resorting to a Hubel–Wiesel type of geniculocortical-connectivity mechanism.

M.N. Shirazi
Osaka Institute of Technology, Osaka, Japan
e-mail: shirazi@is.oit.ac.jp

R. Wang et al. (eds.), *Advances in Cognitive Neurodynamics*,

Method

In my previous article [3], I developed a physiologically-plausible computational model for showing how a mature foveal V1 could, in principle, create cortical excitatory/inhibitory orientation biases from non-oriented thalamic inputs. To develop the model, I adopted the Marr's information-theoretic approach. According to Marr's prescription, in order to understand the intracortical information processing that underlies the emergence of orientation biases in V1, we need to answer the following interrelated questions: (1) what is the computational goal of V1? (2) how does V1 achieve its computational goal? and (3) how does the V1's hardware implement its computational goal? In that article, I provided an answer to the first question by formulating a probabilistic computational theory for the emergence of orientation selectivity in V1. The formulated theory comprised: (1) a computational scenario, (2) a two-layer hierarchical Markov random field, which was assumed to generate the the activity patterns of the lateral geniculate nucleus (LGN) cells, and (3) a Maximum-A-Posteriori (MAP) estimation of the activity pattern of the orientation-selective cortical cells for a given LGN activity pattern, which was envisaged as the computational goal of V1. There, an answer was also provided for the second question by developing a physiologically-plausible parallel algorithm that enables V1 to achieve its computational goal. In this article, I introduce, very briefly, a spiking neuromorphic model as an answer to the last question.

The Orientation-selective Computational Models

For the sake of concreteness, let's consider the following system of local updating rules and doubleton-clique energies which describe a horizontally-tuned physiologically-plausible Bayes–Markovian computational model.

The Local Updating Rules

$$\tilde{x}_{ij}(n+1) = \arg \max_{x_{ij} \in \{\underline{X}, \overline{X}\}} \left\{ - \sum_{C \in \mathcal{C}_{ij}^{Y}} \mathcal{E}(y_{ij}, y_{C'} \mid x_{ij}; \beta, T) \right.$$

$$- \max \left\{ - \sum_{C \in \mathcal{C}_{ij}^{Y}} \mathcal{E}(y_{ij}, y_{C'} \mid x_{ij}; \beta, T), \sum_{C \in \mathcal{C}_{ij}^{Y}} \mathcal{E}(y_{ij}, y_{C'} \mid x_{ij}; \beta, T) \right\}$$

$$\left. - \sum_{C \in \mathcal{C}_{ij}^{X}} \mathcal{E}(x_{ij}, \tilde{x}_{C'}(n); \gamma(n)) \right\} \tag{7.1}$$

for all $(i, j) \in \mathcal{L}$, where $\mathcal{L}$ denotes an $N \times N$ rectangular lattice.

The Doubleton Clique Energies

For all horizontal doubleton cliques of the LGN process,

$$\mathcal{E}(y_{ij}, y_{C'} \mid \overline{X}; \beta, T) = -\beta S(y_{ij}, y_{C'}; T) + \beta \overline{S}(y_{ij}, y_{C'}; T) \tag{7.2}$$

and

$$\mathcal{E}(y_{ij}, y_{C'} \mid \underline{X}; \beta, T) = \beta S(y_{ij}, y_{C'}; T) - \beta \overline{S}(y_{ij}, y_{C'}; T) \tag{7.3}$$

whereas, for the non-horizontal doubleton-cliqes,

$$\mathcal{E}(y_{ij}, y_{C'} \mid \overline{X}; \beta, T) = \beta S(y_{ij}, y_{C'}; T) - \beta \overline{S}(y_{ij}, y_{C'}; T) \tag{7.4}$$

and

$$\mathcal{E}(y_{ij}, y_{C'} \mid \underline{X}; \beta, T) = -\beta S(y_{ij}, y_{C'}; T) + \beta \overline{S}(y_{ij}, y_{C'}; T) \tag{7.5}$$

and finally for all doubleton cliques of the SCI process,

$$\mathcal{E}\left(x_{ij}, \tilde{x}_{C'}(n); \gamma(n)\right) = -\gamma(n) I\left(x_{ij}, \tilde{x}_{C'}(n)\right) \tag{7.6}$$

where $\beta > 0,\ \gamma_0 > 0,\ \Gamma(0) = 0,\ \lim_{n\to\infty} \Gamma(n) = 1$, furthermore $S(\circ,\ \circ)$, $\overline{S}(\circ,\ \circ)$, and $I(\circ,\ \circ)$ denote similarity, dissimilarity, and identity operators, respectively. (For a clear understanding of the computational model, its Bayes–Markovian architecture, dynamics, and computations, and the definitions of the symbols and parameters used in describing the model, see [3].)

A Spiking Horizontally-tuned Neuromorphic Model

A recurrent neural network of Hodgkin–Huxley (HH) type spiking cells was constructed to implement the computational model. The network consists of four layers as shown in Fig. 7.1. The spiking neural network stands between the LGN layer and a layer of orientation-selective, horizontally-tuned, striate cortical (OSC) cells, receives inputs from the LGN layer, and generates signals that control the states of the OSC cells. The four-layered neural network consists of spatially interactive modules which are in a retinotopically one-to-one relationship to the LGN cells. Each module comprises a network of neuromorphic spiking microcircuits designed to implement the computational model's local binary operators.

Figure 7.1 shows the excitatory/inhibitory synaptic connections of the ijth module projected on the plane that passes through the module's principal LGN and OSC cells, i.e., the ijth LGN and OSC cells, and their corresponding horizontally-aligned neighboring LGN and OSC cells. The excitatory/inhibitory synaptic connections projected on the planes that pass through the ijth LGN and OSC cells and their corresponding 45°-, 90°-, and 135°-aligned neighboring LGN and OSC counterparts

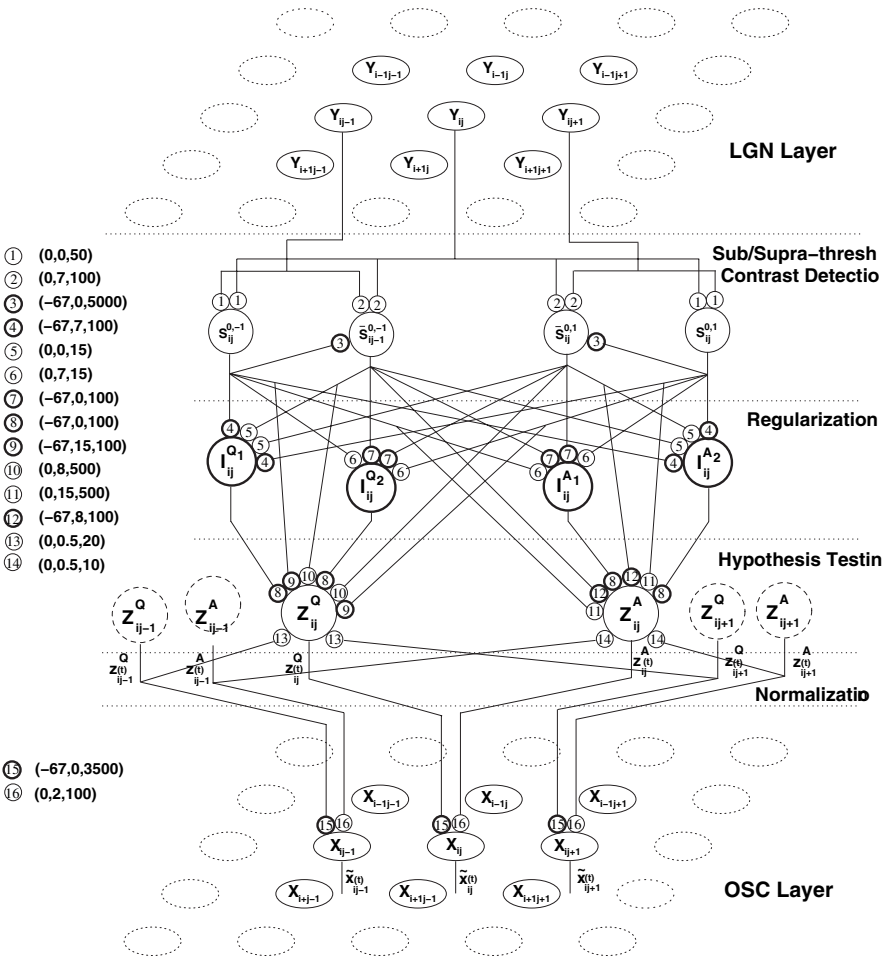

Fig. 7.1 The ijth module's excitatory/inhibitory connectivity pattern projected on the plane passing through the horizontally-aligned neighboring LGN and OSC cells. All cells are assumed to be HH-type spiking cells. Synapses are characterized by three parameters, v_{rev}(mV), d_s(ms), and g_s(μS), where v_{res} denotes the synaptic reversal potential, d_s denotes the synaptic delay, and g_s the synaptic conductance. Synapses with $v_{rev} = -67$(mV) are inhibitory and those with $v_{rev} = 0$ are excitatory

are exactly the same as shown in Fig. 7.1 except the excitatory synapses associated with the sub/supra-threshold contrast cells that should be changed to inhibitory and vice versa.

Simulation Results

The performance of the orientation-selective spiking neural network was studied by using the NEURON simulator. Figure 7.2 shows some of our simulation results.

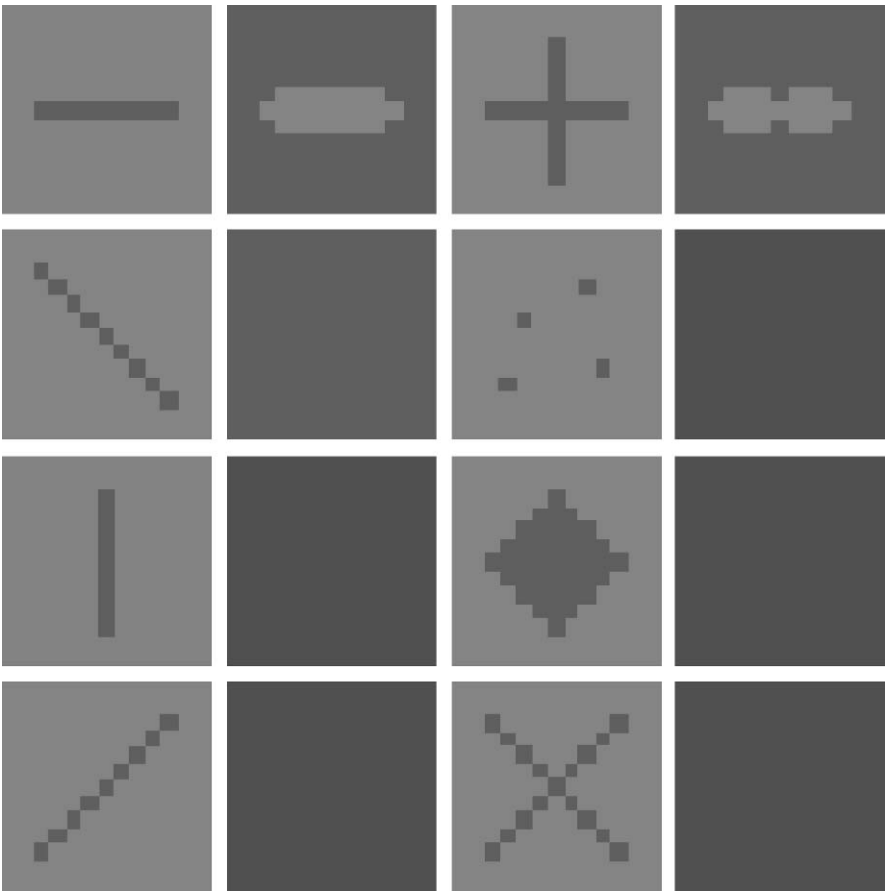

Fig. 7.2 The 1st and 3rd rows show the activity patterns of 15×15 LGN cells, whereas the 2nd and 4th rows show the response patterns of the corresponding 15×15 horizontally-tuned OSC cells. Dark gray in the 2nd and 4th rows denotes zero action potential (AP) per one LGN AP, whereas the light gray denotes one AP per one LGN AP. The simulations were carried out for 80(msec)

References

1. Cruetzfeldt, O.D. and Ito, M.: Functional synaptic organization of primary visual cortex neurons in cat. Exp. Brain Res. 6 (1968) 324–352.
2. Sillito, A.M.: Inhibitary circuits and orientation selectivity in the visual cortex. Models of the Visual Cortex, Eds. D. Rose and V.D. Dobson, (1985) 396–407.
3. Shirazi, M.N.: Emergence of orientation - selective inhibition in the primary visual cortex: a Bayes–Markov computational model. Biol. Cybern. 91 (2004) 115–130.

Chapter 8
Stress Affects Synaptic Plasticity and Basal Synaptic Transmission in the Rat Hippocampus *In Vivo*

Amer Kamal, Ivan Urban and Willem Hendrik Gispen

Abstract Acute as well as prolonged stress produces cognitive deficits. Long term potentiation (LTP) and depression (LTD) in the hippocampus are cellular basic mechanisms implicated in learning and memory. Male Wister rats were used to evaluate the effect of stress on hippocampal synaptic plasticity *in vivo*. The hippocampus CA1 area was implanted with stimulating and recording electrodes. The field excitatory post synaptic responses were recorded before and after induction of stress (unexpected 15 electrical shocks to the feet of the animals during 10 min/twice daily for 2 days). Results showed that the base line synaptic transmission was increased in the stressed rats compared to the control. The induction of LTP (by 100 Hz trains of stimulation) was inhibited in the stressed animals. We concluded that this protocol affected significantly the hippocampal synaptic plasticity. This may explain the effect of stress on some aspects of hippocampus function like learning and memory.

Introduction

Exposure to acute as well as prolonged stress produces cognitive deficits ([1], review) that can be long lasting [2]. Learning is thought to occur through long-lasting, activity-dependent changes in synaptic efficacy. Two opposite synaptic modifications, long-term potentiation (LTP) and long-term depression (LTD) have been identified so far. In many brain areas, including the hippocampus, the direction and the degree of synaptic changes depend primarily on postsynaptic depolarization: LTD is obtained following low levels of depolarization whereas LTP is induced by stronger ones [3]. But the susceptibility to synaptic plasticity also depends on behaviour. Acute [4] and chronic stressors [5] virtually abolish the induction of LTP in hippocampus. We showed that chronic stress affected the performance of rats in water maze, and also inhibited the induction of LTP in the hippocampus [6]. Treatment of the animals with antidepressants (imipramine) or enrichment of

A. Kamal
Rudolf Magnus Institute of Neurosciences, Utrecht University, College of Medicine, Utrecht The Netherlands
e-mail: amerha@agu.edu.bh

R. Wang et al. (eds.), *Advances in Cognitive Neurodynamics*,

their environment [7] reverses these defects. In this study we investigated the effect of stress (in the form of electrical shock delivered to rats) on the basal synaptic transmission and LTP induction in the hippocampus *in vivo*.

Materials and Methods

Young male adult Wister rats (300–350 gm body weight) were used. The hippocampi were implanted with stainless steels wires steriotaxically. The recording electrodes were surgically implanted in the dendritic layer of CA1 field, and the recording electrodes were placed on the Schaffer's Collaterals. Operations were done under general anesthesia, and the hippocampus was reached steriotaxically. After implantation, the site of the electrodes was confirmed by stimulating the afferent fibers and recording the specific responses. The electrode wires were then fixed into sockets which were then screwed to the skull and cemented. The animals were given 2 weeks to recover from the operation. The animals were placed in the recording box which connected the rats to the recording machine and the stimulator. Pulses (of about 70–120 μA) were delivered to the Schaffer collateral afferent fibers and the responses were recorded and fed into a computer for analysis (Spike 2 software). The responses for five different current intensities (I1–I5) were used to evoke threshold to maximum responses. The intensity-response curve was determined, and the current intensity that evoked half maximum responses was used to complete the experiment. Stable base line responses were recorded for at least 1 h. Every rat was transferred into a special treatment cage. One group of animals ($n = 5$) where subjected into electrical shocks through the metal bars of this cage into their feet. The shocks were given unexpectedly, and for a period of 10 min (a total of 15 shocks). This was repeated twice daily for 2 days. Control animals were placed in the same cages but they did not receive electrical shocks. After that, the animals were transferred again into the recording box, and the base line responses were recorded for another 60 min. Three trains of high frequency stimulations (HFS, 100 Hz) were delivered through the recording electrode, and the responses were recorded for further 50 min.

Results

The data are presented as averages ±SEM. The base line responses were set as 100% and the responses after HFS or while measuring the intensity-response relation were expressed as a percentage changes from the base line responses. Student t-test was used to detect significant differences between the groups and before and after HFS.

Figure 8.1 showed that the range of the synaptic responses were not different between the groups. The responses towards the different five current intensities were not significantly different between the groups ($p \geq 0.05$).The effect of acute stress on the basal synaptic responses was measured. Responses before and after stress are

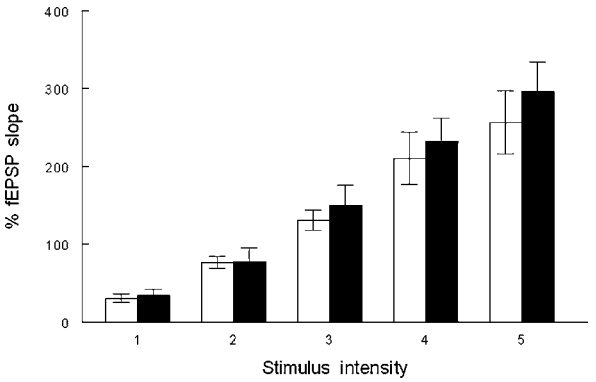

Fig. 8.1 The frequency-response curve in the stressed and control groups of animals. The responses towards five increasing intensities of stimulation (ranging from threshold to maximum responses) were not different in both groups. Empty bar = Control, Black bars = Stressed animals

presented in Fig. 8.2a. The slope of the evoked field excitatory post synaptic potentials (fEPSP) elevated from base line values of $92.72 \pm 4.47\%$ to $119.51 \pm 13.4\%$ measured 45 min after the shock delivery. ($p < 0.05$). No significant change in the fEPSPs slope was recorded in the control animals (100.67 ± 2.64 before the transfer to the treatment cage, and $90.91 \pm 5.8\%$ after 45 min further recording, $p > 0.05$).

Figure 8.3 showed results of LTP induction in the CA1 field of the hippocampus in the stressed and control animals. The conditioning stimulations were 100 Hz (HFS). In the electrically shocked animals there was no significant induction of LTP by this protocol (base line responses were $107.38 \pm 5.12\%$ compared to $110.89 \pm 10.28\%$ of the baseline values recorded 1 h after the application of HFS, $p > 0.05,\ n = 5$). In the control animals however, HFS induced significant LTP induction (base line values were $102.86 \pm 7.67\%$, which were potentiated by HFS into $143.42 \pm 12.56\%$ of base line values 1 h after the HFS, $p < 0.05,\ n = 6$).

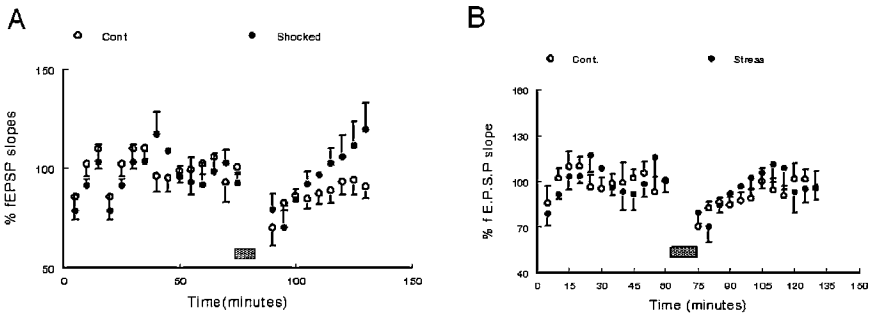

Fig. 8.2 The effect of stress (a) and conditioned stress (b) on the synaptic transmission in the hippocampus. Filled circles refer to stressed group and empty circles to control. Stress potentiates the baseline responses when compared to the control animals (a). In (b) the graph shows that conditioned stress has no effect on the baseline values

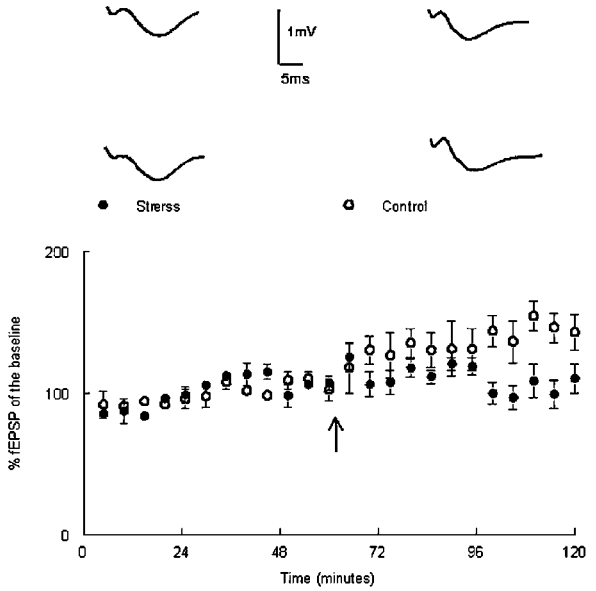

Fig. 8.3 LTP induction in the stressed and control animals. Three trains of HFSs resulted in significant LTP induction in the control animals (empty circles), while it failed to induce potentiation of the responses in the stressed animals (filled circles). Inset: Typical traces from control and stressed animals recorded before and 60 min after the HFS. Calibrations: vertical = 1 mV, Horizontal = 5 ms

Discussions

In this paper we linked between stress and hippocampal synaptic plasticity. It is well known that the hippocampus is playing a role in learning and memory. We showed that defects in learning water maze in rats were associated with defects in hippocampal synaptic plasticity [8]. Our data showed that acute stress induced by unexpected electrical shock to rats caused an increase in synaptic transmission in the hippocampus CA1 area *in vivo*. The slope of the induced fEPSP was significantly higher after the stress. In the other experiment, placing the animals in the treatment box without delivering electrical shock (conditioned stress) did not change the slope of the fEPSP significantly. This could be explained that the responses were already high, and the threshold for further potentiation was increased. We showed earlier that potentiation of a synapse depends also on the state of the synapse before the application of HFS [7]. The same reason may be implicated in the failure of the HFS in LTP induction in the stressed group of animals. The data demonstrated that 3 trains of HFS (100 Hz) were not successful in LTP induction in these animals, while there was a significant potentiation of the responses in the control group. Already potentiated synapses may need more powerful conditioning stimulation to show further LTP. We demonstrated that a defect in LTP induction in stressed rats

was associated with increased sensitivity towards LTD induction [6]. The stressed animals thus showed less LTP but more LTD induction.

In conclusion, our protocol for induction of stress in rats, when applied for 2 days caused an increase in the amplitude of the responses of the hippocampal synapses in rats *in vivo*. The same intensity of current stimulation evoked larger responses after the electrical shock compared to the responses before the shock-induced stress. The results showed also that conditioned stress was not effective in changing the fEPSP responses. This may be due to in part to the fact that the responses were already potentiated by previous stress induced by the electrical shock. The same mechanism may be implicated in the failure of stressed rats to show LTP after HFS.

References

1. De Kloet, E.R., Oitzl, M.S., Joels, M. Stress and cognition: are corticosteroids good or bad guys? 1999: Trends Neurosci; 22: 422–426.
2. Von Frijtag, J.C., Reijmers, Van der Harst, J.E., Leus, I.E., Van den Bos, R., Spruijt, B.M. Defeat followed by individual housing results in long-term impaired reward-and cognition-related behaviours in rats. 2000: Behav Brain Res; 117: 137–146.
3. Dudek, S.M., Bear, M.F. Homosynaptic long-term depression in area CA1 of hippocampus and effects of N-methyl-D-aspartate receptor blockade. 1992: Proc Natl Acad Sci, USA; 89: 4363–4367.
4. Xu, L., Anwyl, R., Rowan, M.J. Behavioural stress fascilitates the induction of long-term depression in the hippocampus. 1997: Nature; 387: 497–500.
5. Gerges, N.Z., Aleisa, A.M., Schwarz, L.A., Alkhadi, K.A. Reduced basal CaMKII levels in hippocampal CA1 region: possible cause of stress-induced impairment of LTP in chronically stressed rats. 2004: Hippocampus; 14: 402–410.
6. Von Frijtag, J.C., Kamal, A., Reijmers, L.G., Schrama, L.H., Van den Bos, R., Spruijt, B.M. C. Chronic imipramine treatment partially reverses the long-term changes of hippocampal synaptic plasticity in socially stressed rats. 2001: Neurosci Lett; 309: 153–156.
7. Artola, A., von Frijtag J.C., Fermont, P.C.J., Gispen, W.H., Schrama, L.H., Kamal, A., Spruijt, B.M. Long-lasting modulation of the induction of LTD and LTP in rat hippocampal CA1 by behavioural stress and environmental enrichment. 2006; Eur J Neurosci; 23: 261–272.
8. Kamal, A., Biessels, G.J., Duis, S.E.J., Gispen, W.H. Learning and hippocampal synaptic plasticity in streptozotocin-diabetic rats: interaction of diabetes and ageing. 2000: Diabetologia; 43: 500–506.

Chapter 9
Physiological Evidence for Cantor Coding Output in Hippocampal CA1

Yasuhiro Fukushima, Makoto Yoneyama, Minoru Tsukada, Ichiro Tsuda, Yutaka Yamaguti and Shigeru Kuroda

Abstract In rat CA1 pyramidal neurons, our previous study showed Cantor coding like property, which is theoretically proposed by Tsuda and Kuroda. In this study, we analyzed the clustering properties by one and two steps before the sequences of electrical stimulation in CA1 pyramidal neurons after many action potentials. The membrane responses after action potentials were significantly clustered as many as in a few action potential conditions. Our results suggest that Cantor coding like processing was also observed in many action potential conditions.

Keywords Cantor coding · hippocampus · clustering property

Introduction

Tsuda and Kuroda [1, 2, 3] theoretically reported the possibility of Cantor coding in CA3-CA1 network. Cantor coding is an information coding scheme for temporal sequences of events. Our previous study showed that Cantor coding like property in hippocampal CA1 neurons, and the clustering property was dependent on input current strength (Fukushima et al., submitted). However, previous stimulation was applied continuously, so there's some possibility to induce neurons' fatigue when inducing many action potentials by very strong current input. To clarify whether many action potentials affect subsequent clustering property of the neurons, we changed the stimulation pattern of random sequences, and analyzed clustering properties in many action potential conditions.

Y. Fukushima
Brain Science Institute, Tamagawa University, 6-1-1, Tamagawagakuen, Machida 194-8610, Japan
e-mail: y-fukusi@lab.tamagawa.ac.jp

R. Wang et al. (eds.), *Advances in Cognitive Neurodynamics*,

Materials and Methods

Patch-clamp recording was made from pyramidal neuron of CA1 area in rat hippocampal slice. EPSPs were induced by extracellular electrical stimulation using two theta glass electrodes. The tips of the two electrodes were set to the Schaffer collaterals, proximal and distal sites to the soma Successive ten pulses (33 Hz) random sequence electrical stimulations, one of four patterns, was applied at 10 s intervals for 20 min. The four patterns of electrical stimulation were as follows: (1) electrical stimulation through both electrodes ("11" type), (2) electrical stimulation through one electrode ("10" type), (3) electrical stimulation through the other electrode ("01" type), and (4) no electrical stimulation ("00" type).

"Cluster index" indicates how well the distribution of responses is clustered by the patterns of electrical stimulation. Cluster index was calculated as our previous experiments (Fukushima et al., submitted). Each response was categorized into four groups by the pattern, one preceding pattern, or two preceding pattern of electrical stimulation. The clustering index indicates the probability that the distance between "its value and weighted-center of its own group" is not shortest among the four distances between "its value and weighted center of all four groups".

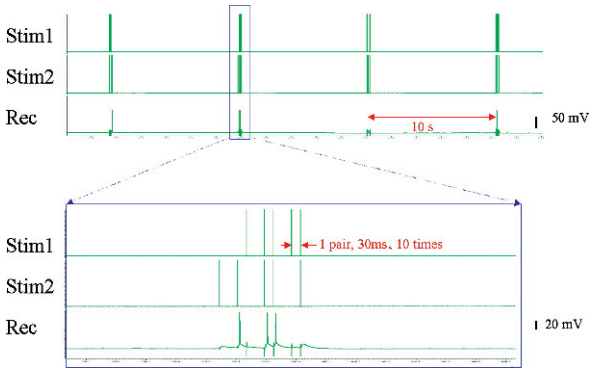

Fig. 9.1 New stimulating pattern

Results and Discussions

Cluster indexes were compared among three conditions: (1) electrical stimulation induced no action potentials (V_r), (2) electrical stimulation induced a few action potentials (V_{th}) (3) electrical stimulation induced many action potentials (V_{spikes}). Clustering index in many action potential condition (V_{spikes}) were significantly lower than randomized control at one and two steps before the sequences, and were similar to those in a few action potential conditions (V_{th}) at clustering by one and two step before in the sequences (Fig. 9.2).

These properties were similar to theoretical Cantor coding system. In additions, our results suggest the possibility that action potentials do not cancel the previous membrane information, but affect subsequent neural processing.

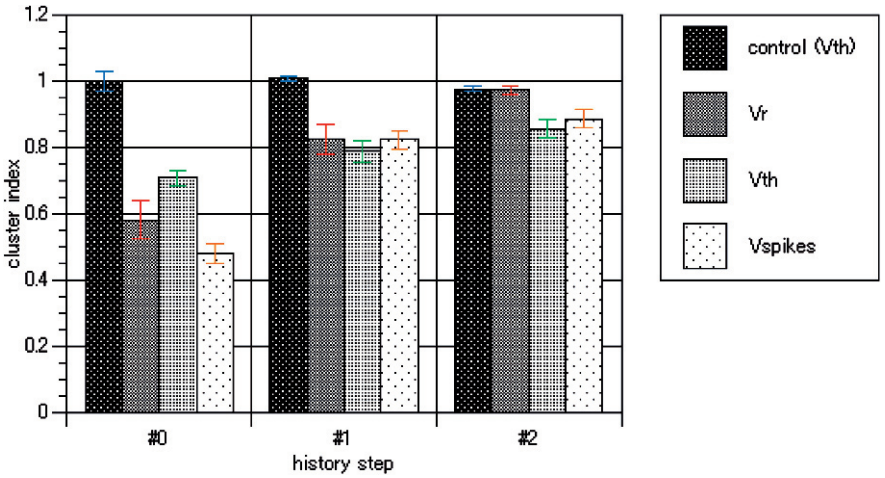

Fig. 9.2 Cluster index at one and two steps before in the sequences

Acknowledgments This study was supported by Grant-in-Aid for a COE Fellow (Y. F) from the Ministry of Education, Culture, Sports, Science and Technology (MEXT) of Japan and by the 21st Century Center of Excellence Program (Integrative Human Science Program, Tamagawa Univ.). One of the authors (I.T.) was supported by Grant-in-Aid for Scientific Research on Priority Areas - Integrative Brain Research - from the Ministry of Education, Culture, Sports, Science and Technology of Japan (18019002), and also supported by Grant-in-Aid for Scientific Research on Priority Areas - Understanding of Mobiligence – from the Ministry of Education, Culture, Sports, Science and Technology of Japan (18047001).

References

1. Tsuda I.: (2001a) Toward an interpretation of dynamic neural activity in terms of chaotic dynamical systems. Behavioral and Brain Sciences 24(5): 793–847.
2. Tsuda I., Kuroda S.: (2001b) Cantor coding in the hippocampus. Japan J Indust Appl Math 18: 249–258.
3. Tsuda I., Kuroda S.: (2004) A complex systems approach to an interpretation of dynamic brain activity II: Does Cantor coding provide a dynamic model for the formation of episodic memory. P Erdi et al. (Eds.): Cortical dynamics, LNCS 3146: 129–139.
4. Fukushima Y., Tsukada M., Tsuda I., Yamaguti Y., Kuroda S.: (2007) Spatial Clustering property and its self-similarity in membrane potentials hippocampal CA1 pyramidal neurons for a spatio-temporal input sequence. Cognitive Neurodynamics 1:305–316.

Chapter 10
Theta Phase Coding and Suppression of Irrelevant Plastic Change Through STDP in the Entorhino-Hippocampal System amid Background Noise

Jun Igarashi and Hatsuo Hayashi

Abstract We investigated sequence learning in the entorhino-hippocampal system using a network model of the entorhinal cortex layer II with entorhino-hippocampal loop connections. Afferent signals to the entorhinal cortex layer II, whose frequencies were different from each other, were encoded by the phase of stellate cell firing with respect to theta rhythm. It is also demonstrated that a LTD window in the range of positive spike-timing may suppress enhancement of irrelevant loop connections due to background noise.

Keywords Entorhinal cortex layer II · network model · loop circuitry · theta-phase coding · STDP · sequence learning · noisy circumstance

Introduction

The entorhinal cortex (EC) and the hippocampus (HC) are crucial brain areas for sequence learning. Place cells have been found in HC [1], and it has been supposed that a sequence of places is encoded by the phase of place cell firing with respect to theta rhythm (i.e. theta phase coding) [2]. Moreover, the phase of place cell firing advances when the animal traverses a place field (i.e. phase precession) [3].

EC layer II (ECII) receiving afferent signals from the neocortex sends signals to HC, and then HC sends signals to EC layer V (ECV). Since projections from ECV to ECII exist, loop circuitry is formed in the EC-HC system and reverberation activity in the gamma range occurs. This gamma activity may be superimposed on the theta rhythm generated in ECII. This is a reminiscence of the theta phase coding.

On the other hand, low-rate random EPSPs (i.e. background noise) occur spontaneously in stellate cells. Occasional firing of stellate cells due to the background

J. Igarashi
Department of Brain Science and Engineering, Graduate School of Life Science and Systems Engineering, Kyushu Institute of Technology, 2-4 Hibikino, Wakamatsu-ku, Kitakyushu 808-0196, Japan
e-mail: igarashi@brain.kyutech.ac.jp

R. Wang et al. (eds.), *Advances in Cognitive Neurodynamics*,

noise may be a cause of plastic change in synaptic weight if synapses in this area are subject to spike-timing-dependent plasticity (STDP).

In this paper, first, we will show that afferent signals to ECII stellate cells, whose frequencies are different from each other, are encoded by the phase of stellate cell firing with respect to theta rhythm, using an ECII network model with loop connections that mimic the EC-HC loop circuitry. Secondly, we will show that a LTD window in the range of positive spike-timing works to suppress enhancement of irrelevant loop connections due to background noise.

Theta Phase Coding in the Entorhino-Hippocampal System

The present ECII network model consists of 30 stellate cells and one inhibitory interneuron (Fig. 10.1a). The EC-HC loop circuitry was mimicked by simple delay lines (transmission delay = 20 ms) that connected stellate cells in all-to-all fashion, whereas the stellate cells were not mutually connected through excitatory synapses within the ECII network. Loop connection weights were subject to a STDP rule. The stellate cell was a multi-compartmental biophysical model [4] that was obtained by modifying the stellate cell model developed by Fransén et al. [5]. Interneuron was exactly the same as that developed by Fransén et al.

The present ECII network model causes theta rhythm as synchronized subthreshold oscillations of stellate cells. As stellate cell firing keeps pace with the theta rhythm, each stellate cell fires around a phase of the theta rhythm determined by the frequency of the afferent signal to the cell. A 40 Hz afferent signal (pulse train) was fed to one stellate cell (cell A) and an afferent signal below 40 Hz was fed to another cell (cell B). When cell B received an afferent signal around 30 Hz, the spike time difference between the cells, A and B, was about 20 ms and the pre-post spike-timing (spike-timing between presynaptic spikes entered from cell A to cell B through the loop connection and postsynaptic spikes of cell B) distributed within the LTP window of ±10 ms. Consequently, the loop connection was enhanced.

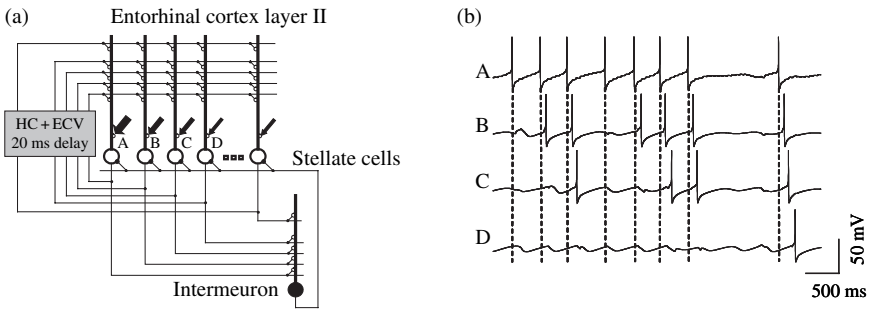

Fig. 10.1 (a) ECII network model with loop connections that mimic EC-HC loop connections (*lines passing through the gray box*). *Arrows* indicate afferent signals. (b) Firing of ECII stellate cells whose loop connections are potentiated, using a Mexican hat STDP rule. Stellate cell *A* alone was stimulated by an afferent signal

Four afferent signals whose frequencies were 40, 30, 20, and 10 Hz were fed to four stellate cells, A, B, C, and D, respectively, during the first period of 40 s and then another four groups of four stellate cells, B-E, C-F, D-G, and E-H, were successively stimulated by the afferent signals every 40 s on the assumption that the animal traverses a place field. Consequently, loop connections, A → B, B → C, C → D, D → E, and E → F, were selectively potentiated. After the establishment of the potentiation, stellate cell A alone was stimulated by a 40 Hz afferent signal. Firing of stellate cell A triggered successive firing of stellate cells, B, C, and D (Fig. 10.1b). This implies that a phase coding was established. Then, stellate cell B alone was stimulated by the 40 Hz afferent signal. Firing of cell B triggered successive firing of stellate cells C-E, and those firing phases advanced. This replicates the phase precession.

Suppression of Plastic Change in Irrelevant Loop Connections

In this section, we used thee types of STDP rules (Fig. 10.2a–c). Loop connections between stellate cells receiving afferent signals whose frequencies were appropriately different were selectively enhanced regardless of the types of STDP rule. However, an asymmetric STDP rule being used, irrelevant loop connections between stellate cells, which received a high-frequency afferent signal and a random signal each, were potentiated, whereas, the Mexican-hat and the Nishiyama STDP rules

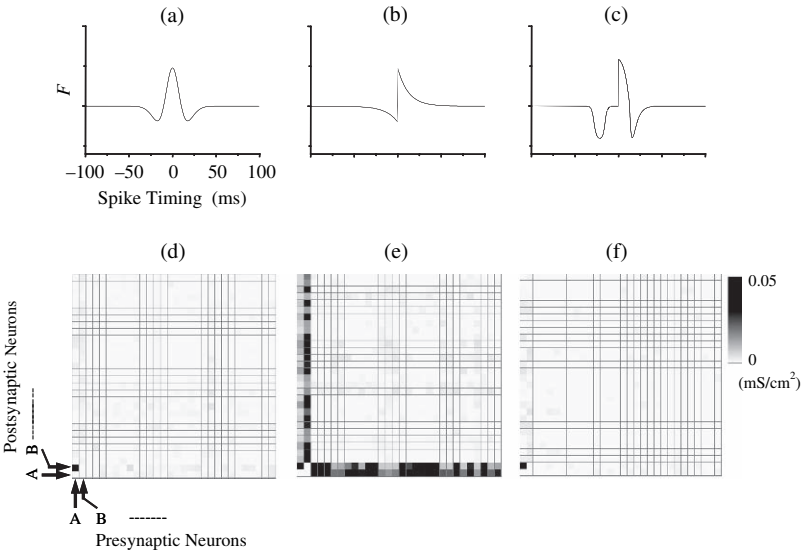

Fig. 10.2 Leaning rules: (a) Mexican hat, (b) asymmetric, and (c) Nishiyama STDP rules. Connection matrices (d)–(f) correspond to the STDP rules (a)–(c) respectively. Stellate cells, *A* and *B*, were stimulated by afferent signals. Each of the other stellate cells was stimulated by a random signal alone

being used, those irrelevant loop connections were not potentiated (Fig. 10.2d–f). The pre-post spike-timing is positive in this situation and the asymmetric STDP rule has only a LTP window in the range of positive spike-timing, while Mexican-hat and Nishiyama STDP rules have a LTD window in the same range.

When the frequency of the afferent signal was below 20 Hz, irrelevant loop connections were potentiated even in the case of Mexican-hat and Nishiyama STDP rules. Those potentiated loop connections were however suppressed with the progress of sequence learning. On the assumption that the animal approaches the center of the place field, the frequency of the afferent signal increases and the irrelevant loop connections were finally suppressed. In contrast, in the case of the asymmetric STDP rule, potentiated irrelevant loop connections remained to the last.

Discussion

In general, the frequency of sensory signals encodes intensity of sensory stimuli. Therefore, the frequency of sensory signals that conveys information about places closely ahead of the animal would be high. In fact, the firing rate of place cells increases when the animal approaches the center of the place field [3]. Probably, the frequency of afferent signals to ECII is low when the animal passes the edge of the place field, and then increases when the animal approaches the center of the place field. As a result, route information would be stored as a sequence of discrete places selected by afferent signals whose frequencies are appropriately different.

A LTD window in the range of positive spike timing works to suppress enhancement of irrelevant loop connections between stellate cells receiving afferent and random signals each, as mentioned above. Another factor in the robust sequence learning is the transmission delay of loop connections. If the transmission delay is more than 10 ms, even synaptic weights between stellate cells receiving only random signals are depressed, because firing phases of the stellate cells were clustered together around a later phase of the theta rhythm and the pre-post spike timing distributes in the range of negative spike timing. STDP rules having a LTD window in the range of positive spike timing and loop connections having a relatively long transmission delay are suitable for robust sequence learning amid background noise.

Acknowledgments This work was supported by the COE program (center #19) granted by MEXT of Japan and KAKENHI (19500126) granted by JSPS.

References

1. O'Keefe, J., Recce, M.L.: Phase relationship between hippocampal place units and the EEG theta rhythm. Hippocampus 3 (1993) 317–330.
2. Jensen O., Lisman J.E.: Hippocampal CA3 region predicts memory sequences: accounting for the phase precession of place cells. Learn. Mem. 3 (1996) 279–287.

3. Skaggs W.E., McNaughton B.L., Wilson M.A., Barnes C.A.: Theta phase precession in hippocampal neuronal populations and the compression of temporal sequence. Hippocampus 6 (1996) 149–172.
4. Igarashi J., Hayashi H., Tateno K.: Theta phase coding in a network model of the entorhinal cortex layer II with entorhinal-hippocampal loop connections. Cogn. Neurodyn. 1 (2007) 169–184.
5. Fransén E., Alonso A., Hasselmo M.E.: Simulations of the role of the muscarinic-activated calcium-sensitive nonspecific cation current INCM in entorhinal neuronal activity during delayed matching task. J. Neurosci. 22 (2002) 1081–1097.

Chapter 11
Effect of Low-Frequency Stimulation on Spontaneous Firing in Cultured Neuronal Networks

J. van Pelt, I. Vajda, P.S. Wolters, G. Ramakers and A. van Ooyen

Abstract Cultured neuronal networks from dissociated rat cortical tissue show spontaneous firing activity from about the end of the first week in vitro. Multielectrode recordings have shown slow developmental changes in the firing activity at the individual electrode sites. Here we report that a short period of low-frequency electrical stimulation is able to induce lasting changes in the spontaneous firing activity, significantly larger than developmental changes over similar periods of time.

Introduction

When dissociated rat cortical tissue is brought into culture, neurons readily grow out by forming axonal and dendritic arborizations and synaptic connections. These developing neuronal networks display spontaneous firing activity from about the end of the first week in vitro. Firing rates, recorded with multielectrode arrays, show slow developmental changes, small on time scales of hours [1, 2, 3, 4, 5]. Here we investigated the sensitivity of spontaneous firing activity to short periods of low-frequency electrical stimulation.

Methods

Cell Cultures on Multielectrode Arrays

Dissociated E18 rat neocortical neurons were cultured on planar multi-electrode arrays (MEA) from MultiChannel Systems [2, 6]. Hexa-MEA types were mainly used, with a hexagonal pattern of electrodes with diameters of 10, 20 and 30 μm, respectively. The latter one was used for electrical stimulation.

J. van Pelt
Department of Experimental Neurophysiology, Center for Neurogenomics and Cognitive Research, VU University Amsterdam, De Boelelaan 1085, 1081 HV Amsterdam, The Netherlands
e-mail: jaap.van.pelt@falw.vu.nl

R. Wang et al. (eds.), *Advances in Cognitive Neurodynamics*,

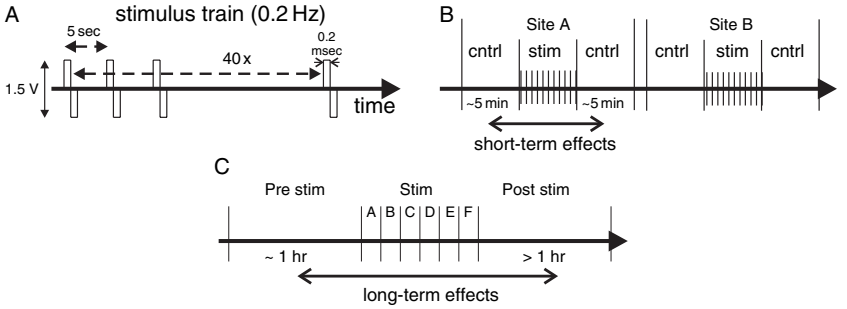

Fig. 11.1 (a) Pattern of low-frequency stimulation, consisting of a train of 40 bipolar pulses of 1.5 V (peak-peak) of 0.2 ms width (single phase), delivered with 5 s intervals (0.2 Hz). (b) Each pulse train is preceded and followed by a period of about 5 min for recording spontaneous activity in the network. (c) Pulse trains are successively applied to six different electrodes in the Hexa MEA multielectrode array

Pattern of Electrical Stimulation

The scheme of electrical stimulation is shown in Fig. 11.1. Individual trains of 40 bipolar pulses at 0.2 Hz were delivered at six successive sites, with a test period of about 5 min before and after each train. Before stimulation at the first site and after stimulation at the sixth site, spontaneous activity was measured for a period of at least 1 h.

Comparing Mean Firing Rates at Individual Sites Between Two Periods

Scatter plots (Fig. 11.2) were constructed in which each individual site is represented by a data point with the mean firing rates for pre-stimulus and post-stimulus periods as coordinates, respectively. Data points at the diagonal line indicate sites with equal firing rates for both periods. The relative deviation *rd* of a data point from the diagonal was calculated as the ratio of its distance to the diagonal and the 3 standard deviation (3σ) distance expected for a Poisson distributed spike train (dashed lines). For a group of data points the mean relative deviation *mrd* was calculated. Data points outside the $\pm 3\sigma$ areas may indicate significant differences in firing rates between the pre- and post-stimulus period.

Results

Long-Term Effects

Figure 11.3 illustrates the long-term effects of low-frequency stimulation on the spontaneous firing rates. The left panel compares the firing rates between the first and the second half of the prestimulus period. All the data points are within the

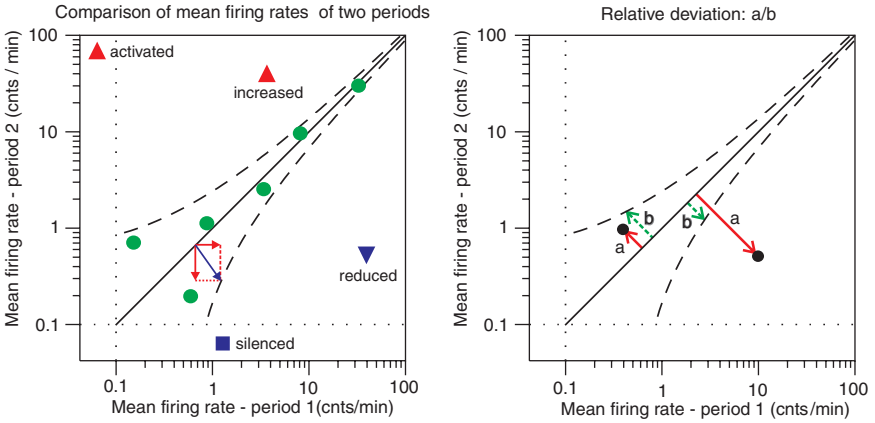

Fig. 11.2 (Left panel) Comparison of mean firing rates at individual sites between pre- and post-stimulus periods. Data points at the diagonal lines indicate sites with equal firing rates for both pre- and post-stimulus periods. The dashed lines indicate 3-standard deviation (SD) boundaries assuming a Poisson distributed spike train. (Right panel) The relative deviation of a data point from the diagonal is expressed by the ratio of the distance of the data point from the diagonal (a) and the 3-SD distance (b)

area bounded by the dashed lines. The central panel compares the firing rates in the second half of the prestimulus period with those in the first half of the poststimulus period. Here, many data points scatter outside the dashed line area, indicating significant changes in firing rates between pre- and post-stimulus period. The right panel compares between the first and the second half of the post-stimulus period. Again all data points are within the dashed lines area indicating that the altered firing rates have maintained in the post-stimulus period. The increased scatter of the data points in the pre-stim post-stim comparison is also shown by the *mrd* values (Fig. 11.4).

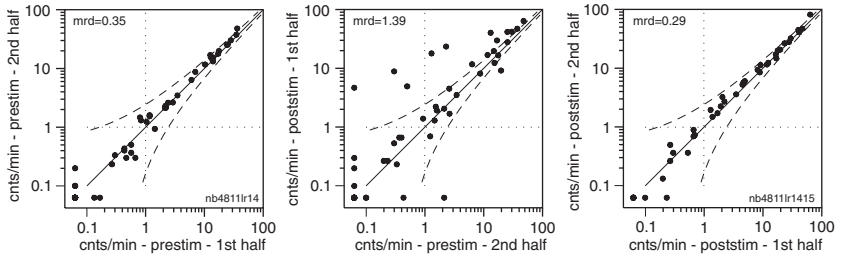

Fig. 11.3 Spontaneous firing rates on individual sites measured one hour before and one hour after a stimulation session. The left panel compares the first half and second half hour of spontaneous activity before the stimulation session. The central panel compares the second half hour of the prestimulation period and the first half hour of the poststimulation period. The right panel compares the first and second half hour of spontaneous activity after the stimulation session. The mean relative deviation (*mrd*) of the data points from the diagonal is indicated in the upper left corner of each panel

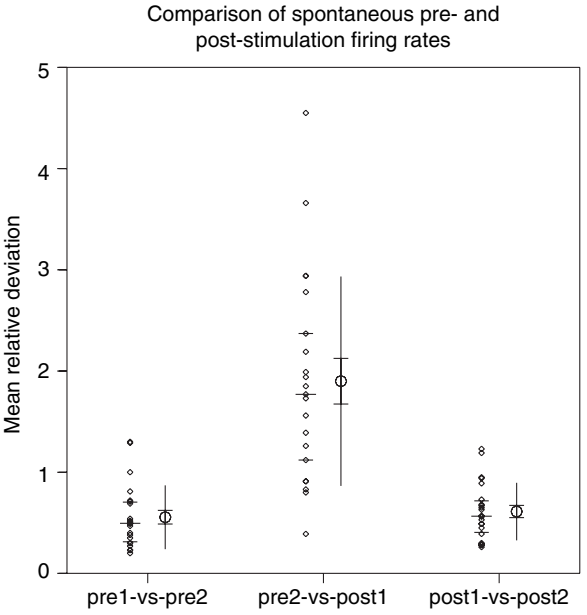

Fig. 11.4 Individual *mrd* values (dots) of 17 stimulus experiments for the pre1-pre2, pre2-post1 and post1-post2 comparisons, as well as their population means (circles) and SD and SEM values (open and closed bars, respectively)

Short-Term Comparison

The results of 12 experiments for the spontaneous firing rates before and after an individual train of 40 stimulus pulses are summarized in the scatter plot of Fig. 11.5. For each experiment, and for each of the six stimulus trains, the spontaneous firing rates in the pre- and post-train periods of 200 sec are plotted as an individual symbol. The symbols appear to scatter equally around the diagonal indicating that there is no systematic difference between pre- and post stimulus firing rates. Several data points scatter outside the dashed lines area.

Discussion

Cultured neuronal networks show ongoing spontaneous activity from the end of the first week in vitro. Firing rates show small developmental changes on time scales of hours [2, 3], indicating a level of robustness in the patterns of spontaneous firing. The present study has shown that low-frequency stimulation is able to induce lasting changes in these firing patterns, significantly larger than developmental changes over the same periods of time (data not shown). Short-term comparisons indicated that even a single stimulus train could be effective. But variable occurrences of network bursts may also have contributed to the scatter in the data points. These findings demonstrate that the intrinsic firing dynamics in cultured neuronal networks maintains a subtle balance between stability under spontaneous conditions and

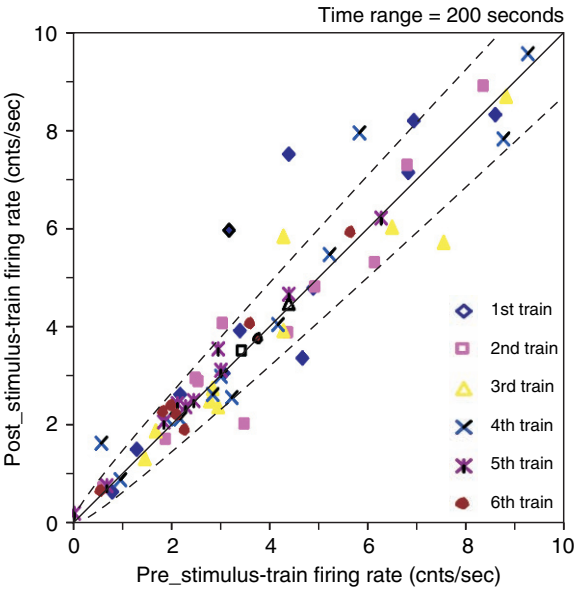

Fig. 11.5 Scatter plot of spontaneous firing rates in a period of 200s before and after a stimulus train. Data from 12 independent experiments. Dashed lines denote 3-SD intervals expected for a Poisson distributed spike train

sensitivity for making transitions to other patterns by even low-frequency external electrical stimulation.

References

1. Shahaf, G. and Marom, S. Learning in networks of cortical neurons. J Neurosci. 21 (2001) 8782–8788
2. Van Pelt, J., Wolters, P.S., Corner, M.A., Rutten, W.L.C. and Ramakers, G.J.A. Long-term characterization of firing dynamics of spontaneous bursts in cultured neural networks. IEEE-TBME 51 (2004a) 2051–2062
3. Van Pelt, J. Corner, M.A., Wolters, P.S., Rutten, W.L.C. and Ramakers, G.J.A. Longterm stability and developmental changes in spontaneous network burst firing patterns in dissociated rat cerebral cortex cell cultures on multi-electrode arrays. Neurosci. Lett. 361 (2004b) 86–89
4. Chiappalone, M., Bove, M., Vato, A., Tedesco, M. and Martinoia, S. Dissociated cortical networks show spontaneously correlated activity patterns during in vitro development. Brain Res. 1093 (2006) 41–53
5. Le Feber, J., Rutten, W.L.C., Stegenga, J., Wolters, P.S., Ramakers, G.J.A. and Van Pelt, J. Conditional firing probabilities in cultured neuronal networks: a stable underlying structure in widely varying spontaneous activity patterns. J. Neural Eng. 4 (2007) 54–67
6. Ramakers, G.J.A., Winter, J., Hoogland, T.M., Lequin, M.B., Van Pelt, J. and Pool, C.W. Depolarization stimulates lamellipodia formation and axonal, but not dendritic branching in cultured rat cerebral cortex neurons. Dev. Brain Res. 108 (1998) 205–216

Chapter 12
Modeling Neurons of the Inferior Colliculus

**Harry Erwin, Mark Elshaw, Adrian Rees,
David Perez-Gonzalez and Stefan Wermter**

Abstract The MiCRAM project has been developing detailed neural models of the inferior colliculus (IC) as the basis for understanding the neural networks that underlie early auditory processing at that level. The initial phase of this project has been to develop biologically plausible models of the physiologically distinct cell types of the IC. This has led to the recognition that some of the gross behavior that produces delay sensitivity may be the result of detailed dynamic interactions between multiple channels.

Keywords Neural modeling · neurodynamics · audition

Introduction

The MiCRAM project is a collaborative study involving the Universities of Sunderland and Newcastle in developing a biologically plausible model of auditory processing at the level of the inferior colliculus (IC). This is being done to clarify the roles of the spectral and temporal representations in the IC and investigate how they interact with auditory processing to focus attention and select sound sources for analysis.

The IC is organized tonotopically into parallel frequency lamina, each with a collection of disc and stellate cells with a variety of response patterns to pure tone stimuli [1]. The IC might be seen as a large set of full and partial spectral representations. Sound sources at different locations or with different characteristics activate the IC spectral representations differently for different sound sources. Understanding how this takes place will provide insight into the auditory processes in acoustically cluttered environments.

The first step towards this goal is the development of biologically realistic GENESIS [2] models of individual IC. That requires us to explore statistically valid models of the firing patterns of these cells.

H. Erwin
School of Computing and Technology, University of Sunderland, SR6 0DD, UK
e-mail: Harry.Erwin@sunderland.ac.uk

R. Wang et al. (eds.), *Advances in Cognitive Neurodynamics*,

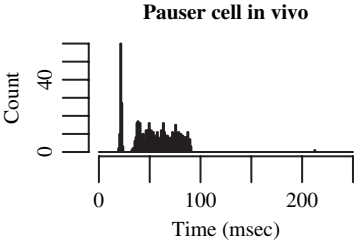

Fig. 12.1 Pauser cell PTSH, 100 *in vivo* trials, pure tone stimulus lasting 75 ms, 1 ms bins (see [1])

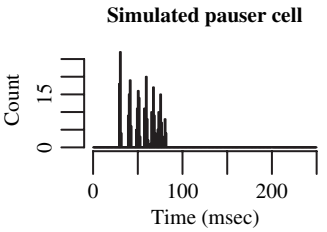

Fig. 12.2 PTSH showing effect of afterhyperpolarisation in simulated pauser cell

A number of research groups are doing research into the area of statistically valid cell models [3, 4, 5]. Since spike trains are binary in form, evaluating goodness of fit is more difficult than for continuous processes [6]. Although IC disk cells fire in a reliable way to repeated presentations of the same stimulus, they often respond quite differently if the intensity or structure of the stimulus is changed, which makes it difficult to use quantitative models to classify these cells [1].

The PSTH classifications in Rees et al. [1] emphasize the spiking rate modulation of IC cells in response to pure tone stimuli *in vivo* and so reflect the cell's membership in neural networks. This can be seen most clearly in pauser cells that spike a variable number of times initially, then become quiet for a period, and finally spike continuously or at a modulated rate (Fig. 12.1). After hyperpolarisation can produce a similar but distinct pattern (Fig. 12.2), that is more regular with a single spike reliably appearing in each burst.

The contribution of specific membrane conductances to the generation of these response patterns has been reported by Sivaramakrishnan and Oliver [7]. The MiCRAM program is modeling these cell types to explore their dynamics and incorporate them into large scale network models of the IC.

Methods

The MiCRAM program models these cell types using the GENESIS neural modeling tool. The channel properties are based on the models in [8]. The simulations replicate their experiments, with a medium goal of constructing networks of different classes of these cells.

Results

Generally, we have been able to replicate in GENESIS simulations the firing patterns described in Sivaramakrishnan and Oliver [7]. Of some interest are the dynamics of the currents in rebound cells. Those cells respond to the end of hyperpolarizing current injection with a membrane potential rebound to values more depolarized than the resting potential of the cell. This 'rebound hump' is believed to be produced by the interaction of relatively slow voltage-activated Ca++ channels with the Na+ and K+ Hodgkin-Huxley (HH) channels that drive spike generation. Figure 12.3 illustrates the underlying conductances and the resulting membrane potentials in our modeling. *In vivo* the Ca++ rebound appears to be a simple hump of depolarization with superimposed spikes, but the modeling suggests that it has a more complicated internal structure, involving the damping of a forced Hodgkin-Huxley system by Ca++ conductances.

Discussion and Conclusions

The rebound spike mechanism has been suggested as playing a role in measuring time delays between sounds [9], and the detailed interaction between channels that we have modeled with GENESIS may play a role in decreasing the variability of the timing of the rebound spike. Live animals seem to perform accurate measures

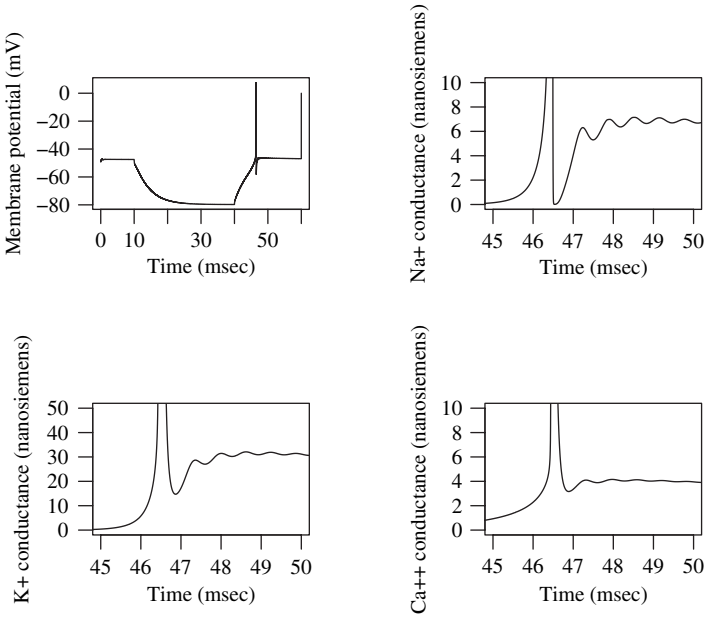

Fig. 12.3 Rebound cell dynamics

of time delays between sounds – jitter sensitivity of 10–100 ns has been reported by Simmons et al. [10] – and this channel mechanism may underlie auditory time delay hyperacuity.

Acknowledgments This work was supported by the Engineering and Physical Sciences Research Council.

Address for Reprint Requests

H. Erwin, University of Sunderland, School of Computing & Technology, PO Box 299, Sunderland, SR6 0YN, United Kingdom.

References

1. Rees, A., et al.: Regularity of Firing of Neurons in the Inferior Colliculus. Journal of Neurophysiology. 77 (1997) 2945–2965.
2. Wilson, M., et al.: GENESIS, the Caltech Neural Network Simulator. (1991) Available from: ftp://genesis.caltech.edu/
3. Wiener, M.C. and B.J. Richmond: Decoding Spike Trains Instant by Instant Using Order Statistics and the Mixture-of-Poissons Model. Journal of Neuroscience. 23 (2003) 2394–2406.
4. Kass, R.E. and V. Ventura: A Spike-Train Probability Model. Neural Computation. 13 (2001) 1713–1720.
5. Eden, U.T., et al.: Dynamic Analysis of Neural Encoding by Point Process Adaptive Filtering. Neural Computation. 16 (2004) 971–998.
6. Brown, E.N., et al.: The Time-Rescaling Theorem and Its Application to Neural Spike Train Data Analysis. Neural Computation. 14 (2001) 325–341.
7. Sivaramakrishnan, S. and D.L. Oliver: Distinct K Currents Result in Physiologically Distinct Cell Types in the Inferior Colliculus of Rat. Journal of Neuroscience. 21 (2001) 2861–2877.
8. De Schutter, E. and J.M. Bower: An Active Membrane Model of the Cerebellar Purkinje Cell: I. Simulation of Current Clamps in Slice. Journal of Neurophysiology. 71 (1994) 375–400.
9. Olsen, J.F.: Processing of Biosonar Information by the Medial Geniculate Body of the Mustached Bat, Pteronotus parnelli. Washington University (1986).
10. Simmons, J.A., et al.: Discrimination of Jittered Sonar Echoes by the Echolocating Bat, Eptesicus fuscus: the Shape of Target Images in Echolocation. Journal of Comparative Physiology A. 167 (1990) 589–616.

Chapter 13
Synchronization Effects in Networks of Striatal Fast Spiking Interneurons – Role of Gap Junctions

Johannes Hjorth, Lennart Hedlund, Kim T Blackwell and Jeanette Hellgren Kotaleski

Abstract Recent studies have found gap junctions between striatal fast spiking interneurons (FSN). Gap junctions between neocortical FSNs cause increased synchrony of firing in response to current injection, but the effect of gap junctions in response to synaptic input is unknown. To explore this issue, we built a network model of FSNs. Each FSN connects to 30–40% of its neighbours, as found experimentally, and each FSN in the network is activated by simulated up-state synaptic inputs. Simulation experiments show that the proportion of synchronous spikes in coupled FSNs increases with gap junction conductance. Proximal gap junctions increase the synchronization more than distal gap junctions. During up-states the synchronization effects in FSNs coupled pairwise with proximal gap junctions are small for experimentally estimated gap junction conductances; however, higher order correlations are significantly increased in larger FSN networks.

Keywords Fast spiking interneurons · gap junctions · synchronization · striatum · computational modeling

Introduction

The input stage of the basal ganglia, the striatum, is populated by four different neuronal types [1]. The medium spiny projection neurons (MSN), which project to the output stages of the basal ganglia, account for more than 90% of the neurons. Another neuron type is the fast spiking interneuron (FSN), which provides strong feed-forward inhibition to the MSNs. Gap junctions between neocortical and hippocampal FSNs increase spike synchrony; therefore, synchronization of striatal FSNs through recently discovered FSNs gap junctions [2, 3] may significantly affect MSN spike timing. We have previously investigated the role of gap junction location and gap junction conductance for synchronization of pairwise coupled FSNs [4] in

J. Hjorth
School of Computer Science and Communication, KTH, AlbaNova University Center, 106 91 Stockholm, Sweden
e-mail: hjorth@csc.kth.se

R. Wang et al. (eds.), *Advances in Cognitive Neurodynamics*,

response to synaptic inputs. Here we extend the previous results and investigate the global synchronization of FSN networks.

Methodological Approaches

To explore synchronization effects of gap junctions in striatal FSNs, we built a network model of FSNs: Each FSN connects to 30–40% of its neighbours, as found experimentally [2, 3], and all FSNs in the network are activated by simulated up-state synaptic inputs (a period of high frequency input). A detailed description of the FSN model and how the up-state synaptic input is generated can be found in [5].

Estimates of the number of FSNs that project to one single MSN have varied between 1–4 [3] and 4–27 [2]. Here we explore the degree of synchronization in a six cell network forming a ring structure. This structure both fulfills the criteria that each FSN is coupled to other FSNs with 30–40% probability, and also this number of cells is within the range of neurons projecting to single MSNs.

To quantify the synchronization between pairs of FSNs a Joint Peristimulus Time Histogram (JPSTH) was constructed (see Fig. 13.1) and then a previously derived "surprise" measure [6, 7] was used for estimation of statistical significance.

A different method must be used to evaluate spike synchronization in networks of multiply connected FSNs, such as the ring structure described above. Each simulated FSN trace was divided into identical bins (10 ms were used), and the total number of spikes from the six cells was counted in each bin. The number of bins with zero to >3 were stored in a 2×5 contingency table, see e.g. [8], and the chi-square test of independence was used to evaluate the probability that the distribution of these spike counts differed between the uncoupled and coupled FSNs (significance level 1%). Data from 100 s of simulated up-states were used.

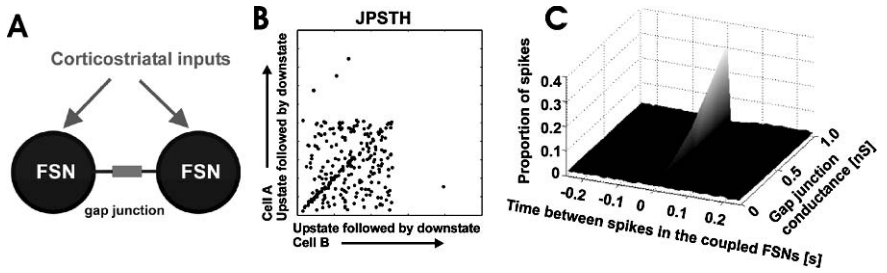

Fig. 13.1 Synchronization effects in pairwise coupled FSNs. (a) Pairs of FSNs were coupled with proximal gap junctions, either on the soma or primary dendrites. (b) The "raw" Joint Peristimulus Time Histogram, JPSTH, is shown (gap junction conductance 0.5 nS). The diagonal represents spike synchronization. (c) Although the proportion of synchronous spikes increases with gap junction conductance, synchronous effects are moderate for gap junction conductances within the physiological range

Results and Discussion

Simulation experiments explored the effects of gap junction location, gap junction conductance, and type of input on synchrony and firing frequency. Results show that the proportion of synchronous spikes in pairwise coupled FSNs increases with increasing gap junction conductance (Fig. 13.1). Proximal gap junctions increase the synchronization more than distal gap junctions, see e.g. [4]. Nonetheless, the synchronization effects in FSNs during up-states are moderate for experimentally estimated gap junction conductances (range 0.013–0.586 nS) [9]. This degree of synchrony is in contrast to effects seen when using supra-threshold current injection.

Simulations are repeated for a ring of six FSNs coupled with 0.5 nS gap junctions located on the primary dendrites. All neurons in the ring had a different set of synaptic inputs, but the time of the up-states was synchronous. Despite moderate spike synchronization in pairwise electrically coupled FSNs, the probability of many cells firing together within a 10 ms time interval was significantly increased in the six cell network (Fig. 13.2). These simulations differ from previous simulations not only in using synaptic inputs, but also in using near threshold inputs producing low firing frequencies [10, 11]. Thus, our simulations predict that small networks of striatal FSNs may play a role in synchronizing spiking despite the rather low firing frequency seen during typical up-states [12]. The results are robust when proximal gap junctions, with conductances in the upper physiological range, are used, and also applies when each FSN has slightly different current-frequency characteristics (result not shown).

The present simulation result is in accordance with recent experimental findings in the retinal network [13]. Future directions of research will address how electrically

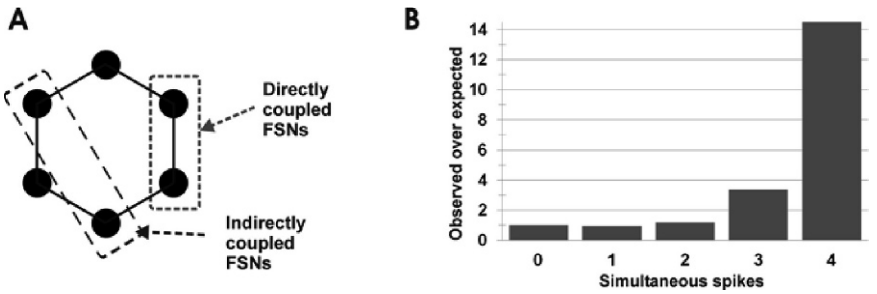

Fig. 13.2 Synchronization in networks of electrically coupled FSNs receiving up-state inputs. (a) Six FSNs coupled to each other with a probability of 30–40% form a ring structure, and were used in the present study. (b) Histogram of observed simultaneous spikes (within 10 ms). The number of 10-ms bins with zero to four spikes were counted and compared with the number expected if assuming the spike trains from each FSN were Poisson distributed and independent of other FSNs. This latter scenario describes the network behaviour when devoid of gap junctions. A maximum of four simultaneous spikes were seen in our simulations. The increased occurrences of three and four simultaneous spikes imply that indirectly coupled FSNs spike simultaneously more often than expected

coupled FSNs affect MSN spiking, and which consequences synchronization might have for the striatal network dynamics.

Acknowledgments This research was supported by the Swedish Research Council.

References

1. Bolam, J.P., Hanley, J.J., Booth, P.A.C., Bevan, M.D. Synaptic organization of the basal ganglia. J. Anat. 196 (2000) 527–542.
2. Koos, T., Tepper, J.M. Inhibitory control of neostriatal projection neurons by GABAergic interneurons. Nat. Neurosci. 2 (1999) 467–472.
3. Tepper, J.M., Koos, T., Wilson, C.J. GABAergic microcircuits in the neostriatum. TINS 27 (2004) 662–669.
4. Hjorth, J., Hanna Elias, A., Hellgren Kotaleski, J. The significance of gap junction location in striatal fast spiking interneurons. Neurocomputing 70 (2006) 1887–1891.
5. Kotaleski, J.H., Plenz, D., Blackwell, K.T. Using potassium currents to solve signal-to-noise problems in inhibitory feedforward networks of the striatum. J. Neurophysiol. 95 (2006) 331–441.
6. Aertsen, A.M.H.J., Gerstein, G.L., Habib, M.K., Palm, G. Dynamics of neuronal firing correlation: Modulation of "effective connectivity". J. Neurophysiol. 61 (1989) 900–917.
7. Palm, G., Aertsen, A.M.H.J., Gerstein, G.L. On the significance of correlations among neuronal spike trains. Biol. Cybern. 59 (1988) 1–11.
8. Marques de Sa, J.P. Applied Statstistics using SPSS, STATISTICA and MATLAB (2003) Springer.
9. Galarreta, M., Hestrin, S. Electrical and chemical synapses among parvalbumin fast-spiking GABAergic interneurons in adult mouse neocortex. PNAS 99 (1999) 12438–12443.
10. Traub, R.D., Kopell, N., Bibbig, A., Buhl, E.H., LeBeau, F.E.N., Whittington, W.A. Gap junctions between interneuron dendrites can enhance synchrony of gamma oscillations in distributed networks. J. Neurosci. 21 (2001) 9478–9486.
11. Mancilla, J.G., Lewis, T.J., Pinto, D.J., Rinzel, J., Connors, B.W. Synchronization of electrically coupled pairs of inhibitory interneurons in neocortex. J. Neurosci. 27 (2007) 2058–2073.
12. Blackwell, K.T., Czubayko, U., Plenz, D. Quantitative estimate of synaptic inputs to striatal neurons during up and down states in vitro. J. Neurosci. 23 (2003) 9123–9132.
13. Schneidman, E, Berry, M.J., Segev, R., Bialek, W. Weak pairwise correlations imply strongly correlated network states in a neural population. Nature 440 (2006) 1007–1012.

Chapter 14
Multilayer In-Place Learning Networks with Adaptive Lateral Connections: Models and Simulations

Weiya Shi, Juyang Weng, Mingmin Chi and Xiangyang Xue

Abstract In this paper, the Multilayer In-place Learning Networks with Adaptive Lateral Connections (MILN-ALC) is proposed to develop both afferent and lateral connections simultaneously, simulating the development of primary visual cortex through sensory experiment. The experimental results using isotropic Gaussian spots and grating indicate that the lateral connections are statistically strongly correlated among nearby neurons, and also show that both afferent and lateral connections depend on input patterns.

Introduction

Neuroscience studies indicate that the representations in the cerebral cortex are epigenetically developed, depending on sensory experience and genetic mechanisms [1, 2]. Many models have been proposed to simulate the cortical self-organizing process, at different degrees of biological plausibilities. In these models, the self-organizing map (SOM) [3] is well known, but lateral connection is not explicitly modeled. Neurobiological experiments indicate that lateral connections are adaptive [4]. Alexander et al. [5], Bartsch and van Hemmen [6], and Miikkulainen et al. [7] proposed several models with adaptive lateral connections.

In our previous work, the Multilayer In-place Learning Networks (MILN) [8] has been proposed to develop internal representations for cerebral development. It uses a new model for neuronal development, called Lobe Component Analysis (LCA) where the learning is automatically and optimally determined based on signal energy, statistical efficiency, and plasticity scheduling. However, the MILN model only considers static lateral connections among neurons with a complete connection between layers. For biological plausibility and further computational studies, in this paper, we extend the MILN model further with adaptive lateral connections. In addition, we also consider the local connections among neurons.The proposed

J. Weng
Department of Computer Science and Engineering, Fudan University, Shanghai, China
e-mail: weng@cse.msu.edu

R. Wang et al. (eds.), *Advances in Cognitive Neurodynamics*,

extended model is called Multilayer In-place Learning Networks with Adaptive Lateral Connections (MILN-ALC). The results using isotropic Gaussian spots and grating indicate that the lateral and afferent connections are developed simultaneously, forming a rich array of representation that enables further studies.

Proposed MILN–ALC model

It is well-known that all areas in the cerebral cortex have 6 (laminar) layers. Among the 6 layers, the Layer 4 (L4) and the Layer 2/3 (L2/3) are function ones [9] and the other layers play assistant roles [10]. For the lack of space, in the paper we only show the function layers, i.e., L4 and L2/3 in Fig. 14.1. In greater detail, for a given neuron i in the L2/3, there are three types of connections.

1. Afferent (bottom-up) excitatory connection. It links input patterns from the L4.
2. Lateral excitatory connection. It links other neurons in the same layer to the i-th neuron within radius d_1, the size of lateral excitatory distances.
3. Lateral inhibitory connection. It links other neurons in the same layer to this neuron within radius d_2, the size of lateral inhibitory distances.

Due to limited space, the work reported here does not consider the supervised signal from the top layer (top–down connections). Therefore, at time t, the response z from the neuron i can be written as

$$z^{(t)} = g\left(\sum_{r_1} \mathbf{w}_b^{(t)} \cdot \mathbf{y}^{(t)} + a_e \sum_{d_1} \mathbf{w}_{he}^{(t)} \cdot \mathbf{z}^{(t-1)} - a_h \sum_{d_2} \mathbf{w}_{hi}^{(t)} \cdot \mathbf{z}^{(t-1)}\right) \tag{14.1}$$

where g is the sigmoid function defined by $g(x) = \frac{1}{1+\exp(-x)}$, $\mathbf{y}$ is the input pattern in the lower layer and $\mathbf{z}$ is the response of other neurons in the same layer, r_1 is the size of afferent receptive fields, the constant factors a_e and a_h represent the influence strengths of the excitatory and inhibitory lateral connections, respectively. The weights of a neuron are updated only when the neuron fires and the updating strategy depends on the pre- and post-synaptic activities shown as follow:

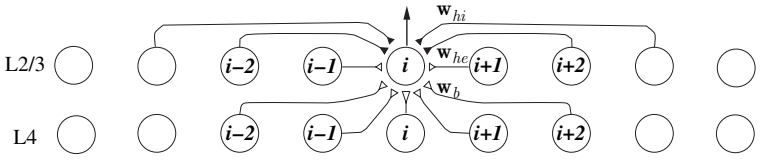

Fig. 14.1 Function layers of the MILN–ALC. Only the afferent connection (weights $\mathbf{w}_b$), excitatory lateral connections (weights $\mathbf{w}_{he}$) and inhibitory lateral connections (weights $\mathbf{w}_{hi}$) of one neuron at position i are shown, but all the neurons in the primary visual layer are similarly connected. White and black triangles indicate excitatory and inhibitory connections, respectively

$$\begin{cases} \mathbf{w}_b^{(t)} = w_1 \mathbf{w}_b^{(t-1)} + w_2 z^{(t)} \mathbf{y}^{(t)} \\ \mathbf{w}_{he}^{(t)} = w_1 \mathbf{w}_{he}^{(t-1)} + w_2 z^{(t)} \mathbf{z}^{(t-1)} \\ \mathbf{w}_{hi}^{(t)} = w_1 \mathbf{w}_{hi}^{(t-1)} + w_2 z^{(t)} \mathbf{z}^{(t-1)} \end{cases} \tag{14.2}$$

where w_1 and w_2 are maturity-dependent weights that control the plastic schedule. We also use the amnesic mean technique [8] for automatic scheduled plasticity which gradually "forgets" old "observations" in the updating processes.

Experiments

In this experiment, we study what the afferent, lateral excitatory and lateral inhibitory connections are generated and updated using the MILN–ALC model.

We use isotropic Gaussian spots and grating to simulate the input to the L4. The L4 has 24×24 neurons and the L2/3 has 18×18 neurons. Each neuron in the L2/3 is locally connected to the 7×7 neurons in the L4. The excitatory lateral radius d_1 is set to 5 and the inhibitory lateral radius d_2 is set to 15. At the beginning, all the lateral connections are set to random values.

The algorithm runs for 10,000 stimulus presentations. Figure 14.2 shows the developed afferent and lateral connections, where each square corresponds to one

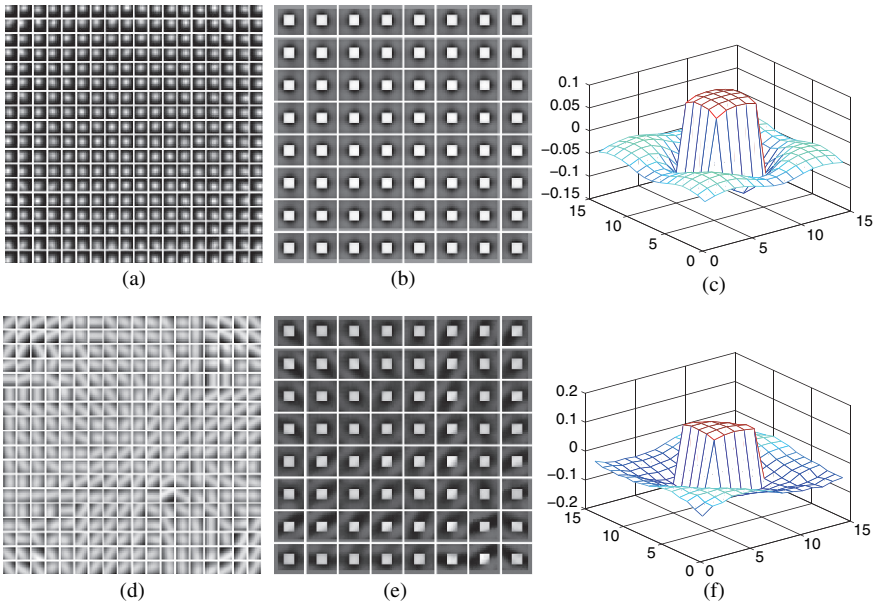

Fig. 14.2 Developed connections of the L2/3 with the 18×18 neurons trained by isotropic Gaussian spots shown in (a, b, c) and grating shown in (d, e, f). Each square corresponds to one neuron. (a, d) The developed afferent connections. (b, e) Combined lateral connections (excitatory - inhibitory connections) of the central 8×8 neurons. (c, f) Detailed plot of the combined lateral connections of the neuron at (10, 10)

neuron. Figure 14.2a shows the afferent connection of each neuron which develops into the Gaussian shape covering the Gaussian input patterns in the visual field when trained using isotropic Gaussian spots. Figure 14.2d shows that the developed afferent connections have different orientation when trained using grating. These results confirm that the shape of receptive field depends strongly on the input patterns. The afferent weights of many neurons correspond to oriented local features, consistent with biological findings [7].

The combined lateral connection (inhibitory connections is subtracted from excitatory connections) is given in Fig. 14.2b and Fig. 14.2e, as well as Fig. 14.2c and Fig. 14.2f in greater detail. As can be seen, the shape of the combined lateral connections takes the shape of symmetrical (asymmetrical) Mexican-hat, similar to that of the models in [7], while our neuronal model is LCA, different from that of [7]. From the results, we can see that the lateral connections are local and patchy, consistent with our intuition that nearby inputs have stronger statistical correlations than far-away inputs, and therefore, picked up effectively by the developed lobe components.

Conclusions

The Multilayer In-place Learning Networks with Adaptive Lateral Connections is a simple, unified and biologically plausible computational model. Our result of adaptive lateral connections indicated that neurons that detect similar features are linked by strong lateral inhibitory connections. The results developed from isotropic Gaussian spots and grating stimuli indicate that lateral and afferent connections are developed simultaneously. The lateral connections store information about correlations among neurons. We plan to further study the properties of adaptive lateral connections.

References

1. Kandel, E.R., Schwartz, J.H., Jessell, T.M., eds.: Principles of Neural Science. 4th edn. McGraw-Hill, New York (2000).
2. Sur, M., Rubenstein, J.L.: Patterning and plasticity of the cerebral cortex. Science **310** (2005) 805–810.
3. Kohonen, T.: Self-Organizing Maps. 3rd edn. Springer-Verlag, Berlin (2001).
4. Gilbert, C.D., Hirsch, J.A., Wiesel, T.N.: Lateral interactions in visual cortex. Cold Spring Harbor Laboratory Press (1990).
5. Alexander, D.M., Bourke, P.D., Konstandators, O., Wright, J.J.: Intrinsic connections in tree shrew v1 imply a global to local mapping. Vision Research **44** (2004) 857–876.
6. Bartosch, A.P., van Hemmen, J.L.: Combined hebbian development of geniculocortical and lateral connectivity in a model of primary visual cortex. bioc **84** (2001) 41–55.
7. Miikkulainen, R., Bednar, J.A., Choe, Y., Sirosh, J.: Computational Maps in the Visual Cortex. Springer, Berlin (2005).
8. Weng, J., Zhang, N.: In-place learning and the lobe component analysis. In: Proc. IEEE World Congress on Computational Intelligence, Vancouver, BC, Canada (July 16–21 2006).
9. Buonomano, D.V., Merzenich, M.M.: Temporal information transformed into a spatial code by a neural network with realistic properties. Science **267** (1995) 1028–1030.
10. Grossberg, S., Seitz, A.: Laminar development of receptive fields, maps and columns in visual cortex: the coordinating role of the subplate. Cerebral cortex **13** (2003) 852–863.

Chapter 15
Stimulus-Induced Pairwise Interaction Can Be Revealed by Information Geometric Approach

Hiroyuki Nakahara, Masanori Shimono, Go Uchida and Manabu Tanifuji

Abstract Understanding the interaction of neural activities is one of the most important themes in neuroscience. To resolve this question, cross-covariogram analysis of two neurons' activities is one of most extensively used techniques. This analysis is conducted mostly against the null hypothesis of independent firing. Here, we argue that an additional analysis is required to understand the role of correlation with respect to behaviourally relevant parameters such as visual stimulus. Specifically, we propose conducting this analysis against the null hypothesis of the activity in a control period. We show that information geometric approach can achieve this task. Furthermore, we demonstrate the validity of this method using data taken from the inferior temporal cortex. The results indicate the possible existence of a stimulus-modulated correlation.

Keywords Pairwise interaction · correlation · information geometry · neural firing · inferior temporal cortex

Introduction

The multi-unit recordings of many neural activities have become widely available, and to make best of such massive data, methods of analysis need to be further developed. As an attempt to achieve this goal, we previously proposed information geometry (IG) approach to decipher interactions of neural firing [4]. In this paper, we illustrate this approach by focusing on the simplest case of analysis, namely an examination of cross-correlation between two neurons.

We previously noted [1] that, although cross-covariogram analysis usually examines correlated activity against the null hypothesis of no correlation, it is often more appropriate to evaluate such correlated activity against the activity in a control period. Section 'Preliminaries' clarifies this issue. The IG approach

H. Nakahara
Lab for Integrated Theoretical Neuroscience, RIKEN Brain Science Institute, 2-1 Hirosawa, Wako, Saitama, 351-0198, Japan
e-mail: hn@brain.riken.jp

R. Wang et al. (eds.), *Advances in Cognitive Neurodynamics*,

allows us to easily handle such a test, which is explained in Section 'Information Geometric-Approach'. In Sections 'Experimental Setting' and 'Results' we demonstrate the method by using real data recorded from the inferior temporal (IT) cortex. The results suggest that a stimulus-modulated correlation exists. Finally, a short discussion is given in Section 'Discussion'.

Preliminaries

Cross-Covariogram Analysis

Cross-covariogram analysis is most extensively used for analyzing the cross-correlation of a pair of two neurons. This analysis implicitly presumes wide-sense stationarity, so all of the arguments below, are made under this assumption. This analysis is mostly combined with the shuffled predictor, called the conventional cross-covariogram analysis in this paper. The shuffled predictor creates a distribution of the null hypothesis that retains the mean firing rate of each neuron but has no correlation between their firings, i.e. they are independent firings. Thus, such an analysis can only reveal whether neural firing is correlated or not within a period of interest in comparison to no correlation.

Analysis Against the Null Hypotheses of Control Period

We now propose that an equally important test is to examine whether neural firing in a period is correlated in comparison with the firing in another period.

To understand why this is important, by way of example, let us consider a single-unit recording using control and test periods. In the control period, the experimental manipulation is usually kept to a minimum, so activity in this period is regarded as being in resting mode. In the test period, some manipulations are done, e.g. showing a visual stimulus, to examine how a neuron responds to the manipulation. The firing in the test period is tested against the firing in the control period. If significant, the firing in the test period is considered test-related. Note that we would not call the firing test-related if we performed the test against zero firing, even if significance was found by that test.

The same argument can be applied to the cross-covariogram analysis. To examine whether a test-related correlation exists, we should examine the correlation in the test period against that in the control period, i.e. against the null hypothesis of the correlation in the control period, but not as done by conventional cross-covariogram analysis. Obviously, this type of argument is generalized for examining the firing between any two periods of interest.

Information-Geometric Approach

Information geometry (IG) provides useful tools and concepts, including the orthogonality of coordinate parameters and the Pythagoras relation in the

Kullback-Leibler divergence [2]. Using the IG approach, a novel method can be constructed to evaluate the interaction of neural firing in a systematic manner [1, 3]. The method allows us to decompose the interactions of neurons of various orders, e.g. pairwise, triplewise and higher order interactions [1]. It can also be applied to analyze and compare different models used for a spike train of single neurons [4]. This further allows us to construct, relatively easily, a hypothesis test under the framework of a log likelihood ratio test [1]. This generality allows us to examine a test of correlation against any null hypothesis [1].

For the cross-correlation (under wide-sense stationarity), we use the IG mixed coordinates $(\eta_1, \eta_2, \theta_3)$ (see [1] for more details). θ_3 is the term measuring the interaction. The Fisher information matrix induces a natural metric, by which we can verify the orthogonality between η and θ components. Such orthogonality cannot generally hold if we replace θ_3 by the interaction term used by the cross-covariogram analysis, denoted here by c. In fact, only when $c = 0$, i.e., there is no correlation, does the orthogonality hold between η and c, and this is why a cross-covariogram analysis is convenient only for a test of no correlation.

Experimental Setting

Experimental details are published elsewhere [5, 6], so only a brief summary is provided here. We conducted simultaneous recording of multi-unit activity from the IT cortex of two anesthetized macaque monkeys. Both control and stimulus periods had 1 sec length, where a visual stimulus is presented in the stimulus period. Correlation is estimated by the IG mixed coordinates for each period, using a 5-ms bin size. In the following, we report the results of correlation at a time lag of zero, i.e. simultaneous coincident firing.

Results

In this section, we report the results of 21 pairs of neurons, where each pair is categorized as either an R-R or R-NR pair. Here, R indicates that one neuron's firing is task-related (Wilcoxon test, $p < 0.05$), whereas NR indicates that one neuron's firing is not. We found 11 R-R pairs and 10 R-NR pairs.

First, we tried to perform a conventional cross-covariogram, for which we used the IG approach by setting the null hypothesis as $\theta_3 = 0$, since it is essentially equivalent. We found that *all* pairs had significant correlation, even in the control period, and further that almost all pairs (precisely, all except one R-NR pair) also had significant correlation in the test period. Thus, in this data, the conventional cross-covariogram is not informative for comparing the correlation between the two periods. However, if we still wanted to use this test to determine whether the correlation had changed from the control to the test period, one way might be to indicate whether the significance had changed between the above two results, i.e. Fig. 15.1 left; in this case, almost all pairs would be classified as unmodulated.

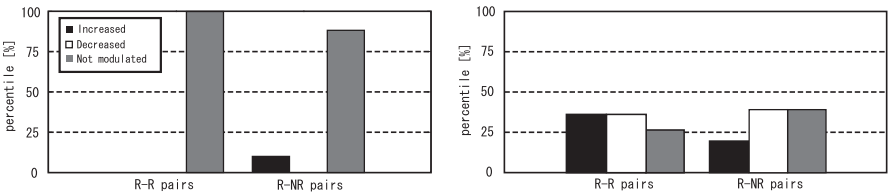

Fig. 15.1 Correlation in stimulus period is examined in comparison with that in control period, indirectly (left) or directly (right). See main text for details. Black, white, and hatched bars indicate the percentage of the number of pairs with correlation significantly increased, significantly decreased, or non-modulated, respectively

Now let us directly examine by the IG approach whether the correlation in the test period is significantly different from that in the control period (Fig. 15.1 right). We find that R-NR pairs have more decreased correlation whereas R-R pairs equally have both increased and decreased correlation. Clearly, this result is more informative in that it reveals either increased or decreased modulation for more number of pairs. It appears that the simultaneous correlation may be differentially modulated for R-R and R-NR pairs. More specifically, given the results of other analyses we performed [6], it will be particularly interesting if further analysis will lead to the observation that the correlation is increased for two neurons if both have task-related activity but decreased for two neurons if one of them does not have task-related activity. To confirm, though, we still need to examine with a greater number of samples.

Discussion

We presented one utility of the IG approach, specifically the flexible use of any null hypothesis, by using real data from the monkey IT cortex in a cross-correlation analysis. The results are promising for further investigations.

Acknowledgments We thank M. Tatsuno for his technical assistance. HN is supported by Grant-in-Aids on Priority Areas Research (C) from MEXT and for Young Scientists (A) from JSPS.

References

1. Nakahara, H., Amari, S.: Information geometric measure for neural spikes. Neural Comput. **14** (2002) 2269–2316.
2. Amari, S., Nagaoka, H.: Methods of Information Geometry. American Mathematical Society/Oxford Univ. Press, Providence (2000).
3. Nakahara, H.: Comments on analysis of neural coding by information geometric measure. International Symposium on Nonlinear Theory and its Applications, NOLTA2004, Fukuoka, Japan, Nov 29–Dec 3, 2004, Proceedings. (2004) 31–34.

4. Nakahara, H., Amari, S., Richmond, B.J.: A comparison of descriptive models of a single spike train by information geometric measure. Neural Comput. **18** (2006) 545–568.
5. Uchida, G., Fukuda, M., Tanifuji, M.: Correlated transition between two activity states of neurons. Phys. Rev. E **73** (2006) 031910.
6. Uchida, G., Fukuda, M., Sato, T., Nakahara, H., Tanifuji M.: Stimulus-dependent modulation of synchronous activities of neurons in area TE of anesthetized macaque monkeys. (submitted).

Chapter 16
A Dynamical Model of Fast Intrinsic Optical Signal of Neural Burstings

Jianzhong Su, Hanli Liu and Yuanbo Peng

Abstract Recent advances in optical imaging techniques allow us to acquire the structure of living nerve cells and their changes. While the commonly used dye-stained extrinsic optical signal mimics the intracellular voltage or the ion currents of the membrane directly, the fast intrinsic optical signal measures longer term physiological changes such as cell structure and sub-cellular level properties after a sustained intracellular spike under the electric and other stimulations. We build a 2-D computational model to simulate the dynamic behavior from neurons' activity leading to optical functional imaging. Such a simulation model requires structural information (cellular volume) at the neuronal level to quantify optical scattering coefficients and a realistic Hodgkin-Huxley model of the neuron to be constructed. Initial computational results show the model as a good indication of the fast intrinsic optical signal.

Keywords Mathematical model · intrinsic optical imaging · bursting neurons

Introduction

Two major neuronal monitoring methods are intrinsic optical imaging (**Shtoyerman** et al. [1] 2000 and others) or extrinsic optical imaging with voltage (or calcium)-sensitive dye. While the dye-stained optical signal mimics the intracellular voltage or Ion current of the membrane directly (<1 ms), the considered fast intrinsic optical signal measures optical properties with a longer term (signals started after 10–100 ms and lasted several seconds) physiological consequence in functional imaging (Salzberg et al. [2] 1983 and its references). Yet, this is different from slow optical signals (in 1–10 s to minutes range) caused by hemodynamic changes that have used in the standard modality for optical imaging. The fast intrinsic optical signal/imaging offers a window for studying the links between electrophysiological activities and functional behavior. However, the fundamental mechanism as how

J. Su
Department of Mathematics, University of Texas at Arlington, Arlington, TX 76019, USA
e-mail: Su@uta.edu

R. Wang et al. (eds.), *Advances in Cognitive Neurodynamics*,

neuronal activities at cellular- or subcellular-scale lead to observable changes in optical imaging is not well understood [3]. It calls for a mathematical modeling study and improved method for processing the measurement data.

We construct a 2-D computational model to simulate the dynamic behavior from a single neuron's activity to optical functional imaging, a process crossing multiple orders of temporal as well as spatial scales. Such a simulation model requires structural information (cellular volume) at the neuronal level, and a realistic Hodgkin-Huxley model of the neuron to be constructed. Later on, we can further perform calculation of light intensity distribution of optical imaging in continuous wave or time domain based on these biophysical changes.

Background in Fast Optical Imaging for Neural Activities

The main hypothesis for the fast optical signal is based upon cell (fiber) volume changes during the action potential change within the 10 ms to several seconds range after stimulations. This mechanism is well documented by Cohen [4] for giant axons of squid and many others, and it is considered the dominant signal in the NIR spectrum region. The cause of change in cell volume and the extra-cellular space is attributed to the change in osmotic pressure due to ion concentration and water movement.

Neural Models for Fast Optical Signals

To understand the connection between electrophysiological activities of neurons and light scattering signals observed from experiments, we start with a modified Hodgkin-Huxley (HH) model to describe the intracellular electrophysiological activities of sensory neuron, and the neuron is assumed (for now) to be a long 1-dimensional nerve fiber. The function $V(x,\ t)$ represents the trans-membrane potential, and (m, n, h)(x,t) represents the variables involved in potassium and sodium currents. To model a specific area of the spinal cord [5], our neural model takes classical HH parameter values except $\overline{g_{\mathrm{na}}} = 50,\ g_{\mathrm{l}} = 0.7,\ V_{\mathrm{l}} = -77.5,\ \overline{g_{\mathrm{k}}} = 2.6$;

$$\begin{aligned}
&\frac{\partial V}{\partial t} = \frac{1}{CM}(D\Delta V - (\overline{\mathrm{g_{na}}}m^3h(V - V_{\mathrm{na}}) + \overline{\mathrm{g_k}}n^4(V - V_{\mathrm{k}}) + \mathrm{g_l}(V - V_{\mathrm{l}})) + I_{\mathrm{app}});\\
&\frac{\partial h}{\partial t} = (h_{\mathrm{inf}}(V) - h)/\tau_h(V);\quad \frac{\partial n}{\partial t} = (n_{\mathrm{inf}}(V) - n)/\tau_n(V);\\
&\frac{\partial m}{\partial t} = (m_{\mathrm{inf}}(V) - m)/\tau_m(V)
\end{aligned} \tag{16.1}$$

We denote the difference of ion concentration across the cell membrane as $C(x,\ t)$, and cellular water volume as $R(x,\ t)$, and the diameter of the fiber as $D(x,\ t)$. Then it holds:

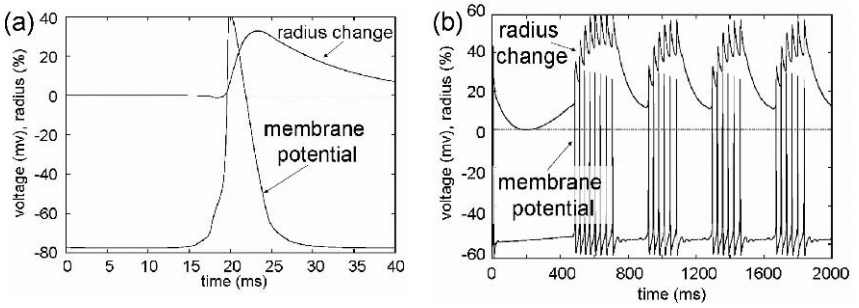

Fig. 16.1 The trans-membrane potential and the cell radius varying with time in a single potential spike (a) and a bursting scenario (b)

$$\frac{\partial C}{\partial t} = \kappa \Delta C - (\overline{g_{na}} m^3 h(V - V_{na}) + \overline{g_k} n^4 (V - V_k) + g_l (V - V_l)) - \gamma g(C, V) \tag{16.2a}$$

$$\frac{\partial R}{\partial t} = \mu C \tag{16.2b}$$

where Eq. (16.2a) describes the concentration change due to intracellular ion flows as well as leaking and pumping effects, and Eq. (16.2b) reflects the water flow rate to be proportional to osmotic pressure generated by concentration difference. The diameter of the nerve fiber, D, is related to volume, R, in $R = MD^2$, and the scattering coefficient of optical signals is given by $D' = KR^{-n}$ based on Mie theory [6] (reciprocal of a power of cross-sectional area). The correlation between one spike and the change in fiber radius is shown in Fig. 16.1a.

When the effect of Calcium flux was included in consideration, experimental evidence [7] indicated the calcium-dependence of K-channel:

$$\overline{g_k} = \overline{g_{k,0}} + \mathrm{Ca}, \quad \frac{\partial \mathrm{Ca}}{\partial t} = \varepsilon f(V + V_{\mathrm{Ca}}, \mathrm{Ca}, m, n, h) \tag{16.3}$$

where we take $V_{Ca} = -55\,\mathrm{mV}$ as the threshold for Ca^{2+} flow, and Ca^{2+} is taken as a simplified model (one threshold). Then bursting is presented in Fig. 16.1b. Super-imposed is the corresponding changes in radius during the bursting.

Simulated Optical Signals of Neuron Activities

The preliminary model study for optical signals of neuron activities was simulated for a 50-μm-diameter iso-potential cell, using XPPAUT software [8]. The effect of soma, myelination was not included in the model. Specific membrane capacitance was 1 $\mu F/cm^2$, specific longitudinal resistance was 110 Ω-cm, and temperature was 20 °C. The cell was divided into 99 segments. XPPAUT used the Runge-Kutta

method for integration ($dt = 0.01$ ms). The calculation was performed on SGI Origin 2000 by Unix version of XPPAUT [8].

We set the applied current, I_{app}, at zero in our first case. The procedure of numerical simulation was as follows. We raised the membrane potential of the first segment $V_1 = -45.0$ mV from equilibrium (-77.5 mV) while ion currents remain at equilibrium. All other segments were left unchanged at equilibrium. An action potential spike was generated in segment 1 first, and then propagated along the fiber. We detected the action potential changes in segment 10, immediately followed by cell radius changes as shown in Fig. 16.1a. This figure demonstrates that the trans-membrane potential and the cell radius at segment 10 vary with time t. Within 1 ms of the voltage spike, the cell radius increases 30% and then retreats slowly to a normal level.

In our second simulation, we raised I_{app} to 12 μA at a constant value, where as the neuron was in hyperexcitability state, but otherwise performed the same simulation. The initial stimulation led to a neuron bursting (a sustained period of intensive spikes before a large influx of Ca Ions terminated active phase). As shown in Fig. 16.1b, the radius of the cell is also changed after each spike and accumulated to a greater level after the active phase before retreating. The two superimposed curves show that the intensity of the spike forces the continued increase of cell radius. The time interval between spikes is not long enough to allow retreating to balance. The increase in radius can be as large as 60% and can provide a much stronger optical signal for the bursting.

Unlike the single spike case, even in the quiescent phase of bursting, the radius remains at 16% increase at its low. This is consistent with 20% radius change observed in experiments [9].

Acknowledgments JS and HL are partially supported by NIH grant 1 R21 NS052850-01A1.

References

1. Shtoyerman, E, Arieli, A, Slovin, H, Vanzetta, I and Grinvald, A "Long-Term Optical Imaging and Spectroscopy Reveal Mechanisms Underlying the Intrinsic Signal and Stability of Cortical Maps in V1 of Behaving Monkeys". J. Neurosci., 20(21) (2000) 8111–8121.
2. Salzberg, BM, Obaid, AL and Gainer, H "Large and rapid changes in light scattering accompany secretion by nerve terminals in the mammalian neurohypophysis". J. Gen. Physiol., 86 (1985) 395–411.
3. Holthoff, K and Witte, OW "Intrinsic optical signals in rat neocortical slices measured with near- infrared dark-field microscopy reveal changes in extracellular space". J. Neurosci., 16 (1996) 2740–2749.
4. Cohen, K and Landowns "Changes in light scattering that accompany the action potential in giant axons: Potential-dependent components". J. Physiol., 224 (1972) 701–725.
5. Amir, R, Michaelis, M and Devor, M "Burst discharge in primary sensory neurons: triggered by subthreshold oscillations, maintained by depolarizing afterpotentials". J. Neurosci., 22 (2002) 1187–1198.
6. Graaff, R, et al., Appl. Opt., 31 (1992) 1370–1376.

7. Liu, CN, Michaelis, M, Amir, R and Devor, M “Spinal nerve injury enhances subthreshold membrane potential oscillations in DRG neurons: relation to neuropathic pain”. J. Neurophysiol., 84 (2000) 205–215.
8. Ermentrout, B “Simulating, analyzing, and animating dynamical systems: a guide to XPPAUT for researchers and students”. SIAM, Philadelphia (2002). (http://www.math.pitt.edu/∼bard/xpp/xpp.html).
9. Ransom, BR, Yamate, CL and Connors BW “Activity-dependent shrinkage of extracellular space in rat optic nerve: a developmental study”. J. Neurosci. 5 (1985), 532–535.

Chapter 17
The Mechanism of Bifurcation-Dependent Coherence Resonance of Morris-Lecar Neuron Model

Guangjun Zhang, Jianxue Xu, Jue Wang, Zhifeng Yue, Chunbo Liu, Hong Yao and Xiangbo Wang

Abstract The mechanism of bifurcation-dependent coherence resonance (CR) of excited neuron model is related to the system motion random transitions between attractors on two sides of bifurcation point. In this paper, the relation between the random transitions and the mechanism of bifurcation-dependent CR is examined in Morris-Lecar (ML) neuron model. Here we show that there exist different attractors on two sides of ML neuron model Hopf bifurcation point and that the system motion may transit between attractors on two sides of bifurcation point at the presence of noise. And the frequency of transitions tend towards a certain frequency for a certain optimal noise intensity, the signal-noise-ratio of system response evaluated at this certain frequency is maximal at the optimal noise intensity, CR occurs.

Keywords Coherence resonance · transition · bifurcation point · Morris-Lecar neuron model

Introduction

The phenomenon of stochastic resonance (SR) in nonlinear dynamical systems perturbed by noise has attracted considerable attention over the last two decades [1, 2]. It is well known that neurons work in a noisy environment, and it is therefore of great interest to study how information is encoded and transmitted when neurons work in such a nosy environment. Recent studies have shown that excitable sensory neurons can use the mechanism of SR to detect weak subthreshold periodic and aperiodic signals, and noise plays a constructive role in the transmission of information in neurons [3, 4, 5]. Other studies [6, 7, 8, 9, 10, 11, 12] has also shown that, for an excitable neuron model with only noise input, noise activates the excitable system producing a sequence of pulses and the coherence of the noise-induced

G. Zhang
School of Aerospace, Xi'an Jiaotong University, Xi'an, P.R. China
e-mail: zhanggj3@126.com

R. Wang et al. (eds.), *Advances in Cognitive Neurodynamics*,

oscillations is shown maximal for a certain noise intensity. Thus CR, which is an SR-like resonance phenomenon, has been observed in the noisy excitable neuron model.

As a noise-induced ordering phenomenon, CR is of particular importance in neurophysiology, where large ensembles of neurons at the absence of input signal become orderly due to interaction with a noisy environment. Gong and Xu studied the factors that have effects on coherence resonance in an excitable neuron [7]. But in their studies the mechanism of CR is not revealed out. Therefore, it is very necessary to study the mechanism of CR of excitable neuron. Zhang and Xu researched the mechanism of CR of FHN and HR neuron model [13, 14]. In order to draw several universal conclusions in this present work, we investigate the mechanism of bifurcation-dependent CR of Morris-Lecar neuron model.

The Bifurcation Characteristic of the Unforced ML Neuron Model

We consider the unforced Morris-Lecar neuron model in the following form [15]:

$$\begin{aligned} C\frac{dV}{dt} &= -\bar{g}_{\mathrm{ca}} m_\infty(V)(V - V_{\mathrm{Ca}}) - \bar{g}_{\mathrm{k}} w(V - V_{\mathrm{k}}) - \bar{g}_L(V - V_L) + (I_0 + D_i\xi_1(t)) \\ \frac{dw}{dt} &= \phi\frac{[w_\infty(V) - w]}{\tau_w(V)} + D_e\xi_2(t) \end{aligned} \tag{17.1}$$

With steady states for the Ca^{2+} and K^+ Current fractions and a transition rate:

$$\begin{aligned} m_\infty(V) &= 0.5 * \left\{1 + \tanh\left[\left(V - V_1\right)/V_2\right]\right\} \\ w_\infty(V) &= 0.5 * \left\{1 + \tanh\left[\left(V - V_3\right)/V_4\right]\right\} \\ \tau_\infty(V) &= 1/\cosh\left[\left(V - V_3\right)/\left(2 * V_4\right)\right] \end{aligned}$$

Where each parameter in equation above is the same as one in reference [15]. The variable v is the transmembrane potential and w is a slow recovery variable, which denotes the open probability for potassium channel. In the paper we fix the values of the other parameters to $V_1 = -1.2,\ V_2 = 18,\ V_3 = 2,\ V_4 = 30,\ \bar{g}_{Ca} = 4.4,\ C = 20,\ \bar{g}_K = 8,\ \bar{g}_L = 2,\ V_k = -84,\ V_L = -60,\ V_{Ca} = 120,\ \phi = 0.04$, only I_0 is considered as control parameters.

According to reference [15] one may see that when $I_0 = 93.86$ a subcritical Hopf bifurcation occurs. On the left of bifurcation point there exists one stable fixed point in ML neuron model, on the right of bifurcation point there exists a stable limit cycle oscillation, a spike or firing occurs in ML neuron model. The attractors of ML neuron model without noise on two side of Hopf bifurcation point are shown as Fig. 17.1 respectively.

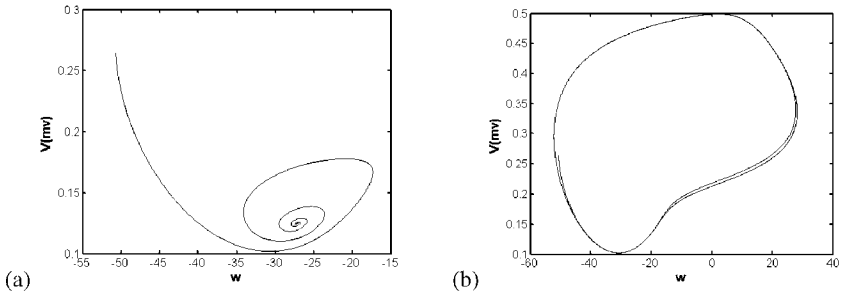

Fig. 17.1 The phase figure of attractors of ML neuron model without noise in two cases of bifurcation parameter, (a) $I_0 = 92.1$; (b) $I_0 = 93.9$

The Mechanism of Bifurcation-Dependent CR of ML Neuron Model

In this paper, the Gaussian distributed white noise $\xi(t)$ is used for perturbing the system. The mean and autocorrelation function are as follows respectively:

$$\begin{cases} < \xi(t) >= 0 \\ < \xi(t)\xi(s) >= 0 \end{cases} \tag{17.2}$$

In this paper it will be denoted as D_i and D_e for the internal and external noise respectively.

According to the section 'The Bifurcation Characteristic of the Unforced ML Neuron Model', one can see that there exist different attractors respectively on two sides of bifurcation point. In the small neighborhood of bifurcation point under the perturbation of noise the system motion may transit between the attractors on two sides of bifurcation point [13, 14].

To illustrate that the viewpoint above is tenable for ML neuron model, the internal and external noise are added to Eq. (17.1). Thus, the differential equation of ML neuron model is:

$$\begin{aligned} C\frac{dV}{dt} &= -\bar{g}_{ca}m_\infty(V)(V - V_{Ca}) - \bar{g}_k w(V - V_k) - \bar{g}_L(V - V_L) + (I_0 + D_i\xi_1(t)) \\ \frac{dw}{dt} &= \phi\frac{[w_\infty(V) - w]}{\tau_w(V)} + D_e\xi_2(t) \end{aligned} \tag{17.3}$$

where each parameter in Eq. (17.3) is the same as one in Eq. (17.1).

The stochastic differential Eq. (17.3) is integrated using the fourth-order Runge-Kutta method with time step $\Delta t = 0.1$ ms. After the mean value of bifurcation parameters of system is fixed to $I_0 = 92.1$ the time history of the system response in two cases of noise is shown respectively in Fig. 17.2. From Fig. 17.2 one may see that at the presence of internal noise the motion trajectory of system transits between

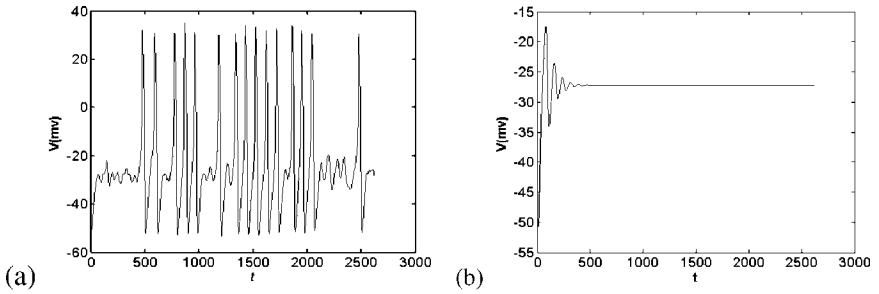

Fig. 17.2 Time history of a realization of ML neuron model response, $I_0 = 92.1$; (a) $D_\mathrm{i} = 4.0$; (b) $D_\mathrm{i} = 0.0$

attractors respectively on two sides of bifurcation point. According to reference [16, 17], the bifurcation point of Hopf bifurcation system will slightly shift to the left or to the right under the perturbation of Gaussian distributed external noise. According to [13, 14], for the FHN and HR neuron model, the transitions between attractors on two sides of Hopf bifurcation point induce CR to occur, however, in the present study, the question whether CR could be induced by this kind of transitions arises naturally in this context. In order to investigate the frequency of random transitions of ML neuron model without periodic signal, the spectrum of response of system in this case is shown in Fig. 17.3. As shown in Fig. 17.3, one may see that under the perturbation of appropriate noise a peak of power spectrum of system response at a certain frequency will appear. That is to say that the frequency of random transitions spontaneously is in accordance with a certain frequency. To measure the coherence of the system at the certain frequency, as in [12] we define the signal-noise-ratio as follow:

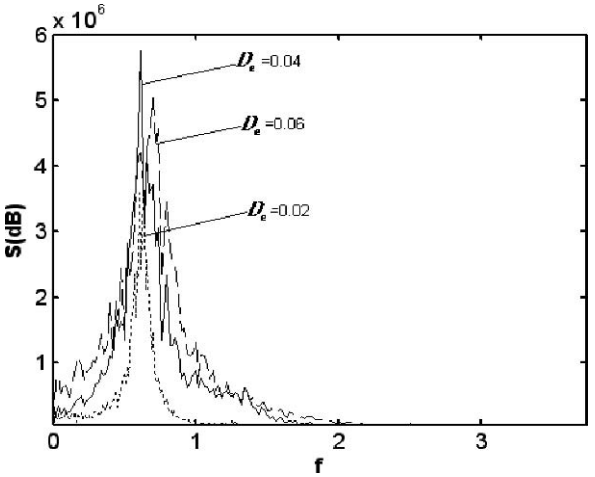

Fig. 17.3 Power spectrum of ML neuron model without periodic stimulus for several values of external noise D_e, $I_0 = 92.1$

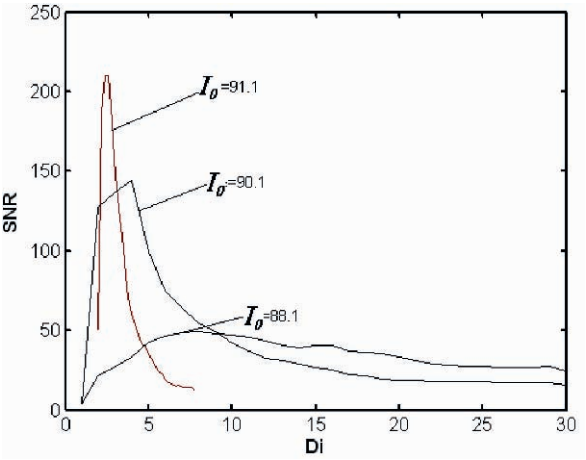

Fig. 17.4 The SNR of ML neuron model response with internal noise only versus internal noise intensity

$$SNR = \frac{H}{w} \tag{17.4}$$

where $w = \Delta\omega/\omega_p$, ω_p is the certain spontaneous frequency above, $\Delta\omega$ is width at the half-maximum height in the power spectrum depends on the noise intensity. H is the power of system response at the spontaneous frequency ω_p mentioned above. When the curve of the SNR defined above as a function of noise intensity is a unimodal curve coherence resonance occurs [2, 10, 12].

Therefore, after the bifurcation parameter without internal noise being fixed to a certain value, the SNR of ML neuron model under the perturbation of internal or external noise is obtained respectively. The curves of SNR as a function of noise intensity D_i or D_e are shown in Figs. 17.4, 17.5 respectively. As shown in Figs. 17.4, 17.5 in two cases of noise CR occurs, and the value of optimal noise intensity D_{opt}

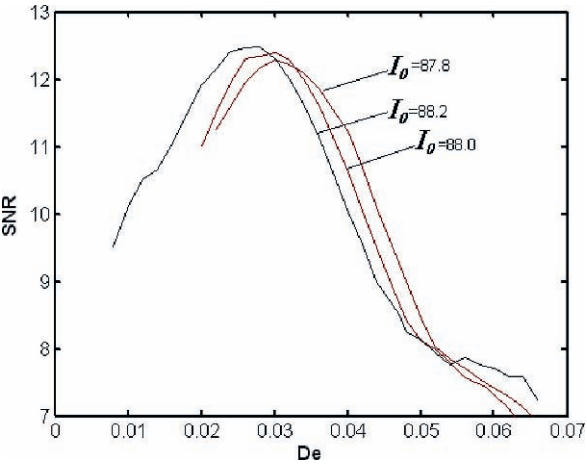

Fig. 17.5 The SNR of ML neuron model response with external noise only versus external noise intensity

decreases as I_0 moves close to the critical firing onset value. This is in accordance with the result of Gong and Xu in [7] and Zhang and Xu in [13, 14]. According to analysis above the conclusion can be drawn, that the mechanism of bifurcation-dependent CR of ML neuron model at the presence of internal or external noise is related to the random transitions between attractors on the two sides of bifurcation point respectively.

Conclusion

In this paper the mechanism of bifurcation-dependent CR of ML neuron model at the presence of internal or external noise have been investigated. The results are as follows:

(1) The random transitions between attractors on two sides of bifurcation point respectively occur in ML neuron model without periodic signal.
(2) The frequency of motion random transitions spontaneously is in accordance with a certain frequency under the perturbation of appropriate noise, and the SNR at the certain frequency as a function of noise intensity is a unimodal curve. Coherence resonance occurs.
(3) The mechanism of bifurcation-dependent CR of excited neuron model at the presence of internal or external noise is related to the random transitions between attractors in the two sides of bifurcation point respectively.

Acknowledgments The National Science Foundation under Grant 10432010, 30670660 and Shaanxi Province Science Foundation supports the work reported in this paper.

References

1. Benzi R., Sutera A. and Vulpiani A. The mechanism of stochastic resonance, J. Phys. A, 14 (1981) L453–L457.
2. Gammaitoni L, Hanggi P et al. Stochastic resonance, Rev. Mod. Phys., 70 (1998) 223–287.
3. Gong Y.F. and Xu J.X. Stochastic resonance: When does it not occur in neuronal models? Phy. Lett. A, 243 (1998) 351–359.
4. Longtin A. Stochastic resonance in neuron model, J. Stat. Phys., 70 (1992) 309–327.
5. Gong P.L., Xu J.X., Global dynamics and stochastic resonance of forced FitzHugh-Nagumo neuron model, Phys. Rev. E., 63 (2001) 031906.
6. Longtin A, Bulsara A, Moss F. Time-interval sequences in bistable systems and the noise induced transmission of information by sensory neurons, Phys. Rev. Lett., 67 (1991) 656–659.
7. Gong P.L and Xu J.X. Coherence resonance in a noise-driven excitable neuron model, Chaos, Solitons Fractals, 13 (2002) 885–895.
8. Pikovsky AS, Kurths J. Coherence resonance in a noise-driven excitable system, Phys. Rev. Lett., 78 (1997) 775–778.
9. Casado JM. Noise-induced coherence in an excitable system, Phys. Lett. A, 235 (1997) 489–492.

10. Longtin A. Autonomous stochastic resonance in bursting neuron, Phys. Rev. E, 55 (1997) 868–876.
11. Robert C. Hilborn, Rebecca J. Erwin. Coherence resonance in models of an excitable neuron with noise in both the fast and slow dynamics, Phys. Lett. A, 322 (2004) 19–24.
12. Gu HG, Yang MG et al. Dynamics of autonomous stochastic resonance in neural period adding bifurcation scenarios, Phys. Lett. A, 319 (2003) 89–96.
13. Zhang GJ, Xu JX et al. The mechanism of bifurcation-dependent CR of Rose-Hindmarsh neuron model, dynamics of continuous, discrete and impulsive system 14 (2007) 52–56.
14. Zhang GJ and Xu JX. The mechanism of bifurcation-dependent CR of FHN neuron model, 2006, International Journal of Nonlinear Sciences and Numerical Simulation, 4 (2006) 447–450.
15. Xie Y, Xu JX, et al. A novel dynamical mechanism excitability for integer multiple spiking, 2004, Chaos, Solitons Fractals 21 (2004) 177–184.
16. Zhang GJ and Xu JX. Stochastic Resonance induced by novel random transitions of motion of FitzHugh-Nagumo neuron model, Chaos, Solitons Fractals 23(4) (2005) 1439–1449.
17. Sri Namachchivaya N and Ariaratnam ST. Stochastically perturbed Hopf bifurcation, International Journal of Nonlinear Mechanics, 22(5) (1987) 363–372.

Chapter 18
Noise-Induced Coherence Resonance in Morris-Lecar Neuron System

Bao-Hua Wang, Qi-Shao Lu and Xiao-Juan Sun

Abstract Noise-induced coherence resonance of square coupled ML neuron models is studied. It is found that an intermediate level noise can make the system produce ordered structure. There also exist optimal fluctuation amplitude and coupling strength resulting in the maximal coherence.

Keywords Coherence resonance · spatial pattern · neuron

The Stochastic Morris-Lecar Neural Model

The Morris-Lecar model is a simple mathematical model of the barnacle giant muscle fiber, in which an equivalent electrical circuit for a patch of sarcolemma membrane is described by the calcium current, the potassium current and the leak current [1]. In the present work, the pattern formation is induced by Gaussian white noise in this coupled excitable model, and the effects of noise and coupling on the spatiotemporal behavior of this system is studied. The optimal noise level and coupling intensity are also analyzed by a measure function β which is related to the power spectrum of the firing-rate.

The reduced ML model is adopted here, coupled into a two-dimensional lattice network of $N \times N$ neurons ($N = 128$) with periodic boundary conditions in the present of noise excitation:

$$\begin{aligned} C\frac{dv_{i,j}}{dt} &= -g_{Ca}m_\infty(v_{i,j})(v_{i,j}-V_{Ca}) - g_K w_{i,j}(v_{i,j}-V_K) - g_L(v_{i,j}-V_L) \\ &\quad + I + D(v_{i-1,j}+v_{i+1,j}+v_{i,j-1}+v_{i,j+1}-4v_{i,j}) + \sigma\xi_{i,j}, \qquad (18.1) \\ \frac{w_{i,j}}{dt} &= \tau_w(v_{i,j})(w_\infty(v_{i,j})-w_{i,j}), \end{aligned}$$

Q.-S. Lu
School of Science, Beijing University of Aeronautics-Astronautics, Beijing 100083, China
e-mail: qishaolu@hotmail.com

R. Wang et al. (eds.), *Advances in Cognitive Neurodynamics*,

where the subscript (i, j) indicates that the neuron is at the *ith* unit in the horizontal and *jth* unit in the vertical direction, and $v_{i,j}$ is the neural membrane voltage and $w_{i,j}$ is the corresponding fraction of open K^+ channels. The input current is represented by I. D denotes the coupling strength and σ is the intensity of the noise $\xi_{i,j}$. Here $\xi_{i,j}$ is assumed to be Gaussian white noise satisfying $< \xi_{i,j} >= 0$ and $< \xi_{i,j}(t)\xi_{m,n}(t') >= \delta(t - t')\delta_{i,m}\delta_{j,n}$. $m_\infty(v_{i,j})$ and $w_\infty(v_{i,j})$ are the fractions of the open Ca^{2+} and K^+ channels at the steady state, respectively, varying in a sigmoid way with the membrane voltage. The rate constant for the open K^+ channel is denoted by $\tau_w(v_{i,j})$, which is also related to $v_{i,j}$. The dependence is introduced by the following functions:

$$\begin{aligned} m_\infty(v) &= 0.5\left[1 + \tanh\left(\frac{v - V_1}{V_2}\right)\right], \\ w_\infty(v) &= 0.5\left[1 + \tanh\left(\frac{v - V_3}{V_4}\right)\right], \\ \tau_w(v) &= \phi \cosh\left(\frac{v - V_3}{2V_4}\right). \end{aligned} \tag{18.2}$$

The parameters values are taken from [2].

Spatial Wave Patterns

In order to understand the noise influence in the square coupled system, the coupling strength is fixed at 1 and keeps unchanged at first. Spatial patterns induced by different noise intensities are presented in Fig. 18.1. For a very small noise amplitude, the neurons cannot fire and there is no visible pattern shown in Fig. 18.1a. When the noise level increases and exceeds a subthreshold value, regular patterns appear drastically in the network. The system gains different collectivity actions when the intensity gradually increases as shown in Fig. 18.1b–e. In Fig. 18.1b there are at least three sources on the left of the lattice and two on the left at $\sigma = 0.005$. Circular wave structures are formed when the waves diffuse from these local portions to global areas. These circular waves propagate and then intersect, leading to a triangular wave. As the noise value is enhanced to 0.02 (Fig. 18.1c), the structure is more regular with several rings piling up. The waves on the left and right collide to exhibit a diamond wave. Along with the rising of fluctuation level, similar phenomena appear, but there are more centers and circles become more dense. It is seemed that bigger noise values will excite more neurons. Larger noise spoils the resonance and the pattern becomes rather random as in Fig. 18.1f. From Fig. 18.1 it is evident that a proper global noise intensity will enhance the excitability of the exciting system and produce coherence resonance in the lattice.

Besides, the coupling strength can also affect the behavior of stochastic systems in the present of noise. For a faint value of D, obvious patterns can not be seen since

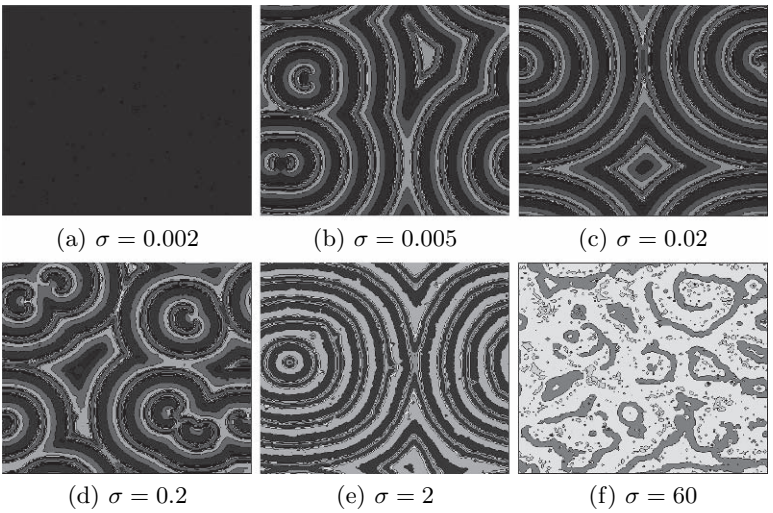

Fig. 18.1 Patterns in a coupled neuronal lattice with a global noise ($D = 1$)

the voltage diffuse suffocated at gap junction. While for larger D, local excitations propagate too quickly beyond the bound before the next wave waking, so spatial regular structures can't be observed. As the couple strength takes intermediate values, special patterns emerge. For a slightly small D, there exist many sources trying to proliferate such that waves impact each other. At this moment, there is no big radius circular wave because little D decelerate the propagating velocity of waves. With D increasing, the circular wave appears and becomes larger. They expand and collide to bring forth beautiful spatial patterns.

The Coherence Resonance

Considering the influence of noise and coupling strength, it seems that there exist optimal levels of σ and D such that the coherence trends to achieve the maximal value. In order to characterize the degree of coherence, a measure β based on the power spectrum of the firing-rate function Π is employed:

$$\beta = H\frac{\omega_p}{\Delta\omega}, \tag{18.3}$$

where w_p is the frequency of the main peak for the spectrum of Π, H is the peak height, and $\triangle\omega$ is the half-width of the peak. The neuron fires if the membrane voltage $v_{i,j}$ reaches a threshold value. The firing-rate function $\Pi(t)$ is used to portray the rate of firing of neurons in the lattice at a given time. When $\Pi = 0$, there is no firing, while for $\Pi = 1$ the whole system fires. In Fig. 18.2 several firing-rate curves are shown for diverse D when $\sigma = 0.2$.

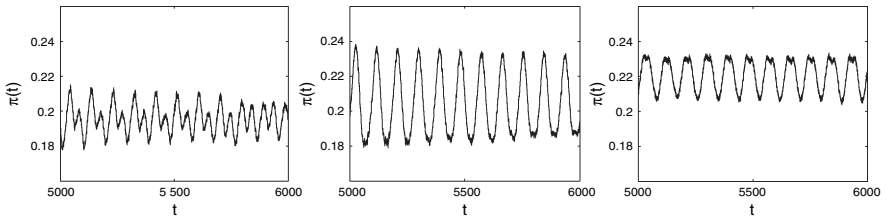

(a) $D = 0.5$ (b) $D = 0.75$ (c) $D = 1$

Fig. 18.2 The firing-rate of the system with different coupling strengths at $\sigma = 0.2$

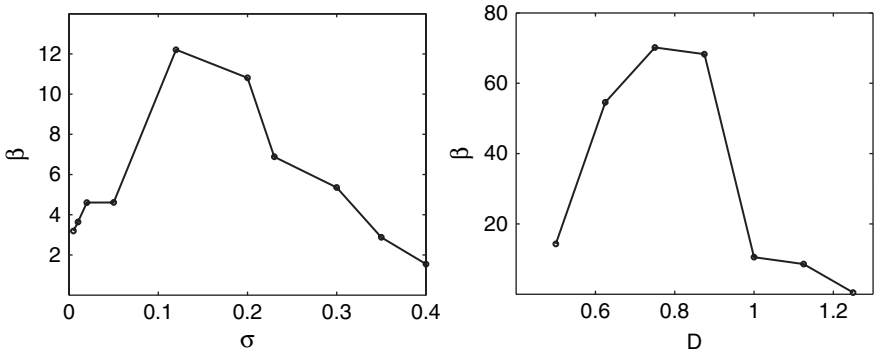

(a) $D = 1$ (b) $\sigma = 0.2$

Fig. 18.3 The coherence factor β of the firing-rate: (a) for fixed coupling strength $D = 1$; (b) for fixed noise level $\sigma = 0.2$

In what follows, the quantity β is computed for different values of the noise level and the coupling strength, respectively, in which small noise amplitude is considered. First, the value of D equals 1 and σ is changed, the simulation results are shown in Fig. 18.3a. With increasing the noise amplitude, β increases at the beginning, and after attaining the peak it turns to decrease in Fig. 18.3a. So there must exits an optimal noise level making the coherence resonance maximal. If the coupling strength varies and the noise level is fixed, from Fig. 18.3b the changing of β for enhanced coupling strength is similar to the upper case; in other words, there also exist an optimum coupling intensity at which the coherence resonance is more pronounced.

Conclusions

To be summarized, coherence resonance is studied for the coupled ML neuron model in the presence of noise. There exists an intermediate level of external random forcing and coupling, which can make the square coupled system produce ordered

spatial wave structure. In addition, there also exist optimal fluctuation amplitude and coupling strength to make the coherence more distinct.

Acknowledgments This work was supported by the National Natural Science Foundation of China (No.10432010).

References

1. Morris C., Lecar H.: Voltage oscillations in the barnacle giant muscle fiber. Biophys. J. **35** (1981) 193–213.
2. Rinzel J., Ermentrout G.B.: Analysis of neural excitability and oscillations. Methods in Neural Modelling (the MIT Press) (1989) 135–171.

Appendix

The parameters values used in this paper [2]: $C = 20\mu\text{F cm}^{-2}$, $g_K = 8.0\mu\text{S cm}^{-2}$, $g_L = 2.0\mu\text{S cm}^{-2}$, $g_{Ca} = 4.4\mu\text{S cm}^{-2}$, $V_{Ca} = 120\,\text{mV}$, $V_L = -60\,\text{mV}$, $V_K = -84\,\text{mV}$, $V_1 = -1.2\,\text{mV}$, $V_2 = 18\,\text{mV}$, $V_3 = 2\,\text{mV}$, $V_4 = 30\,\text{mV}$, $\phi = 0.04$, $I = 88\,\mu\text{A cm}^{-2}$

Chapter 19
Chaotic Burst Synchronization in a Small-World Neuronal Network

Yanhong Zheng, Qishao Lu, Qingyun Wang and Fang Han

Abstract The effects of the topological probability, the coupling strength and the noise intensity on synchronization of a small-world neuronal network are studied. Chaotic burst synchronization can be observed as the probability and the coupling strength are large enough. Moreover, the bursting activity and the spatiotemporal patterns are robust to small noise.

Keywords Neuronal network · small-world burst synchronization

Introduction

Brain is a complex network that can real-time extract and integrate various information perfectly from external and internal stimuli. A single neuron in the vertebrate cortex connects to more than 10,000 postsynaptic neurons via synapses in the forming of complex neural networks [1]. Clinically, the connection between burst and synchronization is extremely important, since synchronization in large neural populations is widely viewed as a hallmark of seizers. It is necessary to explore how burst synchronization appears or disappears in a neuronal network. Here we study the burst synchronization in a small-world network of chaotic HR neuron model with electrical coupling under noise environment. We mainly focus on how the topological probability, defined as the fraction of random shortcuts, the coupling strength and the noise intensity affect the spatiotemporal evolution of small-world neuronal networks.

The Neuronal Network with a Small-World Structure

The three-variable HR model of action potential was proposed as a mathematical representation of the firing behaviour of neurons. It can display rich dynamics

Q. Qishao
School of Science, Beijing University of Aeronautics and Astronautics, Beijing 100083, China
e-mail: qishaolu@hotmail.com

R. Wang et al. (eds.), *Advances in Cognitive Neurodynamics*,

including periodic and chaotic behaviour. Dynamics of the HR neuron is described by a set of differential equations given in [2]. Now we consider the dynamics of a complex network consisted of N coupled HR neurons with gap junction. Starting from a regular ring, which comprises N identical chaotic HR neurons, each neuron is connected to its two nearest neighbors. Links are then randomly added between non-nearest vertices [3], where the new coupling is to be wired randomly with the probability p. In the limit case $p = 1$, all neurons are coupled to each other, that is to say, globally coupled, the network contains $N(N-1)/2$ edges. The dynamics of the HR neuron network can be described by the following equations:

$$\begin{cases} \dot{x}_i = y_i - ax_i^3 + bx_i^2 - z_i + I_{ext} + \xi_i + g\sum_{j=1}^{N} a_{ij}(x_j - x_i), \\ \dot{y}_i = c - dx_i^2 - y_i, \\ \dot{z}_i = r[s(x_i - \chi) - z_i], \end{cases}$$

where $i = 1, 2, \ldots, N$; N is the number of neurons, x_i is the membrane potential, y_i is associated with the fast current Na^+ or K^+, and z_i with the slow current, for example, Ca^{2+}. ξ_i denotes the Gaussian white noise in the ith neuron with $< \xi_i >= 0$, and $< \xi_i(t)\xi_j(t') >= D\delta_{i,j}\delta(t - t')$. D represents the noise intensity, g is the coupling strength and the coefficients a_{ij} take 1 or 0 depending on whether or not there exists electrical coupling between neurons i and j. Here we take the parameters $a = 1$, $b = 3$, $c = 1$, $d = 5$, $s = 4$, $r = 0.006$, $\chi = -1.6$, and $I_{ext} = 3.0$ so as to make any neuron chaotic in the case of without noise and coupling. Numerical simulation are performed by using the fourth order Runge-Kutta method with a time step $\Delta t = 0.01$ ms. All neurons are identical except for distinct initial states and noise terms ξ.

Chaotic Burst Synchronization

Firstly, we investigate the effect of the topological probability p on burst synchronization in a small-world neuronal network under weak noisy environment. Here, we fix the noise intensity $D = 0.0005$, $g = 0.1$ and $N = 32$. Spatiotemporal patterns of all neurons with electrical coupling in the complex networks are displayed in Fig. 19.1. It is shown that burst synchronization among neurons can be strengthened with the probability increasing. Initially, without random shortcuts, the coupled neurons locate in chaotic states, and the HR neurons show rather irregular and nonsynchronous bursts as shown in Fig. 19.1a, where $p = 0$ corresponds to a ring structure. However, when a certain number of random shortcuts is added (e.g. $p = 0.015$), there appear some regular ones as shown in Fig. 19.1b. As the topological probability p is increased to 0.3, the coupled neurons eventually achieve chaotic burst synchronization as showed in Fig. 19.1c. It is evident that the number of random shortcuts is increased and the synchronous action between neurons is strengthened. The above results can also be observed under other weak noisy or noiseless environment.

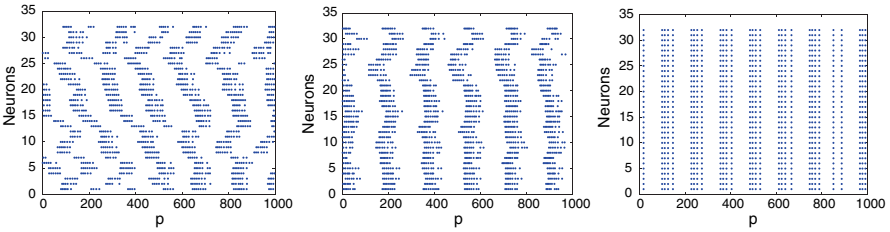

Fig. 19.1 Spatiotemporal patterns in a raster plot, the corresponding probability p is: (a) 0, (b) 0.015, (c) 0.3, respectively. Noise intensity $D = 0.0005$ and $g = 0.1$ for $N = 32$

To study the synchronization degree of neuronal networks, a synchronization parameter δ is introduced as [4]. $\delta =< \delta(k) >$ with

$$\delta(k) = \sqrt{\frac{(1/N)\sum_{j=1}^{N}(t^j(k))^2 - ((1/N)\sum_{j=1}^{N}(t^j(k))^2}{N-1}}, \quad k = 1, 2, \ldots, N_{min}$$

where the number of the spike train of the jth neuron is $N_j (j = 1, 2, \ldots, N)$ in the prescribed time interval, and $N_{min} = min(N_1, N_2, \ldots, N_N)$. The $< \cdot >$ denotes the average value of $\delta(k)$ over k. It is obvious that the more synchronous is a neuronal network, the smaller is the synchronization parameter. Synchronization parameter δ is calculated as illustrated in Fig. 19.2a when $N = 16$, 32, 48 and 100, respectively. It is shown that δ is decreased as the probability p increases. This fact implies the enhancement of neural synchronization. Moreover, synchronization among neurons may be enhanced with the number of neurons increasing if the probability p is above a certain value, for example, $p > 0.125$. On the other hand, a characteristic correlation time τ is introduced to measure the ordered behaviour of neurons [4]. $\tau =< \tau_{i,c} >$ with $\tau_{i,c} = \frac{1}{N_0 \Delta t}\sum_{k=1}^{N} c_i^2(\tau_k)\Delta t$ and

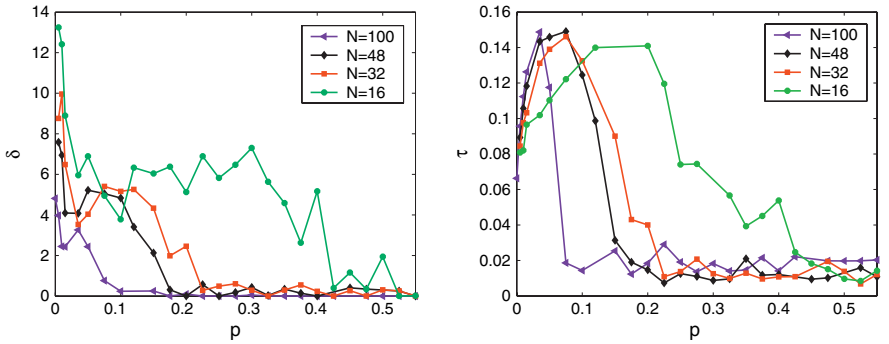

Fig. 19.2 (a) The variation of the synchronization parameter δ, (b) The variation of the characteristic correlation time τ with respect to the probability p for $N = 16$, 32, 48 and 100, respectively

$$c_i(\tau_d) = \frac{< (x_i(t) - < x_i(t) >)(x_i(t+\tau_d) - < x_i(t) >) >}{< (x_i(t) - < x_i(t) >)^2 >}$$

where $x_i(t)$ is the membrane potential of the ith neuron at time t, τ_d is the time delay, $< \cdot >$ denotes an average over time, $\tau_k = k\Delta t$ with Δt being the sampling time, and $N_0\Delta t$ being the length of time series.The more ordered is a neuronal network, the longer is its characteristic correlation time. Therefore, it can be used to measure the degree of spatiotemporal order of the neuronal networks. The curve of τ versus p is displayed in Fig. 19.2b for $N = 16$, 32, 48 and 100, respectively. There is a clear peak in each curve, indicating the occurrence of explicit ordered temporal behavior. The value of p for the peak becomes smaller with increasing the number of neurons and the resonance peak becomes narrower. It indicates that for larger neuron number, the smaller the number of randomly added shortcuts is needed for the system to achieve chaotic burst synchronization.

Secondly, in order to study the influence of coupling strength, we carried out the calculations for other three coupling constants $g = 0.01$, 0.05, 0.1 and 0.15 with $D = 0.0005$ and $p = 0.2$. Similar evolutions of spatiotemporal patterns are found. It shows that chaotic burst synchronization among neurons can be achieved with the coupling strength increasing. When g is small, the HR neurons show rather irregular and nonsynchronous bursts. As g increases to 0.15, the coupled neurons eventually achieve burst synchronization. This indicates that the spatiotemporal chaos of neurons can behave as burst synchronization with the coupling strength being large enough.

To check the effect of noise level, the synchronization parameter and characteristic correlation time are also calculated for the other three typical noise levels $D = 0.005$, 0.05 and 0.1 at $g = 0.05$. We find that for different values of D the spatiotemporal patterns change slightly and the evolution of the characteristic correlation time keeps little change with changing p. This means that the variation of the appropriate noise level exerts a slight influence on the bursting activity, and the spatiotemporal patterns are robust to it.

Conclusion

In this paper, the dynamics of chaotic HR neurons in a small-world network with noise is investigated. It is observed that chaotic burst neurons in this network can achieve burst synchronization when the topological probability and the coupling strength are above a certain value. Burst synchronization likely plays subtle information processing roles in healthy neural tissue. The more the number of neurons is, the easier the burst synchronization for the network shows. However, the burst synchronization cannot be enhanced when the noise is increasing.These results may be instructive to understand firing patterns and information transmission in neural systems under noisy background.

Acknowledgments This work was supported by the National Natural Science Foundation of China (No. 10432010).

References

1. Gerstner W., Kistler W. M.: Spiking Neuron Models, Cambridge University Press, Cambridge, (2002)
2. Hindmarsh J. L., Rose R. M.: A model of neuronal bursting using three coupled first order differential equations, Proc. R. Soc. Lond. B, 221 (1984) 87–102
3. Newman M. E. J., Watts D. J.: Renormalization group analysis of the small-world network model, Phys. Lett. A, 263 (1999) 341–346
4. Wang Q. Y., Lu Q. S., Chen G. R.: Ordered bursting synchronization and complex wave propagation in a ring neuronal network, Physica A, 374 (2007) 869–878

Chapter 20
A Stochastic Resonance Memory Mechanism of Hippocampus

Yan Chuankui and Liu Shenquan

Abstract Using the hippocampal cell channel model, the transmission features of hippocampal system are under the research. The process of memory is simulated by stochastic resonance. By synaptic model, the hippocampus model is constructed, which analyzes the summation of postsynaptic currents in the network. The strong capacity of spatiotemporal encoding in the network indicates the features of CA3 network during the information transmission process in the hippocampus. Analyzing the memory expression in CA1 under PP signal from entorhinal cortex or SC postsynaptic current respectively, results show that the reason is that single subthreshold signal cannot cause memory and stochastic resonance of them. The modeling result with time delay of the synaptic transmission is in accordance with the experimental phenomena of action potential in the hippocampus.

Keywords Hippocampus · stochastic resonance · memory pattern · ISI

Introduction

The function of noise was found first when Benzi explained some questions of ice age. The phenomenon that peak value appears when Signal-to-Noise (SNR) increases rapidly under certain strength of noise is named stochastic resonance [1]. Longtin pointed out that stochastic resonance is very important to neurophysiology and the noise plays a key role in neuron encoding [2, 3]. Outside signal accepted from the distal end of nerve is usually very weak when it reaches our brain, which can be strengthened by noise. A memory recognition process will be explained based on stochastic resonance.

For the hippocampus, Traub founded a simplification model with 19 pyramidal cells to describe the structure of CA3 in 1982 [4]. The result of this model shows that the bursting discharge of a pyramidal cell is very complicated, and that the

Y. Chuankui
Department of Mathematics, Hangzhou Normal University, Hangzhou 310036, China
e-mail: yanchuankui@163.com

R. Wang et al. (eds.), *Advances in Cognitive Neurodynamics*,

number of cells considered is too less. Afterwards, Traub and Jeffyerses carried on an improvement over the original model, building up a CA3 network with 100 pyramidal cells [5]. The excitory synapse among pyramidal cells is random, which indicates that the strong synaptic connection is a necessary condition of the synchronous bursting discharges. In 1998, Tateno, Hayashi and Ishizuka further amplified cells scale to 256 pyramidal cells and 25 interneurons in a CA3 network [6], in which the influence of synaptic strength on action potential had been studied thoroughly in this model. In various models, CA3 is studied alone, or is investigated just with CA1; however, the influence of MF connection of DG upon CA3 is often neglected. This paper is concerned with perfecting the structure of system, adding DG network and EC's effects to the system and analyzing the memory process.

The Hippocampal Neuron Model

There are two kinds of cells in the hippocampus: excitory neurons (mainly granulosa cells in DG and pyramidal cells in CA1 and CA3) and inhibitory neurons (mainly interneurons in CA1, CA3 and DG). Generally, the following model is employed to describe excitory neurons:

$$\begin{aligned} C\frac{\mathrm{d}V}{\mathrm{d}t} &= g_{\mathrm{Na}}m^3h(V_{\mathrm{Na}}-V)+g_{\mathrm{Ca}}s^2r(V_{\mathrm{Ca}}-V)+g_{\mathrm{Ca(low)}}s_{\mathrm{low}}^2r_{\mathrm{low}}(V_{\mathrm{Ca}}-V)\\ &\quad+g_{\mathrm{K(DR)}}n(V_{\mathrm{K}}-V)+g_{\mathrm{K(A)}}ab(V_{\mathrm{K}}-V)+g_{\mathrm{K(AHP)}}q(V_{\mathrm{K}}-V)\\ &\quad+g_{\mathrm{K(C)}}c\min(1,\chi/250)(V_{\mathrm{K}}-V)+g_{\mathrm{L}}(V_{\mathrm{K}}-V)+g_{\mathrm{af}}(V_{\mathrm{syn(e)}}-V)\\ &\quad+I_{\mathrm{syn}}+I_{\mathrm{stim}} \end{aligned} \tag{20.1}$$

$$\frac{\mathrm{d}z}{\mathrm{d}t}=\alpha_z(1-z)-\beta_z z,\quad z \text{ stands for } m,h,s,r,s_{\mathrm{low}},r_{\mathrm{low}},n,a,b,q,c \tag{20.2}$$

$$\frac{\mathrm{d}\chi}{\mathrm{d}t}=-\phi I_{\mathrm{Ca}}-\beta_\chi\chi \tag{20.3}$$

In addition to a large number of excitory neurons, there are a few interneurons in CA3 and DG. Despite its small proportion, interneurons play an important role in maintaining the equilibrium between excitation and inhibition in the hippocampus. The interneuron model can be described in the following way:

$$C\frac{\mathrm{d}V}{\mathrm{d}t}=g_{\mathrm{Na}}m^3h(V_{\mathrm{Na}}-V)+g_{\mathrm{K(DR)}}n^4(V_{\mathrm{K}}-V)+g_{\mathrm{L}}(V_{\mathrm{L}}-V)+I_{\mathrm{syn}} \tag{20.4}$$

$$\frac{\mathrm{d}z}{\mathrm{d}t}=\alpha_z(1-z)-\beta_z z,\quad z \text{ stands for } m,h,n \tag{20.5}$$

Equations 4 and 5 can be adopted to describe the interneurons in the hippocampus. While neurons are connected by synaptic model, these models can analyze the nerve system of the hippocampus.

The Hippocampal Memory Model

The Introduction of Network and Synaptic Model

In order to analyze the system of the hippocampus, firstly a network structure should be constructed. For the sake of convenience, each pyramidal cell excites 8 pyramidal cells around in the network, and each interneuron inhibits 16 pyramidal cells around, which is subjected to the excitation from these 16 pyramidal cells. Hence, two adjacent interneurons together inhibit four common pyramidal cells (the shadows in Fig. 20.1a).

Here suppose DG has the similar network to CA3 (CA1), hence ○ in Fig. 20.1a indicates granulosa cells, and then a hippocampal network is attained in Fig. 20.1b. The cells form network by synaptic connection, which is given below. Each presynaptic action potential always causes an impulse of postsynaptic cells.
The impulse of postsynaptic cells is as follows.

$$I_{\text{syn}} = g_{\text{syn}}(V_{\text{syn}} - V) \tag{20.6}$$

$$g_{\text{syn}} = C_{\text{syn}}(\exp(-t/\tau_1) - \exp(-t/\tau_2)) \tag{20.7}$$

Stochastic Resonance Memory Recognition

A memory object "A" is considered. First it was accepted by cortex and converted into PP current signal which is input into the network of 16×16. For those neurons covered, $W_{\text{perep}} = 0.08$; otherwise, $W_{\text{perep}} = 0$. The potential of the neurons is indicated by the grey level from black to white, that is, near black means resting while near white firing.

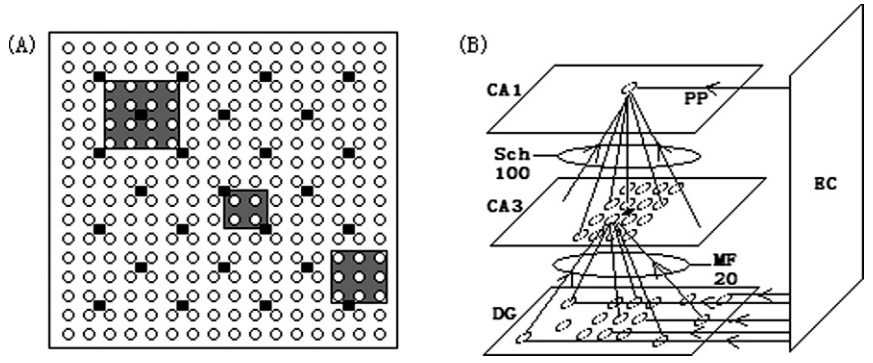

Fig. 20.1 (a) CA1, CA3 or DG network: 16×16.○: pyramidal cell or granulose cell. ■: interneuron. (b) hippocampus system structure. Each pyramidal cell in CA3 is exited by 20 granulose cells with MF connection. Each pyramidal cell in CA1 is exited by 100 pyramidal cells with SC connection. DG and CA1 are exited by PP signal

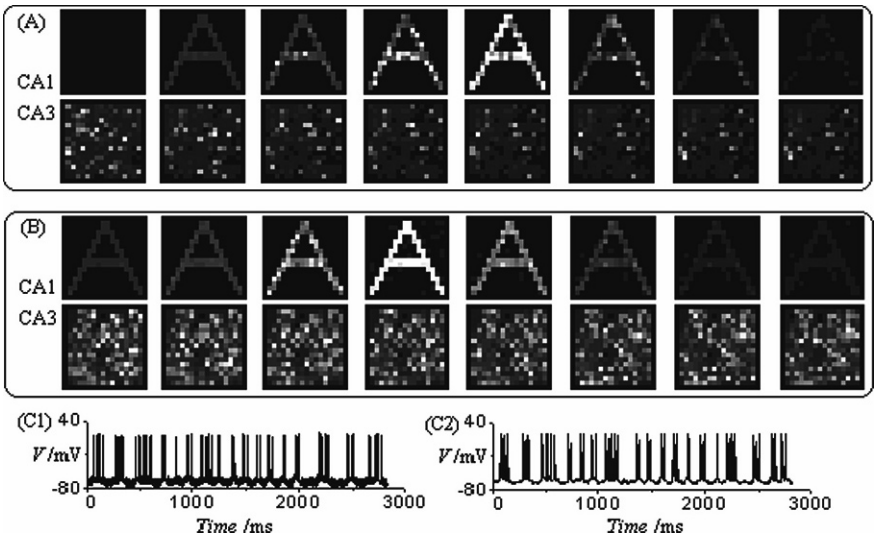

Fig. 20.2 (a) the incomplete memory pattern in the period of sparse pyramidal cells firing; (b) the complete memory pattern in the period of most pyramidal cells bursting synchronously; (C1) CA1 pyramidal cell fires under the incomplete memory pattern; (C2) CA1 pyramidal cell fires under the complete memory pattern

A complete hippocampal system memory is concerned. In Fig. 20.2, the memory is recalled under subthreshold PP signal and SC postsynaptic current in CA1, with the interval between two pictures 0.6 ms. CA3 in the second line is 1 ms ahead of CA1 because of the synaptic delay.

The neurons firing spontaneously are random in CA3-DG structure, and presynaptic neurons of SC connection are also random; therefore, SC postsynaptic current can be regarded as a random variable. Since noise with certain strength is applied into enlarging or detecting subthreshold signals, SC postsynaptic current can be considered as stochastic noise. Using stochastic resonance in the model, the PP subthreshold signal is strengthened by SC stochastic noise, and the memory object is recalled in CA1.

Discussion

A tentative study has been done on the memory mechanism of hippocampus. Memory, as a function, is explained by stochastic resonance. The recognition of a single letter “A” is simulated in the model, which is a relatively good memory expression. Obviously, memory objects in reality are far more complicated than a letter; as a result, in order to recognize complicated information, the input of PP signal should be more complicated, for instance, a word “MEMORY” as a memory object. Suppose the cortex of brain can decompose the object. When it is changed

Fig. 20.3 CA1 expression patterns when memory object is complicated signal "MEMORY"

into PP signal, the basic unit (letter) in this object is output in turn with the frequency of 50 Hz. By this, the memory result of CA1 is obtained (see Fig. 20.3).

Acknowledgments This research was supported by the National Natural Science Foundation of China (Grant Nos. 19902005 and 10432010). The authors wish to thank Katsumi Tateno for his suggestions and help.

References

1. Benzi R., Sutera A., Vulpiani A.: The mechanism of stochastic resonance. J. Phys. A 14 (1981) 453–457.
2. Longtin Andre.: Autonomous stochastic resonance in bursting neurons. Phys. Rev. E 55 (1997) 868–876.
3. Collins J.J., Chow Carson C., Capela Ann C.: Aperiodic stochastic resonance. Phys. Rev. E 54 (1996) 5575–5584.
4. Traub R.D.: Simulation of intrinsic bursting in CA3 hippocampal neurons. Neuroscience 7 (1982) 1233–1242.
5. Traub R.D., Jefferys J.G.R.: Simulations of epileptiform activity in the hippocampal CA3 region in vitro. Hippocampus 4 (1994) 281–285.
6. Tateno K., Hayashi H., Ishizuka S.: Complexity of spatiotemporal activity of a neural network model which depends on the degree of synchronization. Neural Netw. 11 (1998) 985–1003.

Chapter 21
Theta Phase Precession Enhance Single Trial Learning in an STDP Network

Enhua Shen, Rubin Wang and Zhikang Zhang

Abstract Theta phase precession is an interesting phenomenon in hippocampusand may enhance learning and memory. Based on Harris KD et al. and Magee JC's electrophysiology experiments, a biology plausible spiking neuron model for theta phase precession was proposed. The model is both simple enough for constructing large scale network and realistic enough to match the biology context. The numerical results of our model were shown in this paper. The model can capture the main attributes of experimental result. The relationship of phase shift with place shift in experiment was well repeated in our model. An STDP network constructed with our model neurons can memorize place sequence after single time learning with high accuracy. Such a model can mimic the biological phenomenon of theta phase precession, and preserve the main physiology factors underline theta phase precession.

Introduction

Theta phase precession was first discovered by O'Keefe and Recce in rat hippocampus [1]. An important discovery is that the phase shift of individual CA1 neurons with neighboring place fields is observed to be coherent [2]. That is, the neurons with neighboring place fields show nearly fixed phase difference, and phase differences increase with place fields shift. This attribute of theta phase precession will cause the place sequence the rat passed to be represented by a neuron population firing pattern lasting for 0.1 s and repeating in each theta cycle. Such a pattern will enhance the memory of place sequence a lot [3].

E. Shen
Institute for Brain Information Processing and CognitiveNeurodynamics, College of Information Science and Engineering, EastChina University of Science and Technology, 130 Meilong Rd., Shanghai 200237, China
e-mail: {Enhua Shen, sheh}@ecust.edu.cn

R. Wang et al. (eds.), *Advances in Cognitive Neurodynamics*,

Some theoretical models of theta phase precession have been proposed. Some models assumed asymmetric connection weights in the network cause the pattern of theta phase precession [4, 5, 6, 7]. Other models needn't assuming the initially asymmetric connections and generate theta phase precession by some mechanisms in individual neural oscillators [1, 3, 8], while these models are hard to be evaluated by experiment. Based on Harris KD et al. (2002) [9], Magee JC (2001) [10] and Kamondi A et al. (1998) [11], we constructed a model with a basic leakage integrate-and-fire neuron, with adaptation mechanism and slow potassium current. We discard the computational demanding H-H equation in our model, try to capture the major attribute of experimental theta phase precession phenomenon [12].

For study the learning enhancing hypothesis of theta phase precession, an STDP learning network was constructed to study the place sequence memory function in a near real neuron network. We give the network space information only once, and observe the learning ability of the network.

Model

Our single neuron model and network coupling between neurons were described in our previous work [12].

STDP

Spike time dependent of plasticity (STDP) is modeled by following. Take neuron i as presynaptic neuron and neuron j as postsynaptic neuron (the diagonal weights are not involved in Learning, i $\neq$ j), for each postsynaptic spike $\delta(t_j^f)$, $f = 1, 2, \cdots, SNj$, SNj is the total number of spikes neuron j fired, we find a closest presynaptic spike $\delta(t_i^{f^*})$ before it, $t_i^{f^*} < t_j^f$ and $t_i^{f^*+1} > t_j^f$ (or there is no $t_i^{f^*+1}$). Then an increase of weight W_{ij} occurs at time t_j^f. Please note the saturation term $(1 - W_{ij}(t_j^f))$.

$$\frac{dW_{ij}(t_j^f)}{dt} = Cw \bullet \delta(t_j^f) \bullet \tau \bullet e^{\frac{-\tau}{0.004}} \bullet \left(1 - W_{ij}(t_j^f)\right),$$
$$\text{where } \tau = t_j^f - t_i^{f*}, \text{ Cw is a constant to control the learning rate.} \quad (21.1)$$

For each presynaptic spike $\delta(t_i^f)$, $f = 1, 2, \cdots, SNi$, SNi is the total number of spikes neuron i fired, we find a closest postsynaptic spike $\delta(t_j^{f^*})$ before it, $t_j^{f^*} < t_i^f$ and $t_j^{f^*+1} > t_i^f$ (or there is no $t_j^{f^*+1}$). Then an decrease of weight W_{ij} occurred at time t_i^f.

$$\frac{dW_{ij}(t_i^f)}{dt} = -0.03 \bullet Cw \bullet \delta(t_i^f) \bullet \sqrt{\tau} \bullet e^{\frac{-\tau}{0.008}} \bullet W_{ij}(t_i^f)$$

where $\tau = t_i^f - t_j^{f*}$.

An illustration of learning window is given in Fig. 21.2a.

Results

The model was programmed through Simulink of MatLab. We use fixed step ode5 method in simulating. The time step is 0.0002 sec.

Single Neuron Result

The stimulus in simulation of single neuron model is illustrated in Fig. 21.1a. According to [10], in our stimulus, the inhibitory input is: $[-0.2 + 0.2^* \sin(10^*\pi^*t)]$ nA (bottom line). We suppose the rat runs through a line with a length of 60 cm. It will receive a place-specified ramp-like input [10], which illustrated in the top line of Fig. 21.1a. The exciting input has a constant component of 0.7 nA, and a triangle ramp centered at 30 cm with a width of 30 cm. The peak strength of the exciting input is 1.5 nA.

We suppose the rat runs in an average speed of 15 cm/s, with random fluctuations. That is, $P = vt + \xi$, where P is the place of the rat, v is its velocity 15 cm/s, ξ is a Gaussian noise with a mean of 0 and a standard deviation of 1.06 cm. The stimulus strength was selected to match the experiment in [9]. Besides the above we add white noise to the input, the standard deviation is 0.01 nA, and with a mean of 0.

The firing patterns of our model, subjected to input shown in Fig. 21.1a, are shown in Fig. 21.1b. Similar to experiment, we overlapped data from about 20 trails together. It is similar to experiment results in [2]. If we focus on the spikes occur

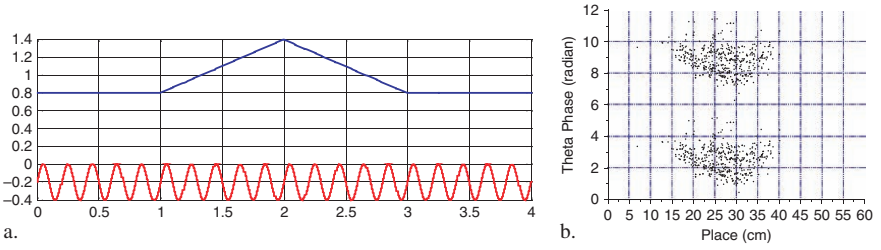

Fig. 21.1 (a) An illustration of input to our model. The top line is an exciting ramp, which is a function of place. The range of the input is about $0 \sim 60$ cm. The bottom line is oscillatory inhibition, whose amplitude is 0.2 nA. It's a function of time. Other details can be found in the text. (b) Data overlapped from 20 single trails

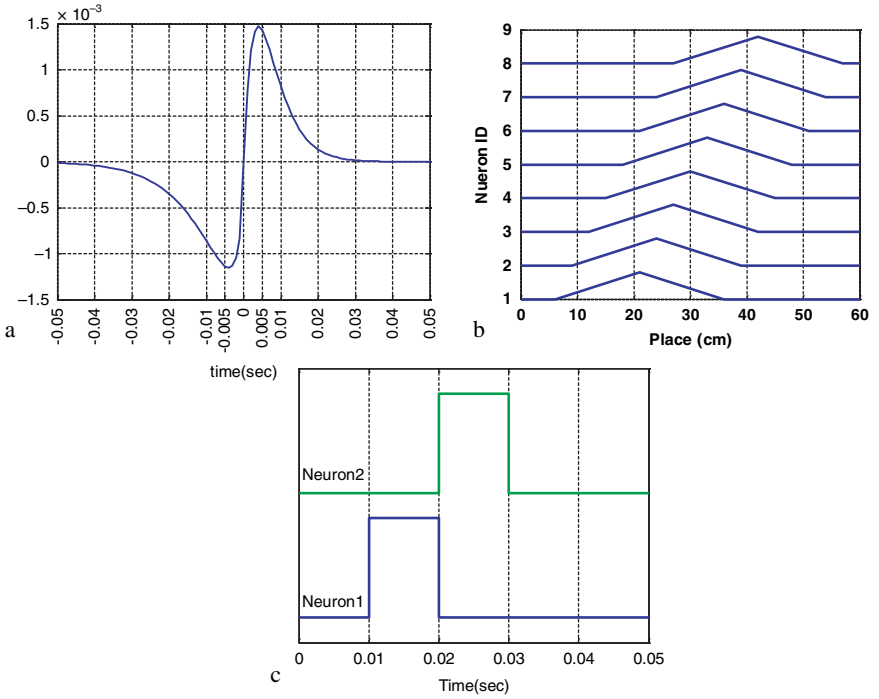

Fig. 21.2 (a) STDP learning window, (b) 8 exciting ramp inputs in learning stage, (c) recall cue, the height is 20 nA

before 30 cm, i.e. before the peak of the ramp input, the phase of spikes advances a lot. While for spikes after 30 cm, the phase doesn't advance but lags. This lag is due to the limitation of adaptation mechanism we currently use. In spite of this shortage, the phase of spike mainly advances in our model.

Place Sequence Memory and Recall in Single-Time-Learning

We constructed a network with 8 model neurons. The connection weights are changeable according to STDP rules during simulation. The shape of learning window is shown in Fig. 21.2a. The simulations were separated into two part, first learning part and then recall part. During the learning part, initial weights were set to random numbers between $0 \sim 0.01$, which is not significant. Parameter WL in Eq. (21.09) is set to 4 at this stage. The input in learning part is similar to previous section. Neighboring exciting ramps are shown in Fig. 21.2b. Simulation at learning stage lasts for 4 s. So a series of neighboring exciting ramps is feed into the network only once.

During the recall part, initial weights were got from the final weights in learning stage. There is no inhibitory theta wave input in this part. The input in recall part is

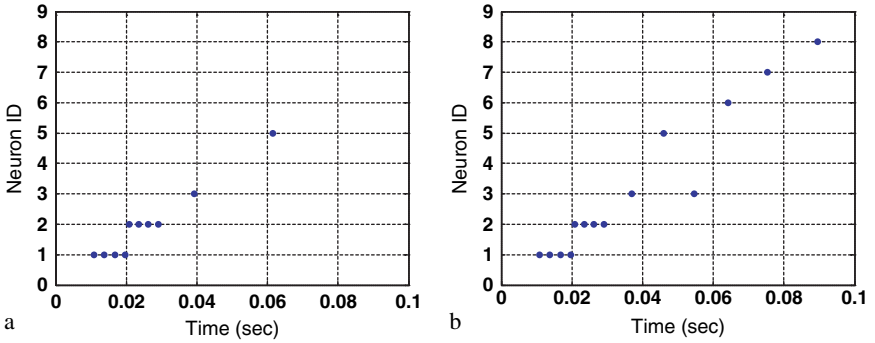

Fig. 21.3 Output in recall stage. Each dot in the figure is a spike fired by a neuron. Spikes of one neuron are plotted along a horizontal line. WL value in (a) is 24, in (b) is 25

two square pulses, only given to neuron 1 and 2. Each pulse lasts for 10 ms and the strength is 20 nA. The strength is very high and will induce a neuron fire 4 spikes. Two pulses are shown in Fig. 21.2c. STDP function is still open at this stage. Simulation in recall stage lasts for 1 s. For effectively activate other neurons, parameter WL in Eq. (21.9) increases a lot at this stage, about seven times. We find, due to noises, weight matrix is very different from each other after each learning process. So at corresponding recall stage, parameter WL need to be set to different value for adapt different learned weight matrix. The value varied from about $25 \sim 34$.

Figure 21.3 shows recall activity under different WL values. We can see if WL is low, only a few neurons (except neuron 1 and 2, which receive strong outside inputs) was activated (a). In a suitable range of WL, most neurons can be activated and represent memory of place sequence (b). The suitable range is narrow, about $2 \sim 3$. If WL is larger than suitable range, at first place sequence still can be represented by spikes, but soon all neurons begin to tonic firing. We can clearly see that in this case the model successfully recall the place sequences, with minor mistake. Please note that the recall process last for 0.1 s, about half a theta cycle, while the learning stimulus last for nearly 4 s.

Not in all cases the model can learn and recall place sequence successfully. In our simulations, about one trial out of five can perform as good as Fig. 21.3b, but it is also hard to find such a thoroughly wrong case.

Conclusion

Inspired by [9] and [10]'s electrophysiology research, we propose in this paper a computational model. In spite of the limitation of adaptation mechanism in this model, the single neuron model shows a firing pattern reserving the major attributes of theta phase precession. Model neurons with neighboring place fields can memorize place sequence after single trail learning in a STDP network.

Acknowledgments This work was supported by the National Natural Science Foundation of China (30270339 and 10672057).

References

1. O'Keefe, J., Recce, M.L.: Phase Relationship Between Hippocampal Place Units and the EEG Theta Rhythm. Hippocampus 3 (1993) 317–330.
2. Skaggs, W.E., McNaughton, B.L., Wilson, M.A., Barnes, C.A.: Theta Phase Precession in Hippocampal Neuronal Populations and the Compression of Temporal Sequences. Hippocampus 6 (1996) 149–172.
3. Yamaguchi, Y.: A Theory of Hippocampal Memory Based on Theta Phase Precession. Biological Cybernetics 89 (2003) 1–9.
4. Tsodyks, M.V., Skaggs, W.E., Sejnowski, T.J., McNaughton, B.L.: Population Dynamics and Theta Rhythm Phase Precession of Hippocampal Place Cell Firing: a Spiking Neuron Model. Hippocampus 6 (1996) 271–280.
5. Jensen, O., Lisman, J.E.: Hippocampal CA3 Region Predicts Memory Sequences: Accounting for the Phase Precession of Place Cells. Learning Memory 3 (1996) 279–287.
6. Wallenstein, G.V., Hasselmo, M.E.: GABAergic Modulation of Hippocampal Population Activity: Sequence Learning, Place Field Development and the Phase Precession Effect. Journal of Neurophysiology 78 (1997) 393–408.
7. Samsonovich, A., McNaughton, B.L.: Path Integration and Cognitive Mapping in a Continuous Attractor Neural Network Model. Journal of Neurophysiology 17 (1997) 5900–5920.
8. Bose, A., Booth, V., Recce, M.: A Temporal Mechanism for Generating the Phase Precession of Hippocampal Place Cells. Journal of Computational Neuroscience 9 (2000) 5–30.
9. Harris, K.D., Henze, D.A., Hirase, H., Leinekugel, X., Dragoi, G., Czurko, A., Buzsaki, G.: Spike Train Dynamics Predicts Theta Related Phase Precession in Hippocampal Pyramidal Cells. Nature, 417 (2002) 738–741.
10. Magee, J.C.: Dendritic Mechanisms of Phase Precession in Hippocampal CA1 Pyramidal Neurons. Journal of Neurophysiology 86 (2001) 528–532.
11. Kamondi, A., Acsady, L., Wang, X.J., Buzsaki, G.: Theta Oscillations in Soma and Dendrites of Hippocampal Pyramidal Cells in vivo: Activity-Dependent Phase-Precession of Action Potentials. Hippocampus 8 (1998) 244–261.
12. Shen, E.-H., Wang, R.-B., Zhang, Z.-K., Peng, J.-H.: A Spiking Neuron Model of Theta Phase Precession. In: Jiao, L., Wang, L., Gao, X. Liu, J., Wu, F. (eds.): Advances in Natural Computation. Lecture Notes in Computer Science, Vol. 4221. Springer-Verlag, Berlin Heidelberg (2006) 214–223.

Chapter 22
A Numerical Mechanism for Square-Wave or Elliptic Bursting of Bursts in a Map-Based Neuron Network

Hongjun Cao and Miguel A.F. Sanjuán

Abstract A network of two identical Rulkov map-based neurons coupled by reciprocal excitatory or inhibitory electrical synapses as a phenomenological example is investigated. This is because on the one hand, this network can exhibit many regular and irregular bursting oscillations, and such behaviors can reflect many functional roles in real neuron assemblies, especially when the information transmission and processing of biological neurons are concerned. On the other hand, this is motivated by experimental studies where the pyloric central pattern generators of the lobster stomatogastric ganglion are coupled by an artificial dynamical current clamp device [Phys. Rev. Lett. 81.5692, 1998]. So it is worthwhile to make a detailed study even for this simple map-based network. Our results demonstrate that there exist multiple cooperative behaviors of bursts. Moreover they can be well explained and predicted by two kinds of different strategies by using a fast-slow dynamics technique and bifurcation analysis. When the electrical coupling is excitatory or inhibitory due to the artificial electrical coupling, separately, a fast-slow analysis is carried out by treating the two slow variables as two different bifurcation parameters. The main contribution of this paper is to present a numerical mechanism for the occurrence of *square-wave* or *elliptic* bursting, which is due to the interaction between multiple stable branches of fixed points of the fast subsystem or two chaotic oscillations with different amplitudes. Particularly, the generation of antiphase synchronization of networks lies in the different switching orders between two pairs of different chaotic oscillations corresponding to the first neuron and the second neuron, respectively.

PACS numbers: 05.45. − a, 84.35. + i, 87.10. + e

H. Cao
Department of Mathematics, School of Science, Beijing Jiaotong University, Beijing 100044, P.R. China
e-mail: hjcao@bjtu.edu.cn

R. Wang et al. (eds.), *Advances in Cognitive Neurodynamics*,

The Coupled Map-Based Neuron System

We consider here a simple neuron network composed of two identical Rulkov map-based neurons [1, 2] coupled through electrical or gap-junctional coupling

$$\begin{aligned} x_{n+1,1} &= \frac{\alpha}{1+x_{n,1}^2} + y_{n,1} + \varepsilon\big(x_{n,2} - x_{n,1}\big), \\ y_{n+1,1} &= y_{n,1} - \eta\big(x_{n,1} - \sigma\big), \\ x_{n+1,2} &= \frac{\alpha}{1+x_{n,2}^2} + y_{n,2} + \varepsilon\big(x_{n,1} = x_{n,2}\big), \\ y_{n+1,2} &= y_{n,2} - \eta\big(x_{n,2} - \sigma\big), \end{aligned} \tag{22.1}$$

where α, ε, η, and σ are parameters. When η is very small, then the evolution of $y_{n,i}$ $(i = 1, 2)$ is much slower than that of $x_{n,i}$ $(i = 1, 2)$. Thus, we refer to $x_{n,i}$ as the fast variables and $y_{n,i}$ as the slow variables, and the parameter ε denotes the electrical synaptic coupling strength.

Motivation

The motivation of this paper is to show that even in this ensemble of two identical neurons, usually, the two slow variables given in Eq. (22.1) assume different values at any given time. It seems to be much more reasonable and predictable to use two different bifurcation parameters rather than to use only one, when bifurcation theory and geometric singular perturbation theory are applied.

Main Results

The main result of this paper is to propose a mechanism for the occurrence of *elliptic* bursting when the electrical coupling is inhibitory. In this case, the fast subsystem includes two different slow variables no matter how small the coupling strength is. The *elliptic* bursting oscillation is due to the interaction between two chaotic oscillations with different amplitudes. Moreover, the generation of antiphase synchronization of networks lies in the different switching orders between two pairs of different chaotic oscillations of the first neuron and the second neuron. The mechanism is in agreement with experimental studies where two coupled neurons are coupled by an artificial dynamical current clamp device [3]. Most importantly, these results could be extended to large-scale networks.

References

1. N. F. Rulkov, Regularization of synchronized chaotic bursts, Phys. Rev. Lett **86**, 183 (2001).
2. G. de Vries, Bursting as an emergent phenomenon in coupled chaotic maps, Phys. Rev. E **64**, 051914–1 (2001).
3. R. C. Elson, A. I. Selverston, R. Huerta, N. F. Rulkov, M. I. Rabinovich, H. D. I. Abarbanel, Synchronous behavior of two coupled biological neurons, Phys. Rev. Lett **81**, 5692 (1998).

Chapter 23
Sub-Threshold Oscillation and Transient Response in Neural Coding

Jianxue Xu

Abstract In this paper, the viewpoints that the information characteristics in neural coding are not only transmitted by neural firing pulse but also by sub-threshold oscillation of activity potential of a neuron is provided through the analysis of dynamics of two kinds of neuron models. Besides, it is revealed that some information characteristic of stimulus and steady state responses for a neuron can be found from transient responses.

Keywords Neural firing pulse · interspike interval · bursting · sub-threshold oscillation · steady state response · transient state response

Introduction

Neural science has been intersected and combined with nonlinear science for exhibiting nonlinear properties of its objects studied. Neural coding is viewed as the quantity and metric of neural activities in the field of bio-neural science. Recently, nonlinear science (nonlinear dynamics) is well developed, and its theory has been employed to analyze the behaviors and mechanisms of the neuron activities.

Sensing information outside and adapting and affecting the circumstances are reached by nerve systems and exhibited the activities of nerves. In the field of neural science, it is paid much attention to how the information are processed by neuron fiber in such situations, and how the patterns of the interspike interval (ISI) sequence of a neuron and the assembly features of neurons caused by stimulus outside and inner physical and chemical activities and processes are regarded as a kind of neural coding. In the brain neural science, the neural coding is used to mean a measurement and metric of neuronal activity [1]. Besides, the Shannon information theory has also been introduced in studying the problem of neural coding [2].

Recently, a lot of the behaviors and mechanisms of neuron activities is found and revealed using the nonlinear dynamics theory, see references [3, 4, 5, 6, 7] as

J. Xu
Xi'an Jiaotong University, Xi'an, P.R. China
e-mail: jxxu@mail.xjtu.edu.cn

R. Wang et al. (eds.), *Advances in Cognitive Neurodynamics*,

example. Here, the viewpoints that the information characteristics in neural coding are not only transmitted by neural firing pulse but also by sub-threshold oscillation of activity potential of a neuron are provided through the dynamics analysis of two kinds of neuron models, and some information characteristic of stimulus and steady state responses for a neuron can be found from transient responses are presented.

Neural Coding Concept Related with Nonlinear Dynamics

The concept of neural coding from the viewpoint of nonlinear dynamics possesses three meanings; the generation of various pattern of response information of a neuron resulted by neuron activities under stimulus or by neuron self activities only (spontaneous firing), the way of information characteristics of specific stimulus transmitted to response of a neuron, and the forms of elementary element constituting various neural information.

It is well known that the biology experiments and analysis of neuron model have provided a lot of evidences that neural activity and neural firing possess rich and variant nonlinear dynamical behavior of response. These behaviors are regarded as the neural coding generated from neuron activities under stimulus or neuron self-activities. This neural coding is expressed by nonlinear steady state response, transient state response, and slow varying processes response. For instance, for same periodic stimulus the steady state responses of a neuron can be different: static, periodic, quasi-periodic, and chaos. The same situation can be met in the spontaneous firing of a neuron. The neural coding is also to state how the characteristic of stimulus after the cooperating or processing by the neuron activity can appear in the response. The neural coding is also employed for identifying the dynamics behavior (neural information) in the complicate dynamics behavior, like chaos.

Coding by Sub-Threshold Oscillation Response

It is found that the information characteristics in neural coding are not only transmitted by neural firing pulse but also by sub-threshold oscillation of neuron activity potential through the dynamics analysis of two kinds of neuron models.

The case of 4-dimension Hodgkin-Huxley neuron under periodic stimulus signal is studied:

$$\begin{aligned}
\dot{u} &= I - \left[120m^3h(u+115) + 36n^4(u-12) + 0.3(u+10.599)\right] \\
\dot{m} &= (1-m)\psi\left(\frac{u+25}{10}\right) - m\left(4\exp\left(\frac{u}{18}\right)\right) \\
\dot{n} &= 0.1(1-n)\psi\left(\frac{u+10}{10}\right) - n\left(0.125\exp\left(\frac{u}{80}\right)\right)
\end{aligned}$$

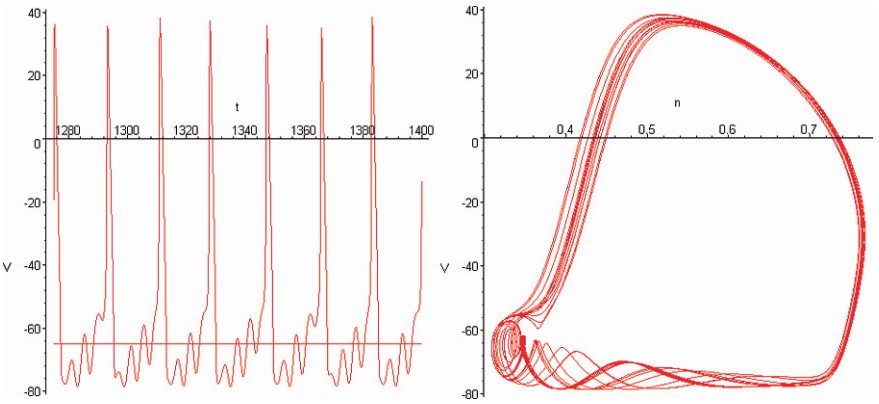

Fig. 23.1 Steady state response of chaotic ISI rhythm of Hodgkin-Huxley neuron model under sinusoid wave current excitation with amplitude of 12.0: Time wave form in time interval t = 1280–1400 ms, and Phase portrait in time interval t = 1100–1400 ms

$$\dot{h} = 0.07(1-h)\exp\left(\frac{u}{20}\right) - h \Big/ \left(1+\exp\left(\frac{u+30}{10}\right)\right)$$
$$\psi(x) = x/(\exp(x)-1) \tag{23.1}$$

By the numerical calculations, the periodic-one, periodic-three, and chaotic ISI rhythm steady state responses under sinusoid wave ($Im\sin(1.57t - 48.67)$) excitation of amplitudes Im, 11.9, 12.0, and 13.0 are obtained.

In the whole time wave of the chaotic ISI rhythm response including peak pulse of firing and sub-threshold oscillation, the waves of time interval between two neighbor sub-threshold oscillation sub-wave peak being approximately equal to the period, 4 ms of sinusoid wave of current stimulus, $I = 12\ \sin(1.57t - 48.67)$ are appeared clearly. which exhibit the characteristics of the periodic stimulus signal. The time wave of a part of the steady state response (after 1280 ms) of this chaotic rhythm and its phase portrait are shown in Fig. 23.1. This situation also occurs in the periodic rhythm case of the periodic stimulus amplitudes 11.9 and 13.

Coding in Transient State Responses

In general situation, a time interval of the transient state response is needed to study until reaching the steady state response of neural firing of a neuron after stimulus, and the environment change is sensed through the neuron activity immediately. Hence, the transmitting of information and the corresponding between stimulus and response at the period of transient state is more important and more complex.

Correspondence of Stimulus and Transient Responses

The characteristics of transient responses of a neuron fiber under a stimulus signal can be described through similar items specified for steady state response case, but some of those are just viewed as at transient state, for instances: transient chaotic dynamics natures. During biological neural information are transmitted from stimulus to transient response along a neuron fiber, how the information characteristics of stimulus signal being coded into the response through neuron activities can also similarly be provided as those in the steady state response case.

The dynamical analysis of four dimensional Hodgkin-Huxley neuron model under sinusoid excitation and three dimensional β-Rinzel model under constant current excitation are employed for indicating these argument. For the former, the periodic-one, chaotic, and periodic-three ISI rhythms transient response under sinusoid wave $Im\sin(1.57t-48.67)$ excitation of amplitudes *Im*, 11.9, 12.0, and 13.0 are obtained. After first pulse, it is seen on the figure of chaotic rhythm case ($Im = 12.0$), that the sub-threshold oscillation waves of the transient responses with time interval between two neighbor wave peak being approximately equal to the period of 4 of sinusoid wave of stimulus have begun occurring, which are just the evidence for exhibiting the information characteristic of excitation (stimulus). This situation also occurs in the periodic rhythm case of the periodic stimulus amplitudes 11.9 and 13.

For square wave excitation cases, the same expressions can be inspected.

Corresponding Between Transient Response and Steady State Response

The β-Rinzel neuron spontaneous firing model of three state variables, *V, n, Ca* [8] is studied. The initial conditions are $V_0 = -40,\ \mathrm{Ca}_0 = 0.62,\ n_0 = 0.1$.

The dynamics characteristic of the chaotic ISI rhythm steady state response may occur in the time interval of first several pulse of the transient response in spontaneous firing of β–Rinzel neuron of calcium-potassium current constant 26,000. For the periodic ISI rhythm steady state response case, the steady state response appears quickly after first several pulse of the transient response. Figure 23.2 shows that the periodic-7 steady state response of β-Rinzel neuron spontaneous firing model of calcium-potassium current constant 26,085 appears after just 52 ms.

Coding in the Process Depending Slowly Varying

A kind of processes of neuron activities or neural firing are often met, of which the dynamics of neuron activities or the patterns of neural firing trains depending a slowly varying parameter vary qualitatively, substantially, and systematically at the slowly varying parameter passing some specific values. This qualitative variation is named as dynamic bifurcation, which is different from usual bifurcation

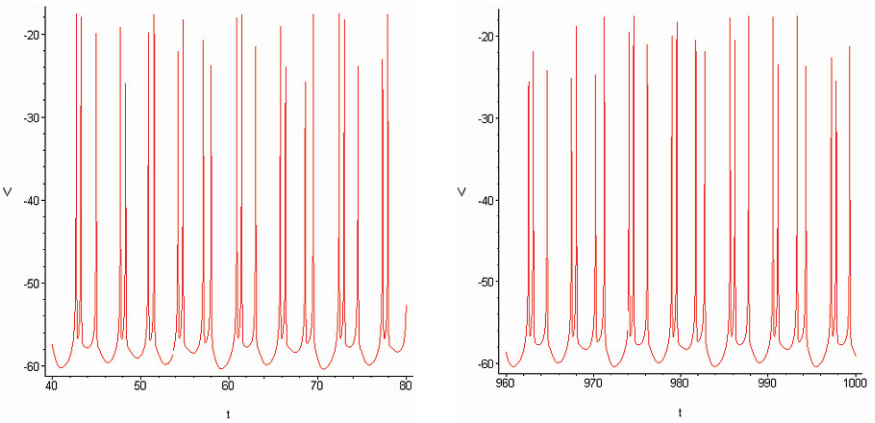

Fig. 23.2 Periodic-7 response of β-Rinzel neuron spontaneous firing model with calciumpotassium current constant 26,085 appears after just 52 ms: transient response, and steady state response

of qualitative variation of dynamics resulting from "condensing", fixing the slowly varying parameter (as bifurcation parameter) value in its varying process. For instance, the injured end of a neuron of the mouse is immersed in a solution, and the density of a medicine of this solution varies slowly with time, then, the qualitative variation of firing patterns of neuron, i.e. dynamic bifurcation may occur. Obviously, this process is neither transient state nor the steady state, but a long-term dynamic process, and its neural coding will be very complicate.

Conclusions

In this paper, the emphases are: (1) Not only spike or bursting firing pulses of responses of neuron activities, but also sub threshold oscillation contains the neural information and affect the neural coding. (2) The analysis of neural coding in the transient response is important.

It is expected the consideration of this paper may be of some help to know and find the mechanisms of the transmitting and processing of bio-neural systems.

Acknowledgments This work is supported by grant of National Natural Science Foundation of China, No: 10432010. The author thanks to Mr. Zhifeng Yue for his help in using Maple software.

References

1. Karl J. Friston. Another neural code? Neuroimage, 1997, 5: 213–220.
2. Jos J. Eggermont. Is there a neural code? Neuroscience & Biobehavioral Reviews, 1998, 22 (2): 355–370.

3. Eugene M. Izhikevich. Neural excitability, spiking and bursting. International Journal of Bifurcation and Chaos, 10 (6): 1171–1266.
4. Xu Jian-xue, Gong Yunfan, Ren Wei, Hu Sanjue, Wang Fuzhou. Propagation of Periodic and Chaotic action potential trains along nervous fibers. Physica D, 1997, 100: 212–224.
5. Gong Yunfan, Xu Jianxue, Ren Wei, Hu Sanjue, Wang Fuzhou. Determine degree of chaos from analysis of ISI time series in nervous system: a comparison between correlation dimension and nonlinear forecasting method. Biological Cybernetics, 1998, 78 (2): 159–165.
6. Ren W., Hu S.J., Zhang B.J., Wang F.Z., Gong Y.F., Xu J.X. Period-adding bifurcation with chaos in the interspike intervals generated by an experimental neural pacemaker. International Journal of Bifurcation and Chaos, 1997, 7 (8): 1867–1872.
7. Gong Pulin, Xu Jianxue. Global dynamics and stochastic resonance of forced FitzHugh-Nagumo neuron model. Physical Review E., 2001, 63 (3): 031906-01–031906-10.
8. Rinzel T., Shorman A., Stokes C. Channels, coupling, and synchronized rhythmic bursting activity. In “Analysis and Modeling of Neural System”, eds. Eeckman FH, Kluner Academic Publisher, 1989: 29–45.

Chapter 24
Setting Up New Memories: The Ideal Job for The Mammalian Dentate Gyrus

Gergely Papp and Alessandro Treves

Abstract Most of the core memory operations carried out by the hippocampus may be implemented in the standard cortical circuitry of its CA3 network, largely conserved from pre-mammalian times. We propose that the new mammalian DG-CA3 circuitry has evolved in order to facilitate one particular process: the formation of novel memories, uncorrelated from those already stored on CA3 recurrent connections. Such teaching aid is shown here to be effective not only in producing discrete memory states, but also for establishing quasi-continuous spatial charts.

Keywords Hippocampus · episodic memory · information theory · one-shot learning

Pattern Completion and Retrieval Capacity

David Marr [1] elaborated ideas about the memory role of the hippocampus and took them as the starting point to understand the organization of hippocampal circuits. His theoretical approach has been enormously influential, even though, in detail, it only 'explained' pattern completion by recurrent connections, a prominent anatomical feature of CA3 pyramidal cells [2] but also presumably of the original, pre-mammalian paleocortex. Marr thought in terms of discrete memory states, and he devoted an entire section of his paper to *capacity calculations*, realizing early on how they could be a central contribution of mathematical network models. The model later introduced by John Hopfield [3] proved suitable for such calculation when it was analyzed by Amit, Gutfreund and Sompolinsky [4]. The generic result is that an autoassociative memory network with C recurrent connections per unit can retrieve, i.e. complete, up to

$$p_c \approx 0.2 - 0.3\, C/[a\ \ln(1/a)] \tag{24.1}$$

G. Papp
SISSA – Cognitive Neuroscience, via Beirut 2, 34014 Trieste, Italy
e-mail: papp@sissa.it

R. Wang et al. (eds.), *Advances in Cognitive Neurodynamics*,

patterns of activity, where a is their sparsity value (in the sparse, $a << 1$ regime; see [5]). Marr did not conceive of any interesting role for the dentate gyrus (DG), and he summarily dismissed granule cells as effectively 'extended dendritic trees' for CA3 cells, which he accordingly labeled as *collector* cells.

The Dentate as a Generator of CA3 Activity

With their 1987 review, McNaughton and Morris [6] rekindled interest in the Marr approach by discussing several 'Hebb-Marr' associative memory architectures, including some similar to the Hopfield model, and whether they resembled hippocampal networks. The operation of such models can be more readily analyzed if the memory patterns to be stored are assigned 'by hand', rather than self-organized under the influence of on-going inputs. One can imagine that a system of strong one-to-one connections from another area may effectively 'transfer' a pattern of activity from the other area, where it is determined by some unspecified process, to the associative memory network. McNaughton and Morris took the strong 'detonator' synapses on the MF projections from DG to CA3 as an approximate implementation in the real brain of such one-to-one connections. The distributions of activity to be stored in memory would be effectively generated in DG, perhaps by expansion recoding and then simply *transferred* to CA3. The detonator proposal thus addresses the most salient feature of the mammalian hippocampus, whereas many connectionist hippocampal models, like Marr's, do not really go beyond the reptilian stage.

A Quantitative Analysis

As clarified by Treves and Rolls [7], for the DG to 'impose' a novel pattern of activity onto CA3, it need not transfer its own, and one-to-one connections are not necessary. What matters is that the MF synapses be *strong, sparse*, and *conveying sparse activity* from DG. This is sufficient to effectively select a limited ensemble of CA3 cells to represent a new memory, unrelated to ensembles which are co-activated in other, previously stored memories, and which would tend to be reinstated by the collateral effect. Quantitatively, an associative network of N units can retrieve up to

$$I_{\max} \approx 0.2 - 0.3N \cdot C \text{ bits} \tag{24.2}$$

of total information – cumulating the contribution of all memory patterns – an amount proportional to the number of synapses NC, and which does not depend much on sparsity. This implies that if patterns are uncorrelated, each should contain at least

$$i \approx N\, a\, \ln(1/a) \text{ bits} \tag{24.3}$$

of new information. Efficient use of the CA3 retrieval capacity then requires that its pyramidal units encode this much new information in a pattern of activity. Analytical estimates derived for a simple model with discrete attractor states [7] suggest that this challenge can be met by afferent inputs with the characteristics and strength of the mossy fibers, but not by those, conveyed by the perforant path to CA3, relayed by synapses which are presumably similar to recurrent synapses, but fewer in number. To make full contact with experimental recordings of CA3 activity, and with recent ones of DG activity [8], the argument has to be generalized and applied to models in which CA3 units encode spatial representations, not just discrete attractor states.

The Random Drawing of a Chart

Samsonovich and McNaughton's chart model [9] demonstrated how one could conceive of fixed points organized in *multiple* 2D continuous manifolds, each of which maps the animal position in a distinct environment. The number of such charts, that can be held simultaneously in the network, is limited approximately by the critical value [10].

$$p_{\text{charts}} \approx 0.1\ C / \ln\,(1/a) \tag{24.4}$$

How can such charts be established? As with discrete memories, an important role may be played by ACh modulation, which is thought to suppress recurrent transmission while enhancing plasticity during storage [11]. Storing quasi-continuous arrays of context-dependent position codes poses, however, additional challenges: at short distances the would-be continuous attractors are fragmented [12]; at longer distances they easily collapse; and periodic inputs from grid cells in medial Entorhinal cortex [13] may induce correlation among non-adjacent position codes, expressed as multiple peaks in CA3 fields.

With simulations, one can investigate the emergence of new charts in models with and without a layer modeling the DG. Figure 24.1 shows the results of simulations, in which a model CA3 network was trained as a virtual rat explored a new environment, with model grid cells as its only source of cortical information. The DG layer, if present, is modeled here with single-field granule units and one-to-one detonator synapses to CA3 units, and is active only during training. At testing, DG is turned off, and CA3 cells, activated by the model perforant path and under the influence of recurrent collaterals, both modified during training, show scattered spatial responses before training, self-organizing into smoother fields after training. The DG teaching input modifies, in this simulation, both the perforant path and the recurrent collateral weights, and both contribute to the response properties of CA3 units. As the perforant path, which at testing relays only a partial cue, is made to gradually fade over 10×12.5 ms iterations, towards the end of the iteration cycle the cue is largely completed by the collateral effect. If the useful role of DG inputs is only in establishing new spatial representations in CA3, as in the model of the figure, lesioning DG or blocking MF transmission should have no effect on memory

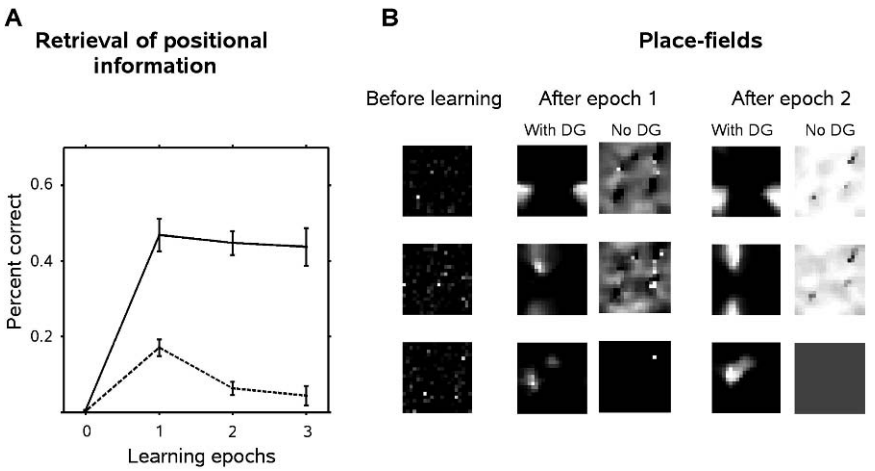

Fig. 24.1 Development of CA3 place field codes with and without a model DG. The percent correct localization afforded by decoding the entire population of 2500 CA3 units increases with the first training epoch (a). Examples of firing rate maps of three model CA3 units are shown before and after $2 \times 10'$ exploration sessions of a new environment (b). Without DG, the fields never develop single peaks, the increase in localization accuracy is smaller (dashed line), and it reverses with successive training epochs. Note that single peaks occurring across the toroidal boundary conditions appear as double when the torus is displayed as a square box

retrieval. This prediction is so far consistent with *behavioral* results obtained in two independent experimental approaches [14, 15].

References

1. Marr, D.: Simple memory: a theory for archicortex. Phil. Trans. R. Soc. Lond. B 262 (1971) 23–81.
2. Amaral, D.G., Ishizuka, N., Claiborne, B.: Neurons, numbers and the hippocampal network. Prog. Brain. Res. 83 (1990) 1–11.
3. Hopfield, J.J.: Neural networks and physical systems with emergent collective computational abilities. Proc. Natl. Acad. Sci. USA 79 (1982) 2554–2558.
4. Amit, D.J., Gutfreund, H., Sompolinsky, H.: Statistical mechanics of neural networks near saturation. Ann. Phys. (N.Y.) 173 (1987) 30–67.
5. Treves, A., Rolls, E.T.: What determines the capacity of autoassociative memories in the brain? Network 2 (1991) 371–397.
6. McNaughton, B.L., Morris, R.G.M.: Hippocampal synaptic enhancement and information storage within a distributed memory system. Trends Neurosci. 10 (1987) 408–415.
7. Treves, A., Rolls, E.T.: Computational constraints suggest the need for two distinct input systems to the hippocampal CA3 network. Hippocampus 2 (1992) 189–199.
8. Leutgeb, J.K., Leutgeb, S., Moser, M.-B., Moser, E.I.: Pattern separation in the dentate gyrus and CA3 of the hippocampus. Science 315 (2007) 961–966.
9. Samsonovich, A., McNaughton, B.L.: Path integration and cognitive mapping in a continuous attractor neural network model. J. Neurosci. 17 (1997) 5900–5912.

10. Battaglia, F.P., Treves, A.: Attractor neural networks storing multiple space representations: a model for hippocampal place fields. Phys. Rev. E 58 (1998) 7738–7753.
11. Hasselmo, M.E., Schnell, E.: Laminar selectivity of the cholinergic suppression of synaptic transmission in rat hippocampal region CA1: Computational modeling and brain slice physiology. J. Neurosci, 14 (1994) 3898–3914.
12. Papp, G., Treves, A.: Continuous attractors come fragmented. Soc. Neur. Abs. (2006) 68.13.
13. Hafting, T., Fyhn, M., Molden, S., Moser, M.-B., Moser, E.I.: Microstructure of a spatial map in the entorhinal cortex. Nature 436 (2005) 801–806.
14. Lassalle, J.-M., Bataille, T., Halley, H.: Reversible inactivation of the hippocampal mossy fiber synapses in mice impairs spatial learning, but neither consolidation nor memory retrieval, in the Morris navigation task. Neurobiol. Learn. Mem. 73 (2000) 243–257.
15. Lee, I., Kesner, R.P.: Encoding versus retrieval of spatial memory: double dissociation between the dentate gyrus and the perforant path inputs into CA3 in the dorsal hippocampus. Hippocampus 14 (2004) 66–76.

Chapter 25
Neural Network Model Generating Symbol Sequence for Songs of Bengalese Finch

Junichirou Kotani, Yasukuni Mori and Ikuo Matsuba

Abstract Bengalese Finch (*Lonchura striata var. domestica*) sings more sophisticated songs than other birds and the grammar of their songs has been found to be described with probabilistic finite state automaton (PFA). In the present paper, we propose a multilayer neural network model that succeeds in reproducing the qualitatively similar symbol sequence by taking into account the memory process. The use of the present method is illustrated for the songs of Bengalese Finch with particular emphasis on issues of input delay that is necessary to obtain the correct grammar. It is found that the grammar obtained from the simulated symbol sequence using the PFA agrees well with the real one.

Introduction

Neurobiology of birdsong started in 1960s and has been studied in more than 60 laboratories. It has now been established that the symbol sequence generated from the songs of Bengalese Finch is described by the PFA [1, 2]. An important point for the previous reports is that the hierarchical structure embedded in the symbol sequence comes from the bird's cerebral nerve system revealed from physiological experiments [3]. Little, however, is rigorously known about the correct role of each nucleus in generating the symbol sequence.

In the present paper, we propose a multilayer neural network model that permits us to study the symbol sequence generated from the birdsongs and helps in understanding the basic ingredients underlying their grammar although the proposed network is a simple one.

J. Kotani
Graduate Course of Advanced Integration Science, Chiba University 1-33 Yayoi-cho, Inage-ku, Chiba-shi, 263-8522 Japan
e-mail: kotani@graduate.chiba-u.jp

R. Wang et al. (eds.), *Advances in Cognitive Neurodynamics*,

Neurobiology of Birdsong

Birdsong consists of syllables separated by brief periods of silence. Each syllable represented by an alphabet shown in Fig. 25.1 is grouped into sequential blocks according to its meaning. Such a sequential block is called *chunk*, and it turn out that the birdsong is considered to be a set of chunks. In general, the collective dynamical behaviors of neural networks emerge from the properties of neurons. From this point of view, it would be interesting to investigate the grammar using artificial neural networks, and check whether the similar grammar is obtained.

Figure 25.2 is a known circuit concerned with production of songs in a bird brain in which RA (Robust Nucleus of the Archistriatum), HVC (High Vocal Center), NIf (Nucleus Interface), etc. are nuclei which are assemblies of neurons. Experiments carried on these nuclei lead to an idea that the birdsong is generated from a hierarchical structure of neural networks in which these nuclei play the follwoing roles:

– RA generates syllables.
– HVC generates chunks from syllables.
– NIf controls the whole system of the song of Bengalese Finch.

Network Model

In this section we propose a simple neural network based on the birdsong control system. Figure 25.3 shows the proposed network in which only the HVC and the NIf are considered since we focus on the sequence generation of the birdsong control

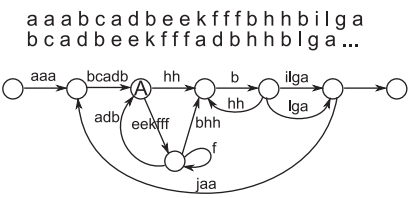

Fig. 25.1 Example of a structure of chunks obtained from syllables

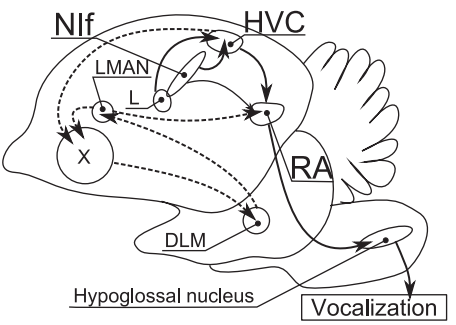

Fig. 25.2 Circuit concerned with production of birdsongs

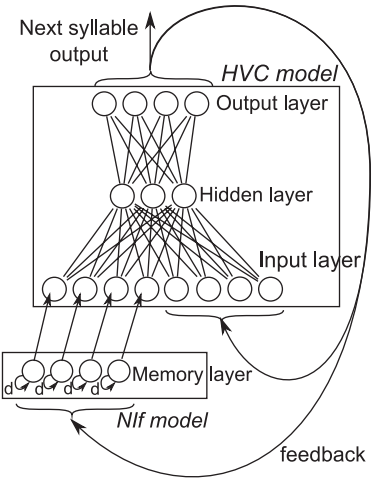

Fig. 25.3 Schematic diagram of the proposed network

system and the RA is considered to be responsible only for the transformation of the signals from HVC to motor signals controlling the vocalization of syllables.

This network is derived based on the following assumptions:

1. The HVC is assumed to play a role to generate a signal pattern that represents a syllable as a response to a previously input syllable fed back from the ears.
2. The NIf is assumed to store some previously vocalized syllables and to send a signal to HVC, which gives complexity to the songs of Bengalese finch (It is well shown that damage to NIf results in structural changes embedded in symbol sequence [3]).

From the first assumption we model the HVC based on a multilayer perceptron (MLP) [4]. The MLP is fed a previously generated syllable together with a signal stored in the NIf. As a response of these signals the MLP outputs a next syllable that is thus fed back to the NIf and HVC through the ears. From the second assumption we introduce the NIf that is a layer composed of self-feedback neurons. The self-feedback has a fixed weight $d(0 \leq d \leq 1)$ which represents a degree of decrease in memorizing of incoming signals. The dynamics of the network is thus defined by the following equations:

$$\mathbf{O}_{t+1} = \varphi\Big(W_{o-m} \cdot \varphi\left(W_{m-i} \cdot [\mathbf{I}_t^T \ \mathbf{C}_{t-1}^T]^T\right)\Big),$$
$$\mathbf{C}_t = d\mathbf{C}_{t-1} + \mathbf{I}_t,$$

where $\mathbf{I}_t$ is an input vector representing a syllable at time t, $\mathbf{O}_t$ is an output vector, W_{m-i} and W_{o-m} are weight matrices of the MLP, $\varphi(\cdot)$ is a activation function (we use a sigmoid function here), and $\mathbf{C}_t$ is a memory process at time t, namely, it represents an amount of stored syllables at time t.

Simulation

To investigate the ability of the proposed network, we performed a numerical simulation. The steps of the simulation are as follows:

1. Generate sequences of symbols according to the automaton shown in Fig. 25.1.
2. Let the network learn the sequences by employing the back propagation method. The binary encoded data are presented to the network in a continuous stream, whose input, hidden, and output layer are configured as set of 26, 8, and 13 units. Output neurons are fed back to the input layer as well as to the NIF network to extract an inherent structure in sequence.
3. The trained network is used to generate sequences of the symbols as follows.
   (a) Input the starting symbol of the grammar 'a' at first.
   (b) The network outputs a next symbol to 'a'.
   (c) The output symbol is in turn fed back to the network.
   (d) The network outputs a second symbol in response to the input of the first output symbol.
   (e) Repeat (a)–(d) until we have an enough number of symbols for the later analysis.
4. Construct an automaton from the generated sequence by employing the Variable-length N-gram model [5, 6] by regarding a history of symbol sequence of variable length as a state of the automaton. Histories having similar probability distributions of preceding symbols are considered to be in the same state. Similarity of probability distributions is measured by the Kullback-Leibler divergence

$$D(P(\cdot|\alpha)||P(\cdot|\beta)) = \sum_{w} P(w|\alpha) \log \frac{P(w|\alpha)}{P(w|\beta)}, \tag{25.1}$$

where α and β are symbol sequences, w is a symbol, and $P(w|\alpha)$ is a conditional probability for w provided α.

To give an idea of chunks obtained by the Variable-length N-gram model, we perform simulation by varying the transition probability p at Node A in Fig. 25.1 where the automaton moves to 'hh' with probability p and to 'eekfff' with probability $1 - p$. Other branching nodes are assumed to have fixed transition probabilities. For $p = 0.5$, a typical automaton obtained by the trained network is depicted in Fig. 25.4, which should be compared with the original one illustrated in Fig. 25.1. The resultant automaton yields chunks with probability $q(p)$ as a function of p as shown in Fig. 25.5.

Summary

In the present paper, we proposed a multilayer neural network based on the birdsong control system and let it learn sequences of symbols from which the approximately correct automaton is obrained. After learning the network extracts correlation

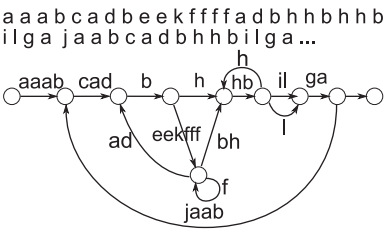

Fig. 25.4 Syllables and chunks obrained by the trained network

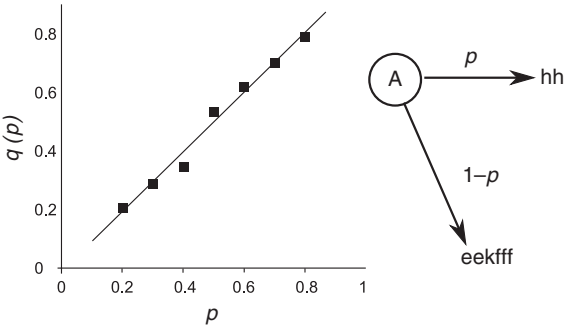

Fig. 25.5 Simulated transition probability $q(p)$ as a function of p

between successive symbols that is enabled by using a history of symbols. It can be said that songs of Bengalese Finch might be produced by combining two network modules, (1) memory storing module NIf and (2) symbol transformation module HVC. The results reported in this paper will prove the assumptions described in Section 'Network Model'. To the best of our knowledge, there is no prior theoretical work on this kind of automaton for the birdsongs.

References

1. Okanoya, K.: The Bengalese Finch: A window on the behavioral neurobiology of birdsong syntax. Behavioral Neurobiology of Birdsong, **1016** (2004) 724–735.
2. Honda, E., Okanoya, K.: Acoustical and syntactical comparisons between songs of the White-backed Munia (Lonchura striata) and its domesticated strain, the Bengalese Finch (Lonchura striata var. domestica)(Biochemistry). Zoological Science, **16** (1999) 319–326.
3. Hoshino, T., Okanoya, K.: Lesion of a higher-order song nucleus disrupts phrase level complexity in Bengalese finches. Neuroreport, **11** (2000) 2091–2095.
4. Simon, H.: Neural Networks: A Comprehensive Foundation. Prentice hall (1999).
5. Dana, R., Yoram S., Naftali, T.: The power of amnesia: Learning probabilistic automata with variable memory length. Machine Learning, **25** (1996) 117–150.
6. Kita, K.: Computation and Language Volume 4: Probabilistic Language Model. University of Tokyo Press (in Japanese) (1999).

Chapter 26
A New Method for Characterizing the Variability of the Spike Trains

Ying Du, Qi-Shao Lu and Shi-Min Wang

Abstract Characterizing the pattern of a spike train is essential to the study of variability in neuroscience and genetic sequences in molecular biology. In neuroscience, traditional methods for sequence comparisons rely on the mean spike count and its variance measured in short time windows. A new method for encoding patterns of spike train is introduced for characterizing features of neural spike trains. This new method is applied to investigate the variability of responses to stimuli and is more effective compared with other methods.

Keywords Spike train · neural system · stimuli · response

Method

In paper [1], a new method was approached to quantify the temporal structures of spikes in neural firing. A recorded neural spike train was characterized by a bounded variation function $q(t)$ called response function as follows:

$$q(t) = i, \quad t_i \leq t < t_{i+1}, \quad (i = 1, 2, \ldots\ldots) \tag{26.1}$$

where t_i is the firing moment of the i-th spike, $q(t)$ is a monotonic function of time. It can completely reflect the temporal rhythm structures (or patterns) of spikes and the information of stimuli. Then the Newtons methodology is adopted to investigate the first and second derivative of the response function defined as follows:

The First Formal Derivative

$$Fr = \frac{1}{N_0 - 1} \sum_{i=1}^{N_0 - 1} \frac{1}{ISI(i)} \tag{26.2}$$

Q.-S. Lu
School of Science, Beijing University of Aeronautics and Astronautics, Beijing 100083, China
e-mail: qishaolu@hotmail.com

R. Wang et al. (eds.), *Advances in Cognitive Neurodynamics*,

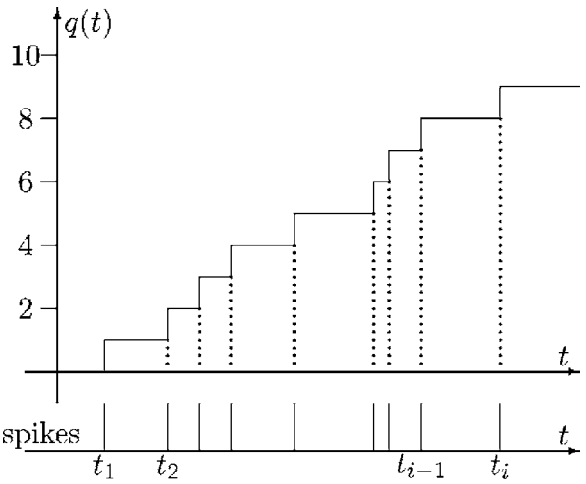

Fig. 26.1 The response function of a spike train

where N_0 is the total spike count in a time bin T. *Fr* is an averaged firing rate over [0 T]. Mathematically, it measures whether spikes gather together or separate each other within interval.

The Second Formal Derivative

$$Sr = \frac{1}{N_0 - 1} \sum_{i=1}^{N_0 - 1} \frac{Fr(i+1) - Fr(i)}{2min[ISI(i), ISI(i+1)]} \tag{26.3}$$

It characterizes the spike train by describing the change of two adjacent *ISIs*, indicates the increasing/decreasing tendency of *ISIs*.

The Integration of Response Function

The area increment from t_0 to $t_0 + T$ can be expressed as:

$$Ar = q(t_0) \cdot T + q(t_0 + T) \cdot (T - t_{N_0}) + \sum_{k=1}^{N_0 - 1} k \cdot ISI(k) \tag{26.4}$$

where N_0 is the total number of spikes fired within the interval $[t_0, t_0 + T]$, t_{N_0} is the firing moment of the last spike.

Characterize the Spike Train Variability to Stimuli

Old Measure

Kreiman and Krahe [2] used two methods to quantify inter-trial spike train variability in response to repeated presentations of the same RAM stimulus. First, they computed the spike count variance as a function of the mean spike count in fixed time windows of length T. But this method did not offer a reliable indication of spike train variability. Then they used a measure of spike timing jitter by using the notion of spike train distances introduced by Victor and Purpura [3]. This measure of variability is obtained by computing an average distance between spike trains obtained in response to the same random electric field AMs(RAMs). This measure was widely applicable to neuronal responses, irrespective of the type of stimuli used, but the choice of the spike moving cost q is so discretional, this measure seemed too intricate.

New Method

First, we use a model of Poisson neuron to produce spike trains. The properties of the model random threshod determine the variability of the resulting spike trains, and the mean voltage threshold determines the mean firing rate of the model [4].

The upper panels of Fig. 26.2, each raster of spikes (10 per panel, 500 ms long) illustrates the range of responses to repeating RAMs recorded under a variety of stimulus conditions and mean firing rates. They represent different spike trains of a Poisson neuron belonging to the same statistical ensemble, which satisfies the assumption of stationary and ergodicity.

We find that spike trains exhibit a broad range of variability when the parameters of stimulus change. A clear locking of the responses to the stimulus is usually observed at high firing rate (mfr $>$ 100 spike/s) and cutoff frequencies(f_c $>$ 40 Hz) (Fig. 26.2, upper panels of b and c). Decreasing the cutoff frequency or the mean firing rate tends to decrease the reproducibility of the spike occurrence times. We can see from the figure that at low firing rates (mfr $<$ 80 spike/s), P-receptor afferent responses do not show clear trends of change in reproducibility with stimulus parameters. (Fig. 26.2, upper panels of a and d). These preliminary observations suggest that the variability across the trials of Poisson neuron spike trains, which is depended on stimulus parameters as well as on the mean firing rate of the units.

Then we use two formal derivatives and integration of response function to characterize the variability of spike trains. From the lower panels of Fig. 26.2, when the spike trains are locking to the stimuli (b and c), the corresponding values of characteristic variables are close too, but when the patterns of spike trains are widely disorder(a and d), corresponding values also have large fluctuation.

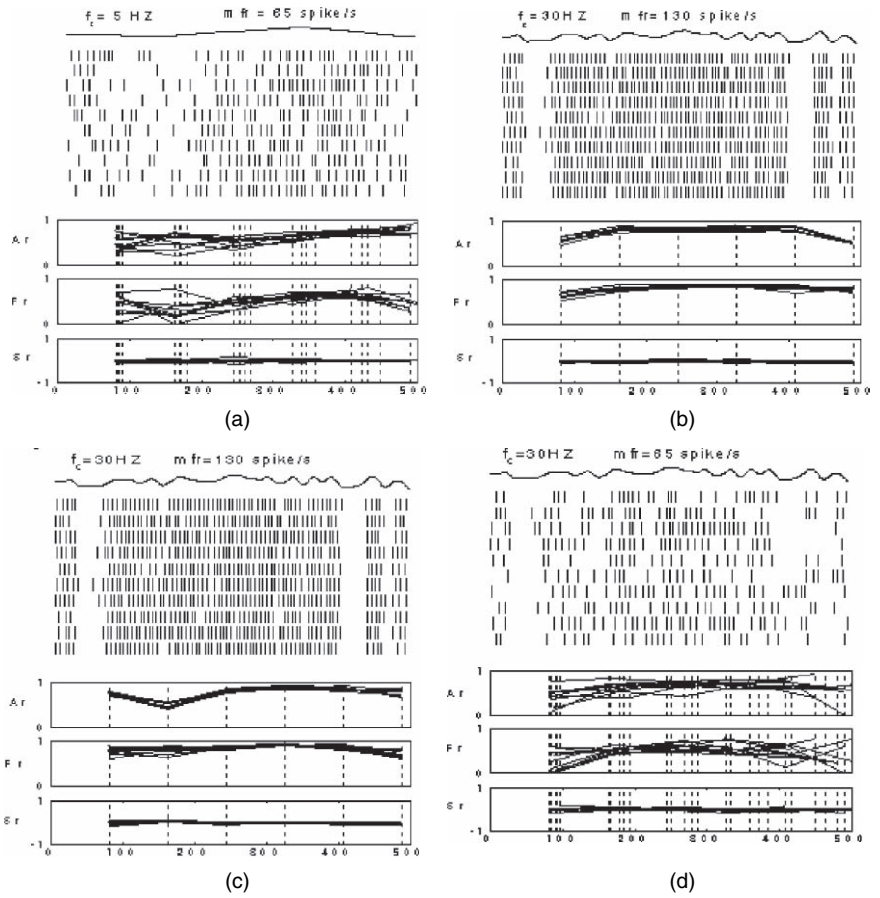

Fig. 26.2 The features of spike trains can be expressed by three characterizing variables. The variability of spike trains to the stimulus can also be reflected

Conclusions

In conclusion, a method is presented to quantify spike trains with a group of variables based on characterizing exact temporal structures of *ISI* series. The work dealing with spike trains can be transformed to treat a group of data defined at sequential moments. This method is used to quantify the variability of spike trains reflected different stimuli. It is seen that this method can characterize the variability more conveniently through three variables of the response function due to their straightforward and intuitionistic quality. If these variables are regarded as the discrete time history of neural response, this quantification leads to a potential way of relating spike trains to dynamic stimuli for searching what aspects of stimulus are encoded in the spike train.

Acknowledgments This work was supported by the National Natural Science Foundation of China (No. 10432010 and 10672006).

References

1. Wang S.M., Lu Q.S., Du Y.: A method for quantifying temporal and spatial patterns of spike trains, Lect. Notes. Comput. Sci. **3610**(2005)480–489
2. Kreiman G., Krahe R., Metzner W., Koch C., Gabbiani F.: Robustness and variability of neuronal coding by amplitude sensitive afferents in the weakly electric fish eigenmannia. J. Neurophysiol. **84**(2000)189–204
3. Vicyor J.D., Purpura K.P.: Nature and precision of temporal coding in visual cortex: a metric-space analysis. J. Neurophysiol. **76**(1996)1310–1326
4. Koch C., Segev I.: Method in neuronal modeling: from ions to networks. MIT Press, Cambridge (1998)

Part II
Mesoscopic Cognitive Neurodynamics; Transitions Between Levels

Chapter 27
Proposed Renormalization Group Analysis of Nonlinear Brain Dynamics at Criticality

Walter J. Freeman and Tian Yu Cao

Abstract Perception is characterized by the formation of spatiotemporal patterns of neural activity that embody mental categories of the material events provided by the senses. The patterns are constructed by modifications of the background activity, which is maintained and self-regulated at criticality, such that all frequencies and wavelengths coexist in neural activity. Patterns form when a null spike in the Rayleigh noise, which is generated by mutual excitation coincides with the sensory-selected activity from a Hebbian nerve cell assembly from past learning that is mobilized by the limbic system. The neural mechanisms of the phase transition that mediates perception may be subject to analysis in terms of renormalization group theory by systematic segmentation of the temporal spectra of various measures of brain activity.

Keywords Action-perception · dissipative structure · EEG · non-equilibrium thermodynamics · phase transition · renormalization · self-organized criticality

Introduction

The central process in perception is the mental construction of categories formed inductively over repeated sensory samples taken in the material world. The subset of equivalent microscopic sensory receptors that is activated by each sample is incomplete and never twice identical, even if the stimulus is invariant, so material events are unknowable. The features of each material sample are transduced into generator potentials in the receptors and conveyed by action potentials in serial neurons to each primary sensory area in the cerebral cortex. The impact of the sensory-derived action potentials results in representations of the stimuli by the microscopic firing of cortical neurons. Thereafter in each sensory area two or three unimodal mesoscopic activity patterns in frames [1, 2, 3, 4] emerge in rapid succession by interactions

W.J. Freeman
Department of Molecular & Cell Biology, University of California at Berkeley, CA 94720, USA
e-mail: dfreeman@berkeley.edu

R. Wang et al. (eds.), *Advances in Cognitive Neurodynamics*,

among cortical and subcortical neurons. These frames are followed by two or more macroscopic frames that are synchronized across all sensory areas and the limbic system [5]. The mesoscopic unimodal categorical patterns and subsequent macroscopic multimodal conceptual patterns are continually updated with each new sample, which is taken by limbic controls of sniffs, saccades and whisks, and which is rendered knowable through the cognitive processes of abstraction and generalization. The global patterns are candidates for the neural embodiments of percepts. The aim of this report is to describe the physics of the construction process in perception from the particular to the categorical, the microscopic to the mesoscopic, which constitutes the transposition of matter into mind.

The process is conceived through analysis of observations and measurements of the spatiotemporal patterns in cortical fields of electric (EEG) and magnetic (MEG) potential governed by Maxwell's equations. The fields manifest neural activity that is measured in scales of time and space ranging from microscopic molecules of neurotransmitters in chemical gradients through action potentials (spikes, pulses) measured in μm and ms to mesoscopic local dendritic potentials (waves, ECoG, LFP) and to macroscopic widespread field potentials observed with EEG, MEG and fMRI and measured in s and cm. The formation of each pattern of gradients in potential, spikes and waves requires use by brains of metabolic energy, so the self-organized mesoscopic and macroscopic patterns qualify as the dissipative structures of Prigogine and the order parameters of Haken.

The action-perception cycle of Merleau-Ponty [6] occurs across all space-time scales of brain activity. An intentional act begins at the macroscopic brain level with the intent to collect information from the world by thrusting the body into the environment while predicting the microscopic sensory consequences of that action at the chemical and atomic level and assimilating to them by synaptic changes with learning at the mesoscopic neural level [7]. Brains make hypotheses (predictions) by extrapolating from retrieved memories of knowledge that is stored in the modified synaptic connections that mediate neural interactions. Strengthening of connections in associative learning creates Hebbian nerve cell assemblies that amplify foreground inputs. Habituation to unreinforced input sharpens the assemblies and attenuates background inputs. Each assembly sustains an attractor in cortical dynamics that activates a learned category of perception. The collection of learned inputs that might be expected consequent to an act of observation are predicted by a landscape of attractors. The synaptic changes in the interdigitated cell assemblies support spatiotemporal pattern formation. The patterns are seen in segments (frames) of EEG that sustain phase-locked oscillatory potentials [8, 9] having carrier frequencies in the beta (12–30 Hz) and gamma (30–80 Hz) ranges. The patterns are spatial amplitude modulations (AM) of the common waveform [1, 2]. The processes of forming and accessing the memory stores are mediated by cortical background activity [3]. The predictions of the consequences and the updating of memory stores are by modification of the background activity. Hence background activity offers a key to unlock the enigma of perception. We propose that renormalization group theory [10, 11] can turn the key.

Nonlinear Coupling Among Neurons Creates Background Activity

Cortical neurons have high packing density ($10^4/\text{mm}^3$) and high spatial divergence/convergence (10^4 synapses/neuron), yet sparse connectivity (1% of neurons within the radius of dendritic branches of most neurons (0.1 mm). Cortical neurons are >80% excitatory and <20% inhibitory; >90% of cortical synapses are by axons originating intracortically; <10% originate subcortically from sensory neurons. Therefore, cortical neural interactions are dominated by excitation among excitatory neurons. Each neuron sustains regenerative activity through positive feedback by multisynaptic serial transmission of spikes, so it interacts with its surround, not with any countable neurons in networks. The feedback to a neuron from a single spike by that neuron can be modeled as a modified 1-D diffusion process [12]. Spike formation is limited by refractory periods; each spike triggers a recovery process during which the neuron cannot fire or can only do so with diminished probability. Yet connection densities are so great that neurons maintain self-sustained interactions. The spike trains of single neurons from mutual excitation yield interval histograms that start at zero probability, rise to a peak, and decay exponentially to a non-zero steady-state baseline, so they can be described as modified Poisson processes manifesting random walks. Summation over a local interactive excitatory population (designated KIe [12]) gives a pulse density function of axonal output and a wave density function of dendritic output, each with a Gaussian amplitude density distribution and a $1/f^{\alpha}$ power spectral density (PSD) in log-log coordinates with exponent α ranging between 2 and 3 (brown vs. black noise [13], slopes -2 and -3) depending on the sensitivities of synapses at dendrites (relating mainly to Ca^{++}) and refractory periods (relating mainly to K+) at the trigger zones of axons [12], which relate also to the degree of behavioral arousal, as shown by the pulse-wave relation (Fig. 27.1b).

Owing to these properties the background activity of a KIe population can be described as that of a lattice with such fine grain that it can be treated as a continuum, and its dynamics can be modeled with derivatives given by ordinary differential equations (ODE) [12]. The densities are locally limited by the refractory periods instead of by their thresholds or by inhibitory interneurons. They are globally controlled by neuromodulatory chemicals that are distributed by subcortical nuclei to all areas of cortex in the maintenance of appropriate levels of behavioral arousal and sleep. The continuum of the neuropil is bounded between scales of neurons (1 ms for spike duration, 1 μm for axon diameter) and scales of brains (cortical circumference ~0.5 m, lifespan ~70 years, $10^{13.7}$ neurons and $10^{17.7}$ synapses in each hemisphere). The coupling across scales between ions and spikes is calculated with the Hodgkin-Huxley equations. That between spikes and waves is calculated from the normalized probability of spike firing conditional on the amplitude, time delay and relative frequency of wave amplitude [12]. Sections through the 3-D table of normalized conditional pulse probability density in time and amplitude yield pulse probability waves in designated frequency ranges in time and the sigmoid curve

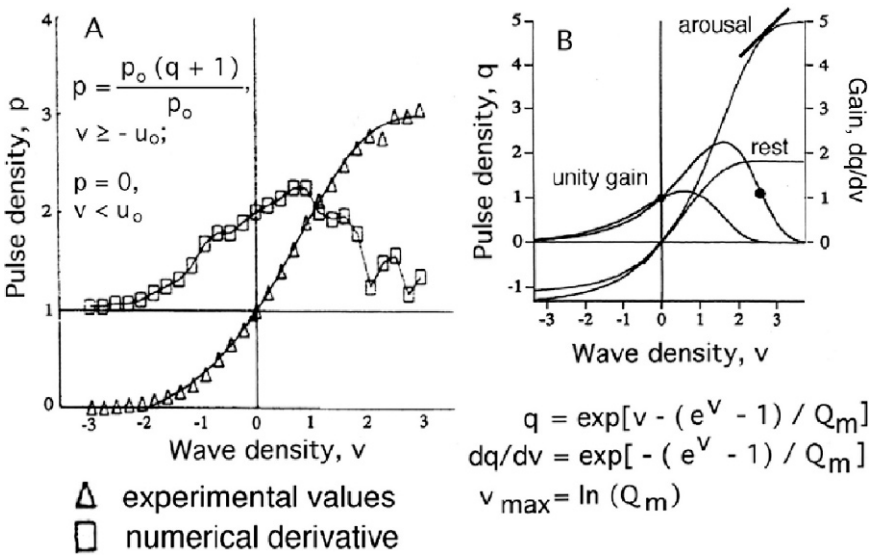

Fig. 27.1 Calculation of the normalized pulse probability of spikes on EEG amplitude gives the sigmoid curve and its derivative (a numerical, b analytic) that represents nonlinear gain under light anesthesia ("rest") and awake ("arousal"). From [3]

(Fig. 27.1) showing the nonlinear population dependence of pulse density on wave density. The lower asymptote is imposed by threshold. The upper asymptote Q_m is imposed by refractory periods. The asymmetry reflects the exponential increase in firing probability of single neurons as the wave amplitude approaches threshold from below, as modeled by the Hodgkin-Huxley equations. Other couplings across EEG frequencies are explored with the high temporal resolution enabled by the Hilbert transform [8, 14].

The derivative of the sigmoid curve with respect to wave density gives the nonlinear part of the forward gain of the two limbs of the feedback loop [12]. The two values of unity gain designate two operating points (B). Unity at high wave density designates the stable operating point of steady-state wave and pulse densities of KIe populations that provide the excitatory bias required by mixed populations (designated KIIei) of excitatory (KIe) and inhibitory (KIi) neuron populations for oscillations in negative feedback. KIIei populations generate the oscillatory patterns observed in the EEG; they have an operating point of unity gain at the lower value of wave density that designates a conditionally stable operating point of mean pulse density P_o and normalized mean wave density $V_o = 0$.

Most neurons spend ~99.9% of their lifetimes in steady state just below their thresholds, firing ~1/s for ~1 ms and mostly randomly with respect to other neurons. This feature and the local statistical continuum enable piece-wise linear approximation of population dynamics near the two operating points by means of ODE, in which the nonlinear gain of each local population is replaced by a coefficient given by the slope (Fig. 27.1b) of the tangent to the sigmoid curve at the

operating point. The KIe population proved [12] to be bistable with a point attractor at zero activity (as in deep anesthesia) and a non-zero point attractor that determines a pole at the origin of the complex plane (zero eigenvalue) for every level of arousal and background activity given by Q_m.

The KIIei population described by piece-wise linearization is also bistable. KIIei maintains a conditionally stable limit cycle attractor at a frequency near 40 Hz, which is represented by a complex conjugate pole pair on the imaginary j-ω axis of the complex plane near 250 rad/s, and which is governed by the KIe point attractor represented by the real-valued pole at the origin [3, 12]. With no intentional engagement into the environment the KIe population goes to a rest state with a point attractor that gives output with normally distributed amplitude and near $1/f^2$ PSD in time (PSD_T) and distance (PSD_X) [2]. The broad spectra document simultaneous genesis of activity densities at all frequencies and wavelengths [3, 10, 11, 15]. Engagement with the environment tends to induce repetitive spontaneous symmetry breaking [16] with transition between a receiving phase and a transitory transmitting phase [2, 3, 12]. Arousal from rest is accompanied by emergence of local peaks in the PSD_T of the EEG peaks in the experimentally observed theta (3–7 Hz), alpha (8–12 Hz), beta and gamma ranges; the PSD_X loses its $1/f^\alpha$ linear relation [1]. These changes reveal the emergence of both local and global spatiotemporal structures that emerge from the background noise that is generated mutual excitation.

A Far-From-Equilibrium Thermodynamic Model of Cortex

The neural systems that support perception may be regarded as essentially scale-free in functioning simultaneously at all levels, ranging from the atomic and molecular events in sensory receptors, trigger zones and central synapses through the microscopic exchanges based in spikes and synaptic potentials in local neural networks, mesoscopic local field potentials, and multiple spike densities to macroscopic brain patterns that are visualized with EEG, MEG and fMRI relating to intentional behaviors. The correlation distances vary widely and may often include much or perhaps all of each cerebral hemisphere for both EEG [17, 18] and MEG [19]. The very broad synchrony over both local and immense correlation distances poses the need for new theory [16, 18] and provides strong justification for proposing the applicability of renormalization group theory. The scales are imposed by observers owing to the necessity for measurement at each level of function. Self-similarity in spatiotemporal patterns is indicated by the power-law distributions found in PSD_T and PSD_X, and also in measures of the durations, diameters, and recurrence intervals of phase patterns [2, 3, 8, 9]. Hence transitions of cortical dynamics between receiving and transmitting phases in the perceptual process take place simultaneously at all hierarchical levels in forms that must be interrelated between levels [10, 11].

A useful framework for assembling the diverse data is provided by treating the brain as a thermodynamic system that is operating far from equilibrium. A convenient starting point is to consider the static phase diagram of water with three phase boundaries, one of which terminates at a critical point (Fig. 27.2a).

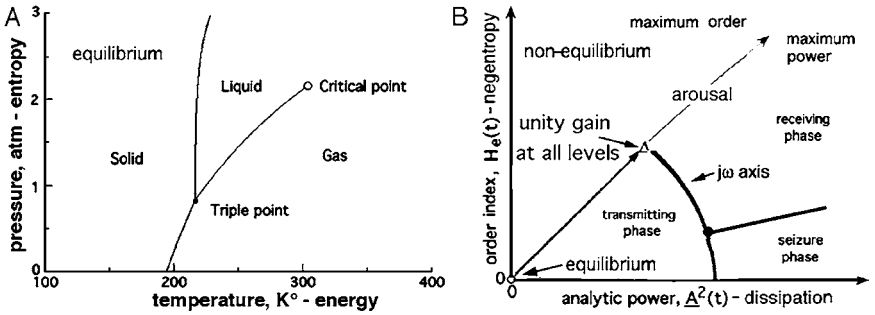

Fig. 27.2 (a) Static thermodynamic phase diagram adapted from [20]. (b) Dynamic non-equilibrium states are represented by fixing the origin of the plot at the critical point and introducing two new dynamic state variables: the rate of increase in order parameter and the mean rate of energy dissipation. Both quantities are calculated from the EEG recorded from 64 electrodes in a high-density array on the surface of sensory cortex. From [3]

This phase diagram holds only for closed systems at equilibrium. Brains are open systems with constant throughput of energy and matter. Chemical energy is delivered by blood flow in the form of glucose, which is converted to high-energy phosphate bonds and stored in glycogen and ATP, and mainly in the maintenance of ionic gradients, which are the most immediate source of potential energy for conversion to kinetic energy in the form of ionic fluxes that yield the observable electric and magnetic fields of Faraday and Maxwell. The mobilization of energy from ionic gradients into electric current is instantaneous compared with the rate of replacement of the gradients by metabolism [21]; the heat from resistance to current is likewise instantly taken up by the watery medium, so the energy transformations are not rate-limiting.

The static portrait in energy vs. entropy is replaced (Fig. 27.2b) by a dynamic portrait with rate of increase in order (negentropy) as a function of rate of dissipation of free energy (power). Derivation of the vectorial order parameter and its scalar index denoted pragmatic information, $H_e(t)$, are described elsewhere [8, 9]. The heat that brains produce by burning glucose is dissipated in blood flow. Brain temperature, pressure, mass and volume are kept within narrow limits, so they are not useful variables. The origin in Fig. 27.2b specifies a critical point at zero ("equilibrium"), when under deep anesthesia the brain waves are flat with no spikes. This state is symmetric with no dissipation by electric current, so it may serve as a vacuum state [16]. Recovery through rest into arousal brings increasing order that appears in a succession of symmetry breakings [16], always based in self-regulated background activity that is supported by metabolism at steady state. The process of awakening and arousal is symbolized by the shift of the critical point upwardly along a diagonal line. The greater is the shift, the greater is the power in the background activity, as shown by the increase in pulse and wave densities from rest to arousal in Fig. 27.1b for the KIe set. Pari passu the rate of increase in order increases.

Testing by impulse input shows that the KI and KIIei sets are self-stabilized at criticality [3, 12]. Analysis of the impulse responses in the near-linear domain

around the critical point is done by measuring the impulse responses with linear basis functions and replacing the nonlinear gain curve (Fig. 27.1) with coefficients from the slopes of tangents fitted to the gain curve at the prevailing operating point. A phase boundary appears in the linear approximation that corresponds to the imaginary jω-axis of the complex plane in the coordinates of frequency in rad/s and decay rate in 1/s. To the left of the axis is the receiving phase and to the right is the transmitting phase. In the thermodynamic graph the phase boundary appears in the coordinates of negentropy and power. The operating point of the KIIei set is revealed by impulse input to cortex that perturbs the amplitude of cortical dynamics outside its self-regulated range. That operating point is seen as a non-zero point attractor that appears as a pair of complex conjugate poles that are located to the left of the jω-axis in the complex plane but to the right of the phase boundary in Fig. 27.3a. Sensory input that also activates the KIe set drives the operating point further in the direction of arousal (Mode 1e) with increased power and increased order. Centrifugal input that bypasses the KIe set shifts the operating point in the direction of increased power and decreased order (Mode 1i). Both types of input move the operating point away from the phase boundary in the direction of enhanced stability and de-amplification.

When test impulse amplitude is fixed to give an impulse response within the self-regulated range of output, repeated samples show "spontaneous variation" along trajectories that converge to a limit cycle attractor [12] with increasing response amplitude (Fig. 27.3a). This finding implies that cortex in the receiving

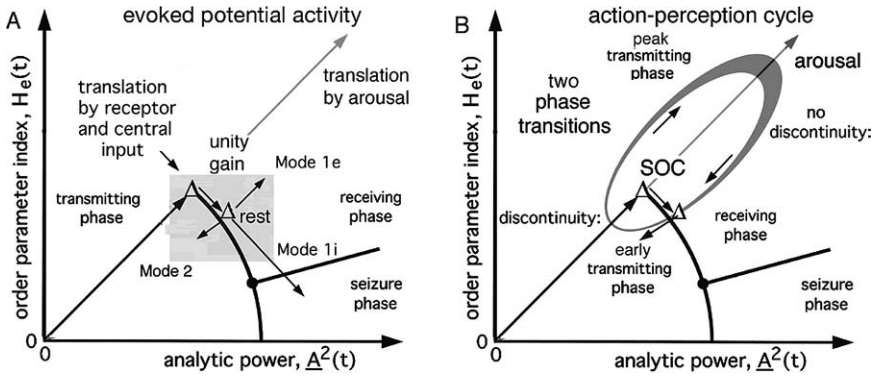

Fig. 27.3 (a) The critical point is translated by arousal toward increased dissipation and order (right upward). The operating point is displaced toward increased dissipation and decreased order by input from other parts of the brain (Mode 1i). The conjoint increase in order and dissipation is replicated by afferent electrical stimulation (Mode 1e). Spontaneous variation leading to symmetry breaking (Mode 2) is attributed in part to the noise fluctuations shown in Fig. 27.4. The gray area shows that part of the complex plane that was used for linear analysis [12]. (b) SOC: self-organized criticality. Early in a phase transition the power and order both decrease. Next order increases; thereafter power increases; after peaking both decrease to the receiving phase, so that the cycle rotates clockwise. The ellipse is a projection into the plane of a helix in time, with 2 to 6 repetitions in an action-perception cycle. From [3]

phase "spontaneously" tends toward the transition boundary (Mode 2), at which the amplitude in response to input undergoes marked amplification. The operating point is translated in the direction of decreased order and decreased dissipation by spontaneous fluctuations in background power and toward the occult limit cycle attractor near 250 rad/s in piece-wise linear approximations using the root locus method [3, 12].

Source of Spontaneous Symmetry Breaking in Rayleigh Noise

The source of the "spontaneous variation" is revealed by the analytic signal from the Hilbert transform. Analytic amplitude in the receiving phase intermittently plunges to near zero ($<10^{-4}$ from peak values) at irregular intervals. The analytic phase is poorly defined, so the spatial standard deviation of phase at multiple sites increases markedly, as shown in Fig. 27.4a of [9] and simulated in Fig. 7, B of [2]. These null spikes resemble vortices: near-zero amplitude and undefined phase; the angular velocity is imposed by the band pass filtering in the beta or gamma range. The null spikes are frequency-specific to pass bands determined by inhibitory feedback delays in local vs. long loops (gamma vs. beta frequency ranges). Return to high amplitude defines the onset of a frame of variable duration, typically longer for beta frames than for gamma frames [1]. The analytic frequency (step-wise temporal phase difference in rad/digitizing step in s) stabilizes to a nearly constant value in each frame; the center value differs on average in successive frames by ± 60 rad/s or more [9]. The spatial pattern of phase values has the form of multiple overlapping radially symmetric phase gradients ("phase cones"), so that the background activity in each cortical area resembles a pan of boiling water [2]. Histograms of the durations and diameters of the phase cones have power-law distributions within limits

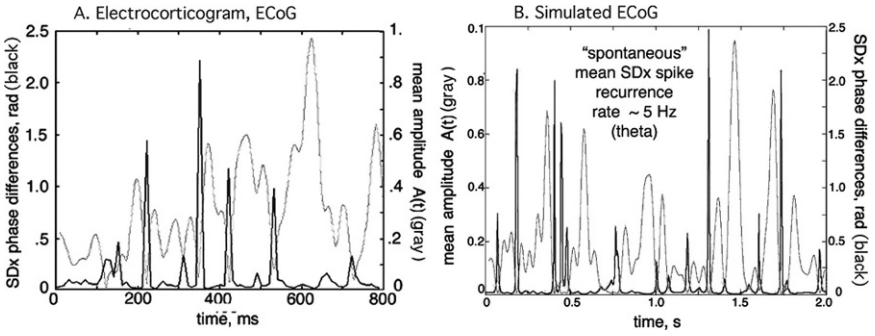

Fig. 27.4 (a) Mean analytic amplitude, $A(t)$, and the spatial $SD_X(t)$ are inversely correlated. The inhibitory feedback acts as a band pass filter on the KIe output, which results in episodic decreases in noise power with amplitude histograms that closely resemble that of Rayleigh noise. The wide range of feedback frequencies is supported by the power-law distribution of feedback distances and delays. (b) Simulation is by band pass filtered $1/f^2$ brown noise that can be generated by summing multiple (e.g., 10,000) time series of random numbers [13]. From [2]

of observability. These overlapping fluctuations at multiple temporal and spatial frequencies manifest the maintenance of cortex in a state of self-regulated criticality.

Phase transitions occurred at null spikes, as shown by the initiation of each transition not with the increase in power expected on the impact of a volley of spikes from a conditioned stimulus but with decrease in power preceding the emergence of a categorizable AM pattern that in turn precedes increased power on termination of the null spike. The categorized frames had durations of three to five cycles of the carrier frequency; their incidence in histograms of frame duration exceeded the expected numbers in the resting power-law distribution, and their carrier frequencies appeared as peaks above the resting power-law PSD. These features showed that the cortical activity during behaviorally correlated EEG frames created dissipative structures that emerged from the background noise. The feature vectors by which AM patterns were categorized came equally from all electrodes of the array measuring each AM pattern; contributions were equal from all electrodes whether their signal amplitudes were high or low. Then the description of each node in the virtual lattice required subsidiary local functions governing learning processes by which the connections of each node with near and remote neighbors were formed, maintained, and updated. The fine details of the innumerable cortical synapses that effected associative learning and related processes of habituation and normalization were inaccessible. They were incorporated into matrices of nonlinear ODE as local averages implemented by modifiable connection matrices serving to coarse-grain the statistical continuum at the limit of observability. The matrix coefficients played the same role in modeling as the gain coefficients replacing the nonlinear sigmoid curve (Fig. 27.1) in the ODE in the procedure for piece-wise linearization: constructing and embedding subsidiary describing functions in matrices of ODE. These techniques employing local averages enabled and facilitated otherwise intractable analyses owing to the immense number of synapses and the sparseness of those modified by the different types of learning.

The cortical events postulated in an action-perception are summarized in Fig. 27.3b. In the receiving phase (A) the rest point (lower right Δ is continually deflected in the direction of diminished dissipation and order by null spikes that simultaneously raise the sensitivity of cortex and the signal-to-noise ratio (Mode 2) [12]. Background input deflects the point away from the phase boundary with increased dissipation and either increased order (receptor input, Mode 1e) or decreased order (centrifugal input, Mode 1i). A phase transition occurs during a null spike only if the receptor input concomitantly contains action potentials that signal a learned stimulus for long enough to ignite a Hebbian nerve cell assembly, which then guides the cortical trajectory into a basin of attraction for the category of the stimulus. When the background activity returns to high power, it bears the AM pattern that is imposed by the attractor to which the cortex converges. In the event that a novel stimulus has sufficient saliency, it ignites an “I don’t know” attractor that elicits a non-specific orienting response by which an aroused animal explores the unknown. An essential step for successful categorization is to normalize each frame by dividing all 64 values by the frame standard deviation [1]. This normalization removes the $1/f^2$ dependence of global amplitude on mean carrier frequency, giving

additional documentation of the self-similarity of AM patterns across the temporal spectrum and the applicability of renormalization group analysis.

The high signal-to-noise ratio in the null spike can explain how a faint whisper, odor or glimpse can capture the cortical readout in literally the blink of an eye. After phase re-setting by a discontinuity and then resynchronization with AM pattern selection, the power and order rise together to a maximum, at which the entire primary sensory cortex broadcasts a stable pattern for 3–5 cycles of the relatively fixed carrier frequency and then returns to the receiving phase with no temporal discontinuity in phase. The cycle repeats two or more times in a helix between the onsets of stimulus and response [3], with expanding time and space scales that include multiple areas of the brain, thereby implementing an action-perception cycle that is completed by assimilation.

Source of Spontaneous Symmetry Breaking in Rayleigh Noise

The property of the cortical dynamics that suggests the suitability of renormalization group analysis is the unity of events across scales. Yet wave packets emergent by phase transition are nearly stationary for ~60–160 ms; the transitions by which they form are shorter by two orders of magnitude; the processes of metabolic energy replenishment are longer by two orders of magnitude, because concentration gradients of ions across membranes drive the dendritic and axonal currents. Hence the coupling of neural events to metabolism and heat dissipation, while essential, is remote, as evidenced by the disparity in scales between EEG/MEG measurements in ms and fMRI measurements in s.

It is the coupling of activities at frequencies across spectra that is most in need of exploration. Given the typical brown noise "$1/f^2$" spectrum [13] in awake resting subjects, a convenient way to segment the spectra for cross-spectral study is to divide them in multiples of 2 [11] (Table 27.1). Supposing that the sample interval is 2 ms for a digitizing rate of 500/s, the Nyquist frequency is 250 Hz. A segmentation of the spectrum that approximates the clinical partitioning in pass bands is given in multiples of the Nyquist frequency.

The opportunity for renormalization group theory opens by analysis of the coupling between bands. The coupling between action potentials and epsilon activity

Table 27.1 Partitioning of the EEG power spectral density

Name	Empirical (Hz)	Geometric (Hz)	Multiples of Nyquist
Epsilon	80–250	100–200	1/2.5–1/1.25
High gamma	50–80	50–100	1/5.0–1/2.5
Low gamma	30–50	25–50	1/10–1/5.0
Beta	12–30	12.5–25	1/20–1/10
Alpha	7–12	6.25–12.5	1/40–1/20
Theta	3–7	3.125–6.25	1/80–1/40

is documented in the chatter of repetitive spike trains in mutual excitation [12]. The coupling between pulse densities and beta/gamma oscillations is documented by calculating pulse probability conditional on wave amplitude [12]. Gamma-high-theta and beta-low-theta coupling have been shown in field potentials from cats and rabbits [1]; beta-theta and beta-alpha coupling have been shown in scalp EEG [14, 17]. These empirical relationships call for theory. Other properties in need of explanation are repeated resynchronization over relatively immense correlation distances; de-amplification of noise-driven activity outside the range of self-regulation; amplification of input in spontaneous null spikes with approach to a limit cycle attractor posing a singularity; and the neural mechanisms by which Hebbian and non-Hebbian modifications of synaptic connectivity support the construction of attractor landscapes. Of special significance here is the Kondo problem, in which very sparse iron impurities at the atomic level in copper modify the macroscopic properties of the metal [10]. While not of great importance in itself, the problem has spawned numerous studies owing to its tractability. The analogy to the effects on cortical dynamics of modified synapses seen as "impurities" enhances the likelihood that renormalization group theory will be useful, if it can be used to model the multiple "impurities" endowed by Hebbian nerve cell assemblies that support the attractor landscapes from which diverse AM patterns or "unitarily inequivalent ground states" [16] emerge through the retrieval of memories from knowledge gained through experience.

References

1. Freeman, W.J.: Origin, structure, and role of background EEG activity. Part 3. Neural frame classification. Clin. Neurophysiol. 116 (5) (2005): 1118–1129.
2. Freeman, W.J.: Origin, structure, and role of background EEG activity. Part 4. Neural frame simulation. Clin. Neurophysiol. 117 (3) (2006): 572–589.
3. Freeman, W.J.: Proposed cortical 'shutter' in cinematographic perception. Invited Chapter in: Neurodynamics of Cognition and Consciousness. Kozma, R. and Perlovsky, L. (eds.): Springer, Heidelberg, (2007) ISBN 978-3-540-73266-2, pp. 11–38.
4. Lehmann, D., Strik, W.K., Henggeler, B., Koenig, T. and Koukkou, M.: Brain electric microstates and momentary conscious mind states as building blocks of spontaneous thinking. I. Visual imagery and abstract thoughts. Int. J. Psychophysiol. 29 (1998): 1–11.
5. Freeman, W.J. and Burke, B.C.: A neurobiological theory of meaning in perception. Part 4. Multicortical patterns of amplitude modulation in gamma EEG. Int. J. Bifurcat Chaos 13: 2857–2866 (2003).
6. Merleau-Ponty, M.: The structure of behavior (Fischer A.L., Trans.). Beacon Press, Boston MA (1942/1963).
7. Freeman, W.J. How brains make up their minds. Columbia U.P., New York (2001).
8. Freeman, W.J.: Origin, structure, and role of background EEG activity. Part 1. Analytic amplitude. Clin. Neurophysiol. 115 (2004): 2077–2088. http://repositories.cdlib.org/postprints/988.
9. Freeman, W.J.: Origin, structure, and role of background EEG activity. Part 2. Analytic phase. Clin. Neurophysiol. 115 (2004): 2089–2107. http://repositories.cdlib.org/postprints/987.
10. Wilson, K.G.: The renormalization group: Critical phenomena and the Kondo problem. Rev. Mod. Phys. 47 (1975): 773–840.

11. Wilson, K.G.: The renormalization group and critical phenomena. Rev. Mod. Phys. 55 (1983): 583–600.
12. Freeman, W.J.: Mass action in the nervous system. Academic Press, New York (1975/2004).
13. Schroeder, M.: Fractals, Chaos, Power Laws. W.H. Freeman, San Francisco CA (1991).
14. Freeman, W.J., Burke, B.C. and Holmes, M.D.: Aperiodic phase re-setting in scalp EEG of beta-gamma oscillations by state transitions at alpha-theta rates. Hum Brain Mapp 19 (4) (2003): 248–272.
15. Linkenkaer-Hansen, K., Nikouline, V.M., Palva, J.M. and Iimoniemi, R.J.: Long-range temporal correlations and scaling behavior in human brain oscillations. J. Neurosci. 15 (2001): 1370–1377.
16. Freeman, W.J. and Vitiello, G.: The dissipative quantum model of brain and laboratory observations. Electronic J. Theoretical Physics 4 (2007): 1–18. http://dx.doi.org/10.1016/j.plrev.2006.02.001.
17. Freeman, W.J., Burke, B.C., Holmes, M.D and S. Vanhatalo, S.: Spatial spectra of scalp EEG and EMG from awake humans. Clin. Neurophysiol. 117 (6) (2003): 1228–1243.
18. Kozma, R. Puljic, M., Balister, P., Bollabás, B, and Freeman, W.J.: Phase transitions in the neuropercolation model of neural populations with mixed local and non-local interactions. Biol. Cybern. 92 (2005): 367–379.
19. Bassett, D.S., Meyer-Lindenberg, A., Achard. S., Duke, T. and Bullmore, E.: Adaptive reconfiguration of fractal small-world human brain functional networks. PNAS 103 (2006): 19518–19523.
20. Blauch, D.N.: Exercises and tutorials in thermodynamics (2006). http://www.chm.davidson.edu/ChemistryApplets/PhaseChanges/PhaseDiagram5.html.
21. Abbot, B.C.: Heat production in nerve and electric organ. J. Gen. Physiol. 43 (1960): 119–127.

Chapter 28
Regulating Cortical Neurodynamics at Different Scales

Hans Liljenström

Abstract In this paper, I review some mechanisms by which cortical neurodynamics may be regulated, at different organisational scales. We use computational methods to describe the relation between structure, dynamics and function of cortical structures, and focus here on the regulatory mechanisms at subcellular (microscopic), cellular (mesoscopic) and network (macroscopic) levels of neural systems. The aim is to gain a better understanding of the neural mechanisms responsible for changes in the neurodynamics, which include phase shifts in the cellular spiking patterns, as well as in the EEG dynamics.

Keywords Neurodynamics · neuromodulation · ion channel · network connectivity · EEG · computational model

Introduction

It should be important for the nervous system of any organism to rapidly be able to change its dynamics, in order to cope with rapid changes in the environment. Such changes at time scales of fraction of seconds to minutes could be imagined take place at different levels of neural organization: subcellular (microscopic), cellular (mesoscopic), network (macroscopic), and systems (super macroscopic) levels. It could involve the relative composition of ion channels in the membranes of neurons, the synaptic efficacy and the neuronal excitability, spontaneous activity of certain neurons, and possibly ephaptic effects due to electromagnetic field effects. Most of these effects would be due to some neuromodulators, or some collective network or system effects (top-down), as a reaction to some external stimuli or change of internal state of the animal.

The functional significance of this behavior is, however, yet to be ascertained. Supposedly, the dynamics of certain cortical structures, and perhaps of the brain as a

H. Liljenström
Department of Biometry and Engineering, SLU, P.O. Box 7032, SE-75007 Uppsala, Sweden and Agora for Biosystems, Box 57, SE- Sigtuna, Sweden
e-mail: hans.liljenstrom@bt.slu.se

R. Wang et al. (eds.), *Advances in Cognitive Neurodynamics*,

whole, reflect an evolutionary pressure to make the neural information processing as efficient as possible [1, 2]. The oscillations could amplify weak signals and sustain an input pattern for more accurate information processing, and the chaotic behavior could increase the sensitivity in initial, exploratory states.

Neurodynamical Regulation

The complex neurodynamics of cortical systems can be regulated by various mechanisms acting at different levels, influencing neuronal excitability, spiking pattern, or synaptic transmission. These regulatory mechanisms result in a balance between stability and flexibility ensuring an efficient information processing [1]. We use a computational approach as a complement to experimental methods in understanding the complexity of biological systems and processes. For the studies presented here, we have used different kinds of models, both of the three-layered paleocortex (olfactory cortex and hippocampus), and neocortex, with either population type or spiking network units.

Ion Channel Composition

The density of voltage-gated ion channels varies between different neurons and varies dynamically in a single neuron. These variations can affect the single cell activity, and possibly also the network neurodynamics. Neurons can supposedly alter their active channel density configurations in response to some cue, resulting in a switch between oscillatory regions (see [2], and references therein), but a change could also be due to some externally applied drug. Selective blocking or activation of ion channels, an important principle in the action of certain anaesthetics and anti-epileptics, will have different effects on the oscillatory activity, depending on the relative selectivity and the intrinsic activity of the active network. Likewise, up-regulation of Na and K channels will induce different activity patterns, depending on their relative densities. Different combinations of sodium and potassium permeability constants, P_{Na} and P_K, cause different oscillatory behaviours at constant stimulation. There are also regions in the $P^*{}_{Na}/P^*{}_K$ plane where there are no oscillations at all.

In our computational study [3], we have focused on network effects of variations in the density of certain ion channels in single cells, and investigated the relation between ion channel density (at the single neuron level) and global connectivity (at the network level) in a network of Frankenhaueser-Huxley neurons. We show how parameters at both of these levels can have similar effects on the global dynamics. More specifically, we have studied how the dynamics of a simple excitatory/inhibitory neural network model depend on the channel densities in single neurons and on the synaptic strengths, and we demonstrate the importance of neural properties in a network consisting of different neuron types.

Our simulations have shown that the network dynamics can change specifically in response to variations in the density of ion channels and/or network connectivity.

We have thus demonstrated that similar qualitative changes in the global dynamics can be obtained by mechanisms at two different levels in the system; either by regulating the K channels in a subsystem of neurons, or by altering the global connection strength.

Neuromodulatory Effects on Excitability and Synaptic Transmission

Neuromodulators, such as acetylcholine, influence the neurodynamics of cortical structures. These neuromodulatory effects may play an important role in setting the functional properties of cortical regions. In the piriform (olfactory) cortex, application of carbachol enhances the persistence of gamma-frequency oscillations in response to stimulation of the lateral olfactory tract and gradually induces a state of high amplitude theta rhythm oscillations [4]. Also in the hippocampus, there is strong evidence for cholinergic induction of theta rhythm oscillations. Understanding the role of acetylcholine in cortical oscillations requires that these influences be linked to specific neuromodulatory effects of acetylcholine at the cellular level.

We have used our computational model of paleocortical oscillatory dynamics for examining how the neuromodulatory effects of acetylcholine, by suppressing neuronal adaptation and synaptic transmission, influence cortical oscillatory properties [5]. We have shown how implementation of cholinergic modulation within the model can simulate effectively the effects of cholinergic modulation on the response to shock stimulation of the lateral olfactory tract (LOT), the development of high amplitude theta rhythm oscillations in vivo, and the development of theta rhythms in cortical brain-slice preparations. This work suggests that induction of theta oscillatory dynamics in some preparations could depend upon the time constant of adaptation rather than the time constants of inhibition.

Spontaneous Neuronal Activity (Noise)

Noise appears at the subcellular (microscopic) and cellular (mesoscopic) levels, but it is uncertain to what degree this noise is affecting the network (macroscopic) level. Irregular (high-dimensional) chaotic-like behavior could be generated by the interplay of neural excitatory and inhibitory activity at the network level. This activity could also contain noise, but in contrast to a chaotic dynamics, which can be controlled and shifted into oscillatory states, noise is not equally controllable and cannot shift into completely different dynamics. However, a varied noise intensity would be comparable to a change in base line activity.

Using our cortical network models, we show that fluctuations can result in state transitions [6, 7]. An increased noise level in all network units can result in a transition from a stationary to an oscillatory state, or vice versa, or alternatively, in a shift between two oscillatory states. Even if only a few network units are noisy (have a high intrinsic random activity) and the rest are quiescent, coherent oscillatory

activity can be induced in the whole network under certain circumstances. The onset of global oscillatory activity depends on, for example, connectivity, the noise level, the number and density of noisy units, and the duration of the noise activity. The location and spatial distribution of these units in the network is also important for the onset of oscillations. If the noisy units are separated beyond a certain distance, or if the noise level is too low, no oscillations occur. Likewise, no transition to global oscillations occurs if the noise "frequency" is too low. This is a clear example of how microscopic events can be amplified and give rise to macroscopic and coherent oscillations in the entire network.

Attention Modulated Neuronal Synchronization

Recently, we have developed a neural network model of the primary visual cortex, to investigate cellular and network mechanisms underlying some recent analytical results from visual attention experimental data [8]. We use our model to simulate findings that attention to a stimulus causes increased gamma-frequency synchronization in the superficial layers, and increased beta-frequency synchronization in the deep layers. Our computer simulations suggest that different attention modulation effects on the oscillations at superficial and deep layers are related to the different functional roles of the neurons, as well as to their connection circuitry in different layers for visual signal discrimination, selection, amplification, and integration.

Conclusions

With computational models of cortical neural networks we have shown that changes at cellular or synaptic levels can, under certain circumstances, have effects at the network level. For example, a change in neuronal excitability or spiking pattern, as well as in the synaptic efficacy, can result in the overall network dynamics, causing a shift between various oscillatory or chaotic modes. The mechanisms discussed above result in a more efficient information processing, primarily expressed as a faster and/or more accurate response to an external input pattern. We believe these results shed new light on the interaction between processes at different neuronal scales, linking microscopic molecular events to macroscopic cortical dynamics and cognitive functions and consciousness levels.

References

1. Liljenström, H.: Cognition and the Efficiency of Neural Processes, In: Århem, P., Liljenström, H., Svedin, U. (eds.): Matter Matters? On the Material Basis of the Cognitive Activity of Mind. Springer, Heidelberg (1997) 177–213.

2. Århem, P., Liljenström, H.: Fluctuations in Neural Systems: From Subcellular to Network Levels. In: Moss, F., Gielen, S. (eds.): Handbook of Biological Physics: Neuro-Informatics and Neural Modelling. North-Holland, Amsterdam (2001) 83–129.
3. Halnes, G., Liljenström, H., Århem, P.: Network Dynamics Dependence on Connectivity and Ion Channel Density. BioSystems 89 (2007) 126–134.
4. Biedenbach, M.A.: Effects of Anesthetics and Cholinergic Drugs on Prepyriform Electrical Activity in Cats. Exp. Neurol. 16 (1966) 464–479.
5. Liljenström, H., Hasselmo, M.E.: Cholinergic Modulation of Cortical Oscillatory Dynamics. J. Neurophysiol. 74 (1995) 288–297.
6. Liljenström, H.: Global Effects of Fluctuations in Neural Information Processing. Int. J. Neural Systems **7** (1996) 497–505.
7. Basu, S., Liljenström, H.: Spontaneously Active Cells Induce State Transitions in a Model of Olfactory Cortex. BioSystems 61 (2001) 57–69.
8. Gu, Y., Liljenström, H.: A Neural Network Model of Attention-Modulated Neurodynamics. Cogn. Neurodyn. 1 (2008) 275–285.

Chapter 29
A Thermodynamic Model of the Action-Perception Cycle in Brain Dynamics

Walter J. Freeman

Abstract Computational models of brain dynamics fall short of performance in speed and robustness of pattern recognition, especially in detecting minute but highly significant pattern fragments. A novel model uses the properties of thermodynamic systems operating far from equilibrium. Such systems construct order by dissipating energy. Conditioned stimuli in reinforcement learning establish categories of patterns in cortical connectivity that create phase domains. Retrieval of a selected category of stored knowledge is by phase transition that is induced by a conditioned stimulus. The key property is cortical background noise, which is simulated by band pass filtering brown noise ($1/f^2$) in the beta (12–30 Hz) or gamma (30–80 Hz) ranges. The noise displays aperiodic null spikes at which analytic amplitude approaches zero. These events resemble vortices. Phase transitions in recall occur at null spikes owing to high signal/noise ratio in the presence of even very weak activity evoked by conditioned stimuli.

Keywords Action-perception cycle · dissipative structures · ECoG electrocorticogram · non-equilibrium thermodynamics · phase transition · reinforcement learning · self-organized criticality

Introduction

Cognitive neurodynamics describes the process by which brains direct the body into the world and learn by assimilation from the sensory consequences of their actions. Repetition of the process constitutes the action-perception cycle by which knowledge is accumulated in increments, each new step being provided by a frame of input in each of the sensory cortices. The expanding knowledge base is expressed in attractor landscapes in each of the cortices. The memory store is based in a rich hierarchy of landscapes of increasingly abstract generalizations. At the base in the first step of the acquisition of new knowledge is the landscape of attractors for the

W.J. Freeman
Department of Molecular & Cell Biology, University of California at Berkeley, CA 94720, USA
e-mail: dfreeman@berkeley.edu

R. Wang et al. (eds.), *Advances in Cognitive Neurodynamics*,

primary categories of sensory stimuli in each modality, for example, the repertoire of odorant substances that an animal can seek, identify, and respond to at any one stage of its experience. Each attractor is based in a nerve cell assembly of cortical neurons that have been pair-wise co-activated in prior Hebbian learning. Its basin of attraction is determined by the total subset of receptors that has been accessed during learning. Convergence in the basin to the attractor gives the process of abstraction and generalization to the category of the stimulus. This categorization process holds in all sensory modalities. The convergence and holding of a cortical state by an attractor provides a frame that typically includes the entire primary sensory cortex and lasts about a tenth of a second. The action-perception cycle includes 3–5 frames plus transition times between frames, giving repetition rates in the theta range (3–7 Hz).

The aim of cognitive neurodynamics is to model the cycle. There is no question that brains are open thermodynamic systems operating far from equilibrium. Brains burn glucose to store glycogen and high-energy adenosinetriphosphate (ATP); they dissipate free energy in driving ionic currents that create the electric and magnetic fields and mediate the action-perception cycle. Brain imaging techniques such as fMRI are indirect measures of metabolic dissipation of free energy, relying on secondary increases in blood flow and oxygen depletion. The dendrites dissipate 95% of the metabolic energy in summed excitatory and inhibitory ionic currents; the axons use only 5% in action potentials that carry the summed output of dendrites by analog pulse frequency modulation. The aim of this report is to show how dendritic potentials recorded as electrocorticograms (ECoG) or electroencephalsograms (EEG) can be used to describe brains as thermodynamic engines that produce mind and behavior.

Thermodynamic Diagram of States from Dendritic Potentials

Examples of cognitive brain dynamics are drawn from the olfactory system, which is the simplest and phylogenetically the precursor of the other sensory systems. Asleep, at rest and engaged with the environment the work of dendrites is revealed by robust background activity with Gaussian amplitude distributions and canonical $1/f^2$ 'brown noise' power spectra. Amplitude increases with arousal (Fig. 29.1a). Oscillations occur in the gamma range (30–80 Hz) in bursts triggered by inhalations at frame rates in the theta range (3–7 Hz). In the presence of learned odorant substances the gamma waves synchronize over the olfactory bulb and carry one of a set of amplitude modulation (AM) patterns. The patterns are recorded with 8×8 electrode arrays and plotted as points in 64-space. Projection into 2-space reveals clusters that reflect the underlying attractor landscape (Fig. 29.1b).

The bulb is bistable, having a receiving phase during which the landscape is latent, and a transmitting phase during which the landscape is brought on line by the sensory receptor input during inhalation. Selection by sensory input of one of the basins of attraction precipitates spontaneous symmetry breaking [3] in the form

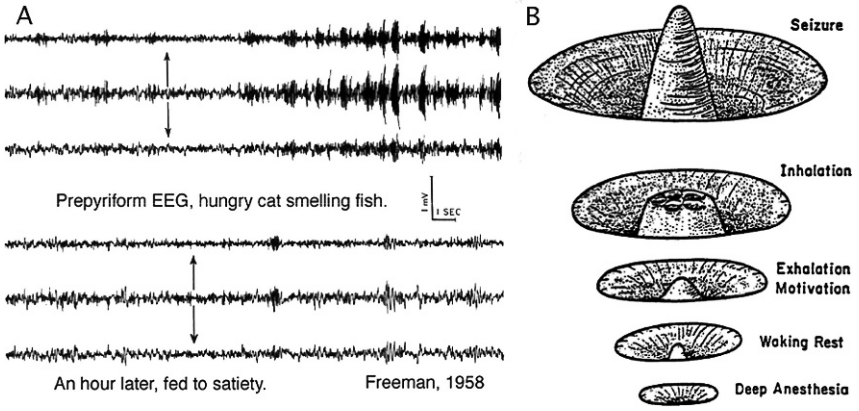

Fig. 29.1 (a). Cat olfactory cortical ECoG [1]. (b) Olfactory attractor landscape. From [2]

of a phase transition from the receiving phase to the transmitting phase. During exhalation another phase transition returns the bulb to the receiving phase. These properties are schematized by adapting the phase diagram for water (Fig. 29.2a), which is the static relation between energy and entropy at equilibrium, to the relation (B) between the rate of increase in order (negentropy) and power (rate of energy dissipation). The order parameter is indexed mainly by the inverse of the Euclidean distance between successive digitizing steps in 64-space ($H_e(t)$); a small step indicates a high degree of order. Power is estimated from mean square analytic amplitude, $A^2(t)$, that is derived applying the Hilbert transform to the ECoG to calculate the analytic signal [3, 4].

The critical point that governs the cortical system is identified with a non-zero point attractor, which arises in the course of mutual excitation among neurons in very large numbers. The interaction is modeled by two 2nd order ordinary

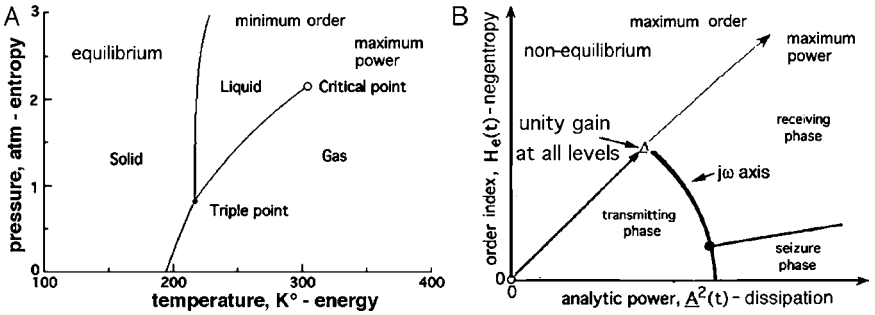

Fig. 29.2 (a) Static thermodynamic phase diagram [4]. (b) Adaptation to pseudo-equilibrium by translation of the origin to the critical point and introducing two dynamic state variables: the rate of increase in order parameter and the mean rate of dissipation of energy, both calculated from the ECoG recorded from 64 electrodes in a high-density array on the surface of sensory cortex. $H_e(t)$ is defined in [5, 6] From [7]

differential equations that form a positive feedback loop between transmitting and receiving neuron pools that are continuously renewed [1].

The refractory periods of the neurons limit the forward gains, providing a soft boundary condition. Perturbation in the near-linear range gives impulse responses that decay to the steady state with a rate constant proportional to the evoked amplitude [1]. Extrapolation to threshold gives zero decay rate, which implies self-stabilization at unity gain. This gives the steady state excitatory bias that is necessary for oscillation by negative feedback, which increases with arousal under brain stem neurohumoral control, always self-stabilized. The point attractor appears as a closed loop pole at the origin of the complex plane [1]. In Fig. 29.2b this pole Δ is matched with the critical point, and the imaginary axis in the upper half of the complex plane is matched with the phase boundary between the receiving and transmitting phases [7].

The inhibitory neurons in cortex are required not for stabilization but for the oscillations in the beta (12–30 Hz) and gamma (30–80 Hz) ranges through a wide range of feedback delays, giving broad spectral bands (Fig. 29.1) that can be modeled with ODE in multiple negative feedback loops [1]. Superposition holds in small-signal ranges, so that the pass bands can be simulated with transfer functions for linear filters. When ECoG is filtered in the beta or gamma range, the analytic signal from the multichannel ECoG both at rest and at work give fluctuating peaks of mean amplitude, $A(t)$, separated by sharp null spikes at which $A(t)$ approaches zero (Fig. 29.3a) [8].

At null spikes the phase, $f(t)$, is undefined, so that the spatial standard deviation function of time, $\mathrm{SD}_X(t)$, across channels increases in a sharp spike, contrasting with the fixed $\mathrm{SD}_X(t)$ and mean $f(t)$ in the intervening peaks of $A(t)$. The simulation is undertaken by summing over random numbers [9] to get $1/f^2$ brown noise and filtering the sum with a band pass filter in the beta or gamma range [10]. This simple

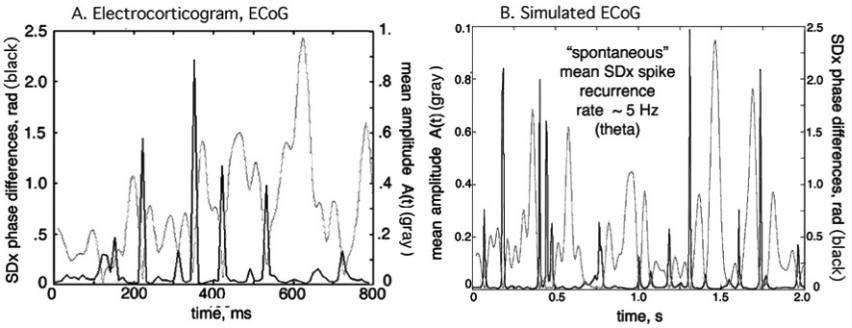

Fig. 29.3 (a). Mean analytic amplitude, $A(t)$, and the spatial $\mathrm{SD}_X(t)$ are inversely correlated. The inhibitory feedback acts as a band pass filter on the KIe output, which results in episodic decreases in noise power with amplitude histograms that closely resemble that of Rayleigh noise. The wide range of feedback frequencies is supported by the power-law distribution of feedback distances and delays. (b). Simulation is by band pass filtered $1/f^2$ brown noise that can be generated using multiple time series of random numbers [9]. From [11]

operator reproduces the inverse relation between $A(t)$ and $SD_X(t)$ (Fig. 29.3b) that is revealed in the ECoG and EEG [7].

Conclusion

The hypothesis is proposed that the first phase transition in a primary sensory cortex that initiates the formation of a unimodal wave packet and the second phase transition that initiates the formation of a multimodal wave packet as the basis for perception are contingent on the coincidence of two endogenous events. One is the occurrence of a null spike that persists for only 1–3 ms. The other is the arrival of a surge of input to the sensory cortices, the onset of which is under limbic control, and the duration of which may be some tens of ms, such that it may coincide with multiple null spikes, each of which may precipitate the formation of a wave packet. In this view the phase transition constitutes an event of spontaneous symmetry breaking [3], in the sense that order in the form of an AM pattern emerges from unpatterned background activity [2]. It is conceived that the Hebbian cell assemblies constituting the attractor landscapes in the sensory cortices, which are maintained under limbic control by corollary discharges, are made accessible by the act of sniffing, whisking, or glancing that destabilizes the cortices (Fig. 29.1). The null spike reduces the background noise and amplifies the input signal [2, 8], which increases the signal-to-noise ratio as in the eye of a hurricane and enables the ignition of an assembly by the action potentials deriving from an expected stimulus. The energy for the transmission of a wave packet is provided by the background activity now modulated by the cell assembly, which is determined by synaptic modifications that embody prior learning and therefore constitute the memory of that category of input. Hence the AM pattern is not a representation of the stimulus; it is an expression of the knowledge about the stimulus in the brain of the observer.

References

1. W. J. Freeman, Mass Action in the Nervous System, New York, Academic (1975/2004).
2. C. A. Skarda and W. J. Freeman, How brains make chaos in order to make sense of the world. Behav. Brain Sci. 10: 161–195 (1987).
3. W. J. Freeman and G. Vitiello, The dissipative quantum model of brain and laboratory observations. Electronic J. Theoretical Physics 4, 1–18 (2007). http://dx.doi.org/10.1016/j.plrev.2006.02.001.
4. D. N. Blauch, Exercises and tutorials in thermodynamics (2006). http://www.chm.davidson.edu/ChemistryApplets/PhaseChanges/PhaseDiagram5.html.
5. W. J. Freeman, How Brains Make Up Their Minds, New York, Columbia UP (2001).
6. W. J. Freeman, Origin, structure, and role of background EEG activity. Part 1. Analytic amplitude. Clin. Neurophysiol. 115, 2077–2088 (2004). http://repositories.cdlib.org/postprints/988.
7. W. J. Freeman, Proposed cortical 'shutter' mechanism in cinematographic perception. In: Neurodynamics of Cognition and Consciousness. R. Kozma and L. Perlovsky (eds.): Heidelberg: Springer, Verlag, 11–38 (2007).
8. W. J. Freeman, Origin, structure, and role of background EEG activity. Part 2. Analytic phase. Clin. Neurophysiol. 115, 2089–2107 (2004). http://repositories.cdlib.org/postprints/987.

9. M. Schroeder, Fractals, Chaos, Power Laws. W. H. Freeman (1991).
10. W. J. Freeman, Origin, structure, and role of background EEG activity. Part 3. Neural frame classification. Clin. Neurophysiol. 116 (5), 1118–1129 (2005). http://repositories.cdlib.org/postprints/2134.
11. W. J. Freeman, Origin, structure, and role of background EEG activity. Part 4. Neural frame simulation. Clin. Neurophysiol. 117 (3), 572–589 (2006). http://repositories.cdlib.org/postprints/1480.

Chapter 30
Dynamic Field Theory as the Interface Between Neuronal Dynamcis and Embodied Cognition

Gregor Schöner

Researchers in computational neuroscience aiming to account for of neuronal function based on detailed biophysically realistic models share two assumptions. First, neural realism is assumed to provide a firm grounding in experiment and, second, the insistance that models "compute" is assumed to link to neuronal function, avoiding epiphenomena. Such work must straddle a deep, historically rooted devide. The first assumption is linked to the epistomology of the biologically based neurosciences, based on extensive description. The second assumption is ultimately linked to psychology, which has approached behavior with an epistomological framework closer to physics, directed at uncovering laws, regularities, and constraints. One obvious reason is that behaviors are not readily reproducible unless the environmental situation, the behavioral history, or more generally the task are controlled.

The conceptual framework of information processing has been, perhaps, the most successful attempt to date to reduce this dependence of behaviors on multiple factors. Extensive description of cognition would be achieved by identifying the complete architecture of computational modules with well-defined input-output relationships. The concept of computation suggests such a feedforward directionality of processing and much current work in computational neuroscience has implicitly or explictly embraced this framework. Information processing has, however, come under serious criticism in multiple ways. In neuroscience, the discovery of pervasive functional modulation of neuronal networks [1] and pervasive plasticity [2] have undermined the fixed assigment of function to neuronal circuits. In cognitive science, the insight arose, that modular information processing architectures make unreasonable demands on abstraction and invariance [3].

Thus, computational neuroscience must confront the long-standing conflict between the conceptual frameworks of extensive description vs. constraint discovery head on. What does it mean that a particular, neuronally realistic and detailed model "accounts for" a neuronal function? The best work shows how detailed models exhibit the same kind of activity pattern as neuronal recordings from behaving animals

G. Schöner
Institut für Neuroinformatik, Ruhr-Universität Bochum, Germany
e-mail: gregor.schoener@neuroinformatik.rub.de

R. Wang et al. (eds.), *Advances in Cognitive Neurodynamics*,

do and may even provide estimates of behavioral measures such as reaction times (e.g., [4]). Ironically, these complex and brilliantly conceived dynamical models are thus tested in paradigms that where defined based on static conceptions of information processing. I propose that a strategy to overcome this limitation is to define a principled interface between neuronal dynamics and behavior that is capable to dealing with the close link between cognition and sensory and motor processes, with the dependence on context, behavioral and stimulus history, and is open to learning and development. Here I sketch the main ideas (see [5, 6] for recent review).

Space-Time Continuity

Behavior unfolds continuously in time and is continuously linked to sensory information. There are no behavioral signatures of the temporal discreteness of neuronal spiking events. Similarly, a continuum of motor behaviors, characterized by movement parameters, is generated by nervous systems. Percepts unfold over continuous features spaces. Perceptual categories are unrelated to the discreteness of neurons. Instead, neurons have strongly overlapping and broad tuning curves, so that any single instance of a stimulus or motor task activates populations of neurons and different instances activate partially overlapping populations.

The neuronal activation field is thus an oppropriate interface between neuronal function and behavior. A continuum of activation variables are defined over a relevant behavioral dimension (e.g., movement parameters, retinal space, or feature dimensions, see Fig. 30.1). Distances along the dimension reflect the metrics of a perceptual or motor task. Localized peaks of activation are units of representation indicating both the presence of information through the increased level of activation as well as the metric estimate of information through the location of the peak. Although initially tied to the neuroanatomy of cortex and thalamus [7], activation fields can be constructed for populations of neural activation irrespective of topographical order [8].

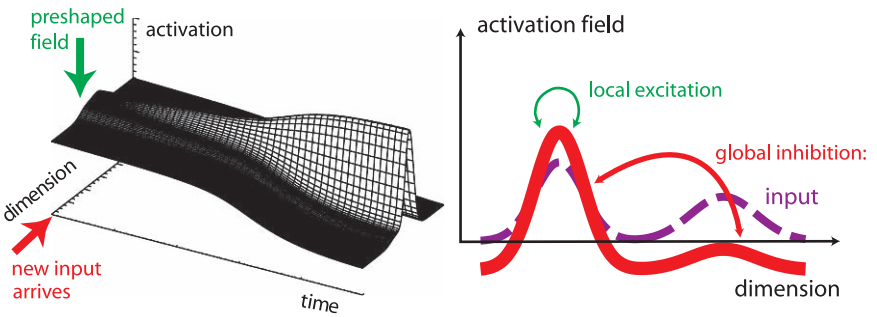

Fig. 30.1 Left: Activation fields defined over relevant behavioral dimensions evolve continuously in time as described by a field dynamics which integrates inputs and interaction. Right: The generic interaction of local excitation and global inhibition stabilizes peak solutions against decay and diffusion

No Separation Between Estimation, Detection, and Selection

What is the function of activation fields? In classical information processing terms, activation fields can be viewed as a form of encoding of sensory or motor information in a generalization of the space code principle [9]. Time plays a role only in the sense of delays that reflect computational effort. In real dynamical neuronal networks, in contrast, activation patterns are continuously coupled both to ongoing sensory inputs as well as to many other neuronal processes that vie for control. Similarly, real behavior always comes from somewhere and goes somewhere. The laboratory situation of waiting for a stimulus to arrive and then producing a single response is a misleading extreme limit case.

Neuronal patterns that matter for behavior must therefore possess stability, that is, the capacity to resist perturbations. Such stability is provided by the dynamics of activation fields as illustrated in Fig. 30.1. The temporal evolution of activation fields is influenced by inputs (here an input from a memory trace that has preshaped the field initially and a new input), but also by neuronal interaction. The generic form of such interaction stabilizes peak solutions as sketched on the right: local excitatory interaction stabilizes peaks against decay, global inhibitory interaction stabilizes peaks against diffusion. Sigmoidal nonlinearities arise because only activated field locations contribute to interaction.

In such dynamic fields, all functional states are attractors. To change state, dynamic fields go through instabilities. Detection, the decision to generate a peak in response to input, amounts to an instability, for instance, in which a subthreshold input-driven solution becomes unstable and the system switches to a peak solution whose location is dictated by local maxima of input [10]. Once a detection decision has been made, that decision is stabilized against fluctuating or competing inputs. Similarly, the capacity to select among multiple inputs arises through an intability from a fusion regime, in which inputs are averaged. Sustained activation, the basis for working memory, arises through an instability from the input regime as the relative weight of interaction is increased (see [11] for seminal analysis). The instabilities lead to qualitatively different dynamics, different modes of operation as simple, parametric changes are brought about either by changing inputs or through simple forms of learning (such as from a memory trace or from Hebbian change of synaptic efficacy). This makes it possible to understand how fields may provide different cognitive function out of the same neuronal structure (see, for instance, [6] for how working memory, selection, update of reference frames and discrimination all arise in this way out one dynamic field architecture).

Behavioral Experiment as a Probe of Neural Dynamics

How may theories based on this interface be validated? The strategy is to seek direct behavioral signatures of the postulated neuronal dynamics, typically in multiple convergent settings and using convergent measures. The set of well-studied

scenarios includes perseverative reaching in infants [12], the structure of working spatial memory [13], the preparation and initiation of movement [14, 15], the perceptual organization of visual motion [16], or the habituation to visual stimuli [17].

Conclusion

Dynamic field theory provides a framework for understanding elementary forms of cognition, that are continously linked to the sensory and motor surfaces and depend on environmental context, on task, and an behaviral history and learning. The empirical constraints for this form of theory are rich sets of behavioral and neuronal data. The goal of providing accounts for neural function on the basis of biophysically realistic models can be realized by deriving the functional dynamics of neuronal activation fields rather than by accounting directly from neuronal or behavioral data.

References

1. Marder, E.: From biophysics to models of network function. Annual Review of Neuroscience **21**(1) (1998) 25–45.
2. Buonomano, D.V., Merzenich, M.M.: Cortical plasticity from synapses to maps. Annual Reviews in Neuroscience **21** (1998) 149–186.
3. Brooks, R.A.: Intelligence without representation. Artificial Intelligence **47** (1991) 139–160.
4. Wong, K.F., Wang, X.J.: A recurrent network mechanism of time Integration in perceptual decisions. The Journal of neuroscience **26**(4) (2006).
5. Schöner, G.: Dynamical systems approaches to cognition. In Sun, R., ed.: Cambridge Handbook of Computational Cognitive Modeling, Cambridge, UK, Cambridge University Press (2007).
6. Spencer, J.P., Simmering, V.R., Schutte, A.R., Schöner, G.: What does theoretical neuroscience have to offer the study of behavioral development? insights from a dynamic field theory of spatial cognition. In Plumert, J., Spencer, J.P., eds.: The emerging spatial mind, Oxford University Press (2007).
7. Wilson, H.R., Cowan, J.D.: A mathematical theory of the functional dynamics of cortical and thalamic nervous tissue. Kybernetik **13** (1973) 55–80.
8. Erlhagen, W., Bastian, A., Jancke, D., Riehle, A., Schöner, G.: The distribution of neuronal population activation (DPA) as a tool to study interaction and integration in cortical pepresentations. Journal of Neuroscience Methods **94** (1999) 53–66.
9. Seung, H.S., Sompolinsky, H.: Simple models for reading neuronal population codes. Proceedings of the National Academy of science (U.S.A.) **90** (1993) 10749–10753.
10. Bicho, E., Mallet, P., Schöner, G.: Target representation on an autonomous vehicle with low-level sensors. The International Journal of Robotics Research **19** (2000) 124–447.
11. Amari, S.: Dynamics of pattern formation in lateral-inhibition type neural fields. Biological Cybernetics **27** (1977) 77–87.
12. Thelen, E., Schöner, G., Scheier, C., Smith, L.: The dynamics of embodiment: A field theory of infant perseverative reaching. Brain and behavioral Sciences **24** (2001) 1–33.
13. Schutte, A.R., Spencer, J.P., Schöner, G.: Testing the dynamic field theory: working memory for locations becomes more spatially precise over development. Child Development **74** (2003) 1393–1417.

14. Erlhagen, W., Schöner, G.: Dynamic field theory of movement preparation. Psychological Review **109** (2002) 545–572.
15. Wilimzig, C., Schneider, S., Schöner, G.: The time course of saccadic decision making: Dynamic field theory. Neural Networks **19** (2006) 1059–1074.
16. Hock, H.S., Schöner, G., Giese, M.A.: The dynamical foundations of motion pattern formation: Stability, selective adaptation, and perceptual continuity. Perception & Psychophysics **65** (2003) 429–457.
17. Schöner, G., Thelen, E.: Using dynamic field theory to rethink infant habituation. Psychological Review **113**(2) (2006) 273–299.

Chapter 31
The Task of Cognitive Neuroscience

Christoph von der Malsburg

What is Cognition?

To be concrete, I will work here with a tentative definition of cognition. Our mind is cognitive in being able to deal with the environment on the basis of insight, in being able to know what is going on outside and to represent the present situation for practical purposes, including the ability to imagine potential outcomes. This cognitive ability is possible only in a world that is dominated by regularities that we can learn in the past and apply in the future. Only very little information is given to us directly by our senses in any given situation. If we see an object, we would like to know how it will look from other perspectives, how it will feel if we touch it, what operations we could perform with it and so on, and all this information is available to us only on the basis of previous experience. Psychologists have long known that the scene that we "see" is to an overwhelming extent a mental construct, erected on the basis of world knowledge. Given the tremendous variability in detail of our environment, this ability to actively construct representations cannot be understood in terms of literal recall. Rather, our cognitive apparatus must be able to construct new representations by combining structural elements according to rules of combination. Our mind is a compositional, self-organizing model box. The task of cognitive neurodynamics is to describe the mechanisms of the neural system to actively construct scene-representations.

Problems with AI, ANN and Bayes

Artificial Intelligence (AI) is the attempt to instill the computer with intelligence just by writing appropriate programs. The universality of the computer seems to set no limit to this project, and one day we will surely have a tin box programmed such as to be a cognitive system. AI, however, invested the bulk of its activities in writing

C. von der Malsburg
Frankfurt Institute for Advanced Studies, Frankfurt, Germany
e-mail: malsburg@fias.uni-frankfurt.de

R. Wang et al. (eds.), *Advances in Cognitive Neurodynamics*,

specific programs to deal with specific applications (such as playing chess), instead of focussing all its energy on the equivalent of neurodynamics. The limits of AI became clear when it turned out that such applications as vision or language understanding are vastly too complicated to be manually programmed into the computer.

The progress with Artificial Neural Networks (ANN) lies with the attempt to replace the programmer's insight by mechanisms of learning and self-organization. There are some impressive demonstrations of that ability, and ANN technology is actually applied broadly to practical problems. However, a fundamental unsolved problem with ANN is that they do not scale up to the extent needed to understand cognitive systems. Thus, painful and extended experience teaches that ANN learning is restricted to applications where input patterns have limited information content, are all taken from the same context, and where the neural system itself is relatively small. Beyond these limits, convergence times get out of hand. Learning structural regularities from examples, the central idea of ANN, has to play, without any doubt, an important role in cognitive systems, but an important further conceptual step will be necessary to unlock its potential.

Similar remarks probably apply to Bayesian networks. There is good reason to surmise that our whole brain is one very large network of belief propagation, its nodes corresponding to more or less elementary structures, together with a representation of uncertainty over a range of alternatives. The links of the network would implement constraints reigning between values represented in the nodes. With proper construction, these constraints help to reduce uncertainties in the nodes, so that the network quickly converges to a highly trustworthy representation of the situation. This "Bayesian dream" is far from realization as a viable theory of brain function, as the concrete applications realized so far are limited to very small networks which, moreover rely heavily on human design instead of on learning and self-organization. Open are issues like how to decide what quantities to represent, how to formulate the constraints and how to ensure rapid convergence in larger networks. As with ANN, only very small systems can be realized, and these depend to a large extent on manual construction.

The Need to Second-Guess the Structure of the World

The reality of our brain stands in stark contradiction to the tight constraints to which AI, ANN and Bayesian networks are subject. The neural network in our brain is very large, and it would be very foolish to assume that the evolution process that has structured it is in any sense equivalent to the manual design of our artificial models of intelligence. Indeed, the amount of genetic information in our genome, about a Gigabyte, falls short by a factor of a million of the quantity of information needed to record the wiring of cortex alone (10^{15} bits: 10^{14} synapses, each requiring 33 bits of information to specify one target neuron out of more than 10^{10}). The genome thus contains enough information to specify a very small part of the network in detail (perhaps some networks in the mid-brain and the periphery, plus some

gross aspects of the wiring of the rest), plus information to formulate a game of self-organization and learning that is responsible for the overwhelming rest of the structure, overwhelming by a factor of a million.

For a theoretician, this is very good news. It will not be necessary to painstakingly record every detail of the brain's wiring, all it needs is to find out the rules of the game, plus a trace of pre-structuring. This is the promise of large booty! Now, there are cautionary signs, in the form of the no-free-lunch-theorems [1] or the bias-variance dilemma [2]. There is no catch-all optimization or learning system, or stated the other way round, for any given system that is highly successful in some application domain it is easy to construct a nasty sample domain on which the system miserably fails. The cognitive neurodynamics of our brain evidently is very successful in this world, and the conclusion must be that our world is not a hodge-podge of disparate structures, such that any cognitive system that were successful with some of the environmental structures would have to fail on other, nasty, structures. The fact that an individual can learn for a decade or two (or that evolution can learn over an eon or two), and then is highly successful in dealing in future situations with what it has learned in the past, is proof that there is a tremendous structural coherence in our environment, in spite of all variation in detail.

If the earthly environment is dominated by one coherent structure, what is it? This is a question worthy of our collective attention. Indeed it is the crown of all intellectual ventures. Understanding some phenomenon means reducing all its particular patterns to some abstract schema. Characterizing the environment to the extent that it can be captured by our brain means coming up with the abstraction of all abstractions. Evolution has done the job of developing a cognitive architecture that is in tune with the world, and we only have to find out the dynamic rules implicit in the cellular repertoire of our organism and the genetic regulatory structures that play on that repertoire.

Fortunately we are not at square zero of this guessing game. We know that neural dynamics is dominated by network self-organization: The stochastic activity in a network is shaped by excitatory and inhibitory connections such as to express signal correlations and anticorrelations. These act back on the network by mechanisms of synaptic plasticity, in turn leading to changes in signal correlations. This interplay comes to a halt (as long as external input is constant) when connectivity and signal correlations have reached a state of mutual correspondence. The specific network patterns that are dynamic attractors of this interplay dominate the structure of the brain, and it is an important issue what they are. It seems clear that attractor networks are sparse (few connections per node), and that those connections are optimally cooperative, with several alternate pathways between two given nodes, which help each other to create those signal correlations in the two nodes that favor the connections by synaptic plasticity. According to one hypothesis [3], attractor networks are of topological structure. A topological network can be arranged (under preservation of connections) in a low-dimensional (e.g., two-dimensional) space such that connectivity is dominated by nearest-neighbor connections. The local (local in this display space) cliques of intensely connected neurons create local firing

events which in turn stabilize the local connectivity, and the total network is, in time, covered by such local firing events like a topological space by its open sets.

If network self-organization takes place also on the fast functional time scale of seconds, as I have proposed [3], then the "permanent" connectivity of the brain is, in a given situation, reduced to a very sparse sub-network between the currently active neurons. According to this view, the brain is an overlay of many connectivity structures, each one appropriate to a specific context, and rapid network self-organization reduces the connectivity to one that implements the functionality and the representations called for at the moment.

If attractor networks are the universal code of our brain, in what way do they capture the structure of the world? Let me just give two aspects that cover part of the territory: differentiation hierarchies and schema application. Space and time in our world are topological in nature, and the structures that we encounter form nested hierarchies, such that an individual, detailed, structure can naturally be embedded in coarse-grained structures. Thus, perception of the scene surrounding us progresses by first capturing it as an office scene or street scene or what the case may be, by perceiving the coarse arrangement of elements, then progressing to identifying objects according to general type (persons, pieces of furniture etc.), then resolving objects into parts and identifying them individually. The detailed structure that we eventually perceive at the end of a process of gradual differentiation is thus embedded in a nested hierarchy, without us needing to back-track again and again in the process. Similarly, before writing down the detailed proof of a theorem, a mathematician conceives it in vague outline, illustrating again a differentiation hierarchy.

Of equally fundamental import is the mechanism of schema application. We can deal with the ever-new structures we encounter only by relating them to abstract schemas. The recognition of a schema in a concrete object makes it possible for our brain to engage appropriate behavior and makes it possible to identify that narrow subsystem of our memory domain where this pattern can be found or is to be stored. We humans are evidently born with a schematic description of the human face, allowing the infant to single out faces from the environment as significant pattern, to store all facial patterns in one narrow part of the brain, and to know what to do in response to the face. An abstract schema presumably is represented in the brain as a structured network, with nodes encoding specific features, and links encoding topological relations between features. The process of schema application then amounts to graph matching, the problem being to identify a subset of nodes and links in the instance (e.g., the concrete face in primary visual cortex) that is isomorphic to the abstract schema network. As modelled in [4], this process of graph matching can be implemented naturally in terms of network self-organization, the attractor structure being composed of the schema network, the isomorphic sub-network embedded in the instance, and the activated links between pairs of corresponding nodes in schema and instance. If the schema and the instance are of homomorphic topological structure, the links knitting them together point-by-point just turn them into a larger topological topological network.

Conclusion

How do these ideas address the problems of AI, ANN and Bayes networks – limitation to small systems and dependence on manual construction? Manual construction is replaced by self-organization, by which the system states contract, on several time scales, to highly structured connectivity states, which form a comparatively narrow sub-universe of network patterns. This sub-universe captures, in a general way, the nature of our environment. This process of construction is guided intensely by the application of abstract schemas. Recognizing a schema in a specific situation amounts to gaining insight, and induces relations between situations that are different in detail but agree in terms of applicability of the abstract schema.

The spontaneous, rapid contraction of a network to a topological structure essentially surrounds each node of the network with its own small environment of other nodes, which all have much to do with each other. Selective attention is an important aspect of this process of state contraction. Inspection of a complex scene is organized as a sequence of flashes of attention. As a first step, the whole scene is taken in, but only in its coarse layout. Recognizing the scene by relation to an abstract scene schema immediately permits to restrict the memory domain to the relevant small sub-sector. In consecutive attention flashes, smaller parts of the scene are singled out, again by relation to schemas, each flash of attention amounting to a contraction of activity in the brain to a very small sub-system – a small segment of visual input, a small segment of memory, a specific functional circuit applicable to the recognized pattern and so on – in which the statistical learning of ANN is now possible, and in which one may perhaps see the realization of a sparse Bayesian network. One may speak of schema-based learning: The animal is born with a complement of schematic descriptions of biologically significant scene components (the schema "coherent object moving relative to the background", the mother's face in the infant, or mother goose in Lorenz' imprinting paradigm) which helps it single out patterns in the otherwise confusing environment, extract them selectively and map them into the appropriate sector of the memory domain.

These ideas may be wrong in detail, but I think it is inescapable that neurodynamic state contraction has to be enlisted to dynamically create the small subsystems that ANN learning requires, and that this state contraction must be guided by principles that put the brain in tune with the structure of the world in a principled way.

Acknowledgments This work was supported by the Hertie Foundation and the EU Project Daisy.

References

1. Wolpert, D.H. and Macready, W.G. (1997), "No Free Lunch Theorems for Optimization." IEEE Transactions on Evolutionary Computation 1, 67.
2. Geman, S., Bienenstock, E. and Doursat, R. (1992), " Neural Networks and the Bias/Variance Dilemma". Neural Computation 4, 1–58.

3. v.d. Malsburg, C. 1994 “The Correlation Theory of Brain Function,” (Reprint of a report of 1981) In: Models of Neural networks II, E. Domany, J.L. van Hemmen and K. Schulten (editors) chapter 2, 1994 (Springer, Berlin) pp. 95–119.
4. Wiskott, L. and v.d. Malsburg, C. (1996), “Face Recognition by Dynamic Link Matching.” In: Lateral Interactions in the Cortex: Structure and Function. Electronic book, Sirosh, J. and Miikkulainen, R. and Y. Choe (editors), chapter 4, 1996. (ISBN 0-9647060-0-8). http://www.cs.utexas.edu/users/nn/web-pubs/htmlbook96

Chapter 32
Functional Roles of Feedback Signals from Higher-Order Areas to Lower-Order Areas in the Visual Cortical Pathways

Tiande Shou

Abstract The functional role of feedback projections from high-order cortical areas to lower-order areas is an important problem unsolved due to the complex reciprocal connections between numeral areas in the visual pathways. Here we described recent studies on this issue using optical imaging of areas 17 and 18 combined with pharmacological manipulating the excitation of high-order areas 21a and PMLS in the cat. The results showed that area 21a feedback not only increased visual response of neurons in areas 17 and 18, but also improved their spatial frequency tuning. Area 21a enhanced the neural oblique effect of area 17 by shifting neurons' preferred orientations. Area PMLS changed preferred direction of area 17 neurons, but not orientation preference. We hypothesized that feedback signals from a distinct higher-order cortex along either the visual motion or form information stream tend to modulate the same type of information processing in the lower-order cortices.

Keywords Feedback · area 21a · PMLS · area 17 · orientation · direction · visual cortex · optical imaging

Introduction

In virtually all primates and carnivores with frontally positioned eyes, visual information from the outside of the world is originated from the retina and sent to the visual cortex through the dorsal lateral geniculate nucleus (LGNd) by a number of largely parallel 'information channels' [1, 2, 3]. In the retino-geniculo-cortical pathway of the cat, the parallel streams of neural signals consist of the so-called W, X and Y channels. Correspondingly, in macaque monkeys they consist of the analogous, if not homologous, information processing streams, so-called as koniocellular, parvocellular and magnocellular channels (for reviews see [1]). In monkey's extrastriate cortices, the parallel information channels to a large extent, go feedforward through

T. Shou
Vision Research Lab, Center for Brain Science Research, School of Life Sciences, Fudan University, 220 Handan Road, Shanghai 200433, P.R. China
e-mail: tdshou@fudan.edu.cn

R. Wang et al. (eds.), *Advances in Cognitive Neurodynamics*,

two parallel information-processing streams that are often referred to as the 'what' and 'where' pathways [2, 3] or as the 'form/pattern' ('ventral' or 'perception') and 'motion' ('dorsal' or 'action') streams ([4, 5]; for reviews see [1]).

For more than five decades, a substantial amount of data has also been gathered concerning the role of the feedforward cortico-cortical, associational, projections from the 'lower-order' cortical areas to 'higher-order' cortical areas. On the other hand, there are equally prominent associational 'feedback' projections from the higher-order visual cortical areas onto the same region (i.e., feedback connections). Several lines of evidence indicate that in cats or macaque monkeys, the feedback signals from the higher-order visual cortical areas, such as area posteromedial lateral suprasylvian (PMLS or area MT), area 18 (or area V2), and area 21a (or V4) modulate many response properties of neurons in the 'lower-order' visual cortical areas [6, 7, 8, 9]. However, the detailed function of the corticocortical feedback projections has not been fully understood.

In the cat, higher-order cortical areas 21a and PMLS belong to form and motion visual streams, respectively and send feedback signals to areas 17 and 18. In recent years, we investigated the functional role of areas 21a and PMLS feedback signals in modulation of areas 17 and 18 in the visual cortical pathways. The purposes of the study are to probe (1) the property of corticocortical feedback signals; (2) the relationship between these properties and visual perception; (3) the general principle of corticocortical feedback connections.

Using optical imaging based on intrinsic signals combined with single unit electrical recording and local pharmacological methods, the visual responses of neurons of areas 17 and 18 to stimulus gratings of different spatial orientations and drifting directions were studied in the anesthesed, paralysed cats when the exitation of areas 21a and PMLS were manipulated by administration of glutamate or GABA reversely.

Results and Discussion

Previous electrophysiological studies showed that the feedback projections from area 21a mainly exert an excitatory influence on the responsiveness of area 17 cells in the cat [9]. However, the detail functions of these feedback projections in a large cortical area are still unclear. Using optical imaging we showed that the response of orientation maps of both areas 17 and 18 elicited by grating stimuli was decreased by microinjecting GABA in area 21a and increased by bicuculline, a GABAa receptor antigonist [10]. This implies indicating the excitatory modulation from area 21a on areas 17 and 18. Furthermore, the global spatial frequency tuning curves of both areas 17 and 18 was flatened by application of GABA or the liquid nitrigen lesion in area 21a. This suggests that the feedback signal from area 21a plays a role in sharpening the spatial frequency tuning property of neurons in areas 17 and 18. Since the results were obtained from anesthesed cats it is speculated that in the awake animal the promotive effect of the feedback on visual spatial property may be more significantly.

Since the intrinsic signal optical imaging has a high spatial resolution (24 × 24 μm) it allows to do the pixel-by-pixe l analysis of a composition map, which resulted from several orientation maps evoked by differntly oriented grating stimuli. Using optical imaging combined with a single unit elelctrophysiological recording, we discovered that neurons in area 21a were functional organized in a slab-like architecture in orientation preference like those in area 17, but with a finer structure. These neurons in area 21a exhibited much stronger neural oblique effect, a well-known psychological or behavioral phenominon that the visual ability in horizontal and versitical meridians are better than the oblique ones in humans and animals, than those in area 17. Figure 32.1 shows a mean overpresentation of horizontal and vertical preferences in area 21a (24%) was 4.6 times more than that in area 17 (5.2%) of the cat [11]. Obviously, the overpresentation of horizontal and vertical meridians in area 17 is too small to initiate a psychological or behavioral oblique effect while the large overpresentation in area 21a is surfficient to do so although many investigators have referred this effect to the overpresentation of neurons in

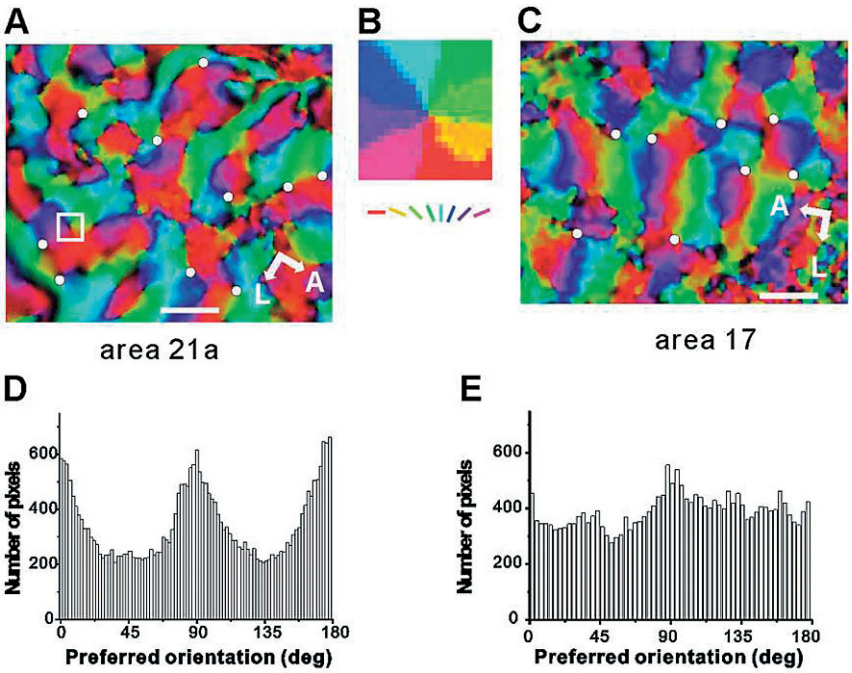

Fig. 32.1 Oblique effect revealed by optical imaging based on intrinsic signals in areas 21a and 17 in the cat. (a) and (c) The overall color-coded orientation maps showing functional organization of areas 21a and 17, respectively. A complete set of 4–6 single-condition orientation maps were color-coded pixel to pixel on the two maps according to the color code presented in the middle (b). The preferred orientation was spatially continuous along the surface of the imaged cortical areas. Scale bar: 1 mm in A. (d) and (e) Preferred orientation histograms of the functional maps of areas 21a and 17 of a cat, respectively. Note that both the histograms exhibit a W-like distribution of preferred orientation with two peaks at horizontal (0° or 180°) and vertical (90°) meridians, suggesting the neural oblique effect in the two areas (From Huang et al. [11])

area 17 previously. It remains to study how area 21a become so strong in neuronal oblique effect.

Generally, the preferred orientation of visual cortical cells were thought to be rather solid. Surprisedly, we found that activation of area 21a by glutamate application altered the preferred orientation in some cortical neurons (about 6%) in area 17 of the cat. These neurons shifted their preferred orientaions from the oblique toward the horizantal and vertical. On the other hand, inactivation of area 21a by

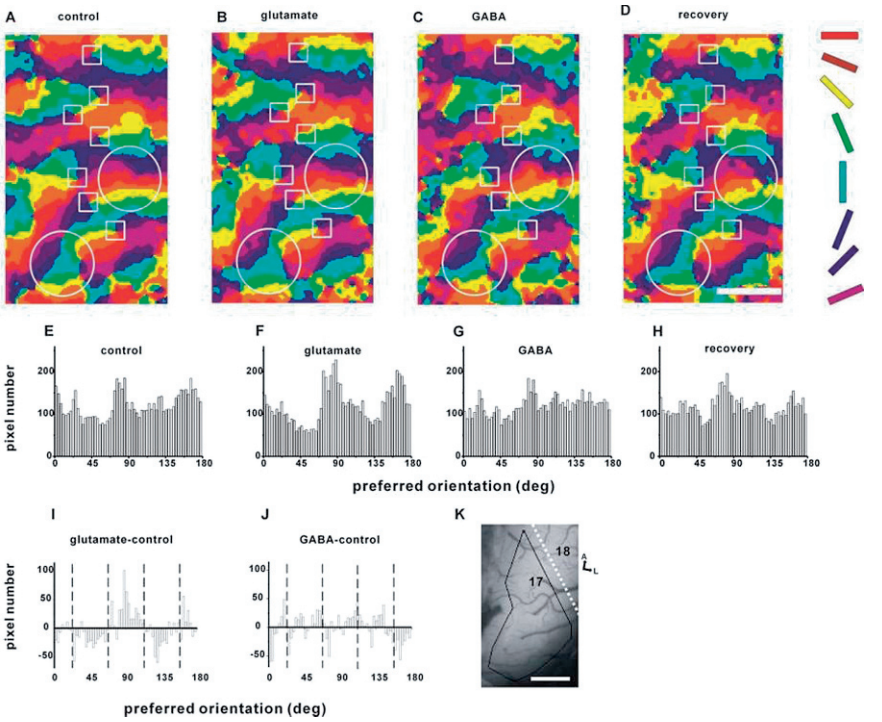

Fig. 32.2 Changes in neural oblique effect observed in functional orientation maps of area 17 due to injection of glutamate (0.2 mM) and GABA (400 mM) in area 21a. (a–c) Color-coded orientation maps recorded under normal (a), glutamate (b) and GABA (c) injection and recovery (d) conditions for one cat. Scale bar: 1mm. (e–h) Preferred orientation distribution histograms of pixels in the same region of interest in area 17 under conditions of (a), (b), (c) and (d). Note that the W-shaped distribution is significantly enhanced by glutamate and reduced by GABA. (i–j) Subtracted histograms of preferred orientation distributions in the region of interest of area 17 obtained for glutamate injection minus control (i), and GABA minus control (j). The pixels of negative values mean those pixels in the functional map changed their original preferred orientations to new ones which were denoted by the positive values. Panel (h) shows that injection of glutamate caused a clear shift in many pixels from preferring oblique orientations to horizontal and vertical ones; in panel (i), more pixels turned from preferring horizontal and vertical orientations to oblique ones. (k) The surface view of the area 17 of the cat studied. The ROI denoted by solid line. A white dotted line indicates the boundary between areas 17 and 18 which was determined by subtracting the orientation map elicited by a spatial frequency 0.58 c/d grating from the one by 0.14 c/d. Scale bar: 1 mm (From Liang et al. [12])

GABA application induced a preferred orientation shifting from the horizontal and vertical toward the oblique (Fig. 32.2 [12]). These results provide the first evidence of the neural besis of the cortical feedback for modulating the oblique effect in the low-order cortical areas. It is speculated that the coavctivation of areas 21a and 17 would contribute more substantially to the psychological oblique effect in the normal condition than in anesthesized condition.

In another study, we investigated the influence of feedback signals originating from area posteromedial lateral suprasylvian (PMLS), the dominant motion-processing region of the parietal cortex, on responses of cortical neurons' orientation and direction maps of cats' area 17. The inactivation of area PMLS by local application of GABA resulted in a reduction of the responses of direction maps of area 17 which is mainly involved in form information processing rather than motion in the cat. Furthermore, inactivation of area PMLS abolished the global layout of direction maps in area 17, but did not affect the basic structure of the orientation maps [13]. Therefore, feedback projections from higher-order visual cortex both within and across information-processing streams are important in information integration in the visual cortex. Now, we hypothesized a general principle that feedback signals from a distinct higher-order cortex along either the visual motion or form information stream tend to modulate the same type of information processing in the lower-order visual cortices.

References

1. Burke, W., Dreher, B., Wang, C.: Selective block of conduction in Y optic nerve fibres: significance for the concept of parallel processing. Eur. J. Neurosci. 10 (1998) 8–19.
2. DeYoe, E.A., Felleman, D.J., Van Essen, D.C., McClendon, E.: Multiple processing streams in occipitotemporal visual cortex. Nature 371 (1994) 151–154.
3. Van Essen, D.C., Felleman, D.J., DeYoe, E.A., Olavarria, J., Knierim, J.: Modular and hierarchical organization of extrastriate visual cortex in the macaque monkey. Cold Spring Harb. Symp. Quant. Biol. 55 (1990) 679–696.
4. Young, M.P.: Objective analysis of the topological organization of the primate cortical visual system. Nature 358 (1992) 152–155.
5. Goodale, M.A., Milner, A.D.: Separate visual pathways for perception and action. Trends Neurosci. 15 (1992) 20–25.
6. Alonso, J.M., Cudeiro, J., Perez, R., Gonzalez, F., Acuna, C.: Influence of layer V of area 18 of the cat visual cortex on responses of cells in layer V of area 17 to stimuli of high velocity. Exp. Brain Res. 93 (1993) 363–366.
7. Galuske, R.A., Schmidt, K.E., Goebel, R., Lomber, S.G., Payne, B.R.: The role of feedback in shaping neural representations in cat visual cortex. Proc. Natl. Acad. Sci. U. S. A. 99 (2002) 17083–17088.
8. Hupe, J.M., James, A.C., Payne, B.R., Lomber, S.G,, Girard. P., Bullier, J.: Cortical feedback improves discrimination between figure and background by V1, V2 and V3 neurons. Nature 394 (1998) 784–787.
9. Wang, C., Waleszczyk, W.J., Burke, W., Dreher, B.: Modulatory influence of feedback projections from area 21a on neuronal activities in striate cortex of the cat. Cereb. Cortex 10 (2000) 1217–1232.

10. Huang, L., Chen, X., Shou, T.: Spatial frequency-dependent feedback of visual cortical area 21a modulating functional orientation column maps in areas 17 and 18 of the cat. Brain Res. 998 (2004) 194–201.
11. Huang, L., Shou, T., Chen, X., Yu, H., Sun, C., Liang Z.: Slab-like functional architecture of higher-order cortical area 21a showing oblique effect of orientation preference in the cat. Neuroimage 32 (2006) 1365–1374.
12. Liang, Z., Shen, W., Shou, T.: Enhancement of oblique effect in the cat's primary visualo cortex via orientation preference shifting induced by excitatory feedback from high-order cortical area 21a. Neuroscience 145 (2007) 377–383.
13. Shen, W., Liang, Z., Chen, X., Shou, T.: Posteromedial lateral suprasylvian motion area modulates direction but not orientation preference in area 17 of cats. Neuroscience 142 (2006) 905–916.

Chapter 33
Dynamics of Population Decoding with Strong Inhibition

Thomas Trappenberg

Abstract Decoding information from a population of noisy neurons can be achieved efficiently with center-surround recurrent networks. Here we study such networks with continuing external input and investigate the dynamics of decoding with varying inhibition strength in the network. We find that the best decoding is achieved at the onset of the memory regime in such networks.

Introduction

In the brain, information is typically represented by a population of neurons. For example, while individual neurons in the primary visual cortex respond maximally to specific orientations of line segments, they also respond to a lesser extend to neighboring orientations. Thus, even with a 'pure' image there are many neurons that respond. This is important as such states are likely to represent probabilities of specific events [1]. Furthermore, cortical neurons are very noisy and their firing rates are low so that decoding the information from a population becomes crucial for reliable information processing in the brain.

Mathematically it is well established how to decode information in specific situations [2]. For example, if we consider Gaussian tuning curves we could fit a Gaussian through the data points given by the neuron response to achieve a maximum likelihood (ML) estimate of the stimulus which is optimal with these assumptions. While optimal decoding is of some theoretical and practical interest, much more important for brain processing is its efficient implementation. Several researcher have pointed out that ML estimation in the above mentioned case can be achieved with recurrent networks [3, 4]. This is significant as these networks enable fast computation consistent with the functional mechanisms of the cortex as captured by neural fields theory [5, 6, 7]. Furthermore, while the optimality can be proven in some cases [4], optimality in a statistical sense is not fundamentally required.

T. Trappenberg

Dalhousie University, Halifax, NS, Canada
e-mail: tt@cs.dal.ca

R. Wang et al. (eds.), *Advances in Cognitive Neurodynamics*,

Instead, it is possible that this is the principle decoding mechanism in the brain and this mechanism should therefore be studied in more general circumstances, such as in the case of multiple inputs.

Decoding mechanisms with neural fields have been studied mainly in a model where noisy input was applied as initial states of the network and where the asymptotic state of sustained activity packets (bubbles) are used for optimal decoding. In this paper we explore the dynamics of decoding when input is sustained for some time, resembling more closely transient input in the brain. We then explore the regime with strong lateral inhibition and show that this regime is well suited for fast population decoding.

Population Decoding with Recurrent Networks

We consider a standard recurrent rate neural network model with N nodes in which the time evolution of the internal state u_i is given by

$$\tau \frac{\mathrm{d}u_i(t)}{\mathrm{d}t} = -u_i(t) + \sum_j w_{ij} r_j(t) \Delta x + I_i^{\mathrm{ext}}(t), \tag{33.1}$$

where τ is a time constant, I_i^{ext} is the external input applied to the network and $\Delta x = 2\pi/N$ is a scale factor. The rate r_i is related to u_i by a sigmoidal gain function $g(u) = 1/(1 + \exp(-\beta u))$ with a slope parameter $\beta = 0.1$. Applications of this model to population decoding commonly use a gain function with divisive inhibition [8], but the principal findings reported here do not depend critically on the form of the gain function. The weight matrix, $\boldsymbol{w}$, describes center-surround interactions in the network with a shifted Gaussian profile,

$$w_{ij} = A_{\mathrm{w}} \left(\mathrm{e}^{-((i-j)*\Delta x)^2/2\sigma_w^2} - C \right). \tag{33.2}$$

This dynamic model exhibits several regimes characterized by different possible asymptotic states [7]. If the inhibition, C, is low compared to excitation in the network, then the excitation will spread through the network resulting in runaway activity. In contrast, if inhibition is dominating, then any activity in the field will decay without external reinforcement. In an intermediate regime it is possible to have activity packets where localized activity is stable. We call this mode of the model the memory regime.

The later two regimes are depicted in Fig. 33.1 in the context of population decoding. In these experiments we supply a static noisy input to the field over 20 timesteps. This input was chosen as a Gaussian around the middle node ($x_0 = 50$) with additive white noise of strength $n_\eta = 0.5$,

$$I_{\mathrm{ext}} = I_0 + A(\mathrm{e}^{-((i-j)*\Delta x)^2/2\sigma^2} + \eta_\eta \eta, \tag{33.3}$$

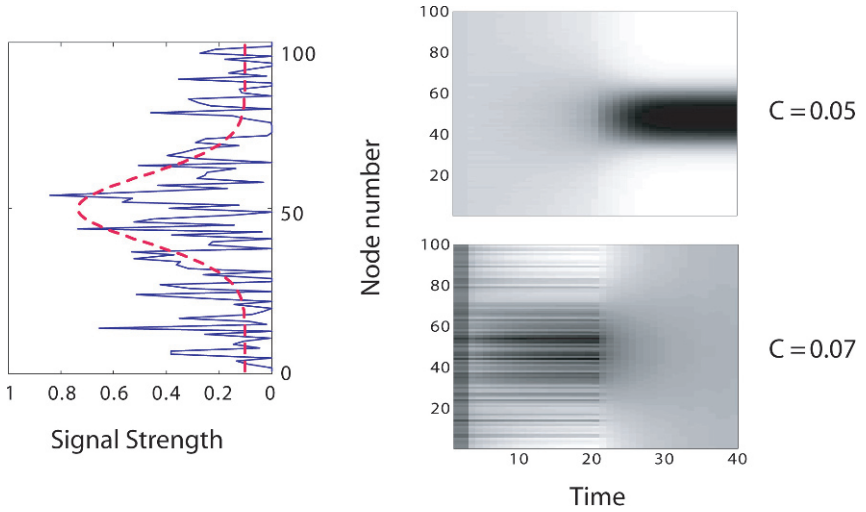

Fig. 33.1 Noisy population decoding with weak and strong inhibition in neural fields. The noisy input derived from the dashed line on the left is applied until $t = 20$ to the neural fields shown on the right

where I_0 is a background field and η is a normal distributed random number. When an inhibition constant of $c = 0.05$ is used, the field developed into a clean bubble around the middle node after the input was removed at time $t = 20$, demonstrating perfect decoding. The sustained localized activity in the neural field without external input demonstrates the above mentioned memory regime.

Traces of the noisy input are not apparent in the $c = 0.05$ case, and it seems one has to wait until the bubble forms to perform accurate decoding. This is different when running the same simulation with larger inhibition. Figure 33.1 shows the case for $c = 0.07$. Traces of the noisy input are now also visible during the time the external input is supplied, which is partly enhanced by the fact that a smaller range of values is depicted by the gray scale in the figure. The inhibition is now too large to sustain an activity packet after input is removed. However, the increased competition facilitates a cleaning of the signal even during the time when the signal is applied so that some form of population decoding is supported. While this might be less accurate than in the previous case, an advantage would certainly be that the decoding can be achieved much earlier. This assertion is investigated in Section 'Quality of Decoding with Varying Inhibition Over Time'.

Quality of Decoding with Varying Inhibition Over Time

To assess the quality of decoding with time and different inhibition constants we ran decoding experiments over 100 trials in each condition. While we have used signals with static noise in Fig. 33.1, we report now on the results when changing the noise after each unit of time, simulating ongoing fiuctuations in the input signal over time.

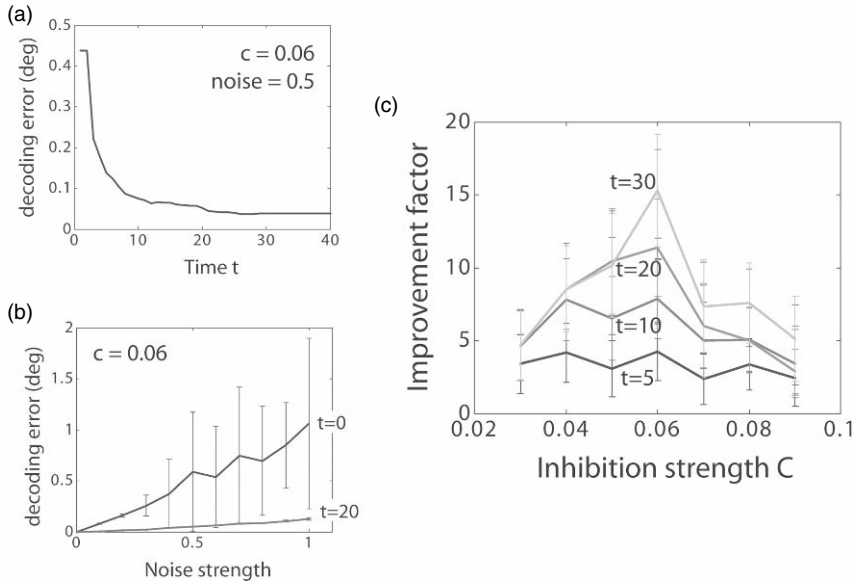

Fig. 33.2 Temporal aspects and decoding quality with different levels of inhibition

This represents a more plausible implementation of decoding conditions in the brain although we found similar results in the static noise case.

To assess the decoding quality we use a center of mass scheme to determine the prediction of the feature value encoded in the neural field. This was done for the original input signal and at each time step during the dynamic decoding in the recurrent network. An example trace of the decoding error is shown in Fig. 33.2a. For the shown strength of inhibition, the decoding error continuously decreases even while external input is supplied. The decoding error only improves slightly after the external input is removed at $t = 20$. The decoding error increases with increasing noise level as shown in Fig. 33.2b, but the decoding error at $t = 20$ is always much smaller than the center of mass decoding of the original signal. Finally, a major question motivating this study was to determine which network regime, in terms of inhibition strength, would be most suitable for decoding in such networks. The results of these studies are summarized in Fig. 33.2c which shows the decoding improvement at different time steps for different inhibition parameters. Early on there is little dependence of the results on the strength of inhibition, but later there is some advantage for inhibition values around 0.06. Interestingly, this is close to the transition region between the domain of decaying input and the domain of sustained activity.

Conclusion

In this study we analyzed population decoding with recurrent networks with biologically motivated modifications. We thereby included sustained input, a simplified and non-global gain function, and different levels of inhibition. We found that population

decoding with such competitive networks is very powerful even when continuously driven by external input. We also found that inhibition levels at the onset of the memory regime showed best decoding performances.

References

1. Zemel, R., Dayan, P., Pouget, A.: Probabilistic interpretation of population code. Neural Computation **10** (1998) 403–430.
2. Pouget, A., Dayan, P., Zemel, R.: Information processing with population codes. Nature Reviews Neuroscience **1** (2000) 125–132.
3. Pouget, A., Zhang, K., Deneve, S., Latham, P.: Statistically efficient estimation using population coding. Neural Computation **10** (1998) 373–401.
4. Wu, S., Amari, S., Nakahara, H.: Population coding and decoding in a neural field: a computational study. Neural Computation **14** (2002) 999–1026.
5. Wilson, H., Cowan, J.: A mathematical theory of the functional dynamics of cortical and thalamic nervous tissue. Kybernetik **13** (1973) 55–80.
6. Grossberg, S.: Contour enhancement, short-term memory, and constancies in reverberating neural networks. Studies in Applied Mathematics **52** (1973) 217–257.
7. Amari, S.: Dynamics of pattern formation in lateral-inhibition type neural fields. Biological Cybernetics **27** (1977) 77–87.
8. Deneve, S., Pouget, A., Latham, P.: Divisive normalization, line attractor networks and ideal observers. Advances in Neural Information Processing Systems **11** (1999) 104–110.

Chapter 34
Global Oscillations of CA3 Neural Fields

Francesco Ventriglia

Abstract The conditions which cause in the hippocampal CA3 field global oscillatory activities behaviorally important for their links to learning and memory, such as theta and gamma rhythms, have been analyzed with great details. To this aim, the theoretical framework devised years ago by the present author for the study of activities of large neural fields, has been enhanced in such a way to take into account basic biological features. By using that methodology, a two-dimensional model of the entire CA3 field has been described and its activity, originated by the several external inputs impinging on it, has been computer simulated. As a consequence of these investigations, a hypothesis has been elaborated on the relationship between global oscillatory activities of CA3 and engram formation.

Introduction

The Hippocampus is a fundamental station in the chain of neural structures along which the neural information flows in brain, going from the primary (sensorial) cortices to superior areas and back. In fact, several lines of evidence remark the great importance of this structure for learning and memory in rat, monkey and man [1, 2, 3, 4]. The modality according which the information is coded within the activities of the neural fields of Hippocampus and the way with which they produce the laying in brain of memory traces, or *engrams*, specifically related to sensory events, constitute a very elusive problem and no clear elucidation about its nature exists yet.

A hypothesis on the possible rules governing the production of engrams is presented in this article. It takes into account global oscillatory activities of neural populations of Hippocampus. In fact, synchronous waves of activity constitute one of the most characteristic aspects of the working brain and are associated closely

F. Ventriglia
Istituto di Cibernetica *E. Caianiello*, CNR, Via Campi Flegrei 34, 80078 - Pozzuli (NA), Italy
e-mail: franco@ulisse.cib.na.cnr.it

R. Wang et al. (eds.), *Advances in Cognitive Neurodynamics*,

to essential behavioral states. Rhythmic oscillations in the theta (4–12 Hz) and in the gamma (20–80 Hz) ranges are among the most prominent patterns of activity in Hippocampus, and neuroscientists believe that both rhythms reflect aspects of the hippocampal functions related to learning and memory. It is commonly supposed that activity coming from Medial Septum and Entorhinal Cortex are nedeed to induce the theta rhythm in Hippocampus. Vice versa, the hypothesis that the gamma rhythm is generated intrinsically by the network of inhibitory interneurons in Hippocampus is supported by recent experimental and theoretical articles. Both rhythms are present during the exploratory activity in awake animals.

The Kinetic Model

The kinetic theory of neural systems, formulated several years ago [5, 6] to describe the activity of large neural fields, has been utilized here for the description of the activity of the CA3 neural field. The most original aspect of such a theory is the statistical description of the neuronal interaction. In fact, the action potentials traveling along the axonic branches are represented as massless particles, the *impulses*, having only statistical links to the axonic structure. They move freely within the neural field until they *collide* with a neuron. The collision can possibly result in the absorption by the neuron of the impulse and, hence, in the increasing or decreasing of its subthreshold membrane potential. If the threshold value is exceeded, the neuronal *firing* occurs and a stream of new impulses is emitted within the neural field.

The functions $f_s(\mathbf{r},\ \mathbf{v},\ t)$ and $g_{s'}(\mathbf{r},\ e,\ t)$ describe, respectively, the velocity distribution of impulses and the distribution of the subthreshold neuronal excitation within the neural field. The function $\psi_{s'}(\mathbf{r})$ denotes the local density of neurons.

Differently from the assumptions of earlier articles, we surmise here that the impulses can be absorbed by large extension of the neural field, reflecting the span of the dendritic trees. In this setting, defined as non-local absorption model, it can be demonstrated that the time evolution of the distribution functions $f_s(\mathbf{r},\ \mathbf{v},\ t)$ and $g_{s'}(\mathbf{r},\ e,\ t)$ is governed by the following set of coupled differential equations:

$$\begin{aligned}\nabla_t f_s(\mathbf{r},\mathbf{v},t) + \mathbf{v}\cdot\nabla_{\mathbf{r}} f_s(\mathbf{r},\mathbf{v},t) + f_s(\mathbf{r},\mathbf{v},t)\left(\Sigma_{s'}\int_{D(\mathbf{r})}\psi_{s'}(\mathbf{r}')\mid\mathbf{v}\mid\sigma_{s's}d\mathbf{r}'\right) = \\ S_s(\mathbf{r},\mathbf{v},t)\delta(s-s_{ex}) + f_s^*(\mathbf{r},\mathbf{v})N_{s'}(\mathbf{r},t)\delta(s-s_{in}) \\ + f_s^0(\mathbf{v})\int_A \xi_{s's}(\mathbf{r},\mathbf{r}')\,d\mathbf{r}'\int f'(v')N_{s'}\left(\mathbf{r}',t-\frac{|\mathbf{r}-\mathbf{r}'|}{v'}\right)dv'\delta(s-s_{in})\end{aligned} \tag{34.1}$$

$$\begin{aligned}\nabla_t g_{s'}(\mathbf{r},e,t) + \mu(e_r-e)\nabla_e g_{s'}(\mathbf{r},e,t) = \\ [g_{s'}(\mathbf{r},e-\epsilon,t) - g_{s'}(\mathbf{r},e,t)]\,(1-\delta(\epsilon)) \\ + N_{s'}(\mathbf{r},t-\tau_{s'})\delta(e-e_r) + M_{s'}(\mathbf{r},t)\theta(\epsilon)\delta(e-e_0)\end{aligned} \tag{34.2}$$

Where, ϵ (the net excitatory effect on single neurons), $N_{s'}(\mathbf{r},\ t)$ and $M_{s'}(\mathbf{r},\ t)$ (the probable number of neurons in firing or hyperpolarized state, respectively), can be computed as functions of f and g. Moreover, $f^*(\mathbf{r},\ \mathbf{v})$, $f^0(\mathbf{v})$ are structural parameters linked to the velocity spectra of impulses emitted in different conditions and $\xi_{s's}(\mathbf{r},\ \mathbf{r}')$ is an origin/destination matrix for long-range impulses, while $f'(v')$ denotes the velocity distribution along these paths. This matrix is based on experimental data about the geometry of pyramidal association projections along Schaffer collaterals ($CA3 \rightleftharpoons CA3$) [7].

Ca3 Global Activity Simulation

The non-local model has been utilized to carry out several series of computer simulations to study the activity of the entire CA3 field of the rat – as reported in the Atlas of Rat Brain [8]. The neuronal densities and parameters of connectivity have been computed from values in literature (see [9], where estimates of several structural parameters are reported). According to those values, the neuronal families of the simulated CA3 field were constituted by about 300.000 pyramidal neurons and 30.000 fast and 30.000 slow inhibitory neurons. As regards to the inputs, it is well known that pyramidal neurons of Entorhinal Cortex (EC) innervate CA3 both via Dentate Gyrus (through the mossy fibers) and by a direct path. Dentate Gyrus is also under the inhibitory control of the Hilus, an hippocampal field which receives input from several sub-cortical nuclei, such as Medial Septum (MS) and diagonal band, Raphe and Corpus Coeruleus, related to attentional or emotional reactions [10].

In all the computer simulations, stimuli caming from Entorhinal Cortex, Dentate Gyrus, and Medial Septum were simulated. In some simulations inhibitory input, selectively inhibiting the inhibitory neural populations of CA3, have been considered.

The space-time course of some macroscopic parameters computed by $f_s(\mathbf{r},\ \mathbf{v},\ t)$ and $g_{s'}(\mathbf{r},\ e,\ t)$ – i.e. local frequency of spikes, local mean sub-threshold excitation, number of firing neurons – which have close analogy with the *in vivo* recorded activity of the hippocampal CA3 field (i.e., population spike trains, local field potentials) has been analyzed in the search of parameter values which induced oscillating hippocampal activity.

Results and Discussion

The computer simulation of the neural activity of the CA3 field shed light on some remarkable features of its dynamics. Under appropriate driving inputs, self-organized activities within the pyramidal neuronal population spread to the entire CA3 region. In their wake, stable oscillatory activities occurred within the inhibitory neural populations. They presented a persistent remnant, or trace, of the spatio-temporal behavior of the vanishing pyramidal activity, lasting for much longer time than that of pyramidal one. During this time, the pyramidal neurons could not

generate new activities, being very efficiently inhibited. The inhibition of the slow inhibitory neurons could modulate the duration of the inhibitory periods. This was obtained by simulating an inhibitory input on CA3 inhibitory populations originating from Medial Septum. In different simulations the frequency of the global pyramidal activity could range from 3 Hz to 11 Hz. Hence, the global activity of the CA3 field was organized in such a way to present specific time windows for the generation of pyramidal (excitatory) activities, separated by long periods of patterned inhibition. This suggests that a sort of temporal coding is associated to the function of the entire CA3 field, which seems to operate as follows. Among all the inputs arriving to CA3 through EC, only those which reach it in appropriate time intervals, which are also under the control of activities in emotion-linked sub-cortical nuclei (like Locus Coeruleus and Median Raphe), are able to trigger global activities and to produce effects on the brain regions driven by CA3. Other cortical activities, which arrive either too late or too early with respect to the time windows imposed by attentional-emotional control, are unable to modify the ongoing CA3 activity, and the information they convey is not allowed to go beyond CA3. In such a way, a free period of time with a duration of 50–80 ms is reserved to the successful cortical inputs to CA3, during which they can drive activities in other cortical regions without interferences by competing inputs. They may result in learning, memory and other cognitive effects.

References

1. Milner B.: Disorders of learning and memory after temporal lobe lesions in man. Clinical Neurosurg. **19** (1972) 421–446
2. Mishkin M.: A memory system in the monkey. Phil. Trans. R. Soc. Lond. B **298** (1982) 85–95
3. Squire L. R., Shimamura A.P. and Amaral D. G.: Memory and the hippocampus. In Neural Models of Plasticity (eds Byrne J. H. and Berry W. O.) Academic Press, San Diego (1989) 208–239
4. Wilson M. A. and McNaughton B.: Dynamics of the hippocampal ensemble code for space. Science **261** (1993) 1055–1058
5. Ventriglia F.: Towards a kinetic theory of cortical-like neural fields. In Neural Modeling and Neural Networks (ed Ventriglia F.) Pergamon Press, Oxford-New York (1994) 217–249
6. Ventriglia F.: Kinetic approach to neural systems.I. Bull. Math. Biol. **36** (1974) 534–544
7. Ishizuka N., Weber J. and Amaral D. G.: Organization of intra-hippocampal projections originating from CA3 pyramidal cells in the rat. J. Comp. Neurol. **295** (1990) 580–623
8. Paxinos G. and Watson C.: The rat brain in stereotaxic coordinates. Academic Press, San Diego (1986)
9. Ventriglia F.: Computational experiments support a competitive function in the CA3 region of the hippocampus. Bull Math Biol. **60** (1998) 373–407
10. Vertes R. P.: Brainstem modulations of hippocampus: anatomy, physiology, and significance. In The Hippocampus (eds Isaacson R. L. and Pribram K. L.), Vol. 4 Plenum Press, New York (1986) 41–75

Chapter 35
Behaviour Signatures of Continuous Attractors

Si Wu

Abstract Continuous attractors are promising models for describing the encoding of continuous stimuli in neural systems. In this study we investigated two general properties associated with the unique dynamics of continuous attractors, namely, the logarithm reaction time and the asymmetric neural correlation. These two behaviour signatures can serve as important clues for experimental data to check whether continuous attractors are really applied in neural systems.

Introduction

The recent progress in both experimental and theoretical studies have suggested that there may exist a new form of memory structure, called continuous attractor, in biological systems (see [1, 2] and references therein). This type of attractor is appealing for encoding continuous stimuli, such as the orientation, the moving direction and the spatial location of objects, or the continuous features of a class of objects that underlying their categorization.

In a continuous attractor, the stationary states of the system are properly aligned in the state space according to the stimulus values they represent. They form a continuous parameter space, on which the system is neutrally stable. This neutral stability is the key that distinguishes a continuous attractor from a discrete one. Intuitively think, neutral stability implies that the system state can be easily changed along the attractor space under a small external drive. For a discrete attractor, such as the Hopefield model [3], the memory states are trapped in their basins (see the illustration in Fig. 35.1a,b).

A continuous attractor has many computationally desirable properties, for instance, it enables a neural system to track time-varying stimuli in real-time, a

S. Wu
Department of Informatics, University of Sussex, UK
e-mail: siwu@sussex.ac.uk

R. Wang et al. (eds.), *Advances in Cognitive Neurodynamics*,

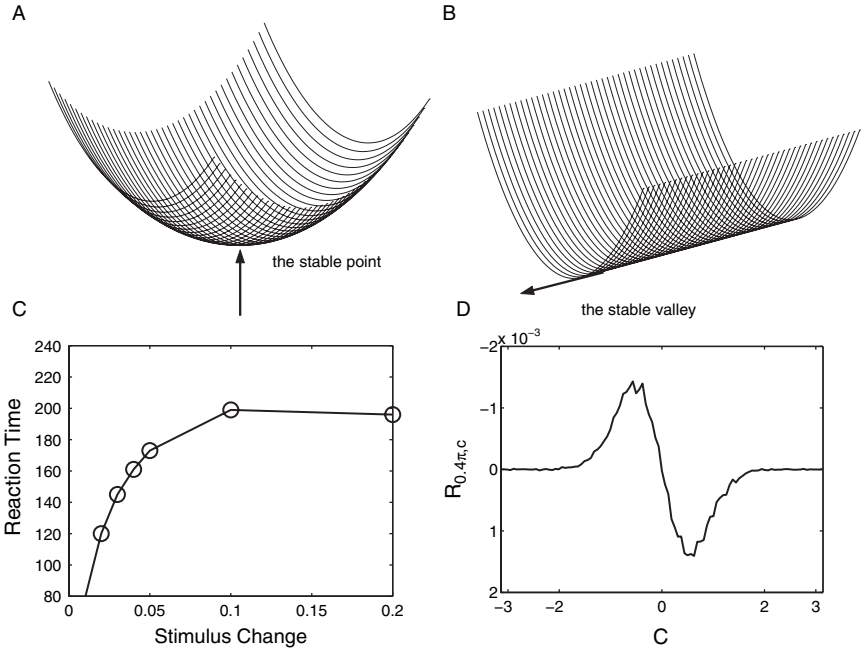

Fig. 35.1 (a) An example of a discrete point attractor. The system is only stable at the bottom of the bowl. (b) An example of line attractor, the one-dimensional version of continuous attractor. The system is neutrally stable along the valley. (c) The reaction time vs. the abrupt stimulus change. (d) Illustrating the asymmetric neural correlation

capacity which is crucial for the brain to carry out many important tasks, such as motion control and spatial navigation. Although continuous attractors have these attracting properties, their implementation in neural systems has not been fully confirmed. In this study we will explore two behaviour signatures associated with the unique dynamics of continuous attractors, namely, the logarithm reaction time and the asymmetrical neural correlation. They can serve as important clues for experimental data to check whether continuous attractors are really applied in neural systems.

Dynamics of Continuous Attractors

For simplicity, we will consider a simple continuous attractor model, which allows us to solve the network dynamics analytically. The final conclusions, however, can be easily extended to general cases.

Consider a one-dimensional continuous stimulus x is encoded by an ensemble of neural clusters, whose preferred stimuli are denoted as c, with $c \in (-\infty,\ \infty)$. We

denote γ_c the firing rate of the cluster c, and U_c the population-averaged input. The network dynamics is given by

$$\tau \frac{dU_c}{dt} = -U_c + \rho \int_{c'} J_{c,c'} \gamma_{c'} dc' + I_c^{ext}, \tag{35.1}$$

$$\gamma_c = \frac{U_c^2}{1 + k\rho \int_{c'} U_{c'}^2 dc'}, \tag{35.2}$$

where τ the time constant, ρ the neural cluster density, k a small positive constant and I_c^{ext} the external input. The recurrent interaction $J_{c,c'}$ is set to be $J_{c,c'} = Je^{-(c-c')^2/2a^2}/(\sqrt{2\pi}a)$ with J a constant.

It is straightforward to check that the network holds a continuous family of stationary states when $I_c^{ext} = 0$, i.e.,

$$\bar{U}_c(z) = \frac{A\rho J}{\sqrt{2}} e^{-(c-z)^2/4a^2}, \tag{35.3}$$

$$\bar{\gamma}_c(z) = Ae^{-(c-z)^2/2a^2}, \tag{35.4}$$

where A is a proper constant. These stationary states are of the Gaussian-bell shape, agreeing with the experimental data. They are parameterized by a single free variable $z \in (-\infty, \infty)$, i.e., the peak position of the bump.

We choose the external drive I_c^{ext} to be

$$I_c^{ext} = \alpha \bar{U}_c(x) + \sigma \xi_c(t), \tag{35.5}$$

where both α and σ are small positive constants, and $\xi_c(t)$ is Gaussian white noise with zero mean and unit variance. The first term, $\alpha \bar{U}_c(x)$, represents the stimulus signal, whose effect is to drive the system to the location of the stimulus x.

To proceed, let us first see how neutral stability shapes the network dynamics. Suppose the discrepancy, $\delta U_c = U_c(z) - \bar{U}_c(z)$, is sufficiently small, we linearize eq. (1) in the vicinity of a stationary state peaked at z, and obtain

$$\tau \frac{d\delta U_c}{dt} = -\delta U_c + \rho \int_{c'} F_{c,c'} \delta U_{c'} dc' + I_c^{ext}, \tag{35.6}$$

where the matrix $F_{c,c'}(z) = \int_{c''} J_{c,c''}(\partial \bar{r}_{c''}(z)/\partial \bar{U}_{c'}(z))dc''$.

Neutral stability implies that the matrix $\mathbf{F}(z)$ has one right eigenvector whose eigenvalue is one and all the other eigenvalues are smaller than one. It can be checked this is indeed the case. The eigenvector of unit eigenvalue is along the tangent of the attractor space, which is given by

$$e_c^I(z) \sim \bar{U}_c'(z) = D_I(c - z)e^{-(c-z)^2/4a^2}. \tag{35.7}$$

The fact that $\mathbf{e}^I(z) = \{e_c^I(z)\}$ is the right eigenvector of $\mathbf{F}(z)$ with unit eigenvalue implies that the projection of $\{\delta U_c(z)\}$ on $\mathbf{e}^I(z)$, corresponding to the bump movement along the valley, is sustained under the attractor dynamics; whereas, the projections of $\delta U_c(z)$ on the other directions, corresponding to the distortion of the bump shape, decay exponentially. This tells us that the dynamics of a continuous attractor under the driving of small external inputs is dominated by its position shift along the attractor space. Therefore, we can reasonably project the network dynamics Eq. (35.1) on the direction $\mathbf{e}^I(z)$, and simplify it as a one-dimensional Ornstein-Uhlenbeck process, which is given by

$$\tau \frac{dz}{dt} = -\alpha(z - x) + \beta\epsilon(t), \tag{35.8}$$

where β is given by $\beta = \sigma/\sqrt{\int_c [\bar{U}_c'(z)]^2 dc}$. The meaning of this equation is straightforward: when the bump is not at the stimulus position, the stimulus signal generates a force, $-\alpha(z-x)$, which pulls the bump to the stimulus position ($z = x$). The noise effect, $\beta\epsilon(t)$, on the other hand, tends to shift the bump position randomly.

Based on Eq. (35.8), we now investigate two properties associated with the continuous attractor dynamics. Firstly, we quantify the reaction time for the system to catch up abrupt stimulus change. Consider a scenario in which the stimulus value is abruptly changed from initial $z(0)$ to 0. The reaction time is measured by the mean of the first passage time for the bump peak crossing 0. We get

$$\langle T \rangle = \frac{\tau}{\alpha}\sqrt{\pi} \int_{d_1}^{0} e^{u^2} [1 + erf(u)]\, du, \tag{35.9}$$

where $d_1 = -z(0)\sqrt{\alpha\tau}/\beta$. This equation reveals that the reaction time of the continuous attractor increases logarithmically with the size of abrupt stimulus change $|z(0)|$ (see Fig. 35.1c).

Secondly, we calculate the correlation between neural response variabilities, which is defined to be

$$R_{c,c'} = < (r_c - \bar{r}_c)(r_c - \bar{r}_{c'}) > . \tag{35.10}$$

Since the network dynamics is dominated by the bump movement along the attractor space, we have $r_c(z) \approx \bar{r}_c(x) + \bar{r}_c'(x)(x - z)$. Therefore, we get

$$\begin{aligned} R_{c,c'} &\sim \bar{r}_c'(x)\bar{r}_c'(x), \\ &\sim (x - c)(x - c')e^{-(c-x)^2/2a^2} e^{-(c'-x)^2/2a^2}. \end{aligned} \tag{35.11}$$

This correlation structure is asymmetric with respect to the stimulus value, in the sense of that $R_{c,c'} > 0$ if $(x - c)(x - c') > 0$, and $R_{c,c'} < 0$ if $(x - c)(x - c') < 0$ (see the illustration in Fig. 35.1d).

Conclusions

The present study investigated two general properties of continuous attractors, namely, the logarithm reaction time and the asymmetric neural correlation. Since these two properties are determined by the unique neutral stability of continuous attractors, they can serve as important clues for checking in experiments whether continuous attractors are really applied in neural systems. For instances, the logarithm reaction time may be checked by the mental rotation experiment, and the asymmetrical neural correlation may be checked by the multi-unit recording. We will carry out research to confirm these two properties in our future work.

References

1. Trappenberg, T.: Continuous attractor neural networks. Recent Developments in Biologically Inspired Computing. Leandro Nunes de Castro and Fernando J. Von Zuben ed., Idea Group Inc., (2004) http://books.google.co.uk/books?id=s_Q5YZ2nh2kC&dq=Recent+Developments+in+biologically+inspired+computing+2003&lr
2. Wu, S. & Amari, S.: Computing with continuous attractors: stability and on-line aspects. Neural Comput 17 (2005) 2215–2239.
3. Hopfield, J. J.: Neurons with graded responses have collective computational properties like those of two-state neurons. Proc Natl Acad Sci USA 81 (1984) 3088–3092.

Chapter 36
Statistical Outliers in Neuron Population and Myelinated Fiber Development in Human Neocortex

David L. Cooper, James E. Gentle and James L. Olds

Abstract Between 1939 and 1967, JL Conel performed detailed histological examinations of 54 human subjects at eight observations ages ranging from newborns to 6 years old. He made detailed observations of neuron densities, Weigert and Golgi-Cox stained fibers, fiber diameters, and cell sizes by neocortical layer for up to 43 neocortical areas for each age. Here we use this data to construct standard sample columns to calculate changes between observation ages, and show that it is well matched by a gamma distribution. We then show that a developmental distance metric (DDM) transformation facilitates a statistical exploration of inter-area differences during development.

Keywords Developmental distance · gamma distribution

Introduction

JL Conel's [1] four million observations of neuron density, layer thickness, somal size, Golgi-Cox and Weigert-stained fiber densities from human subjects through 6 years of age ($N = 54$), provides a unique source of information below current imaging resolution. Shankle et al. [2] used a multivariate ordination technique called correspondence analysis to reduce Conel's data into 1727 feature profiles for the 43 regions of the human neocortex that Conel examined. The profiles reveal distinct time-phased changes; for example, neuron packing density decreases with age, while fiber myelinization increases. This analysis provided a compelling argument for a broad developmental pattern of changes across individuals.

However, correspondence analysis does not preserve information on the distributions of change for the individual measurements, and thus does not highlight differences between neocortical areas. Those differences, if they existed, might well be of functional importance. Here we apply a novel transformation method that

D.L. Cooper
Krasnow Institute of Advanced Study, 4400 University Drive, Mail Drop 2A1, George Mason University, Fairfax, VA 22030, USA
e-mail: dcoopere@gmu.edu

R. Wang et al. (eds.), *Advances in Cognitive Neurodynamics*,

preserves that information on distributions, while expanding information on the temporal details of development. We show that the measurement of neurons and myelinated fibers in the human neocortex during development conforms to gamma distributions.

Methods

We employed two transformations to Conel's neuron density and Weigert-stained (myelinated) fiber density. The first transformation was to convert density information by cortical area and layer into standard sample columns (SSCs). In the case of neuron populations, Conel made his measurements for standard volumes of $100\,\mu m^3$. For fiber populations, he counted stained fibers in a sample volume of $50\,\mu m \times 50\,\mu m \times 25\,\mu m$. SSCs were constructed using Conel's layer thickness measurements for these unit volumes. When Conel reported the densities for sublayers rather than complete layers, we used the mean density for the layer. Here, we produced SSCs corresponding to 19 sample Brodmann Areas related to audio and visual processing.

The second transformation was to create DDMs using the changes between ages within each SSC type (neuron or fiber). We treated Conel's measurements at the eight observation ages as eight experiments on a neocortical macroarray, comparable to microarray analysis of gene or protein expression (for example, [3]). Similar to Strand et al., we first took the log proportion of neuron or fiber populations within each observation age [Eq. (36.1)]. Next, rather than the z-score method used in Strand et al., we normed changes to the log proportions across observation ages by using the pooled variance [Eq. (36.2)]. Finally, as in Strand et al., we examined for clustering of the scores by taking the Euclidean distances between the normed scores area-by-area. Conel made his observations at eight different ages from newborn to 6 years of age, so the DDMs provide cumulative double-normed measures for seven sets of changes.

$$LP(\text{Area}_i) = \log(\text{Count}_i / \sum\nolimits_j \text{Count}_j) \tag{36.1}$$

$$D = (\mu_1 - \mu_2)^2/(\sigma_1^2 + \sigma_2^2) \tag{36.2}$$

To examine the change data, we first measured unadjusted SSC change data for each layer, and then examined the distributions created by double-normed DDMs.

Results

Overall neuron change data for the 54 brains shows a negative mean and negative skewness (Fig. 36.1a). On average, a layer lost 36.9 neurons within a $100\,\mu m^2$ cross-section between any two observation ages. Skewness for an entire SSC was -1.74. The myelinated fiber changes have positive skewness (2.36 for the SSC) and a

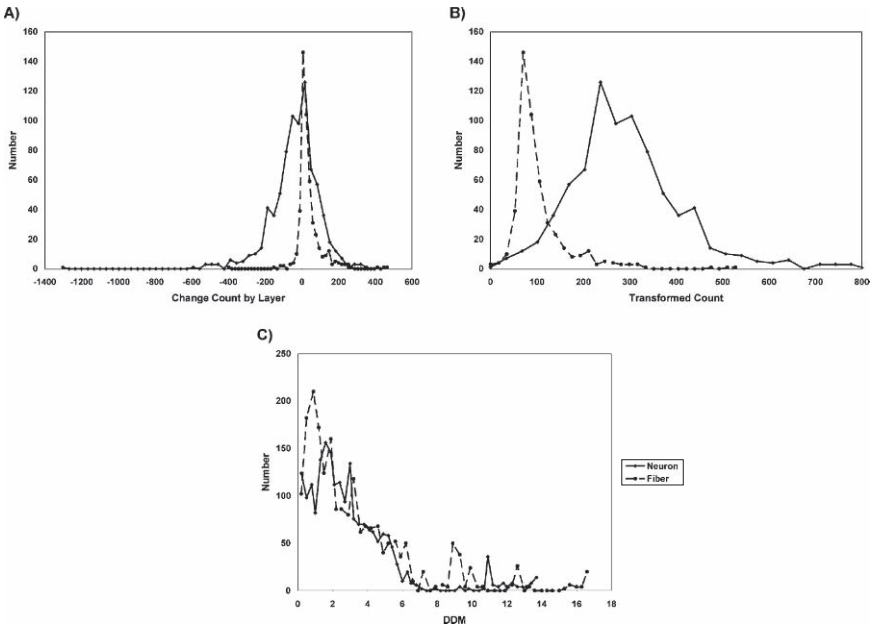

Fig. 36.1 Neuron and myelinated fiber distributions. Neuron histograms use solid lines. Fiber histograms use dashed lines. (a) changes to neuron and fiber counts in a layer for 19 neocortical areas. (b) comparison of change data for neuron losses and fiber increases by layer. (c) DDM neuron and fiber distributions

positive mean (23.2 for a 50 μm^2 cross-section for each layer). To test for a gamma fit, we compared neuron losses to myelinated fiber gains (Fig. 36.1b). We reflected the neuron change data about an axis equal to the maximum value, and translated fiber data toward the origin, excluding the six disconnected negative outliers in Fig. 36.1a. The distributions then became positively skewed over a non-negative range. We compared these empirical distributions to both a gamma distribution and a lognormal distribution with corresponding values based on maximum likelihood estimates. We then applied a Kolmogorov-Smirnov goodness-of-fit test for these distributions against a cumulative density function equal to the mean of a 10,000-iteration random function with the corresponding estimated parameters. P-values appear in Table 36.1. This reveals that a gamma distribution models the empirical data well.

For an SSC, maximum likelihood estimates for gamma parameters for neurons are $\alpha = 5.4764$ (95 pct confidence interval = [4.9787, 6.0239]), and $\beta = 0.0745$ (95 pct confidence interval = [0.0675, 0.0824]). The P-value from a Kolmogorov-Smirnov goodness-of-fit test is 0.3116. For myelinated fibers $\alpha = 4.3359$ (95 pct confidence interval = [3.8409, 4.8946]), and $\beta = 24.8831$ (95 pct confidence interval = [21.8824, 28.2952]). The associated P-value is 0.3334.

Although double-normed DDMs are gamma-like (the Kolmogorov-Smirnov P-value is 0.1546 for 48 and 72 months for neurons, and higher for myelinated

Table 36.1 *P*-values associated with Kolmogorov-Smirnov goodness-of-fit tests for gamma and lognormal distributions compared to the mean cumulative density function from 10,000 iterations using estimated parameters for neuron population and myelinated fiber data by layer

P-value	Neuron gamma	Neuron lognormal	Fiber gamma	Fiber lognormal
Layer I	0.3759	0.3755	0.4219	0.4169
Layer II	0.3582	0.3428	0.4038	0.4026
Layer III	0.2435	0.1405	0.3553	0.3391
Layer IV	0.3899	0.3897	0.2671	0.3045
Layer V	0.3840	0.3649	0.3732	0.3618
Layer VI	0.3839	0.3605	0.2961	0.1588

fibers), their histograms appear to be multimodal (Fig. 36.1c). A 50-bin histogram of the cumulative distances at 72 months, for example, has two local maxima to the left of the overall maximum, and has several local maxima at the right tail separated from the rest of the distribution by empty bins. Generally, the shortest double-normed neuron distances correspond to Layer IV (the thalamic input layer) for most of the 19 areas, whereas the longest double-normed distances pertain to primary visual cortex (BA 17), the anterior cingulate cortex (BA 24), and the dorsolateral prefrontal cortex (BA 9). Extreme distances for fibers correspond to primary motor cortex (BA 4).

Discussion

DDMs appear to "unfold" the state-space associated with neuron losses and myelinated fiber gains during development from birth through 6-years of age. The distance metric embeds the change data in a higher-dimensional manifold and enables the separation of change factors that are initially nearly adjacent in state space [4]. The presence of layer or area-specific associations in the outlier areas indicates that this is a promising avenue to pursue in future research.

References

1. Conel JL (1939–1967) Postnatal development of the human cerebral cortex, Vols 1–8. Harvard University Press.
2. Shankle WR, Romney AK, Landing BH, Hara J (1998) Developmental patterns in the cytoarchitecture of the human cerebral cortex from birth to 6 years examined by correspondence analysis. Proc Nat Acad Sci USA 95:4023–4028.
3. Strand AD, Aragaki AK, Baquet ZC, Hodges A, Cunningham P, Holmans P, Jones KR, Jones L, Kooperberg C, Olson JM (2007) Conservation of regional gene expression in mouse and human brain. PLoS Genet 3(4): e59 doi:10.1371/journal.pgen.0030059.
4. Grassberger P, Procaccia I (1983) Measuring the strangeness of strange attractors. Physica D 9:189–208.

Chapter 37
Studies on Synchronization Using KIV Model

Mark H. Myers, Robert Kozma and Walter J. Freeman

Abstract The KIV model is a biologically inspired neural network that can exhibit non-linear electrical brain activity found in the limbic system of the brain. One such behavior exhibited in brain activity is cognitive processing. Spatial patterns of beta-gamma EEG emerged following sudden jumps in cortical activity called "phase transitions". The interaction between entorhinal cortex (EC), amygdala, and hippocampal and cortical areas in vertebrate brains is studied using the dynamical K model approach. Other biological attributes defined by Freeman et al. [1] are applied to display the biological relevance of the KIV model.

Keywords Chaotic neurodynamics · KIV model · EEG · cognitive phase transitions · Hilbert transform

Introduction

Sensory input differentiates itself from the periodic oscillations of the background noise of the cortex, and has an amplitude and phase modulation that is different from the periodic oscillations. The synchronization of the myriad of neuron domains can be quantitatively measured by the phase differences of the EEG electrode data collection channels [2]. Hilbert Transformation decomposes the EEG time series into Analytic Amplitude (AA) and Analytic Phase (AP) [3]. Through the use of Hilbert transformations, we can calculate the phase differences over time which correspond to the rapid firing of the large domains of neurons and provide a means to display the synchronizations of those domains when the cortex is exhibiting a cognitive or learning process [4]. Details of the model simulations are given by the next section, followed by the results of the analysis of various spatio-temporal characteristics. The obtained results may provide a basis for the interpretation of experimental EEG data measured in various cognitive states.

M.H. Myers
Computational Neurodynamics Laboratory, Department of CS, University of Memphis, Memphis, TN 38152, USA
e-mail: mhmyers@memphis.edu

R. Wang et al. (eds.), *Advances in Cognitive Neurodynamics*,

The KIV Model

The KIV model is a biologically inspired neural network [5]. K-set family includes hierarchy of K models of increasing complexity. They represent different aspects of the vertebrate brain. KIV is the mathematical model of the hemisphere. It has the functionality of sensory perception and action selection. Figure 37.1 provides the architecture of the KIV model which is represented by three major parts; the KIII cortex, KIII hippocampus and the KII amygdala. Hippocampus models include navigation functions. The cortex models sensory processing and pattern recognition in various sensory modalities. The amygdala is the unit where the activations from the cortex and hippocampus are projected and decision is made concerning the next action, based on the fusion of the signals from other brain areas. With proper weight selection between the components of KIV, this network can maintain non-convergent chaotic oscillations. The balanced weights between these chaotic networks, WA, WB, and WC provide the manner in which we can model electrical neuronal activity found in a human EEG.

Signal Processing Methodology

Hilbert Transformations decomposes the EEG time series, one for Analytic Amplitude (AA), and the other for Analytic Phase (AP) [4]. Once the complex part of the signal is calculated through Hilbert Transformations, the analytical phase is calculated by the arctangent of the ratio of the imaginary part to the real part. The average unwrapped phase is calculated by adding Π radians on each channel. The average unwrapped phase was marked by repeated jumps known as "phase slip" above or below the mean difference [3]. A raster plot of the curves and phase slip were plotted, and upward or downward deviation from the mean differences.

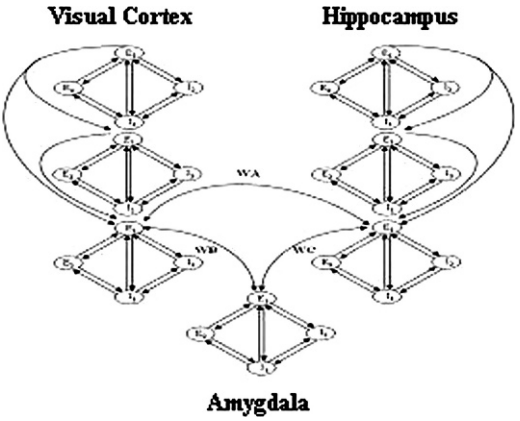

Fig. 37.1 Analytic amplitude with standard deviation of phase slips

KIV Simulations

The weights connecting the two KIII networks and the KII network are increased, while the signal bias in the KIII is set to a value much greater value (1.5) than the bias of the signal generated from the KII network (0.1). Noise is not added to the network, which would normally aid in amplifying the signal to display phase synchronizations [6]. Lower parameter values for the weighting between the networks, as well as lower biases in the KIII networks did not display phase synchronizations over time. The standard deviation of the phase differences across time display the phase slips across the mean of the phases, see Fig. 37.2. The standard deviation of phase differences measures the synchronization in the system. Low values of standard deviation (SDt) indicate where we would expect to find the synchronizations of the analytic amplitude; whereas high values of SDt of the phase differences isolate and bookend where the analytic amplitude of the phase should occur. The high values of SDt revealed the time periods when spatial patterns were changing rapidly [1]. Figure 37.3 shows a example of the oscillating SDt during a 4 s long experimental period.

A series of experiments have been conducted with a range of initial conditions in order to derive statistically relevant information on the phase transitions. A histogram of the standard deviation of the phase differences SDt is shown in Fig. 37.4a, in semilogx coordinate.

For SDt $<$ 0.1, the distribution is log-normal, however, the phase transitions are manifested in a long tail of the distribution function from SDt $=$ 0.1 to the max value of about Π rad. The tail of the distribution is analyzed in detail in Fig. 37.4b, in loglog coordinates. A regression analysis shows, that the size of the jumps in SDt has a scale-free fractal distribution, with regression behavior log (phase) $=$ 0.41–0.98 log(SDt). Time domain analysis yields a waiting time of 189$\pm$89 ms between jumps, while the jumps take just 6 ms in average.

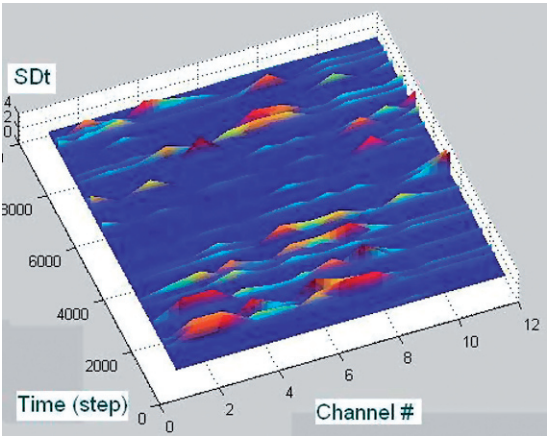

Fig. 37.2 The 12 columns show the near-coincidence of the sudden phase jumps

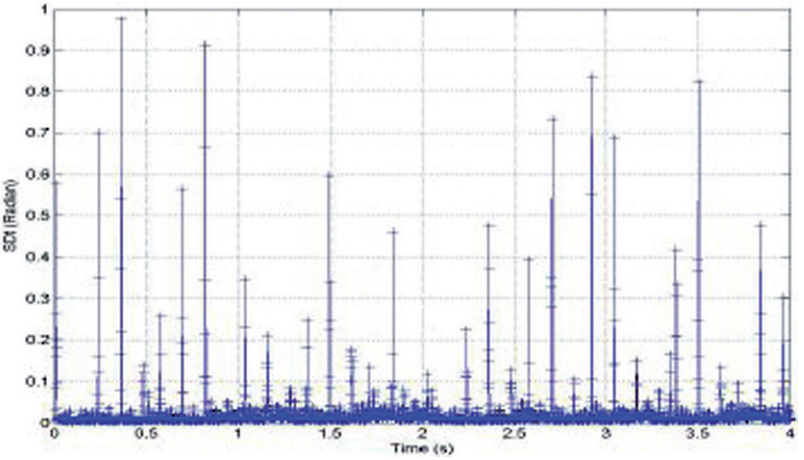

Fig. 37.3 Standard deviation of analytic phase differences across the cortical array

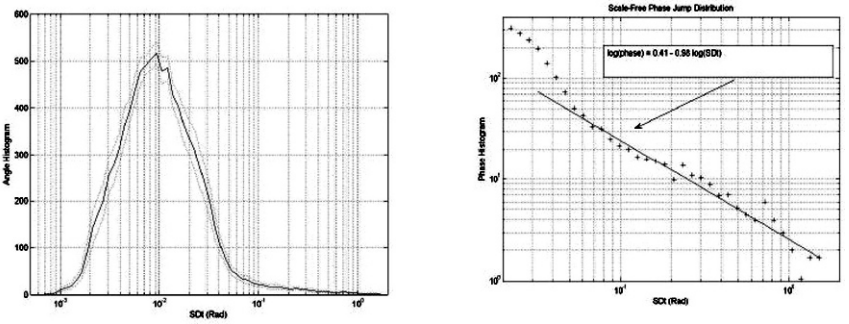

Fig. 37.4a–b Histogram of the phase standard deviation SDt. The left panel shows details of the phase jumps

Conclusion

By using Hilbert transforms we were able to capture fast global synchronized spatial patterns of amplitude modulation. Our results indicate various phase transitions in the cortex which has been observed in EEG patients engaged in cognitive tasks.

References

1. Freeman, W. J.: Origin, Structure, and Role of Background EEG Activity, Part 1, Analytic Amplitude. Clinical Neurophysiology 115 (2004) 2077–2088.
2. Freeman, W. J., Burke, Brian, Holmes, Mark D.: Origin, Structure, and Role of Background EEG activity, Part 2, Analytic Phase. Clinical Neurophysiology 115 (2004) 2089–2107.
3. Kozma R., Myers M.: Analysis of Phase Transitions in KIV with Amygdale during Simulated Navigational Control. IEEE IJCNN05, Montreal, Canada (2005).

4. Freeman, Walter J.: Origin, Structure, and Role of Background EEG Activity, Part 1, Analytic Amplitude. Clinical Neurophysiology (2004) 9–47.
5. Kozma R., Freeman W. J., Erdi P.: The KIV Model – Nonlinear Spatio-Temporal Dynamics of the Primordial Vertebrate Forebrain. Neurocomputing 52–54 (2003) 819–826.
6. Liljenstrom, H., Wu X.: Noise-Enhanced Performance in a Cortical Associative Memory Model. International Journal of Intelligent Systems 6 (1995) 19–29.

Chapter 38
Synchronous Firing and Its Control in Neuronal Population with Time Delay

Xianfa Jiao and Rubin Wang

Abstract We propose a stochastic model of a neuronal population in cases where synaptic delays and also inhibitory coupling are present. We investigate the firing patterns and its control of a neuronal population by means of Fokker-Planck approach. Numerical simulations show that synaptic transmission delay can suppress oscillatory synchronization of neuronal firing and enhance synchronized firing behavior. Neuronal stimulation also indicate that effective desynchronization occur by external stimulation.

Introduction

Synchronous firing in a neuronal population has received considerable attention as a possible candidate mechanism for neural information processing. For instance, Kreiter and Singer demonstrated that neurons in the monkey brain that responded to two independent images of a bar fired asynchronously when the bars were moving in different directions, but fired synchronously when the same bars moved together [1]. It appeared that two different aspects of the same object were encoded by synchronous firing of neurons in a neuronal population. Eckhron, Singer have suggested that synchronous oscillation in primary visual cortex link distant neurons involved in representing different aspects (color, shape, movement, etc.) of the same visual perceptions and bind together features of a sensory stimulus [2, 3].

Taking into account stochastic aspect in the nervous system, collective behaviors of a neuronal population have been investigated by using Fokker-Planck approach [4, 5, 6, 7, 8, 9]. Tass has investigated collective firing patterns in a neuronal population by considering the cluster of oscillators as a model of interacting neurons, where the single neuron is approximated by means of a phase oscillator [4].

In this paper, motivated by real nervous system where synaptic transmission delay can be significant, we explore the synchronized firing patterns of a neuronal population in cases where synaptic delays and also inhibitory coupling are present.

X. Jiao
School of Science, Hefei University of Technology, Hefei 230009, China
e-mail: xfjiao@126.com

R. Wang et al. (eds.), *Advances in Cognitive Neurodynamics*,

Stochastic Model

We consider the dynamics of a neuronal population with excitatory and inhibitory connection. For convenience, we assume that the coupling strength between excitatory neurons is time dependent, and the coupling strength between inhibitory neurons is a constant. The dynamical equation is described by the following set of equations:

$$\dot{\psi}_i = \omega_i + \frac{1}{N}\sum_{j=1}^{N_1} K_{ij} M(\psi_j - \psi_i) + \frac{1}{N}\sum_{j=N_1+1}^{N} a\,Q(\psi_j - \psi_i) + S(\psi_I) + \xi_i(t) \tag{38.1}$$

$$\dot{K}_{ij} = -\frac{1}{\tau}K_{ij} + \alpha H(\psi_j - \psi_i) + \eta_{ij}(t)\ (i = 1, \ldots, N; j = 1, \ldots, N_1) \tag{38.2}$$

where ψ_i describes the phase of the ith neuronal oscillator, ω_i is its eigenfrequency without mutual interacting. $M(\psi_j - \psi_i)$ and $Q(\psi_j - \psi_i)$ are coupling functions representing, respectively, excitatory and inhibitory interactions. K_{ij} is a time-dependent coupling strength between excitatory oscillators, the second term on the right-hand side describes the contribution of active level of two excitatory oscillators connected to the coupling strength, we assume that it is the function of phase difference with amplitude α. a is a time-independent coupling strength between inhibitory oscillators. $\xi_i(t)$ and $\eta_{ij}(t)$ are random forces acting on the phase and the coupling strength, respectively. For the sake of simplicity, the random forces are modeled by Gaussian white noise with following first-order and second-order moments:

$$\langle \xi_i(t) \rangle = 0 \left\langle \xi_i(t)\xi_j(t') \right\rangle = 2D_1\delta_{ij}\delta(t - t') \left\langle \eta_{ij}(t) \right\rangle = 0,$$

$$\left\langle \eta_{ij}(t)\eta_{mn}(t') \right\rangle = 2D_2\delta_{im}\delta_{jn}\delta(t - t') \left\langle \xi_i(t)\eta_{mn}(t') \right\rangle = 0,$$

where $\langle\ \rangle$ denotes an ensemble average, constants D_1 and D_2 are the intensities of the Gaussian white noises.

If η is short transmission delay compared to the period of an oscillation, we assume that the transmission delay creates only a simple phase shift in function H, namely $H(\psi_j(t - \eta) - \psi_i) = H(\psi_j - \psi_i - \theta)$, the case is considered as in [10].

To investigate the collective behavior of neural networks, in the limit of $N \to \infty, N_1 \to \infty$, $n_E(\psi, K, t)$ denotes the average number density of neuronal oscillators with phase ψ and coupling strength K in the excitatory population at time t, $n_I(\psi, t)$ denotes the average number density of neuronal oscillators with phase ψ in the inhibitory population at time t. $n_E(\psi, K, t)$, $n_I(\psi, t)$ is governed by following equations, which is derived as in [8].

$$\frac{\partial n_E}{\partial t} = -\omega\frac{\partial n_E}{\partial \psi} - \frac{\partial}{\partial \psi}\left[n_E S(\psi)\right] - \frac{\partial}{\partial \psi}\left[n_E \int_0^{2\pi}\int_0^{+\infty} K' M(\psi - \psi') n_E(\psi', K', t) d\psi' dK'\right]$$
$$-a\frac{\partial}{\partial \psi}\left[n_E \int_0^{2\pi} Q(\psi - \psi') n_I(\psi') d\psi'\right] + \frac{1}{\tau}\frac{\partial}{\partial K}(K n_E)$$
$$-\alpha\frac{\partial}{\partial K}\int_0^{2\pi} H(\psi - \psi') n_E(\psi', K, t) d\psi' + D_1\frac{\partial^2 n_E}{\partial \psi^2} + D_2\frac{\partial^2 n_E}{\partial K^2} \tag{38.3}$$

$$\frac{\partial n_I}{\partial t} = -\omega\frac{\partial n_I}{\partial \psi} - \frac{\partial}{\partial \psi}\left[n_I \int_0^{2\pi}\int_0^{+\infty} K' M(\psi - \psi') n_E(\psi', K', t) d\psi' dK'\right]$$
$$-a\frac{\partial}{\partial \psi}\left[n_I \int_0^{2\pi} Q(\psi - \psi') n_I(\psi') d\psi'\right] + D_1\frac{\partial^2 n_I}{\partial \psi^2} \tag{38.4}$$

In order to analyze the firing pattern of neural population, we consider the marginal probability distribution $n_E(\psi, t) = \int_0^{+\infty} n_E(\psi, K, t) dK$. We took $n(\psi, t)$ as a number density of the same phase in the neuronal population, viz. $n(\psi, t) = n_E(\psi, t) + n_I(\psi, t)$. For spiking neurons, a neuron is modeled by means of a phase generating a spike whenever its phase equals ψ_0, where ψ_0 is a constant. Therefore, $p(t) = n(\psi_0, t)$, called "population activity", describes the density of firing neurons at time t, which serves as a link between the experimentally observed firing of a population of neurons and the ensemble dynamics.

Numerical Simulations

The functions $M(x)$, $Q(x)$, $S(x)$ and $H(x)$ are all 2π-periodic functions, which are expanded by Fourier modes for numerical simulation. For simplicity's sake, we take $M(x) = \sin(x)$, $Q(x) = \cos(x)$, $H(x) = \cos(x)$, here I is stimulation amplitude. We also assume that a coupling strength between two excitatory neurons can't increase unboundedly, in the present paper, the variation of coupling strength K is in the interval (0, 2). Transmission delay phase $\theta = 0.01\pi$. Synchronized firing patterns in a neuronal population are represented by peaks in $p(t)$. Numerical simulation indicates that inhibitory connection can cause the oscillatory synchronized firing in a neuronal population (Fig. 38.1a). Whereas synaptic transmission delay is taken into account in our model, we find that synaptic transmission delay can decrease oscillation, and enhance synchronized firing (Fig. 38.1b).

Synchronized firing in a neuronal population is important for neuronal information processing. However, synchronization is not always desirable. For instance, several neurological diseases, such as essential tremor and Parkinson's disease, are caused by oscillatory synchronized firing in the neuronal population. To explore an effective desynchronized neuronal firing pattern by external stimulation, we take stimulation pattern $S(x) = I\cos(x)$ for numerical simulations. The result of numerical simulation is presented in Fig. 38.2. Our result indicates that appropriate external stimulation can effectively control synchronized firing behavior.

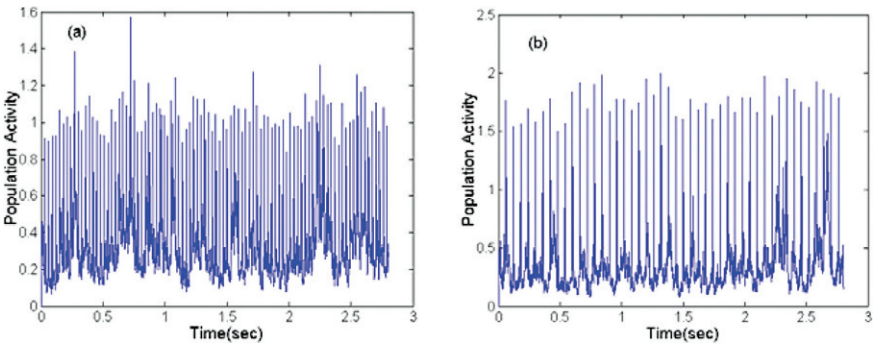

Fig. 38.1 Firing patterns of the neuronal population. (a) without transmission delay, (b) with transmission delay. Parameters: $\Omega = 2\pi$, $\tau = 20$, $D_1 = 0.5$, $D_2 = 0.2$, $\alpha = 0.01$, $a = 0.5$, $\theta = 0.01\pi$

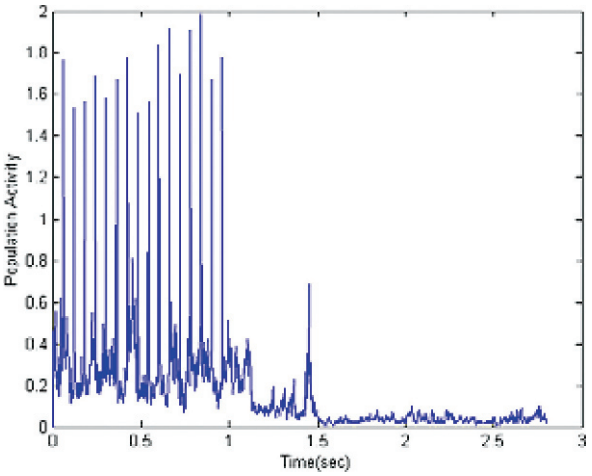

Fig. 38.2 Firing patterns of the neuronal population with transmission delay. Parameters: $\Omega = 2\pi$, $\tau = 20$, $D_1 = 0.5$, $D_2 = 0.2$, $\alpha = 0.01$, $a = 0.5$, $\theta = 0.01\pi$, $I = 10$

Conclusions

We have taken into account the property of real neuronal population, and proposed the stochastic model of a neuronal population in cases where synaptic delays and also inhibitory coupling are present. We investigate the firing patterns and its control of a neuronal population by means of Fokker-Planck approach. Numerical simulations show that synaptic transmission delay can suppress oscillatory synchronization of neuronal firing and enhance synchronized firing behavior. Neuronal stimulation also indicate that effective desynchronization occur by external stimulation.

Acknowledgments This work was supported by the National Natural Science Foundation of China under Grant 10672057, the Anhui Provincial Natural Science Foundation under Grant 070416231.

References

1. Kreiter, A.K. and Singer, W.: Stimulus-dependent synchronization of neuronal responses in the visual cortex of the awake macaque monkey, J. Neurosci., 16 (1996) 2381–2396.
2. Eckhorn, R., Bauer, R., Jordan, W., Brosch, M., Kruse, W., Munk, M. and Reitboeck, H.J.: Coherent oscillations: A mechanism of feature linking in the visual cortex? Multiple electrode and correlation analyses in the cat, Biol. Cybern., 60 (1988) 121–130.
3. Singer, W.: Consciousness and the structure of neuronal representations, Philos. Trans. R. Soc. Lond. B Biol. Sci., 353 (1998) 1829–1840.
4. Tass, P. A.: Phase resetting in Medicine and Biology, Springer-Verlag, Berlin (1999).
5. Wang, R., Zhang, Z.: Nonlinear stochastic models of neurons activities, Neurocomputing, 51 (2003) 401–411.
6. Wang, R., Zhang, Z.: Analysis of dynamics of the phase resetting on the set of the population of neurons, Int. J. Nonlinear Sci. Numer. Simul., 4 (2003) 203–208.
7. Jiao, X., Wang, R.: Synchronization in neuronal population with the variable coupling strength in the presence of external stimulus. Appl. Phys. Lett., 88 (2006) 203901.
8. Wang, R., Jiao, X.: Stochastic model and neural coding of large-scale neuronal population with variable coupling strength, Neurocomputing, 69 (2006) 778–785.
9. Jiao, X., Wang, R,: Nonlinear dynamic model and neural coding of neuronal network with the variable coupling strength in the presence of external stimuli, Appl. Phys. Lett., 87 (2005) 083901.
10. Izhikevich Z.M., Phase models with explicit time delays, Phys. Rev. E, 58 (1998) 905–908.

Chapter 39
Sequence Memory with Dynamic Synapses and Chaotic Neurons

Min Xia, Zhijie Wang and Jian'an Fang

Abstract A sequence memory with dynamic synapses and chaotic neurons is proposed. Ascribing to dynamic synapses, the sequence memory has features of short transition time and high stability of sequence. Owing to chaotic neurons, the steady-state period in the sequence memory can be adjusted by changing the parameter values of chaotic neurons. Simulation results demonstrating the performance of the sequence memory are presented.

Keywords Sequence memory · dynamic synapse · chaotic neurons

Introduction

Sequential information processing, for instance the sequence memory, plays an important role on many functions of brain. Neural networks are often utilized to model the sequence memory. Unlike a conventional autoassociative neural network which evolves to settle at a stable steady state [1], a neural network model for sequence memory switches orderly among the patterns that stored in the network. This requires the neural network model to have an ability to get out of a stable equilibrium [2]. Several neural network models have been proposed to model the sequential learning and memory [3, 4, 5, 6, 7, 8].

Based on the strategy of asymmetric synaptic weight [3] (SMAS), the present paper first proposes a sequence memory with dynamic synapses (SMDS), then gives a sequence memory with chaotic neurons (SMCN), finally constructs a sequence memory with dynamic synapses and chaotic neurons (SMDSCN). The present paper investigates the performances of SMDSCN by comparing it with other models through simulation. Ascribing to dynamic synapses, the sequence memory in SMDS has features of short transition time and high stability of the sequence. Owing to chaotic neurons, the steady-state period in SMCN can be adjusted by changing the

Z. Wang
College of Information Science and Technology, Donghua University, Shanghai 201620, China
e-mail: wangzj@dhu.edu.cn

R. Wang et al. (eds.), *Advances in Cognitive Neurodynamics*,

parameter values of chaotic neurons. The simulation results further indicate that SMDSCN benefits from both the effects of dynamic synapses and chaotic neurons.

Model of the Sequence Memory

The neuron in the network is characterized by binary state $\{s_i\}_{i=1}^{N} = \{-1, 1\}$. A set of patterns $\left\{x^u = (x_1^u, \ldots, x_N^u)\right\}$ are stored in the network, where $u = 1, 2, \ldots, p$. Each element x_i^u is generated with $prob\left[x_i^u = 1\right] = prob\left[x_i^u = -1\right] = 0.5$. The sequence consists of q stored patterns with $q \leq p$.Traditional sequence memory models usually use the asymmetric synapses (SMAS). The synaptic weights are composed of a symmetric part m_{ij}^c and an asymmetric part w_{ij}^c. In Eq. (39.2) $x_i^{q+1} = x_i^1$.

$$m_{ij}{}^c = \frac{1}{n}\sum_{u=1}^{p} x_i^u x_j^u \quad for \quad i \neq j. \tag{39.1}$$

$$w_{ij}{}^c = \frac{1}{n}\sum_{u=1}^{q} x_i^{u+1} x_j^u \quad \text{for } i \neq j. \tag{39.2}$$

The state of each neuron in the network is updated as follows:

$$s_i(t+1) = \begin{cases} 1 & h_i(t) \geq 0, \\ -1 & h_i(t) < 0, \end{cases} \tag{39.3}$$

$$h_i(t) = \sum_{j=1}^{n} m_{ij}(t) s_j(t) + \sum_{j=1}^{n} w_{ij}(t) \frac{\lambda}{G} \sum_{k=1}^{t} \varphi\,(k) s_j(k), \tag{39.4}$$

where $m_{ij}(t) = m_{ij}^c$, $w_{ij}(t) = w_{ij}^c$ for the model of SMAS Eqs. 1–4. $\frac{1}{G}\int_0^G \varphi(t)dt = 1$. We assume $\varphi(k) \equiv 1$. G is the total number of time steps of the simulation. The closeness between the $s(t)$ and the x^u is defined by:

$$z^u(t) = \frac{1}{N}\sum_{i=1}^{N} x_i^u s_i(t). \tag{39.5}$$

The synaptic weight $m_{ij}(t)$ and $w_{ij}(t)$, evolve with time t as follows [9]:

$$w_{ij}(t+1) = w_{ij}{}^c r_j(t) \tag{39.6}$$

$$m_{ij}(t+1) = m_{ij}{}^c r_j(t) \tag{39.7}$$

$$r_j(t+1) = \begin{cases} r_j(t) + \dfrac{1 - r_j(t)}{\tau_1} - \delta_1 r_j(t) & \text{if } s_j(t) = 1, \\ r_j(t) + \dfrac{1 - r_j(t)}{\tau_2} + \delta_2 r_j(t) & \text{if } s_j(t) = -1, \end{cases} \tag{39.8}$$

where $r_j(t)$ denotes the fraction of synaptic resources available for a postsynaptic current, $\tau_1,\ \tau_2$ ($\tau_1, \tau_2 > 1$) and $\delta_1,\ \delta_2$ ($\delta_1, \delta_2 < 1$) are the parameters for synaptic depression. The model of SMDS can be described by Eqs. 1–4 and 6–8.The SMCN is constructed and is described by Eqs. 1, 2, 4, and 9–11:

$$h_i(t+1) = h_i(t) + \beta h_i(t), \tag{39.9}$$

$$c_i(t+1) = \begin{cases} \alpha_1 c_i(t) - \theta_1 s_j(t) + a_1 & \text{if } s_j(t) = 1, \\ \alpha_2 c_i(t) - \theta_2 s_j(t) + a_2 & \text{if } s_j(t) = -1, \end{cases} \tag{39.10}$$

$$s_i(t+1) = \begin{cases} 1 & f(c_i) \geq \zeta \\ -1 & f(c_i) < \zeta \end{cases} \quad \zeta \in (0, 1), \tag{39.11}$$

where $a_1 \geq 0$ and $a_2 \geq 0$ denote the sum of the threshold and the temporally constant external input, $\theta_1 \geq 0$ and $\theta_2 \geq 0$ are the refractory scaling parameters. $f(c_i) = 1/(1 + \exp(-(h_i(t+1) + c_i(t+1))/\varepsilon))$ is the logistic function with the steepness parameter ε. $h_i(t+1)$ and $c_i(t+1)$ are the internal states of neuron i. $\alpha_1,\ \alpha_2$ are the decay parameters for the refractoriness, and β is the decay parameters for the feedback inputs.The SMDSCN is described by Eqs. 1, 2, 4, and 6–11.

Simulation Results

As the transition time is defined as the time period during which the network switches from one pattern to anther. It is denoted by Δt. Figure 39.1 shows that the transition time for SMDS is shorter than that for SMAS. Figure 39.1 also shows that during some steps (for example T) the network wander beyond stored patterns of SMAS. Therefore, the stability of the sequence[1] of SMDS is higher than that of SMAS.

Figure 39.2 presents the numerical results for SMCN. The SMCN switches more frequently between the patterns than SMAS, viz., the average steady-state period[2] of SMCN is smaller than that of SMAS. Figure 39.2 also implies that the steady-state period can be adjusted by the parameter values of $\theta_1 - a_1$ and $\theta_2 + a_2$.

---

[1] Stability of the sequence is defined in this paper as $\rho = \chi / G$, where χ is the number of the time steps, at each of which one of the stored patterns is recalled exactly.G is the total time steps of the simulation.

[2] Steady-state period defined in this paper is the period during which the network settles at one pattern in a cycle.

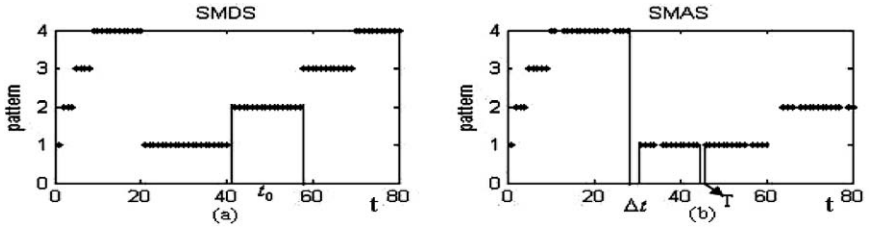

Fig. 39.1 Simulation results of SMDS and SMAS. The parameter values are $N = 400,$ p=6, $q = 4,\ \lambda = 1,\ G = 80,$ and $z^u(t) \geq 0.88$. The the parameters for synaptic depression in (a) are $\tau_1 = \tau_2 = 1.2,\ \delta_1 = 0.02,\ \delta_2 = 0$

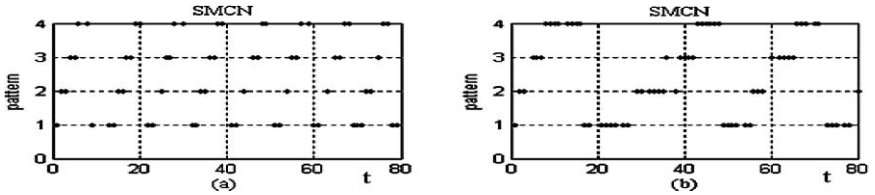

Fig. 39.2 Simulation results of SMCN. The parameter values are $N = 300,\ p = 6,\ q = 4,\ \lambda = 1,\ G = 80,\ \beta = 0.12,\ \alpha_1 = \alpha_2 = 1,\ \xi = 0.26,$ and $z^u(t) \geq 0.88$. In (a) $\theta_1 - a_1 = 0.5,\ \theta_2 + a_2 = 0.4,$ in (b) $\theta_1 - a_1 = 0.18,\ \theta_2 + a_2 = 0.15$

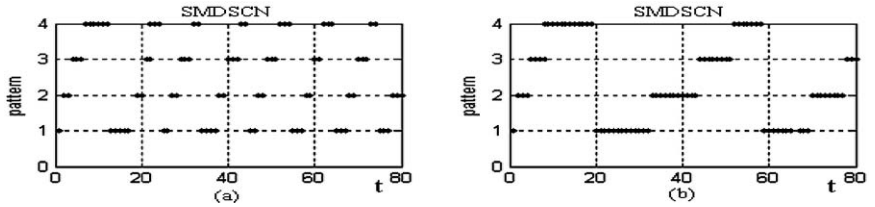

Fig. 39.3 Simulation results of SMDSCN. The parameter values of the chaotic neurons in SMDSCN (Fig. 39.3a and b) are set the same as that in SMDS (Fig. 39.2a and b, the dynamic synapses in SMDSCN (Fig. 39.3) are set the same as that in SMDS (Fig. 39.1a)

Figure 39.3 presents the numerical results for SMDSCN. SMDSCN in Fig. 39.3 has the features of short steady-state period, which is similar to that of SMDS in Fig. 39.2. Figure 39.3 shows that SMDSCN has also the features of short transition time and high stability of sequence owing to the dynamic synapses. Thus, SMDSCN possesses of both the characteristics of SMDS and SMCN.

Summary

We investigated the influence of dynamic synapses and chaotic neurons on the performance of the sequence memory. By introducing dynamic synapses into a sequence memory, the transition time between patterns in the sequence can be

shortened and that the stability of the sequence can be enhanced. Owing to chaotic neurons, the steady-state period in the sequence memory can be adjusted by changing the parameter values of chaotic neurons.

References

1. J.A. Anderson, A simple neural network generating interactive memory, Mathematical Biosciences, 14 (1972) 197–220.
2. A. Sandberg, A. Lansner, Synaptic depression as an intrinsic driver of reinstatement dynamics in an attractor network, Neurocomputing 44–46 (2002) 615–622.
3. H. Sompolinsky, I. Kanter, Temporal association in asymmetric neural networks, Physical Review Letters 57(22) (1986) 2861–2864.
4. M. Rehn, A. Lansner, Sequence memory with dynamical synapses, Neurocomputing, 58–60 (2004) 271–278.
5. L Olivia. White, D. L Daniel., H. Sompolinsky., Short-term memory in orthogonal neural networks. Physica Review Letters 92(14) (2004) 14812–148104.
6. P. Seliger, L. S. Tsimring, M. I. Rabinnovich, Dynamics-based sequential memory: Winnerless competition of patterns, Physical Review E 67 (2003) 011905.
7. Rubin Wang, Jing Yu, Zhiakng Zhang, A neural model on cognitive process. Lecture Notes in Computer Science. ISNN 2006, LNCS3971. pp. 50–58.
8. Y. Yamaguchi., A theory of Hippocampal memory based on Theta phase precession. Biological Cybernetics 89 (2003) 1–9.
9. L. Pantic, J. J. Torres, H. J. Kappen, Associative memory with dynamic synapses, Neural Computation, 14(12) 2903–2923, 2002.

Chapter 40
Interacting Turing and Hopf Instabilities Drive Pattern Formation in a Noise-Driven Model Cortex

Moira L. Steyn-Ross, D.A. Steyn-Ross, M.T. Wilson and J.W. Sleigh

Abstract Using a recently reported analysis of gap-junction density in the cat visual cortex, we have augmented a standard mean-field model of the cortex to include a dense network of diffusive connections between inhibitory neurons. Provided the diffusive connection strength exceeds a critical threshold, our augmented cortical model predicts the spontaneous emergence of Turing structures, patterned regions of high- and low-firing cortical activity distributed across the brain. In this paper we demonstrate that these patterns will become self-modulating if a second model parameter, the rate-constant for the inhibitory post-synaptic potential, is made sufficiently small, allowing a low-frequency Hopf temporal instability to emerge. This interaction between Turing and Hopf instabilities may explain the slow oscillations in coherent brain activity observed in BOLD (blood oxygen-level-dependent) imagery, and may have relevance to brain pathologies which are characterized by abnormally low (e.g., schizophrenia) or abnormally high (e.g., Parkinson's disease) levels of cross-cortical neural synchrony.

Keywords Cortical modeling · pattern formation · gap junctions · schizophrenia · Parkinson's disease

Background

The formation of spatiotemporal patterns in network models of the cerebral cortex has been the focus of considerable research activity over many years (e.g., [1, 2, 3]). Unlike these earlier continuum models that are based on neuron communication via *chemical* synapses, the present work investigates the implications of incorporating a dense reticulum of *electrical* or *gap-junction* synapses linking the dendrites of neighbouring inhibitory neurons. We have demonstrated theoretically [4] that inhibitory gap-junction coupling can lead to the spontaneous formation of

M.L. Steyn-Ross
Department of Engineering, University of Waikato, Private Bag 3105, Hamilton 3240, New Zealand
e-mail: msr@waikato.ac.nz

R. Wang et al. (eds.), *Advances in Cognitive Neurodynamics*,

Turing patterns: spatially structured regions of high- and low-firing neuron activity distributed across the brain. This prediction is based on a detailed analysis of a standard synaptic-transmission model of the cortex that has been supplemented with gap-junctions providing direct resistive connections between adjacent neurons. The standard model, used previously to study the induction of anesthesia [5] and the cycles of natural sleep [6, 7], describes the interaction behaviors of *populations* of excitatory and inhibitory neurons in terms of their population-averaged firing *rates* (rather than spike generation in individual neurons). It uses physiologically-based parameters that represent the spatially averaged properties of the $\sim 10^5$ neurons contained within $\sim 1\,\mathrm{mm}^3$ of cortical tissue, so provides a reasonable match with what can be measured with on-scalp or on-cortex EEG electrodes.

The incorporation of gap-junction connectivity into the standard model is motivated by a recent report by Fukuda *et al*. [8] that provides convincing evidence for dense gap-junction connectivity between inhibitory neurons in the cat visual cortex, each neuron making 60 ± 12 (mean $\pm$ SD) gap-junction dendritic connections not only with proximal inhibitory neurons, but also with distal inhibitory neurons in adjoining orientation columns. These resistive connections provide a source of diffusive current to the receiving neuron, supplementing the chemical-synaptic currents generated by incoming action-potential spike activity. Fukuda *et al*. [8] describe how the gap junctions form a dense and homogeneous electrical coupling of interneurons, and propose that this diffusion-coupled network provides the substrate for synchronization of neuronal populations. Our schematic representation for the synaptic and diffusive current sources is illustrated in Fig. 40.1.

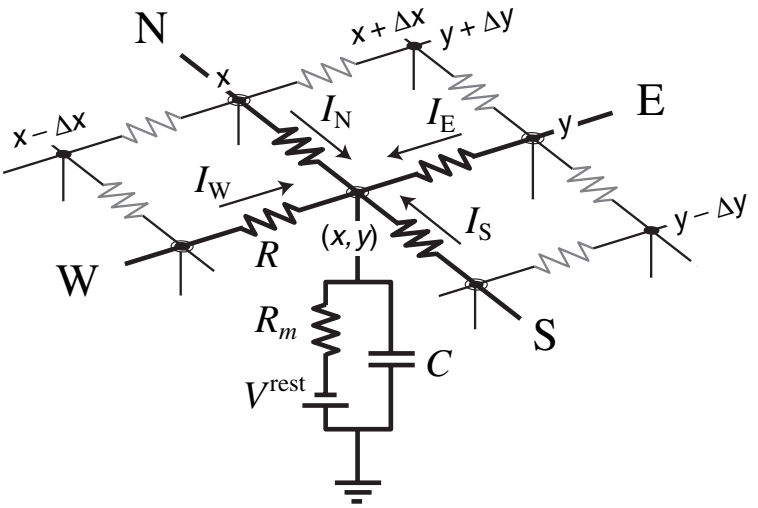

Fig. 40.1 Cortex modelled as a 2D rectangular network of diffusively-coupled neurons. Each neuron is an RC integrator of membrane resistance R_m and capacitance C. The neuron at node (x, y) receives diffusive currents from the four neighboring diffusion cells labeled N, S, W, E. (From [4].)

Model for Diffusive Coupling in the Cortex

Our continuum model is expressed in terms of the population-average excitatory and inhibitory soma voltages, V_e and V_i,

$$\tau_e \frac{\partial V_e}{dt} = V_e^{\text{rest}} - V_e + [\rho_e \psi_{ee} \Phi_{ee} + \rho_i \psi_{ie} \Phi_{ie}] + D_1 \nabla^2 V_e, \tag{40.1}$$

$$\tau_i \frac{\partial V_i}{dt} = V_i^{\text{rest}} - V_i + [\rho_e \psi_{ei} \Phi_{ei} + \rho_i \psi_{ii} \Phi_{ii}] + D_2 \nabla^2 V_i. \tag{40.2}$$

where $\tau_{e,i}$ are the neuron time-constants, $V_{e,i}^{\text{rest}}$ are the respective resting voltages, $\rho_a \psi_{ab} \Phi_{ab}$ (with labels $a, b \in \{e,\ i\}$) are the voltage perturbations due to spike-rate activity Φ_{ab} from distant and local neurons of type a arriving at the soma of a neuron of type b; ψ_{ab} are normalized synaptic reversal-potential functions; and $\rho_{e,i}$ are chemical-synaptic strengths with $\rho_e > 0,\ \rho_i < 0$. The four Φ_{ab} fluxes obey second-order differential equations; two of these (for Φ_{ee} and Φ_{ei}) are driven by long-range and local spike flux, plus white-noise sources representing non-specific cortical stimulation from the subcortex.

The terms in square brackets [. . .] are elements of the standard mean-field cortical model whose derivation has been described in detail previously [5]. The new feature is the addition of excitatory, (inhibitory) diffusive voltage terms $D_1 \nabla^2 V_e,\ (D_2 \nabla^2 V_i)$. While inhibitory ($i \leftrightarrow i$) gap junctions are plentiful, excitatory ($e \leftrightarrow e$) gap junctions are rare, so we assume D_1 is a small fraction of D_2. Applying simple mean-field arguments, we have derived an expression for the inhibitory coupling strength, D_2,

$$D_2 = \frac{a N^{\text{gap}}}{4} \cdot \frac{R_m}{R_g}, \tag{40.3}$$

where N^{gap} is the number of gap-junction contacts per neuron, a is the per-neuron area of diffusive sensitivity, R_m is the membrane resistance of the soma, and R_g is the resistance of a single gap-junction connection. Using Fukuda's measurements we obtain $D_2 = 0.6\,\text{cm}^2$.

Predictions: Turing Structures and Hopf Oscillations

We apply a linear stability analysis, and, intriguingly, find that this $D_2 = 0.6\,\text{cm}^2$ value for the diffusive coupling strength is close to the critical value required to destabilize the homogeneous steady state: larger values of D_2 cause the cortex to crystallize into random maze-like Turing structures (see Fig. 40.2). These are centimetre-scale spatial patterns in which regions of high-firing activity are intermixed with regions of low-firing activity. Such structuring may be the basis for the large-scale brain-activity images detected from the BOLD (blood oxygen-level-dependent) signal reported by Fox *et al*. [9].

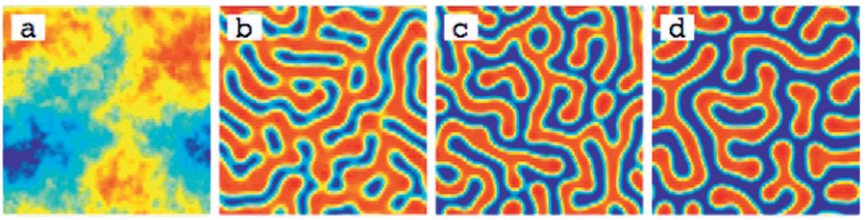

Fig. 40.2 Selection of diffusion-induced Turing patterns in a square cortex of side 25 cm. Inhibitory diffusion, D_2, increases *to the right* with values a. 0; b. 1; c. 3; d. 6 cm^2. Each panel shows a snapshot of the noise-driven cortex after 4 s of evolution from a homogeneous initial state. Panel-a shows the case of zero diffusion: the cortex organizes into a diffuse, cloud-like pattern, but fails to generate a Turing structure. All other cases evolve into stable serpentine Turing patterns containing alternating regions of low- (blue) and high-firing (red) states. (Modified from [4].)

Thus strong inhibitory diffusion can provoke a Turing instability. From previous work [7], we know that the standard cortical model possesses a low-frequency (~ 1 Hz) *Hopf instability* that emerges when γ_i, the rate-constant for the IPSP (inhibitory post-synaptic potential) is reduced (i.e., the time-to-peak for the hyperpolarizing GABA response is delayed). This raises the interesting possibility that the Hopf and Turing instabilities might interact to produce modulated Turing patterns whose amplitudes oscillate at the slow Hopf frequency. This is illustrated in the Fig. 40.3 firing-rate time-series recorded for 30 sample points, regularly spaced across the 25-cm width of the model cortex: the evolution into stable "up" (active) and "down" (quiescent) firing states in Fig. 40.3a is replaced by a coherent whole-cortex slow oscillation of patterned neural activity in Fig. 40.3b.

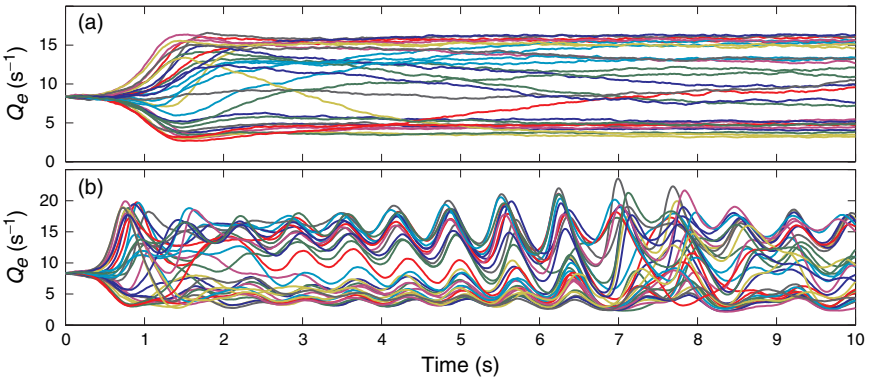

Fig. 40.3 Ten-second simulation runs showing that the precipitation into stable Turing states in (a) is replaced by Turing structures that oscillate in place when the Hopf instability is triggered. Settings: (a) $\gamma_i = 58.6\,\text{s}^{-1}$; (b) $\gamma_i = 29.3\,\text{s}^{-1}$. Diffusion strength is $D_2 = 1.0\,\text{cm}^2$ for both runs

Clinical Relevance

There is now a body of clinical evidence suggesting that unusual gap-junction densities in the brain might be relevant to certain neural pathologies such as schizophrenia and Parkinson's disease. The neurotransmitter dopamine – a potent gap-junction blocker [10] – is implicated in both of these brain dysfunctions: dopamine is present in excess in schizophrenia patients, and is markedly deficient in the brains of Parkinson's sufferers. For the schizophrenic brain, our theory predicts that the excess dopamine will close gap junctions and disrupt Turing formation, diminishing the likelihood of long-range correlated neural activity. This prediction is consistent with recently reported observations from fMRI/BOLD studies that schizophrenics exhibit weaker low-frequency correlations between specific regions of the cortex than is observed in normals [11]. This lack of long-range synchrony is also seen in the EEG signals recorded from schizophrenics [12].

Reversing our prediction for the case of Parkinson's disease, if the dopamine is present in levels far below normal, then the gap-junction-mediated Turing connections might become "too strong," plausibly resulting in the abnormal levels of synchronous neuronal firing that typify Parkinsonian tremors.

References

1. Destexhe, A.: Oscillations, complex spatiotemporal behavior, and information transport in networks of excitatory and inhibitory neurons. Physical Review E **50** (1994) 1594–1606.
2. Jirsa, V.K., Haken, H.: A field theory of electromagnetic brain activity. Physical Review Letters **77** (1996) 960–963.
3. Hutt, A., Bestehorn, M., Wennekers, T.: Pattern formation in intracortical neuronal fields. Network: Computation in Neural Systems **14** (2003) 351–368.
4. Steyn-Ross, M.L., Steyn-Ross, D.A., Wilson, M.T., Sleigh, J.W.: Gap junctions mediate large-scale Turing structures in a mean-field cortex driven by subcortical noise. Physical Review E **76** (2007) 011916.
5. Steyn-Ross, M.L., Steyn-Ross, D.A., Sleigh, J.W.: Modelling general anaesthesia as a first-order phase transition in the cortex. Progress in Biophysics and Molecular Biology **85** (2004) 369–385.
6. Steyn-Ross, D.A., Steyn-Ross, M.L., Sleigh, J.W., Wilson, M.T., Gillies, I.P., Wright, J.J.: The sleep cycle modelled as a cortical phase transition. Journal of Biological Physics **31** (2005) 547–569.
7. Wilson, M.T., Steyn-Ross, D.A., Sleigh, J.W., Steyn-Ross, M.L., Wilcocks, L.C., Gillies, I.P.: The slow oscillation and K-complex in terms of a mean-field cortical model. Journal of Computational Neuroscience **21** (2006) 243–257.
8. Fukuda, T., Kosaka, T., Singer, W., Galuske, R.A.W.: Gap junctions among dendrites of cortical GABAergic neurons establish a dense and widespread intercolumnar network. The Journal of Neuroscience **26** (2006) 3434–3443.
9. Fox, M.D., Snyder, A.Z., Vincent, J.L., Corbetta, M., van Essen, D.C., Raichle, M.E.: The human brain is intrinsically organized into dynamic, anticorrelated functional networks. Proceedings of National Academy of Sciences, USA **102** (2005) 9673–9678.
10. Hampson, E.C.G.M., Vaney, D.I., Weile, R.: Dopaminergic modulation of gap junction permeability between amacrine cells in mammalian retina. The Journal of Neuroscience **12** (1992) 4911–4922.

11. Bluhm, R.L., Miller, J., Lanius, R.A., Osuch, E.A., Boksman, K., Neufeld, R.W.J. et al.: Spontaneous low frequency fluctuations in the bold signal in schizophrenic patients: Anomalies in the default network. Schizophrenia Bulletin **33**(4) (2007) 1004–1012.
12. Uhlhaas, P.J., Linden, D.E.J., Singer, W., Haenschel, C., Lindner, M., Maurer, K., Rodriguez, E.: Dysfunctional long-range coordination of neural activity during perception in schizophrenia. The Journal of Neuroscience **26** (2006) 8168–8175.

Chapter 41
Context-Dependent Processing of Spatiotemporal Patterns Based on Interaction Between Neurodynamical Systems

Takashi Hasuo, Ken Yamane and Masahiko Morita

Abstract Dynamics of traditional neural network models are generally time-invariant. For that reason, they have limitations in context-dependent processing. We present a new method, dynamic desensitization, of varying neurodynamics continuously and construct a basic model of interaction between neurodynamical systems. This model comprises two nonmonotone neural networks storing sequential patterns as trajectory attractors. The dynamics of respective networks are modified according to the states of other networks. Using numerical experiments, we also show that the model can recognize and recall complex sequences with identical patterns in different positions.

Introduction

The brain can be regarded as an assemblage of dynamical systems comprising many neurons that perform spatio-temporal pattern processing. Consequently, neurodynamical systems comprising artificial neural networks with recurrent connections and continuous-time dynamics are thought to offer great potential for brain-like information processing. However, existing neurodynamical systems have limited capability, particularly in terms of context-dependent processing.

Two explanations for this limited ability are the following. First, the dynamics are usually time-invariant (at least in the short run). For that reason, the system always makes the same transition at the same state unless it receives external input. Second, no appropriate method is known for making different neurodynamical systems interact. If two networks are interconnected in a usual manner, they constitute a single neurodynamical system with time-invariant dynamics, rather than two different systems. In such a case, the influence of system A on system B depends on the state of A, but not on that of B.

T. Hasuo
Graduate School of Systems and Information Engineering, University of Tsukuba, Tsukuba-city, 305-8573, Japan
e-mail: hasuo@bcl.esys.tsukuba.ac.jp

R. Wang et al. (eds.), *Advances in Cognitive Neurodynamics*,

In this paper, we propose a method of varying the dynamics of a recurrent neural network according to another network. We construct a model for context-dependent processing such as recognition and recall of complex sequential patterns.

Dynamic Desensitization

As a method of varying the dynamics of a neural network discretely, Morita et al. [1] proposed selective desensitization. This method desensitizes about half of the neurons or renders their output as neutral, depending on a given modification pattern. Through this operation, the modified state of the network is projected onto a subspace of the state space, and produces transitions according to the dynamics in the subspace. If trajectory attractors [2] are formed in different subspaces, the network state reaches different target patterns according to modification patterns, as shown schematically in Fig. 41.1a.

In this model, however, the modification pattern is restricted to a static pattern so that trajectory attractors can be formed within individual subspaces. For that reason, we call this "static desensitization."

Here we propose "dynamic desensitization" by extending the modification pattern of static desensitization to a dynamic or spatiotemporal pattern. Then the set of desensitized neurons, or the subspace onto which the network state is projected, varies continuously with time, as depicted in Fig. 41.1b. In this case, a single trajectory attractor to the target state cannot be formed. If the change of the modification pattern is sufficiently slow, however, the network state makes short transitions in each of a series of subspaces and can thereby reach the target.

Model

Using the method described above, we constructed a basic model of interaction between neurodynamical systems (Fig. 41.2). This model consists of two nonmonotone neural networks that have the same number of neurons and obey the same dynamic equation.

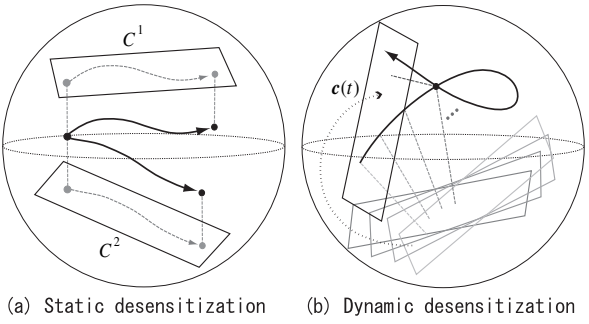

Fig. 41.1 Methods of varing neurodynamics: Thick arrows represent trajectories of the network state. Planes represent subspaces. The dashed arrows represent trajectory attractors in the subspaces

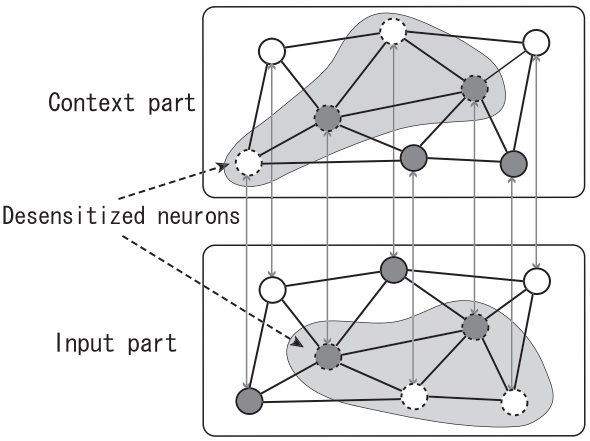

Fig. 41.2 Model structure

Specifically, the i-th neuron ($i = 1, \ldots, \mathrm{n}$) of either network acts according to

$$\tau \frac{\mathrm{d}u_i}{\mathrm{d}_t} = -u_i + \sum_{j=1}^{n} w_{ij} y_j + z_i, \;\; y_i = g(v_i) \cdot f(u_i), \tag{41.1}$$

where u_i denotes the instantaneous potential, y_i is the output, z_i is the external input. In addition, w_{ij} represents the synaptic weight from the j-th neuron of the same network, v_i is the instantaneous potential of the corresponding neuron of the other network, and τ is a time constant. Also, $g(v_i)$ is a sigmoid function which takes a value from 0 to 1, and $f(u_i)$ is a nonmonotonic output function [2]. If v_i takes a positive large value, the output is $y_i \simeq f(u_i)$, but if v_i takes a negative large value, then $g(v_i)$ and y_i are nearly zero, which means that the neuron is desensitized. Here we consider $x_i \equiv \mathrm{sgn}(u_i)$ ($\mathrm{sgn}(u) = 1$ for $u > 0$ and -1 for $u \leq 0$) and refer to the binary vector $\boldsymbol{x} = (x_1, \ldots, x_n)$ as the current state of the network.

The two networks have a similar structure, but they differ in function (Fig. 41.3). One network receives an input of complex spatiotemporal patterns from the outside and stores them. This network is termed the input part, but it also shows the recalled pattern when no input pattern is fed. The other network, termed the context part, does not receive the external input directly, but it autonomously changes its state from a fixed initial state O', via some branch points, to a terminal state C^μ in accordance with the state transitions of the input part.

Computer Simulation

We carried out simulation experiments using the 10 spatiotemporal patterns $\boldsymbol{s}^1, \ldots, \boldsymbol{s}^{10}$ presented in Table 41.1. Their dimensions (and size of each network) were $n = 800$ and their temporal length was $T = 20\tau$. We also generated $\boldsymbol{c}^\mu = \{O' \bullet \bullet \bullet C^\mu\}_T$ ($\mu = 1, \ldots, 10$) corresponding to $\boldsymbol{s}^\mu$, where $\bullet$ represents a branch point described above. Subsequently, we trained the model by giving $\boldsymbol{s}^\mu$ and $\boldsymbol{c}^\mu$ as

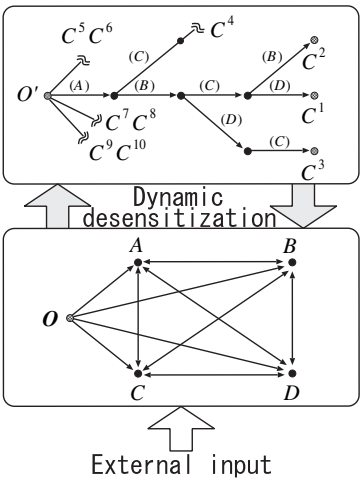

Fig. 41.3 State transition diagram

Table 41.1 Input sequences: Letters represent n-dimensional binary patterns selected randomly; $\{OABCD\}_T$ denotes a spatiotemporal pattern changing from a pattern O via A, B and C into D over a period of T. Each trajctory overlaps with others in every unit section, e.g., $\{AB\}$ is included in $\boldsymbol{s}^1$, $\boldsymbol{s}^2$ and $\boldsymbol{s}^3$, and $\{BC\}$ is included in $\boldsymbol{s}^1$, $\boldsymbol{s}^2$ and $\boldsymbol{s}^5$

$\boldsymbol{s}^1 = \{OABCD\}_T$	$\boldsymbol{s}^2 = \{OABCB\}_T$
$\boldsymbol{s}^3 = \{OABDC\}_T$	$\boldsymbol{s}^4 = \{OACBD\}_T$
$\boldsymbol{s}^5 = \{OBCBD\}_T$	$\boldsymbol{s}^6 = \{OBDAC\}_T$
$\boldsymbol{s}^7 = \{OCADB\}_T$	$\boldsymbol{s}^8 = \{OCADA\}_T$
$\boldsymbol{s}^9 = \{ODADC\}_T$	$\boldsymbol{s}^{10} = \{ODCDA\}_T$

learning signals to the input and context parts, respectively, to store them as trajectory attractors (see references [2] and [1] for the learning algorithm).

After completion of 30 training cycles, we gave various input patterns and examined the behavior of the model. Figure 41.4 presents two examples in which (a) $\boldsymbol{s}^2$ was fed with 10% noise and with temporal expansion and contraction, and (b) only short sections of $\boldsymbol{s}^9$ were fed. The state of the context part reaches C^2 in (a) and C^9 in (b), meaning that the model recognized the input pattern as $\boldsymbol{s}^2$ or $\boldsymbol{s}^9$. It is also apparent that a spatiotemporal pattern similar to the original is recalled in the input part.

This result, together with those of many other experiments, indicates that the two networks act autonomously and cooperatively through mutual dynamic desensitization.

Concluding Remarks

We have proposed a dynamic desensitization method to modify a neurodynamical system using another system. We have also shown that two systems which are interconnected by this method can recognize and recall complex sequences with many

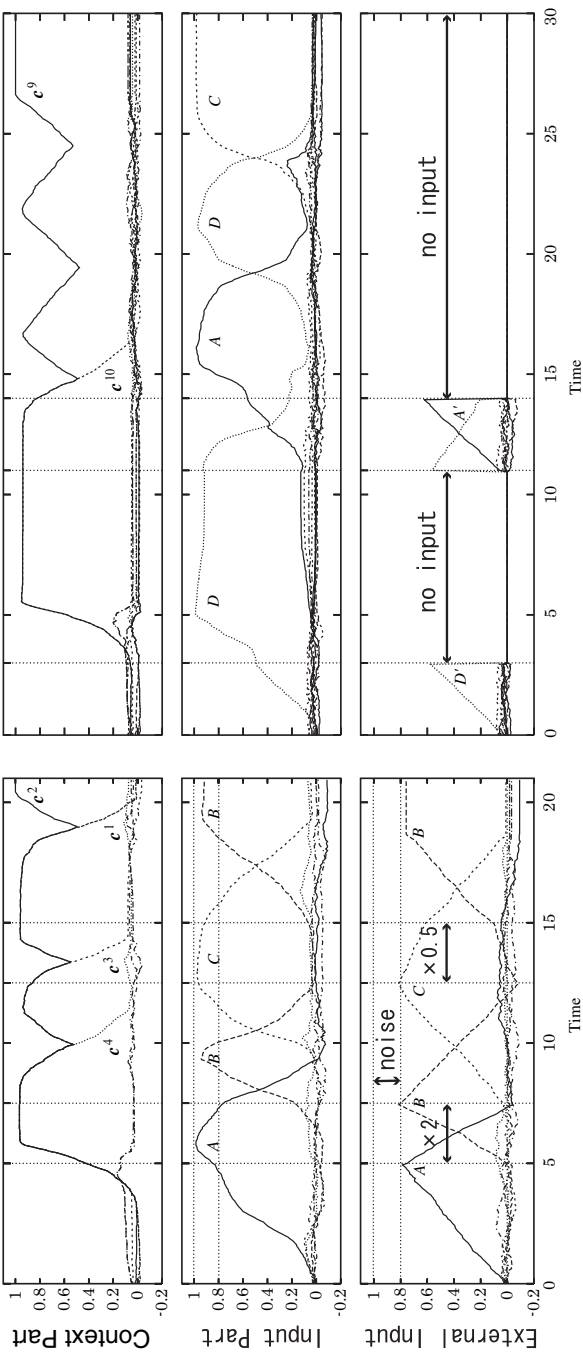

Fig. 41.4 Behavior of the model: Similarities of the network state (upper and middle graphs) or the current input (lower graph) to reference patterns are plotted against time scaled by the time constant τ

overlapping sections, even if they have substantial noise, have some blank sections, or are temporally expanded or contracted.

Interaction through dynamic desensitization differs greatly from interaction which takes place through ordinary synaptic connections between neurons: the influence on dynamics of one system depends on the states of both systems. This method also presents an advantage in that the number of interconnections required is merely n. By developing this method, more than two neurodynamical systems can interact to provide more powerful capability, which remains as a subject for future study.

References

1. Morita, M., Murata, S., Morokami, S.: Context-dependent sequential recall by a trajectory attractor network with selective desensitization. Proceedings of the Third International Conference on Neural Networks and Artificial Intelligence (2003) 235–238.
2. Morita, M.: Memory and learning of sequential patterns by nonmonotone neural network. Neural Networks **9** (1996) 1477–1489.

Chapter 42
The Synchronization and Associative Memory of Izhikevich Neural Network

Wei Zhang, Qingli Qiao, Xuyuan Zheng and Xin Tian

Abstract A new neural network with Izhikevich neuron model and Hopfield-like structure is presented in this paper. The stored memory patterns are coded with the connection weight. The output of network is represented by the synchronous periodic firings in the network. When the network is presented with two corrupted input patterns, the stored memory pattern can be retrieved through the associative memory. It is shown that synchronization plays an important role in the associative memory of the brain.

Keywords Synchronization · associative memory · Izhikevich neuron model

Introduction

There are as many as 10^{11} neurons in the human brain, and each can have more than 10,000 synaptic connections with other neurons. Individual neurons may show irregular behavior, while ensembles of neurons can synchronize in order to process biological information or to produce regular, rhythmical activity [1].

Synchrony is observed in many situations both in the laboratory and in nature. The pendula of identical pendulum clocks placed near to each other are known to synchronize due to extremely weak coupling from air movements and vibrations. Synchrony also occurs between organisms. In the brain, synchrony of spikes plays a critical role in the processing of information, and it is the foundation of associative memory [2, 3]. The synchronization occurred when there is noise in the system.

Feeble input information (such as a weak signal) can be amplified and optimized by the assistance of noise, that is the so called stochastic resonance [4]. Stochastic resonance is important in neurobiology. It can help us to understand the role of noise in neural coding.

In this paper, a neural network composed of 200 Izhikevich neuron models is presented that can implements the retrieval of stored memory patterns and use

Q. Qiao
Department of Biomedical Engineering, Tianjin Medical University, Tianjin 300070, P.R. China
e-mail: qlqiao@gmail.com

R. Wang et al. (eds.), *Advances in Cognitive Neurodynamics*,

the spatio-temporal coding mechanism to process information. The stored memory patterns are represented by the synchronous periodic firings in the network. It will help us to understand the mechanisms of associative memory of real brains.

The Neural Network Model

Izhikevich neuron model proposed recently by Izhikevich [5] combines the biologically plausibility of Hodgkin–Huxley-type dynamics and the computational efficiency of integrate-and-fire neurons. Depending on four parameters, the model can reproduce spiking and bursting behavior of known types of neurons.

The structure of the network is shown in Fig. 42.1:

The structure of the network is similar to the Hopfield neural network [6, 7, 8]. The differential equations of the neuron models in the neural network are [9]:

$$v_i' = 0.04v_i^2 + 5v_i + 140 - u_i + \gamma I_i + \sum_{j=1}^{N} w_{ij}(v_j - v_{eq}) + \xi_i(t) \tag{42.1}$$

$$u_i' = a(bv_i - u_i) \tag{42.2}$$

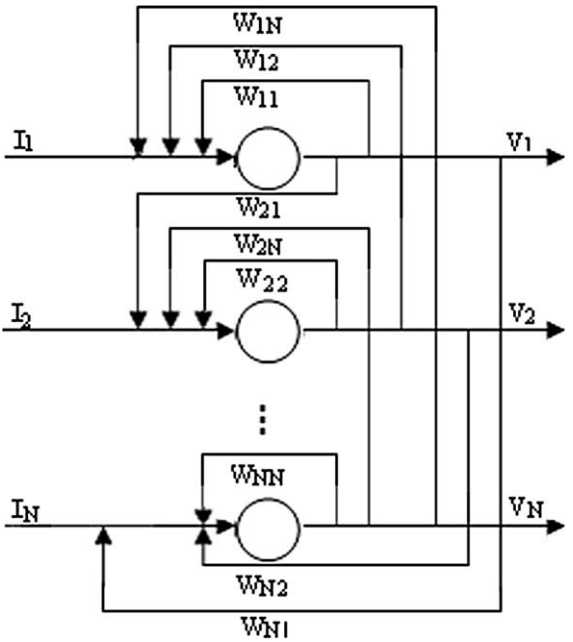

Fig. 42.1 The structure of the neural network

$$\text{If } v_i \geq 30, then \begin{cases} v_i \leftarrow c \\ u_i \leftarrow u_i + d \end{cases} \tag{42.3}$$

$$\left\{\xi_i(t)\xi_j(t')\right\} = D\delta_{ij}\delta(t - t') \tag{42.4}$$

Where v_i and u_i are dimensionless variables, and $' = \mathrm{d}/\mathrm{dt}$, where t is the time; The variable v_i represents the membrane potential of the neuron i; v_j represents the membrane potential of the neuron j; and u_i represents a membrane recovery variable of the neuron i, which provides negative feedback to v_i. Synaptic currents or injected dc-currents are delivered via the variable I_i. $a = 0.02$; $b = 0.2$; $c = -65$; $d = 8$; $\xi_i(t)$ is Gaussian white noise; w_{ij} is the connection weight from neuron j to neuron i, v_{eq} is the equilibrium value.

According to the Hebbian paradigm [10]:

$$w_{ij} = \frac{\sigma}{Na_0(1 - a_0)} \sum_{\mu=1}^{P} (\zeta_i^u - a_0)(\zeta_j^u - a_0) \tag{42.5}$$

where σ is the connection strength; a_0 is the mean value of all the input patterns of all the neurons; N represents the number of neurons in the neural network; ζ_i^u represents the memoried patterns of the network, P represents the number of the stored memory patterns.

The external input γI_i is:

$$I_i = x_i\theta(t), x_i \in \{0, 1\} \tag{42.6}$$

$$\theta(t) = \begin{cases} 1, & t \geq 0 \\ 0, & \text{others} \end{cases} \tag{42.7}$$

Where x_i is the binary factor which determines whether the input is injected to the i-th neuron or not, γ is the strength of external input.

The Storage and Retrieval of Memory Patterns

In our network, the stored memory is represented by the synchronous periodic firings of the neurons which store 1's. The storage and retrieval of memory patterns is achieved through the synchronous periodic firings of the neurons in the network. The stored memory pattern is defined as follows:

$$\zeta = \begin{cases} 1 & 100 \leq i \leq 150 \\ 0 & \text{others} \end{cases} \tag{42.8}$$

Where i represents the index of the neuron. The stored memory patterns are coded with the connection weight in the network.

When the input to the network is:

$$\zeta_{in1} = \begin{cases} 1 & 110 \le i \le 150 \\ 0 & \text{others} \end{cases} \tag{42.9}$$

The output of the network is presented in Figs. 42.2 and 42.3, from which it can be shown that the neurons in the range from 100 to 150 fire synchronously, it means the memory and retrieval of the stored memory pattern ζ is successful.

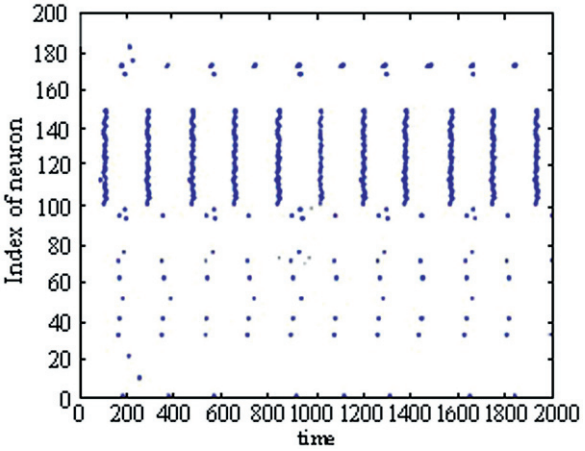

Fig. 42.2 The firing times of all the neurons when: $D = 0.002,\ \gamma = 0.32,\ \sigma = 0.6$

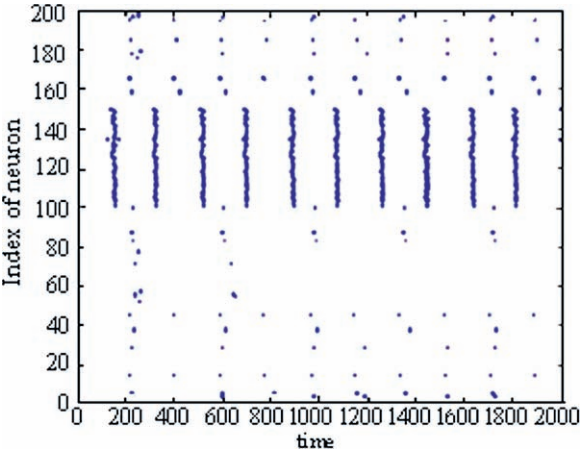

Fig. 42.3 The firing times of all the neurons when: $D = 0.005,\ \gamma = 0.32,\ \sigma = 0.6$

When the input to the network is:

$$\zeta_{in2} = \begin{cases} 1 & 90 \le i \le 150 \\ 0 & \text{others} \end{cases} \tag{42.10}$$

The neurons in the range from 100 to 150 fire synchronously too, it means that the associative memory and retrieval of the stored memory pattern ζ is successful too when the network is presented with another corrupted input pattern ζ_{in2}.

Conclusion

In this paper, a network composed of Izhikevich neuron model is presented with a structure similar to that of the Hopfield network, in which memory patterns are coded with the connection weight.

In the experiment, the stored memory patterns composed of 0/1 digits are retrieved through the synchronous periodic firings in the network. Adding proper amount of noise can enhance spatiotemporal patterns. Synchrony of spikes plays a critical role in the associative memory of human brain.

Due to the extreme computational simplicity of the Izhikevich neuron model, we can simulate networks consisting of thousands of spiking neurons in real time with 1 ms resolution.

Acknowledgments The work is supported by National Basic Research Program of China (973 Program 2005CB724302).

References

1. Robert C. Elson, Allen I. Selverston, Ramon Huerta, Nikolai F. Rulkov, Mikhail I. Rabinovich, Henry D. I. Abarbanel: Synchronous Behavior of Two Coupled Biological Neurons. Phys. Rev. Lett. 81 (1998) 5692–5695.
2. Fujii H., Hiroyuki Ito, Kazuyuki Aihara, Natsuhiro Ichinose, Minoru Tsukada: Dynamical cell assembly hypothesis-theoretical possibility of spatio-temporal coding in the cortex. Neural Netw 9 (1996) 1303–1350.
3. Gray C. M., Gray C. M., Konig P., Engel A. K., Singer W.: Oscillatory responses in cat visual cortex exhibit inter-columnar synchronization which reflect global stimulus properties. Nature 338 (1989) 334–337.
4. Kitajo K., Yamanaka K., Ward L. M., Yamamoto Y.: Stochastic resonance in attention control. Europhys Lett 76 (2006) 1029–1035.
5. Izhikevich, E. M.: Simple model of spiking neurons. IEEE Trans Neural Netw 14 (2003) 1569–1572.
6. Hopfield J. J.: Neural networks and physical systems with emergent collective computational abilities. Proc Natl Acad Sci 79 (1982) 2554–2558.
7. Hopfield J. J.: Neurons with graded response have collective computational properties like those of two-state neurons. Proc Natl Acad Sci 81 (1984) 3088–3092.

8. Hopfield J. J.: Pattern recognition computation using action potential timing for stimulus representation. Nature 376 (1995) 33–36.
9. André Longtin.: Autonomous stochastic resonance in bursting neurons. Phys Rev E 55 (1997) 868–876.
10. Hebb D O.: The organization of behavior. John Wiley, New York (1949).

Chapter 43
Connectivity Dependent Effects in Cognitive Neurodynamics of Mental Disorders

Hans Liljenström and Yuqiao Gu

Abstract Computational modeling was applied to investigate how cortical neurodynamics may depend on network connectivity. In particular, we study effects of pruning of cortical networks, which may be related to the onset of different mental disorders. In addition, we study changes in EEG pattern of depressed patients, following ECT (electroconvulsive therapy). The aim is to gain a better understanding of the neural mechanisms responsible for these changes, which include phase shifts in the EEG dynamics. This understanding is intended to provide clinical guidance, predicting ECT dose and response in depressed patients. Finally, we discuss the relevance of these results to clinical and experimental neuroscience and speculate on a link between neural instability and mental disorders.

Keywords Neurodynamics · network connectivity · EEG · ECT · pruning · mental disorder · computational models

Introduction

It appears that some mental disorders and their treatments are related to the connectivity pattern in various cortical structures. In particular, it has been hypothesized that the onset of pruning of the cortical neural networks is related to maturation and possible mental disorders [1, 2]. In the last major step in brain development, some 40% of the neuronal synapses are eliminated. When the pruning is shut down too soon (early maturers), according to this hypothesis, the synaptic density will be high and could be subject to mutual electrochemical influences. These tend to synchronise neighbouring neurons, which might be locked into a pattern of paroxysmal activity which complicates central nervous system (CNS) function. In contrast, in late maturers the synaptic density will be below optimal, because of failure to shut down the pruning process. The reduced synaptic density and the associated tendency

Hans Liljenström
Department of Biometry and Engineering, SLU, P.O. Box 7032, SE-75007 Uppsala, Sweden Agora for Biosystems, Box 57, SE- Sigtuna, Sweden
e-mail: hans.liljenstrom@bt.slu.se

R. Wang et al. (eds.), *Advances in Cognitive Neurodynamics*,

to desynchronisation could lead to a general break-down of circuitry. Both too early and too late shut down of the pruning process could lead to mental disorders. In early maturers, mano-depressive psychosis is more common, while late maturers more often get schizophrenia [1].

When it comes to clinical treatment, electroconvulsive therapy (ECT) is one of the most successful treatments of depression and other mental disorders, presumably by altering the cortical connectivity [3, 4]. ECT stimulus can generate an intracerebral current flow to induce a generalized seizure in the CNS [3]. Clinical ECT EEG data show complex neurodynamical patterns, but the anatomic and physiological mechanisms behind such dynamical patterns are poorly known [5].

We have used computer models of cortical network structures, in order to investigate the effect of connectivity changes on system performance [6, 7, 8]. The objective of our studies is to gain a better understanding of the neural mechanisms correlated with changes in mental states and processes, which include phase shifts in the EEG dynamics. This understanding is intended to provide clinical guidance, for example by predicting ECT dose and response in depressed patients.

Cortical Network Models

We have used computational models of the three-layered distributed structure of paleocortex [6] and the six-layered, columnar structure of neocortex [7, 8] to investigate the relation between structure, dynamics and function of these systems, with a focus on maintenance of the balance between stability and flexibility in such systems and the response to external and internal disturbances. For our paleocortical model, we have used Hopfield-type of network nodes, with a continuous input-output relation, mimicking the firing density representing populations of neurons. For our neocortical model, we have primarily used spiking neuronal model of Fitzhugh-Nagumo type. The mean activity in both types of networks has been taken as the cortical neurodynamics, relating to the observed EEG signals. The connectivity pattern of the networks resembles the anatomy of the real structures, with excitatory and inhibitory neurons with varying properties.

Network connectivity is varied in terms of cell types and number of neurons and short and long distance connections. In particular, we investigate how a variation in the balance between excitation and inhibition affects the network dynamics. By varying the connectivity patterns, we mimic the effects of sprouting, pruning and synaptic modification that are supposed to be related to the processes involved in shifts between mental stability and instability. Details are given in references [6, 8].

Simulation Results

Effects of Network Pruning

With reference to the pruning hypothesis, the connectivity effects that we found with our computer simulations could point at a shift in the balance between stability and

flexibility of the neural networks of the brain, which possibly could be reflected in a similar shift at a cognitive/mental level. It is also conceivable that a suboptimal timing of the extensive pruning process that occurs during development could well have an effect on the stability-flexibility balance of the mental processes in later stages of life.

Our simulations showed that the system is extremely stable against network pruning, maintaining much of its learning capacity even when a majority of the initial connections were pruned away. However, when pruning was applied, synchronization of network activity was increased. A pruned network is also more efficient in terms of energy usage (less synapses involved) and network activity levels, and it gives a more accurate learning/recall. However, pruning results in a less flexible network, where fewer patterns can be stored, as the number of modifiable connections is reduced.

The simulations further show that a regulated complex neurodynamics, which can shift its balance between sensitivity and stability, can result in an efficient information processing. A high interconnectivity, with extensive long-range excitatory connections, and more local inhibitory connections, can be extremely robust to network pruning and external or internal fluctuations. An oscillatory dynamics, resulting from a proper balance between excitation and inhibition, is another factor that provides both flexibility and stability to the system. In addition, such a dynamics is more energetically advantageous than a non-oscillatory dynamics.

Simulation of ECT Effects

Our simulations with ECT EEG showed a rather good resemblance with clinical data where the changes in mean activity of our network Neurodynamics resembled the change in EEG of patients treated with ECT. By changing the connectivity, we obtain network structures that react on ECT in a way resembling the clinical signals in a real situation (Fig. 43.1). By mimicking the assumed re-generation of neurons and forming of new connections, as a result of ECT, we find changes in the neurodynamics corresponding to the changes seen in subsequent EEG traces during a normal three week ECT treatment.

We found that the collective dynamics of neurons varies with connection topology and neuron density in different layers, the balance between excitatory and inhibitory

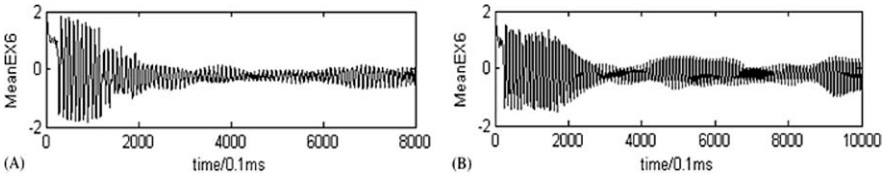

Fig. 43.1 The mean membrane potential of excitatory neurons in layer VI neurons. (a) Shows the effect of long-distance excitatory lateral connections. (b) Shows the effect of density and long-distance inhibitory connections. The decreased neuron density in layers V and VI result in higher-amplitude synchronous oscillations in these two layers

strength and neuronal intrinsic parameters. The collective dynamical behavior not only depends on the structure and parameters of the network but also depends on the neuronal intrinsic oscillatory property and external input. From this multi-dependence feature we postulate that the collective dynamics of the cortex after external stimulation is kind of a "resonance" between the network, neuronal oscillators and external input.

Discussion

We have used two types of computational models of cortical networks to investigate the role of synaptic connectivity for system performance. In particular, we have used these models to address the stability-flexibility dilemma of neural systems, assuming a close relation between neural processes and mental processes and disorders.

An efficient neural information processing supposedly requires an appropriate balance between flexibility and stability of the system. Ideally, the balance can shift depending on internal and external circumstances. Our computer simulations show that a regulated complex neurodynamics, which can shift its balance between sensitivity and stability, can result in an efficient information processing. A high interconnectivity, with extensive long-range excitatory connections, and more local inhibitory connections, can be extremely robust to network pruning and external or internal fluctuations. An oscillatory dynamics, resulting from a proper balance between excitation and inhibition, is another factor that provides both flexibility and stability to the system. In addition, such a dynamics is more energetically advantageous than a non-oscillatory dynamics.

In addition to more or less permanent changes in connectivity, also effects of synaptic modification due to neuromodulators, or a change in synaptic efficacy could result in more temporary and reversible connectivity changes. We have used our computational models also for investigating such effects, which has been reported elsewhere. Finally, our simulations show that a certain amount of disorder is beneficial for the system, and optimal levels of randomness have been found. Too much order can clearly be detrimental to the system (e.g. by getting stuck in a limit cycle attractor, corresponding to a repetitive cognitive or motor behavior).

References

1. Saugstad, L.F.: The Maturational Theory of Brain Development and Cerebral Excitability in the Multifactorially Inherited Manic-depressive Psychosis and Schizophrenia. Int. J. Psychophysiol. 18 (1994) 189–203.
2. Siekmeier, P.J., Hoffman, R.E.: Enhanced Semantic Priming in Schizophrenia: A Computer Model Based on Excessive Pruning of Local Connections in Association Cortex. British J. Psychiatry 180 (2002) 345–350.
3. Beyer, J.L., Weiner, R.D., Glenn, M.D.: Electroconvulsive Therapy. Am. Psych. Press, Washington DC (1998).

4. Wahlund B, von Rosen D. ECT of Major Depressed Patients in Relation to Biological and Clinical Variables: A Brief Overview. Neuropsychopharmacology 28 (2003) S21–26.
5. Gu, Y., Wahlund, B., Liljenström, H., von Rosen, D., Liang, H.: Analysis of Phase Shifts in Clinical EEG Evoked by ECT. Neurocomputing 65–66 (2005) 475–483.
6. Liljenström, H.: Neural Stability and Flexibility - A Computational Approach. J. Neuropsychopharmac. 28 (2003) S64–S73.
7. Gu, Y., Halnes, G., Liljenstrom, H., Wahlund, B.: A Cortical Network Model for Clinical EEG Data Analysis. Neurocomputing 58–60 (2004) 1187–1196.
8. Gu, Y., Halnes, G., Liljenström, H., Liang, H., von Rosen, D., Wahlund, B.: Modelling ECT Effects by Connectivity Changes in Cortical Neural Networks. Neurocomputing 69 (2006) 1341–1347.

Chapter 44
Corticopetal Acetylcholine: A Role in Attentional State Transitions and the Genesis of Quasi-Attractors During Perception

Hiroshi Fujii, Kazuyuki Aihara and Ichiro Tsuda

Abstract The Role(s) of corticopetal acetylcholine (ACh) in perception and conscious flow is largely unknown. The attention hypothesis may well be established experimentally. The aim of this talk is to give a small review, and then try to extend further the arguments, on the role of corticopetal ACh in perception from a dynamical systems standpoint, to search for its possible role in perceptual *binding*, and in the transient genesis of quasi-attractors through the mechanism of changing synchrony.

Keywords Corticopetal acetylcholine · nucleus basalis of Meinert · complex hallucinations · perceptual binding · attentions · binding through synchrony · quasi-attractors · muscarinic receptor · cortical state transitions

Corticopetal Acetylcholine: Backgrounds

Corticopetal Cholinergic Afferents Originating in the NBM are Critical to Attentional Processing

Recent evidence shows that *acetylcholine* (ACh) is involved, not only in global brain activation during arousal, but also in mediating attentional mechanisms based on the nucleus basalis of Meynert (NBM) situated at the basal forebrain (BF).

A blockage of NBM ACh, either by disease-related or drug-induced, causes a severe loss of attentions: *selective* attention, *sustained* attention, and *divided* attention, together with a *shift* of attention. Also studies using immunotoxin provide consistent evidence of the role of ACh in attentions. For example, ACh release at mPFC is reported to depend strongly on cholinergic neurons of NBM (but, not of

H. Fujii
Department of Intelligent Systems, Kohyama Center for Neuroscience, Kyoto Sangyo University, Kyoto 603-8555, Japan
e-mail: fujii@bacco.kyoto-su.ac.jp

R. Wang et al. (eds.), *Advances in Cognitive Neurodynamics*,

the diagonal band of Broca), and this circuit is essential in maintaining sustained attention [1].

Sarter *et al*. [2] hypothesize that cholinergic inputs from NBM might be the critical control system which may trigger various kinds of attentions receiving convergent inputs from other sensory and association areas.

Cholinergic Drugs and Hallucinogenesis

Lewy Body Dementia (LBD) is a disease caused by a continual death of cholinergic cells in NBM. One of the most salient symptoms of LBD patients is *complex visual hallucinations* (CVH).[1]

Perry and Perry [3] reported a parallelism between hallucinations by LBD and muscarinic blockade. Images are generally vivid and colored, continues for a few minutes (neither seconds nor hours). It is noted also that many of these hallucinatory experiences are enhanced during *eye closed* and relieved by visual input, and nicotinic antagonists, such as mecamylamine, are not reported to induce hallucinations.

Attention Induces State Transitions with Changing Synchrony in Collaboration with *G*lutamatergic and *C*holinergic Afferents

Attention Causes a 'Local' Transition of Cortical States

Fries *et al*. [4] observed increase of synchrony in high-gamma range in accordance of *selective attention*. (See, also Buschman *et al*. [5], and Niebur et al. [13].) Kay *et al*. [6] observed a cascade of brain events at the successive stages of the task as 'expectation' and/or 'attention' during perceptual processing in a *local* brain system, that is, the olfactory-limbic axis. They observed 'local' transitions of cortical states indicated by modulations of the structure of EEG signals as gamma amplitude, periodicity, and coherence in the olfactory structures. They also observed the *local* dynamics *transiently* falls into attractor-like states. Such 'local' transitions of states were postulated to be triggered by 'top down' and 'bottom up' communications by means of glutamatergic spike packets.

However, as we shall explain later, such brain events including the changing synchrony could be a result of collaboration of glutamatergic spike volleys and ACh afferents from NBM.

---

[1] Perry and Perry [3] gave a comparative description of mental symptoms of LBD as compared with those caused by ACh blockade by muscarinic antagonist scopolamine or atropine. The authors noted those hallucinatory LBD patients who see 'integrated images of *people* or *animals* which appear real at the time', 'insects on walls', or 'bicycles outside the fourth storey window'.

Posterior Cortical-Prefrontal-BF Circuitry

Golmayo *et al*. [7] made an electrophysiological study suggesting the existence of a parietal cortex → prefrontal cortex → NBM → sensory cortex *triangular amplification circuit*, which may modulate sensory responses in visual and somatosensory cortical areas in rat. The triangular circuitry consists of modules that target specific control areas. Region-specific regulation of cortical functions recruited by the prefrontal cortex (PFC), enhances detection, processing of stimuli of a particular modalty.

Attention and Dynamical Binding Through Synchrony

In order that *perception* of an object makes sense, its features must be bound as a unity. As has been suggested in Treisman and Gelade [8], binding may require 'attention'. Before the arrival of attention, features are 'free floating'. (See also, [9].) If attention is diverted, arbitrary rearrangements of binding might appear as a dramatic breakdown of bindings shown by some neurological patients.

Before the arrival of attention, 'internal states', or 'fragmental' cell assemblies, activated by external stimuli which may represent features are free floating. *Binding* of mosaics of fragmental cell assemblies, and large-scale *integration* of brain activity representing stimuli or events are mediated by *synchrony* over multiple frequency bands [5, 6, 10]. The emergent integrated state induced by *top down attention* through synchrony is a 'transiently stable' state. We may regard such processes as the basic brain dynamics in perception, and might be conceptualized as a 'quasi-attractor' state. The function of the muscarinic receptors, mAChR could be regarded as a *slow variable* which may control the transitions of the system state. In fact, most neurons alter their resting potential when glutamatergic action potentials concomitantly arrive with ACh afferents. The activation of mAChR is a process with a slower onset and *longer* lasting process providing G-protein-coupled second messenger generation.

Hasselmo and McGaughy [11] emphasize the ACh role in memory as: 'high acetylcholine sets circuit dynamics for attention and encoding; low acetylcholine sets dynamics for consolidation', which is based on some experimental data on selective *pre-synaptic* depression and facilitation.

However, in view of the potential role of attentions in local *bindings* or global *integrations*, we may pose an alternative (but not necessarily exclusive,) *scenario* on the ACh function as temporarily modifying the quasi-attractor landscape, in collaboration with glutamatergic spike volleys.

Hypothesis and Discussions

We hypothesize that a possible role of corticopetal ACh in perception is to work as a *prompter* for state transitions and changing synchrony through top down attention.

Top down attention may trigger corticopetal ACh projections through the posterior cortex – PFC – NBM attentional circuitry. Evidence accumulates that *binding* and *large-scale integration* of brain activity representing stimuli or events are mediated by *synchrony* over multiple frequency bands [5, 6, 10]. The temporal organization of a transiently stable state functionally connected by a large-scale *transient synchrony* could be conceptualized as an orbit approaching to *a state of quasi-attractor*.

How can corticopetal ACh transiently modify synchrony and, the landscape of quasi-attractors? What are the basic means for organizing such brain events? Possible means are, first, *post-synaptically* by changing the level of resting potentials of neurons, and second, *pre-synaptically* by selectively modifying synaptic transmissions. The former might cause modification of collective behavior of cell assemblies, and the latter might modify connectivity within, e.g., layer 2 of the cortex, and also effective inter-layer connectivity, and probably between thalamic relay cells and the layer 4 neurons causing facilitation/depression of thalamocortical projections.

Such hypothetical arguments must be verified by both experimental and model-based theoretical studies with a focus on state transitions and transient synchrony at the *workfront* of ACh, i.e., the cortical six layers. However, the situation around experimental data appears to be so complicated. Gullege *et al*. [12] challenged the classical data because of unrealistic assumptions on 'default' ACh concentrations in the *in vivo* brain. The function of GABAergic projections from NBM, which are believed to be twice more abundant than cholinergic projections, is another indeterminate factor.

Together with those studies, understanding of the complex hallucinations would give us an insight how 'normal' perceptions and conscious flow may take place in the human brain, and should be an important subject of future studies.

References

1. Behrendt, R.-P., Young, C.: Hallucinations in schizophrenia, sensory impairment, and brain disease: A unifying model. Behav. Brain Sci. 27 (2004) 771–787.
2. Sarter, M., Gehring, W.J., Kozak, R.: More attention should be paid: The neurobiology of attentional effort. Brain Res. Rev. 51 (2006) 145–160.
3. Perry, E.K., Perry, R.H.: Acetylcholine and hallucinations: disease-related compared to drug-induced alterations in human consciousness. Brain Cognit. 28 (1995) 240–258.
4. Fries, P., Reynolds, J.H., Rorie, A.E., Desimone, R.: Modulation of oscillatory neuronal synchronization by selective visual attention. Science 291 (2001) 1560–1563.
5. Buschman, T.J., Miller, E.K.: Top–down versus bottom–up control of attention in the prefrontal and posterior parietal cortices. Science 315 (2007) 1860–1862.
6. Kay, L.M., Lancaster, L.R., Freeman, W.J.: Reafference and attractors in the olfactory system during odor recognition. Int. J. Neural Systems 4 (1996) 489–495.
7. Golmayo, L., Nunez, A., Zaborsky, L.: Electrophysiological evidence for the existence of a posterior cortical-prefrontal-basal forebrain circuitry in modulating sensory responses in visual and somatyosensory rat cortical areas. Neuroscience 119 (2003) 597–609.
8. Treisman, A. M., Gelade, G.: A feature-integration theory of attention. Cognit. Psychol. 12 (1980) 97–136.

9. Kenet, T., Bibitchkov, D., Tsodyks, M., Grinvald, A., Arieli, A.: Nerve cell activity when eyes are shut reveals internal views of the world. Nature 425 (2003) 954–956.
10. Varela, F., Lachaux, J.-P., Rodriguez, E., Martinerie, J.: The Brainweb: phase synchronization and large-scale integration. Nature Rev. Neurosci. 2 (2001) 229–239.
11. Hasselmo, M.E., McGaughy, J.: High acetylcholine sets circuit dynamics for attention and encoding; Low acetylcholine sets dynamics for consolidation. Prog. Brain Res. 145 (2004) 207–231.
12. Gulledge, A.T., Susanna, S.B., Kawaguchi, Y., Stuart, G.J.: Heterogeneity of phasic signaling in neocortical neurons. J. Neurophysiol. 97 (2007) 2215–2229.
13. Niebur, E., Hsiao, S.S., Johnson, K.O.: Synchrony: a neuronal mechanism for attentional selection?. Curr. Opin. Neurobiol. 12 (2002) 190–194.

Chapter 45
Cortical Anatomy and the Spatiotemporal Learning Rule

J.J. Wright and P.D. Bourke

Abstract A model of the self-organization of synapses in the visual cortex is presented. Subject to Hebbian learning with decay, evolution of synaptic strengths proceeds to a stable state in which all synapses have either maximum, or minimum, pre/post-synaptic coincidence. The most stable configuration gives rise to anatomically realistic "local maps", each of macro-columnar size, and each organized as Mobius projections of retinotopic space. A tiling of V1, constructed of approximately mirror-image reflections of each local map by its neighbors is formed, accounting for orientation-preference singularities, linear zones, and saddle points—with each map linked by connections between sites of common orientation preference. Ocular dominance columns, the occurrence of direction preference fractures always in odd numbers around singularities, and effects of stimulus orientation relative to velocity of motion, are accounted for. Convergence to this configuration is facilitated by the spatio-temporal learning rule.

Introduction

We have presented a theoretical account of the self-organization of synapses during development of the visual cortex (V1) [1]. This theory deduced the most stable configuration of synapses to emerge under a Hebbian learning rule. No consideration was given to pre-synaptic interaction, nor was a specific physiology of synaptic modification invoked. The spatiotemporal learning rule [2, 3] – which was developed in relation to work in the hippocampus – allows for pre-synaptic interactions, and relates pre- and post-synaptic interactions to long-term-potentiation (LTP) and depression (LTD). This paper summarizes the earlier theory of V1 self-organization, and concludes with comments on the relevance of the spatiotemporal rule in this further anatomical context.

J.J. Wright
Department of Psychological Medicine, University of Auckland, Auckland, New Zealand
e-mail: jj.w@xtra.co.nz

R. Wang et al. (eds.), *Advances in Cognitive Neurodynamics*,

Theory

Synaptic Densities in V1

In V1 and cortex generally, the density of synaptic couplings generated by each neuron declines with distance from the soma of the cell of origin, at two principal scales – that of the local intra-cortical connections (at the V1 macrocolumnar scale), versus the longer intracortical connections spanning a substantial fraction of the extent of the V1, which are continuous with interareal connections [4, 5, 6]. Via polysynaptic transmission, information can reach each macrocolumn-sized area, from the whole, or a substantial part, of V1, thus modulating direct visual pathway inputs. We will describe the emergent unit organization on the smaller, macrocolumnar, scale as the *local map*, and V1 itself as the *global map*.

Visual Cross-Correlation and Synchronous Fields

Because of the decline of synaptic density with distance, the spatial covariance of activity (synchronous oscillation) between any pair of pyramidal neurons in V1 declines with distance [7, 8, 9, 10]. Visual stimuli exhibit a decline in spatial covariance with distance, and impose this property upon activity in V1. Thus, covariance of activity in V1 declines with distance at both the global, V1, scale, and the local, macro-columnar, scale, and as will be shown, this provides a metric for organization of connections.

Learning Rule

A simple Hebbian rule, with decay can be initially applied. At each synapse the co-incidence of pre and post synaptic activity, $r_{Q\varphi}$, over a short epoch, t, is given by

$$r_{Q\varphi}(t) \propto \sum\nolimits_t Q_e(t) \times \varphi_e(t) \tag{45.1}$$

where $Q_e(t) \in \{0, 1\}$ is the post-synaptic firing rate, and $\varphi_e(t) \in \{0, 1\}$ is the pre-synaptic firing rate. A Hebbian multiplication factor, H_s, operating on the gain of synapses at steady states of pre- and post-synaptic firing is given as

$$H_s = H_{\max} \exp\left[-\lambda / r_{Q\varphi} \right] \tag{45.2}$$

where λ is a suitable constant. With changes in $r_{Q\varphi}$, H_s can increase or decline over time.

Stability at Individual Synapses

It is shown in [1] that under this learning rule synapses can approach a stable state, only by approaching either one of two extremes – either *saturated* or *sensitive*.

In the saturated state, H_s and $r_{Q\varphi}$ are at maxima, while in the sensitive state, H_s and $r_{Q\varphi}$ are at minima. Conversely, $\frac{dH_s}{dr_{Q\varphi}}$, the sensitivity to change in synaptic gain, is at a minimum for saturated synapses and a maximum for sensitive synapses – hence the choice of the names. No specific physiological state was assumed as the basis of saturation or sensitivity.

Metabolic Uniformity

Competition occurring for metabolic resources within axons adds a constraint to Hebbian rules [11]. Metabolic energy supply of all small axonal segments remains approximately uniform, while the metabolic demand of saturated synapses, which have high activity, will be much greater than for sensitive synapses. Therefore the proportion of saturated and sensitive synapses must be approximately uniform along axons, and consequently the densities of both saturated and sensitive synapses must decline with distance of pre-synapses from the cell bodies of origin.

The Impact of Distance/Density and Saturation/Sensitivity on Overall Synaptic Stability

All positions in V1, $\{P_{j,k}\}$, can be given an ordered numbering in the complex plane, $1 \ldots, j, \ldots, k, \ldots, 2n$, and all positions within a macrocolumn located at P_0, $\{P_{j,k}\}$, can be similarly numbered. The total perturbation of synaptic gains for the synapses from V1 entering the macrocolumn, $\Psi(pP)$, and the total perturbation of synaptic gains within the macrocolumn, $\Psi(pp)$, can thus be written as

$$\Psi(pP) = \sum_{j=1}^{j=n}\sum_{k=1}^{k=n} \sigma_{SAT}(p_j P_k) S_{SAT}(p_j P_k) + \sum_{j=1}^{j=n}\sum_{k=1}^{k=n} \sigma_{SENS}(p_j P_k) S_{SENS}(p_j P_k) \tag{45.3}$$

$$\Psi(pp) = \sum_{j=1}^{j=n}\sum_{k=1}^{k=n} \sigma_{SAT}(p_j p_k) S_{SAT}(p_j p_k) + \sum_{j=1}^{j=n}\sum_{k=1}^{k=n} \sigma_{SENS}(p_j p_k) S_{SENS}(p_j p_k) \tag{45.4}$$

where $\sigma_{SAT}(p_j P_k, p_j p_k)$ and $\sigma_{SENS}(p_j P_k, p_j p_k)$ are densities of saturated and sensitive synapses respectively, and $S_{SAT}(p_j P_k, p_j p_k)$ and $S_{SENS}(p_j P_k, p_j p_k)$ are the corresponding variations of synaptic gains over a convenient short epoch.

Since densities of synapses decline with distances of cell separation, then as a simple arithmetic property of sums of products, minimization of $\Psi(pp)$ requires neurons separated by short distances to most closely approach maximum saturation, or maximum sensitivity. Yet metabolic uniformity requires that both sensitive and saturated synaptic densities must decline with distance from the cell bodies of origin, and remain in equal ratio. An apparent paradox arises, since sensitive synapses must link pre- and post-synaptic neurons with minimal pre- and post-synaptic pulse co-incidence, yet the reverse is true for saturated synapses. Also apparently paradoxically, minimization of $\Psi(pP)$ requires that saturated connections afferent to any p_j arise from highly covariant, and therefore closely situated, sites in V1, while sensitive connections afferent to p_j must arise from well-separated sites. Yet again, metabolic uniformity requires that both sensitive and saturated pre-synapses arise from cells at any single site. The paradoxes exist only in the Euclidean plane, and can be resolved as follows.

Mobius Projection, and the Local Map

By re-numbering $\{P_{j,k}\}$ as $\{P_{j1,j2,k1,k2}\}$, and $\{p_{j,k}\}$ as $\{p_{j1,j2,k1,k2}\}$, the subscript numbers $1, \ldots, j1, \ldots, j2, \ldots, n, (n+1), \ldots, j2, \ldots, k2, \ldots, 2n$ can be ascribed in the global map so that $j1$ and $j2$ are located diametrically opposite and equidistant from P_0, while in the local map $j1$ and $j2$ have positions analogous to superimposed points located on opposite surfaces of a Mobius strip. This generates a *Mobius projection* (the *input map*) from global to local, and a *Mobius ordering* within the local map. That is,

$$\frac{P_{jm}^2}{|P_{jm}|} \rightarrow p_{km} \quad m \in \{1, 2\} \tag{45.5}$$

$$p_{jm} \rightarrow p_{km} \qquad m \in \{1, 2\} \tag{45.6}$$

In Eq. (45.5) the mapping of widely separated points in the global map converge to coincident points on opposite surfaces of the local map's Mobius representation. In the Eq. (45.6) the density of saturated synaptic connections now decreases as $|j1-k1|$ and $|j2-k2|$, while the density of sensitive couplings decreases as $|j2-k1|$ and $|j1-k2|$.

The anatomical parallel requires $j1$ and $j2$ in the local map to represent two distinct groups of neurons. To attain maximum synaptic stability within the local map an intertwined mesh of saturated couplings forms, closed after passing twice around the local map's centre, with sensitive synapses locally linking the two turns of the mesh together. In this fashion both saturated and sensitive synapses decline in density with distance, as required. The input map is of corresponding form, conveying an image of the activity in V1 analogous to projection onto a Mobius strip.

Evolution of these patterns of synaptic connections is shown in Figs. 45.1 and 45.2.

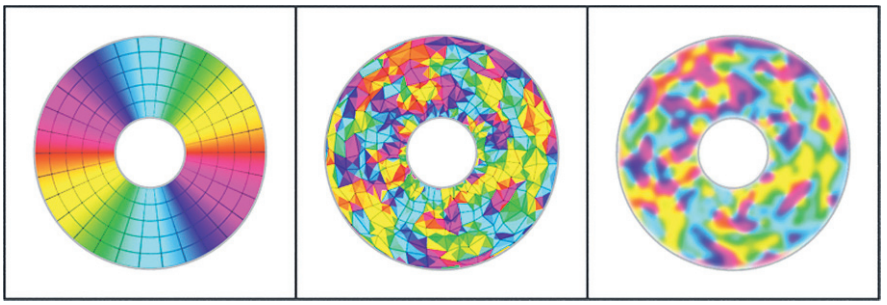

Fig. 45.1 Initial conditions for local evolution of synaptic strength. *Left*: The global field (V1) in polar co-ordinates. Central defect indicates the position of a local area of macro-columnar size. Polar angle is shown by the color spectrum, twice repeated. *Middle*: Zones of random termination (shown by color) of lateral axonal projections from global V1 in the local area. Central defect is an arbitrary zero reference. *Right*: Transient patterns of synchronous oscillation generated in the local area, mediated by local axonal connections

Fig. 45.2 Evolution of synaptic strengths to their maximally stable configuration. *Left*: The global field (V1), as represented in Fig. 45.1. *Middle*: Saturated synaptic connections input from the global field now form a Mobius projection of the global field, afferent to the local map, forming an input map. *Right*: Saturated local synapses within the local map form a mesh of connections closed over 0–4π radians. The central defect now corresponds to the position within the local map, of the local map within the global map. Sensitive synapses (not shown) link adjacent neurons as bridges between the 0–2π and 2π–4π limbs of the mesh of saturated connections. Wright et al. 2006

Monosynaptic Interactions Between Adjacent Local Maps

The input and local maps can, in principle, emerge with any orientation, and with either left or right-handed chirality. However, chirality and orientation of adjacent local maps is also constrained by requirement for overall stability. Adjacent local maps should form in approximately mirror image relation, as shown in Fig. 45.3, because in that configuration homologous points within the local maps have densest saturated and sensitive synaptic connections, thus meeting minimization requirements analogous to those of Eq. 45.3a,b.

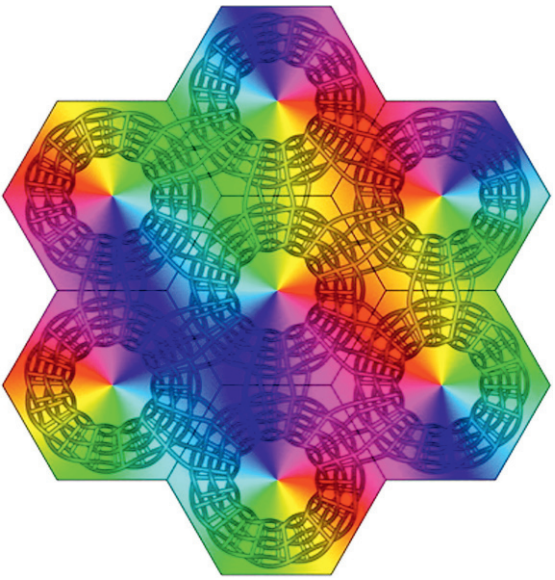

Fig. 45.3 Organization of saturated coupling within and between local maps, and the approximate mirror symmetry of orientation preference in adjacent local maps [1]

Consequences of Projection of Object Configuration and Motion from the Global to the Local Map

The emergent input and local maps form a 1:1 representation of points in the global map. As described in [1], this accounts for response preferences of V1 neurons to visual stimuli – notably orientation preference singularities, linear zones and saddle points, and connections between cells of similar orientation preference in adjacent macrocolumns [12]. Ocular dominance columns [13], which arise in parts of V1 with binocular input, can be explained as a special case of the application of similar mechanisms to those operating in monocular cortex. The occurrence of direction preference fractures always in odd numbers around singularities [14] is explained by the Mobius configuration of the local map, and axonal conduction lags from the global to the local maps accounts for the dynamic variation of orientation preference which occurs with changes in stimulus velocity when, stimulus orientation is not orthogonal to the direction of motion [15].

Application of the Spatiotemporal learning Rule and its Relationship to LTP and LTD

The explanation of self-organization of the synaptic connections in V1 given in[1] is deficient in two respects.

Firstly, no particular physiological synaptic mechanism is associated with the descriptive terms “saturated” and “sensitive”, and these idealized states may never be attained physiologically. However, at least on the appropriate time-scale, saturation

of a synapse may be equated with the LTP state, and sensitivity of a synapse with the LTD state, as indicated in [2, 3].

Secondly, the approach of all synapses to their maximally stable condition has been assumed, without any mechanism being proposed to assist convergence towards maximum stability. The spatiotemporal rule has been recently specified in relation to LTD/LTP of conventional Hebbian type [16]. The operation of this learning rule, which facilitates the mapping of adjacent afferent connections, has the properties required to bring about convergence to stability, since the global-to-local mapping depends on the preservation of the same relation between spatial covariance and distance at both local and global levels.

References

1. Wright JJ, Alexander DM, Bourke PD (2006) Contribution of lateral interactions in V1 to organization of response properties. Vision Research 46: 2703–2720.
2. Tsukada M, Aihara T, Saito H (1996) Hippocampal LTP depends on spatial and temporal correlation of inputs. Neural Networks 9: 1357–1365.
3. Tsukada M, Pan X (2005) The spatio-temporal learning rule and its efficiency in separating spatiotemporal patterns. Biological Cybernetics 92: 139–146.
4. Scholl DA (1956) The Organization of the Cerebral Cortex. Wiley, New York.
5. Braitenberg V, Schuz A (1991) Anatomy of the Cortex: Statistics and Geometry. Springer-Verlag, New York.
6. Liley DTJ, Wright JJ (1994) Intracortical connectivity of pyramidal and stellate cells: estimates of synaptic densities and coupling symmetry. Network 5: 175–189.
7. Wright JJ (1997) EEG simulation: variation of spectral envelope, pulse synchrony and 40 Hz oscillation. Biological Cybernetics 76: 181–184.
8. Robinson PA, Rennie CJ, Wright JJ (1998) Synchronous oscillations in the cerebral cortex. Physical Review E 57: 4578–4588.
9. Wright JJ, Bourke PD, Chapman CL (2000) Synchronous oscillation in the cerebral cortex and object coherence: simulation of basic electrophysiological findings. Biological Cybernetics 83: 341–353.
10. Chapman CL, Bourke PD, Wright JJ (2002) Spatial eigenmodes and synchronous oscillation: coincidence detection in simulated cerebral cortex. Journal of Mathematical Biology 45: 57–78.
11. Grossberg S, Williamson JR (2001) A neural model of how horizontal and interlaminar connections of visual cortex develop into adult circuits that carry out perceptual grouping and learning. Cerebral Cortex 11: 37–58.
12. Bosking WH, Zhang Y, Schofield B, Fitzpatrick D (1997) Orientation selectivity and the arrangement of horizontal connections in tree shrew striate cortex. Journal of Neuroscience 17: 2112–2127.
13. Obermayer K, Blasdel GG (1993) Geometry of orientation and ocular dominance columns in monkey striate cortex. Journal of Neuroscience 13: 4114–4129.
14. Swindale NV, Shoham D, Grinvald A, Bonhoeffer T, Hubener M. (2000) Visual cortical maps are optimised for uniform coverage. Nature Neuroscience 3: 822–826.
15. Basole A, White LE, Fitzpatrick D (2003) Mapping multiple features of the population response of visual cortex. Nature 423: 986–990.
16. Tsukada M, Yamazaki Y, Kojima H (2007) Interaction between the spatiotemporal learning rule (STRL) and Hebb type (HEBB) in single pyramidal cells in the hippocampal CA1 area. Cognitive Neurodynamics 1: 1871-4080.

Chapter 46
Theta Phase Precession for Spatial Representation in the Entorhinal-dentate Gyrus-ca3 Network

Colin Molter and Yoko Yamaguchi

Abstract In rats, the hippocampus plays a crucial role in spatial representation. This ability is related to cells firing at specific locations in the environment. Recently, it has been reported that entorhinal cells, which convey the major cortical input to the hippocampus, have a very different spatial pattern of firing activity. Each cell fires at several locations in an environment, these locations forming a grid-like pattern. Both the entorhinal 'grid cells' and the hippocampal 'place cells' fire with theta phase precession; the phase between the spiking activity and the theta local field potential continuously precesses while traversing a receptive field. Previously, the authors demonstrated that this mechanism is sufficient to explain the transformation of entorhinal grid fields to dentate gyrus place fields. This paper investigates the necessary conditions for the appearance of place fields in the CA3 network.

Introduction

In rats, hippocampal neuron activities are well characterized as 'place cells', each cell firing in a confined location of the environment, the 'place field' [1]. Furthermore, during exploratory behavior, firing rate of the place cell is modulated by theta oscillation of local field potential in term of 'theta phase precession'[2]: the relative firing phase unidirectionally shifts in advanced way when the rat crosses the place field. Located one synapse upstream, recent observations have shown that cells in the layer II of the medial entorhinal cortex (mEC) have a different spatial pattern of activity; these so-called 'grid cells' fire at several locations in every environment the animal visits, with the locations forming a regular triangular grid-like pattern [3, 4]. Again, theta phase precession is observed when the rat traverses every activity field of the grid cell [5].

C. Molter
Laboratory for Dynamics of Emergent Intelligence, RIKEN-BSI, Wako, Japan
e-mail: cmolter@brain.riken.jp

R. Wang et al. (eds.), *Advances in Cognitive Neurodynamics*,

Several authors suggested that the conjunctive activity of grid cells could explain the apparition of hippocampal place cells [6, 7, 8]. However, results appeared not convincing enough, suggesting that a fundamental mechanism was missing. In a precedent paper [9], the authors suggested that this mechanism could be the theta phase precession. Thankful to this mechanism, the activity of multiple grid cells synchronize only when the rat simultaneously enters their grid fields. Since hippocampal cells work as coincident detectors of their inputs, phase precession is sufficient to sculpt the representation of hippocampal place cells from randomly connected grid cells. In agreement with experimental data [10], it was observed that dentate gyrus (DG) cells (hippocampal cells driven mainly by EC cells) were characterized by the presence of numerous cells having two or more associated place fields.

It has been hypothesized that the two distinct input systems (EC and DG) to the hippocampal CA3 network are necessary for efficient information storage in the CA3 [11]. Inline, this paper investigates what are the necessary conditions for the apparition of single place field cells in the CA3 network; i.e. how a refinement from DG spatial representation to CA3 spatial representation can occur.

Materials and Methods

This study aims to investigate the activity patterns of DG and CA3 cells obtained after simulating phenomenologically the activity of mECII grid cells when the rat wanders freely in an open-field area (Fig. 46.1). The grid field properties of each MEC cell is randomly assigned (random space phase, orientation, and the distance between grid vertices is chosen from a uniform distribution [30 cm–60 cm]). When crossing each individual grid field, the firing activity is driven by the theta rhythm according to theta phase precession; i.e. a complete crossing of the field results in the phase of the spiking activity going from $\pi/2$ to $-\pi/2$.

DG cells are massively driven by EC cells through the perforant pathway (PP); each cell receives connections from all EC cells. CA3 cells are driven both by EC cells through the PP and by DG cells through Mossy Fibers (MF). Mossy fibers provide sparse connections; each CA3 cells received connections from 50 DG cells randomly selected. Inhibitory interneurons are assumed to maintain sparse DG and CA3 activations:

$$x_i^{\mathrm{dg}} = \Theta\left(\sum_j w_{ij}^{\mathrm{pp.dg}} x_j^{\mathrm{ec}}\right) \tag{46.1}$$

$$x_i^{\mathrm{ca3}} = \Theta\left(\alpha^{\mathrm{pp}} \sum_j w_{ij}^{\mathrm{pp.ca3}} x_j^{\mathrm{ec}} + \alpha^{\mathrm{mf}} \sum_j w_{ij}^{\mathrm{mf}} x_j^{\mathrm{dg}}\right) \tag{46.2}$$

where α^{pp} and α^{mf} regulate the relative strengths of the perforant path and the mossy fibers. The function Θ simulates the activity of inhibitory neurons by maintaining a

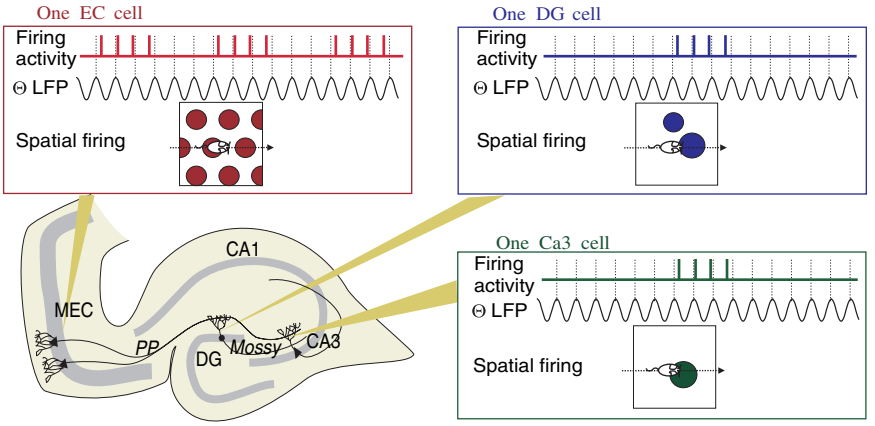

Fig. 46.1 Anatomical view of the three networks modeled in this paper; the medial entorhinal cortex (mEC), the dentate gyrus (DG) and the CA3 network. The correlate of behavioral activity of typical cells found on these network is schematically plotted. Grid fields, one or multiple place fields and one place field characterize respectively entorhinal cells, dentate cells and CA3 cells. All cells' firing activity precesses continuously relatively to the theta rhythm

constant level of sparseness in the network (see [12]) such that $(\sum_i x_i)^2 / \sum_i x_i^2$ is lower than a given constant, here set to 3.

The presence of NMDA receptors at perforant path synapses, suggests the use of an associative rule for the plasticity. Differently, mossy fibers supports a form of plasticity induced predominantly by presynaptic activity [11]:

$$\Delta w_{ij}^{\text{pp.dg}} = k^{\text{pp.dg}} x_i^{\text{dg}} x_j^{\text{ec}} \quad \Delta w_{ij}^{\text{pp.ca3}} = k^{\text{pp.ca3}} x_i^{\text{ca3}} x_j^{\text{ec}} \quad \Delta w_{ij}^{\text{mf}} = k^{\text{mf}} x_j^{\text{dg}} \tag{46.3}$$

where $k^{\text{pp-dg}}$, $k^{\text{pp-ca3}}$ and k^{mf} regulate the respective learning strengths. To maintain bounded synapses and to avoid the "dark side" of synaptic potentiation [13], the synapses of each cell are constantly scaled down such that the equality: $\sum_j w_{ij}^2 = 1$ is preserved.

To identify the presence of place fields in firing maps, the following procedure is followed. The product of convolution between the firing map and a circular field of variable diameter ϕ_d is computed. For each diameters, peaks of maximum intensity ($I_M(\phi_d)$) are identified. For a given peak, the optimum diameter ϕ'_d is such that $I'_M(\phi'_d)/\phi'^2_d$ is maximum. Finally, a place field of diameter ϕ'_d is identified at a peak location if the local firing rate inside the place field is three times larger than the average firing rate.

Results

Each layer contains 1000 units. Initially, synaptic weights are chosen randomly in a uniform distribution. Computations simulate a rat running at 24 cm/s in a square meter open-field, following a random trajectory. At each computational time step,

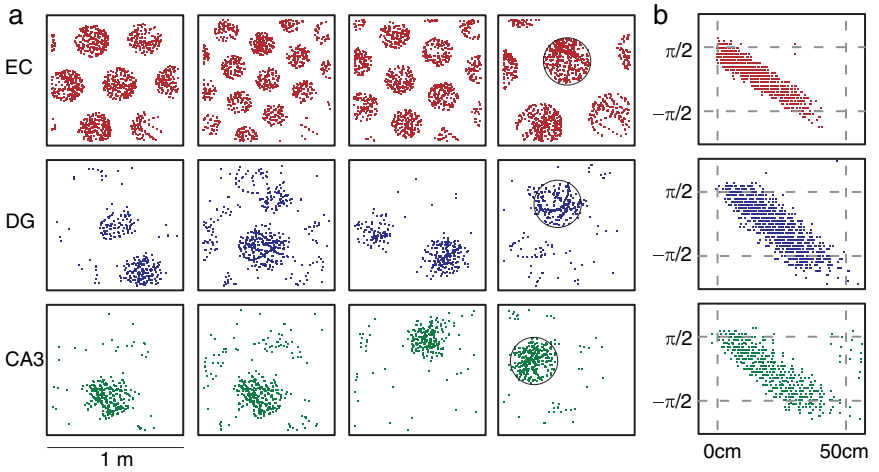

Fig. 46.2 (a) Firing maps of 4 different EC (top), DG (middle) and CA3 (bottom) cells. (b) For cells in the last row, while the rat is crossing the field highlighted, theta phase of the firing activity is plotted of the distance traveled in that field

the rat advances 0.2 cm ($\sim$ 10 ms) and the activity of all units are updated. In the following, two phases are simulated; first, a short learning phase lasting 2 min (with $k^{\text{pp.dg}} = k^{\text{pp.ca3}} = k^{\text{mf}} = 10^{-4}$ in Eq. 46.3), then activity is observed during 8 min (with $k^{\text{pp.dg}} = k^{\text{pp.ca3}} = k^{\text{mf}} = 0$).

Figure 46.2 shows the results obtained when both the PP and the MF pathways are accounted for. The PP coefficient α^{pp} in Eq. 46.2 is set to 1. During the learning phase, mossy fibers are strongly driving CA3 activities, with a decreasing factor α^{mf} going linearly from 10 to 1. After learning, the MF factor α^{mf} is set to 1. EC cells' firing activity is phenomenologically simulated; all cells fire at several locations in the environment, these locations forming grids (first row in Fig. 46.2a), and the firing activity across a place field is characterized by theta phase precession (first row in Fig. 46.2b). DG cells are characterized by the presence of several cells having two place fields. CA3 cells have more selective location of firing activity. Fig. 46.2b shows the firing phase, relatively to the theta rhythm, in function of the distance traveled in a place field (selected with a circle in Fig. 46.2a). It appears that theta phase precession is inherited by the DG and in the CA3 networks.

Figure 46.3 shows statistical analyses of place fields in the EC, the DG and the CA3 network. In very good agreement with experimental data, the DG is characterized by the presence of cells having two or more place fields while CA3 cells are more likely to have only one place field.

Discussion

In a previous paper [9], the authors demonstrated that entorhinal phase precession is inevitable in the transformation of EC grid cells representation to DG place cells

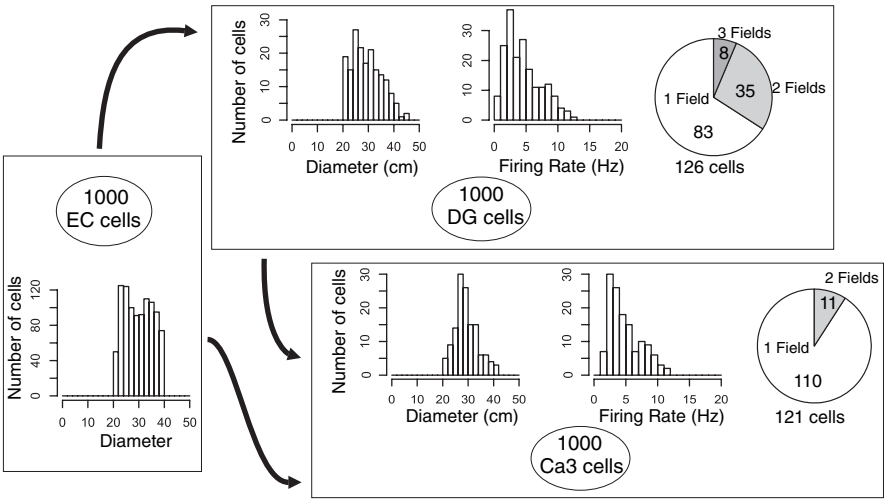

Fig. 46.3 Statistical analyses of place fields in the EC the DG and the CA3 network. Three analyzes are performed; the distribution of place fields' diameter, the distribution of the place fields' firing rate, and finally, the number of place fields found per cell. Firing rates of place fields in EC cells is more of less constant and equal to 15 Hz. All EC cells have three or more place fields

representation. Here, we show that in addition to the direct EC inputs, the presence of DG cells, mediating the EC activity, helps to organize CA3 place cells with single place fields in agreement with experimental observations.

By relying on a computational model, the EC-hippocampal network is simulated when a rat is exposed to a new environment. During the first period, CA3 cells' representations are mostly driven by DG inputs, providing a supervised way to potentiate associatively the EC-CA3 synapses. During observation, EC cells and DG cells are equally responsible for the CA3 activity. In agreement with experimental data [10], results show that while a large number of DG cells are characterized by more than one place field, most of CA3 place cells have only one place field. These results indicate that besides the role played by the DG in forcing the storage of the information in the CA3 network, the MF pathway is also important in refining the hippocampal spatial representation.

The appearance of place fields in the CA3 network requires a balance between the EC and the DG inputs. Preliminary results (not shown here) indicate that increasing the impact of DG inputs leads to increase the number of CA3 place cells having multiple place fields. By contrary, decreasing the impact of DG inputs leads to decrease the number of CA3 place cells, the remaining place cells having weak spatial selectivity. This suggests that feedback inhibition from the CA3 to the DG could give a simple mechanism to regulate the relative strength of the DG inputs. Still further investigations should be performed.

Our findings confirm the hypothesis that hippocampal phase precession is instantaneously inherited from entorhinal phase precession [14]. Moreover, it appears that phase precession defines place field boundaries, in agreement with recent observations of hippocampal cell assemblies [15].

Synchronization of spiking activity appears very important for our understanding of cognitive functions, such as the famous binding problem [16]. By assuming that cells work as coincident detectors, phase locking to the gamma frequency, characterized by very narrow peaks ($\sim$ 20 ms), can efficiently synchronize the activity of many cells; theta frequency, with its broad peaks ($\sim$ 125 ms), can hardly synchronize any cells. However, we demonstrate here that the mechanism of theta phase precession, which sharpens the time windows of activity during theta, provides a powerful mechanism for synchronizing spiking activity between the EC and the hippocampal network and within the hippocampal network.

References

1. OKeefe, J., Dostrovsky, J.: The hippocampus as a spatial map: preliminary evidence from unit activity in the freely moving rat. Brain Research **34** (1971) 171–175.
2. OKeefe, J., Recce, M.: Phase relationship between hippocampal place units and the eeg theta rhythm. Hippocampus **3** (1993) 317–330.
3. Fyhn, M., Molden, S., Witter, M., Moser, E., Moser, M.: Spatial representation in the entorhinal cortex. Science **305** (2004) 1258–1264.
4. Hafting, T., Fyhn, M., Molden, S., Moser, M.B., Moser, E.I.: Microstructure of a spatial map in the entorhinal cortex. Nature **436** (2005) 801–806.
5. Hafting, T., Fyhn, M., Moser, M.B., Moser, E.I.: Phase precession and phase locking in entorhinal grid cells. Abstract Viewer/Itinerary Planner Atlanta, GA: Society for Neuroscience. Program No. 68.8 (2006).
6. Solstad, T., Moser, E.I., Einevoll, G.T.: From grid cells to place cells: a mathematical model. Hippocampus **16** (2006) 1026–1031.
7. McNaughton, B., Battaglia, F., Jensen, O., Moser, E., Moser, M.B.: Path-integration and the neural basis of the cognitive map. Nature Reviews Neuroscience **7** (2006) 663–678.
8. Rolls, E.T., Stringer, S.M., Elliot, T.: Entorhinal cortex grid cells can map to hippocampal place cells by competitive learning. Network: Computation in Neural Systems **15** (2006) 447–465.
9. Molter, C., Yamaguchi, Y.: Theta phase precession mediates the entorhinal to hippocampal transformation of space representation in agreement with hippocampal global remapping. Abstract Viewer/Itinerary Planner San Diego, CA: Society for Neuroscience. Program No. xxx (2007).
10. Leutgeb, J., Leutgeb, S., Moser, M.B., Moser, E.I.: Pattern separation in the dentate gyrus and ca3 of the hippocampus. Science **315** (2007) 961–966.
11. Treves, A., Rolls, E.: Computational constraints suggest the need for two distinct input systems to the hippocampal ca3 network. Hippocampus **2** (1992) 189–199.
12. Rolls, E., Deco, G.: Computational Neuroscience of Vision. Oxford University Press, Oxford (2002).
13. Turrigiano, G.: Homeostatic plasticity in neuronal networks: the more things change, the more they stay the same. Trends Neuroscience **22** (1999) 221–227.
14. Yamaguchi, Y.: A theory of hippocampal memory based on theta phase precession. Biological Cybernetics **89** (2003) 1–9.
15. Maurer, A.P., Cowen, S.L., Burke, S.N., Barnes, C.A., McNaughton, B.L.: Organization of hippocampal cell assemblies based on theta phase precession. Hippocampus **16** (2006) 785–794.
16. Singer, W.: Neuronal synchronization: a solution to the binding problem? In: The Mind-Brain Continuum. Sensory Processes. MIT Press, Cambridge (1996) 100–130.

Chapter 47
Optical Imaging of Visual Feature Representation in the Awake, Fixating Monkey

Anna Roe

The cerebral cortex houses the main computational power in the brain. Its size and complexity serves to differentiate humans from other animals (e.g. [1, 2]). Akin to the architecture of a computer in which there are repeating components, computational circuits reside in fundamental submillimeter-sized building blocks called cortical columns. The activation of specific populations of these cortical columns underlies how the brain achieves specific behavioral repertoires. A major goal of modern neuroscience, therefore, is to understand which networks of columnar activation underly specific behaviors and how their dysfunction leads to specific diseases of brain and behavior.

One approach to understanding the role of these columns (or modules) in behavior and cognition is to visualize them with with optical imaging methods in the alert animal. Indeed, understanding how networks of modules within and across cortical areas achieve vision or memory or emotion is a primary challenge of systems neuroscience. Visualization of such modular activations during behavior is tantamount to watching the brain at work. Over the past decade, we and others have developed methods to visualize activations through implanted 'windows on the brain'. By applying these methods to the awake, behaving animal, it is hoped that this method can open new vistas in our understanding of the neural basis of cognitive function. Furthermore, the ability of these studies to forge a critical link between a large body of work on animal models and functional imaging in humans will be invaluable.

Towards this goal, we have developed an optical window which permits long-term viewing of cortical activity [3, 4]. The window employs a clear, artificial dura which does not interfere with cortical function and prevents infection and dural regrowth. Repeated imaging experiments can be conducted on the same cortical region in the same animal. Electrophysiological recordings can also be conducted. Using these methods, we have examined relationship between different featural maps in V1, V2, and V4 of the alert fixating monkey. To examine featural representation, we used luminance gratings, isoluminant color gratings, and depth stimuli induced by

A. Roe
Vanderbilt University, USA
e-mail: anna.roe@vanderbilt.edu

R. Wang et al. (eds.), *Advances in Cognitive Neurodynamics*,

random dot stimuli. To examine retinotopy, we used 0.1 deg stimulus rings centered on the fovea, 0.1 deg bars oriented radially, 0.5 or 1 deg spots, and full field stimuli. To quickly map the field of view within the imaged window, we have developed a rapid spot imaging method for mapping the imaged field of view [5].

In V2 of the awake monkey, we see several featural maps responsive to color/brightness, contour, motion and disparity. Similar to findings in the anesthetized monkey, these maps exhibit a clear correspondence with the thin, pale, and thick cytochrome oxidase stripes of V2 (cf. [6, 7]). The thin stripes exhibit clear preferential response to color over luminance [8]. Comparison of color/gray and gray/gray isoluminant stimuli of the same luminance contrast revealed preferential activation of thin stripes by color contrast and thick stripes by luminance contrast. Within the thin stripes, focal activations with preferential response to red, green, or blue are mapped topographically, consistent with Felleman's results in the anesthetized monkey. With respect to contour, we find strong contour invariance in the thick and pale stripes of V2. We have previously demonstrated in the anesthetized monkey that orientation maps in V2 exhibit similar response to both real contours (real lines or gratings) and illusory contours [9]. We now show in alert monkeys that this invariance of response in V2 includes not only real and illusory contours, but also motion contrast contours [10]. This provides strong support that orientation domains in V2 are higher order than those in V1. Although it was previously thought that V2 contained little motion signal, in the alert monkey, we find that there is quite strong motion selectivity in thick stripes of V2 and that there is a topographic pattern for directional selectivity in the thick stripes. With respect to disparity, we find activations in V2, and not V1, exhibit topographically organized maps for Near to Far depth percepts induced by random dot stereograms [11]. These findings suggest that organized disparity response, previously shown to exist in later visual areas such as MT, may first arise in V2. Thus feature-specific signals in V2 are poised to contribute both to form information processing in the ventral pathways and to motion and disparity specific processing in the dorsal pathways. Based on these and other findings, we suggest a new view of V2's role in form and motion processing.

In V4, electrophysiological studies have identified neuronal selectivity for different types of visual features, such as orientation, color, and binocular disparity. However, the functional organization of these properties is unknown [12]. Neither is much known about the topographic map within the foveal region [13]. Here, we obtained optical maps through a chronic chamber over the portion of V4 (and the adjoining V2) representing foveal visual space ($< 2^{\circ}$ eccentricity) [14]. Spot and line stimuli activated foveal V4 topographically, in a manner consistent with overall topography of V4. The general retinotopic representation for color, orientation, and disparity stimuli was similar. In general, activations were clustered in appearance, and small stimuli activated domains more strongly than the full-screen gratings, consistent with presence of strong surround suppression in V4. However, color, orientation, and disparity features mapped in different locations within foveal V4. Non-orientation-specific luminance- and color-preferring domains in this region of V4 mapped most caudally, alternating with a band-like appearance. Within luminance- and color-preferring domains, different colors activated separate sets

of sub-domains. In a region just anterior to these domains, orientation selective domains were observed. Further anterior was a large disparity responsive zone (induced by red/green anaglyph random dot patterns). It is possible that details of specific functional organizations may exhibit some variability between animals. These results extend our understanding of V4 functional topography to regions of foveal representation and indicate a distinct compartmentalization of different visual features (orientation, luminance, color, and binocular disparity) in foveal V4.

References

1. Kaas JH (2007) The evolution of sensory and motor systems in primates. In: Evolution of Nervous Systems, Vol 4, pp 35–57 (ed, Kaas JH. Elsevier Academic Press, Elsevier, Amsterdam).
2. Rakic P, Kornack DR (2007) The development and evolutionary expansion of the cerebral cortex in primates. In: Evolution of Nervous Systems, Vol 4, pp 243–259 (ed, Kaas JH. Elsevier Academic Press, Elsevier, Amsterdam).
3. Chen LM, Heider B, Healy FL, Ramsden BR, Williams GV, Roe AW (2002) A chamber and artificial dura method for long-term optical imaging in primates. J Neurosci Methods 113:41–49.
4. Roe AW (2007) Long-term optical imaging of intrinsic signals in anesthetized and awake monkeys. Appl Opt 46:1872–1880.
5. Lu HD, Chen G, Ts'o DY, Roe AW (2008) A rapaid topographic mapping and eye alignment method using optical imaging in Macaque visual cortex. Neuroimage, in press.
6. Lu HD, Roe AW (2008) Functional organization of color domains in V1 and V2 of Macaque monkey revealed by optical imaging. Cerebral Cortex 18(3): 512–533.
7. Lu HD, Roe AW (2007) Optical imaging of contrast response in Macaque monkey V1 & V2. Cerebral Cortex 17(11): 2675–2695.
8. Roe AW, Lu HD, Crewther D (2007) Blue color activation in V1 and V2 of Macaque monkey. Soc Neurosci Meeting, San Diego, CA.
9. Ramsden BM, Hung CP, Roe AW (2001) Real and illusory contour processing in area V1 of the primate – a cortical balancing act. Cereb Cortex 11:648–665.
10. Lu HD, Roe AW (2007c) Response to motion and motion boundary in monkey V2. Vision Sciences Society, Sarasota, FL.
11. Chen G, Lu HD, Roe AW (2008) A map of horizontal disparity in primate V2. Neuron, 58: 442–450.
12. Ghose GM, Ts'o DY (1997) Form processing modules in priamte area V4. J Neurophysiol 77:2191–2196.
13. Gattass R, Sousa AP, Gross CG (1988) Visuotopic organization and extent of V3 and V4 of the macaque. J Neurosci 56:1402–1405.
14. Tanigawa H, Lu HD, Chen G, Roe AW (2007) Functional organization of foveal V4 revealed by optical imaging in the behaving Macaque monkey, Soc Neurosci Meeting, San Diego, CA.

Chapter 48
Mechanisms of Spatial Integration in Primary Visual Cortex of the Primate

Alexander Thiele and Mark Roberts

Abstract Attention can selectively enhance neuronal responses and exclude external noise. To investigate these effects and their neuronal mechanisms we investigated spatial integration and the underlying neuronal mechanisms in primary visual cortex. We found evidence for spatial filtering mechanisms, whereby attention reduced spatial integration in macaque V1 neurons. To study possible mechanisms of this effect, we measured length tuning in V1 in the presence and absence of externally applied acetylcholine. The effects of acetylcholine application and attention in V1 were largely similar. Acetylcholine reduced spatial integration by reducing the neuron's summation area. Thus, attention can alter perceptual and neuronal spatial integration, and acetylcholine may contribute to these task dependent receptive field dynamics.

Keywords Attention · V1 · acetylcholine · spatial integration

Introduction

A variety of studies have demonstrated that attention can influence neuronal firing rates [1], it affects spatial integration of extrastriate cortical neurons [2], as well as the location of cortical receptive fields [3]. The reduction in spatial integration that has been demonstrated with spatial attention could underlie increased perceptual accuracy, reduced influence by external noise [4] and increased resolution at attended locations. While effects of attention on neuronal firing rates and perception are well established, the underlying mechanisms are poorly understood. Many studies highlight the importance of changes in neuronal gain with attention [5, 6, 7, 8], others argue in favor of altered filtering properties [2, 4, 9, 10]. Here we test how attention affects spatial integration in V1 and determine possible neuropharmacological mechanisms.

A. Thiele
Institute of Neuroscience, University of Newcastle upon Tyne, Newcastle Upon Tyne, NE2 4HH, UK
e-mail: alex.thiele@ncl.ac.uk

R. Wang et al. (eds.), *Advances in Cognitive Neurodynamics*,

Methods and Results

If attention alters spatial integration, then neurons at some level have to alter their filtering properties. Such alterations could be mediated by feedback projections from 'higher' cortical areas [11]. In addition to feedback, the neuromodulator Acetylcholine (ACh) is often considered to play an important role in the mediation of attention [12, 13]. Acetylcholine could mediate changes in spatial integration, i.e. change spatial filtering properties of neurons. Such a proposal is based on *in vitro* studies, which demonstrate that ACh selectively reduces the efficacy of lateral cortical connections via a muscarinic mechanism [14, 15], while boosting the efficacy of thalamocortical/feed-forward connections via a nicotinic mechanism [16]. *In vivo* ACh should thus reduce centre-surround interactions of neurons in primary visual cortex, making cells more reliant on feed-forward information. Within the framework of attention it would mean that local sensory information is boosted by spatial attention, while distracting surround information is filtered out. To test whether ACh indeed affects spatial integration in vivo, we recorded neurons from primary visual cortex in the anaesthetised marmoset monkey (Callthrix Jacchus), in the presence and absence of applied ACh. We measured spatial integration by determination of the preferred length of V1 neurons. We found that ACh application in the majority of cells (66%) increased the firing rate of V1 neurons. In line with our prediction it also reduced spatial integration, shifting the preferred bar length towards shorter bars. We fitted a Difference of Gaussian Model to our data, thereby determining mechanisms that underlie these changes in spatial integration. The analysis yielded that ACh significantly reduces the size of the summation area, while having no systematic effect on either the size of the inhibition area, or the excitation or inhibition gains [17].

If ACh is involved in the mediation of attention, then selective attention should have similar effects on spatial integration of V1 neurons. We tested this by determining the preferred length of V1 neurons while three animals attended to the receptive field of the neuron under study, and when they attended away. In two of three animals we recorded from a group of cells with parafoveal receptive field locations (within 2–3° from the fovea), and from cells with more peripheral receptive field locations ($> 6°$ from the fovea). In both cell groups we found that attention usually enhanced the neuronal activity ($p < 0.001$, t-test). For the parafoveal cell group we additionally found that attending to the receptive field of the neuron under study significantly reduced the preferred length. Fitting a Difference of Gaussian to our data, revealed that the reduction in preferred length ($p < 0.01$, signed rank test) was mediated by a reduction in the summation area ($p < 0.01$, signed rank test), while the other parameters (size of inhibition area, excitation gain, and inhibition gain) were not consistently affected. Thus, attention at parafoveal locations affects spatial integration in a manner comparable to ACh. Surprisingly, the effects of attention on cells with more peripheral receptive fields were opposite to those at parafoveal sites. Although attention still increased firing rates ($p < 0.001$, t-test), it shifted the preferred length towards larger bar lengths ($p < 0.001$, signed rank test). These changes were mediated by an increase in summation area ($p < 0.01$, signed rank test), an increase

in excitation gain ($p < 0.01$, signed rank test), and an increase in inhibition gain ($p < 0.01$, signed rank test). We hypothesize that an increase in spatial integration at more peripheral locations could aid in the highlighting of these locations in the saliency map, and label them for impending eye-movements towards these locations. The differential effects of attention on spatial integration at parafoveal and peripheral sites could reflect specific task demands. In our task animals had to detect a very small and subtle change in brightness at the attended location. If neurons at parafoveal sites have better contrast sensitivity, the necessity to pool across neurons might be reduced for these locations. Conversely, increased pooling among neurons with lower contrast sensitivity at peripheral locations might benefit task performance and thus result in increased spatial integration with attention.

If ACh is part of the mechanism that mediates attention, blocking the cholinergic receptors should significantly reduce attentional effects, while animals 'attend' to the receptive field of the neurons under study. To investigate this we developed and employed a novel pipette electrode combination [18], and recorded neuronal activity from V1 neurons while animals attended to and away from the receptive field of the neuron under study. This was done while muscarinic (scopolamine) or nicotinic (mecamylamine) antagonists were locally iontophoretically either applied or not applied. We performed a 3-Factor ANOVA for each cell to determine whether attention significantly affected neuronal activity (factor 1), whether drug application significantly affected neuronal activity (factor 2), whether bar length had an effect on activity (factor 3), and whether these factors interacted. If cells were significantly affected by attention and drug application, or if there was a significant interaction between these two we selected the cells for further analysis. For these cells we analysed whether blocking muscarinic or nicotinic receptors significantly altered attentional modulation. Attentional modulation was quantified by calculating the receiver operating characteristic between the attend RF and attend away condition. We found that nicotinic blockade hugely reduced sensory transmission (firing rates were on average reduced by $> 50\%$), but had no significant effect on attentional modulation ($p > 0.05$, signed rank test). Blocking muscarinic receptors reduced firing rates much more modestly. Importantly, it resulted in a significant reduction of attentional modulation ($p < 0.001$, signed rank test). The action of ACh on muscarinic receptors is thus one of the mechanisms that is important for the mediation of attention.

Discussion

We investigated whether attention affects spatial integration in V1 and a possible contribution of ACh to these effects. We found that attention alters spatial integration in V1 for cells with parafoveal receptive fields, by reducing their spatial summation area. Thereby these cells are less influenced by stimuli presented in their receptive field surrounds, effectively enhancing local analysis of visual scenes. External application of ACh in V1 of anaesthetized marmoset monkeys equally resulted in a reduction of spatial integration by reducing a cell's summation area. Moreover,

in the awake macaque attentional modulation was significantly reduced during application of muscarinic antagonists, supporting our hypothesis that acetylcholine enables states of attention. We do not, however, dispute the importance of feedback projections in the mediation of attentional selection. We rather hypothesize that the appropriate amount of ACh acting on muscarinic receptors allows neurons to change their conductance [19, 20], such that they are more susceptible to small inputs at peripheral dendritic locations, possibly more susceptible to weak modulatory feedback input, and possibly more susceptible to engage in high frequency synchronization [21, 22], that has been associated with attention.

Acknowledgments The work was supported by the BBSRC (BBS/B/09325), the Wellcome Trust (070380/Z/03/Z), and the MRC (G0100407; G78/7853).

References

1. Treue, S. and J.H.R. Maunsell, Attentional modulation of visual motion processing in cortical areas MT and MST. Nature, 1996. 382: p. 539–541.
2. Reynolds, J.H., L. Chelazzi, and R. Desimone, Competitive mechanisms subserve attention in macaque areas V2 and V4. J Neurosci, 1999. 19(5): p. 1736–1753.
3. Womelsdorf, T., et al., Dynamic shifts of visual receptive fields in cortical area MT by spatial attention. Nat Neurosci, 2006. 9: p. 1156–1160.
4. Lu, Z.L., L.A. Lesmes, and B.A. Dosher, Spatial attention excludes external noise at the target location. J Vis, 2002. 2(4): p. 312–323.
5. McAdams, C.J. and J.H.R. Maunsell, Effects of attention on orientation tuning functions of single neurons in macaque cortical area V4. J Neurosci, 1999. 19: p. 431–441.
6. Treue, S. and J.H.R. Maunsell, Effects of attention on the processing of motion in macaque middle temporal and medial superior temporal visual cortical areas. J Neurosci, 1999. 19: p. 7591–7602.
7. McAdams, C.J. and J.H.R. Maunsell, Attention to both space and feature modulates neuronal responses in macaque area V4. J Neurophysiol, 2000. 83: p. 1751–1755.
8. Williford, T. and J.H. Maunsell, Effects of spatial attention on contrast response functions in macaque area V4. J Neurophysiol, 2006. 96(1): p. 40–54.
9. Spitzer, H., R. Desimone, and J. Moran, Increased attention enhances both behavioral and neuronal performance. Science, 1988. 240: p. 338–340.
10. Dosher, B.A. and Z.L. Lu, Noise exclusion in spatial attention. Psychol Sci, 2000. 11(2): p. 139–146.
11. Moore, T. and K.M. Armstrong, Selective gating of visual signals by microstimulation of frontal cortex. Nature, 2003. 421(6921): p. 370–373.
12. Robbins, T.W., Arousal systems and attentional processes. Biol Psychol, 1997. 45(1–3): p. 57–71.
13. Robbins, T.W., Chemical neuromodulation of frontal-executive functions in humans and other animals. Exp Brain Res, 2000. 133(1): p. 130–138.
14. Hasselmo, M.E. and J.M. Bower, Cholinergic suppression specific to intrinsic not afferent fiber synapses in rat piriform (olfactory) cortex. J Neurophysiol, 1992. 67(5): p. 1222–1229.
15. Kimura, F., Cholinergic modulation of cortical function: a hypothetical role in shifting the dynamics in cortical network. Neurosci Res, 2000. 38(1): p. 19–26.
16. Gil, Z., B.W. Connors, and Y. Amitai, Differential regulation of neocortical synapses by neuromodulators and activity. Neuron, 1997. 19(3): p. 679–686.

17. Roberts, M.J., et al., Acetylcholine dynamically controls spatial integration in marmoset primary visual cortex. J Neurophysiol, 2005. 93(4): p. 2062–2072.
18. Thiele, A., et al., A novel electrode-pipette design for simultaneous recording of extracellular spikes and iontophoretic drug application in awake behaving monkeys. J Neurosci Methods, 2006. 158(2): p. 207–211.
19. McCormick, D.A., Cellular mechanisms underlying cholinerig and noradrenergic modulation of neuronal firing mode in the cat and guinea pig dorsal lateral geniculate nucleus. J. Neurosci, 1992. 12: p. 278–289.
20. McCormick, D.A. and D.A. Prince, Two types of muscarinic response to acetylcholine in mammalian cortical neurons. Proc Natl Acad Sci U S A, 1985. 82(18): p. 6344–6348.
21. Rodriguez, R., et al., Short- and long-term effects of cholinergic modulation on gamma oscillations and response synchronization in the visual cortex. J Neurosci, 2004. 24(46): p. 10369–10378.
22. Fries, P., et al., Modulation of oscillatory neuronal synchronization by selective visual attention. Science, 2001. 291(5508): p. 1560–1563.

Chapter 49
Coding of Peripheral Olfactory Information in the Olfactory Bulb of Small Animals

Fuqiang Xu, James Shafer, Nian Liu, Douglas L. Rothman, Fahmeed Hyder and Gordon M. Shepherd

Abstract The activity pattern in the olfactory bulb is generally believed to code for the peripheral olfactory information. To reveal how chemical structure and experimental parameters are represented by the patterns, high resolution functional MRI was used to map the responses of the bulb to various stimuli under different conditions. The results revealed that different odorants elicited specific and reproducible patterns. Pattern similarity (difference) parallels structure similarity (difference). Experimental parameters, such as odorant concentration and exposure duration, strongly affect pattern intensity, but have little effects on the pattern topography. The results provided evidence for the hypothesis that the pattern intensity codes for the stimulation strength and pattern topography codes for chemical structure.

Keywords fMRI · olfactory bulb · information coding · rat and mouse

Introduction

The activity pattern in the glomerular layer of the olfactory bulb (OB) is believed to code peripheral olfactory information [1]. It contains the information of the absolute activity of each glomerulus, defining the pattern intensity, as well as the relative activity and the spatial relations among all glomeruli, defining the pattern topography [2]. Ever increasing evidence shows that a given odor can activate many glomeruli, and a glomerulus can be activated by many odorants [3]. Highly activated glomeruli frequently cluster together, forming module, or focus, domains [4]. However, further analysis of how chemical structures and physical parameters of olfactory stimuli are represented by the activity patterns is limited by the methods currently available. Global methods, such as 2-deoxyglucose and c-fos mapping, test single odors in terminal experiments, preventing comparison of responses to

F. Xu
Wuhan Institute of Physics and Mathematics, Chinese Academy of Science, Wuhan 430071, China
e-mail: fuqiang.xu@wipm.ac.cn

R. Wang et al. (eds.), *Advances in Cognitive Neurodynamics*,

different odors in the same animal. Optical methods, such as florescent and intrinsic imaging, are limited to a small portion of the OB (the accessible dorsal surface), preventing the comparison of the patterns across the OB. To overcome these limitations, we have developed functional MRI (fMRI) to map the activity patterns with high spatial resolution to reveal how the chemical and physical properties of olfactory stimuli are coded in the OB. Specifically, we will test the hypothesis that the chemical nature is mainly represented by pattern topography, while the physical parameters are mainly represented by pattern intensity.

Experimental

Animal Preparation

Male rats were anesthetized with 1–2% halothane, and the skin overlying the OB was removed to expose the skull. Before the mouse was placed in the magnet the anesthesia was switched to urethane (i.p. 1.0 mg/g initial; 0.1 mg/g/h supplemental). The surgical procedure was approved by the Yale Animal Care and Use Committee (YACUC no. 10004).

Odor Delivery

The odor-delivery system was made of Teflon and glass with a dead volume of 5 ml. Mineral oil was used as the solvent to prepare the odor solution. The flow rate of the extra-pure air passing over the odorant solution was kept at 3 l/min, generating odorized airflow at selected odor concentrations. The concentrations of the solutions were adjusted so that the vapor concentrations of different odorants were approximately the same.

Anatomical MRI and fMRI

Experiments were performed on horizontal-bore Bruker spectrometers. The magnetic field homogeneity was optimized by manual shimming. T1-weighted fast low-angle single-shot (FLASH) anatomical images were obtained (image dimension = 128 × 128 pixels; in-plane resolution = 100 × 100 μm; slice thickness = 200 μm; repetition delay = 5.0 s; echo time = 16 ms; flip angle = 90°) with variable inversion recovery weighting per slice. Each multislice fMRI experiment consisted of a series of 128 T^*2-weighted FLASH images (image dimension = 64 × 64 pixels; in-plane resolution = 200 × 200 μm; slice thickness = 200 μm; repetition delay = 400 ms; echo time = 16 ms; flip angle = 5–15°).

Data Processing

Data processing and analysis were performed as described previously [3]. Statistical methods such as normalized dot-product, spatial correlation coefficient, and regression coefficient will be used to reveal pattern reproducibility, similarity and difference.

Results

Reproducibility and Specificity

The hypotheses have the prerequisites of the pattern reproducibility for repeated stimulations and specificity for different stimuli. The patterns of heptanal, amyl and ethyl acetate in two exposures (Fig. 49.1) are highly reproducible. The patterns elicited by the two esters are rather similar, but are very different from that of the aldehyde. The results demonstrate that odorants with similar/different structures evoke similar/different activity patterns in the OB.

Concentration Effects on Patterns

Concentration is one of the most important attributes for an olfactory stimulus. Although odor can be detected over a broad range of concentration, most odorants usually have similar odor-quality but different intensities [5]. The pattern intensity increases with concentration for all three tested odorants, indicating that the OB responses are not saturated under the experimental concentrations (Fig. 49.2). However, when the pattern of low concentration is normalized to the higher concentration, the pattern topography is very similar. Statistical analysis shows that the topography of patterns from different concentrations is rather similar. The signals of the same pixels are concentration dependent, but are highly correlated. The correlation coefficients for patterns of the same concentrations (reproducibility) and the

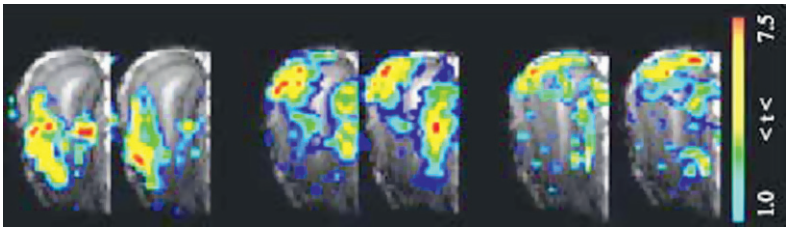

Fig. 49.1 Reproducibility and specificity of fMRI patterns in a coronal slice elicited by odorants heptanal, (left), amyl acetate (middle), and ethyl acetate (right)

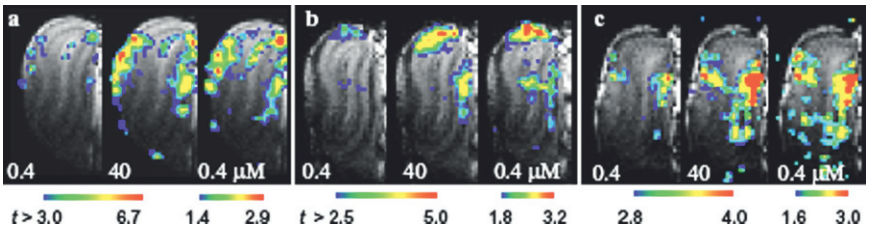

Fig. 49.2 Variability of pattern intensity and invariability of pattern topography for different odorant concentrations. The patterns of 0.4 μM of all three odorants, amyl acetate (**a**), carvone (b) and heptanal (c), are normalized to the same percentage of the 40 μM stimulus (30%) to show similarity of pattern topography

patterns of different concentrations are high and not significantly different among them, while the correlation coefficients between the pattern of any concentration of odorant and air are near zero. These results show that the pattern topography is concentration independent and the intensity is concentration dependent.

Adaptation Effects on Patterns

Exposure history, another physical feature of a stimulus, describes the concentration, exposure duration, and time elapsed of the earlier exposures. The daily experience and animal behavior show that the odor-quality is maintained in multiple, or prolonged exposures, while the perceived intensity is attenuated, even disappeared [6]. Indeed, the fMRI pattern intensity decreases accordingly with different exposure histories. With same inter-stimulation interval, more adaptation is observed for longer exposure duration. The response is less attenuated when longer time is elapsed but with the same exposure duration. However, when the adapted patterns are normalized to the first exposures, conservation of the pattern topography is apparent (Fig. 49.3). The quantitative analysis shows that these images are highly

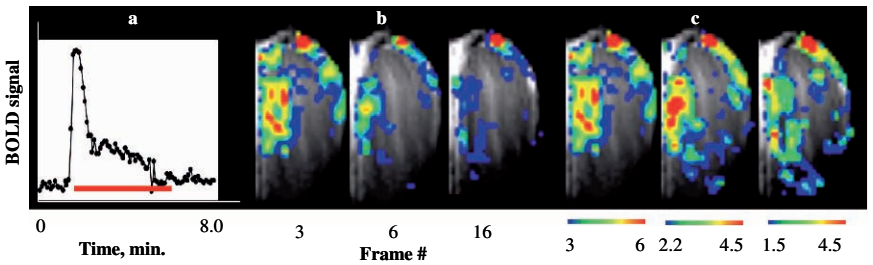

Fig. 49.3 The variability of pattern intensity and variability of pattern topography of activity pattern during prolonged exposure. a. Time course of fMRI signal, red bar represents the exposure duration; b. Patterns at frame #3, 6 and 16 to show the change of intensity, c. The same images as in (b), but normalized to show the similarity of topography

correlated, among the unadapted, and the adapted. Therefore, the data demonstrated that for a given odorant, the pattern topography is independent of the exposure history, while the pattern intensity varies consequently.

Conclusions

The results have shown that all tested physical parameters affect the pattern intensity, but not the pattern topography of a given odorant. OB neurons respond to olfactory stimulation can be excitatory, inhibitory, or null. A neuron rarely changes from one to another type under different conditions of the same odorant [7]. The concentration dependent of intensity and independent of topography have been revealed from honeybee, turtle, salamander, and rat by methods measuring different signals, such as electrical recording, optical imaging, fMRI, and 2-deoxyglucose mapping [4, 8]. These techniques have very different temporal and spatial resolutions, and field of view. However, all is consistent with the observations reported here.

References

1. Xu, F., Greer, C. A., Shepherd, G. M.: Odor maps in the olfactory bulb. J. Com. Neurobiol. 422 (2000) 489–495.
2. Xu, F.: That's your left foot and. . .. Trend Neurosci. 24 (2001) 549–550.
3. Xu, F., Liu, N., Kida, I., Rothman, D.L., Hyder, F, Shepherd, G.M.: Odor maps of aldehydes and esters revealed by functional MRI in the glomerular layer of the mouse olfactory bulb, Proc. Natl. Acad. Sci. USA 100 (2003) 11029–11034.
4. Uchida. N., Takahashi, Y.K., Tanifuji, M., Mori, K.: Odor maps in the mammalian olfactory bulb: domain organization and odorant structural features. Nat. Neurosci. 3 (2000) 1035–1043.
5. Youngentob, S.L., Markert, L.M., Mozell, M.M., Hornung., D.E.: A method for establishing a five odorant identification confusion matrix task in rats. Physiol. Behav. 47 (1990) 1053–1059.
6. Chaput, M.A., Holley, A.: Responses of olfactory bulb neurons to repeated odor stimulations in awake freely-breathing rabbits. Physiol. Behav. 34 (1985) 249–258.
7. Duchamp-Viret, P., Duchamp, A., Sicard, G.: Olfactory discrimination over a wide concentration range. Brain Res. 517 (1990) 256–262.
8. Johnson, B.A., Leon, M.: Modular representations of odorants in the glomerular layer of the rat olfactory bulb and the effects of stimulus concentration. J. Comp. Neurol. 422 (2000) 496–509.

Chapter 50
Neural Ensembles and Local Field Potentials in the Hippocampal-Prefrontal Cortex System During Spatial Learning and Strategy Shifts in Rats

Francesco P. Battaglia, Karim Benchenane, Mehdi Khamassi, Adrien Peyrache and Sidney I. Wiener

Abstract To better understand the mechanisms of hippocampal-cortical signalling for mnemonic function and behavior, we recorded ventral hippocampal local field potentials (LFPs) simultaneously with ensemble neural activity and LFPs in the prefrontal cortex in rats learning and switching strategies in a Y-maze variant of the Wisconsin Card Sorting Task. Behaviorally correlated activity of individual neurons changed after task contingency changes or as the animal adopted different strategies. Curiously, within ensembles of simultaneously recorded neurons, individual neurons showed different responses to contingency or strategy while others did not change at all. Furthermore some prefrontal neurons are significantly modulated by hippocampal theta activity and also by hippocampal sharp waves (with 150 Hz ripples). Finally we present data showing that coherence between the hippocampus and prefrontal cortex in the theta band is behaviorally modulated. These observations provide evidence for engagement of hippocampal signals by prefrontal neurons as a mechanism underlying learning this task.

Keywords Memory · EEG · unit recordings · theta · coherence · prelimbic area

Introduction

The hippocampus and prefrontal cortex are sometimes attributed complementary functions for memory processing (memory consolidation and working memory respectively), which must be reconciliated with the fact that there is a direct hippocampal-prefrontal pathway in the rat. The problem may however be a problem of interpretation, since experimental interventions inducing local inactivation in one

F.P. Battaglia
Graduate School of Neurosciences Amsterdam, University of Amsterdam, Faculty of Science, Swammerdam Institute for Life Sciences, Center for Neuroscience, 1090 GB, Amsterdam, The Netherlands
e-mail: battagli@science.uva.nl

R. Wang et al. (eds.), *Advances in Cognitive Neurodynamics*,

structure or the other often lead to the assignment of distinct functions to individual structures. Thus neuropsychological studies employing inactivation protocols must be complemented by other approaches such as unit activity recordings. However interpretation of many recording studies of this system is hampered by experiments being carried out on overtrained animals. Thus the experiments described here concern cell activity in animals still learning.

While recordings of single neurons, of evoked potentials and of images of brain activation shed light on fundamental processes, it is our belief that it is also important to focus on recordings of ensemble activity and its relations with local field potentials in order to integrate findings at these three orders of magnitude and hence elucidate dynamic functional mechanisms for cognitive functions. Of particular interest is synchronous oscillatory activity which has received much recent attention as a reference for phase coding of neuronal discharges, and may also underlie mechanisms of synchronization and privileging communication among select distant brain areas, as in 'binding'.

Thus we developed a variant of the Wisconsin Card Sorting Task for rats. Performance in this task is known to be impaired in neurological patients suffering from damage to the prefrontal cortex. Once the rats had been familiarized with the maze, tetrode recordings were made of local field potentials in ventral hippocampal CA1 and prefrontal (prelimbic area) as well as ensemble activity of prelimbic neurons.

Methods

Prefrontal neurons as well as prefrontal and hippocampal LFPs were recorded from multiple tetrodes in rats successively learning four reward contingency strategies on a Y maze: go right, go to the lit arm, go left, then go to the dark arm (the lit arm was selected randomly). Rats were required to return to the start arm after consuming the chocolate milk reward. A delay of 5 s was imposed between trials.

In analyses, modulation by theta was defined as the amplitude of the sine-wave fitting the phase histograms of one cell spikes' phases relative to theta. Modulation by sharp waves is taken as the logarithm of the ratio between mean firing rate of a cell in a 100 ms window surrounding ($\pm$ 25 ms) ripples' amplitude peak and the mean firing rate of the cell in a window lasting from 1 s to 50 ms before ripple peaks.

Results

Hippocampal LFP and medial prefrontal neurons and LFP were recorded in five freely moving rats during 98 recording sessions in a Y maze and in previous and subsequent sessions of quiet repose.

Task-Related Shifts in Behavioral Correlates

In 238 of the 1894 neurons analysed, there were abrupt changes in firing correlates following changes in the task rule ($n = 99$) or in the rat's strategy ($n = 139$). These changes included appearance of a new behavioral correlate or reduction in behaviorally correlated activity. Other neurons discriminated from the same tetrode showed no such changes reducing the risk that this corresponds recording instability. Within groups of simultaneously recorded neurons, the reaction to the task or strategy shift varied.

Hippocampal Theta Modulation and Sharp Wave ('Ripple') of Prefrontal Neurons

In 35% of the 2230 cells analysed, action potentials were significantly phase modulated by hippocampal theta during task performance (Rayleigh test, $p < 0.05$) as shown previously. Furthermore, in 21%, firing rates increased (11%) or decreased (10%) during hippocampal ripples occurring during previous or subsequent resting periods (t-test, $p < 0.05$). (Modulation by sharp waves is taken as the logarithm of the ratio between mean firing rate of a cell in a window surrounding (± 25 ms) ripples' peak and the mean firing rate of the cell in a window lasting from 1 s to 50 ms before ripples' peak.) In 10% of the cells there was significant modulation by both theta and ripples, and the amplitude of these respective modulations was significantly correlated (Pearson's correlation test, $p < 0.05$). This correlation may correspond to the strength of hippocampal afferences to the respective neurons and their local circuits, suggesting that the hippocampal/prefrontal interaction is mediated by the same population of prefrontal cells both during sleep and active behavior.

LFP Coherence Between Hippocampus and Prefrontal Cortex in the Theta Band

A robust theta rhythm at 6–8 Hz was observed in the prefrontal LFP. During learning, high hippocampal-PFC coherence (values > 0.7) in the theta band (5–10 Hz) was observed. This occurred principally at the decision point in the maze, suggesting heightened communication between hippocampus and PFC at the moment of behavioural choice.

Discussion

These results demonstrate that the hippocampal-prefrontal system was engaged by this variation of a set-shifting task that is used to diagnose prefrontal dysfunction in human patients. The transitions in cell activity corresponded to the rat's strategy

shifts may reveal an underlying mechanism of prefrontal action in this task. In previous recordings of rats switching strategies (albeit with triggering cues) [1] we observed comparable changes in responses in prefrontal afferent zones of the nucleus accumbens, but not hippocampal place cells which also project to accumbens [2].

This is consistent with the hypothesis that this 'set-shifting' activity is mediated by the prefrontal cortex.

The observation of prefrontal neurons modulated by hippocampal theta oscillatory activity and by hippocampal sharp waves demo nstrates nevertheless that there is a powerful hippocampal influence on a subset of prefrontal neurons. This is hypothesized to correspond to a pathway transmitting signals for executing strategies requiring contextual information such as spatial position.

The behaviorally modulated coherence of simultaneously recorded hippocampal and prefrontal LFPs reinforces the latter evidence for hippocampal influences on the prefrontal cortex. Conversely, the reduced modulation during behaviors other than the decision period suggests that perhaps other brain areas are oscillating coherently with the prefrontal cortex then. This is reminiscent of the observations of greater incidence of cross-correlations between neurons of the hippocampus and the nucleus accumbens during approaches to a goal site, but not during return visits [3]. This suggests that certain circuits can be selectively gated in a behaviorally relevant manner.

Acknowledgments Supported by EC ICEA, BACS and NeuroProbes.

References

1. Shibata, R., Mulder, A.B., Trullier, O., Wiener, S.I.: Position sensitivity in phasically discharging nucleus accumbens neurons of rats alternating between tasks requiring complementary types of spatial cues. Neuroscience 108 (2001) 391–411.
2. Trullier, O., Shibata, R., Mulder, A.B., Wiener, S.I.: Hippocampal neuronal position selectivity remains fixed to room cue in rats alternating between place navigation and beacon approach tasks. Eur. J. Neurosci. 11(12) (1999) 4381–4388.
3. Tabuchi, E., Mulder, A.B., Wiener, S.I.: Position and behavioral modulation of synchronization of hippocampal and accumbens neuronal discharges in freely moving rats. Hippocampus 10 (2000) 717–728.

Chapter 51
Temporal and Spatial Characters of Retinal Ganglion Cells' Response to Natural Stimuli

Ying-Ying Zhang, Xin Jin, Hai-Qing Gong and Pei-Ji Liang

Abstract Results from physiological, theoretical, and computational studies suggest that the visual cortex processes natural sensory information with a strategy of sparse coding. To investigate whether this is also the case for retinal ganglion cells (RGCs), neuronal activities were recorded from a group of chicken RGCs in response to natural, time-varying images (movies) using extracellular multi-electrode recording system. The response of single RGC in exposure to natural stimulation showed sparse activity, while the ensemble responses did not. Such result may suggest that at the RGC level, the single unit activity is kept at a low level in response to natural stimuli for energy-saving, but the neuronal population are often activated in a correlated manner to achieve efficient information transmission.

Keywords Natural movie · retinal ganglion cell · life-time sparse activity · population activity

Introduction

The task of the visual system is primarily to process information in natural environment, it is therefore important to explore the visual information processing in response to natural stimuli [1]. It is suggested that the central visual system can use a strategy of sparse coding to optimize itself to match the natural scenes, which are inherently sparse in statistical structure [2, 3]. Sparse coding refers to the phenomenon that only a small portion of neurons are activated at a given time in response to a given stimulation [4], and at the mean time, the single neuronal activities are kept at a low level most of the time during stimulation. Sparse representation makes the structure in nature scenes explicit and simpler

Y.-Y. Zhang
Department of Biomedical Engineering, Shanghai Jiao Tong University, 800 Dong-Chuan Road, Shanghai 200240, China
e-mail: zcyyz@sjtu.edu.cn

R. Wang et al. (eds.), *Advances in Cognitive Neurodynamics*,

for the subsequent neurons to read out with high memory capacity and metabolic efficient [5].

Sparseness can be defined in two terms, lifetime sparseness and population sparseness. The fourth moment (i.e., the kurtosis) of the response distribution of a single neuron over time, and that of the firing rates distribution of the population neurons in response to a certain state of the natural stimuli can be applied to quantify the lifetime sparseness (K_L) and population sparseness (K_P) respectively.

In the present study, the activities of several dozens of RGCs in response to natural stimuli (movies) were recorded simultaneously from isolated chicken retina using a multi-electrode array (MEA). To represent the natural stimuli, each single neuron showed sparse representation while the ensemble neuronal activities are correlated. These results provide further experimental evidence from the earliest stage of the visual system to support the hypothesis that the nervous system can be well adapted to efficiently represent the natural input using a strategy of sparse coding combined with population correlation.

Methods

Electrophysiology Recordings and Visual Stimulation

Detailed extracellular-recording procedure can be found elsewhere [6, 7]. Spikes from ganglion cells were recorded by MEA electrodes (8×8) using a commercial multiplexed data acquisition system with a sampling rate of 20 kHz.

The stimulation protocols were: (1) Full-field white light flashes (1-s light-ON duration vs 9-s light-OFF intervals) to test the functional condition of the neurons being investigated; (2) Digitized segments of grayscale video recording (1920 frames, 128×128 pixels, refresh rate being 10 Hz) of natural outdoor scenes containing trees, rocks, streets, houses etc (download from the website of Hateren's lab, http://hlab.phys.rug.nl/vidlib/index.html; see also [8]). The images were projected onto the retinal piece via an optical lens system and covered the whole area of the multi-electrode array.

Data Analysis

Kurtosis is the fourth moment of a distribution for measuring the "peakedness" of the distribution [9]:

$$K = \left\{ \frac{1}{n} \sum_{i=1}^{n} \left[\frac{r_i - r^-}{\sigma_r} \right]^4 \right\} - 3 \tag{51.1}$$

This value is close to zero for a Gaussian distribution and a high positive value is related with a heavy-tailed peaky distribution, such as the case for sparse response of the neuronal activity.

Results

The firing probability distribution of an example neuron's response (firing rates counted in 1-s segments) in exposure to the natural movie is with a sharp peak as compared to the surrogate Gaussian distribution (Fig. 51.1a), with a K_L value being 1.8837 (the K_L value of the surrogate Gaussian data is -0.0390 ± 0.2761 (mean $\pm$SD, $n = 100$)). All the K_L values of the 21 ganglion cells recorded from the same piece of isolated retina are significantly larger than the K_L values of the surrogate Gaussian distribution data (Fig. 51.1b and c). These results demonstrate that the null hypothesis that the firing probability distribution follows a Gaussian distribution can be rejected for the single neurons' responses to natural movie, which gives evidence that the lifetime sparseness is a character of single neurons' responses to natural stimulation.

The response distribution of the neuronal population in exposure to an example segment of the natural movie (lasted for 1 s) is sharply peaked, but the data are more widely distributed (Fig. 51.2a), and the relevant K_P value is -0.21889 (with

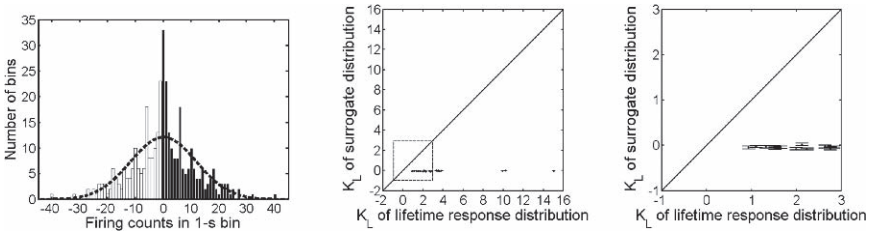

(*a*) (*b*) (*c*)

Fig. 51.1 (a) Response probability distribution (RPD) (filled bars, bin size = 1 s, with mirror values given in blank bars) for an example cell in exposure to the natural movie is compared to a Gaussian distribution (*dashed line*) which shares the same mean value and standard deviation with the reflected RPD to be analyzed. (b) Scatter plot of the K_L values of all the 21 neurons' surrogate Gaussian distribution against that of the RPDs. (c) Truncated from the dashed box in (b)

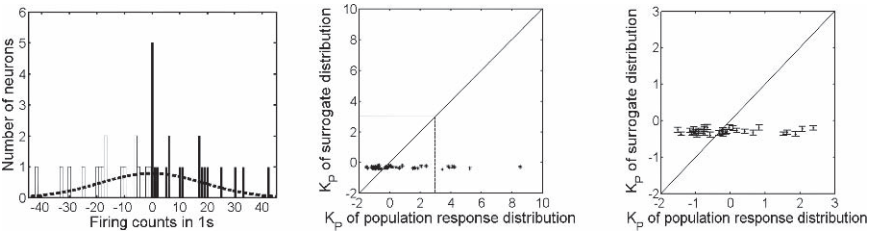

(*a*) (*b*) (*c*)

Fig. 51.2 (a) Response distribution (*filled bar, with mirror values given in blank bars*) for the population of 21 cells to 1-s segment of the natural movie is compared with a Gaussian distribution (*dashed line*) which shares the same mean value and standard deviation with the reflected response distributions to be analyzed. (b) Scatter plot of the K_P values of the surrogate Gaussian distribution against that of the response distribution of 40 segments of the movie (each lasted for 1 s). (c) Truncated from the dashed box in (b)

the K_P value of the surrogate Gaussian data being -0.19866 ± 0.68109 (mean $\pm$SD, $n = 100$)). Quite a portion of the neurons fired at a relatively low rate within the time window being investigated, but with a correlated manner. Figure 51.2b and c show that the K_P values of the response distribution in response to 40 segments of the movie (each lasted for 1 s) are widely distributed, while the K_P values of the surrogate Gaussian distributions are relatively constant. These results indicate that the population sparseness can not be detected and the activities of population RGCs in response to the natural stimuli in a correlated manner to provide an efficient information transmission.

Summary

Our results from temporal and spatial responses of the RGCs in exposure to natural movie provide further experimental evidence at the RGC level to support the hypothesis that the nervous system can be well adapted to efficiently represent the natural input using a strategy of sparse coding and suggest that the correlation among the population neurons is critical for efficiently encoding and transmitting the natural stimuli.

References

1. Reinagel, P.: How do visual neurons respond in the real world? Curr. Opin. Neurobiol. 11 (2001) 437–442.
2. Field, D.J.: Relations between the statistics of natural images and the response properties of cortical cells. J. Opt. Soc. Am. A 4 (1987) 2379–2394.
3. Simoncelli, E.P., Olshausen, B.A.: Natural image statistics and neural representation. Annu. Rev. Neurosci. 24 (2001) 1193–1216.
4. Olshausen, B.A., Field, D.J.: Natural image statistics and efficient coding. Network 7 (1996) 333–339.
5. Olshausen, B.A., Field, D.J.: Sparse coding of sensory inputs. Curr. Opin. Neurobiol. 14 (2004) 481–487.
6. Chen, A.H., Zhou, Y., Gong, H.Q., Liang, P.J.: Luminance adaptation increased the contrast sensitivity of retinal ganglion cells. Neuroreport 16 (2005) 371–375.
7. Jin, X., Chen, A.H., Gong, H.Q., Liang, P.J.: Information transmission rate changes of retinal ganglion cells during contrast adaptation. Brain Res. 1055 (2005) 156–164.
8. van Hateren, J.H., van der Schaaf, A.: Independent component filters of natural images compared with simple cells in primary visual cortex. Proc. R. Soc. Lond. B 265 (1998) 359–366.
9. Willmore, B., Watters, P.A., Tolhurst, D.J.: A comparison of natural-image-based models of simple-cell coding. Perception 29 (2000) 1017–1040.

Chapter 52
Synchronization of Chaotic Neuronal Networks with Small-world Topology

Fang Han, Qi-Shao Lu and Yan-Hong Zheng

Abstract Synchronization of coupled chaotic neuronal network with small-world topology is explored in this paper. The synchronization condition of chaotic HR neuronal network is obtained by using the master stability function as a general criterion for synchronization stability of neuronal networks. Numerical simulation is performed in a small-world network with hundreds of neurons. It is shown that master stability function is effective for determining synchronization condition of neuronal networks and chaotic small-world neuronal networks can synchronize by setting the coupling strength properly.

Keywords Neuronal network · master stability function · small-world · synchronization region · coupling strength

Introduction

Synchronization of coupled neurons could play a key role in intercommunications among neurons. However, the synchronization of real neuronal network has long been a difficult problem as the topology of real neuronal network has not been very clear so far. The small world network models, which were introduced by Watts and Strogatz in 1998, simultaneously realize dense local connections and short pairwise distances. Many biological neural networks have been reported to have the small-world properties. In this paper, complete synchronization of chaotic HR neurons with small world topology is explored by using the master stability function [1] as a general criterion for synchronization stability of coupled neuronal networks.

In general, we consider n identical chaotic neurons coupled through their first state variables as follows:

Q.-S. Lu
School of Science, Beijing University of Aeronautics-Astronautics, Beijing 100083, China
e-mail: qishaolu@hotmail.com

R. Wang et al. (eds.), *Advances in Cognitive Neurodynamics*,

$$\dot{\mathbf{X}}_i = \mathbf{F}(\mathbf{X}_i) + \sigma \sum_{j=1}^{N} g_{ij}\mathbf{H}(\mathbf{X}_j), \quad i = 1, 2, \cdots, N \tag{52.1}$$

where $\mathbf{X}_i \in R^m$ is a m-dimensional vector for the ith neuron, σ is the coupling strength, $G = \{g_{ij}\}_{N\times N}$ is the coupling matrix, a symmetric matrix with zero row-sum and real spectrum, $\mathbf{H}$ is the output function and is taken to be $\mathbf{H} = diag\{1, 0, 0, \cdots 0\}$ for every node.

To assess the linear stability of the synchronous state $\{\mathbf{X}_i = \mathbf{s}(t), \forall i\}$, we need to diagonalize the variational equations $\dot{\boldsymbol{\xi}} = [\mathbf{1}_N \otimes D\mathbf{F}(\mathbf{S}) + \sigma G \otimes D\mathbf{H}(\mathbf{s})]\boldsymbol{\xi}$, and check that the perturbations transverse to the synchronization manifold are damped. The diagonalization of G transforms the variational equation into n blocks of the form

$$\dot{\boldsymbol{\xi}}_k = [D\mathbf{F}(\mathbf{s}) + \sigma\gamma_k D\mathbf{H}(\mathbf{s})]\boldsymbol{\xi}_k, \quad k = 0, 1, \cdots, N-1 \tag{52.2}$$

which only differs in the eigenvalues of the topology matrix $G : \{\gamma_k, k = 0, 1, \cdots, N-1\}$. The synchronous state linked to $\gamma_0 = 0$ is stable if the remaining $(N-1)$ blocks, associated with the graph eigenmodes transverse to the synchronization manifold, have negative Lyapunov exponents [2].

Generally, we consider the system

$$\dot{\boldsymbol{\eta}} = [D\mathbf{F} + \alpha D\mathbf{H}]\boldsymbol{\eta} \tag{52.3}$$

The largest Lyapunov exponent $\lambda_{\max}$ of network (3), which is a function of α for given functions $\mathbf{F}$ and $\mathbf{H}$, is referred to as the master stability function. The region S for negative α, where $\lambda_{\max}$ is also negative, is called the synchronized region of network (1). For network (2), we obtain the generic requirement $\sigma\gamma_k \in S$ for the synchronous state to be linearly stable. Hence, given coupling matrix G in network (1), we can tune the coupling strength σ to locate the products $\sigma\gamma_k$ within the synchronization region S.

The coupled HR neuronal network is expressed as follows:

$$\begin{aligned}
\dot{x}_i &= y_i - ax_i^3 + bx_i^2 - z_i + I + \sigma \sum_{j=1}^{N} g_{ij}x_j, \\
\dot{y}_i &= c - dx_i^2 - y_i, \\
\dot{z}_i &= r[s(x_i + \chi) - z_i]. \quad i = 1, 2, \cdots, N
\end{aligned} \tag{52.4}$$

where parameters are chosen as $a = 1, b = 3, c = 1, d = 5, s = 4, r = 0.006, \chi = 1.6, I = 3$ to exhibit chaotic dynamics. The master stability function of coupled chaotic HR neurons is shown in Fig. 52.1. It can be seen that the synchronization region of coupled chaotic HR neurons is $\alpha > \alpha_1$, where $\alpha_1 \approx -0.85$. That is, whatever the network topology is, when all of the products $\sigma\gamma_k > \alpha_1 (k = 1, \cdots, N-1)$, synchronization will happen.

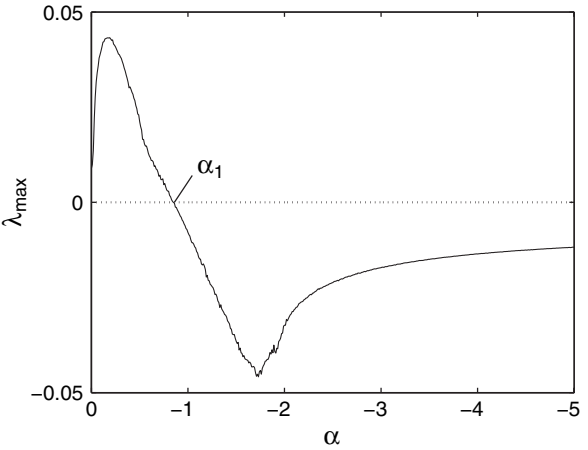

Fig. 52.1 The master stability function of coupled chaotic HR neurons

To obtain the small-world network structure, we use the rewiring procedure of Watts and Strogatz. The networks have the neurons number $N = 500$ and a mean connectivity $C = 5$ per neuron. Since coupling matrix G is a real symmetric and irreducible matrix, we have the eigenvalues for small world networks $0 = \gamma_0 > \gamma_1 \geq \cdots \geq \gamma_{N-1}$.

By the principle of $\sigma\gamma_k \in S$, the critical coupling strength for synchronization of the chaotic HR neuronal network with small-world structure can be deduced.As the synchronization region is half bounded, the synchronization condition will be satisfied only if $\sigma\gamma_1 > \alpha_1$. Namely, the critical synchronization coupling strength is $\sigma_c = \frac{\alpha_1}{\gamma_1}$. Numerical values of σ_c as function of p is shown in Fig. 52.2.

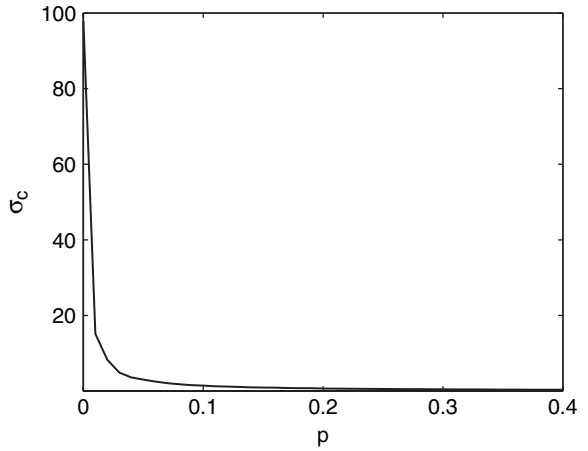

Fig. 52.2 The critical synchronization coupling strength σ_c versus p

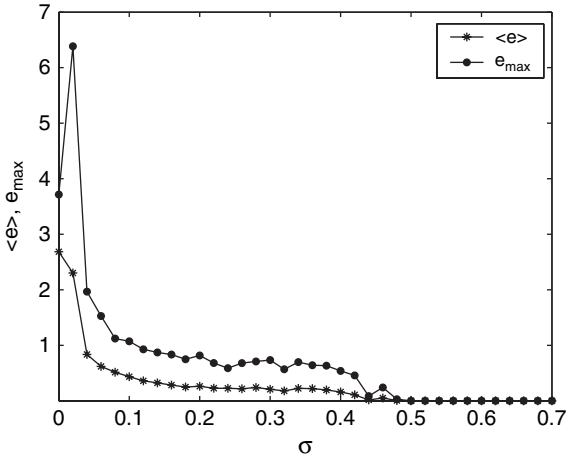

Fig. 52.3 The synchronization error $\langle e\rangle$ and e_{max} versus coupling strength σ

It can be seen that the synchronization coupling strength is considerably large for the regular network ($p = 0$), so it is really difficult to synchronize for regular network. However, σ_c drops suddenly as p increases. Namely, the introduction of short-cuts in regular network will greatly benefit synchronization.

Simulation is performed in a chaotic neuronal network. For any given small-world structure (such as when $p = 0.3$), the eigenvalues of the network can be calculated (here is a case $\gamma_1 = -1.8057$) and the coupling strength for synchronization can be deduced ($\sigma_c \approx 0.47$). The dynamical behavior of the network under different coupling strength is simulated. The average synchronization error $\langle e\rangle$ and the maximum synchronization error $e_{\max}$ are used as the characteristic measures with the definitions given as follows [3]: $\langle e\rangle = \frac{1}{N-1}(\sum_{i=2}^{N}\langle e_i\rangle)$, where $e_i = \sqrt{(x_i - x_1)^2 + (y_i - y_1)^2 + (z_i - z_1)^2}$, $(i = 2, 3, \cdots, N)$ and $\langle\cdot\rangle$ denote the average with respect to time, $e_{\max} = \max(e_i)$. Simulation result is shown in Fig. 52.3. Obviously, $\langle e\rangle$ and $e_{\max}$ become both zeros when $\sigma > 0.48$, which accords with the anticipation ($\sigma_c \approx 0.47$). Hence, it can make a chaotic small-world neuronal network synchronize to set the coupling strength properly.

This paper proposes a general method for determining synchronization condition of neuronal networks. It also shows that setting the coupling strength properly can make small-world neuronal networks synchronize.

Acknowledgments This work was supported by the National Natural Science Foundation of China (No.10432010).

References

1. Fink K.S., Johnson G., Carroll T., Mar D., Pecora L. Three coupled oscillators as a universal probe of synchronization stability in coupled oscillator arrays. Phys. Rev. E 61 (2000) 5080–5090.

2. Barahona M., Pecora L.M. Synchronization in small-world systems. Phys. Rev. Lett. 89 (2002) 054101.
3. Wang H.X., Lu Q.S., Wang Q.Y. Complete synchronization in coupled chaotic HR neurons with symmetric coupling schemes. Chin. Phys. Lett. 22 (2005) 2173–2175.

Chapter 53
Effects of Time Delay on Synchronization and Temporal Order in a Square Lattice Noisy Neuronal Network

Qing-Yun Wang, Zhi-Sheng Duan and Qi-Shao Lu

Abstract Synchronization and temporal order characterized by the rate of firing are studied in a spatially extended map neuron network with coupling time delay. It is shown that there exist an intermediate noise level, where synchronization and temporal order are maximum irrespectively of the coupling time delay. Furthermore, it is found that temporal order is weakened when the coupling time delay appears. However, the coupling time delay has two-fold effects on synchronization, one associated with its increasing, the other with its decreasing. This clearly manifests that random perturbations and time delay play a complementary role in synchronization and temporal order.

Introduction

Traditionally, it is considered that random noise is a nuisance because it can destroy signal detection and transduction. However, the effects of noise on nonlinear dynamical systems are very complicated and often counter-intuitive. The ability of noise to induce temporal order (that is, temporal periodic behaviour) in nonlinear systems is a well-known fact. It is well known that, for instance, random fluctuations enhance the response to weak periodic driving, as observed in many different physical, chemical and biological scenarios [1, 2, 3]. This is called stochastic resonance (SR). For a more intriguing perspective, stochastic resonance without external periodic forces, where noise extracts a hidden intrinsic time scale of the system dynamics, has been found and termed as coherence resonance (CR) (or autonomous stochastic resonance (ASR)) [4, 5, 6]. This phenomenon has been predicted theoretically in a wide variety of models, and observed experimentally in fields as diverse as physical, neuroscience and chemical systems. There are still many other examples demonstrating that noise can lead to more order in dynamics [7].

Q.-Y. Wang
State Key Laboratory for Turbulence and Complex Systems, Department of Mechanics and Aerospace Engineering, College of Engineering, Peking University, Beijing 100871, China
e-mail: nmqingyun@163.com

R. Wang et al. (eds.), *Advances in Cognitive Neurodynamics*,

It is commonly accepted that a single neuron in the vertebrate cortex connects to more than 10,000 postsynaptic neurons via synapses–forming complex networks. Meanwhile, since neurons are known to be noisy analogue units, noisy neurons coupled via synapses can carry out highly complex and advanced operations with cognition and reliability. As far as these perspectives are concerned, it is evident that neural tissue combines features of being both a noisy and a spatially extended structure. Hence, the effect of noise on neural networks should be studied extensively so as to get better insight into complex collective rhythm and cooperative operation of neuronal firings.

Time delays are inherent in neuronal transmissions. It is well known that human brain is the most complex system, which is composed of millions of neurons. The information flow in coupled systems is not generally instantaneous, because of both infinite propagation velocities in the conduction of signals along neurites and the delays in the synaptic transmission at chemical synapses. For experimental relevance, it has testified that the speed of signal conduction through unmyelinated axonal fibers is on the order of 1 m/s resulting in time delays up to 80 ms for propagation through cortical network. Therefore, it is important to understand how delays affect the nonlinear characteristics of the neuron systems.

It is interesting to know whether synchronization and temporal order exist in spatially extended neuronal systems with the coupling time delay, and how they depend on the noise and coupling time delay. For this goal we use a discrete-time Rulkov map neuron with time delay to construct a spatially extended network system, which is arranged in a $N \times N$ square grid. Each grid element is defined by the discrete map neuron and is diffusively coupled to its neighbours. The results in the present study show that synchronization and temporal order can exist in noisy neuronal network with the coupling delay. Moreover, there exists an optimal noise level, where synchronization and temporal order are maximum. Hopefully, our work outlines some possibilities for future experimental work in the field of neural networks in which time delay and noise exist spatially in general.

Map Neuron Model in a Square Lattice

We consider an ensemble of identical two dimensional Rulkov map neurons [8], coupled diffusively with its nearest neighbours and arranged in a square lattice of size $N \times N$. This coupling implies the interaction of electrical synapses among neurons. The spatial-temporal evolution of this lattice network is governed by

$$\begin{aligned} x^{(i,j)}(n+1) &= \alpha f(x^{(i,j)}(n)) + y^{(i,j)}(n) + \sigma \xi^{(i,j)}(n) \\ &\quad - D(4x^{(i,j)}(n) - x^{(i+1,j)}(n-\tau) - x^{(i-1,j)}(n-\tau) \\ &\quad - x^{(i,j+1)}(n-\tau) - x^{(i,j-1)}(n-\tau)) + A\sin(2\pi\omega n) \\ y^{(i,j)}(n+1) &= y^{(i,j)}(n) - \beta x^{(i,j)}(n) - \gamma, \quad i,j = 1,2,\ldots,N \end{aligned} \tag{53.1}$$

where $x^{(i,j)}(n)$ is the membrane potential of the neuron labelled (i, j), $y^{(i,j)}(n)$ is the variation of ion concentration, and they represent the fast and slow dynamics, respectively. The slow evolution of $y^{(i,j)}(n)$ is due to the small values of the positive parameters β and γ, say, $\beta = \gamma = 0.001$ in this paper. n is the discrete time index, while α is a model control parameter. $f(x) = \frac{1}{1+x^2}$ is a nonlinear function, σ denotes the level of noise and $\xi^{(i,j)}$ the Gaussian white noise for the (i, j)th space neuron. D is the diffusive coefficient. A and ω are the amplitude and frequency of external stimulus, respectively. In what follows, the periodic boundary condition of the coupling is used.

In order to capture the essence of neuronal resonant dynamics quantitatively, the rate of firing is defined as follows. For a rough illustration, we call a Rulkov map neuron firing when the membrane potential x reaches its threshold value $x_{th} = -0.2$ from below at certain time. Suppose that m neurons fire at given discrete time n, then we define a function $\Pi(n) = \frac{m}{N^2}$. This statistical function can simply measure the proportion of firing neurons in the square lattice neuronal network and is called as the rate of firing of this network.

To quantitatively investigate the synchronization and temporal order, we introduce the following two important quantities. One is the average of the rate of firing Π, which can show the number of the fired neurons at given time. We call it the synchronization index and denote as $Syn_{index} = \langle \Pi \rangle$. It is obvious that the larger is Syn_{index}, the more neurons can synchronize at given time. The other is the characteristic correlation time, which is characterized by an autocorrelation function as $\tau = 1/T \int_T c^2(t)dt$. The autocorrelation function of the rate of firing is defined as $c(\tau) = \langle \Pi(t)\Pi(t + \tau) \rangle$, where Π is the rate of firing, τ the time delay, and $\langle \cdot \rangle$ denotes the average over time. It is well known that the more ordered this neuronal network is for time, the longer is its characteristic correlation time. Therefore, it is called the order index and can be used to measure the degree of temporal order for this neuronal network.

As illustrated in Fig. 53.1a, when the noise level $\sigma = 0.003$, synchronization index reaches a maximum irrespectively of whether it is no delay or delay. Hence, there exist an optimal noise level, at which, synchronization of this square neuronal network is maximal. Furthermore, it is found that synchronization is decreased with the noise being beyond the optimal level when the coupling delay appears. On the contrary, if the noise is slightly below the optimal value, the coupling delay can enhance synchronization of neural networks. Hence, the coupling delay can exhibit two-fold effects on synchronization. At the same time, order index is shown in Fig. 53.1b as the noise level increases for different delays. We also find that there is an optimal noise level, where the order index achieves a maximal value irrespectively of whether there is delay or not, and with the time delay appearing, order can be weakened. More importantly, it is found that there is an equally optimal noise level, at which the maximum of temporal order and synchronization is achieved simultaneously. Hence, temporal order is in good agreement with synchronization in the present system studied.

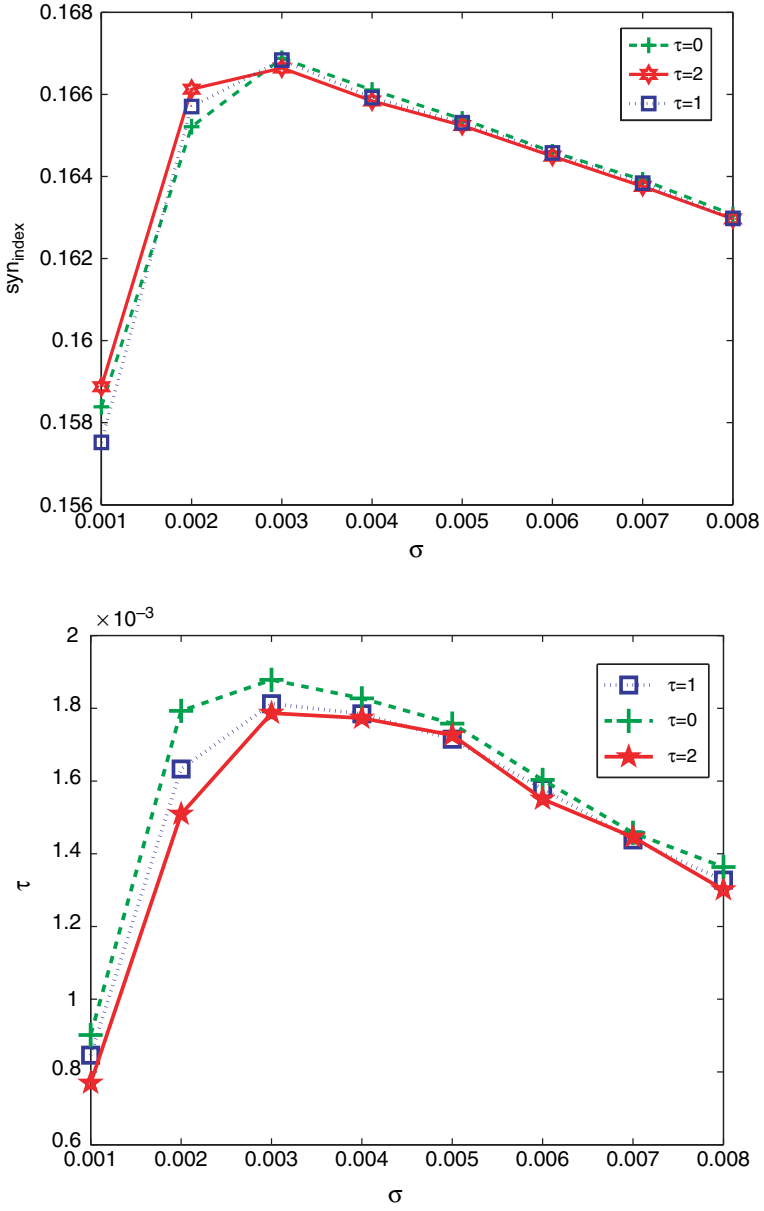

Fig. 53.1 (a) Synchronization index with respect to the noise for different delays. (b) Order index with respect to the noise for different delays

Conclusion

Our results showed that spatial extended discrete neuron models with the coupling delay could exhibit the like-resonance phenomena of temporal order and synchronization at the optimal noise level. Furthermore, it was shown that there are nontrivial effects of time delay on synchronization and temporal order. Consequently, the results in this Letter have potential meanings for understanding the synchronization, and we will adopt more real biological neuron models for further study.

Acknowledgments This work was supported by the National Natural Science Foundation of China (Nos. 10702023 and 60674093) and Postdoctoral Foundation of China (No. 20070410022).

References

1. Gammaitoni L., Hanggi P., Jung P., Marchesoni F.: Stochastic resonance. Rev. Mod. Phys. 70 (1998) 223–287.
2. Ray F., Sengupta S.: Stochastic resonance in underdamped, bistable systems. Phys. Lett. A 353 (2006) 364–371.
3. Neiman A., Sung W.: Memory effects on stochastic resonance. Phys. Lett. A 223 (1996) 341–347.
4. Hu G.: Stochastic resonance without external periodic force. Phys. Rev. Lett. 71 (1993) 807–810.
5. Longtin A.: Autonomous stochastic resonance in bursting neurons. Phys. Rev. E 55 (1997) 868–877.
6. Pikovsky A.S., Kurths J.: Coherence resonance in a noise-driven excitable system. Phys. Rev. E 78 (1997) 775–778.
7. Zhu L.Q., Lai Y.C., Liu Z.H., Raghu A.: Can noise make nonbursting chaotic systems more regular? Phys. Rev. E 66 (2002) 015204.
8. Jiang Y.: Multiple dynamical resonances in a discrete neuronal model. Phys. Rev. E 71 (2005) 057103.

Chapter 54
The Attractor Type of Complex Networks

Tan Ning, Huang Jing, Zhang Wei and Yang Fenghong

Abstract In this paper, the bistable differential system is introduced to each unit of a complex network, the affections of network topology fabrics on the attractor type of the network are studied numerically. It is found that the tendency probability to fixed point is decreasing according to the average connectivity but the tendency probability to periodic attractor is increasing simultaneously. The probability rewiring each edge at random has little influence on the aforementioned phenomenon.

Keywords Complex network · small world · attractor · dynamics

Introduction

Complex network has been a hotspot in study of abroad fields and achieves many meaningful results in mathematics, physics, biology, communication, economics and sociology. In fact any complex system in nature can be modeled as a network, where vertices are the elements of the system and edges represent the interactions between them. The study and characterization of the statistical properties of complex networks has received much attention in the last few years. It is shown by Barabási, Newman, Watts and many other researchers that a great variety of real networks exhibit a small world property and scale-free character [1, 2]. However, network dynamics study is equally important. One can define a network by characteristics of topology then introduce dynamical elements into it to probe its global dynamical behaviors.

Theoretical and experimental studies suggest that the ordered (stable) dynamics exhibited by complex networks may represent a distinct phenotype and function. One famous result is Kauffman's study on random networks under Boolean law rule [3, 4]. Kauffman has made three simplifying assumptions in his study, but it is well known that real networks exhibit more abundant property. Analysis on the

Z. Wei
College of Mechanical Engineering, Beijing University of Technology, Beijing 100022, China
e-mail: sandyzhang0@yahoo.com

R. Wang et al. (eds.), *Advances in Cognitive Neurodynamics*,

dynamical convergence of complex networks and uncovering which main factors determining the dynamical convergence is still in continual investigation.

In this paper, the relation between network topology and attractor type is numerically studied. The bistable differential system is introduced to each unit of a network. The network topology is considered as small world network, WS model. It is found that the tendency probability to fixed point is decreasing according to the average connectivity K but the tendency probability to periodic attractor is increasing simultaneously. The probability rewiring each edge at random, p, has little influence on the aforementioned phenomenon.

Dynamical Model

In many natural networks, their unit exhibits bistable probability. For example, the excitation of each neuron in neuron networks can be roughly described as rest state and spiking state. Therefore, the bistable differential system is introduced to each unit of networks in this study.

Consider a dynamical network consisting of N identical units. The dynamical control equation accorded to each unit is $\dot{x} = ax - bx^3$, where x is the state variable. If $a,\ b > 0$, there are two stable equilibrium points, $\pm\sqrt{\frac{a}{b}}$, and one unstable equilibrium point, 0.

The connection matrix $\mathrm{A} = (a_{ij}) \in R^{N\times N}$ is used to describe the topology of a N-dimensional network, where the element a_{ij} denotes the action of unit j on unit i. Although the detailed form of actions is not clear, the effect of actions can be grouped into two aspects, namely, active or inactive. To simplify the analysis, let $a_{ij} = 1$ denote the active effect and $a_{ij} = -1$ denote the inactive effect in the following.

To a N-dimensional dynamical system, the governing equations are:

$$\dot{x}_i = ax_i - bx_i^3 + \sum_{j=1}^{N} a_{ij}x_j \quad i = 1, 2, \cdots, N \tag{54.1}$$

Thus the vector $X(t) = [x_1(t), x_2(t), \ldots, x_N(t)]^{\mathrm{T}} \in R^N$ can describe the state of the network at time t.

Network Topology

It is reported that the connection topology of biology networks, like the circuitry in the cortex and genetic regulation networks, is neither completely regular nor completely random, showing small world property [5, 6, 7]. They are highly clustered like regular lattices, yet have small characteristic path lengths like random networks. So we attribute small world property to networks.

The model we use is called as Watts-Strogatz model (**WS** model) [1]. We generate a regular network as nearest-neighbor couplings with N vertices and KN

edges, where K is the average value of connections per node. Then rewiring each edge randomly with a probability p, the regular lattice can be turned to a random network in a continuous way as $p = 1$. When $0 < p < 1$, we can get networks with small world property.

Applied the aforementioned method, an undirected small world network can be obtained. Then we can attribute the regulation effect and direction randomly to each edge. Here let 1 denote the active effect and -1 denote the inactive effect.

Results

Enough interconnected networks are sampled. Then we will study the dynamical steady state of each network leaving from the same initial state point. The network steady state has three types, an equilibrium point, a periodic orbit, a chaotic attractor (nonperiodic orbit).

Let M be the total number of gathered network, M_e be the number of networks with an equilibrium steady state, M_p be the number of networks with a periodic steady state, and M_c be the number of networks with a chaotic steady state. Define $p_i = \frac{M_i}{M}$ $i = e, p, c$ as the steady state tendency probability to each attractor type i.

Fix p But Change K

From Fig. 54.1, it is shown that networks' steady state is apt to ordered attractor. The tendency probability to chaotic attractor is too small that we omit it in figures. But the steady state tendency gradually transfers from equilibrium point to periodic orbit, along with increasing K.

Fix a and b But Change p

From Fig. 54.2, it is shown that the probability rewiring each edge at random, p, has little influence on the aforementioned phenomenon.

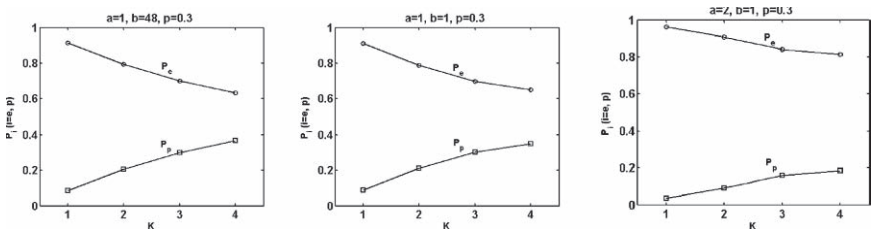

Fig. 54.1 The steady state tendency gradually transfers from equilibrium point to periodic orbit, along with increasing K, where $p = 0.3$

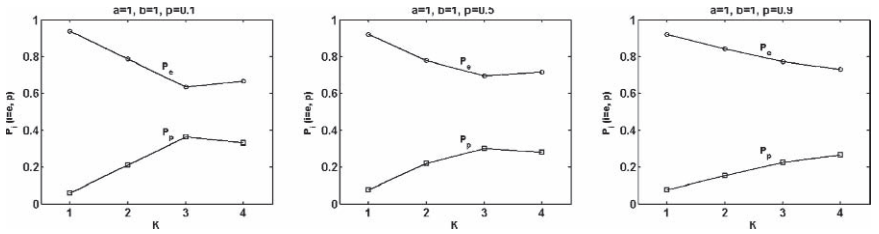

Fig. 54.2 The probability rewiring each edge at random, p, has little influence on the aforementioned phenomenon shown in Fig. 54.1

Conclusion

In this paper, the relation between network topology and attractor type is numerically studied. The bistable differential system is introduced to each unit of a small world network. It is found that the tendency probability to fixed point is decreasing according to the average connectivity K but the tendency probability to periodic attractor is increasing simultaneously. However, the probability rewiring each edge at random, p, has little influence on the aforementioned phenomenon.

The dynamics attractor exhibited by complex networks may represent a distinct cellular phenotype and function [5, 6, 7]. Distinct phenotypic states of cells in multicellular organisms and the switch transitions between the cell fates are all rest with the types of attractor and dynamical bifurcations. If the architecture of a functional network is mutative because of some diseases, the phenotypic states of the network will change. The normal function can not be carried out. Our work may be helpful to understand the function and structure of biological system.

Acknowledgments The authors gratefully acknowledge the support of the National Science Foundation for Distinguished Young Scholars of China (No.10425209), the National Natural Science Foundation of China (Nos. 10602003, 10372008, 10328204) and the Natural Science Foundation of Beijing (No. 3032006).

References

1. Watt D.J., Strongatz S.H.: Collective dynamics of 'small-world' network. Nature 393 (1998) 440–442.
2. Barabási A.L., Albert R.: Emergence of scaling in random networks. Science 286 (1999) 509–512.
3. Kauffman S.A.: Antichaos and adaptation. Sci. Am 265 (1991) 78–84.
4. Kauffman S. A.: Origin of Order. Oxford University Press, Oxford (1993).
5. Huang S., Eichler G., Bar-Yam Y., Ingber D.E.: Cell fates as high-dimensional attractor states of a complex gene regulatory network. Phy. Rev. Lett. 94 (2005) 128701: 1–4.
6. González-Burgos G., Barrionuevo G., and Lewis D.A.: Horizontal synaptic connections in monkey prefrontal cortex: an *in vivo* electrophysiological study. Cereb. Cortex 10 (2000) 82–92.
7. Roxin A., Riecke H. and Solla S.A.: Self-sustained activity in a small-world network of excitable neurons. Phy. Rev. Lett. 92 (2004) 198101: 1–4.

Chapter 55
Asymptotical Stability of Delayed BAM Neural Networks with Generalized Activation Functions by Comparison Approaches

Yuguo Chen and Wudai Liao

Abstract Asymptotical stability of delayed bi-directional associative memory (BAM) neural networks with generalized activation functions is studied. Essentially speaking, BAM neural networks can be viewed as a linear system perturbed by the outer input. Under this point of view, by adopting the variation of coefficient of liner differential equations and comparison approaches, some delay-independent stability algebraic criteria are obtained. The results obtained in this paper need only to compute the norm of some matrices constructed by the parameters of the neural networks which are very convenient to verify in system synthesis.

Introduction

The stability problem of BAM neural networks with Sigmoid output functions has been widely studied [1, 2, 3, 4, 5], and for the delayed BAM neural networks, there also have lots of results [6, 7], and the results obtained in these papers were mainly used the Lyapunov direct method and the Razumikhin-type theorems.

In engineering applications, we sometimes select the generalized activation function (not always the sigmoid types) to be the output function of BAM neural networks. And from the point of research approaches, we can treat BAM neural networks as a linear system perturbed by the outer input [8]. Based on this point, we introduce the variation of coefficient of differential equations, instead of Lyapunov direct method, to study the stability problem of the delayed BAM neural networks.

Y. Chen
School of Electrical and Information Engineering, Zhongyuan University of Technology, 450007, Zhengzhou, Henan, China
e-mail: cygzzti@163.com

R. Wang et al. (eds.), *Advances in Cognitive Neurodynamics*,

Delayed BAM neural network's equations are as following:

$$\begin{aligned}
&\dot{x}_i(t) = -c_i x_i(t) + \sum_{j=1}^{n} a_{ij} g_j\left(y_j\left(t-\tau_{yj}\right)\right), \quad t \geq 0, \ \ i = 1, 2, \cdots, m,\\
&\dot{y}_j(t) = -d_j y_j(t) + \sum_{i=1}^{m} b_{ji} f_i\left(x_i\left(t-\tau_{xi}\right)\right), \quad t \geq 0, \ \ j = 1, 2, \cdots, n,\\
&x_i(t) = \phi_{xi}(t) \in C\big([-\tau, 0]; \mathbb{R}\big), \quad y_j(t) = \phi_{yj}(t) \in C\big([-\tau, 0]; \mathbb{R}\big). \qquad (55.1)
\end{aligned}$$

Where, $c_i > 0,\ d_j > 0$ are constants, a_{ij} is the connected weight from neuron y_j to neuron x_i, and b_{ji} is the connected weight from neuron x_i to neuron y_j, $\tau_{yj},\ \tau_{xi}$ are time delays of neuron y_j and neuron x_i separately, $\tau = \max\{\tau_{xi},\ \tau_{yj}\}$. $f_i(\cdot), g_j(\cdot)$ are the activation functions of neuron x_i and neuron y_j separately and there exist constants $\alpha_i > 0, \beta_j > 0$ such that the conditions

$$f_i(0) = g_j(0) = 0, \quad |f_i(u)| \leq \alpha_i |u|, \quad |g_j(u)| \leq \beta_j |u| \qquad (55.2)$$

hold for $i = 1, 2, \cdots, m,\ j = 1, 2, \cdots, n$.

In the following, we will give some preliminaries [9, 10, 11], including the stability criteria of linear differential difference equations and some properties of eigenvalues of a matrix.

Definition 1. *A real matrix $A = (a_{ij})_{n\times n}$ is called an M-matrix, if*

1) $a_{ii} > 0$, $i = 1, 2, \cdots, n$, $a_{ij} \leq 0$, $i \neq j$, $i, j = 1, 2, \cdots, n$;
2) The determinants

$$\begin{vmatrix} a_{11} \cdots a_{1i} \\ \cdots\cdots\cdots \\ a_{i1} \cdots a_{ii} \end{vmatrix} > 0, \quad i = 1, 2, \cdots, n.$$

Lemma 1. *For a matrix $A = (a_{ij})_{n\times n}$, assume that $a_{ii} > 0$, $i = 1, 2, \cdots, n$, $a_{ij} \leq 0$, $i \neq j$, $i, j = 1, 2, \cdots, n$. The matrix A is an M-matrix if and only if one of the following conditions holds.*

1) There exist positive constants c_j, $j = 1, 2, \cdots, n$, such that

$$\sum_{j=1}^{n} a_{ij} c_j > 0, \quad i = 1, 2, \cdots, n.$$

2) $-A$ is a stable matrix, that is, all eigenvalues of the matrix $-A$ have negative real parts.

Now, we consider the following linear differential difference equation

$$\dot{x}(t) = Ax(t) + Bx(t-\tau)) \qquad (55.3)$$

where $x \in \mathbb{R}^n$, $A, B \in \mathbb{R}^{n\times n}$, $x(t-\tau) = (x_1(t-\tau_1), \cdots, x_n(t-\tau_n))^T$, $0 \le \tau_i \le \tau$, $i = 1, 2, \cdots, n$ are constant delays.

The characteristic polynomial of Eq. (55.3) is defined as following:

$$h(\lambda, \tau) = \det\Big(\lambda E - A - B \cdot \operatorname{diag}\big(e^{-\lambda\tau_1}, e^{-\lambda\tau_2}, \cdots, e^{-\lambda\tau_n}\big)\Big) \tag{55.4}$$

where E denotes $n \times n$ unit matrix.

Lemma 2. *The equilibrium $x = 0$ of System (3) is delay-independent asymptotic stability if and only if*

1) $A + B$ is a stable matrix, that is, each eigenvalue λ of character equation

$$h(\lambda, 0) = 0$$

has negative real part;

2) For any $\omega \in \mathbb{R}$ and any $\tau \ge 0$, $h(j\omega, \tau) \ne 0$, j is the imaginary unit.

Main Results

Integrate the first m equations in System (1) by using the method of variation of coefficient, we have

$$x_i(t) = e^{-c_i t}x_i(0) + \int_0^t e^{-c_i(t-s)} \sum_{j=1}^{n} a_{ij} g_j\Big(y_j\big(s-\tau_{yj}\big)\Big)\mathrm{d}s, \quad t \ge 0,$$

and by using the properties of the activation functions (2), we have

$$|x_i(t)| \le e^{-c_i t}|x_i(0)| + \int_0^t e^{-c_i(t-s)} \sum_{j=1}^{n} |a_{ij}| \cdot \beta_j \cdot |y_j(s-\tau_{yj})|\mathrm{d}s := z_i(t).$$

Similarly, we have

$$|y_j(t)| \le e^{-d_j t}|y_j(0)| + \int_0^t e^{-d_j(t-s)} \sum_{i=1}^{m} |b_{ji}| \cdot \alpha_i \cdot |x_i(s-\tau_{xi})|\mathrm{d}s := u_j(t).$$

Differentiate both sides of equations above:

$$\begin{aligned} \dot{z}_i(t) &\le -c_i z_i(t) + \sum_{j=1}^{n} |a_{ij}|\beta_j|u_j(t-\tau_{yj})|, \quad t \ge 0, \ \ i = 1, 2, \cdots, m \\ \dot{u}_j(t) &\le -d_j u_j(t) + \sum_{i=1}^{m} |b_{ji}|\alpha_i|z_i(t-\tau_{xi})|, \quad t \ge 0, \ \ j = 1, 2, \cdots, n. \end{aligned} \tag{55.5}$$

We have the result: System (5) asymptotically stable $\Rightarrow$ System (1) asymptotically stable. The characteristic polynomial of System (5) is $h(\lambda,\ \tau) = \det(G)$,

$$G(\lambda, \tau) = \lambda E - \begin{pmatrix} -C & A\mathrm{diag}(e^{-\lambda\tau_{y1}}, \cdots, e^{-\lambda\tau_{yn}}) \\ B\mathrm{diag}(e^{-\lambda\tau_{x1}}, \cdots, e^{-\lambda\tau_{xm}}) & -D \end{pmatrix},$$

where, $C = diag(c_1, c_2, \cdots, c_m)$, $D = diag(d_1, d_2, \cdots, d_n)$, $A = (|a_{ij}|\beta_j)_{m\times n}$, $B = (|b_{ji}|\alpha_i)_{n\times m}$, $E = E_{m+n}$ is $(m+n)$-dimension unit matrix.

Theorem 1. *If the matrix M is an M-matrix, then the trivial equilibrium $x_i = y_j = 0$ of delayed BAM neural network (1) is globally asymptotically stable, where*

$$M = \begin{pmatrix} C & -A \\ -B & D \end{pmatrix}.$$

Proof. Because M ia an M-matrix, by Lemma 1, $-M$ is a stable matrix, this implies that all eigenvalues of $h(\lambda, 0) = \det(\lambda E + M)$ are all negative real parts;

Again, use Lemma 1, there exist positive constants $k_1, \cdots, k_m,\ k_{m+1}, \cdots, k_{m+n}$, such that

$$k_i c_i > \sum_{j=1}^{n} k_{m+j}|a_{ij}|\beta_j, \quad i = 1, 2, \cdots, m,$$

$$k_{m+j} d_j > \sum_{i=1}^{m} k_i |b_{ji}|\alpha_i, \quad j = 1, 2, \cdots, n.$$

Denote $K = \mathrm{diag}(K_1, K_2)$, $K_1 = \mathrm{diag}(k_1, \cdots, k_m)$, $K_2 = \mathrm{diag}(k_{m+1}, \cdots, k_{m+n})$, consider

$$G(j\omega, \tau)K = \begin{pmatrix} (j\omega E_m + C)K_1 & A\mathrm{diag}(e^{-\lambda\tau_{y1}}, \cdots, e^{-\lambda\tau_{yn}})K_2 \\ B\mathrm{diag}(e^{-\lambda\tau_{x1}}, \cdots, e^{-\lambda\tau_{xm}})K_1 & (j\omega E_n + D)K_2 \end{pmatrix}$$

Notice that for any $\omega \in \mathbb{R}$, $\tau \geq 0$,

$$|(j\omega + c_i)k_i| \geq k_i c_i > \sum_{j=1}^{n} k_{m+j}|a_{ij}|\beta_j = \sum_{j=1}^{n} k_{m+j}|a_{ij}||e^{-j\omega\tau_{yj}}|\beta_j,$$

$$i = 1, 2, \cdots, m,$$

$$|(j\omega + d_j)k_{m+j}| \geq k_{m+j} d_j > \sum_{i=1}^{m} k_i |b_{ji}|\alpha_i = \sum_{i=1}^{m} k_i |b_{ji}||e^{-j\omega\tau_{xi}}|\alpha_i,$$

$$j = 1, 2, \cdots, n,$$

We can know that the matrix $G(j\omega, \tau)K$ is diagonal-dominated, and so, it is non-singular, that is $\det(GK) = \det(G)\det(K) \neq 0$. From this, $h(j\omega, \tau) = \det(G) \neq 0$

for any $\omega \in \mathbb{R}$, $\tau \geq 0$. From Lemma 2, the desired result of this theorem is obtained. The proof is complete.

Acknowledgments This work was supported in part by the National Natural Science Foundation of China under grant No. 60474001 and Natural Science Foundation of Henan Province of China (0611054500).

References

1. Kosko, B.: Adaptive Bi-directional Associative Memories. Applied Optics, 26(23) (1987) 4847–4860.
2. Koskok, B.: Bi-directional Associative Memories. IEEE Transactions on Systems Man, and Cybernetics, 18 (1988) 49–59.
3. Liao, W., Liao, X.: Stability Analysis of Cellular Neural Networks. Control Theory and Applications, 20(1) (2003) 89–92.
4. Michel, A.N., Liu, D.: Qualitative Analysis and Synthesis of Recurrent Neural Networks, 1st ed. Marcel Dekker, Inc. New York (2002).
5. Cao, J.: Stability Analysis of Discrete Hopfield Bi-directional Associated Memory Neural Networks. Acta Automatica Sinica, 25(5) (1999) 606–612.
6. Liao, X., Wu, Z., Qin, Z.: Global Attraction Analysis of Delayed BAM Neural Networks. Computer Researches and Development, 37(7) (2000) 833–837.
7. Shen, Y., Jiang, M., Liao, X.: Global Exponential Stability of Cohen-Grossberg Neural Networks with Time-varying Delays and Continuously Distributed Delays. In: JunWang Xiaofeng, and Liao ZhangYi (Eds.): Advances in Neural Networks – ISNN 2005. LNCS 3496. Springer-Verlag, Berlin, Heidelberg (2005) 156–161.
8. Liao, X.: Studies on Mathematic Meaning of Physic Parameters in Hopfield Neural Networks. Science in China (Series E), 33(2) (2003) 127–136.
9. Liao, X.: Stability Theory and Applications on Power Systems. National Defence Industry Press, Beijing (2000).
10. Hale, J.: Theory of Functional Differential Equations. Springer-Verlag, New York (1977).
11. Qin, Y., Liu, Y., Wang, L.: Motion Stability of Dynamical Systems with Time-Delays. 2nd ed. Science Press, Beijing (1989).

Chapter 56
Chaotic Synchronization of Hindmarsh-Rose Neurons Coupled by Cubic Nonlinear Feedback

Xiaoling Fang and Hongjie Yu

Abstract The chaotic synchronization of two cubic nonlinear coupling Hindmarsh-Rose (HR) neurons is discussed. A nonlinear coupling feedback term with higher order form of membrane potential is studied, and adds it to different position of the HR equation. Numerical simulation shows when the cubic nonlinear coupling feedback term only added to the first differential equation, in a quite large region of coupling strength, the two neurons cannot achieve full synchronization. On this condition, if the square form of membrane potential added to the second differential equation, the two neurons can achieve full synchronization in special coupling strength region. The synchronization stability has been proved by the calculation of the maximum conditional Lyapunov exponent. This investigation proposes the harmony theory of complex neuron network to some extent and provides a theoretical foundation for next step of research.

Introduction

In present, chaos has been found from microcosmic neurons, neural network dynamics to macroscopical electroencephalography (EEG) and magnetoencephalograph (MEG) both in theory and experiment [1, 2, 3, 4, 5]. It's generally realized that synchronization of neuron's activities featured by chaotic synchronization is important for memory, calculation, motion control and diseases such as epilepsy. Moreover, it plays an important role in the realization of associative memory, image segmentation and binding. For the universality of neurons' synchronization, it's necessary to study the mechanism of chaotic synchronization for the coupling neurons using some typical neuron equations such as Fitzhugh-Nagumo neuron equation and Hindmarsh-Rose neuron equation.

Hindmarsh-Rose (HR) model was constructed from voltage clamp data to provide a simple description of the patterned activity seen in molluscan neurons. It is a

X. Fang
Institute of Mechanobiology and Medical Engineering, Shanghai Jiao Tong University, Shanghai 200240, China
e-mail: {Xiaoling Fang, fxlarlene}@126.com

R. Wang et al. (eds.), *Advances in Cognitive Neurodynamics*,

system with time-multiple scale, an important characterization of which is the irregular bursting chaos. The research shows that the communication in brain mainly by burst but not by single impulse or fire. Therefore, the HR model can be used in the simulation of the brain activity and investigate the chaotic synchronization.

In 1998, Pecora and Carroll [6] put forward the main stability equation of synchronization coupling system and solved the synchronization stability problem of many oscillators by random linear coupling, and then, a series of results about the chaotic synchronization of Hindmarsh-Rose neuron was obtained. Shuai and Durand [7] studied the phase synchronization of two coupling HR neurons. He and his co-workers [8] studied the dynamic behavior of coupling HR neuron in the event of weak coupling and found that the weak coupling between fast changing variables can drive the high-dimensional hyperchaos of coupled time-multiple scale system into periodic state with functional phase relation. In 2003, A method (SC method) based upon the stability criterion of linear systems for synchronizing chaotic systems was proposed by Yu and Liu [9], and was expanded in 2004 [10]. This method has been used to examine the stability of synchronous state of all-to-all coupling [11] and star coupling [12] in HR neural networks. However, in almost all the research, the linear coupling between neurons is considered only by far. For the nonlinear coupling, that is, coupling with membrane voltage square and higher order, only few papers [11, 12, 13] deal with it. Nonlinear coupling, include high order nonlinear coupling, is an important coupling form in real systems. In the mean time, coupling feedback is only applied to the right side of the first differential equation in the current study. The effect on system synchronization by applying coupling feedback to the second differential equation isn't considered and even it is thought as noneffective to system motion [14]. Therefore, it is creative to study the effect on the system's chaotic synchronization by applying higher order coupling feedback to the second differential equation.

In this paper, we construct a cubic nonlinear coupling Hindmarsh-Rose (HR) neural network, and add the square form of membrane potential to the second differential equation, by changing the coupling strength, the chaotic synchronization was achieved. The stability of chaos has been proved by the calculation of the maximum conditional Lyapunov exponent.

Chaotic Synchronization of Two Cubic Nonlinear Coupling Feedback Hindmarsh-Rose Neurons

In paper [11] and [12], Yu described Hindmarsh-Rose neuron model in detailed. Now we considering a network of two HR neurons connected by nonlinear coupling feedback term $({x_i}^3 - {x_j}^3)$, and add it to the right hand of the first differential equation:

$$\begin{cases} \dot{x}_1 = y_1 - a{x_1}^3 + b{x_1}^2 + I_{ext} - z_1 + \alpha({x_1}^3 - {x_2}^3) \\ \dot{y}_1 = c - dx_1^2 - y_1 \\ \dot{z}_1 = r(S(x_1 - \bar{x}) - z_1) \end{cases} \tag{56.1}$$

$$\begin{cases} \dot{x}_2 = y_2 - a{x_2}^3 + b{x_2}^2 + I_{ext} - z_2 + \alpha({x_2}^3 - {x_1}^3) \\ \dot{y}_2 = c - dx_2^2 - y_2 \\ \dot{z}_2 = r(S(x_2 - \bar{x}) - z_2) \end{cases} \tag{56.2}$$

Assume that the initial condition is $x_1(0) = 0.3,\ y_1(0) = 0.3,\ z_1(0) = 3.0,\ x_2(0) = 0.2,\ y_2(0) = 0.35,\ z_2(0) = 3.2$, and other parameters are the same as before. Numerical simulation shows when in a quite large region of coupling strength, $\alpha \in [0.0001, 0.5]$, the system has not achieve any synchronization.

In HR neuron equation, recovery variable y is influenced by the outward flow of potassium ions immediately after the discharge of the action potential [15], The potassium ion currents slower the returning of membrane potential to the threshold value and the frequency of repeating discharge, and allow a delay between excitable simulate and action potential [16]. From the point view of neurophysiology, introducing the square form of membrane voltage between two neurons $({x_i}^2 - {x_j}^2)$ as coupling feedback into the flow of potassium ions, that is, exerting coupling feedback on the right side of the second differential equation, which means the change of potassium ion, and modulate the burst interval of HR neuron, so the chaotic synchronization of two neurons may be affected. The resulting differential equations of system motion are as follows:

$$\begin{cases} \dot{x}_1 = y_1 - a{x_1}^3 + b{x_1}^2 + I_{ext} - z_1 + \alpha({x_1}^3 - {x_2}^3) \\ \dot{y}_1 = c - dx_1^2 - y_1 + \beta({x_1}^2 - {x_2}^2) \\ \dot{z}_1 = r(S(x_1 - \bar{x}) - z_1) \end{cases} \tag{56.3}$$

$$\begin{cases} \dot{x}_2 = y_2 - a{x_2}^3 + b{x_2}^2 + I_{ext} - z_2 + \alpha({x_1}^3 - {x_2}^3) \\ \dot{y}_2 = c - dx_2^2 - y_2 + \beta({x_2}^2 - {x_1}^2) \\ \dot{z}_2 = r(S(x_2 - \bar{x}) - z_2) \end{cases} \tag{56.4}$$

Initial values and the other parameters are as mentioned above. Numerical simulations show that system can achieve complete synchronization as long as β reaches a certain region regardless of α. Figure 56.1 show that when $\alpha = 0.1,\ \beta = 1.1$, the burst time series, synchronization error and time interval of two HR neurons, apparently they are full synchronized.

Different α and β values to achieve complete chaotic synchronization are given in Table 56.1.

The evolutional equation of the difference e(t) is as follows:

$$\dot{e} = \begin{bmatrix} \dot{x}_1 - \dot{x}_2 \\ \dot{y}_1 - \dot{y}_2 \\ \dot{z}_1 - \dot{z}_2 \end{bmatrix} = \begin{bmatrix} \dot{e}_1 \\ \dot{e}_2 \\ \dot{e}_3 \end{bmatrix} = \begin{bmatrix} e_2 - e_3 - 3(a - 2\alpha){x_2}^2 e_1 + 2bx_2 e_1 \\ -e_2 + 2(2\beta - d)x_2 e_1 \\ rse_1 - re_3 \end{bmatrix} \tag{56.5}$$

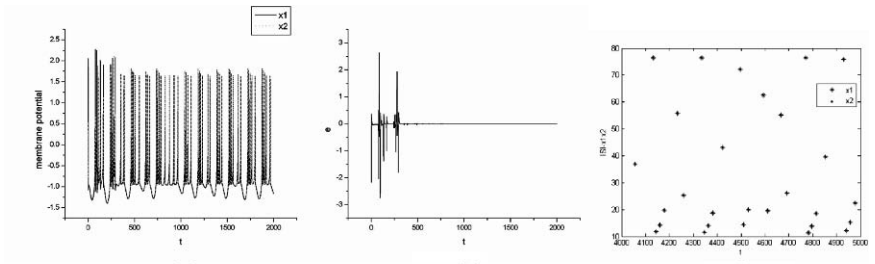

(a) (b) (c)

Fig. 56.1 The burst time series (a), synchronization error (b) and time interval (c), when $\alpha = 0.1, \beta = 1.1$

Table 56.1 The system achieved full synchronization with different α and β

α	0.1	0.01
β	[1.0, 1.9]	[0.8, 3.0]

So calculate the maximum conditional Lyapunov exponent, we find that the maximum conditional Lyapunov exponents are all negative when coupling strength are shown as Table 56.1, see Fig. 56.2., which means that the synchronization is stable.

It can be seen from calculation above that chaotic synchronization of two cubic nonlinear coupling HR neurons can be realized effectively by exerting the square form of the output membrane voltage on the right side of the second differential equation. Assuming that the nonlinear coupling strength on the first differential equation is α and the nonlinear coupling strength on the second differential equation is β, Bigger is α, the range of β is smaller.

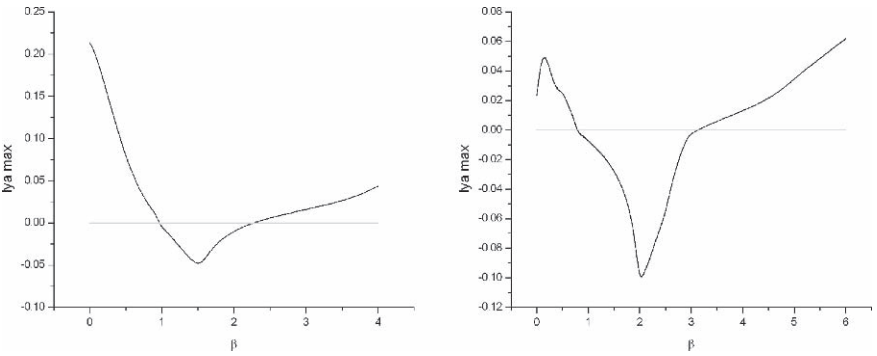

(a) $\alpha = 0.1$ (b) $\alpha = 0.01$

Fig. 56.2 The maximum Lyapunov exponent, lyamax vs. β

Conclusion

In this paper, the chaotic synchronization of two cubic nonlinear coupling HR neurons is discussed. A nonlinear coupling feedback term with higher order form of membrane potential is studied, and adds it to different position of the HR equation. Through numerical simulations, we can get the following conclusion:

(1) No chaotic synchronization occurs in a considerable range of coupling strength when cubic nonlinear coupling feedback is exerted on the first differential equation only.
(2) On this condition, if the square form of membrane potential added to the second differential equation, the two neurons can achieve full synchronization in special coupling strength region. Assuming that the nonlinear coupling strength on the first differential equation is α and the nonlinear coupling strength on the second differential equation is β, the system can achieve complete synchronization with different α and β in a certain range. Bigger is α, the range of β is smaller. The maximum conditional Lyapunov exponent can identified the synchronization stability.

This study proposes a possible explanation on the generation mechanism of synchronization between neurons in brain. On the other hand, the basis is also provided for the chaotic synchronization of higher-order nonlinear coupling neurons. The mechanism of coordination in the complex neural system is revealed in a certain extent, which has laid a foundation for the future study.

Acknowledgments This work was supported by the National Natural Science Foundation of China (10572086) and the Doctoral Program foundation of Institution of Higher Education of China (20050248031).

References

1. Aihara, K., Takabe, T., Toyoda, M.: Chaotic neural networks. Phys. Lett. A 144 (1990) 333–340.
2. Freeman, W.J.: The physiology of perception. Sci. Am. 264 (1991) 78–85.
3. Wang, W., Perez, G., Cerdeira, H.A.: Dynamical behavior of the firings in a coupled neuronal system. Phys. Rev. E 47 (1993) 2893–2898.
4. Femat, R., Alvarez-Ramirez, J., Zarazua, M.: Chaotic behavior from a human biological signal. Phys. Lett. A 214 (1996) 175–179.
5. Xu, J.-X., Gong, Y.-F., Ren, W., Hu, S.-J.: Propagation of periodic and chaotic action potential trains along nerve fibers. Phys. D 100 (1997) 212–231.
6. Pecora, L.M., Carroll, T.L.: Master stability functions for synchronized coupled systems. Phys. Rev. Lett. 80 (1998) 2109–2112.
7. Shuai, J.W., Durand, D.M.: Phase Synchronization in two coupled chaotic neurons. Phys. Lett. A 264 (1999) 289–296.
8. He, D.H., Hu, G., Zhan, M., Lu, H.P.: Periodic states with functional phase relation in weakly coupled chaotic Hindmarsh-Rose neurons. Phys. D 156 (2001) 314–324.

9. Yu, H.-J., Liu, Y.-Z.: Chaotic synchronization based on stability criterion of linear system. Phys. Lett. A 314 (2003) 292–298.
10. Yu, H.-J., Liu, Y.-Z.: Synchronization of symmetrically nonlinear-coupled chaotic systems. Acta Phys. Sin. 54 (2005) 3029–3033 (in Chinese).
11. Yu, H.-J., Peng, J.-H.: Chaotic synchronization of Hindmarsh-Rose neural networks using special feedback function. International conference on intelligent computing. ICIC2006 Kunming, China, August 2006 Proceedings, Part I. Lecture Notes in Computer Science 4113 63–68.
12. Yu, H.-J., Peng, J.-H.: Chaotic synchronization and control in nonlinear-coupled Hindmarsh-Rose neural systems. Chaos Solitons Frac 29 (2006) 342–348.
13. Ali, M.K., Fang, J.Q.: Synchronization of chaos and hyperchaos using linear and nonlinear feedback function. Phys. Rev. E 55 (1997) 5285–5290.
14. Pyragas, K.: Continuous control of chaos by self-controlling feedback. Phys. Lett. A 170 (1992) 421–428.
15. Milne, A.E., Chalabi, Z.S.: Control analysis of the Rose–Hindmarsh model for neural activity. IMA J. Math. Appl. Biol. Med. 18 (2001) 53–75.
16. Levitan, I.B., Kaczmarek, L.K.: The neuron cell and molecular biology. New York: Oxford University Press Inc. (1997).

Part III
Macroscopic Cognitive Neurodynamics

Chapter 57
When Is It Worth Working: Calculating the Motivational Value of Working

Barry J. Richmond, Giancarlo LaCamera, Alex Lerchner and Takafumi Minamimoto

Abstract To determine what factors influence motivated behavior, we have worked to identify behavioral and neurophysiological correlates related to motivation. In these studies we have used behavioral paradigms in which monkeys must carry out one or more simple operant behavioral trials, detecting when a visual target changes from red-green, which when done correctly, allows that monkey to either move to another identical trial or obtain a reward. Visual cues appearing at the beginning of the trials indicate whether a trial will be rewarded, or not. Monkeys react to these cues, with the number of errors related to how long in the future the reward will be, but also contingent on how much work has been already completed. The performance, both overall, and dynamical can be nicely modeled with simple modifications of temporal difference learning models.

Most, if not all, exploration of the world relies on seeking goals or rewards. Learning which circumstances lead to rewards it is necessary to learn the association between environmental stimuli and/or actions and the rewards (or which stimuli or actions to take to avoid adverse outcomes). Both experimental psychology and economic theory have worked on the circumstance leading to this stimulus-outcome learning from different points of view. The field of learning theory grew up to describe the dynamics and outcomes of experiments delving into this learning. In economics the same behaviors are of great interest because the actions of individuals affects individual behavior, and these behaviors affect financial markets.

We have been studying the how motivation arises, and particularly, what factors govern when and how hard an animal will work to obtain a goal. In our experiments monkeys are taught to touch a bar to start single trials and to release the bar when a red target spot turns to green, i.e., a simple sequential red-green color discrimination. Monkeys generally learn to do this well in about 4–6 weeks (with red waiting times of 2–4 s). After learning this 'operant' task, the monkeys are required to perform 1, 2, 3 or 4 of these red-green discrimination trials to obtain a reward. A visual cue

B.J. Richmond
Bldg 49, Rm 1B80, Section on Neural Coding and Computation, Laboratory of Neuropsychology, National Institute of Mental Health, Bethesda, MD 20892, USA
e-mail: bjr@ln.nimh.nih.gov

R. Wang et al. (eds.), *Advances in Cognitive Neurodynamics*,

appears at the beginning of each trial. In the valid condition, there is a particular cue associated with each state. In the random condition, the cue is chosen at random from the set of cues. Thus, in the valid condition the monkeys can know which state is current, and they can learn how many trials must be performed to obtain a reward. In a variant of the task, the monkey needs to perform only one trial, but, in the valid condition the cue will signal how long the monkey will have to wait to obtain the reward, that is, how postponed the reward will be.

In both tasks, the monkeys make few errors when the cues are chosen randomly. In the valid cue condition, the monkeys make errors in trials that are not immediately rewarded. The number of errors becomes larger as the number of remaining trials, or postponement period increases [1, 2, 3, 4, 5, 6, 7]. Thus, the value of trials decreases as the time before reward increases. This is a well-known result and the temporal difference model describes this well. However, the temporal difference model predicts that when the agent (here the animal) has control over the situation, the performance should improve to maximize reward. However, the monkeys do not show that effect. There behavior remains stable for years with the errors being proportional to the delay before reward.

To model this behavior we have modified the temporal difference model of Sutton and Barto [8]. They derived the temporal difference model for a machine-learning. They sought an algorithm that could drive learning of a wide variety of tasks. This model is formulated with a reward being given for every successful performance of the desired function, and the algorithm was predicated on maximizing the long term reward. This is achieved by increasing the values of actions or states that were followed by a reward. The approach is wonderfully successful and can be used to teach machines to perform a wide variety of tasks very well.

To model the behavior we used to the temporal difference model for learning the state values, but removed the adaptation that maximizes the reward. In this form the model matches the performance of the monkeys very closely by learning the values of all states, even those that are not rewarded. This latter requirement must be achieved or there would be no motivation to continue performing in unrewarded circumstances. In addition to predicting the behavior in the valid cue condition, the model predicts that the monkeys will perform well in all trials of the random condition. This occurs because value is mapped to errors through a sigmoidal function, and the overall average of value maps into a low error rate, that is, the average value maps to a low error rate.

In economic theory it is shown that states equally far from reward should be equally valuable. In our experiments, we observed that the values of states equally far from a reward, say a penultimate trial, depended upon number of trials already performed in the current state. In penultimate trials, the monkeys made fewer errors when more trials had already been performed. This behavior cannot be explained with conventional temporal difference models because they look ahead only, discounting future reward. By including a term that is algebraically similar to temporal discounting, the value can be increased according to the number of trials already performed, with the algebra depending only on the preceding state. It is not necessary to count the number of preceding trials. This latter effect is similar

to framing as described by Kahnemann and Tversky [9, 10]. In framing the local context affects the value of state, which is just what is happening to the monkeys. Thus, with the simple algebra of temporal difference modeling we can capture many of the important features of reward schedule behavior.

Because our monkeys learn to associate the stimuli with the state values, we have used this as a tool to probe the abilities of monkeys to form generalizable categories. If different sets of cues, for example, dogs, cats or rats, are presented with different states in variants of reward schedule tasks the monkeys quickly show that they have generalized these categories through their error rates and reaction times. This provides a rapid and powerful means to explore perceptual categorization in monkeys. We can further to study the relation between different brain regions and the formation of categories. We have found that monkeys with complete lateral prefrontal lesions form generalizable categories and are as capable of making extradimensional shifts (e.g., they can shift from categorizing by color to categorizing by shape) as normal monkeys. Thus, perceptual rule shifting does not seem to require lateral prefrontal cortex.

References

1. Bowman EM, Aigner TG, Richmond BJ (1996) Neural signals in the monkey ventral striatum related to motivation for juice and cocaine rewards. J Neurophysiol 75:1061–1073.
2. Liu Z, Richmond BJ (2000) Response differences in monkey TE and perirhinal cortex: stimulus association related to reward schedules. J Neurophysiol 83:1677–1692.
3. Liu Z, Richmond BJ, Murray EA, Saunders RC, Steenrod S, Stubblefield BK, Montague DM, Ginns EI (2004) DNA targeting of rhinal cortex D2 receptor protein reversibly blocks learning of cues that predict reward. Proc Natl Acad Sci U S A 101:12336–12341.
4. Ravel S, Richmond BJ (2006) Dopamine neuronal responses in monkeys performing visually cued reward schedules. Eur J Neurosci 24:277–290.
5. Shidara M, Richmond BJ (2002) Anterior cingulate: single neuronal signals related to degree of reward expectancy. Science 296:1709–1711.
6. Shidara M, Aigner TG, Richmond BJ (1998) Neuronal signals in the monkey ventral striatum related to progress through a predictable series of trials. J Neurosci 18:2613–2625.
7. Sugase-Miyamoto Y, Richmond BJ (2005) Neuronal signals in the monkey basolateral amygdala during reward schedules. J Neurosci 25:11071–11083.
8. Sutton RS (1988) Learning to predict by the methods of temporal differences. Mach Learn 3:9–44.
9. Kahneman D, Tversky A (1984) Choices, values, and frames. Am Psychol 39:341–350.
10. Tversky A, Kahneman D (1981) The framing of decisions and the psychology of choice. Science 211:453–458.

Chapter 58
The Physiological and Biochemical Bases of Functional Brain Imaging

Louis Sokoloff

Functional brain imaging techniques are now widely used to identify regions of the brain involved in cognitive and various other neurological functions. These methods are all based on the display of the local activities of physiological and/or biochemical processes related to functional activity within images of the brain.

Tissues that do physical work, as, for example, mechanical work by heart and skeletal muscles and chemi-osmotic work by kidney, derive the energy needed to support that work from the metabolism of substrates supplied to them by the blood. The greater the work load, the greater is the demand for energy and the higher the tissue's rate of energy metabolism. Although the physical nature of the work done by brain is less obvious, the pathways of its energy metabolism are similar to those of other tissues. In man the normal adult male's brain comprises only about 2% of total body mass, yet it consumes approximately 20% of the body's total basal oxygen consumption. This probably indicates that even at rest the brain is functionally very active. The brain's oxygen consumption ($CMRO_2$) is almost entirely for the oxidative metabolism of glucose which in normal physiological conditions is the almost exclusive substrate for the brain's energy metabolism [1]. As far back as 1892 Roy and Sherrington [2] had hypothesized that mechanisms exist in brain that adjusts its rate of blood flow (CBF) to the nutritional demands of its energy metabolism. If so, then CBF should vary with the rate of energy metabolism and reflect the level functional activity in the brain. In comparison with other organs the brain is extraordinarily heterogeneous with regard to both structure and function with different neurological functions localized to specific regions of the brain. Probably for that reason methods that measured average $CMRO_2$ and CBF in the brain as a whole failed to show a clear relationship between normal physiological functional activities and rates of blood flow and metabolism. What was needed were methods for measuring rates of blood flow and/or energy metabolism in the brain locally within the various structures of the brain.

L. Sokoloff
National Institute of Mental Health, National Institutes of Health, Building 49, Room 1B80, 49 Convent Drive MSC 4415, Bethesda, MD 20892, USA
e-mail: louissokoloff@mail.nih.gov

R. Wang et al. (eds.), *Advances in Cognitive Neurodynamics*,

The first step in the evolution of functional brain imaging was the development of the [^{131}I]trifluoroiodomethane ($CF_3{}^{131}I$) method for measuring local rates of blood flow within the various structures of the brain (lCBF) [3]. This method utilized a unique quantitative autoradiographic technique in which the optical densities in autoradiographs of sections of the brain were quantitatively related to the local tissue concentrations of the radioactive tracer, and these concentrations were in turn determined by the rate of blood flow to the tissue. Essentially, the method provided pictorial maps of the local rates of blood flow throughout the brain exactly within each of its anatomic structures. This method was used to show that retinal stimulation with photoflashes markedly increased local CBF in all the structures of the visual pathways of the conscious cat, and these local increases were clearly visible in the autoradiographs [4]. This study confirmed the validity of the Roy and Sherrington hypothesis and was the first true example of functional brain imaging.

The mechanisms by which CBF adjusts to changes in functional activity are still largely undefined, probably because there are so many of them. It was long believed that CBF is adjusted to the level of energy metabolism because increased CO_2, and reduced oxygen tensions, decreased pH, and increased adenosine concentration in the tissue, all consequences of increased energy metabolism, dilate cerebral blood vessels, and when these are changed in the opposite direction during reduced energy metabolism, the vessels constrict. Neurogenic control of the cerebral circulation is always a possibility but never proven. Vascular effects of neurotransmitters, such as glutamate, dopamine, GABA, etc., and nitric oxide, a very potent vasodilator, have all been implicated. It may well be that all contribute to some extent and to varying degrees in different parts of the brain so that none can be ruled out. Regardless of the mechanism, however, measurement of local CBF can be used to localize local functional activity.

Compared with blood flow, it should be expected that local energy metabolism would be more closely, more directly, and more specifically related to local functional activity because both processes are localized to the same individual cells. No individual cells, however, have their own private blood flows, and, therefore, blood flow should increase more diffusely in areas surrounding the activated cells. Furthermore, energy metabolism is influenced only by events within the cells, but blood flow is also influenced by chemical factors in the blood perfusing the tissue. All in all, it is to be expected that measurement of local energy metabolism should provide a more specific marker and better spatial localization of functional activity in the brain.

The development of the [^{14}C]deoxyglucose) ([^{14}C]DG) method made it possible to measure local rates of glucose utilization ($lCMR_{glc}$) throughout the brain [5]. This method employed a quantitative autoradiographic technique like that of the ($CF_3{}^{131}I$) method but, subsequently, added computerized processing techniques that scanned the autoradiographs and redisplayed them in color with the actual rates of $lCMR_{glc}$ encoded in a calibrated color scale. It measured $lCMR_{glc}$ quantitatively accurately with a spatial resolution (Full-Width-Half-Max, FWHM) of about 200 μm [6], but it could qualitatively visualize and display altered $lCMR_{glc}$ in areas as small as 25 μm. Numerous applications of this method in both conscious and

anesthetized animals clearly established that increased functional activity stimulates and decreased functional activity diminishes $lCMR_{glc}$ in anatomical components of the activated pathways [7]. A surprising finding was that the increases in glucose consumption evoked by functional activation are confined to synapse-rich regions, i.e., neuropil which contains axonal terminals, dendritic processes, and also the astrocytic processes that envelop the synapses [8, 9]. It was also shown that the magnitudes of these increases are directly and linearly related to the frequency of action potentials in the afferent pathways and not to the activity of the target neurons in their projection zones [8–10]. $lCMR_{glc}$ is, therefore, increased in the projection zone of an activated pathway regardless of whether the pathway is excitatory or inhibitory. To determine which requires examining $lCMR_{glc}$ in the next synaptic station of the pathway. Regions rich in neuronal cell bodies do consume glucose, but their rates are essentially unaffected by neuronal functional activation [8, 9]. Presumably, the glucose metabolized in neuronal cell bodies is mainly to support cellular vegetative and house-keeping processes, e.g., axonal transport, biosynthesis of nucleic acids, proteins, phospholipids and other lipids, as well as other energy-consuming processes not related directly to action potentials.

Studies with the [^{14}C]DG method in neural tissue slices showed that the activation of energy metabolism by functional activation is due mainly, if not entirely, to stimulation of Na^+,K^+-ATPase activity [11]. Action potentials reflect the uptake of Na^+ into and extrusion of K^+ from the cells, thus depolarizing the cell membranes. These ion shifts stimulate the activity of Na^+,K^+-ATPase, the enzyme that pumps the Na^+ back out and the K^+ back into the cells, a process dependent on the energy derived from the breakdown of ATP. The breakdown of ATP in turn stimulates glucose metabolism to restore the ATP that had been consumed. In short, it appears then that the energy-requiring work of the brain supported by the increased $lCMR_{glc}$, during neuronal functional activation is due mainly to activation of Na^+,K^+-ATPase activity to restore the ionic gradients across the cell membrane and the membrane potentials that were degraded by the spike activity.

The [^{14}C]DG method lacks the cellular and subcellular resolution needed to identify the elements in neuropil, e.g., axonal, dendritic, and astrocytic processes, that contribute to the functional activation of $lCMR_{glc}$. This issue has been approached indirectly by studies *in vitro* with cultured neurons and astroglia in which the incubation medium is manipulated to simulate changes expected to occur *in vivo* during neuronal functional activation, e.g., increased extracellular K^+ concentration ($[K^+]_o$), opening Na^+ channels and raising intracellular Na^+ concentration ($[Na^+]_i$), and raising extracellular neurotransmitter concentrations [12, 13]. Membrane depolarization by raising $[K^+]_o$ stimulated glucose utilization in cultured neurons but not in astroglia [13], and opening Na^+ channels by addition of veratridine or monensin markedly stimulated glucose utilization in both types of cells. These stimulations were all blocked by addition of ouabain, an inhibitor of Na^+,K^+-ATPase, confirming a role for this enzyme in the mechanism of the increased glucose utilization. Of particular interest was the finding that addition of L-glutamate to the medium markedly stimulated glucose utilization in the cultured astroglial cells [12, 13]. This stimulation was unaffected by inhibitors of NMDA or non-NMDA receptors but

blocked by ouabain and absent in Na^+-free medium, excluding glutamate receptors but implicating Na^+,K^+-ATPase in the mechanism of this stimulation as well [12, 13].

L-glutamate is the most prevalent excitatory neurotransmitter in brain and is released by the axonal terminals in the synapses in the projection zones of glutamatergic pathways. Extracellular glutamate is extraordinarily toxic to neurons, but they are normally protected from toxic extracellular glutamate concentrations by the avid uptake of glutamate by the astrocytes. This uptake is mediated by a Na^+/glutamate co-transporter that transports the glutamate together with Na^+ into the astrocytes [14] where the glutamate is converted to glutamine by glutamine synthetase, another ATP-consuming enzymatic process. On the basis of these observations made in cultured neurons and astroglia and anatomical evidence that capillaries in brain are largely surrounded by astrocytic end-feet, Magistretti and Pellerin [15] have hypothesized that oxidative metabolism of glucose in brain is compartmentalized between astrocytes and neurons, first uptake of glucose by astrocytes where it is converted by glycolysis to lactate and then the export of this lactate to the neurons where it is oxidized to CO_2 and water by the tricarboxylic cycle. This hypothesis, combined with what is already known about cerebral biochemistry, leads to the following scenario. Functional activation of a pathway is associated with increased spike activity and the release of neurotransmitters in its terminal projection zone. This neurotransmitter is mainly glutamate in most excitatory pathways. The released glutamate is cleared from the extracellular space by the co-transport of the glutamate and two to three Na^+ ions into the astrocytes. The glutamate taken up by the astroglia is converted by glutamine synthetase to glutamine which can then be released and recycled for use by neurons. The rise in intracellular Na^+ content in the astroglia stimulates Na^+,K^+-ATPase activity to pump out the Na^+ ions, and one molecule of ATP is consumed in the pumping out of three Na^+ ions. The conversion of one molecule of glutamate to glutamine also consumes one molecule of ATP. Therefore, each glutamate molecule that is released by neuronal functional activation, then taken up along with Na^+ into the astroglia, and converted there into glutamine results in the consumption of two molecules of ATP, the net amount of ATP produced by the glycolytic conversion of one molecule of glucose to two molecules of lactate. The lactate molecules thus produced in the astrocytes are exported to the neurons where they are oxidized by the tricarboxylic acid cycle to produce an additional 36 molecules of ATP. These ATP molecules are used by Na^+,K^+-ATPase to restore the ionic gradients in the axonal terminals and dendritic processes that were partially degraded by the spike activity. The energy metabolism supporting functional activity in brain is then shared by neurons and astroglia in a symbiotic relationship. Glucose is the essential substrate for the brain's energy metabolism, but different segments of the overall pathway in its metabolism are to some extent segregated in the two cell types, glycolysis in astrocytes and oxidation in neurons.

This lactate-shuttle hypothesis has raised some controversy [16]. Its relevance has been questioned because it is based mainly on studies of cells in culture, and also as originally presented, appeared to propose exclusive assignments of glycolysis to

astrocytes and oxidative metabolism of the glycolytic products, lactate and pyruvate, to neurons. It is true that in astroglia in culture the rate of glycolytic metabolism of glucose far exceeds that of oxidation so that excessive lactate is formed and released into the medium. Neurons in culture, however, are also able to metabolize glucose in the medium to pyruvate and lactate and then to oxidize these glycolytic products to CO_2 and water, and astroglia are able to some extent to oxidize glucose and lactate to CO_2 and water [17]. The neurons, however, do show a kinetic preference to oxidize lactate than glucose to CO_2. For example, progressive increases in lactate concentration in the medium produce correspondingly progressive inhibition of glucose oxidation by neurons whereas glucose in the medium does not inhibit the oxidation of lactate [17]. This would indicate that the direct utilization by glucose by neurons depends on the lactate concentration in the medium. The lactate-shuttle hypothesis is probably valid mainly in regions of the brain with major glutamatergic inputs where spike activity in the afferent pathway releases glutamate in the synapses. The glutamate is then taken up along with Na^+ by the astrocytes which stimulates glucose utilization to pyruvate and lactate. The ATP formed by glycolysis is consumed in the astrocytes to pump the Na^+ out of the cells and convert the glutamate to glutamine, and the lactate is released into the extracellular space. The rise in extracellular lactate concentration leads to preferential uptake and oxidation of lactate and inhibition of glucose utilization by the neurons. The ATP generated by the oxidation of the lactate provides the energy needed to restore the ionic gradients and membrane potentials degraded by the spike activity in the neuronal synaptic membranes. This compartmentalization is probably of lesser magnitude and importance in regions with input pathways that use transmitters other than glutamate, and in no case is the compartmentalization of glycolytic and oxidative metabolism of glucose between astrocytes and neurons complete and fully obligatory.

Because of their use of autoradiography, the $CF_3{}^{131}I$ and [^{14}C]DG methods for measuring local CBF and glucose utilization were limited to studies in animals. Both methods were, however, subsequently adapted for use in humans by substituting positron-emitting tracers and positron emission tomography (PET) in place of autoradiography, i.e., $H_2{}^{15}O$ instead of $CF_3{}^{131}I$ to measure blood flow [18] and [^{18}F]fluorodeoxyglucose (^{18}FDG)in place of [^{14}C]DG to measure glucose utilization [19, 20]. These PET methods, however, have far lesser spatial resolution than the autoradiographic methods, e.g., FWHM in the mm instead of μm range. Although these PET methods contributed very little to define the mechanisms that relate blood flow and energy metabolism to functional activity in the brain, their applications did initiate and establish the field of functional brain imaging in humans.

The advent of nuclear magnetic resonance imaging (MRI) introduced a new and now the most convenient and commonly used method for functional brain imaging (fMRI) in both animals and humans. It is based on the physical property of atomic nuclei that, when first oriented in a magnetic field and then temporarily reoriented by radiofrequency pulses, emit during their return to their previous orientation in the magnetic field radio signals at resonance frequencies and intensities characteristic of their chemical species, concentrations, and environment. The strongest signals are those obtained from hydrogen nuclei because they are in water and thus most

prevalent. This physical phenomenon has been exploited for fMRI by taking advantage of the so-called Blood-Oxygen-Level-Dependent (BOLD) effect [21, 22]. The physical basis of this effect is as follows. Reduced hemoglobin, mainly in venous blood, is paramagnetic which causes it to alter and attenuate the MRI signal. Oxyhemoglobin, most prevalent in the arterial blood is diamagnetic and has no such effect. Blood flow is increased by dilatation of the blood vessels which augments the inflow of arterial blood and its oxyhemoglobin content into the tissue. If this increased blood flow and oxygen input is not matched by a proportionate increase in oxygen consumption and extraction of oxygen from the blood by the tissue, the venous blood draining the tissue within the field of view contains more of oxyhemoglobin and less deoxyhemoglobin. This leads to a small increase in the MRI signal, i.e., the BOLD effect. Functional activation, at least initially, increases inflow of arterial blood more than the oxygen extraction which results in reduced hemoglobin content within the field of view and produces the signal exploited by fMRI to localize functional activity in the brain [22, 23].

The physiological basis of the discrepancy between the magnitudes of the changes in blood flow and oxygen extraction that lead to the BOLD effect evoked by functional activation is still unclear. It has been attributed to increases in blood flow without, despite comparable increases in glucose utilization, proportionate rises in oxygen consumption that would extract the oxygen from the blood [24, 25]. This is highly unlikely because the same intracellular changes produced by increased functional activity that stimulate glucose utilization also stimulate oxidative phosphorylation and the oxidation of the pyruvate and lactate produced by glycolysis. A more likely explanation is that there is a temporal dissociation between the increased rates of glycolysis and the oxidation of its products. The time course of increased oxygen consumption is likely to be delayed, acutely less intense, and more spread out over a longer time period than the increase in blood flow. The lactate and pyruvate produced by the initial stimulation of glycolysis may be oxidized more slowly but over a longer time span that extends beyond the end of the functional activation [26]. Another likely contributor to the BOLD effect is the different spatial distributions of the changes in blood flow and oxygen consumption within the field of view. Functional activation stimulates energy metabolism only in functionally activated cells. No cells, however, have their own private blood flows. When cells are activated, blood flow is increased not only to those cells but also to surrounding unaffected cells. The venous blood draining the mixture of activated and unaffected cells in the field of view then contains higher oxyhemoglobin and lower reduced hemoglobin contents giving the impression that functional activation increases blood flow more than oxygen consumption. The blood flow is disproportionately higher because it includes the increased blood flow in the surrounding tissues within the field of view that were not functionally activated. In addition, one must consider the potential role of the Munro-Kellie doctrine [27] which addresses the fact that because the brain is enclosed in a rigid box, the cranium, any increase in any one fluid compartment must be at the expense of one or more of the other fluid compartments in the brain. Because the brain is incompressible, this leaves only arterial and venous blood and cerebrospinal fluid susceptible. During functional

activation the arterial blood vessels are dilated bringing in more oxygenated blood which must displace venous blood and/or CSF. The exit channels for CSF have much higher resistance than those for the venous blood, and so the input of arterial blood mechanically displaces mainly venous blood which would give rise to a BOLD effect.

Even though the physiological basis of the BOLD effect during functional activation in brain is still undefined, it is clear that fMRI provides a potent method for localizing functional activities in the brain. It is non-invasive, uses no ionizing radiations, is very rapid so that numerous repeated scans can be done within one session and control and stimulated conditions compared, and provides better spatial resolution than PET. Its main disadvantage is that baseline conditions without functional activation between subjects cannot be compared.

References

1. Clarke, D. D., and Sokoloff, L. (1999) Circulation and energy metabolism of the brain. In: Siegel, G., Agranoff, B., Albers, R. W., and Fisher, S. (Eds.): Basic Neurochemistry: Molecular, Cellular, and Medical Aspects, Sixth Edition. Lippincott-Raven, Philadelphia, pp. 637–669.
2. Roy, C. S., Sherrington, C. S. (1890) On the regulation of the blood supply of the brain. J. Physiol. 11: 85–108.
3. Landau, W. M., Freygang, W. H., Rowland, L. P., Sokoloff, L., and Kety, S. S. (1955) The local circulation of the living brain: values in the unanesthetized and anesthetized cat. Trans. Am. Neurol. Assoc. 80: 125–129.
4. Sokoloff, L. (1961) Local cerebral circulation at rest and during altered cerebral activity induced by anesthesia or visual stimulation. In: Kety, S. S., and Elkes, J. (Eds.): The Regional Chemistry, Physiology and Pharmacology of the Nervous System. Pergamon Press, Oxford, pp. 107–117.
5. Sokoloff, L., Reivich, M., Kennedy, C., Des Rosiers, M. H. Patlak, C. S., Pettigrew, K. D., Sakurada, O., and Shinohara, M. (1977) The [^{14}C] deoxyglucose method for the measurement of local cerebral glucose utilization: theory, procedure, and normal values in the conscious and anesthetized albino rat. J. Neurochem. 28: 897–916.
6. Goochee, C., Rasband, W., and Sokoloff, L. (1980) Computerized densitometry and color coding of [^{14}C]deoxyglucose autoradiographs. Ann. Neurol. 7: 359–370.
7. Sokoloff, L. (1981) Localization of functional activity in the central nervous system by measurement of glucose utilization with radioactive deoxyglucose. J. Cereb. Blood Flow Metab. 1: 7–36.
8. Sokoloff, L. (1999) Energetics of functional activation in neural tissues. Neurochem. Res. 24: 321–329.
9. Kadekaro, M., Crane, A. M., and Sokoloff, L. (1985 Differential effects of electrical stimulation of sciatic nerve on metabolic activity in spinal cord and dorsal root ganglion in the rat. Proc. Natl. Acad. Sci. U.S.A. 82: 6010–6013.
10. Yarowsky, P., Kadekaro, M., and Sokoloff, L. (1983) Frequency-dependent activation of glucose utilization in the superior cervical ganglion by electrical stimulation of cervical sympathetic trunk. Proc. Natl. Acad. Sci. U.S.A., 80: 4179–4183.
11. Mata, M., Fink, D. J., Gainer, H., Smith, C. B., Davidsen, L., Savaki, H., Schwartz, W. J., and Sokoloff, L. (1980) Activity-dependent energy metabolism in rat posterior pituitary primarily reflects sodium pump activity. J. Neurochem. 34: 213–215.

12. Takahashi, S., Driscoll, B. F., Law, M. J., and Sokoloff, L. (1995) Role of sodium and potassium ions in regulation of glucose metabolism in cultured astroglia. Proc. Natl. Acad. Sci. U.S.A. 92:. 4616–4620.
13. Pellerin, L., and Magistretti, P. J. (1994) Glutamate uptake into astrocytes stimulates aerobic glycolysis: a mechanism coupling euronal activity to glucose utilization. Proc. Natl. Acad. Sci. U.S.A. 91: 10625–10629.
14. Flott, B., and Seifert, W. (1991) Characterization of glutamate uptake in astrocyte primary cultures from rat brain. Glia 4: 293–304.
15. Magistretti, P. J., and Pellerin, L. (1996) Cellular bases of brain energy metabolism and their relevance to functional brain imaging: evidence for a prominent role of astrocytes. Cereb. Cortex 6: 50–61.
16. Dienel, G. A., and Hertz, L. (2001) Glucose and lactate metabolism during brain activation. J. Neurosci. Res. 66: 824–838.
17. Itoh, Y., Esaki, T., Shimoji, K., Cook, M., Law, M. J., Kaufman, E., and Sokoloff, L. (2003) Dichloroacetate effects on glucose and lactate oxidation by neurons and astroglia in vitro and on glucose utilization by brain in vivo. Proc. Natl. Acad. Sci. U.S.A. 100: 4879–4884.
18. Herscovitch, P., Markham, J., and Raichle, M. (1983) Brain blood flow measured with intravenous $H_2^{15}O$. I. Theory and error analysis. J. Nucl. Med. 24: 782–789.
19. Reivich, M., Kuhl, D., Wolf, A., Greenberg, J., Phelps, M., Ido, T., Cassella, V., Fowler, J., Hoffman, E., Alavi, A., Som, P., and Sokoloff, L. (1979) The [^{18}F]fluoro-deoxyglucose method for the measurement of local cerebral glucose utilization in man. Circ. Res. 44: 127–137.
20. Phelps, M. E., Huang, S. C., Hoffman, E. J., Selin, C., Sokoloff, L., and Kuhl, D E. (1979) Tomographic measurement of local cerebral glucose metabolic rate in humans with (F-18)2-fluoro-2-deoxy-d-glucose: validation of method. Ann. Neurol. 6: 371–388.
21. Ogawa, S., Lee, T. M. Kay, A. R., and Tank, T. W. (1990) Brain magnetic resonance imaging with contrast dependent on blood oxygenation. Proc. Natl. Acad. Sci. U.S.A. 87: 9868–9872.
22. Ogawa, S., Tank, D. W., Menon, R., Ellerman, J. M., Kim, S. G., Merkle, H., and Ugurbil, K. (1992) Intrinsic signal changes accompanying sensory stimulation: functional brain mapping with magnetic resonance imaging. Proc. Natl. Acad. Sci. U.S.A. 89: 5951–5955.
23. Kwong, K. K., Belliveau, J. W., Chesler, D. A., Goldberg, I. E., Weisskoff, R. M., Poncelet, B. P., Kennedy, D. N., Hoppel, B. E., Cohen, M. S., Turner, R., Cheng, H. M., Brady, T. J., and Rosen, B. R. (1992) Dynamic magnetic resonance imaging of human brain activity during primary sensory stimulation. Proc. Natl. Acad. Sci. U.S.A. 89: 5675–4679.
24. Fox, P. T., and Raichle, M. E. (1986) Focal physiological uncoupling of cerebral blood flow and oxidative metabolism during somatosensory stimulation in human subjects. Proc. Natl. Acad. Sci. U.S.A. 83: 1140–1144.
25. Fox, P. T. Raichle, M. E., Mintun, M. A., and Dence, C. (1988) Nonoxidative glucose utilization during focal physiologic neural activity. Science 241: 462–464.
26. Madsen, P L., Cruz, N F., Sokoloff, L., and Dienel, G A. (1999) Cerebral oxygen/glucose ratio is low during sensory stimulation and rises above normal during recovery: excess glucose consumption during stimulation is not accounted for by lactate efflux from or accumulation in brain tissue. J. Cereb. Blood Flow Metab. 19: 393–400.
27. Wolff, H. G. (1936) The cerebral circulation. Physiol. Rev. 16: 545–596.

Chapter 59
Through Attention to Consciousness

J.G. Taylor

Abstract There is presently a vigorous ongoing debate about the relation between attention and consciousness. This is being fuelled by results from experimental paradigms which probe various features of the interaction of attention and consciousness, such as the attentional blink, object substitution masking and change blindness. We present here simulations of these three paradigms which can all be produced by use of a single model of attention. This model helps suggest an explanation of consciousness as created through attention, and helps explore the complex nature of attention. It indicates how it is possible to accommodate the relevant experimental results without needing to regard consciousness and attention as independent processes. We continue by analysis of the early stages of attention (the first 200 ms post-stimulus) and show how these can support the original CODAM model introduced by us earlier. The paper concludes with a discussion.

Introduction

The debate is intensifying between those who believe attention is necessary (but not sufficient) for consciousness [1, 2, 3] and those who regard these two brain processes as independent [4, 5]. The debate presently is based on arguments of the latter protagonists, who assume that attention and consciousness are each simple processes. However neither of these processes is likely to be simple. The complexity of attention is indicated by the subtle nature of priming and masking effects, and by a variety of deficits in attention such as neglect and extinction, as well as phenomena like the attentional blink. The complexity of consciousness arises from the wealth of different states of consciousness: in the normal waking state, under various drugs, in meditation (such as in so-called pure consciousness), in dreaming, hypnosis, dissociation of identity disorder, and so on. In order to advance

J.G. Taylor
Department of Mathematics, King's College, Strand, London WC2R2LS, UK
e-mail: john.g.taylor@kcl.ac.uk

R. Wang et al. (eds.), *Advances in Cognitive Neurodynamics*,

the debate, we explore more fully some of these complex features of attention by use of a recent model providing a deconstruction of attention, and thence of consciousness [6, 7, 8, 9, 10, 11]. The model extends to attention the recently successful applications of engineering control concepts to motor control [12, 13, 14, 15]. Thus modules acting as inverse model controllers and forward models are extended from the motor control domain to attention control. Considerable support has been given for this engineering control approach to attention from recent brain imaging results [16].

The resulting model uses the efference copy or corollorary discharge of the attention movement control signal to give a precursor signal to the posterior cortical sensory working memory buffer site for the creation of content consciousness. This precursor signal has been proposed [6, 7, 9, 10] as that generating the experience of 'ownership' or of 'being there' [17], and leading to the important mental property of 'immunity to error through misidentification of the first person pronoun' [18]. That is why the resulting model is termed the COrollary Discharge of Attention Movement (CODAM). It has been used to give an initial explanation of the main ERP sequence as observed in the brain during the creation of consciousness [11]. The suggestion of the importance of the corollary discharge of attention movement in understanding consciousness also allows for the beginnings of a rapprochement between science and religion through the explanation, by CODAM, of the meditative state of pure consciousness seen to be at the basis of the religious experience of God across all the world's major religions [8, 19]. The CODAM model is applied in this paper to give detailed explanations of the various paradigms now available and used in the arguments by one side or the other of this division on attention and consciousness. It is later considered in terms of how attention is developed in a bottom-up manner, relating particularly to the N2 signal (and more particularly the N2pc) as an indication of the detailed dynamics of the development of attention in the brain.

We proceed in the next section to give a brief review of the basic CODAM model which we use to bolster our argument that attention is the main stepping stone for consciousness. In the following section we give a short review of how the attentional blink is explained by CODAM, extending the results of [20] to include explicit control of distracter inhibition on the buffer working memory site by the attention movement corollary discharge. The section on 'Modeling Object Substitution' treats the phenomenon of object substitution, again with a simulation showing how an attention control approach allows some of the details of the phenomenon to be explained quantitatively, with results indicating that again the manipulation of awareness of stimuli in the paradigm is to be explained by attention processes inside the CODAM model. In the section on 'Modeling Change Blindness' we consider the phenomenon of change blindness, with similar results. The section on 'Further Paradigms Against an Attention-Basis for Consciousness' has a brief discussion of the results of further paradigms supposedly proving that attention and consciousness are disparate entities, and show how this is not the case. A final discussion concludes the paper.

The CODAM Model

The basic architecture of the model is shown in Fig. 59.1. The modules present arise as those observed by brain imaging of attention paradigms [16], plus an extension by use of engineering control models to include an efference copy buffer. The proposed sites of the various modules of CODAM are given in Table 59.1.

The modules in Fig. 59.1 consist of those for input processing (oriented bar analyzers, etc), for object representations (the object map), a goals module, an inverse model controller (IMC: creating a feedback attention signal to the object map and input modules, so as to move the focus of attention, as biased by the goals module), a working memory buffer site (to hold attention-amplified activity for report and awareness), a corollary discharge buffer (as a copy of the attention movement signal, to give an early prediction of the expected report signal from lower cortices on the buffer working memory), and finally a monitor module (to create an error signal so as to correct for possible attention errors).

There are numerous macroscopic electrical signals in the brain which signal important information processing events. These are the event-related potentials (ERPs) that arise from interactive processing of inputs up and down the hierarchy of modules (in vision this hierarchy involves V1, V2, V3, V4, TEO and TE for the ventral route and V1, V5/MT, LIP for the dorsal one) with a stimulus attempting to reach its sensory buffer being given a boost by the corollary discharge signal. As seen from the application of CODAM to the attentional blink [20] (as discussed further below) these signals give a description both of activity in the various sites as processing time proceeds, as well as how the various sites interact through either excitatory or inhibitory feed-forward or feedback effects. These interactions are enhanced when a number of stimuli are present in a short period. In this condition the excitatory effects from the corollary discharge signal are seen to enhance the growth of the sensory buffer signal, together with the possibility that the inhibition from the corollary discharge signal and the sensory buffer combined inhibit further processing in

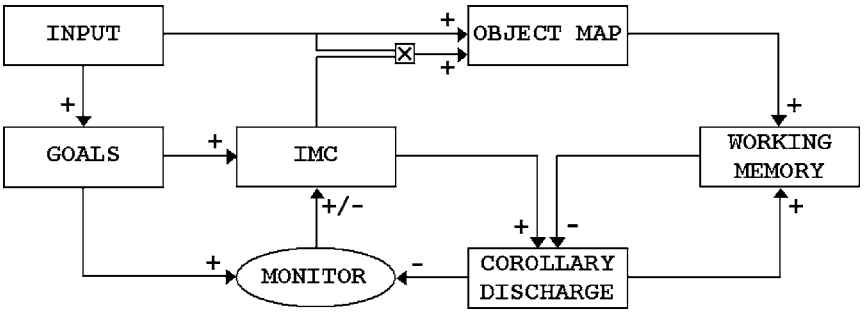

Fig. 59.1 The CODAM model. The various modules are those of engineering control, and discussed in the text and in Table 59.1

Table 59.1 Comparison of variables in engineering control theory and attention

Variable	In Engineering control	In attention	Suggested brain sites for modules
$X(,t)$	State of plant	State of lower level cortical activity	Sensory cortices (occipital, temporal)
X(IMC)	Control signal to control plant in some manner	Control signal to move attention to a spatial position or to object features	Superior parietal lobes; tempero-parietal junction (TPJ)
X(goal)	Desired state of plant	Desired goal causing attention to move	Prefrontal Cortices (DLPFC & cingulate)
X(CD)	Corollary discharge signal to be used for control speed-up	Corollary discharge to speed-up attention movement	Presently unknown, but expected in parietal/prefrontal
X(WM)	Estimated state of plant (as at present time or as predictor for future use) often termed an observer	Estimated state of attended lower level activity (at present time or as predictor for future use)	WM Buffers in posterior parietal and hippocampal areas

the attention movement signal generation module. These interactions are now being observed in the attentional blink paradigm [23].

Modeling the Attentional Blink

The attentional blink requires a subject to be able to recognize a given letter, say, as the first target (T1) in a rapid visual stream of stimuli being presented at about 10 Hz, and then requires the subject to recognize a further second letter target (T2) presented several lags later. The success level in recognizing T2 as the lag is increased from 1 to 10 has a well-established U-shape, with the dip of the U being for a lag of about 3 or for a time gap between T1 and T2 being about 300 ms. A detailed simulation of the attentional blink has been presently recently [20]. This uses the interaction between the P3 of T1 (assumed to be created on the sensory buffer) and the N2 of T2 (assumed created from an efference copy of the attention movement control signal.). The N2 is itself observed to be complex [21, 22].

The results of an extension of the original model of [20] by addition of inhibition from the corollary discharge buffer (WMcd) to the other nodes on the sensory buffer site (WMsens) are shown in Fig. 59.2, for levels of the inhibitory connection strengths of 0, 0.5 and 1.0, As seen from the figures there is progressive change of the activity at various lags as the inhibition is increased. This is particularly clear for the P3 of T1.

We note that the results of Fig. 59.2 can be compared with the recent results of [23], which showed that there is an inhibitory effect, in the case of awareness of T1, from the N2 of T2 to the P3 of T1. This effect is observed most clearly in the above Fig. 59.2c, with inhibitory connection of 1.00. The fall-off of the WMsens

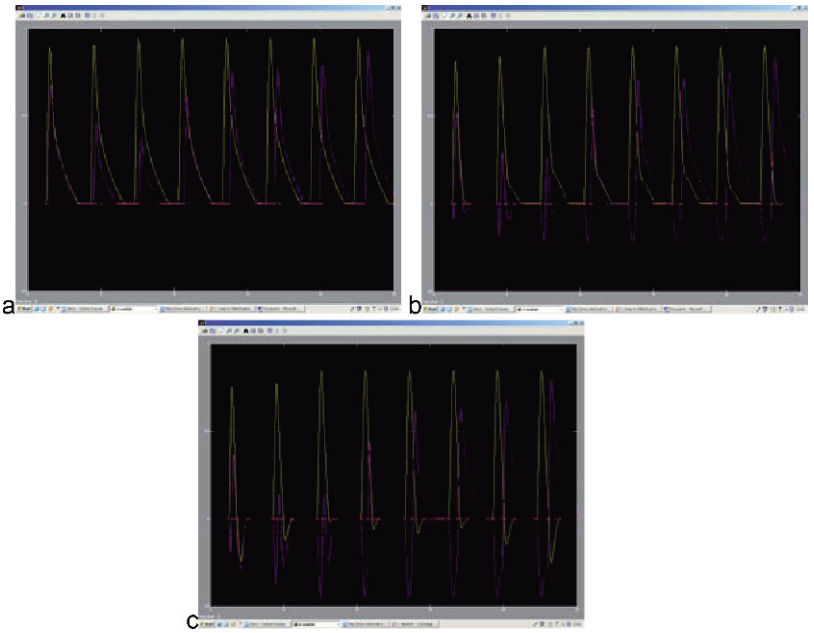

Fig. 59.2 Simulation results from CODAM, showing the P3 of T1 (in yellow, only detection of T1) and of T2 (in magenta: detection of both T1 and T2) for different lags for the presentation of T2, Note the increased reduction of the P3 of T2 as the feedback inhibition from the sensory buffer to the corollary discharge buffer increases, from Fig. 59.2a to b to c. (a) INHIBITION = 0 (Yellow = T1/Magenta = T2), (b) INHIBITION = 0.5 (Yellow = T1/Magenta = T2), (c) INHIBITION = 1 (Yellow = T1/Magenta = T2)

activity of T1 is largest, becoming negative, with largest inhibitory effect of T2s WMcd signal onto it.

Thus we interpret the results of [23] as evidence for the crucial mechanism posited for the Attentional Blink in [20], that of the prior boosting of the sensory buffer activity by that of the efference copy for the same code, with corresponding inhibition from the P3 to all positions on the attention movement signal generator (inverse model controller).

The success of this model supports the view that attention is well described as a control system, in engineering control terms (the basis of the original CODAM model [6, 7, 8, 10, 11, 19]). Moreover the manipulation of consciousness would necessarily need to arise from the internal dynamics of neural processes inside CODAM, and not some further external activation, as evidenced by the correlation of the level of awareness of T2 as the lag between T1 and T2 is varied and the level of activity in the WM buffer module.

Modeling Object Substitution

A related question is that of understanding the results presented on object substitution masking in [24]. When a subject is presented with a masked object, the

experimenters observed an N2 to the object even though it did not reach awareness. This would correspond in CODAM to the presence of the WMcd signal, but with no WMsens signal above report threshold. We simulated this by sending two objects at the same time to the object map, with one of them persisting longer than the other (so as to represent the four dots) The first object was on for 83 ms, the second starting at the same time as the first but either co-terminating or continuing on for another 600 ms (in the object substitution case). In the second case we expected a lower level of WMsens for the first object, although there should be a WMcd signal in both cases. Noise could then be added to obtain more detailed fits. However we tested, with no noise, if the WMsens level is lower for the first (83 ms exposure) stimulus when the second continues on for 500 ms.

The results are shown in Fig. 59.3.

As seen in Fig. 59.3c, in the co-termination phase, the target activity is twice as large as the mask, so leading us to expect awareness of the target in this case. In the delayed offset phase the mask is considerably more active than the target, so awareness will switch to the mask. However in both phases the WMcd activity of the target is very closely the same between the phases. Thus if the N2 for the target can be detected in the co-termination phase, so can it in the delayed phase. That agrees with the results in reference [24]; see also reference [25].

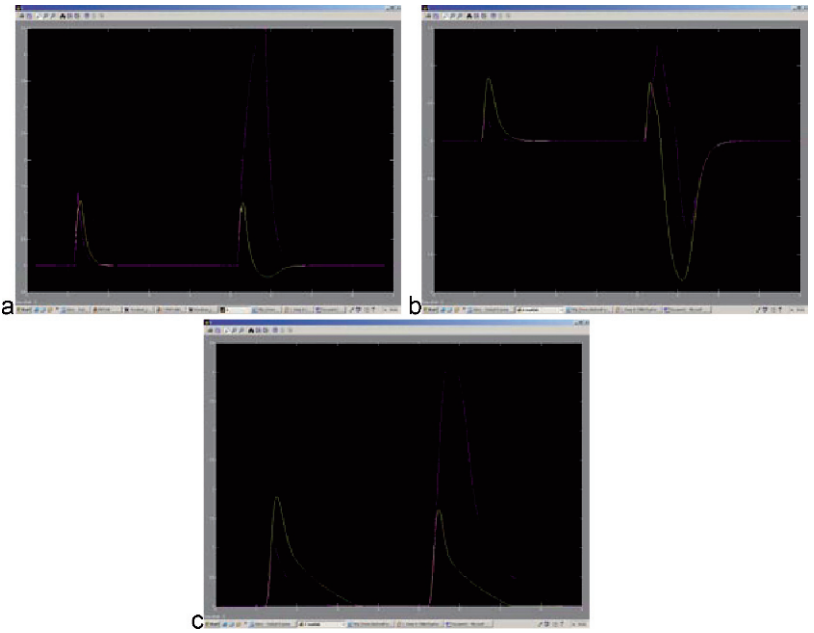

Fig. 59.3 Object map activations in the CODAM-based object substitution paradigm. (a) OBJECT MAP ACTIVATIONS are plotted in the figure (where Yellow = TARGET/Magenta = DOTS). (b) COROLLARY DISCHARGE ACTIV/S (Yellow = TARGET/Magenta = DOTS). (c) WORKING MEMORY ACTIVATIONS (Yellow = TARGET/Magenta = DOTS)

Modeling Change Blindness

Change blindness has been studied by many different paradigms [2]. A number of these involve realistic outdoor scenes but do not give quantitative data relevant to the problem of differentiating between attention and consciousness. However this is different for the CB paradigm of Fernandez-Duque and Thornton [26], see also [27] in which:

I. 8 objects are presented simultaneously, placed equally round a circle (so the spatial map is that of a circle);
II. After 500 ms a uniform grey mask is presented for 200–1500 ms (so that only the dorsal route is uniformly activated, with zero activation in the ventral route);
III. There is re-presentation of objects, with one of them possibly changed (but with no change of positions overall of the objects, nor more specifically of the unchanged objects), until the subject responds as to there being a change of orientation to an object at a cued position..

There are 3 cue conditions:

C1: A cue to where to look for a change of object is presented during the first presentation of the objects (by increasing the activation of the position of the relevant object);
CM: A cue to where to look for a change of object is presented during the presentation of the mask (by again increasing the activation of the position of the relevant object);
C2: A cue to where to look for a change of object is presented during the second presentation of the objects (again by increasing the activation of the position of the relevant object).

The task is to determine, under any of the three cue conditions, if the relevant object at the cued position has been changed during the presentation of the mask. The results for subjects [26] were that accuracy levels respectively for C1, CM and C2 were 100%, 90% and 60%. This corresponds, as expected, to perfect memory for the cued object and its comparison, a slight loss of memory when cued during the mask and a greater loss of remembered objects at the relevant positions when cued after the mask.

A general description of what is happening during the processing for the various cue states could go as follows (in a CODAM-based approach):

C1: Attention is directed to the object at the cued position, and it is held in working (or more permanent) memory until the report stage is reached; this is expected to lead to 100% accuracy, as observed, and already noted in [27].
C2: The subject does not know which object needs to be remembered until report, so can either (a) attempt to store all of the objects as a general picture (they are all expected to be inside the focus of covert attention in the paradigm) or (b) select as many as possible to remember and serially rehearse. In case

(a) there will be degradation of the 'picture' during the mask so that only imperfect recall will occur. In case (b) only of order of 4 objects can be stored, so explaining the 60% level of accuracy observed.

CM: This will correspond to an intermediate position between the cue conditions C1 and C2, and so lead to an intermediate accuracy level between these two, as observed.

We now consider how these cases can be simulated using CODAM. There is progression of increased accuracy as learning occurs in the subjects; that can be considered as arising by the subjects changing from the naïve strategies of (a) and (b) above applied to the direct visual images to coding the images as H or V in a sequence, and learning the sequence of 8 H's and V's. This is a chunking process which should end up with about 100% accuracy through the masking period, as observed in subjects at session 3 in [27]. We will only consider the naïve subject results here.

We have two choices: try to keep to only one CODAM model, representing some fusion of the dorsal spatial processing route or double up the CODAM models, so that one represents the dorsal route, the other the ventral. Connections between these two routes must be established accordingly.

Let us first consider the single CODAM model, especially since this would present a certain economy of architecture. To proceed we consider the single CODAM model as the dorsal route, with the orientations coded in SEF/FEF as possible goals and also in the other modules (IMC, plant map, monitor, buffer WMs). The nodes in each of these maps are doubled up at each spatial point, so that each pair of nodes represents a vertical and a horizontal bar; only one was allowed to be active at any time. The requisite cueing is assumed to create a relevant goal in the spatial prefrontal map, so as to bias the spatial attention signal and thence to amplify by attention the relevant object activity at that position.

The most important assumption to be made in the simulation is the manner in which the cue is used by each subject. For C1, it is assumed that the cue acts in the goal map to hold the orientation of the object at the cued position in the buffer working memory, for use in report after the second stimulus offset. For C2, it is assumed that each subject holds activity representing the whole set of objects in buffer working memory. However the capacity of that buffer is only 4, so not all 8 objects can be held efficiently at once. We suppose that the subject tries to preserve an activation of shapes as observed in the first stimulus presentation period. This could be done by a sequential focusing on each shape, as in case (b) mentioned above, with only 4 stimulus representations being able to be held efficiently. Over numerous tests, on average only 4 would be able to be stored in this manner. However the results of the CM cueing case indicate that more shapes are initially held in the buffer, possibly solely as a general spatial map which has then to be questioned by the cue. This questioning would correspond to modifying the attention signal so as to focus more tightly on only the one cued position. During the mask period there is decay, but if the cue appears early in the mask period there will still be a sharper effect of the shape map (less degradation by noise) and so there will be a

higher level of accuracy. As the mask period continues before the cue is presented in the CM cueing condition, there will be successive reduction of ability to detect a shape above the background noise. Finally in the final period the C2 cue will only have 4 stimuli to be able to pick out, as corresponds to the known capacity of the buffer. The alternative strategy (of case a) mentioned earlier for C2) uses the strategy of the subject to rehearsing the orientations of as many as possible of the bars, so as to have those still available for inspection when the cue finally comes on in the stimulus period 2.

What arises from this discussion is that there could be a continued representation on the WM sensory buffer from all the stimuli having been attended to in the stimulus 1 period, although the amplification by attention would be lower on the object map, hence a lower WM buffer activity, due to the increased competition between the objects on the IMC. There would also be increased competition on the WM buffer due to WMcd competing inhibition onto the WM buffer amongst the various object nodes (either of these competitions being a source of the capacity limit of 4). The WM buffer representation will continue through the rest of the mask period, and so be able to be used in the stimulus period, or questioned during the mask period. The resulting decay with time of the cue is richly explored experimentally in [27], and a similar rich analysis of the simulation results is possible to compare with this data.

The alternative architectural approach is to take two CODAM models, one for the dorsal and one for the ventral routes, as duplicates of the circuits of Fig. 59.1. The dorsal route would simply code for the 8 positions of the bars round a circle; eh ventral route would code for the orientations of each of those objects Thus the ventral object map would consist of two dedicated nodes, one for a vertical bar, the other for a ventral one. There would be hard-wired connections between the ventral route object map and the dorsal spatial map, so that if a change of orientation occurred during the mask period, this would be implemented by a corresponding change of connections of the object and spatial map. Similar connections could be taken between the buffer WMs for the object and spatial maps, as we report below.

In either architecture, we are most interested in the level of activity in the buffer WM persisting in stimulus period 2 that can be used for report of the orientation of the bar at the relevant cued position. In the single route architecture this will be the activity at the cued position in the single buffer WM at the end of stimulus period 2. For the dual route architecture the relevant activity is that in the cued position in the ventral WM buffer map.

The nature of the task for the subject is to determine if there has been a change in orientation of the bar at the cued position. We assume that the level of the buffer WM for the orientation, in either architecture, gives the memory of the orientation in the first stimulus period. This can then be compared against the actual bar orientation in the second stimulus period, which can be taken from the actual stimulus input. Hence it is the level of buffer WM activity of the orientation for the relevant bar in the second stimulus period which would be expected to determine the level of accuracy of the change detection. However, on being cued, either during the mask period or in the stimulus two period, a subject will be expected to immediately query

what the orientation is of the object at the cued position (where in the stimulus two period, the new stimulus can be 'left out' in the outside world until it is needed in the comparison stage They will then store the result of the query about the old stimulus in some form of rehearsal memory, so as to be available when they prepare to look at the new set of stimuli and compare the new orientation at the cued position with what the orientation they have stored. So the crucial quantity, for each time of cueing, is the maximum level of the old target stimulus, during the mask. The activations during the stimulus presentation (with no stimulus two interference, as corresponds to the above strategy) are shown for various cue times in Fig. 59.4.

Let us repeat the interpretation made of the sequence of curves in Fig. 59.4. It is assumed that a subject, once cued to a position expected to be asked about after the

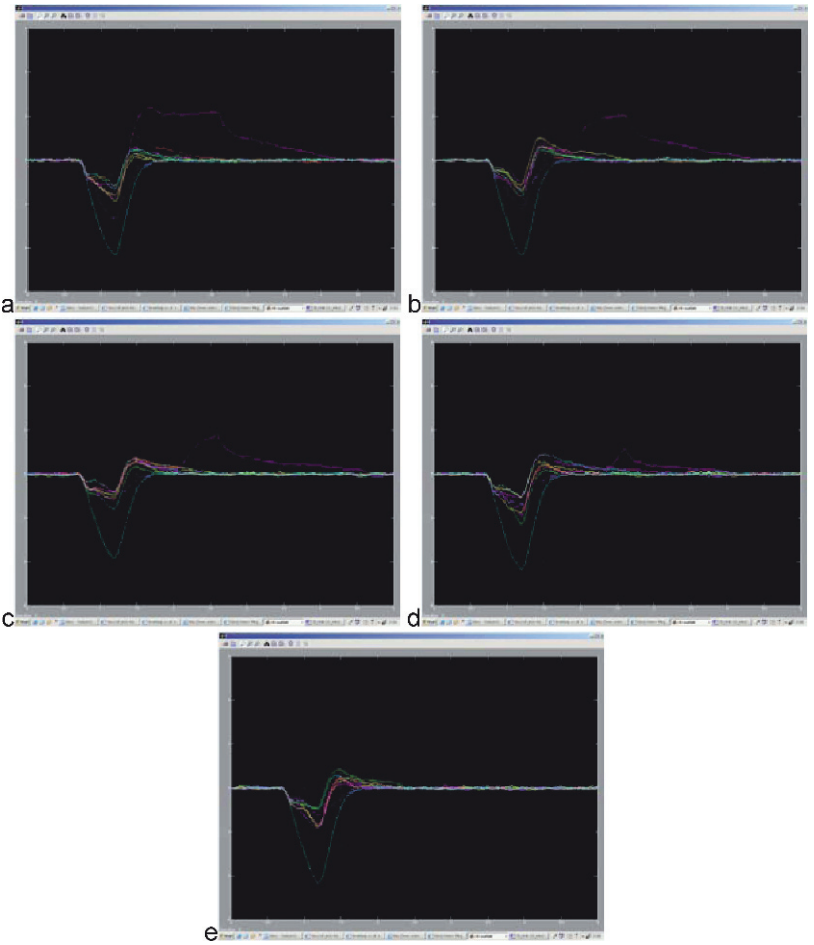

Fig. 59.4 WMsens activations during the paradigm, for different cue times. (a) CUEING AT: 0. (b) CUEING AT: 300. (c) CUEING AT: 600. (d) CUEING AT: 900. (e) CUEING AT: 1200

masking, will query in their sensory buffer which stimulus orientation occurs at the cued position. This will then be remembered, say using an 'H' or 'V' mnemonic. The querying is assumed to be correct with a probability proportional to the maximum height of the cued stimulus activity on their sensory buffer. These values, read off from the figures, are:

0 ms: 2.1; 300 ms: 2.0; 600 ms: 1.5; 900 ms: 1.2; 1200 ms: 0.

Thus there is a decrease of probability (as measured by the membrane potential) of recall of the cued orientation as the cue is presented increasingly later in the mask period. This fits qualitatively with the results of [27], although there is not as great persistence of activity in the WM sensory in the simulation as in the reported experiment (which was shown to last at least for 1800 ms). A more detailed analysis of report probability as determined by membrane potential on the sensory buffer, is needed to attempt a quantitative fit, and will be given elsewhere.

Further Paradigms Against an Attention-Basis for Consciousness

There is also controversy over the question as to attention being THE gateway to consciousness in the light of recent claims [4, 5, 28] that consciousness and attention have a certain degree of independence. The main thrust of our argument here is that attention itself is far more complex than considered in [4, 5, 28]. More specifically attention is known to be present in two forms – sensory and motor [29], it possesses the possibility of multiple foci (at least for vision) [30], and it controls the transfer of laborious sequences of motor actions, for example, to chunked versions, with each chunk being able to be run off automatically, without attention, in different brain sites [31]. It also not only arises from top-down control circuitry but has many components of the top-down circuitry involved in bottom-up 'break-through' [32]. These properties allow us to re-analyse the data presented in [4, 5, 28] so as to show how attention is still to be regarded as a filtering operation before consciousness can arise, such that consciousness occurs only when attention is directed to a stimulus.

For Koch & Tsuchiya, the relevant experimental data is that subjects do possess the ability to report, without increased response time, on the presence or absence of animal figures in stimuli presented simultaneously in the periphery with a central letter task. This clearly depends on the amount prior training undergone by subjects and also the presence of possible multiple attentional foci. Due to lack of suitable data the strong conclusion drawn by [5] need not be accepted, and only the simpler hypotheses that either suitable automatic response patterns had been learnt over the training time [31] or that two attention foci had been used [30]. Either explanation does not require consciousness and attention to be independent.

For Lamme [4] (in which working memory properties of the visual system were claimed to be impossible to explain by use of attention) we refer to the explanation of the relevant data in reference [11], which uses a standard engineering control

approach (that of CODAM as described above in the section on 'The CODAM Model').

The results of the authors in [28] (that increased inhibitory priming of a motor action arose from subliminal commands whilst decreased inhibition occurred in response to reportable commands) can be explained as involving two forms of attention: motor and sensory. The former produces these counterintuitive effects: direct stimulus input to motor command centers in the subliminal case increase motor IOR, whereas the aware stimulus would have been processed in a visual working memory and are expected to activate a different circuit than the direct lower level visual input in the subliminal case, and cause inhibition of IOR effects.

In all cases there is no need to attempt to separate attention from consciousness, and attention is still seen as a necessary condition for consciousness.

Bridging the Bottom-Up Gap

One outstanding question is that of the observational foundation of the attention movement corollary discharge signal. We have already presented evidence from the attentional blink for the presence of this attention copy signal in the case of endogenous or top-down attention movement control (as expected to occur in the attentional blink and as used in the CODAM model). There is not the same level of experimental support for the existence of the attention copy signal in bottom-up attention control. In this there is 'attention capture', say by salient distracters. Thus in the paradigm of [33] a salient distracter (color) causes an initial bottom-up capture of attention (as evidenced by an initial N2pc contra-lateral to the distracter side) before there is a switch of the hemispheric side of this attention capture to be contra-lateral to the target side (some 50 ms later).

In this section we will consider how this and similar data on behavioral effects of varying target-distracter distance [34] can be incorporated in the more complete CODAM model, initially constructed to describe top-down attention movement.

The interaction between bottom-up and top-down attention movement has already been considered in [35]. The paradigm considered was associated with the distracter-devaluation (DD) effect, in which inhibited distracters have been discovered to acquire a lower emotional evaluation than targets (36). In the paradigm modeled in [35] pairs of faces were presented, one in each hemisphere, and the color of the face of a specific gender (M or F) was reported by the subject. A little later a trustworthiness evaluation of either face was then asked for from the subject. The DD effect was observed in that distracter (non-target) faces were evaluated with lower trustworthiness than the target faces.

The simulated model explain this DD effect using a top-down template or bias on the module for face coding, so amplifying the output from the nodes coding for

the target face, and inhibiting those for the distracter. These nodes then feed back activity to a model of V4 with separate nodes coding for either gender together with hermaphroditic nodes coding equally for both. Thus there is also amplification of the relevant target-coding nodes in V4. The subject has no prior information on the hemispheric side of these input stimuli (the M and F faces); there must be a search for the relevant target face (given gender). In the model this is guided by a competition on the spatial posterior parietal cortex map, which excited nodes on the component of V4 in the same hemisphere and inhibits those in the opposite hemisphere. This competition then ultimately singles out the target nodes for the correct gender in V4 and beyond.

The paradigm of [33] has a salient 'pop-out' for a colour distracter, as observed by the earlier distracter-driven N2pc, to be followed by the target N2pc on the opposite side. The switch of attention focus back to the target contra-lateral side of the brain requires some error-correcting mechanism. In our model [37] we insert a monitor that assesses if the target has been amplified most on V4; if not then inhibition of other sites is implemented to prevent distracter processing and resultant errors.

The resulting model is thus close to CODAM, possessing all of the CODAM modules except for an explicit attention copy module and its use in speeding up attention processing, as discussed there. There is also no buffer working memory module (WM), but that is needed for report in any case, so is assumed present in all the models.

In the model there are two main attention signals: top-down and bottom-up. The former is one set up beforehand as a bias on the nodes at intermediate cortical level (say in temporal lobe, such as the face fusiform gyrus or hippocampal place area). Thus the only dynamic signal relevant to the entering into awareness of the target stimulus (say the appropriate gender face in the DD paradigm described earlier) is that arising from the parietal cortical (PPC) spatial attention signal, as a feedback signal to V4 to amplify that input activity on the correct side for the target stimulus.

Our question is thus: is there a copy of the PPC attention control signal sent to any other high cortical sites in order to help speed up access to the buffer working memory module. To answer this question, we need to consider where such WM sites are sited in the brain. In the case of object representations (faces, houses, etc) the appropriate WM module is very likely placed in parahippocampal regions. Thus we need evidence of an earl activation in such sites (say at the time of the N2, and more specifically around the N2pc).

There is in fact good evidence for sources of the N2 being in the hippocampal region. This was discussed in some detail in [11], where the emphasis was on the encoding in the hippocampus as part of the pre-reflective self. However the references cited in [11] also support the existence of sources of the N2 ERP in regions of the parahippocampal gyrus, so allowing for some early neural activations being sited in buffer working memory sites. It is this activity which may also be crucial in providing an ownership experience in the case of bottom-up (and also top-down) attention movement.

Discussion

Summary of Results

Each of the main paradigms of interest has been simulated satisfactorily by our CODAM model; further paradigms have been explored and also found not to pose any serious difficulty to attention being THE basis for consciousness.. Thus we can use the interpretations of the various CODAM modules to begin to tackle the thorny problem of the relation between attention and consciousness. To begin with we consider in more detail the implications of the model in understanding attention.

Implications for Attention

The simulations give more support to the general type of model of which CODAM is a particular case: the ECA (efference copy of attention) type of model. This general class of models is of an engineering control form, with many varieties, as can be seen from the range of motor control models proposed as existing in the brain. But in particular there is support given for the interpretation of the corollary discharge of the attention movement control signal as that observed in part of the N2 signal.

Implications for Consciousness

The ECA-type of models have been interpreted as possessing support for both phenomenal experience of content as well as of phenomenal experience itself (as the sense of the 'inner self'). This latter experience is proposed in CODAM to have arisen from the signal on the corollary discharge buffer, itself being used to stimulate the relevant code on the sensory buffer, and hence leading uniquely to the relevant experience of content. It is this which has been noted as corresponding to the 'immunity to error through misidentification of the first person pronoun [18].

We note the presence of cases of subjects being unaware to change blindness yet sensing it occurred [26]. We note their result that accuracy was highest for cases without awareness when the change occurred close to fixation, as also occurs in trials with awareness. We can attempt to explain these effects by the dragging of attention to the new object by the use of the efference copy of the attention movement signal, without or with access to the sensory working memory buffer being achieved as a result in the two cases (unaware and aware). How would this mechanism lead to the 'sense' of an orientation change, even though it was outside awareness? We can assume that the response to a stimulus is governed by the strength of that stimulus on the object map; if that is amplified by attention movement signal, even though it was not enough to reach the sensory buffer, it would still lead to a more rapid response, and hence to a sense of having observed change blindness.

Implications for the Relation Between Attention and Consciousness

The ECA type models in general have a boosting effect from the efference copy to speed up the access of stimulus activations from lower semantic maps onto their associated buffer for report and use at a cognitive level. They also provide various levels of inhibition of distracters to prevent their access to buffer sites. Overall the process of consciousness creation involves activation of two sites in these ECA type models: ownership on the efference copy buffer, and content on the sensory buffer. The second of these activations is expected to have correlated lower-level activations (possibly through synchronisation or amplitude correlation). The ownership activity is not so created, but may still involve a network of similar sites to provide a sense of unity of self.

In all this dynamical process there is a clear message: attention is necessary for consciousness, where by attention is meant a signal generated by the attention movement controller. Without that there will be no efferent copy, nor any amplification of semantic level activity to achieve access to its sensory buffer.. But with these attention signals there will still not necessarily be consciousness unless both the efference copy and the amplified semantic activity access their appropriate buffers. If various modules involved in this are damaged then the sense of self will be compromised. This can occur in schizophrenia or in AD, as well as in other diseases of a cognitive nature. At the same time the varieties of consciousness (in dreams, under drugs, etc) begin to be explicable in terms of the deconstruction process that CODAM, and more generally ECA type models, allow one to perform on attention and consciousness.

Acknowledgments The author acknowledges support from the BBSRC of the UK for financial support, and the EC IST for support under the grant GNOSYS. He also thanks his colleague Dr N Fragopanagos for considerable work performing the simulations reported in the paper, as well as many discussions about the various topics involved in attention control.

References

1. James W (1890) The Principles of Psychology. London: Macmillan.
2. Mack & Rock (1998) Inattentional Blindness. Cambridge MA: MIT Press.
3. Rensink RA, O'Regan JK & Clark JJ (1997) To see or not to see: the need for attention to perceive changes in a scene. Psychological Science 8:363–373.
4. Lamme V (2003) Why visual attention and awareness are different. Trends in Cognitive Sciences 7:12–18.
5. Koch C & Tsuchiya N (2006) Attention and consciousness: two distinct brain processes. Trends in Cognitive Sciences 11(1):16–22.
6. Taylor JG (2000) A control model for attention and consciousness. Society for Neuroscience Abstracts 26:2231#839.3.
7. Taylor, JG (2002). Paying attention to consciousness. Trends in Cognitive Sciences 6(5):206–210.
8. Taylor JG (2002) From matter to mind. Journal of Consciousness Studies 6:3–22.
9. Taylor JG (2003) Paying attention to consciousness. Progress in Neurobiology 71:305–335.

10. Taylor JG (2005) Mind and consciousness: Towards a final answer? Physics of Life Reviews 2:1–45.
11. Taylor JG (2007) On the neurodynamics of the creation of consciousness. Cognitive Neurodynamics 1(2):97–118.
12. Kawato M (1999) Internal models for motor control and trajectory processing. Current Opinion in Neurobiology 9:718–727.
13. Sabes M (2000) The planning and control of reaching movements. Current Opinion in Neurobiology 10:740–746.
14. Desmurget M & Grafton S (2000) Forward modeling allows feedback control for fast reaching movements. Trends in Cognitive Sciences 4:423–431.
15. Wolpert DM & Ghahramani Z (2000) Computational principles of movement neuroscience. Nature Neuroscience 3:1212–1217.
16. Corbetta M & Shulman GL (2002) Control of goal-directed and stimulus-driven attention in the brain. Nature Reviews, Neuroscience 3:201–215.
17. Nagel T (1974) What is it like to be a Bat? Philosophical Review 83:434–450.
18. Shoemaker S (1968) Self-reference and self-awareness. Journal of Philosophy 65:556–570.
19. Taylor JG (2006) The Mind: A User's Manual. London: Wiley & Son.
20. Fragopanagos N, Kockelhoren S & Taylor JG (2003) A neurodynamic model of the attentional blink. Cognitive Brain Research 24:568–586.
21. Hopf JM, Lucj SJ, Girelli M, Hagnar T, Mangun GR, Scheich H & Heinze H-J (2000) Neural sources of focussed attention in visual search. Cerebral Cortex 10:1233–1241.
22. Ioannides AA & Taylor JG (2003) Testing models of attention with MEG. Proceedings of IJCNN'03.
23. Sergent C, Baillet S & Dehaene S (2005) Timing of the brain events underlying access to consciousiness during the attentional blink. Nature Neuroscience 8:1391–1400.
24. Woodman GF & Luck SJ (2003) Dissociations among attention, perception, and awareness during object-substitution masking Psychological Science 14(6):605–611.
25. Woodman GF & Luck SJ (1999) Electrophysiological measurements of rapid shifts of attention during visual search. Nature 4000:867–869.
26. Fernandez-Duque D & Thorton IM (2000) Change detection without awareness. Visual Cognition 7:323–344.
27. Landman R, Spekreijse H & Lamme VAF (2003) Large capacity storage of integrated objects before change blindness. Vision Research 43:149–164.
28. Sumner P, Tsai P-C & Nachev P (2006) Attentional modulation of sensorimotor processes in the absence of awareness. Proceedings of the National Academy of Sciences of the United States of America 103(27):10520–10525.
29. Rushworth MFS, Paus T & Sipila PK (2001) Attention systems and the organization of the human parietal cortex. Journal of Neuroscience 21(14):5262–5271.
30. McMains SA & Somers DC (2004) Multiple spotlights of attentional selection in human visual cortex. Neuron 42:677–686.
31. Pollmann S & Maertens M (2005) Shift of activity from attention to motor-related brain areas during visual learning. Nature Neuroscience 8(11):1494–1496.
32. Balan PF & Gottlieb J (2006) Integration of exogenous input into a dynamical salience map revealed by perturbing attention. Journal of Neuroscience 26(36):9239–9249.
33. Hickey C, McDonald JJ & Theeuwes J (2006) Electrophysiological evidence of the capture of visual attention. Journal of Cognitive Neuroscience 18(4):604–613.
34. Caputo C & Guerra S (1998) Attention selection by distracter suppression. Vision Research 38(5):660–689.
35. Fragopanagos et al. (2007) Modeling the distracter-devaluation effect (submitted).
36. Raymond JE, Fenske MJ & Tavaosli NT (2003) Selective attention determines emotional response to novel visual stimuli. Psychological Science 14:537–542.
37. Fragopanagos et al. (2007) Modeling the interaction between attention to salient stimuli (in preparation).
38. Kanswisher N & Wojciulik E (2000) Visual attention: insights from brain imaging. Nature Reviews Neuroscience, 1:91–100.

Chapter 60
What Do Infants Infer? – Modelling Simple Cognition

J.G. Taylor and M. Hartley

Abstract We develop a minimal neural architecture for explaining the major features of the developments of an infant of one year old in its powers of inferring about unexpected or expected stimulus movements. We start from a minimal reasoning architecture of internal models and working memory buffer modules, and extend them by addition of suitable long-term memories and a novelty detection system. We argue that these are capable of explaining the observations of Gergely and Csibra on such infants, so helping defuse somewhat higher level cognitive processing structures and enable them to function at a much lower and more realistic level. It makes a cognitive machine defined by these components more powerful than expected.

Introduction

We are interested in building a cognitive machine following processes occurring during the maturation of a child. We have already indicated how we might build a machine which has the reasoning powers of a chimpanzee or corvid [1]. We explore in this paper how this might be extended to include some of the cognitive powers of a one-year old child. It turns out that we can define simple but specific components to be added to the chimpanzee brain which allow this extension, granting it what would seem to be considerable further discriminatory powers.

There is obviously a considerable amount of information processing occurring in the brains of most advanced animals at a non-linguistic level, as indicated by their success in inhabiting and controlling their particular niche domains. It is natural to ask the question as to how much of this non-linguistic processing extends into humans, especially in their early non-linguistic stages up to one year of age. The issue is controversial, with some researchers proposing that there is already at this age a level of mentalistic competence with respect to the theory of mind of others [2, 3]. An interesting counter-answer to such 'theory of mind' powers in one-year

J.G. Taylor
Department of Mathematics, King's College, Strand, London WC2R 2LS, UK
e-mail: john.g.taylor@kcl.ac.uk

R. Wang et al. (eds.), *Advances in Cognitive Neurodynamics*,

old children has been proposed by Gergely and Csibra [4, 5, 6]. These authors suggest that such children possess a 'teleological stance', in that they can infer one of the three components from the other two in the triplet: goal, means action (to achieve the goal), constraints, when observing an actor performing an action on an object in a given constraining environment. Moreover the children possess an understanding of the level of rationality of the agent they are observing embodied in the so-called 'principle of rationality': the watching children expect the agent to perform the means action in the most efficient manner (either as needing least effort or least time to complete; shortest distance may not be most important).

We start the paper by presenting a minimal architecture that the children must possess. This arises from our earlier analysis of animal reasoning powers, which we assume also to be possessed by such children (an assumption we discuss in the section 'The Minimal Brain Architecture'). A detailed discussion of the way that this minimal architecture can explain some of the results of Gergely and Csibra is then presented. Extensions to the minimal architecture are considered and a discussion is then given to complete the paper, with a new slant being given on the results of Gergely and Csibra, that reduces one-year old children's powers to below the level conjectured by the above authors. We conclude that children most especially possess a novelty-detecting predictive system composed of a suitable set of internal models plus a novelty/familiarity detecting system [7, 8] for that set of internal models. There is also an inferential component that has been developed for seemingly autonomous agents as to their possession of goals in their own right. We term this system the 'Interpretive System for Rational Analysis'.

The Minimal Brain Architecture

Certain higher animals have recently been discovered to possess some form of reasoning powers [9, 10]. In particular chimpanzees and New Caledonian crows have been found to be able to perform non-trivial sequences of deduction to work out how to solve simple tasks. Let us consider briefly one of these simple paradigms.

The 'two stick' paradigm involves a chimpanzee which is presented with a short and a longer stick and a food reward set beyond the reach of the animal (or when it possesses the shorter stick). If the animal can gain the longer stick then it could reach the food reward. However, it can only reach the longer stick by using the shorter stick (within its reach) to pull the longer stick towards itself.

Our previous work on the higher cognitive powers of animals [1] able to solve these paradigms suggested that there were periods when the animal was stationary and was 'reasoning'. During these reasoning periods the animal used a set of internal forward and inverse models to 'reason' how best to achieve the required food reward. In the process we proposed that the animal employed a system of reward manipulation, allowing it to set up new sub-goals considered worth working towards before the final food reward goal could be obtained.

We thus assume that children of one year of age also have such reasoning powers as being able to solve the two stick paradigm (although we do not know of any tests

made to determine that). Beyond this we assume that such children possess at least a similar architecture to that of chimpanzees and crows which we conjectured [1] were used in the reasoning tasks we just discussed. Thus in details we assume these children posses a set of inverse control models for arm motor control as discussed in [1], representations of goals and rewards.

These models need to be expanded to include an associated working memory buffer site to allow temporary storage of the results of reasoning before they are actually put into practice. Such working memory buffers need to be trained on the material they are required to store over short periods of seconds or so. The material has also to be specified. It will certainly include goals, represented by object stimulus representations, as considered by [11] and many others since then. There is experimental support for the short-term holding of high level motor plans in pre-motor cortex(PMC) [12], thus we might assume that there is a buffer working memory for motor plans in PMC at least.

Explaining the Teleological Stance of Children: Beyond Lower Animals?

Let us now consider how we might use the above architecture to explain the results of Gergely and Csibra cited earlier. We begin with a brief summary of these results.

Firstly (and mainly) there is a class of results based on extended looking of children of one year of age at the motion of a small circular stimulus across a screen in the presence or absence of an obstacle, as shown in Fig. 60.1.

There are two classes of children being considered in the paradigm of Fig. 60.1: the experimental and the control group. The former are exposed to the 'rational' stimulus movement, where the small circle moves in such a way as to most effectively jump the vertical barrier between it and the large circle (to be regarded as the goal of the small circle's motion). The control group is exposed to a similar trajectory of the small circle, including the vertical jump in the middle of its trajectory, but now in the absence of the vertical barrier requiring this jump. On being exposed to either this old but irrational action or the movement of the small circle in a straight line to the large one, in the absence of the vertical barrier (these two trajectories being termed the 'test' trajectories), the experimental group spent more looking time at the old irrational trajectory compared to the rational straight line movement, whilst the control group looked equally long at both test trajectories.

How can a minimal architecture based on internal models as described in the section, 'The Minimal Brain Architecture' begin to explain these results? We propose that the exposure of either the experimental or control group causes them involuntarily to train the relevant internal models to capture the information presented in the initial stimulus exposures. Thus for the experimental group there is an internal IMC (inverse model controller) which allows the child to produce, from the pair of initial and final state the required trajectory of the moving small circle. We can simplify the more complex curved trajectory necessary to pass the obstacle by reducing it to

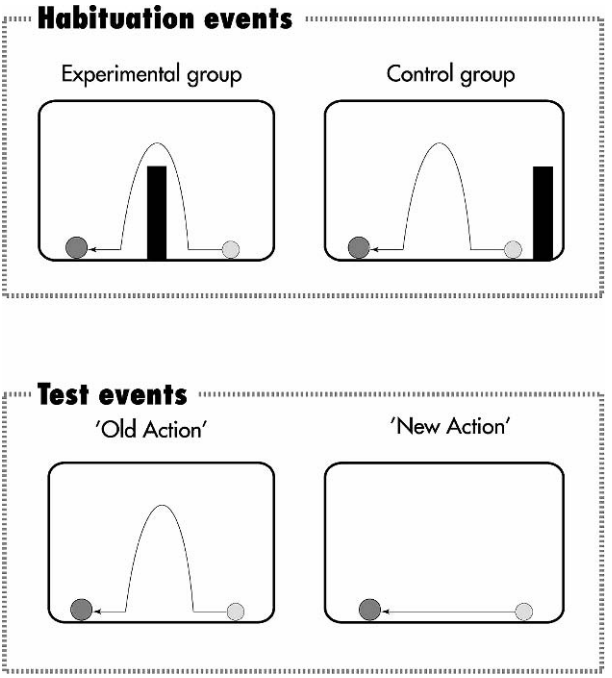

Fig. 60.1 Explanation of the results contained in the text

two linear movements, one from the start position to the top of the obstance, and a second from there to the goal position.

Given the experimental group of children had experienced the trajectory encoded by their created internal IMC model what should their responses be to the test stimuli? The 'irrational' test case (involving a jump in the trajectory of the small circle at the place previously occupied by the vertical obstacle but now empty) caused the children longer looking compared to the original experimental exposure. The rational (straight line) trajectory did not cause such longer looking (although this is not explicitly stated: did they look longer at the rational test case than the original experimental case?). Under the assumption of longer looking at the irrational test case than either the rational one (which they may already have been exposed to in the real world) or the experimental stimulus, it would appear that the difference between the various stimuli is that of the novelty of the irrational test case (or lack of exposure to this).

Returning to the original paradigm of Gergely and Csibra cited above we now consider how we might explain the response of the control group to the two sets of stimuli (irrational and rational). According to the results presented in [13] there was no differential looking pattern in the children's responses. This can be explained, using the assumed architecture of the section 'The Minimal Brain Architecture' by the fact that the control group had been exposed to the irrational trajectory, as well as (we assume) the linear (rational) test trajectory at earlier times. Thus these would

possess no novelty and hence not cause any differential looking times between the two sorts of trajectory; these control children possessed both an IMC trained for both situations.

The overall conclusion we draw from the above considerations is that the various looking times for the paradigm of Fig. 60.2 of [13] can be explained by a set of internal models, some already present, others created by leaning through exposure to the stimuli of the paradigm. All that is needed to explain these results in detail is a further extension to add in some novelty detection system, as we will consider later.

Modelling the Simple Paradigm

We can construct a simple model using our suggested minimal architecture, incorporating the inputs to the system in the forms of an inferred goal, constraints, and the observed action, and the internal processing system based around the IMC.

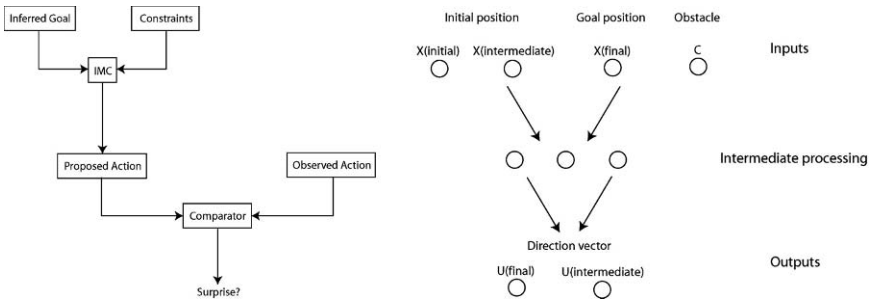

Fig. 60.2 Simple architecture for solving the trajectories problem

The left panel shows the overall modular architecture of the system. We assume a visual system that extracts information from the scene, and processing sufficient to be able to identify the goal (both from initial and target positions), and the constraints. This information is then fed to the inverse model, which produces an expected action, in the form of a trajectory – either the straight or indirect path. This is compared to the observed trajectory, and if a mismatch occurs, surprise is generated.

The right panel shows details of the IMC – an inputs layer with four nodes representing the possible start and end positions, and the presence of the obstacle. The outputs layer consists of two nodes – one of two direction vectors for either the direct or indirect path. There is a middle 'hidden' layer with three nodes (to allow more general training to be done). The network can be trained via the backpropagation algorithm, using inputs that represent either the control or experimental groups of the experimental paradigm. We can then measure the 'surprise' generated by comparing the strength of the model's predicted output trajectory node activation with the demonstrated trajectory.

Early results from the simulation show that the simulated "experimental group" that habituate to the situation involving an obstacle, show larger surprise values for the old action event, whereby the indirect trajectory is used despite lack of a barrier than the 'control group'. These results are to be examined in more detail.

Further Paradigms of Gergeley and Csibra

The next of these paradigms was presented in figure 3 of [13]. Beside the one already considered above there is one involving covering the area under the jump of the small circle so that the presence of the obstacle causing that jump cannot be determined by the child. Here children, after removal of the cover, looked longer at the case where there was no obstacle causing the jumping than if there were. Such a result cannot be explained solely by the creation of internal models. The child had to create an internal model with structure that was consistent with the curved structure of the trajectory, and appeared to explain it. In that way the absence of a vertical barrier would be unexpected, after removal of the cover.

Let us consider ways that a child could try to puzzle out what was being covered up:

(1) It assumes, from prior knowledge, that there is an obstacle present, which is causing the trajectories curvature; this prior knowledge would lead to a corresponding IMC, but one in which there is a slot which is only filled by the observation of a suitable obstacle on removal of the cover. Otherwise the complete trajectory would be novel as far as its predictability by an IMC is concerned.
(2) It makes a guess as to the presence or absence of such an obstacle. However this guess would have to be consistently that there is an obstacle present across all children in the group, so is rather unlikely.

Thus it would seem that there needs to be extra knowledge (from long-term-memory) as to the nature of trajectories of small objects in movement in the presence of obstacles. Such knowledge is compatible with what would be expected for such children, and will be assumed here. Thus the results of figure 3C can be explained by the extension of the reasoning system to both a novelty detector and a set of long-term memories of previously observed trajectories in natural situations (footballs, tennis balls, etc in movement).

There is also a further paradigm tested as part of the experiments associated with figure 3 of Gergely and Csibra: that of figure 3B, where a larger moving ball either does or does not fuse with a smaller one it seems to be pursuing on the other side of a partial barrier, which the larger ball has to detour round to meet up with the smaller one. Here the child is longer looking at the case when the larger ball does not fuse with the smaller one. We can explain this in terms of a suitable predictor created in the child's brain as a forward model which takes account of the apparent

pursuit process of the smaller ball by the larger one. This leads to the child being surprised when the larger ball ignores the smaller one, when it could fuse with the smaller one on the other side of the barrier. Again the child is to be assumed to possess long-term memories appropriate for it to expect the larger circle to be in pursuit of the smaller one in order to fuse with it.

In all then, the further extension seems to be, beyond the ability to create internal models and the novelty detector addition, the ability to use past memories to impart agency properties to small moving objects. Thus the larger circle pursuing the smaller one is able to be endowed with a goal: 'Catch the smaller circle and fuse with it'. In the case of the cover over the obstacle, the child is assumed to be able to extract from its memories cases of obstacle avoidance causing swerving motion of an agent.

For the case of the paradigm of figures 4 and 5 of [13], we can assume that the experimental group, who were exposed to both effortful and effortless trajectories with no alternatives, created what we will call the IMC (effortful/no alternative). The control group, on the other hand, being exposed to both effortful and effortless trajectories with a lesser effort but a curved path alternative, created the IMC (effortful/longer effortless path not used). The test stimulus trajectories of shortest path or least effort would be expected to be looked at longer:

(a) The shortest path cases for the experimental group, since they have not seen the control alternatives, and so will be expected (using past memories of trajectories created with least effort) to look longer at the shorted path case as a novelty compared to any past IMCs or memories of only shortest paths;
(b) The least effort cases for the control group, since the least effort cases have not been created from the habituation events, so do not have associated IMCs and hence will cause longer looking due to their novelty.

Therefore this set of results can be explained using the above architecture and its extension as later to a novelty detector system.

Finally the results of the discussion in section 7 of [13] on the emulation versus imitation of observed actions can be analysed as follows. The paradigm considered is of an agent who is observed to strike a box in front of them with their forehead so as to cause a light to go on. The extension of this paradigm by [5] was to use two separate cases: a hands-free paradigm and a hands-full case. The former required the agent to have performed an action (drape a blanket round their shoulders) and then released their hands; the latter uses a similar paradigm with the blanket, but requires the agent to continue clutching the blanket whilst striking the box with their head.

This can be understood in terms of the associated IMC created in either case: IMC (free) or IMC (full). In the case of IMC (free), then the reason why the agent did not use their hands is unknown but assumed exists, by the child. Hence it also will tend to create a similar IMC (free), using the head as the main instrument to strike the box. In the hands-full case the IMC created in the child is expected no to include the observed constraint, since it is not one the child has constraining it.

Thus the child will use any means, mainly with their free arms, to strike the box. This fits as observed. It uses that IMCs are created using the constraints observed by the child, and also inferred by the child by using its memory as to why such things could occur and be relevant.

Thus, beyond novelty detection amongst its internal models, the child is expected to be able to ascribe goals to moving objects as they might to moving pets they observe. Whether or not they ascribe autonomy to the moving objects is unclear, but may not be needed. . It also needs to be able to incorporate constraints into the IMC constructed (as in the case of the box-striking paradigm). This is all eminently reasonable, given the environments in which a child of one lives.

Extensions Needed

We have thus seen that the following three components of the brain architectures for one-year olds are needed beyond those of 'The Minimal Brain Architecture' section above:

(1) A novelty/familiarity detector system for internal models;
(2) An agency ascription system for apparently autonomously moving objects, allowing at least goal ascription to the moving object.
(3) Presence of long-term memories that allow the inferring of various types of obstacles to cause trajectories to be non-straight, or cause non-immediate usage of the simplest means at the child's disposal.

In [8] we developed a model of a set of novelty and familiarity detectors in the hippocampus which possess unique properties. This is based on recent experimental data obtained from deep intercranial electrodes placed in the hippocampal region of patients about to undergo surgery for intractable epilepsy [7]. The experimenters found two typed of neuronal response: novelty detectors (ND) which responded well to novel stimuli on their first showing but only to the new novel stimuli on a later showing, and familiarity detectors (FD) which had no response to initial novel stimuli, but were activated by any now-familiar stimuli. In [8] the model uses both inhibition and disinhibition, together with a suitable function on the output of the prefrontal object representations, to create the separate novelty and familiarity detectors with the observed properties.

Such a novelty system could serve to provide the relevant signal to cause longer looking in a child until it has learnt the stimuli previously novel to it. Thus the ND units may act so as to alert the attention system of the child to attend to the stimulus and hence turn off the ND units and activate the FD units. The simplest way that the ND units could be sensitive to the appearance of an unexpected stimulus or stimulus movement would be if there was no appropriate model allowing for prediction of the motion. For then no forward prediction could be made, so that the stimulus at some point would appear novel. As such it will activate the ND system, and so bring about

longer looking time. This would last until a suitable forward model or predictor had been learnt, by when the stimulus would only activate the FD neurons, not any ND neurons.

A Final Discussion

Do the extra components require the functionality posited by Gergely and Csibra? This is very likely not necessary. What we have required above

are the two components at the end of the previous section. What Gergely and Csibra proposed were:

(a) Rationality (picking out the most efficient trajectory of moving object), involving assessment of effort, etc.;
(b) Teleological representation of goal-directed actions, allowing inference by the child of any one of the triplet of goals, means-directed actions to the goals, constraints producing the specific actions.

The rationality was deduced from the longer looking times at 'irrational' object trajectories. Our analysis has shown that these longer times can be explained by the difference between looking times for novel and familiar situations.

The teleological representations were deduced from the inferential powers of children in the presence of trajectories of a variety of sorts arising from the cases of absence of visual stimuli representing one or other of goal, means action and constraints. In particular:

(1) Deduction of the goal of an action (as in figure 3B) by the use of a suitable forward model;
(2) Deduction of the action to achieve a known goal (as in figure 3A) by the use of an existent IMC;
(3) Deduction of the constraints imposed on an action (as in figure 3C) is explained by the use of a combination of internal models and suitable memory. The latter provide a memory of how the trajectory was arrived – what constraint was present when observed in the past.

Finally we come back to the question as to the relevance of our analysis to the problem of creating a cognitive machine. Cognition has many components, but one of them is certainly reasoning. However we know that a child develops beyond understanding only about the mechanics of the world and being able to reason mechanically. A 1-year old child apparently possesses greater powers, especially possessing powers associated with the interesting 'teleological principle' and the 'rational principle' of Gergely and Csibra. However these principles, besides leading to remarkably advanced behaviour, are somewhat mystical in character. To understand them more fully we have resorted to attempting to construct a machine which

would have these powers. To achieve that we had to add to the components for reasoning (internal models and short-term-memory) a novelty component (causing further looking at unexpected events) as well as further memory components. With these extras we could begin to explain these two principles, as shown in the paper. There may be other solutions, but we suggest our proposal has an attractive incremental property about it. But only experiment can finally decide.

References

1. Hartley, M. and J.G. Taylor, *Neural models of reasoning in animals*. Submitted. 2007.
2. Call, J. and M. Tomasello, *A nonverbal false belief task: the performance of children and great apes*. Child Dev, 1999, **70**(2): pp. 381–95.
3. Keleman, D., *The scope of teleological thinking in preschool children*. Cognition, 1999, **70**: pp. 241–272.
4. Gergely, G. and G. Csibra, *Teleological reasoning in infancy: the infant's naive theory of rational action. A reply to Premack and Premack*. Cognition, 1997, **63**(2): pp. 227–33.
5. Gergely, G. and G. Csibra, *Teleological reasoning in infancy: the nai;ve theory of rational action*. Trends Cogn Sci, 2003, **7**(7): pp. 287–292.
6. Csibra, G., *Teleological and referential understanding of action in infancy*. Philos Trans R Soc Lond B Biol Sci, 2003, **358**(1431): pp. 447–58.
7. Rutishauser, U., A.N. Mamelak, and E.M. Schuman, *Single-trial learning of novel stimuli by individual neurons of the human hippocampus-amygdala complex*. Neuron, 2006, **49**(6): pp. 805–13.
8. Taylor, N. and J.G. Taylor, *A novel novelty detector*. ICANN 2007, accepted, 2007.
9. Weir, A.A., J. Chappell, and A. Kacelnik, *Shaping of hooks in New Caledonian crows*. Science, 2002, **297**(5583): p. 981.
10. Limongelli, L., S.T. Boysen, and E. Visalberghi, *Comprehension of cause-effect relations in a tool-using task by chimpanzees (Pan troglodytes)*. J Comp Psychol, 1995, **109**(1): pp. 18–26.
11. Baddeley, A., et al., *Dementia and working memory*. Q J Exp Psychol A, 1986, **38**(4): pp. 603–18.
12. Schwartz, A.B., D.W. Moran, and G.A. Reina, *Differential representation of perception and action in the frontal cortex*. Science, 2004, **303**(5656): pp. 380–3.
13. Gergely, G., *What should a robot learn from an infant? Mechanisms of action interpretation and observational learning in infancy*. Connection Science, 2003, **15**(4): pp. 191–209.

Chapter 61
The Time Dimension for Scene Analysis

DeLiang Wang

Abstract Although humans perform scene analysis with little effort, automatic scene analysis remains a tremendously challenging problem. One reason is the binding problem, which refers to how the coherence of a pattern as a large collection of features is represented in a neural network. I argue that introducing the dimension of time is essential for solving the binding problem. I will discuss oscillatory correlation as an adequate representation theory to address the binding problem. To turn this representation theory into an effective computational mechanism requires solutions to several problems in oscillatory dynamics. LEGION networks, which can rapidly synchronize an assembly of locally coupled oscillators and desynchronize multiple oscillator assemblies, have successfully solved these problems. LEGION has been applied to a variety of tasks in visual and auditory scene analysis, and this presentation will show several such examples that demonstrate the computational utility of oscillatory correlation theory.

Introduction

A remarkable accomplishment of the perceptual system is its scene analysis ability, which involves two basic perceptual processes: The segmentation of a scene into a set of coherent patterns (objects) and the recognition of familiar patterns. Closely related to scene segmentation are figure-ground separation, which emphasizes segmentation of one object from the rest of the scene (background), and perceptual organization. Although humans perform scene analysis with little effort, automatic scene analysis is a tremendously challenging problem despite many years of intense research in neural networks, and related fields such as computer vision and computational audition.

D. Wang
Department of Computer Science and Engineering and Center for Cognitive Science, The Ohio State University, Columbus, OH 43210-1277, USA
e-mail: dwang@cse.ohio-state.edu

R. Wang et al. (eds.), *Advances in Cognitive Neurodynamics*,

This presentation focuses on scene analysis in the field of neural computation, with emphasis on scene segmentation as pattern recognition has been a central theme of neural network research since the very beginning [1]. Compared to recognition, less research has been devoted to scene segmentation. The importance of scene segmentation is, however, increasingly recognized as pattern recognition is being applied in real-world situations.

In his classic book more than forty years ago, "Principles of neurodynamics," Frank Rosenblatt [2] summarized a list of problems facing the study of perceptron theory at the time. Two problems among the list "represent the most baffling impediments to the advance of perceptron theory" (p. 580). These are the problems of figure-ground separation and the recognition of topological relations. The development of neural networks in the ensuing years has largely validated the foresight of Rosenblatt. In particular, major progress has been made in the understanding of error-correction procedures for training multi-layer and recurrent perceptrons. On the other hand, progress has been limited in addressing Rosenblatt's two chief problems. One reason that scene analysis is particularly difficult for neural networks is the binding problem, which refers to how the coherence of a pattern as a large collection of features is represented in a neural network. I will discuss two theoretical proposals to the binding problem. One proposal is the grandmother-cell representation, which claims that individual neurons can become so selective as to represent individual objects. Multiple objects in a scene would be represented by the coactivation of multiple cells [3]. Another proposal, known as temporal correlation [4], encodes the binding by the correlation of temporal activities of feature-detecting cells. A special form of temporal correlation is oscillatory correlation, where basic units are neural oscillators.

This presentation argues that introducing the dimension of time is essential for a systematic attack on Rosenblatt's challenge, which is intrinsically related to the binding problem. Oscillatory correlation offers an adequate representation theory to address the binding problem. To turn this representation theory into an effective computational mechanism, however, requires satisfactory solutions to several problems in oscillatory dynamics. The development of Locally Excitatory Globally Inhibitory Oscillator Networks (LEGION), which build on relaxation or other nonlinear oscillators, has successfully solved these problems [5, 6]. LEGION networks can rapidly synchronize an assembly of locally coupled oscillators and desynchronize multiple oscillator assemblies. LEGION dynamics provides a solution to the well-known Minsky-Papert connectedness problem [7, 8], which represents an important example of the binding problem. LEGION has been applied to a variety of tasks in both visual and auditory scene analysis, and this presentation will show several such examples that demonstrate the computational utility of the oscillatory correlation theory.

I will also discuss the neurobiological relevance of the oscillatory correlation theory. Finally, the time dimension is argued to be necessary for versatile computation.

The details for much of this presentation can be found in Wang [9].

References

1. M.A. Arbib, Ed., Handbook of brain theory and neural networks. 2nd ed., Cambridge, MA: MIT Press, 2003.
2. F. Rosenblatt, Principles of neural dynamics. New York: Spartan, 1962.
3. H.B. Barlow, Single units and cognition: a neurone doctrine for perceptual psychology, Percept., vol. 1, pp. 371–394, 1972.
4. C. von der Malsburg, The correlation theory of brain function, Internal Report 81-2, Max-Planck-Institute for Biophysical Chemistry (Reprinted in Models of neural networks II, E. Domany, J.L. van Hemmen, and K. Schulten, eds., Berlin: Springer, 1994), 1981.
5. D. Terman and D.L. Wang, Global competition and local cooperation in a network of neural oscillators, Physica D, vol. 81, pp. 148–176, 1995.
6. D.L. Wang and D. Terman, Locally excitatory globally inhibitory oscillator networks, IEEE Trans. Neural Net., vol. 6(1), pp. 283–286, 1995.
7. M.L. Minsky and S.A. Papert, Perceptrons. Cambridge, MA: MIT Press, 1969.
8. M.L. Minsky and S.A. Papert, Perceptrons (Expanded edition). Cambridge, MA: MIT Press, 1988.
9. D.L. Wang, The time dimension for scene analysis, IEEE Trans. Neural. Net., vol. 16, pp. 1401–1426, 2005.

Chapter 62
Implications for Psychiatry of a Thermodynamic Model of Brain Operating Far from Equilibrium

Walter J. Freeman

Abstract Phenomenologists hold that perception works by the creation of meaning through chaotic dynamics that forms hypotheses about the environment, and that adapts through learning. Experimental evidence for creative thermodynamics in brains is briefly sketched. The explanation is offered that brains, being finite systems, work this way in order to cope with the infinite complexity of the world. All that brains can know is the hypotheses they construct and the results of testing them by acting into the environment, and learning by assimilation from the sensory consequences of their actions. The process is intentionality, using the action-perception cycle. The cost is the progressive isolation of individuals. Socialization and the acquisition of shared knowledge require emergence of new personality structure by self-organization through chaotic dissolution of existing structure. Dissolution is most clearly seen in crisis situations as regression to earlier stages of development. A thermodynamic model of this unlearning is proposed.

Keywords Action-perception cycle · dissipative structures · ECoG electrocorticogram · non-equilibrium thermodynamics · phase transition · reinforcement learning · self-organized criticality · unlearning

Introduction

The identification by the Young Turks in the middle of the 19th century of the action potential as an electrochemical wave revolutionized neurobiology. The conception of the transmission of animal spirit or of élan vitale was replaced with a conception of energy or Newtonian force in the brain of the kind that was shared by all other forms of matter, not just living things. The subsequent discovery by Helmholtz of the First Law of Thermodynamics, the conservation of energy, profoundly impacted the formulations of brain dynamics by neurobiologists, neurologists, and psychiatrists.

W.J. Freeman
Department of Molecular & Cell Biology, University of California at Berkeley, CA 94720, USA
e-mail: dfreeman@berkeley.edu

R. Wang et al. (eds.), *Advances in Cognitive Neurodynamics*,

The reconceptualization of brain dynamics in terms of the flows of nerve force culminated in 1895 with Freud's publication of "The Project of a Scientific Psychology":

> "This approach is derived from clinical observations concerned with 'excessively intense ideas' in hysteria and obsessional neurosis. . .. What I have in mind is the *principle of neuronic inertia*, which asserts that neurones tend to divest themselves of quantity (Q). . .. We arrive at the idea of a 'cathected' neurone (N) filled with a certain quantity. . .. The principle of inertia finds expression in the hypothesis of a *current*, passing from the dendrites to the axone. . .. The secondary function [memory] is made possible by supposing that there are *resistances* in contacts between the neurones which function as barriers. The hypothesis of 'contact-barriers' is fruitful in many directions" (pp. 356–359).

Freud saw very clearly the psychiatrists' need for a firm foundation in normal physiology and dynamics of brain function to explain nervous and mental disorders. Yet he experienced doubts following his euphoria. In a letter to Fliess on May 25, 1895 Freud wrote [1]:

> "I am tormented by two aims: to examine what shape the theory of mental functioning takes if one introduces quantitative considerations, a sort of economics of nerve forces; and, second to peel off from psychopathology a gain for normal psychology. Actually, a satisfactory general conception of neuropsychotic disturbances is impossible if one cannot link it with clear assumptions about normal mental processes."

By 1898 Freud's optimism had completely evaporated. On September 22, 1898 he wrote to Fliess:

> "I am not at all in disagreement with you, not at all inclined to leave psychology hanging in the air without an organic basis. But apart from this conviction, I do not know how to go on, neither theoretically nor therapeutically, and therefore must behave as if only the psychological were under consideration. Why I cannot fit it together [the organic and the psychological] I have not even begun to fathom."

Clearly Freud lacked the requisite tools for his Project, yet he had unprecedented powers of imagination in conceiving brain mechanisms and describing them by inventing a form of symbolic logic that has been codified by Freudians into the quasi-religious dogma of psychoanalysis. The most specific cause of his failure was the fact that nerve energy and nerve force are not conserved. A classic example comes from the work of the founder of British and American neurology, J. Hughlings Jackson [2]:

> ". . .we speak of the dynamics of the nervous system. . .. A normal discharge starting in some elements of the highest centres overcomes the resistance of some of the middle, next the resistance of some of the lowest centers, and the muscles are moved.". . . "A fit of epilepsy is an excessive caricature of normal physiological processes during what is called a voluntary action. . .. We have, in the case of 'discharging lesions,' to consider not only the quantity of energy liberated, but the rate of its liberation."
>
> "*Resistances* will be considered later." (pp. 42–44)

Years later a note initialed by JHH in his hand on the margin of his author's copy by the editor of his selected works:

> "No more of this was published."

The concept of neural resistance or of psychological resistance can readily be related to Freuds's "contact barriers", 2 years later named "synapses" by Foster and Sherrington [3], but use of the concept of "electrical resistance" was only a metaphor. The misidentification of resistance in a physical system with attenuation or inhibition at synapses constituted what Gilbert Ryle [4] termed a "category mistake"; it led to the collapse of the entire enterprise. Psychiatry splintered into competing schools and even into the black-box mentality of behaviorism, a catastrophe from which it has yet to recover.

We now have the necessary tools – nonlinear dynamics, nonequilibrium thermodynamics, random graph theory, and quantum field theory – and can resume where Freud abandoned his project. My approach is to treat the brain as a thermodynamic system that is self-stabilized at criticality, as this is defined in a physical medium such as water. The dynamical phase space of the brain as a medium can be conceived as having multiple compartments, the most salient and experimentally accessible being three phases: receiving, transmitting, and seizure. These phases are separated by phase boundaries. In the phase diagram of water the phase boundary between liquid and gas terminates at the critical point. This is the point at which all frequencies and wavelengths coexist, where the system has maximal flexibility and information content. That point in brain thermodynamics is hypothesized to be the critical point at which brains self-stabilize.

Owing to the fact that brains are open systems with throughput of energy and matter, the static 19th century phase diagram is inappropriate. Two new state variables are introduced in order to describe nonequilibrium brain dynamics. Temperature, which in any case in homeotherms is kept constant, as a measure of energy is replaced by power as a time-varying measure of the rate of dissipation of free energy as heat. Entropy that is estimated by pressure or volume, likewise held constant in brains, is replaced by a measure of the rate of increase in order (negentropy). In thermodynamic systems operating far from equilibrium the property of self-organization emerges in the form of dissipative structures [5] that feed on energy. Brains maintain their background activity by mutual excitation, which is self-stabilized by refractory periods at all levels of arousal, as demonstrated by calculating the feedback gain and showing that it is maintained at unity, giving steady state excitatory output.

In a demonstration of the promise offered by these new tools, the concept of intention will be described as the outward thrust of the body controlled by motor systems that are embedded in massive positive feedback among cortical excitatory cells. Evidence will be cited that the maintenance of this background is in significant part by gaba-ergic neurons that are loaded with chloride ions under the modulation by histamine, which makes the action of GABA excitatory by opening the GABA-A receptors to the outflow of chloride, resulting in the depolarizing action of GABA [6]. It is noteworthy that the benzodiazepines are antihistamines, so it is postulated that their anxiolytic action is due to the reduction in the level of output from mutual excitation, which can be modeled in terms of thermodynamics as a reduction in the rate of dissipation of free energy and a consequent reduction in the degree of order or negentropy.

Numerous other examples in addition to arousal (motivation, desire, drive, etc.) might be presented, depending on the time available, by which intention, attention,

perception, decision-making, the action-perception cycle, abstraction, generalization, memory retrieval, and consciousness can be re-defined and explained in terms of nonlinear brain dynamics [7], using the concepts of phase transition, spontaneous symmetry breaking, and the conceptualizations offered by scale-free dynamics operating simultaneously across the micro-meso-macroscopic levels that characterize contemporary neuroscience.

References

1. Freud S (1895) The project of a scientific psychology. Chapter in: The Origins of Psycho-Analysis. Bonaparte M, Freud A, Kris E (eds.), Mosbacher E, Strachey J (trans.). New York: Basic Books 1954.
2. Jackson JH (1884) Evolution and dissolution of the nervous system. Lecture III. In: Taylor J (ed.) Selected Writings. New York: Basic Books 1958. p. 72.
3. Foster M, Sherrington CS (1897) A textbook of physiology. III. the central nervous system. London: MacMillan 7th Ed., p. 929.
4. Ryle G (1949) The concept of mind. New York: Barnes and Noble.
5. Prigogine I (1980) From being to becoming: time and complexity in the physical sciences. San Francisco: W H Freeman.
6. Freeman WJ (1975) Mass action in the nervous system. New York: Academic Press.
7. Freeman WJ (2006) Definitions of state variables and state space for brain-computer interface. Part 1. Multiple hierarchical levels of brain function. Cognitive Neurodynamics 1(1): 1871–3080 (print) 1871–4099 (Online) http://dx.doi.org/10.1007/s11571-006-9001-x.

Chapter 63
Optical Imaging of Plastic Changes Induced by Fear Conditioning in The Auditory Cortex of Guinea Pig

Yoshinori Ide, Jan Lauwereyns, Guy Sandner and Minoru Tsukada

Abstract In this study, the plastic change in the auditory cortex induced by a fear conditioning with pairing of sound (Conditioned Stimulus, CS) and electric foot-shock (Unconditioned Stimulus, US) was investigated by using of an optical recording. To investigate the effect of association learning, optical signals in the auditory cortex to CS (12 kHz pure tone) and non-CS (8 and 16 kHz pure tone) were recorded before and after the conditioning. As a result, the response area only to CS increased after the conditioning. On the other hand, to investigate whether auditory information could be retrieved by electric foot-shock after association learning or not, auditory response to foot-shock was also investigated before and after the conditioning. As a result, the optical response in the auditory cortex to only electric foot-shock without any sound stimuli could not be observed before the conditioning but clearly appeared after the conditioning.

Keywords Auditory cortex · optical imaging · fear conditioning · plasticity

Introduction

Fear conditioning using sound and electric stimuli is commonly used in the researches of emotional memory, many researches of plasticity in the auditory cortex using this paradigm have been carried out. Weinberger et al. reported that receptive field in the auditory cortex are plastically changed by fear conditioning and the best frequency strongly tunes to the frequency used for the conditioning [1]. The information in the auditory cortex is spatially represented as the tonotopic map. Merzenich et al. reported that the response region to the training frequency in the primary auditory cortex of a monkey enhanced after the frequency discrimination

Y. Ide
Brain Science Institute, Tamagawa University, 6-1-1 Tamagawa-gakuen Machida, Tokyo 194-8610, Japan
e-mail: yide@lab.tamagawa.ac.jp

R. Wang et al. (eds.), *Advances in Cognitive Neurodynamics*,

task [2]. In this work, to verify the results for those researches, response in the auditory cortex to CS sound and non-CS sound was investigated before and after the conditioning. Furthermore, to investigate whether auditory information could be retrieved by electric foot-shock after association learning or not, auditory response to foot-shock was also investigated before and after the conditioning.

Methods

Guinea pigs of 250–450 g, 3–6 weeks old female were used as an experimental subject. After the animal was anesthetized, the trachea was incised and cannulated for the artificial respiration. The scalp was detached and a hole (approximately 10 by 10 mm^2) was drilled in the left temporal bone and the dura and arachnoid membrane were removed. The auditory cortex was stained for 40–60 min with a voltage-sensitive dye, RH795 (0.125 mg/ml, dissolved in saline; molecular Probes). Then, the animal was artificially respirated, and optical recording was carried out before and after the conditioning. While a pure-tone (duration: 5 s, frequency: 4, 8, 12, 16 kHz, acoustic pressure: 65 dB SPL) was presented to the right ear or an electric shock (duration: 0.5 s, current intensity: 0.5–1.5 mA) was applied to hind legs, response from the left auditory cortex was recorded. 100 × 100 ch MOS imaging device (MiCAM ULTIMA, Brain Vision) was used for recording the fluorescent signals from the cortex. Fear conditioning was carried out by using sound stimulus (CS) and electric foot shock (US). A pure-tone (duration: 5 s, frequency: 4 or 12 kHz) was presented to the right ear as CS, and an electric shock (duration: 0.5 s, current intensity: 0.5–1.5 mA) was applied to hind legs as US. Electric shock was applied just after the sound presentation, this paring was defined to be one trial, and 70 trials were carried out in total. The interval between each trial was randomly 60–120 s.

Results

Auditory responses to pure tone with a frequency of 8, 12 and 16 kHz was recorded before and after the conditioning. As shown in Fig. 63.1, the auditory response area markedly increased only for CS sound (12 kHz) after the conditioning, while such an increase of auditory response area could not be observed for the other non-CS sounds.

Auditory responses for electric foot-shock alone was investigated without presenting any sound stimuli before and after the conditioning. Figure 63.2 shows the time course of those auditory responses. As shown in Fig. 63.2, it was found that auditory response that could not be observed before the conditioning clearly appeared after the conditioning. Besides, in a normal time course for a pure tone (gray solid line), the peak onset latency was approximately 40 ms and the offset latency was approximately 100 ms, however, in the time course for electric foot-shock alone

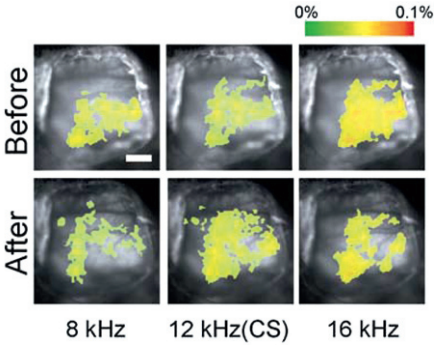

Fig. 63.1 Auditory responses to CS (12 kHz) and non-CS (8, 16 kHz) recorded before and after conditioning

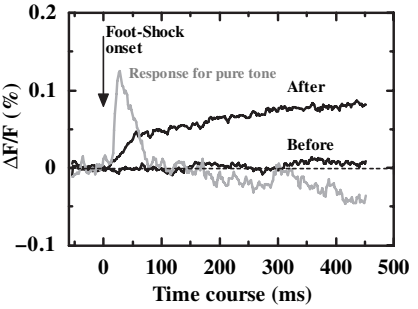

Fig. 63.2 Time course of auditory response to electric foot-shock alone before and after conditioning

(red solid line), the onset latency was similar to that for a pure tone, while the rising until the peak was very gentle and the duration was over 450 ms, suggesting that the time course for electric foot-shock was very different from that for pure tone.

Next, the comparison between auditory response area for CS sound and electric foot-shock was investigated. Figure 63.3 shows the auditory responses for CS sound and electric foot-shock when the CS sound was 12 kHz pure tone.

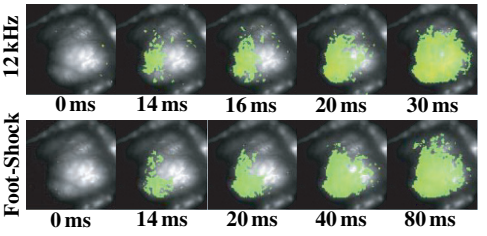

Fig. 63.3 Auditory responses to CS sound and electric foot-shock when CS sound was 12 kHz pure tone

As shown in Fig. 63.3, when the conditioning with a CS sound of 12 kHz was carried out, the auditory response area to the electric foot-shock considerably corresponded to that for CS sound. Similar results were obtained when CS sound was 4 kHz.

Discussions

It has been reported that an optical imaging may record responses mainly from the layer II and III in the cerebral cortex. Furthermore, it has also been reported from the pharmacological experimental data in vivo that responses for acoustic stimuli recorded by using optical imaging consists of the three main components as follows: (i) non-NMDA (N-methyl-D-aspartate) glutamate receptor dependent excitatory postsynaptic potential (EPSP), which is a fast response component, (ii) NMDA glutamate receptor dependent EPSP, which is a slow response component and (iii) GABA (γ-amino butyric acid) receptor dependent inhibitory postsynaptic potential (IPSP) [3]. On the other hand, acetylcholine (ACh) released from basal forebrain to cortex affects NMDA glutamate receptor in layer II/III of cortex and promotes plastic changes in auditory cortex [4]. Excitatory neuron activities based on NMDA glutamate receptor laterally exists beyond the isofrequency band in tonotopic map of auditory cortex [3], suggesting that the increase of auditory response area for CS sound (12 kHz) after the conditioning based on NMDA glutamate receptor dependent LTP in the layer II/III. Furthermore, it has been reported that layer II/III is important for plastic changes in somatosensory cortex, and LTP was induced in horizontal connection of layer II/III in motor cortex. From these viewpoints, rising velocity of auditory response shown in Fig. 63.2 was slow and a large response was obtained in a late time region of after 50 ms, suggesting that NMDA glutamate receptor dependent late-EPSP is a dominant component of the auditory response to foot-shock. Therefore, it might be thought that LTP was induced in the NMDA glutamate receptors by the fear conditioning and EPSP was induced by electric foot-shock in the same NMDA glutamate receptors where LTP was induced by conditioning. Thus there was a correlation between auditory response area for CS sound and electric foot-shock, implying that the acoustic information about CS sound was retrieved by electric foot-shock.

References

1. J. S. Bakin and N. M. Weinberger (1990) “Classical conditioning induces CS-specific receptive field plasticity in the auditory cortex of the guinea pig.” Brain Res., 536: 271–286.
2. G. H. Recanzone, C. E. Schreiner and M. M. Merzenich (1993) “Plasticity in the frequency representation of primary auditory cortex following discrimination training in adult owl monkeys.” J. Neurosci., 13: 87–103.

3. J. Horikawa, Y. Hosokawa, M. Kubota, M. Nasu and I. Taniguchi (1996) “Optical imaging of spatiotemporal patterns of glutamatergic excitation and GABAergic inhibition in the guinea-pig.” J. Physiol., 497: 629–638.
4. N. M. Weinberger and J. S. Bakin (1998) “Learning induced physiological memory in adult primary auditory cortex: Receptive field plasticity, model, and mechanisms.” Audiology & Neuro-Otology, 3: 145–167.

Chapter 64
Learning in Sparse Attractor Networks with Inhibition

Si Wu and Thomas Trappenberg

Abstract Attractor networks are important models for brain functions on a behavioral and physiological level, but learning on sparse patterns has not been fully explained. Here we show that the inclusion of the activity dependent effect of an inhibitory pool in Hebbian learning can accomplish learning of stable sparse attractors in both, continuous attractor and point attractor neural networks.

Introduction

Recurrent attractor neural networks (ANNs) are a fundamental ingredient in many models of brain functions [1, 2]. Probably best known are point attractor neural networks (PANNs) which are trained on random patterns with a Hebbian covariance rule, such as the one popularized by [3]. Another popular type is that of continuous attractor neural networks (CANNs) where the weight matrix is commonly chosen to be of the on-center-off-surround type [2, 4]. Such models have been proposed from basic physiological principles [5] as well as from their ability to describe the dynamics of cognitive functions [6]. While basic Hebbian training has long been described in PANNs [7, 8, 9], training on sparse patterns through activity dependent inhibition in PANNs and training in CANNs have not been fully addressed. By sparsity we mean that only a small portion of nodes are active in the network when a single memory pattern is retrieved. In this paper we show that training with inhibition can stabilize sparse network activity in both PANNs and CANNs.

Learning in CANNs

We consider a simple CANN model, as used in [2]. The nodes are uniformly distributed in a feature space of range $(-\pi, \pi]$ with periodic conditions. The neuronal states take on binary values of 0 and 1, and the memory patterns, μ, are sparse

S. Wu
Sussex University, UK
e-mail: siwu@sussex.ac.uk

R. Wang et al. (eds.), *Advances in Cognitive Neurodynamics*,

attractors of localized activity packets (bumps) in the sense that in each pattern $d \ll 2\pi$ consecutive nodes are activated. We further consider that the network holds a continuous family of memory patterns uniformly distributed in the feature space. Conventional studies (e.g.[2]) often assume this form of the recurrent interactions. Here, we derive the recurrent interaction structure based on a properly modified Hebbian learning rule.

We propose a general Hebbian covariance learning rule which is augmented with an additional inhibition constant, C, describing the effect of inhibitory internodes,

$$w_{i,j} = \frac{2\pi}{M} \sum_{m=1}^{M} (\mu_i^m - < \mu_i >)(\mu_j^m - < \mu_j >) - C, \tag{64.1}$$

where M denotes the number of training patterns, and the average activity of the ith node over all patterns is $< \mu_i > = \sum_m \mu_i^m / M = d/(2\pi)$.

Since the neural field is translation invariant, the interaction between two nodes is determined by their distance in feature space. Without loss of generality, we can thus calculate the interaction between nodes at locations 0 and x. Under the continuous field approximation, $M \to \infty$ with pattern density is $\rho = M/(2\pi)$, the weight is given by

$$w(x) = \int_{-\pi}^{\pi} \mu_0^y \mu_x^y dy - C - d^2/2\pi, \tag{64.2}$$

with $\mu_x^y = 1$ when $y \le x \le y + d$ and $\mu_x^y = 0$ otherwise. We get:

$$\begin{aligned} &- \text{when } 0 < |x| < d : w(x) = d - |x| - C - d^2/(2\pi) \\ &- \text{when } d < |x| < \pi : w(x) = -C - d^2/(2\pi) \end{aligned}$$

Thus, the weight profile describes short-range excitatory and long-range inhibitory interactions as demanded by the center-surround neural field theory [2, 4].

Stability Under the Network Dynamics

We denote the network states at time t with $\mathbf{S}(t) = \{S_i(t)\}$. Under the continuous field approximation, the network dynamics can be written as:

$$S(x) = \Theta[\int_{-\pi}^{\pi} w(x - z) S(z) dz], \tag{64.3}$$

where $\Theta(x)$ is a threshold function. We can check the stability of a memory pattern, μ, of a bump at location $[0, d]$, under the network dynamics. This requires:

$$\mu(x) = \Theta[\int_{-\pi}^{\pi} w(x-z)\mu(z)dz. \quad (64.4)$$

Since the inputs received by nodes in the middle of the bump are always larger than that at the boundaries (due to short-range excitation and long-range inhibition), it is adequate to only check the stability of the boundary points. The recurrent input received by the boundary point, 0, is given by

$$h(0) = \int_0^d w(z)dz = \int_0^d (d-z-C-d^2/(2\pi))dz = d^2/2-Cd-d^3/(2\pi). \quad (64.5)$$

The activity packet (bump) is stable when $h(0) = 0$. From the above equation we see that in case of a pure covariance rule ($C = 0$) the size of the bump can only be $d = \pi$. That is, the memory patterns are not sparse. In order to hold sparse patterns, a inhibition of $C \neq 0$ is required.

In the following, we absorb the constant term from the covariance learning rule (the third term on the right-hand side of Eq. 63.5) in a revised inhibition constant C. Then, the condition for stabilizing sparse patterns of size d in CANNs is $C = d/2$. It is straightforward to check that this is also the sufficient condition: consider the network state starts from a bump larger than d, then it will shrink due to the recurrent interactions, and if the initial state is smaller than d, it will enlarge.

For training patterns with width d we can modulate the retrieval width $\tilde{d} < d$ with different inhibition values:

$$-\tilde{d} < d : h(0) = \int_0^{\tilde{d}} (d-z-C)dz = \tilde{d}(d-\tilde{d}/2-C).$$

Thus, the bump width, obtained by $h(0) = 0$, is $\tilde{d} = 2(d-C)$. From the requirement $0 < \tilde{d} < d$, this implies $d/2 < C < d$.

$$-\tilde{d} > d : h(0) = \int_0^d (d-z-C)dz - \int_d^{\tilde{d}-d} Cdz = d^2/2 - C\tilde{d}.$$

The bump width is therefore $\tilde{d} = d^2/(2C)$. From the condition $\tilde{d} > d$, we have $C > d/2$.

These analytic solutions are compared to simulations in Fig. 64.1a.

Learning in PANNs

Learning sparse representations in the point attractor networks (PANNs) can also be solved with global inhibition. Again, we consider the Hebbian learning rule with global inhibition,

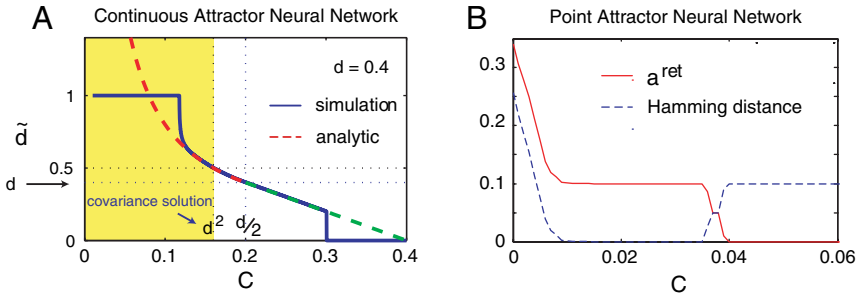

Fig. 64.1 The effect of inhibition on learning in attractor networks. (a) The solid line represents the simulations of a CANN model and shows the ratio of active nodes after 10 iterations from an initial memory pattern. The results compare well with the analytic results (dashed line) for appropriate values of C. Too small or too large inhibition leads to a loss of the memory states. (b) Average retrieval sparseness, a^{ret}, and Hamming distance between network state and memory pattern for a point attractor network for different inhibition constants, C. Due to the attractor dynamics, a range of inhibition values around the analytic solution can support sparse memory states

$$w_{i,j} = \frac{1}{\sqrt{M}} \sum_m (\mu_i^m - a)(\mu_j^m - a) - C, \tag{64.6}$$

where a denotes the sparseness of patterns which is the probability for a node to be active in each pattern (the ratio between the number of active nodes and the total number of nodes). The commonly used network update rule [7] is given by:

$$S_i = \Theta[h_i] = \Theta[\frac{\sqrt{M}}{N} \sum_{j=1}^{N} w_{ij} S_j], \tag{64.7}$$

so that the activity of the ith node is determined by the sign of the input, h_i. In the limit of many patterns, and under the condition that the network is homogenous, h_i becomes Gaussian distributed with mean and variance given by:

$$< h_i >= -Ca, \quad \sigma^2 =< h_i^2 >= a^3(1-a)^2. \tag{64.8}$$

Thus, the probability of the ith node to be active is $P(h_i > 0)$ and to be inactive is $P(h_i < 0)$. On the other hand, the probability for the ith node to be active is also equal to a. Thus, under the self-consistent requirement, it must hold that

$$\frac{P(h_i > 0)}{P(h_i < 0)} = \frac{a}{1-a}, \tag{64.9}$$

from which the relationship between the inhibition, C, and the sparseness, a, can be derived:

$$a = \frac{1}{2} - erf(\frac{Ca}{\sqrt{2}\sigma}). \tag{64.10}$$

From this condition, we see that when $C = 0,\ a = 0.5$, that is, the retrieved patterns are not sparse. However, patterns with the correct retrieval sparseness $a^{\text{ret}} = a$ can be maintained for a range of inhibition values as shown in Fig. 64.1b.

Conclusion

We showed here that sparse attractor networks can be trained with Hebbian learning if inhibition is taken into account, and we calculated how the spareness of retrieved states is related to the inhibition constant.

References

1. Caianello, E.R.: Outline of a theory of thought processes and thinking machines. Journal of Theoretical Biology **2** (1961) 204–235
2. Amari, S.: Dynamics of pattern formation in lateral-inhibition type neural fields. Biological Cybernetics **27** (1977) 77–87
3. Hopfield, J.: Neural networks and physical systems with emergent collective emergent computational abilities. Proceeding of the National Academy of Science **79** (1982) 2554–2558
4. Grossberg, S.: Contour enhancement, short-term memory, and constancies in reverberating neural networks. Studies in Applied Mathematics **52** (1973) 217–257
5. Wilson, H., Cowan, J.: A mathematical theory of the functional dynamics of cortical and thalamic nervous tissue. Kybernetik **13** (1973) 55–80
6. Schöner, G. Dynamical systems approaches to cognition. In: R. Sun, The Cambridge Handbook of Computational Psychology, Cambridge University Press, April 2008 (ISBN-13: 9780521674102)
7. D.J. Amit, H. Gutfreund, H.S.: Storing infinite numbers of patterns in a spin-glass model of neural networks. Physical Review Letters **55** (1985) 1530–1533
8. Zhang, K.: Representation of spatial orientation by the intrinsic dynamics of head-direction cell ensembles: a theory. Journal of Neuroscience, **16** (1996) 2112–2126
9. Stringer, S., Trappenberg, T., Rolls E., Araujo, I.: Self-organising continuous attractor networks and path integration: One-dimensional models of head direction cells. Network: Computation in Neural Systems **13** (2002) 217–242

Chapter 65
Dynamic Analysis of Motor Imagery EEG Using Kurtosis Based Independent Component Analysis

Xiaojing Guo, Lu Wang, Xiaopei Wu and Daoxin Zhang

Abstract This paper investigates the possibility of using independent component analysis (ICA) to analyze EEG dynamics of motor imagery. Considering the non-stationary characteristics of the motor imagery EEG, the online Independent Component Analysis by kurtosis maximization is proposed to detect the mu rhythm changes during left and right hand movement imagination. The experiment results show that the kurtosis based online ICA can concentrate the mu rhythm in raw EEG channels to one output channel, but the batch ICA fails to do that. The study in this paper also show that the elements of dynamic mixing matrix are more sensitive to mu rhythm dynamic changes, which means the parameters of dynamic mixing model online ICA can be used to monitor the dynamic changes of mu rhythm during motor imaginations. The results in this paper demonstrate that the online ICA may be a promising tool for the analysis of EEG dynamics.

Keywords Motor imaginary · EEG · online independent component analysis · kurtosis

Introduction

ICA is a novel approach for blind source separation and feature extraction, which has caught broad attention of many researchers in recent years. According to published papers and research reports, most of ICA algorithms used for EEG source separation belong to the class of static ICA algorithm with batch data processing. It is well known that EEG is a non-stationary bioelectricity signals. For example, conscious (or unconscious) mental activities will activate the different cortex region, which means EEG source may have dynamic changes during the EEG acquisition process. In this case, static ICA algorithm often fails to get the valuable results from raw EEG data [1, 2].

X. Guo
The Key Laboratory of Intelligent Computing & Signal Processing of MOE, Anhui Univesity, Hefei 230039, Anhui Province, China
e-mail: jing886@sina.com

R. Wang et al. (eds.), *Advances in Cognitive Neurodynamics*,

Researches have shown that when the subject performs or even imagines limb movement, the μ rhythm in EEG is (de)synchronized over the contralateral (ipsilateral) sensorimotor area. This phenomenon is known as Event-Related (De) synchronization (ERD/ERS) [3, 4]. Based on this phenomenon, people attempt to develop a new brain-computer interface (BCI) system based on motor imagination, which concerns with the reliable EEG pattern extraction and the online signal processing algorithm [3, 4]. This paper attempts to analyze the EEG signals of motor imagery using online independent component analysis based on kurtosis maximization, and some valuable results are achieved.

Kurtosis-Based Independent Component Analysis

The definition of ICA can be described simply as follow: given a set of observations of random variables $x = [x_1, x_2, \ldots, x_N]^T$, assume that they are generated as a linear mixture of independent components: $\mathbf{x} = \mathbf{As}$, where $\mathbf{A}$ is some unknown matrix. The aim of ICA is to find a separation matrix $\mathbf{W}$, so that the random variables u_i ($\mathbf{u} = \mathbf{Wx}$) are as independent as possible. Kurtosis is often used as a quantitative measure of independence of a random variable or signal. The ICA algorithm based on kurtosis maximization is described bellow.

Let $\mathbf{x}$ be the input random variables, $\mathbf{w}_t$ be one row of the matrix, $u = \mathbf{w}_t^{\mathrm{T}}\mathbf{x}$ the corresponding independent component. The learning rules for separation matrix based on kurtosis maximization are as follows:

$$\mathbf{w}_{t+1} = \mathbf{w}_t + \mu \frac{\partial J(\mathbf{w})}{\partial \mathbf{w}}\bigg|_{\mathbf{w}=\mathbf{w}_t} = \mathbf{w}_t + \mu \cdot sign[kurt(u)] \cdot E\left\{(\mathbf{w}_t^T\mathbf{x})^3 \cdot \mathbf{z}\right\} \tag{65.1}$$

where μ is the learning rate of the gradient descent, sign () is the symbol function, t is learning times, $J(w)$ is the cost function:

$$J(\mathbf{w}) = |kurt(u)| = \left|kurt(\mathbf{w}^T\mathbf{x})\right| \tag{65.2}$$

After removing the expectation operation in Eq. (65.1), we get the online estimation algorithm based on new updating sample x_{t+1}.

$$\mathbf{w}_{t+1} = \mathbf{w}_t + \mu \frac{\partial J(\mathbf{w})}{\partial \mathbf{w}}\bigg|_{\mathbf{w}=\mathbf{w}_t} = \mathbf{w}_t + \mu \cdot sign[kurt(u)] \cdot \left(\mathbf{w}_t^T x_{t+1}\right)^3 \cdot x_{t+1} \tag{65.3}$$

where, Eq. (65.4) is employed to estimate the $kurt(u)$.

$$kurt = \frac{E[u^4]}{\left(E\left[u^2\right]\right)^2} - 3 \tag{65.4}$$

Application to Motor Imagery EEG

EEG Data

The raw EEG data is from the motor imagery EEG database of Austrian Graz scientific and technical university. Figure 65.1a is the mu rhythms of one trial EEG data (C3, C4) while the subject imagines left hand movement (the raw EEG data is filtered by 8–12 Hz band-pass filter). From Fig. 65.1a, We can easily observe the ERD (ERS) phenomenon: after 3 s, the mu rhythm on the ipsilateral electrode (C3) is strengthened while on contralateral electrode (C4) is suppressed. Based on the mu rhythm pattern, the type of motor imagination can be correctly classified by commonly used classification method, such as the method of energy comparison between C3 and C4 channels, etc. But not all EEG trials have the obvious ERD/ERS as in Fig. 65.1a. In some cases, the ERD (ERS) is very weak (as shown in Fig. 65.1b, according to the true label provided by the database, which belongs to the class of right hand movement imagination). For this kind of EEG trial, the commonly used methods for motor task classification fail to get correct answer.

Experiments and Analysis

For the purpose of mu rhythm enhancement, ICA method is employed to deal with the EEG trial in Fig. 65.1b. First, the classic FastICA algorithm is used, The outputs of FastICA are shown in Fig. 65.2a. Comparing it with the row EEG data in Fig. 65.1b, we can find that FastICA algorithm cannot enhance the mu rhythm.

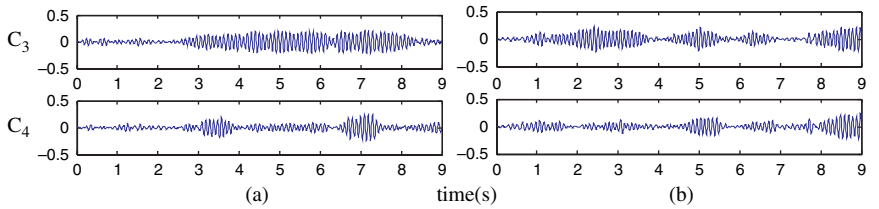

Fig. 65.1 The μ rhythm of motor imagery EEG on electrode C3 and C4: (a) left hand; (b) right hand

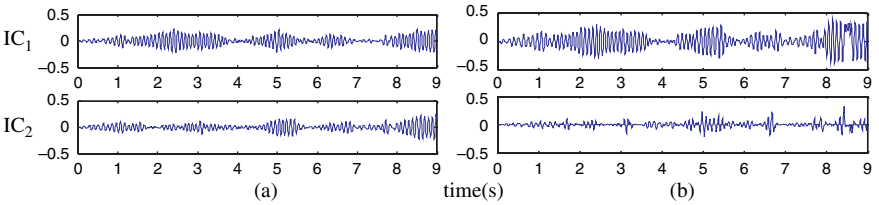

Fig. 65.2 The outputs of ICA applying to EEG in Fig.64.1(b): (a) Fast ICA; (b) Dynamic ICA

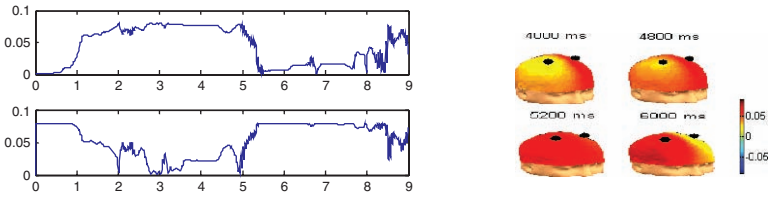

(a) time(s) (b)

Fig. 65.3 (a) The curve of dinamic mixing matrix estimated by DICA based on kurtosis maximization. (b) The dynamic distribution of μ rhythm on the electrodes C3 and C4 in the process of right hand motor imagination (4–6 s)

Then, The online ICA algorithm defined in Eq. (65.3) is used to deal with the same EEG data in Fig. 65.1b. Figure 65.2b is the output of kurtosis-based online ICA, It is easy to see that the mu rhythm is separated to the first independent component (IC1). According to the linear mixing model, the first column of $\mathbf{A}_t$: $\mathbf{a}_1 = [a_{11}(t),\ a_{21}(t)]^{\mathrm{T}}$ can be used to describe the distribution of mu rhythm on electrode position C3 and C4 during the motor imagination. Figure 65.3a gives the time courses of $|a_{11}(t)|,\ |a_{21}(t)|$. Based on them, the dynamic 3D brain topographic map between 4–6 s is given in Fig. 65.3b. From the results, we can see that the kurtosis-based online ICA can separate the mu rhythm from raw EEG to one output channel even in the case of weak ERD. Furthermore, we notice that the elements of the mixing matrix changes apparently at 5 s as shown in Fig. 65.3a, which correspond to the dynamic changes of mu rhythm distribution on electrode C3 and C4 in Fig. 65.3b. That means, before and after 5 s, the energy of the μ rhythm on electrode C3 changes from more to less, while on electrode C4 it changes from less to more. That is to say, the subject was really undergoing the right hand movement imagination.

Conclusion

In this paper, we have studied kurtosis-based online independent component analysis and its application to EEG of motor imagery. The results demonstrate that online ICA based on kurtosis maximization can detect the mu rhythm from motor imagery EEG. The column of estimated mixing matrix can accurately reflect the ERD phenomenon. So it may be a valuable method for study of EEG dynamics and BCI implementation. It is worth mentioned that kurtosis-based ICA algorithm is seldom directly used in traditional ICA applications because the kurtosis is very sensitive to outlier appeared in data. But our research show that online ICA based on kurtosis maximization principle performs better in extracting the basic rhythm of the EEG than other ICA algorithm does. We think this is a quite interesting phenomenon and worth further studying.

Acknowledgments This research is supported by Nature Science Foundation of Anhui province (070412038) and National Nature Science Foundation (60771033).

References

1. T.-W. Lee: Independent Component Analysis–Theory and application[M]. Kluwer Academic, Boston (1998) 27–64.
2. S.I. Amari: Supereffeciency in blind source separation[J]. IEEE Transactions on Signal Processing (1999) 47(3): 936–944.
3. G. Pfurtscheller, C. Neuper: Motor imagery and direct brain-computer communication. Proceedings of IEEE (2001) 89(7): 1123–1134.
4. Eleanor A. Curranab, Maria J. Stokesa: Learning to control brain activity: A review of the production and control of EEG components for driving brain–computer interface (BCI) systems. Brain and Cognition (2003) 51(3): 326–336.

Chapter 66
Quantifying the Sequential Structure of Psychotic Behavior

P.E. Rapp

Abstract In its simplest form, a random reinforcement, choice task experiment is one in which the subject makes choices in an attempt to guess the outcome of a random number generator. The subject does not know that the pattern is random and will try to construct different strategies to increase the frequency of correct guesses. Differences in the pattern of choices are observed when clinical populations are compared against healthy controls. Additionally, the choice sequences of animals obtained before and after the administration of drugs can show marked differences. This contribution identifies mathematical methods from symbolic dynamics that can be used to provide a quantitative characterization of the sequential structure of behavior.

Introduction

In 1983 Frith and Done [1] published a seminal study of behavioral stereotypy in schizophrenia. This investigation has been the model for several subsequent studies. In a sequence of trials, subjects had to guess if a cross would appear on the left or right side of the screen. The position was assigned randomly. The subject did not know that the pattern is random and tried to construct different strategies to increase the frequency of correct guesses. In the Frith and Done study, normal controls, manic depressive subjects, patients presenting senile dementia and acute schizophrenics with positive symptoms (hallucinations, delusions, bizarre behavior) generated sequences of guesses that were "relatively random." Acute schizophrenics with negative symptoms (affective flattening, alogia, apathy, anhedonia) and chronic schizophrenics generated a high incidence of stereotyped alternating LRLR sequences. Chronic schizophrenics presenting both negative symptoms and intellectual deterioration produced repetitive sequences (LLLL. . ... or RRRR. . ...). These results were largely confirmed by Lyon et al. [2]. A large literature examining choice

P.E. Rapp
Uniformed Services University, Bethesda, MD, USA
e-mail: prapp@usuhs.mil

R. Wang et al. (eds.), *Advances in Cognitive Neurodynamics*,

behavior in clinical populations has subsequently appeared [3, 4, 5, 6, 7, 8, 9]. In most investigations, the analysis is largely limited to determining (1) the frequency of each choice, (2) switching percentages, (3) the number of appearances of each of the 16 possible tetragrams (RRRR, LLLL, RLRL,. . ..), (4) the appearances of each trigram and (5) appearance of each two element pair. (As will be discussed, Paulus [5] and Magnusson [10] are a notable exceptions in this regard.) The purpose of this contribution is to identify measures from symbolic dynamics that can provide a more systematic characterization of the sequential structure of choice behavior.

Mathematical Methods

The simplest measure of a symbol sequence is its Shannon information [11]. Suppose a message (symbol sequence) is constructed from an alphabet of k symbols, and suppose that p_i is the probability of the appearance of the i-th symbol in the message. The Shannon information is

$$I = -\sum_{i=1}^{k} p_i \log_2 p_i$$

It can be shown that the maximum value of I is $I = 1$, and that this is obtained when $p_i = 1/k$ for all i. Frith and Done [1] found differences in information between different populations, but Lyon et al. [2] did not. Upon reflection it is seen that Shannon information will provide a very incomplete characterization of a message because it is not sequence sensitive. Consider the messages:

$M_1 =$ AAAAAAAAAABBBBBBBBBBCCCCCCCCCCDDDDDDDDDDEEEEEEEEEE

$M_2 =$ BCBADCDAEBCDAAAEAAEEBCCDDEDACCBEDBDBAEEBEDCCABECDB

Though they are qualitatively very different, their corresponding value of information, $I = 1$, is the same since $p_1 = p_2 = \cdots\cdots = p_5 = .2$ in both cases. Alternative measures are sensitive to sequential structure.

Previous analyses of choice behaviors have looked for different substrings (words) in the behavior sequence. This can be made more rigorous by calculating the topological entropy of a message [12]. Again suppose a message is constructed from an alphabet of k symbols. With an alphabet of k symbols, the maximum number of possible words of length n is k^n. By definition, all possible words appear in a random message. In a non-random message the number of observed words of length n grows with n, but not as rapidly as it does for a random message. Let $N(n)$ be the number of words of length n actually observed in the message. $N(n)$ grows exponentially at the rate $H_T n$ where H_T, the topological entropy is between zero and one.

$$N(n) \alpha\, k^{H_T n} \leq k^n$$

If $\log_k N(n)$ is plotted as a function of n, it will have slope H_T. Strictly, H_T is defined in the limit of infinitely long messages:

$$H_T = \lim_{n\to\infty} \frac{\log_k N(n)}{n}$$

If the message is random, then $N(n) = k^n$ and $H_T = 1$. Suppose the message is constructed by repeating a single symbol ($M = \text{LLLLL}\ldots..$). In that case, $N(n) = 1$ and $H_T = 0$. Intermediate values of H_T can be generated by chaotic sequences.

The topological entropy is sensitive to the appearance of each substring of length n, but it is insensitive to the frequency of each appearance. In contrast, the metric entropy incorporates a dependence on the relative frequency of each substring [13]. Let S_n denote a substring of length n. Let $F(S_n)$ denote the number of times that it appears. The probability of S_n is $P(S_n)$.

$$P(S_n) = F(S_n) \Big/ \sum_{\text{all}S_n} F(S_n)$$

I_n is the information obtained from observing substrings of length n.

$$I_n = -\sum_{\text{all } S_n} P(S_n) \log P(S_n)$$

The information content of a substring increases with its length.

$$I_n \,\alpha\, H_M n$$

If I_n is plotted as a function of n, it should have a slope H_M, which is the metric entropy. As in the case of topological entropy, metric entropy is defined mathematically as a limiting case.

$$H_M = \lim_{n\to\infty} I_n/n = \lim_{n\to\infty} \left\{ \frac{-\sum_{\text{all } S_n} P(S_n) \log_2 P(S_n)}{n} \right\}$$

If the message is composed from an alphabet of k symbols, there are k^n possible substrings of length n. In the case of a random sequence, each substring appears with equal probability, $P(S_n) = 1/k^n$. For the case of a random sequence, the sum contains k^n identical terms.

$$H_M = \lim_{n\to\infty} \left\{ \frac{-\sum_{\text{all } S_n} \frac{1}{k^n} \log_2 \frac{1}{k^n}}{n} \right\} = \log_2 k$$

If the message is constructed by repeating a single symbol, there is only one substring of length n in the message, and the probability of its appearance is one. No information is obtained by observing a process that has a certain outcome. $I_n = 0$ and hence $H_M = 0$.

Several other methods for characterizing order in symbol sequences should be noted briefly. Frith and Done [1] reported that for healthy controls and several patient groups the choice pattern was "relatively random." The Lempel-Ziv complexity [14] is an important method for characterizing the degree of randomness in a symbol sequence. A normalization of Lempel-Ziv complexity that reduces its sensitivity to the length of the message has been constructed [15, 16]. We have published elsewhere a detailed didactic presentation of this measure along with pseudocode for its calculation [17]. The topological entropy, metric entropy and Lempel-Ziv complexity give low values for regular sequences and high values for random sequences. A number of investigators have published definitions of complexity that give low values for both regular and random processes and higher values for irregular deterministic chaotic processes [18, 19, 20, 21]. In a series of publications, Paulus and his colleagues have used sequence sensitive methods to characterize choice behavior in schizophrenia patients [4, 5, 6, 22]. The fluctuation spectrum of local substring entropies was calculated. They observed that "schizophrenic patients exhibited significantly less consistency in their response selection and ordering, characterized by a greater contribution of both highly perseverative and highly unpredictable subsequences or responses within a test session [4]."

What Symbolic Dynamics Doesn't Measure

An analysis of choice behavior with methods from symbolic dynamics proceeds without reference to whether or not a guess was correct. Measures that, for example, determine the frequency of implementation of a win-stay strategy are not generated by an examination of the response sequence alone. The frequency of a win-stay strategy can be informative. Its frequency is reduced in schizophrenic subjects [2]. The latencies (time required to respond) are not incorporated into an analysis based on symbolic dynamics. Magnusson [10] has constructed a measure that is sensitive to both choice sequence and latency. It has been applied to data obtained from schizophrenics by Lyon and Kemp [23]. Using this measure they found that schizophrenic and manic patients showed more complex patterns than controls. The complexity of the response structure was reduced by clozapine. It should be noted that it is not necessary to chose between measures. Several measures can be incorporated into a multivariate discrimination. The coefficient of determination can be used to determine which measures are most effective in discriminating between different groups of subjects.

Discussion

The analysis of choice task behavior is not limited to studies of schizophrenia. Studies of perseverative behavior have been conducted with autistic patients and with traumatic brain injury patients [24]. The experimental paradigm of choice and

random reinforcement has a long history in animal studies [25]. Animal experiments are important in providing a bridge between human clinical studies and investigations of animal models of schizophrenia [26]. For example, Evenden and Robbins [27, 28] observed psychotic choice behaviors in rats treated with amphetamine. Similarly, stereotyped behavior has been seen in human control subjects following administration of amphetamine [29]. It is suggested that analysis of behavioral sequences with methods from symbolic dynamics will provide a more finely grained quantitative characterization of behavior. Further studies may show that it is possible to use dynamical measures of human choice performance longitudinally to assess the response to treatment.

Acknowledgments This research was supported by the Naval Medical Research Center. We also acknowledge support from the Traumatic Injury Research Program of the Uniformed Services University. The opinions and assertions contained herein are the private ones of the authors and are not to be construed as official or reflecting the views of the Department of the Navy or the Department of Defense.

References

1. Frith, C.D., Done, D.J. Stereotyped responding by schizophrenic patients on a two-choice guessing task. Psychological Medicine 13 (1983) 779–786.
2. Lyon, N., Gerlach, J. Perseverative structuring of responses of schizophrenic and affective patients. Journal of Psychiatric Research 22 (1988) 261–277.
3. Crider, A. Perseveration in schizophrenia. Schizophrenia Bulletin 23(1) (1997) 63–74.
4. Paulus, M.P., Geyer, M.A., Braff, D.L. Use of methods from chaos theory to quantify a fundamental dysfunction in the behavioral organization of schizophrenic patients. American Journal Psychiatry 153 (1996) 714–717.
5. Paulus, M.P., Rapaport, M.H., Braff, D.L. Trait contributions of complex dysregulated behavioral organization in schizophrenic patients. Biological Psychiary 49(1) (2001) 71–77.
6. Paulus, M.P., Braff, D.L. (2003). Chaos and schizophrenia: Does the method fit the madness? Biological Psychiatry 53(1) (2003) 3–11.
7. Yogev, H., Hadar,U., Gutman, Y., Sirota, P. Perseveration and over-switching in schizophrenia. Schizophrenia Research 61(2–3), 315–321.
8. Yogev, H., Sirota, P., Gutman, Y., Hadar, U. Latent inhibition and overswitching in schizophrenia. Schizophrenia Bulletin 30(4) (2004) 713–726.
9. Garner, J.P., Meehan, C.L., Mench, J.A. Stereotypies in caged parrots, schizophrenia and autism: evidence for a common mechanism. Behavioral Brain Research 145(1–2) (2003) 125–134.
10. Magnusson, M.S. Discovering hidden time patterns in behavior: T-patterns and their detection. Behavior Research Methods, Instruments and Computers 32(1) (2000) 93–110.
11. Shannon, C.E. A mathematical theory of communication. Bell System Technical Journal 27 (1948) 379–423.
12. Crutchfield, J.P., Packard, N.H. Symbolic dynamics of noisy chaos. Physica D 7 (1983) 201–223.
13. Badii, R., Politi, A. Complexity, Hierarchical Structures and Scaling in Physics. Cambridge: Cambridge University Press (1997).
14. Lempel, A., Ziv, J. On the complexity of finite sequences. IEEE Transactions on Information Theory IT-22 (1976) 75–81.

15. Rapp, P.E., Cellucci, C.J., Korslund, K.E. Watanabe, T.A.A., Jiménez-Montaño, M.-A. An effective normalization of complexity measurements for epoch length and sampling frequency. Physical Review E 64 (2001) 016209-1–016209-9.
16. Rapp, P.E., Cellucci, C.J., Watanabe, T.A.A., Albano, A.M. Quantitative characterization of the complexity of multichannel human EEGs. International Journal of Bifurcation and Chaos 15 (2005) 1737–1744.
17. Watanabe, T.A.A., Cellucci, C.J., Kohegyi, E., Bashore, T.R., Josiassen, R.C., Greenbaun, N.N., Rapp, P.E. The algorithmic complexity of multichannel EEGs is sensitive to changes in behavior. Psychophysiology. 40 (2003) 77–97.
18. Xu, J., Liu, Z.-R., Liu, R. The measure of sequence complexity for EEG studies. Chaos, Solitons and Fractals 4 (1994) 2111–2119.
19. D'Alessandro, G., Politi, A. Hierarchical approach to complexity with applications to dynamic systems. Physical Review Letters 64 (1990) 1609–1612.
20. Wolfram, S. Computation theory of cellular automata. Communications in Mathematical Physics 96 (1984) 15–57.
21. Grassberger, P. Toward a quantitative theory of self-generated complexity. International Journal of Theoretical Physics 25 (1986) 907–938.
22. Paulus, M.P., Perry, W., Braff, D.L. The nonlinear, complex sequential organization of behavior in schizophrenic patients: neurocognitive strategies and clinical correlations. Biological Psychiatry 46 (1999) 662–670.
23. Lyon, M., Kemp, A.S. Increased temporal patterns in choice responding and altered cognitive processes in schizophrenia and mania. Psychopharmacology 172(2) (2004) 211–219.
24. Al-Adawi, S., Powell, J.H., Greenwood, R.J. Motivational deficits after brain injury: a neuropsychological approach using new assessment techniques. Neuropsychology 12(1) (1998) 115–124.
25. Morgan, M.J. Effects of random reinforcement sequences. Journal of the Experimental Analysis of Behavior 22 (1974) 301–310.
26. Robbins, T.W. Synthesizing schizophrenia: A bottom up symptomatic approach. Schizophrenia Bulletin 31(4) (2005) 854–864.
27. Evenden, J.L., Robbins, T.W. Dissociable effects of d-amphetamine, chlordiazepoxide and α-flupenthixol on choice and rate measurement reinforcement in the rat. Psychopharmacology 79 (1983) 180–186.
28. Evenden, J.L., Robbins, T.W. Increased response switching perseveration and perseveration switching following d-amphetamine in the rat. Psychopharmacology 80 (1983) 67–73.
29. Ridley, R.M., Baker, H.F., Frith, C.D., Dowdy, M., Crow, T.J. Sterotyped responding on a 2-choice guessing task by marmosets and humans treated with amphetamine. Psychopharmacology 95(4) (1988) 560–564.

Chapter 67
Machine Learning Framework for Inferring Cognitive State from Magnetoencephalographic (MEG) Signals

Andrey Zhdanov, Talma Hendler, Leslie Ungerleider and Nathan Intrator

Abstract We develop a robust linear classification framework for inferring mental states from electrophysiological (MEG and EEG) signals. The framework is centered around the concept of temporal evolution of regularized Fisher Linear Discriminant classifier constructed from the instantaneous signal value. The value of the regularization parameter is selected to minimize the classifier error estimated by cross-validation. In addition, we build upon the proposed framework to develop a feature selection technique. We demonstrate the framework and the feature selection technique on MEG data recorded from 10 subjects in a simple visual classification experiment. We show that using a very simple adaptive feature selection strategy yields considerable improvement of classifier accuracy over the strategy that uses fixed number of features.

Introduction

The problem of "brain reading" or inferring a person's mental state from accompanying brain signals has been a subject of extensive research in the field of Brain – Computer Interfaces (BCI) [1, 2] and, more recently, functional neuroimaging [3]. Most attempts of "brain reading" adopt a machine learning framework to model the correspondence between brain signals and mental states [4].

An important part of the machine learning approach to mental state inference is the problem of feature selection. While many researchers adopt the ad hoc approach to feature selection, there are several attempts to treat the problem in a systematic fashion [5, 6].

In this work, we construct a framework for inference of mental states that takes into account temporal evolution of brain signals based on electrical recordings by MEG. We utilize this framework to develop a feature selection technique and

A. Zhdanov
Functional Brain Imaging Unit, Tel Aviv Sourasky Medical Center, Tel Aviv, Israel
e-mail: zhdanova@post.tau.ac.il

R. Wang et al. (eds.), *Advances in Cognitive Neurodynamics*,

demonstrate that adopting a very simple adaptive feature selection strategy yields a considerable improvement in classifier performance.

Experimental Setup

During the MEG recording 10 healthy subjects were presented with images from two categories – faces and houses. The images continuously switched between face and house at irregular intervals – approximately every several seconds.

MEG signals were acquired using 275-sensor whole-head CTF-275 system by VSM MedTech Ltd, Coquitlam, Canada. Because of a failure of one of the sensors only 274 channels were recorded. The data was sampled at 60 Hz. The signals were segmented into intervals from 0.33 sec (20 samples) before the stimulus switch to 1 s (60 samples) after. In this manner for each subject we obtained several dozens of signals; each signal contains 274 (number of channels) ^{*81} (number of timeslices) values and is represented as a 274-by-81 *signal matrix*. Each of the signals was associated with class label "face" or "house".

Classifier Construction

Our main goal is to develop a method for inferring correct label from the signal matrix. We assume a time-point-wise correspondence among the signals. This assumption implies entry-wise correspondence of the signal matrices, allowing us to treat each signal as a point in a $274 \times 81 = 22194$ – dimensional feature space. Thus we can formulate our inference problem as a high-dimensional pattern classification problem. To make the classification problem feasible we need to select a small subset out of 22,194 features. First, let us consider a very straightforward feature selection strategy: selecting the set of 274 MEG sensor readings from a single most predictive timepoint, i.e. selecting the most predictive column from the 274 by 81 feature matrix (we call this *default feature selection strategy*; we investigate a more sophisticated feature selection technique later). We evaluate the predictiveness of each timepoint by evaluating the performance of the resulting classifier using 100-fold cross-validation on all the data available.

To solve the resulting 274-dimensional classification problem we use Linear Fisher Discriminant classifier regularized by adding regularization parameter λ to the diagonal elements of the data covariance matrix. We select the value of λ that jointly with timepoint minimizes the prediction error estimated using the cross-validation procedure.

Adaptive Feature Selection Strategy

Once we select optimal timepoint and λ using the default feature selection strategy, the resulting Fisher Linear Discriminant classifier assigns weights to each of the

274 features (instantaneous values from the 274 channels at the best timeslice). The absolute value of each channel's weight may be interpreted as the measure of relevance of the channel to the classification. We use this information to guide channel selection in the proposed *adaptive feature selection strategy*.

The adaptive feature selection strategy selects a subset of n out of 274 best separating features from the best timeslice. The n features selected are the features with the highest absolute values of the weights assigned to them by the classifier.

Results

Figure 67.1 shows the relation between the regularization parameter, classifier error and maps of the weights assigned by the classifier to different MEG sensors when using the default feature selection strategy. One can clearly see the global minimum of the prediction error obtained in the middle of the λ range. The smoothing impact of λ on the weight maps is also clearly visible.

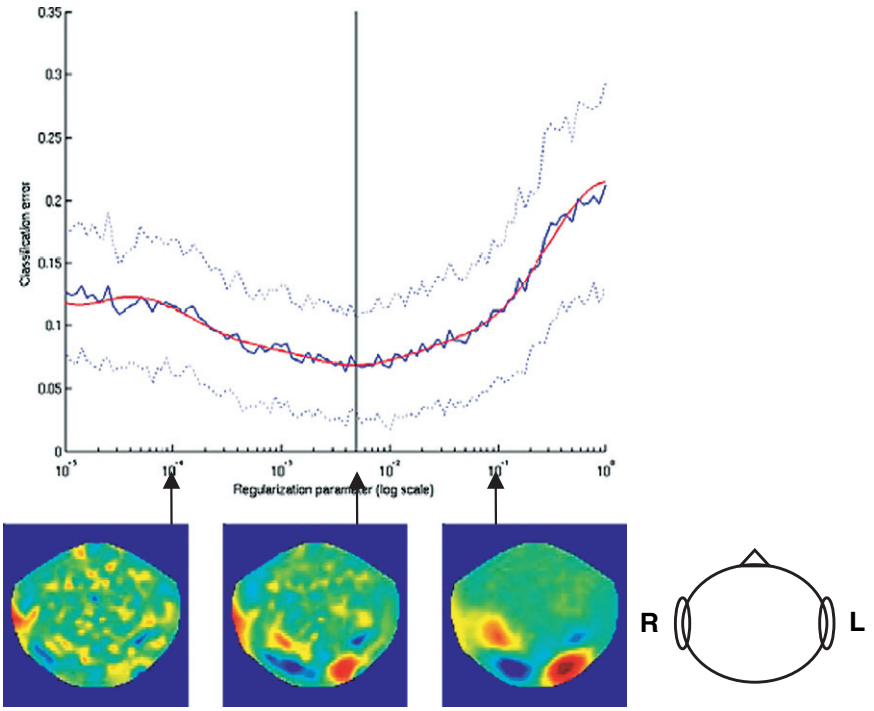

Fig. 67.1 Error rate as a function of regularization parameter for subject ZK. Solid blue line denotes the average error rate over 100-fold cross-validation, dotted lines mark 1-std – wide margin. The vertical line marks the minimum of the smoothed error rate (red line). Three plots below show the distribution of sensor weights corresponding to different values of the regularization parameter

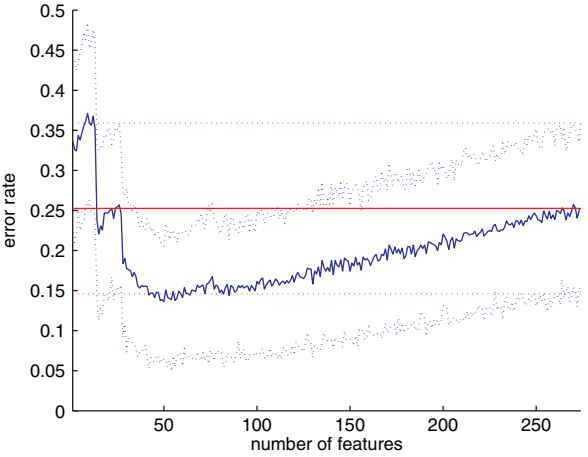

Fig. 67.2 Estimated classification error as a function of number of channels at the optimal separating timeslice for the subject CT. The horizontal (red) line marks the error obtained by using all the 274 channels. Dotted lines mark 1-std – wide margin

Comparison of Feature Selection Strategies

In Fig. 67.2 we compare the performance of the default feature selection strategy to the performance of the adaptive strategy for different sizes n of the feature set (for the subject CT).

As one can see from the plot, the error decreases as the number of features increases until it reaches a clear minimum at approximately 50 sensors. From that point on adding more sensors only increases the classification error – this is a clear example of the over-fitting phenomenon. Similar results were obtained for all 10 subjects – they are summarized in Table 67.1.

Discussion

We have presented a computational framework which allows inference of the subject's cognitive state from brain signals independently of overt response. The importance of each of the sensory inputs is measured by its ability to enable distinction between two mental states (i.e. switch from house to face or switch from face to

Table 67.1 Comparison of the prediction errors for the default and the adaptive feature selection strategies for all subjects

Subject	CT	ER	FB	JMB	JMM	MC	MKN	SH	TE	ZK
Default error	0.25	0.23	0.27	0.13	0.19	0.19	0.25	0.17	0.30	0.06
Adaptive error	0.15	0.14	0.09	0.01	0.12	0.06	0.12	0.13	0.04	0.02
No. of features	50	60	110	70	50	50	70	55	110	50

house). This is radically different than methods which seek the sensory representation that is most associated (correlated) with a certain sensory input (i.e. face or house). We have demonstrated that using classification prediction, it is possible to find optimal interplay between model complexity as affected by the regularization parameter and model fitness as represented by the regression weights. The depicted distributed weights (i.e. maps), thus, represent a model which is more robust and less overfitting to its training data.

Using this computational framework we have been able to infer the number of sensory inputs which should be considered beyond local representations. The map findings clearly indicate that a distributed sensory representation is more informative than local representation, and thus suggesting the importance of a long range network activity in inferring these mental states.

References

1. Fabiani, G. E., McFarland, D. J., Wolpaw, J. R. & Pfurtscheller, G. Conversion of EEG Activity Into Cursor Movement by a Brain-Computer Interface (BCI). IEEE Transactions on Neural Systems and Rehabilitation Engineering, 2004, 12, 331–338.
2. Friehs, G. M., Zerris, V. A., Ojakangas, C. L., Fellows, M. R. & Donoghue, J. P. Brain-Machine and Brain-Computer Interfaces. Stroke, 2004, 35, 2702–2705.
3. Kamitani, Y. & Tong, F. Decoding the Visual and Subjective Contents of the Human Brain. Nature Neuroscience, 2005, 8, 679–685.
4. Haynes, J. & Rees, G. Decoding mental states from brain activity in humans Nature Reviews Neuroscience, 2006, 7, 523–534.
5. Lal, T., Schroder, M., Hinterberger, T., Weston, J., Bogdan, M., Birbaumer, N. & Scholkopf, B. Support Vector Channel Selection in BCI. IEEE Transactions on Biomedical Engineering, 2004, 51, 1003–1010.
6. Schroder, M., Bogdan, M., Hinterberger, T. & Birbaumer, N. Automated EEG Feature Selection for Brain Computer Interfaces. Proceedings of the First International IEEE EMBS Conference on Neural Engineering, 2003.

Chapter 68
Relevant Stimuli Encoding Surface Structural Textures by Touching Plain Woven Fabric

Jiyong Hu, Xin Ding, Rubin Wang and Wei Lin

Abstract In this paper, we investigate the relevant stimuli to SAI afferents encoding surface structural textures of plain woven fabric, via a FE model of fingertip and fabric in contact. By analogizing the neural responses of fingerpad indented by rigid bar to the case of woven fabric in a quasi-static manner, attempts are made to find the relevant mechanical stimuli to SAI units during touching fabric surface. The results show that the surface structural texture is relevant for tactile sensing, and is the invariant attribute of tactual cognition. The maximum tensile strain and strain energy density are probably potential variables of SAI units spatially encoding structural textures of fabric responsible for roughness sensation. These results can also facilitate the understanding of peripheral neural presentation of objects.

Keywords Relevant stimuli · texture · SAI · fingerpad · taction

Introduction

Taction of fabric is a complex process from mechanical and neurophysiologic perspectives. There has been some work to understand the relationship between mechanical stimuli to the finger, neural signals, and perception. However, these studies are lack in elucidating mechanisms of fabric touch. Many studies have looked at rigid surfaces in contact with the fingerpad to elucidate the neural mechanism of form and shape encoding of mechanoreceptors within fingertip [1, 2]. For textiles, the finger contacts apparently with surfaces with similar or greater compliance, and this difference changes the deformation mode of the complex system as both the finger and fabric deform coherently, and leads to different deformation kinetics [3].

Here, A Finite Element (FE) model incorporating the physiological characteristics of fingertip and fabric properties will be developed to investigate the ability of strains in the vicinity of SAI (Slowly Adapting I) units in representing structural undulation of woven fabric surface.

J. Hu
College of Textiles, Donghua University, Shanghai 201620, P.R.China
e-mail: hjydhu@126.com

R. Wang et al. (eds.), *Advances in Cognitive Neurodynamics*,

Modeling and Method

The detailed FE model of human fingertip and fabric in contact can referred to [3] and Fig. 68.1. The model is composed of four-node, quadratic, generalized plain strain elements (Element type: CPEG4).

Relevant stimulus is a property of the mechanoreceptor and does not depend on the mechanical stimuli on the surface [2]. Of deformation parameters, the strain energy density (SED), the maximum strains (MS) [1, 2], whether compressive or tensile, have tentatively been consider as the relevant stimuli to SAI units, associated with the Merkel cells (MC). These quantities are closely related to the stretch experienced by the receptor membrane, which has been shown in biophysical studies to underlie mechanoreceptive ion channel activation [1, 2, 4]. Thus, the spatial sub-surface strains for each indentation at the node depth of 1.0 mm, the maximum sensitive spot (MMS) underneath the symmetric center of fingerpad, where MC locates [1, 2], are calculated. In fact, the size of MCs (80–120 nm in diameter) [4] is several orders of magnitudes smaller than the size of the fingertip and its constituents. It is, therefore, valid to approximate the receptor as a point.

Results and Discussions

Fingertip and Bar

Neural data obtained from a SA-I afferent for the 3.0mm bar by Phillips and Johnson [1] is combined and compared with the subsurface strain measures in the present simulation. Figure 68.2 illustrates that the calculated strain components predict the similar trend for spatial-response profiles of SAI mechanoreceptors at the maximum sensitive spot (MMS), and the clear edge enhancement is observed. Moreover, the strain at depth of 1.0 mm agrees more with the recorded neural data. Therefore, we think that the developed FE model of fingertip can be used to investigate the case of finger indented by objects.

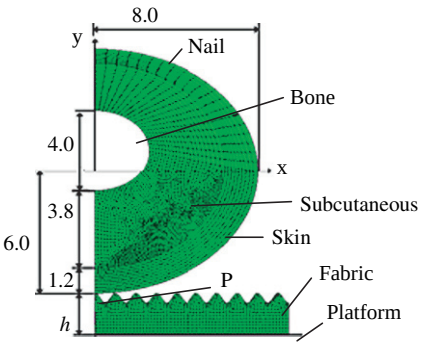

Fig. 68.1 2-D cross-section FE model of fingertip and fabric in contact (Unit: mm)

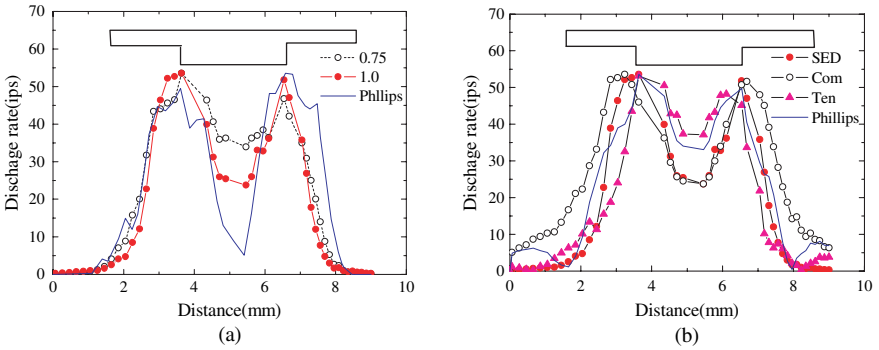

Fig. 68.2 Typical SA spatial response profiles predicted by the 2D model for sequential indentations by 3 mm wide bar are shown. Data from Phillips and Johnson [1] is shown in by the thin line. (a) SED and (b) MSs at depth of 0.75 and 1.0 mm, respectively

Fingertip and Fabric

When fingerpad contacts fabric, the simulated results of relevant quantities are illustrated in Figs. 68.3 and 68.4. Skin surface bends to conform to the sinusoidal wavy-form surface of fabric, and lead to uneven pressure distribution over contact region, as shown in Fig. 68.3. A zero-pressure zone exists during sequential indentions in Fig. 68.3, resulting in small strain values in Fig. 68.4. The reason is that concave of high density texture segment in contact with fingerpad leads to a gap between the skin surface and the fabric surface. Broadly speaking, the distribution of strains inside the medium are the blurred version of pressure distribution on the surface [1, 2]. From the leftmost first peak in these figures, the higher responses to the edge of undulation than that to the flat and textured parts are attributed to the higher change in skin surface curvature under the edge as the skin conforms to it. Combined with the above section on "Fingertip and Bar", these results show a direct spatial relationship between the responses of the SAI and the change in the curvature of the skin surface above MSS, namely the role of packing space of fabric surface in roughness sensation.

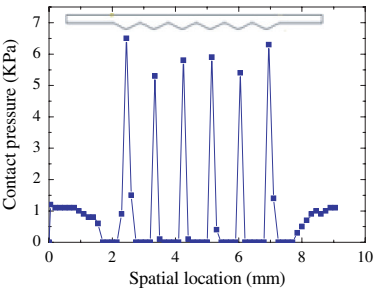

Fig. 68.3 Contact pressure distribution over the spatial location for sequential indentations

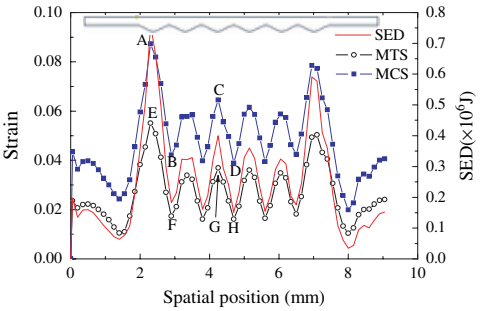

Fig. 68.4 SED and strains at a depth of 1.0 mm for the sequential indentions of fabric

On the other hand, the response of the first convexity indenting into fingerpad different from the next, as shown in Fig. 68.4 is 51.89% and 68.42% at point of A and B, E and F of edge convexity, and 40.49% and 56.37% of multi-convexities at C and D, G and H, respectively. These results indicate that SED and the maximum tensile strains (MTS) give stronger stimuli to SA units, and means more discriminable textures than that of the maximum compressive strains (MCS).

Due to predict a quadratic relationship between neural response and stimulus amplitude, furthermore, SED is eliminated from the relevant stimulus to SAI units by Sripati [2], and the general conclusion is linear over a wide range of indentations by the probe tip [1, 2]. Note, small contact area size of probe in effect is nearly stationary during indentation. Whereas, the contact area increases rapidly at the beginning of fingerpad contacting objects [2, 3]. In fact, Verg-Bermudez [5] observed that the number of probe contacting with fingerpad, equivalently larger contact area, affects nonlinearly the neural response of SAI afferents. The apparently increasing contact area enhances the probability of gross mechanical coupling between stimulus sites, namely recruiting more SAI afferents in effect. For the textiles, the equivalent contact-area radius spreads apparently on fingerpad contacting fabric. Therefore, SED is considered as a candidate proximal stimulus to SAI afferents for its good prediction. If the Merkel cell receptors generate a neural impulse rate proportional to the strain energy density in their neighborhood, then the receptors can have a fixed location and orientation relative to the skin surface and yet code with high fidelity the different mechanical stimuli imposed on the skin surface.

Conclusion

Skin's material properties determine that it effectively acts as a low-pass filter in transmitting the mechanical signals, and the mechanoreceptors respond to the blurred version of the surface pressure distribution, thus spatially encode the shape of the objects in terms of its surface curvatures.

As the compliance of the skin and its substrata, the rapidly spreading contact region on contacting leads to recruiting more and more SAI afferents in "influence region" when fingerpad is in contact with fabric, so that the general linear

relationship between indentation amplitude and neural response is dubitable. It means that SED is probably the relevant stimuli to SAI units.

From rigid bar to soft fabric, the tentative conclusion is draw, namely MS and SED is the potential variables encoding the surface texture by touching plain woven fabric. These results are instructive to design virtual tactile rendering device of fabric.

Acknowledgments The National Natural Science Foundation through grant number 10672057.

References

1. Phillips, J.R., Johnson, K.O.: Tactile Spatial Resolution. III A Continuum Mechanics Model of Skin Predicting Mechanoreceptor Responses to Bars, Edges and Gratings. J. Neurophysiol. 46 (1981) 1204–1225.
2. Sripati, A.P., Bensmaia, S.J., Johnson, K.O.: A Continuum Mechanical Model of Mechanoreceptive Afferent Responses to Indented Spatial Patterns. J. Neurophysiol. 95 (2006) 3852–3864.
3. Hu, J., Ding, X., Wang, R.: Dependence of Softness on Fabric Surface Quality and Compressibility. J. Donghua University (Eng. Ed.) 23 (2006) 59–63.
4. Moll, I., Roessler, M., Brandner, J.M., et al.: Human Merkel Cells – Aspects of Cell Biology, Distribution and Functions. European Journal of Cell Biology 84 (2005) 259–271.
5. Verga-Bermudez, F., Johnson, K.O.: Surround Suppression in the Response of Primate SAI and RA Mechanoreceptive Afferents Mapped with A Probe Array. Journal of Neurophysiology 81 (1999) 2711–2719.

Chapter 69
Robust Auditory-Based Speech Feature Extraction Using Independent Subspace Method

Qiang Wu, Liqing Zhang and Bin Xia

Abstract In recent years many approaches have been developed to address the problem of robust speaker recognition in adverse acoustical environments. In this paper we propose a robust auditory-based feature extraction method for speaker recognition according to the characteristics of the auditory periphery and cochlear nucleus. First, speech signals are represented based on frequency selectivity at basilar membrane and inner hair cells. Then, features are mapped into different linear subspaces using independent subspace analysis (ISA) method, which can represent some high order, invariant statistical features by maximizing the independence between norms of projections. Experiment results demonstrate that our method can considerably increase the speaker recognition accuracy specifically in noisy environments.

Introduction

In speaker recognition system, feature extraction is one of important tasks, which aims at finding succinct, robust, and discriminative features from acoustic data. Acoustic features such as linear predictive cepstral coefficients (LPCC) [1], mel-frequency cepstral coefficients (MFCC) [1], perceptual linear predictive coefficients (PLP) [1] are commonly used, and the most popular data modeling techniques in current speaker recognition are based on the gaussian mixture model (GMM) [2]. Recently the computational auditory nerve models attract much attention from both neuroscience and speech signal processing communities. Lewicki et al. [3] demonstrated that efficient coding of natural sounds could explain auditory nerve filtering properties and their organization as a population. Smith et al. [4] proposed an

Q. Wu
Department of Computer Science and Engineering, Shanghai Jiao Tong University, Shanghai 200240, China
e-mail: johnnywu@sjtu.edu.cn

R. Wang et al. (eds.), *Advances in Cognitive Neurodynamics*,

algorithm for learning efficient auditory codes using a theoretical model for coding sound in terms of spikes.

However, the conventional feature extraction methods for speaker recognition are often affected by the environmental noise or channel distortions. In this paper, we investigate statistical approaches of constructing a basis function for encoding patterns including spectral and temporal information. This method attempts to extract the robust speech features by mapping the frequency selectivity characteristics at cochlea into independent subspace. The extraction features may model the differences of speakers and reduce the disturbances of noise. Furthermore, we employ the support vector machine as a classifier to test the effectiveness and recognition performance.

Method

As we know, the human auditory system can accomplish the speaker recognition easily and be insensitive to the background noise. In our approach, the first step is to obtain the frequency selectivity information by imitating the process performed in the auditory periphery and pathway. And then we represent the robust speech feature as the projections of the extracted auditory information mapped into a feature subspace via independent subspace analysis. A diagram of the feature extraction method and speaker recognition is shown in Fig. 69.1. For the auditory-based processing of speech signals, we implement three modules of auditory system as what is described in Fig. 69.1 to obtain the representation in the auditory periphery and pathway.

In order to raise the energy for frequency components located in the high frequency domain, we implement traditional pre-emphasis to model the combined outer and middle ear as a band-pass function i.e. $H(z) = 1 - 0.97z^{-1}$.

The frequency selectivity of peripheral auditory system is simulated by a bank of cochlear filters which represent frequency selectivity at various locations along the basilar membrane in a cochlea. The cochlear filterbanks have an impulse response as $g(t) = at^{n-1}e^{2\pi bERB(f_c)t}cos(2\pi f_c t + \phi)$, where n is the order of the filter, f_c is the center frequency, ϕ is the phase, $a, b \in R$ are constants where b determines the rate of decay of the impulse response, which is related to bandwidth, $ERB(f_c)$ is the equivalent rectanglar bandwidth (ERB) of the auditory filter with a quadratic formula i.e. $ERB = 24.7(4.37f_c/1000 + 1)$.

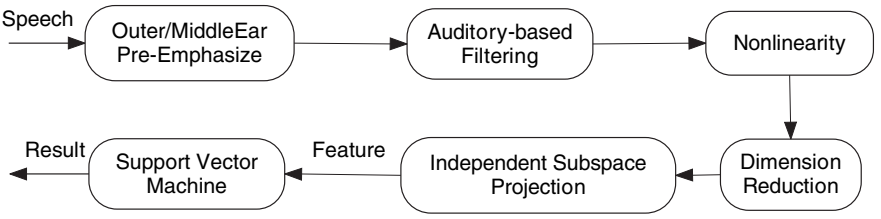

Fig. 69.1 Extraction of auditory feature by independent subspace method and recognition

In order to model nonlinearity of the inner hair-cells, the power of each band in every frame with a logarithmic nonlinearity was calculated by following equation i.e. $x(k) = log(1 + \gamma \sum_{t \in frame\ k} \{x_g(t)\}^2)$, where $x(k)$ is the output power, γ is a scaling constant, $x_g(t)$ is the output of cochlear filterbanks. This result can be considered as average firing rates in the inner hair-cells, which simulate the higher auditory pathway.

In this paper we apply independent subspace analysis to learn an optimal basis function which can give a robust representation of speech signals. The motivation of independent subspace analysis [5] (ISA) is to achieve such an extension which generalizes the assumption of component independence to independence between groups of components. Compared to the ordinary ICA model, the components s_i in ISA model are not assumed to be all mutually independent. Instead, s_i can be divided into n-tuples and the s_i inside a given n-tuple may be dependent on each other, but dependencies among different n-tuples are not allowed. A stochastic gradient ascent algorithm can be described as:

$$\Delta \mathbf{w}_i \propto \mathbf{x} \left(\mathbf{w}_i^T \mathbf{x} \right) g \left(\sum_{i \in S_j} \left(\mathbf{w}_i^T \mathbf{x} \right)^2 \right). \tag{69.1}$$

where $\mathbf{w}_i$ is the vector of demixing matrix, $\mathbf{x}$ is the observed signal, $g = p'/p$ is a nonlinear function that incorporates the information on the sparseness of the norms of the projections. In order to speed up the convergence, we prewhite the signals and constrain the vectors $\mathbf{w}_i$ to be orthogonal and unit norm. More information about ISA can be found in [5].

Experiments and Results

In order to evaluate the efficiency of our method, a text-independent speaker identification experiment was conducted. We used Grid speech corpus to test the performance of our feature extraction method in section (Methods). The Grid speech Corpus contains 17000 sentences spoken by 34 speakers (18 males and 16 females).

In our experiments the sampling rate of speech signals was 8 kHz. For the given speech signals, we employed every window of length 8000 samples(1s) and time duration 20 samples (2.5 ms) and 36 gammatone filters were selected. In order to reduce the computational complexity, principle component analysis was performed for the dimension reduction. As described in section (Methods), we calculated the basis function using independent subspace analysis after the calculation of the average firing rates in the inner hair-cells. 170 sentences (five sentences each person) were selected randomly as the training data for learning basis function and 40 independent feature subspaces were obtained which subspace dimension was chosen to be 4.

In order to test the efficiency and robustness of our feature extraction method, we employed support vector machine as the classifier. 1700 sentences (50 sentences each person) were used as training data and 2040 sentences (60 sentences each person) mixed with different kinds of noise were used as test data. The test data

was mixed with babble, factory, f16 and white noises in SNR intensities of 15dB, 10dB, 5dB and 0dB.

For comparison, we implemented a baseline GMM system that used conventional MFCC. In the system, each frame was modeled by 13-component vector, derived from a 40-channel Mel-scale filter bank, and the popular data modeling method GMM was used to build the recognizer with 32 gaussian mixtures. From Fig. 69.2a

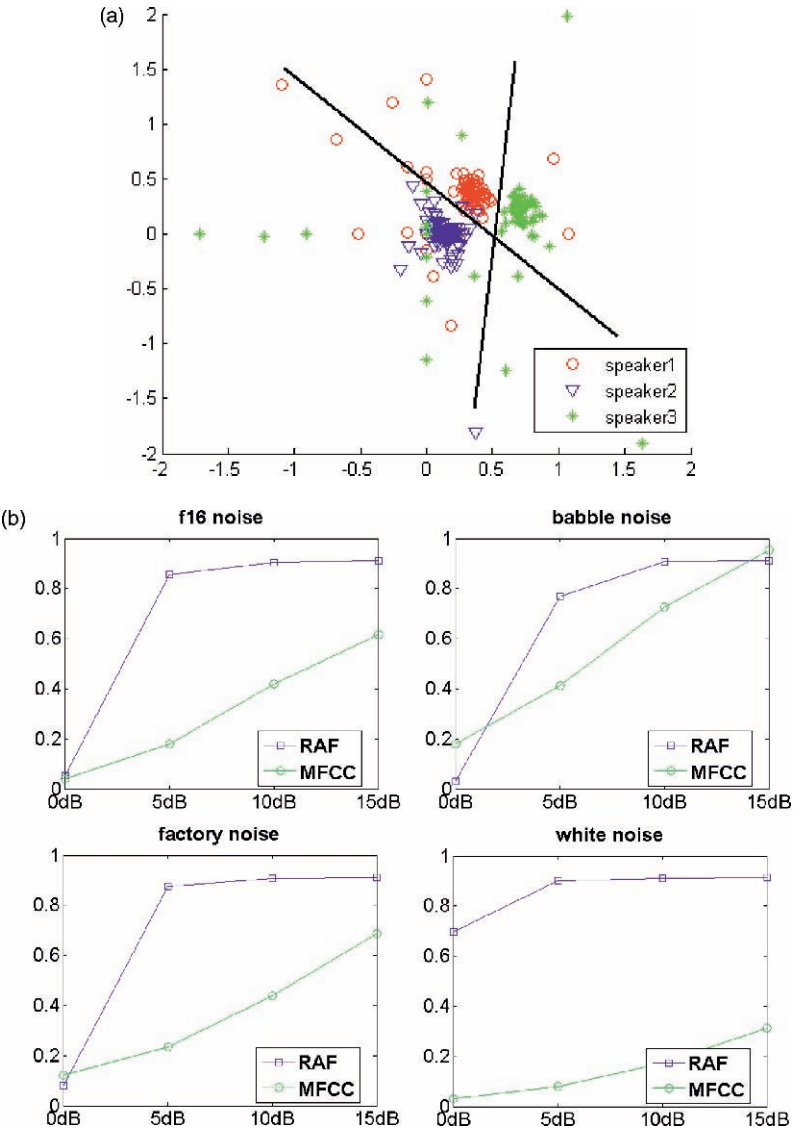

Fig. 69.2 Feature space for classification and identification accuracy. (a) depicts projections onto two-dimensional feature space using PCA. The data was mixed with white noise in SNR 5dB. (b) shows the identification accuracy in different noise conditions

we can observe the classification boundaries among different speakers clearly which is beneficial to the identification. Figure 69.2b presents the identification accuracy obtained by the robust auditory-based feature (RAF) and baseline system in all tested conditions.

The result demonstrates that the performance degradation of RAF is little with noise intensity increase. It performs significantly better than MFCC in the high noise conditions. Such as 0dB condition of white noise, RAF maintains results close to the low noise condition, while MFCC has dropped sharply. The result can suggest that this auditory-based method is robust against the noise and improves the recognition performance.

Conclusions

An auditory-based feature extraction method applied to a text-independent speaker recognition task was presented in this paper, and according to the experiments results, the robustness and effectiveness were confirmed. This method is designed to extract the robust speech features by mapping the frequency selectivity characteristics at cochlea into independent subspace by learning a basis function. The goal of finding a optimal basis function using independent subspace analysis was to increase the robustness of feature by removing the noisy components and improve the recognition scores.

Acknowledgments The work was supported by the National High-Tech Research Program of China (Grant No.2006AA01Z125) and the National Basic Research Program of China (Grant No. 2005CB724301).

References

1. L.R. Rabiner, B. Juang: Fundamentals on Speech Recognition. Prentice Hall, New Jersey (1996).
2. D.A. Reynolds, R.C. Rose: Robust text-independent speaker identification using gaussianmixture speaker models. Speech and Audio Processing, IEEE Transactions **3** (1995) 72–83.
3. M.S. Lewicki: Efficient coding of natural sounds. Nature neuroscience **5** (2002) 356–363.
4. E.C. Smith, M.S. Lewicki: Efficient auditory coding. Nature **439** (2006) 978–982.
5. A. Hyv arinen, P. Hoyer: Emergence of phase-and shift-invariant features by decomposition of natural images into independent feature subspaces. Neural Computation **12** (2000) 1705–1720.

Chapter 70
Intra- and Interpersonal Coordination of Goal-Oriented Movements in a Working Scenario

Cordula Vesper, Sonja Stork, Mathey Wiesbeck and Anna Schubö

Abstract We present a scenario for examining mechanisms of goal-oriented movement coordination in humans. Our aim is to determine behavioral rules and constraints that shape movement execution. Therefore, trajectories of hand and finger movements are recorded while participants perform a simple construction task. We measure different parameters of reaching and grasping and compare performance in a single-person versus a two-person condition. First results of a pilot study are shown. Finally, we discuss our scenario with respect to possible applications in human-robot interaction in a factory environment.

Introduction

Movement coordination with other people is an important aspect of our everyday social life. For example, we are able to catch a ball thrown by a member of our basketball team or we avoid collisions when walking through a crowded shopping mall. In all these apparently easy situations, the human motor system faces a variety of challenges related to motor planning and movement coordination, e.g. how to select the right motor program regarding the fact that motor tasks can be performed in an infinite number of ways [1], the so-called "degrees-of-freedom" problem. A different, but related problem is the necessity to adapt movements online to a changing environment. For example, static or moving obstacles (such as objects or another person's limbs) have to be avoided. Furthermore, a question that is still under debate is how motor actions can be learned [2].

Research in cognitive psychology and neuroscience has attempted to detect the underlying mechanisms of these complex human abilities. Most current theories on the motor system assume three different types of mechanisms that allow an individual to execute, plan and monitor motor actions [2]. First, motor commands

C. Vesper
Department of Psychology, Experimental Psychology, Ludwig-Maximilians-Universität München, Leopoldstr. 13, 80802 Munich, Germany
e-mail: Cordula.Vesper@Campus.LMU.de

R. Wang et al. (eds.), *Advances in Cognitive Neurodynamics*,

are sent out via reafferences from the motor system to the periphery where they are executed and transformed into consequent sensory feedback. Second, the same motor commands are fed into an internal forward model that uses these efference copies of the motor commands to predict the sensory consequences of possible movements before they actually happen. Third, an inverse internal model works in the opposite direction by computing motor commands with respect to the goal movement, i.e. the motor system determines what muscles need to be used in order to reach a certain sensory effect.

Although the internal model approach works well on an individual actor's level, motor control is even more complicated in interaction situations as the other person's next movements and action goals have to be inferred [4]. However, Wolpert et al. assume that the same general mechanisms can also apply to group situations [4]: the motor commands from person A will provide communicative signals that the interaction partner B can perceive to understand A's movement and use this information to coordinate his or her own motor actions with the partner. Thus, the theory of internal models can account both for intra- and interpersonal motor control.

In addition, several constraining mechanisms of the motor system have been specified. First, constraints arise from the movement kinematics themselves, e.g. trajectories are normally smooth and have a bell-shaped velocity profile. Different parameters determine the exact form of a movement, including shape and material of a to-be-grasped object [3], movement direction, the relation of object size and movement speed or the timing of the maximal grip aperture [1]. Another constraining mechanism is to plan movements according to their end-goal [5]: particular movements are chosen with respect to the comfort of the goal posture ("endstate-comfort effect") or dependent on the subsequent movement [6]. Finally, a hierarchy of constraints [5] is set up for each motor task determining the priorities of single task steps. For example, when carrying a tray of filled water glasses, keeping the balance is more important than moving quickly.

In the remaining part of this paper, we introduce a scenario that aims at examining general mechanisms of human movement coordination in an assembly task in order to transfer results to situations in which humans and robots work together.

The Ball Track Scenario

The ball track scenario consists of the relatively simple task of building a ball track (i.e. a children's toy to let marbles run down) from wooden blocks. Its advantage lies in its flexible design and the large amount of possible parameters that can be examined with it.

In our scenario, participants build a ball track from wooden blocks (height 4 cm, width 4 cm, length between 4 and 16 cm) while their arm and hand movement parameters are assessed. They sit alone or next to a second person at a table with the ball track blocks and a screen in front of them. In each trial, the participants' task is to grab the blocks from a predetermined initial position and to stack them

Fig. 70.1 (a) Example of goal ball track (*top*) and an initial block position (*bottom*); (b) Marker of Polhemus Fastrak; (c) Temporal coordination in joint performance: vertical movements of one pair of participants (*smooth lines*: person A, *dotted lines*: person B) in 3 trials (same condition)

according to a visual instruction showing the goal ball track (Fig. 70.1a). Our main focus with this task lies on the temporal aspects of movement coordination. We analyze movement onset time, latency and length of individual performance steps (e.g. grasp and transport components), velocity, and acceleration patterns and overall variances of movements. A Polhemus Fastrak, a magnetic motion tracker with a six degree-of-freedom range (X, Y and Z coordinates and azimuth, elevation and roll), is used for this movement recording (sampling rate: 120 Hz). The receiver markers are mounted on the back of the hand or on the index finger and thumb of the participants (Fig. 70.1b). In a later project phase, we plan to additionally use the electroencephalogram (EEG) to measure electrical brain potentials while the block stacking task is performed.

This scenario allows the examination of a variety of different aspects of human movement coordination. As our main interest concerns the interaction of two persons, a main comparison is between *individual and joint performance*. We hypothesize that, when people work in a group, the kinematics and temporal aspects of the interaction partner's movements will be taken into account and used to adapt the own motor actions. Consequently, similarities between single and joint performance should be observable. A second parameter we will examine is *uni- versus bimanual working*, i.e. we compare the condition in which one hand is used to the condition in which participants work with both hands. Moreover, we intend to analyze "two persons, one hand" and "one person, two hands" conditions. Similar movement patterns in these conditions would support the idea that the own motor system is used to understand and predict other peoples' actions [7]. A further experimental variation concerns the relation of *initial and goal block orientation*. Based on the above described findings on the dependence of end-goal on movement planning, as, e.g., the endstate-comfort effect [5], we want to examine hand orientation at pick up and put down sites. We expect individuals to use different initial hand orientations that depend both on the initial and on the goal position of the blocks. Similarly, by varying the goal positions of the blocks, we can look at mechanisms of *obstacle avoidance*. In our scenario, this becomes necessary when the workspaces of the interaction partners overlap. Consequently, we expect to find timing delays in the movement patterns if the other person's actions have to be carried out before the subsequent movement can be started. Finally, we will also vary *timing constraints* imposed to our participants as well as *task complexity*.

In a pilot study with three pairs of participants, we found first evidence for some of the hypothesized effects. As can be seen in Fig. 70.1c, people systematically coordinate the timing of their responses. In specific, the onset of a movement (both at pick up and put down positions) is strongly coupled with the partner's movement pattern. This is especially striking in the case of overlapping workspaces, where a larger movement onset delay can be seen. Finally, we could also observe that hand orientation during grasping depends on the relation of block orientation at the initial and goal position.

Conclusion

The aim of this paper was to introduce our ball track scenario that examines a variety of questions related to movement coordination in humans and robots. We presented the methodology, an overview of relevant variables and first results. A special focus of the scenario is the possibility to apply results to human-human and human-robot interaction in assembly and construction tasks. Progress in the development of robot technology is fast and as a consequence humans and machines will interact to an even greater extent in the future [8]. Thus, the value of understanding the parameters which determine the outcome of internal forward and inverse models in humans is threefold: First, knowledge about principles of human motor control in interaction situations can be used to ergonomically design workspaces and, thus, improve interpersonal coordination in both everyday and professional applications. Second, mechanisms observed in human intrapersonal movement coordination can be used in order to solve the degree of freedom problem in movement trajectory planning of robots. Finally, transferring results from interpersonal movement coordination will enhance adaptive behaviors in machines and allow the safe and efficient collaboration of human workers and robots.

Acknowledgments This work is funded in the Excellence Cluster "Cognition for Technical Systems" (CoTeSys) by the German Research Foundation (DFG). The authors would like to thank their research partners Florian Engstler, Christian Stößel and Frank Wallhoff for fruitful discussions and contributions in the project "Adaptive Cognitive Interaction in Production Environments" (ACIPE).

References

1. Rosenbaum, D.A.: Human Motor Control. Academic Press, San Diego (1991).
2. Wolpert, D.M., Kawato, M.: Multiple paired forward and inverse models for motor control. Neural Networks 11 (1998) 1317–1329.
3. Cujpers, R.H., Smeets, J.B.J., Brenner, E.: On the relation between object shape and grasping kinematics. Journal of Neurophysiology 91 (2004) 2598–2606.
4. Wolpert, D.M., Doya, K., Kawato, M.: A unifying computational framework for motor control and social interaction. Philosophical Transactions of the Royal Society of London 358 (2003) 539–602.

5. Rosenbaum, D.A., Meulenbroek, R.G.J., Vaughan, J.: Planning reaching and grasping movements: Theoretical premises and practical implications. Motor Control 2 (2001) 99–115.
6. Cohen, R.G., Rosenbaum, D.A.: Where grasps are made reveals how grasps are planned: generation and recall of motor plans. Experimental Brain Research 157 (2004) 486–495.
7. Rizzolatti, G., Fogassi, L., Gallese, V.: Neurophysiological mechanisms underlying the understanding and imitation of action. Nature Reviews 2 (2001) 661–670.
8. Thrun, S.: Toward a framework for human-robot interaction. Human-Computer Interaction 19 (2004) 9–24.

Chapter 71
Network Synchronization/Desynchronization Defects in the Pathogenesis of Neuropsychiatric Disorders

R.S. Hernandez and P.E. Rapp

Abstract Classical theory maintained that all significant information transmission in the central nervous system was implemented by the movement of neurotransmitters at axon-to-dendrite synapses. It is now understood that this is an incomplete description. An alternative understanding incorporates other forms of information transmission and emphasizes the role of synchronization in organizing CNS activity. This expanded view has immediate implications for the clinical response to neuropsychiatric disorders. Treatment of neuropsychiatric disorders should not focus exclusively on neurotransmitters acting at chemical synapses. Rather, the focus should expand to include a generic examination of network dysfunction. CNS network defects will, it is hypothesized, result in abnormalities of synchronization that may be diagnostically disclosing.

Introduction: The Failure of the Neuron Doctrine

Once it was simple. The Neuron Doctrine, it was supposed, provided an essentially complete specification of the mechanism of central nervous system (CNS) function. The Doctrine could be presented in five statements.

1. All information processing in the CNS is performed by neurons.
2. Neurons are anatomically discrete units; they do not form a reticulum.
3. All information transmission is unidirectional from axons of the pre-synaptic neuron to dendrites of the post-synaptic neuron.
4. All information transmission is mediated by all-or-nothing, regeneratively propagated action potentials.
5. All information is transmitted from neuron-to-neuron across the synaptic cleft by neurotransmitters.

R.S. Hernandez
Uniformed Services University, Bethesda, MD, USA
e-mail: rhernandez@usuhs.mil

R. Wang et al. (eds.), *Advances in Cognitive Neurodynamics*,

In practice neuroscientists did not hold the Doctrine as stated above inflexibly. All recognized that there were exceptions to each of the five statements. Indeed even Ramón y Cajal who introduced the concept of anatomically discrete neurons (as contrasted with Golgi's hypothesis of neurons forming a continuous syncytium) recognized that there would be exceptions to the principle of neural discontinuity (as cited by Bullock et al. [1]). Assessment of the frequency and magnitude of these exceptions and their operational significance to CNS function is, however, a challenging question that must be addressed. The exceptions are frequent, and they are highly significant because they lead to an expanded view of CNS operation which has immediate implications for the clinical response to neuropsychiatric disorders. As summarized by Bullock et al. [1] and Douglas Fields [2], emerging evidence indicates that the classical Neuron Doctrine is at best an incomplete description of CNS operation. Each of the five assertions made above have been challenged.

The list of exceptions to the Neuron Doctrine indicate that the search for organizing principles that provide a conceptual framework for interpreting CNS operation must expand beyond axon-to-dendrite neurotransmitter mediated communication between neurons. If not the Neuron Doctrine, what? Bullock's view, as presented by Douglas Fields [2] was that "the unparalleled abilities of the human mind arise not as a unique property of our neurons or brain circuitry but as an emergent property of the way its billions of neurons operate cooperatively." This is stated with such breadth that it is almost certainly correct, but it is not mechanistically specific. Most importantly it does not immediately suggest a potentially falsifiable hypothesis. The requirement for a hypothesis driven investigation is addressed by introducing the network synchronization hypothesis.

The Network Synchronization Hypothesis

A long intellectual development has lead to the concept of organization by synchronization. An important contribution to the development of the synchronization hypothesis was made by von der Malsburg in a theory of correlative brain function published as an internal report of the Max-Planck-Institut für Biophysikalische Chemie [3]. A parallel developmental history took the EEG as its starting point. Freeman's book "Mass Action in the Nervous System" [4] begins with the question "What are the neural mechanisms and what is the behavioral significance of the electroencephalogram (EEG)?" Freeman's analysis included an early, perhaps the first, mathematical account of the importance of neural synchronization in ongoing in CNS activity.

In the 1980's investigations of oscillating CNS activity took on an added interest because of the hypothesized role of synchronization in feature binding. The binding problem has been stated with exemplary concision by Revonsuo and Newman [5]. The binding problem is "the problem of how the unity of conscious perception is brought about by the distributed activities of the central nervous system." The problem is often examined in the context of visual processing. How do the distinct

elements of an object, its color, shape, distance, texture and direction and velocity of motion bind together to form a unitary percept? Building on earlier work, notably Bressler and Freemen [6], Singer [7] and Eckhorn [8] proposed that feature binding was accomplished by synchronized oscillations in the visual cortex.

The concept of integration by synchronization has subsequently been generalized beyond the specific context of sensory feature binding to provide a generic dynamical metaphor for CNS organization including cognition [9] Synchronization of EEGs and ERPs (event related potentials) are associated with attention, learning, memory and perception. (A large primary literature is identified in [10]) We must guard against an unduly simplistic conceptualization of the role of synchronized activity. The importance of a cautionary view becomes especially apparent when considering patterns of event related synchronization and desynchronization. Complicated patterns of synchronization and desynchronization can be seen simultaneously at different scalp sites in response to the same stimulus [11, 12, 13] With these complexities of mechanism and interpretation explicitly recognized, we can ask an empirical question: are abnormalities of synchronization and desynchronization associated with neuropsychiatric disorders? The answer is "Yes." A large literature is listed in [10] Table 3. General reviews are given in [14, 15, 16, 17].

Clinical Implications

At present, the principal treatment for psychiatric disorders is pharmacological. These treatments are directed to manipulating synaptic transmission by either facilitating transmission, for example by providing transmitter precursors, or by blocking transmitter receptor sites. The growing list of exceptions to the Neuron Doctrine indicates that synaptic transmission is only a part, possibly a small part, of CNS function. We should look beyond the chemical synapse and try to identify forms of treatment that will have a positive impact on network integrity. It is possible that some forms of treatment already in use act by enhancing network function. Fluoxetine (Prozac) is a widely prescribed serotonin reuptake inhibitor with antidepressant action. Paradoxically, tianeptine (Stablon) which is a serotonin reuptake enhancer also has antidepressant action. Though these drugs have opposite effects on serotonin transport, they have a common action in promoting increased innervation in the forebrain [18]. This result is pertinent to the thesis of the present contribution because the resulting increase in serotonin fiber density in the forebrain would have an effect on network function.

The increased fiber density reported in [18] could be the result of increased arborization of exiting neurons. This is the possibility that they emphasize in the discussion of their results. Other investigations, however, suggest that neurogenesis may be a critical element in antidepressant action. For example, Madsen et al. [19] have shown increased hippocampal neurogenesis in an animal model of electroconvulsive therapy. Malberg et al. [20] showed that chronic antidepressant treatment using several different classes of antidepressant medication increased neurogenesis

in the adult rat hippocampus. Santarelli et al. [21] carried the analysis further with animal studies showing that interventions blocking the neurogenesis effect of antidepressants also blocked the behavioral antidepressant action of these drugs. Similarly, aerobic exercise can have significant antidepressant action [22] and exercise can increase hippocampal neurogenesis to high levels [23]. Ernst et al. [24] have argued that the antidepressant effects of aerobic exercise may be related to its impact on neurogenesis. Treatments that increase fiber density or create new neurons have an impact on the hardware available for network activity.

Conclusions

Neuropsychiatric disorders are disorders of networks. Treatment of neuropsychiatric disorders should not focus exclusively on neurotransmitters acting at chemical synapses. Rather, the focus should expand to include a generic examination of network dysfunction. Among other consequences, CNS network defects will, it is hypothesized, result in abnormalities of synchronization and desynchronization that may be diagnostically disclosing. Additionally, longitudinal time-frequency analysis of event related signals may provide an important technology for assessing the response to treatment.

Acknowledgments This research was supported by the Naval Medical Research Center. We also acknowledge support from the Traumatic Injury Research Program of the Uniformed Services University. The opinions and assertions contained herein are the private ones of the authors and are not to be construed as official or reflecting the views of the Department of the Navy or the Department of Defense.

References

1. Bullock, T.H., Bennett, M.V.L., Johnston, D., Josephson, R., Marder, E., Douglas Fields, R. The Neuron Doctrine, Redux. Science 310 (2005) 791–793.
2. Douglas Fields, R. Beyond the neuron doctrine. Scientific American Mind 17(3) (2006) 20–27.
3. von der Malsburg, C. The correlation theory of brain function. (Internal Report 81-2). Max-Planck-Institut fur Biophysikalische Chemie. (1981) Reprinted in E. Domany, J. L. van Hemen and K. Schulten, eds. Models of Neural Networks II. Berlin: Springer Verlag (1994).
4. Freeman, W.J. Mass Action in the Nervous System: Examination of the Neurophysiological Basis of Adaptive Behavior Through the EEG. New York: Academic Press (1975).
5. Revonsuo, A., Newman, J. Binding and consciousness. Consciousness and Cognition 8 (1999) 123–127.
6. Bressler, S.L., Freeman,W.J. Frequency analysis of olfactory system EEG in cat, rabbit and rat. Electroencephalography and Clinical Neurophysiology 5 (1980) 19–24.
7. Gray, C.M., König, P., Engel, A.K., Singer, W. Oscillatory responses in the cat visual cortex exhibit inter-columnar synchronization which reflects global stimulus properties. Nature 338 (1989) 334–337.
8. Eckhorn, R., Bauer, R., Jordan, W., Brosch, M., Kruse, W., Munk, M., Reitboeck, H.J. Coherent oscillations: A mechanism of feature linking in the visual cortex? Biological Cybernetics 60 (1988) 121–130.

9. Varela, F., Lachaux, J.P., Rodriguez, E., Martinerie, J. The brainweb: Phase synchronization and large scale integration. Nature Reviews Neuroscience 2 (2001) 229–239.
10. Rapp, P.E., Cellucci, C.J., Hernandez, R.S. CNS synchronization/desynchronization abnormalities following blast exposure. (2007) Technical Report. Silver Spring, Maryland: Combat Casualty Care Directorate. Naval Medical Research Center.
11. Pfurtscheller, G. Event-related synchronization (ERS): an electrophysiological correlate of cortical areas at rest. Electroencephalography and Clinical Neurophysiology 83 (1992) 62–69.
12. Pfurtscheller, G. Induced oscillations in the alpha band: functional meaning. Epilepsia 44 Suppl. 12 (2003) 2–8.
13. Neuper, C., Pfurtscheller, G. Event-related dynamics of cortical rhythms: frequency-specific features and functional correlates. International Journal of Psychophysiology 43 (2001) 41–58.
14. Herrmann, C.S., Demiralp, T. Human EEG gamma oscillations in neuropsychiatric disorders. Clinical Neurophysiology 116(12) (2005) 2719–2733.
15. Llinás, R., Ribary, U., Jeanmonod, D., Kronberg, E., Mitra, P.P. Thalamocortical dysrhythmia: a neurological and neuropsychiatric syndrome characterized by magnetoencephalography. Proceedings of the National Academy of Sciences, USA 96 (1999) 15222–15227.
16. Schnitzler, A., Gross, J. Normal and pathological oscillatory communication in the brain. Nature Reviews: Neuroscience 6(4) (2005) 285–296.
17. Uhlhaas, P.J., Singer, W. Neural synchrony in brain disorders: relevance for cognitive dysfunctions and pathophysiology. Neuron 52(1) (2006) 155–168.
18. Zhou, L., Huang, K.-X., Kecojevic, A., Welsh, A.M., Koliatsos, V.E. Evidence that serotonin reuptake modulators increase the density of serotonin innervation in the forebrain. Journal of Neuorchemistry 96(2) (2006) 396–406.
19. Madsen, T.M., Treschow, A., Bengzou, J., Bolwig, T.G. Lindvall, O., Tingstrom, A. Increased neurogenesis in a model of electroconvulsive therapy. Biological Psychiatry 47 (2000) 1043–1049.
20. Malberg, J.E., Eisch, A.J., Nestler, E.J., Duman, R.S. Chronic antidepressant treatment increases neurogenesis in adult rat hippocampus. Journal of Neuroscience 20 (2000) 9104–9110.
21. Santarelli, L., Saxe, M., Gross, C., Surget, A., Battaglia, F., Dulawa,S., Weisstaub, N., Lee, J., Duman, R., Arancio, O., Belzung, C., Hen, R. Requirement of hippocampal neurogenesis for the behavioral effects of antidepressants. Science 301 (2003) 805–809.
22. Dunn, A.L., Trivedi, M.H., Kampert, J.B., Clark, C.G. and Chambliss, H.O. Exercise treatment for depression. Efficacy and dose response. American Journal of Preventive Medicine 28(1) (2005) 1–8.
23. Rhodes, J.S., van Pragg, H., Jeffrey, S., Girard, I., Mitchell, G.S., Garland, T., Gage, F.H. Exercise increases hippocampal neurogenesis to high levels but does not improve spatial learning in mice bred for increased voluntary wheel running. Behavioral Neuroscience 117(5) (2003) 1006–1016.
24. Ernst, C., Olson, A.K., Pinel, J.P.J., Lam, R.W., Christie, B.R. Antidepressant effects of exercise: evidence for an adult-neurogenesis hypothesis? Journal of Psychiatry and Neuroscience 31(2) (2006) 84–92.

Chapter 72
Exploring Causal Relationships in the Phase Functions of Coupled Van der Pol Oscillators

C.J. Cellucci and P.E. Rapp

Abstract We investigate whether causal relationships in coupled Van der Pol oscillators can be determined. Using the instantaneous phase of computer generated time series, which are unidirectionally and time dependently coupled, the technique of lagged mutual information is tested to determine its usefulness in detecting information transmission. If successful, it could assist in improving our understanding of the role of information transmission in organizing CNS activity.

Introduction

The study of Van der Pol oscillators has been of interest since Balthasar van der Pol's work on oscillations in a triode circuit led to the development of the Van Der Pol equation [1, 2]. The equation of motion for the Van der Pol oscillator can be written as,

$$\ddot{x} + \mu \left(x^2 - 1\right) \dot{x} + \omega_0 x = 0 \tag{72.1}$$

The linear term represents a constant force which determines the natural frequency. The self-sustained oscillations are modified by the nonlinear damping term. There is positive damping or energy is dissipated from the system when $|x| > 1$, and there is negative damping or energy is added to the system when $|x| < 1$.

Rewriting (1) as first order equations, the coupled system being studied is,

$$\begin{aligned} &\textbf{System 1}\ \frac{dx_1}{dt} = y_1 \quad \textbf{System 2}\ \frac{dx_2}{dt} = y_2 \\ &\frac{dy_1}{dt} = -\mu_1 \left(\hat{x}_1^2 - 1\right) y_1 - \omega_{01} x_1 \quad \frac{\mathrm{dy}_2}{\mathrm{dt}} = -\mu_2 \left(\hat{\mathrm{x}}_2^2 - 1\right) \mathrm{y}_2 - \omega_{02} \mathrm{x}_2 \end{aligned} \tag{72.2}$$

where $\hat{x}$ is the coupling term, and ε is the coupling parameter;

C.J. Cellucci
Aquinas, LLC, Berwyn, PA, USA
e-mail: cellucci@gmail.com

R. Wang et al. (eds.), *Advances in Cognitive Neurodynamics*,

$$\hat{x}_1 = \varepsilon_{2,1} x_2 + (1 - \varepsilon_{2,1}) x_1 \quad \hat{x}_2 = \varepsilon_{1,2} x_1 + (1 - \varepsilon_{1,2}) x_2 \tag{72.3}$$

Physically, this means that the two oscillators are coupled only through the damping term. For $\varepsilon_{1,2} = \varepsilon_{2,1} = 0$, we have two uncoupled oscillators whose limit cycles are determined by the damping constants μ_1 and μ_2, and the natural frequency terms ω_{01} and ω_{02}.

Although there are different methods for calculating the phase of a signal, we chose an approach based on the Hilbert Transform. This technique was originally applied by Gabor [3]. For an arbitrary signal $s(t)$, an analytic signal of the form,

$$\Psi(t) = s(t) + s_{SH}(t) = A(t)\, e^{i\phi(t)} \tag{72.4}$$

is defined, where $s_{\mathrm{SH}}(t)$ is the Hilbert Transform of $s(t)$, $A(t)$ is the instantaneous amplitude, and $\varphi(t)$ is the instantaneous phase [4].

A fourth order Runge-Kutta algorithm was used for the numerical integration of the system Eqs. 2. The parameters chosen were $\varepsilon_{\mathrm{MAX}}\ (t) = 0.3,\ \mu_1 = 0.5,\ \mu_2 = 2,\ \omega_{01} = 7,\ \omega_{02} = 11$, the time step $= 0.1$, and the equations were integrated for 5000 steps. Since we are interested in detecting causal relationships, the coupling terms $\varepsilon(t)$, was unidirectional and time dependent. For the time steps, 1–1000, 2001–3000, and 4001–5000, there was no coupling, i.e., $\varepsilon_{1,2} = \varepsilon_{2,1} = 0$. For the interval 1001–2000, $\varepsilon_{1,2} = 0.3,\ \varepsilon_{2,1} = 0$; that is, the position of system 1 was coupled to the damping term of system 2. Finally, for interval 3001–4000, we set $\varepsilon_{1,2} = 0$, and $\varepsilon_{2,1} = 0.3$.

Causal Relationships

While synchronization measures can be used to prove a correlative relationship between two signals, they cannot establish causal relationships or provide any information concerning the direction or flow of information. In most cases, a quantitative assessment of causal relationships between two systems is built on the following idea. If the measurement of variable X improves the prediction of variable Y, then Y is, in at least this limited operational sense, causally dependent on X. It should be stressed that this relationship is not necessarily unidirectional. It can also be the case that, with the same data, measuring variable Y also improves the prediction of variable X. (This conceptualization of causality appears in Wiener [5]).

An early implementation of this concept was published by Granger [6] in the econometrics literature and popularized by Sims [7]. Granger causality is constructed using linear regression models of stochastic processes. In the sense operationalized by Granger, if past values of X are useful in predicting the current value of Y in a linear regression, then X has a causal relationship with time series Y. There are several variants of this concept. A complementary procedure for the investigation of causal relationships can be constructed by examining delayed mutual information functions.

Lagged Mutual Information

The mutual information of time series X and Y, $I(X, Y)$ is defined as the average number of bits of one variable that can be predicted by measuring the other. Mutual information is symmetrical, that is, $I(X, Y) = I(Y, X)$. Therefore, while mutual information can establish the presence of a nonrandom relationship between time series, it cannot identify causal relations. However, a time lagged mutual information in which one of the two variables is time shifted can be used to determine if, for example, measuring variable X in the past allows prediction of future values of variable Y. We can shift time series X by some time lag τ and calculate $I(X(\tau), Y)$ as a function of τ. Similarly, we can calculate $I(X, Y(\tau))$.

If measuring $X(\tau)$ allows better prediction of Y, than the other way around, then it can be argued that information is transferred from X to Y. The magnitude of the mutual information and the time lag which produces the greatest value of $I(X, Y)$ can be used to quantify both the magnitude of the information transfer and the time delay associated with that transfer. A number of investigators have proposed using lagged mutual information to investigate information transfer in distributed systems [8, 9]. In previous work, Albano [10] found that information transfer, as determined by lagged mutual information calculated between a scalp electrode located near an epileptogenic focus and other electrodes of the montage, increased prior to seizure onset.

Conversely, significant limitations of causality measures based on lagged mutual information have been identified in Schreiber [11]. He argues that "time delayed mutual information fails to distinguish between information that is exchanged from shared information due to common history and inputs." Since that time there have been some significant improvements in the calculation of mutual information, specifically we refer to the development of the CAR algorithm [12]. Because some of the deficiencies of prior methods have been overcome, we believe that a second look at lagged mutual information as a casualty measure is warranted.

After solving the system Eqs. (2) using the parameter values given above, the instantaneous phase for each time series was generated using the Hilbert Transform. Five hundred point epochs were used in calculating the mutual information, and the center of each time interval was used for the temporal location of each epoch. One epoch remains constant while the other epoch is moved forward in time. Past values of the mutual information of one system could then be compared with future values of the mutual information of the other system. Our results are summarized in Fig. 72.1.

Conclusions

These preliminary results suggest that there may still be some potential in the use of lagged mutual information as a casualty measure. Our results showed that an increase in mutual information corresponded in time with unidirectional coupling, and that the increase decayed when the coupling ended. Future questions to be addressed should include determining the noise robustness of this algorithm.

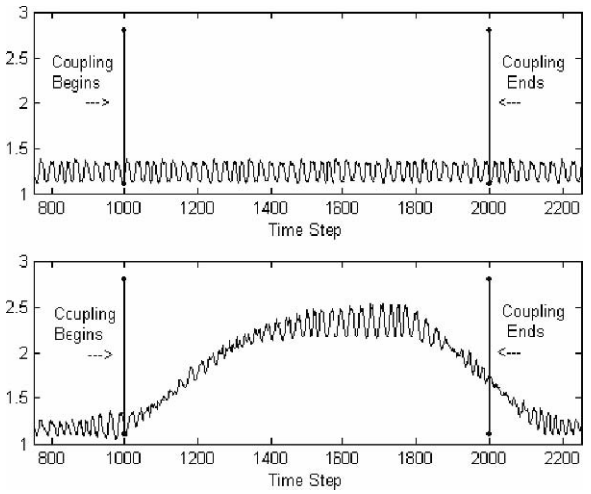

Fig. 72.1 (*Upper plot*) is the mutual information between a 500 point epoch of System 1 centered at time step 1000 and moving forward in time to a position centered at time step 2000, and a stationary 500 point epoch of System 2 centered at time step 1000. Since there is no coupling from System 2 to System 1 we see no change in mutual information. (*Lower plot*) is the mutual information between a 500 point epoch of System 2 centered at time step 1000 and moving forward in time to a position centered at time step 2000, and a stationary 500 point epoch of System 1 centered at time step 1000. There is a significant change in mutual information over the coupling interval. Comparable results were obtained for the time step interval 3001–4000, where System 2 was coupled to System 1

Biological signals, particularly EEG's are generally noisy, so methods whose performance deteriorates significantly with noise are of limited use.

Acknowledgments This research was supported by the Naval Medical Research Center. We also acknowledge support from the Traumatic Injury Research Program of the Uniformed Services University. The opinions and assertions contained herein are the private ones of the authors and are not to be construed as official or reflecting the views of the Department of the Navy or the Department of Defense.

References

1. Van der Pol, B. Forced oscillations in a circuit with non-linear resistance. Philosophical Magazine 3 (1927) 62–80.
2. Van der Pol, B., Van der Mark, J. The heartbeat considered as a relaxation oscillation, and an electrical model of the heart. Philosophical Magazine 6 (1928) 763–775.
3. Gabor, D. Theory of communication. Journal of the Institute of Electrical Engineers (London) 93 (1946) 429–457.
4. Schafer, C., Rosenblum, M.G., Abel, H., Kurths, J. Synchronization in the human cardiorespiratory system. Physical Review E 60(1) (1999) 857–869.
5. Wiener, N. The theory of prediction, In: Beckenback, E.R., (ed.): Modern Mathematics for Engineers. McGraw Hill, New York (1956).

6. Granger, C. W. J. Investigating causal relation by econometric and cross-sectional method. Econometrica 37 (1969) 424–438.
7. Sims, C.A. Money, income, and causality. The American Economic Review 62 (1972) 540–552.
8. Kaneko, K. Lyapunov analysis and information flow in coupled map lattices. Physica 23D (1986) 436–477.
9. Vastano, J.A., Swinney, H.L. Information transport in spatiotemporal systems, Physical Review E 60 (1988) 1773–1776.
10. Albano, A.M., Bedonie, C., Cellucci, C.J., Halkides, D., Miller, V., Ree, J., Torruella, A., Harner, R.N., Rapp, P.E. Spatiotemporal EEG information transfer in an episode of epilepsy. In: Sreenivasan, R., Pradhan, N. and Rapp, P.E.. (eds.) Nonlinear Dynamics and Brain Functioning. Nova Publishing, NY (1999) 411–434.
11. Schreiber, T. Measuring information transfer. Physical Review Letters 85, (2000) 461–464.
12. Cellucci, C.J., Albano, A.M., Rapp, P.E.. Statistical validation of mutual information calculations: comparisons of alternative numerical algorithms. Physical Review E 71(6) (2005) 066208.

Chapter 73
EEG Theta Regulates Eye Saccade Generation During Human Object-place Memory Encoding

Naoyuki Sato and Yoko Yamaguchi

Abstract In this paper, we proposed a computational theory of human memory formation in the hippocampus and determined if electroencephalography (EEG) theta power is associated with eye saccades during object-place memory encoding. EEG theta power and saccade rate is significantly correlated with subsequent recall performance. This result suggests that information acquisition for object-place memory is processed by the theta rhythm network for memory system, attentional regulation and saccades.

Introduction

"A neural dynamics theta phase precession" observed in the rat hippocampus [1] [2] is considered to play an important role in online memory formation of the environment. In this phenomenon, the temporal sequence of place field activation is temporally compressed within the phase of every theta cycle and repeated in several theta cycles [2]. Since the time scale of this phase pattern matches the time-window of the spike-timing dependent plasticity (STDP) [3], theta phase precession results in synaptic plasticity. According to this evidence, Yamaguchi [4] proposed a computational theory: a behavioral input sequence is translated to theta phase precession in the entorhinal cortex, and stored into CA3 unidirectional connections according to STDP. Computer experiments demonstrated that theta phase precession is advantageous in memory formation with respect with various task demands [5].

The theory was further applied to human object-place memory, a model of human episodic memory [6, 7]. In the proposed computational network model [8], a visual input sequence consisting of object and scene information were assumed: the object

N. Sato
Laboratory for Dynamics of Emergent Intelligence, RIKEN Brain Science Institute, Saitama 351-0198, Japan
e-mail: satonao@brain.riken.jp

R. Wang et al. (eds.), *Advances in Cognitive Neurodynamics*,

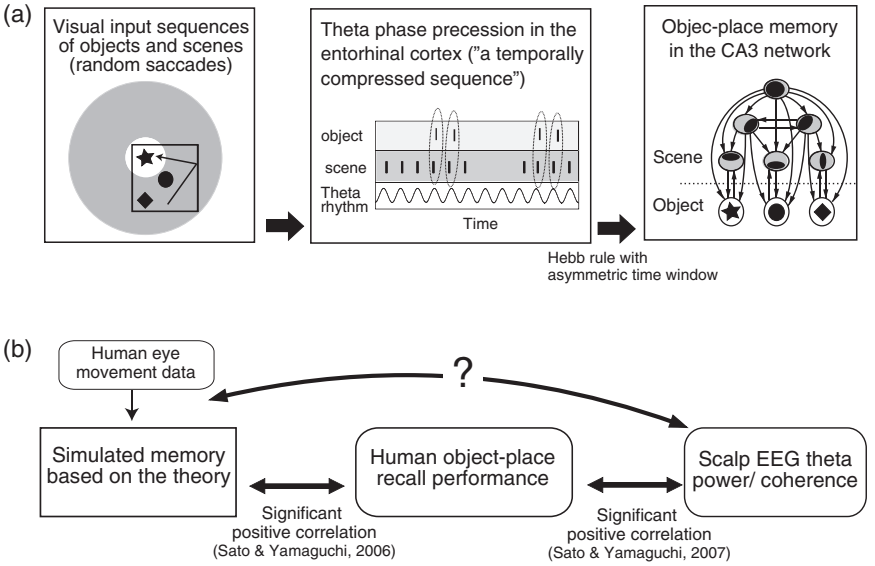

Fig. 73.1 (a) A computational theory of object-place memory formation based on human theta phase precession [8]. (b) Supporting evidences of the computational theory

input in the central visual field changes rapidly in relation to saccades, while the scene input in peripheral visual filed changes continuously through several saccades (Fig. 73.1a).

By using computer experiments, it was found that theta phase precession of the visual input sequence results in a formation of a hierarchical cognitive map including scene unit layers and an object unit layer characterized by asymmetric connections. Thus, theta phase precession observed in the rat hippocampus could contribute to form human episodic memory.

The theoretical predictions of human memory formation have been evaluated in human experiments, as summarized in Fig. 73.1b. First, the scalp EEG theta power during object-place memory encoding was found to significantly correlate with subsequent memory recall [9]. Second, theoretically simulated memory with human eye movement was also found to significantly correlate with human memory recall [10]. These results support the computational theory of human memory formation. In addition to this evidence, this theory would predict a positive correlation between EEG theta and eye saccades during successful memory encoding, although such a relation has not been evaluated.

In this paper, we elucidated the theoretical prediction of the relationship between EEG theta and eye saccades. If EEG theta is essential to encode object-place memory with visual input sequences, the EEG theta power-saccade rate coherence is expected to increase in relation to subsequently successful memory recall.

Methods

Scalp EEG and eye movement data reported in [9] were used. Eleven volunteers performed 350 trials of an object-place memory task that consists of an 8-s encoding of a set of four object-place associations in 3-by-3 grids (subtended 15 by 15 degrees each), a 10-s secondary task of random fixation, and a recall task of the objects configuration on the display using a mouse. During the task, 58-ch scalp EEG signals and 6-ch electro-oculography (EOG) signals were recorded with a Neuroscan amplifier (NeuroScan, US) and eye movement was recorded with a video-based eye-tracker (Eyelink I, SR Research, Canada). In the analysis, ocular artifacts in the EEG were corrected with the RAAA (revised aligned-artifact average) method using horizontal EOG, vertical EOG and radial EOG [11]. The coherence between wavelet EEG power of electrode i and saccade rate was further evaluated with a coherence value C_i defined by

$$C_i(f) = \left(\sum_{t=1}^{N} e_i(f,t) s(t) \right) \Big/ \left(\sum_{t=1}^{N} e_i(f,t) \sum_{t=1}^{N} s(t) \right), \tag{73.1}$$

where f is the frequency, N is the number of time points in a trial, and $e_i(f,t)$ is wavelet power at each time-point t, and $s_i(t)$ is the inter-grid saccade rate calculated by a 2-s sliding window. A Wilcoxon rank-sum test was used to compare the coherence values during encoding in each trial that were later either completely ("successful") or imcompletely recalled ("failed"). As described in the previous report [9], saccade rate itself is not significantly correlated with subsequent memory recall ($t(10) = 1.59,\ p = 0.145 > 0.05$).

Results

Figure 73.2 represents an example of data processing: raw and corrected EEGs, raw and corrected wavelet EEG powers, eye movement, and saccade rate. EEG theta power intermittently increased with increased saccade rate. Note that the ocular artifacts in the lower frequency-range were well corrected as shown in the wavelet EEG power.

Figure 73.3 displays the topographical pattern of the increase in coherence values for each frequency power, in relation to subsequent memory recall. A significant increase of the EEG power-saccade rate coherence was found at the theta range (4.5–6.5 Hz) in the fronto-central region and in occipital region. These results are in a good agreement with the theoretical prediction. Note that the coherence indices of horizontal and vertical EOGs were not significantly correlated with subsequent memory recall, indicating that the coherence increase in theta range is not caused by residuals of EOG artifacts.

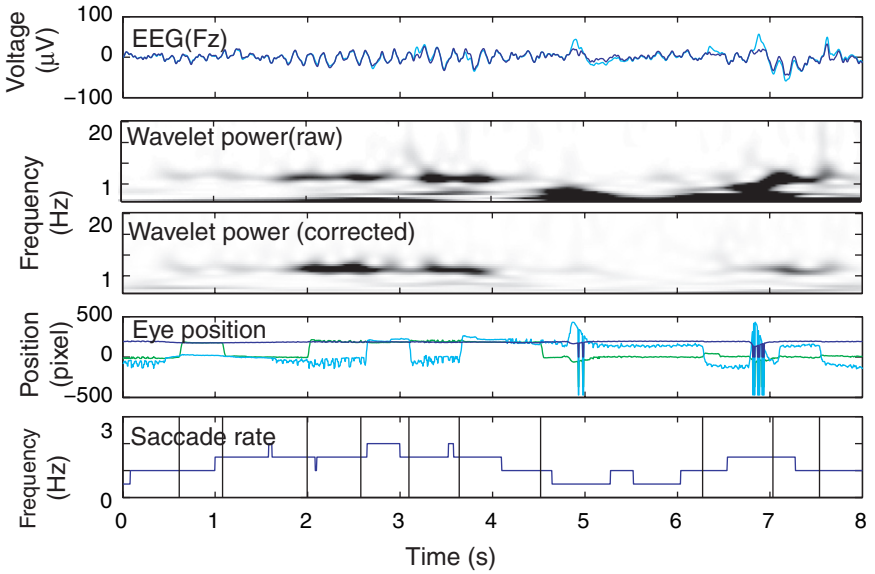

Fig. 73.2 Results of EEG signals and eye movement recordings (subject 4860, Fz electrode, trial 19)

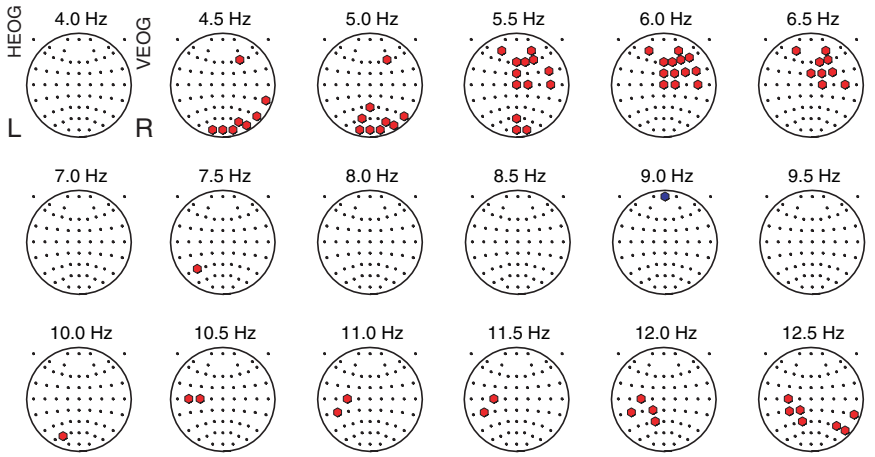

Fig. 73.3 Topographical maps showing Wilcoxon rank-sum values difference of the EEG power-saccade rate coherence values between successful and failed trials. Filled red and blue circles represent electrodes showing a significant increase and decrease in coherence value ($p < 0.05$), respectively

In order to remove residual ocular artifacts in EEG signals, we analyzed the coherence values only during eye fixation periods. The result is shown in Fig. 73.4. A significant coherence increase was again found at theta range (4.0–6.5 Hz) in the fronto-central region, confirming that the EEG theta power-saccade coherence

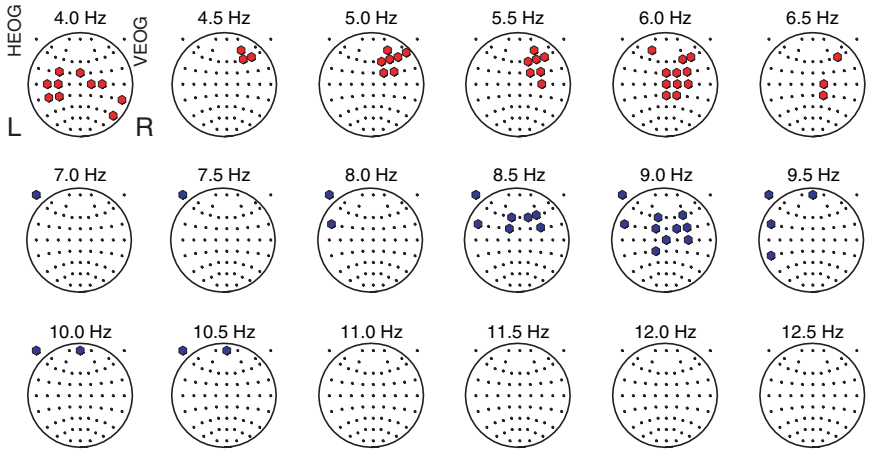

Fig. 73.4 Topographical maps showing Wilcoxon rank-sum values difference of the EEG power-saccade rate coherence values between successful and failed trials, where saccade periods (from one oscillation cycle before saccade onset to one oscillation cycle after saccade offset) are excluded from the analysis

increase is not caused by ocular artifacts. Moreover absence of significant effect in the occipital regions indicates that the subsequent memory effect in the occipital region is more related to periods of saccade occurrence. The subsequent memory effect in the fronto-central region is considered to be more independent of saccade timing.

Discussion

The EEG theta power-saccade rate coherence increase was found to significantly correlate with subsequent memory recall (Figs. 73.2 and 73.3). The effect was found at a lower theta range (4.5–6.5 Hz) in fronto-central region. This difffers from the subsequent memory related EEG power increase at higher theta range (6.5–7.5 Hz) in the posterior region (at 6.5 Hz), the central region (at 7.0 Hz), and the fronto-central region(at 7.5 Hz) (Fig. 73.3 in [9]). According to these results, there are two functional theta synchronization networks: a memory encoding system in higher theta (6.5–7.5 Hz) and a saccade regulation system in lower theta (4.5–6.5 Hz). Acquisition of object-place memory is processed by theta rhythm networks for memory, attentional regulation and saccades. These results support the computational theory of human object-place memory formation based on theta phase precession.

The current result suggests a functional role of the intermittent increase of EEG theta power in the primate hippocampus [12] that is different from a continuous EEG theta observed in the rodent hippocampus [1, 2]. The intermittent EEG theta is expected to generate a set of visual input sequences that helps form an accurate

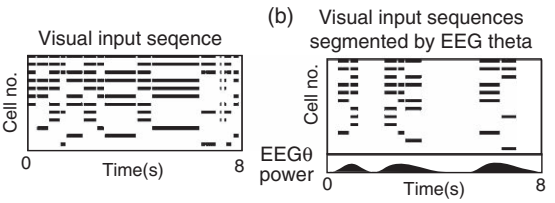

Fig. 73.5 (a) A continuous visual input sequence. (b) A set of visual input sequences segmented by EEG theta

memory within a limited encoding period (Fig. 73.5). The hippocampal local field potential (LFP) theta should increase in primates in relation to saccades, as recently pointed out by Ulanovsky and Moss [13].

References

1. O'Keefe, J., Recce, M.L.: Phase relationship between hippocampal place units and the EEG theta rhythm. Hippocampus **3** (1993) 317–330.
2. Skaggs, W.E., McNaughton, B.L., Wilson, M.A., Barnes, C.A.: Theta phase precession in hippocampal neuronal populations and the compression of temporal sequences. Hippocampus **6** (1996) 149–172.
3. Bi, G.Q., Poo, M.M.: Synaptic modifications in cultured hippocampal neurons: dependence on spike timing, synaptic strength, and postsynaptic cell type. J. Neurosci. **18** (1998) 10464–10472.
4. Yamaguchi, Y.: A theory of hippocampal memory based on theta phase precession. Biol. Cybern. **89** (2003) 1–9.
5. Yamaguchi, Y., Aota, Y., Sato, N., Wagatsuma, H., Wu, Z.: Synchronization of neural oscillations as a possible mechanism underlying episodic memory: a study of theta rhythm in the hippocampus. J. Integ. Neurosci. **3** (2004) 143–157.
6. Smith, M.L., Milner, B.: The role of the right hippocampus in the recall of spatial location. Neuropsychologia **19** (1981) 781–793.
7. Stepankova, K., Fenton, A.A., Pastalkova, E., Kalina, M., Bohbot, V.D.: Object-location impairment in patient with thermal lesions to the right or left hippocampus. Neuropsychologia **42** (2004) 1017–1028.
8. Sato, N., Yamaguchi, Y.: On-line formation of a hierarchical cognitive map for object-place association by theta phase coding. Hippocampus **15** (2005) 963–978.
9. Sato, N., Yamaguchi, Y.: Theta synchronization networks emerge during human object-place memory encoding. NeuroReport **18** (2007) 419–424.
10. Sato, N., Yamaguchi, Y.: An evidence of a hierarchical representation of object-place memory based on theta phase coding: a computational model-human experiment combined analysis, Program No. 366.25, Society for Neuroscience Abstracts, (2006).
11. Croft, R.J., Barry, R.J.: Removal of ocular artifact from EEG: a review. Neurophysiol. Clin. **30** (2000) 5–19.
12. Ekstrom, A.D., Caplan, J.B., Ho, E., Shattuck, K., Fried, I., Kahana, M.J.: Human hippocampal theta activity during virtual navigation. Hippocampus. **15** (2005) 881–889.
13. Ulanovsky, N., Moss, C.F.: Hippocampal cellular and network activity in freely moving echolocating bats. Nat. Neurosci. **10** (2007) 224–233.

Chapter 74
Hippocampal and Parahippocampal Neuronal Responses to Spatial and Non-Spatial Factors in Rats and Monkeys

Hisao Nishijo, Etsuro Hori, Tsuneyuki Kobayashi and Taketoshi Ono

Abstract Rat hippocampal (HF) neurons were recorded while the rat ran on a treadmill affixed to a motion stage that was translocated along a figure 8-shaped track. Comparison of HF spatial firing patterns across different experimental conditions indicated that place neuron activity encodes intra-maze multiple information including location of animals, locomotion, the reinforcement episodes, and vestibular sensation or optic flow. Place neurons were also recorded from the monkey HF during virtual navigation. Most place-differential responses disappeared or changed their spatial tuning (i.e., remapping) when the arrangements of the distal cues were altered/moved in the virtual spaces. The results suggest that the HF encodes multifold information within the maze, which are gated by the extra-maze distal cues.

Keywords Hippocampus · CA1 · place cell · context · episodic memory

Introduction

The relationship between spatial functions and episodic memory in the HF is one of the main issues. Changes in place-related activity (remapping) is suggested to be a neural basis of episodic memory [1, 2]. Basic spatial tuning of place cells is essentially formed by local geometrical intra-maze and idiothetic cues [1, 3, 4]. Other factors modulate this spatial tuning. One of these factors is extra-maze distal cues, which might set orientation of the place fields of place cells or work as contexts to gate local geometrical and idiothetic cues [1, 3]. Another factor is cognitive requirement or task paradigms, which are reported to influence activity of place cells even in the same spatial environment [5]. Thus, these studies suggest that remapping of place fields might be induced by both changes in extra-maze distal

H. Nishijo
System Emotional Science, Graduate School of Medicine and Pharmaceutical Science, University of Toyama, Sugitani 2630, Toyama 930-0194, Japan
e-mail: nishijo@med.u-toyama.ac.jp

R. Wang et al. (eds.), *Advances in Cognitive Neurodynamics*,

cues and cognitive factors such as task requirements. In this chapter, we review our studies in which place cell activity was recorded in rats and monkeys while space, locomotion, and episodes with positive/negative reinforcements were separately manipulated.

Rat HF Neurons

The rat's head was painlessly fixed to a stereotaxic frame on the motion stage, which was translocated along a figure 8-shaped track [6]. The floor of the stereotaxic frame was removed so that the rats could run on the treadmill along with translocation of the motion stage. The track could be navigated by two different routes (Routes 1 and 2 in Fig. 74.1) that shared a common central stem. The stage was paused at the start and end of the routes [Places 1 (P1) and 2 (P2)], where conditioned response tasks with different reinforcements were imposed.

Figure 74.1 shows an example of a place neuron having route-dependent activity. In the first control session, the activity of the neuron increased in Route 1 (Aa), but this neuron exhibited little activity in Route 2 (Ba). Thus, the activity of the neuron in the central stem was route-dependent. The activity of the neuron did not increase on the central stem when the treadmill was turned off (Lo−) during translocation (Ab: session Lo − Ts+). However, the same neuron displayed a clear place field on the central stem of Route 1 without the task (Ts−) (Ac: session Lo + Ts−). In the session Lo − Ts−, the spatial firing patterns in the central stem again disappeared (Ad). In the last control session, Lo+Ts+, the spatial firing pattern observed in the first control session resumed (Ae). These results indicated that the route-dependent activity of the neuron was locomotion-dependent.

The 44 place neurons were analyzed similarly, and 7 (15.9%) showed task-dependent, 20 (45.5%), locomotion-dependent, and 4 (9.1%), task- and locomotion-dependent responses. Furthermore, 13 (56.5%) of 23 route-dependent place neurons were also locomotion-dependent or locomotion-and-task-dependent. It is noted that

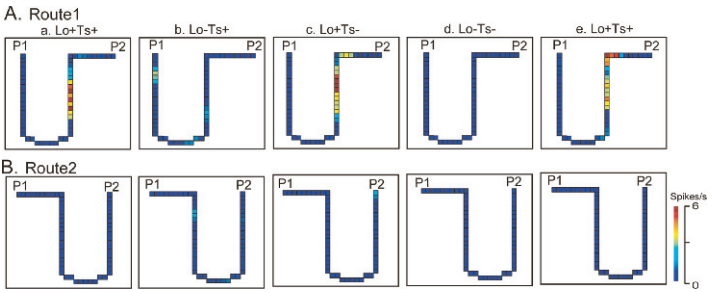

Fig. 74.1 A HF place neuron with locomotion- and route dependent spatial firing patterns on the common central stem of Route 1. Lo−, Lo+: Turning on (−) and off (+) of the treadmill; Ts−, Ts+: without (−) and with (+) imposition of the tasks

some place responses were task- and locomotion-independent. These might code visual (optic flow) and/or vestibular information.

Monkey HF Neurons

The purpose in this section was to investigate effects of extra-maze distal cues on HF place-differential activity of monkeys using a virtual navigation task (VNT) [7]. Monkeys were trained to sit on a chair in front of a screen in a dark room, and viewed 3D visual images of virtual spaces projected on the screen. In the VNT, a large-scale virtual space (diam., 100 m) was created. A circular open field (diam., 20 m; movable arena) surrounded by a wall was located in the center of the virtual space. The movable arena contained five reward areas that were symmetrically placed [North (N), East (E), South (S), West (W), and Center (C)] (Fig. 74.2Aa), and extra-maze distal cues were placed outside the movable arena. In this VNT task, the monkey was required to navigate by manipulating a joystick among the three reward areas aligned in a line (i.e., N–C–S or E–C–W) to acquire a juice reward at each of these three reward areas. There were three different arrangements of the virtual spaces, based on the placement of the extra-maze distal cues (VNT1-3).

Of these 228 neurons recorded from the HF, 72 displayed significant spatial correlate (place-differential neurons). The effect(s) of the extra-maze distal cues on the place-related responses of the monkey HF neuron in the three VNT tasks is shown in Fig. 74.2. Activity of the neuron increased only in the VNT1, but neither in the VNT2 (B) nor VNT3 (C) (i.e., remapping). Of the 127 neurons tested with more than two VNT tasks, 40 displayed place-differential activity in at least one VNT task. Of these 40 place neurons, 27 showed remapping, respectively.

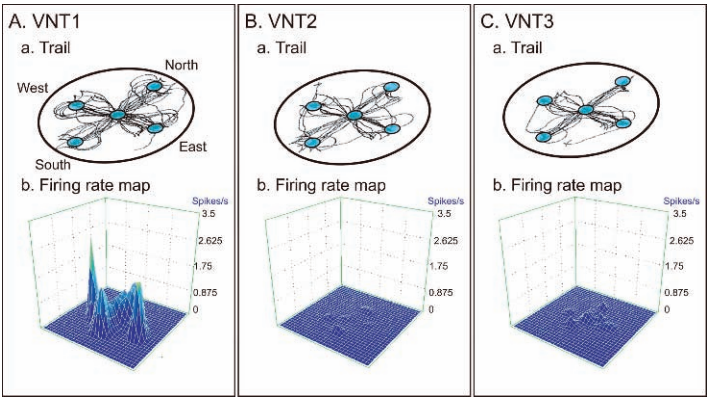

Fig. 74.2 An example of a place neuron that displayed remapping of place-related activity among the three VNT tasks. (A–C): Trails (a) and average firing rate maps (b) of the place-differential neuron in the VNT-1 (A), VNT-2 (B) and VNT-3 (C). Large and small circles in A-a indicate the movable arena and reward areas, respectively

Discussion

Comparison of HF spatial firing patterns across different conditions in rats indicated that these route-dependent spatial firing patterns were sensitive to locomotion, the tasks, and vestibular sensation or visual cues such as optic flow. The results suggest that multifold intra-maze information including location of the animals, trajectory of the routes, idiothetic cues, and reinforcement episode (task) are all encoded in the HF.

The results of monkey HF neurons indicated that the response of most HF place-differential neurons depended on the arrangement of the extra-maze distal cues. These results are consistent with the previous studies in rodents in which place cells were highly sensitive to distal cues [1, 3], and suggest that primate HF neurons share similar characteristics to those of rodents. These results also suggest that distal cues work as a context to gate intra-maze local and idiothetic cues that are essential for spatial tuning within a maze [8]. Furthermore, even in the same experimental room where monkeys navigated by driving a cab, most HF neurons had non-overlapped place fields across the different task [5]. In conclusion, these results indicated that activity of place neurons encoded multifold information including space, proprioception (locomotion), vestibular sensation (or optic flow), nonspatial stimuli including the reinforcements in the task, and contexts (distal cues and task demands). These results further suggest that the HF is crucial for processing of allocentric information (distal cues) to encode as reference frames (contexts), which may be the neural basis of episodic memory [9].

References

1. Jeffery, K.J., Anderson, M.I., Hayman, R., Chakraborty, S.: A proposed architecture for the neural representation of spatial context. Neurosci. & Biobehav. Rev. 28 (2004) 201–218.
2. McNaughton, B.L., Battaglia, F.P., Jensen, O., Moser, E.I., Moser, M.B.: Path integration and the neural basis of the 'cognitive map'. Nature Rev. Neurosci. 7 (2006) 663–678.
3. Jeffery, K.J., Gilbert, A., Burton, S., Strudwick, A.: Preserved performance in a hippocampal-dependent spatial task despite complete place cell remapping. Hippocampus 13 (2003) 175–189.
4. Knierim, J.J., Rao, G.: Distal landmarks and hippocampal place cells: effects of relative translation versus rotation. Hippocampus 13 (2003) 604–617.
5. Matsumura, N., Nishijo, H., Tamura, R., Eifuku, S., Endo, S., Ono, T.: Spatial- and task-dependent neuronal responses during real and virtual translocation in the monkey hippocampal formation. J. Neurosci. 19 (1999) 2381–2393.
6. Dayawansa, S., Kobayashi T., Hori, E., Umeno, K., Tazumi, T., Ono, T., Nishijo, H.: Conjunctive effects of reward and behavioral episodes on hippocampal place-differential neurons of rats on a mobile treadmill. Hippocampus 16 (2006) 586–595.
7. Hori, E., Nishio, Y., Kazui, K., Umeno, K., Tabuchi, E., Sasaki, K., Endo, S., Ono, T., Nishijo, H.: Place-related neural responses in the monkey hippocampal formation in a virtual space. Hippocampus 15 (2005) 991–996.
8. Hayman, R.M., Chakraborty, S., Anderson, M.I., Jeffery, K.J.: Context-specific acquisition of location discrimination by hippocampal place cells. Eur. J. Neurosci. 18 (2003) 2825–2834.
9. Nadel, L., Willner, J.: Context and conditioning. Physiol. Psychol. 8 (1980) 218–228.

Chapter 75
Oscillatory Event Synchrony During Steady State Visual Evoked Potentials

François B. Vialatte, Justin Dauwels, Tomasz M. Rutkowski and Andrzej Cichocki

Abstract In this paper we study the dynamics of distributed neuronal assemblies, through the event synchrony of EEG oscillatory bursts. We recorded EEG signals before, during and after steady-state visual evoked potentials (SSVEP) in medium (16 Hz) and high frequency (32 Hz) ranges. The time-frequency oscillatory events are extracted using bump modeling. Thereafter, the recently introduced stochastic event synchrony (SES) method is applied to compare these patterns between brain areas. Significant effects are shown, demonstrating that not only the background activity is affected by flickering stimulation, but also oscillatory patterns.

Introduction

Local synchrony of neural assemblies induces bursts of oscillatory activities. In EEG signals, these activities usually appear as successions of oscillatory patterns that can be observed using time–frequency representations. Synchrony among oscillating neural populations is a plausible candidate to mediate functional connectivity, and therefore to allow the formation of spatiotemporal structures [1]. Such neural assemblies can be considered as distributed local networks of neurons, transiently linked by reciprocal dynamic connections [2].

Steady-state visual evoked potentials (SSVEP) are characterized by constituent discrete frequency components remaining closely constant[1] in amplitude and phase over a long stimulation time [3]. There is generally little knowledge, for SSVEP, concerning the trial-by-trial detail of oscillatory patterns dynamics. Studies in neuroscience use classical methods to study the SSVEP responses: superposition, averaging, frequency analysis (narrow band Fourier power), or correlation analysis. Whereas efficient tools for time–frequency analysis were used proficiently for evoked potential or event-related responses investigation [4, 5], time-frequency

F.B. Vialatte
RIKEN Brain Science Institute, Saitama, Japan
e-mail: fvialatte@brain.riken.jp

[1] This holds only for average of trials. Single trials usually do not show constant activity.

R. Wang et al. (eds.), *Advances in Cognitive Neurodynamics*,

analysis of SSVEP were unfortunately seldom investigated [6, 7]. We will here make the first attempt to investigate oscillatory pattern synchrony during SSVEP induced by a flickering light stimulus.

In this paper, a sparse "bump" model of the most prominent time–frequency oscillatory events is used [8]. For each trial, we quantify the pairwise synchrony between bump model approximations of the EEG signals using the Stochastic Event Synchronization (SES) method [9].

Methods

Human scalp EEG was recorded in a dark room, while a subject was exposed to flickering light. Stimulus consisted of a single flashing white square with constant time interval EEG data was recorded from 64 sites on the scalp, based on the extended 10–20 standard system. A Biosemi system with average reference was used. Sampling rate was set to 2048 Hz (yielding good frequency resolutions), with offline high pass filter above 3 Hz. Trials were recorded with SSVEP induced at 16 and 32 Hz during a four second stimulation (51 trial per frequency range, thus total $=$ 102 trials). As a first step, wavelet time–frequency maps are computed using complex Morlet wavelets. The complex Morlet wavelet results in the optimal resolution in time and frequency; it has also proven to be well-suited for EEG signals [4, 5, 10]. Here, time–frequency representations were restricted to the frequency ranges of SSVEP, *i.e.* 15–17 Hz or 31–33 Hz, with adequate time and frequency borders for bump modeling [8]. Epochs were analyzed before, during and after stimulation. A frequency dependent z-score normalization [11] was applied comparatively to the pre-stimulus period of each trial:

$$z(f,t) = \frac{c(f,t) - \mu_f}{\sigma_f}, \tag{75.1}$$

where μ_f and σ_f are the mean and standard deviation of the wavelet map at frequency f, during the pre-stimulus period.

The resulting z-score maps are approximated as a sum z_{bump} of basis (half ellipsoid) functions b, referred to as "bumps" ([8], Fig. 75.1):

$$z(f,t) \simeq z_{\text{bump}}(\theta) = \sum_{k=1}^{N_b} b(\theta_k). \tag{75.2}$$

After bump modeling, the 64 electrodes were clustered into nine areas (occipital, parietal left and right, temporal left and right, central, frontal left and right, and prefrontal). Stochastic event synchrony (SES, [9]) quantifies the alignment of two bump models (Fig. 75.1). A fraction ρ_{spur} of bumps appear in one area but not in the other ("spurious" bumps); other bumps are present in both areas at slightly different positions ("non-spurious bumps"). We denote by Δ the average timing offset

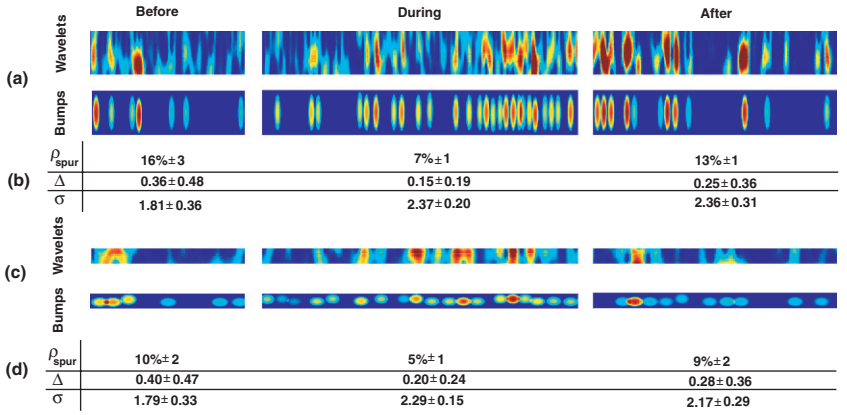

Fig. 75.1 Application of SES to SSVEP signals. Bumps are modeled with central frequencies close to the SSVEP rate ±1 Hz. (a) z-scored wavelet transform (26–38 Hz) and bump modeling of a typical signal with SSVEP at 32 Hz. (b) SES parameters for all signals at 32 Hz. (c) z-scored wavelet transform (13–19 Hz) and bump modeling of a typical signal with SSVEP at 16 Hz. (d) SES parameters for all signals at 16 Hz

between pairs of non-spurious bumps, σ stands for the standard deviation of this offset.

Results and Discussion

A first observation on wavelet maps (Fig. 75.1) is that EEG trials remain organized in oscillatory bursts during SSVEP stimulation: we can observe on z-score maps, during and after as well as before SSVEP, intermittent patterns of activity. The average of a sufficient number of trials would show instead a more constant activity in the frequency range of interest. Earlier investigations [6] also revealed such rhythmic patterns.

We present the first application of oscillatory event synchrony to SSVEP responses in EEG. We first compared EEG periods using magnitude square coherence. "Before vs. During" condition and "During vs. After" condition yields significant p-values ($p < 0.01$, Mann–Whitney test). SES also shows (Fig. 75.2) a general increase of synchrony (ρ_{spur} and $|\Delta|$ decreased significantly) between oscillatory patterns, but with an induced perturbation of organization (σ increases significantly). Note that σ captures fluctuations "within" a trial, whereas the distribution of $|\Delta|$ reveals fluctuations "from trial to trial". Note that with a high ρ_{spur} in the "Before" period, the estimate of σ may be less reliable. Likewise, σ may be small in the "Before" period since there are only few bumps (= fluctuation within a trial); however, the fluctuations in $|\Delta|$ are large (from trial to trial) during this period. We need to investigate this more carefully with surrogate data.

Therefore, during SSVEP, not only background activity increase its coherence, but also oscillatory events. Considering the assumption that oscillations and long

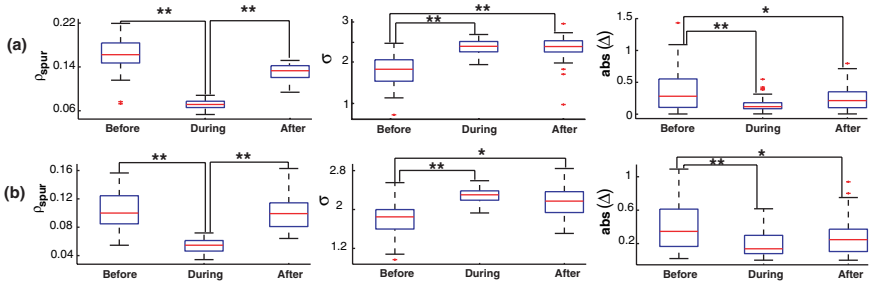

Fig. 75.2 Boxplots of the three SES parameters. * and ** represents respectively significant ($p < 0.05$) and strongly signicant ($p < 0.01$) differences (Mann–Whitney test). Red crosses represents outliers. (a) stimulation at 32 Hz. (b) stimulation at 16 Hz

distance synchrony both play key roles for cognition [2, 1], we can moreover expect from these results that SSVEP stimuli could induce some cognitive side-effects. This conjecture will be verified in our future investigations.

References

1. Cosmelli, D., Lachaux, J.P., Thompson, E.: Neurodynamical approaches to consciousness. In Zelazo, P.D., Moscovitch, M., Thompson, E. (eds.): The Cambridge Handbook of Consciousness. Cambridge University Press, Cambridge (2007).
2. Varela, F., Lachaux, J.P., Rodriguez, E., Martinerie, J.: The brainweb: phase synchronization and large-scale integration. Nat. Rev. Neurosci. **2** (2001) 229–239.
3. Regan, D.: Human Brain Electrophysiology: Evoked Potentials and Evoked Magnetic Fields in Science and Medicine. Elsevier, New York (1989).
4. Tallon-Baudry, C., Bertrand, O., Delpuech, C., Pernier, J.: Stimulus specificity of phase-locked and non-phase-locked 40 Hz visual responses in human. J. Neurosci. **16** (1996) 4240–4249.
5. Ohara, S., Crone, N.E., Weiss, N., Lenz, F.A.: Attention to a painful cutaneous laser stimulus modulates electrocorticographic event-related desynchronization in humans. Clin. Neurophysiol. **115** (2004) 1641–1652.
6. Cui, J., Wong, W.: Optimal Window Length in the Windowed Adaptive Chirplet Analysis of Visual Evoked Potentials. Proceedings of IEEE EMBS, New York (2006).
7. Cui, J., Wong, W.: The adaptive chirplet transform and visual evoked potentials. IEEE Trans. Biomed. Eng. **53** (2006) 1378–1384.
8. Vialatte, F., Martin, C., Dubois, R., Haddad, J., Quenet, B., Gervais, R., Dreyfus, G.: A machine learning approach to the analysis of time-frequency maps, and its application to neural dynamics. Neural Netw. **20** (2007) 194–209.
9. Dauwels, J., Vialatte, F., Cichocki, A.: A Novel Measure for Synchrony and Its Application to Neural Signals. Proceedings of IEEE International Conference on Acoustics and Signal Processing (ICASSP), Honolulu, Hawaii (2007).
10. Herrmann, C.S., Grigutsch, M., Busch, N.A.: EEG oscillations and wavelet analysis. In Handy, T. (eds.): Event-Related Potentials: A Methods Handbook. MIT Press Cambridge, (2005) 229–259.
11. Browne, M., Cutmore, T.R.H.: Low-probability event-detection and separation via statistical wavelet thresholding: an application to psychophysiological denoising. Clin. Neurophysiol. **113** (2004) 1403–1411.

Chapter 76
Information Entropy-Based Penalty for PARAFAC Analysis of Resting EEG

Eduardo Martínez-Montes, Rafael Sarmiento-Pérez, José M. Sánchez-Bornot and Pedro A. Valdés-Sosa

Abstract PARAFAC analysis of time-varying EEG spectra data provides a parsimonious representation in terms of topographic, temporal and spectral signatures, which allows for the identification of functional neural networks. This networks work in a critical state where short and long range connections coexist. Although PARAFAC is unique through usual least squares estimation, the use of penalized least squares allows to incorporate this kind of knowledge into the decomposition. Here we propose the use of Information Entropy-based penalties for obtaining atoms with minimum spectral entropy. They offer sparse spectral signatures corresponding to networks oscillating in a well-defined (sharp) frequency band.

Keywords PARAFAC · penalized least squares · information entropy · EEG

Parallel Factor Analysis

The multidimensional nature of neuroscience data has made the use of multi-way statistical analysis suitable in this field. Many bidimensional approaches such as Independent and Principal Components Analysis (PCA) are very popular but offer non-interpretable results when higher dimensional structure is hidden in the data. Parallel Factor (PARAFAC) analysis is a generalization of PCA to deal with multidimensional data. For example, the EEG time-varying spectra is a three dimensional array ($\mathbf{Y}_{(I\times J\times K)}$), indexed by channels, time points and frequencies [1]. PARAFAC model is then stated as:

$$y_{ijk} = \sum a_{if} b_{jf} c_{kf} + \varepsilon_{ijk} \tag{76.1}$$

where a_{if}, b_{jf}, and c_{kf} are the elements of loading matrices $A_{(I\times F)}$, $B_{(J\times F)}$, $C_{(K\times F)}$ respectively and ε_{ijk} represents the noise. The sum is over $f = 1 \ldots F$, which represents components or atoms. PARAFAC is usually fitted through Alternating Least

E. Martínez-Montes
Neurostatistics Department, Cuban Neuroscience Center, Ave. 25, esq 158, Havana, Cuba
e-mail: eduardo@cneuro.edu.cu

R. Wang et al. (eds.), *Advances in Cognitive Neurodynamics*,

Squares (ALS) algorithm [2], in which, iteratively, each loading is (least squares-) estimated conditionally on the others. This has the advantage that the decomposition is unique under very mild conditions without requiring orthogonality or independence among components. However, physiologically acceptable constraints are of help in the interpretation of results.

Multiple Penalized Least Squares and Information Entropy

Substituting each least squares step in ALS by a penalized least squares (PLS) regression we can introduce constraints in the PARAFAC decomposition. Many types of constraints are now possible, varying from the use of usual Ridge (quadratic) penalty functions to non-convex penalty functions (non-quadratic, continuous and with a singularity at the origin), which has been proposed in PLS to obtain sparse and stable solutions. Some examples are the Lasso, the SCAD, which also produces unbiased estimators and Elastic Net, which is a combination of Ridge and Lasso [3]. These non-linear models are estimated by Local Quadratic Approximation [3], which has been generalized to deal with multiple penalty terms simultaneously, i.e. to tackle Multiple Penalized Least Squares (MPLS) models. Consider the multivariate linear regression model: $\mathbf{y} = \mathbf{X}\beta + \mathbf{e}$, where β is the vector of parameters to estimate; $\mathbf{y}$ the data vector; $\mathbf{X}$ the given design matrix and $\mathbf{e}$ represents unmodeled noise. Then, the MPLS model for β is stated as:

$$\hat{\beta} = \arg\min \left\{ (\mathbf{y} - \mathbf{X}\beta)^T (\mathbf{y} - \mathbf{X}\beta) + \sum \lambda_k p_k(\beta) \right\} \tag{76.2}$$

where $k = 1 \ldots Nk$ indexes different kind of constraints imposed through $p_k(\beta)$, with corresponding weighting parameters λ_k.

When β can be considered as a probability density function (pdf), the Information Entropy is defined as $H(\beta) = -K \sum \beta_j \ln \beta_j$, with $j = 1 \ldots n$ and K a positive constant. This measure will be maximum for all $\beta_j = 1/n$ and minimum (zero) when one β_j is 1 and the rest are 0. Therefore it is a measure of the "peakness" of the pdf. If we use this measure as a penalty in MPLS[1], we are constraining the solution to have minimum Entropy, i.e. to be the sharpest one. Applied to the spectral signature of a PARAFAC decomposition, the use of this penalty would imply to constraint the loadings to have minimum spectral Entropy, which can be interpreted as to find those functional networks with well-defined frequency of oscillation. According to [3] this penalty produces sparse solutions if $K < 2$ but without satisfying the unbiasedness and continuity conditions. However, it is easy to derive a sparse and unbiased estimator by combining the Entropy with a Ridge penalty of the form:

$$p(\beta) = -\sum \beta_j \ln \beta_j + \sum \beta_j^2 / 2 \tag{76.3}$$

[1] Note that this penalty differs from the so-called entropy-penalty or *L0*-penalty [3].

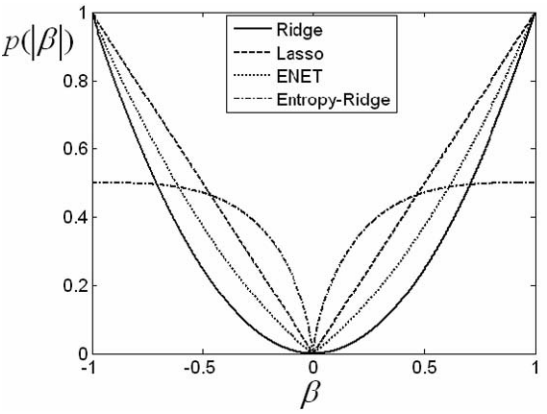

Fig. 76.1 Penalty functions: Ridge (*solid*), Lasso (*dash*), ENet (*dot*), Entropy-Ridge (*dot-dash*)

This will be called the Entropy-Ridge penalty and its shape with some other penalty functions is shown in Fig. 76.1.

Penalized PARAFAC of Resting EEG

The time-varying spectra of resting-state EEG, (indexed by channels, time points and frequencies) were decomposed by unconstrained and constrained PARAFAC into three components with corresponding topographic, temporal and spectral signatures. The latter allowed the identification of spontaneous brain rhythms. Figure 76.2a shows unconstrained spectral loadings which, although presenting clear main peaks, have negative values and some oscillating behavior that might be due to noise fitting. Figure 76.2b presents the smoother loadings given by constrained PARAFAC using Ridge penalty.

Figure 76.3a shows the piece-wise smooth spectral loading as estimated by using Elastic Net penalty and 3b the sparser loadings obtained with the Entropy-Ridge penalty. The three constrained versions are more reasonable and physiologically

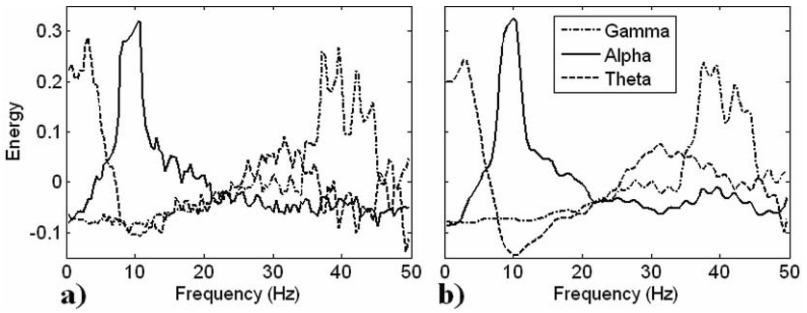

Fig. 76.2 (a) Unconstrained PARAFAC, (b) PARAFAC with MPLS using Ridge penalty. Components are identified as alpha (*solid*), theta (*dash*) and gamma (*dot-dash*)

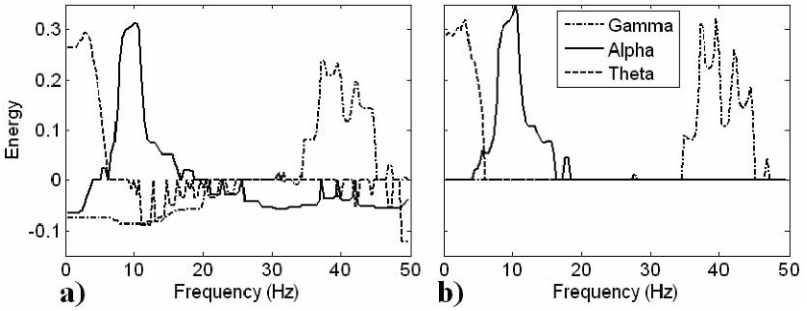

Fig. 76.3 (a) PARAFAC with MPLS using Elastic Net penalty; (b) PARAFAC with MPLS using Entropy-Ridge penalty. Components are identified as alpha (*solid*), theta (*dash*) and gamma (*dot-dash*)

sound options for the interpretability of the results. However, Ridge and ENet solutions do not avoid the negative values and the oscillating behavior for frequencies far from the main peak.

Conclusions

The application of alternating penalized least squares for PARAFAC allows the use of known and yet unexplored types of constraints, resulting in a strong tool for statistical analysis in neuroscience. Through these constraints one can make use of prior knowledge about the underlying functional networks. In this sense, a newly proposed penalty based in the Information Entropy allowed the identification of networks with minimum spectral entropy, which resulted in nonnegative and sparse spectral loadings with PARAFAC. Weighting parameters can be tuned to obtain different degrees of constraints, however, future work is needed on the selection of their optimal values using cross validation or other information criteria.

References

1. Miwakeichi, F., Martínez-Montes, E., Valdés-Sosa, P.A., Nishiyama, N., Mizuhara, H., Yamaguchi, Y.: Decomposing EEG data into space-time-frequency components using parallel factor analysis. Neuroimage 22, 3 (2004) 1035–1045.
2. Bro, R.: Multi-way Analysis in the Food Industry: Models, Algorithms and Applications. Ph.D. Thesis. University of Amsterdam and Royal Veterinary and Agricultural University, Denmark, (1998).
3. Fan, J.Q., Li, R.Z.: Variable selection via nonconcave penalized likelihood and its oracle properties. J. Amer. Statis. Assoc. 96 (2001) 1348–1360.

Chapter 77
PARAFAC Analysis of Neural Correlates of Face Detection

Jhoanna Pérez-Hidalgo-Gato, Valia Rodríguez-Rodríguez and Eduardo Martínez-Montes

Abstract Neural correlates of face processing have been largely studied, but more emphasis has been done in the identification of a particular face. Here we study the neural correlates of the N170 peak corresponding to the correct and incorrect detection of faces through the use of the Bayesian Model Averaging procedure. Moreover, different components of electrical sources are extracted with a PARAFAC analysis of the data. PARAFAC is a generalization of principal component analysis to deal with multidimensional data, offering as a great advantage unique decompositions. PARAFAC analysis of the three-dimensional data formed by the array of BMA inverse solutions for each subject and each experimental condition, provide of characteristic BMA sources with corresponding profiles for subjects and conditions. This allowed the identification of different and common sources for correct and incorrect detection of faces.

Keywords Face processing · N170 · neural correlates · BMA · PARAFAC

Introduction

The face fusiform area (FFA) in human extraestriate cortex is active about twice as strongly when people view faces as when they view other kinds of objects [1]. Bentin et al. (1996) [2] described a negative potential with a mean peak latency of 172 ms (N170), which was elicited by human faces but not by animal faces, cars, or butterflies. This component was larger over the right than the left hemisphere and largest in the posterior temporal areas. They suggested that, although essential for efficient face recognition, the mechanism associated with the N170 component acts on basic physiognomic features and precedes within-category identification. So, the N170 represents probably a mechanism specialized in detecting physiognomic

J. Pérez-Hidalgo-Gato
Experimental Neurosciences Department, Cuban Neuroscience Center, Ave. 25, esq 158, Havana, Cuba
e-mail: jhoanna@cneuro.edu.cu

R. Wang et al. (eds.), *Advances in Cognitive Neurodynamics*,

features and extracting the visual characteristics needed to form an internal representation of a human face.

In this work, we use an experimental paradigm for obtaining the N170 peaks corresponding to correct and incorrect recognition of faces. The neural correlates of this process are sought with the use of source localization techniques in both cases and a multidimensional analysis will be carried out for identifying different sources associated with correct and incorrect detection.

Methods

Experimental Design

The experimental paradigm consisted of presenting a face followed by a mask stimulus. The subject was asked to detect the presence of (1) any face (hereinafter condition D), (2) a specific (predetermined) face and (3) a scrambled face. The presentation time was 30 ms for both face and mask. We recorded the electrical activity and obtained the corresponding N170 event related potential (ERP) [2] for each condition by averaging across trials. 10 subjects volunteered for the experiment.

Source Analysis

Source analysis of ERPs corresponding to right (RA) and wrong answers (WA) in condition D were carried out by Bayesian Model Averaging (BMA) [3]. This method uses a functional segmentation in 67 structures of the MNI brain atlas for defining different models (all combinations of anatomical compartments). Current densities are estimated by constrained LORETA for the relevant models (using a Markov Chain Monte Carlo procedure), and then they are bayesian averaged for obtaining a model-free inverse solution. With this technique deep sources can be found even when other cortical activations are present.

Parallel Factor (PARAFAC) Analysis

PARAFAC analysis is a generalization of Principal Component Analysis (PCA) to deal with multidimensional data that has been increasingly used in neuroscience studies [4]. With PARAFAC the data is decomposed into a sum of atoms, each being the outer product of characteristic signatures for each dimension, thus assuming that the data depends linearly on each of the intrinsic dimensions. Its main advantage is that, unlike PCA, it provides a unique decomposition. However, the number of components is arbitrary although an optimal estimate can be found with the use of the Core Consistency Diagnostic (Corcondia) test [5].

In this study we arranged the BMA inverse solutions obtained for all subjects and conditions RA and WA into a three dimensional array, as represented in Fig. 77.1.

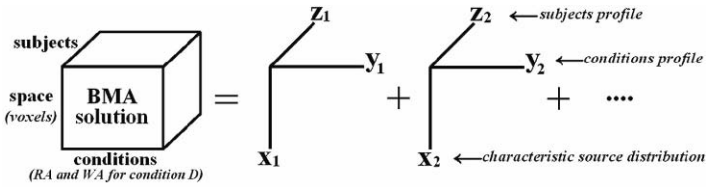

Fig. 77.1 Schematic representation of the PARAFAC analysis of the three-dimensional data formed by the BMA inverse solutions (giving the current density for each voxel) for each condition and subject

PARAFAC model was used for decomposing this array into components with a characteristic source distribution and corresponding profiles for both conditions and subjects.

Results

Amplitude of the Grand Average N170 peak for right answers of D condition was significantly higher ($p = 0.0158$) than for wrong answers (not shown). PARAFAC analysis of the 3D array of current density yielded two components, as assessed by the Corcondia test. Figure 77.2 shows the condition profiles for the two components. Clearly, the first component reflects the data representative of the WA condition and the second the data of the RA condition.

This means that characteristic BMA source distributions for the second component will show the sources activated when the subjects correctly detect the presented face and the first component will show sources when the subject was not able to detect the presence of the face. Figure 77.3 shows the signatures of BMA solutions for the two components. The first component (panel (a)) shows the activation of right temporal and frontal regions (Broadman Areas 6, 21, 22, 24 and 32), while the

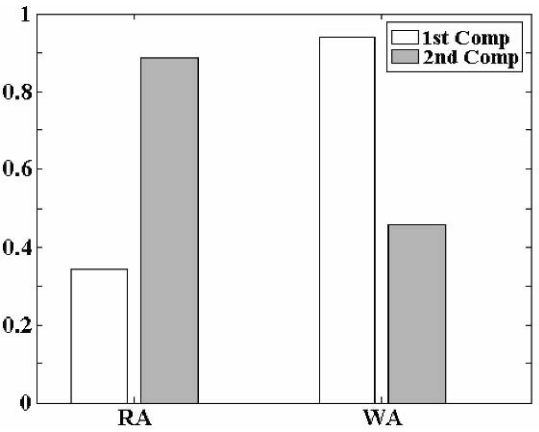

Fig. 77.2 Condition profile for the two components extracted with PARAFAC. The first component has greater contribution from the wrong answers and the second has greater contribution from the right answers (correct detection of faces)

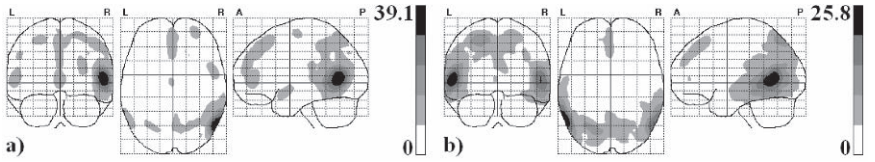

Fig. 77.3 Orthogonal projections of the BMA solution signatures for the two components extracted with PARAFAC. (a) First component; (b) Second component

second (panel (b)) shows higher activation in bilateral temporal and lateral-occipital regions (Broadman Areas 9, 20, 37, and 10).

Conclusions

The use of a PARAFAC model provides a parsimonious and easy-to-interpret representation of the huge amount of data given by the estimated current density for several subjects and experimental conditions. Two components extracted by PARAFAC can be identified as reflecting the sources of the correct and incorrect detection of faces, according to the conditions profile. The corresponding spatial signatures, i.e. the characteristic current densities show these sources for the different components. In this case we found that the FFA and the temporal right area is common to both conditions, while for incorrect detection higher activations are present in the frontal region. Also, it was shown that in addition to the FFA, the face selective region in lateral-occipital cortex is also involved in the correct recognition of faces.

References

1. Grill-Spector, K., Knouf, N., Kanwisher, N.: The fusiform face area subserves face perception, not generic within-category identification. Nat. Neurosci. 7 (2004) 837–843.
2. Bentin, S., Allison, T., Puce, A., Perez, A, McCarthy, G.: Electrophysiological studies of face perception in humans. J. Cognitive Neurosci. 8 (1996) 551–556.
3. Trujillo-Barreto N.J., Aubert-Vázquez, E., Valdés-Sosa, P.A.: Bayesian model averaging in EEG/MEG imaging. Neuroimage 21, 4 (2004) 1300–1319.
4. Miwakeichi, F., Martínez-Montes, E., Valdés-Sosa, P.A., Nishiyama, N., Mizuhara, H., Yamaguchi, Y.: Decomposing EEG data into space-time-frequency components using parallel factor analysis. Neuroimage 22, 3 (2004) 1035–1045.
5. Bro, R.: Multi-way Analysis in the Food Industry: Models, Algorithms and Applications. Ph.D. Thesis. University of Amsterdam and Royal Veterinary and Agricultural University, Denmark, (1998).

Chapter 78
Human Vision Can Predict Semi-Random but the First-Order Linear Process

Manabu Shikauchi and Tomohiro Shibata

Abstract This study aims at investigating prediction in human vision, particularly prediction of semi-random target sequences that cannot be predicted simply based on the memory of a part of target sequence whose length is typically determined by an estimated period of the sequence. In this article, we propose a novel experimental paradigm in which the Auto-Regressive (AR) process was used to generate the semi-random sequence, and to generate the random sequence which is designed to have the same variance with the semi-random sequence. Optimal prediction can be achieved by learning and using the AR model parameter that is used to generate the semi-random sequence. In our experiment, a visual target was presented on a monitor one by one from a sequence, and subjects were asked to predict the next target position using saccades. Results suggest that human vision can well predict semi-random first-order linear processes presumably based on learning their generative processes.

Keywords Prediction · AR process · vision · saccades

Introduction

Prediction of changes in the environment is crucial for humans as well as animals. When the change of a target sequence is periodic or the length of a sequence is sufficiently short, learning and prediction of the sequence are not difficult; there have been many studies reporting such learning and prediction in humans as well as monkeys [1, 2, 3, 4, 5]. Although many previous studies assumed memory-based learning in which a short sequence was memorized as it was, or one period of a sequence was memorized for a periodic sequence, such a memory-based method is computationally inefficient when it is not necessary to memorize a whole sequence

M. Shikauchi
Graduate School of Information Science, Nara Institute of Science and Technology, 8916-5 Takayama, Ikoma, Nara, Japan
e-mail: manabu-s@is.naist.jp

R. Wang et al. (eds.), *Advances in Cognitive Neurodynamics*,

as a simple rule is used to generate a sequence. Furthermore, such a memory-based method cannot handle semi-random or aperiodic target sequences.

This study examined whether human vision can predict semi-random target sequences that cannot be predicted by a memory-based approach but can be well predicted if the brain extracts a simple rule which was used to generate the sequence. In this article, we propose a novel experimental paradigm in which Auto-Regressive (AR) process is employed as a sequence generator. There are three other advantages of employing the AR process. First, it enables systematic design of unpredictability of the target sequences. Second, an optimal predictor exists for each target sequence. Third, a completely unpredictable (random) sequence can be easily generated from an AR sequence, a sequence generated by an AR process.

Methods

Our experiment was composed of six tasks each of which used a different target sequence: AR_1, AR_{21}, AR_{22}, and three random sequences generated for control tasks from the AR sequences. One task consisted of 500 trials. Fig. 78.1b illustrates the procedure for one trial. In a target gaze period at the T-th trial, a target $S(T)$ appeared on the monitor, and each subject was instructed to gaze at the target until the target disappeared 1500 ms later with a notification sound. Then, the subject was required to predict the next target position by saccades and to keep gazing at the position until the subject heard another notification sound. After a 1000-ms rest, the next trial was started. The visual target was drawn as a small circle of 0.16° and was presented on the graduated ruler. The ruler had 9.2° view angle.

The novel feature of our experimental paradigm is that the AR process was employed to generate the target sequence. An AR sequence $\{S(T);\ (T = 1, \cdots, N)\}$ was generated by $S(T) = \sum_{i=1}^{M} a_i S(T-i) + \xi(T)$, where T is discrete time, a_i is an AR model parameter, M is the model order, and $\xi(T)$ is the system noise input. The system noise $\xi(T)$ followed a normal distribution $N(\mu_s,\ \sigma_s^2)$, where the mean μ_s and the standard deviation σ_s were set to 0.0° and 0.72° of view angle, respectively. In this study, three AR sequences, each of which was composed of 500 positions for 500 trials, were used. One sequence, called AR_1 sequence, was generated by a first-order AR process $S(T) = 0.9S(T-1) + \xi(T)$, and the other two, called AR_{21} and AR_{22} sequences were generated by second-order AR processes: $S(T) = a_1 S(T-1) + a_2 S(T-2) + \xi(T)$, where $(a_1, a_2) = (0.6,\ 0.3)$ and $(1.3,\ -0.7)$, respectively.

For the control task of this experiment, we generated random sequences each of which had the same variance with a mother AR sequence; they could not be predicted at all, i.e., the all random sequence did not have any dynamics. Just shuffling the order of an AR sequence provides a random sequence. Examaple AR and random sequence employed in this study are presented in Fig. 78.1a.

If the optimal prediction is achieved by a subject, the distribution of the prediction error should be close to the system noise distribution of the corresponding

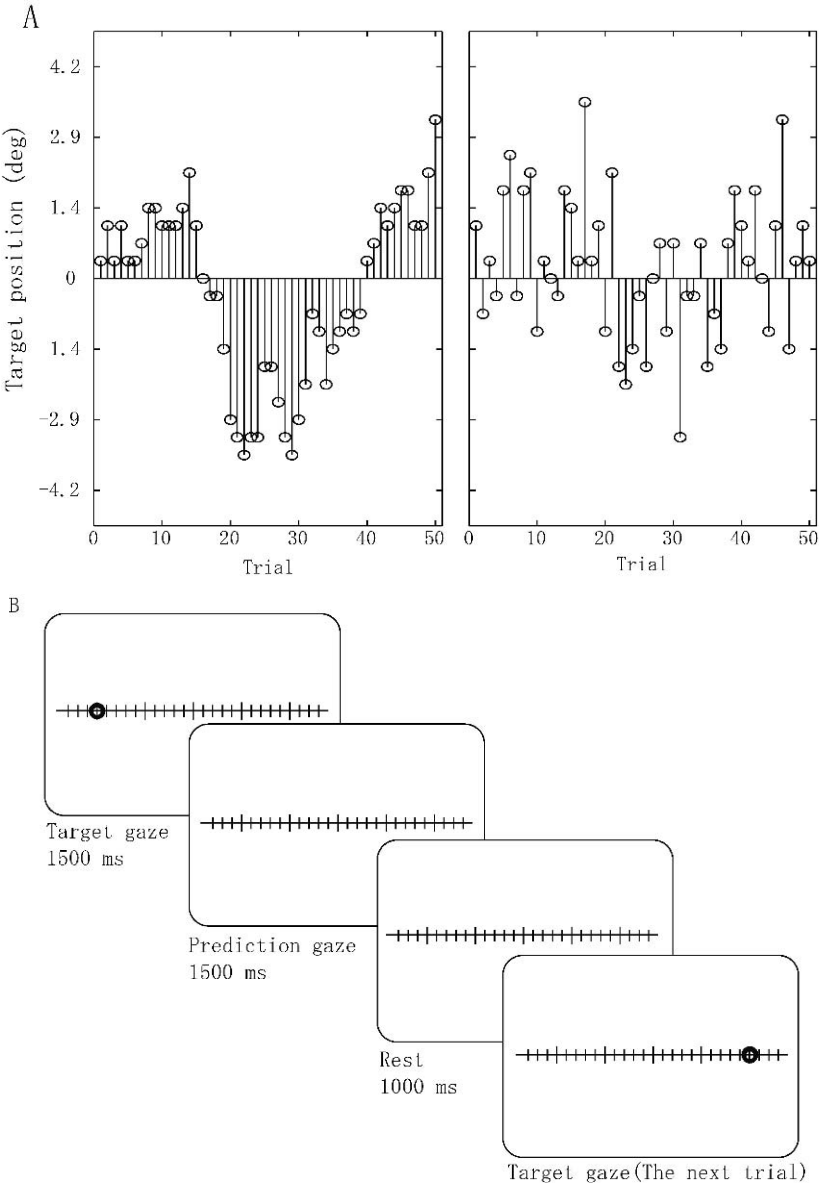

Fig. 78.1 Sample target sequences and task procedure. (a) Target sequence generated by an AR process (left), and a random sequence (right), (b) Task procedure for one trial (see text in detail)

AR process. The prediction error $E(T)$ was calculated by $P(T) - \hat{P}(T)$, note that $\hat{P}(T)$ is the optimal prediction $\sum_{i=1}^{M} a_i S(T-i)$, where $S(T-i)$ are past target positions presented on the monitor. Root mean square error (RMSE) of prediction was calculated by $\sqrt{\frac{1}{N}\sum_{T=1}^{N} E(T)^2}$, where N denotes the number of trials.

As the first analysis, comparison of the prediction error between the AR sequence and the pairing random sequence was made. The RMSE of prediction was calculated for each task where $N = 500$ as the number of trial in each task. $RMSE_{ar}$ and $RMSE_{rnd}$ denote the RMSE of prediction in an AR task and in a random task, respectively. The second analysis was made to investigate whether learning AR model parameters occurred during a task. The initial phase and the ending phase of $RMSE_{ar}$, called $RMSE_{init}$ and $RMSE_{end}$, respectively, were calculated and compared. The initial phase and the ending phase specify the first 150 trials and the last 150 trials of one task, respectively.

In addition, AR model orders presumably used for prediction were estimated from the subjects' behavioral data. The aim of this was to investigate how much complicated model each subject actually utilized. We used Bayesian Information Criterion [6] $\hat{p} = \underset{p}{\operatorname{argmin}}\, BIC(p)$, to determine the model order $\hat{p}$. $BIC(p) = N \log \sigma_p^2 + p \log N$, where σ_p^2 is the estimated variance of the residual error when p-th order AR model is assumed. In this study, $0 \leq p \leq 10$ was searched for.

Following local ethical committee approval, five healthy male volunteers (KT, MO, NN, TY, and KY) gave their informed consent to participate. All subjects had normal or corrected-to-normal vision, and were naive of this oculomotor experiments. Because each task required strong powers of concentration, two subjects, MO, NN were participated in all tasks, whereas others a part of the tasks; detailed assignment are shown in Fig 78.2. Eyelink II (SR Research) was used for eye-movement measurements with a sampling frequency of 500 Hz. A bite bar and a chin rest were used to fix the subject head.

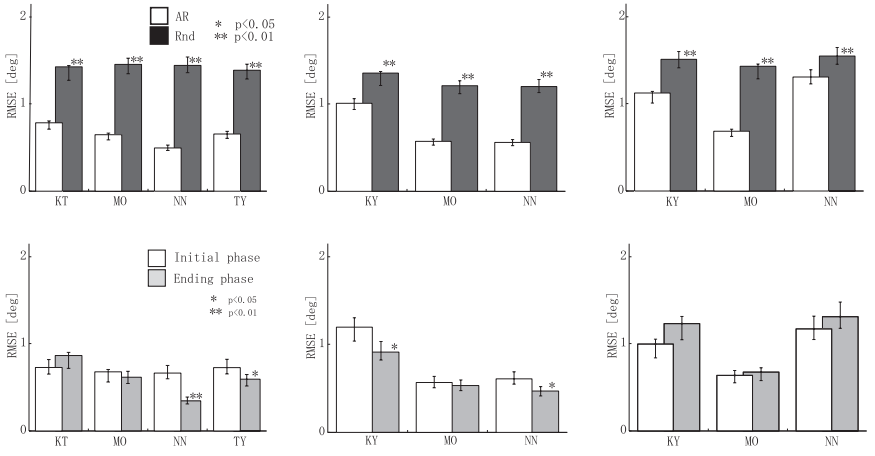

Fig. 78.2 Comparison of prediction errors. The upper panel compares $RMSE_{ar}$ and $RMSE_{rnd}$. The left, the middle, and the right columns correspond to the AR_1, AR_{21} and AR_{22} task. respectively. The lower panel compares the RMSE of prediction of the initial and the ending phase. The column order is the same with the upper panel (*, $p < 0.05$; **, $p < 0.01$; Error-bars, 95% confidence intervals)

Results

In all experiments for all subjects, $RMSE_{ar}$ was significantly smaller than $RMSE_{rnd}$ (chi-square test, $p < 0.01$, Fig. 78.2, upper). In the AR_1 task, there were significant differences between $RMSE_{init}$ and $RMSE_{end}$ for two subjects (NN and TY) (chi-square tests, $p < 0.01$ for NN, $p < 0.05$ for TY, Fig. 78.2, lower). In the AR_{21} task, there were significant differences between $RMSE_{init}$ and $RMSE_{end}$ for other two subjects (KY and NN) (chi-square tests, $p < 0.05$ for both, Fig. 78.2, lower). In the AR_1 and AR_{21} task, the decrease of $RMSE_{ar}$ was observed for each of two subjects (NN and TY). The estimated model orders were the first-order for all tasks where AR sequences were used, whereas it was the second order for one subject (KY) in the AR_{21} task. In contrast, it was always zero-th for all tasks where random sequences were presented.

Discussion

The first analysis (upper panel, Fig. 78.2) show that all subjects made better performance for AR sequences than random sequences. The second analysis (lower panel, Fig. 78.2) suggests that the better prediction performances for the AR sequences could be caused by learning of the AR process. The additional analysis in which the model order was estimated for each subject's prediction partly supports the above suggestion because it clearly shows that all subjects were able to detect whether the current sequence had a dynamics or not. The first analysis (upper panel, Fig. 78.2) also indicates that the predictive performances for the AR sequences were not optimal, and that the performances for AR_{22} were much worse than the one for other AR sequences.

In summary, this study illuminates a novel possibility for human vision to predict semi-random sequences that cannot be predicted by a memory-based approach. The possibility, however, might be allowed only for the sequence generated by a first-order linear process.

References

1. G.R. Barnes and P.T. Asselman. The mechanism of prediction in human smooth pursuit eye movements. *J Physiol*, 439:439–461, 1991.
2. J. Tanji and K. Shima. Role for supplementary motor area cells in planning several movements ahead. *Nature*, 371:413–416, 1994.
3. R. Kawashima, J. Tanji, K. Okada, M. Sugiura, K. Sato, S. Kinomura, K. Inoue, A. Ogawa, and H. Fukuda. Oculomotor sequence learning: a positron emission tomography study. *Exp Brain Res*, 122:1–8, 1998.
4. J.C. Eliassen, T. Souza, and J.N. Sanes. Human brain activation accompanying explicitly directed movement sequence learning. *Exp Brain Res*, 141:269–280, 2001.
5. L.A. Murotek, C.C.A.M. Gielen, and M. Flanders. Manual tracking in three dimensions. *Exp Brain Res*, 171:99–115, 2006.
6. G. Schwartz. Estimating the dimension of a model. *Ann Stat*, 6:461–464, 1978.

Chapter 79
Memory Formation of Object Representation: Natural Scenes

Eiichi Hoshino, Fumihiko Taya and Ken Mogi

Abstract It has been suggested that the parahippocampal region collects spatial information in relation to navigational objects, in a joint encoding of space (Nature Neuroscience 7: 673–677, 2004). The navigational object may play a role of "landmark" when the episodically dispersed snapshots are combined into comprehensive spatial information of an individual space. Here we study the nature of object recognition in the long-term memory in human cognition that is learnt during scene-integration as regards the viewing angle under attention control. Based on the result, it is suggested that objects in a scene without attention may be processed into a 2-D representation bound to the background scene as a texture.

Introduction

The interpretation of spatial relationships is an important factor in contextual behaviours and the formation of episodic memory. The classic key idea of spatial information processing has been analysed by O'Keefe and Nadel [1]. Together with discovery of "place cells" and concept of "cognitive map" [2], they proposed the cognitive map theory in which place cells, dead reckoning system and landmark navigation are combined into allocentric map-based navigation in hippocampus formation. On the other hand, Yamaguchi has proposed a mechanism of hippocampal memory encoding of episodic events from novel temporal inputs caused by theta phase precession [3]. More recently, Janzen and van Turennout demonstrated that the parahippocampal region collects spatial information in relation to various objects, in a joint encoding of space and objects [4]. To produce allocentric long-term memory (LTM), it is necessary that the egocentric representations primarily obtained from perceptual information are combined together. In a case of absence of self motion, the production of allocentric LTM crucially relies on the integration

E. Hoshino
Tokyo Institute of Technology, Tokyo 152-8552, Japan
e-mail: eiichi@brn.dis.titech.ac.jp

R. Wang et al. (eds.), *Advances in Cognitive Neurodynamics*,

of different scenes. If scenes are episodically dispersed, it is required that there be navigational landmarks in the scenes to combine these scenes into coherent allocentric representations.

Current study focuses on the observation of object recognition underlying human cognition after episodically dispersed views are combined into comprehensive spatial information of an individual space. Additionally, attention enhances the visual LTM (VLTM) of previously attended objects embedded in a natural scene [5], which is supported by a dynamic evolution model on attention and memory [6], suggesting that object representations in LTM may also be affected by attention. Thus, we also study the effect of attention on the object representations revealed in a later recognition task.

Experiments

To investigate the nature of object representations within human cognition in LTM that is learnt during scene-integration, experiment 1 was designed especially as regards the viewing angle with attention control, in the context of integration of the spatial information. In the leaning phase, participants were, in turn, viewed two dispersed views in which the several objects were located. They were instructed to remember objects on green bases and their position while those on blue bases were distractors at the moment. After the learning phase, they were required to conduct a two-alternative forced-choice recognition test. The objects presented in the test phase were divided into three types; i.e. objects viewed from same angle as the learning phase, those from different angles and novel objects. The objects were chosen from everyday use objects in same basic-level category (i.e. chairs, in this study) to make the different visual angle recognition easy because the aim of the experiment is to study the nature of object representations in LTM, but not in short-term memory (STM) in which the multi-angle object representations would be more easily established than those in LTM. Consequently, experiment 2 was carried out as the same as experiment 1 but the background in learning phase were changed to monochromatic.

Results

The rate of correct judgement (RCJ) (familiar or new) was significantly higher for the attended objects (green bases) compared to the unattended objects (blue bases). A 2 by 2 repeated-measures analysis of variance (ANOVA) (attention by visual angle) on the RCJ showed a significant effect of attention ($F(1, 8) = 7.977,\ p = 0.022 < 0.05$), whereas no significant effect of visual angles and no interaction between same and different visual angles ($F(1, 8) = 0.397,\ p = 0.546$) (Fig. 79.1a). The RCJ on unattended objects viewed from the same visual angle was higher than that for rotated objects, although the difference was not statistically significant

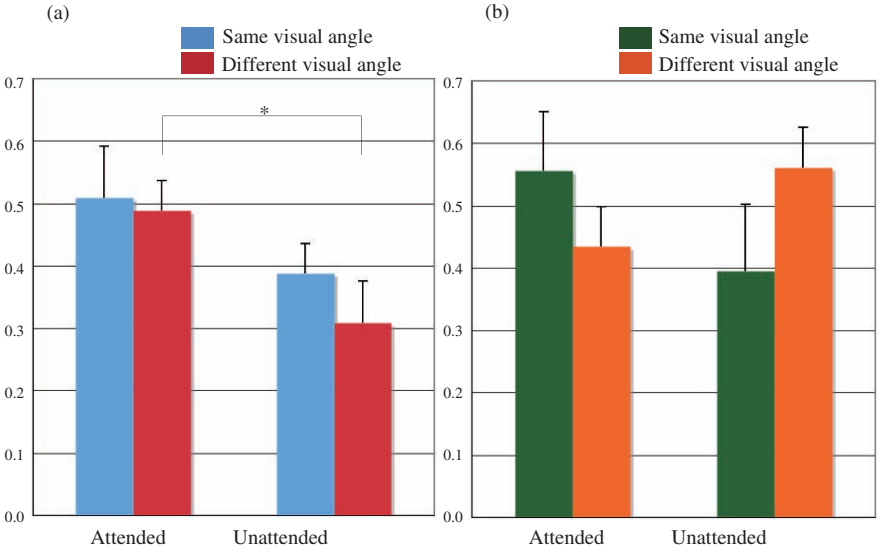

Fig. 79.1 Rate of correct judgement (RCJ) for the objects in experiments 1 and 2. (a) RCJ for attended and unattended objects viewed from same and different visual angles in experiment 1. (b) That in experiment 2. Error bars are standard errors across participants

(Fig. 79.1a). The RCJ on unattended objects viewed from different visual angle was significantly lower than that on attended objects, ($p < 0.05$), while that on attended objects had no significance. The RCJ on objects located at a certain spatial configuration, such as right- or left turn corner and crossroads, was not consistent in conditions with any particular visual angles. A few participants reported that remembering the objects and their location was too difficult and could not confidentially discriminate familiar or new for the most of the objects. However the tendency in less RCJ on the unattended objects presented from different visual angle was observed among participants. A motivated participant showed that good performances in both types of RCJ for attended objects, but again his RCJ for unattended objects viewed from different angles was significantly poor.

In experiment 2, no statistically significant difference was observed among the four conditions, although both types of RCJ of objects from different visual angles appeared to be higher than that of objects from same visual angles (Fig. 79.1b).

Discussion

The result that overall VLTM of attended objects was relatively well established compared with that of unattended objects is consistent with previous work by Hollingworth [5], supporting that attention to objects in a scene enhanced the consolidation of memory for navigational landmark representations. Moreover, the

accuracy on attended object recognitions from different visual angles indicates the role of attention is producing the angle invariant object representations.

The inconsistency between the succeeded recognition for object from particular visual angles and the spatial configurations suggests that the memory of object representations do not include the spatial configurations around the object. [But see Hollingworth (2006) [8]]. This supports Mallot and Gillner's finding that the local views and objects are recognised individually and not recognised as configurations among objects when navigating in a large-scale environment [9]. The selective activation for navigational objects previously showed in a scene but not for non-navigational objects, found by Janzen and van Turennout, in the parahippocampal gyrus [4] may not support encoding of spatial configurations around the objects. The result that the RCJ vary according to attention could predict that the nature of object representations would reflect only object intrinsic representations, again consistent with Mallot and Gillner's finding. The VLTM of object representations is strongly bound to a presented scene [8]. If attention plays a role in extracting focal information, a cognitive stage of object representations may be produced by attention. Therefore, attention may support to obtain the view-invariant or 3-D representations of objects from a scene, but in absence of attention, such representations are never obtained. Rather the object-to-scene binding gives rise to a perception of objects as a texture in the scene. In this view, the failure of recognition in unattended and depth rotation may arise from the object-to-scene binding.

Whereas unattended objects in a scene might be primarily treated as a texture bound to the scene in the VLTM without any 3-D structural information. The failure to recognise rotated objects whose orientation is novel for subjects may reflect the strong object-to-scene binding where an object is regarded as a part of plain surface of a scene, resulting in inhibition priming.

References

1. O'Keefe, J., Nadel, L.: The Hippocampus as a Cognitive Map. Oxford, Clarendon (1978).
2. O'Keefe, J., Dostrovsky, J.: The Hippocampus as a Spatial Map. Preliminary Evidence from Unit Activity in the Freely-Moving Rat. Brain Research. Vol. 34. No. 1. (1971) 171–175.
3. Yamaguchi, Y.: A Theory of Hippocampal Memory Based on Theta Phase Precession. Biological Cybernetics. Vol. 89. No. 1. (2003) 1–9.
4. Janzen, G., van Turennout, M.: Selective Neural Representation of Objects Relevant for Navigation. Nature Neuroscience. Vol. 7. No. 6. (2004) 673–677.
5. Hollingworth, A., Henderson, J.M.: Accurate Visual Memory for Previously Attended Objects in Natural Scenes. Journal of Experimental Psychology. Vol. 28. No. 1. (2002) 113–136.
6. Wang, R., Yu, J., Zhang, Z.: A Neural Model on Cognitive Process. Lecture Notes in Computer Science. ISNN 2006. LNCS3971. (2006) 50–58.
7. Hollingworth, A.: The Relationship Between Online Visual Representation of a Scene and Long-Term Scene Memory. Journal of Experimental Psychology. Vol. 31. No. 3. (2005) 396–411.

8. Hollingworth, A.: Scene and Position Specificity in Visual Memory for Objects. Journal of Experimental Psychology. Vol. 32. No. 1. (2006) 58–69.
9. Mallot, H.A., Gillner, S.: Route Navigating without Place Recognition: What is Recognised in Recognition-Triggered Responses? Perception. Vol. 29. (2000) 43–55.
10. Hoshino, E., Taya, F., Mogi, K., Egocentric Space and Object Perception. Posted on : SfN2006 (Society for Neuroscience). (2006).

Chapter 80
Dynamical Model of Action Reinforcement by Gated Working Memory

Adam Ponzi

Abstract Phasic dopamine response is thought to provide a reward prediction error as a teaching signal for adjustment of an action selection policy. Here we propose a simple neural network dynamical system model based on the dopamine modulated cortical basal ganglia thalamic loops. The system produces a realistic dopamine response and combines it with a gated working memory model, to reinforce the policy when the dopamine signal is above baseline and reverse the policy when below baseline. We illustrate the model with application to the learning of a simple cue action delay reward task.

Introduction

Cortico-basal ganglia loops are critical for the learning of rewarded cued procedures and in cued working memory (WM) tasks. Dopamine is thought to play the role of *reward prediction error* [1], where the burst firing of dopamine cells is increased by unexpected rewards and reduced if an expected reward is omitted. The striatum and cortex recieves a rich innervation from the midbrain dopaminergic system [2]. The basal-ganglia, the prefrontal cortex and the midbrain dopamine nuclei are also strongly implicated in WM. Persistent neural activity in recurrent circuits play a central role in the maintenance of information in WM [3]. Some theories also ascribe a direct gating role to dopamine, such that dopamine release is required for read-in to WM. The integration of gating and neuromodulation within and between basal ganglia and cortex provides a set of important, and as yet underexplored, issues [3]. Dopamine also can seemingly paradoxically suppress or enhance striatal and cortical activity, and can extend the duration of enhanced activity. This is due to the complex action of the D1 and D2 dopamine receptors [2]. Our model brings a few of these observations together in uniting action selection, dopamine reward prediction and WM gating in a cortical basal ganglia based model.

A. Ponzi
Laboratory for Dynamics of Emergent Intelligence, RIKEN BSI, Saitama, Japan
e-mail: adam@brain.riken.jp

R. Wang et al. (eds.), *Advances in Cognitive Neurodynamics*,

Model

The network model is depicted in Fig. 80.1a. The input layer consists of a set of units which respond to the external environment. These inputs $I_i(t),\ i = 0, .., N$, are modeled very simply as $I_i(t) = 0, 1$, where the unit is firing at a constant rate if it is activated and completely silent otherwise. (More complex receptive fields are perfectly possible however.) The input units project in a one-to-one way to a recurrent layer described by activities $p_i(t)$. It is simply given by,

$$\frac{dp_i}{dt} = -k_1 p_i + k_2 g\left(\sum_{j\neq i} w_{ij} p_j\right) f(T(t) - T_X) + k_3 I_i(t) f(T_X - T(t)), \quad (80.1)$$

$$\frac{dw_{ij}}{dt} = k_4 p_i - k_5 p_i p_j - k_6 w_{ij}. \quad (80.2)$$

Here the activities $p_i(t)$ may represent membrane potentials or firing rates and we do not model spiking explicitly. The $w_{ij}(t)$ are modifiable synaptic efficacies associated with the recurrent collaterals between the N cells, simply modeled by competitive Hebbian learning, where $k_4, k_5, k_6 > 0$ are parameters and the k_6 term produces between trial exponential decay. In Eq. (80.1) $g(x)$ is a sigmoidal function which limits the activity from the recurrent collaterals and produces the non-linearity. The terms $f(T(t)-T_X)$ and $f(T_X-T(t))$ where $f(x) = x,\ x > 0,\ f(x) = 0$ otherwise, models the action of the thalamus which here switches on an off the WM and gates the input. When $T_X > T(t)$ input from the primary layer is allowed through but the recurrent collaterals are suppressed. During this time the weights Eq. (80.2) of the activated cells i with $I_i(t) = 1$, are increased by the term $k_4 p_i$. However when $T_X < T(t)$ the recurrent collaterals are switched on and the system becomes a winner-take-all system with the winner the most recently and strongest p cell activated. The input is down-gated during this time so that p cells with active input during this time do not interfere with the winner selection.

The action layer cells $m_i(t)$ represent actions and the layer is modeled exactly the same way as Eqs. (80.1, 80.2) except that the input term is not topographic and

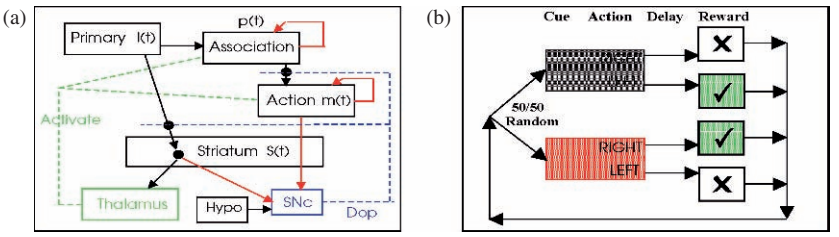

Fig. 80.1 (a) Anatomy of the model system described. The black lines are excitatory projections, the red lines inhibitory. The blue dashed line depicts the dopamine LTP/LTD modulation and the green dashed line depicts the thalamus gating and WM activation signal. (b) Task described. One of two cues, red or black is presented at random each trial. During this time the animal makes an action. After a delay a green signal is shown and a reward is given if correct action selected

is replaced by an all-to-all projection from the association layer so that the term $I_i(t)$ in Eq. (80.1) is replaced by $J_i(t) = \sum_j x_{ij} p_j(t)$. Otherwise the equations are the same, including the thalamus gating. Here the $x_{ij}(t)$ are modifyable synaptic weights between the p and m layers given by,

$$\frac{dx_{ij}}{dt} = -x_{ij}(t) + f((\alpha(t) - \alpha_c)m_i p_j + e_c \epsilon_{ij}(t) + x_{ij}(t)). \tag{80.3}$$

In this Eq. (80.3) $\alpha(t)$ is the dopamine concentration in the vicinity of the synapse and $(\alpha(t) - \alpha_c)$ represents the D1/D2 dopamine receptors controlling LTP or LTD at these synapses [2, 4]. The term $\epsilon_{ij}(t)$ is an i.i.d noise term and e_c is a parameter. For the results shown in this paper $e_c = 0$ so the system is deterministic but we leave the noise term for generality [5]. The striatum MSN neurons $S(t)$ are modeled as,

$$\frac{dS_i}{dt} = -S_i + f\left(\sum_j Y_{ij}(t) I_j - k_7 \sum_i S_i + k_8 S_i\right), \tag{80.4}$$

where again the $Y(t)$ are modifyable synaptic weights modulated by dopamine,

$$\frac{dY_{ij}}{dt} = -Y_{ij}(t) + f((\alpha(t) - \alpha_c) S_i I_j + Y_{ij}(t)). \tag{80.5}$$

This system Eq. 80.4 is also a winner-take-all system. Here the input layer $I_i(t)$ projects all-to-all to the MSN cells. In this model the striatum controls the thalamus $T(t)$ reactivation and gating activity and the dopamine concentration $\alpha(t)$. The thalamus activity is given by, $\tau_T \frac{dT}{dt} = -T(t) + T_X + \sum_i S_i(t)$ so that it is activated by the striatum cells $S_i(t)$ and τ_T is a time scale and T_X is its base level. The dopamine signal is given by, $\tau_\alpha \frac{d\alpha}{dt} = -\alpha(t) + \alpha_c - \sum_i S_i(t) - \sum_i m_i(t) + R(t)$. Dopamine is activated by $R(t)$ which is the primary reward signal from the hypothalamus activated when food is found and inihibited by the actions $m_i(t)$. The inhibition from $m_i(t)$ is necessary to stabilize the learning at the association layer to action layer synapses in Eq. 80.3. Dopamine is also inhibited by the striatum cells $S_i(t)$, which are also the ones which activate the thalamus $T(t)$. The idea here is that $I_i(t)$ states which coincide with reward $R(t)$ learn through the striatum system Eqs. (80.4), (80.5) to *balance* the reward signal $R(t)$. At the same time this allows rewarded states to activate $T(t)$ which controls the gating and WM as described. Therefore states $I_i(t)$ which are rewarded *part of the time*, as given by the current action selection policy will activate $T(t)$ sometimes in the presence of positive dopamine and sometimes with negative dopamine.

Here we only have two actions and one is selected according to the sign of $F(t)$ at the end of the action selection period where $\frac{dF}{dt} = m_1(t) - m_2(t)$ is summed over the action selection period during the cue presentation period and $F(t)$ is reset to zero between trials. All equations were integrated using fourth order Runge-Kutta.

Results and Discussion

The model is best understood through studying examples of its time series, see Fig. 80.2. In this task one of two cues, red I_1, or black I_2 is presented each trial at random. The animal makes an action and a third signal I_3 green is shown with or without reward. Figure 80.2a shows the association layer $p_i(t)$ time series. Figure 80.2b shows early in learning. The dopamine signal resembles the reward prediction error of Rescorla-Wagner. The animal initial action selection policy is such that red is correctly associated to action 1, while black is incorrectly associated to action 1. The positive dopamine signal generated by primary reward associates the coincindent green signal I_3 to the thalamus $T(t)$ reactivation via an MSN cell $S_i(t)$ gradually over several trials. For the first time at $t \approx 6700$ (Fig. 80.2b) this is strong enough to enable the gating of the cue signal (together with the selected action $m_i(t)$) into WM. Positive dopamine now strongly reinforces the cue-action association during WM maintenance. In Fig. 80.2c the black signal is encountered with the incorrect action and the black cue and the incorrect action it selected are gated into WM. The negative dopamine signal reduces the incorrect x_{ij} weight via Eq. (80.3) while the green signal I_3 maintains the cue and incorrect action in WM. Maintainence is necessary to allow LTD to occur without reducing the postsynaptic selected action m_i activity. If postsynaptic activity is reduced in a noiseless winner-take-all system, the action cannot be reversed since the weights x_{ij}, Eq. (80.3), cannot cross, (they just oscillate a fixed point). This allows the reversal of the black cue

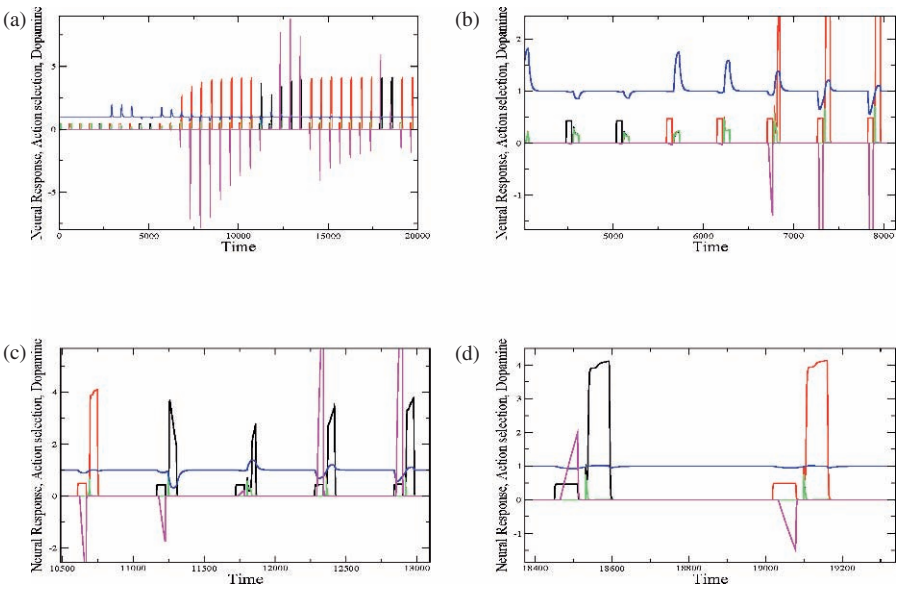

Fig. 80.2 (a) Association layer $p_i(t)$ time series over many repeated trials. $p_1(t)$ black, $p_2(t)$ red, $p_3(t)$ green. Dopamine $\alpha(t)$ blue. Action selector $F(t)$ pink. (b), (c) and (d) segments from time series in (a)

action assignment which is then positively reinforced next trial. In Fig. 80.2d we see that at full learning the dopamine signal has relaxed to a *no surprise* level where the system is fully predicted. A previous version of this model is to appear in [5] and Roelfsema et al. [6] describe a related model of attention gated reinforcement learning.

References

1. Schultz, W. (1998), J. Neurophysiol., **80(1)** 1–27.
2. Reynolds, J.N.J., Hyland, B.I., Wickens, J.R., (2001), Nature, **413**, 67.
3. Gruber, A.J., Dayan, P., Gutkin, B.S., Solla, S.A., (2006), J. Comput. Neurosci. **20** 153–166.
4. Nakahara,H., Amari, S., Hikosaka, O., (2002), Neural Comput, **14** 819–844.
5. Ponzi, A. (2008), Neural Networks, **21** 322–330.
6. Roelfsema, P.R., Van Ooyen, A., (2005), Neural Comput **17** 2176–2214.

Chapter 81
Quantum Representation Theory for Nonlinear Dynamical Automata

Peter beim Graben

Abstract Nonlinear dynamical automata (NDAs) are implementations of Turing machines by nonlinear dynamical systems. In order to use them as parsers, the whole string to be processed has to be encoded in the initial conditions of the dynamics. This is, however, rather unnatural for modeling human language processing. I shall outline an extension of NDAs that is able to cope with that problem. The idea is to encode only a "working memory" by a set of initial conditions in the system's phase space, while incoming new material then acts like "quantum operators" upon the phase space thus mapping a set of initial conditions onto another set. Because strings can be concatenated non-commutatively, they form the word semigroup, whose algebraic properties must be preserved by this mapping. This leads to an algebraic representation theory of the word semigroup by quantum operators acting upon the phase space of the NDA.

Introduction

One of the most crucial problems in cognitive neurodynamics is the realization of symbolic processing capabilities in the human brain. While the traditional cognitivistic account assumes that cognition is essentially rule-driven manipulation of symbols [1, 2], the dynamical systems approach to cognition models cognitive processes by the (transient) dynamics of nonlinear systems, such as neural networks [2, 3] or nonlinear dynamical automata (NDA) [2, 4, 5]. The latter are piecewise affine linear maps on the unit square whose symbolic dynamics exhibits the computational power of Turing machines.

Therefore, NDAs have been suggested for modeling syntactic language processing [2, 5] and language-related brain potentials (ERPs) [6]. It is the aim of this paper to discuss one particular problem of this approach, the issue of nondeterminacy of

P.B. Graben
School of Psychology and Clinical Language Sciences, University of Reading, UK
e-mail: p.r.beimgraben@reading.ac.uk

R. Wang et al. (eds.), *Advances in Cognitive Neurodynamics*,

parsing [7], and to present a solution in terms of interactive computation [8] such that environmental perturbations act upon the system's phase state similar to quantum operators.

Nonlinear Dynamical Automata

In this section, we construct an NDA that is able to process the material from the study of Osterhout et al. [6] investigating sentences such as "the judge believed the defendant was lying". In a first step, the sentence is described by a phrase structure tree as in Fig. 81.1.

In order to derive a context-free grammar (CFG) from this tree, we first discard the lexical material, regarding the nodes d, n_1, v_1, n_2, a, and v_2 as terminal symbols. The CFG is then given by the rules: (1) $S_1 \to NP_1\ VP_1$, (2) $NP_1 \to d\ n_1$, (3) $VP_1 \to v_1\ S_2$, (4) $S_2 \to NP_2\ VP_2$, (5) $NP_2 \to d\ n_2$, and (6) $VP_2 \to a\ v_2$. Following [5], the variables of that CFG are next Gödel encoded by integers from a g-adic number system. Let $G(d) = 0$, $G(n_1) = 1$, $G(v_1) = 2$, $G(n_2) = 3$, $G(a) = 4$, $G(v_2) = 5$, $G(NP_1) = 6$, $G(NP_2) = 7$, $G(VP_1) = 8$, $G(VP_2) = 9$, $G(S_1) = A$, and $G(S_2) = B$, where $A \equiv 10$, $B \equiv 11$. Then, the sentence "the judge believed the defendant was lying" is mapped onto the string 0120345, being interpreted as a fraction 0.0120345_6 where $g_T = 6$ is the number of terminal symbols. The total number of variables is $g_V = 12$.

Syntactic language processing (parsing) generally describes the mapping of a sentence to its phrase structure tree, such as in Fig. 81.1. Yet, the most simple parsers for CFGs are push-down automata which merely decide whether an input string can be generated by a grammar. In the following, we shall discuss a simple top-down parser. Its state descriptions comprise the input string w and a stack memory γ. Table 81.1 gives the sequence of state descriptions of a parser processing the string 0120345 according to the Gödel encoding of the CFG.

In order to map the state descriptions in Table 81.1 onto the dynamics on the NDA, we have to compute the Gödel numbers

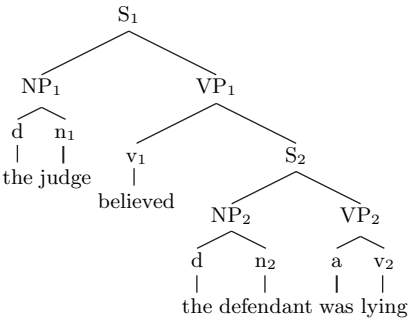

Fig. 81.1 Phrase structure tree of the example sentence

Table 81.1 Sequence of state descriptions of a top-down parser processing the string 0120345. The operations are indicated as follows: `predict(X)` means prediction according to rule (X) in the CFG; `attach` means cancelation of successfully predicted terminals both from stack and input; and `accept` means acceptance of the string as being well-formed

Time	Stack γ	Input w	Operation
0	A	0120345	`predict (1)`
1	68	0120345	`predict (2)`
2	018	0120345	`attach`
3	18	120345	`attach`
4	8	20345	`predict (3)`
5	2B	20345	`attach`
6	B	0345	`predict (4)`
7	79	0345	`predict (5)`
8	039	0345	`attach`
9	39	345	`attach`
10	9	45	`predict (6)`
11	45	45	`attach`
12	5	5	`attach`
13	ε	ε	`accept`

$$G_{V|T}(x) = \sum_{i=1}^{|x|} G(x_i) g_{V|T}^{-i} + \sum_{i=|x|+1}^{\infty} \eta_i g_{V|T}^{-i} \tag{81.1}$$

in the bases $g_V,\ g_T$, respectively. Here, $|x|$ denotes the lengths of the strings $x = \gamma$ or w and η_i are random digits in the respective base. By virtue of (1), the parser's state descriptions are represented by clouds of points $(G_V(\gamma),\ G_T(w))$ randomly scattered across rectangles in the unit square $X = [0,\ 1]^2$. Correspondingly, Table 81.1 is represented by a sequence of those rectangular macrostates evolving due to a nonlinear map $\Phi\colon X \to X$ [2, 4, 5]. Figure 81.2a displays the parsing trajectory processing the string 0120345 according to Table 81.1.

Quantum Representation Theory

The initial conditions of the NDA model are given by the whole string $w = 0120345$ in the input. However, this is cognitively implausible for two reasons: (1) Hearing or reading supplies lexical material successively to the human mind and not at once as modeled above. The same holds for psycholinguistic experiments with a word-by-word presentation paradigm [6]. (2) The NDA's dynamics is deterministic for a given initial condition. Hence, the preparation of initial conditions by the whole string w, yields a completely predictable trajectory in phase space. By contrast, the human parser is often trapped by garden path interpretations resulting from unpredicted continuations [6, 7].

In order to remedy this shortcoming, I suggest the following solution: (1) Restrict the parser's input to a *working memory* of finite length, say, $w = w_1 w_2,\ |w| = 2$ [7].

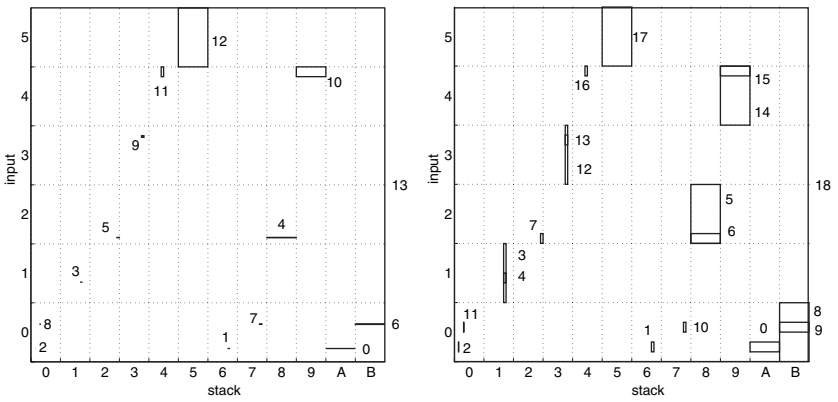

(a) (b)

Fig. 81.2 Parsing trajectories for the string $w = 0120345$. (a) Fully encoded in the initial conditions. The indices correspond to the time steps in Table 81.1. (b) Only working memory encoded in the initial conditions and representing the `scan` operation

(2) After each attachment (i.e. when $w = w_2$) the next symbol A is scanned from an *information source* [9]. (3) Define a map $\texttt{scan}(A): w \mapsto w'$, such that $w' = w_2 A$. A parser described in this way, is not longer a closed system. Now, it is interacting with its environment which perturbs its state descriptions [8]. What does this mean for the corresponding NDA?

Since the NDA is characterized by a nonlinear dynamics $\Phi: X \to X$, the scanned input A must be *represented* by another map $\rho(A)$: $X \to X$. Such representations are well-known in algebraic quantum theory [10], where observables $A,\ B \in \mathcal{A}$ are described by their abstract commutation relations. A representation is then a C*-algebra homomorphism $\rho: \mathcal{A} \to \mathcal{B}(\mathcal{H})$ from a C*-algebra $\mathcal{A}$ into the set of bounded operators $\mathcal{B}(\mathcal{H})$ acting upon a Hilbert space $\mathcal{H}$.

In terms of quantum representation theory, the construction of the representation $\rho(A)$ in the NDA's phase space is straightforward. After attaching w_1, the working memory only contains the most significant digit $w = w_2$, thus, by (1), possessing the Gödel code $G_T(w) = G(w_2)g_T^{-1} + \sum_{i=2}^{\infty} \eta_i g_T^{-i}$. Inserting A into the second most significant position by the `scan` operation, yields $w' = w_2 A$. Therefore, the representation $\rho(A)$ is given by

$$\rho(A)\big[(G_V(\gamma), G_T(w))\big] = (G_V(\gamma), G_T(w'))$$

$$G_T(w') = G(w_2)g_T^{-1} + G(A)g_T^{-2} + \sum_{i=3}^{\infty} \eta_i g_T^{-i}. \qquad (81.2)$$

Supplementing the top-down parser from Section 'Nonlinear Dynamical Automata' with the `scan` operation and representing it by (2) in the NDA's phase space, the parsing trajectory in Fig. 81.2b is obtained. After each attachment, the macrostate coincides with one of those rectangles partitioning the unit square.

Immediately afterwards, `scan` fetches the next symbol from the information source that acts like a quantum operator upon the unit square thereby squeezing the rectangular macrostate vertically.

References

1. Newell, A., Simon, H.A.: Computer science as empirical inquiry: symbols and search. Communications of the Association for Computing Machines 19 (1976) 113–126.
2. Graben, P.B.: Incompatible implementations of physical symbol systems. Mind and Matter 2 (2004) 29–51.
3. Smolensky, P.: Harmony in linguistic cognition. Cognitive Science 30 (2006) 779–801.
4. Moore, C.: Unpredictability and undecidability in dynamical systems. Physical Review Letters 64 (1990) 2354–2357.
5. Graben, P.B., Jurish, B., Saddy, D., Frisch, S.: Language processing by dynamical systems. International Journal of Bifurcation and Chaos 14 (2004) 599–621.
6. Osterhout, L., Holcomb, P.J., Swinney, D.A.: Brain potentials elicited by garden-path sentences: evidence of the application of verb information during parsing. Journal of Experiment Psychology: Learning, Memory, & Cognition 20 (1994) 786–803.
7. Frazier, L., Fodor, J.D.: The sausage machine: a new two-stage parsing model. Cognition 6 (1978) 291–325.
8. Wegner, P.: Interactive foundations of computing. Theoretical Computer Science 192 (1998) 315–351.
9. Shannon, C.E., Weaver, W.: The Mathematical Theory of Communication. University of Illinois Press, Urbana (1949).
10. Haag, R.: Local Quantum Physics: Fields, Particles, Algebras. Springer, Berlin (1992).

Chapter 82
Superior Colliculus and Basal Ganglia Control the Saccadic Response in Motion Discrimination Tasks

Jiaxiang Zhang and Rafal Bogacz

Abstract Recent physiological studies suggest that in motion discrimination tasks, neurons in the lateral intraparietal (LIP) area integrate sensory evidence during decision making process by carrying persistent response selective to the saccadic response. LIP neurons also discharge at high frequency shortly before the saccade onset. We propose that the later response is due to the activity form the bursting neurons in the Superior Colliculus (SC). To test the hypothesis we developed a decision making model with populations of neurons in LIP, Basal Ganglia (BG) and SC where BG and SC process the threshold detection and action generation. The model successfully describes the LIP activity from the experiment, and is also consistent with the behavioral measurements.

Keywords LIP · basal ganglia · superior colliculus · decision making

Introduction

During perceptual decision making tasks a motor response is generated on the basis of sensory stimuli. Neurophysiological studies suggest that certain cortical areas integrate noisy sensory information over time to provide a more accurate decision, and once the accumulated evidence satisfies certain decision threshold, the integration process terminates and the decision is made by behavioral response [1]. Neural correlates of decision making are typically investigated in a two-alternative motion discrimination task [2, 3]. Subjects are shown a display of randomly moving-dots in which a fraction of dots move coherently to one direction (left or right). The task is to identify the direction of the majority of dots and make a saccadic eye movement towards this direction. The required time of response can be controlled by the experimenter or the subject itself, yielding two versions of the task: fixed-duration (FD) and free-response (FR), respectively, as illustrated in Fig. 82.1.

J. Zhang
Department of Computer Science, University of Bristol, Bristol BS8 1UB, UK
e-mail: Jx.Zhang@bristol.ac.uk

R. Wang et al. (eds.), *Advances in Cognitive Neurodynamics*,

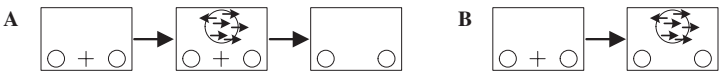

Fig. 82.1 Versions of the motion discrimination task: (a) fixed-duration (FD) and (b) free-response (FR). At the beginning of a trial a monkey is presented with a fixation point (cross) and two targets (circles). In FD the monkey has to fixate during stimulus presentation until the cross disappears, in FR it is free to make a saccade at any time

In single neuron recording data from both FD and FR tasks [2], most neurons in the lateral intraparietal (LIP) area exhibit persistent activity during motion viewing period, whose magnitude correlates with the motion strength. Indeed, LIP neurons accumulate information from sensory area (i.e., extrastriate visual cortex) to form the decision [3]. LIP neuron response also presents a stereotyped increase that is independent of motion strength in the final epoch ($\sim$ 100 ms) before the saccade. In RT task, it is thought to be a reflection of decision threshold crossing by many decision making model proposed so far. However, in FD task, since subjects have to render their decision during pre-fixed delay and keep it in the working memory, the final phase of LIP activity cannot be explained by threshold crossing.

In this work we describe the hypothesis that the increasing activity of LIP in FD task before saccade onset is a reflection of downstream activity from subcortical areas, i.e., basal ganglia (BG) and superior colliculus (SC). We design a population model involving cortical areas, BG and SC based on the existing knowledge of their connectivity. The model is consistent with both behavior and physiological data.

Proposed Decision Making Model

Our model describes three proceeding stages: accumulation of decision evidence from sensory input, threshold detection, and motor response generation. Each stage is mainly controlled by one cortical/subcortical area (Fig. 82.2a). In the first stage, two populations of LIP neurons implement a leaky-competing-accumulator network [4]. I.e., each population integrates input supporting one of the two alternatives, and competes with each other by lateral inhibition. Since the sensory information is biased to the correct alternative, the decision is determined by the winning LIP population which has higher mean firing rate.

The second stage is a mechanism that can detect whether the amount of evidence in LIP in favor of one alternative reaches a threshold and is ready to render a decision. The model applies a common concept that BG is involved in threshold detection [5]. Substantia nigra pars reticulate (SNr), the output nucleus of BG, sends high tonic inhibition to downstream areas to suppress any action response. When the striatum (STR) receives sufficient large excitatory input (e.g., from LIP), it inhibits SNr, and hence SNr decreases its inhibitory output to release downstream activity. In the model, a working memory (MEM) is proposed to effectively receive input from both LIP and SNr (possibly via the thalamus). When LIP activity reaches the threshold, the inhibitory input from SNr is removed and MEM caches the temporal

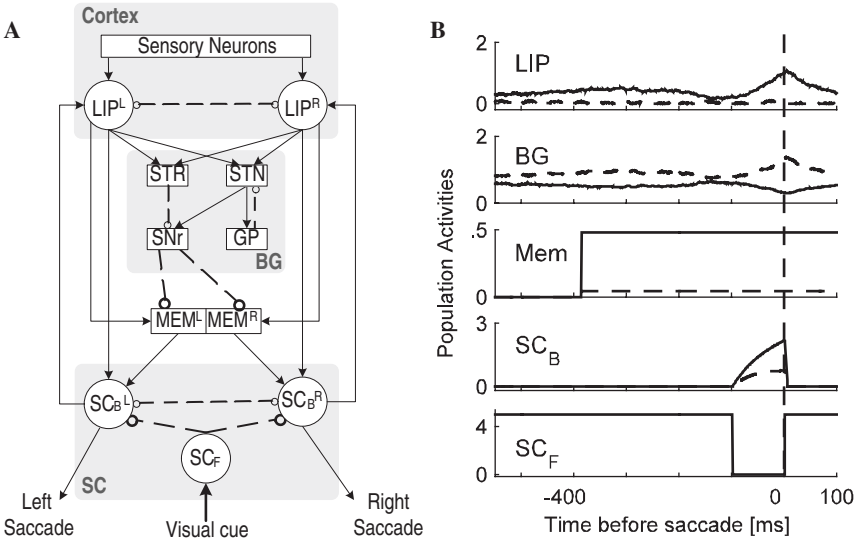

Fig. 82.2 Proposed model and its responses. (a) Schematic architecture. LIP populations send excitatory projections to BG, MEM, and SC_B. The bypass circuit in BG between subthalamic (STN) and globus pallidus (GP) nucleuses are required to implement asymptotically optimal threshold detection mechanism [8]. When decision threshold is reached in BG, SNr opens the gates of MEM by disinhibition to cache the preferred choice from LIP. LIP and SC_B units are modeled as leaky integrators with bounds at baseline zero to avoid negative firing rate. The superscripts on the units indicate the population's selectivity to left (L) or right (R) stimulus. Solid and dash lines represent excitatory and inhibitory connections, respectively. Strong outputs are shown in thicker lines (i.e., outputs from SNr and SC_F). (b) Responses of populations on a sample simulated FD trial, aligned to initiation of the saccade (denoted by the vertical dashed line). Motion viewing time is 1000 ms. Solid and dashed curves respectively denote the activity of population selective to R and L stimulus when the correct choice is R

LIP activity (i.e., the decision result) to guide later response. As we proposed before such working memory is critical in FD task. However the neural mechanism of working memory for saccade movement is still an open question. Some studies suggest it would be implemented in the BG [5] or prefrontal cortex [6].

In the final stage, the decision results stored in the working memory are passed down to motor center (SC) to generate saccade command. SC includes two types of neurons: the fixation (SC_F) and burst neurons (SC_B). SC_F generates tonic inhibition during visual fixation and suppress most saccades, as a "No-Go" signal [7]. SC_B is normally silent but have high firing rates ($\sim$ 200 Hz) just before saccade onset, as a "Go" signal [7]. In FD task the subject was trained to gaze on the fixation point while it is present during stimulus viewing (Fig. 82.1a) hence we assume SC_F is active and inhibits saccades during this period. When the fixation point disappears, the inhibition of SC_F is removed allowing the saccade. In FR task, during stimulus viewing, there is no fixation point (Fig. 82.1b) and hence no inhibition from SC_F, allowing a saccade as soon as the threshold in BG is exceeded.

Simulation Results and Conclusion

Stimulations are performed to illustrate the dynamics of the model's response in FD task. On a sample trial (Fig. 82.2b), threshold crossing happens $\sim$ 380 ms before saccade onset in BG. Then the MEM starts to maintain the preferred choice from LIP by increasing MEM^R. Due to the high inhibition from SC_F, SC_B are inactive until 100 ms before saccade, when the disappearance of fixation point induces a sharp drop in SC_F activity. The burst response in SC_B before saccade also increases LIP activity via excitatory connections. This effect is more obvious in average LIP activity across trials (Fig. 82.3a). During motion viewing period LIP activity depends on the motion strength, followed by a stereotyped increase in the final 100 ms before saccade onset. The model predictions are consistent with experiment data [2, 3]. Moreover, the model is naturally consistent with behavioral measurements [2, 3] (Fig. 82.3b) as it extends the model [4] previously shown to capture these data. The model can be also simulated in FR task [9] by neglecting the effect of fixation point.

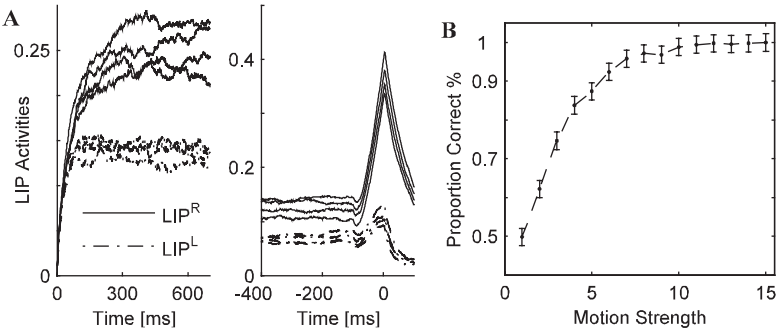

Fig. 82.3 (a) Time course of LIP activity under different motion strengths. On the left panel LIP responses are aligned to the motion onset. On the right panel responses are aligned to the saccade time. Each line is averaged over 200 trials. (b) The accuracy from 500 trials against different motion strengths with error bars showing standard error. The logarithmic increasing of accuracy is consistent with the experiment observations [2, 3]

References

1. Smith, P.L., Ratcliff, R.: Psychology and neurobiology of simple decisions. Trends Neurosci., 27(3):161–168 (2004).
2. Roitman, J.D., Shadlen, M.N.: Response of neurons in the lateral intraparietal area during a combined visual discrimination reaction time task. J. Neurosci., 22(21):9475–9489 (2002).
3. Shadlen, M.N., Newsome, W.T.: Neural basis of a perceptual decision in the parietal cortex (area lip) of the rhesus monkey. J. Neurophysiol., 86:1916–1936 (2001).
4. Usher, M., McClelland, J.L.: On the time course of perceptual choice: the leaky competing accumulator model. Psychol. Rev., 108:550–592 (2001).
5. Hikosaka, O., Takikawa, Y., Kawagoe, R.: Role of the basal ganglia in the control of purposive saccadic eye movements. Physiol. Rev., 80(3):953–978 (2000).

6. O'Reilly, R.C., Frank, M.J.: Making working memory work: a computational model of learning in the frontal cortex and basal ganglia. Neural Comput., 18:283–328 (2006).
7. Munoz, D.P., Wurtz, R.H.: Saccade-related activity in monkey superior colliculus. I. Characteristics of burst and buildup cells. J. Neurophysiol., 73(6):2313–2333 (1995).
8. Bogacz, R., Gurney, K.: The basal ganglia and cortex implement optimal decision making between alternative actions. Neural Comput., 19:442–477 (2007).
9. Lo, C.C., Wang, X.J.: Cortico-basal ganglia circuit mechanism for a decision threshold in reaction time tasks. Nat. Neurosci. (9):956–963 (2006).

Chapter 83
A Synergetic Model for Operant Behaviors Under the Control of Fixed Interval Reinforcement Schedules

Shih-Che Lin and Jay-Shake Li

Abstract This study presents a nonlinear dynamical model for operant responses under the FI reinforcement schedule based on the synergetic concept. The model simulates different types of behavioral dynamics seen in the extended return map (ERM) patterns, as well as the "scalloped-curve" using data averaged over a whole session. We compared our results with the performance of a very popular model for operant behaviors, Machado's LeT model. It was found that although both models can successfully reproduce the scalloped-curve built from the averaged data, only the synergetic model is capable of simulating the real time dynamics of FI-responses revealed in the ERM-patterns.

Keywords Operant · FI schedule · synergetic · extended return map · LeT

Introduction

In an operant conditioning paradigm an organism's behavior is reinforced, if it is contiguously followed by an appetitive stimulus, the so-called reinforcer, which increases the organism's motivation to get more by repeating that behavior. The behavior which is reinforced is called operant behavior. After successful training the organism's behavior becomes an intended action elicited by a specific context, and the appearance of a reinforcer is usually a consequence of the action.

One of the most important variables that influence operant behaviors is the schedule by which the reinforcers are made available. In natural environments, it is uncommon that same actions lead exactly to the same outcomes. Thus, applying an intermittent reinforcement schedule is more realistic than using a continuous reinforcement (CRF) in the experimental design. For example, in a fixed-interval (FI) reinforcement schedule only the first response occurring after a pre-defined, fixed time interval will be rewarded. After intensive training, organisms exhibit a temporal

S.-C. Lin
Departmet of Psychology, National Chung Cheng University, 168 University Road, 621 Ming-Hsiung, Chia-Yi, Taiwan
e-mail: psyjsl@ccu.edu.tw

R. Wang et al. (eds.), *Advances in Cognitive Neurodynamics*,

control of responding. The response rate increases as a function of time elapsed since the delivery of the previous reinforcer. This type of responding dynamics can be seen in a cumulative record as a concave-upward curve, which is called the "scalloped-curve". There were several attempts to model this responding curve, for example, the SET model by Gibbon [1], the BeT model by Killen and Fetterman [2], and the LeT model by Machado [3]. They all successfully reproduced the scalloped curve described above. However, the responding curve these models described was constructed by data averaged across multiple trials in one session. None of them touched the issue of real time dynamics of the FI-responding.

Ever since the pioneering works of Skinner, variations of operant responding have been found not only between individual organisms, but within subject between sessions and trials as well [4, 5]. It has been suggested that a nonlinear, more complicated dynamical system might be responsible for the behavioral patterns under the FI-schedule. A graphical method "extended return map (ERM)" has been developed to analyze the real time dynamics of operant behaviors [6]. Furthermore, it was found that it is possible to construct a model that can successfully simulate the scalloped curve, yet shows a completely different dynamics of behaviors as revealed by the ERM-patterns. Previous works also suggested that the behavioral dynamics of FI responses can be regarded as switching between operant and alternative behavioral states [7].

Synergetic Model for the FI-Response

In the present study, we built a model for operant responses under the FI reinforcement schedule based on the synergetic concept. The formulation of the model is similar to the synergetic model for the verbal transformation effect developed previously [8, 9]. While in the verbal transform model the order parameters ξ_k incorporated the strength of perceptual states, they described in our FI-response model the strength of behavioral states. The operant behavior is denoted as ξ_o, and the alternative behavior as ξ_a. The total energy V of the system consists of two parts: the V_i coming from the original synergetic model of perception, and a new potential term V_r implementing the effect of reinforcers. Here we assumed that the delivery of a reinforcer weakened the operant behavior while enhancing the alternative behaviors. Its impact declined exponentially with time. Formally, the original potential V_i, and the new term V_r are defined by:

$$V_i = -\frac{1}{2}\sum_{k'=1}^{M}\lambda_{k'}\xi_{k'}^2 + \frac{B}{4}\sum_{k\neq k'}^{M}\xi_k^2\xi_{k'}^2\left[1 - 4\alpha_{kk'}\frac{\xi_k^2 - \xi_{k'}^2}{\xi_k^2 + \xi_{k'}^2}\right] + \frac{C}{4}\left(\sum_{k'=1}^{M}\xi_{k'}^2\right)^2 \quad (83.1)$$

and

$$V_r = \frac{1}{3}R\left(\xi_o^3 - \sum_{k'=1,k'\neq o}^{M}\xi_{k'}^3\right)e^{-T/\tau} \quad (83.2)$$

The impact of reinforcement declines exponentially with a speed determined by a time constant τ. T denotes the time elapsed since the delivery of the previous reinforcer. For the time evolution of the strength of behavioral states, the equations of motion were defined by:

$$\dot{\xi}_k = -\frac{\partial V}{\partial k}, \quad k = 1 \cdots M \tag{83.3}$$

That leads to the dynamics of ξ_o and ξ_a determined by:

$$\dot{\xi}_o = \xi_o \left[\lambda_o - B\xi_a^2 \left(1 - \alpha \left(1 - \frac{2\xi_a^4}{(\xi_a^2 + \xi_o^2)^2} \right) \right) - C\left(\xi_o^2 + \xi_a^2\right) - \xi_o \, \mathrm{Re}^{-T/\tau} \right] \tag{83.4}$$

and

$$\dot{\xi}_a = \xi_a \left[\lambda_a - B\xi_o^2 \left(1 + \alpha \left(1 - \frac{2\xi_a^4}{(\xi_a^2 + \xi_o^2)^2} \right) \right) - C\left(\xi_o^2 + \xi_a^2\right) + \xi_a \, \mathrm{Re}^{-T/\tau} \right] \tag{83.5}$$

The goal of the modeling study is to correctly simulate the "scalloped-curve" using data averaged over a whole session, and to reproduce different types of behavioral dynamics seen in the ERM-patterns. Furthermore, we implemented the LeT model developed by Machado [3], and compared the simulation results with the synergetic model. It was found that although both models can successfully reproduce the scalloped curve built from averaged data (Fig. 83.1), only the synergetic model is capable of simulating the real time dynamics of FI-responses revealed in the ERM-patterns (Fig. 83.2).

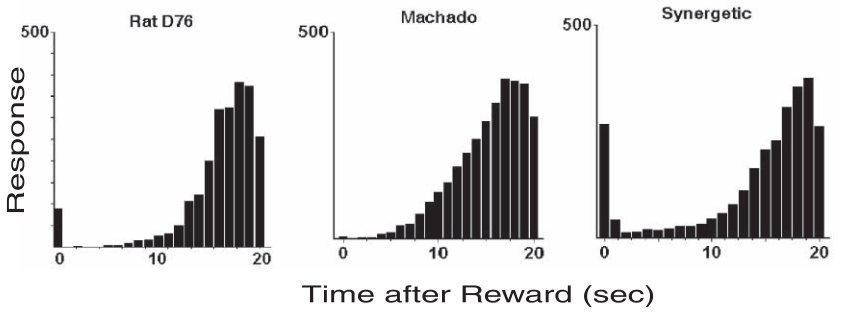

Fig. 83.1 Average response rate in a fixed-interval (FI) 20 s schedule. Left: average lever-press rate of a real rat. Central: prediction of the LeT model. Right: prediction of the synergetic model

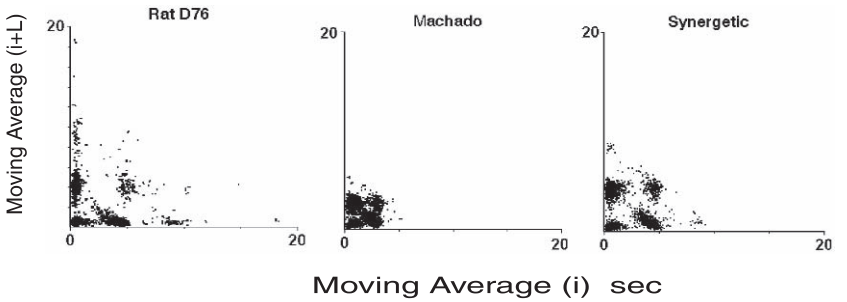

Fig. 83.2 The ERM-patterns. Left: a real rat data. Central: prediction of the LeT model. Right: prediction of the synergetic model model

References

1. Gibbon, J.: Scalar Expectancy Theory and Weber's Law in Animal Timing. Psychological Review 84 (1977) 279–325.
2. Killeen, P., Fetterman, G.: A Behavioral Theory of Timing. Psychological Review 95 (1988) 274–295.
3. Machado, A.: Learning the Temporal Dynamics of Behavior. Psychological Review 104 (1997) 241–265.
4. Hoyert, M.S.: Order and Chaos in Fixed? Interval Schedules of Reinforcement. Journal of the Experimental Analysis of Behavior 57 (1992) 336–339.
5. Palya, W.L.: Dynamics in the fine structure of schedule? Controlled Behavior. Journal of the Experimental Analysis of Behavior 57 (1992) 267–287.
6. Li, J.-S., Huston, J.P.: Nonlinear Dynamics of Operant Behavior: A New Approach via the Extended Return Map. Reviews in the Neurosciences 13 (2002) 31–57.
7. Li, J.-S., Huston, J.P., Krauth, J.: Operant Behavior of Rats Under Fixed-Interval Reinforcement Schedules: A Dynamical Analysis Via the Extended Return Map. Nonlinear Dynamics, Psychology, and Life Sciences 10 (2006) 215–240.
8. Ditzinger, T., Haken, H. A synergetic model of multistability in perception. In: P. Kruse and M. Stadler (eds.), Ambiguity in Mind and Nature: Multistable Cognitive Phenomena, Springer Verlag, Berlin, 1995, pp. 255–274.
9. Ditzinger, T., Tuller, B., Haken, H., Kelso, J.A.S.: A synergetic model for the verbal transformation effect. Biological Cybernetics 77 (1997) 31–40.

Chapter 84
Adaptable Intermittency and Autonomous Transitions in Epilepsy and Cognition

Elan Liss Ohayon, Hon C. Kwan, W. McIntyre Burnham, Piotr Suffczynski, Fernando H. Lopes da Silva and Stiliyan Kalitzin

Abstract In this paper we investigate the mechanisms underlying transitions in epilepsy and cognition by exploring intermittency in simple recurrent neural network models. We demonstrate that neural activity can change dynamical phases without requiring plasticity or reliance on external cues. However, we also demonstrate that the characteristic of the resultant phases can undergo modification with localized parametric alteration. By modifying a single connection in the network we can change the trajectory of the dynamics and thus illustrate that intermittency mechanisms are compatible with more traditional models of ictal transitions that depend on alteration in structural parameters. Finally, we argue that intermittency-based neural transitions coupled with weight adaptation mechanisms can apply beyond epilepsy and might form a foundation for autonomous neurodynamics in biological systems. As such, the implications of these intermittent models may be extended to sleep, emotion, attention and other transitions in cognition seen in autonomous embodied agents.

Keywords Attention · autonomous neurodynamics · computer model · epilepsy · intermittency · neural network · plasticity · seizure

Introduction

How does the brain transition between epilepsy and non-epileptic dynamics? Are these transitions dependent on the external environment? Do these transitions depend on changes to network structure or to constituent unit properties? What about transitions in attention and other cognitive states? Rapid transitions in activity are a fundamental feature of neurodynamics. Epilepsy is a striking example for which the mechanisms of transitions remain largely unknown. Theories regarding transitions in and out of seizures have most often focused on two possible mechanisms: (1) parametric alteration and (2) multi-stable systems. In the first case, the brain

E.L. Ohayon
University of Toronto Epilepsy Research Program, Toronto, Canada
e-mail: ohayon@chass.utoronto.ca

R. Wang et al. (eds.), *Advances in Cognitive Neurodynamics*,

properties are assumed to change such that a new seizure state – or attractor – is either formed or made more prominent. The parametric change can (a) lead to a bifurcation that directly brings about a seizure or (b) modify the system such that a stimulus that in the past may not have had any discernable effect will now fall within the enlarged basin of attraction and trigger a seizure. Kindling might be an example of such a process. According to the second, related, hypothesis (2) a transition is envisioned as a jump between two or more pre-existing attractors. In this multi-stability scenario, the attractor for a seizure already exists and the ictal phenomenon is brought about when the brain is pushed into the seizure state as the result of either an external or internal perturbation. The perturbation may be a sensory stimulus as in the case of certain reflex epilepsies or it may be random noise in which case the onset of the seizure becomes unpredictable. These scenarios are related in that they posit attractors that correspond to the seizure state. For a review of these attractor-based theories see: [1, 2, 3]. More recently, our group has suggested an alternate possibility in which intermittent transitions are an inherent feature of a network's dynamics [4, 5]. In such networks the activity autonomously switches between two (or more) phases without perturbation from either the environment or another brain structure. We have demonstrated that such dynamics can be sustained in a network even if the structure is static. The implications of such models are that transitions to seizure – and indeed, transitions between any cognitive conditions – may take place even in the absence of environmental input, stochastic fluctuations (noise) or plasticity. Here we expand on this model by showing that although autonomous transitions do not require external input or network alterations, intermittent systems are also compatible with structural change mechanisms. Specifically, we demonstrate that intermittent activity can be modified in a continuous fashion by local synaptic change and illustrate how these structural changes may alter the distribution and trajectory of the intermittent neural activity.

Methods

To explore these intermittent dynamics we used computational models of recurrent networks with random connections and initial conditions. The networks were fully connected including both inhibitory and excitatory weights as well as self-feedback ($w_0..w_j$). The total input (E_i) for a unit (i) was the weighted sum of the activations of the input units (S_j) such that:

$$E_i = \sum_j w_{ij} S_j \tag{84.1}$$

Units had radial basis activation functions (RBF):

$$S(E_i) = e^{(-E_i)^2} \tag{84.2}$$

Simulations included networks of up to 100 units with 10,000 connections and various plasticity algorithms. However, to illustrate that mechanisms require neither complex structural nor plasticity assumptions, we present results for static networks with only 5 units and 25 connections. Network dynamics were categorized using variants of close return and Lyapunov exponent algorithms. For details regarding the analytic approach see [4].

Results

Intermittency in Recurrent Networks

We began by generating random networks and then excluded networks that exhibited simple fix-point and limit-cycle oscillations. Some networks exhibited multistability activity patterns depending on the initial conditions. For a discussion of the distribution of dynamical categories in random networks see [6]. For the purposes of this study we selected networks that exhibited intermittent activity. Figure 84.1a–c illustrates intermittent behaviour in which the activity autonomously switched from laminar to turbulent epochs. Although weight changes were not required for obtaining ictal transitions in any of these simulations, we found that changes in connectivity *could* influence the properties of the intermittent activity in a generally continuous manner. Graphs 1(a), (b) and (c) show a progressive decrease in the duration of laminar periods corresponding to increasing the strength of a single recurrent connection.

The properties of the activity were also modifiable by external input but the intermittency could persist under a wide range of perturbations including ongoing

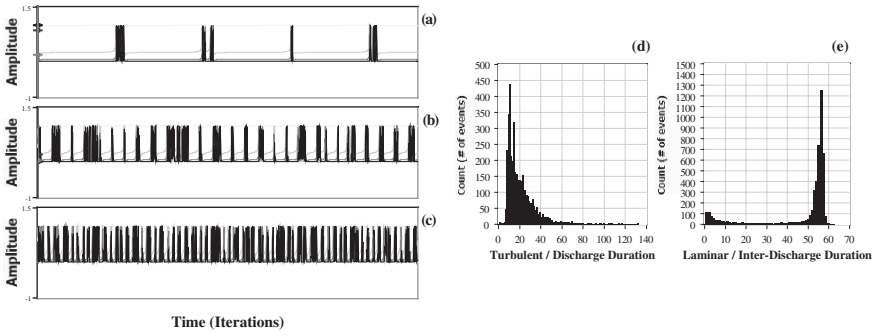

Fig. 84.1 *A*ctivity Traces and Statistics of Intermittent Networks: (a), (b), (c) are the activity traces for three networks exhibiting intermittent activity. Each graph shows the superimposed activity traces of 5 units over 2000 iterations. These graphs illustrate the large change in laminar duration as a result of the modification of a single weight. Histogram (d) is the distribution of the turbulent epochs for the middle network (b). Histogram (e) is the distribution of the laminar durations for the same network

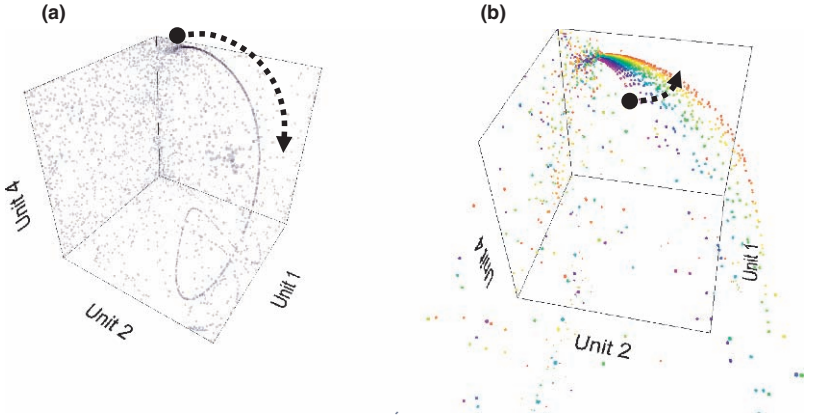

Fig. 84.2 Intermittent neural network activities and alteration of the laminar trajectory with weight change: (a) Illustrates the states of three units over 10,000 iterations in 3-dimensional activity space (or phase space) [4]. (b) Changes in the trajectory of the intermittent activity as a single connection in the network is incremented in steps of 0.1. The output associated with each weight change is represented by a unique color. The arrow highlights the manner in which the laminar trajectory rotates in space as the weight is changed

noise injection and varied initial conditions (not shown). Figure 84.1d illustrates the distribution of the turbulent epochs and 1(e) is the distribution of the laminar durations for the middle trace (b). These event duration histograms show a statistical profile characteristic of Type I intermittency. The turbulent epoch distribution (d) had a sparsely populated long tail. The laminar events distribution (e) had two peaks, a minor one at the short durations and a peak at long intervals marking the maximal length of a laminar phase.

Activity Space and Trajectory Modification with Weight Changes

In order to better illustrate the nature of the changes to the dynamics we plotted the activity in phase space (Fig. 84.2). The cloud of points in Fig. 84.2a corresponds to the turbulent activity and the arrow indicates the trajectory of the laminar activity. Figure 84.2b illustrates changes to the laminar activity trajectory in phase space as a result of changes to connectivity.

Discussion

The network model illustrates that dynamical transitions do not require: (i) a triggering input (including noisy processes) (ii) changes in the intrinsic cell properties nor (iii) ongoing changes to the network structure (plasticity). The model thus raises the possibility that intermittent dynamics need not be a consequence of changes

to synaptic connectivity nor external perturbation but rather could be a recurring event entirely due to intrinsic network properties. The fact that the properties of these transitions are modifiable through synaptic changes demonstrates that these intermittency mechanisms are compatible with a parametric change scenario.

Implications to Epilepsy

The model forwards a novel way to understand autonomous seizure transitions. Once network connectivity is set to exhibit intermittency, ictal events can occur intermittently without further changes or extrinsic triggering. There is no requirement for synaptic or gap junction modification nor changes in individual neuronal properties. However, these intermittency-based autonomous transitions do not preclude the involvement of other mechanisms such as parameter-based bifurcations [1, 2] or multi-stability [3]. Indeed, here we show that parametric weight modulation can directly alter the duration and distribution of turbulent and laminar phases. That is, even small changes in the weights of a network might directly affect the response characteristics of the system. These findings suggest that the appearance of a seizure can be independent of network changes but subtle changes in connectivity could alter seizure duration, interictal duration, and other seizure-related signal features. The model may thus help us understand the factors governing the genesis and abolition of seizure susceptibly. The statistical signatures may suggest new ways of identifying such mechanisms in clinical studies, diagnosis and therapy of epilepsy. For example, we note that if epileptic seizures are induced by random parameter fluctuations or noise-driven transitions between states in multi-stable systems, the transitions may be unpredictable. However, if the transitions are intermittency-based, our model offers the possibility of early warning for the turbulent phase. Using a variant of Lyapunov exponent analysis, we have shown that the spectrum changes when entering the "point of no return" to a turbulent phase [4]. As such, the method indicates that the onset or duration of certain intermittent seizures may be predictable depending on whether the turbulent phase corresponds to the ictal or interictal period.

Implications to Cognition

Although it might be simplest to conceive of the laminar epoch as a quiescent interictal state and the turbulent epoch as representing a seizure, it is the turbulent activity that may correspond best to healthy forms of complex neurodynamics. The distinction between the epochs and the relation of dynamic categories to cognitive states ultimately requires consideration of functional embodied behaviour [6]. Nonetheless, the fact that a simple random network without more complex connectivity assumptions such as small world connectivity can exhibit intermittency illustrates that this is a viable mechanism to implement rapid transition in neurodynamics. The

simulations highlight the possibility that certain transitions in cognition may be best characterized as a continuous trajectory in a system with heterogeneous dynamics rather than alternations between distinct attractors (or states). Although these networks can respond to external stimuli, the ability to implement transition independently of the environment suggests that intermittency could play an important role in autonomous cognitive transitions including changes to attention, alertness and emotions. The model helps show that such transitions do not require plasticity. However, the present study also demonstrates that structural changes, including single synapse and unit modification, can affect intermittency dynamics. The fact that the change is local opens the possibility for biologically plausible learning algorithms. Moreover, the autonomous nature of the transitions coupled with the potential for adaptivity make this a candidate mechanism in embodied biological systems that depend on quick transitions, autonomy and the ability to learn.

References

1. Lopes da Silva F.H., Blanes W., Kalitzin S.N., Parra J., Suffczynski P., Velis D.N.: Dynamical Diseases of Brain Systems: Different Routes to Epileptic Seizures. IEEE Transactions on Biomedical Engineering 50 (2003) 540–548.
2. Lopes da Silva F.H., Blanes W., Kalitzin S.N., Parra J., Suffczynski P., Velis D.N.: Epilepsies as Dynamical Diseases of Brain Systems: Basic Models of the Transition Between Normal and Epileptic Activity. Epilepsia 44:s12 (2003) 72–83.
3. Suffczynski P., Kalitzin S., Lopes da Silva F.H.: Dynamics of Non-Convulsive Epileptic Phenomena Modeled by a Bistable Neuronal Network. Neuroscience 126 (2004) 467–484.
4. Ohayon, E.L., Kwan, H.C., Burnham, W.M., Suffczynski, P., Kalitzin, S.: Emergent Complex Patterns in Autonomous Distributed Systems: Mechanisms for Attention Recovery and Relation to Models of Clinical Epilepsy. Proceedings of IEEE SMC (2004), 2066–2072.
5. Ohayon E.L., Kwan H.C., Burnham W.M., Suffczynski P., Kalitzin S.: Introduction and Abolition of Autonomous Seizure Transitions in Random Networks Through Weight Changes. Epilepsia 46 (2005) 206.
6. Ohayon E.L., Kalitzin S., Suffczynski P., Jin F.Y., Tsang P.W., Borrett D.S., Burnham W.M., Kwan H.C.: Charting Epilepsy by Searching for Intelligence in Network Space with the Help of Evolving Autonomous Agents. Journal of Physiology-Paris 98 (2004) 507–529.

Chapter 85
A Computational Approach to the Control of Voluntary Saccadic Eye Movements

Jeremy Fix

Abstract We present a computational model of how several brain areas involved in the control of voluntary saccadic eye movements might cooperate. This model is based on anatomical and physiological considerations and lays the emphasis on the temporal evolution of the activities in each of these areas, and their potential functional role in the control of saccades.

Introduction

Primates use two kinds of voluntary eye movements to bring objects of interest onto the fovea : saccades and pursuits. In this article, we focus exclusively on saccadic eye movements that involve several areas widespread in the cortex; a subcortical pathway also exists and is involved in reflexive saccades. A visual stimulation exciting the retina produces a signal that travels (not necessarily sequentially) to the visual cortex, the lateral intraparietal sulcus (LIP), the frontal eye fields (FEF), the supplementary eye fields (SEF), the dorsolateral prefrontal cortex (dlPFC) to finally excite the superior colliculus (SC) that will provide downstream subcortical areas with the parameters of a saccadic eye movement to trigger [1, 2]. We first review biological studies on the functional role of these areas and introduce a computational model based on these data to illustrate how these areas might cooperate.

In the last few years, several studies have led to a better understanding of the representation of visual information in LIP. Both experimental measurements and computational models have shed the light on an eye-centered representation [3]. The neurons in LIP are also strongly modulated by the position of the eye, head and body parts. Andersen and Cohen [3] have shown, for example, that the activity of the neurons in this area depends on the eccentricity of the eye, while always exhibiting

J. Fix
Loria, Campus Scientifique, BP239, 54506 Vandoeuvre-les-Nancy, France
e-mail: Jeremy.Fix@Loria.fr

R. Wang et al. (eds.), *Advances in Cognitive Neurodynamics*,

a maximal response at a given retinal position. Computational modelings [4] have provided strong results that indicate that the representation of the information in a common eye-centered representation, modulated by the position of the eye, head and body parts, can be decoded in several frames of reference, namely eye-, head- and body-centered.

The neurons in FEF receive strong topographically organized projections from the posterior parietal cortex. Bruce and Goldberg [5] distinguish three types of neurons in FEF. *Visual neurons* (FEFv) respond to visual stimuli but not to the initiation of a saccade. On the opposite, *movement related neurons* (FEFm) fire before and during saccades, whether or not the saccade is triggered by a visual stimulus. *Visuomovement neurons* (FEFvm) have both visual and movement-related activity. Among these three types of cells, only the ones related to movement project to the superior colliculus and to the caudate nucleus [1]. The first projection carries the target of the saccade while the second determines when the movement is executed.

An enhanced activity in the supplementary eye field (SEF) is recorded when the selection of a target (among several possible stimuli) for a saccadic eye movement is based on internal factors such as motivation or reward expectation [6, 7]. The SEF has been thought to represent the targets of saccadic eye movements in a craniocentric frame of reference [8]. More recently, [9] have shown that the encoding in SEF is much more complex than a simple craniocentric representation and that there coexists a continuum of eye-, head- and space/body-centered representations for gaze coding. Finally, [10] have provided evidences for the role of the dorsolateral prefrontal cortex in spatial working memory.

While more and more is known about the different structures involved in the control of saccadic eye movements, the way these areas cooperate to select the relevant stimuli, to decide which of them is the next target to focus on, to memorize these targets when the task at hand requires it is still unclear. We propose in the next section a neural network architecture relying on the previously introduced anatomical considerations and illustrate its functioning with a classical double-step task.

Architecture of the Model

The model we propose, depicted in Fig. 85.1, is based on the Continuum Neural Field Theory [11, 12], a framework of dynamical lateral interactions within a neural map. It consists in several two dimensional sets of units, each of them characterised by an activity which depends on the activity of lateral units in the same map or afferent units in other maps. We generally use a *mexican-hat* weight function and compute the integration of the inputs for a given unit with a classical weighted sum. In some specific cases, we also use a weighted sum of the product of inputs' activity, as we have shown in [13] that these sigma-pi integrations provide an efficient way to remap a visual information across saccadic eye movements and is used in the presented model to compute transformations of frame of reference.

The labels of the maps indicate what could be the binding between the biological areas and the computational maps, under the strong restriction that not all the properties of the biological areas are covered by the model.

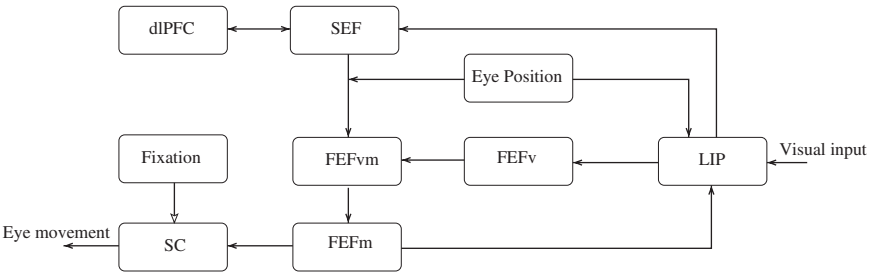

Fig. 85.1 A possible architecture of how the major brain areas involved in the control of voluntary saccadic eye movements might cooperate. (Refer to the text for details)

A visual stimulation excites LIP. As described in section 'Introduction', the neurons in LIP have retinotopic receptive fields and are modulated by the position of the eyes. From this representation, it is possible to extract eye- and head-centered representations of the visual information. LIP projects onto FEFV with topographically organised connections; the neurons in FEFV are then sensitive to visual stimulations. LIP also projects to SEF. As shown in the introduction, SEF is a continuum of several frames of references. We consider here that SEF represents the visual stimuli in a head-centered frame of reference, this represention depending on internal factors such as reward expectation. If we consider a double-step task, all the presented stimuli must be memorised since the task requires to perform an eye movement toward each of them. If we consider an antisaccade task, SEF migth represent the location of the antisaccade target. In the case a stimulus must be memorised, DLPFC is shown to be active during the delay, and we consider it here as a component of a short term memory built with the SEF-DLPFC recurrent circuit. SEF and FEFV project onto FEFVM. While the FEFV and FEFVM maps both represent the stimuli in an eye-centered frame of reference, the projection from SEF to FEFVM, from a head-centered to an eye-centered representation, are modulated by the current position of the eye, using the same sigma-pi mechanism that we used in [13]. The FEFVM map represents all the potential targets for an impeding eye movement. These targets can be a direct consequence of a visual stimulation (FEFV) or a target computed from internal factors (SEF). The map FEFVM then projects onto FEFM in which only one saccadic target emerges. The competition is performed with lateral connections with a mexican-hat shape, which leads to similar results than a winner-take-all but in a dynamic and distributed way. The feedback projection from FEFM onto LIP is supposed to represent visual attention. It is shown in several studies that the target of an impeding eye movement is enhanced in areas such as LIP. Studies have shown that fixation units in FEF and SEF fire vigorously when the eyes must keep still. Moreover, the inhibitory pathway from FEF to SC going through the caudate nucleus and the substantia nigra reticulata is supposed to signal when a saccade must be executed. We model this pathway with inhibitory projections from the FIXATION map to SC. The units in the FIXATION map are active when the eyes must keep still and silent when the movement must be triggered. The decision to trigger the saccade can originate from exogenous (a fixation cue is switched off) or endogenous factors (the location of the target of the saccade is computed internally).

Discussion

The presented architecture was successfully applied to a classical double-step task.[1] The aim of the model was not to reproduce all the physiological properties reported on the areas involved in the control of voluntary saccadic eye movements. Rather, we wanted to test a possible way in which these areas might cooperate emphasizing the functional role and the dynamic behavior of each of them. One of the limitations of this model is that the selection of the target of the saccade emerges from lateral competition in the FEFM map, giving the opportunity to all the potential stimuli to be selected while one may desire to avoid selecting a previously focused one. A bias toward non previously focused stimuli may be achieved by adjoining a working memory to the FEF maps as illustrated in [13].

References

1. Goldberg, M.: The control of gaze. In: Kandel, E.R., Schwartz, J.H., Jessell, T.M., Principles of Neural Science. The McGraw-Hill Companies, Chapter 39, (2000) 782–800.
2. Krauzlis, R.: The control of voluntary eye movements: new perspectives. The Neuroscientist **11** (2005) 124–137.
3. Cohen, Y., Andersen, R.: Multimodal spatial representations in the primate parietal lobe. In: Spence, C., Driver, J., Crossmodal Space and Crossmodal Attention. Chapter 5, Oxford University Press Inc., USA (2004) 99–122.
4. Pouget, A., Deneve, S., Duhamel, J.: A computational perspective on the neural basis of multisensory spatial representations. Nature Reviews Neuroscience **3** (2002) 741–747.
5. Bruce, C., Goldberg, M.: Primate frontal eye fields: I. single neurons discharging before saccades. Journal of Neurophysiology **53** (1985) 603–635.
6. Coe, B., Tomihara, K., Matsuzawa, M., Hikosaka, O.: Visual and anticipatory bias in three cortical eye fields of the monkey during an adaptive decision-making task. The Journal of Neuroscience **22** (2002) 5081–5090.
7. Amador, N., Schlag-Rey, M., Schlag, J.: Reward-predicting and reward-detecting neuronal activity in the primate supplementary eye field. Journal of Neurophysiology **84** (2000) 2166–2170.
8. Schlag, J., Schlag-Rey, M.: Evidence for a supplementary eye field. Journal of Neurophysiology **57** (1987) 179–200.
9. Martinez-Trujillo, J., Medendorp, W., Wang, H., Crawford, J.: Frames of reference for eye-head gaze commands in primate supplementary eye fields. Neuron **44** (2004) 1057–1066.
10. Funahashi, S., Bruce, C., Goldman-Rakic, P.: Dorsolateral prefrontal lesions and oculomotor delayed-response performance: evidence for mnemonic scotomas. The Journal of Neuroscience **13** (1993) 1479–1497.
11. Amari, S.: Dynamical study of formation of cortical maps. Biological Cybernetics **27** (1977) 77–87.
12. Taylor, J.: Neural bubble dynamics in two dimensions. Biological Cybernetics **80** (1999) 5167–5174.
13. Fix, J., Vitay, J., Rougier, N.: A distributed computational model of spatial memory anticipation during a visual search task. In: Butz, M.V., Sigand, O., Pezzulo, G., Baldassarre, G. (eds.): ABiALS. Springer Verlag, LNAI 4520 (2006) 170–188.

[1] A video showing the temporal evolution of the model is available at http://www.loria.fr/~fix/demo.php?demo=iccn

Chapter 86
Spatial Considerations of Feedback Control for the Suppression of Epileptic Seizures

Beth A. Lopour and Andrew J. Szeri

Abstract Control of epileptic seizures through brain electrical stimulation is currently the focus of experimental and theoretical research. Here we use a mean-field model of the human cortex to study spatial issues related to two types of feedback control. We start with a 14th order set of stochastic partial differential equations from Kramer et al. (Journal of Computational Neuroscience 22:63–80, 2007), add either proportional or differential control, and then simulate the effect on seizure-like behavior. We analyze the results based on changes in electrode size, electrode spacing, and the number of electrodes in the grid.

Background and Model

There are millions of people in the US that are affected by epileptic seizures, and roughly one in five do not respond to medication [1]. For those that do not respond to anti-epileptic drugs, the available treatments are invasive and dangerous. It may even be necessary to surgically resect the seizing portion of the cortex. During pre-surgical evaluations, doctors found that applying pulses of electrical stimulation to the cortex can suppress epileptiform afterdischarges, which are often precursors to full-blown seizures [2]. In addition, it has been found that sinusoidal voltages can be applied to various brain structures and nerves to reduce the severity of epileptic seizures [3, 4]. Going one step further, some researchers have experimented with the application of electric fields via feedback control [5]. Currently, the mechanism by which brain electrical stimulation works is unknown, and no *optimal* techniques have been developed. However, research in this area may eventually lead to implanted devices that can automatically stop seizures when they occur, or perhaps even prevent them.

Because experiments in electrical stimulation can be dangerous for humans, mathematical models are useful for exploring these ideas. Here, we utilize a

A.J. Szeri
Department of Mechanical Engineering, University of California, Berkeley, California 94720, USA
e-mail: aszeri@me.berkeley.edu

R. Wang et al. (eds.), *Advances in Cognitive Neurodynamics*,

mesoscale stochastic PDE model of the cortex that was first developed in the 1970's [6] and has since undergone revisions and improvements [7]. It has not only been used to study epilepsy [8, 9], but also anesthesia [10] and sleep [11]. The 14th order model consists of dimensionless partial differential equations in space (x) and time (t). The equations contain four stochastic terms, which represent subcortical inputs and are approximated by Gaussian-distributed white noise (scaled in space and time), in addition to several nonlinear terms. We will incorporate two different feedback controllers and analyze their utility for stopping epileptic seizures.

While the model contains a large number of states and parameters, there are only three that are central to the results described here: (1) $\mathbf{h_e}$ – a variable that represents the mean soma voltage of the neurons in the model and is assumed to be proportional to the voltage that can be measured via EEG. Because it is related to an observable quantity, h_e is the variable that will be used for feedback control. (2) $\boldsymbol{\Gamma_e}$ – a parameter that represents the influence of excitatory input on the averaged soma voltage. (3) $\mathbf{P_{ee}}$ – a parameter that represents the subcortical input to the excitatory neurons in the cortex. For a full statement of the model, the reader is directed to [9].

Simulations and Results

At typical values of the parameters described above, $\Gamma_e = 1.42 \times 10^{-3}$ and $P_{ee} = 11.0$, the simulated cortical voltage resembles the fluctuations of a typical EEG signal. The variation in voltage is roughly 8 mV centered around -52 mV. However, if we change the values of Γ_e and P_{ee} we observe remarkably different behavior. In a "hyper-excited" state, with $\Gamma_e = 0.8 \times 10^{-3}$ and $P_{ee} = 550.0$, we see repeated large-amplitude oscillations in the model that are reminiscent of a seizure. The variation in voltage increases to roughly 50 mV centered around -60 mV. Because we believe h_e to be related to the electric fields measured and induced by electrodes on the cortex, this variable is a prime candidate for feedback control. The goal is to use feedback to stop seizures that are in progress and move the cortex back to its normal operating range.

In order to implement this type of control, we need to measure the electric field on the cortex through a set of electrodes, use those values to calculate the control, and then apply the control voltages to the brain via a different set of electrodes. There are several assumptions we make in order to simulate this process. First, we assume that h_e is directly proportional to the EEG measurement, so we may use h_e to calculate the control [12]. Next, we ignore the spread of the electric field beyond the electrode edges. Lastly, we assume that the output of the electrode adds directly to the electric field of the neuron itself; in the model, this means that we can simply add the control law to $\partial h_e/\partial t$. With these in mind, we model *proportional control* by adding an $a(x,t)\bar{h}_e$ term to the first equation of the model:

$$\frac{\partial \tilde{h}_e}{\partial \tilde{t}} = 1 - \tilde{h}_e + \cdots + a(x,t)\bar{h}_e. \tag{86.1}$$

Here, $a(x,t)$ represents the gain, which can vary across the cortex, and $\bar{h}_e$ is a local spatial average of $\tilde{h}_e$. The number of points in the average is equal to the size of the simulated electrode. Also, by setting the gain to zero in strategic locations, we can delineate individual electrodes. These parameters allow analysis of the effects of changing the electrode size, electrode spacing, and number of electrodes.

Alternatively, we could add the term $a(x,t)(\bar{h}_e[t]-\bar{h}_e[t-\tau])$ to model *differential control*. As before, $a(x,t)$ represents the discrete controller gain, but we have now incorporated a delay time τ. This method of control has been shown to stop seizure-like behavior in the model [8], with the added benefit of using voltages that are less likely to damage brain tissue.

Because the simulation parameters present a seemingly infinite number of possible combinations, we have focused on three key issues:

1. **Number of electrodes**: This defines the number of electrodes placed side-by-side on the cortex, similar to electrode grids used in experiments; the gain $a(x,t)$ is set to zero for all spatial steps outside the grid.
2. **Electrode size**: To represent electrodes covering multiple spatial points, we determine the average of h_e over the points and use it to calculate one control voltage. We then apply that voltage to all of the points covered by the electrode.
3. **Spacing between electrodes**: To simulate locations unaffected by the applied electric field, the gain $a(x,t)$ is set to zero for all points determined to be between electrodes.

In this analysis, we do not address the issue of sensing and controlling at different cortical locations, and we have assumed that the electric fields applied by each electrode are constant in space. For simplicity, we neglect extracellular electrochemical changes in the immediate vicinity of the electrodes.

We simulated feedback control of the stochastic PDE's using a predictor-corrector algorithm written in Matlab. The stochastic terms were incorporated using the Euler–Maruyama method, which ensures that the quality of the noise remains the same regardless of the integration step sizes. While more sophisticated solvers would provide better convergence and stability properties, this method was chosen due to the complexity of the system.

The following parameters were used in all simulations: the gain $a(x,t) = 0$ for $0 \leq t \leq 0.5$; for $t > 0.5$ within the electrode grid, $a(x,t) = -2$ for proportional control, and $a(x,t) = -10$ with a delay of $\tau = 20$ ms for differential control; the integration was performed over 10,000 time steps with a step size of 0.1 ms; 50 spatial steps were used with a step size of 7 mm; $\Gamma_e = 0.8 \times 10^{-3}$; P_{ee} was normally distributed in space with a maximum of 550; the magnitude of the stochastic terms was $\alpha = 16$. These parameter choices were based on those in [8].

Proportional Control Results

A typical simulation of proportional control is shown in Figure 86.1a shows the resulting cortical voltage h_e when control is applied to four 35 mm electrodes with

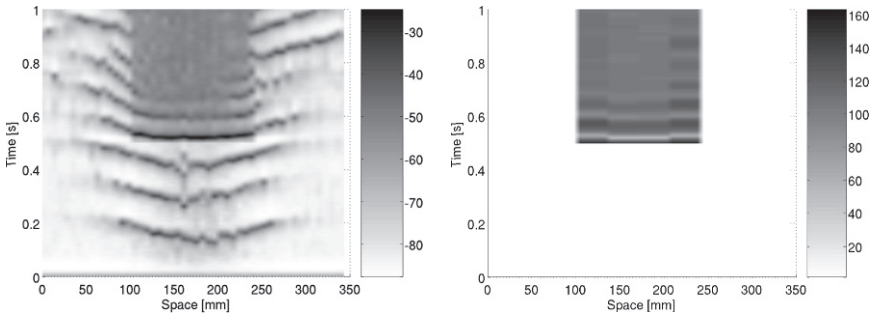

Fig. 86.1 Simulation of proportional control. (a) h_e output for four 35 mm electrodes with 0 mm spacing. The strong wavelike solutions emanating from the center of hyper-excitation for $t < 0.5$ are those associated with a seizure. (b) Control effort for the same parameters as in (a)

0 mm spacing. Figure 86.1b depicts the voltage applied to the cortex by the controller. In the locations where electrodes have been applied, the proportional control succeeds in stopping the seizure-like oscillations; note that when the controller is turned on at $t = 0.5$, h_e quickly moves to a steady voltage of roughly -50 mV. This result can be obtained with electrodes of *any* size. However, there are several aspects of this control that are not optimal. While the controller works well wherever electrodes are applied, new large-amplitude waves appear to emanate from the controlled area. This seems to occur regardless of the number of electrodes in the grid. Also, the required control effort consists of a large positive voltage, which could potentially damage cortical tissue.

Simulations with non-zero spacing mimic the results presented here. Proportional control is effective at stopping seizure-like oscillations at the electrodes, but does not necessarily prevent waves from occurring in the gaps. Hence, the electrode size is not as critical as the length of spacing between them.

Differential Control Results

Figure 86.2 shows a simulation of differential control. As with proportional control, Fig. 86.2a shows the resulting h_e voltage while Fig. 86.2b displays the calculated control effort. The simulation was done with six 14 mm electrodes at a spacing of 0 mm. In the ideal case, with an electrode size of 7 mm (one nondimensional step) and 0 mm spacing, the controller completely halts the large-amplitude oscillations and brings the cortical voltage to roughly -70 mV. However, with larger electrodes, we see that small sections of high voltage persist even after the controller is turned on. This effect is enhanced as electrode size and spacing are increased – more and more segments of the wavefront remain until the controller is not capable of stopping the seizure-like oscillations. Also, note that the equilibrium value of -70 mV does not match the typical mean soma potential associated with $\Gamma_e = 1.42 \times 10^{-3}$ and $P_{ee} = 11.0$. On the other hand, differential control does offer several advantages

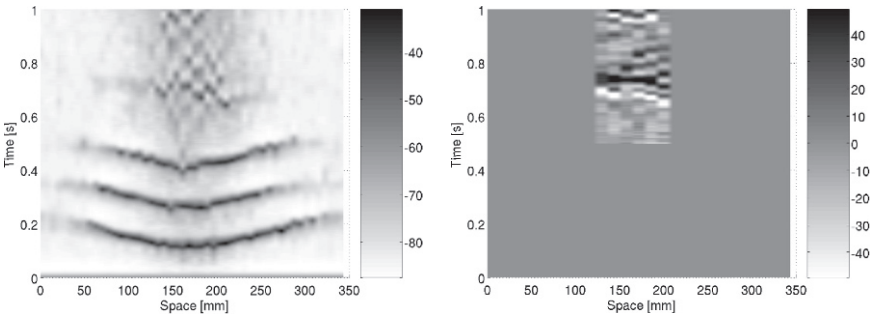

Fig. 86.2 Simulation of differential control. (a) h_e output for six 14 mm electrodes with 0 mm spacing. (b) Control effort for the same parameters

over proportional control. First, despite the fact that the grid is smaller than the extent of the traveling waves, the controller is able to stop the seizure-like oscillations. No new waves develop at the edge of the electrode grid. Second, the control effort used in this case is lower amplitude and oscillates between positive and negative values. This type of signal is much safer for cortical tissue, as discussed in [8] and the references therein.

Discussion

Overall, both proportional and differential control have advantages and disadvantages. Proportional control is effective regardless of electrode size, and it also returns h_e to its typical value of roughly -50 mV. However, the large positive voltages it uses could potentially be damaging to cortical tissue, and it sometimes causes new oscillations to arise. Alternatively, differential control uses safer voltages and requires smaller grid sizes, but its effectiveness quickly deteriorates with increasing electrode size and spacing. It also has an equilibrium value of approximately -70 mV, which does not match the typical cortical state.

Some of these results may be connected to neuro-physiological properties. For example, the degree of correlation between spatial points on the cortex is related to P_{ee}; this relationship may give insight into the size of electrode needed to stop a seizure. Future work will investigate such ideas.

Acknowledgments This material is based upon work supported under a National Science Foundation Graduate Research Fellowship. We also personally thank Alexandre Bayen for helpful discussions.

References

1. The Epilepsy Foundation: Epilepsy: An Introduction. World Wide Web, http://www.epilepsyfoundation.org (2005).

2. Motamedi, G.K., Lesser, R.P., Miglioretti, D.L., Mizuno-Matsumoto, Y., Gordon, B., Webber, W.R.S., Jackson, D.C., Sepkuty, J.P., Crone, N.E.: Optimizing parameters for terminating cortical afterdischarges with pulse stimulation. Epilepsia **43** (2002) 836–846.
3. Durand, D.M., Bikson, M.: Suppression and control of epileptiform activity by electrical stimulation: a review. Proceedings of the IEEE **89** (2001) 1065–1082.
4. Bikson, M., Inoue, M., Akiyama, H., Deans, J.K., Fox, J.E., Miyakawa, H., Jeffreys, J.G.R.: Effects of uniform extracellular dc electric fields on excitability in rat hippocampal slices in vitro. Journal of Physiology **577** (2004) 175–190.
5. Gluckman, B.J., Nguyen, H., Weinstein, S.L., Schiff, S.J.: Adaptive electric field control of epileptic seizures. Journal of Neuroscience **21** (2001) 590–600.
6. Wilson, H., Cowan, J.: Excitatory and inhibitory interactions in localized populations of model neurons. Biophysical Journal **12** (1972) 1–24.
7. Steyn-Ross, M.L., Steyn-Ross, D.A., Sleigh, J.W., Whiting, D.R.: Theoretical predictions for spatial covariance of the electroencephalographic signal during the anesthetic-induced phase transition: increased correlation length and emergence of spatial self-organization. Physical Review E **68** (2003) 021902.
8. Kramer, M.A., Lopour, B.A., Kirsch, H.E., Szeri, A.J.: Bifurcation control of a seizing human cortex. Physical Review E **73** (2006) 041928.
9. Kramer, M.A., Szeri, A.J., Sleigh, J.W., Kirsch, H.E.: Mechanisms of seizure propagation in a cortical model. Journal of Computational Neuroscience **22** (2007) 63–80.
10. Wilson, M.T., Sleigh, J.W., Steyn-Ross, A., Steyn-Ross, M.L.: General anesthetic-induced seizures can be explained by a mean-field model of cortical dynamics. Anesthesia **104** (2006) 588–593.
11. Wilson, M., Steyn-Ross, D., Sleigh, J., Steyn-Ross, M., Wilcocks, L., Gillies, I.: The k-complex and slow oscillation in terms of a mean-field cortical model. Journal of Computational Neuroscience **21** (2006) 243–257.
12. Liley, D.T.J., Cadusch, P.J., Dafilis, M.P.: A spatially continuous mean field theory of electrocortical activity. Network: Computation in Neural Systems **13** (2002) 67–113.

Chapter 87
EEG Scaling Difference Between Eyes-Closed and Eyes-Open Conditions by Detrended Fluctuation Analysis

Tingting Gao, Dan Wu and Dezhong Yao

Abstract The electroencephalogram (EEG) data from two rest conditions of eyes-closed and eyes-open were analyzed using a nonlinear method named detrended fluctuation analysis (DFA). The results showed that the EEG fluctuations exhibited scaling behavior in two regions with two scaling exponents (β1 and β2). These two scaling exponents were significantly different between the two conditions, and according to anyone of the two scaling exponents we could distinguish the two rest conditions easily. The results also provide evidence that the differences between eyes-closed and eyes-open rest conditions are not only in the alpha frequency bands, but also in the lower and higher frequencies bands.

Keywords Detrended fluctuation analysis (DFA) · electroencephalogram (EEG) · nonlinear, scaling behavior

Introduction

The electroencephalogram (EEG) provides plentiful information about human brain dynamics and is a popular method to investigate human brains. The most common methods of EEG analyses such as event-related potential and Fourier decomposition are based implicitly on assumptions of linearity. But the scalp EEG arises from a large number of neurons whose interactions are generally nonlinear [1], so it could not be best described by linear analyses, and nonlinear analyses are needed. However, the classical nonlinear method such as correlation dimension and Kolmogorov entropy are very sensitive to noise and require the stationary condition, but EEG signals often show highly non-stationary [2]. It was also indicated that the scalp EEG can not be represented by entirely low-dimensional chaos [3]. Recently, a nonlinear method named detrended fluctuation analysis (DFA) was introduced to analyzing the scaling behavior of EEG [2, 4]. DFA is known for its robustness

D. Yao
Center of NeuroInformatics, School of Life Science and Technology, University of Electronic Science and Technology of China, Chengdu 610054, China
e-mail: dyao@uestc.edu.cn

R. Wang et al. (eds.), *Advances in Cognitive Neurodynamics*,

against non-stationarity [2] and by using this method the assumptions of linearity and low-dimensional chaos can be avoided.

In this paper, we used a direct DFA method [4] to discuss the EEG scaling difference between eyes-closed and eyes-open rest conditions. It is well known that the alpha (α) wave is strong in eyes-closed condition, and it may disappear in eyes-open condition. In this work, we found significant differences in the frequency bands besides the α band in these two rest conditions by using the nonlinear DFA method.

Paper Preparation

Materials

The EEG data from 14 healthy, right-handed student subjects (8 males, 6 females, mean ± S.D. age, 21.83 ± 2.04) in eyes-closed and eyes-open rest conditions were recorded for about 2 min respectively, using the 128-channel EGI System 200 with a sampling frequency of 500 Hz (0.1∼48 Hz band-pass filter). The reference electrode was located at the top of the head (Cz) and lengths of 10 s continuous artifact-free EEG from four scalp locations of F3, F4, PO3 and PO4 were extracted from the raw data of each subject in each condition for the DFA process.

Detrended Fluctuation Analysis (DFA)

We used the direct DFA method which was introduced in Hwa's work [4]. To be brief, let an EEG time series be denoted by $y(t)$ with a length of N. First, the entire time series are divided into equal time windows of size k, discarding any remainder; Then, the least-square fitted line denoted by $y_k(t)$ is computed for each window and the EEG time series $y(t)$ is detrended by subtracting the local trend $y_k(t)$ from the original data in each window; Finally, the average root-mean-square fluctuation of this detrended time series $F(k)$ is computed as:

$$F(k) = \sqrt{\frac{1}{N}\sum_{t=1}^{N}\left[y(t) - y_k(t)\right]^2} \tag{87.1}$$

The study of the dependence of $F(k)$ on the window size k, which ranges from 10 to 1000 in this work, is the essence of DFA. If it is a power-law behavior of $F(k) \propto k^{\beta}$, then the scaling exponent β is an indicator of the nonlinear complexity of the EEG dynamics [1, 2, 4]. According to Hwa's work, there may have two scaling regions and two exponents (denoted by β1 and β2 in this study) for the human EEG. These two scaling exponents were analyzed next.

Statistical Analysis

Multivariate ANOVA with β1 and β2 as dependent variables, conditions and positions as factors were performed on the obtained scaling exponents, followed by Post-Hoc tests. All statistical analyses were performed using the statistical software package SPSS PC (version 13.0) at a significant level of $p < 0.05$.

Results

A typical log-log plot of $F(k)$ as a function of k in this study was showed in Fig. 87.1a. Consistent with Hwa's work, there were obviously two scaling regions in the $\ln F - \ln k$ plot. To quantify the two scaling exponents, we performed a linear fit in region I for $2.9 < \ln k < 3.7$ with a slope denoted by β1, and in region II for $4.5 < \ln k < 6.0$ with a slope denoted by β2. The average position of the bend between these two regions was located approximately at $\ln k \approx 4.0$. Since the time scale k is associated with the period of a sine wave with frequency f by $f = r/k$ [4], where the data sampling rate is $r = 500$ points/s in this work, it means that the bend in $F(k)$ at $\ln k \approx 4.0$ is associated with the traditional dominant frequency of α band (8–13 Hz). Thus, we can conclude that region I corresponds to fluctuations over short time scales (> 13 Hz) and region II corresponds to fluctuations over long time scales (< 8 Hz).

Tests of between-subjects effects showed that there were significant main effects of conditions and positions for both β1 and β2 (all at $p < 0.001$), while the interaction effects were not significant. Post-Hoc tests of conditions showed significant differences between the eyes-closed condition and the eyes-open condition for both β1 and β2 (all at $p < 0.001$). Post-Hoc tests of positions showed significant differences between F3 and PO3, F3 and PO4, F4 and PO3, F4 and PO4 (all at $p < 0.005$), while the differences between F3 and F4 or PO3 and PO4 were not significant. The

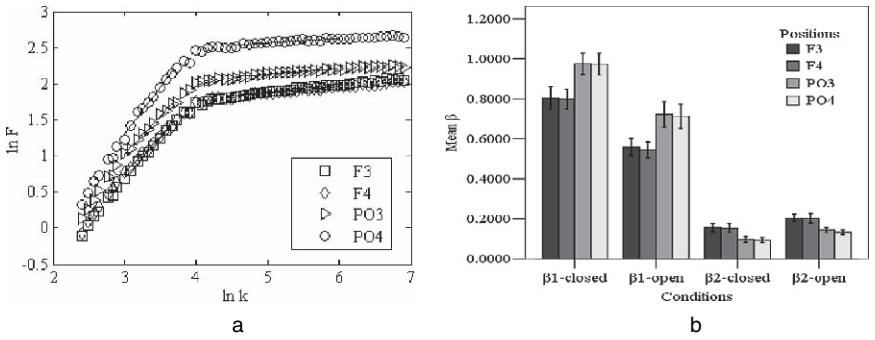

Fig. 87.1 Log-log plot of $F(k)$ versus k for a subject during eyes-closed rest condition (a) and mean β1 and β2 for the eyes-closed and eyes-open rest conditions ($n = 14$) with error bars represented the standard error of the mean (b)

results of mean β1 and β2 for the two conditions and the four positions were showed in Fig. 87.1b. The statistical results clearly showed that according to anyone of the two scaling exponents we could distinguish states of eyes-closed rest and eyes-open rest easily.

Discussion

As the statistical results shows, there exists a common scaling behavior in EEG with two different scaling exponents of two scaling regions respectively. According to anyone of the two scaling exponents we could distinguish states of eyes-closed rest and eyes-open rest easily. Especially, when discussing the difference between eyes-closed and eyes-open conditions, most previous researches focused on the EEG α band [5]. But what about the other EEG frequency bands besides α wave? In this work, significant differences are also found in the high frequency bands above α and the low frequency bands below α though the nonlinear DFA processing. This may suggest a new promising way to investigate the internal mechanism of the resting EEG.

Conclusion

In this work, the human EEG during two rest conditions of eyes closed and eyes open were investigated by using the nonlinear method of direct DFA. The results show that according to anyone of the two scaling exponents (β1 and β2) we can distinguish states of eyes-closed rest and eyes-open rest easily. Our results also indicate that there exist significant differences between the eyes-closed and eyes-open rest conditions in the frequency bands besides generally discussing α band.

Acknowledgments This work was supported by the 973 project 2003CB716106 and NSFC No.60571019.

References

1. Linkenkaer-Hansen, K., Nikouline, V.V., Palva, J.M., Ilmoniemi, R.J.: Long-Range Temporal Correlations and Scaling Behavior in Human Brain Oscillations. J. Neurosci. 21 (2001) 1370–1377.
2. Lee, J.M., Kim, D.J., Kim, I.Y., Park, K.S., Kim. S.I.: Detrended Fluctuation Analysis of EEG in Sleep Apnea Using MIT/BIH Polysomnography Data. Comput. Biol. Med. 32 (2002) 37–47.
3. Pritchard, W.S., Duke, D.W., Krieble, K.K.: Dimensional Analysis of Resting Human EEG II: Surrogate-data Testing Indicates Nonlinearity but not Low-dimensional Chaos. Psychophysiology 32 (1995) 486–491.
4. Hwa, R.C., Ferree, T.C.: Scaling Properties of Fluctuations in the Human Electroencephalogram. Phys. Rev. E 66 (2002) 021901.
5. Yao, D., Wang, L., Nielsen, K.D., Arendt-Nielsen, L.,Chen A.C.N.: Cortical Mapping of EEG Alpha Power Using a Charge Layer Model. Brain Topogr. 17(2) (2004) 65–71.

Chapter 88
Closure Positive Shifts Evoked by Different Prosodic Boundaries in Chinese Sentences

Weijun Li, Lin Wang, Xiaoqing Li and Yufang Yang

Abstract Spoken language is structured into phrases. Electroencephalography (EEG) was used in this study investigating the perception of prosodic hierarchical boundaries. It was found that the closure positive shift (CPS) can be evoked by phonological phrase boundaries and intonational phrase boundaries respectively; the CPSs are different in onset and peak latency. The deflection elicited by prosodic word boundaries is more positive compared with the one elicited by syllable boundaries.

Introduction

Prosodic phrasing is central to spoken language comprehension. In recent years, a growing number of researches have been conducted to address the prosodic phrasing [1], and a novel electrophysiological correlate to major intonational phrase (IPh) boundaries has been found and termed the Closure Positive Shift (CPS). Unlike LAN, N400 and P600, the CPS mainly reflects prosodic phrasing, rather than semantic or syntactic processing. It is a bilateral, centroparietal positive shift [2].

The pioneering neurophysiological study investigating the role of prosody in spoken language comprehension was conducted by Steinhauer et al. (1999) using ERP measures [3]. They used two types of sentences with different prosodic structures. The data of ERPs showed that IPh boundaries in both types of sentences elicited the CPS. Further study suggested that even the pause after IPh boundaries were removed, the CPS was still induced. To explore whether the CPS exclusively relying on the prosodic information, Pannekamp et al. (2005) used four types of stimuli in which the linguistic content was systematically reduced [4]. The results showed that IPh boundaries in these sentences all evoked the CPS. In addition, Steinhauer and Friderici (2001) found that commas in the silent reading also elicited the CPS with smaller amplitude and shorter duration compared with the speech-induced CPS [5].

Y. Yang
State Key Lab of Brain and Cognitive Science, Institute of Psychology, Chinese Academy of Sciences, Beijing 100101, China
e-mail: yangyf@psych.ac.cn

R. Wang et al. (eds.), *Advances in Cognitive Neurodynamics*,

The CPS also has been found in music [6], which has a similar topography and amplitude, but different latency and duration. It seems that whenever the listeners or readers segment the current stimulus into phrases, the CPS will be evoked.

Up to now, the CPS has only been investigated at IPh boundaries. However, as we all know, there are other prosodic units in a sentence except for IPh, such as prosodic words (PW) and phonological phrases (PPh). Some researchers found that the acoustic-phonetic cues to the prosodic boundaries are systematically changed, and listeners can differentiate these different boundaries [7]. It is suspected that the CPS may also be found at other prosodic boundaries. The aims of present study are to investigate: (I) whether the CPS can be elicited by different prosodic boundaries in a sentence; (II) if yes, what are the differences between these CPSs.

Experimental Procedures

Subjects

Twenty students of the Capital Normal University (10 men; mean age 22.0 years) participated in the experiment and were paid for their participation. All of them were native speakers of Chinese with normal hearing and normal or corrected-to-normal vision.

Stimuli and Experimental Protocol

Fifty groups of sentences were produced by a male native speaker of standard Chinese and recorded in a soundproof chamber. In each group there are four sentences with the same target disyllable and the same length. The boundaries between the two target syllables in the four sentences are boundaries of syllables within a word, PW, PPh and IPh boundaries respectively. The position of the target disyllables in sentences is the same in each group but different among groups. The duration of pre-boundary syllable, the duration of pre-boundary and silence, and the lowest pitch value for all target syllables were measured and statistically analyzed. A group of listeners were asked to evaluate the size of boundaries. The results indicated that the materials are proper for the experiment.

The 200 experimental sentences were intermixed with 100 filler sentences and presented auditorily in a pseudo-randomized order in four blocks of 75 trials. Block order was counterbalanced across subjects. The structure of each trial was as follows: a fixation star appeared at the center of a computer monitor 300 ms before the voice of “ding” started, and remained visible until the end of the sentence; after the “ding”, an auditory sentence presented. During the experiment the listeners were asked to answer yes or no to comprehension questions in 20% of the trials. The experimental session lasted about 1 h, including electrode application.

EEG Recording and Analysis

The subjects' brain potentials (EEG) were recorded continuously from 64 cap-mounted Ag/AgCl electrodes with a sampling rate of 250 Hz. The electrooculogram (EOG) was recorded from electrodes placed at the left and right outer canthus of each eye, and above and below the left eye. On line, the system was referenced to the left mastoid, and the system was re-referenced offline to linked mastoid. Impedances were kept below 5 kΩ.

The EEG data were processed with the software NeuroScan 4.3. EEG epochs containing eye blinks were firstly processed with "ocular artifact reduction". Epochs comprised the 200 ms preceding and 1500 ms following the pre-boundary syllable onset. As can be seen in Fig. 88.1, relative to syllable boundaries, PPh and IPh boundaries elicit positive deflections separately, which both start about 260 ms after onset of the critical syllable. We classified the positive deflections as the CPS, since its latency and topography (not reported because of space limits) fit the standard characteristics of the CPS. Based on the literature and the visual inspection of the grand averages, 300–800 ms were selected for analysis of the shifts elicited by PW, PPh and IPh boundaries, the data were analyzed with a three-way repeated-measures ANOVA with mean amplitude as dependent factor, with condition (4 levels: syllable, PW, PPh, IPh), region (frontal vs. central vs. parietal), and hemisphere (left vs. mid-line vs. right) as independent factors. To establish the onsets of the boundary effects, we conducted a series of onset analyses in consecutive mean amplitude latency bins of 10 ms wide (e.g. 100–110 ms, 110–120 ms, etc.) for PW, PPh, IPh compared with syllable boundaries. To further compare peak latency and amplitude of the CPSs

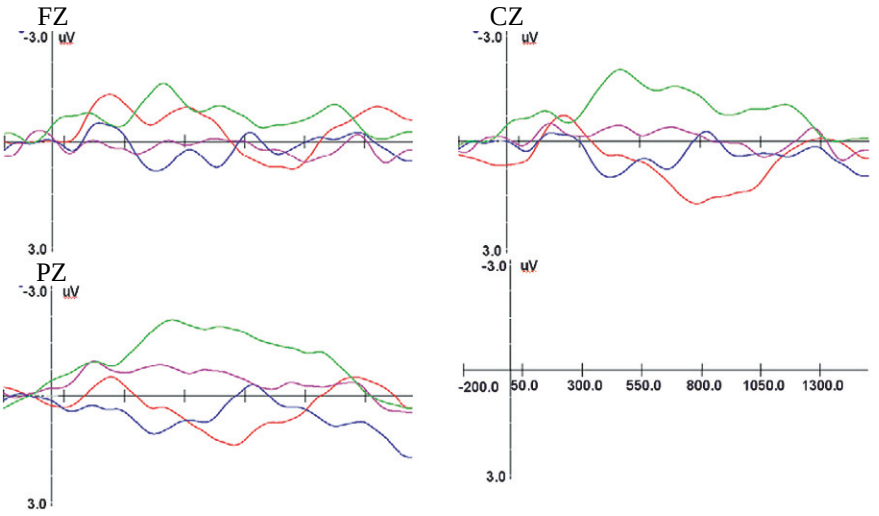

Fig. 88.1 Closure positive shift. Grand-average ERPs at the FZ, CZ, PZ. The waveforms in the conditions of syllable (green), PW (pink), PPh (blue) and IPh (red) are superimposed. The onsets of pre-boundary syllables are aligned to the time axis

elicited by PPh and IPh boundaries, we select the time window from 300 to 1200 ms to get peak (baseline to maximum peak) and latency (onset to maximum peak) value for each condition per subject. The data were analyzed with three-way repeated-measures ANOVA with condition, region, and hemisphere as independent factors.

Results and Discussion

EEG traces are shown in Fig. 88.1. In the time window 300–800 ms, the statistical analysis revealed a main effect of conditions, $F(3, 57) = 14.915,\ p < 0.01$. Further post hoc tests indicated that pair-wise comparisons were significant between syllable ($M = -1.251,\ \mathrm{SD} = 0.229$) and PW boundaries ($M = -0.277,\ \mathrm{SD} = 0.267$), $p < 0.01$; syllable and PPh boundaries ($M = 0.647,\ \mathrm{SD} = 0.277$), $p < 0.01$; syllable and IPh boundaries ($M = 0.074,\ \mathrm{SD} = 0.251$), $p < 0.01$. The analysis of onsets of the boundary effects revealed that it started in 320–330 ms latency bin for PPh boundaries, 370–380 ms for IPh boundaries, but 400–410 ms for PW boundaries for the midline electrodes

For the amplitude, it showed amplitude of the CPS elicited by IPh boundaries ($M = 3.106,\ \mathrm{SD} = 0.227$) is larger than the one elicited by PPh boundaries ($M = 2.932$uv, $\mathrm{SD} = 0.310$), but not reach significant, $F(1, 19) = 0.357,\ p > 0.05$. However, the analysis of peak latency revealed that the CPS elicited by IPh boundaries ($M = 862.959,\ \mathrm{SD} = 29.013$) is significantly different from the one elicited by PPh boundaries ($M = 539.556,\ \mathrm{SD} = 15.611$), $F(1, 19) = 98.277,\ p < 0.01$.

Present experiment shows that the CPS is evoked not only by IPh boundaries but also by PPh boundaries, whereas PW boundaries cannot elicit it. It mainly reflects the processing of prosodic phrases. The amplitudes of the CPSs at different boundaries are similar, but not for onset and peak latency. It seems that the bigger the prosodic boundary is, the later of the CPS onset and the longer of peak latency. ERP data of this experiment indicate that the prosodic boundaries at different levels can induce systematic changes of brain response.

Studies about the CPS in music suggested that it is influenced by the variations of acoustic cues in the vicinity of the phrase boundary such as pause length, length of the last tone preceding the pause [6]. The boundaries markers of PPh and IPh are different in acoustic cues, we suspect this is why the CPS they evoked are different. Future studies are needed to explore this problem.

Acknowledgments Thanks to the Laboratory of Learning and Memory, Capital Normal University for their offering experiment facilities.

References

1. Frazier, L., Carlson, K., Clifton, C.: Prosodic phrasing is central to language comprehension. Trends in Cognitive Science 10 (2006) 244–249.

2. Steinhauer, K.: Electrophysiological correlates of prosody and punctuation. Brain and Language 86 (2003) 142–164.
3. Steinhauer, K., Alter, K., Friederici, A. D.: Brain potentials indicate immediate use of prosodic cues in natural speech processing. Nature Neuroscience 2 (1999) 191–196.
4. Pannekamp, A., Toepel, U., Alter, K., Hahne, A., Friederici, A. D.: Prosody-driven sentence processing: An event-related brain potential study. Journal of Cognitive Neuroscience 17 (2005) 407–421.
5. Steinhauer, K., Friederici, A. D.: Prosodic boundaries, comma rules, and brain responses: The closure positive shift in ERPs as a universal marker for prosodic phrasing in listeners and readers. Journal of Psycholinguistic Research 30 (2001) 267–295.
6. Neuhaus, C., Knösche, T. R., Friederici, A. D.: Effects of musical expertise and boundary markers on phrase perception in music. Journal of Cognitive Neuroscience 18 (2006) 1–22.
7. Yang, YF.: Perception of prosodic structures of sentences. Chinese Journal of Acoustics 23 (1998) 163–169.

Chapter 89
Structure–Function Relationship in Complex Brain Networks by Multilevel Modeling

Changsong Zhou, Lucia Zemanová, Claus C. Hilgetag and J. Kurths

Abstract We try to illuminate the relationship between structural and functional connectivity by studying synchronization dynamics based on realistic anatomical network of cat cortical connectivity. A multilevel model is considered, where each cortical area is modeled by a subnetwork of interacting excitable neurons. We show that the model displays biologically plausible dynamics, and the synchronization patterns reveal a hierarchical cluster organization in the network structure. A group of brain areas involved into multimodal association can be identified by comparing the dynamical clusters to the topological communities of the network.

Introduction

Investigation of brain in the last years has put significant emphasis on large-scale *network connectivity* between brain areas, both structurally and functionally. The analysis of the anatomical connectivity of the mammalian cortex [1] and the functional connectivity of the human brain [2] has shown that large-scale cortical networks display typical features of small-world networks. An important problem in cognitive neuroscience is the understanding of the relationship between anatomical and functional connectivity. We investigate dynamical behavior of a realistic network of corticocortical connections and study the relationship between the dynamical organization and the network connectivity at the level of cortical areas. The dynamics of the cortical network is simulated by a *multilevel model*, where each cortical area is modeled by a subnetwork of interacting excitable neurons. Correlation between the mean activity of the areas is compared to the anatomical network to understand the relationship between them.

C. Zhou
Department of Physics, Hong Kong Baptist University, Kowlong Tong, Hong Kong
e-mail: cszhou70@yahoo.de

R. Wang et al. (eds.), *Advances in Cognitive Neurodynamics*,

Multilevel Model of Cat Cortex

We use the cat corticocortical network as an example for large-scale anatomical connectivity. The cortex of a cat can be parcellated into 53 areas, linked by about 830 fibers of different densities [3] into a weighted complex network as shown in Fig. 89.1a. This cortical network exhibits a hierarchical community organization [4]. There exist a few topological communities that broadly agree with four functional cortical sub-divisions: visual cortex (V, 16 areas), auditory (A, 7 areas), somatomotor (SM, 16 areas) and fronto-limbic (FL, 14 areas).

We consider an ensemble of local neurons to be coupled with a small-world topology to reproduce basic biological features: neurons are mainly connected to their spatial neighbors, but a few long-range projections are also present [5]. Our model also includes other realistic, experimentally observed features: 25% of the neurons are inhibitory and only a small number of neurons (about 5%) in one area receive excitatory synapses from other areas [6]. Individual neurons are described by the FitzHugh–Nagumo excitable model. A weak noise is added to each neuron so that isolated units exhibit sparse, Poisson-like irregular spiking patterns, as in realistic neurons. The model thus represents a rest state of the brain. More details of the model are presented in [7].

Main Results

We present biologically plausible behavior of the model, typical for weak coupling, where the neurons have a low frequency of irregular spiking and irregular mean activities (Fig. 89.1c), similar to those observed experimentally (e.g., EEG data). The correlation matrix R_{IJ} in Fig. 89.1b shows that the dynamics of the multilevel model has a nontrivial organization and an intriguing relationship to the underlying network topology.

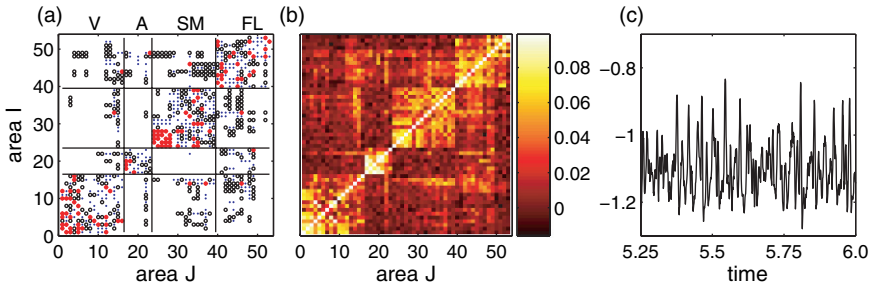

Fig. 89.1 (a) Connection matrix M^A of the cortical network of the cat brain. The different symbols represent different connection weights: 1 (○ sparse), 2 (● intermediate) and 3 (∗ dense). The organization of the system into four topological communities (functional sub-systems, V, A, SM, FL) is indicated by the solid lines. (b) Correlation matrix. (c) Typical mean activity V_I of one area (subnetwork)

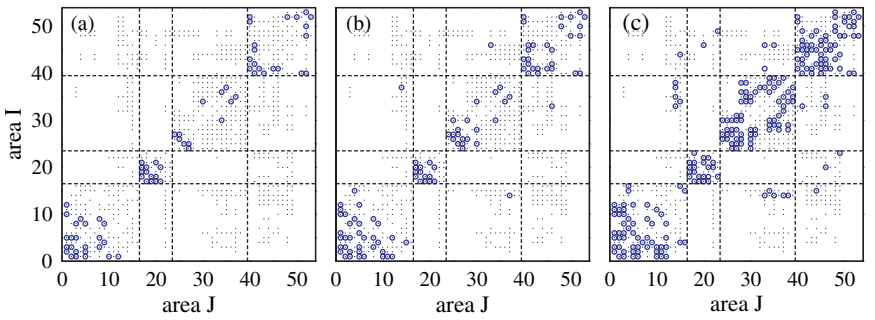

Fig. 89.2 The functional networks M^F (○) at various thresholds R_{th}. A pair of areas is considered to be functionally connected if $R_{ij} \geq R_{th}$. (a) $R_{th} = 0.070$, (b) $R_{th} = 0.065$, (c) $R_{th} = 0.055$. The small dots indicate the anatomical connections

To study the structure-function relationship, we extract *functional networks* M^F from the model by applying a threshold R_{th} to the matrix R_{IJ}. Typical patterns of functional connectivity are shown in Fig. 89.2, showing that the dynamics display hierarchical cluster organization. When R_{th} is close to the maximal value of R, only some areas with reciprocal projections are functionally connected; e.g., at $R_{th} = 0.07$, about 2/3 of areas but only 10% of the reciprocal links are present in M^F (Fig. 89.2a). Interestingly, within each anatomical community V, A, SM, and FL, a core subnetwork is functionally manifested in the form of connected components without intercommunity connections. At lower R_{th}, more areas from the respective communities are included into these components, and a few intercommunity connections appear to join them (Fig. 89.2b). This observation suggests the existence of a core subnetwork within each community that performs specialized functions. At a smaller R_{th}, only about 1/3 of the anatomical reciprocal links and very few unidirectional links can already connect all of the cortical areas into a single functional network (Fig. 89.2c). With such low connection density M^F already resembles the main properties of M^A: high clustering and community structure. The additional anatomical connectivity provides high robustness and many parallel paths of information processing.

We analyzed the most prominent clusters of the dynamics (Fig. 89.3). They follow closely the four anatomical communities – C_1 (V), C_2 (A), C_3 (SM), C_4 (FL).

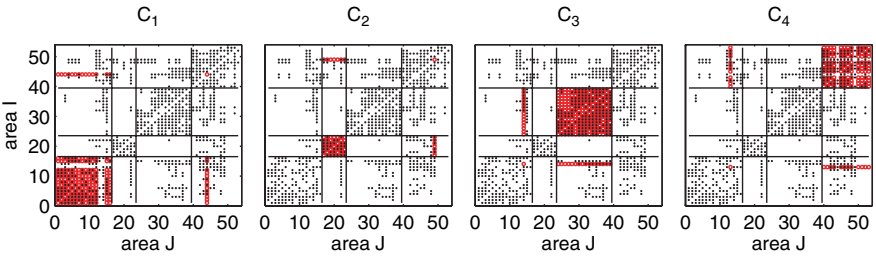

Fig. 89.3 Major dynamical clusters (○), compared to the anatomical connections (·)

Table 89.1 Cortical areas involved in multimodal association, identified in simulations

Index	Area	Location	Functions (response)
14	7	parietal cortex	visual, auditory and somatosensory stimuli, visuo-motor coordination
15	AES	ectosylvian sulcus	multimodal: auditory, visual, somatosensory
22	EPp	ectosylvian gyrus	visual and auditory association area
43, 44	Ia, Ig	insular cortex	multimodal stimuli, homeostatic function
46	CGp	cingulate cortex	processing top-down and bottom-up stimuli, multisensory stimuli
48	36	perirhinal cortex	multimodal sensory stimuli; memory

However, there are a few nodes which belong to one anatomical community but join another dynamical cluster. For example, the area $I = 14$ (anatomically named 'area 7') of the visual system appears in the dynamical cluster C_3 mainly composed of areas from the somato-motor system (Fig. 89.3 (C_3)). Interestingly, this area is associated to both visual and somatosensory. A closer inspection shows that these nodes bridging different anatomical communities and dynamical clusters are exactly the areas sitting in one anatomical community but in close connectional association with the areas in other communities [3], i.e., they are involved into multimodal associations. We can obtain different groups of these areas in different realization of the simulations. A list of some of the areas and the corresponding multimodal functions of them [3] are listed in Table 89.1.

To conclude, with a simplified model of cortical networks, we demonstrated that the cortical dynamics displays nontrivial clustered organization, constrained by the anatomical connectivity. Cortical areas involved in multimodal association can be identified as bridging nodes in the dynamical clusters. Many more details can be found in [7, 8, 9].

References

1. Sporns O, Chialvo DR, Kaiser M and Hilgetag CC: Trends Cogn. Sci. **8** (2004) 418–425.
2. Bassett DS and Bullmore E: Neuroscientist **12** (2006) 512–523.
3. Scannell JW, Burns GAPC, Hilgetag CC, O'Neill MA and Young MP: Cereb. Cortex **9** (1999) 277–299.
4. Hilgetag CC and Kaiser M: Neuroinformatics **2** (2004) 353–360.
5. Buzsaki G, Geisler C, Henze DA and Wang XJ: Trends Neurosci. **27** (2004) 186–193.
6. Young MP: Spatial Vis. **13** (2000) 137–146.
7. Zemanová L, Zhou CS and Kurths J: Physica D **224** (2006) 202–212.
8. Zhou CS, Zemanová L, Zamora G, Hilgetag CC and Kurths J: Phys. Rev. Lett. **97** (2006) 238103.
9. Zhou CS, Zemanová L, Zamora G, Hilgetag CC and Kurths J: New J. Phys. **9** (2007) 178.

Chapter 90
Model of Attention Allocation for Car Driver by Driving Plan and Prediction of Environment Change

Takashi Omori, Yuki Togashi and Koichiro Yamauchi

Abstract In this study, we try to construct a computational model of car driver attention allocation that can explain real world driver behavior. In our previous work, we proposed a model of a driver's eye glances that consists of bottom-up and top-down attention submodels. In this model, top-down eye motion is determined based on the driver's driving plan, which designates desired attention allocation, whereas the bottom-up eye motion is determined based on predicted locations of moving objects.

Keywords Eye motion model · driving plan · map maintenance

Introduction

Car safety systems are improving as intelligent transport systems (ITS) evolve. One way of making driving safer is supporting drivers by reminding them of objects that may be hazards. To achieve this effectively, the system has to recognize the cognitive status and attention allocation of the driver. However, it is not easy to achieve such recognition only by observing the driver's behaviors. To overcome this problem, the system needs to predict the cognitive status and attention allocation using a model of human driver behavior. Several researchers have already proposed models of human driving behavior [1, 2, 6]. These models, however, describe only driver behaviors but not the driver's internal cognitive processes. In this study, we focused on eye motion during driving and constructed a model of the cognitive process behind the eye motion that represents attention allocation.

T. Omori
Tamagawa University Tokyo, Japan
e-mail: omori@lab.tamagawa.ac.jp

R. Wang et al. (eds.), *Advances in Cognitive Neurodynamics*,

Model for Driving with Plan

Driving Plan for Steering and Saliency

We have already constructed an eye motion model that consists of two submodels: the eye motion process for active collection of information for steering operation, and passive eye motion in response to normal visual stimuli (Fig. 90.1) [3].

This model yields a probability distribution function of eye motion at any given time based on its driving environment. This model enabled us not only to estimate what kind of information processing is going on, but also to detect a driver's internal attention and processing by calculating the likelihood of actual eye motion data at a given time.

However, when we observe the eye motion of a driver in an actual driving scene, we noticed a lack of driving plan factor. To improve this, we introduced an effect of intention (driving plan) into the model, and calculated a probability distribution of eye motion based on a driving plan that actually describes attention allocation of the moment.

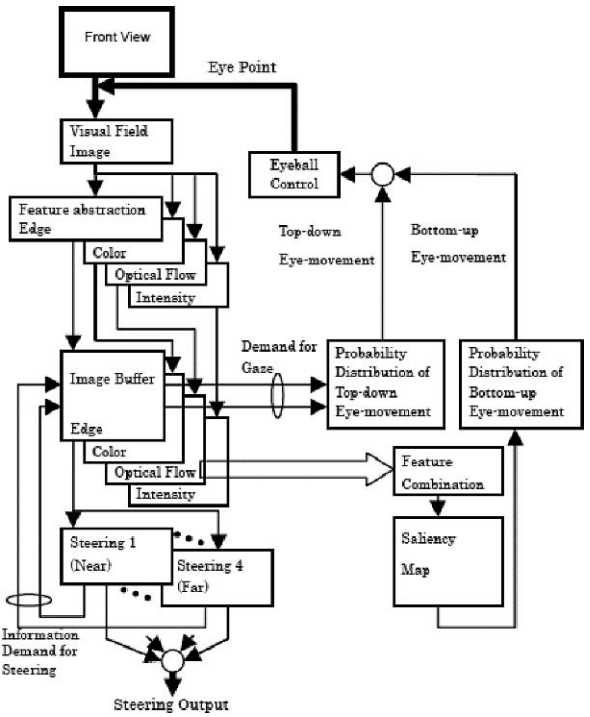

Fig. 90.1 Model of eye motion and steering operation

Driving Plan and Plan Relevance Map

While driving, the system repeats recognition of environmental objects. Plans are associated with the layout of objects and attention allocation to conduct the plan, and a plan can be selected in a competitive base when the layout matches the actual object position. The selection of a driving plan from several plan candidates and eye motion depending on the selected plan are executed repeatedly. The selection of the plan automatically allocates attention of the moment for driving.

The eye motion process was simulated using the model that incorporates the saliency map [5]. During driving, plans compete for their execution by calculating their score values based on an object's attributes and the distance between the car and objects. This information is stored in the recognition results buffer, and, the most appropriate driving plan with the highest score is selected. Each plan consists of conditions for selection, action, and observation to monitor the evolving situation. Driving actions are determined by the selected driving plan, which is described by steering angle, accelerator operation, and observation for a moment of plan selection.

The driving plan can be divided into master plans and subplans. A master plan is a global plan such as "go straight, turn left, turn right" and so on. The subplans denote condition for executing the corresponding master plan. The master plan is selected if all conditions are satisfied. If one of the master plans is selected, the corresponding subplans are activated. Then, the activated sub plans are evaluated by calculating estimation value E, and a subplan with the maximum value is selected for execution.

To achive actions in the selected subplan, a plan relevance map (PRM) is introduced. The PRM denotes the position and width of target objects using normal distributions.

Computer Simulation and Human Behavior

In our experiment, we examined a driver's eye motion, and evaluated the validity of the model by comparing the driver behavior to that of the driving simulator [4]. A set of scenes is presented to human subjects and their eye motion is measured. The same scene is also given to the driving simulator and its eye motion is recorded. Fig. 90.2 shows comparison of the eye motion by human subjects and that by model simulation.

As a result, the distributions of eye motion were comparatively close to real driving one of immediately before beginning to pass a stopped car. However, human bottom-up eye movements to observe the surroundings were less frequent than those predicted by the model. Moreover, the lack of eye motion suggests that people often observe the environment using peripheral vision.

Inclusion of Object Motion Prediction Model

To improve precision of the model, we are planning to introduce a space map maintenance system in the model. The structure of the new model is shown in Fig. 90.3.

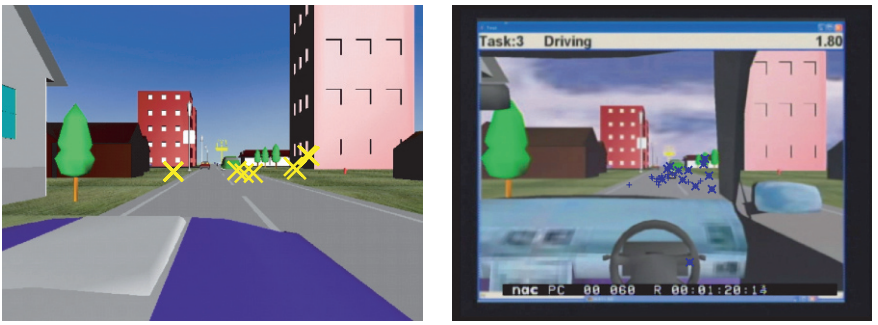

(a) Directions of model's glances (b) Directions of subject's glances

Fig. 90.2 Glance distribution during drive straight plan

The bottom-up eye motion part of the previous model is included in the saliency eye movement calculated in the image processing system (Fig. 90.3a). The top-down eye motion is included in the plan-dependent eye movement calculated in the driving plan system (Fig. 90.3d). A new model corresponds to the eye motion calculated in the object image processing system (Fig. 90.3b) and the space map maintenance system (Fig. 90.3c). The evaluation result with the model will be shown during the talk.

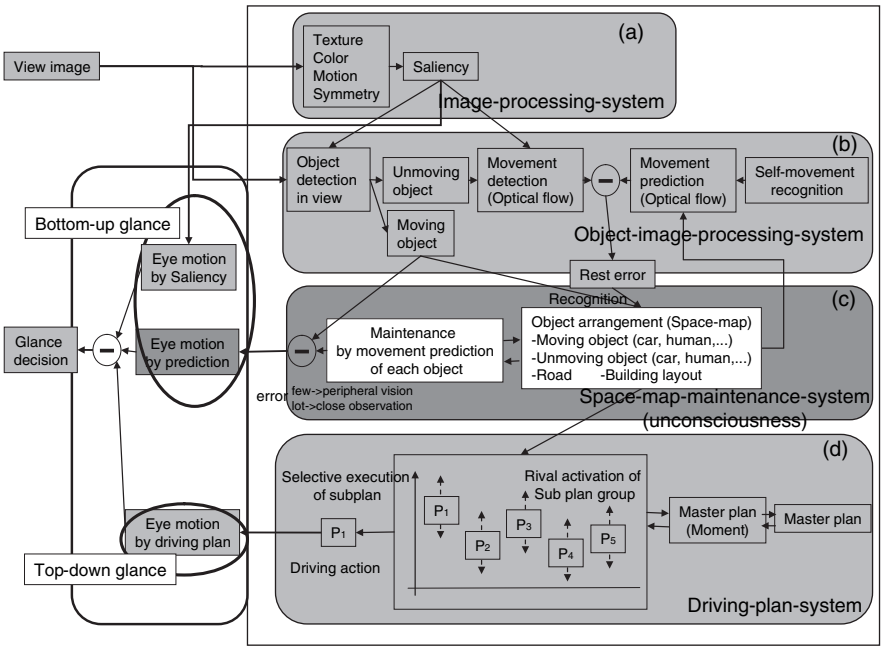

Fig. 90.3 Eye motion decision process with space map maintenance

Conclusion

In this paper, we discussed the necessity to construct a model of human eye movement and attention allocation behind driving actions. In the model, a driver predicts the movement of objects in the environment and directs glances at objects that move differently than expected. The model is expected to predict observational eye movement that is similar to human behavior.

References

1. D.D. Salvucci and T. Siedlecki: Toward a unified framework for tracking cognitive processes. In Proceedings of the 25th Annual Conference of the Cognitive Science Society (2003) 1023–1028.
2. T. AI-Shihabi and R.R. Mourant: A framework for modeling humanlike driving behavior for autonomous vehicles in driving simulators. In The Fifth International Conference on Autonomous Agents (2001) 286–291.
3. K. Mizutani and T. Omori A feasibility study of driver's cognitive process estimation from driving behavior. IEEJ Transactions on Electronics, Information and Systems vol. 125-C, no. 6 (2005) 967–975.
4. Y. Togashi, T. Omori, K. Yamauchi: Model of driver eye motion based on driving plan and prediction of changes in the environment. Proceedings of Symposium on Foundation of Computational Intelligence (2007) 289–295.
5. L. Itti, C. Koch and E. Niebur: A model of saliency-based visual attention for rapid scene analysis. IEEE Transactions on Pattern Analysis and Machine Intelligence vol. 20, no. 11 (1998) 1254–1259.
6. S.-J. Park, S.-W. Ban, J.-K. Shin and M. Lee: Implementation of visual attention system using bottom-up saliency map model. in Artificial Neural Network and Neural Information Processing - ICANN/ICONIP (2003) 678–685.

Chapter 91
Top-Down Object Biased Attention Using Growing Fuzzy Topology ART

Young-Min Jang, Byungku Hwang, Sang-Woo Ban and Minho Lee

Abstract In this paper, we propose a top-down object biased attention model which is based on human visual attention mechanism integrating feature based bottom-up attention and goal based top-down attention. The proposed model can guide attention to focus on a given target object over other objects or feature based salient areas by considering both the object preferable bottom-up attention mechanism and the object biased attention mechanism. We proposed a growing fuzzy topology ART that plays important roles for object biased attention, one of which is to incrementally learn and memorize features of arbitrary objects and the other one is to generate top-down bias signal by competing memorized features of a given target object with features of an arbitrary object. Experimental results show that the proposed model performs well in successfully focusing on given target objects, as well as incrementally perceiving arbitrary objects in natural scenes.

Keywords Top-down object biased attention · bottom-up attention · growing fuzzy topology ART

Introduction

Human vision system can effortlessly detect an arbitrary object in natural or cluttered scenes, and incrementally perceive an interesting object in dynamic visual scene. Such a visual search performance will require both bottom-up and top-down control sources to be considered and balanced against one another [1]. In Desimone and Duncan's biased competition model, the biased competition view of visual search proposed two general sources for the control of attention: bottom-up sources that arise from sensory stimuli present in a scene and top-down sources that arise from the current behavioral goals [1, 2].

Y.-M. Jang
School of Electrical Engineering and Computer Science, Kyungpook National University, 1370 Sankyuk-Dong, Puk-Gu, Taegu 702-701, Korea
e-mail: ymjang@ee.knu.ac.kr

R. Wang et al. (eds.), *Advances in Cognitive Neurodynamics*,

Based on the biased competition mechanism, we proposed a biologically motivated top-down object biased attention model.

The proposed attention model consists of two parts. One is the bottom-up attention part that can pop-out salient areas by calculating the relativity of primitive visual features such as intensity, edge, and color [3]. Moreover it provides object preferable attention by considering symmetrical feature since every object with form has symmetry information [3]. The other is the top-down object biased attention part. In order to generate object biased signal, we need object perception and memorization mechanism such as working memory in a human brain. In this model, we propose a new growing fuzzy topology adaptive resonance theory (TART) model for object perception and memorization that makes object feature clusters in an incremental mode. The proposed growing fuzzy TART not only increases stability in conventional fuzzy ART while maintaining plasticity, but it also preserves topology structures in input feature spaces that are divided by color and form domains in an object. Finally, the growing fuzzy TART makes clusters in order to construct an ontology map in the color and form domains. The growing fuzzy TART can activate the target object related features among memorized features and compare the activated features with features of an arbitrary object in order to generate a proper top-down bias signal that can make a target object area in an input scene become the most salient area. Moreover, the clustered information in the growing fuzzy TART is relevant for describing specific objects, and thus it can automatically generate an inference for unknown objects by using learned information. Experimental results show that the proposed model properly guides top-down object biased attention.

The Proposed Model

When humans pay attention to a target object, the prefrontal cortex gives a competitive bias signal, related with the target object, to the infero-temporal (IT) and the V4 area. Then, the IT and the V4 area generates target object dependant information, and this is transmitted to the low-level processing part in order to make a competition between the target object dependant information and features in every area in order to filter the areas that satisfy the target object dependant features.

Figure 91.1 shows the overview of the proposed model during training mode. As shown in the lower part of Fig. 91.1, the bottom-up attention part generates a bottom-up SM based on primitive input features such as intensity, edge and color opponency. Moreover, the bottom-up attention part can generate object preferable SM by considering symmetry feature. Fukushima's biologically based model is adapted to obtaining local symmetry feature from edge information [4]. In training mode of the proposed model, each salient object decided by bottom-up attention is learned by the growing fuzzy TART. For each object area, the log-polar transformed features of HIS and the log-polar transformed Gabor filtered features of edge information

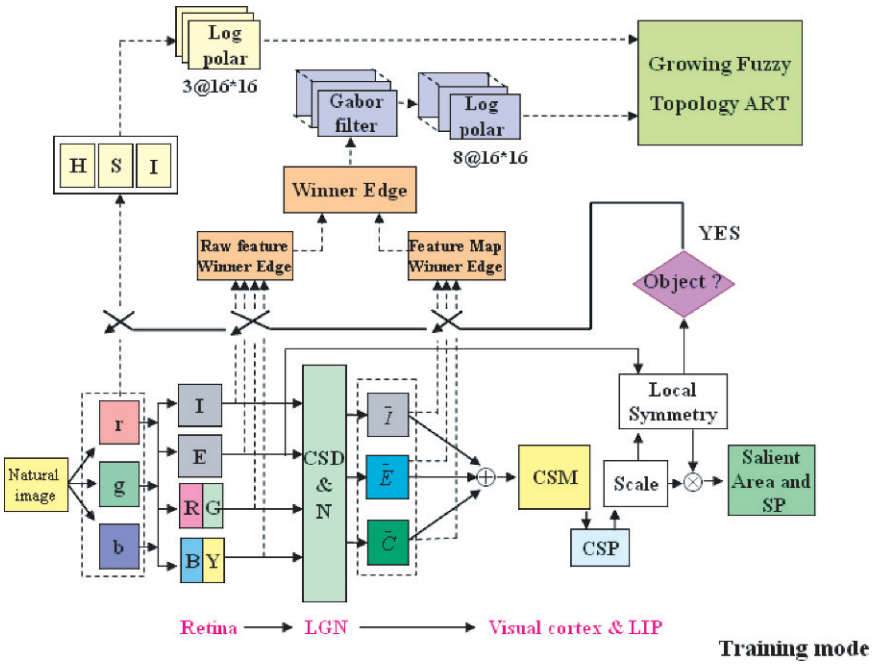

Fig. 91.1 Overview of the proposed model during training mode (r: red, g: green, b: blue, I: intensity feature, E: edge feature, RG: red-green opponent coding feature, BY: blue-yellow opponent coding feature, LGN: lateral geniculate nucleus, CSD&N: center-surround difference and normalization, $\bar{I}$: intensity feature map, $\bar{E}$: edge feature map, $\bar{C}$: color feature map, CSM: candidate saliency map, CSP: candidate salient point, H: hue, S: saturation, I: intensity)

are used as color features and form features for representing an object, respectively. Those are used as input of the growing fuzzy TART.

In the top-down object biased attention mode, which is shown in Fig. 91.2, the growing fuzzy TART activates the memorized form and color features of the target object when a task of target object searching is being given. The activated form and color features related with the target object are involved in competition with the form and color features extracted from each bottom-up salient object area in an input scene. By such a competition mechanism, as shown in Fig. 91.2, the proposed model can generate a top-down signal that can bias the target object area in the input scene. Finally the top-down object biased attention model can generate a top-down object biased saliency map, in which the target object area is popped out. Therefore, the growing fuzzy TART works the most important role for the top-down object biased attention. In this model, the proposed growing fuzzy TART is implemented by integrating the conventional fuzzy ART, with the topology-preserving mechanism of the growing cell structure (GCS) unit [5]. In the growing fuzzy TART, each node in the F2 layer of the conventional fuzzy ART network was replaced with GCS units.

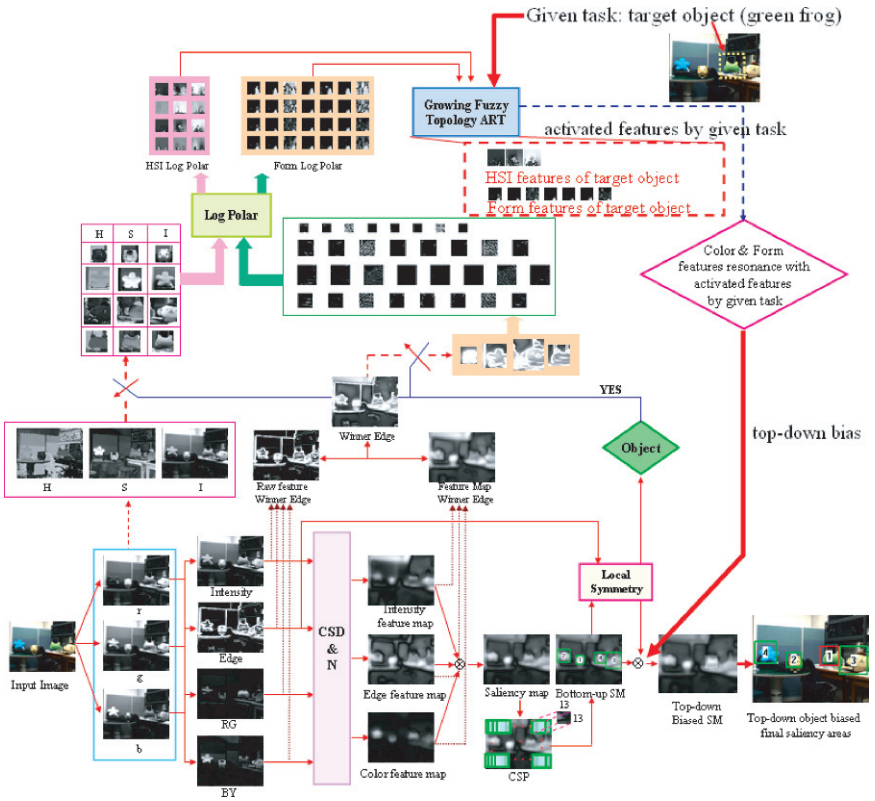

Fig. 91.2 Top-down biased attention results of the proposed model

Experimental Results and Conclusion

Figure 91.2 shows the simulation results of the proposed top-down object biased attention model. As shown in a bottom-up SM result image in Fig. 91.2, the target object, green frog, is not mostly salient area but the 4th salient area when based on only bottom-up features without considering top-down bias. However, the target object became the most salient area after considering top-down bias in conjunction with bottom-up attention as shown in the top-down object biased final saliency areas result image in Fig. 91.2. Moreover, the proposed model can infer an unknown object from known object features memorized in the growing fuzzy TART.

In conclusion, we proposed a biologically motivated selective attention model that can provide a proper visual object search performance based on top-down biased competition mechanism considering both spatial attention and goal oriented object based attention.

Acknowledgments This research was partially funded by the Brain Neuroinformatics Research Program of the Ministry of Commerce, Industry and Energy in Korea, and the research project by ADD (Agency of defense development).

References

1. Vecera, S. P.: Toward a Biased Competition Account of Object-Based Segregation and Attention. Brain and Mind 1 (2000) 353–384.
2. Desimone, R., Duncan, J.: Neural Mechanisms of Selective Visual Attention. Annual Review of Neuroscience 18 (1995) 193–222.
3. Won, W. J., Yeo, J., Ban, S. W., Lee, M.: Biologically Motivated Incremental Object Perception Based on Selective Attention. International Journal of Pattern Recognition & Artificial Intelligence 21 (2007) 1293–1305.
4. Fukushima, K.: Use of Non-uniform Spatial Blur for Image Comparison: Symmetry Axis Extraction. Neural Network 18 (2005) 23–22.
5. Marsland, S., Shapiro, J., Nehmzow, U.: A Self-Organising Network that Grows When Required. Neural Networks, Special Issue 15, 8–9 (2002) 1041–1058.

Chapter 92
Saliency Map Models for Stimulus-Driven Mechanisms in Visual Search: Neural and Functional Accounts

Jun Saiki, Takahiko Koike and Matthew deBrecht

Abstract Saliency map models have been influential in neurocognitive modeling of visual attention. Despite recent applications to complex visual scenes, some basic characteristics of the model remain elusive. Here, we address two issues; neural plausibility of saliency computation, and functional account of search asymmetry phenomenon by a saliency map model. With some modifications, we showed that saliency can be computed by a neurally plausible way, and that search asymmetry can be accounted for only by stimulus-driven mechanisms.

Introduction

The visual system cannot process a massive amount of information from the environment in parallel. Visual attention selects a subset of this information, certain locations, objects, or features, for thorough processing. However, when there are many objects in the visual scene, how does the visual system choose which object to focus on? This has been a topic of research for many years, and the visual search task is one of the methods that have been used to help clarify how the visual system chooses which objects to attend to.

Saliency map models [1, 2] has been influential both in computational modeling, and in neurophysiological studies on attention and visual search. The original idea was quite simple: selection of target of attentional deployment is determined by winner-take-all mechanism on a saliency map, where saliency is defined by a mixture of feature values. Recently, the saliency map models expand to incorporate various top-down mechanisms, and are applied to more complex real-life settings. However, there are still some unresolved problems in basic architecture of saliency map models. This work picked up two such problems; (1) neural network implementation of saliency map, and (2) saliency-map-based account of search asymmetry.

J. Saiki
Unit of Cognitive Science, Graduate School of Human and Environmental Studies, Kyoto University Yoshida-Nihonmatsucho, Sakyo-ku, Kyoto 606-8501, Japan
e-mail: saiki@cv.jinkan.kyoto-u.ac.jp

R. Wang et al. (eds.), *Advances in Cognitive Neurodynamics*,

Neural Network Model of Saliency Map

It has been some concerns whether saliency map can be implemented as a neurally plausible model. There are at least three potential problems: (1) over-competition problem, (2) normalization problem, and (3) temporal dynamics problem.

Over-competition problem arises when competition within a map continues for a long period. Because of the property of winner-take-all mechanism, even a tiny difference in activation ends up with elimination of a competitor. Furthermore, over-competition can be even more of a problem in heterogeneous visual scenes, where slightly less salient stimuli tend to be completely eliminated and as a result do not get represented in the saliency map. The non-salient target may not be represented at all, and so the saliency map could not guide attention to its location.

Normalization during saliency processing is necessary in order for the saliency map to be applicable under a wide variety of stimulus and environmental conditions. In addition, the activity of each feature map must be kept within a reasonable range to assure that a single feature dimension does not dominate visual search. Although the saliency map models include normalization, it is not implemented in a biologically plausible manner.

Finally, the model proposed by Itti and Koch does not give a description of the time course of saliency computation, but it is desirable to have quantitative estimates of the time required to calculate saliency so that we know the time restraints for using saliency information. In addition, it is of interest to be able to model the processing of salience for dynamic scenes.

deBrecht and Saiki [3] addressed these issues, and proposed a neural network model to solve these problems. Their model uses synaptic depression [4] to keep neural activity and competition within a reasonable range, ensuring that stimuli activity is not eliminated in the saliency map due to continuous competition. The model shows how a stimulus with unique features will be more salient than other stimuli with common features, describes the time course of saliency computation and and also explains the high saliency of sudden onset stimuli [5], which has not been considered with standard models.

Stochastic Saliency Map and Search Asymmetry

Although visual search behavior involves highly complex interaction of top-down and bottom-up mechanisms of visual attention, it is useful to explore how far bottom-up mechanisms alone can account for visual search. We have been investigating search asymmetry phenomenon to understand functional roles of saliency-based bottom-up mechanisms.

The phenomenon of search asymmetry, for example, searching for a Q among Os is easier than vice versa [6], is robust and observed with various types of visual

stimuli. Yet, the underlying mechanism of search asymmetry is still unknown. Some accounts postulate top-down mechanisms regarding target identity. For example, saliency-based search model with a task-related saliency map [8] can explain human performance in some visual search tasks showing search asymmetry. However, we recently found that search asymmetry is observed even when target-identity is uncertain (i.e., singleton search) [9], and the model cannot explain search asymmetry in such a case.

To explain why search asymmetry occurs even in singleton search tasks, Koike and Saiki [7] employed a different approach. Instead of adding top-down control mechanisms, they modified the existing bottom-up saliency-based models to account for the search asymmetry in the singleton search.

The modified model incorporated the following mechanisms to account for search asymmetry in the singleton search: stochastic winner-take-all (WTA) and inter-feature competition. These modifications made the model sensitive to relative magnitude of saliency as well as rank order, which could successfully simulate various psychological data showing search asymmetry without top-down control.

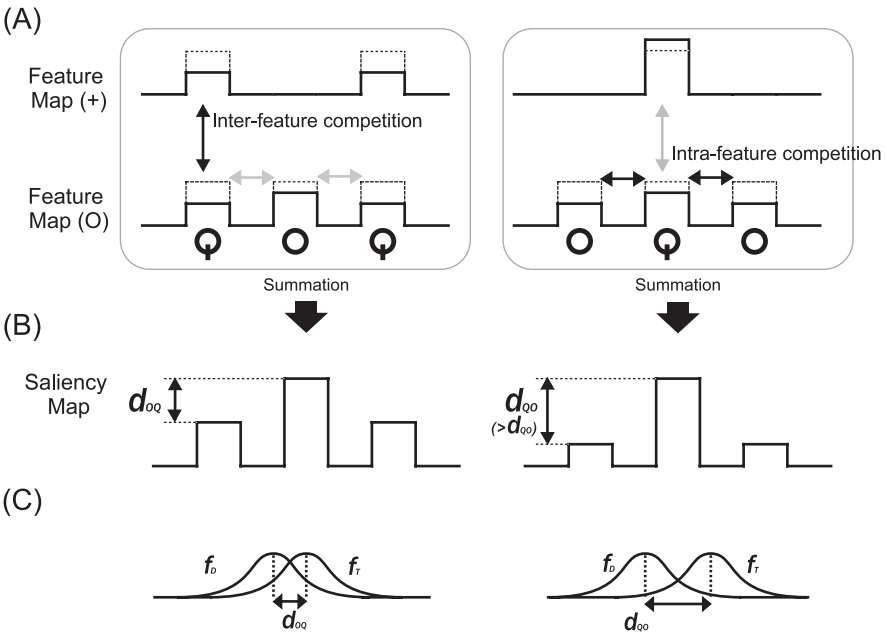

Fig. 92.1 Schematic illustration of the two modifications in the model in [7]. (a) intra- and inter-feature competition, (b) competitions lead to saliency maps with different relative magnitudes depending on the target, and (c) stochastic winner-take-all is sensitive to relative magnitude, not simply rank-order, of saliency

Extension of Models

Two models discussed here focus on different levels; one neural and one functional. However, it appears that the idea of stochastic saliency map can be implemented by the proposed temporal dynamics of neural network, because the reduction of over-competition by synaptic depression enables quick decision-making, which leads to more stochastic behavior of the model. Another future direction is to apply these models to visual cognition phenomena other than visual search. For example, the neural network model with precise temporal dynamics [3] can be applied to attentional capture, in paricular, capture by sudden onset [5]. Also, the functional saliency map model can be extended to visual short-term momory, and we are currently developing a model to account for basic findings of visual short-term memory research [10]. It is no doubt that more technically-sophisticated saliency map models can achieve human-like visual cognition and behevior in the near future, but simpler versions of saliency map models are still useful as tools for investigating basic characteristics of biological mechanisms of visual attention.

Acknowledgments This work was supported by PRESTO "Intelligent cooperation and control" from Japanese Science and Technology Agency (JST), Grants-in-Aid for Scientific Research from JMEXT (#19500226) and the 21st Century COE Program from JMEXT (D-2 to Kyoto University).

References

1. Itti, L., & Koch, C. (2000). A saliency-based machanism for overt and covert shifts of visual attention. *Vision Research, 40*, 1489–1506.
2. Koch, C., & Ullman, S. (1985). Shifts in selective visual attention: towards the underlying neural circuitry. *Human Neurobiology, 4*, 219–227.
3. deBrecht, M., & Saiki, J. (2006). Neural network implementation of saliency map. *Neural Networks, 19*, 1467–1474.
4. Abbott, L. F., Varela, J. A., Sen, K., & Nelson, S. B. (1997). Synaptic depression and cortical gain control. *Science, 275*, 220–224.
5. Yantis, S. (1993). Stimulus-driven attentional capture. *Current Directions in Psychological Science, 2*, 156–161.
6. Treisman, A., & Souther, S. (1985). Search asymmetry: a diagnostic for preattentive processing of separable features. *Journal of Experimental Psychology: General, 114*, 285–310.
7. Koike, T., & Saiki, J. (2006). Stochastic saliency-based search model for search asymmetry with uncertain targets., *Neurocomputing, 69*, 2112–2126.
8. Navalpakkam, V., & Itti, L. (2005). Modeling the influence of task on attention. *Vision Research, 45*, 205–231.
9. Saiki, J., Koike, T., Takahashi, K., & Inoue, T. (2005). Visual search asymmetry with uncertain targets. *Journal of Experimental Psychology: Human Perception and Performance, 31*, 1274–1287.
10. Luck, S. J., & Vogel, E. K. (1997). The capacity of visual working memory for features and conjunctions. *Nature, 390*, 279–281.

Chapter 93
Extraction of Single-Trail N400 Event-Related Potentials Based on Dynamic Independent Component Analysis

Wen-Juan Li and Xiao-Pei Wu

Abstract The Independent Component Analysis (ICA) method has a good application in EEG. But ICA algorithm is mostly a combination of static model and batch optimization algorithm. Considering the non-stationary characteristics of event-related potentials, the Dynamic Independent Component Analysis (DICA) based on kurtosis maximization was proposed to single-trail extract the event-related potential N400 which is induced by the Chinese idioms whose last word is incorrect. The DICA method achieved satisfactory results.

Keywords Event-related potential (ERP) · EEG · signal-trail extraction · dynamic independent component analysis (DICA).

Introduction

Event-related Potential (ERP) reflects neural activity of the brain in cognitive process, It has a widely application in clinical medicine and cognitive science [1]. But ERP is often heavily contaminated by many noises. It is necessary to extract ERP signal from the strong background noises.

Traditional method for extracting ERP is the simple method of averaging. But the method has some limitations. Commonly, the experiment duration is long and the signal is non-stationary. Also repeating stimulate can make the nervous system tired and make the stimulate familiar to the brain. All those factors will influence the ERP's time non-stationary. In later 1990s, Independent Component Analysis was emerged as a blind source separation technology. The ICA method has a good application in EEG.

W.-J. Li
The Key Laboratory of Intelligent Computing & Signal Processing of Ministry of Education, Anhui University, Hefei 230039, China
e-mail: iamliwenjuan@yahoo.com.cn

R. Wang et al. (eds.), *Advances in Cognitive Neurodynamics*,

But ICA algorithm is mostly a combination of static model and batch optimization algorithm. As we know, EEG is a biological signal of highly non-stationary nature. So the static ICA algorithm is often hard to obtain valuable results.

Single-trail extraction of the N400 event-related potentials based on the kurtosis maximization ICA algorithm performed an important physiological significance and more accurate result in this paper.

N400 Event-Related Potentials

N400 event-related potential is a commonly used ERP component in language processing. In 1980s American scholars Kutas and Sillyard first reported that in a statement read tasks, the semantic mismatch of the last word in a sentence can induce a language-related negative element. Because the negative element is about 400 ms, it was know as N400. N400 can be induced by various language operational tasks [2]. It mainly reflects the cognitive function of neural activity.

Most research on the N400 is based on the English text material. Chinese is different from Western alphabet. Therefore, using Chinese characters as stimulating material has an important significance.

In this paper, the experiment data is acquired by the stimulation of Chinese idioms. When the last word is incorrect, it can induce N400 event-related potentials. We used the Scan 4.3 acquisition system to record the experiment data. Electrodes placed under international 10–20 system.

Dynamic ICA Algorithm

Independent component analysis [3] can be simply described as follows: given a set of observations of random variables $\mathbf{X} = [x_1(t),\ x_2(t), \ldots x_N(t)]^T$, where t is the time or sample index, assume that they are generated as a linear mixture of independent component $\mathbf{X} = \mathbf{AS}$. Independent component analysis now consist of estimating both the matrix $\mathbf{A}$ and the $\mathbf{S}$, when we only observe the $\mathbf{X}$. Alternatively, we could define ICA as follows: find a linear transformation given by a matrix $\mathbf{W}$ as in formulation $\mathbf{Y} = \mathbf{WX}$, so that the random variables $y_i,\ i = 1, 2, \ldots N$ which are in the matrix $\mathbf{Y}$ are as independent as possible.

Kurtosis (4-order cumulant) is a commonly used method for measuring the independence of the random variables. The idea generated from the statistical theory of the central limit theorem. The central limit theorem states: under certain conditions, the joint of the independent non-Gaussian random variables effected approximation Gaussian distribution. So in the independent component extraction, using kurtosis to measure the independence between the separating components is a good method. With a zero mean random variable $\mathbf{X}$, a normalized kurtosis defined as follows:

$$kurt(x) = \frac{E\{x^4\}}{(E\{x^2\})^2} - 3 \tag{93.1}$$

Denote the importation of random vectors by $\mathbf{x}$, $\mathbf{w_t}$ is a line vector of separation matrix, $\mathbf{y} = \mathbf{w_t}^{\mathbf{T}}\mathbf{x}$ is a output independent component. The ICA separation matrix algorithm [4] based on kurtosis maximization is as follows:

$$\mathbf{w}_{t+1} = \mathbf{w}_t + \mu \cdot sign[kurt(u)] \cdot E\{(\mathbf{w}_t^T \mathbf{x})^3 \cdot \mathbf{z}\} \tag{93.2}$$

μ is the learning step of the gradient method, sign () is the symbol function, t is the number of learning. (2) is the batch method of ICA algorithm. DICA algorithm use a single input sample one time for estimating and updating the separation matrix. It is not difficult to see that only the removal of the mean can become the DICA algorithm [5]. Formulation as (3).

$$\mathbf{w}_{t+1} = \mathbf{w}_t + \mu \cdot sign[kurt(y)] \cdot (\mathbf{w}_t^T x_t)^3 \cdot x_t \tag{93.3}$$

Dynamic Independent Component Analysis for Single-Trail N400 Extraction

The original EEG signals were got by a university man whom is induced by the Chinese idioms. Twenty-nine observation signals are drew in Fig. 93.1.

Figure 93.2 is the separated results using the dynamic ICA algorithm. From Fig. 93.2, it is clear to know that S1 is the eye signal, S2 is the extracted ERP.

In order to get clearer ERP signal, first used the wavelet transform for pretreatment, then use DICA for separation. Figure 93.3 is the final result. Based on the above analysis, the S2 signal in Fig. 93.3 is the final extracted ERP signal. We drew it as Fig. 93.4.

Conclusion

This paper applied the dynamic independent component analysis based on kurtosis maximization to extraction of single-trail N400 event-related potentials and achieved satisfactory result. For the Dynamic ICA algorithm has the capability of online operation, this method has important practical value. Because extraction of the event-related potentials is an important issue, we must work hard for extracting the signal more accurate and rapid.

Acknowledgments This research is supported by Nature Science Foundation of Anhui province (070412038)

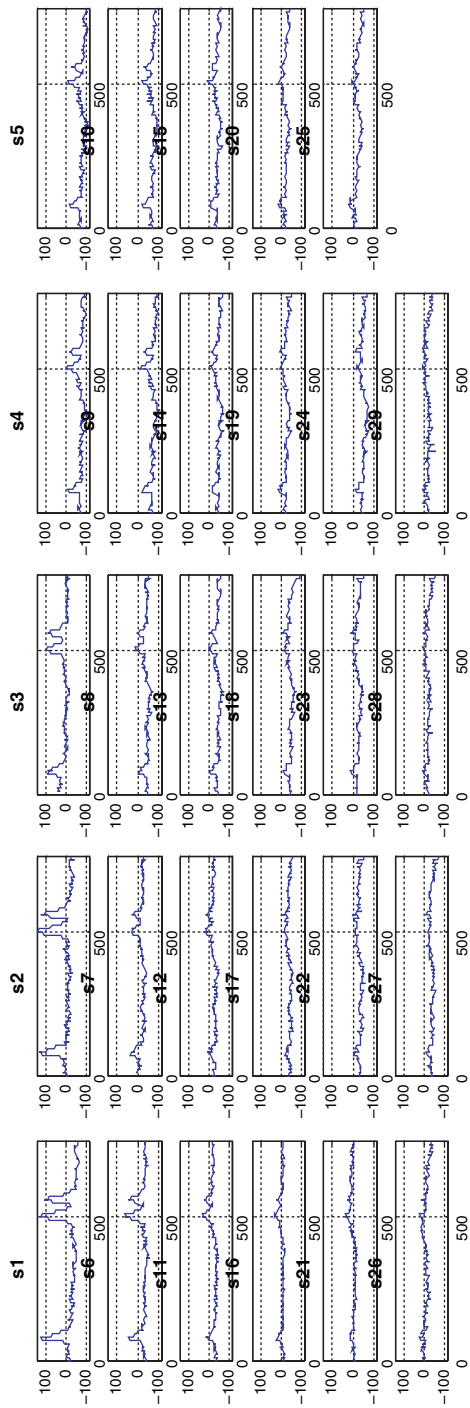

Fig. 93.1 Original EEG

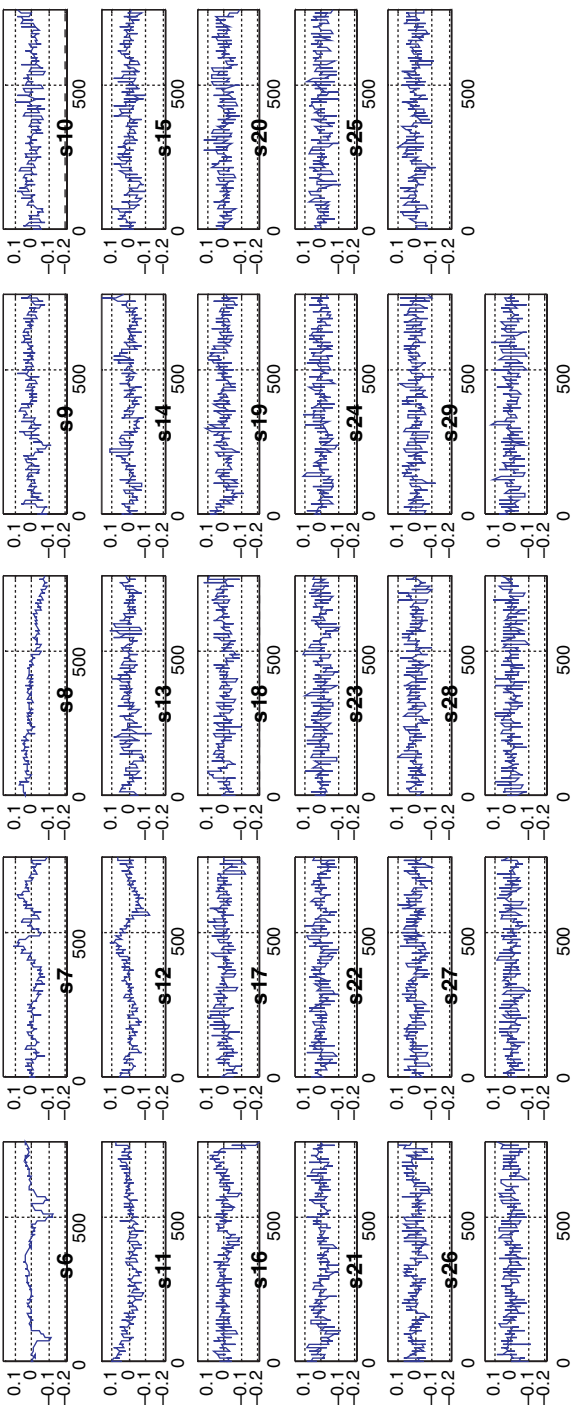

Fig. 93.2 Separate signals using DICA

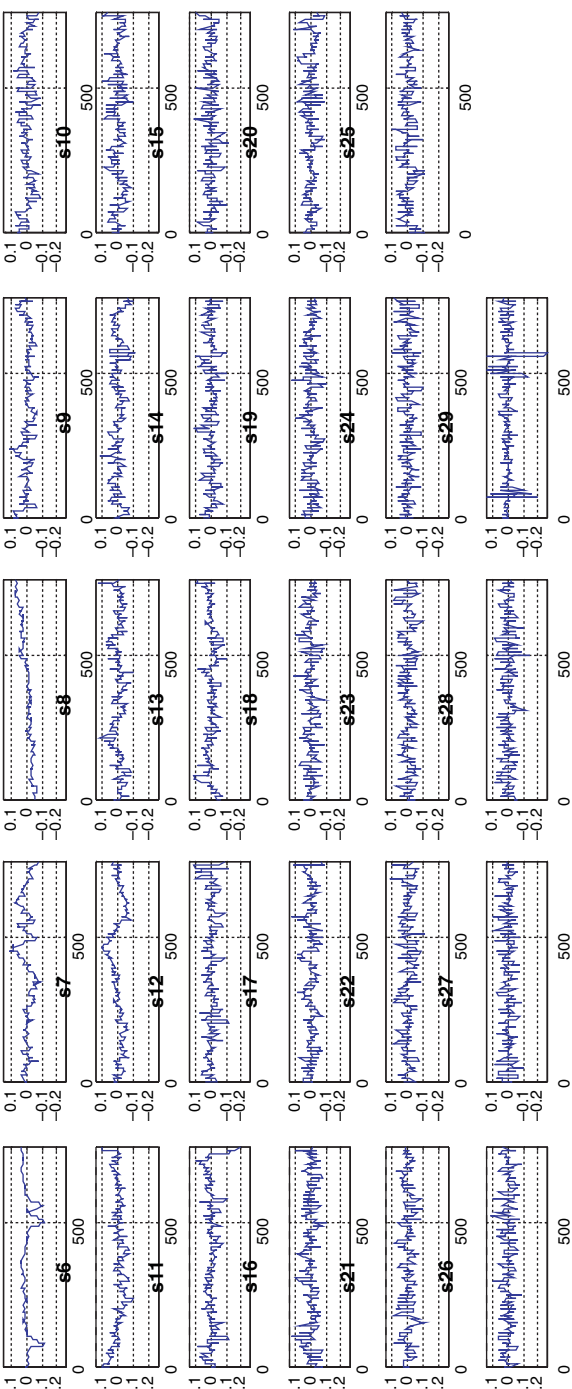

Fig. 93.3 Separate signals using wavelet transform pretreatment and DICA

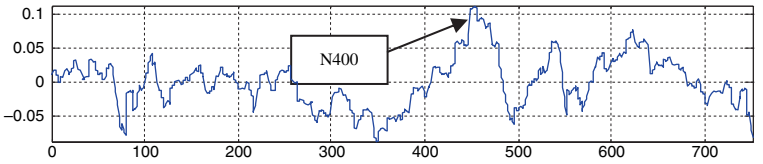

Fig. 93.4 ERP signal

References

1. Pan YF.: Evoked potentials in medical practice. 2nd edn. Beijing: People's Medical Publishing House (2000): 579–622.
2. Kutas M, et al.: Event-related potentials symmetries during the reading sentences. Electroencephalography and Clinical Neurophysiology (1988) 69: 23–218.
3. Hyvarinen, A., Karhunen, J., Oja, E.: Independent component analysis[M]. New York, A Wily-Interscience Publication (2001): 165–178.
4. Makeig, S., Bell, A.J., Jung, T., & Sejnowski, T.J. Scott Making: Independent Component Analysis of Electroencephalographic Data. Advances in Neural Information Processing Systems [J] (1996) 8: 145–151.
5. Xiao-Pei Wu, Zhong-Fu Ye, Xiao-Jing Guo, Dao-Xin Zhang, Ren-Jun Hu: Independent Component Analysis Based on Sliding Window[J]. Journal of Computer Research and Development (2007) 44(1): 185–191.

Chapter 94
Characterizing Individual Interest by a Computational Model of Reading

J. Ignacio Serrano, M. Dolores del Castillo and Ángel Iglesias

Abstract Individual topic interest seems to be strongly related to reading attention and depth of processing. Although there exists a lot of research about the study of the relationship between the latter aspects, there is little work in the quantification of this interaction during reading. This paper presents a way for the detection and quantification of the influence of individual interest in the reading process by using several parameters that characterize a computational model of reading called CRIM. Experiment results have pointed out a certain dependency between the implicated issues, motivating further and deeper research.

Introduction

Individual interest, also known as personal interest, is related to specific topics and it is persistent over time [1]. It derives from the subjective long-term goals and desires. It has to be distinguish from situational interest, which refers to short-term processing changes influenced by the immediate context [2]. Although there exists much more research about the latter type of interest, empirical studies concerning individual interest have been carrying out for twenty years. Among the published results, it can be found out that personal or individual interest is related to prior knowledge [3] and also that there exists a relationship between personal interest, attention and processing depth [4]. Some models of this interaction has been proposed, such as the long-term model by Alexader [5], and the "real time" model by Schiefele [6]. However, these models lack a fine characterization and quantification of the cited relationships. In this paper, the parameters of an existent computational model of reading are presented as indicators and quantifiers of the mentioned dependencies.

J.I. Serrano
Instituto de Automática Industrial, Spanish National Research Council. Ctra. Campo Real km 0.200 - La Poveda. 28500 Arganda del Rey, Madrid, Spain
e-mail: nachosm@iai.csic.es

R. Wang et al. (eds.), *Advances in Cognitive Neurodynamics*,

Computational Model of Reading

The base framework used to model individual interest was CRIM (Cognitive Reading Indexing Model) [7]. CRIM is a connectionist model of reading which sequentially processes words in order to generate a semantic representation from the corresponding input text. The representation formalism is a net of semantically associated concepts, and each of them includes a significance degree with respect to the main semantic of the text that has been read. The system operates in two stages. In the first one, a background semantic knowledge is constructed from a collection of free language texts. In the second stage, the model of reading applies its mechanisms on the background knowledge to obtain a semantic representation from any input text.

Construction of the Background Knowledge

CRIM represents the background semantic knowledge as a net of concepts, associated one to another by weighted connections that indicate semantic relationship degrees. It is considered that a concept is semantically related to another if they co-occur within the same context. In this case, the context is not the typical word window but a context of variable size, the sentences themselves. This context makes the model dependent on the texts, thus supporting the psychological plausibility. The connections between concepts are not symmetrical, as well as they are not for human beings. The asymmetry is represented by the direction of the connections as well as by the relative weights. The weights are the relative frequency of co-occurrence between the source concept and the destination concept.

Construction of Semantic Representation of Texts

Once the background knowledge is constructed, the model can apply the cognitive procedures on the text to be read using the former knowledge. This semantic extraction mechanism is a process over time in which cognitive factors like perception, memory, inference and forgetting take part.

The model dynamics is as follows. The words in the texts are processed following the order in which they appear. Every time a word is read or perceived, the model searches for the corresponding concept in the background knowledge. If the concept is present, i.e. the word is already known, it is added to the current semantic representation in the working memory with a base activation level. Then, the inferences come into play by propagating the activation of the perceived concept through the background knowledge. The activation is multiplied by the connection weights and spread from one concept to another associated concepts until one of the following two conditions is fulfilled: the activation to be propagated is lower than a certain threshold, called propagation threshold, or the activation has passed through a certain number of concepts from the perceived one (maximum propagation level).

All the concepts reached in the propagation process are then retrieved and added to the current semantic representation with the activation level they received, together with the weighted semantic connections between them. If a perceived or inferred concept was already in the working memory then its current activation is increased by the activation level obtained either after perceiving or inferring. Every certain time interval, called the forgetting interval, all concepts currently in the working memory lose a portion of activation, called forgetting factor. Since words are sequentially processed, the time interval can be expressed as a number of consecutive words. To be psychologically plausible, the forgetting interval was decided to be determined by the sentences themselves. Thus, every sentence that is read involves that the activation level of the concepts in the current semantic representation is decreased, so that if a concept is not reinforced either directly by perception or indirectly by inference along the reading process, the concept is forgotten. When the activation of a concept is below the so-called forgetting threshold the concept is removed from the working memory and so forgotten. Thus, the most activated concepts in final representation conform the text topics and their activation level depicts the semantic significance with respect to those topics. Since attention might be related to deeper inferences and better understanding [2], the propagation threshold and forgetting factor parameters were evaluated as indicators of the individual interest and its interaction with attention.

Characterization of Individual Interest

In order for testing the validity of the propagation threshold and forgetting factor as individual interest indicators, an experiment was carried out: 20 subjects, with university and science academic degree, were asked to rank five topic categories depending on their personal individual interest. Then, the subjects were asked to summarize five news belonging to the former five categories just after reading each of them, placing first the more important issues of each text in their opinion. The reading time was also measured for each subject and each text. Next, the CRIM system was used to construct a background knowledge from a collection of university academic level texts and news. The model generated several semantic representations for each of the five news varying the values of the propagation threshold and forgetting factor parameters.

The subject's summaries were transformed into lists of concepts in order of appearance. The CRIM representations were transformed into lists of concepts decreasingly sorted by their activation level. Then, the human's lists and CRIM lists from the same news were then compared, obtaining a measure of similarity between CRIM representations and human summaries. The similarity was computed by the average difference of the normalized positions of concepts belonging to the intersection of both lists. Thus, for each subject and each text, the parameter values which allow the model to generate the most similar representation to the subject summary were obtained. These values are grouped by the interest ranking position that the subject assigned to the corresponding text. For example, the values are assigned

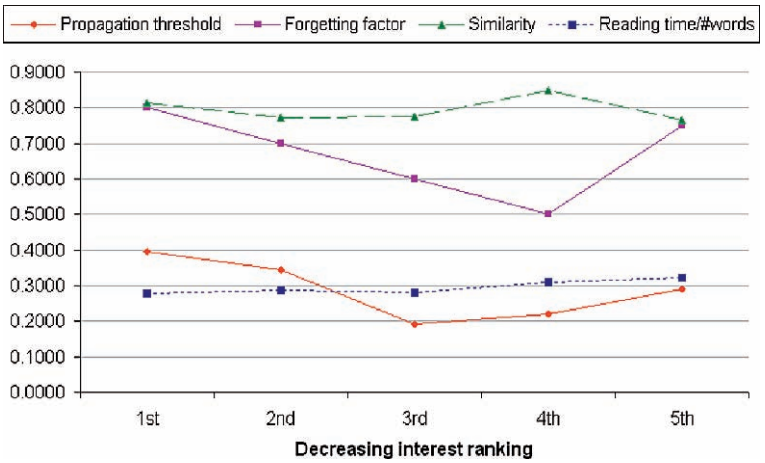

Fig. 94.1 Average values of propagation threshold, forgetting factor, similarity with humans and time rate spent for different levels of interest

to group 2 if those values produce the most similar representation to the summary corresponding to the second most interesting text category for the subject. The average values of each group are presented in Fig. 94.1. The x-axis contains the interest ranking groups(1st the most interesting, 5th the least one) and the y-axis the average values for the parameters, the similarity and the spent time rate (time/number of words in the text).

The results showed that the time rate slightly increases when the interest decreases, as expected. Similarity values between model and humans seem not to be influenced by the individual interest variation. On the opposite, there is a dependency between individual interest and propagation threshold and forgetting factor. As expected, when the interest is high the propagation threshold is low, i.e. more concepts are inferred which implies more attention, and the forgetting factor is high too, i.e. concepts are retained more time in memory. The latter values decrease as the interest does excepting for the lowest interest, where both parameters take high values again, although not so significant as for high interest. Since prior knowledge seems to be related to individual interest [3], it is likely that subjects need to pay more attention and intention to memorize text surface elements when the topic is not familiar to them (and not interesting). This is the case pointed out by the results, which is indeed psychologically plausible.

Conclusions and Future Work

A connectionist computational model of reading, called CRIM, has been used to characterize and quantify the individual interest in such task. Concretely, two parameters of such model, related to attention and memory capacity, have been proven

to be good indicators of the subject individual interest, by the study of the similarity between CRIM output text representations and human summaries for different levels of subjective topic interest. Since individual interest and prior knowledge might be related [3], it is planned to characterize the former aspect in the same terms as in this work and to extract the dependency type and quantification of that relationship. It is also intended to study the detection of reading disorders by means of the characterized issues.

References

1. Schraw, G., Lehman, S.: Situational Interest: A Review of the Literature and Directions for Future Research. Educational Psychology Review 13 (2001) 23–52.
2. Hidi, G.: Interest, Reading and Learning Theoretical and Practical Considerations. Educational Psychology Review 13, (2001) 191–209.
3. Tobias, S.: Interest, Prior Knowledge and Learning. Review of Educational Research 64 (1994) 37–54.
4. Schiefele, U.: Interest and Learning from Text. Scientific Studies Reading 3 (1999) 257–280.
5. Fox, E., Alexander, P. A.: A Developmental Model of Interest, Knowledge, and Strategy Use in Text Comprehension. In C. M. Kardash (Chair), *The Role of Affect in Text Processing/Comprehension: Implications for Theory, Research, and Practice*, Symposium of the annual meeting of the American Educational Research Association, San Diego (2004).
6. Schiefele, U.: Topic Interest and Levels of Text Comprehension. In Renninger, A., Hidi, S. and Krapp, A. (eds.), *The Role of Interest in Learning and Development*, Erlbaum, Hillsdale, NJ (1992) 151–182.
7. Serrano, J. I., del Castillo, M. D.: Text Representation by A Computational Model of Reading. In King, I. et al. (eds.), *Lecture Notes in Computer Science*, Springer-Verlag Berlin 4232, (2006) 237–246.

Chapter 95
Overview of Diffusion Tensor Imaging in Multiple Sclerosis and Neuromyelitis Optica

Chunshui Yu

Abstract Diffusion tensor imaging (DTI) is a powerful quantitative technique with the potential to detect *in vivo* microscopic abnormalities of brain tissue. It has been successfully applied to study the occult damage in multiple sclerosis (MS) and neuromyelitis optica (NMO), providing information otherwise inaccessible on the pathological substrates. DTI has also been used to differentiate these two diseases. Several image-analysis approaches have been employed, including region of interest, histogram, and tractography. This review focuses on the use of DTI to investigate MS and NMO.

Keywords Diffusion tensor imaging · multiple sclerosis · neuromyelitis optical

Introduction

Diffusion is the microscopic random translational motion of molecules, and water diffusion can be measured using diffusion weighted imaging, in terms of an apparent diffusion coefficient [1]. Since diffusion is affected by the properties of the medium where molecular motion occurs, the measurement of diffusion inside biological tissues provides information about tissue structure at a microscopic level [2]. Pathological processes, which change the microstructural environment, such as neuronal size, extracellular space and tissue integrity, result in altered **diffusion** [3, 4]. In some tissues with an oriented microstructure, such as brain white matter, the molecular mobility is not the same in all directions. This property is called anisotropy, and results in a variation in the measured diffusivity [5]. Within a highly ordered white matter tract, water molecules diffuse faster in the direction parallel to the tract than perpendicular directions, because axonal membranes and myelin sheaths restrict transverse **diffusion** [6, 7]. Under these conditions, diffusion characteristics can be described by a tensor [8]. From the tensor, it is possible to derive some scalar

C. Yu
Department of Radiology, Xuanwu Hospital, Capital Medical University, No.45, Chang-Chun Street, Xuanwu District, Beijing, China
e-mail: Chunshuiyu826@yahoo.com.cn

R. Wang et al. (eds.), *Advances in Cognitive Neurodynamics*,

indices that reflect the diffusion characteristics of the tissue. Mean diffusivity (MD) reflects the average magnitude of molecular motion and fractional anisotropy (FA) reflects its directionality [8]. They are calculated from three orthogonal diffusion tensor eigenvalues (λ_1, λ_2 and λ_3), which represent the diffusion coefficients along the major, median and minor axes of the diffusion ellipsoid.

Diffusion tensor tractography can visualize white matter tracts *in vivo* and its reliability has been validated by comparison with known anatomy [9, 10]. Subsequently tract-based quantitative analyses of diffusion indices were developed, and analysis has been performed by either considering a tract as an entire ROI or defining ROIs along the tract [11, 12, 13]. These methods may partly overcome the limitations of conventional ROI-based analyses, improve the reliability of defining a ROI of a tract, and detect both the local and global changes of the tract.

DTI technique seems like a promising tool for the quantification of tissue damage and for improving our understanding of conditions that affect the integrity of brain tissues. The pathological changes of multiple sclerosis (MS) and neuromyelitis optica (NMO) have the potential to alter the permeability or geometry of structural barriers to water molecular diffusion in the brain. The present review outlines the major contributions given by DTI for the quantification of MS and NMO-related damage, for the understanding of their pathophysiology, and for the differentiation of these two diseases.

Multiple Sclerosis

Multiple sclerosis (MS) is an inflammatory demyelinating disease, typically occurs in the 30–40 years of age, and the disease course varies greatly from patient to patient. According to the disease course, MS can be divided into three subtypes: relapsing-remitting (RR), secondary progressive (SP) and primary progressive (PP).

Lesions Visible on Conventional MR Images

All DTI studies have shown higher MD and lower FA in T2 visible lesions [14, 15, 16, 17]. However, water diffusion abnormalities are different in different types of MS lesions. All researchers have shown higher MD values in non-enhancing T1-hypointense than in non-enhancing T1-isointense lesions [14, 16, 17]. Although conflicting results have been achieved when comparing MD in enhancing vs. non-enhancing lesions, FA has always been found lower in enhancing than in non-enhancing lesions [16, 17]. Some studies have shown that water diffusivity is markedly increased in ring-enhancing lesions when compared to homogeneously enhancing lesions [14, 18], or in the non-enhancing portions of enhancing lesions when compared with enhancing portions [18]. Markedly reduced FA values have also been found in ring-enhancing lesions [14]. The above findings confirm the pathological heterogeneity of MS lesions and indicate that measures derived from

DTI have the potential to improve our ability to define and monitor the mechanisms underlying MS tissue damage, since the various pathological substrates of MS have a different impact on the integrity of brain tissue.

Normal-Appearing White Matter

DTI studies in MS have shown that MD values of normal-appearing white matter (NAWM) are higher than those of corresponding white matter from controls and lower than those measured in T2-visible lesions, while FA values of NAWM are lower than those of corresponding white matter from controls and higher than those of T2-visible lesions [14, 15, 16, 17, 19]. These results are consistent with pathologic findings from patients with MS, including diffuse astrocytic hyperplasia, patchy edema, perivascular infiltration, gliosis, abnormally thin myelin and axonal loss [20]. While all these processes might reduce FA, myelin and axonal loss should lead to increased water diffusivity. The possible reasons for these subtle NAWM changes may result from Wallerian degeneration of axons transversing large lesions or the presence of small focal abnormalities beyond the resolution of conventional MRI.

Gray Matter

Traditionally, MS was regarded as a demyelinating disease that mainly involved in the white matter. More and more evidence supported the involvement of brain gray matter in this disease. Based on the histogram analysis, some studies [15, 21, 22, 23] showed that MD histogram of brain GM from MS patients was different from that of brain GM from sex- and age-matched healthy volunteers. This indicates that brain GM is not spared by the MS pathological process and is consistent with a previous post-mortem study [24] which showed that lesions are relatively frequent in the cerebral GM of patients with MS. As a consequence, one explanation of this finding might be the presence of a certain amount of discrete MS lesions in the GM of MS patients, which go undetected on conventional MRI. An alternative explanation of the MD changes in GM might be Wallerian degeneration of GM neurons secondary to the damage of fibers transversing MS white matter lesions, which is supported by the correlations found between T2 lesion volume and GM MD [25]. The presence of GM damage in MS fits well with the frequent demonstration of cognitive impairment in patients with MS [26].

Cognitive Impairment

Cognitive impairment can be seen in approximate 50% of MS patients [27], including deficits in processing speed [28], memory [29] and higher executive function

[30]. Rovaris et al. [31] examined the relationship between DTI and cognition in RRMS patients with mild neurological disability. They found a moderate correlation between MD of the GM and impairments of memory, speed of information processing and verbal fluency. Lin et al. [32] found that the MD of the corpus callosum correlated with cognitive impairment. Moreover, Benedict et al. [33] indicates diffusion weighted imaging can predict cognitive impairment in MS.

Neuromyelitis Optica

Neuromyelitis optica (NMO) is a severe demyelinating disease characterized by selective involvement of the spinal cord and optic nerves and is considered to frequently spare the brain. Recently using quantitative MRI techniques, some authors have investigated whether NMO has occult damage in the brain. Filippi et al. [34] did not find any significant changes in 8 NMO patients using magnetization transfer imaging (MTI). Rocca et al. [35] found occult damage in the NAGM of 10 patients with NMO with the use of MTI and DTI. Using DTI histogram analysis, Yu et al. [36] found significant abnormalities in the NAWM and NAGM in NMO patients. Then using ROI analysis, they found that NMO patients had a higher average MD and a lower average FA in ROIs being the continuation of the spinal white matter tracts or optic nerve and a normal average MD and FA in corpus callosum without direct connection with them. To further explain the diffusion abnormalities of brain NAWM in NMO, Yu et al. [37] studied diffusion indices of the corticospinal tract (CST), corpus callosum (CC), optic radiation (OR) and cingulum in NMO patients without visible lesions in the brain. Compared with controls, both global and regional analyses showed significant increases in MD and λ_{23} of the CST and OR in NMO, but not in any of the diffusion indices of the CC and cingulum. In NMO, MD and λ_1 of the CST were correlated with motor function scores and MD and λ_1 of the OR were correlated with visual function scores. They concluded that axonal degeneration secondary to lesions in the spinal cord and optic nerves is a cause for NAWM damage in NMO.

Differentiating RRMS and RNMO

Both relapsing NMO (RNMO) and RRMS are recurrent demyelinating diseases. Although they are different in onset age, sex preponderance, lesion distribution, attack severity, CSF profile, pathological findings, and immunopathologic characteristics [38, 39, 40, 41], they also have overlapping clinical manifestations, MRI and CSF findings, which bring difficulties in differentiation. Since the optimal treatments for the two disorders are different [42, 43], correct diagnosis critically affects the therapeutic outcome. To differentiate these two diseases, two methods have proposed: two-dimensional histogram of MD and FA [44] and diffusion indices of corpus callosum [45]. The former using two-dimensional histogram of MD and FA as

classification feature, obtained a correct recognition rate of 85.7%, which was much higher than that using feature of ADC or FA separately (59.5% for ADC, 76.2% for FA). The latter used the MD or FA of the corpus callosum as classification feature to differentiate these two diseases, The sensitivity and specificity for differentiation were 92.31% and 93.48% for the FA and 88.46% and 89.13% for the MD.

Conclusion

DTI allows to quantify the amount of tissue damage of MS lesions and to detect occult changes occurring in NAWM and GM of MS and NMO. With the technique of DTI, we can speculate on the possible pathological substrates of such changes. Post-mortem studies correlating DTI findings with histopathology are needed, as well as longitudinal studies of patients with various MS phenotypes to elucidate the correlation between evolving diffusion abnormalities and the development of irreversible disability.

References

1. Le Bihan D., Breton E., Lallemand D., Grenier P., Cabanis E., Laval-Jeantet M.: MR imaging of intravoxel incoherent motions: application to diffusion and perfusion in neurologic disorders. Radiology 161 (1986) 401–407.
2. Le Bihan D., Turner R., Moonen C.T., Pekar J.: Diffusion and perfusion imaging by gradient sensitization: design, strategy and significance. J. Magn. Reson. Imaging. 1 (1991) 7–8.
3. Anderson A.W., Zhong J., Petroff O.A., Szafer A., Ransom B.R., Prichard J.W., Gore J.C.: Effects of osmotically driven cell volume changes on diffusion-weighted imaging of the rat optic nerve. Magn. Reson. Med. 35 (1996) 162–167.
4. Sevick R.J., Kanda F., Mintorovitch J., Arieff A.I., Kucharczyk J., Tsuruda J.S., Norman D., Moseley M.E.: Cytotoxic brain edema: assessment with diffusion-weighted MR imaging. Radiology 185 (1992) 687–690.
5. Chenevert T.L., Brunberg J.A., Pipe J.G.: Anisotropic diffusion in human white matter: demonstration with MR techniques in vivo. Radiology 177 (1990) 401–405.
6. Beaulieu C., Allen P.S.: Water diffusion in the giant axon of the squid: implications for diffusion-weighted MRI of the nervous system. Magn. Reson. Med. 32 (1994) 579–583.
7. Nomura Y., Sakuma H., Takeda K., Tagami T., Okuda Y., Nakagawa T.: Diffusional anisotropy of the human brain assessed with diffusion-weighted MR: relation with normal brain development and aging. Am. J. Neuroradiol. 15 (1994) 231–238.
8. Basser P.J., Pierpaoli C.: Microstructural and physiological features of tissues elucidated by quantitative-diffusion-tensor MRI. J. Magn. Reson. B. 111 (1996) 209–219.
9. Basser P.J., Pajevic S., Pierpaoli C., Duda J., Aldroubi A.: In vivo fiber tractography using DT-MRI data. Magn. Reson. Med. 44 (2000) 625–632.
10. Jones D.K., Simmons A., Williams S.C., Horsfield M.A.: Non-invasive assessment of axonal fiber connectivity in the human brain via diffusion tensor MRI. Magn. Reson. Med. 42 (1999) 37–41.
11. Berman J.I., Mukherjee P., Partridge S.C., Miller S.P., Ferriero D.M., Barkovich A.J., Vigneron D.B., Henry R.G.: Quantitative diffusion tensor MRI fiber tractography of sensorimotor white matter development in premature infants. Neuroimage 27 (2005) 862–871.

12. Lin F., Yu C., Jiang T., Li K., Li X., Qin W., Sun H., Chan P.: Quantitative analysis along the pyramidal tract by length-normalized parameterization based on diffusion tensor tractography: application to patients with relapsing neuromyelitis optica. Neuroimage 33 (2006) 154–160.
13. Partridge S.C., Mukherjee P., Berman J.I., Henry R.G., Miller S.P., Lu Y., Glenn O.A., Ferriero D.M., Barkovich A.J., Vigneron D.B.: Tractography-based quantitation of diffusion tensor imaging parameters in white matter tracts of preterm newborns. J. Magn. Reson. Imaging 22 (2005) 467–474.
14. Bammer R., Augustin M., Strasser-Fuchs S., Seifert T., Kapeller P., Stollberger R., Ebner F., Hartung H.P., Fazekas F.: Magnetic resonance diffusion tensor imaging for characterizing diffuse and focal white matter abnormalities in multiple sclerosis. Magn. Reson. Med. 44 (2000) 583–591.
15. Cercignani M., Bozzali M., Iannucci G., Comi G., Filippi M.: Magnetisation transfer ratio and mean diffusivity of normal appearing white and grey matter from patients with multiple sclerosis. J. Neurol. Neurosurg. Psychiatry 70 (2001) 311–317.
16. Filippi M., Cercignani M., Inglese M., Horsfield M.A., Comi G.: Diffusion tensor magnetic resonance imaging in multiple sclerosis. Neurology 56 (2001) 304–311.
17. Werring D.J., Clark C.A., Barker G.J., Thompson A.J., Miller D.H.: Diffusion tensor imaging of lesions and normal-appearing white matter in multiple sclerosis. Neurology 52 (1999) 1626–1632.
18. Nusbaum A.O., Lu D., Tang C.Y., Atlas S.W.: Quantitative diffusion measurements in focal multiple sclerosis lesions: correlations with appearance on T1-weighted MR images. Am. J. Roentgenol. 175 (2000) 821–825.
19. Lin F., Yu C., Jiang T., Li K., Chan P.: Diffusion tensor tractography based group mapping of the pyramidal tract in relapsing-remitting multiple sclerosis patients. Am J Neuroradiol AJNR 28 (2007) 278–282.
20. Allen I.V., McKeown S.R.: A histological, histochemical and biochemical study of the macroscopically normal white matter in multiple sclerosis. J. Neurol. Sci. 41 (1979) 81–91.
21. Bozzali M., Cercignani M., Sormani M.P., Comi G., Filippi M.: Quantification of brain gray matter damage in different MS phenotypes by use of diffusion tensor MR imaging. Am. J. Neuroradiol. 23 (2002) 985–988.
22. Oreja-Guevara C., Rovaris M., Iannucci G., Valsasina P., Caputo D., Cavarretta R., Sormani M.P., Ferrante P., Comi G., Filippi M.: Progressive gray matter damage in patients with relapsing-remitting multiple sclerosis: a longitudinal diffusion tensor magnetic resonance imaging study. Arch. Neurol. 62 (2005) 578–584.
23. Rovaris M., Gallo A., Valsasina P., Benedetti B., Caputo D., Ghezzi A., Montanari E., Sormani M.P., Bertolotto A., Mancardi G., Bergamaschi R., Martinelli V., Comi G., Filippi M.: Short-term accrual of gray matter pathology in patients with progressive multiple sclerosis: an in vivo study using diffusion tensor MRI. Neuroimage 24 (2005) 1139–1146.
24. Kidd D., Barkhof F., McConnell R., Algra P.R., Allen I.V., Revesz T.: Cortical lesions in multiple sclerosis. Brain 122 (1999) 17–26.
25. Iannucci G., Rovaris M., Giacomotti L., Comi G., Filippi M.: Correlation of multiple sclerosis measures derived from T2-weighted, T1-weighted, magnetization transfer, and diffusion tensor MR imaging. Am. J. Neuroradiol. 22 (2001) 1462–1467.
26. Peyser J.M., Edwards K.R., Poser C.M., Filskov S.B.: Cognitive function in patients with multiple sclerosis. Arch. Neurol. 37 (1980) 577–579.
27. Rao S.M., Leo G.J., Bernardin L., Unverzagt F.: Cognitive dysfunction in multiple sclerosis. I. Frequency, patterns, and prediction. Neurology 41 (1991) 685–691.
28. Archibald C.J., Fisk J.D.: Information processing efficiency in patients with multiple sclerosis. J. Clin. Exp. Neuropsychol. 22 (2000) 686–701.
29. Rao S.M., Grafman J., DiGiulio D., Mittenberg W., Bernardin L., Leo G.J., Unverzagt F., Luchetta T.: Memory dysfunction in multiple sclerosis: Its relation to working memory, semantic encoding, and implicit learning. Neuropsychology 7 (1993) 364–374.

30. Beatty W.W., Monson N.: Problem solving by patients with multiple sclerosis: comparison of performance on the Wisconsin and California Card Sorting Test. J. Int. Neuropsychol. Soc. 2 (1996) 134–140.
31. Rovaris M., Iannucci G., Falautano M., Possa F., Martinelli V., Comi G., Filippi M.: Cognitive dysfunction in patients with mildly disabling relapsing-remitting multiple sclerosis: an exploratory study with diffusion tensor MR imaging. J. Neurol. Sci. 195 (2002) 103–109.
32. Lin X., Tench C.R., Morgan P.S., Niepel G., Constantinescu C.S.: 'Importance sampling' in MS: use of diffusion tensor tractography to quantify pathology related to specific impairment. J. Neurol. Sci. 237 (2005) 13–19.
33. Benedict R.H., Bruce J., Dwyer M.G., Weinstock-Guttman B., Tjoa C., Tavazzi E., Munschauer F.E., Zivadinov R.: Diffusion-weighted imaging predicts cognitive impairment in multiple sclerosis. Mult. Scler. 13 (2007) 722–730.
34. Filippi M., Rocca M.A., Moiola L., Martinelli V., Ghezzi A., Capra R., Salvi F., Comi G.: MRI and magnetization transfer imaging changes in the brain and cervical cord of patients with Devic's neuromyelitis optica. Neurology 53 (1999) 1705–1710.
35. Rocca M.A., Agosta F., Mezzapesa D.M., Martinelli V., Salvi F., Ghezzi A., Bergamaschi R., Comi G., Filippi M.: Magnetization transfer and diffusion tensor MRI show gray matter damage in neuromyelitis optica. Neurology 62 (2004) 476–478.
36. Yu C.S., Lin F.C., Li K.C., Jiang T.Z., Zhu C.Z., Qin W., Sun H., Chan P.: Diffusion tensor imaging in the assessment of normal-appearing brain tissue damage in relapsing neuromyelitis optica. Am. J. Neuroradiol. 27 (2006) 1009–1015.
37. Yu C.S., Lin F.C., Li K.C., Jiang T.Z., Qin W., Sun H., Chan P.: Pathogenesis of brain normal-appearing white matter damage in neuromyelitis optica: diffusion tensor MRI. Radiology (in press).
38. Ghezzi A., Bergamaschi R., Martinelli V., Trojano M., Tola M.R., Merelli E., Mancardi L., Gallo P., Filippi M., Zaffaroni M., Comi G.: Italian Devic's Study Group (IDESG). Clinical characteristics, course and prognosis of relapsing Devic's Neuromyelitis Optica. J. Neurol. 251 (2004) 47–52.
39. Lucchinetti C.F., Mandler R.N., McGavern D., Bruck W., Gleich G., Ransohoff R.M., Trebst C., Weinshenker B., Wingerchuk D., Parisi J.E., Lassmann H.: A role for humoral mechanisms in the pathogenesis of Devic's neuromyelitis optica. Brain. 125 (2002) 1450–1461.
40. Mandler R.N., Davis L.E., Jeffery D.R., Kornfeld M.: Devic's neuromyelitis optica: a clinicopathological study of 8 patients. Ann. Neurol. 34 (1993) 162–168.
41. Wingerchuk D.M., Weinshenker B.G.: Neuromyelitis optica: clinical predictors of a relapsing course and survival. Neurology 60 (2003) 848–853.
42. Keegan M., Pineda A.A., McClelland R.L., Darby C.H., Rodriguez M., Weinshenker B.G.: Plasma exchange for severe attacks of CNS demyelination: predictors of response. Neurology 58 (2002) 143–146.
43. Saida T., Tashiro K., Itoyama Y., Sato T., Ohashi Y., Zhao Z.: Interferon Beta-1b Multiple Sclerosis Study Group of Japan. Interferon beta-1b is effective in Japanese RRMS patients: a randomized, multicenter study. Neurology 64 (2005) 621–630.
44. Lin F., Yu C., Jiang T., Li K., Zhu C., Zhu W., Qin W., Duan Y., Xuan Y., Sun H., Chan P.: Discriminative analysis of neuromyelitis optica and multiple sclerosis based on two-dimensional histogram from diffusion tensor imaging. Neuroimage 31 (2006) 543–549.
45. Yu C.S., Zhu C.Z., Li K.C., Xuan Y., Qin W., Sun H., Chan P.: Relapsing neuromyelitis optica and relapsing-remitting multiple sclerosis: differentiation at diffusion-tensor MR imaging of corpus callosum. Radiology 244 (2007) 249–256.

Chapter 96
^{1}H MRS Characterization of Cerebral Metabolic Changes in Transgenic Mouse Models of Alzheimer's Disease

Xiaoxia Du and Hao Lei

Abstract Recently developed transgenic mouse models of Alzheimer's disease (AD) exhibit many features of human AD pathology. Proton magnetic resonance spectroscopy (1H MRS) is a useful tool for characterizing and monitoring the metabolic changes and the progression of the disease in both human AD patients and transgenic mouse models of AD. In this paper, we review recent 1H MRS findings in the transgenic mouse models of AD and compare the results obtained from the animal models to those observed in human patients. The main 1H MRS findings in the transgenic mouse models are significantly reduced cerebral N-acetyl aspartate (NAA) and glutamate levels and significantly increased cerebral myo-inositol level. These results agree well with the findings in human AD brains. It can be expected that the combined use of 1H MRS and transgenic mouse models of AD will help us accelerate drug discovery for AD.

Keywords Alzheimer's disease · magnetic resonance spectroscopy · animal model · transgenic mouse · brain · metabolism

Introduction

Alzheimer's disease (AD) is the most common cause of dementia in the elderly. The two main hallmarks of the disease are deposition of β–amyloid (Aβ) plaques and neurofibrillar tangles [1]. Currently a definitive diagnosis of AD is only possible by postmortem evaluation. There is a great clinical need of biomarkers that can be used for the diagnosis of AD with high specificity and sensitivity and for the preclinical drug test. Transgenic (Tg) mouse models of AD have been developed for mechanistic studies of the disease as well as for testing therapeutics. The Tg mice express familial AD-related mutated amyloid precursor protein (APP) or presenilin

H. Lei
State Key Laboratory of Magnetic Resonance and Atomic and Molecular Physics, Wuhan Institute of Physics and Mathematics, Chinese Academy of Sciences, Xiaohongshan West 30#, Wuhan, Hubei, P.R. China
e-mail: leihao@wipm.ac.cn

R. Wang et al. (eds.), *Advances in Cognitive Neurodynamics*,

(PS1 or PS2) genes [2], and show many features of AD pathology including the development of extra-cellular Aβ deposits.

^{1}H magnetic resonance spectroscopy (MRS) offers a non-invasive way to assay cerebral metabolism in vivo, and has been widely applied in the studies of neurodegenerative disorders. It has been shown that AD patients often exhibit abnormalities in cerebral metabolism, and AD-related metabolic alterations are thought to be related to the pathological processes at the molecular or cellular level [3]. In this paper, we review the recent reports on ^{1}H MRS-observable changes of cerebral metabolism in the Tg mouse models of AD, and compare the findings in the animal models to those observed in the AD patients.

Changes of NAA in AD

N-acetyl aspartate (NAA) is an amino acid found only in neurons of the adult brain, and has been proposed as a putative marker of neuronal density. NAA level is also reported to be related to the metabolic state of neurons [4]. A reduction of NAA is commonly interpreted as a result of neuronal dysfunction or neuronal loss. The brain of AD patients shows diffuse NAA reductions, involving a network of brain regions including hippocampus, medial temporal lobes, parietal lobes, occipital lobes and frontal lobes [5, 6].

Compared to the wild-type (WT) mice, the APP and SP2APP Tg mice show significantly reduced NAA/total creatine (tCr) ratio in the frontal cortex [7, 8], and the APP-PS1 Tg mice have reduced NAA/Cr ratio in both the cortex and the hippocampus [3, 9, 10]. These observations are in accordance with the ^{1}H MRS findings in human AD patients.

Different strains of Tg mouse were found to have plaque load at different ages, and ^{1}H MRS-observed NAA reduction in the Tg mice correlates well with the courses of plaque load and disease progression [8]. Significant NAA reduction was found to occur the earliest in the APP-PS1 Tg mice at 6.5 to 9 months after birth [10] and the latest in the PS2APP Tg mice at 20 to 24 months of age [8]. Clinically reduction of NAA has been used as an indicator of disease progression in the AD patients, and to differentiate stable mild cognitive impairment (MCI) from progressive MCI [11].

Changes of Glu and Gln in AD

Glutamate is an important and abundant excitatory neurotransmitter in the central nervous system (CNS). At clinical field strengths (i.e., 1.5-3T), the resonance of Glu overlaps severely with that of glutamine (Gln) so that the two metabolites are often measured together as glutamate + glutamine (Glx) [12]. Measurements of cerebral Glx level in AD patients have yielded somewhat inconsistent results. There are reports showing that the Glx level is reduced in the occipital gray matter [13] and cingulate region of AD patients [14], and the amplitude of Glx reduction is

correlated with Mini-Mental State Examination scores [14]. However, there are also results showing elevated Glx/tCr ratio in the temporal lobe of AD patients [15].

Compared to the WT mice, all three strains of Tg mouse showed significantly reduced Glu/tCr ratio in the brain [3, 7, 8, 9, 10]. In addition, von Kienlin et al. found a negative (though non-significant) correlation between cerebral Glu level and plaque load [8]. Oberg et al. found a significant negative correlation between the cerebral Glu level and the age of the Tg and WT animals [10]. More importantly, with the Tg mouse models it would be possible to measure Glu and Gln individually at high field strength so that the roles of the two metabolites in the pathology of AD can be evaluated separately.

Changes of mIns and Tau in AD

Myo-inositol is a sugar alcohol that is thought to be a marker for osmotic stress and astrogliosis. Many previous 1H MRS studies have found significant increased levels of mIns in the temporal, parietal and occipital lobes of AD patients [12, 13, 15, 16]. However, there are also studies reported unchanged mIns levels in the paratrigonal white matter and temporal lobe [11, 17]. Using NAA/mIns ratio as a marker for AD has showed enhanced diagnostic sensitivity and specificity [18].

Cerebral mIns level has been found to change significantly with age in the APP-PS1 Tg mice. Compared to the WT mice, The Tg mice have similar cerebral mIns levels before 400 days of age [3, 10], but drastically increased cerebral mIns levels after the age of 600 days [3, 9]. The increase in the cerebral mIns level has been attributed to microglial activation, which may accelerate around 20 postnatal months [3, 9]. The cerebral mIns level in the frontal cortex APP mice was found to be similar to that in the WT mice. However, this strain of Tg mouse showed significantly elevated level of taurine (Tau), a metabolite predominantly present in the glia, in the frontal cortex [7]. No increase of cerebral mIns level or any other indicator of gliosis was observed in the PS2APP Tg mice before 24 months of age [8].

Conclusion

^{1}H MRS provides a useful tool in AD research. Noninvasive measurements of NAA, mIns and Glu by ^{1}H MRS in the Tg mouse models of AD correlate well with the plaque load and histological results, thus can be used as surrogates for monitoring the progression of the disease. More importantly, these Tg mice exhibit ^{1}H MRS profiles analogous to that present in human AD patients. Therefore it would be attractive to use ^{1}H MRS, because of its noninvasive and repeatable nature, for treatment monitoring and response prediction when the Tg mouse models of AD are used for drug test [19].

Acknowledgments The work is supported by an 863 project (2006AA02Z4A1) from the Ministry of Science and Technology of China.

References

1. Braak, H., Braak, E.: Diagnostic criteria for neuropathologic assessment of Alzheimer's disease. Neurobiol. Aging 18 (1997) S85–S88.
2. German, D.C., Eisch, A.J.: Mouse models of Alzheimer's disease: insight into treatment. Rev. Neurosci. 15 (2004) 353–369.
3. Marjanska, M., Curran, G.L., Wengenack, T.M., Henry, P.G., Bliss, R.L., Poduslo, J.F., Jack, C.R., Jr., Ugurbil, K., Garwood, M.: Monitoring disease progression in transgenic mouse models of Alzheimer's disease with proton magnetic resonance spectroscopy. Proc. Natl. Acad. Sci. U. S. A. 102 (2005) 11906–11910.
4. Bates, T.E., Strangward, M., Keelan, J., Davey, G.P., Munro, P.M., Clark, J.B.: Inhibition of N-acetylaspartate production: implications for 1H MRS studies in vivo. Neuroreport 7 (1996) 1397–1400.
5. Ackl, N., Ising, M., Schreiber, Y.A., Atiya, M., Sonntag, A., Auer, D.P.: Hippocampal metabolic abnormalities in mild cognitive impairment and Alzheimer's disease. Neurosci. Lett. 384 (2005) 23–28.
6. Valenzuela, M.J., Sachdev, P.: Magnetic resonance spectroscopy in AD. Neurology 56 (2001) 592–598.
7. Dedeoglu, A., Choi, J.K., Cormier, K., Kowall, N.W., Jenkins, B.G.: Magnetic resonance spectroscopic analysis of Alzheimer's disease mouse brain that express mutant human APP shows altered neurochemical profile. Brain Res. 1012 (2004) 60–65.
8. von Kienlin, M., Kunnecke, B., Metzger, F., Steiner, G., Richards, J.G., Ozmen, L., Jacobsen, H., Loetscher, H.: Altered metabolic profile in the frontal cortex of PS2APP transgenic mice, monitored throughout their life span. Neurobiol. Dis. 18 (2005) 32–39.
9. Jack, C.R., Jr., Marjanska, M., Wengenack, T.M., Reyes, D.A., Curran, G.L., Lin, J., Preboske, G.M., Poduslo, J.F., Garwood, M.: Magnetic resonance imaging of Alzheimer's pathology in the brains of living transgenic mice: a new tool in Alzheimer's disease research. Neuroscientist 13 (2007) 38–48.
10. Oberg, J., Spenger, C., Wang, F.H., Andersson, A., Westman, E., Skoglund, P., Sunnemark, D., Norinder, U., Klason, T., Wahlund, L.O., Lindberg, M.: Age related changes in brain metabolites observed by (1)H MRS in APP/PS1 mice. Neurobiol. Aging (2007).
11. Metastasio, A., Rinaldi, P., Tarducci, R., Mariani, E., Feliziani, F.T., Cherubini, A., Pelliccioli, G.P., Gobbi, G., Senin, U., Mecocci, P.: Conversion of MCI to dementia: Role of proton magnetic resonance spectroscopy. Neurobiol. Aging 27 (2006) 926–932.
12. Jones, R.S., Waldman, A.D.: 1H-MRS evaluation of metabolism in Alzheimer's disease and vascular dementia. Neurol. Res. 26 (2004) 488–495.
13. Moats, R.A., Ernst, T., Shonk, T.K., Ross, B.D.: Abnormal cerebral metabolite concentrations in patients with probable Alzheimer disease. Magn. Reson. Med. 32 (1994) 110–115.
14. Antuono, P.G., Jones, J.L., Wang, Y., Li, S.J.: Decreased glutamate + glutamine in Alzheimer's disease detected in vivo with (1)H-MRS at 0.5 T. Neurology 56 (2001) 737–742.
15. Herminghaus, S., Frolich, L., Gorriz, C., Pilatus, U., Dierks, T., Wittsack, H.J., Lanfermann, H., Maurer, K., Zanella, F.E.: Brain metabolism in Alzheimer disease and vascular dementia assessed by in vivo proton magnetic resonance spectroscopy. Psychiatry Res. 123 (2003) 183–190.
16. Kantarci, K., Petersen, R.C., Boeve, B.F., Knopman, D.S., Tang-Wai, D.F., O'Brien, P.C., Weigand, S.D., Edland, S.D., Smith, G.E., Ivnik, R.J., Ferman, T.J., Tangalos, E.G., Jack, C.R., Jr.: 1H MR spectroscopy in common dementias. Neurology 63 (2004) 1393–1398.
17. Frederick, B.D., Lyoo, I.K., Satlin, A., Ahn, K.H., Kim, M.J., Yurgelun-Todd, D.A., Cohen, B.M., Renshaw, P.F.: In vivo proton magnetic resonance spectroscopy of the temporal lobe in Alzheimer's disease. Prog. Neuropsychopharmacol. Biol. Psychiatry 28 (2004) 1313–1322.

18. Parnetti, L., Tarducci, R., Presciutti, O., Lowenthal, D.T., Pippi, M., Palumbo, B., Gobbi, G., Pelliccioli, G.P., Senin, U.: Proton magnetic resonance spectroscopy can differentiate Alzheimer's disease from normal aging. Mech. Ageing Dev. 97 (1997) 9–14.
19. Jessen, F., Traeber, F., Freymann, K., Maier, W., Schild, H.H., Block, W.: Treatment monitoring and response prediction with proton MR spectroscopy in AD. Neurology 67 (2006) 528–530.

Chapter 97
WLC Analysis of Lamprey Neural System

Liu Shenquan, Chen Shuchun and Wang Rubin

Abstract The paper simulates membrane potential of Lamprey neural circuit based on WLC model. The influences parameter of RS and SR neuron stimulation are numerically analyzed. The results show that left or right motoneuron will appear alternately spike in circumstance of external stimulation. In alternate-current stimulation the ISI sequences of motoneuron will have periodical increase. Also it shows transforming of motoneuron frequent from left to right motoneuron. These results explain the experiment phenomena when lamprey was influenced by electrical stimulation.

Keywords Lamprey · ISI · motoneuron · stretch receptor neuron

Introduction

The Vertebrate neural system of mammals is very complex. Its structure contains numerous neurons form different central pattern generators. There are many specialists doing research in lamprey experiment, especially on the rhythm caused by central pattern generator [1]. The experiments study the influence of synaptic strength and lamprey pattern activity by modulating dopamine concentrations and reveal essential properties.

In order to analyze the rhythm of neuron in the lamprey system, we not only use the motoneuron rhythm to analyze the locomotor behavior, but also study the lamprey locomotor influenced by external stretching. For example, we can compute the ISI (interspike interval) sequence of neuron spike, and then analyze the relationship between external stimulation and locomotor frequency. As the lamprey system is inhibited neural network the WLC model is used to describe the inhibition of the system, which is composed of brain part and 1-segment neurons. We analyze the influence of motoneuron inputted by external stimulation and discuss the changes

L. Shenquan
Department of Applied Mathematics, School of Mathematical Sciences, South China University of Technology, Guangzhou 510640, China
e-mail: mashqliu@scut.edu.cn

R. Wang et al. (eds.), *Advances in Cognitive Neurodynamics*,

of the neuron ISI sequence. The simulation results here explain the experiment phenomena when we vary the external stimulation.

The Lamprey Network

Based on Sten Grillner's experiment results [2], the lamprey network contains four parts: brainstem neuron, stretch receptor neuron, CPG and motoneuron. There are two kinds of stretch receptor neurons: SR-E neuron is excitatory stretch receptor neuron, while SR-I neuron is inhibitory stretch receptor neuron. CPG is composed of E, I, L neuron. These three neurons can generate motor rhythm. In CPG, E is an excitatory interneuron, while L and I are two kinds of inhibitory interneurons. L neuron can inhibit I neuron in the ipsilateral side. I neuron can inhibit spinal cord cell in the contra lateral side. M is included in every segment.

The lamprey network's synaptic connection is mainly inhibitory synaptic. So we can use WLC model to simulate the head of lamprey neural system [3]. While the excitatory synaptic in the lamprey network can be considered as the perturbation to neuron. The WLC model including excitatory synaptic is described as followed:

$$\frac{dx_i(t)}{dt} = \frac{1}{\tau_1}\left\{x_i(t) - \frac{1}{3}x_i^3(t) - y_i(t) - z_i(t)[x_i(t) - v] + 0.35 + S_i\right\} + \sum_{j\neq i} E_{ji}x_j(t) \tag{97.1}$$

$$\frac{dy_i(t)}{dt} = x_i(t) - by_i(t) + a \quad i = 1, 2, \cdots, 14 \tag{97.2}$$

$$\frac{dz_i(t)}{dt} = \frac{1}{\tau_2}\left\{\sum_j g_{ji}G[x_j(t)] - z_i(t)\right\} \tag{97.3}$$

Where E_{ji} is the strength of excitatory synaptic, which describes as jth neuron excite ith. The parameters of WLC model can be seen references [3].

The Lamprey Model Analysis

Motoneurons Influenced by the Constant Stimulation to SR or RS Neurons

1. The ISI sequence of motoneuron is analyzed when we give a constant external stimulation $S_i = I_i$ to SR neuron or RS neuron. If we choose a set of parameters of the model the alternating spike from neuron RS, L, E, I rhythms appear in Fig. 97.2. These results conform to the experiment phenomena of lamprey [2]. We add constant stimulation to neuron SR-E or SR-I on the left or right side of

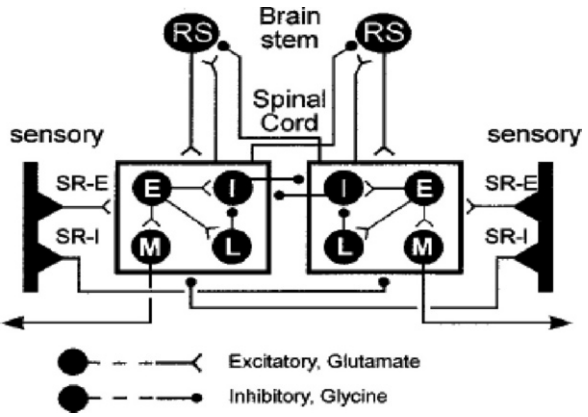

Fig. 97.1 The head network of lamprey

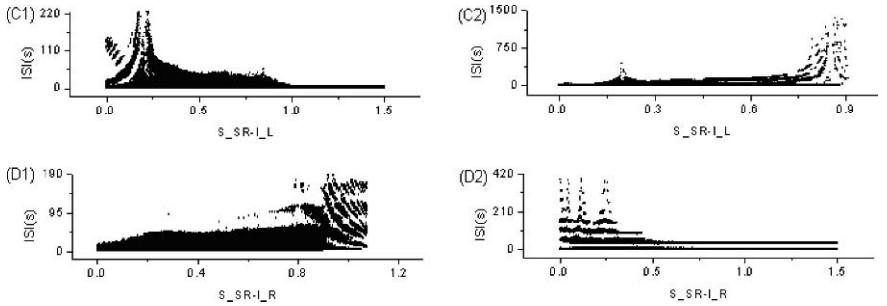

Fig. 97.2 ISI sequence of M neuron by constant stimulation of left SR-I

lamprey network and compute the ISI sequence. Figure 97.2 show, when left SR-I is given an increasing constant stimulation, the rhythm frequency of left M will become slow first and then become fast. While we increase constant stimulation to right SR-I, the rhythm frequency of left M will become fast first and then become slow. These results conform to the experiment phenomenon mentioned in reference [4].

2. When RS neuron is given constant stimulation, lamprey also shows alternate property on two sides of neurons. In Fig. 97.3, it is apparent to see that RS neurons have more information in increasing period phenomena. These results show the head of lamprey controls the body movement. The general rule of controlling movements can be studied by more segments in lamprey network.

The reference [5] shows, when the two sides of spinal cord are given a 100–200 μA pulse or 20 Hz alternate stimulation, the symmetric rhythm phenomena would appear in the neurons in lamprey's dorsal. These results can be explained by model results here.

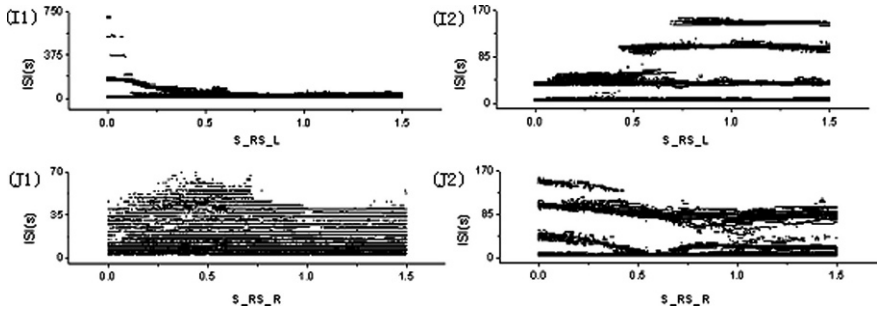

Fig. 97.3 ISI sequence of M neuron by constant stimulation of left RS

Motoneurons Influenced by the Alternate Stimulation of SR or RS Neurons

1. We will study the influences of motoneurons when stretch receptor neuron or RS neuron is given by alternate stimulation, $S_i = I_i \cdot \cos(wt)$. The ISI results can be seen in the following, Fig. 97.4.
2. From Fig. 97.4, we can apparently see that ISI sequence of single motoneuron occur symmetric phenomena. These phenomena can be described as alternate

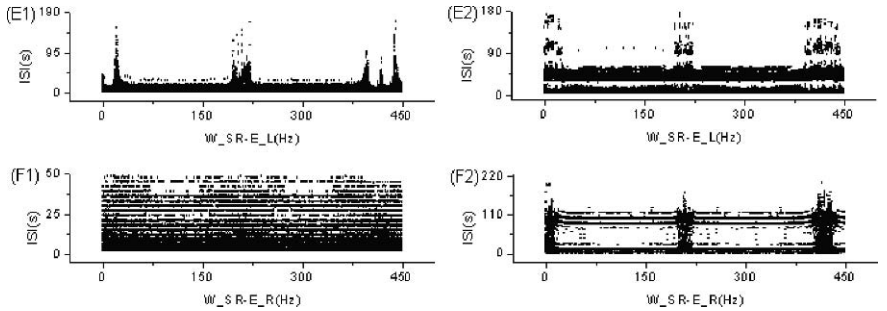

Fig. 97.4 ISI sequence of M neuron by alternate stimulation of SR-E

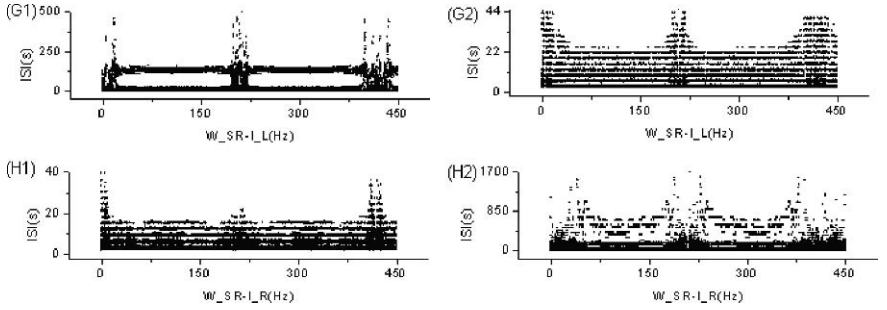

Fig. 97.5 ISI sequence of M neuron by alternate stimulation of SR-I

activity of lamprey. From Figs. 97.4-E1 and 97.4-F2, one can see the alternate stimulation frequency of left or right SR-E increases, the general motor frequency has no difference. In the same way, we can analyze the ISI sequence of single motoneuron when left or right SR-I is given alternate stimulation. These results can be seen in Fig. 97.5.

Discussion

In lamprey spinal cord, our numerical analysis shows the rhythm activity of the two sides motoneuron. The result here shows, WLC model can describe the alternate rhythm of neuron in two sides of lamprey system very well. We also use constant or alternate stimulation of two sides SR neurons to analyze the influence of lamprey rhythm. When single SR neurons are inputted by constant stimulation, the motor frequency of two sides motoneuron will occur alternate phenomena. So that two sides of muscles will transform from the contracting status to the relaxing status or the inverse. This transformation can explain the forward swim or turning of lamprey. When a single SR neuron is inputted by alternate stimulation, the general motor frequency of one side motoneuron will be fast, while the general motor frequency of the other side motoneuron will be slow. So the lamprey will bend from one side to the other side. The ISI results here can explain lamprey's spinal cord has stable ability of controlling movements. This result shows that lamprey's system has high efficiency of information transmission. Using lamprey's system to control robot's movement is also the hot spot of many specialist researches.

Acknowledgments This research was supported by the National Natural Science Foundation of China (Grant Nos. 19902005 and 10432010).

References

1. Örjan Ekeberg, Sten Grillner, Anders Lansner. The Neural Control of Fish Swimming Studied Through Numerical Simulations. Adaptive Behavior, 1995(3): 363–384.
2. Sten Grillner, Peter Wallen. Cellular Bases of a Vertebrate Locomotor System-Steering Intersegment and Segmental Co-Ordination and Sensory Control. Brain Research Reviews, 2002(40): 92–106.
3. Rabinovich M., Volkovskii A., Lecanda P. et al. Dynamical Encoding by Networks of Competing Neuron Group: Winnerless Competition. Physical Review Letters, 2001(068102): 1–4.
4. Andrew D., McClellan, André Hagevik. Descending Control of Turning Locomotor Activity in Larval Lamprey: Neurophysiology and Computer Modeling. The Journal of Neurophysiology, 1997(78): 214–228.
5. Fagerstedt P, Zelenin PV, Deliagina et al. Crossed reciprocal inhibition evoked by electrical stimulation of the lamprey spinal cord. Experimental Brain Research 2000(134): 147–154.

Chapter 98
Hydrocephalus: A Realistic Porous-Media Model with Geometry Based on Neuroimaging

Guillermo Narsilio, Xiaobin Shen, Hongxin Wang, David Smith and Gary Egan

Abstract Hydrocephalus is a condition characterized by abnormal cerebrospinal fluid flow and is usually diagnosed through shape measurements of the ventricular system. In this work, actual brain and skull geometries obtained from MRI scans are incorporated into numerical simulations of the cerebrospinal fluid flow throughout the brain parenchyma Intracranial pressure and fluid velocity fields in the brain tissue in hydrocephalus are calculated using finite element methods. A case-study is used to summarize the procedure.

Keywords Hydrocephalus · intracranial pressure · CSF · numerical modeling · MRI · finite element method

Introduction

Hydrocephalus is a condition where abnormal flow of cerebrospinal fluid (CSF) leads to pressure accumulation inside the skull leading to brain damage and other complications [1] as a result of brain deformation. CSF is mainly produced in the choroid plexus through rather complex process of fluid leaving capillaries and subsequently being modified by ependymal cells. Its production rate ranges from about 100 to 500–600 ml/day depending on age and weight [2]. CSF overproduction, under-reabsortion in arachnoid granulations or obstructions of normal CSF pathways due to birth defects, accidents or infections, may prompt pressure redistributions in the brain, and a change in the CSF volume.

Computational simulations of the CSF space and flow are still in their early stages [3], thus a better hydrodynamic understanding of this condition may lead to new and innovative treatments. Although some brain models for hydrocephalus have been published during the last few years [4, 5] these models extensively simplify the geometry and boundary conditions.

G. Narsilio
Biomedical Engineering Centre, The University of Melbourne, Parkville VIC 3010, Australia
e-mail: narsilio@unimelb.edu.au

R. Wang et al. (eds.), *Advances in Cognitive Neurodynamics*,

In this paper, a novel use of a porous media fluid flow model with realistic domain geometry of the brain and skull based on MRI (Magnetic Resonance Imaging) scans is proposed and implemented. The central aim is to demonstrate body forces arising from fluid gradients on the neural tissue lead to the abnormal growth during development of the brain. A case-study is used to exemplify these ideas.

Brain Model Geometry

Realistic geometries of brains and skulls from MRI scans are incorporated into the multiphysics COMSOL finite element package. This requires three steps: (1) MRI data acquisition, (2) Tissue classification segmentation, (3) Importation and meshing.

Data from a 1.5 Tesla MR scanner are used (T1W, 1.5 mm coronal slices, TR 35 ms, TE 9 ms, 18 cm field of view; and T2W, 3 mm coronal slices, TR 4000 ms, TE 60/160 ms). Tissue classification segmentation is done using the Warfield's adaptive, template-moderated, spatially-varying statistical classification [6]. Similarly, axial slides are segmented based on pixel (rather than voxel) values. To facilitate our purpose, we focus on two (coronal and axial) slices (Fig. 98.1).

Hydraulic Model

It is assumed brain tissue can be treated as a porous material, with fluid flow through the extracellular compartments of the brain [4, 5]. A Darcy's model is employed to simulate the basic physics of porous media fluid flow in a hydrocephalus patient.

The movement of CSF through the porous brain parenchyma is given by:

$$U = \left(k \big/ \rho_{CSF} \cdot g\right) \nabla p \tag{98.1}$$

where U is the (Darcian) filtration velocity [m/s], k is the hydraulic conductivity [m/s], ρ_{CSF} is the fluid density [1000 kg/m^3], g is the acceleration of gravity

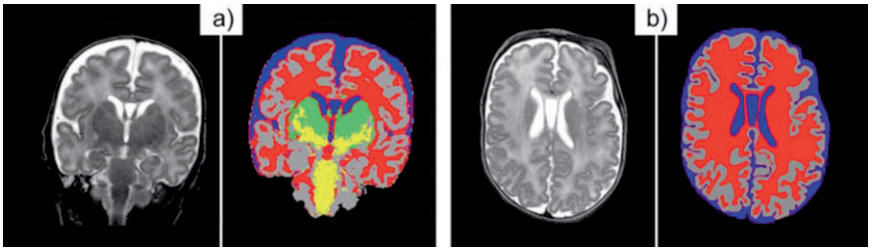

Fig. 98.1 Coronal (**a**) and axial (**b**) MRI and tissue classification segmentation: White matter (red), gray matter (gray), CSF (blue), myelinated white matter (yellow), basal-ganglia (green)

[9.81 m/s^2] and ∇p is the pressure gradient [Pa/m]. Conservation of fluid mass (assuming no CSF absorption in the brain tissues – this assumption may be easily relaxed, but evidence for this is yet to be established), yields the governing equation under quasi-steady state conditions:

$$\nabla \cdot \left[k \big/ (\rho_{CSF} \cdot g) \nabla p \right] = 0 \tag{98.2}$$

Equation (98.2) must be supplemented with appropriate boundary conditions: CSF production rate in the ventricles (i.e. a flux boundary conditions), no flux through the skull, and pressure boundary condition in the subdural space, together with continuity of fluid pressure and flow at the interface between white and grey matter.

We distinguish two regions with different hydraulic conductivity k based on tissue type (Fig. 98.1): $k_w = 1.542 \times 10^{-7}$ m/s for the white matter [7], and a range varying between $k_g = 1.542 \times 10^{-8}$ m/s and $k_g = 1.542 \times 10^{-9}$ m/s for the gray matter [5, 7].

The CSF production rate is estimated in 100 ml/day for the infant analyzed here [2], and the pressure in the inner surface of the skull is prescribed at $p_b = 650$ Pa (typical value for venous blood pressure) [4, 8].

Results and Discussion

We solve Eq. 98.2 numerically using the finite element method, on realistic 2D geometries (Section 'Brain Model Geometry'). In this preliminary study, we explore the effect of the likely k-values for the gray matter. Figure 98.2 summarizes the results, showing CSF pressure and velocity fields. Figure 98.2a shows pressure distributions in the coronal and axial slices, for the case where $k_w = 1.542 \times 10^{-7}$ m/s and $k_g = 1.542 \times 10^{-9}$ m/s (*high contrast hydraulic conductivity*); and when $k_g = 1.542 \times 10^{-8}$ m/s (*low contrast hydraulic conductivity*). Figure 98.2b shows the corresponding velocity fields. In other words, we compare cases where the hydraulic conductivity differs in the gray matter by one order of magnitude. CSF flow paths are perpendicular to pressure equipotential lines.

Velocity and pressure fields are computed using these realistic domain geometries for the first time, overcoming the usual simplified geometries currently found in the literature. We have effectively developed procedures to include these realistic geometries and parameters from MR images into numerical simulations.

In case of obstructive hydrocephalus, a large proportion of the CSF produced in the ventricles flows throughout the brain parenchyma encountering much greater resistance than following the normal ventricular and canal pathways. We note that in poroelasticity theory, pressure gradients through the brain act as body forces in the equilibrium equations describing balance of momentum. We postulate that these body forces lead to mechanical deformation of the brain, abnormal growth during development, and the characteristic shape of the head in hydrocephalus.

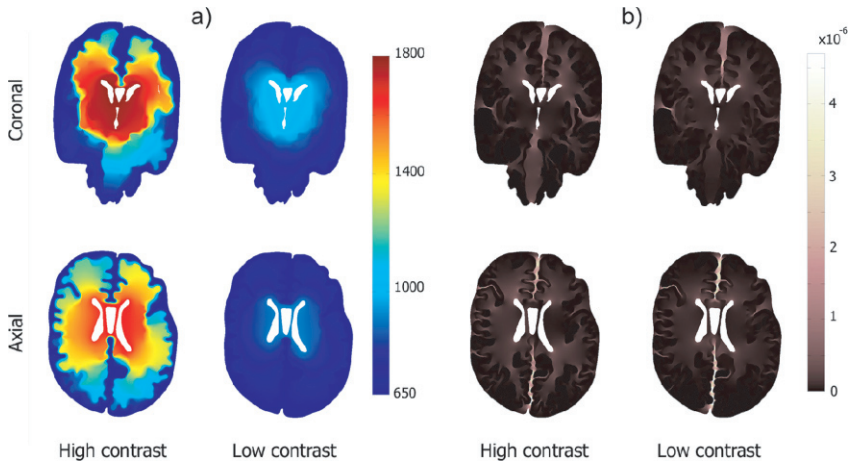

Fig. 98.2 Pressure [Pa] (**a**) and velocity [m/s] (**b**) fields for a coronal and an axial slice. Comparison between high hydraulic conductivity impedance with $k_w = 1.542 \times 10^{-7}$ m/s and $k_g = 1.542 \times 10^{-9}$ m/s (high contrast); and lower contrast when $k_g = 1.542 \times 10^{-8}$ m/s (low contrast)

In Fig. 98.2 (*high contrast*), the larger hydraulic conductivity impedance of the gray matter concentrate the largest pressure gradients in the gray matter. This modeling suggests that traction is applied to the outer cortex of the brain, pulling the developing brain outward, followed by the deformation of the tissue upstream, and dragging the ventricles walls outward.

Finally, further investigation will be done considering 3D geometry, anisotropy in the hydraulic conductivity, losses of fluid into the venous and lymphatic, deformations predicted by poroelasticity, and evaluations of the re-distribution of hydraulic pressure with the introduction of a shunt.

Acknowledgments Support for this research was provided by the University of Melbourne. The Royal Children Hospital MR Centre, Victorian Infant Brain Study provided the MR images. Thanks Simon Warfield for use of "Tissue Classification Segmentation" software (coronal).

References

1. Van De Graaff, K.: Human Anatomy, Wm. C. Brown Publishers, Dubuque, IO (1984).
2. Yasuda, T., Tomita, T., McLone, D., Donovan, M.: Measurement of Cerebrospinal Fluid Output Through External Ventricular Drainage in One Hundred Infants and Children: Correlation with Cerebrospinal Fluid Production, Pediatr. Neurosurg. 36, 22–28 (2002)
3. Kurtcuoglu, V., Soellinger, M., Summers, P., Boomsma, K., Poulikakos, D., Boesiger, P., Ventikos, Y.: Reconstruction of Cerebrospinal Fluid Flow in the Third Ventricle Based on MRI Data. In: Duncan, J., Gerig, G. (eds.) 8th International Conference on Medical Image Computing and Computer-Assisted Intervention – MICCAI 2005, Vol. 3749 LNCS, pp. 786–793. Springer Verlag, Heidelberg (2005).

4. Sivaloganathan, S., Stastna, M., Tenti, G., Drake, J.: A Viscoelastic Model of the Brain Parenchyma with Pulsatile Ventricular Pressure, App. Math. Comput. 165, 687–698 (2005).
5. Smillie, A., Sobey, I., Molnar, Z.: A Hydroelastic Model of Hydrocephalus, J. Fluid Mech. 539, 417–443 (2005).
6. Warfield, S.: Fast k-NN Classification for Multichannel Image Data, Pattern Recog. Lett. 17, 713–721 (1996).
7. Kaczmarek, M., Subramaniam, R.P., Neff, S.R.: The Hydromechanics of Hydrocephalus: Steady-State Solutions for Cylindrical Geometry, Bull. Math. Biol. 59, 295–323 (1997).
8. Pairaudeau, P.W., Smith, S.L., Hames, T.K., Hall, M.A.: Strain-Gauge Fontanometry – an Advance in Noninvasive Intracranial-Pressure Measurement, Clin. Phys. Physiol. Meas. 11, 125–134 (1990).

Chapter 99
Pattern Classification of Visual Evoked Potentials Based on Parallel Factor Analysis

Jie Li, Liqing Zhang and Qibin Zhao

Abstract Visual Evoked Potentials (VEPs) reflect the brain's mental process to specific stimuli, including perception and recognition. Feature analysis of VEPs evoked by geometric figures is of significance in understanding visual neural mechanism and has potential applications in the field of brain computer interface and biomedical engineering. We use Parallel Factor (PARAFAC) model to extract features of the VEPs triggered by three classes of geometric figures, and construct the computational model for class discrimination. PARAFAC is used to decompose the wavelet transformed VEPs. Then by the proposed computational model, we can project single trial data into the subspace spanned by *channel* $\times$ *frequency* $\times$ *time* of the factors to obtain the feature vectors. We further use SVM to classify the feature vectors of the selected two classes, achieving the highest classification accuracy 80%.

Introduction

Visual Evoked Potentials (VEPs) represent the EEG response to visual stimuli triggered by a series of flashes presented to the subject's eyes, and are contaminated by other ongoing background EEG activity. Analysis of the EEG activity in $channel \times time \times frequency$ has been proven to be an effective method to extract the features of evoked potentials [1, 2, 3, 4]. The traditional feature extraction methods such as PCA and ICA, can only analyze such data by unfolding the multi-way arrays into matrices, and it excludes the specific information endorsed by the modalities. The multi-way model PARAFAC has been an exploratory tool in analysis of these data [5, 6].

J. Li
Department of Computer Science and Engineering Shanghai Jiao Tong Univeristy, Shanghai 200240, China
e-mail: lijie1216@sjtu.edu.cn

R. Wang et al. (eds.), *Advances in Cognitive Neurodynamics*,

In this paper, we use PARAFAC model to analyze spatial-temporal-frequency features of VEPs evoked by geometric figures, and construct a computational model for class discrimination of single trial data.

Experiment Setup and Data Acquisition

Three healthy male subjects, aged from 21 to 30, participated in the experiment. In each trial, one of geometric figures, the circle, square and triangle, was presented to the subjects according to the sequence illustrated in Fig. 99.1. The frequency of stimulus is about 15 Hz.

EEG signals were recorded, sampled at 1000 Hz and bandpass filtered between 0.1 Hz and 200 Hz by the NeuroScan System. Sixty-four channels of signals including 62 channels of EEG and two channels of EOG were recorded. Each trial lasted 3500 ms. The data were cut into epochs(-200 ms to $+1000$ ms).

The PARAFAC Analysis

In this section, we will briefly introduce the PARAFAC model and propose a computational model for class discrimination of VEPs.

The PARAFAC Model

A Parallel Factors Model (PARAFAC) of an N-way array $\mathcal{T}$ is a decomposition of $\mathcal{T}$ in a minimal sum of rank-1 factors [7]. The classical approach of estimating the PARAFAC model is using Alternating Least Squares (ALS), minimizing

$$f(A, B, C) = \| \mathcal{T} - \sum_{r=1}^{n} (A_r \circ B_r \circ C_r) \|^2 . \tag{99.1}$$

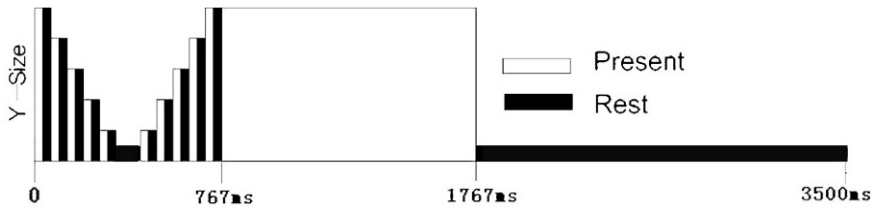

Fig. 99.1 A stimulus sequence in one trial. The X and Y axis show the duration of the presence of the figure stimulus and the relative size of the figure respectively

where, the $A_r \circ B_r \circ C_r$ is the outer product of the r-th factor's mode matrices (To simplifying the illustration, we take the PARAFAC model of a 3-way array for example).

In this paper, neither multi-way array, nor the mode matrices, can take negative values, therefore the Non-negative Multi-Way Factorization (NMWF) algorithm [8] was employed.

The Computational Model for Class Discrimination

A 4-way ($channel \times frequency \times time \times class$) array of the Event-Related Spectral Perturbation (ERSP) in assemble average data, $\mathcal{ERSP}^{(Nd \times Nf \times Nt \times Nc)}$, where Nd, Nf, Nt, Nc is the number of channels, steps of frequency, time points, and classes respectively, can be decomposed by the PARAFAC model and expressed by the 4-mode matricization:

$$ERSP^{(Nc \times NdNfNt)} = D(C \odot B \odot A)^T, \tag{99.2}$$

where, the A, B, C and D is the channel, frequency, time and class mode matrix, and the $C \odot B \odot A$ is the Khatri Rao product of C, B and A. Given the ERSP of a single trial data, denoted by $\mathcal{X}$, the class mode matrix D' of $\mathcal{X}$ can be obtained by projecting $\mathcal{X}$ into the subspace spanned by the $C \odot B \odot A$ using least squares.

$$D' = (P^T P)^{-1} P^T X^{NdNfNt \times 1}, \tag{99.3}$$

where $P = (C \odot B \odot A)$, and the $X^{NdNfNt \times 1}$ is the 4-mode matricization of the multi-way array $\mathcal{X}^{Nd \times Nf \times Nt}$.

Simulations and Results

In this section, PARAFAC is applied to wavelet transformed VEPs, and the application and performance of the proposed computational model will be given.

The VEPs exhibit a great diversity between subjects. For a certain subject, the wavelet transformed EEG data given by ERSP is calculated in assemble average data. The 4-way of $\mathcal{ERSP}_{(c,f,t,c)}$ is the ERSP at channel c at frequency f at time t in class c, which is calculated in the channel-time-frequency range (62 channel; −200–1000 ms; 5–100 Hz) for each class. A twenty-factor PARAFAC model is calculated to detect similarity and difference of the VEPs evoked by different figures. Among those decomposition factors, two factors present significantly differences between class 1, 2 and class 3 in the dorsal stream as shown in Fig. 99.2. It is clear that those factors could reveal the differences among three classes especially between class 1, 2 and class 3.

By the proposed computational model, we obtain the class features of single trial VEPs, then use the SVM as the classifier, in which the Gaussian Radial Basis

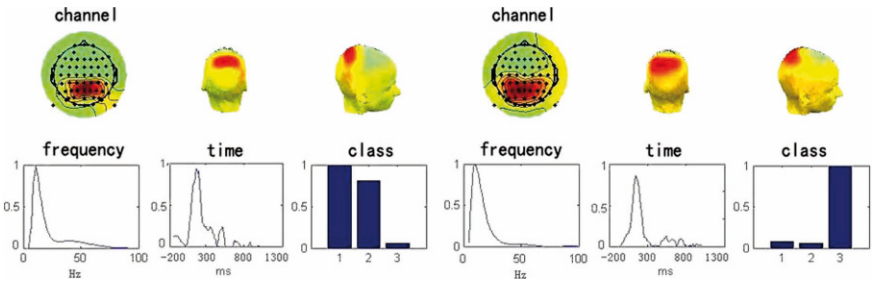

Fig. 99.2 Two factors present significantly differences between class 1, 2 and class 3

Table 99.1 The classification results

Subject	Circle square %	Circle triangle %	Square triangle %
sub1	67.0	81.0	76.0
sub2	68.0	70.0	75.0
sub3	65.0	76.0	75.0

function (RBF) is used as the kernel function. The classification results are listed in Table 99.1.

Discussions and Conclusions

The 4-way ($channel \times frequency \times time \times class$) analysis of wavelet data (ERSP) by PARAFAC model signify the VEPs evoked by figures could be detected in the dorsal stream. Then the computational model for class discrimination is applied to single trial VEPs, and the classification results demonstrate the proposed model is efficient for classifying VEPs. However, the classification accuracy is still not satisfactory, it is assumed that the EEG data is rather nosiy, resulting in some single trial VEPs deviated too much from the mean activity.

Acknowledgments The work was supported by the National Basic Research Program of China (Grant No. 2005CB724301) and the National High-Tech Research Program of China (Grant No.2006AA01Z125).

References

1. Gruber, T., Malinowski, P., Muller, M.: Modulation of oscillatory brain activity and evoked potentials in a repetition priming task in the human EEG. Eur. J. Neurosci. **19** (2004) 1073–1082.
2. Gruber, W., Klimesch, W., Sauseng, P., Doppelmayr, M.: Alpha phase synchronization predicts P1 and N1 latency and amplitude size. Cereb. Cortex **15** (2005) 371–377.
3. Jansen, B., Hegde, A., Boutros, N.: Contribution of different EEG frequencies to auditory evoked potential abnormalities in schizophrenia. Clin. Neurophysiol. **115** (2004) 523–533.

4. Jones, K., Begleiter, H., Porjesz, B., Wang, K., Chorlian, D.: Complexity measures of event related potential surface laplacian data calculated using the wavelet packet transform. Brain Topogr. **14** (2002) 333–344.
5. Miwakeichi, F., Nez-Montes, E., Valdes-Sosa, P., Nishiyama, N., Mizuhara, H., Yamaguchi, Y.: Decomposing EEG data into space-time-frequency components using parallel factor analysis. NeuroImage **22** (2004) 1035–1045.
6. Mørup, M., Hansen, L., Herrmann, C., Parnas, J., Arnfred, S.: Parallel factor analysis as an exploratory tool for wavelet transformed event-related EEG. NeuroImage **29** (2006) 938–947.
7. Lathauwer, L., Moor, B., Vandewalle, J.: On the best Rank-1 and Rank-(r1, r2, . . ., rn) approximation of higher-order tensors. Society for Industrial and Applied Mathematics **21** (2000) 1324–1342.
8. Mørup, M., Hansen, L., Parnas, J., Arnfred, S.: Decomposing the time-frequency representation of EEG using non-negative matrix and multi-way factorization. Technical reports (2006).

Chapter 100
How Can We Justify the Use of Lower Animal Models to Understand the Pathophysiology of Schizophrenia?

Anne-Laure Boutillier, Carlos Eduardo Macedo, Marie-Josée Angst and Guy Sandner

Abstract Schizophrenia may result from an alteration of the communication between neurons which results in the perturbation of cognitive functions difficult to analyse since symptoms do not exist in lower animals and most cognitive functions are differently expressed than in humans. In the standard developmental model of "Lipska–Weinberger", a number of passively acquired memories were weaker than in normal animals, whereas more stringent forms of learning were less impaired, what reminds the difficulties of patients. They were interpreted as mismanagements of the capacity to attend automatically to relevant factors of the environment. But, our attempts to model the precise mismanagement of attention still remained unsuccessful. We suggest that more refined behavioural investigations are needed, especially for understanding the management of mental representations. Considering the cellular mechanisms of the disease is an other insight necessary for the development of new therapeutic strategies.

Keywords Models of schizophrenia · brain development · attention · learning · memory · classical conditioning · instrumental learning · histone methylation

Introduction

New prospects for understanding psychopathological processes arose recently. They were based on lower animal research, especially about schizophrenia. Any pathophysiological study has to consider two facets: *simulating the cause of a disease* and *evaluating the consequences* of the simulation. Simulating the cause needs to speculate and focus on a specific cause of the disease (based on epidemiological, clinical or biological findings in patients). We have to produce it experimentally. This can be done only in lower animals for obvious ethical reasons. New prospects

G. Sandner
U666 INSERM & ULP, 11 Rue Humann, 67085 Strasbourg, France
e-mail: sandner@ neurochem.u-strasbg.fr

R. Wang et al. (eds.), *Advances in Cognitive Neurodynamics*,

were provided by the dysconnection hypothesis of schizophrenia. It corresponds to an alteration of the efficiency of information exchanges between separate neuronal networks in the brain. This dysconnection would be the consequence of an abnormal development of the brain combined with some epigenetic factors occurring during puberty [1]. We simulate them by perturbing the brain development with a neonatal lesion of the ventral hippocampus [2], knowing that it elicits abnormal neuronal networks especially at the level of the nucleus accumbens. In other words, the early suppression of the contribution of the hippocampal inputs to this brain area is partially compensated which creates an altered meso-cortico-limbic network [3]. It constitutes a prototypal neuronal dysconnection (modified brain connectivity).

A crucial cognitive disability in patients is their difficulty to manage complex mental representations of the world [4]. The linkage between the fragments of memories is believed to result from neuronal synchrony between distant brain areas [5]. Synchrony is detectable in EEG records and gamma wave activity was related to the synchronization process [6]. The hierarchy of memories could result from their indexation by hippocampal oscillatory neuronal activities [7]. A coherent memory representation is crucial since it guides the acquisition of new memories through proper management of attention, which has been reported to be altered in schizophrenia as soon as in its initial description [8]. It is postulated that the alteration of specific aspects of attention would model what happens in schizophrenia. We postulate three attention management mechanisms to be essential: (1) an inwired form of attention, tested by owershadowing of stimuli during learning where the addition of a stimulus to a target to be remembered decreases its memories, (2) a retrospective form of attention, tested by latent inhibition where the initial familiarisation with a stimulus delays the capacity of an animal to predict a significant outcome, and (3) a prospective form of attention where a targeted action enhances the memory of the target.

We shall illustrate this approach with a number of data, some of which being recently published [9], others being original.

General Methods

We used the classical Lipska–Weinberger model based on neonatal hippocampus lesions in rats. Rats were anesthetized by isoflurane inhalation. Ibotenic acid (lesion) or artificial cerebrospinal fluid (control) was bilaterally infused into the brain. The tip of the injection needle was aimed at the ventral hippocampus. Once adults, the lesioned rats were anesthetized for 15 min and MRI was performed on a scanner operating at 4.7 T (SMIS). The brain was scanned from the frontal cortex to the cerebellum by using consecutive 1-mm-thick coronal slices with a T_2-weighted, spin-echo fast imaging method sequence to detect the lesions. Rats selected for their lesion and sham operated rats were used. Only rats with a substantial bilateral lesion were included. They were submitted to different learning protocols to be described below.

Associative (Pavlovian) and Instrumental Learning with a Reward as Outcome

Method

Two experiments were simultaneously conducted in two sets of rats. In one experiment, a light or a tone preceded the delivery of two sweet food pellets on five occasions every day. Rats explore progressively more and more the food recess towards the end of the light or tone when it signals the occurrence of food (CS +) but not when no food is provided (CS−). This corresponds to pure associative learning (tone or light => food). In the other experiment, the rat had to learn to press 20 times (RR20) a bar to get a sweet beverage. The increasing bar-pressing rates – and to some extend the nose poke activity searching for the reward – is indicative of learning the action-rewarding outcome relationship. This corresponds to a typical instrumental learning (action => beverage).

Result for Associative (Pavlovian) Conditioning

The graph represents the increasing nose poke durations during the last five seconds of the stimulus that announced the pellets. It increased less for the lesioned rats and not at all for the CS-control condition. This means that the lesion impaired but did not totally suppress this form of learning.

Result for Instrumental Conditioning

The bargraph at the right of the figure represents the number of sessions required to get stable bar-pressing rates. Both control (C) and lesioned (L) rats showed the same capacity to learn the task. When tested after this learning stage, in conditions were the outcome had been suppressed (extinction conditions) no difference was found according to the reward used (polycose or sucrose), nor to the lesion status, nor to the progressive extinction process.

Intermediate Conclusion

The most elementary learning method proved to be the more sensitive to the neonatal lesion. It did not consist of a suppression of learning but a decrease of its effect. This is reminiscent of some difficulty that did not exist when instrumental conditioning was used. The major difference between both situations is that rats had to trigger an activity in instrumental learning that necessitated more arousal and some self-awareness. This is supposed to change the level of attention to the situation experienced by the rat. For this reason, we had to explore the contribution

of this factor. The diversity of protocols that may be used to explore attention let us postulate that at least three different forms of management of attention must be considered in lower animals. The first one (called "inwired form") expresses no more than the competition of simultaneously occurring stimuli. It generates the "overshadowing" phenomenon. The second one expresses a competition between the earlier memories of a situation and ongoing experience. It can be tested through the "latent inhibition" phenomenon. The third one considers that animals predict the outcome of their actions and pay attention to such outcomes much more that for events that occur by chance. We developed original experimental strategies for testing the latter.

Overshadowing and Latent Inhibition

Method for Testing Overshadowing

We tested several conditioning methods in which a stimulus was added to the to-be-conditioned stimulus to decrease its salience. All of them provided the same result with lesioned rats. We illustrate these results with the most standard method, using conditioned emotional response. Briefly, a thirsty rat drinks water from a tube. While it drinks, a flashing light is switched on. Basically, the rat remains at drinking. But when the light had been used to announce an electrical shock administered to the rat's paws, it stops drinking for a more or less long period of time beginning with the onset of the light. This arrest of activity, called freezing, was shorter when a tone had been switched on simultaneously to the light during conditioning (not during the test). It "overshadowed" the light.

Result of the Overshadowing Experiment

The bargraph represents the freezing durations in a logarithmic scale. Comparing the durations between lesioned rats (left two bars) with the controls (right two bars) shows a decrease elicited by the lesion. This means that for such a Pavlovian protocol also, there was a reduced expression of conditioning in lesioned rats. Noteworthy, it was not a reward that was used as outcome like in the preceding experiments, but a punishment. There was a similar difference between the grey and hatched bars in control and lesioned rats. The deleterious effect of the presence of a distracting stimulus (the tone) during conditioning was the same in the control and lesioned rats. Its effect in controls was of the same magnitude as the effect of the lesion.

Method for Testing Latent Inhibition

We illustrate also these results with the most standard method, i.e. using conditioned emotional response. Based on its definition (see the slide), latent inhibition appears

as a decrease in the effect of conditioning when a familiar stimulus is used at conditioning rather than a new one. We used a tone. Testing latent inhibition requires a three stage experiment: (1) pre-exposure to the to-be-conditioned stimulus – none or another one being used in the control condition – (2) conditioning and testing.

Result of the Latent Inhibition Experiment

The bargraph represents the freezing durations in a logarithmic scale. Comparing the durations between lesioned rats (left two bars) with the controls (right two bars) shows the usual low conditioning elicited by the lesion. It illustrates that the reduced expression of conditioning in lesioned rats was reproducible. The difference between the grey and hatched bars was the same in control and lesioned rats. This difference expressed the deleterious effect of the pre-exposures on memories. Its effect was of the same magnitude as the effect of overshadowing.

Second Intermediate Conclusions

The decreased sensitivity to the deleterious effect of lesion obtained in instrumental conditioning cannot be explained by a basic difficulty to manage vigilance, awareness or attention.

Prospects

Biological Modifications Within the Nucleus Accumbens

The neonatal lesion was done just when the axonal endings become stabilized by their activity. The subsequent deprivation of some inputs to nucleus accumbens target cells (and also target cells in other brain areas) may produce some modifications in the expression of the DNA in such cells. This reminds that such modifications have been reported as possible causes of the disease. We started to investigate such effects and found an hypo-expression of dimethylated histones together with an over-expression of BDNF. It would be interesting to elicit directly such changes, i.e. without destroying the ventral hippocampus. It could be achieved by injecting into the brain methylating agents or other drugs known to interfere with the expression of the DNA. But the critical question is to select where the modification has to be produced (nucleus accumbens or prefrontal cortex?) and when (early postnatal period?). Such a decision is bound to pathophysiological hypotheses of schizophrenia.

The Necessity to Focus on Specific Target Cognitive Processes

Many psychopathological models rest on basic behavioural observations. This seems inappropriate for understanding their mechanism. Two directions of research

may become helpful: (1) those evidencing archetypes of self-awareness in lower animals and (2) those studying the biological mechanisms [10] and cognitive phenomena [11, 12] by which the brain constructs a representation of the world. Research on cognitive deficits of schizophrenic patients indicated that it is at this level that may reside the key of the pathophysiology of schizophrenia.

References

1. Stephan KE, Baldeweg T, Friston KJ. Synaptic plasticity and dysconnection in schizophrenia. Biol Psychiatry. 2006;59:929–39.
2. Lipska BK, Weinberger DR. A neurodevelopmental model of schizophrenia: neonatal disconnection of the hippocampus. Neurotox Res. 2002;4:469–75.
3. Goto Y, O'Donnell P. Delayed mesolimbic system alteration in a developmental animal model of schizophrenia. J Neurosci. 2002;22:9070–7.
4. Danion JM, Cuervo C, Piolino P, Huron C, Riutort M, Peretti CS, Eustache F. Conscious recollection in autobiographical memory: an investigation in schizophrenia. Conscious Cogn. 2005;14:535–47.
5. Abeles M, Hayon G, Lehmann D. Modeling compositionality by dynamic binding of synfire chains. J Comput Neurosci. 2004;17:179–201.
6. Cho RY, Konecky RO, Carter CS. Impairments in frontal cortical gamma synchrony and cognitive control in schizophrenia. Proc Natl Acad Sci U S A. 2006;103:19878–83.
7. Eichenbaum H. Hippocampus: mapping or memory? Curr Biol. 2000;10:785–7.
8. Braff DL. Information processing and attention dysfunctions in schizophrenia. Schizophr Bull. 1993;19:233–59.
9. Angst MJ, Macedo CE, Guiberteau T, Sandner G. Alteration of conditioned emotional response and conditioned taste aversion after neonatal ventral hippocampus lesions in rats. Brain Res. 2007;1143:183–92.
10. Bevilaqua LR, Rossato JI, Clarke JH, Medina JH, Izquierdo I, Cammarota M. Inhibition of c-Jun N-terminal kinase in the CA1 region of the dorsal hippocampus blocks extinction of inhibitory avoidance memory. Behav Pharmacol. 2007;18:483–9.
11. Ostlund SB, Balleine BW. Orbitofrontal cortex mediates outcome encoding in Pavlovian but not instrumental conditioning. J Neurosci. 2007;27:4819–25.
12. Petrovich GD, Ross CA, Holland PC, Gallagher M. Medial prefrontal cortex is necessary for an appetitive contextual conditioned stimulus to promote eating in sated rats. J Neurosci. 2007;27:6436–41.

Chapter 101
Monkey Prefrontal Neuronal Activity Modifications after Training in a Cognitive Task

Xue-Lian Qi, Travis Meyer and Christos Constantinidis

Abstract In order to study how training to perform a cognitive task modifies activity of neurons in the primate prefrontal cortex, we recorded neuronal discharges and local field potentials from monkeys before and after training. Prior to training, neurons responded to visual stimuli, demonstrated spatial and feature selectivity, and maintained persistent discharges after the stimulus was offset. Neurons maintained these properties after training. Additionally, after training, activity during the stimulus presentation was decreased in error trials compared to correct trials. Local field potential power below 20 Hz was also diminished during stimulus presentations, after training. These results demonstrate the effects of training on prefrontal neuronal activity as monkeys learn to perform a cognitive task.

Keywords Monkey · neurophysiology · prefrontal cortex · learning · memory · cognition

Introduction

The prefrontal cortex is known to play an important role in higher cognitive functions. Prefrontal lesions cause deficits in the ability to represent information in memory and to plan future actions, and prefrontal dysfunction has been implicated in mental illnesses such as schizophrenia [1]. Several previous experiments have sought to uncover how the discharges of prefrontal cortical neurons relate to sensory and remembered information and to the execution of higher cognitive functions. Early experiments revealed that prefrontal cortical neurons continue to discharge after the offset of sensory stimuli that animals are required to remember [2, 3]. This persistent activity is generally thought to constitute the neural correlate of working

X.-L. Qi
Wake Forest School of Medicine, Department of Neurobiology and Anatomy, Medical Center Blvd, Winston-Salem, NC 27157-1010, USA
e-mail: xqi@wfubmc.edu

R. Wang et al. (eds.), *Advances in Cognitive Neurodynamics*,

memory. In recent years, research has sought to identify neural correlates of more complex operations [4, 5, 6].

These experiments have verified that the prefrontal cortex is activated during the execution of complex cognitive tasks, however previous neurophysiological studies have been performed in animals highly conditioned to perform a stereotypical behavior for hundreds of trials every day. Our understanding of prefrontal cortical physiology relies heavily on the assumption that the patterns of activation observed in monkeys trained to perform a task that engages working memory or higher cognitive functions are the same under more natural conditions. We therefore wished to examine how prefrontal cortical neurons encode the properties of visual of stimuli before the animals have been trained to associate stimuli and responses, and what the effects of training to perform a cognitive task are on prefrontal neuronal responses.

Methods

Two male, rhesus monkeys (*Macaca mulatta*) with no prior training were used in the experiments. Neural recordings were performed in areas 46, 8, 45, and 12 of the prefrontal cortex. Monkeys were first trained to fixate and were rewarded for simply maintaining fixation while visual stimuli were presented in the screen. In each trial two stimuli were presented with a 1.5 s delay period between them. The second stimulus was also followed by a second delay period of 1.5 s, after which the fixation point was extinguished and monkey was rewarded.

The monkeys were subsequently trained to perform an active task, requiring them to remember the two stimuli presented in sequence and determine if they matched each other or not. The active task involved the same stimuli used prior to training. Additionally, after the second delay period, a green and blue square were presented on the screen. The monkey was required to saccade to the green target if the two original stimuli were the same, and to the blue target otherwise. The locations of blue and green targets changed randomly from trial to trial.

Single neuron recordings were performed with arrays of 4–8 microelectrodes. The electrical signal from each electrode was amplified, band-pass filtered between 500 and 8 kHz, and recorded. Local Field Potential (LFP) signals were sampled at 500 Hz and recorded at the same time from each electrode.

We determined whether a neuron responded to visual stimuli by compared neuronal firing during stimulus presentation with the activity during fixation (paired t-test; $p < 0.05$). We also compared neuronal activity between correct trials and error trials in the active task. Neuronal firing rate was normalized for each neuron by the best response in the correct trials. The difference between error trials and correct trials was accessed by comparing averaged firing rate of the best response stimuli (paired t-test, $p < 0.05$).

We performed a power spectrum analysis of LFP recording and calculated power in different frequency ranges. Paired t-tests were performed for each frequency

range between baseline and stimulus presentation. The population response was also collected from all the locations and response from each location were averaged and normalized by the peak power within the block.

Results

We recorded from 855 prefrontal neurons prior to training, during the passive fixation task. We also recorded from 302 neurons after training, while the monkeys performed the active task. We base our analysis on this dataset.

Pre-training

Prior to training, 254 (30%) neurons responded to visual stimuli with a significant elevation of their firing rate above the baseline fixation (paired t-test; $p < 0.05$). We refer to these as "visually responsive" neurons. Of those neurons 171 (67%) neurons had significant selectivity for the spatial location of the stimuli (ANOVA test, $p < 0.05$). Also, 87 (34%) neurons had significant selectivity for the features of the visual stimuli we used. Of the visually responsive neurons, 52 (20%) continued to discharge in the delay period following the first visual stimulus, with a significant elevation in discharge rate over the baseline fixation (paired t-test; $p < 0.05$, corrected for multiple comparisons).

We recorded local field potentials from 105 sites. LFP signals were averaged across trials and power spectrum analysis was performed. LFP power spectra had generally decreasing power for higher frequencies. We also observed two peaks at the 10–20 and 40–60 Hz range.

Post Training

After we trained monkeys to perform a match/non-match task, 93 (31%) neurons responded to visual stimuli with a significant elevation of their firing rate above the baseline fixation. Of those neurons, 41 (44%) neurons had significant selectivity for the spatial location of the stimuli (ANOVA test, $p < 0.05$) and 18 (19%) neurons had significant selectivity for the feature of the visual stimuli. We also observed 25 (27%) neurons with persistent discharges in the delay period following the first stimulus.

These results were based on analysis of correct trials, when the monkey correctly identified whether the two stimuli presented on the screen matched each other, or not. We additionally analyzed error trials in which the monkey incorrectly identified a stimulus as a match instead of a non-match, and vice versa. We observed that in error trials neuronal activity during the cue presentation was significantly decreased than neuronal activity in correct trials (paired t-test, $p < 0.05$).

We also recorded LFP results from 138 sites. LFP power showed that, compared with pre-training, post-training power during stimulus presentation decreased in the frequencies below 20 Hz.

Discussion

Our experiments addressed how responses of neurons in the prefrontal cortex are modified by training to perform a cognitive task, requiring recognition of visual stimuli. Our results suggested that prefrontal cortical neurons responded to visual stimuli in a selective manner for their spatial location and features, even prior to any training. A population of prefrontal neurons discharged in a persistent manner after the offset of the stimuli, even though the monkeys were not trained or required to remember them.

After training, we observed almost identical percentage of neurons that responded to visual stimuli, and no further increase in the percentage of spatially and feature selective neurons. There was only a slight increase in the percentage of neurons that exhibited significant persistent, delay activity.

After training, the activity observed during the stimulus presentation could predict whether a trial was likely to result in an erroneous discrimination. Error trials were characterized by reduced mean firing rate during the stimulus presentation.

Local field potentials prior to and after training had similar spectral properties, and we only observed a slight decrease in spectral power in frequencies below 20 Hz after training, specifically during the second stimulus presentation.

Our results suggest that training to perform a cognitive task does not alter radically the properties of prefrontal cortical neurons, and that the prefrontal cortex of experimentally naïve animals already displays most of the properties that have been described in animals trained to perform cognitive tasks.

Acknowledgments This work was supported by NIH grant EY017077 and Whitehall Foundation grant 2004-05-50.

References

1. Goldman-Rakic, P.S.: Circuitry of the prefrontal cortex and the regulation of behavior by representational knowledge. In: Plum, F., Mountcastle, V.B. (eds.): Handbook of Physiology. American Physiological Society, Bethesda, MD. (1987) 373–417.
2. Fuster, J.M., Alexander, G.E.: Neuron activity related to short-term memory. Science 173 (1971) 652–654.
3. Kubota, K., Niki, H.: Prefrontal cortical unit activity and delayed alternation performance in monkeys. J. Neurophysiol. 34 (1971) 337–347.
4. Kim, J.N., Shadlen, M.N.: Neural correlates of a decision in the dorsolateral prefrontal cortex of the macaque. Nat. Neurosci. 2 (1999) 176–185.
5. White, I.M., Wise, S.P.: Rule-dependent neuronal activity in the prefrontal cortex. Exp. Brain Res. 126 (1999) 315–335.
6. Freedman, D.J., Riesenhuber, M., Poggio, T., Miller, E.K.: Categorical representation of visual stimuli in the primate prefrontal cortex. Science 291 (2001) 312–316.

Chapter 102
Neural Substrates During Finding Target Objects and Observing Natural Phenomena: An fMRI Study

Jun-Ki Lee, Jin-Su Jeong, Il-Ho Yang and Yong-Ju Kwon

Abstract This study investigated neural substrates underlying subjects' intentional visual search while finding target objects and observing natural phenomena using fMRI. Eight healthy, male, right-handed subjects participated in this study. Sets of finding target objects and observing natural phenomena tasks were presented to and performed by the subjects. The bilateral SPL and the occipital gyrus were activated by both task sets, bilateral fusiform gyrus was activated only during finding target objects tasks. The left precentral gyrus, the left inferior frontal gyrus and the culmen were activated only during observing natural phenomena tasks. The right inferior frontal gyrus was found to be active in the main effect of observing natural phenomena and the left postcentral gyrus was activated in the main effect of finding target objects. Thus, expectation-controlled search may be associated with comparison processes and goal-controlled search is related to both spatial and attentional processes.

Keywords Visual search · top-down attention · bottom-up attention · superior parietal lobule · fusiform gyrus · left inferior frontal gyrus

Introduction

Visual search is a complex mental process. Everyday visual search is guided not only by sensory input, but is also largely determined by mental processing activities, such as perception, object recognition, and attention. Perception is a process by which sensations are selected, organized and interpreted [1, 2] and is strongly influenced by an individual's experience, education and cultural values to interpret input received by the body's sensory receptors [1]. Object recognition is needed to represent a combination of perceptual and semantic processes [2]. Visual search is also engaged in multiple forms of attentional processing, including bottom-up

J.-K. Lee
Department of Biology Education, Korea National University of Education, Chungbuk 363-791, Korea
e-mail: cryptogams@hanmail.net

R. Wang et al. (eds.), *Advances in Cognitive Neurodynamics*,

(exogenous, stimulus driven) and top-down (endogenous, cognitively driven) mechanisms [3]. According to studies on functional neuroimaging, current models of visual search suggest that visual search is mediated by a widely distributed neural network, with critical components located in frontal and parietal regions [3, 4, 5, 6]. These previous studies, however, have not examined real world intentional visual search. Although many neurophysiological studies have tried to investigate visual search, few have done so under natural conditions with highly complicated visual environments and intentional free viewing. In the real world, objects rarely appear instantaneously or in isolation. Instead, they are usually encountered in the situation of exploring visually complex environments for intended objects.

Intentional visual search is controlled by a top-down mechanism which is based on the observer's current goals or expectation [7]. According to this notion, there are two types of intentional visual searches: goal-controlled and expectation-controlled. Good examples of these two types of searches are finding target objects and observing natural phenomena. What happens in a subject's brain when she/he observes natural phenomena and finds target objects? This study investigated the neural substrates underlying a subject's intentional visual search while finding target objects and observing natural phenomena.

Materials and Methods

Eight healthy adults (all male, right-handed, aged 30–39) took part in the study with informed consent and with the approval of the Ethics Committee of Korea National University of Education. Two kinds of visual task sets were presented to the subjects: a 'finding target objects' task set that required them to find specified natural objects within an extremely puzzling picture related to the nature and an 'observing natural phenomena' task set that compelled them to observe a scene associated with natural phenomena such as animals or plants. Figure 102.1 below provides an illustration of the experimental design. After scanning, the subjects were provided with two kinds of questionnaires; one on the finding target objects task set and the other on the observing natural phenomena task set. Subjects were asked to write down objects found and phenomena observed during the tasks. They also partook in semi-structured interviews regarding cognitive strategies used during the tasks.

Blood oxygen level-dependent (BOLD) images were obtained with a T2*-weighted echo planar imaging (EPI) gradient echo sequence from a 3.0T MR scanner (ISOL, KOREA) with standard head coil. The image parameters were as follows: TR 3000 ms; TE 35 ms; a matrix size of 64×64 FOV 220×220 mm; and 5 mm slice thickness with no gaps. Thirty axial EPI BOLD images were acquired.

The fMRI data were analyzed using SPM2. Statistical analysis was carried out using one sample t-test to determine significant activation at group level. Voxels were considered to be significantly activated when they passed a statistical threshold of $p < 0.0005$, uncorrected.

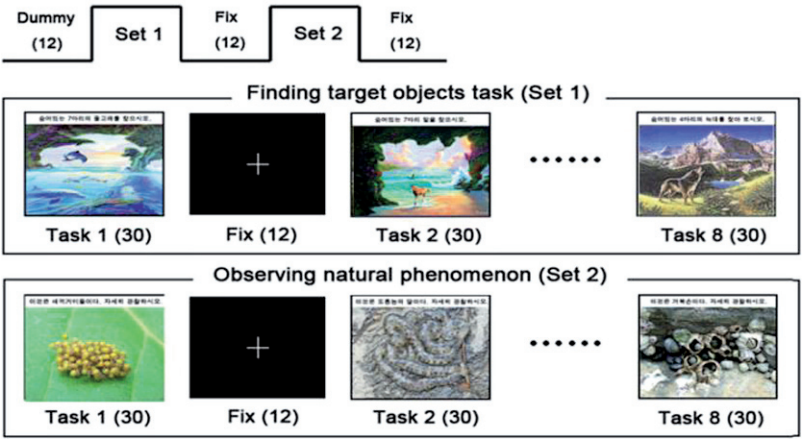

Fig. 102.1 The Experimental task set. Participants were instructed to find specified objects within an extremely puzzling picture for the finding target objects task set, while the other task set required them to observe and figure out biological phenomena in a natural picture

Results

Behavioral scores and the results of semi-structured interviews indicated that subjects performed the tasks in the expected manner. The mean numbers of found objects and observed phenomena in each picture for the two tasks are shown in Fig. 102.2. On average, participants found 5.19 ($\pm$2.55) objects in each picture for the finding target objects task, and 5.02 ($\pm$1.74) objects in each picture for the observing natural phenomena task. There was no significant difference between the mean numbers ($t = 0.44$, $p = 0.658$). Retrospective reports, obtained by the semi-structured interviews after fMRI scanning, highlighted phenomenal

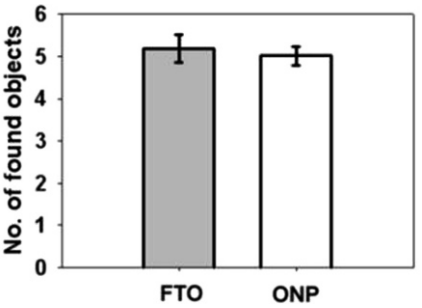

Fig. 102.2 The behavioral results of biologists' finding target objects and observing natural phenomena. The shaded bar indicates the averaged number of objects found in each picture during the finding target objects (FTO) tasks. Similarly, the white bar indicates the averaged number of objects found in each picture during the observing natural phenomena (ONP) tasks. Error bars represent standard errors

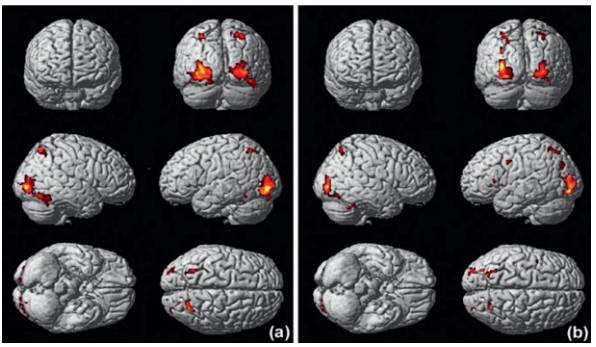

Fig. 102.3 Surface-rendered brain areas activated by (**a**) finding target objects and (**b**) observing natural phenomena are shown here after having been compared to the baseline condition ($p < 0.0005$, uncorrected for multiple comparisons)

differences between the two conditions. Briefly, participants concentrated on finding the specified goal objects during the finding target objects tasks whereas during the observing natural phenomena tasks, they focused their attention on finding any natural phenomena since there were no given goal objects.

fMRI results of simple effects are summarized in Table 102.1 and Fig. 102.3. The simple effect of finding target objects (finding target objects – baseline) showed enhanced activation in the bilateral superior parietal lobule, the bilateral occipital gyrus, the cuneus and the bilateral fusiform gyrus. The simple effect of observing natural phenomena (observing natural phenomena – baseline) revealed activation in the left precentral gyrus, the left inferior frontal gyrus, the bilateral superior parietal lobule, the bilateral occipital gyrus, the cuneus and the right culmen.

Discussion

Furthermore, activation of the left inferior frontal gyrus was found in the simple effect of observing natural phenomena, whereas the right inferior frontal gyrus (BA 47) was found to be active in the main effect of observing natural phenomena only. Right prefrontal engagement in the main effect may be due to the fact that this process may exceed semantic processing [6]. In addition, the right inferior frontal gyrus mediate explicit retrieval processes, involving comparison processes with newly observed phenomena [6]. Thus, observing natural phenomena may be associated with comparison processes, acceptance or rejection of observed phenomena during expectation-controlled search. On the other hand, the result of the main effect of finding target objects revealed activation in the left postcentral gyrus (BA 40). Multiple PET and fMRI studies reported brain activity related to spatial memory tasks in BA 7 or 40 [6]. Moreover, it was emphasized the role of this region in attentional top-down processed during mental imagery [8]. It is thus possible that the left postcentral gyrus activation in the main effect of finding target objects reflects both spatial and attentional processes.

In conclusion, the bilateral superior parietal lobule (BA 7) and the bilateral occipital gyrius (BA 17, 18, 19) were activated by both the finding target objects

Table 102.1 Talairach coordinates of cortical activations during the tasks of finding target objects and observing natural phenomena as revealed by whole-brain analysis

Lobe	Cortical region	BA & Side	x	y	z	z-value	x	y	z	z-value
Simple Effect				**FTO – Base**				**ONP – Base**		
Frontal	Precentral gyrus	6 L					–2	4	35	3.74
	Inferior frontal gyrus	13/45 L					–38	22	6	3.93
		45 L					–32	28	8	3.60
Parental	Superior parietal lobule	7 R	30	–59	55	4.69	30	–61	56	3.95
		7 R	22	–63	58	4.32	30	–58	45	3.36
		7 R	32	–54	45	3.59				
		7 L	–30	–59	55	4.38	–26	–65	53	3.83
		7 L	–22	–64	46	3.53	–22	–64	46	3.69
		7 L					–30	–55	56	3.65
Occipital	Superior occipital gyrus	19 L					–32	–72	31	4.14
	Middle occipital gyrus	18 L					–26	–84	–3	5.31
		19/18 L					–42	–83	2	3.98
		18 L	–28	–84	–1	4.97				
		18 L					–30	–81	11	5.03
		18 R	36	–83	1	4.56				
		17 R	22	–85	3	4.42				
	Inferior occipital gyrus	19 L	–32	–76	–5	4.73				
	Lingual gyrus	17 R					22	–85	1	4.22
		17 L	–18	–88	–2	5.74				
	Cuneus	17 R	24	–79	11	4.97	26	–81	11	4.50
	Fusiform gyrus	37 L	–36	–44	–16	4.14				
		37 R	44	–53	–12	4.25				
		37 R	46	–65	–9	3.75				
		37 R	48	–59	–16	3.60				
Cerebellum	Culmen	R					42	–52	–26	4.49
		R					34	–49	–18	3.72
Main Effect				**(FTO – Base) – (ONP – Base)**				**(ONP – Base) – (FTO – Base)**		
Frontal	Inferior frontal gyrus	47 R					28	29	–1	3.66
Parietal	Postcentral gyrus	40 L	–50	–29	51	3.81				

Note: Whole-brain analysis was applied ($N = 8$) for activations during the two types of tasks by comparing each activated region on a task to the baseline condition. A threshold of $p < 0.0005$ (uncorrected) was used. For each region, Brodmann's Areas (BA) number, locations in the coordinate space of Talairach and Tournoux (1988), the brain hemisphere: left (L) or right (R), and z-values are given. FTO indicates finding target objects. ONP indicates observing natural phenomena.

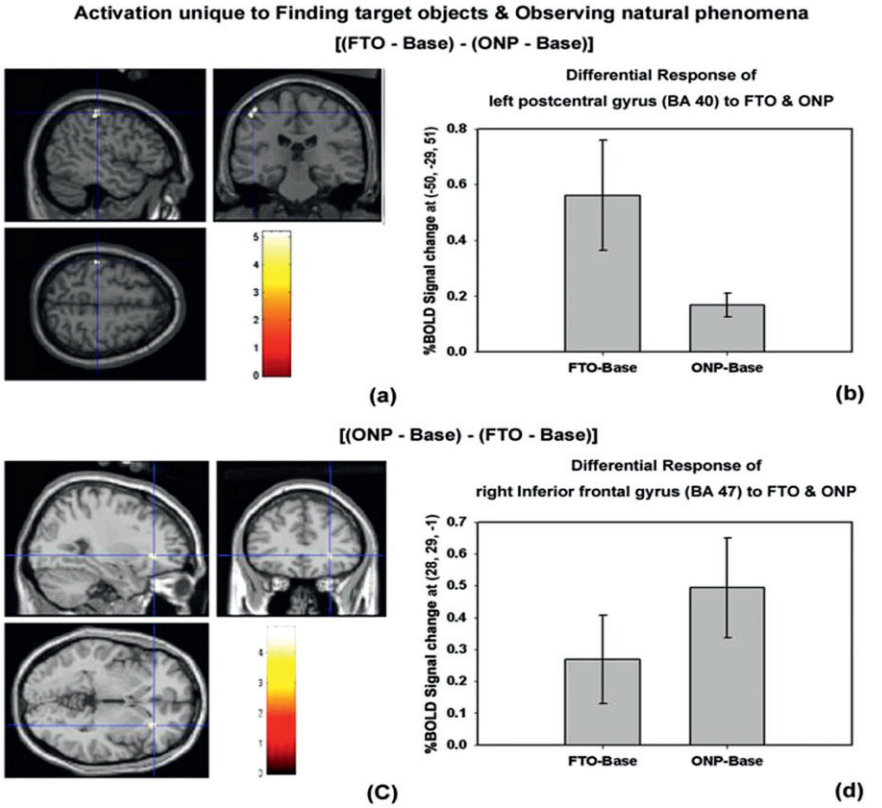

Fig. 102.4 (**a**) The main effect of finding target objects [(finding target objects – baseline) – (observing natural phenomena – baseline)] revealed activation in the left postcentral gyrus (BA 40) (-50, -29, 51; $Z = 3.81$). (**b**) %BOLD Signal change at (-50, -29, 51) show that the left postcentral gyrus is more activated during finding target objects than observing natural phenomena. (**c**) The main effect of observing natural phenomena [(observing natural phenomena – baseline) – (finding target objects – baseline)] showed significant activation in the right inferior frontal gyrus (BA 47) (28, 29, -1; $Z = 3.66$). (**d**) %BOLD Signal change at (28, 29, -1) show that the right inferior frontal gyrus is more activated during observing natural phenomena than finding target objects

and the observing natural phenomena tasks which suggests that the superior parietal lobule is associated with target identification, visuospatial selection, spatial working memory, attention shift, and top-down attention, while the occipital gyrus is related to the extraction of visual features as well as to shape analysis and recognition. The bilateral fusiform gyrus (BA 37) was activated only in the finding target objects tasks proposing that this region is important for the perception of object form and features. The left precentral gyrus (BA 6), the left inferior frontal gyrus (BA 13, 45), and the culmen were activated only during the observing natural phenomena tasks showing that the activation of these regions may reflect semantic encoding and retrieval and the increase of verbal working memory for verbal strategy usage. Furthermore, the

right inferior frontal gyrus (BA 47) was found to be active in the main effect of observing natural phenomena and the left postcentral gyrus (BA 40) was activated in the main effect of finding target objects. Thus, expectation-controlled search may be associated with comparison processes, acceptance or rejection of observed phenomena during observing natural phenomena. It is thus possible that goal-controlled search is related to both spatial and attentional processes.

References

1. Curry, D.V., Meyer, J.E., McKinney, J.M., 2006. Seeing versus perceiving. Prof. Saf. 51, 28–34.
2. James, T.W., Gauthier, I., 2004. Brain areas engaged during visual judgments by involuntary access to novel semantic information. Vision Res. 44, 429–439.
3. Madden, D.J., Spaniol, J., Whiting, W.L., Bucur, B., Provenzale, J.M., Cabeza, R., White, L.E., Huettel, S.A., in press. Adult age differences in the functional neuroanatomy of visual attention: A combined fMRI and DTI study. Neurobiol. Aging 28, 450–476.
4. Colby, C.L., Goldberg, M.E., 1999. Space and attention in parietal cortex. Annu. Rev. Neurosci. 22, 319–349.
5. Huettel, S.A., Misiurek, J., Jurkowski, A.J., McCarthy, G., 2004. Dynamic and strategic aspects of executive processing. Brain Res. 1000, 78–84.
6. Wolf, R.C., Vasic N., Walter, H., 2006. Differential activation of ventrolated profrontal cortex during working memory retrieval. Neuropsychologia 44, 2558–2563.
7. Desimone, R., Duncan, J., 1995. Neural mechanisms of selective visual attention. Annu. Rev. Neurosci. 18, 193–222.
8. Mechelli, A., Price, C.J., Friston, K.J., Ishai, A., 2004. Where bottom–up meets top–down: neuronal interactions during perception and imagery. Cereb. Cortex 14, 1256–1265.
9. Knauff, M., Mulack, T., Kassubek, J., Salih, H.R., Greenlee, M.W., 2002. Spatial imagery in deductive reasoning: a functional MRI study. Brain Res. Cogn. Brain Res. 13, 203–212.

Chapter 103
Changes in Brain Activation Induced by Training of Hypothesis Generation Skills: An fMRI Study

Yong-Ju Kwon, Jun-Ki Lee, Jin-Su Jeong, Dongkook Park and Il-Ho Yang

Abstract The aim of the present study was to investigate the learning-related changes in brain activation that were induced by the training of hypothesis generation skills about biological phenomena. Eighteen undergraduate participants were scanned twice with fMRI before and after training during a two-month interval. The experimental group was trained through eight biological hypothesis generation programs, but the control group was not given any hypothesis generation program during the two-month period. The results have shown that the brain activation of the trained group was increased in the left inferior and the superior frontal gyri which were related to working memory load and higher-order inferential processes. However, the activation after training was decreased in the occipito-parietal route which was associated with the perception and analysis processes of visual information. Furthermore, the results have suggested that the DLPFC region is the critical area for training of hypothesis generation skills.

Keywords Brain activation change · training-induced activation · hypothesis generation skills · inferior frontal gyrus · superior frontal gyrus · fMRI

Introduction

A hypothesis is a proposition proposed as a tentative causal explanation for an observed situation [1]. Generating and testing scientific hypotheses are key components of the modern scientific method [2]. Specifically, hypothesis generation has been regarded as one of the core reasoning processes in creative thinking for scientific discovery [1]. From a cognitive psychological perspective, hypothesis generation has been regarded as a causal inference [1, 3]. Making causalities include the perception and analysis of sensory information, the retrieval and activation

Y.-J. Kwon
Department of Biology Education, Korea National University of Education, Chungbuk 363-791, Korea
e-mail: kwonyj@knue.ac.kr

R. Wang et al. (eds.), *Advances in Cognitive Neurodynamics*,

of information within long-term memory, the short-term retention of information within working memory, and the encoding of information into long-term memory [4].

On the neurological level, the left inferior prefrontal region mediates the retrieval and stage of information within working memory [4]. The left superior prefrontal cortex has been implicated in establishing higher-order inferential processes [5]. Thus, it is possible to suggest that the left inferior and superior frontal gyri play a crucial role in generation of scientific hypothesis. In addition, the occipito-parietal route is primarily responsible for perception and analysis of visual information, while integration components are localized in the prefrontal cortex [5].

A number of studies have linked neuroanatomical changes to cognitive development and the training of cognitive skills [6, 7]. Furthermore, Booth et al. (2003) showed that greater frontal activation was associated with better performance on cognitive tasks and better selective attention performance was associated with less activation in parietal areas on visual perception tasks. Also, they suggested that maturation is not only associated with increased activation in critical areas for task performance, but also with decreased activation in non-critical areas.

According to prior studies, understanding the correlation of cognitive development with neurological changes is valuable for improving thinking and reasoning skills [1, 8], and learning language, science and math [6]. However, no brain imaging studies have explored developmental changes of brain activation before and after receiving biological hypothesis generation training. Therefore, the present study investigated brain activation patterns during biological hypothesis generation and brain activation changes related to the training of persons in hypothesis generation.

Methods

Eighteen undergraduate participants (all female and right-handed, 20–25 years of age) were scanned twice with fMRI, during two-month interval. All participants had no history of neurological, psychiatric or major medical illness. The participants gave informed consent for their participation in the study, which was approved by the Ethics Committee of Korea National University of Education. Participants were divided into two groups; each group consisted of nine persons. The trained group was educated through eight programs of biological hypothesis generation for 60 min each week throughout a two-month period that took effect between two fMRI scanning sessions. The other nine participants comprised the control group and were not given skill training throughout the two months. By utilizing the abduction model for hypothesis generation [3], eight biological hypothesis generation programs were developed and administered to the trained group. Each weekly training program consisted of six steps: observing a situation, generating a causal question, analyzing the question, representing experienced phenomena, cause representation, and constructing hypothesis. For example, in the root pressure activity, participants observed a figure of sap oozed from a tomato stump and made a causal question, such as "Why does the sap oozed from the stump?" After the analysis of the question, they

represented similar phenomena and causes of the similar phenomena. Finally, they constructed a biological hypothesis by using the causes, such as osmosis and root pressure.

All participants were scanned twice with fMRI: before and after the two-month period. During the fMRI session, three visual tasks were presented to trained and control groups. In each task participants were shown a biological picture with a causal question (e.g., Why is the monkey covered with white fur?). They were asked to generate a biological hypothesis, i.e. a tentative causal explanation for the question. Each task was performed for 30 s followed by a baseline stimulus of a white crisscross on a black background for 12 s. Immediately after scanning, participants were asked to write down hypotheses generated during the three visual tasks. Once this requirement was fulfilled, participants then partook in semi-structured interviews regarding cognitive strategies used during the tasks.

The participants' biological hypotheses generated during fMRI scanning were assessed. An explanation score was given to each hypothesis and represented an averaged score for the three biological hypotheses. Each hypothesis was scored by counting the number of explanations included in its hypothesis. For example, if a participant wrote, "sugar particles moved from a more concentrated area to a less concentrated area," the hypothesis scored 4; for "sugar melted," the hypothesis scored 2. A comparison of explanation scores was made between pre-and post-scanning tests to assess changes associated with hypothesis generation training. The statistical significance of hypothesis generation skill training was tested through an analysis of covariance (ANCOVA).

Blood oxygen level-dependent (BOLD) images were obtained with a T2*-weighted echo planar imaging (EPI) gradient echo sequence from a 3.0T MR scanner (ISOL, KOREA) with standard head coil. The image parameters were as follows: TR 3000 ms; TE 35 ms; a matrix size of 64 × 64 FOV 220 × 220 mm; and 5 mm slice thickness with no gaps. 30 axial EPI BOLD images were acquired.

Structural and functional images were analyzed using SPM2. Voxels were considered to be significantly activated when they passed a statistical threshold of $p < 0.0005$, uncorrected. This paper assessed the main effects of biological hypothesis generation (hypothesis generation–baseline), the increase training effects (post-training–pre-training) in each group and the decrease training effects (pre-training - post-training) in each group. In addition, to precisely determine the effect of training, BOLD signal changes were compared and the analyses of time courses of hemodynamic responses were performed on four regions of interest (ROIs) which were selected based on the effects of training and previous studies [4, 5]. The ROIs were: the left superior frontal gyrus (BA 6), the left inferior frontal gyrus (BA 9), the right insula (BA 13), and the left inferior parietal lobule (BA 40).

Results

The results of semi-structured interviews indicated that participants performed the fMRI tasks in the expected manner. All of the participants successfully generated biological hypotheses. In retrospective reports, all participants answered that they had

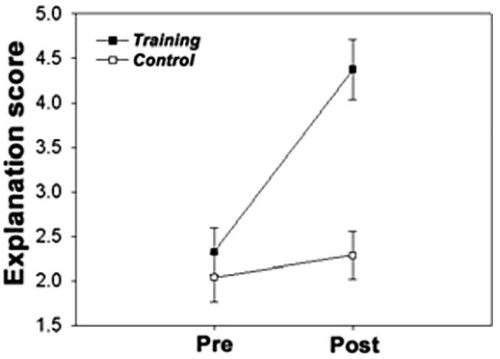

Fig. 103.1 Variation of the means of explanation scores for biological hypothesis generation. Black boxes indicate the average scores of trained group and white boxes indicate the average score of control group. Pre = pre-training, Post = post-training. Error bars represent the standard mean error

focused their attention on generating biological hypotheses. Participants comprising the trained group showed significantly higher explanation scores than those of the control group due to training in the generation of biological hypothesis. The mean score of the trained group was 2.33 (SD = 0.71) on the pre-test and 4.59 (SD = 1.10) on the post-test whereas the mean score of the control group was 2.00 (SD = 0.75) on the pre-test and 2.26 (SD = 0.72) on the post-test. Figure 103.1 shows the variation of the means of explanation scores for the two groups.

Figure 103.1 highlights significant discrepancy between the scores of the control and trained groups on the pre-training test. Therefore, ANCOVA was conducted to determine statistical difference between the post-training scores of the two groups were. The means of post-training scores were compared using the pre-training scores as a co-variate. The results of ANCOVA showed that the explanation score of the trained group was significantly higher than that of the control group [$F(1, 17) = 25.00$, $p < 0.01$].

The fMRI results are summarized in Table 102.1, Figs. 103.2 and 103.3. The main effect (hypothesis generation – baseline) of hypothesis generation as shown in Table 103.1 and Fig. 103.2a was activation in the left superior frontal gyrus (BA 6), the left middle frontal gyrus (BA 6), the left inferior frontal gyrus (BA 9), the right cingulate gyrus, and the bilateral cuneus (BA 17).

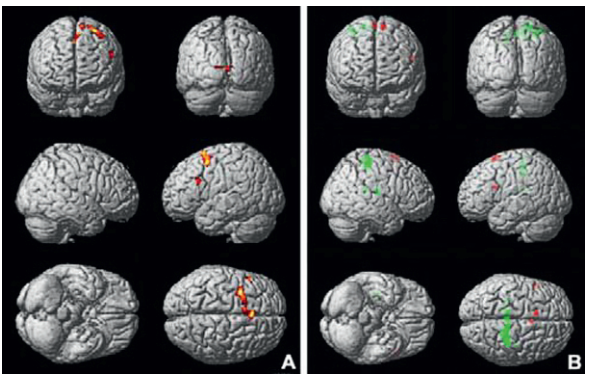

Fig. 103.2 Surface-rendered brain areas activated by the main effect (**a**) in all participants, and the increased areas of activation due to training (red blobs of **b**) and the decreased areas of activation due to training (green blobs of **b**) in the trained group participants. (See Table 102.1 for details)

Table 103.1 Talairach coordinates of cortical activations during the task of biological hypothesis generation by whole-brain analysis

Cortical region	BA and side	Talairach coordinates			
		X	*Y*	*Z*	Z-value
Main effect (Hypothesis – baseline)					
Frontal					
Superior frontal gyrus	6 L	–8	15	62	4.43
	6 L	–4	22	52	4.4
Middle frontal gyrus	6 L	–24	13	58	4.63
		–38	10	49	4.18
Inferior fontal gyrus	9 L	–51	19	23	3.66
Limbic					
Cingulate gyrus	32 R	2	21	41	4.4
Occipital					
Cuneus	17 L	–4	–79	11	4.98
		–12	–79	8	4.45
	17 R	6	–77	9	4.26
Training effect in control group					
Increase *[(Post – baseline)] – [(Pre – baseline)]*					
No survival voxels					
Decrease *[(Pre – baseline)] – [(Post – baseline)]*					
No survival voxels					
Training effect in Training group					
Increase *[(Post – baseline)] – [(Pre – baseline)]*					
Frontal					
Superior frontal gyrus	6 R	2	8	67	3.8
	6 L	–12	14	67	3.8
Inferior fontal gyrus	9 L	–41	12	21	3.52
Decrease *[(Pre – baseline)] – [(Post – baseline)]*					
Frontal					
Precentral gyrus	4/6 R	26	–28	53	4.37
	4/6 R	18	–28	62	4.34
Paracentral lobule	6 L	–12	–25	47	4.25
Parietal					
Inferior parietal lobule	40 L	–30	–25	38	3.68
Others (Sub lobar)					
Thalamus		–10	–34	16	3.68
		–10	–24	16	3.7
		8	–32	15	3.8
Caudate		–18	–36	22	3.5
		–20	–36	20	3.78
Insula	13 R	38	–15	15	4.02
		42	–12	23	3.36

Coordinates indicate location in Talairach space of the maximally significant voxel within each significant cluster of activation ($P < 0.0005$, uncorrected). L = left hemisphere, R = right hemisphere, Pre = pre-training, Post = post-training. *Z*-value refers to the *Z*-transformed *t*-statistic for the maximally significant voxel within a cluster.

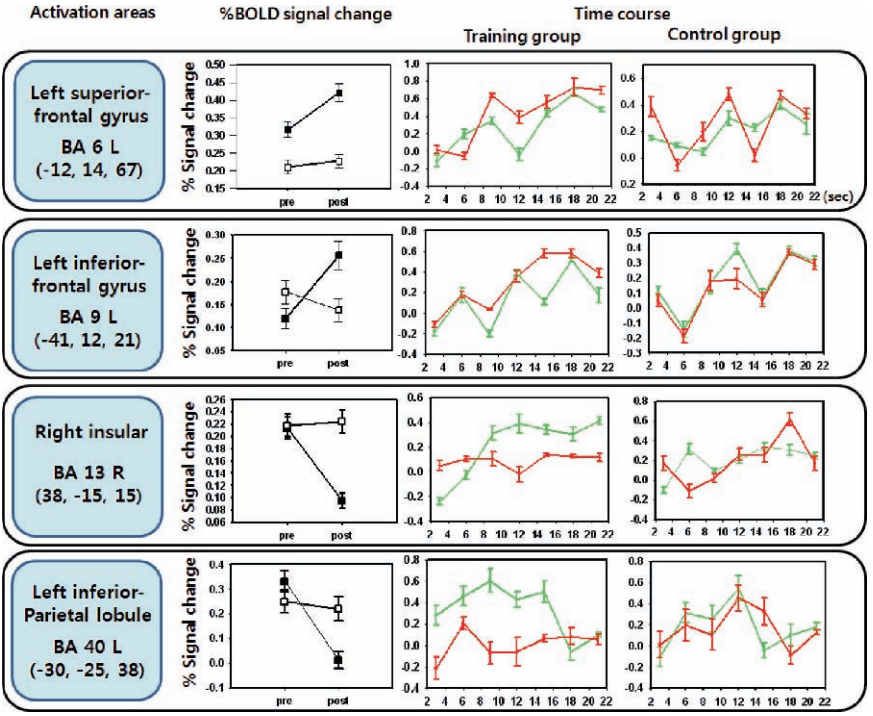

Fig. 103.3 %BOLD signal changes according to the effect of training and the time courses of hemodynamic responses on four regions of interest (ROIs): the left superior frontal gyrus (BA 6 L), the left inferior frontal gyrus (BA 9 L), the right insula (BA 13 R), and the left inferior parietal lobule (BA 40 L). On the %BOLD signal changes charts, black boxes indicate the average scores of the trained group and white boxes indicate the average score of the control group. On the time course charts, two types of %BOLD signal changes are plotted: green curves represent pre-training and red curves represent post-training. Error bars represent standard mean error

In control group, there were no significant modifications of brain activations from pre-training to post-training or vice-versa. On the other hand, both increased and decreased areas of brain activation training due to were observed in the trained group. The increased areas of activation illustrated in Fig. 103.2b via red blobs showed activation in the bilateral superior frontal gyrus (BA 6) and the left inferior frontal gyrus (BA 9). The green blobs in Fig. 103.2b, on the other hand, highlighted the decreased areas of activation i.e. less activation in the right precentral gyrus (BA 4/6), the left paracentral lobule (BA 6), the inferior parietal lobue (BA 40), the thalamus, the caudate, and the right insula (BA 13).

The results of %BOLD signal change computations and time course of the hemodynamic response in the left superior frontal gyrus (BA 6) and the left inferior frontal gyrus (BA 9) revealed an increase in %BOLD signals in the trained group on the post-training test as shown in Fig. 103.3. The %BOLD signal changes of the trained group on the post-training test were significantly higher than those of the

control group in the left superior frontal gyrus (BA 6) [$F(1, 17) = 10.53$, $p < 0.01$, ANCOVA] and the left inferior frontal gyrus (BA 9) [$F(1, 17) = 46.97$, $p < 0.01$, ANCOVA]. For the other two ROIs: the right insula (BA 13) and the left inferior parietal lobule (BA 40), the results of ROI analyses showed a decrease in %BOLD signals in the trained group due to the experimental training. The %BOLD signal changes of the trained group on the post-training test were significantly lower than those of control group in the insula (BA 13) [$F(1, 17) = 0.16$, $p < 0.01$, ANCOVA] and the left inferior parietal lobule (BA 40) [$F(1, 17) = 9.08$, $p < 0.01$, ANCOVA].

Discussion

The hypothesis generation training produced increased activations of the bilateral superior frontal gyrus (BA 6) and the left inferior frontal gyrus (BA 9) in trained group (Fig. 103.2b, red blobs). On the other hand, decreased activations where seen in the right precentral gyrus (BA 4/6), the left paracentral lobule (BA 6), the inferior parietal lobue (BA 40), the thalamus, the caudate, and the right insula (BA 13) in trained group (Fig. 103.2b, green blobs). These findings are consistent with the suggestion that cognitive development is supported by changes in patterns of brain activation, including an increase of activation in critical areas and a decrease in others [9]. Furthermore, the present results might be explained by "the neural efficiency hypothesis" [10]. According to the hypothesis, participants that generate hypotheses well used a limited number of brain circuits, thus requiring minimal glucose usage while participant poor at generation used more circuits, some of which were inessential to the generation of hypotheses which reflected higher overall brain glucose metabolism.

Figure 103.3 shows that the results of %BOLD signal change computations and time courses of the hemodynamic response on the left superior frontal gyrus (BA 6) and left inferior frontal gyrus (BA 9) reveal increased activations because of training. The increasing patterns of %BOLD signal changes in these regions are consistent with the increasing pattern of explanation scores of behavioral results. These brain areas have been claimed to be involved in higher-order inferential processes (the left superior frontal gyrus) and working memory (the left inferior frontal gyrus) [4]. Therefore, it is suggested that the trained group's increased ability to generate hypotheses might be correlated with the acceleration of working memory retrieval and higher-order inferential processes.

The results of %BOLD signal change computation and time courses of the hemodynamic response on the insula (BA 13) and the left inferior parietal lobule (BA 40) highlighted decreased activations because of training. Several studies have suggested that the insula (BA 13) is associated with uncertainty in linking cognitive and affective components [11]. Thus, it is possible that the decreased activation of the insula reflected the trained group's increased confidence in hypothesis generation after experiencing the experimental training. Moreover, the signal decrease in the left inferior parietal lobule (BA 40) hints at a practice-associated disengagement of visual analysis processing. The inferior parietal lobule has been shown to play a

relevant role during the processing of visually complex stimuli [12]. Therefore, it is suggested that the participants in trained group more efficiently analyzed the visual situation for biological hypothesis generation after receiving training than before experiencing the training.

In conclusion, results of the main effect showed that recruitment of the left inferior frontal gyrus was driven by increased working memory load and superior prefrontal cortex recruitment reflected higher-order inferential processes during hypothesis generation. In addition, activation of the occipito-parietal route was due to perception and processes involved in visual information analysis. Furthermore, trained participants showed more frontal areas and less occipito-parietal route activations which are associated with better performance. It may be concluded that developmental changes are associated with an increase of activation in critical areas as well as a decrease of activation in non-critical areas in biological hypothesis generation.

References

1. Lawson, A.E., 1995. Science Teaching and the Development of Thinking. Wadsworth Publishing Company, CA.
2. McPherson, G.R., 2001. Teaching and learning the scientific method. Am. Biol. Teach. 63, 242–245.
3. Kwon, Y., Jeong, J., Park, Y., 2006. Roles of abductive reasoning and prior belief in children's generation of hypotheses about pendulum motion. Sci. Edu. 15, 643–656.
4. Kuperberg, G.R., Lakshmanan, B.M., Caplan, D.N., Holcomb, P.J., 2006. Making sense of discourse: An fMRI study of causal inferencing across sentences. NeuroImage 33, 343–361.
5. Smith, E.E., Jonides, J., 1997. Working memory: a view from neuroimaging. Cogn. Psycho. 1, 5–42.
6. Kassubek, J., Schmidtke, K., Kimmig, H., Lcking, C.H., Greenlee, M.W., 2001. Changes in cortical activation during mirror reading before and after training: an fMRI study of procedural learning. Cogn. Brain Res. 10, 210–217.
7. Olsen, P.J., Westernberg, H., Klingberg, T., 2004. Incresed prefrontal and parietal activity after training of working memory. Nat. Neurosci. 7, 75–79.
8. Grossberg, S., 1988. Studies of Mind and Brain: Neural Principle of Learning, Perception, Development, Cognition and Motor control. Reidel Publishing Company, Dordrecht.
9. Booth, J.R., Burman, D.D., Meyer, J.R., Lei, Z., Trommer, B.L., Davenport, N.D., Li, W., Parrish, T.B., Gitelman, D.R., Mesulam, M.M., 2003. Neural development of selective attention and response inhibition. NeuroImage 20, 737–751.
10. Haier, R.J., Siegel, B.V., MacLachlan, A., Soderling, E., Lottenberg, S., Buchsbaum, M.S., 1992. Regional glucose metabolic changes after learning a complex visuospatial/motor task: A positron emission tomographic study. Brain Res. 570, 134–143.
11. Paulus, M.P., Rogalsky, C., Simmons, A., Feinstein, J.S., Stein, M.B., 2003. Increased activation in the right insula during risk-taking decision making is related to harm avoidance and neuroticism. NeuroImage 19, 1439–1448.
12. Small, S.L., Burton, M.W., 2002. Functional magnetic resonance imaging studies of language. Curr. Neurol. Neurosci. Rep. 2, 505–510.

Chapter 104
Early Access and Integration of Meaning Indicated by Pitch Accent: A Mismatch Negativity Study

Xiaoqing Li and Yufang Yang

Abstract Mismatch negativity (MMN) was used to examine the on-line processing of pitch accent relative to different information state. An oddball design, using Chinese spoken sentences and picture context, was applied. It was found that mismatch response were significantly larger for experiment condition than for control condition. The results indicated that listeners could access and integrate the meaning of pitch accent into discourse context in the early stage of processing.

Keywords MMN · pitch accent · information state · semantic integration

Introduction

Pitch accent reflects the relative prominence of a particular word, or phrase in a certain prosodic structure. Speakers tend to place pitch accent on new information, while leaving given information deaccented. Compared with inconsistent accentuation, consistent accentuation facilitates speech processing [1]. Recently, ERP has also been used to study pitch accent processing. Some studies found that both missing pitch accent on new information and superfluous pitch accent on given information, evoked negative-going effect resembling N400 component [2]. However, other studies found that only missing pitch accent on new information evoked a negative deflection [3].

For the role of pitch accent in speech processing, many questions remain open. First, behavioral studies indicated that crucial information about incoming words and their context can be processed within 200 ms after the onset of the critical word [4]. It was unknown whether, in the early time window, the meaning conveyed by pitch accent can be accessed and integrated into discourse context. Previous studies couldn't answer this question because of the latency of N400. Second, whether

Y. Yang
State Key Laboratory of Brain and Cognitive Science, Institute of Psychology, Chinese Academy of Sciences, China
e-mail: yangyf@psych.ac.cn

R. Wang et al. (eds.), *Advances in Cognitive Neurodynamics*,

both missing pitch accent on new information and superfluous pitch accent on given information evoke ERP responses.

The aim of this study was to investigate the on-line processing of pitch accent relative to different information state during the early stage of access. Mismatch negativity (MMN) was used which is elicited by infrequent acoustic events (deviant stimuli) occasionally occurring among frequently repeated sounds (standard stimuli). The MMN usually peaks around 100–250 ms after a stimulus change [5], so it was suitable for studying the physiological basis of the early speech comprehension processes. The oddball design was used in two conditions. First, two pictures were presented visually to serve as discourse context for a spoken sentence. Second, spoken sentence was presented without context.

Experimental Procedures

Subjects and Stimuli

Sixteen right-handed subjects participated in the experiment; all of them were native speakers of Mandarin Chinese. None of them had any neurological impairment.

Two pictures were presented visually in succession. During the appearance of the second picture, a spoken sentence was presented (随后红色的方形出现了, then a red rectangle appears) with an embedded critical word "red". The critical word was either accented or deaccented. The sentences were edited to keep the word preceding "red" (namely, "then") was exactly the same in all conditions.

In the experiment situation, first, "accented-new" (standard): a blue rectangle followed by a red rectangle made the word "red" as new which was consistently accented. Second, "accented-given" (deviant): a red triangle followed by a red rectangle made "red" as given which was inconsistently accented. Third, "deaccented-new" (deviant): a blue rectangle followed by a red rectangle made "red" as new which was inconsistently deaccented. In addition, for the word preceding "red" (namely, "then") in "accented-given" and "accented-new" condition, there is no correspondence between pitch accent and information structure, just the mere effect of "picture" (red-triangle vs. blue-rectangle). In the control situation, just the sentences were presented. Sentences with "red" accented served as standard stimuli, the deaccented version as deviant stimuli, hence just mere effect of "pitch" (deaccentuation vs. accentuation).

Evoked Potential Recording and Analysis

EEG was recorded (0.01–40 Hz, sampling rate 500 Hz) from 64 Ag/AgCl electrodes. EEG and EOG data were amplified with DC amplifiers (Neuroscan). All electrodes were referenced to the left mastoid online, and were re-referenced offline to linked mastoids. Impedances were kept below 5 kΩ.

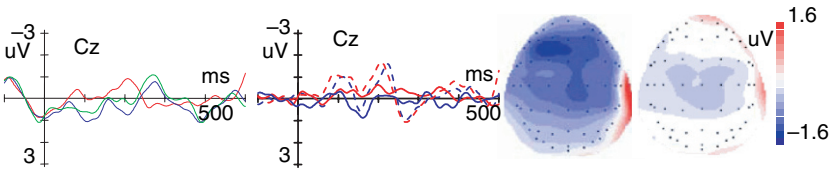

Fig. 104.1 Left: Grand-averaged ERPs for the deaccented-new (red) and accented-given (green) as compared to frequent accented-new (blue); difference waveforms dNew (dashed red), Pitch (dashed blue), aGiven (solid red), and Picture (solid blue). Left: scalp potential distributions for difference waveforms: "deaccented-new"–"accented-new", "accented-given"–"accented-new"

Subjects were asked to watch the pictures appearing on the screen, and neglect the sentence. The effective measuring time of 90 min was divided into two sessions with five blocks for experiment session (standard: 75%, 800 trials; deviant: 25%, 100 trials) and two blocks for control session (standard: 75%, 300 trials; deviant: 25%, 100 trials). The order of the two sessions was counterbalanced between subjects.

The raw EEG data were 1–30 Hz bandpass filtered and were screened for eye movements, muscle artifact, electrode drifting, and amplifier blocking in a critical window ranging from 100 ms before to 800 ms after critical word onset. Trials containing such artifacts were rejected (5.5% overall).

The mismatch response was obtained by subtracting the averaged response to the standard stimuli from the averaged response to each deviant stimuli (dNew: "deaccented-new"–"accented-new"; aGiven: "accented-given"–"accented-new"; Pitch: "deaccentuation"–"accentuation"; Picture: "red-triangle"–"blue-rectangle") per subject.

Mean amplitude computed in the time window of 160–220 ms (MMN) was used. The ANOVAs were conducted on electrodes (F3/Fz/F4; C3/Fz/C4; P3/Pz/P4). First, two ANOVAs were performed based on original waves: "*DN ANOVA*" with Deaccented-new (deaccented-new vs. accented-new), Laterality (left, midline, right) and Anteriority (frontal; central; parietal) as independent factors; "*AG ANOVA*" with Accented-given (accented-given vs. accented-new), Laterality and Anteriority as independent factors. Second, another two ANOVAs were performed based on difference waves. One was "*Missing-pitch ANOVA*", Missing-pitch (dNew vs. Pitch) × Laterality × Anteriority; the other was "*Superfluous-pitch ANOVA*", Superfluous-pitch (aGiven vs. Picture) × Laterality × Anteriority.

Results and Discussion

"*DN ANOVA*" revealed a significant interaction between Deaccented-new and Anteriority [$F(2, 15) = 4.35$, $p < 0.05$] and a main effect of Deaccented-new [$F(1, 15) = 24.34$, $p < 0.0001$], indicating that "deaccented-new" evoked a larger negative deflection than "accented-new". Subsequent simple-analysis showed that the Deaccented-new effect reached significance in all of the three levels of

Anteriority (frontal, central and parietal) [$F(1, 15) = 20.13$, $p < 0.0001$; $F(1, 15) = 28.13$, $p < 0.0001$; $F(1, 15) = 10.05$, $p < 0.01$], but showed maximum effect in the central areas. "*AG ANOVA*" resulted in a significant main effect of Accented-given [$F(1, 15) = 5.28$, $p < 0.05$), indicating that "accented-given" evoked a larger negative deflection than "accented-new".

"Missing-pitch ANOVA" and "Superfluous-pitch ANOVA" resulted in main effect of Missing-pitch [$F(1, 15) = 5.34$, $p < 0.05$], main effect of Superfluous-pitch [$F(1, 15) = 6.57$, $p < 0.05$] respectively, indicating that difference wave "dNew" being more negative than difference wave "Pitch", and difference wave "aGiven" being more negative than the difference wave "Picture".

The major results of this study were that "deaccented-new" and "accented-given" elicited larger negative deflections (MMN) than consistent pitch accent respectively. Further analysis revealed that the MMN effects were indeed evoked by the correspondence between pitch accent and information state, not just by the differences in the physical feature of the stimuli, since the MMN effects in the experimental condition were significantly larger than those in the control conditions.

Previous ERP studies have already proved that pitch accent influenced on-line discourse processing [2, 3]. The novel finding of this study was that the effect of pitch accent on discourse comprehension occurred in the early time window. Around within the first 200 ms after critical word onset, the listener had accessed the meaning indicated by pitch accent and integrated it into discourse context. This study also proved that both the missing pitch accent on new information and superfluous pitch accent on given information are identified in the early stage of processing.

The results of this study also had important indications for MMN itself. At beginning, the MMN was found to be an indicator of acoustic change detection. Subsequently MMN response characteristics were also found to change with the lexical status of a stimulus, with grammaticality of a word string, and with the meaning of words [6]. This study deepened previous studies by showing that MMN was sensitive to the semantic match between the meaning indicated by pitch accent and discourse context indicated by pictures, and that the MMN could appeared even when the spoken stimuli were exact the same and only the visually context being different. Those added evidences to the insight that MMN can indicate processes at "higher" levels of language processing, such as semantic context integration.

References

1. Li, X.Q., Yang, Y.F.: The role of accentuation in spoken discourse comprehension. Acta Psychologica Sinica (2004) 36, 393–399.
2. Magne, C., Astésano, C., Lacheret-Dujour, A., Morel, M., Alter, K., Besson, M.: On-line processing of "pop-out" words in spoken French dialogues. Journal of Cognitive Neuroscience (2005) 17, 740–756.
3. Johnson, S.M., Breen, M., Clifton, C., Jr, Morris Florak, J.: ERP investigation of prosodic and semantic focus. Poster presented at Cognitive Neuroscience, New York City (2003).
4. Rastle, K., Davis, M.H., Marslen-Wilson, W.D., Tyler, L.K.: Morphological and semantic effects in visual word recognition: a time-course study. Language and Cognitive Processes (2001) 15, 507–537.

5. Naätänen, R., Tervaniemi, M., Sussman, E., Paavilainen, P., Winkler, I.: 'Primitive intelligence' in the auditory cortex. Trends in Neurosciences (2001) 24, 283–288.
6. Pulvermüller, F., Shtyrov, Y.: Language outside the focus of attention: The mismatch negativity as a tool for studying higher cognitive processes. Progress in Neurobiology (2006) 79, 49–71.

Chapter 105
Electric Stimulation of Optic Nerve Fiber: A Simulation Study

Qingli Qiao, Wei Zhang, C.L. Vencent and Qiushi Ren

Abstract A mathematical model optic nerve fiber was presented. In the model, the main active nodal channels include fast Na^+, persistent Na^+, slow K^+ and a fast repolarizing K^+ (A-current), and activation and inactivation parameters expressions are given at 22°C. By computer simulation, the main features underlying action potentials (AP) in optic nerve fibers can be able to generate. The simulation results is consistent with the experimental data and that of other models.

Keywords Optic nerve · mathematical model · ionic channels

Introduction

The optic nerve is a key object regarding research on visual prosthesis [1]. More precisely an insight on stimulation threshold is a key point for optic nerve selective stimulation hoping for artificial vision. Previously, the FCM model had been developed especially for the retinal ganglion cell based on voltage clamp studies in tiger salamander and rat retina [2]. These studies have identified at least five intrinsic ion currents, which appear to play a role in generating nerve impulses. A Model for the Electrically Stimulated Retina has been constructed by Rattay using FCM model [3]. However, due to the thin diameter of optic nerve fibers, extensive channels dynamics studies cannot be conducted directly, but previous pharmacological and electrical studies has pinned down the main features of the mechanisms underlying the nerve impulse in the rat optic nerve (RON). Based on existing membrane models and pharmacological experimental data, a model of optic nerve was presented by Oozeer et al. [4]. which is called here OVLD model though through adjusting the maximum conductances and the gating kinetics of three ionic currents: Fast potassium current Persistent sodium current Slow potassium current [4].

In this paper, a new version of complete OVLD model was presented by adding leakage conductance and leakage Nernst potential value E_L. The leakage Nernst

Q. Qiao
Department of Biomedical Engineering, Tianjin Medical University, Tianjin 300070, China
e-mail: qlqiao@gmail.com

R. Wang et al. (eds.), *Advances in Cognitive Neurodynamics*,

potential value E_L was selected for the system to remain in equilibrium at the resting potential. As ion channel gating is usually specified for a given temperature, the activation and inactivation parameters expressions in the model are given at 22°C. Because of its interest in vision prosthesis, the main phenomenon underlying action potentials (AP) in those myelinated fibers is reproduced.

Model of Optic Nerve

The RON experiments [5, 6] had shown the rough mechanism of AP generation in RON is widely believed to be as follows: in presence of 4-aminopyridine (4-AP), increase of spike duration, depolarizing afterpotential (DAP) followed by a spike frequency dependent and tetraethylammonium (TEA) sensitive hyperpolarizing afterpotential (AHP).

Based on various experimental facts, The depolarization of AP of RON is due to fast Na^+ channels, the repolarization to a 4-AP-sensitive K^+ current is similar to the A-current found in other experiments [7]. The DAP present in mammalian motor axons was suggested to be due to a persistent, noninactivating Na^+ current, the AHP being attributed to a slow K^+ current [8].

In a space–clamp condition, a single node model with ionic currents (including leakage) and capacitive current being summed according to Kirchoff's law:

$$c\frac{dv}{dt} + \sum_{\text{ionic}} i_{\text{ionic}} = i_{\text{stim}} \tag{105.1}$$

where t is the time (ms), v is the transmembrane potential (mV), c is the membrane capacitance ($\mu\text{F}\,\text{cm}^{-2}$) and i_{stim} is the applied stimulation current density ($\mu\text{A}\,\text{cm}^{-2}$).

Following the Hodgkin-Huxley theory [9], the general form of the ionic current density is

$$i_{\text{ion}} = g_{\text{ion}} x^p y^q (v - E_{\text{ion}}) \tag{105.2}$$

where g_{ion} is the maximum conductance density for a given ionic current ($\text{mS}\,\text{cm}^{-2}$), x and y are, respectively, the activation and inactivation gating variables, ranging from 0 to 1, with associated exponents p and q, E_{ion} is the Nernst potential for the ion underlying the current. For a non-inactivating current, $y = 1$, while $x = y = 1$ for a passive leakage current.

The time and voltage dependence for the gating variable x (or y) are given by:

$$\frac{dx}{dt} = \alpha_x(v)(1 - x) - \beta_x(v) \cdot x \tag{105.3}$$

The activation and inactivation parameters expressions at 22°C are given below.

Fast sodium current:

$$I_{\mathrm{Na}} = g_{\mathrm{Na}} m^3 h (v - E_{\mathrm{Na}}) \tag{105.4}$$

$$\begin{aligned} \alpha_m(v) &= \frac{5.65(v+20.4)}{1 - e^{(-20.4-v)/10.3}}; \quad \beta_m(v) = \frac{-0.2612(v+25.7)}{1 - e^{(v+25.7)/9.16}}; \\ \alpha_h(v) &= \frac{-0.0876(v+102)}{1 - e^{(v+20.4)/11}}; \quad \beta_h(v) = \frac{3.2478}{1 + e^{-(v+19.8)/13.4}} \end{aligned} \tag{105.5}$$

Fast potassium current:

$$I_A = g_A a^3 b (v - E_K) \tag{105.6}$$

$$\begin{aligned} \alpha_a(v) &= \frac{0.1134(v+40)}{1 - e^{-(v+40)/5}}; \quad \beta_a(v) = 0.0088 \cdot e^{-(v+36.5)/18.4}; \\ \alpha_b(v) &= 0.152 e^{-(v+60)/20}; \quad \beta_b(v) = \frac{2.28}{1 + e^{-(v+30)/10}} \end{aligned} \tag{105.7}$$

Persistent sodium current:

$$I_p = g_p p^3 (v - E_{\mathrm{Na}}) \tag{105.8}$$

$$\alpha_p(v) = \frac{0.0342(v+27)}{1 - e^{-(v+27)/10}}; \quad \beta_p(v) = \frac{-0.000571(v+34)}{1 - e^{(v+34)/10}} \tag{105.9}$$

Slow potassium current:

$$I_s = g_s s (v - E_K) \tag{105.10}$$

$$\alpha_s(v) = \frac{0.064}{1 + e^{-(v+77.5)/0.5}}; \quad \beta_s(v) = \frac{0.0154}{1 + e^{-(V+102.5)}} \tag{105.11}$$

Leakage current:

$$\frac{dx}{dt} = \alpha_x(v)(1 - x) - \beta_x(v) \cdot x \tag{105.12}$$

Simulation Procedure

A space–clamp system was simulated. Ionic current models from different existing membrane models were considered:

$$\begin{aligned} c\frac{dv}{dt} = &-g_{\mathrm{Na}} m^3 h (v - E_{\mathrm{Na}}) - g_A a^3 b (v - E_K) \\ &- g_p p^3 (v - E_{\mathrm{Na}}) - g_s s (v - E_K) - g_L (v - E_L) + i_{\mathrm{stim}} \end{aligned} \tag{105.13}$$

Table 105.1 The parameters in the space–clamp model

Parameters	Values
Nodal capacitance (c)	$2\,\mu F\,cm^{-2}$
Maximum fast Na^+ conductance (g_{Na})	$750\,mS\,cm^{-2}$
Na^+ Nernst potential (E_{Na})	48 mV
Maximum persistent A-current conductance (g_A)	$446\,mS\,cm^{-2}$
K^+ Nernst potential (E_K)	−98.6 mV
Maximum persistent Na^+ conductance (g_p)	$1.41\,mS\,cm^{-2}$
Maximum slow K^+ conductance (g_s)	$40\,mS\,cm^{-2}$
Nodal leakage conductance (g_L)	$2\,mS\,cm^{-2}$
Leakage reversal potential (E_L)	−90 mV
Resting potential (v_r)	−80 mV

The stimulus was delivered as a current injection in the node. Equations system was solved using backward Euler implicit integration scheme [10] in Matlab, with an integration time step of 0.005–0.05 ms. The parameters in the simulation is shown in Table 105.1.

The resulting models of ionic currents were able to reproduce the action potential kinetics consistent with these of the original OVLD model [4].

Results

The resulting model has threshold values (Fig. 105.1) consistent with anterior study [4]. The rheobase value is $0.43\,mA\,cm^{-2}$. For a 0.2 ms current pulse, the stimulating threshold is about $620\,\mu A\,cm^{-2}$.

The response of the space–clamp system to a 0.2-ms suprathreshold mono-current pulse is illustrated in Fig. 105.2. Action potential duration was doubled and reached 3 ms when the A-current was suppressed.

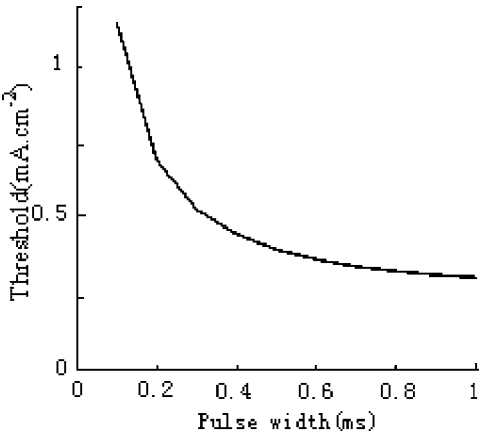

Fig. 105.1 Strength-duration curve computed for the complete model

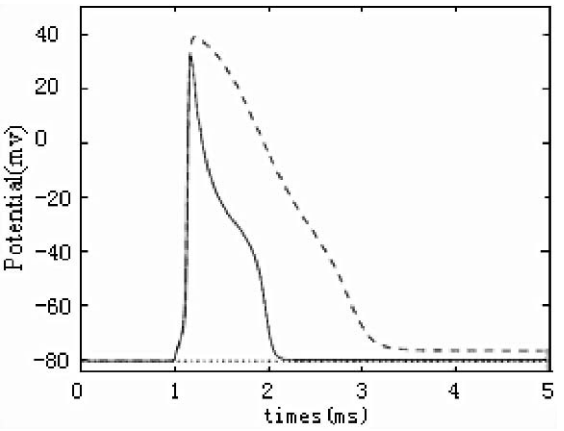

Fig. 105.2 Response to a mono-stimulation. Response of the complete model with (continuous line) and without (dashed line) the persistent A-current

When repetitive stimulation ($I = 600\,\mu$A, PW $= 0.2$ ms) was applied at 100 Hz, each pulse elicited an action potential. As shown in Fig. 105.3, at the end of the train, a small afterpotential occurred. When IA was set to zero, an AHP also followed the spike train, but this time it was larger. In normal conditions there is no AHP. In presence of 4-AP there is an activity dependent AHP. Action potentials are truncated. Simulation matched well with experimental recordings [5, 6].

In Fig. 105.4, the post-action potential threshold variations with time are illustrated. A 1-ms 150% suprathreshold conditioning stimulus was followed by an identical successive test stimulus and amplitude of the second spike was determined. The ratio of the amplitude of the second spike to the first spike is introduced and plotted against the inter-stimulus interval. The excitability of second spike expressed by its amplitude is increased with the inter-stimulus interval. Simulation matched well with experimental recordings [5].

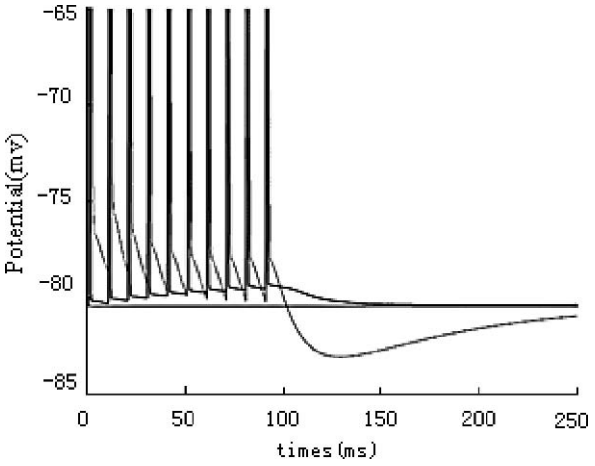

Fig. 105.3 Membrane potential response to a 100 Hz, 100 ms duration suprathreshold stimulation, with (bold line) and without (thin line) the persistent A-current

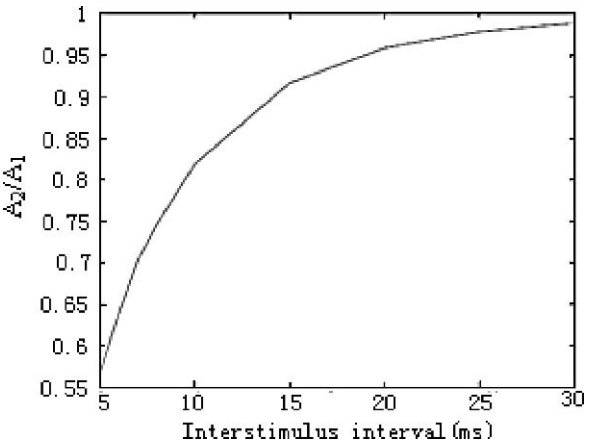

Fig. 105.4 Amplitude refractoriness. Two identical successive stimuli were delivered to the model and generated two AP. The ratio of the amplitude of the second spike to the first spike is plotted against the inter-stimulus interval

Conclusions

The work in this paper proposes a mathematical model in which the main active nodal channels including fast Na^+, persistent Na^+, slow K^+ and a fast repolarizing K^+ (A-current) were added. The model was able to generate the following features: in presence of 4-AP, increase of spike duration, depolarizing afterpotential (DAP) followed by a spike frequency dependent and tetraethylammonium (TEA) sensitive hyperpolarizing afterpotential (AHP).

Acknowledgments Supported by grants National Basic research Program of China (973 Program: 2005CB724302).

References

1. Veraart, C., Raftopoulos, C., Mortimer, J.T., Delbeke, J., Pins, D., Michaux, G., Vanlierde, A., Pairini, S., Wanel-Defalque, M.C. Visual sensations produced by optic nerve stimulation using an implanted self-sizing spiral cuff electrode. Brain Research 813 (1998) 181–186.
2. Fohlmeister, J.F., Coleman. P.A., Miller, R.F. Modeling the repetitive firing of retinal ganglion cells. Brain Research 510 (1990) 343–345.
3. Resatz, S., Rattay, F. A model for the electrically stimulated retina. Mathematical and Computer Modelling of Dynamical Systems 10 (2004) 93–106.
4. Oozeer, M., Veraart, C., Legat, V., Delbeke, J. A model of the mammalian optic nerve fibre based on experimental data. Vision Research 46 (2006) 2513–2524.
5. Gordon, T.R., Kocsis, J.D.,Waxman, S.G. Evidence for the presence of two types of potassium channels in the rat optic nerve. Brain Research 447(1) (1988) 1–9.
6. Gordon, T.R., Kocsis, J.D., Waxman, S.G. Pharmacological sensitivities of two afterhyperpolarizations in rat optic nerve. Brain Research 502(2) (1989) 252–257.
7. Lukasiewicz, P., Werblin, F. A slowly inactivating potassium current truncates spike activity in ganglion cells of the tiger salamander retina. Journal of Neuroscience 8(12) (1988) 4470–4481.

8. McIntyre, C.C., Richardson, A.G., Grill, W.M. Modeling the excitability of mammalian nerve fibers: Influence of afterpotentials on the recovery cycle. Journal of Neurophysiology 87(2) (2002) 995–1006.
9. Hodgkin, A.L., Huxley, A.F. A quantitative description of membrane current and its application to conduction and excitation in nerve. Journal of Physiology (London) 117 (1952) 500–544.
10. Mascagni, M., Sherman, A. (Eds.). Numerical Methods for Neuronal Modeling, 2nd Ed. Methods in Neuronal Modeling: From Ions to Networks. MIT Press, Cambridge, MA, USA 1996.

Chapter 106
EEG Dynamics During Nitrous Oxide Inhalation in Healthy Male Participants

Brett L. Foster, Mathew P. Dafilis, Nicholas C. Sinclair and David T.J. Liley

Abstract Despite nitrous oxides (N_2O) wide and historic clinical use, its quantitative effects on electrical brain function are still poorly characterised. Here we report on improved attempts to characterise the quantitative EEG dynamics of N_2O inhalation in healthy males. Results show varying concentrations do not suppresses resting spectra, but rather enhance alpha/beta power.

Introduction

Research into the utility of the processed electroencephalogram (EEG) as an index of patient state during anaesthesia has sharply risen over the past decade. Although many of these monitoring devices show promise, there are consistent insensitivities across monitors for specific types of anaesthetic agents [1], in particular the dissociative agents such as nitrous oxide (N_2O). N_2O is widely employed as an analgesic and sedative agent, often used as an adjuvant gas with other general anaesthetics (GA) for surgical anaesthesia. However, recent investigations have shown that a number of monitors inadequately index the effects of N_2O inhalation on the EEG [2, 3, 4], and thus patient state (i.e. anaesthetic depth).

Common GA agents (e.g. sevoflurane) produce an approximately dose-dependent suppression of EEG resting frequencies (alpha: 8-15 Hz & beta: 15+ Hz), resulting in a sleep-like slow wave dominance. N_2O, together with other dissociative agents ketamine and xenon (Xe) are of special interest owing to their somewhat paradoxical, though understudied, enhancement of resting EEG [2, 5, 6], promoting alpha and beta power.

Most GA achieve their clinical effects by the suppression of large scale neural populations [7] via the potentiation of gamma-amino-butyric-acid (GABA)

B.L. Foster
Brain Dynamics Research Unit, Brain Sciences Institute, Swinburne University of Technology, Melbourne, Australia
e-mail: bfoster@bsi.swin.edu.au

R. Wang et al. (eds.), *Advances in Cognitive Neurodynamics*,

inhibitory neurotransmission at $GABA_A$ receptors [8]. In contrast, dissociative agents are believed to act by antagonising the excitatory glutamatergic *N*-methyl-*d*-aspartate (NMDA) receptor [9].

Although there have been serious attempts to quantitatively characterise the spatio-temporal EEG during general anaesthesia [10], dissociative anaesthetics have only received relatively minimal quantitative investigation (e.g. [11]). Therefore, the following study aimed to quantify EEG dynamics induced by N_2O inhalation in healthy male participants.

Method

With approval of the authors' institutional human ethics committee, participants were recruited for a single recording session, each being randomly allocated to one of three possible conditions. The three conditions constituted three levels of N_2O (1: 20%, 2: 40% & 3: 60%), each accompanied with oxygen (O_2, 1: 80%, 2: 60% & 3: 40%, respectively). All participants had to pass a general medical examination and be in good health before involvement in the study, along with providing informed written consent.

Recording sessions involved three five minute baseline EEG recordings of eyes-open, eyes-closed and eyes-closed auditory continuous performance task (aCPT). After these baselines a 20-min N_2O condition EEG recording was performed. For the N_2O condition the first 5 min involved equilibration of the required gas concentration. Once equilibrated, the concentration was maintained for 10 min, followed by a 5-minute washout period of pure O_2. During the entire condition participants performed the same aCPT.

EEGs were recorded using two coupled EEG systems resulting in a 64 channel montage. Sixty-two channels where dedicated to the acquisition of scalp EEG, whilst the remaining two electrodes where used for auxiliary electrooculogram (EOG) and electromyogram (EMG). The 62 channel EEG montage was positioned and digitized according to the international 10:20 standard system, with a linked ear lobe reference. Electrode impedance was maintained below 10 kΩ for all recordings. All electrophysiological data was acquired continuously (non-epoched) with 500-Hz sampling and bandpass filter (0.1–70 Hz) in a noise minimized recording laboratory.

Mixed gases were delivered via a closed Bain co-axial breathing circuit, with expired gases being collected in a large capacity Douglas bag. Estimation of gas absorption was performed via an infrared gas analyzer, which provided values of N_2O content, carbon dioxide (CO_2) content and respiratory frequency via a low volume sampling line. Heart rate and O_2 saturation were obtained using pulse oximetry.

Results

Time series acquired from 14 participants were analysed, where for condition 1 (20%) $n = 5$, condition 2 (40%) $n = 5$ and condition 3 (60%) $n = 4$. However, two participants from condition 3 did not complete the full testing protocol. Preliminary

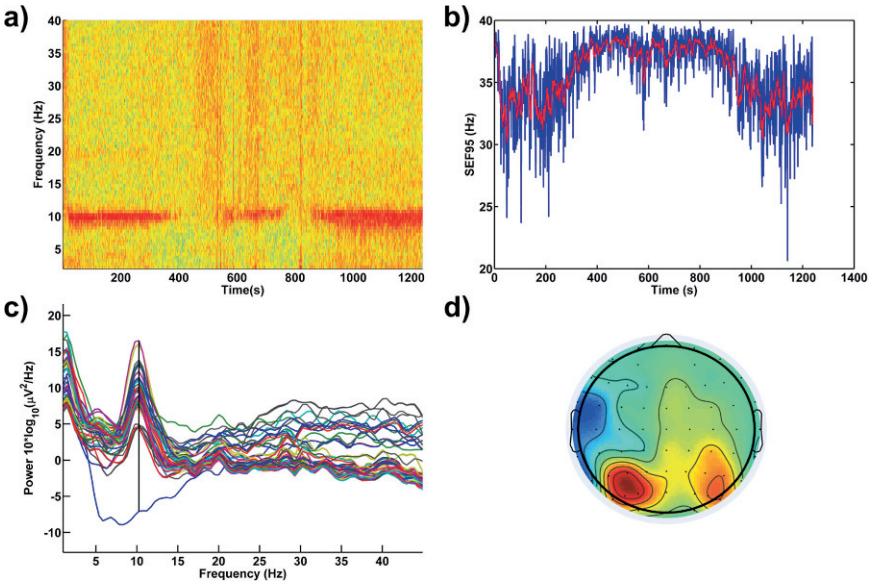

Fig. 106.1 60%, participant 3. (**a**) spectrogram for channel Oz, with (**b**) showing the SEF 95% for this channel. (**c**) Power spectrum for all channels, over the period of 600–700 s, with (**d**) showing the topographic distribution of 10 Hz as marked (black line) in (**c**)

inspection of frequency power suggested that none of the conditions produced any major suppression of the resting EEG spectrum. In most cases an alpha (≈10 Hz) power oscillation was dominant. Curiously in the 60% condition alpha power is suppressed not long after gas equilibration, and reemerges several minutes later, before being once more suppressed (at Oz). However, with the loss of alpha power there is an increase in the 95% spectral edge frequency (SEF 95%), suggesting a spectral shift to the right. This unforseen effect was shown also in the other eligible 60% participant. Inspection of anterior electrode sites showed a similar though less defined time course for the alpha band. Figure 106.1 presents the findings for a single participant under condition 3.

Discussion

Sedative concentrations of N_2O/O_2 mixture did not greatly modify the standard resting eyes closed EEG spectra. Like other dissociative anaesthetics N_2O either maintained or promoted resting alpha/beta frequencies depending on concentration. This finding supports the growing literature which suggests that NMDA based anaesthetics produce electrocortical arousal, differing from the suppression of $GABA_A$ based GA [12]. Interestingly, at the highest concentration of 60%, two participants showed a systematic return of alpha power during the maintained concentration. Such findings are likely to underlie the insensitivities of most anaesthesia monitors to N_2O/O_2 adjuvant anaesthesia and dissociative anesthesia more

generally. As linear measures provide a limited explanation for the paradoxical relationship between drug effect and EEG response, nonlinear time series analysis methods are currently being implemented by the authors. Indeed, future parameters for DOA monitoring will have to incorporate such effects in the development of more stable diagnostic devices.

References

1. Bowdle, T.A.: Depth of anesthesia monitoring. Anesthesiol Clin 24(4) (2006) 793–822.
2. Rampil, I.J., Kim, J.S., Lenhardt, R., Negishi, C., Sessler, D.I.: Bispectral EEG index during nitrous oxide administration. Anesthesiology 89(3) (1998) 671–677.
3. Barr, G., Jakobsson, J.G., Owall, A., Anderson, R.E.: Nitrous oxide does not alter bispectral index: study with nitrous oxide as sole agent and as an adjunct to i.v. anaesthesia. Br J Anaesth 82(6) (1999) 827–830.
4. Anderson, R.E., Jakobsson, J.G.: Entropy of EEG during anaesthetic induction: a comparative study with propofol or nitrous oxide as sole agent. Br J Anaesth 92(2) (2004) 167–170.
5. Goto, T., Nakata, Y., Saito, H., Ishiguro, Y., Niimi, Y., Suwa, K., Morita, S.: Bispectral analysis of the electroencephalogram does not predict respon- siveness to verbal command in patients emerging from xenon anaesthesia. Br J Anaesth 85(3) (2000) 359–363.
6. Hirota, K.: Special cases: ketamine, nitrous oxide and xenon. Best Pract Res Clin Anaesthesiol 20(1) (2006) 69–79.
7. Erchova, I.A., Lebedev, M.A., Diamond, M.E.: Somatosensory cortical neuronal population activity across states of anaesthesia. Eur J Neurosci 15(4) (2002) 744–752.
8. Rudolph, U., Antkowiak, B.: Molecular and neuronal substrates for general anaesthetics. Nat Rev Neurosci 5(9) (2004) 709–720.
9. Yamakura, T., Harris, R.A.: Effects of gaseous anesthetics nitrous oxide and xenon on ligand-gated ion channels. Comparison with iso urane and ethanol. Anesthesiology 93(4) (2000) 1095–1101.
10. John, E.R., Prichep, L.S., Kox, W., Valdes-Sosa, P., Bosch-Bayard, J., Aubert, E., Tom, M., di Michele, F., Gugino, L.D.: Invariant reversible QEEG effects of anesthetics. Conscious Cogn 10(2) (2001) 165–183.
11. Johnson, B.W., Sleigh, J.W., Kirk, I.J., Williams, M.L.: High-density EEG mapping during general anaesthesia with xenon and propofol: a pilot study. Anaesth Intensive Care 31(2) (2003) 155–163.
12. Tsuda, N., Hayashi, K., Hagihira, S., Sawa, T.: Ketamine, an NMDA-antagonist, increases the oscillatory frequencies of alpha-peaks on the electroencephalographic power spectrum. Acta Anaesthesiol Scand 51(4) (2007) 472–481.

Chapter 107
Penalized Regression Methods in the Source Analysis of Face Recognition

Mayrim Vega-Hernández, Eduardo Martínez-Montes, Jhoanna Pérez-Hidalgo-Gato, José M. Sánchez-Bornot and Pedro Valdés-Sosa

Abstract Recent developments in the field of variable selection through penalized least squares regression provide means for the analysis of neuroscience data. Particularly, combinations of non-convex penalties allow for sparse solutions and other unexplored properties that are especially attractive in their application to e.g. EEG/MEG inverse problem. Here, we explore the use of these techniques for the source analysis of a cognitive process, namely, the recognition of faces. Found sources are in agreement with previous studies and new methods, based on combination of penalties, provided for more physiologically plausible solutions.

Keywords Multiple penalized least squares · EEG · inverse problem

Introduction

Currently, the need for developing advanced statistical tools that deal with a huge amount of data has become apparent, especially in Neuroscience, where the main challenge is the analysis of neuroimaging data in which the number of hidden parameters to estimate is much greater than the number of observations. This is the case of the well-known inverse problem (IP) of the Electroencephalogram (EEG), which consists in the identification of the neural current sources inside the brain generating the voltage field measured over an array of sensors distributed on the scalp surface. The mathematical relation between these voltages ($\mathbf{v}$) and the Primary Current Density (PCD, $\mathbf{j}$) can be written as a system of linear equations:

$$\mathbf{v} = \mathbf{K}\mathbf{j} + \boldsymbol{\varepsilon} \tag{107.1}$$

where $\mathbf{K}$ comprises the geometrical and electrical properties of the model assumed for the head and is known as the electric lead field. This system is highly

M. Vega-Hernández
Neurostatistics Department, Cuban Neuroscience Center, Ave. 25, esq 158, Havana, Cuba
e-mail: mayrim@cneuro.edu.cu

R. Wang et al. (eds.), *Advances in Cognitive Neurodynamics*,

underdetermined since the number of unknown generators inside the brain is much higher than the number of sensors. Therefore, there is no unique solution and the IP is ill-posed.

The additional or prior information or constraints used for obtaining a unique solution characterizes each of the known inverse solutions [1]. Also, different approaches have been used (Bayesian, Dipole fitting) but the most popular is the regularization, which is equivalent to a penalized least squares (PLS) regression. Here we will formulate the IP as a general multiple penalized least squares (MPLS) model that encompasses most of known inverse solutions as particular cases. The use of non-convex penalty functions allows to obtain new types of inverse solutions, whose performance is explored here in the source analysis of face recognition.

Multiple Penalized Least Squares Model for EEG Inverse Problem

PLS models have been recently addressed as multivariate linear regressions with regularization with efficient and flexible techniques to solve variable selection problems. Interestingly, the use of non-convex penalty functions (non-quadratic, continuous and with a singularity at the origin) has been proposed to obtain sparse and stable solutions, such as the LASSO [2]. Moreover, this approach can be extended to use any combination of penalties, leading to solutions sharing properties such as smoothness and sparseness, e.g. Elastic Net (ENet) combines an $l1$-norm (LASSO) term and an $l2$-norm (Ridge). These non-linear models are estimated by modified Newton-Raphson algorithms such as the Local Quadratic Approximation [2] and the Minorization-Maximization [3], which have been generalized to deal with multiple penalty terms simultaneously, i.e. to tackle MPLS models [4]. The EEG inverse problem can be expressed as a MPLS model in the form:

$$\hat{\mathbf{j}} = \arg\min \left\{ \|\mathbf{v} - \mathbf{K}\mathbf{j}\|_2^2 + \sum \lambda_m P_m(\mathbf{j}) \right\} \tag{107.2}$$

where $\sum \lambda_m P_m(\mathbf{j})$, with $m = 1 \ldots M$, includes all prior information given by the penalty functions $P_m(\mathbf{j})$, weighted by corresponding regularization parameter λ_m. Several inverse solutions can be obtained as particular cases of Eq. 107.2 [5]. Here we will compute those shown in Table 107.1. As a first approximation, optimal values for λ_m will be found by generalized cross-validation [6].

The data set analyzed corresponds to an experiment in which subjects are presented faces or non-faces images followed by a mask image after 30 ms. They are required to respond if a face was presented or not. Sources of the evoked N170 peak were sought separately for correct and incorrect responses, averaged across 80 trials. Since the PCD is a vector field, the Hotelling's T^2 statistic was computed across 10 subjects for each condition and for the difference between them.

Table 107.1 Some inverse solutions derived from MPLS model. $\boldsymbol{M}$ ($\boldsymbol{m}_j$ as j-th row) and $\boldsymbol{R}$ are linear operators. $\boldsymbol{I}$ is the identity matrix and $\boldsymbol{L}$ a discrete version of laplacian operator

Name	$\sum \lambda_m P_m(\mathbf{j})$	Inverse solution
Ridge	$\lambda \mathbf{j}^T \mathbf{M}^T \mathbf{M}\mathbf{j}$	If $M = I \rightarrow$ Minimum Norm; If $M = L \rightarrow$ Loreta
Lasso	$\lambda \sum \lvert \mathbf{m}_j \mathbf{j} \rvert$	If $M = I \rightarrow$ Lasso; If $M = \mathbf{L} \rightarrow$ Lasso Fusion
ENet	$\lambda_1 \mathbf{j}^T \mathbf{R}^T \mathbf{R}\mathbf{j} + \lambda_2 \sum \lvert \mathbf{m}_j \mathbf{j} \rvert$	If $M = R = I \rightarrow$ ENet; If $M = R = L \rightarrow$ ENet L

Source Localization of Face Recognition

Figure 107.1 shows the maximum projection in the coronal view of the estimated Hotelling's T^2 images by the three methods for each condition: correct response (top row), incorrect response (middle row) and difference between correct and incorrect responses (bottom row).

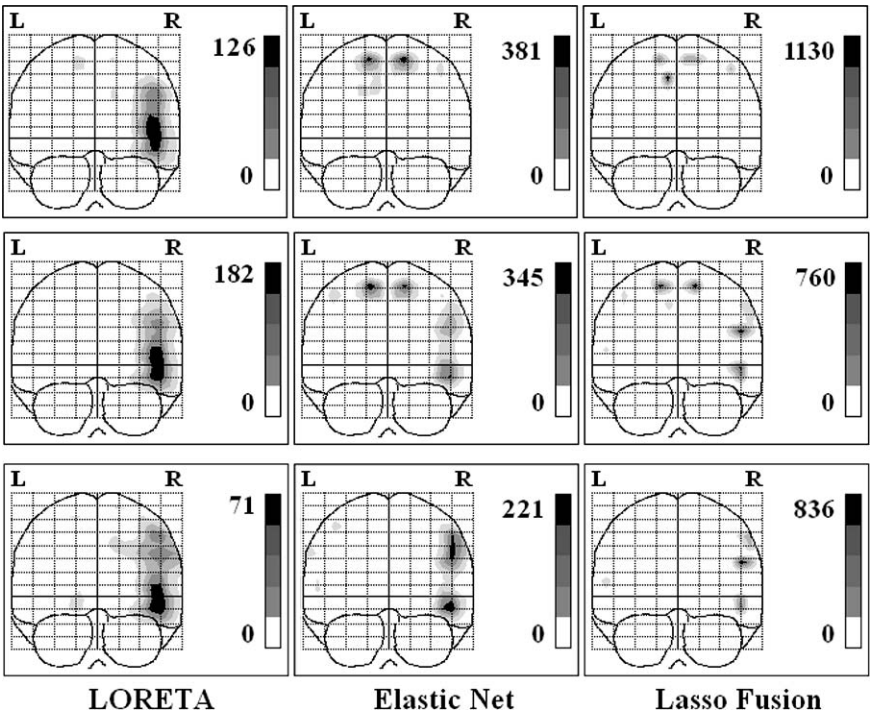

Fig. 107.1 Hotelling's T^2 images of sources of evoked N170 peak corresponding to correct face detection (upper panel), incorrect face detection and (middle panel) and the difference between correct and incorrect detection (bottom panel)

Significant activations for the correct and incorrect detection of faces were found in the inferior and superior temporal gyrus right, in the middle frontal gyrus (right and left) and in the middle occipital gyrus right, although with different degree of activation. These areas are in agreement with previous fMRI studies on the conscious perception of faces [7]. Significant differential sources were located mainly in the inferior temporal gyrus right and middle occipital gyrus right.

On the other hand, it can be seen that the use of $l1$-norm (Lasso Fusion) allows for much more concentrated (sparser) solutions, dividing the usual low resolution image given by LORETA in several sources. ENet L, in turn, offers solutions with intermediate degrees of sparseness and smoothness (that can be tune through the regularization parameters) and are more physiologically plausible.

Conclusions

In this work we have studied the applicability of a general statistical tool, namely, MPLS, to the source analysis of face recognition. Three inverse solutions (one known, LORETA and two newly proposed, Lasso Fusion and ENet) found sources in agreement with previous studies with fMRI. Also, it was shown that by combining $l1$ and $l2$-norm terms, ENet L offers solutions with intermediate levels of blurring between LORETA (too smooth) and Lasso Fusion (too sparse). However, this method strongly depend on the selection of optimal regularization parameters, therefore, further research on the use of appropriate (non-linear) methods is needed.

In general, the formulation of the EEG inverse problem in terms of an MPLS model, offers the possibility of exploring a wide range of new kind of inverse solutions.

References

1. Pascual-Marqui, R.D.: Review of methods for solving the EEG inverse problem. Int. J. Bioelectromagnetism 1 (1999) 75–86.
2. Fan, J.Q. and Li, R.Z.: Variable selection via nonconcave penalized likelihood and its oracle properties. J. Am. Stat. Assoc. 96 (2001) 1348–1360.
3. Hunter, D.R. and Lange, K.: A tutorial on MM algorithms. Am. Stat. 58 (2004) 30–37.
4. Valdés-Sosa, P.A.; Sánchez-Bornot, J.M.; Vega-Hernández, M.; Melie-Garcia, L.; Lage-Castellanos, A. and Canales-Rodriguez, E.: Granger Casuality on Spatial Manifolds: applications to Neuroimaging. Handbook of Time Series Analysis: Recent Theoretical Developments and Applications. Chapter 18 (2006). ISBN: 3-527-40623-9.
5. Vega-Hernández, M., Sánchez-Bornot, J.M., Lage-Castellanos, A., Martínez-Montes, E. and Valdés-Sosa, P.A.: Penalized regression methods for solving the EEG inverse problem. Available on CD-Rom in Neuroimage 27 1 (2006).
6. Golub, G., Heath, M. and Wahba, G.: Generalized cross-validation as a method for choosing a good ridge parameter. Technometrics 21 (1979) 215–223.
7. Kanwisher, N., McDermott, J. and Chon, M.M.: The fusiform area: a module in human extrastriate cortex specialized for face perception. J. Neurosci. 17 (1997) 4302–4311.

Chapter 108
Brain Activation During Scientific Hypothesis Generation in Biologists and Non-biologists

Il-Sun Lee, Jun-Ki Lee, Jin-Su Jeong and Yong-Ju Kwon

Abstract Functional magnetic resonance imaging was used to investigate neural substrates during scientific hypothesis generation, in particular, the differences between biologists and non-biologists. Eight biologists and eight non-biologists were scanned while they performed eight scientific hypothesis generation tasks. The results of this study revealed that activation of the left inferior and middle frontal gyri were driven by increased working memory load. The superior medial prefrontal cortex reflected higher-order inferential processes. The activation of the right hippocampus reflected the retrieval and encoding of information in long-term memory. The increased activity in the occipito-parietal route was due to perception and visuo-spatial working memory. Furthermore, the biologists' exceptional abilities for hypothesis generation were correlated with the acceleration of memory retrieval and higher-order inferential processes.

Keywords Scientific hypothesis · biologist · non-biologist · causal inference · prefrontal cortex · hippocampus · occipito-parietal route

Introduction

A hypothesis is a proposition proposed as a tentative causal explanation for an observed situation [1]. Generating a scientific hypothesis is a key component of modern scientific method [2]. How do scientists generate hypotheses in actual scientific situations? From a cognitive psychological perspective, hypothesis generation has been regarded as a causal inference [1]. It has been suggested that making causality is clearly rooted in perceptual experience. However, it goes beyond perception in inferring relationships. It includes the retrieval and activation of information within long-term memory (LTM), the appropriate selection of relevant semantic information, the short-term retention of information within working memory, and

I.-S. Lee
Department of Biology Education, Korea National University of Education, Chungbuk 363-791, Korea
e-mail: yis213@hanmail.net

R. Wang et al. (eds.), *Advances in Cognitive Neurodynamics*,

the encoding of information into LTM [3]. The left inferior prefrontal cortex mediates the controlled retrieval and selection of information for integration and encodes new information in LTM, which is associated with the hippocampus [4]. Both the posterior inferior prefrontal cortices and the dorsolateral prefrontal regions are implicated in short-term retention of verbal semantic information within working memory. However, previous studies have not examined real causal inference for scientific hypothesis generation, and the studies were only performed on populations with a relatively normal range of intelligence. Therefore, the present study investigated neural substrates during scientific hypothesis generation, in particular, the differences between biologists and non-biologists.

Methods

Eight healthy biologists (all male, right-handed, aged 30–39) and eight healthy non-biologists (all male humanists, right-handed, aged 26–39) took part in the study with informed consent and with the approval of the Ethics Committee of Korea National University of Education. All of the biologists had doctorate degrees in biology while three of the non-biologists had doctorate degrees in the humanities or social sciences and the remaining five non-biologists were students currently undertaking postgraduate study in the department of elementary education. Eight visual tasks were presented to the biologists and non-biologists. In each task, participants were shown a biological picture with a causal question (e.g., Why is the monkey covered with white fur?). They were asked to generate a scientific hypothesis, a tentative causal explanation for the question. Each task was performed for 30 s followed by a baseline stimulus of a white crisscross on a black background for 12 s. Blood oxygen level-dependent (BOLD) images were obtained with a $T2^*$-weighted echo planar imaging (EPI) gradient echo sequence from a 3.0T MR scanner (ISOL, KOREA) with standard head coil. The image parameters were as follows: TR 3000 ms; TE 35 ms; a matrix size of 64×64 FOV 220×220 mm; and 5 mm slice thickness with no gaps. 30 axial EPI BOLD images were acquired.

After scanning, participants were asked to write down all hypotheses generated during the eight visual tasks. They were also asked to express the degree of confidence in their hypotheses by checking a point on the Likert seven-point scale – 0, least confident; 6, most confident. Once these requirements were fulfilled, participants then partook in semi-structured interviews regarding cognitive strategies used during the tasks. Structural and functional images were analyzed using SPM2. Statistical analysis was carried out using one sample t-test to determine significant activation at group level. Voxels were considered to be significantly activated when they passed a statistical threshold of $p < 0.0005$, uncorrected.

Results

The results of semi-structured interviews indicated that the participants performed the tasks in the expected manner. All of the participants, except one non-biologist

on only one task, successfully generated scientific hypotheses. On average, the biologists' the degree of the confidence was 3.18 (±0.48) and the non-biologists' was 2.10 (±0.64). There was significant difference between the mean confidences ($t = 3.784$, $p < 0.005$). In retrospective reports, all participants answered that they had focused their attention on generating scientific hypotheses.

The fMRI results are summarized in Fig. 108.1. The 'main effect' (hypothesis generation – baseline) of hypothesis generation as shown in Fig. 108.1a revealed activation in the left superior frontal gyrus, the left middle frontal gyrus, the bilateral precentral gyri, the left medial frontal gyrus, the left inferior frontal gyrus, the right superior parietal lobule, the left precuneus, the right hippocampus, the left superior occipital gyrus, the bilateral lingual gyri, the bilateral middle occipital gyri, the bilateral culmens, the right declive, and the right insula. The 'expert effect' [(biologist – baseline) – (non-biologist – baseline)] illustrated in Fig. 108.1b via red

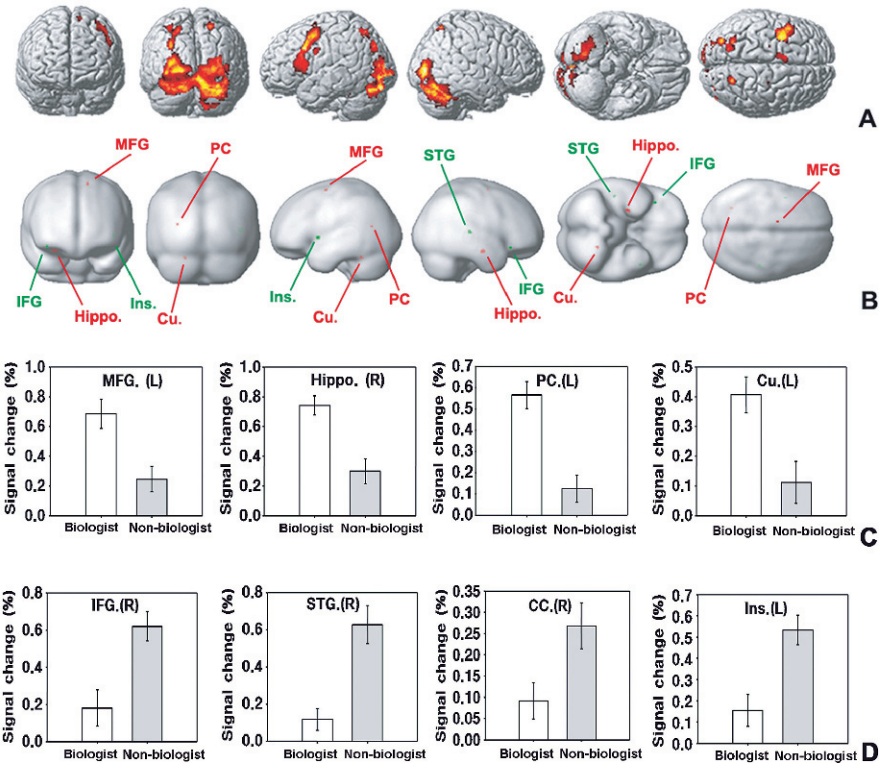

Fig. 108.1 Surface-rendered brain areas activated by the main effect (a), expert effect (red blobs of b), and non-expert effect (green blobs of b). The signal changes (%BOLD signal changes) by the expert effect are greater in biologists than non-biologists in four regions (c): MFG.(L) = the left medial frontal gyrus, Hippo.(R) = the right hippocampus, PC.(L) = the left posterior cingulate, and Cu.(L) = the left culmen. The %BOLD signal changes by the non-expert effect are greater in non-biologists than biologists in four regions (d): IFG.(R) = the right inferior frontal gyrus, STG.(R) = the right superior temporal gyrus, CC.(R) = the right corpus callosum, and Ins.(L) = the left insula

blobs showed activation in the left medial frontal gyrus, the right hippocampus, the left posterior cingulate, and the left culmen. The green blobs in Fig. 108.1b, on the other hand, highlighted the 'non-expert effect' [(non-biologist – baseline) – (biologist – baseline)] i.e. activation in the right inferior frontal gyrus, the left superior temporal gyrus, the right corpus callosum, and the right insula.

Discussion

According to the main effect (Fig. 108.1a), the left inferior prefrontal gyrus (BA 44, 45) as well as the left dorsolateral prefrontal (BA 6, 9) regions appear to hold information within working memory [3]. Several working memory studies have also revealed activation of the left frontal cortex and the right cerebellum to be associated with increased working memory demands [5]. Therefore, it is possible that the recruitment of the left inferior and middle frontal gyri and the culmen were driven by the increased working memory load associated with establishing inference to generate scientific hypothesis. In addition, the left superior medial prefrontal cortex (BA 6) has been implicated in establishing integration of information [6]. Thus, it is also possible that activation of the left superior medial prefrontal cortex during hypothesis generation reflects higher-order inferential processes. Additionally, the main effect was found to be consistent with the suggestion that the right hemisphere possesses an advantage for causality perception and the left hemisphere has a greater ability to infer causality [7]. In the frontal lobe, the left hemispheric distribution observed in present study may have been predominantly achieved through left hemisphere processing for inferring causality during scientific hypothesis generation.

The expert effect produced activations of the left medial frontal gyrus (BA 6), the right hippocampus, the left posterior cingulate (BA 31) and the right culmen during hypothesis generation (Fig. 108.1b). The computations of %BOLD signal change in these four regions also showed that activities in all regions were greater in biologists than non-biologists (Fig. 108.1c). These areas have been claimed to be involved in higher-order inferential processes (the left medial frontal gyrus), episodic memory retrieval (the posterior cingulate) and long-term memory (the hippocampus) [4, 6]. Therefore, it is suggested that the biologists' exceptional abilities for hypothesis generation may be correlated with the acceleration of memory retrieval and higher-order inferential processes.

On the other hand, the non-biologist revealed activations of the right inferior frontal gyrus (BA 47), the left superior temporal gyrus (BA 41), the right corpus callosum, the right insula (BA 13) during hypothesis generation (Fig. 108.1b). The %BOLD signal change in these four regions also showed that activities in all regions were greater in non-biologists than biologists (Fig. 108.1d). Several studies have suggested that the insula is associated with uncertainty in linking cognitive and affective components [8] and the right inferior frontal gyrus is involved in hard task conditions [9]. Thus, it is possible that the activations of the insula and the inferior frontal gyrus during hypothesis generation reflected non-biologists' low hypothesis

confidence. Actually, behavioral results showed that non-biologist confidence in generated hypotheses was lower than biologist confidence.

In conclusion, this study showed that the recruitment of the left inferior and middle frontal gyri and the culmen were driven by the increased working memory load, and the superior medial prefrontal cortex reflected higher-order inferential processes during hypothesis generation. In addition, the activation of the right hippocampus reflected retrieval and encoding of information in LTM, and the increased activity in the occipito-parietal route was due to perception and visuo-spatial working memory of visual information. Furthermore, the biologists' exceptional abilities for hypothesis generation were correlated with the acceleration of memory retrieval and higher-order inferential processes, and the non-biologists' low hypothesis confidence was linked to the activations of the insula and the inferior frontal gyrus.

References

1. Lawson, A.E., 1995. Science Teaching and the Development of Thinking. Wadsworth Publishing Company, CA.
2. McPherson, G.R., 2001. Teaching and learning the scientific method. The American Biology Teacher 63, 242–245.
3. Kuperberg, G.R., Lakshmanan, B.M., Caplan, D.N., Holcomb, P.J., 2006. Making sense of discourse: An fMRI study of causal inferencing across sentences. Neuroimage 33, 343–361.
4. Eldridge, L.L., Knowlton, B.J., Furmanski, C.S., Bookheimer, S.Y., Engel, S.A., 2000. Remembering episodes: A selective role for the hippocampus during retrieval. Nat. Neurosci. 3, 1149–1152.
5. Petersen, S.E., Fox, P.T., Posner, M.I., Mintun, M., Raichle, M.E., 1988. Positron emission tomographic studies of the cortical anatomy of single-word processing. Nature 331, 585–589.
6. Ferstl, E.C., von Cramon, D.Y., 2002. What does the frontomedian cortex contribute to language processing: Coherence or Theory of Mind? Neuroimage 17, 1599–1612.
7. Fugelsang, J.A., Roser, M.E., Corballis, P.M., Gazzaniga, M.S., Dunbar, K.N., 2005. Brain mechanisms underlying perceptual causality. Cogn. Brain Res. 24, 41–47.
8. Paulus, M.P., Rogalsky, C., Simmons, A., Feinstein, J.S., Stein, M.B., 2003. Increased activation in the right insula during risk-taking decision making is related to harm avoidance and neuroticism. Neuroimage 19, 1439–1448.
9. Goel, V., Dolan, R.J., 2000. Anatomical segregation of component processes in an inductive inference task. J. Cogn. Neurosci. 12, 1–10.

Chapter 109
Wavelet Analysis of ERP Recordings for Dual Tasks in Man

Jie Wu, Zhuo Yang and Tao Zhang

Abstract The study was to examine the application of wavelet packet method to electrophysiological responses recorded during single and dual task performance. Relative energies of both EEG alpha and beta frequency bands were significantly higher in the single task conditions compared with that of the dual task condition ($P < 0.05$). The data demonstrated that relative energy measurements based on wavelet transform could be a useful alternative approach to analyzing short duration EEG signals on a time scale of seconds.

Introduction

EEG and ERP data sets are non-stationary in both time and space. Furthermore, the specific components and events tend to be transient, prominent over certain scalp regions, and restricted to certain ranges of temporal and spatial frequencies [1]. Nonlinear dynamics have been shown to characterize a large number of complex physiological systems, however, the techniques and algorithms for nonlinear analysis used so far have been derived from low-dimensional dynamic systems [2]. It is hard to apply the techniques and algorithms in calculating EEG signals, which have a high-dimensional structure. Another approach to measurement of nonlinear trends in EEG data is quantification of complexity from the point of view of information theory. To this end, EEG data can be analyzed with the help of entropy measurements such as approximate entropy (ApEn) and sample entropy (SampEn) [3]. The wavelet packet transform (WPT) represents a generalization of the wavelet methods and it has recently been applied to various science and engineering fields with great success. Based on wavelets and their related function called wavelet packets wavelet method could efficiently measure and manipulate non-stationary signals, such EEG and ERP. Wavelet analysis could provide flexible control over

T. Zhang
Key Laboratory of Bioactive Materials, Ministry of Education, College of Life Science, Nankai University, Tianjin 300071, PR China
e-mail: zhangtao@nankai.edu.cn

R. Wang et al. (eds.), *Advances in Cognitive Neurodynamics*,

the resolution with which neuro-electric components and events can be localized in time, space, and scale. There are some relations between nature brain rhythms and functions. For example, alpha frequency responses have been reported in association with, e.g., attention, alertness and semantic memory and beta frequency responses have been associated with the activity of the motor cortices and recently also with cognitive processing [4, 5]. In this investigation, wavelet packet method was used to analysis short time series EEG data collected from participants in both single and dual task conditions. It has been proposed that cognitive control mechanisms are required to orchestrate performance of more than one task at a time [3]. If this is the case then it is expected that the energy distribution of the EEG signals should be different in the multiple task condition compared with the single task condition.

Method

None of the participants were taking medication, have a history of head injury, substance abuse, or any significant medical or psychiatric problems that may impact on electrophysiological responses. There were two conditions: single task and dual task. The experimental stimuli and participants behavioural responses were controlled and collected using the Superlab (SL, Cedrus Corporation, Phoenix, USA) software program. The details of experimental tasks and data Acquisition can be seen in reference [3].

Wavelet Packet Transforms

A wavelet family $\psi_{a,b}$ is the set of elemental functions generated by scaling and translation of a unique admissible mother wavelet $\psi(t)$:

$$\psi_{a,b}(t) = |a|^{-1/2}\,\psi\left(\frac{t-b}{a}\right) \tag{109.1}$$

where $a, b \in R$, $a \neq 0$, are the scale and translation parameters, respectively, and t is the time. The continuous wavelet transform (CWT) of a signal $S(t) \in L^2(R)$ is defined as the correlation between the function (signal) $S(t)$ with the family wavelet $\psi_{a,b}(t)$ for each a and b

$$(W\psi S)(a,b) = |a|^{-1/2}\int S(t)\psi^*\left(\frac{t-b}{a}\right)dt = (S, \psi_{a,b}) \tag{109.2}$$

where the symbol of * is complex conjugation and $(S, \psi_{a,b})$ are the wavelet coefficients. $E_\mathrm{s} = \sum_k |s(k)|^2$. And the relative energy is defined as $E_\mathrm{sr} = \frac{E_\mathrm{s}}{E_\mathrm{t}}$ Where E_t is the total energy, which is calculated by adding E_s here [6].

Statistics

All the data are expressed as the mean ± SEM. Analysis of variance (ANOVA) was used for statistical analysis of the data, allowing within and between task comparisons to be made and significant differences were presented when $P < 0.05$.

Results

The comparison of relative energy measurements between AST and ADT data in channel fp1 and fp2 on rhythm alpha and beta is shown in Fig. 109.1. For the single auditory task, it can be seen that the group values ($n = 13$) of relative energy measurements for the rhythm alpha (0.011 ± 0.001 for fp1 and 0.016 ± 0.002 for fp2) is significantly higher ($P < 0.01$) than that of ADT group (0.027 ± 0.004 for fp1 and 0.031 ± 0.003 for fp2). Meanwhile, it can be found that for AST the relative energy measures of rhythm beta (0.049 ± 0.005 for fp1 and 0.068 ± 0.008 for fp2) is also statistically higher ($P < 0.05$) than that of ADT groups (0.117 ± 0.014 for fp1 and 0.130 ± 0.013 for fp2).

Figure 109.2 gives the relative energy measurements for rare tone stimuli in the single auditory task and the auditory-motor dual task ($n = 13$) on rhythm alpha and beta, respectively. The relative energy values of the alpha rhythm in the auditory single task condition were high compared to that of the auditory dual task condition, but there were only 11 channels (Fig. 109.2a) where significant differences of relative energy between them were obtained ($P < 0.05$). Meanwhile, the relative energy values of the beta rhythm for the most of the electrodes (expect for six channels of total 26, Fig. 109.2a) in the AST condition were significantly higher than that of the ADT condition ($P < 0.05 - 0.001$).

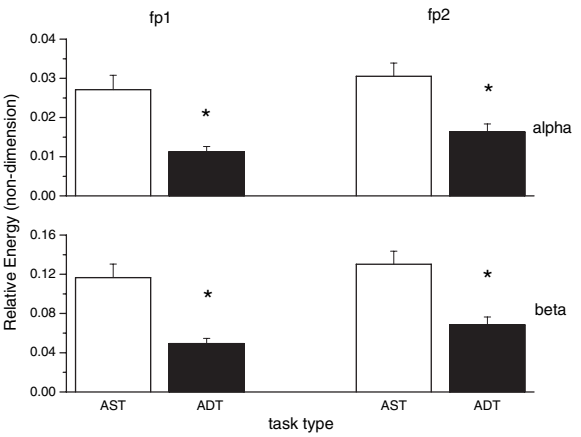

Fig. 109.1 Statistical comparisons were taken between the relative energy AST data (open bars) and ADT (solid bars) in channel fp1 and fp2 on rhythm alpha and beta, respectively. The group data are expressed as the Mean ± SEM, $^{*}P < 0.05$

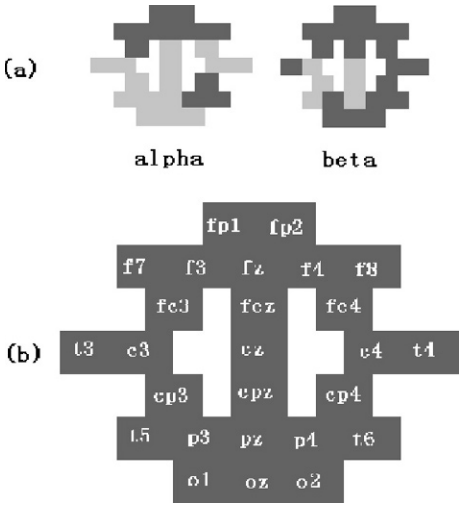

Fig. 109.2 (**a**) Comparison values of relative energy between AST and ADT. Dark colour was taken for indicating significant differences between AST & ADT and light colour for statistically insignificant differences. (**b**) International 10/20 electrode placement system

Discussions

Various investigations have shown that applying nonlinear dynamical methods to time series of brain electrical activity provides new information about the complex dynamics of the underlying neuronal networks [1, 7]. However, it is hard to provide clearly biological meanings based on the results obtained from analysis of nonlinear dynamical measurements.

It is known that certain events can block or desynchronize the ongoing alpha and beta activity. This may be considered to be due to a decrease in synchrony of the underlying neuronal populations, which is called event-related desynchronization (ERD) [7]. In the previous study it was found that the entropy values, obtained from the algorithm of SampEn, in ADT were significantly lower than that in AST [3]. At the present study, it can be seen that the relative energy values of either alpha or beta rhythms in the auditory single task condition were significantly lower than that of the auditory dual task condition. The results suggest that the neural information transmission or communication in the participants when performing auditory/motor dual task could be isolated and was impaired compared to when participants only performed the single auditory task.

In conclusion, the findings of this study have demonstrated that wavelet packet method could be alternative approaches for analyzing ERP signals using short-term time series. The method further show promise as a quantitative measure of nonlinear dynamic systems behaviour and psychological changes, such as single compared with dual tasks challenges, where the nonlinear dynamical approaches, have been challenged since they are limited in their ability to present only global information of the system.

Acknowledgments NSFC (30470453, 30640037), TMSTC (06yfjwjc09400).

References

1. Samar, V. J., Bopardikar, A., Rao, R., Swartz, K.: Wavelet analysis of neuroelectric waveforms: a conceptual tutorial. Brain Lang, 66(1).(1999) 7–60.
2. Zhang, T., Johns, E. J.: Chaotic characteristics of renal nerve peak interval sequence in normotensive and hypertensive rats. Clin Exp Pharmacol Physiol, 25(11).(1998) 896–903.
3. Zhang, T., Tang, X. J.,Yang, Z.: Comparison of complexity and regularity of ERP recordings between single and dual tasks using sample entropy algorithm. Lect Notes Comput Sci, 3610.(2005) 806–810.
4. Pesonen, M., Bjornberg, C. H., Hamalainen, H., Krause, C. M.: Brain oscillatory 1-30 Hz EEG ERD/ERS responses during the different stages of an auditory memory search task. Neurosci Lett, 399(1-2).(2006) 45–50.
5. Ward, L. M.: Synchronous neural oscillations and cognitive processes. Trends Cogn Sci, 7(12).(2003) 553–559.
6. Rosso, O. A., Martin, M. T., Figliola, A., Keller, K., Plastino, A.: EEG analysis using wavelet-based information tools. J Neurosci Methods, 153.(2006) 163–182.
7. Pfurtscheller, G., Aranibar, A.: Event-related cortical desynchronization detected by power measurements of scalp EEG. Electroencephalogr Clin Neurophysiol, 42(6).(1977) 817–826.

Chapter 110
Neocortical and Neocerebellar Synchronization of Fast Oscillations: Role in the Dynamic Organization of Rapid Temporal Processing

John P. Welsh, Xiao-Hui Zeng, Paulo Rodrigues and Eric Washburn

Abstract We investigated the role of neuronal synchrony and oscillation for rapid temporal processing in both the sensory and motor domains. A novel technique for genetically blocking neuronal gap junctions in the fully-developed brain using lentiviral knockdown of connexin36 was applied to the inferior olive of the medulla and inhibitory interneurons in primary auditory neocortex in behaving rats. Functional studies of normal and uncoupled neural networks at the behavioral level using multiple electrode recordings in vivo and intracellular recording in vitro demonstrated the important of connexin36-mediated gap junctions for sensory and motor precision in the range of 20–50 ms. Such precision allows synchronous muscle activity during movement and for the perception of rapidly presented auditory stimuli during a two-tone auditory task. At both the in vivo and in vitro levels, our studies suggest a general importance of the synchronous oscillations of neuronal ensembles for rapid temporal processing.

Keywords Gap junction · electrical synapse · connexin36 · behavior · oscillation · synchrony · auditory

Introduction

The olivocerebellar system is perhaps the best example of a system in the mammalian brain in which we are beginning to ascribe a behavioral function to electrical synapses. The inferior olive (IO), the origin of the olivocerebellar system, was the first structure in the mammalian brain in which both electrical synapses [1] and gap junctions [2] were identified. Now, over 30 years later, it is accepted that the IO has the highest density of neuronal gap junctions in the adult brain [3, 4, 5] and, more generally, that electrical synapses are important for brain function [6, 7]. The physiological effect of gap junctions within the IO is manifested in electrotonically

J.P. Welsh
Department of Pharmacology and Physiology, Drexel University College of Medicine, Philadelphia, PA, USA
e-mail: john.welsh2@drexelmed.edu

R. Wang et al. (eds.), *Advances in Cognitive Neurodynamics*,

coupled potentials in vivo [1] and in vitro [8] and is the basis for the synchrony of the 10 Hz oscillations in membrane potential that are subthreshold for spiking. Electrotonic coupling among IO neurons triggers synchronous complex spikes in groups of Purkinje cells in the cerebellar cortex [9, 10], as detected with multielectrode arrays. The synchronous triggering of cerebellar complex spikes is very tight, and occurs with sub-millisecond precision. Patterns of complex spike synchrony are significantly correlated with the performance of a skilled operant movement [10, 11] and reorganize "on-line" in the tens-of-milliseconds time domain as skilled movement is being performed. Studies have shown that removing the IO disrupts the timing of skilled movement [12]. Thus, there is good evidence to suggest that the ability of ensembles of IO neurons to synchronize their activity may be fundamental for cerebellar motor control. Indeed, the dynamic reconfiguration of electronic coupling within the IO may be the substrate that facilitates the recombination of muscle synergies during movement [13].

Among the various bandwidths of neocortical activity, the so-called gamma ("40-Hz") rhythm has received an extraordinary amount of attention. This is because: (1) the relation of the gamma rhythm to higher sensory and cognitive function is becoming understood, and (2) many biophysical features of thalamocortical circuits that give rise to the gamma rhythm have been identified [7]. The gamma rhythm represents synchronous electrical events, recurring at 30–90 Hz, that are sufficiently coherent within large volumes of cortex to generate strong electrical fields. The gamma oscillation forms a large component of the low-voltage, high frequency EEG of wakefulness. The period of the gamma oscillation ($\sim$20 ms) in auditory cortex evoked by a click predicts the shortest interval that humans could distinguish two successive clicks as separate events [14] and implies that the upper limit of brain speed ($\sim$50 Hz) is reflected in the gamma rhythm.

Both olivocerebellar 10-Hz oscillation and the neocortical gamma oscillation have been shown to require neuronal gap junctions mediated by connexin36. We developed a lentiviral (LV) method for disrupting connexin36 in adult rats that can be used to electrically uncouple local brain circuits. Our LV method employs a dominant-negative mutation of connexin36 that prevents wild-type connexin36 from being trafficked to the neuronal membrane [15]. Application of our LV method in adult rat brain circumvented the developmental compensation that can occur after embryonic gene deletion. We applied this method to the functional study of electrical synapses in awake and behaving rats performing simple motor tasks requiring 10-Hz olivocerebellar function and complex cognitive tasks that engage 40-Hz gamma rhythm in neocortex for the purpose of elucidating the functional meaning of neural synchronization for motor and cognitive function.

Experimental Findings

Our experiments unilaterally blocked gap junctions in the IO using lentivector based gene-transfer of the dominant-negative connexin36 under stereotaxic control. We found that unilateral blockade of gap junctions in the IO desynchronized harmaline

tremor on the contralateral side of the body without blocking the tremor or affecting the ipsilateral side [16]. This was quantified using six-site EMG recording where we found that there was a 15–40-ms dispersion in the EMG burst onset times from muscles at cervical to lumbar levels on the body side controlled by the uncoupled IO. This contrasted with the unaffected side of the body which had EMG burst onset times that were close to synchronous with little temporal variation. We found that genetically uncoupled IO neurons were unable to express robust, large amplitude and continuous oscillations in their membrane potential, but instead expressed low-voltage oscillations that were ~10% of normal amplitude and which could not be sustained longer than 2 s [17]. The experiments demonstrated that gap junctional coupling between neurons, specifically mediated by connexin36, allows a continuous network oscillation to emerge from a population of weak and episodic cell oscillators.

We used a multielectrode approach to record gamma oscillations in the primary auditory cortex of awake rats performing an auditory task of rapid temporal processing [18]. Rats were trained in an operant paradigm using tongue protrusion as the conditioned response (CR) to differentially respond to auditory stimuli comprised of 8 ms, 80 dB, 10 kHz tones. An excitatory conditioned stimulus (CS+) consisted of two tones and was reinforced with a drop of water onto the tongue upon a CR after the second tone; a conditioned inhibitor (CS−) consisted of a single tone and was not reinforced. For conditioning, the intertone interval for the CS+ was 200 ms and differentiation of responding occurred over 80 daily sessions (120 trials/session) such that the CS+ elicited 69 ± 6% CRs while the CS− elicited 35 ± 6% CRs. After differentiation, the intertone interval during the CS+ was varied randomly (10–400 ms) in a psychophysical test to determine the minimal interval at which the second tone could be heard. This test revealed that 10–15 ms is the threshold interval at which rapid temporal processing in the auditory domain occurs. We recorded local field potentials (LFPs) from 15 sites from primary auditory cortex during differential conditioning and the psychophysical test. During rapid temporal processing, there were two bursts of gamma oscillation to the first tone and an evoked burst to the second tone; however, there was only a single evoked burst to the first tone in rats not trained for rapid temporal processing. LFPs recorded during the cognitive test also indicated a decrease in gamma strength after local LV blockade of connexin36.

Conclusions

Our data with vector-based gene transfer to knock down connexin36 function in the normally developed brain demonstrated a functional role for neuronal synchrony in the inferior olive for “motor binding,” by which is meant the ability to rapidly control the contraction of independent muscles in the temporal domain for coordinated movement, a behavioral property that emerges from the ability of electrical coupling to permit ensemble rhythms. In the auditory cortex, the findings indicated that bursts of gamma oscillation may be learned and therefore predictive, perhaps to prime a perceptual response for rapidly presented sounds that are temporally predictable.

Acknowledgments Supported by research grant R01 NS31224 from the United States National Institutes of Health and Autism Speaks.

References

1. Llinás, R., Baker, R., Sotelo, C.: Electrotonic coupling between neurons in cat inferior olive. J Neurophysiol 37 (1974) 560–571.
2. Sotelo, C., Llinás, R., Baker, R.: Structural study of inferior olivary nucleus of the cat: morphological correlates of electrotonic coupling. J Neurophysiol 37 (1974) 541–559.
3. DeZeeuw, C.I., Ruigrok, T.J., Holstege, J.C., Jansen, H.G., Voogd, J.: Intracellular labeling of neurons in the medial accessory olive of the cat: II. Ultrastructure of dendritic spines and their GABAergic innervation. J Comp Neurol 300 (1990) 478–494.
4. Condorelli, D.F., Parenti, R., Spinella, F., Trovato Salinaro, A., Belluardo, N., Cardile, V., Cicirata, F.: Cloning of a new gap junction gene (Cx36) highly expressed in mammalian brain neurons. Eur J Neurosci 10 (1998) 1202–1208.
5. Teubner, B., Degen, J., Sohl, G., Guldenagel, M., Bukauskas, F.F., Rexler, E.B., Verselis, V.K., DeZeeuw, C.I., Lee, C.G., Kozak, C.A., Petrasch-Parwez, E., Dermietzel, R., Willecke, K.: Functional expression of the murine connexin 36 gene coding for a neuron-specific gap junctional protein. J Membr Biol 176 (2001) 249–262.
6. Bennett, M.V.L.: Electrical synapses: a personal perspective (or history). Brain Res Rev 32 (2000) 16–28.
7. Connors, B.W., Long, M.A.: Electrical synapses in the mammalian brain. Ann Rev Neurosci 27 (2004) 393–418.
8. Llinás, R., Yarom, Y.: Electrophysiology of mammalian inferior olivary neurons in vitro: different types of voltage-dependent ionic conductances. J Physiol 315 (1981) 549–567.
9. Sasaki, K., Bower, J.M., Llinás, R.: Multiple Purkinje cell recording in rodent cerebellar cortex. Eur J Neurosci 1 (1989) 572–586.
10. Welsh, J.P., Lang, E.J., Sugihara, I., Llinás, R.: Dynamic organization of motor control within the olivocerebellar system. Nature 374 (1995) 453–457.
11. Welsh, J.P., Schwarz, C., Garbourg, Y.: The cerebellum as a neuronal prosthesis machine. Prog Brain Res 130 (2001) 297–315.
12. Welsh, J.P.: Systemic harmaline blocks associative and motor learning by the actions of the inferior olive. Eur J Neurosci 10 (1998) 3307–3320.
13. Welsh, J.P., Llinás, R.R.: Some organizing principles for the control of movement based on olivocerebellar physiology. Prog Brain Res 114 (1997) 449–461.
14. Joliot, M., Ribary, U., Llinas, R.: Human oscillatory brain activity near 40 Hz coexists with cognitive temporal binding. Proc Natl Acad Sci USA 91 (1995) 11748–11751.
15. Placantonakis, D.G., Cicirata, F., Welsh, J.P.: A dominant negative mutation of neuronal connexin 36 that blocks intercellular permeability. Mol Brain Res 98 (2002) 15–28.
16. Placantonakis, D.G., Bukovsky, A.A., Zeng, X.H., Kiem, H.P., Welsh, J.P.: Fundamental role of inferior olive connexin 36 in muscle coherence during tremor. Proc Natl Acad Sci USA 101 (2004) 7164–7169.
17. Placantonakis, D.G., Bukovsky, A.A., Aicher, S.A., Kiem, H.P., Welsh, J.P.: Continuous electrical oscillations emerge from a coupled network: a study of the inferior olive using lentiviral knockdown of connexin36. J Neurosci 26 (2006) 5008–5016.
18. Rodriques, V.P., Zeng, X.-H. Welsh, J.P.: Gamma oscillation in auditory cortex underlies auditory perception in a rapid temporal processing task. Abstr Soc Neurosci (2007).

Part IV
Applications

Chapter 111
A Road-Map Towards Cognitive Machines

J.G. Taylor

Abstract We present a first draft for a Road Map towards the creation of Cognitive Machines. We start by raising a set of basic questions relevant to the creation of such machines. In the following sections we propose a set of answers to the most crucial of them. The paper finishes with conclusions as to the most viable and interesting directions to be pursued to create cognitive machines.

Introduction

Industry, commerce, robotics and many other areas are increasingly calling for the creation of cognitive machines. These are machines which have 'cognitive' powers similar to those of humans. Guidance from our understanding of human cognitive powers will therefore be one important route to guide in the construction of such machines. Other routes must be tried as well (machine learning, fuzzy logic, evolutionary algorithms, etc) and these can also contribute strongly. However we have to accept that as we develop ever more powerful machines the human guidance, especially as to how we create decent/non-threatening human beings by education in the family and school, must be ever more strongly appealed to and used – implying the need for some emotional abilities of such advanced machines.

At the same time, whilst the cognitive powers of humans are the most developed of all other animals it is also valuable to consider, in order to gain a further handle on human cognition, how animals can also possess cognitive powers, although at a lower level than humans.

We therefore see that the topic of cognitive machines is a very broad one, covering as it does animal intelligence, human intelligence and machine intelligence. These disciplines are to be used as guidance to create a machine that can think, reason, set up goals and work out how to attain them, be aware of its surroundings

J.G. Taylor
Department of Mathematics, King's College Strand, London WC2R2LS, UK
e-mail: john.g.taylor@kcl.ac.uk

R. Wang et al. (eds.), *Advances in Cognitive Neurodynamics*,

and what it is doing, and even be aware in the sense of being conscious. This leads to a range of problems that should be addressed as part of the program of creating cognitive machines:

1. What is human cognition in general?
2. What are the crucial processing components of human cognition?
3. What are the bases of these processing components in the human brain?
4. How can human cognition be modelled in neural terms?
5. What are the powers of animal cognition as presently understood?
6. How can various powers of animal cognition, such as animal reasoning, be understood in information processing terms?
7. How can animal cognitive powers be modelled in neural terms?
8. How important is language in achieving a cognitive machine?
9. What are the benchmark problems that should be able to be solved by a cognitive machine so as to be allowed to be able to be described as 'cognitive'?
10. Does a cognitive machine have to be built in hardware or can it work solely in software?
11. How can hybridisation (in terms of fusing computational neuroscience and machine intelligence methods) help in developing truly cognitive machines?
12. Is consciousness crucial for cognition, and if not what is?

Human Cognition (Question 1–4)

Cognition means many things to many people, but here I take it necessarily to include the higher-level information processing stages in the human brain: thinking, reasoning and eventually consciousness. Each if these can occur without necessarily any language, but they each require processing of a different order than that involved in perceiving external stimuli with suitable sensors (cameras, microphones or whatever) or performing motor actions with suitable effectors (wheels or grippers). In order to lift the neural processing up to the high level expected to be involved in cognition, it is necessary to filter out distracters (especially in a complex environment), using attention. This is a brain processing mechanism which is now well-studied.

Attention is now understood as involving biasing of the position of the focus of attention, either top-down from some endogenous goal state set up in prefrontal cortex or bottom-up by a competitive 'breakthrough' of salient information to change the attention focus to the most salient input stimulus. Such modification of the focus of attention can be encapsulated in an engineering control framework [1] so bringing in various functional modules such as the plant (posterior cortex), an inverse model controller generating a signal to move the focus of attention (in parietal lobes), a goal site (in prefrontal cortex, for both exogenous and endogenous attention movement), an error monitor (for rapid error correction, say in cingulate cortex), an attention copy signal or corollary discharge (in parietal lobe), and so on. The difference between engineering control and attention control is that in the former an estimate of the state of the planet is made to speed up and improve the accuracy of the control;

in the latter it is only the attended state of the world that is of relevance (and is used in any predictive model to speed up the movement of the focus of attention).

It is possible to develop models of various cognitive processes in terms of this control model of attention. Special additional sites are needed to act as buffer working memory sites to hold for a few seconds the neural activity amplified by attention. This activity will thereby stand out from the surrounding distracters. In these terms one of the fundamental process of cognition – that of rehearsing attended neural activity on the relevant buffer – can be attained by setting up as a goal the condition to preserve the buffer activity above a certain threshold level; if it drops below it then attention will be redeployed to the stimulus on the buffer (or at a lower level). This was achieved in [2] by use of the monitor (mentioned above as arising as part of the engineering control approach to attention); the decaying stimulus is then refreshed by refocusing of attention onto it.

A further level of cognition is that of manipulating an 'image' on a buffer site so as to become another desired image, such as being upside down or fusing into an eagle. This can be achieved by setting up the top-down template so as to achieve the final stimulus configuration. Then attention will be directed to alter the input stimulus representation to the final desired goal stimulus on the buffer (and its related lower cortices). Such manipulation allows comparisons to be made between different images, which may be different or only rotated versions of each other.

Reasoning can be seen to require additions to the sensory attention system considered above. Besides sensory attention there is also a parallel system of motor attention [3] which is based in the left hemisphere, in comparison to the sensory attention system in the right hemisphere. These two systems are apparently fused in sets of pairs of internal control models associated with motor control: an inverse model (IMC: generating an action to attain a desired goal state from a present state), and a forward model (FM: predicting the new state caused by a given action on a present state); the states here are all taken as sensory. The reasoning process can then use these sets of FM/IMC pairs determine which virtual sequences of actions would attain a given goal. This is a planning problem, taking place in the space of concepts.

Animal Cognition (Questions 5–7)

There are numerous observations of animals using reasoning to solve tasks. A well-known example is that of Betty the Crow [4], who worked out how to use a bent piece of wire to extract a small basket with food in it from the bottom of a transparent tube. Betty was even able to make a suitably bent wire from a straight one in several cases when no bent wire was present. On the other hand chimpanzees are able to solve a paradigm such as the '2 sticks' paradigm. In this a chimpanzee is put in the situation of having a small stick within reaching distance which, however, is too short to retrieve a reward such as a grape outside its cage. There is also a longer stick further away outside the cage, which can only be reached by use of the shorter

stick. The chimp is able to work out, apparently by reasoning that it has first to use the shorter stick to pick up the longer one, and then use the longer one to obtain the food reward.

In addition to this apparatus of internal models (including the functional models of attention mentioned above) there is need for manipulation of rewards for the various stimuli. We have suggested elsewhere [5] that altering rewards expected from stimuli allows an animal to arrange the external stimuli in order of their being attained, as a set of sub-goals, so that the modified rewards carry a memory of the reverse order in which the sub-goals must sequentially be obtained. In this way autonomous flexible planning occurs in the animal: the rewards act as a set of drives causing response to attain the sequence of goals determine by the order of goal values.

There are extended features of cognition displayed in infants [6], in which infants are observed to detect novelty in various stimulus motions, observed by longer looking time at a novel stimulus display than at one already observed. It is possible to include this level of cognition in a neural model by the introduction of a novelty detector which directs attention to the novel stimulus until it becomes familiar [7].

The set of modules I have so far introduced (coupled IMC/FM pairs and reward lists that can be manipulated, plus a novelty detector system) needs to have further modules to enable effective planning. In particular both motor and sensory attention are needed in order to keep down errors and reduce the computational complexity of the overall reasoning process. Together with the buffer site, the overall system allows for efficient and flexible reasoning to be attained.

Language Powers (Question 8)

Language grants amazing powers to human beings. Without it and the cumulative written records encoding the accumulated wisdom of the cultures, it is expected that much less civilizing and technological advances would have occurred. The task of introducing language in a machine system is not insuperable, provided we accept that the system is able to learn continuously in the manner we do in growing from the first few months into adulthood. If such learning is allowed then an initial vocabulary of say 500 words (the size of a basic vocabulary for some parts of the world) can soon expand to tens of thousands words. The nature of syntax, in terms of phrase structure analysis, can be seen as part of learning time series of concepts, and that by means of recurrent networks (of which there are plenty in the prefrontal cortex and sub-cortical sites, especially the basal ganglia).

In this paper we take the position that language can be learnt through attaching sensory feature codes to the associated words that the system hears, so giving proper grounding in the world (represented by sensory codes in the brain). This grounding can be extended to grounding action words (verbs) in the action codes in the brain. Such a possibility requires considerable work to achieve in software, although the principles would appear accessible, and the computational complexity is currently approaching the possible, using grid or Beowulf computing.

Given a linguistic system like that above we can then ask how it might be used to achieve reasoning powers. Chunks of syllogistic reasoning processes would be expected to be learnt more by rote initially, so they could then be used recurrently to allow for more powerful syllogistic reasoning. Mathematical reasoning would also depend on the building of suitable simple rules, in terms of the axioms of the mathematical system being used (such as the Peano postulates). Again it would then be possible to use mathematical arguments of great sophistication on the basis of these rules and postulates (such as in the case of solving Fermat's last theorem).

Benchmarking Problems (Question 9)

It is necessary to have some problems that can act as a standard and that thereby allow testing the abilities of various reasoning systems, In the case of computational neuroscience these problems will be those able to be carried out by animals and children of various ages, so that the level of progress of a cognitive machine can be tested against its competitors.

We have already considered several of these, in particular the 2-stick paradigm and the basket retrieval paradigm. There are numbers of others, for example in [8], to which we refer the reader.

Hardware Versus Software (Question 10)

There has always been the debate between these two modes of implementation. Software is usually easier to implement quickly, although it is more difficult to incorporate embodiment into a software environment without careful interfacing (see the results of the EC GNOSYS program, in which a cognitive robot was designed and created: http://www.cs.forth.gr/gnosys). The need for embodiment to be at the basis of any cognitive system has been argued strongly for some time [9]. However there are examples of people who have lost all peripheral feedback (from a viral infection) who can still continue with unabated cognitive powers; these people need to attend solely to walking around for example, otherwise they will fall down. Thus embodiment may not play such as truly fundamental role, but it clearly plays an important role in survival and response development.

At the same time there is the question as to whether or not a machine with some level of consciousness could ever exist only in a software state. For the analogy of a model of the weather is relevant here. A software model of weather patterns cannot be wet or dry itself, nor hot or cold. All that the model can do is make predictions about the numbers (wind speeds, rainfall levels, etc) associated with these features in a particular region. But it cannot be raining in the model nor can any other of the modes of action of the modelled weather act like those modes in real life. For consciousness it would seem that the same situation would occur: the cognitive machine would need to be implemented in hardware in order for the

'conscious experience' ever to arise in the machine (in the real world, based on activity levels of nerve cells).

Consciousness (Question 11)

The nature of consciousness is still very controversial, although it has now become a legitimate subject of scientific study. Various models have been suggested [10] although none has yet gained universal acceptance. Any model worth its salt should be able to give a sense of 'inner self' as well as provide that self with 'immunity to error through misidentification of the first person pronoun' [11, 12]. Such a model can be constructed using attention as the gateway to consciousness, and in particular relates the inner self or 'owner' of the content of consciousness to the signal arising as a copy of the attention movement signal. It is this attention copy model (more technically termed the CODAM model, from Corollary Discharge of Attention Model) which can be related to various paradigms sensitive to loss of awareness, such as the attentional blink [13], but at the same time can lead to there being no misidentification of the inner self as belonging to someone else. Such immunity to error arises because the attention copy signal is used to speed up access to awareness (on a buffer memory site) as well as inhibit possible distracters. Thus the ownership signal is also a guarantee that 'what you are about to receive (into consciousness) is exactly what you wanted to receive' (including awareness of highly salient sudden stimuli which are also set up in frontal lobes as a goal, so are processed in a similar manner to the top-down attended stimuli).

Future Avenues

In all then, possible neural implementation of the architectures to solve the various questions 1–11 above have been suggested in this brief paper. There will certainly be many improvements and alternative approaches to these architecturs, although it is to be expected that the main outlines will remain. Given such a situation, what is to be seen as the important avenues for future development, both from a theoretical or architectural point of view as well as from an applied position? There are several steps:

1. Extend (and if necessary modify as needed) the CODAM model and other neural models of consciousness, so as to test them against all available psychological and related brain imaging data. In the process further tests of the models by such approaches will become clear, refining the testing even further. Hopefully the main framework of a suitable model will become clear by such a down-to-earth scientific approach.
2. Create software able to function as the higher regions of the brain of a human (including if necessary various sub-cortical sites suggested as also important for helping create consciousness [14, 15];

3. Develop hardware platforms for providing embodiment for the software brain;
4. Develop hardware chips of semi-realistic neurons able to provide a physical realization of the neuron processing in the brain (so as to go beyond pure software simulation to hardware emulation);
5. Allow the embodied/cognitive chips system to train on suitably simple (but increasingly complex) environments so as to build autonomous internal representations of stimuli through vision (and other possible modalities) as well as develop internal models of actions and of the affordances associated to stimuli whose representations at different feature levels are being learnt.
6. Expose the embodiment/hardware brain to develop suitable internal models to solve simple reasoning tasks (the benchmark animal level ones).

Ultimately a language understanding component must be included in order to allow the overall system to begin to attain adult human cognitive capabilities. However that is some if not many decades away.

References

1. Taylor JG (2003) Paying Attention to Consciousness. Progress in Neurobiology 71:305–335
2. Korsten N, Fragopanagos N, Hartley M, Taylor N & Taylor JG (2006) Attention as a Controller. Neural Networks 19:1408–1421
3. Schluter N, Krams M, Rushworth MFS Passingham RE (2001) Cerebral dominance for action in the human brain: the selection of actions. Neuropsychologia 39:105–113
4. Weir AAS, Chappell J & Kacelnik A (2002) Shaping of tools in New Caledonian Crows. Science 297:981–983
5. Hartley M, Taylor N & Taylor JG (2007) Neural Models of Reasoning in Animals and Robots. KCL preprint and submitted.
6. Gergely G (2002) Gergely G, Csibra G (2003). Teleological reasoning in infancy: the naive theory of rational action. Trends in Cognitive Sciences 7: 287–292
7. Hartley & Taylor (2007) ICANN07 paper
8. Hurley S & Nudds M (eds) (2006) Rational Animals? Oxford: Oxford University Press.
9. Damasio A (2000) Descartes' Error. New York: Picador Press
10. Taylor JG (1999) The Race for Consciousness. Cambridge: MIT Press
11. Taylor JG (2006) The Mind: A User's Manual. Chichester Wiley & Sons
12. Shoemaker S (1968) Self reference & self-awareness. Journal of Philosophy 65:555–567
13. Fragopanagos N, Kockelkoren S & Taylor JG (2005) A neurodynamic model of the attentional blink. Cognitive Brain Research 24:568–586
14. Crick F & Koch C (2005) What is the function of the claustrum? Philosophical Transactions of the Royal Society of London Series B 360:1271–1279
15. LaBerge D (1998) Defining awareness by the triangular circuit of attention. PSYCHE, 4(7), June, 1998 (http://psyche.cs.monash.edu.au/v4/psyche-4-07-laberge.html)

Chapter 112
Comprehensive EEG Signal Analysis for Brain–Computer Interface

Shangkai Gao, Xiaorong Gao and Bo Hong

Abstract A brain–computer interface (BCI) is a direct communication channel between brain and external devices without any use of peripheral nerves and muscles. The key issues in BCIs are brain signal recordings and interpretations. Scalp EEG-based BCI is a non-invasive technology, and probably the most acceptable systems for the subjects to use. The comprehensive EEG signal analysis in EEG-base BCI are described in this paper, and the designs of the on-line EEG-based BCI systems are also presented.

Keywords Brain–computer interface · electroencephalography (EEG) · signal analysis

Brain–Computer Interface (BCI) is a direct communication channel between brain and computer or external devices, in which the commands from subjects are sent to the external world without passing through brain's normal output pathways of peripheral nerves and muscles. BCI research has become a rapid growth area in neural engineering [1].

The essential parts of a BCI system are brain signal recording and interpretation so that the system can recognize the specific patterns of brain activities and translate it into commands for controls. General speaking, the brain signal could be recorded through electroencephalography (EEG), electrocorticography (ECoG), local field potentials (LFPs) and single-neuron action potential recordings (single units). Among them, scalp EEG-based BCI is the only fully non-invasive technology, and probably the most acceptable systems for the subjects to use.

However, the EEG signals recorded from the scalp are very week with low signal-to-noise ratio and low spatial resolution due to the low conductivity of the skull and the ambient noises. It seriously restricts the development of practical BCI systems. To overcome these obstacles, advanced signal processing technology is absolutely important.

S. Gao
Department of Biomedical Engineering, School of Medicine, Tsinghua University, Beijing 100084, China
e-mail: gsk-dea@tsinghua.edu.cn

R. Wang et al. (eds.), *Advances in Cognitive Neurodynamics*,

The framework of information processing in BCI is composed of the commonly known steps: pre-processing, feature extraction, feature selection/dimensionality reduction, feature classification and post-processing [2]. Here, we will emphasize several key issues of signal processing in the design of practical EEG based BCI systems. They are real-time on-line processing, parameter optimization and co-adaptive learning [3, 4, 5].

A practical BCI system has to be applied in real time. Causality is thus a must for the algorithm. Another problem that needs considering is the operating speed of the system. An algorithm with heavy computation load can hardly be applied to on-line system; even its performance is rather good in off-line analysis.

Performance of the processing system in BCI is closely related with various parameters of the system, such as electrode location, time window, frequency band and the dimension of features. It is necessary to select optimal parameters for each subject. Moreover, the parameters have to be changed with time to adapt the non-stationarity of EEG.

During the operation of a BCI system, the analyzed brain activities are transformed into corresponding control commands and the outside world will be influenced when the commands are executed. To adapt itself with the changed outside world, the brain has to adjust its activation according to biofeedback and the pattern of EEG will then be changed. The algorithm for analyzing brain information must be adjusted in time so as to interpret the brain commands correctly.

Among the currently existing BCI systems, those based on steady-state visual evoked potential (SSVEP) and imagery movement are most prospective. Our recent work in the designs and implementations of the BCI systems based on SSVEP and imagery movement will be introduced. The results show that by adequately synthesize the problems encountered in signal processing, system design and parameter optimization, it is really possible to gain the most useful information about brain activities using least electrodes. At the same time, system cost could be greatly decreased and usability could be readily improved. All of these are the significant progresses toward applicable BCI systems.

Acknowledgments This work is supported in part by the National Natural Science Foundation of China (60318001 and 30630022).

References

1. Mason, S. G., Bashashati, A., Fatourechi, M., Navarro, K. F., Birch. G. E. A comprehensive survey of brain interface technology designs. *Annals of Biomedical Engineering*, 2007, 35(2):137–169.
2. Bashashati, A., Fatourechi, M., Ward, R. K., Birch, G. E. TOPICAL REVIEW: A survey of signal processing algorithms in brain – computer interfaces based on electrical brain signals. *Journal of Neural Engineering*, 2007, 4: R32–R57.
3. Wang, Y. J., Wang, R. P., Hong, B., et al. A practical VEP-based brain–computer interface. *IEEE Transactions on Neural System and Rehabilitation Engineering*, 2006, 14(2):234–239.

4. Wang, Y. J., Hong, B., Gao, X. R., Gao, S. K. Phase synchrony measurement in motor cortex for classifying single-trial EEG during motor imagery. In *Proceedings of the 28th International IEEE EMBS Conference*, p75–78. 2006.
5. Wang, Y. J., Hong, B., Gao, X. R., Gao, S. K. Design of a novel electrode layout for the motor imagery based brain – computer interface. *Electronics Letters*, 2007, 43(10):557–558.

Chapter 113
Unsupervised Extraction and Supervised Selection of Features Based on Information Gain

Soo-Young Lee, Chandra Shahard Dhir, Paresh Chandra Barman and Sangkyun Lee

Abstract For robust recognition we first extract features from sensory data without considering the class labels, and then select important features for the classification. The unsupervised feature extraction may incorporate Principle Component Analysis, Independent Component Analysis, and Non-negative Matrix factorization. For the supervised selection of features we adopt Fisher Score and Information Gain (IG). To avoid the calculation of multivariate joint probability density functions, instead of the IG, we use Mutual Information (MI) between a feature and the class variable. However, in this case the MI among selected features reduces the effectiveness of the feature selection, and the statistically-independent ICA-based features result in the best performance.

Keywords Feature extraction · feature selection · Fisher score · information gain · mutual information · independent component analysis

Introduction

Features are the basic components for recognition. At the earlier stage of learning one first extract features from sensory data without knowing the meaning, and latter relates these features to the meanings provided by others. At this second stage some of the extracted features may turn out to be more useful than the others, and only these important features may be selected for further processing. This feature selection is important for robust and efficient recognition.

At the first stage the features are extracted by unsupervised learning from sensory data. The Principal Component Analysis (PCA) results in non-local features [1],

S.-Y. Lee
Brain Science Research Center, Korea Advanced Institute of Science and Technology, Daejeon 305-701, Korea
e-mail: sylee@kaist.ac.kr

R. Wang et al. (eds.), *Advances in Cognitive Neurodynamics*,

while Independent Component Analysis (ICA) results in localized basis features [2]. The Non-negative Matrix Factorization (NMF) comes with non-negative constraints which is useful to images and spectrogram, and usually results in regional features, i.e., between the global and local features [3].

We adopt Fisher Score [4] and Information Gain (IG) as the selection criteria, and the latter is approximated by Mutual Information (MI) [5] for computational simplicity. Its is investigated for the three different feature extraction algorithms.

Unsupervised Feature Extraction

The two important issues of feature extraction and selection are *redundancy* and *multivariate prediction*. The redundancy problem occurs when some features share common information, while the multivariate prediction problem occurs when some feature are important only with other features. The unsupervised feature extraction resolves the redundancy problem by making the extracted features as independent as possible. Also, it is expected to resolve the multivariate prediction problem by forming complex features from multiple features.

Let $\mathbf{f}_i = [f_{1i} \dots f_{Ni}]^T$ with $1 \leq i \leq M$ be the unknown features, and $\mathbf{x} = [x_1 \dots x_N]^T$ be the observed data vector which is considered as a linear mixture of feature vectors. Here, N and M are the number of pixels and the number of features, respectively. The mixing model can be written in a matrix form as

$$x = Fs \tag{113.1}$$

where $\mathbf{F} = [\mathbf{f}_1 \dots \mathbf{f}_M]$ is a matrix consisting of all the feature vectors as the columns, and $\mathbf{s} = [s_1 \dots s_M]^T$ is a vector consisting the mixing coefficients. The feature extraction algorithms find the unknown features $\mathbf{F}$ from many observed data $\mathbf{x}$'s only. This is an underdetermined problem, and additional constraints are usually required. The popular choices are orthogonal basis images for PCA, linear independence for ICA, and non-negativity of NMF.

PCA is probably the most commonly used technique for image processing tasks. PCA computes a set of orthogonal subspace basis vectors for an image database, and project the images into the compressed subspace. PCA generates compressed data with minimum mean-squared reproduction error, and is an unsupervised learning that produces global feature vectors [1].

ICA decomposes data image into linear combination of statistically independent mixtures. While PCA is based on the second-order statistics of the images, ICA decorrelates the high-order moments of the input in addition to the second-order moments. The ICA-based features are locally supported and usually very sparse [2].

NMF imposes non-negative constraints on both the features and coefficients, which results in parts-based features. Both quadratic error function and entropy-like cost function are utilized for the adaptive learning.

In Fig. 113.1 the extracted features from the three algorithms are shown for lip-reading. It clearly shows the global characteristics of PCA-based features and

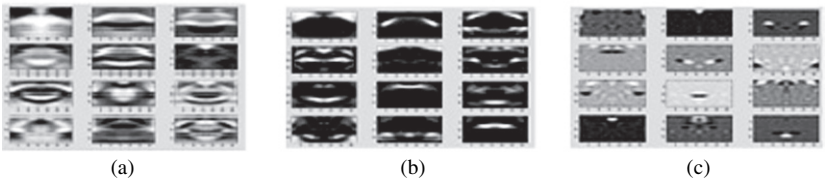

(a) (b) (c)

Fig. 113.1 Features of lip motion by (**a**) PCA, (**b**) NMF, and (**c**) ICA. The PCA-based features are global, while ICA-based features are the sparsest

sparseness of ICA-based features. The NMF-based features show parts of the images with the middle sparseness [6].

In Fig. 113.2a ICA-based spatial features are shown for EEG signals from left-vs-right hand motor imagery tasks. In Fig. 113.2b the temporal features are also extracted from the 15th spatial feature.

Supervised Feature Selection

We adopted Fisher Score and Information Gain for the criteria of feature selection. The Fisher Score is defined as the ratio between inter-class difference and within-class difference, and may be effective for Gaussian-like well-distributed clusters. The Information Gain may of a feature on the classification system is defined as the difference between the system information with and without the feature. However, the calculation requires estimation of high-dimensional joint probability functions, which may be very difficult for large number of features with small database. Instead we would like to use Mutual Information (MI) between a feature and the class

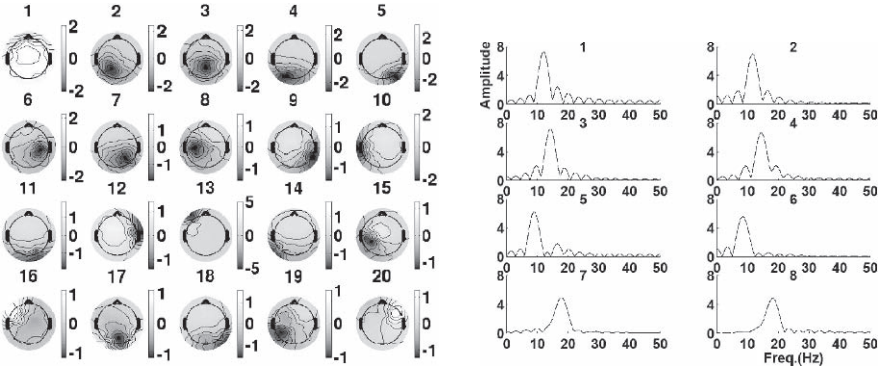

(a) (b)

Fig. 113.2 ICA-based features of EEG from the binary class (left vs. right hand) motor imagery tasks. (**a**) 20 spatial maps, and (**b**) top eight temporal bases components in frequency domain from the 15th spatial

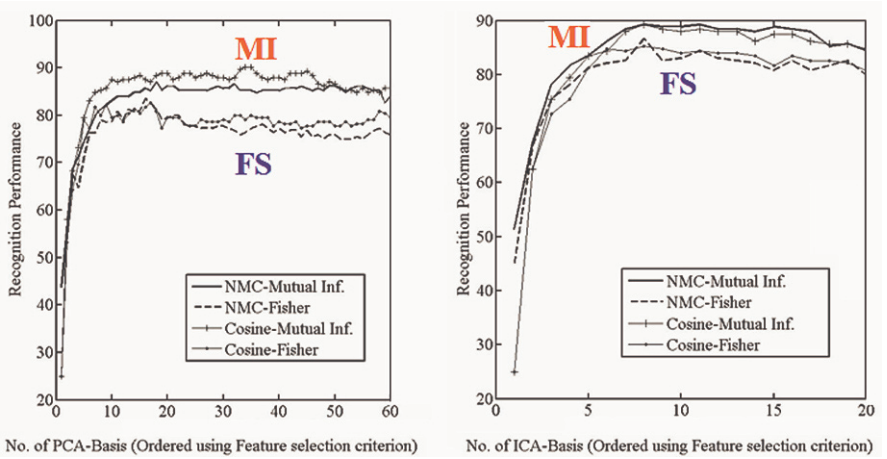

Fig. 113.3 Performance of emotion recognition from facial images by (**a**) PCA-based features and (**b**) ICA-based features. The recognition rates are plotted as functions of the number of features used for the classifier, and the features are sorted by FS or MI

variable *without considering the other features*, and KL divergence is used for the MI as

$$I(C;F) = \sum_{c}\sum_{f} p(c,\, f)\log\left[\frac{p(c,\, f)}{p(c)p(f)}\right] \geq 0 \qquad (113.2)$$

Provided all the features are statistically independent, it will be the same as Information Gain.

Although the three feature extraction algorithms come up with somewhat independent features, the ICA algorithm specifically impose independence among features as much as possible. Therefore, the ICA-based features are expected to provide the best classification performance with the MI selection criteria.

In Fig. 113.3 we show the classification performance of emotion recognition from facial images with features extracted by PCA or ICA and then selected by FS or MI.

Conclusion

In this paper we demonstrate that the ICA-based features result in better classification performance than PCA-based features with the same number of features. Also, the difference between FS and MI selection criteria becomes smaller for ICA-based features.

Acknowledgments This research was supported as the Brain Neuroinformatics Research Program by the Korean Ministry of Commerce, Industry, and Energy.

References

1. Turk, M., and Pentland, A.: Eigenfaces for recognition. Journal of Cognitive Neruoscience 3 (1991) 71–86.
2. Bartlett, M., Lades, H., and Sejnowski, T.: Independant component representations for face recognition. In T. Rogowitz, B. and Pappas (Ed.): Proceedings of the SPIE Symposium on Electronic Imaging: Science and Technology; Human Vision and Electronic Imaging III, 3299, January 1998. SPIE Press, San Jose, CA, pp. 528–539.
3. Lee, D.D., and Seung, H.S.: Learning the parts of objects by non-negative matrix factorization. Nature 401 (1999) 788–791.
4. Bishop, C.: *Neural Networks for Pattern Recognition*, 2nd ed. New York: Oxford University Press, (1995).
5. Wang, G., and Lochovsky, F.H.: Feature selection with conditional mutual information maxim in text categorization. *Proceedings of the thirteenth ACM international conference on Information and Knowledge Management* (2004) 342–349.
6. Lee, K.D., Lee, M.J., and Lee, S.Y.: Extraction of frame-difference features based on PCA and ICA for lip-reading. IEEE International Joint Conference on Neural Networks, IEEE Computer Society Press, Los Alamitos (2005) pp. 232–237.

Chapter 114
Stability and Instability in Autonomous Systems

Hans Liljenström

Abstract Behaving systems, biological as well as artificial, need to respond quickly and accurately to changes in the environment. The response is dependent on stored memories, and novel situations should be learnt for the guidance of future behavior. A highly nonlinear system dynamics is required in order to cope with a complex and changing environment, and this dynamics should be regulated to match the demands of the current situation, and to predict future behavior. If any of these regulatory systems fail, the balance beween order and disorder can be shifted, resulting in an inappropriate and unpredictable behaviour. I discuss how such "mental disorders" might be related to the structure and dynamics of any autonomous cognitive system.

Keywords Efficiency · stability-flexibility dilemma · information processing · complex neurodynamics · cognitive disorders · robots

Order and Disorder in Cognitive Systems

While we are still far away from being able to construct artificial cognitive systems or robots that are human-like in any sense, other than superficially, we will no doubt get closer and closer. If our artificial systems eventually become enough human-like to have many of the cognitive and mental functions that humans have, one can wonder whether they would also be capable of having "mental disorders" like humans. What, in that case, would it mean for an artificial system (robot) to suffer from cognitive or mental disorders? In this paper I wish to explore this possibility and what it could imply. First, I will outline some basic relations between structure, dynamics, and function, that I believe could be common to cognitive functions of both humans and humanoid robots, and then discuss where things can go wrong.

As my outset, I will consider a well-functioning autonomous system, human or other, one (1) which has an efficient information processing with regard to the

H. Liljenström
Department of Biometry and Engineering, SLU, P.O. Box 7032, SE-75007 Uppsala, Sweden
e-mail: hans.liljenstrom@bt.slu.se

R. Wang et al. (eds.), *Advances in Cognitive Neurodynamics*,

environment, (2) which has a way to regulate its balance between stability and flexibility, and (3) which has a predictable behaviour and appropriate interaction with its "society".. Many other aspects of a healthy system could be listed, but I have chosen these for reasons that will become clear shortly.

Mental disorders could be of different kinds, characterized e.g. as depression, schizophrenia, autism, or Alzheimer's syndrome. Symptoms include memory deficits, unpredictable and erratic behaviour, impairment of social interaction, lack of initiative, apathy, thought disorders, inappropriate emotional responses, reduced attention span, and an inability to plan ahead. For example, schizophrenia could arise as a failure of linking representational knowledge and behaviour [1], and could be a result of a late shutdown in the pruning of cortical networks [2]. Normally, our brains are continuously updating our inner models of reality, and thereby guide our behaviour. If we fail in this task, perception becomes fragmented and our behaviour becomes dominated by the impulses of the moment, rather than by the evened-out influence of past and current information [3].

Living organisms have to survive in a complex and changing environment. This implies, among other things, to be able to respond and adapt to environmental events and changes at several time scales. For an organism with a nervous system, there are (at least) three different time scales, relating to the life span of the individual: (1) a large one based on genetic changes (evolution), (2) an intermediate one based on synaptic changes (learning), and (3) a small one based on neuronal activity changes (neurodynamics), directly related to cognitive functions. The interaction with the environment, behaviour in animals, depends upon the present (dynamical) state of the organism, as well as on previous experiences stored in its molecular and cellular structures.

It has become clear that also artificial cognitive or intelligent systems have to have the capacity to adapt to environmental changes at different time scales. The lesson from the original AI approach is that cognition and intelligence cannot really be built into an artificial system, it has to develop through an exploratory interaction with the environment [3].

For artificial systems, we, the constructors, have taken care of the longer, "evolutionary" time scale, by building on (biological) experience that can be transferred to the artificial system in the construction of its structure and dynamics, and where a clear purpose is implemented. We want the system (robot) to perform certain tasks, we endow it with purpose and goals. However, the adaptation at an intermediate scale, i.e. at the scale of experience through interaction with the environment, can be taken care of by the artificial system, for example through the use of artificial neural networks. Finally, the rapid adaptation that has to do with rapid changes in the momentary environment, also has to be reflected through the internal dynamics of the artificial system (robot).

Even if we could construct complex artificial systems that learn through experience, and more or less follow the rules and goals we have given them, the more complex they become, the more likely they could go wrong. Also wrong in a sense we could refer to as "mentally disturbed". Such behaviour could include repetitive and "compulsory" behaviour, erratic or chaotic behaviour, where small,

apparently insignificant events could result in a completely unpredictable and "crazy" behaviour. It's also imaginable that such cognitive robots could get "depressed" or "schizophrenic", in the sense that they would become slow and inefficient, with impaired and inappropriate interaction with the environment, inable to perform the tasks given to them.

Efficiency of Cognitive Processes

For any autonomous system that interacts with an environment it is important that this interaction is efficient in terms of energy, time and accuracy. Normally, there is an interdependence, or trade-off, between these quantities, and different processes seem to be optimized with respect to either one of these. This optimization also determines the efficiency of the system [4]. Whether the system is biological or artificial, this implies that the response to an external input should give a sufficiently "accurate" and robust output at an acceptable (low) cost in terms of time and energy. It should be able to solve the problem of being stable to noise and external perturbance and, at the same time, be flexible and adapt to significant environmental changes. In general, to achieve a high accuracy requires a long processing time, whereas if the system can suffice with a lower accuracy, processing time can be reduced. In many cases it is most important to minimize processing time. For example, the response or reaction time of an animal in a natural environment or a robot in an industrial real-time operation.

An advanced system would be able to shift the strategy for different situations, and oscillations could be an appropriate way to deal with this. First, oscillatory or complex dynamics provides a means for fast response to an external input. If sensitivity to small changes in the input is desired, a chaotic–like dynamics should be optimal, but a too high sensitivity should be avoided. Oscillations can also be used for enhancing weak signals and by "resonance" large populations of neurons can be activated for any input. Secondly, such "recruitment" of neurons in oscillatory activity can eliminate the negative effects of noise in the input, by cancelling out the fluctuations of individual neurons. Noise can, however, also have a positive effect. Finally, from an energy point of view, oscillations in the neuronal activity should be much more efficient than if a static neuronal output (from large populations of neurons) was required. In engineering, great efforts are made to eliminate oscillations in the system, but if the system can perform as well (or better) with oscillations, energy can be saved [4, 5].

The Stability-Flexibility Dilemma

An autonomous cognitive system has to be flexible and adaptive, while maintaining a sufficient stability. There is a trade-off between the two: a greater stability is achieved at the expense of a lesser flexibility (adaptability), and vice-versa. Yet, it is essential that the system is stable to short-term fluctuations, or common insignificant events, while it should also be able to react to weak signals and rare

important events, as well as adapting to long-term changes. This so-called stability-flexibility dilemma has to be dealt with by any autonomous system, and should be reflected in both structure and dynamics. The structure should partly be "hard-wired" and partly be adapted trough experience. The problem of keeping a (dynamical) balance between stability and flexibility, or more generally, between order and disorder, is likely to apply also to mental processes and disorders [6].

Our computer simulations of cortical network structures show that a self-regulated complex neurodynamics, which can shift the balance between stability and flexibility, and with optimal noise levels, can result in an efficient information processing [5, 6].

Appropriate Interaction with the Environment

All cognitive autonomous systems have to develop and act in constant interaction with the environment. The late Rodney Cotterill emphasized the crucial link between movement and cognition, both for biological and artificial systems: "The relevant stimulus is the animal's own muscular movement, the relevant response being the sensory feedback from the surroundings" [7]. Mental disorders often involve deficits in such interaction, which sometimes can be related to impairments of the neural circuitry in the brain. In particular, autism can be characterized by social isolation, resistance to novelty, and stereotyped behaviour, communication or language deficits, but there are altogether some twenty different autistic characteristics [3, 7]. In some mental disorders develops after triggering events in the environment, but almost always there are internal factors, that can be either genetically based or due to neuronal processes affecting cortical structures, or a disturbance in the neurochemical balance.

Conclusion

I have here tried to outline some of the properties I believe can be associated with a well-functioning autonomous system. I have also pointed at some disorders that could result in a less well-functioning system. Even though my examples are primarily based on biological systems, and in particular associated with human cognition and mental disorders, it is conceivable that similar characteristics would apply also to artificial cognitive systems or robots. This would be an issue for future robot psychiatry.

References

1. Goldman-Rakic, P.S.: Prefrontal Cortical Dysfunction in Schizophrenia: the Relevance of Working Memory. In: Carrol, B.J., Barrets, J.E. (eds.): Psychology and the Brain. Raven Press, New York (1991).

2. Saugstad, L.F.: The Maturational Theory of Brain Development and Cerebral Excitability in the Multifactorially Inherited Manic-depressive Psychosis and Schizophrenia. Int. J. Psychophysiol. 18 (1994) 189–203.
3. Cotterill, R.M.J.: Enchanted Looms – Conscious Networks in Brains and Computers. Cambridge University Press, Cambridge (1998).
4. Liljenström, H.: Cognition and the Efficiency of Neural Systems. In: Århem, P., Liljenström, H., Svedin, U. (eds.): Matter Matters? On the Material Basis of the Cognitive Activity of Mind. Springer, Heidelberg (1997) 177–213.
5. Liljenström, H.: Autonomous Learning With Complex Dynamics. Int. J. Intell. Syst. 10 (1995) 119–153.
6. Liljenström, H.: Neural Stability and Flexibility – A Computational Approach. J. Neuropsychopharmacol. 28 (2003) S64–S73.
7. Cotterill, R. M. J.: An Inside-Out Paradigm for Consciousness and Intelligence. In: Liljenström, H., Århem, P. (eds.): Consciousness Transitions – Phylogenetic, Ontogenetic, and Physiological Aspects. Elsevier, Amsterdam (2007) 177–191.

Chapter 115
The Neuroinformatics Portal of the International Neuroinformatics Coordinating Facility

Jan G. Bjaalie

There is a clear need in the neuroscience community for databases extending from genes to cognition and disease mechanisms, for data sharing, and for modeling and use of computational tools at different levels [1, 2]. For this reason, the Global Science Forum (GSF) of the OECD (Organization of Economic Cooperation and Development) has initiated an International Neuroinformatics Coordinating Facility (INCF), to facilitate the development of Neuroinformatics. Each member nation contributes in relation to Research and Development expenditure in the particular nation [3], (see also INCF platform documents at http://www.incf.org/med/INCF_Understanding.pdf and http://www.incf.org/med/INCF_BusinessPlan.pdf). The current member nations are Belgium, the Czech Republic, Finland, France, Germany, Italy, Japan, the Netherlands, Norway, Poland, Sweden, Switzerland, the United Kingdom, and the United States. INCF also receives support from the European Commission. The central Secretariat of the INCF is located in Stockholm. Each member has established, or is about to establish, a National node. The nodes will contribute with infrastructure developments and neuroinformatics research in the context of the global network of member nations.

The mission of the INCF Secretariat and the global network of National nodes is to:

- coordinate and foster international activities in neuroinformatics in general
- contribute to the development of scalable, portable, and extensible applications that can be used to further knowledge of the human brain and its development, function and disease
- contribute to the development and maintenance of specific database and other computational infrastructures and support mechanisms
- focus on developing mechanisms for the seamless flow of data, information, and knowledge among government agencies, academics and libraries, the publication industry and private enterprises.

J.G. Bjaalie
International Neuroinformatics Coordinating Facility, Secretariat, Karolinska Institutet, SE - 171 77 Stockholm, Sweden
email: jan.bjaalie@incf.org

R. Wang et al. (eds.), *Advances in Cognitive Neurodynamics*,

The INCF will establish a strong external operative representation. Directed to the world-wide, open and diverse neuroscientific community, such a basic representation will be based on a unifying web portal, the INCF Neuroinformatics Portal. This new portal will serve as a platform for providing research oriented services to the neuroscience community world-wide, in agreement with the INCF work plan (http://www.incf.org/med/INCF_BusinessPlan.pdf). The present report provides a brief outline of the current plans for the INCF portal.

State-of-the-Art and International Coordination

A large number of neuroinformatics resources are currently available, including data repositories, advanced database applications, software tools for data visualization, analysis, and modeling of brain function at multiple levels. Also biophysically specified computational models are to some extent shared. Several neuroscience portal services, general or focused, have been initiated around the world over the last few years, such as:

- BIRN portal / Biomedical Informatics Research Network portal (https://portal.nbirn.net/)
- Neurocommons (http://sciencecommons.org/projects/data)
- NDG / Neuroscience Database Gateway (http://www.sfn.org/ndg)
- NIF / Neuroscience Information Framework (http://neurogateway.org)
- Japan Node/The Portal system for Neuroinformatics in Japan (http://www.neuroinf.jp)

Creating synergies and collaborations among the existing portals will be a key strategy in INCF operations.

INCF Portal: Goals and Basic Approach

A major component of the new INCF portal will be services for navigation and integration of distributed resources, across continents, within specific domains of neurosciences. The portal effort will act on two levels: (1) It will help shepherd diverse protocols of interoperability across the world. This will facilitate the development of consensus positions on standards and “best practice”. Specifically, it will provide a final international vetting body for neuroscience-specific ontologies and related ontologies in other fields. (2) It will then implement these consensus international interoperability standards and provide example and exemplar resources and data sets and test suites.

To facilitate the process of establishing such services, the status of different portal initiatives as well as the collaborative dividing of maintenance and development tasks will be dealt with in the INCF workshop series, with major stakeholders

present. A sound basis for a collaborative effort exists, since the INCF portal initiative and several of the existing portal developments have emerged from a relatively similar background.

INCF Portal: Domain Oriented Services

The rationale for providing domain oriented services, allowing navigation and integration of distributed resources, is that the gathering of comprehensive sets of available resources on the internet and through other available channels requires a substantial effort in the form of manual searching and coordination. A large number of different and isolated systems are used for access, referencing, technical standards, user interface principles, and quality standards. This poses problems at several levels when using distributed resources in cutting-edge research. INCF will use its technical and coordinating capabilities as well as its domain authority established via the INCF Workshops series and INCF Expert panels, to address these issues. At a general level, examples of approaches to be taken by the domain oriented services include database mediation, data fusion and mining, data driven navigation, specialized multi-level categorization, and search engines. Among the values to be reached by establishing domain oriented services are

- a general information efficiency boost due to less administrative and coordinative overhead on the part of the end user
- scientific information gain by facilitating data fusion and new levels of integrated information refinement
- strategic resource persistence and standardization advantages with regards to quality, referencing and availability
- the establishment of an international community derived authority in the given domains, in connection with INCF Workshops and Expert panels funded by other INCF resources
- general organizational development with regards to cooperation and communication between neuroscientific and technological institutes around the world
- increased opportunities for improved IT-infrastructures in the neuroinformatics community of developers, as a result of a new focus on their deliverables and increased use of these
- the establishment of standards and common principles
- technological spin-offs within fields such as data fusion, database mediation, sensemaking, distributed information services, usability and platform independence

The domain areas to be included in the portal will be decided on by the Governing board of the INCF. Each domain area is critically analyzed by a workshop, with representatives of the main stakeholders in a given area. The INCF workshops deliver penetrating reports that includes recommendations for actions. One report example is provided by the 1st INCF workshop on Large-scale modeling of the nervous

system, available via the INCF web site and via Nature Proceedings [4]. Follow-up of the workshop recommendations are in turn overseen by expert panels, derived with each panel linked to a program officer at the INCF Secretariat. Examples of domain areas that are currently considered for inclusion are:

- Large-scale modeling of the nervous system
- Digital brain atlasing systems
- Integration of fMRI and other neuroimaging data resources
- Neuroanatomical nomenclature and taxonomy

Future domain areas to be considered include also biologically problem-oriented domains, such as Action, Learning and Memory, Vision, and Cellular neurobiology. Building on the workshop and expert panel mechanism, the INCF has at hand the necessary international authority, connected to the community of lead scientists.

INCF Portal: Basic Services

The basic services that will be included in the portal are software provision and general community building support. A broad use of these services is expected. A primary concern is to support the domain oriented services of the portal.

Software Provision

The development, distribution and use of specialized software tools will be facilitated and supported by the portal. This is quite challenging since many of the developers represent small research groups, many specialized approaches are used, few standards are applied, and tracking of the use of tools as well as feedback and reward to the developers are limited. From the perspective of the end users, the concerns that will be targeted include the overhead work involved in finding and getting access to software tools, the problems of quality assurance relative to purpose of use, platform dependency problems, and updating and support. From the perspective of the tools developers, the concerns that will be targeted include tools Lifecycle Management, coordination of user feedback and usage statistics, release management and redistribution, and the interface and buffer between the tools developer community and the user community (by which individuals are often members of both).

In the context of the portal developments, the INCF will aim to identify high quality tools from all relevant resources (helped by its workshops and expert panels) and facilitate access to such tools via the portal services. Further, structural support systems in the form of code repositories, version control and issue tracking mechanism will be provided. Such systems, essential in the context of development of high quality software and associated with a resource overhead often beyond the capacity of individual scientists or small research groups, will be provided. Therefore, state-of-the-art software development support services, tailored for the needs of the

neuroinformatics community, will be developed. Substantial weight will be placed on platform-independency and continuing availability of key software applications through new versions of operating systems and hardware, i.e. forward-porting. A possible solution for some types of software may also be the use of managed servers holding relevant and frequently used software and removing the need to download software.

Community Building Support

General community building support services relates directly to the coordination objectives of the INCF. These services will include functions such as online meeting forums, blogs with emphasis on news and commentaries for the different divisions of the portal, and calendars of neuroscience and neuroinformatics events. Given the focus on domain oriented services, the above functionalities will address the different domains specifically, but also offer integration of communication across domains.

Concluding Remark

A key element in the INCF operation is to work closely with the scientific community in adjusting and translating the INCF work plan to practical action. To the extent possible, actions of the INCF will always seek to build on a careful mapping of existing resources and, when possible, to prepare for the full use of these in combination with new developments. The INCF portal will be one of several instruments that will play a role in establishing a future neuroinformatics capability, the aim of which will be to have the same role in basic and clinical neuroscience as bioinformatics has for genomics and proteomics.

Acknowledgements and Information J.G.B. is the Executive Director of the INCF. R. Ritz and M. Naeslund at the INCF Secretariat have contributed to the development of the portal plan, with valuable input also received from from R.W. Williams and S. Grillner. This article describes principles only. INCF strategies and actions are subject to continuous monitoring and approval by the INCF Governing Board.

References

1. Amari S-I, Beltrame F, Bjaalie JG, Dalkara T, De Schutter E, Egan GF, Goddard NH, Gonzalez C, Grillner S, Herz A, Hoffmann K-P, Jaaskelainen I, Koslow SH, Lee S-Y, Matthiessen L, Miller PL, Silva FMD, Novak M, Ravindranath V, Ritz R, Ruotsalainen U, Sebestra V, Subramaniam S, Tang Y, Toga AW, Usui S, Pelt JV, Verschure P, Willshaw D, Wrobel A (2002) Neuroinformatics: The integration of shared databases and tools towards integrative neuroscience. J Integrative Neurosci. 1:117–128.
2. Gardner D, Toga AW, Ascoli GA, Beatty JT, Brinkley JF, Dale AM, Fox PT, Gardner EP, George JS, Goddard N, Harris KM, Herskovits EH, Hines ML, Jacobs GA, Jacobs RE, Jones EG, Kennedy DN, Kimberg DY, Mazziotta JC, Miller PL, Mori S, Mountain DC,

Reiss AL, Rosen GD, Rottenberg DA, Shepherd GM, Smalheiser NR, Smith KP, Strachan T, Van Essen DC, Williams RW, Wong ST (2003) Towards effective and rewarding data sharing. Neuroinformatics. 1:289–295.
3. Bjaalie JG, Grillner S (2007) Global neuroinformatics: the international neuroinformatics coordinating facility. J Neurosci. 27:3613–3615.
4. Djurfeldt M, Lansner A (2007) Workshop report: 1st INCF Workshop on Large-scale Modeling of the Nervous System. Available from Nature Precedings http://dx.doi.org/10.1038/npre.2007.262.1.

Chapter 116
Neuroinformatics in the Netherlands

Jaap van Pelt and Arjen van Ooyen

Abstract In the past decade the Netherlands has actively participated in the OECD initiatives for an international program in neuroinformatics. Simultaneously, many activities have been unfolded towards a national program in neuroinformatics in the Netherlands. This paper briefly summarizes these activities within the national context and opportunities.

Introduction

From the beginning on, the OECD Global Science Forum initiative to promote Neuroinformatics was supported by the Netherlands. Several factors contributed to this interest. Neuroscience takes a prominent place among the life sciences. Theoretical biology programs at several universities have created a community of researchers trained in modeling in the life sciences, including the neurosciences (computational neuroscience). The Netherlands has an excellent high-speed IT infrastructure for higher education and research (SURFNET), and advanced super-computing facilities, supported by the Netherlands national computing facilities foundation (NWO-NCF). A steering group was established to promote a national neuroinformatics program, by (i) building a neuroinformatics community, (ii) organizing workshops (twice a year), working on awareness of neuroinformatics among governmental and industrial organizations, and (iii) launching a website [1]. It resulted in a Masterplan Neuroinformatics with recommendations to the Netherlands Organization for Scientific Research (NWO). At the 21th of March 2007 NWO signed the agreement with INCF through the joint support of the NWO departments for Health R&D (ZonMw), Earth and Life Sciences (ALW), Social Sciences (MaGW) and Physical Sciences (EW), making the Netherlands the 12th member of INCF.

J. van Pelt
Department of Experimental Neurophysiology, Center for Neurogenomics and Cognitive Research, VU University Amsterdam, De Boelelaan 1085, 1081 HV Amsterdam, The Netherlands
e-mail: jaap.van.pelt@falw.vu.nl

R. Wang et al. (eds.), *Advances in Cognitive Neurodynamics*,

Masterplan Neuroinformatics

Mission

The mission of a Dutch Neuroinformatics Program is to provide a general framework of computational tools and modeling approaches in order to advance our understanding of the working of the brain. The program aims at taking away barriers in neuroscience research of data integration and conceptual insight by enabling research at higher levels of complexity, dynamics and integration. The focus is on three topics: data-basing/data-sharing (developing and applying tools to improve accessibility, sharing, and integration of neuroscientific data); data analysis and visualization (developing and applying mathematical and statistical methods to analyze and visualize the huge quantity and great complexity of neuroscientific data, such as originating from micro-, multielectrode- and photodiode arrays, and brain imaging); and computational and mathematical modeling across all levels, from gene to synapse to cognition).

National Node

The national node is aimed at coordinating neuroinformatics activities at the national level. These include actions towards an education and training program, acquiring enabling resources, and plans for sustainability.

Organization

The size of the Netherlands and the state of modern technology may permit a first stage of organization into research clusters that operate as virtual (distributed) expertise centers composed much more on a content-based definition than on a geographical or institutional organization. The field could get organized around a few common themes to create focus and critical mass such as (Fig. 116.1): (i) Web-based Data-sharing Infrastructure, (ii) Computational Platforms for Data Analysis, and (iii) Computational Modeling as typical neuroinformatics themes, and (iv) Brain Imaging and (v) Brain-Machine Interfacing as typical integrative themes. These centers should also implement a neuroinformatics educational program. Two tracts are foreseen, one aimed at (PhD/Master) students from informatics(-like) science that need education in neuroscience and another one for students in neuroscience that need education in informatics and computational and mathematical modeling.

Funding

Funding for a national neuroinformatics program need to be obtained by the neuroinformatics community itself through regular mechanisms. These include larger

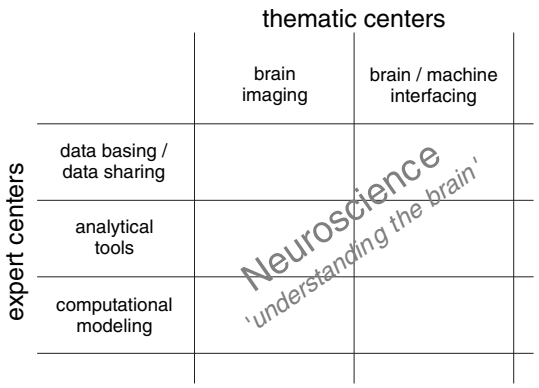

Fig. 116.1 Illustration of how expert centers and thematic centers may form an integrated field of research providing a neuroinformatics platform to help furthering our understanding of the brain

public programs, support from universities and research institutes, as well as the European Commission. Industrial interest for neuroinformatics will create a source for private funding. It is anticipated that these institutions are in particular interested in supporting (joint) expert centers for neuroinformatics research and education/training.

Neuroinformatics Community

Many research groups have expressed their interest in a national neuroinformatics program. They represent a large community of scientists from a full range of specializations encompassing basic, clinical and computational neuroscience, biophysics, mathematics, informatics and computer sciences, cognitive and psychological sciences, and biomedical engineering. Almost all general universities and all technical universities are represented, as well as several research institutes. The scientific programs of these research groups include common themes as (i) physiological processes and information processing in the brain, (ii) structural organization of the brain, (iii) computational platforms for the analysis of images and physiological data, (iv) computational platforms for modeling brain structure and function, (v) non-invasive brain imaging, (vi) data basing and data mining, grid technology, (vii) bio-informatics, and (viii) neural control and man-machine interfacing.

Within these themes research groups have build up specific expertise in experimental and computational studies at a variety of topics such as morphological and functional development of neuronal networks, firing dynamics in neuronal networks, membrane excitability, information processing in biological and artificial neural networks, electrophysiology of cortical micro-circuits, structural and functional brain imaging in development and cognition research, and in neurological (epilepsy) and psychiatric (schizophrenia) disorders, scientific visualization and computer graphics, computational geometry and geometric modeling, pattern

recognition and segmentation in computer vision, analysis and modeling of EEG, MEG, fMRI and VEP time series, neural control of human motor system, data mining and algorithmic analysis of complex data, and autonomic and self-organizing databases.

The inventory also made clear that the participating research groups provide possibilities for a full range of education and training programs on neuroinformatics topics. The neuroinformatics community has the expertise, the quality, the research and educational facilities and, above all, the enthusiasm, for making the Netherlands well prepared to execute a national neuroinformatics program at the highest international competitive standards.

Related National Initiatives

BIG GRID

A proposal for the organization of a national infrastructure for e-science on the basis of grid technology (BIG GRID) has recently been awarded by NWO [2]. The e-Science infrastructure to be built is intended to provide Grid based facilities for data-basing/archiving, data communication and computing power for data analysis. Because these facilities implement basic resources for a neuroinformatics program, the NI steering group has strongly supported this Big Grid proposal. Big Grid facilities are especially beneficial when resource demands are high, such as in the case of image data bases requiring large amounts of storage capacity, and in the case of large scale brain modeling, requiring substantial compute power. Facilities for secure communication with on the fly encryption via dedicated optical links may be highly relevant for ethical and IPR-sensitive applications. The optimal architecture concerning centralized/distributed facilities needs further to be investigated.

Neurofederation

In December 2005 the Dutch Neurofederation formulated her vision on next decade brain research in the *Strategy Plan Brain Research 2005-2015* [3]. There is a great societal need for brain research because of brain diseases, aging, educational challenges, understanding human behavior, and for the development of man-machine interfaces. New challenges are identified at gene-environment interaction, brain & cognition, plasticity and (de)regeneration. Integrative neurosciences and neuroinformatics are seen as key approaches for the realization of these challenges.

Systems Biology

In line with international developments Systems Biology is also an emerging field in the Netherlands, not in the least by the activating work of the Dutch Platform for

System Biology [4]. With the promotion of computational modeling approaches to integrate data and knowledge over different levels of biological organization, there is great resonance with neuroinformatics, focussing on the nervous system.

National Initiative Brain & Cognition

A National Initiative Brain & Cognition is presently in preparation [5]. This initiative aims at bundling and integrating national research of the brain and cognition into a coherent program for fundamental and applied research. Such an integrated program is timely because of the advancements in science and technology now enabling the bridging of cognitive and brain science. With this initiative a platform is formed for applied research towards learning and memory, communication, brain disorders, and integrative cognition and neuroscience. The initiative will put a strong requirement on the integration of data and knowledge and the availability of tools for data analysis and exploration and for computational modeling. Neuroinformatics will therefore play a crucial role in the realization of this initiative.

References

1. http://www.neuroinformatics.nl
2. http://www.nikhef.nl/grid/BIG/
3. http://www.neurofederatie.nl/publications/index.htm
4. http://www.systembiology.net/sbnl/
5. http://www.nwo.nl/nwohome.nsf/pages/NWOA_6TTC8C

Chapter 117
Neuroinformatics Japan Node and Platforms

Shiro Usui

Abstract Since the establishment of NIJC in 2005 at the RIKEN Brain Science Institute, which represents the Japan Node of INCF, Japanese neuroinformatics activities has been enhanced to integrate outstanding research of neuroscience in Japan. We introduce the scheme and resources developed by NIJC. There are nine neuroinformatics platforms so far, including both already developed and under development. The J-Node portal has been accessed about 47,000 times per month on average inside and outside the country. We intend to increase the overseas users of the platforms on the J-Node site.

Keywords Neuroinformatics · INCF · J-Node · platforms · XooNIps

Introduction

Neuroinformatics (NI) is concerned with integrating the diverse and complex neuroscience data through information science in the inter/intranationally organized framework. The international framework is the International Neuroinformatics Coordinating Facility (INCF)[1] established through the Global Science Forum of OECD on November 2005, while the intranational counterpart is the National Node of the INCF member country. The role of the National Nodes includes to coordinate neuroinformatics activities within the country and to promote neuroinformatics development that supports the objectives of INCF.

The Neuroinformatics Japan Center (NIJC) represents the INCF national Node of Japan (J-Node)[2] . Together with the Japan Node Committee and the Platform Committees, NIJC facilitates neuroinformatics research in Japan. Figure 117.1 shows J-Node in the center connected with nine platforms. Platform Committee members

S. Usui
RIKEN Brain Science Institute, Hirosawa 2-1, Wako, Saitama, 351-0198 Japan
e-mail: usuishiro@riken.jp

[1] http://www.incf.org/
[2] http://www.neuroinf.jp/

R. Wang et al. (eds.), *Advances in Cognitive Neurodynamics*,

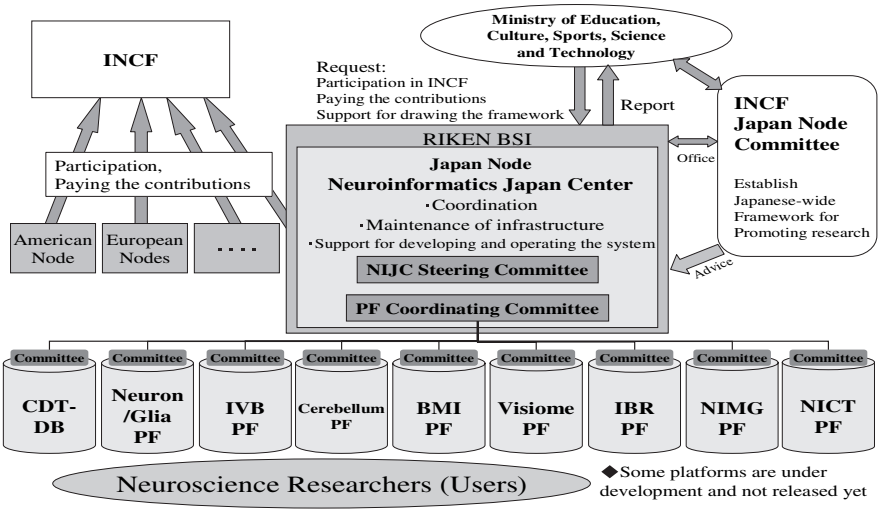

Fig. 117.1 Japan-Node scheme with INCF

collaborate to develop their platforms. Each platform has been developed with a base platform system, XooNIps[3] , which was developed by NI-Team at RIKEN BSI and is operated by NIJC. The registered users of a platform can freely download its contents and upload their own contents on it by a simple procedure with the approval of the platform Committee. These platforms are or will be accessible at the J-Node site.

J-Node Platforms

We here introduce each platform (PF) developed or under development at the J-Node portal site [1].

Cerebellar Development Transcriptome Database

To elucidate the genetic basis for mouse cerebellar development, as a model system, the members analyze all of the transcriptional events (i.e., the transcriptome) responsible for developmental stages. CDT-DB has been developed to combine the large datasets of the expression profile information and the relevant bioinformatics, which not only allows us to delineate the complex genetic mechanisms underpinning cerebellar development but also provides a tool for sharing and mining of our large datasets. [*PF head:* Furuichi, Teiichi (RIKEN Brain Science Institute)]

[3] http://xoonips.sourceforge.jp/

Neuron-Glia PF

Focuses on how neuronal and glial cells and the networks of these cells work in a highly complex and dynamical system of brain and proposes to give mathematical model descriptions to new findings and ideas on neural information processing. Neuron-Glia PF also provides the function to help collaboration of researchers. [*PF head:* Miyakawa, Hiroyoshi (Tokyo University of Pharmacy and Life Sciences)]

Invertebrate Brain PF

IVB PF allows us to share such resources as the physiological and behavioral data from insects and other invertebrate animals. For example, Invertebrate Brain Gallery - a collection of images of nervous systems in various invertebrates - is constructed and managed by the original XooNIps module. Original image data of invertebrate neurons, such as interneuron of antennal lobe of moth brain, are collected on the site. [*PF head:* Kanzaki, Ryohei (University of Tokyo)]

Cerebellum PF

Is a database of the all kinds of information on a cerebellum with an unique structure and role in motor learning. The platform will provide a history of the cerebellar research and the basic concepts of the cerebellar structure and function, references and images, experimental data for the modeling, source codes of neural network models, and other tools for the study of the cerebellum. The members will focus on the two important cerebellum-dependent experimental paradigms, i.e., adaptation of the eye movements and eyeblink conditioning. [*PF head:* Nagao, Soichi (RIKEN Brain Science Institute)]

Brain-Machine Interface PF

BMI is the interface in which mechanical devices provide sensory input to the brain, or are controlled by the motor output signals recorded in the brain. BMI PF is a database of BMI researches covering the research fields of neuroscience, computational theory, robotics etc. It provides organically linked information about BMI to researchers of the field inside and outside the country and support researches to develop their study or understanding of BMI. By using a clickable map of research sites about BMI, users can figure out trends of BMI studies around the world. [*PF head:* Iijima, Toshio (Tohoku University)]

Visiome PF

is a vision science neuroinformatics platform, which was developed by NRV project [2]. Since reproducibility is a key principle of the scientific method, published results must be testable by other researchers using the same methods. The platform collects various kinds of reference files and makes them organized and packaged as a single item in Visiome Binder, which is useful for providing a reading list for students, a collection of models and data with a particular interest, a collection of educative movies in vision science. [*PF head:* Kamiyama, Yoshimi (Aichi Prefectural University)]

Integrative Brain Research PF

The IBR project is comprised of about 300 principal investigators (PIs) from different neuroscience areas. The database committee is planning both top-down and bottom-up types of databases. For the former, the database committee will collect the outcomes of the research of individual PIs and will publish these research outcomes on IBR PF. Although the activity of the project will finish in 5 years, the content will be maintained and updated by the IBR-PF committee under the J-Node afterwards. [*PF head:* Isa, Tadashi (National Institute for Physiological Sciences)]

Neuroimaging PF

NIMG-PF committee members are registering bibliographies, tutorial materials, software contents, experimental data and other information and links related to various neuroimaging technologies such as MRI, MEG, EEG, PET, and NIRS, and their integrations. They are also developing convenient visualization functions for neuroimaging databases, which are capable of an easy-to-use display of 3D brain images and a function of search by pointing locations on the images. In addition, there is a plan of registering MEG multi-dipole analysis software and raw data of MRI and MEG. [*PF head:* Suzuki, Ryoji (Kanazawa Institute of Technology)]

Neuroinformatics Common Tools PF

NICT PF aims to share mathematical theory, algorithm, analytical tool and NI-supporting environment. At present, software tools and NI-supporting environment developed by NI-Team for neuroscientists are being registered, such as (1) Customizable base platform; XooNIps, (2) Personal database software; Concierge, (3) System analysis total environment; SATELLITE, and (4) Visualization tools; Samurai-Graph. [*PF head:* Usui, Shiro (RIKEN Brain Science Institute)]

Concluding Remarks

We have kept track of the access log to the J-Node site regularly since it was revised in July 2006. Figure 117.2 shows the records on monthly basis as of May 31 2007. The average number of site access is approximately 47,000 per month. This number has much increased because the portal was revised to be easier to find the information of users' interests and to provide information in English as well. Figure 117.2 also reveals that the site is accessed not only from jp domain but also from other country domains (us, au, eu, de, and so on). It is necessary to collect significant resources to attract users and promote the J-Node site over the countries.

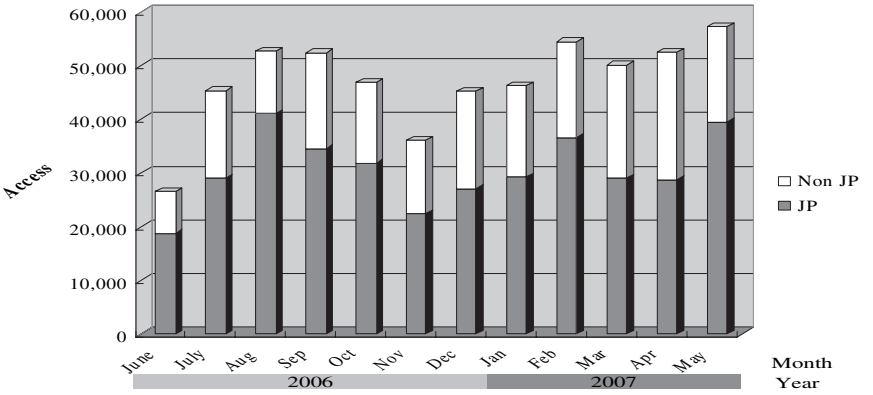

Fig. 117.2 The number of access to the J-Node portal site (June '06 - May '07)

Acknowledgements I would like to thank Dr.Amari, Shun-ichi at RIKEN BSI and all members of the PF Committees for their supports and collaborations.

References

1. Usui, S., Furuichi, T., Miyakawa, H., Ikeno, H., Nagao, S., Iijima, T., Kamiyama,Y., Isa, T., Suzuki, R., Ishikane, H.: Japanese Neuroinformatics Node and Platforms. ICONIP2007 Proceedings, (2007).
2. Usui, S.: Visiome: Neuroinformatics research in vision project. Neural Networks, 16 (2003) 1293–1300.

Chapter 118
Chinese Neuroinformatics Research: Recent Progress and Future Activities

Guang Li, Ling Yin, Yiyuan Tang and Xiaowei Tang

Keywords Neuroinformatics · China · database · progress · activity

Introduction

In September, 2001, the 168th Xiangshan Science Conference, which focusing on the scientific frontier of basic research and important engineering technology of China, entitled "Human Brain Project and Neuroinformatics" was held in Beijing. As a result, the Neuroinformatics Working Group of China was found. Since then, supported by the Ministry of Science and Technology (MOST) of China, neuroinformatics researches have developed fast in China [1, 2].

Recent Progress of Neuroinformatics in China

In recent years, the research in neuroinformatics in China focused on the standard and criterion for neuroinformatics data-sharing, an internationally-distributed neuroinformatics database in china and the promotion on neuroinformatics research [2].

Funded by the National Basic Research Program of China (973 Program), the National Node of Neuroinformatics of China, entitled Brain Bank, was initialized in January 2005. The aim of this project is to collect and normalize existing neuroinformatics resources all over the country, develop informatics processing platform for neuroscience, setup the national web node of China as a part of international neuroinformatics network and provide neuroinformatics resources with local characteristics.

While doing effort on neuroinformatics data-sharing, the Neuroinformatics Working Group of China has promoted on neuroinformatics research. Several

G. Li
National Laboratory of Industrial Control Technology, Institute of Advanced Process Control, Zhejiang University, Hangzhou 310027, China
e-mail: guangli@zju.edu.cn

R. Wang et al. (eds.), *Advances in Cognitive Neurodynamics*,

training courses in neuroinformatics have been held, and several national and international conferences were organized.

Scientific Data Sharing in China

When the world is entering a new era of enormous potential for everyone, that of the Information Society and expanded human communication, Chinese government has realized that data have become both more accessible and more necessary to maintain; more abundant and more complex to manipulate; more global and more expected to share. So the Chinese government started to pay more and more attention on scientific data sharing. In October, 2006, the 20th International CODATA Conference (CODATA 2006), titled "Scientific Data and Knowledge within the Information Society," was held in Beijing. CODATA 2006 intended to promote the use of scientific data and knowledge and harness the benefits of the Information Society to reach scientific and developmental targets.

As a cutting-edge research field in science and technology development today, the studies of biomedicine have already accumulated an enormous volume of data by scientists across the world. Chinese government also realized that although the construction of some databases, for instance the Genbank by the U.S. National Center for Biotechnology Information, has been taken shape and won world recognition, most data resources are still in the private possession of individual scientists or institutes. The shortage of authoritative managing institutions and standardized norms for such data leads to a lot of low-efficient and repeated research. The establishment of global platforms for data management and sharing for biomedical studies becomes one important target for the government. By far, a website called "the Scientific Data Sharing System for Chinese Medicine and Health" [3] has been established to collect every piece of valuable information in fields like pre-clinical medicine, clinical medicine, public health and traditional Chinese medicine. A report on its construction and development during the Conference for Committee on Data for Science and Technology (CODATA) in Beijing last year gained high applause, and the system was regarded as the most comprehensive and promising bio-medical databank in today's world. The data-sharing in neuroinformatics was brought into this system.

As a part of the 20th International CODATA Conference held in Beijing last year, a special session entitled Brain Bank was organized by the Neuroinformatics Work Group of China. And the work of Neuroinformatics Work Group of China were introduced. During the 298th Xiangshan Science Conference held on March 29–31, 2007, entitled "International Symposium on Global Data-sharing Strategy in Biomedicine", neuroinformatics data shring was considered as a good example of data-sharing in biomedicine as well as the Genbank.

Brain Bank – Chinese National Node of Neuroinformatics

The Brain Bank [4] is a professional website developed by the Neuroinformatics Working Group of China and Computer Network Information Center of Chinese

Academy of Sciences (CNIC, CAS), according to general disposition of the Organization of international Economic Cooperation and Development (OECD) – Global Science Forum(GSF) – Neuroinformatics (NI), under the support of the 973 great international cooperation project – Chinese node of the international neuroinformatics network.

The webpages include seven columns: home, international cooperation, research program, research results, services, forum, and free mailbox. Mainly, the databases include the basic neuroscience database, clinical neuroinformatics database, perception, awareness consciousness database, artificial intelligence database and informatics tool database. Additionally, three databases with significant Chinese characteristics are constructed. They are Chinese-western medicine encephalopathy database, acupuncture brain function imaging database and the Chinese cognition and consciousness feeling database.

The main missions of the Brain Bank are to integrate neuroinformatics data resources with Chinese characteristics, to build up a research network environment for global cooperation, to utilize the technique of computer network to link the international databases relevant with brain and neuroinformatics research, to manage data from preservation to sharing and value extraction and addition, to enhance international cooperation on brain research together with international organizations, and to provide scientific data sharing service.

Promotion on Neuroinformatics Research

The Chinese Neuroinformatics Working Group has done effort on neuroinformatics database and internet based collaboration environment as a part of scientific data-sharing, particular the data-sharing in biomedicine.

In October, 2005, the 266th Xiangshan Science Conference, entitled “Neuroinformatics and Scientific Data Sharing” was held in Beijing. The national strategy of the development of neuroinformatics in China was discussed.

(a) (b)

Fig. 118.1 Brain Bank – the Chinese node of the International Neuroinformatics Network, (**a**) Chinese version (**b**) English version

A special session of the 20th International CODATA Conference entitled Brain Bank was organized. The work of Neuroinformatics Work Group of China were reported.

In March 29–31, 2007, the 298th Xiangshan Science Conference, entitled "International Symposium on Global Data-sharing Strategy in Biomedicine" was held in Beijing. It was decided to start cooperation with the National Institute of Biomedical Imaging and Bioengineering of USA in neuroimaging data sharing as one of starting point of Sino-American scientific data-sharing cooperation.

Meanwhile, China is doing effort on promoting research on neuroinformatics. In order to enhance the communication in neuroinformatics, the China–Japan–Korea Joint Workshop on Neurobiology and Neuroinformatics is regularly organized. The 7th China–Korea–Japan Joint Workshops on Neurobiology and Neurinformatics was held in Xiamen in November 2005. The first International Workshop on Nonlinear Brain was held in Hangzhou, June 9–10, 2007. Over 80 scholars from different countries across the world join the workshop.

Future Works

Taking it as one of the pioneers of the scientific data-sharing projects, the Chinese Neuroinformatics Working Group will implement a better web-based coordinating research environment for neuroscience and informatics by improving the overall planning, standardization and operational mechanism of the neuroinformatics data-sharing system,

Furthermore, we will continue to coordinate the neuroinformatics research with Chinese characteristics in China, to integrate the neuroinformatics resources and do effort on the neuroinformatics training programs.

Acknowledgements The work was supported by the National Basic Research Program of China (No. 2004CB720302).

References

1. Li, G., Zhang, J., Gu, F., Yin, L., Tang, Y., Tang, X.: Neuroinformatics Research in China – Current Status and Future Research Activities. In: Wang, L., Chen, K., Ong, Y.S. (eds.): ICNC 2005, Lecture Notes in Computer Science, Vol. 3610. Springer-Verlag, Berlin Heidelberg (2005)1052–1056.
2. Yin, L.: Neuroinformatics and Data-Sharing, 20th International CODATA Conference (CODATA 2006): Scientific Data and Knowledge within the Information Society, 22–25 October 2006, Beijing.
3. The Scientific Data Sharing System for Chinese Medicine and Helath, http://www.ncbi.sciencedata.cn/
4. International Neuroinformatics Network – China: Brain Bank, http://www.brainbank.cn/

Chapter 119
Neuroinformatics in India – Current Status and Future Directions

Nandini Chatterjee Singh

Abstract Neuro-Informatics and computational neuroscience research in India has followed two directions – on the one hand research has focused on the use of computational approaches to understand neural processing. On the other hand research has been directed towards developing new tools that would benefit clinical research. In this paper we describe research initiatives undertaken in both areas and also discuss some new programs that been initiated at the recently commissioned National Facility for Functional Brain Imaging at the National Brain Research Centre.

Keywords Computational neuroscience · India · brain · models · fMRI

Introduction

The field of Neuroinformatics and computational neuroscience research in India has followed two paths (1) Computational analysis and modeling to understand brain function and (2) Development of tools and techniques to aid the aid the clinical community for the analysis and diagnosis of brain disorders. A major role in organizing such research has been played by the National Brain Research Center (NBRC), the first Institute in India, established in 1999, for the development and promotion of fundamental research on Neuroscience. The mandate of NBRC is to carry out research on brain function in health and disease in order to see basic research and technological advances translated into better diagnostic tools and rational therapies for health problems.

In this paper we will outline some of the research undertaken at various centres in India and hope that newer research collaborations with other countries might result from the exchange and sharing of such information. The next few paragraphs describe research in computational neuroscience in different parts of India.

N.C. Singh
National Brain Research Centre, NH-8, Nainwal Mode, Manesar, Haryana 122 050 India
e-mail: nandini@nbrc.ac.in

R. Wang et al. (eds.), *Advances in Cognitive Neurodynamics*,

Language Phonological Maps and Their Applications in Studying Language Disorders

The speech and language laboratory at the National Brain Research Centre (NBRC) headed by Dr. Nandini C Singh have initiated a new approach to study spoken language. Using state of the art signal processing techniques they describe spoken language in terms of information at different time scales. Towards building such a picture, language is 'visualized' as sound in terms of modulations of the amplitude envelope and can thereby be characterized by broadband spectra with energy at many different time scales. In the process this laboratory has developed for the first time a single unified tool called the 'language phonological map' that can capture all aspects of spoken language like rhythm, place of articulation and pitch voicing which is currently being used to study the temporal structure of different languages.

The Development of Speech Motor Skills in Children in Populations of Monolingual and Bilingual Children

To study the development of speech motor skills in typically developing children, the speech and language laboratory at NBRC is setting language phonological maps for children between 4–10 years of age and comparing them with adults. Since this data is being investigated in a population such studies not only provide information on when children achieve adult-like maturation but could potentially also be useful for speech language pathologists in the screening and diagnosis of language disorders associated with speech motor skills [1].

A third area of interest in this laboratory is the to investigate patterns of speech produced by children with autism and how it differs from the patterns exhibited by typically developing children.

Application of Stochastic Resonance and Stability Analysis for Brain Imaging and Therapy: Using Noise to Defeat Noise

A major project in Dr. Prashun Roy's laboratory is to apply the Stochastic Resonance Enhancement paradigm for increasing the efficiency of diagnostic and therapeutic radiology, especially in neuroimaging (MRI, MRS), tomography and tomotherapy [2]. Though CT and MRI have revolutionized the study of brain in health and disease, a major problem is increasing the signal:noise ratio (SNR). This group headed by Dr. Prasun K. Roy has designed the pathways through which perturbation can be administered during the process of MRI, tomography and tomotherapy. SRE is being harnessed to distinguishing between brain tumour recurrence and post-radiotherapy necrosis, whose problematic differential diagnosis is an ordeal for conventional imaging procedure. The stochastic augmentation is also being explored for enhancing the diagnosis of Alzheimer's disease.

Non-equilibrium Information Theory

Dr. Prashun Roy's group at the National Brain Research Centre is elucidating a new generalized theory of information transmission and processing beyond the Shannon paradigm and use the theory to understand and modulate information processing in high throughput conditions of neuronal systems, as in intensive adaptation, plasticity, and epileptic seizures. A new nonlinear non-equilibrium dynamic analysis of information processing and control in the neuronal system is being developed to address these issues.

Modelling the Basal Ganglia

In order to explain how various subcortical nuclei of the basal ganglia are involved in diverse functions like reward-based learning, sequence generation, timing, exploratory behavior, motor preparation, working memory, attention, etc Dr. srinivas Chakravarthy's laboratory at the Indian Institute of Technology at IIT, Madras is currently involved in developing an integrated neural network model of BG. The highlights of their model include a hypothesized role of Subthalamic Nucleus-Globus Pallidus externa subsystem in exploratory behavior. This idea suggests a radically new interpretation of the Direct and Indirect Pathways of BG wherein Direct Pathway is the Timing Pathway and the Indirect Pathway is the Exploration Pathway. This model also captures several aspects of Parkinson disease handwriting like micrographia, jagged contour and abnormal velocity fluctuations [3].

Olfaction and Memory

Dr. Upinder Bhalla's laboratory at the National Centre for Biological Sciences in Bangalore is looking at two specific brain functions: the sense of smell, and memory.

To investigate olfactory neural processing they use imaging, electrical recordings, and odor-guided behavior information from which is being used to build a comprehensive computational model of the olfactory system based on basic biophysical principles that will allow them to predict olfactory behaviour [4].

Research in this laboratory is also are directed towards building a biologically detailed computational model of memory, from molecules to network using data from various chemical circuits.

Learning Mechanisms

Human skill learning using behavioural experiments, functional neuroimaging and neural modelling is being investigated by Dr. Bapi Raju at the University of Hyderabad. They undertakeexperiments to investigate the mechanisms underlying the

acquisition of sequential motor skills (such as typing) triggered by visual cues. A second area of interest in the laboratory is the modeling of biochemical signaling pathways involved in reinforcement learning [5].

Computational Exploration of Neurotransmission in Smooth Muscle

Computational analysis and in silico experimentation of neurochemical processes are fast developing into a new research focus in the neuroscience arena. Dr. R. Manchanda at the Bio-engineering department at the Indian Institute of Technology in Mumbai, is pioneering a research unit that has implemented a discrete electrical model of a 3-D syncytium representing smooth muscle. Theoretical analyses can now be carried out of the effects on smooth muscle electrical activity, measured as syncytial synaptic potentials, of imposed conditions. The conditions that are imposed are chosen such as to mimic experimental conditions or protocols. Experimental application of presumptive uncoupling agents can be modelled as alteration in relevant electrical parameters of the system. Alteration of function at the bundle, rather than cellular, level, can be explored.

Modelling of Receptive Field Formation and Cortex–Retina Interaction

The Department of Electrical Engineering at Indian Institute of Technology – Delhi, has an intensive research team led by Dr B Bhaumik, working in the problem of simulating and analyzing the orientation and direction selectivity of simple cells as well as studying a developmental model for receptive field formation in these cells. To obtain the response of cortical cells to sinusoidal grating input, the retinal layer has been modeled as a 2-D sheet of retinal ganglion cells (RGC) lying one over the other, the first sheet corresponding to ‘on’ center RGCs and the other to ‘off’ center RGSs. The stimuli used in the visual space consists of a moving sinusoidal grating of a given spatial and temporal frequency with varying orientation, this stimulus traverses in the up-and-down direction for each orientation of the grating. The response of cortical cell at a given time is calculated using spike-response model (SRM). This computational experiment show that about 18% cells of the simulated cortex are direction selective, and this model has been a pioneering one for the receptive field formation in directionally selective cells [6].

Analysis of fMRI Data

The major focus of research of the team initiated by S. Purkayastha at Indian Statistical Institute (Kolkata) has been neuroimaging. Current studies of estimation

of hemodynamic sponse function, with special focus on Bayesian methods, is being pursued. They also propose to actively use the software fMRIstat (developed by Keith J. Worsley of McGill University, Montreal, Canada)

National Neuroimaging Facility

A 3T scanner has been installed at the National Brain Research Centre as part of the National Functional Imaging facility and is completely functional. It is open for research to neuroscientists across universities and institutes. Efforts are being directed to develop a National Initiative in Neuroinformatics by involving various Institutes to develop newer models for language and speech processing, analysis of images various other areas of research. Students at post-graduate and the Ph.D. level would undertake projects and rotate through various Institutes depending on the available expertise and thus also facilitate more interaction and develop better networks.

Acknowledgements The author would like to acknowledge all the research laboratories and the National Brain Research Centre for valuable research input and a research grant from the Department of Information Technology, Government of India.

References

1. Singh, L., Singh, N.C.: The development of articulatory signatures in children, *Development Science*, (in press).
2. Roy, P.: Cognitive processing and activation: an analysis using stochastic transition and stochastic resonance. *Journal of Institution of Electronics and Telecommunication Engineers*, 49, 183–95, 2003.
3. Devarajan, S., Prashanth, P.S., Chakravarthy, V.S.: On the exploratory role of complex oscillations in a model of basal ganglia based on reinforcement learning. *International Journal of Neural Systems*, 16(2), 111–124, 2006.
4. Rajan, R., Clement, J.P., Bhalla, U.S.: Rats smell in stereo, *Science*, 311, 666–670, 2006.
5. Wanjerkhede, S.M., Bapi, R.S. (2005). Role of presynaptic reuptake on dopamine modulation of cortico-striatal activity in TD learning. In: The Proceedings of the International Joint Conference on Neural Networks (IJCNN) July 31–Aug 4, 2145–2149, 2005.
6. Mathur, M., Bhaumik, B.: Study of spatial frequency selectivity and its spatial organization in the visual cortex through a feedforward model. *Neurocomputing*, 65–66: 85–91, 2005.

Chapter 120
Emotional States Estimation from Multichannel EEG Maps

**Tomasz M. Rutkowski, Andrzej Cichocki,
Anca L. Ralescu and Danilo P. Mandic**

Abstract The notion of emotional empathy, that is the estimation of responses from electrophysiological signals has recently gained attention among the designers of brain computer/machine interfaces (BCI/BMI). This is largely due to the relative simplicity and convenience of electroencephalograph (EEG) recordings. Whereas this problem is not entirely new, engineering approaches connecting the emotional states of humans and the observed EEG recordings are still in their infancy. In this paper we present an initial set of results on the estimation of basic emotional responses generated while watching short videos with dynamic emotional contents. A novel multichannel EEG analysis approach is proposed in order to discover representative components of the emotional responses. This is achieved based on distinct spatial patterns exhibited within the EEG data recorded over frontal lobes, and averaged over a number of trials and subjects. Simulation results support the proposed approach, and confirm the initial hypothesis.

Introduction

Manifestations of emotional states are normally straightforward to detect and understand by humans, as these are reflected in both the voice and body language [1, 2]. Some of the emotional states generate strong audio-visual responses (such as laughter or anger), whereas other are more difficult to recognize. Indeed, it requires rather special knowledge to discover intent or deception from the behavior of a human, although it is intuitively clear that these ought to be manifested in brain responses. The approach presented here is somewhat related to some previously discussed methods [3, 4, 5], where emotional stages were estimated based on the asymmetry within the frontal brain activity in recorded EEG. In our approach the subjects were presented with videos showing faces exhibiting different flavors of standardized emotional expressions (comprehensive databases showing various emotional stages [6]). Experiments reported in [2, 7] showed that the unconscious mind exerts

T. M. Rutkowski
Brain Science Institute RIKEN, Wako-shi, Saitama, Japan
e.mail: {tomek,cia}@brain.riken.jp

R. Wang et al. (eds.), *Advances in Cognitive Neurodynamics*,

direct control of facial muscles. However, contemporary approaches to emotional state estimation usually deal with a static analysis of facial expressions and seldom consider a dynamic or multimodal analysis. The classic experiments of [7] were conducted using electromyography, in order to capture actual muscle activity of communicators. Results of those experiments revealed that the communicators often do not have total control over their expressed facial emotions. These findings clearly suggest that important aspects of *emotional face–to–face* communication could occur at the unconscious level; this justifies our aim to predict emotional empathy from EEG recorded over the frontal cortex. This activity is naturally expected to precede the muscle activity (muscle reaction planing). The aim of this paper is therefore twofold as follows: (i) to introduce a novel computational framework based on Empirical Mode Decomposition (EMD) convenient for simultaneous data conditioning and feature extraction from EEG data, and (ii) to provide an insight into the information theoretic processing mechanism of the brain based on this technique, in particular, to illustrate the effectiveness of this approach for tracking of emotional empathy from EEG data recorded over frontal lobes.

Experiments with EEG Recording during Emotions Presentation

Experiments were conducted in Advanced Brain Signal Processing Laboratory of Brain Science Institute RIKEN, Japan. Every subject was asked to wear an EEG cap with electrodes connected to the following front head channels *Fp1, Fp2, AF3, AF4, AF7, AF8, F3, F4,* as in extended 10/20 EEG recording systems [8]. Throughout the recording sessions, three different sets of movies from [6] with facial expressions illustrating the emotions of *angry*, *thinking* and *happy* were presented. EEG signals recorded on the scalp levels are usually highly contaminated by noise due to a very low level of electrophysiological signals and due to the presence of different devices in the environment creating electromagnetic interference. To tackle these problems, the current study proposes to use empirical mode decomposition (EMD) [9], a new technique to decompose EEG signals. EMD utilizes empirical knowledge of oscillations intrinsic to a time series in order to represent them as a superposition of components, called *intrinsic mode functions* (IMF), with well defined instantaneous frequencies. In the current approach each recorded channel is first decomposed into IMFs separately. Subsequently those signals which match instead only the frequency bands of δ, θ, α, and β [8] are reconstructed. To obtain a single channel IMF it is necessary to remove local riding waves and asymmetries, which are estimated from local envelope of minima and maxima of the waveform. The technique of finding IMFs corresponds thus to finding band limited semi-orthogonal components of the signal. It also corresponds to eliminating riding-waves from the signal, which ensures that the instantaneous frequency will have no fluctuations caused by an asymmetric wave form. In each cycle, the IMF is defined by zero crossings and involves only one mode of oscillation, thus not allowing complex riding waves. Notice that an IMF is not limited to be a narrow band signal, as it would be in traditional Fourier or wavelets decomposition. In fact, an IMF can be both amplitude and frequency modulated at once, and also non-stationary or non-linear.

The procedure to obtain IMF components from a signal, called sifting [9], consists of the following steps: (i) Identify the extrema of the signal waveform $x(t)$; (ii) Generate "signal envelopes" by connecting local maxima by a cubic spline. Connect signal minima by another cubic spline; (iii) Determine the local mean, m_1, by averaging the two spline envelopes; (iv) Subtract the mean from the data to obtain: $h_i = x(t) - m_i$; (v) Repeat as necessary until there are no more possible IMF to extract; (vi) Proper IMF is a first component containing the finest temporal scale in the signal; (vii) The residue r_i should be generated by subtracting out proper IMF found from the data; (viii) The residue contains information about longer periods which will be further resifted to find additional IMFs. Using the above procedure, EEG signals from chosen electrodes were decomposed separately forming subsets of IMF functions, from which low frequency drifts and high frequency spikes were further removed. From the obtained IMFs, corresponding frequency bands of δ, θ, α, and β [8] were extracted and their combined powers were plotted in form of "head–plots" with specific patterns for different emotional stages generated in response to watched videos were obtained as in Fig. 120.1. Notice differences in power distributions over the frontal head and the asymmetry in *thinking* and *happy* states. The state of *angry* response is characterized by frontally symmetric response in bottom panels in Fig. 120.1.

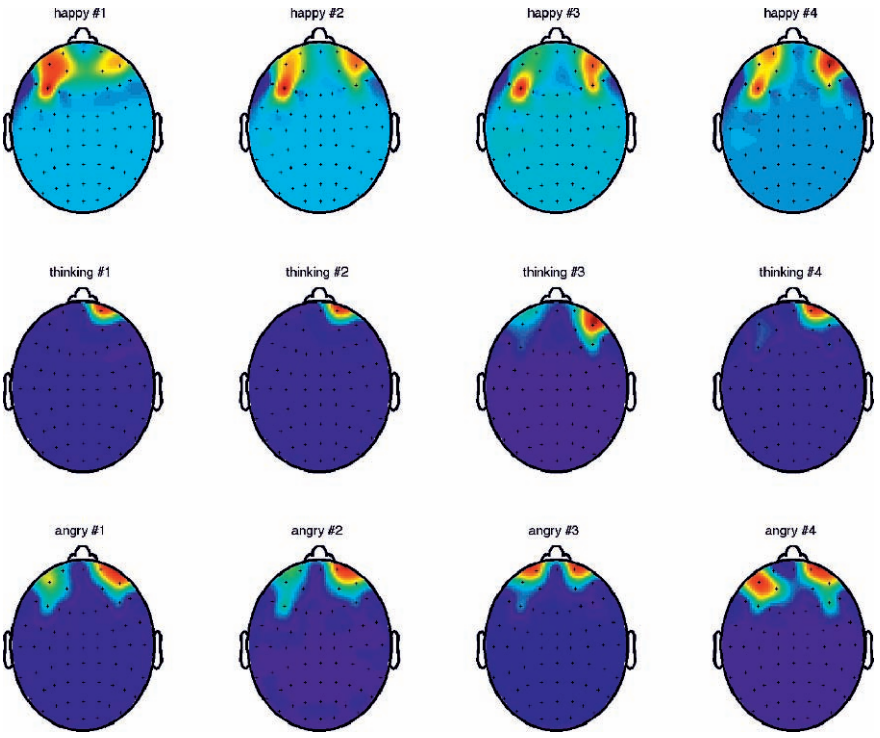

Fig. 120.1 The averaged (over subjects and sessions) EEG power patterns (over the frontal head) during different emotional stimuli

Conclusions

A framework to estimate emotional emphatic response from EEG has been presented as a part of augmented BMI research. This has been achieved by proposing a new EEG decomposition technique, which allows a flexible sub-band signal decomposition while preserving the nonlinear and non-stationary nature of the signals. A set of carefully selected video clips, containing faces showing dynamic emotions, has been shown to allow for the estimation mental feedback. Reactions of the subjects were estimated from EEG recorded synchronously while the users where watching labeled videos, and the EEG patterns elicited during these experiments have been analyzed. This approach is very far from an idea of "thought reading" but indicates the possibility of designing a video stimulus that might generate an expected reaction clearly noticeable from EEG. This is a step forward toward creating user friendly brain–machine–interfaces that would not utilize mentally demanding stimuli.

Acknowledgements This work was supported in part by JSPS and Royal Society under the Japan-UK Research Cooperative Program, 2007.

References

1. Adler, R.B., Rodman, G.: Undestanding Human Communication. Oxford University Press (2003).
2. Pease, A., Pease, B.: The definitive book of body language - How to read others' thoughts by their gestures. Pease International (2004).
3. Ahern, G.L., Schwartz, G.E.: Differential lateralization for positive and negative emotion in the human brain: EEG spectral analysis. Neuropsychologia **23**(6) (1985) 745–755.
4. Coan, J.A., Allen, J.J.B.: Frontal EEG asymmetry as a moderator and mediator of emotion. Biological Psychology **67**(1–2) (2004) 7–50.
5. Esslen, M., Pascual-Marqui, R.D., Hell, D., Kochi, K., Lehmann, D.: Brain areas and time course of emotional processing. NeuroImage **21**(4) (2004) 1189–1203.
6. Baron-Cohen, S.: Mind Reading - The Interactive Guide to Emotions. Jessica Kingsley Publishers, London, UK (2004).
7. Dimberg, U., Thunberg, E., Elmhed, K.: Unconscious facial reactions to emotional expressions. Psychological Science **11**(1) (2000) 149–182.
8. Niedermeyer, E., Da Silva, F.L., eds.: Electroencephalography: Basic Principles, Clinical Applications, and Related Fields. 5 edn. Lippincott Williams & Wilkins (2004).
9. Huang, N., Shen, Z., Long, S., Wu, M., Shih, H., Zheng, Q., Yen, N.C., Tung, C., Liu, H.: The empirical mode decomposition and the Hilbert spectrum for nonlinear and non-stationary time series analysis. Proceedings of the Royal Society A: Mathematical, Physical and Engineering Sciences **454**(1971) (March 1998) 903–995.

Chapter 121
ICA and Complexity Measures of EEG Analysis in Brain Death Determination

Jianting Cao and Zhe Chen

Abstract The concept of brain death has been accepted in worldwide. In many countries, electroencephalography (EEG) is used as a criterion to evaluate the absence of cerebral cortex function in the brain death diagnosis (BDD). Since EEG recordings might be corrupted by some artifacts or various sources of noise interference, studying EEG in noise reduction and the significant differences of EEG measurements is crucial in the process of BDD. This paper presents an EEG data analysis method using independent component analysis (ICA) and complexity measures [IEEE Transactions on Neural Networks 14: 631–645, 2003, Proceedings of International Conference of the IEEE Engineering in Medicine and Biology Society]. A total of 36 patients' EEG data have been analyzed. The reported experimental results illustrate the effectiveness of the proposed method.

Introduction

Brain death is defined as the cessation and irreversibility of all brain and brain-stem functions. Based on this definition, the basic clinical criterion (including the EEG criterion) is typically established in most countries. For example, a relatively strict criterion in Japan is given as (1) Coma test; (2) Pupils test; (3) Brainstem reflexes test; (4) Apnea test; and (5) EEG confirmatory test. Since the standard process of BDD usually involves certain risks and takes a long time (e.g. the need of removing the respiratory machine in the apnea test), it is desirable to develop a practical yet safe and reliable tool for the diagnosis of brain death.

We have introduced an EEG preliminary examination method in the standard BDD process [1, 2]. After (1)-(3) tests, an EEG examination along with real-time data analysis is used to detect the brain activity at the bedside of patient. Provided the examined result is positive, we suggest to accelerate (or bypass) the BDD process, and focus the attention on the medical care.

J. Cao
Department of Human Robot, Saitama Institute of Technology, 1690 Fusaiji, Fukaya-shi, Saitama 369-0293, Japan
e-mail: cao@sit.ac.jp

R. Wang et al. (eds.), *Advances in Cognitive Neurodynamics*,

In order to support the EEG preliminary examination in BDD, we develop a system that includes a portable EEG recording parts and several EEG signal processing tools [1, 2, 3]. It is our belief that if the EEG preliminary examination is reliable and its results are significant, it can provide a simple and risk-free diagnosis tool in the Intensity Care Unit (ICU) of the hospital without jeopardizing the life of the patient.

EEG Data Analysis

ICA with a Robust Pre-whitening for Noise Reduction

Given the measured EEG signal, the signal model can be formulated by

$$\mathbf{x}(t) = \mathbf{A}\mathbf{s}(t) + \boldsymbol{\xi}(t), \tag{121.1}$$

where $\mathbf{x}(t) = [x_1(t), \cdots, x_m(t)]^T$ represent the transpose of m electrodes at time t. Each electrode signal $x_i(t)$ contains n common components represented by the vector $\mathbf{s}(t) = [s_1(t), \cdots, s_n(t)]^T$ and a unique component which is an element in the vector $\boldsymbol{\xi}(t) = [\xi_1(t), \cdots, \xi_m(t)]^T$. The element of matrix $\mathbf{A} \in \mathbb{R}^{m \times n} = (a_{ij})$ reflects the mixing (or propagation) factor between the i-th sensor and the j-th source.

There are two kinds of noise that needs to be reduced or discarded in the EEG data analysis. The first kind is the additive noise that is generated from the individual sensor. The standard ICA approaches usually fail to reduce this kind of noise. Therefore, we will first apply a robust pre-whitening technique [4] in the preprocessing stage to reduce the power of the additive noise. The second kind of noise is a common component such as an interference source. we will apply a robust ICA algorithm based on the parameterized **t**-distribution density model [4] to separate the mixtures of sub-Gaussian and super-Gaussian signals, and discard the common noise components after the source decomposition.

Quantitative Complexity Measures

The quantitative EEG analysis for the coma and quasi-brain-death patients has been reported in [1, 2]. Specifically, four types of complexity measures are used for evaluating the differences between two groups of patients. These four types of complexity measures are : (1) the *approximate entropy* (ApEn); (2) the *time delay-embedded normalized singular spectrum entropy* (NSSE); (3) the C_0 *complexity*; and (4) the α-exponent based on *detrended fluctuation analysis* (DFA). Upon obtaining the quantitative results from these four complexity measures, statistical tests were further applied to evaluate their statistical significance. Specifically, one-way ANOVA (analysis of variance) was applied to these quantitative measures within two groups (coma vs. quasi-brain-death) for each electrode channel.

Experimental Data and Results

The EEG measurements were recorded in the Shanghai Huashan Hospital in affiliation with Shanghai Fudan University, China. The EEG was directly recorded at the bedside of patient where the level of environmental noise was relatively high. Six electrodes and one ground electrode were placed on the forehead of the patient. A total of 36 patients have been examined by EEG from June 2004 to March 2006, with the age range from 17 to 85 years old.

By applying ICA to the 36 patients' EEG, we were able to extract brain activities from 19 patients (see Table 121.1). The β-wave component occurred in some patients due to the effect of medical drug. On the other hand, only noise or interference components (e.g., heartbeat component in some cases) were extracted from the remaining 17 patients. The results from our data analysis were almost identical to the clinical diagnosis.

Based on the clinical diagnosis and the ICA results, the patients were classified into a deep-coma group or a quasi-brain-death group. We applied four types of complexity measures to evaluate the quantitative differences between two groups. The result is summarized in Table 121.2. As seen from the table, statistical tests show significant differences in all complexity measures and all channels for the raw EEG data. For the filtered EEG data (0.5–100 Hz), significant differences between two groups are still found in all or majority of the channels for all complexity measures.

Table 121.1 The results of extracted brain activities from 19 patients (δ band: 1–4 Hz, θ band: 4–8 Hz, α band: 8–12 Hz, β band: 13–30 Hz)

Number	Gender	Age	Analysis results
1	Male	18	θ-wave, α-wave, δ-wave
2	Male	40	θ-wave
3	Male	85	θ-wave, α-wave
4	Male	65	θ-wave
5	Female	64	θ-wave
6	Female	23	δ-wave
7	Male	48	θ-wave
8	Female	17	α-wave
9	Male	18	θ-wave, δ-wave
10	Male	66	θ-wave
11	Female	84	θ-wave, δ-wave, α-wave, β-wave
12	Male	79	θ-wave
13	Male	48	α-wave, θ-wave
14	Female	73	θ-wave
15	Male	64	θ-wave, α-wave
16	Male	83	θ-wave, δ-wave
17	Female	67	α-wave, θ-wave
18	Female	82	δ-wave
19	Male	37	β-wave

Table 121.2 Summary of quantitative statistics applied to the raw and filtered EEG data for two groups: coma (C) vs. brain death (D). For the p-value column, $*$ means $p < 0.05$ and $**$ means $p < 0.01$, and they both show statistical significance

		raw data			filtered data		
measure	chan.	median (C)	median (D)	p value	median (C)	median (D)	p value
ApEn	Fp1	0.227	0.598	**	0.103	0.217	*
	Fp2	0.267	0.727	**	0.123	0.362	**
	F3	0.302	0.836	**	0.115	0.362	**
	F4	0.314	0.853	**	0.135	0.331	**
	F7	0.232	0.755	**	0.097	0.263	**
	F8	0.274	0.798	**	0.097	0.305	**
NSSE	Fp1	0.427	0.659	**	0.236	0.336	**
	Fp2	0.453	0.732	**	0.256	0.412	**
	F3	0.474	0.755	**	0.264	0.411	**
	F4	0.464	0.748	**	0.270	0.398	**
	F7	0.402	0.718	**	0.223	0.363	**
	F8	0.419	0.715	**	0.228	0.393	**
C_0	Fp1	0.040	0.093	**	0.030	0.033	**
	Fp2	0.043	0.109	**	0.033	0.038	*
	F3	0.043	0.1191	**	0.030	0.042	*
	F4	0.049	0.137	**	0.034	0.043	0.063
	F7	0.041	0.096	**	0.028	0.040	**
	F8	0.031	0.112	**	0.023	0.041	**
α-exponent	Fp1	1.212	1.147	*	1.277	1.217	0.088
	Fp2	1.203	1.074	**	1.251	1.152	*
	F3	1.194	1.067	**	1.250	1.161	*
	F4	1.220	1.089	*	1.259	1.178	0.053
	F7	1.245	1.096	**	1.307	1.198	**
	F8	1.217	1.101	**	1.292	1.179	**

Conclusion

We have applied ICA and complexity measures to the EEG data recorded from 36 coma and quasi-brain-death patients. Our experimental results illustrate that the alive deep-coma patient or the quasi-brain-death patient can be distinguished. It is our hope that this method can be useful in assisting physicians and doctors for BDD in clinical practice.

Acknowledgements The authors would like to thank Ms. Juhong Yang at the Saitama Institute of Technology, Dr. Zhen Hong, Dr. Guoxian Zhu and Yue Zhang at the Shanghai Huashan Hospital, Prof. Yang Cao and Prof. Fanji Gu at the Fudan University, China for the EEG recordings and useful comments. This research project was partly supported by the Japan Society for the Promotion Science (JSPS).

References

1. Chen, Z. and Cao, J.: An Empirical Quantitative EEG Analysis for Evaluating Clinical Brain Death. Processings of 29th Annual International Conference of the IEEE Engineering in Medicine and Biology Society, Lyon, France (2007) in print.

2. Chen, Z., Cao, J., Cao, Y., Zhang, Y., Gu, F., Zhu, G., Hong, Z., Wang, B. and Cichocki, A.: Qualitative Evaluation and Quantitative EEG Analysis in Brain Death Diagnosis for Adults: An Empirical Study. submitted to IEEE Transactions on Biomedical Engineering.
3. Cao, J.: Analysis of the Quasi-brain-death EEG Data Based on a Robust ICA Approach. Lecture Notes in Artificial Intelligence 3973 (3) (2006) 1240–1247.
4. Cao, J., Murata, N., Amari, S., Cichocki, A. and Takeda, T.: A Robust Approach to Independent Component Analysis with High-Level Noise Measurements. IEEE Transactions on Neural Networks 14 (3) (2003) 631–645.

Chapter 122
Feature Reduction in Biosignal Processing

Martin Golz and David Sommer

Abstract Feature reduction is common in biosignal analysis, especially in case of quantitative EEG analysis. Mostly, summation in the spectral domain is applied to reduce the number of estimated power spectral density values, which gains between four and twelve band power values. Depending on the problem, on signals under analysis and on methods used for further processing it is an open question if such a strong decrease in the number of features is optimal. Modern Soft Computing methods offer the feasibility of processing a large amount of different features without considerable performance deteriorations. In this paper we apply such methods and compare empirically the case of no feature reduction to four variants of feature reduction. Our data set consist of more than 3,700 examples of microsleep events experienced by young adults in an overnight driving simulation study. More than 4,600 features were extracted from seven EEG and two EOG channels utilizing the modified periodogram method. Results showed that summation in many fixed bands, or in fewer, but freely optimized bands is more optimal than no reduction, or strong reduction to four bands commonly selected in EEG analysis.

Introduction

A very important human factor causing accidents is operator fatigue and loss of attentiveness. It is estimated that fatigue plays a major role in 15 to 20% of all accidents and is exceeding in this respect the importance of alcohol and drugs [1]. Extreme fatigue originates dangerous microsleep events (MSE) which are defined as short intrusions of sleep under the demand of sustained attentiveness. Their detection in spontaneous biosignals still poses a challenge.

It has been shown that the empirical error of MSE recognition sensitively depends on several parameters of the preprocessing, the feature extraction and the

M. Golz
Department of Computer Science, University of Applied Sciences Schmalkalden 98574 Schmalkalden, Germany
e-mail: m.golz@fh-sm.de

R. Wang et al. (eds.), *Advances in Cognitive Neurodynamics*,

classification stages [2]. Considerable improvements can be gained if different signal sources are fused on the feature level [3]. Furthermore, it turned out that feature extraction in the spectral domain is more successful compared to methods in the state space or time domain [3]. Therefore we here report only of feature extraction in the spectral domain and their subsequent reduction.

The common way of EEG feature reduction is summation in spectral bands. The Power Spectral Densities (PSD) are commonly reduced to four or sometimes slightly more bands. Their definition is not fixed and varies to some extend between different authors. Typical values are 0.5–4.0 Hz (delta), 4.0–8.0 Hz (theta), 8.0–12.0 Hz (alpha) and 12.0–30 Hz (beta) [4]. The question arises if this or other choices of feature reduction are optimal for quantitative EEG analysis in order to get accurate MSE detection [5]. Five different cases are presented:

(1) No reduction; all available frequency bins are included,
(2) Feature reduction utilizing Principal Component Analysis (PCA),
(3) Feature reduction by summation over fixed band [4],
(4) Feature reduction by summation over equidistant bands,
(5) Reduction by summation in arbitrary bands utilizing genetic algorithms.

For this, we apply modern Soft Computing methods, like the Support Vector Machine (SVM), which do not suffer from the so-called curse of dimensionality [6]. The detection accuracy, estimated by the mean classification error of the test set, is a valid measure to compare all five cases empirically. For this purpose, multiple hold-out validation is used.

Material and Methods

Experiments were conducted in our real car driving simulation lab. 22 young adults (18–32 years) took part and each of them finished 7 driving sessions (35 min length) which are repeated every hour between 1 a.m. and 8 a.m. During driving the electrical brain activity reflected by the EEG was recorded of seven different locations on the scalp (C3, Cz, C4, O1, O2, A1, A2, common reference). The eye and eyelid movements reflected by the Electrooculogram (EOG) were recorded at two locations (vertical, horizontal). Both were sampled at a rate of 128 s.

MSE are typically characterized by driving errors, prolonged eye lid closures or nodding-off which was scored by two experts independently. In all 3,573 MSE and 6,409 non-MSE were scored. Non-MSEs are periods between MSE where the subject is drowsy but shows no clear or unclear MSE.

Segments of all nine signals were extracted with respect to the observed temporal starting points of MSE or Non-MSE using two free parameters, the segment length and the offset between first sample of segment and starting point of an event. After linear trend removal the PSD values were estimated by the modified Periodogram method utilizing Hann windows. Subsequently, PSD values were scaled logarithmically which has been shown to be important for error diminishing [3].

Table 122.1 Comparison of two classification methods (OLVQ1, SVM) for five different cases of feature reduction. Mean and standard deviation of training and test errors for OLVQ1 and SVM were estimated by Multiple Hold-Out and by Leave-One-Out cross validation, respectively

Case	Number of Features		OLVQ1		SVM	
			E_{TRAIN} [%]	E_{TEST} [%]	E_{TRAIN} [%]	E_{TEST} [%]
(1) No feature reduction	4617	(513 × 9)	22.6 ± 0.5	27.7 ± 0.6	0.0 ± 0	13.1 ± 0
(2) PCA	60	128	10.4 ± 0.2	17.4 ± 0.4	1.4 ± 0	10.9 ± 0
(3) fixed band	36	(4 × 9)	11.6 ± 0.2	17.5 ± 0.4	4.9 ± 0	13.2 ± 0
(4) equidistant bands	216	(24 × 9)	9.3 ± 0.1	15.7 ± 0.4	0.1 ± 0	9.9 ± 0
(5) GA-OLVQ1 optimized	90	(10 × 9)	8.2 ± 0.1	14.1 ± 0.4	0.1 ± 0	9.8 ± 0

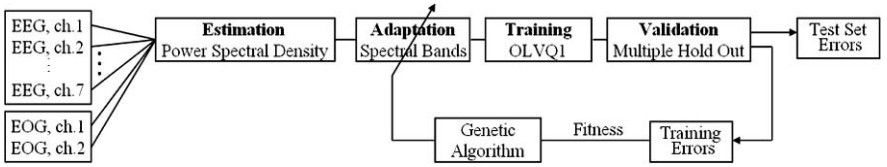

Fig. 122.1 GA-OLVQ1 framework for empirical optimization of band averaging

The above mentioned five cases were utilized in order to evaluate the efficacy of feature reduction. For case (1) each feature vector had a number of components $n_F = 4{,}617$ (Table 122.1) because of sampling in nine channels at 128 Hz and a segment length of 8 s. In order to reduce this large number of features, PCA was utilized (case 2). Alternatively, the common summation of PSD values in the four fixed spectral bands of EEG analysis as mentioned above was examined (case 3). This is a very simple concept and should be optimal if the EEG is dominated by broad-band activity. If not, then case (4) should be more optimal. Here, a flexible number of equidistant bands are generated. Three parameters are to be optimized [3]: lower and upper cut-off frequency and the width of each band. In the most flexible approach (case 5) PSD values were summed in spectral bands of arbitrary location and width. Both parameters were found utilizing a framework (Fig. 122.1) [5] involving Optimized Learning Vector Quantization (OLVQ1) and Genetic Algorithms (GA). We have stopped computations with this GA-OLVQ1 framework after 300 generations. The genetic representation we have fixed in advance to 10 flexible spectral bands for each EEG and EOG channel.

Results

Table 122.1 show that SVM clearly outperforms OLVQ1. Processing a very large number of features (case 1) is acceptable only for SVM and is as good as processing of a relatively low number of features (case 3). But, this is achievable only when a computationally extensive hyperparameter optimization of the SVM has been performed. This way, we achieved mean test errors of 13.1% for the case of no

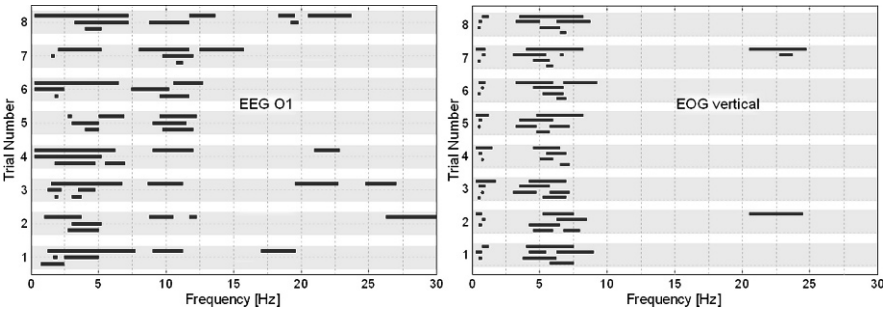

Fig. 122.2 Results of case (5). Eight randomly selected genetic representations (out of 100) which were found for EEG-O1 (left) and vertical EOG (right). Each bar represents both parameters (location and width) of the spectral bands. The plots are limited to 30 Hz whereas optimizations were performed up to 64 Hz

reduction. In case (2) the number of principal components was found to be optimal down to 2% of the original feature space dimensionality (SVM: first 128 principal components, OLVQ1: first 60 principal components). This was a result of empirical investigations not presented here due to space limitations. We achieved worst results when applying common EEG bands (case 3). Much lower errors resulted in case (4). A reduction to 24 small spectral bands for each of the 9 EEG and EOG channels led to errors down to 15.7% (OLVQ1) and 9.9% (SVM). The most flexible approach (case 5) utilized spectral bands arbitrarily in width and location, whereby overlapping spectral bands and differences between channels were allowed. An impression on the variability is shown for two channels (Fig. 122.2). It presents eight examples of the final population.

A summation over all 100 individuals of the final population and subsequent normalization (Fig. 122.3) reveals that broad-band activity in the delta-theta-alpha range is important for MSE detection and that beta as well as gamma activity is much less important. This result of one single channel (EEG-O1) is roughly similar the other EEG channels. For the vertical EOG a narrow-band (6 Hz) and a broad-band (20–45 Hz) is relevant for MSE detection.

In conclusion, moderate feature reductions (cases 4, 5) and modern kernel methods (SVM) should be preferred for quantitative EEG analysis tasks, like event detection.

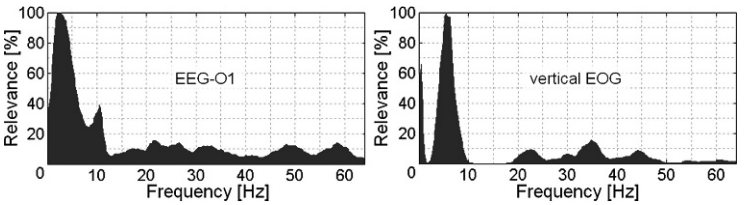

Fig. 122.3 Relevance versus frequency for EEG-O1 (left) and for vertical EOG (right). Results are the outcome of 100 GA-OLVQ1 runs

References

1. T. Akerstedt (2000). Consensus Statement: Fatigue and Accidents in Transport Operations. J Sleep Research 9, 395
2. M. Golz, D. Sommer (2004). Automatic Recognition of Microsleep Events; Biomedizinische Technik 49, 332–333
3. D. Sommer, et al. (2005). Fusion of State Space and Frequency-Domain Features for Improved Microsleep Detection. Proc ICANN 2005; LNCS3697, 753–759, Springer, Berlin.
4. E. Niedermeyer, F. Lopes Da Silva (1999). Electroencephalography; 4th edition, Williams & Wilkins, Baltimore, MD.
5. M. Golz, D. Sommer, M. Chen, U. Trutschel, D. Mandic (2007). Feature Fusion for the Detection of Microsleep Events. J. VLSI Signal Process Syst 49(2), 329–342.
6. Y. Bengio, et al. (2005). The Curse of Dimensionality for Local Kernel Machines. Technical Report 1258, Univ Montréal, Canada.

Chapter 123
An Efficient Encoding Scheme for Dynamic Visual Input Based on the Statistics of Natural Optic Flow

Dirk Calow and Markus Lappe

Abstract Statistically efficient processing schemes focus the resources of a signal processing system on the range of statistically probable signals. Relying on the statistical properties of retinal motion signals during ego-motion we propose a nonlinear processing scheme for retinal flow. It maximizes the mutual information between the visual input and its neural representation and distributes the processing load uniformly over the neural resources. We derive predictions for the receptive fields of motion sensitive neurons in the velocity space. The properties of the receptive fields are tightly connected to their position in the visual field and to their preferred retinal velocity. The velocity tuning properties show characteristics of properties of neurons in the middle temporal area of the primate brain.

Introduction

Although the processing power of the brain is huge compared with contemporary artificial signal processing systems, the range of signals a single neuron can process is limited. The visual pathways of the brain show adaptations to the statistics of the natural environment for an efficient processing of the set of signals that the environment provides. Such adaptations are seen in gestalt laws [1, 2] and in efficient encoding schemes [3, 4], in which the processing pathway is more sensitive for signals that occur very frequently than to signals that are very unlikely to occur. However, in many natural situations the visual input is dynamic because animals move. We aim here to apply the concept of efficient encoding to the realm of motion processing to find properties of motion sensitive neurons, that efficiently encode the set of motion signals generated on the retina by natural behavior in natural environments. Most of the retinal motion in natural situations is generated by ego-motion of the observer. Therefore, we concentrate our investigation on retinal motion signals during ego-motion.

D. Calow
Department of Psychology, Westf.- Wilhelms University, Fliednerstr. 21, 48149 Münster, Germany
e-mail: calow@uni-muenster.de

R. Wang et al. (eds.), *Advances in Cognitive Neurodynamics*,

Statistical Properties of Natural Retinal Flow

Our analysis starts from an analysis of the statistics of motion signals generated by ego-motion. We use a method introduced in [5] to generate a large number of naturalistic retinal motion fields from range images of natural scenes and assumed ego-motions. This approach provides the distributions of true motion signals at each position of the visual field, which then a population of neurons is meant to encode. We use the Brown Range Image Database, a database of 197 range images of outdoor and indoor scenes recorded with a laser range-finder with high spatial resolution [6]. These range images provide the depth map of each scene. The knowledge of the 3D coordinates of each scene point allows the calculation of the projected retinal motion of that point for any given combination of translation and rotation of the observer. We consider as the retina a spherical projection surface with radius 1. The field of view is set to 90° horizontally and 58° vertically. The retinal flow fields are calculated on the inside of this section of the sphere on a 250×160 grid of motion sensors with a resolution of $0.36^\circ \times 0.36^\circ$. The flow vectors obtained for this grid provide our measurement of the true retinal flow field for a certain ego-motion and scene. To calculate the flow field from the scene structure we need the motion parameters of the projection surface. Possible ego-motions for a given scene are derived from properties of the scene and natural parameters of ego-motion. First, we determine areas in each scene which are free from obstacles. We then assumed ego-motion through those areas. Since natural ego-motion involves gaze-stabilizing eye movements [7] we measure eye movements of observers who view images of the scene to collect naturalistic gaze points. We also measure gait dynamics of walking human subjects, particularly their bounce and sway, to allow a naturalistic modeling of the ego-motion trajecory. From these factors (obstacle-free walking direction, gaze point, gait dynamics) we construct a set of naturalistic ego-motions for each range mage scene. From the scenes and the ego-motions we constructed 7136 different naturalistic flow fields and obtain for each position on the retina a distribution of true motion signals (see Fig. 123.1a, left panel). These flow fields serve to estimate the statistical properties of retinal flow.

Efficient Encoding of Natural Retinal Flow

To turn to our aim of finding an efficient encoding scheme we assume a population of neurons that cover a four-dimensional parameter space consisting of retinal position (azimuth and elevation) and velocity (retinal direction (ϕ_i) and speed (v_i)). This population of neurons efficiently encodes the natural distribution of motion signals when the response probability is the same for all neurons of the population. In this case, the information about the original distribution is uniformly distributed over the neuron population. This maximizes the mutual information between the distribution of motion; signals and the distribution of their representation in the neural population, and performs a nonlinear independent component analysis on the original distributions of motion signals. To construct such a population of

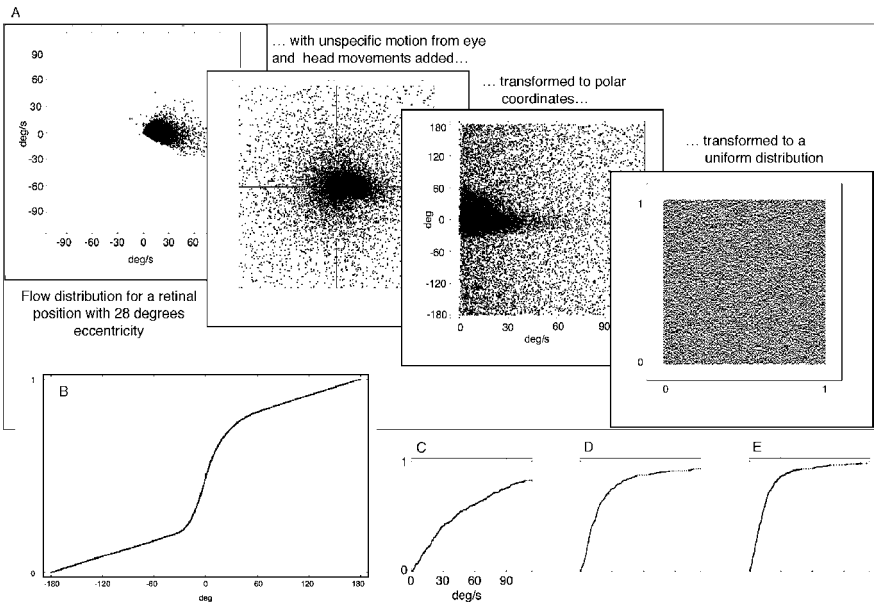

Fig. 123.1 Uniforming procedure, (b) approximation of the transformation function $f_2(\phi)$, C,D and E: approximation of the transformation functions $f_1(v, -180°)$, $f_1(v, -30°)$ and $f_1(v, 0°)$

neurons we search for the transformation functions that maps the distributions of retinal velocities onto a uniform distribution and then cover this uniform distribution uniformly with circular receptive fields (see Fig. 123.1). The actual sensitivity of each neurons for retinal motion signals can then be estimated by the back transformation of the uniform distribution to the original distribution of motion signals. A crucial issue in this procedure is the noise in the signal since the noise level determines the number of neurons necessary to cover the distribution of motion signals and to discriminate between neighboring signals. To each measured distribution therefore we add a set of unspecific motion signals, which is uniform in the distributions of directions and obey a logarithmic normal distribution for retinal speed (see Fig. 123.1a, second panel). To find a mapping from the distributions of retinal velocities to a uniform distribution we use a uniforming procedure referred to as rank ordering. The procedure starts with the rank ordering of the distribution of directions, which results in the approximated transformation function for retinal direction $f_2(\phi)$ (see Fig. 123.1b). The rank ordered data set is then divided into 72 stripes of equal width such that each stripe contains the same number of data points. Regarding each stripe as a one-dimensional data set, the stripes are rank ordered again to yield a set of approximated transformation functions $f_1(v, \phi)$ for retinal speed (see Fig. 123.1c–e). This procedure is an approximation of finding the transformation function $F(v, \phi) = (f_1(v, \phi), f_2(\phi))$ that fulfills $\frac{\partial f_2}{\partial \phi} \frac{\partial f_1}{\partial v} = P(v, \phi)$, where $P(v, \phi)$ is the probability density function of the random variables speed and direction.

Tuning Curves of Efficient Retinal Flow Encoders

The approximation of the transformation functions $F(v, \phi)$ by the uniforming procedure allows to plot the receptive fields in velocity space of neurons which are supposed to encode the distribution of motion signals at a certain position in the field of view. To find the tuning curve of a neuron we have to back-transform from the uniformed space to retinal motion space. Let (v, ϕ) be a retinal motion signal. The mean response $r_i(v, \phi)$ of the i-th neuron to a retinal motion signal is given by $r_i(v, \phi) = r_{max} \exp(-(m_i - F(v, \phi))^2/2\sigma_i^2)$, where $m_i \in [0, 1] \times [0, 1]$ is the center of the receptive field, σ is the width of the receptive field, and $F : \mathbb{R}^2 \longrightarrow [0, 1] \times [0, 1]$, $F(v, \phi) = (f_1(v, \phi), f_2(\phi))$ is the transformation function, which governs the tuning curve of the neuron and which is approximated by the results of the uniforming procedure. The results for a number of example neurons with different receptive field centers m_i are shown in Figs. 123.2 and 123.3. The resulting properties of efficiently encoding neurons show a wide range of selectivity for the parameters retinal speed and direction. We find neurons, whose selectivity is largely restricted to a small domain in the velocity space (Fig. 123.2c). There are also neurons whose selectivity show a crescent-shaped structure (Fig. 123.2b,d). Such structures resemble receptive field properties of motion processing neurons in the middle temporal (MT) area of the primate [8]. Other similarities to properties of MT neurons can be seen in the speed selectivity. Individual neurons can be characterized as low pass (Fig. 123.2a), tuned (Fig. 123.2c), broad band (Fig. 123.2b,d), or high pass (Fig. 123.2e) consistent with neurophysiological recordings [9]. With respect to direction tuning, neurons can be sharply tuned, broadly tuned, or not tuned also similar to neurons in area MT. However, the particular properties of the velocity receptive fields of efficiently encoding neurons depend strongly on the position

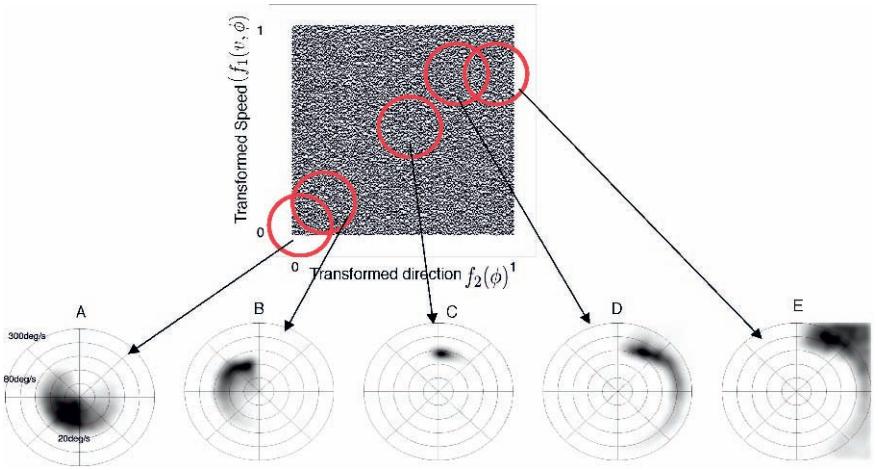

Fig. 123.2 Resulting responsiveness $r_i(v, \phi)$ of a selection of neurons for certain receptive field centers m_i and width $\sigma = 0.1$ at a retinal position of 28 degrees eccentricity

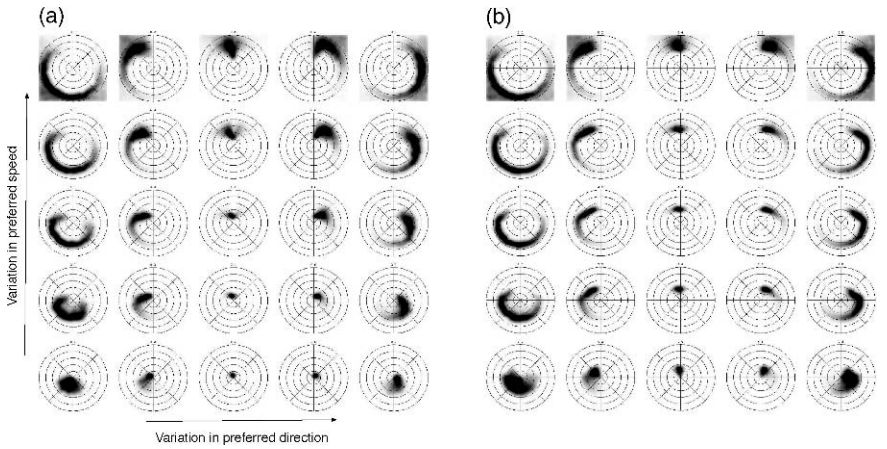

Fig. 123.3 Resulting responsiveness $r_i(v, \phi)$ of a selection of neurons for certain receptive field centers m_i and width $\sigma = 0.1$ for two different positions in visual field, (a) eccentricity 3 degrees, (b) eccentricity 15 degrees

of their receptive field in the visual field (Fig. 123.3). Since the properties of the distributions of retinal motion signals vary from position to position [5], also the population of neurons encoding motion at these positions show differences in their properties. At higher eccentricities, the selectivity for retinal speed shifts to higher speeds and the distribution of preferred directions becomes narrower. This is also similar to findings in area MT [10, 9].

We conclude that the application of the principle of efficient encoding to the processing of retinal motion signals is a valid tool to predict receptive field structures and tuning curves of neurons in the motion processing pathway of the brain. Several interesting issues remain for future work. First, the incfluence of internal noise may be investigated using a Poisson model to describe the response behavior of the neurons. Second, a Bayesian decoding scheme may be applied to develop computational models that detect retinal motion in the statistically likely range. Third, it may be tested experimentally whether humans show a similar characteristics in motion detection.

References

1. E. H. Elder and R. G. Goldberg. Ecological statistics of Gestalt laws for the perceptual organization of contours. *J. Vision*, 2:324–353, 2002.
2. N. Krüger and F. Wörgötter. Multi-modal estimation of collinearity and parallelism in natural image sequences. *Netw.: Comput. Neural Syst.*, 13:553–576, 2002.
3. H. B. Barlow. Possible principles underlying the transformation of sensory messages. In W. A. Rosenblith, editor, *Sensory Communication*, pages 217–234. MIT Press, Cambridge, MA, 1961.
4. S. B. Laughlin. Simple coding procedure enhances a neuron's information capacity. *Z. Naturforsch.*, 36C:910–912, 1981.

5. D. Calow, N. Krüger, F. Wörgötter, and M. Lappe. Statistics of optic flow for self-motion through natural sceneries. In U. Ilg, H. H. Bülthoff, and H. A. Mallot, editors, *Dynamic Perception 2004*, pages 133–138, Ios Press, Amsterdam 2004.
6. J. Huang, A. B. Lee, and D. Mumford. Statistics of range images. *Proc. CVPR*, 1:324–321, 2000.
7. M. Lappe, M. Pekel, and K. -P. Hoffmann. Optokinetic eye movements elicited by radial optic flow in the macaque monkey. *J. Neurophysiol.*, 79:1461–1480, 1998.
8. M. S. Livingstone, C. C. Pack, and R. T. Born. Two-dimensional substructure of MT receptive fields. *Neuron*, 30:781–793, 2001.
9. L. Lagae, S. Raiguel, and G. A. Orban. Speed and direction selectivity of macaque middle temporal neurons. *J. Neurophysiol.*, 69:19–39, 1993.
10. T. D. Albright. Centrifugal directionality bias in the middle temporal visual area (MT) of the macaque. *Vis. Neurosci.*, 2:177–188, 1989.

Chapter 124
Grid Task Scheduling Algorithm R3Q for Evolving Artificial Neural Networks

Yoshiyuki Matsumura, Masashi Oiso, Kazuhiro Ohkura, Noriyuki Fujimoto, Kenichi Hagihara, Jeremy Wyatt and Xin Yao

Abstract Task scheduling algorithms for evolving artificial neural networks (EANNs) in grid computing environments is discussed. In this paper, list scheduling with round-robin order replication (RR) is adopted to reduce waiting times due to synchronization. However, RR is suitable for coarse-grained tasks. For EANNs as medium-grained tasks, we propose a new technique to reduce the communication overhead, called the remote work queue (RWQ) method. We then define round-robin replication remote work queue (R3Q) as RWQ with RR. Our results show that R3Q can reduce both the synchronous waiting time and communication time compared to other methods.

Introduction

Evolving artificial neural networks (EANNs) [1] are the combination of evolutionary algorithms (EAs) and artificial neural networks (ANNs). EANNs are of great interest in some fields, such as evolutionary robotics (ER) [2], traffic flow prediction in telecommunications, breast cancer diagnosis, etc. In particular, ER researchers have proposed EANNs as a methodology for the control of autonomous mobile robots, where artificial evolution is used for designing ANNs. In [3], we investigated the use of evolution strategies (ES) [4] for the automatic design of robotic controllers. In this approach, we bred populations of controllers under artificial selective pressure over many generations. This approach led to a number of advances, including the invention of more efficient evolutionary methods and the use of more powerful ANNs. Despite these advances, it still took considerable amount of time for robot controllers to evolve. This is because, to evolve a controller, every candidate must be evaluated during each successive generation to ascertain its effectiveness. Typically, the candidate controllers are evaluated in simulations of the actual robots in which they are used. This is a very time consuming process. Therefore, to improve this situation, we propose a new approach where the tasks are distributed among many

Y. Matsumura
Shinshu University, 3-15-1 Tokida, Ueda, Nagano, 386-8567, Japan
e-mail: matsumu@shinshu-u.ac.jp

R. Wang et al. (eds.), *Advances in Cognitive Neurodynamics*,

computers in a desktop grid computing environment. In general, EAs methods implemented in a grid environment require synchronizing during each generation. In addition, EAs problems involve a significant communication overhead, because of the fact that they are based on "medium-grained" tasks. We overcome these problems by using a dynamic grid scheduling method without prediction.

In this paper, list scheduling with round-robin order replication (RR) [5] is adopted to reduce the waiting times caused by synchronization. However, RR is mainly suited to coarse-grained tasks. For EANNs as medium-grained tasks, we propose a new technique for reducing the communication overhead, called the remote work queue (RWQ) method. This has the ability to both reduce communication time and obtain efficient forced termination of tasks. We then define round-robin replication remote work queue (R3Q) as RWQ with RR. In recent research [6], the performance of Grid scheduling algorithm R3Q has been evaluated by using tasks that have uniform computational granularity. This paper investigates the effect of Grid scheduling algorithms on non-uniform computational granularity. In order to evaluate task scheduling algorithms, computer experiments on EANNs are conducted using a test procedure that requires a constant number of evaluations, but where varying both calculation time and computer resources in the grid nodes result in different execution times.

Grid Task Scheduling Algorithms

The available computational power on the grid changes all the time because the surplus power supplied by the underlying computers is dynamic and varies as the peak performance of these computers varies. Thus for distributed execution of EAs on a Grid, this paper adopts scheduling algorithms that are dynamic and use no prediction. Examples of dynamic and non-prediction scheduling algorithms are Work Queue (WQ) [7], RR [5] and R3Q [6].

WQ [7] is a classic algorithm and assigns a task to the processor in an idle state, receives the result when the processor of the task is completed, and then assigns the next new task. In a heterogeneous environment such as the Grid, WQ causes some problems that waiting time for synchronization at end of each generation on EAs.

RR [5] improves on WQ by performing task reproduction to reduce the waiting time for synchronization. In addition, RR provides performance guarantee. However, when a medium-grained task like fitness calculation of individuals on EAs is implemented in the Grid, the communication delay due to WQ and RR are significant.

R3Q [6] can reduce the communication time by using the slide transfer method. The master computer submits two tasks to each slave computer. Then, the second task is queued on the slave computer. In which case, the slave computer can carry out this task without having to enter an idle state. As a result, communication time is removed. Furthermore, the waiting time for synchronization is reduced by using RR method simultaneously. The effectiveness of R3Q is demonstrated using uniform medium-grained task.

Computer Experiments

This paper uses cooperative box-pushing problem as an application of EANNs with non-uniform computational granularity. Based on the Sussex approach [2], we construct the minimal simulator for ten Khepera robots in Fig. 124.1. The Khepera robots are able to move around and push objects into the goal. In this test simulation, the field size is 3000×2500 cm. There are three objects in the field. Two robots can bring the small-sized object. Three robots can bring the medium-sized object. Five robots can bring the large-sized object. The Khepera robot itself is 5.5 cm in diameter and the sensor range is approximately 5.2 cm. The Khepera robot is equipped with eight active infrared(IR) sensors, omni-vision and two motor-driven wheels; and it is controlled by recurrent neural networks (RNN) shown in Fig. 124.2. The RNN has 16 sensory inputs, four middle-node and two motor output. In total, the RNN has 132 connections. The connection weights are optimized by ES. Note that each robot has the same recurrent neural networks. The distribution of calculation time of each task in this problem is shown in Fig. 124.3, and an example result of cooperative box-pushing behavior is shown in Fig. 124.4.

We construct the Grid environment using Web service in two environments, LAN and WAN; LAN environment uses 10 slave computers in Hiroshima Uni., and WAN environment uses five computers in Hiroshima Uni. and five computers in Shinshu Uni.. To illustrate the effectiveness of the R3Q algorithm, one scheduler performs 20,000 more communications during a particular experiment, while R3Q reduces both the synchronous waiting time and communication delay time in comparison with WQ and RR. To obtain a more accurate measure, each experiment is performed 10 times and the average is taken. This is accomplished by carrying out 100 gener-

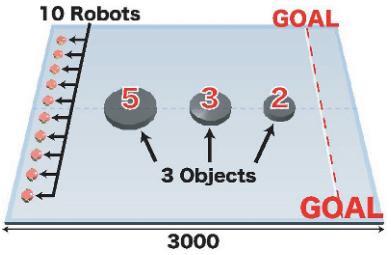

Fig. 124.1 Cooperative box-pushing problem

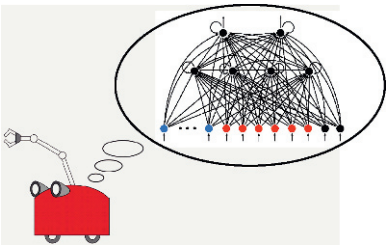

Fig. 124.2 Recurrent neural networks

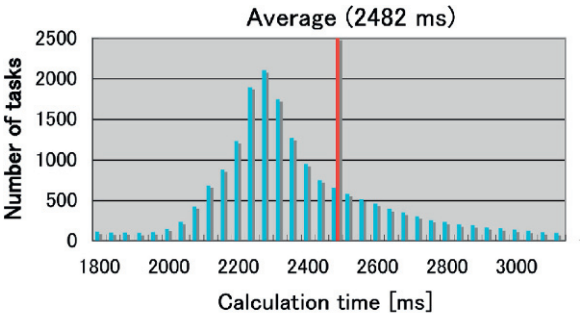

Fig. 124.3 Distribution of calculation time

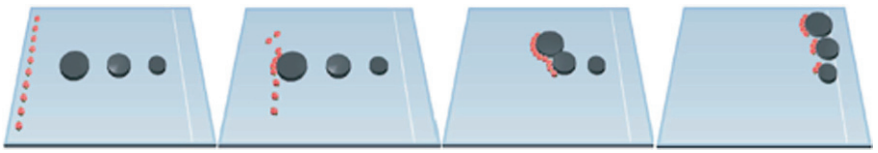

Fig. 124.4 Cooperative box-pushing behavior

ations with (30,200)-ES, measuring the total execution time, synchronous waiting time, and communication time before the 100th generation took place.

The total execution time of each scheduling algorithm in the LAN environment is shown in Fig. 124.5 and that of the WAN environment is shown in Fig. 124.6. The result shows that both RR and R3Q decrease the total execution time in comparison with WQ. It is clear that these algorithms are not influenced by the change of computational granularity because RR and R3Q are dynamic and non-prediction scheduling algorithms and change of execution time on the slave computers does not affect them. As a result, we conclude that RR and R3Q are effective for problems that have non-uniform computational granularity. In addition, R3Q almost eliminates the effect of communication delays in the WAN environment, but the effect of communication delays is significant under RR and WQ in Fig. 124.7.

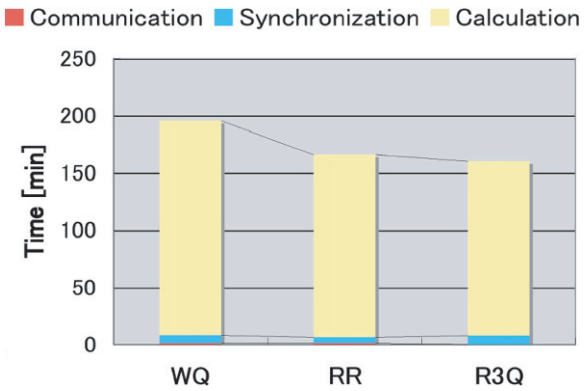

Fig. 124.5 Total time in LAN

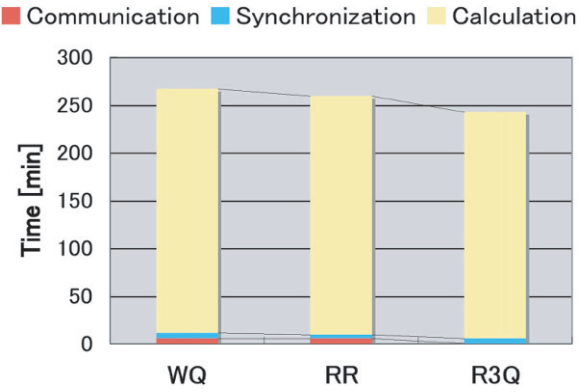

Fig. 124.6 Total time in WAN

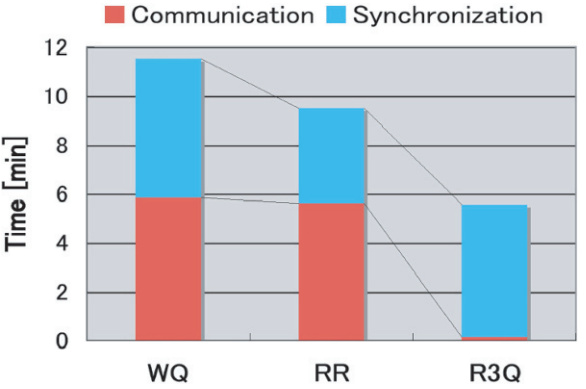

Fig. 124.7 Communication time and synchronous waiting time in WAN

Conclusions

We constructed the Grid environment using Web service and tested three scheduling algorithms using cooperative box-pushing problem that has non-uniform computational granularity as the application of EANNs. The experiment showed that R3Q are more effective than WQ and RR. We will expand the scale of a Grid environment by increasing the number of computers and the number of robots and objects in the application of EANNs. The authors acknowledge financial support in part through Grant-in-Aid for Scientific Research (18700058), (19500192) and also Grant-in-Aid for Global COE Program from the Ministry of Education, Culture, Sports, Science and Technology of Japan.

References

1. X. Yao(1999),"Evolving Artificial Neural Networks", Proceedings of the IEEE, 87, 1423–1447, IEEE press.
2. Harvey, P. Husbands and D. Clif (1993), "Issues in Evolutionary Robotics", From animals to animats 2: Proceedings of the Second International Conference on Simulation of Adaptive Behaviour (SAB92), 364–373, MIT Press, Cambridge.

3. Y. Matsumura, X. Yao, J. Wyatt, K. Ohkura and K. Ueda (2003), “Robust Evolution Strategies Use Adaptive Search Strategies to Design the Continuous-Time Recurrent Neural Networks”, Proceedings of 2nd International Conference on Computational Intelligence, Robotics and Autonomous Systems (CIRAS 2003).
4. T. Bäck and H.-P. Schwefel (1993), “An overview of evolutionary algorithms for parameter optimization”, Evolutionary Computation, 1, 1–24.
5. N. Fujimoto and K. Hagihara (2003), “Near-Optimal Dynamic Task Scheduling of Independent Coarse-Grained Tasks onto a Computational Grid”, Proceedings of the 32nd Annual International Conference on Parallel Processing (ICPP-03), 391–398, IEEE Press, Kaohsiung.
6. Y. Matsumura, K. Ohkura, Y. Matsuura, M. Oiso, N. Fujimoto and K. Hagihara (2007), “Grid Task Scheduling Algorithm R3Q for Evolution Strategies”, Proceedings of IEEE Congress on Evolutionary Computation (CEC 2007), Singapore.
7. R. L. Graham (1966), “Bounds for certain multiprocessing anomalies”, Bell System Technical Journal, 45, 1563–1581.

Chapter 125
Pattern Discrimination of Mechanomyogram Using a Delta-Sigma Modulated Probabilistic Neural Network

Keisuke Shima and Toshio Tsuji

Abstract This paper proposes a discrimination method for mechanomyogram using probabilistic neural network based on delta-sigma modulation. The proposed method includes a statistical model so that the posterior probability for the given input patterns can be estimated. Also, the 1-bit pulse signals with delta-sigma modulators used in this paper improves the calculation speed of the probabilistic neural network implemented in the hardware. Finally, discrimination experiments were conducted using the mechanomyogram measured from an amputee.

Keywords Mechanomyogram · neural network · delta-sigma modulation

Introduction

Bioelectric signals such as electromyograms and electroencephalograms reflect the internal conditions of the human body including the intention regarding body motions. If the motion intention can be estimated from biological signals, it could be used as a control signal for artificial limbs and human-machine interfaces.

The present paper explores the utilization of the mechanomyogram (MMG) [1] for the human-machine interfaces [2, 3]. Unlike electromyograms and electroencephalograms, it is not affected by the change of skin impedance caused by sweating. For the human-machine interfaces, the discrimination of multiple motions is necessary, as well as the estimation of muscular force from the measured MMG signals.

The probabilistic neural networks (PNNs) [4] have been applied to the pattern discrimination problems for bioelectric signals such as electromyograms. Our research group proposed a PNN for the pattern discrimination of bioelectric signals, which is called a log-linearized Gaussian mixture network (LLGMN) [5]. Then, the LLGMN has been used to develop various human-machine interfaces such as myoelectric prosthetic hands [6]. In such systems, the software implementation of

K. Shima
Graduate School of Engineering, Hiroshima University, Japan
e-mail: keisuke@bsys.hiroshima-u.ac.jp

R. Wang et al. (eds.), *Advances in Cognitive Neurodynamics*,

the LLGMN on a general-purpose computer was adopted; however, it has not been applied to human-machine interfaces because of the difficulty to reduce the size of the interface device to be portable.

In this paper, for the aim of estimation of forearm motions from MMGs in a digital hardware, we propose a feature extraction and discrimination method using PNN based on delta-sigma modulation. As delta-sigma modulation and statistical model are included in PNN, the proposed method can realize high accuracy discrimination for the MMGs.

MMG Discrimination Using the Delta-Sigma Modulated PNN

The MMG signals can be measured using acceleration sensors which are attached to the forearm. Then, full-wave rectification and smoothing process by a second low-pass filter, whose cut-off frequency is f_d [Hz], are carried out for the measured MMG. The normalized signals, the sum of which for all channels makes 1, are converted into the input vector $\boldsymbol{x}(t) = [x_1(t), x_2(t), \ldots, x_L(t)]^{\mathrm{T}}$ for time t and are used for pattern discrimination. Also, the user's force information for $\boldsymbol{x}(t)$ is defined as follows:

$$RMS_i(t) = \sqrt{\frac{1}{n}\sum_{\tau=0}^{n-1} MMG_i(t-\tau)^2}, \tag{125.1}$$

$$F_{MMG}(t) = \frac{1}{L}\sum_{i=1}^{L} \frac{RMS_i(t) - RMS_i^{st}}{RMS_i^{max} - RMS_i^{st}}, \tag{125.2}$$

where $MMG_i(t)$ is the preprocessed MMG signal from the ith acceleration sensor; and RMS_i^{max} and RMS_i^{st} are the average of $RMS_i(t)$ at the maximum voluntary contraction of the muscle and at rest, respectively. When $F_{MMG}(t)$ exceeds threshold M_d of the motion occurrence, the movement is estimated from the input vector $\boldsymbol{x}(t)$ using the PNN.

The LLGMN using delta-sigma modulation [7] is used as the discrimination method for MMG, which is based on the Gausian mixture model and the log-linear model of the probability density function (pdf). First, the input vector $x \in \Re^d$ is converted into the modified vector $\boldsymbol{X} \in \Re^H$ as follows:

$$\boldsymbol{X} = \left[1, \boldsymbol{x}^{\mathrm{T}}, {x_1}^2, x_1x_2, \cdots, x_1x_L, x_2^2, x_2x_3, \cdots, x_2x_L, \cdots, {x_L}^2\right]^{\mathrm{T}}, \tag{125.3}$$

where $x_i, i = 1, 2, \ldots, d$, are the elements of x and $H = 1 + L(L+3)/2$. The first layer consists of H units corresponding to the dimension of $\boldsymbol{X}$ and the identity function is used for activation of each unit. In the second layer, each unit receives the output of the first layer weighted by the weight $w_h^{(k,m)}(h = 1, 2, \ldots, H; k = 1, \ldots, K; m = 1, \ldots, M_k)$ and outputs the posterior probability of each Gaussian component. Here, K denotes the number of classes, and M_k is the number of Gaussian

components in class k. The relationships between the input of unit $\{k, m\}$ in the second layer ${}^{(2)}I_{k,m}$ and the output ${}^{(2)}O_{k,m}$ are defined as

$$ {}^{(2)}I_{k,m} = \sum_{h=1}^{H} {}^{(1)}O_h w_h^{(k,m)}, \qquad {}^{(2)}O_{k,m} = \frac{\exp\left[{}^{(2)}I_{k,m}\right]}{\sum_{k'=1}^{K}\sum_{m'=1}^{M_{k'}} \exp\left[{}^{(2)}I_{k',m'}\right]}, \tag{125.4} $$

where $w_h^{(K,M_k)} = 0$. The third layer consists of K units, and the function between the input and the output is described as

$$ {}^{(3)}O_k = {}^{(3)}I_k = \sum_{m=1}^{M_k} {}^{(2)}O_{k,m} \, . \tag{125.5} $$

Delta-sigma modulation is a technique in which the input signal such as multi-bit signals and analog signals is converted into a 1-bit pulse signal, and it has been attracting interests in various fields such as acoustics and communications [8]. The structure of a bipolar-type delta-sigma modulator (DSM) is shown in Fig. 125.1, where the output takes the values "−1" and "+1. " In this figure, the bold line represents multi-bit signals and the thin line 1-bit signals. The output y of the circuit can be expressed in the form of

$$ v = \frac{z^{-1}}{1 - z^{-1}} \{x - \tau y\}, \qquad y = \begin{cases} 1 & (v \geq 0) \\ -1 & (v < 0) \end{cases} \tag{125.6} $$

where x is the input, v is the integrated value of the quantization error, and $\tau > 0$ is the feedback gain. Here, "−1" and "+1" are represented by the low level and the high level in the hardware, respectively.

The structure of the LLGMN based on delta-sigma modulation is shown in Fig. 125.2. The network consists of 1-bit adders, 1-bit multipliers, weight multipliers using DSM, and so on. Here, the input data are normalized to its minimum value of −1 and maximum value of +1 as a prerequisite for pattern discrimination, due to the restriction of the calculable ranges of the 1-bit pulsed NNs. First, the input vector $x(t)$ is interpolated using the linear interpolation method at a sampling frequency f_h [Hz], and nonlinearly transformed using the $(H - L - 1)$ 1-bit multipliers. Next, for

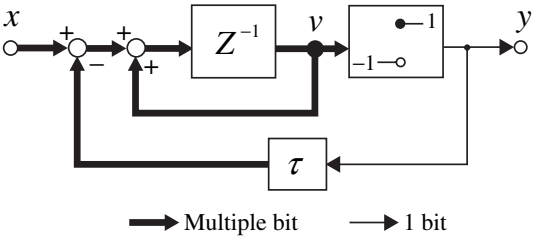

Fig. 125.1 Delta-Sigma modulator [8]

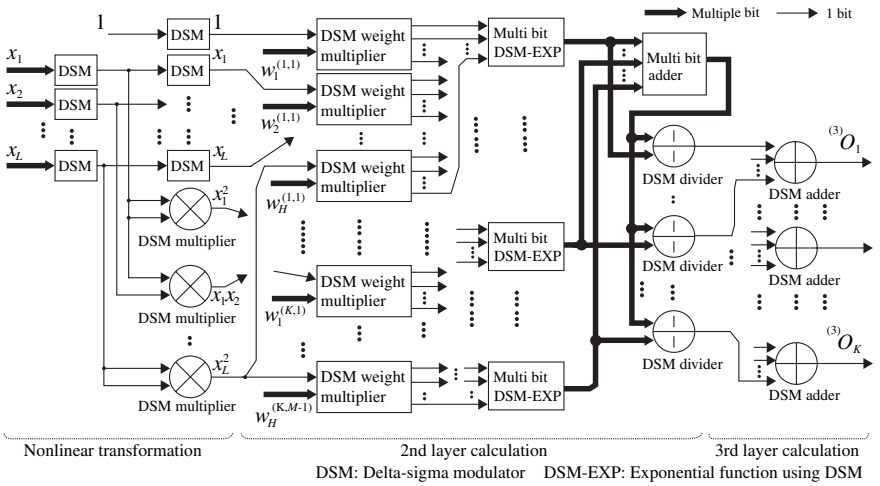

Fig. 125.2 Structure of an LLGMN using delta-sigma modulation

the calculation of the weight coefficients, the input function of the second layer is converted as follows:

$$ {}^{(2)}I_{k,m} = \sum_{h=1}^{H} \sum_{n=1}^{N} {}^{(1)}O_h \frac{w_h^{(k,m)}}{N}, \tag{125.7} $$

where N is an arbitrary positive integer. Further, the exponential function included in (125.4) is approximated as follows by using the Taylor series:

$$ \begin{aligned} \exp[{}^{(2)}I_{k,m}] &= \prod_{h=1}^{H} \prod_{n=1}^{N} \exp\left[{}^{(1)}O_h \frac{w_h^{(k,m)}}{N} \right] \\ &\cong \prod_{h=1}^{H} \prod_{n=1}^{N} \left[\sum_{c=0}^{C} \frac{1}{c!} \left({}^{(1)}O_h \frac{w_h^{(k,m)}}{N} \right)^c \right], \end{aligned} \tag{125.8} $$

where C is the order of the Taylor series ignoring the high-order terms greater than $C+1$. Because the range of the values for the input functions of the second layer (see (125.7)) are restricted between -1 and $+1$ using the appropriate value of N, each term of the right-hand side of (125.8) can be calculated in a range of values between -1 and $+1$. The output function (125.4) in the second layer is then realized by using multipliers and dividers, after it is demodulated to multi-bit signals using low-path filters. Finally, the outputs of the network are calculated by (125.5) by using the 1-bit adder from the outputs in the second layer. Thus, the posterior probabilities of input patterns can be calculated using DSMs.

Experiments

In order to verify the validity of the proposed method, we implemented the delta-sigma modulated PNN on a field programmable gate array (FPGA), and MMG discrimination experiments were conducted. MMG patterns were measured from four healthy subjects (A−D: male) and a right forearm amputee (E: male). First, we measured the acceleration signals at four locations of a forearm using acceleration sensors ($L = 4$, NIHON KOHDEN Corporation) with each subject. The measured signals were recorded at a sampling frequency of 1 [kHz], and filtered by the second band-path filter (bandwidths: 30 – 150 [Hz]) to extract the MMG. The subject was asked to perform the following four motions ($K = 4$) continuously: M1: hand opening, M2: hand grasping, M3: wrist extension, and M4: wrist flexion (see Fig. 125.3). Parameters of proposed method were set as $f_{cut} = 0.5$ [Hz], $f_h = 25$ [MHz], $M_k = 2$, $N = 30$, and $C = 4$.

An example of the measured MMG of subject E is shown in Fig. 125.4. In this figure, four channels of the input MMG are shown. The discrimination rates of the MMG measured from five subjects are shown in Fig. 125.5, which are represented by the software implementation of the LLGMN using C language and the hardware implementation of the LLGMN using DSMs. From this figure, we confirmed that the proposed method has a high accuracy of pattern discrimination in digital hardware. The discrimination rates of all the trials were 94.3 ± 1.65 [%] and 92.48 ± 2.38 [%],

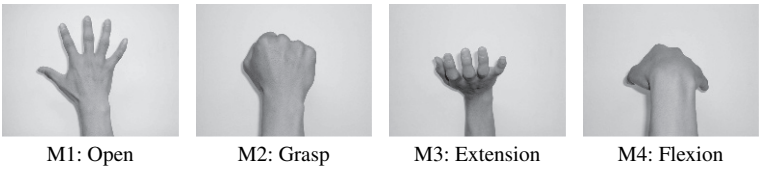

Fig. 125.3 Forearm motions used in the experiments

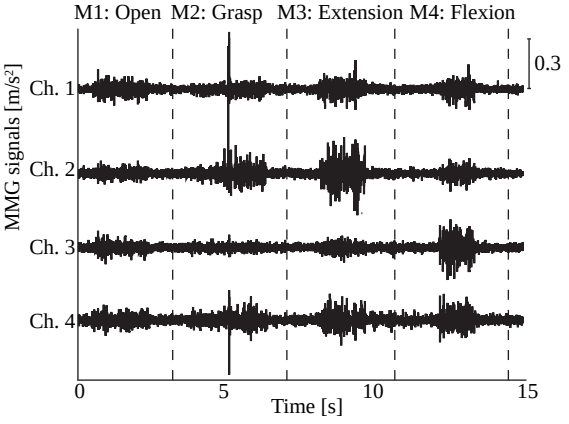

Fig. 125.4 Measured MMG signals of each motion (a forearm amputee)

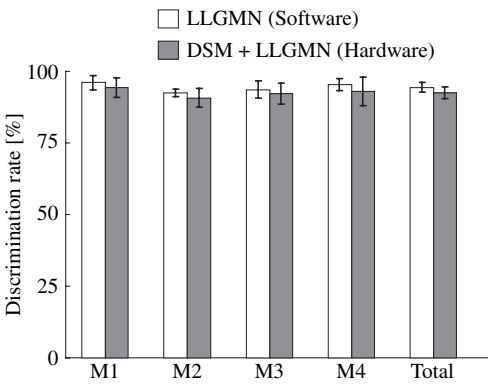

Fig. 125.5 Discrimination results of forearm motions with all subjects

respectively. It should be noted that the feature extraction of the MMG was implemented in the software, and only discrimination of the MMG patterns is performed by an FPGA.

Conclusions and Future Work

In this paper, we proposed the MMG discrimination method using a delta-sigma modulated PNN in digital hardware. Since the discrimination rates of the proposed PNN was 92.48 ± 2.38 [%], it can be concluded that the proposed method has a high performance in the case of the MMG discrimination. In the future, we plan to study the human-machine interface in digital hardware using the proposed method.

References

1. C. Orizio, R. Perini, B. Diemont and A. Veicsteinas: "Muscle sound and electromyogram spectrum analysis during exhausting contractions in man," European Journal of Applied Physiology and Occupational Physiology, 65, 1–7, 1992.
2. T. D. Barry, J. J. Leonard, A. J. Gitter and R. D. Ball: "Acoustic myography as a control signal for an externally powered prosthesis," Archives of Physical Medicine and Rehabilitation, 67, 267–269, 1986.
3. J. Silva, W. Heim and T. Chau: "A Self-Contained, Mechanomyogra-phy-Driven Externally Powered Proshesis," Archives of Physical Medicine and Rehabilitation, 86, 2066–2070, 2005.
4. D. F. Specht: D. F. Specht: "Probabilistic Neural Networks," Neural Networks, 3, 109–118, 1990.
5. T. Tsuji, O. Fukuda, H. Ichinobe and M. Kaneko: "A Log-Linearized Gaussian Mixture Network and its application to EEG pattern classification," IEEE Transactions on Systems, Man, and Cybernetics, Part C, 29, 60–72, 1999.
6. O. Fukuda, T. Tsuji, M. Kaneko and A. Otsuka: "A human-assisting manipulator teleoperated by EMG signals and arm motions," IEEE Transactions on Robotics and Automation, 19, 210–222, 2003.

7. K. Shima and T. Tsuji: “FPGA implementation of a probabilistic neural network using delta-sigma modulation for pattern discrimination of EMG signals,” IEEE/ICME International Conference on Complex Medical Engineering, 403–408, 2007.
8. Y. Murahashi, H. Hotta, S. Doki and S. Okuma: “Pulsed neural networks based on delta-sigma modulation with GHA learning rule and their hardware implementation,” Systems and Computers in Japan, 36, 14–24, 2005.

Chapter 126
HMM-Based Top-Down Attention for Noise-Robust Speech Recognition

Chang-Hoon Lee and Soo-Young Lee

Abstract The top-down attention is extended into hidden Markov model (HMM) classifier with Mel-Frequency Cepstral Coefficient (MFCC) features for noise-robust speech recognition. The attention filter was introduced at the outputs of Mel-scale filterbank and adjusted to maximize the log-likelihood of the attended features with the attended class. Low-complexity constraint was proposed to prevent overfitting, and a confidence measure was introduced on the attention. The proposed algorithm demonstrated in much better recognition rates in noisy environments.

Keywords Attention · top-down · HMM · noise-robustness · speech recognition

Introduction

Although noise-robust feature extractions based on auditory models demonstrated improvements in recognition performance [1], current speech recognition systems still require big performance improvements in noise-robustness. Human beings utilize top-down selective attention from pre-acquired knowledge for confusing patterns. Inspired by Broadbent's 'early filtering' theory [2] and Treisman's modification with attenuation filter [3], we came up with a top-down attention model for the recognition of noisy and/or confusing patterns [4]. Although it shares the same top-down pass with Fukushima's Neocognitron model [5], simple multi-layer Perceptron (MLP) classifier was used.

In this Letter, we extend the top-down selective attention model to HMM classifiers. To avoid over-fitting, the low-complexity restriction is imposed on the attention filter, and a new confidence measure is introduced for the classification.

C.-H. Lee
Brain Science Research Center, Department of BioSystems, Department of Electrical Engineering and Computer Science, Korea Advanced Institute of Science and Technology, Daejeon 305-701, Korea
e-mail: chlee@neuron.kaist.ac.kr and sylee@kaist.ac.kr

R. Wang et al. (eds.), *Advances in Cognitive Neurodynamics*,

Computational Model of Top-Down Attention

Figure 126.1 shows the signal flows with (solid line) and without (dashed line) the top-down attention with the popular MFCC (Mel-Frequency Cepstral Coefficient) features and HMM classifiers. Without the top-down attention the Mel-filterbank outputs go through logarithmic nonlinearity and discrete cosine transform (DCT) to form the MFCC. With the top-down attention a multiplicative attention filter may be placed at the Mel-filterbank output, which is equivalent to an additive adjustment at the log spectrum domain. Then, the log spectrum is transformed into cepstral coefficient by DCT. The cepstral coefficients up to 12th order and energy, and their delta and acceleration coefficients were applied to HMM for speech recognition. The attention filter is updated to estimate best input features for the attended output class.

The proposed speech recognition algorithm using top-down selective attention is summarized as follows:

Step 1: Train HMMs with training set.
Step 2: For a testing pattern, calculate likelihood for all classes and choose N_c best candidates.
Step 3: For each candidate class,

1. Set attention filter to 0.
2. Update attention filter for the expected input.
3. Calculate new likelihood of changed input.
4. Repeat 2 and 3 until likelihood converges
5. Calculate a confidence measure of the class.

Step 4: Choose the class with the maximum confidence measure.

Since the characteristics of a class are modeled as an HMM, the top-down selective attention algorithm at Step 3 estimates the expected input from the test speech for the pre-trained attended class model as

$$\tilde{\mathbf{x}}_i = \arg\max_{\mathbf{x}} P(\mathbf{x}|\lambda_i) \tag{126.1}$$

within reasonable proximity from the original input x. The gradient ascent algorithm for the log-likelihood results in

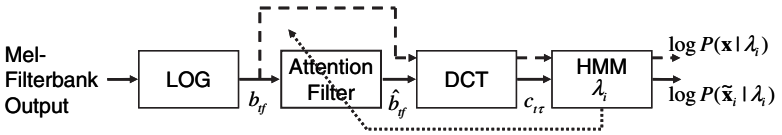

Fig. 126.1 Speech recognition model with top-down selective attention filter

$$a_{tf}[n+1] = a_{tf}[n] + \eta \frac{\partial L}{\partial a_{tf}[n]}, \quad \frac{\partial L}{\partial a_{tf}} = \sum_{\tau} \sum_{t'} \frac{\partial L}{\partial x_{t'\tau}} \frac{\partial x_{t'\tau}}{\partial c_{t\tau}} \frac{\partial c_{t\tau}}{\partial \hat{b}_{tf}} \frac{\partial \hat{b}_{tf}}{\partial a_{tf}} \quad (126.2)$$

where a_{tf} is the attention filter at time t for the f-th Mel-filter and $c_{t\tau}$ is the τ-th cepstral coefficient at time t. The summation over τ is needed for DCT, and the summation over t' is needed for the delta and acceleration coefficients. The derivative of the log-likelihood on speech features was derived in [6] for continuous density HMM.

As the selective attention process goes on, the attended input pattern may move toward the most likely pattern of the attended class, which is independent upon the actual input pattern. To prevent this over-fitting, the attention filter need be regularized by imposing low-complexity constraint.

We propose to represent the attention filter as a bilinear kernel or a linear mixture of Gaussians, i. e.,

$$a_{tf} = \sum_{t'f'} g_{t'f'} \Phi\left(t' - \frac{t}{N_t}, f' - \frac{f}{N_f}\right) \quad \text{or} \quad a_{tf} = \sum_{k=1}^{k} w_k G_k(t, f) \quad (126.3)$$

where each Gaussian may represent one 'spot-light'. The confidence measure is defined as

$$M_i = (1-\gamma) \log P(\mathbf{x}|\lambda_i) + \gamma \log P(\tilde{\mathbf{x}}_i|\lambda_i) \quad (126.4)$$

where the tilde denotes the top-down attended input pattern and γ controls the relative importance.

Experimental Results

Speaker independent isolated word recognition experiments are performed using isolated digit section of AURORA database [7]. The database, which has 11 word vocabulary (the digits 1–9, 'oh', and 'zero'), contains 2412 utterances for training and 1144 utterances for testing.

After pre-emphasis, the input speech signal was framed by 25 ms Hamming window with 10 ms shifting and 23 Mel-scale filterbanks were formed at each time frame. Left-right continuous density HMMs are used. Each HMM has nine states with four Gaussian mixtures with diagonal covariance, and is trained by Baum-Welch algorithm with clean training data. In our experiments we found $\gamma = 0.7$ gives best performance, and $N_c > 7$ does not improve the performance.

In Fig. 126.2 the misclassification rates of top-down attention are compared to those of the baseline HMM classifier. When the proposed low-complexity constraint is added, the recognition performance under noisy condition is greatly improved. Also the performance is not sensitive to the grid size nor the number of Gaussian mixtures. The false recognition rates decrease dramatically up to 10 dB SNR, while

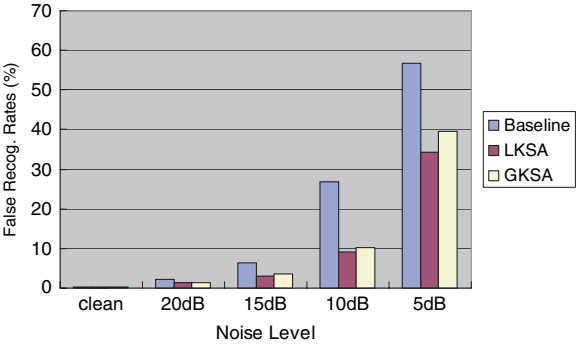

Fig. 126.2 False recognition rates with several noise levels for white Gaussian noise

the reduction becomes smaller for noisier speeches. It is similar to the findings in cognitive science, i.e., the effects of the top-down attention are significant only with familiar input patterns.

Conclusion

A top-down selective attention model with HMM classifier is proposed. The top-down attention iteratively finds the most-likely input pattern from noisy or corrupted input within the proximity of the input pattern. By introducing regularization on the attention filter and also a confidence measure, the top-down attention can greatly improve recognition rates in moderate noisy environments.

Acknowledgements This research was supported as a Brain NeuroInformatics Research Program by Korean Ministry of Commerce, Industry and Energy.

References

1. D.-S. Kim, S.-Y. Lee and R.M. Kil, Auditory processing of speech signals for robust speech recognition in real-world noisy environments. IEEE Transactions on Speech and Audio Processing, vol. 7, no. 1, pp. 55–69, 1999.
2. E. Broadbent, Perception and Communication, Pergamon, London, 1958.
3. A. Treisman, Contextual cues in selective listening. Quarterly Journal of Experimental Psychology, vol. 12, pp. 242–248, 1960.
4. K.-Y. Park and S.-Y. Lee, Out-of-vocabulary rejection based on selective attention model. Neural Processing Letters, vol. 12, pp. 41–48, 2000.
5. K. Fukushima, Neural network model for selective attention in visual pattern recognition and associative recall. Applied Optics, vol. 26, pp. 4985–4992, 1987.
6. S. Moon and J.N. Hwang, Robust speech recognition based on joint model and feature space optimization of hidden markov model. IEEE Transactions on Neural Networks, vol. 8, no. 2, pp. 194–204, 1997.
7. D. Pearce and H.G. Hirsch, The aurora experimental framework for the performance evaluation of speech recognition systems under noisy conditions. In Proceedings of the ICSLP, Beijing, China 2000, pp. 29–32.

Chapter 127
Roving Robot Autonomously Controled by Chaotic Memory Dynamics in Quasi-Layered Recurrent Neural Networks for Sensing and Driving

Tai Tanaka, Yasumasa Miyamoto, Yongtao Li, Daigo Munetaka, So Shimizu, Shuhei Kurata, Shogo Morita and Shigetoshi Nara

Abstract Chaotic dynamics is applied to 2-dimensional motion control. We propose a quasi-layered recurrent neural network consisting of sensing neurons and driving neuros, where in sensing neurons, sensitive response to external input is utilized, whereas in driving neurons, complex dynamics is utilized to generate complex motions. A hardware implementation into a roving robot is shown.

Introduction

The great progress of modern Very Large Scale Integrated Circuit (VLSI) technologies has produced revolutionary devices and/or machines. However, algorithms on conventional computers run into problems with combinatorial explosion and program complexity in realizing flexible functions when there are too many degrees of freedom to control. On the other hand, the rapid progress in studying biological information and control processing, particularly brain functions suggests that they might be based on novel *dynamical mechanisms* that result in excellent functioning and/or controlling. The key idea is to somehow harness the onset of complex nonlinear dynamics in information processing or control systems. This idea arised from the observations of chaos in biological systems, and it is our primary motivation for studying chaotic dynamics in neural networks from the functional point of view.

As an example of studying such functionality, Nara and Davis proposed that chaotic dynamics can occur in a recurrent binary neuron network by changing a system parameter (connectivity between neurons), and they have studied that it can be applied to solving ill-posed problems, for example memory search or synthesis as reported in the previous works [1]. Furthermore, the idea was extended to application of chaotic dynamics to a novel function, the control task that an object should

T. Tanaka
Division of Electronic and Information System engineering, Graduate School of Natural Science and Technology, Okayama University, Japan
e-mail: tanakat@cc.tuat.ac.jp

R. Wang et al. (eds.), *Advances in Cognitive Neurodynamics*,

catch a set target in 2-D maze, or capture a moving target, which were successfully executed in their computer experiments and reported in [2] and [3]. Their consideration not only indicates that the role of chaos is critically important to realize a complex control via simple rule but also enables us to generalize the usefulness of chaos.

In this paper, we attempt to develop their ideas with adding a new neuron module, "sensing neuron module". So, we propose a quasi-layered recurrent neural network consisting of sensing neurons (upper layer) and driving neurons(lower layer). In both layers, chaotic dynamics are used where, in sensing neurons, sensitive response to external input is utilized, while in driving neurons, complex dynamics is utilized to generate complex motions. These two properties are applied to solving two-dimensional mazes by computer experments and an example of hardware implementation into a roving robot is shown.

Attractor & Chaotic Dynamics in Quasi-layered RNNM, and Coding Them into 2-Dimensional Motion

Our study works with an asymmetrical recurrent neural network model(RNNM) consisting of $N/2$ sensing neurons of a upper layer and $N/2$ driving neurons of a lower layer for driving the robot's motors. At time t, the state of the network is represented by a N dimensional state vector $\boldsymbol{S}(t) = [\boldsymbol{x}(t), \boldsymbol{y}(t)]$, where $\boldsymbol{x}(t) = \{x_i(t) = \pm 1 | i = 1, 2, \cdots, N/2\}$ and $\boldsymbol{y}(t) = \{y_i(t) = \pm 1 | i = 1, 2, \cdots, N/2\}$, called as state pattern. The updating rules of the upper layer(sensing) and the lower layer(driving) are defined by

$$\text{Upper: } x_i(t+1) = \operatorname{sgn}\left(\sum_{j \in G_u(r_u)} W_{ij}^{u-u} x_j(t) \right),$$

$$\text{Lower: } y_i(t+1) = \operatorname{sgn}\left(\sum_{j \in G_l(r_l)} \left[W_{ij}^{l-l} y_j(t) + W_{ij}^{u-l} x_j(t) \right] \right)$$

- u: upper layer $\quad l$: lower layer
- W_{ij}^{u-u}: connection weight from neuron x_j of upper layer to neuron x_i of upper layer; W_{ij}^{u-l} and W_{ij}^{l-l} are defined similarly.
- N: the number of neurons
- r: fan-in number for neuron $x_i(y_i)$, named connectivity
- $G_{u,l}(r_{u,l})$: spatial configuration set of connectivity r

The updating rule shows that time development of the network depends on connection weight W_{ij} and connectivity r. By appropriately determined connection weight W_{ij}, a group of arbitrarily designed state patterns can be embedded as cyclic memory attractors. In this paper, the firing states of $N = 40 \times 20 = 800$ neurons are

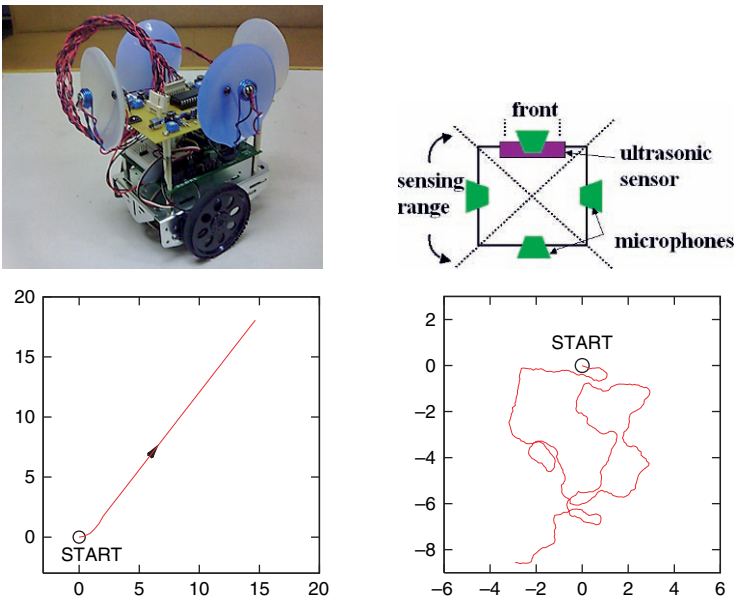

Fig. 127.1 Chaotic motion generated by chaos in driving neurons

employed and we take 24 state pattens consisting of 4 (cycles) $\times$ 6 (patterns per cycle), as embedded memory attractors. As the network evolves with the updating rules, randomly initial state pattern will converge into one of embedded cyclic attractors. When the connectivity r is reduced by blocking signal propagation from other neurons, attractors gradually becomes unstable, finally chaotic dynamics occurs in updating dynamics of the network. Time-dependent firing patterns consisting of 400-neurons (lower layer: driving neurons) can be transfromed into motions in 2-D space by a certain coding format proposed by us [2, 3]. Figure 127.1 show examples.

Control Algorithm and Computer Experiments to Find Detours

By adaptive switching of connectivity r between prototypical motion and chaotic motion, a simple control algorithm is proposed to solve mazes, shown in Fig. 127.2. Depending on the sound signal intensity from target picked by sensing neurons, the firing states of the upper layer changes in real time. Correspondingly, the lower layer sensitively responds to the upper layer and the robot adaptively turn toward the strongest intensity direction quickly due to sensitivity of chaotic dynamics. When there are no obstacles in the range of sensing neurons, the robot moves with sufficiently large connectivity. When there is an obstacle, it moves chaotically with small connectivity and trys to find detour to avoid obstacles.

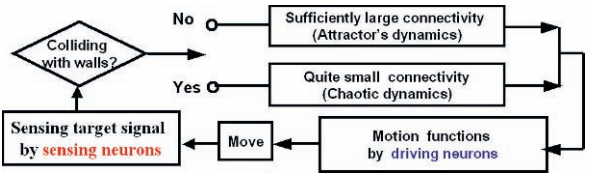

Fig. 127.2 Algorithm of controlling a roving robot

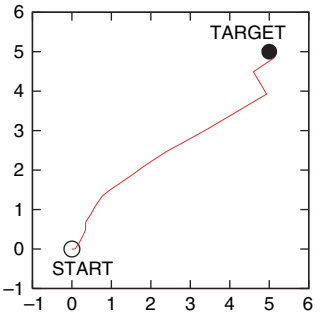

Fig. 127.3 Without obstacle

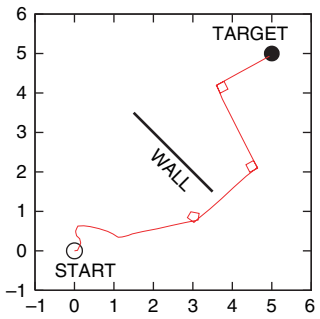

Fig. 127.4 With obstacles

The computer-experimental examples of the robot approaching a target in two dimensional space are shown in Fig. 127.3 (without obstacle) and Fig. 127.4 (with obstacles). We have made elementary hardware implementation of the robot with sensing system and driving system. We are developing the experiment to the case that the robot approaches a target in an unknown environment with obstacles. Detailed report will be done in our forthcoming paper.

Hardware Implementation into a Roving Robot

We employed a roving robot with two driving wheels called Bobot supplied by Parallax Co. in U.S.A. Four directional microphones to receive sound from a set target and two whisker to detect obstcles are equipped. Also, bluetooth system is attached to enable the robot to communicate with a computer in which a neuro-chaos simulator is installed, because a micro-computer of the robot is too poor to install the neuro-chaos simulator.

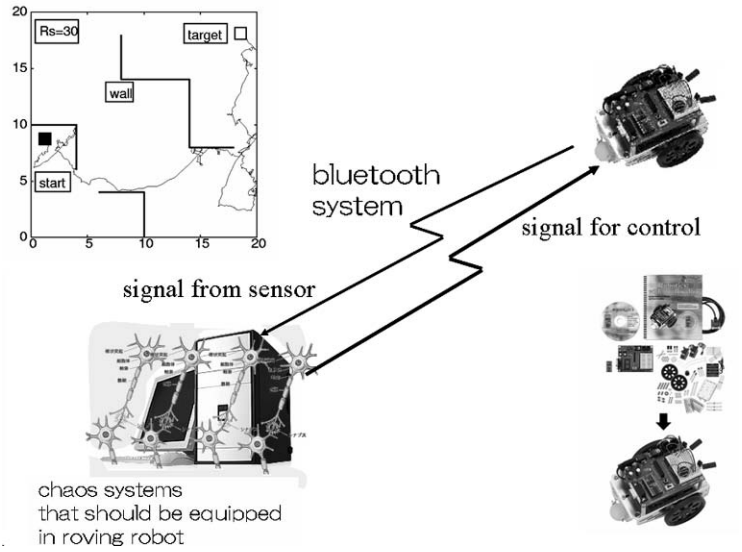

Fig. 127.5 Blocd diagram of our harware implementation

The sound from the set target (3.6 kHz) is received by the four microphones and amplified with elecronic circuits. It should be noted that the hardware implementation is not yet completed but on intermediate stage to finally fabricated form, so a comparator of sound intensity from the four microphones is equipped instead of sensor neurons and a whisker to detect obstacles instead of ultrasonic sensor is attached.

Overall experimental configuration is shown in Figs. 127.5 and 127.6.

We successfully have done many trials to solve maze using this system. The detailed reports and discussions will be given in near future.

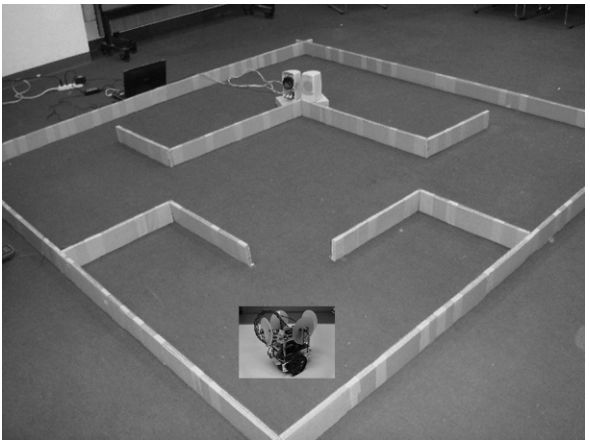

Fig. 127.6 Experimental configuration

References

1. S.Nara: Chaos, 13, 1110–1121 (2003).
2. Y.Suemitsu, S.Nara: Neural Computation, 16, 1943–1957 (2004).
3. Y.Li, S.Nara: accepted for publication in Cognitive Neurodynamics.

Chapter 128
A New Approach to Detect Stable Phase Structure in High-Density EEG Signals

Yusely Ruiz, Guang Li, Eduardo González and Walter Freeman

Abstract The application of Hilbert transform to intracranial EEG recordings have revealed the markers for repetitive phase transitions in neocortex at frame rates in the theta and alpha bands. After those phase transition amplitude a phase modulation patterns could be formed. In this paper a new methodology to detect phase transition and phase modulation patterns is presented. The results are compared with phase patterns obtained from cone fitting in awake, task, sleep and seizure states. High levels of frame coincidence in time are obtained and the different characteristics between states are maintained.

Keywords PM spatial pattern · stable phase structure · frames

Introduction

Amplitude modulation (AM) and phase modulation (PM) spatial patterns can be found in EEGs recorded with high density array electrodes [1, 2, 3, 4]. These patterns often have beta or gamma carrier waves and recurs at rate in the theta range [2, 3]. Studies conducted in animal and human EEGs with electrodes implanted in cortex have shown that AM-PM patterns emerge after sudden jumps in cortical activity called state transition [4]. An abrupt phase resetting to a new value on every channel is the first step for transitions, follow by re-synchronization and spatial pattern stabilization.

Freeman and colleague's latest works had demonstrated that PM patterns have radial symmetry similar to a cone. PM patterns have been studied using cone fitting to the phase structure obtained by Hilbert transform (HT) or Fourier transform (FFT) [2, 3, 5]. Also, those patterns has different characteristic in task, awake, sleep and seizure state [3, 5]. Cone fitting is a high time consuming tool and it is difficult to apply in real time. In this paper a new method to detect stable phase structure is explained. The new cone parameter estimation is presented in task, awake, sleep

Y. Ruiz
Department of Biomedical Engineering, Zhejiang University, Hangzhou, 310027, China
e-mail: yuselyrg79@yahoo.es

R. Wang et al. (eds.), *Advances in Cognitive Neurodynamics*,

and seizure state. Phase structure consider as stable phase cone from HT method where compared with the detected new method stable phase structure. The time coincidence for stable phase structure detected was higher than 70%.

Materials and Methods

The data set used for the present work was selected 1 min recording segments with a subject in four states: awake, sleep, task, and during a typical seizure, more detail about signal recording can by found in [3, 5]. The 64 EEG signals in each segment were preprocessed first by de-meaning to remove channel bias and normalizing to unit standard deviation. A spatial low pass filter was applied to remove channel noise and a temporal band pass filter was applied to get the beta activity [1, 3, 5].

Stable Phase Structure Detection

The 64 channel signals in all state were study using 5 s segments. The analytic amplitude (AA) and analytic phase (AP) were obtained from HT [1, 2]. The AA and AP covariance in each time interval were calculated over the 64 channels. Thresholds for covariance (te1 & te2) were set and a stable phase structure was selected if AP covariance was lower than te1 and AA covariance was higher than te2.

The 64 stable analytic phase value form an 8×8 matrix represent phase structures similar to a cone. The cone gradient was estimated as the slope of the line fitted to the different between every phase value and the other 63 phase value for each interelectrode distance. The others cone parameters frequency, temporal wavelength, spatial wave length, velocity, diameter and duration were calculated using Eqs. (3–7) from [5] during the time intervals that stable phase structure was detected, the gradient sign did not change and the frequency was within the temporal band used.

After that, physiological criterion [3, 5] were applied to detect the final stable phase structure (stable cone or frame) The objective was compare the frame parameter in different states because according to [3, 5] the cone gradient was increased and frame velocity and diameter was reduced previous and during the seizure episode. That fact could be use as a seizure predictor.

Results

According to te1 and te2 value chosen, stable cone using the new method and the classical cone fitting as a coincidence vary from 85% to 40%; but the frame number in the new method is higher. The relation between the new method frame and new method frame that have coincidence with the frame obtained from the classical cone fitting fluctuate from 0.5 to 0.6 (see Fig. 128.1).

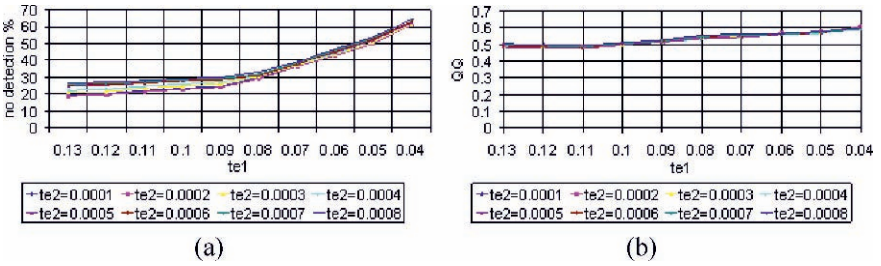

Fig. 128.1 Different te1 and te2 values for seizure state, awake, sleep an task have similar results, (**a**) coincidence of cone detected using new method and the cone fitting method, (**b**) relation new method coincidence cone/ new method cone (QQ)

Te1 value was fix to 0.08 and te2 to 0.0007. Then, each state cone parameters were calculated in 12 segments of 5 s. Task and awake state parameters have similar mean and standard deviation value, sleep state has lightly low frequency and gradient that affect the other parameter estimation. In time domain no significant differences can be found in the EEG segments before seizure and task, awake or sleep state (see Fig. 128.2).

Seizure and task states has similar parameters value in some segment but high gradient values in other, mainly during 15 and 5 s before seizure episode (Pre-1 and Pre-2 Table 128.1) and after it (Seizure-2 Table 128.1). High values in gradient are reflected as a decreased in velocity and cone diameter. Also, seizure state cone quantity is lower than other states, especially during 15 and 5 s before seizure episode and 15 s after it (see Fig. 128.3 and 128.4).

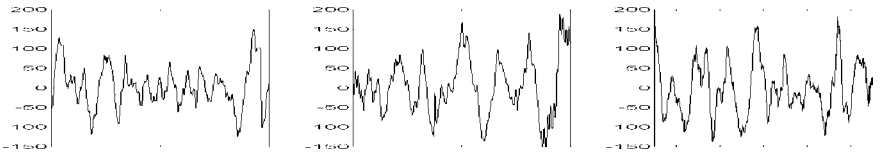

Fig. 128.2 Five seconds mean raw EEG signal. Left to right: task, sleep and 15 s before seizure

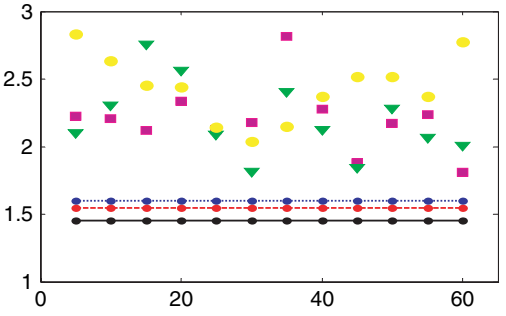

Fig. 128.3 Cone velocity mean value in 5 s segments, (●) sleep, (■) awake, (▼) task, line 15 s before seizure dash line 5 s before seizure and dot line 15 s after seizure

Table 128.1 Stable cone parameter (mean ± SD)

Signal	Time	γ (rad/mm)	B (m/s)	Dx (mm)
Task		0.0458 ± 0.0234	2.2253 ± 1.2567	35.3042 ± 18.1658
awake		0.0472 ± 0.0232	2.1760 ± 1.2436	36.0946 ± 20.7945
sleep		0.0396 ± 0.0230	2.4416 ± 1.4054	42.9158 ± 25.1332
Pre-1	−15	0.0626 ± 0.0166	1.5998 ± 0.5832	26.4534 ± 8.6501
Pre-2	−5	0.0562 ± 0.0299	1.5440 ± 0.4554	24.8704 ± 5.2128
Seizure-2	+15	0.0632 ± 0.0211	1.4547 ± 0.4246	24.1608 ± 7.1592

In task, awake and sleep stated value are the mean of 1-min signal.

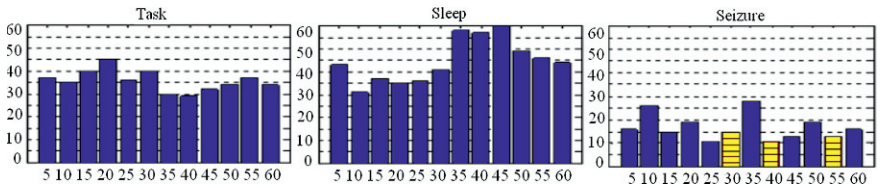

Fig. 128.4 Cone number is 5 s segments

Conclusions

High levels of time coincidence between cone fitting and the new method were obtained. The new methodology reduces the processing time to detect stable cone even when it is used with the cone fitting.

The striking difference between stable cone parameters derived from cone fitting and the new method is the lower gradient values, however the differences between brain states are maintained.

The new methodology is useful to detect stable phase cone in real time so that it is promising to predict epilepsy seizure.

Acknowledgements This research is supported by the National Creative Research Groups Science Foundation of China (NCRGSFC:60421002) and the National Basic Research Program of China (973 Program 2004CB720302). The human data were collected by Professor Mark D. Holmes in the EEG & Clinical Neurophysiology Laboratory, Harborview Medical Center, Seattle WA from an 8 × 8 electrode array that was constructed by Ad-Tech Medical Instrument Corp. Racine WI 53404 in accordance with a Berkeley design, and which was implanted in a human subject by Professor G. Alexander West, Department of Neurological Surgery, University of Washington,
Seattle, WA.

References

1. Freeman, W.J. *Origin, structure, and role of background EEG activity. Part 1. Analytic amplitude*. Clinical Neurophysiology, 2004. **115**(9): p. 2077–2088.
2. Freeman, W.J. *Origin, structure, and role of background EEG activity. Part 2. Analytic phase*. Clinical Neurophysiology, 2004. **115**(9): p. 2089–2107.

3. Freeman, W.J., Holmes, M.D., West, G.A., *et al. Fine spatiotemporal structure of phase in human intracranial EEG*. Clinical Neurophysiology, 2006. **117**(6): p. 1228–1243.
4. Kozma, R., Freeman, W.J. *Classification of EEG patterns using nonlinear dynamics and identifying chaotic phase transitions*. Neurocomputing, 2002. **44–46**: p. 1107–1112.
5. Freeman, W.J., Holmes, M.D., West, G.A., *et al. Dynamics of human neocortex that optimizes its stability and flexibility*. International Journal of Intelligent Systems, 2006. **21**(9): p. 881–901.

Chapter 129
A Tea Classification Method Based on an Olfactory System Model

Eduardo Gonzalez, Guang Li, Yusely Ruiz and Jin Zhang

Abstract In this paper the dynamics and architecture of a neural network derived from olfactory bulb and olfactory cortex are explained. The results of its application in tea classification are shown. The model presents multi-layer structure which is connected by feed forward and feedback lines with distributed delays. Using the same database, the tea classification results of the model are compared with those of the BP network. The new model performed better than the BP network.

Keywords Tea classification · olfactory system · neural network

Introduction

Tea is one of the most popular and oldest beverages around the world. Its components have significant antioxidant properties and its showed important role in the prevention of cancer, cardiovascular diseases, and other chronic diseases ascribed to oxygen toxicity [1]. The aroma and flavour are the two quality features of tea beverage which are produced by hundreds of volatile compounds. Tea flavour is traditionally measured using a combination of conventional analytical instrumentation and human or ganoleptic profiling panels. These methods are expensive in terms of time and labour and also inaccurate due to the lack of either sensitivity or quantitative information [2].

Thanks to the olfactory system have been well studied on last time, many mathematical model have been created to mimic its information processing. Researchers like Freeman [3], Hopfield [4], Li [5], Liljenström [6] and others have developed their own models to represent olfactory systems.

In this paper a chaotic neural network derived from the olfactory system was used to classify different kind of tea. The features of the tea samples were extracted using an gas sensor array. The model performance was compared with the BP network.

E. Gonzalez
Department of Biomedical Engineering, Zhejiang University, Hangzhou 310027, China
e-mail: moreira80@gmail.com

R. Wang et al. (eds.), *Advances in Cognitive Neurodynamics*,

Mathematical Model

The model is composed of two principal parts: the olfactory bulb and the olfactory cortex. The bulb structure is based on Li's model [7] while its dynamics is described by second order differential equations. The architecture and dynamics of cortex are essentially the same as in the olfactory cortex simulations by Liljenström [8].

The output of the olfactory bulb model is transmitted to the olfactory cortex model through the lateral olfactory tract (LOT) and the feedback transmission from the cortex to glomerulus's ensembles in the bulb is via the medial olfactory track (MOT).

Olfactory Bulb

The olfactory bulb in most mammalian consists of excitatory mitral and inhibitory granule cells, as reported in the literature. Each neural ensemble dynamics is described using a second order differential equation obtained from olfactory system physiological experiments.

$$\frac{1}{ab}\left[\ddot{x}(t) + (a+b)\dot{x}_i(t) + abx_i(t)\right] = \sum_{j\neq i}^{N} w_{ij}\, Q\left[x_j(t), q_j\right] + r_i(t) \qquad (129.1)$$

where a and b represent rate constants. $x_i(t)$ and $x_j(t)$ symbolize the dynamic state of the ith and jth neural ensemble respectively in a mammalian olfactory system. The positive, negative or zero value in w_{ij} represents an excitatory, inhibitory or no connection from neural population j to i; therefore, w_{ij} values define the system topology. $Q(x_i, q_i)$ is the asymmetric sigmoidal input/output transformation function used for mitral and granule cells, which is derived from the Hodgkin-Huxley model and q represents the maximum asymptote of the sigmoid function. Bulb olfactory model is mathematically represented by a second order non-autonomous nonlinear ordinary differential equation set.

Olfactory Cortex

The olfactory cortex is developed following Liljenström's cortex model. This model is based on the notion that simple network units with continuous output functions are enough to describe many global dynamical properties of biological neural networks.

In order to calculate how the internal states of the units change with time, nonlinear first-order differential equations are used. With external input, I(t), each unit i is represented by:

$$\frac{du_i}{dt} = \sum_{j=1}^{N} w_{ij} g_j\left[u_j\left(t - t_{ij}\right)\right] - \frac{u_i}{\tau_i} + I_i(t) \qquad (129.2)$$

$$g_j = \frac{1}{2}\left\{1 + \tanh\left[\frac{u_j\left(t - t_j\right) - \theta_j}{\gamma_j}\right]\right\} \tag{129.3}$$

In these equations t_{ij} correspond to the time delay and w_{ij} to the connection weights. The curve shape, g_j, is given by its threshold value, θ_j, and the gain parameter, γ_j.

The model has a laminar structure that can be subdivided into three layers: one feedforward inhibitory layer, one excitatory layer and one feedback inhibitory layer. On the excitatory layer the connections are widely distributed but excitatory-inhibitory and inhibitory-excitatory connections are more local. All connections strengths are dependent of the distance.

Learning Rule

The model was trained in order to form a prototype connections pattern between the nerve cells assembly. The system learns how differentiate classes from training set inputs with Hebbian modification of the excitatory synapses connection strength in the olfactory bulb mitral sets.

After the training session, the connection weights are fixed to perform a pattern classification test. The minimum Euclidian distances from the training patterns cluster centers to output system determine the classifications.

Tea Classification

A sensor array, which consisting of seven metal oxide sensors. (TGS2610, TGS2611, TGS800, TGS813, TGS822, TGS826 and TGS880 from Figaro Co.), was used to acquire the tea aroma. A tea sample was heated before data acquirement. The mean value of the voltage signal during the steady state was acquired as the raw data of this sample. Sometimes there has some peak signal brought by noises. For this reason, a median filter was applied [9].

Firstly a classification between green tea and black tea was made. To build up a testing set, thirty samples were acquired for each kind of tea while training set contains three samples of green tea and three samples of black tea and were trained twice each set. The results are shown in Table 129.1.

In order to show the capacity of the model to the pattern recognition the number of patterns was increases to four, using data set composed of four kind of tea

Table 129.1 Result of classification of two kinds of tea

Tea	Amount	Olfactory model's correction rate (%)
Green tea	30	100.0
Black tea	30	96.7
Total	60	98.4

Table 129.2 Result of classification of four kinds of tea

Tea	Amount	BP's correction rate (%)	Olfactory model's correction rate (%)
Chinese green tea	15	100.0	93.4
Japanese green tea	15	80.0	80.0
Indian black tea	15	66.7	86.7
Chinese black tea	15	93.4	100.0
Total	60	85.0	90.0

(Table 129.2). Fifteen samples of four kind of tea were used to build a testing set and three samples for each kind were utilized twice in the training process. To compare the model performance, a Back-Propagation network (BP) was implemented. Novel model correction rate is higher than BP network.

Conclusions

Traditionally, tea classification has been made by human senses. The fast development of neural network has allowed the introduction of its mathematical model on many areas on last decades. In this paper a novel olfactory system model was applied to tea recognition. The olfactory model has the capacity to learn complex patterns due to Hebbian modification of the M-sets excitatory synapses connection strengths in the bulb. The model showed an efficient performance on tea classification. Performance comparison between BP and novel model show higher correction rate values for the novel model.

Acknowledgements This research is supported by the National Creative Research Groups Science Foundation of China (NCRGSFC: 60421002) and the National Basic Research Program of China (973 Program 2004CB720302).

References

1. McKay, D.L. and J.B. Blumberg: The role of tea in human health: an update. Journal of American College of Nutrition, 2002. **21**(1) p. 1–13.
2. Dutta, R., et al.: Electronic nose based tea quality standardization. Neural Networks, 2003. **16**(5–6) p. 847–853.
3. Chang, H.-J. and W.J. Freeman: Parameter optimization in models of the olfactory neural system. Neural Networks, 1996. **9**(1) p. 1–14.
4. Hopfield, J.J.: Olfactory computation and object perception. PNAS, 1991. **88**(15) p. 6462–6466.
5. Li, Z. and J. Hertz: Odour recognition and segmentation by a model olfactory bulb and cortex. Network: Computation in Neural Systems, 2000. **11**(1) p. 83–102.
6. Aronsson, P. and H. Liljenström: Effects of non-synaptic neuronal interaction in cortex on synchronization and learning. BioSystems, 2001. **63** p. 43–56.
7. Li, Z. and J.J. Hopfield: Modeling the olfactory bulb and its neural oscillatory processings. Biological Cybernetics, 1989. **61**(5) p. 379–392.

8. Liljenström, H.: Modeling the dynamics of olfactory cortex using simplified network units and realistic architecture. International Journal of Neural Systems, 1991. **2**(1–2) p. 1–15.
9. Yang, X., Fu, J., Lou, Z., Wang, L., Li, G. and Freeman, W.J.: Tea classification based on artificial olfaction using bionic olfactory neural network. In: Wangm, X., Zhang, L., Sun, Y., Kim, K.-B., Lu, W., Wu Y., Li, B., Wang, J., Wang, W. and Wang, H. (Eds.): Advances in Neural Networks – ISNN 2006. Lecture Notes in Computer Science, 2006, Springer, Berlin, Heidelberg. pp. 343–348.

Chapter 130
Evolution Architecture Models for Integrated Grid Information Services

Do-Hyeun Kim, Kyung-Woo Kang and Gyung-Leen Park

Abstract Grid information services are an indispensable component of Grid computing and vital part of any Grid software infrastructure, providing fundamental mechanisms for discovery and monitoring, and thus for planning and adapting application behavior. However, existing Grid information services are unable to provide the all information for monitoring Grid resources. Accordingly, this paper presents three steps architecture models for an integrated Grid information service to enable the efficient discovery and monitoring of all Grid resources. These architecture models use the manager-of-managers method, the existing lower layer information systems and API for the discovery and monitoring of all Grid resources. Thereafter, an integrated Grid information system is designed and implemented based on the second architecture model using existing information systems. As such, the integrated Grid information system allows for the discovery and monitoring of all Grid resources, the usability of the system can be proliferated.

Keywords Grid computing · integrated information monitoring

Introduction

The interest in coupling geographically distributed resources is also growing for solving large-scale problems, leading to what is popularly known as Grid computing. In this environment, a wide variety of computational resources, such as supercomputers and clusters, including low-end systems, such as PCs/workstations, visualization devices, storage systems and databases, special class of scientific instruments, computational kernels, and so on, are logically coupled together and presented as a single integrated resource to the user [1]. GRID projects include Globus, Legion, Condor, NWS (Network Weather Services), LSF (Load Sharing Facility),

D.-H. Kim
Department of Computer and Telecommunication Engineering, Cheju National University, Korea
e-mail: kimdh@cheju.ac

R. Wang et al. (eds.), *Advances in Cognitive Neurodynamics*,

NetSolve, Ninf, AppLes, Nimrod/G, and JaWS, all of which have been previously discussed [2].

Accordingly, this paper proposes three steps architecture models for an integrated Grid information service in a Grid environment. The proposed architecture models use the manager-of-managers method, the lower layer information systems and API (Application Program Interface). In addition, an integrated Grid information system is designed and implemented based on the proposed second architecture model using existing lower layer information systems.

Architecture Models

This paper proposes three architecture models for an integrated information service in a Grid environment. First step architecture model is the Grid information system and the lower information systems are layered vertically. The Grid information system collects and processes totally the resource information of each of the lower information systems. The Grid and the lower information systems transfer the resource information using a standard protocol. Figure 130.1 represents the first architecture integrating a number of information systems. The resource information is collected and processed by the lower information system and it is concentrated in the upper information system.

The second model supports a uniform Grid information application. This architecture model uses the existing lower layer information systems and a standard interface. Figure 130.2 illustrates the architecture of a Grid information service that effectively integrates each information system using an application program interface or its proprietary tools. Using the lower layer information systems, these systems collect a part of the information from the Grid resources using the proprietary tools for each Grid information service. The application program interface

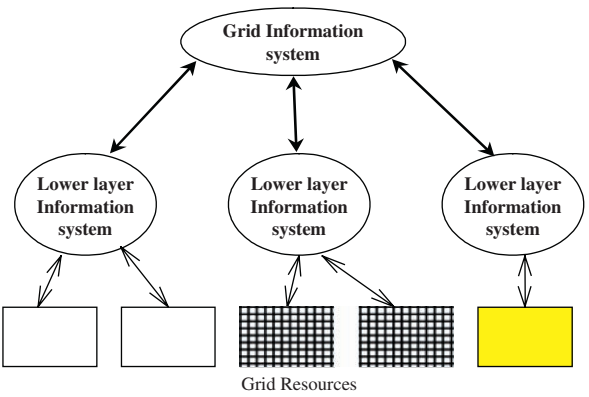

Fig. 130.1 The first architecture model for integrated Grid information service

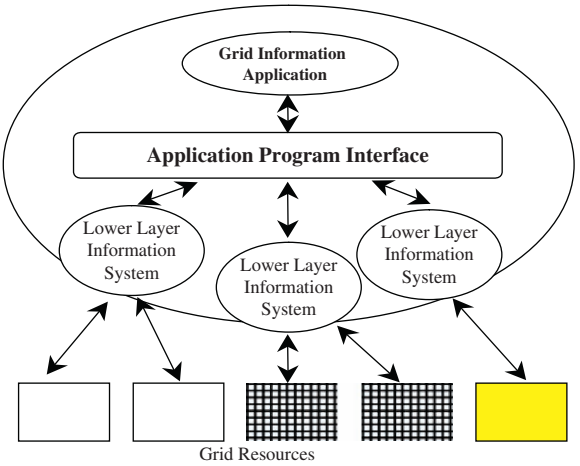

Fig. 130.2 The second architecture model for integrated Grid information service using lower layer information systems

then integrates the Grid resource information that is transferred from the existing lower layer information systems.

If all the Grid resources support a standard protocol, the third architecture is proposed that can be progressively modified into a prior integrated architecture and add a standard protocol to the Grid resources. With a third architecture, the Grid information applications do not each have lower layer information systems. Instead, all the Grid resources are communicated using an API (Application Program Interface). As such, a third architecture is a method of monitoring all the Grid resources using an application program interface. All the Grid resources use a standard protocol, a scheme of Grid resources, and an interface.

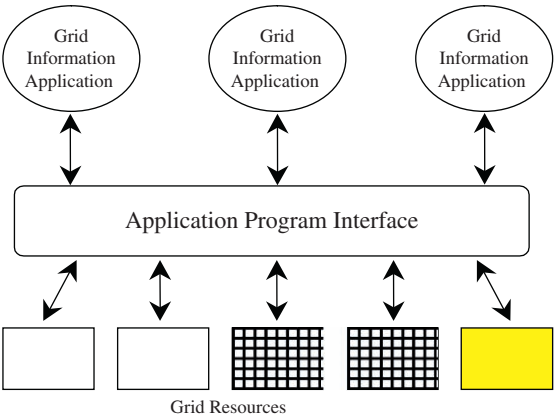

Fig. 130.3 The third architecture model for integrated Grid information service using an API

Therefore, the second architectures can resolve the problem of the first architecture that abandon the existing information systems using the proprietary protocol, and that of the first architecture that needs additional hardware and the installation of a standard protocol in the previous information system. Furthermore, an information system using second architecture can be developed a short period, and its development cost can be lowered by reusing the existing information systems as much as possible and by implementing it on a hardware platform. This architecture has the difficulty the integrated monitoring of all kinds of information systems and resources using various new protocols.

Implementation of Integrated Information System Using Lower Layer Information Systems

Thereafter, an integrated Grid information system is designed and implemented based on the second architecture model using existing information systems, and is able to monitor basic information on each node, the network state, computing state of a cluster, number of nodes and queue state. This system uses the LDAP (Lightweight Directory Access Protocol) as the application program interface, and Condor, MDS (Metacomputing Directory System), NWS, and LDF as the lower layer information systems. Figure 130.4 shows the configuration of the integrated Grid information system for the integrated monitoring and discovery of Grid resources using the second architecture model.

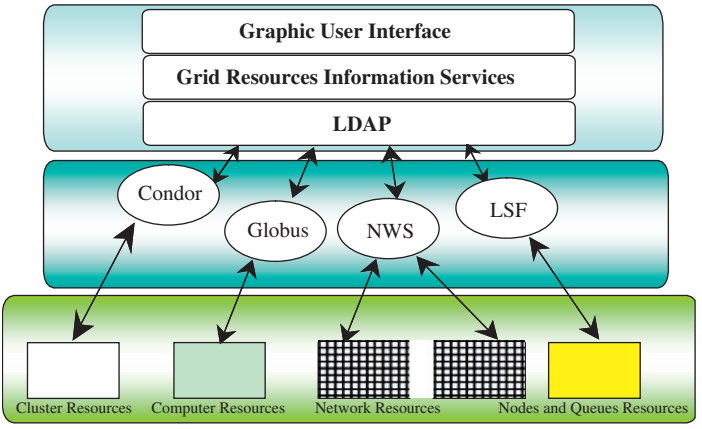

Fig. 130.4 Configuration of integrated information system using the second architecture model

Acknowledgements This research was supported by the MIC (Ministry of Information and Communication), Korea, under the ITRC (Information Technology Research Center) support program supervised by the IITA (Institute of Information Technology Advancement) (IITA-2006-C1090-0603-0040).

References

1. R. Buyya, S. Chapin, D. DiNucci, Architectural Models for Resource Management in the Grid, The First IEEE/ACM International Workshop on Grid Computing (GRID 2000), Springer Verlag LNCS Series, Germany(2000).
2. K. Czajkowski, S. Fitzgerald, I. Foster, C. Kesselman, Grid Information Services for Distributed Resource Sharing. Proceedings of the Tenth IEEE International Symposium on High-Performance Distributed Computing (HPDC-10), IEEE Press (2001).

Chapter 131
Maximizing Parallelism for Single Loops

Sam Jin Jeong

Abstract We review some loop partitioning techniques such as loop splitting method by thresholds and Polychronopoulos' loop splitting method which already developed. We propose improved loop splitting method for maximizing parallelism of single loops with non-constant dependence distances. By using the iteration and distance for the source of the first dependence, we present generalized and optimal algorithms for single loops with non-uniform dependences. The algorithms generalize how to transform general single loops into parallel loops.

Keywords Parallelizing compiler · loop parallelization · loop transformation

Introduction

An efficient approach for exploiting potential parallelism is to concentrate on the parallelism available in loops in ordinary programs and has a considerable effect on the speedup [1, 2].

Through some loop transformations using a dependence distance in single loops [3, 4], a loop can be splitted into partial loops to be executed in parallel without violating data dependence relations, that is, the size of distance can be used as a reduction factor [3], which is the number of iterations that can be executed in parallel. In the case of non-constant distance such that it varies between different instances of the dependence, it is much more difficult to maximize the degree of parallelism from a loop.

When we consider the approach for single loops, we can review two partitioning techniques proposed in [3] which are fixed partitioning with minimum distance and variable partitioning with ceil(d(i)). However, these leave some parallelism unexploited, and the second case has some constraints.

S.J. Jeong
Division of Information and Communication Engineering, BaekSeok University, 115 Anseo-Dong, Cheonan City 330-704, Korea
e-mail: sjjeong@bu.ac.kr

R. Wang et al. (eds.), *Advances in Cognitive Neurodynamics*,

Program Model and Data Dependence Computation

For data-dependence computation in actual programs, the most common situation occurs when we are comparing two variables in a single loop and those variables are elements of a one-dimensional array, with subscripts linear in the loop index variable. Then this kind of loop has a general form as shown in Fig. 131.1a. Here, l, u, a_1, a_2, b_1 and b_2, are integer constants known at compile time.

For dependence between statements S_1 and S_2, to exist, we must have an integer solution (i, j) to Eq. (131.1) that is a linear diophantine equation in two variables. The method for solving such equations is well known and is based on the extended Euclid's algorithm [5].

$$a_1 i + a_2 = b_1 j + b_2 \text{ where } l \leq i, j \leq u \tag{131.1}$$

Related Works

Now, we review some partitioning techniques of single loops. We can exploit any parallelism available in such a single loop in Fig. 131.1a, by classifying the four possible cases for a_1 and b_1, coefficients of the index variable I, as given by (131.2).

$$\begin{aligned} &\text{(a) } a_1 = b_1 = 0, \quad \text{(b) } a_1 = 0, b_1 \neq 0 \quad \text{or} \quad a_1 \neq 0, b_1 = 0, \\ &\text{(c) } a_1 = b_1 \neq 0 \quad \text{(d) } a_1 \neq 0, b_1 \neq 0, a_1 \neq b_1 \end{aligned} \tag{131.2}$$

In case 4(a), because there is no cross-iteration dependence, the resulting loop can be directly parallelized. In the following subsections, we briefly review several loop splitting methods for the case of 4(d).

Loop Splitting by Thresholds

A threshold indicates the number of times the loop may be executed without creating the dependence. In case 4(d), an existing dependence is non-uniform since there is a non-constant distance, that is, such that it varies between different instances of the dependence. And we can consider exploiting any parallelism for two cases when $a_1^* b_1 < 0$ and $a_1^* b_1 > 0$. Suppose now that $a_1^* b_1 < 0$. If (i, i) is a solution to (131.1), then there may be all dependence sources in (l, i) and all dependence sinks in $[i, u]$. Therefore, by splitting the loop at the iteration $I = i$ (called crossing threshold), the two partial loops can be directly parallelized [4].

DO $I = l,\ u$	DO $I = 1,\ N$	DO $I = l,\ 12$
S_1: A($a_1^* I + a_2$)= ...	S_1: A($3I + 1$)= ...	A($3^* I - 2$)
S_2: ... =A($b_1^* I + b_2$)	S_2: ... =A($2I - 4$)	... =A($2^* I + 5$)
ENDDO	ENDDO	ENDDO

Fig. 131.1 (a) A single loop model. (b) Example 1. (c) Example 2

Polychronopoulos' Loop Splitting

We can also consider exploiting any parallelism for the case 4(d) when $a_1{}^*b_1 \geq 0$. We will consider three cases whether it exists only flow dependence, anti-dependence, or both in the range of I. First, let (i, j) be an integer solution to (131.1). If the distance, $d(i)$ depending on i, as given by (131.3), has a positive value, then there exists a flow dependence, and if $\mathrm{d}_a(j)$ depending on j, as given by (131.4), has a positive value, then there exists an anti-dependence. Next, if (x, x) is a solution to (1) (x may not be an integer.), then $\mathrm{d}(x) = \mathrm{d}_a(x) = 0$ and there may exist a flow (or anti-) and an anti-dependence (or flow) before and after $I = \mathrm{ceil}(x)$, and if x is an integer, then there exists a loop-independent dependence at $I = \mathrm{x}$. Here, suppose that for each value of I, the element $\mathrm{A}(a_1{}^*I + a_2)$ defined by that iteration cannot be consumed before $\mathrm{ceil}(\mathrm{d}(i))$ iterations later, and this indicates that $\mathrm{ceil}(\mathrm{d}(i))$ iterations can execute in parallel.

$$\mathrm{d}(i) = j - i = \mathrm{D}(i)/b_1, \text{ where } \mathrm{D}(i) = (a_2 - b_1)^*i + (a_2 - b_1) \tag{131.3}$$

$$\mathrm{d_a}(j) = i - j = \mathrm{D_a}(j)/a_1, \text{ where } \mathrm{D_a}(j) = (b_1 - a_1)^*j + (b_2 - a_2) \tag{131.4}$$

Consider the loop, as given in Fig. 131.1b, in which there exist flow dependences. $\mathrm{d}(i) = \mathrm{D}(i)/b_1 = (i + 5)/2 > 0$ for each value of I and $\mathrm{d}(i)$ have integer values, 3, 4, 5, ... as the value of I is incremented.

Maximizing Parallelism for Single Loops

From a single loop with non-constant distance such that it satisfies the case (d) in (2) and $a_1{}^*b_1 > 0$, we can get the following Lemmas. For convenience' sake, suppose that there is a flow dependence in the loop.

Lemma 1. *The number of iterations between a dependence source and the next source, s_d is given by $|b_1|/g$ iterations where $g = gcd(a_1, b_1)$.*

Lemma 2. *The dependence distance, that is, the number of iterations between the source and the sink of a dependence, is $D(i)/b_1$ where $D(i) = (a_1 - b_1)^*i + (a_2 - b_2)$, and the increasing rate of a distance per one iteration, d' is given by $(a_1 - b_1)/b_1$. And the difference between the distance of a dependence and that of the next dependence, d_{inc} is $|a_1 - b_1|/g$.*

By using the iteration and distance for the source of the first dependence, and concepts defined by Lemma 1 and 2, we obtain the generalized and optimal algorithm to maximize parallelism from single loops with non-uniform dependences.

Procedure MaxSplit shows the transformation of single loops satisfying the case (d) in (2) and $a_1{}^*b_1 > 0$ into partial parallel loops.

Applying Procedure MaxSplit to the loop in Fig. 131.1b, the unrolled version of this result is shown in Fig. 131.2c. As shown in Fig. 131.2, we can know that Procedure MaxSplit is an algorithm to maximize parallelism from single loops with non-constant distances.

I	A(3*I+1)	A(2*I-4)
1	A(04)	A(-2)
2	A(07)	A(00)
3	A(10)	A(02)
4	A(13)	A(04)
5	A(16)	A(06)
6	A(19)	A(08)
7	A(22)	A(10)
8	A(25)	A(12)
9	A(28)	A(14)
10	A(31)	A(16)
11	A(34)	A(18)
12	A(37)	A(20)
13	A(40)	A(22)
14	A(43)	A(24)
15	A(46)	A(26)
16	A(49)	A(28)
…		

(a) Using minimum distance.

I	A(3*I+1)	A(2*I-4)
1	A(04)	A(-2)
2	A(07)	A(00)
3	A(10)	A(02)
4	A(13)	A(04)
5	A(16)	A(06)
6	A(19)	A(08)
7	A(22)	A(10)
8	A(25)	A(12)
9	A(28)	A(14)
10	A(31)	A(16)
11	A(34)	A(18)
12	A(37)	A(20)
13	A(40)	A(22)
14	A(43)	A(24)
15	A(46)	A(26)
16	A(49)	A(28)
…		

(b) Using ceil(d(*i*)).

I	A(3*I+1)	A(2*I-4)
1	A(04)	A(-2)
2	A(07)	A(00)
3	A(10)	A(02)
4	A(13)	A(04)
5	A(16)	A(06)
6	A(19)	A(08)
7	A(22)	A(10)
8	A(25)	A(12)
9	A(28)	A(14)
10	A(31)	A(16)
11	A(34)	A(18)
12	A(37)	A(20)
13	A(40)	A(22)
14	A(43)	A(24)
15	A(46)	A(26)
16	A(49)	A(28)
…		

(c) Our proposed method.

Fig. 131.2 The unrolled versions of transformed loops

Conclusions

In this paper, we have studied the parallelization of single loop with non-uniform dependences for maximizing parallelism. For single loops, we can review two partitioning techniques which are fixed partitioning with minimum distance and variable partitioning with ceil(d(*i*)). However, these leave some parallelism unexploited, and the second case has some constraints. Therefore, we propose a generalized and optimal method to make the iteration space of a loop into partitions with variable sizes. In the proposed method, two algorithms are considered as one for loops with one dependence and the other for loops with multiple dependences. Our algorithm generalizes how to transform general single loops with one dependence into parallel loops.

In comparison with some previous splitting methods, our proposed methods give much better speedup and extract more parallelism than other methods.

Our future research work is to consider the extension of our method to n-dimensional space.

References

1. W. Zhang, G. Chen, M. Kandeemir, and M. Karakoy, Interprocedural Optimizations for Improving Data Cache Performance of Array-Intensive Embedded Applications, in DAC 2003, Anaheim, California (2003).
2. D. S. Park, M. H. Choi, Interprocedural transformations for parallel computing, in Journal of Korean Multimedia Society, vol. 9, no. 12, (2006) 1700–1708.
3. C. D. Ploychronopoulos, Compiler optimizations for enhancing parallelism and their impact on architecture design, in IEEE Transactions on computers, vol. 37, no. 8, (1988) 991–1004.

4. J. R. Allen, and K. Kennedy, Automatic translation of Fortran programs to vector form, in ACM Transactions on Programming Languages and Systems, vol. 9, no. 4, (1987) 491–542.
5. D. E. Knuth, The Art of Computer Programming, vol. 2: Seminumerical Algorithms, Reading, MA: Addison-Wesley (1981).

Chapter 132
The Realtime Workflow for RFID Based Medical Test

Sang Hwan Kung, YunHee Kang and Kyung Woo Kang

Abstract The workflow, one of core features for modern business operation, models common elements and their relationships in business processes. The ultimate goal of the workflow is to automate the business processes found in business or other diverse applications. Once business process is defined with the automated tool, the workflow service is activated by the definition, separating workflow service from the workflow applications. In the paper, we model the workflow system under the ubiquitous environment which is composed of the moving patients with the customer devices such as PDA. The paper defines the role of ubiquitous devices in the system as well as the interaction with the workflow server. The paper also deals with the application analysis in terms of real-time workflow concept. On the other hand, it includes software architecture which shows block diagram of the system.

Keywords Medical test · RFID · workflow · BPR

Introduction

In this paper, we apply the workflow to the health examination process which is comprised of multiple medical tests. Usually, the number of patients needs to be tested at the same time is not usually small, so many of them need to be waited at the test spots. On the other hand, there needs to be many of helpers in order to help them find the next test spot.

We try to resolve this problem, by having a couple of ideas. One of them is to set up the real-time, ubiquitous environment by providing patients with PDA and RFID card, which enables patients move around by themselves without any of helpers. The other is to extend the workflow to have real-time feature, which means the workflow works for the dynamic situation when making a decision on how a patient moves to next spots. We especially consider how many people are waiting on the spot and how long each test spot takes to be finished. The paper covers from the analysis of

S.H. Kung
Division of Information and Communication Engineering, Baekseok University, Korea
e-mail: kung@bu.ac.kr

R. Wang et al. (eds.), *Advances in Cognitive Neurodynamics*,

requirements for the RFID based real-time workflow system to the functional block structures, including a core algorithm.

Researches and standards for enabling Technologies like Workflow and RFID are described in the attached references [1, 2, 3, 4, 5, 6, 7, 8].

Application Service Environment

These days the healthcare examination is popularly done to know if people have any kind of bad symptoms in their health. This type of medical examination is usually performed at the specialized test center which is well facilitated with modernized medical diagnostic equipments.

In many cases, the medical test center is full of patients to be checked, so it is usual cases for the patients to be waited in a long line to take a certain test. So, some helpers guide them to the test spots which might be expected to be minimal waiting.

We decided to use the workflow concept for the medical test, because a total examination process is composed of many individual tests just like a business or manufacturing process.

At every test spot, the tester uses the personal computer to see the patients waiting for the test and to write in the test results. And, in order to provide patients with non-stop services possibly, each patient is given with PDA with RFID function. The RFID chip is attached on the backside of the PDA.

The patient's information stored in this RFID is read by the RFID reader located at each test spot and the indication of patient's arrival is notified to the tester's PC and also moved to database of the server. When the test is finished, its result is given to the database in the server by the tester. Even though some tests make take some days to have the results of the test, this does not become serious matter because the system mainly concerns about only the activities which are performed on the floor.

Once the test result is given, the system tries to decide the next test for the patient by taking care of the defined route, the number of people waiting and average test time. When the conclusion is made, the direction to the test spots is displayed on the PDA. So, the patient do not have any trouble in moving around the entire test spots. The PDA also gives the patient the whole list of tests and the tests he/she has finished.

Analysis of Workflow Feature

A workflow is executed through several processes performed in parallel. The process also includes multiple activities which are performed in parallel or in serial. In our system, the basic element of task will be a specific test, which will be actually a activity. The patient goes through the entire activities belong to a process. Since

```
if(routing type == Random)
  search the all the tests which are not visited yet
  find the least waiting spot by the number of waiting patients and average waiting time of the spot.
  if(next spots with the same waiting time are multiple)
  choose it from the pre-defined path
else // routing type == Random
  find next spot from the pre-defined path
```

Fig. 132.1 Routing algorithm

there could be multiple patients being tested, multiple processes could be handled in parallel in the system also.

The performer who does each activity will be the tester who has its own role. So, he/she chooses a task from to-do list and finishes out one by one. In patient's point of view, to-do list is comprised of multiple different activities. On the other hand, in tester's point of view, to-do list is comprised of same activities.

The process for medical test is activated by the fixed scenario which defines entire sequence of tests. If there is only one patient to be tested, the he or she is supposed to visit the predefined steps. Nevertheless, this can be varied by the healthcare test center, we need to define the all the activities in XML form according to environment and condition of the centers.

The one of important function is to make a real-time decision to move on a certain test spot. The system provides with this function with the routing type, which is either 'F' (*Fixed Routing*) or 'R' (*Random Routing*). Fixed routing means that routing is automatically done depending on the XML script, on the other hand Random routing means that routing from one spot to another is randomly selected. For random routing, we can apply to a algorithm which decides the next spot based on the total waiting time of the spot.

On a certain test spot, the algorithm to make a decision of the next test spot is as in Fig. 132.1.

Architecture of the System

The Fig. 132.2 shows the Block Diagram of the system which consists of core blocks which may explain the brief architecture and behavior of the system. The major blocks of the system are divided into four parts which are the client part, the workflow server main, the workflow application, and the workflow service part. The client part is composed of the device handler and the workflow application. When it wants to be served, it connects to the workflow server main. The workflow service provided at the server side is handled by the workflow application block and the workflow service block. The workflow service block carries out workflow functions independently from the applications. On the other hand, the application-specific processing is performed by the workflow application block.

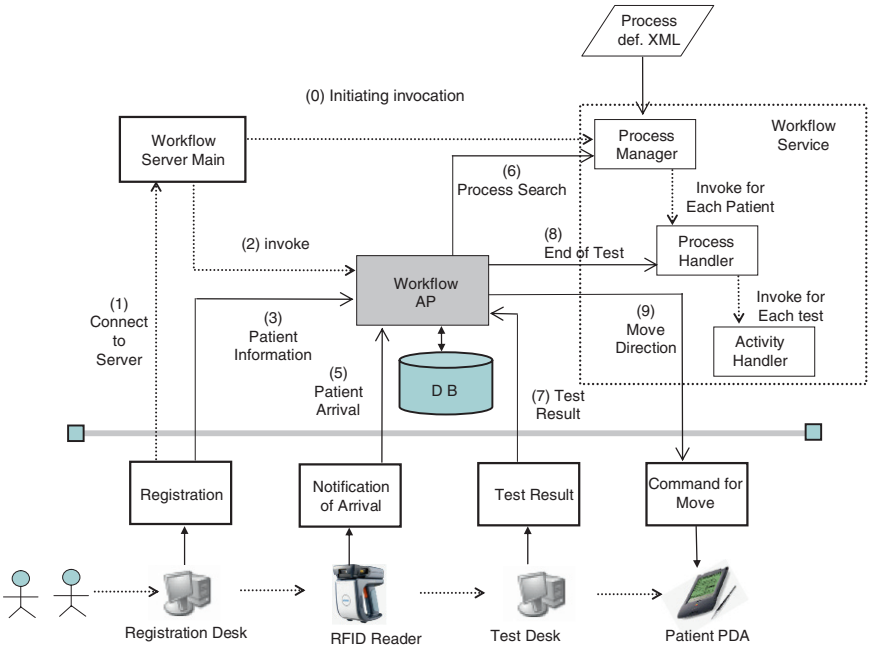

Fig. 132.2 Block diagram of the system

Conclusion

The paper focuses on the design of application and middleware for Medical Test Center. The procedure on the floor for the test needs to be automated in terms of workflow scheme which have been widely popular. On the other hand, the inconvenience discovered on the floor when the patients moves around needs to be facilitated with ubiquitous devices such as PDA and RFID feature.

We concentrated on the design of software architecture for the system realizing the requirements. So, in this paper, we covered from the business scenario and requirement analysis to design of software blocks and important classes. The brief algorithm to make a decision for next move on a spot was also introduced.

Anyhow, we need to improve the design in that more complicated model for the process definition is realistic and the routing algorithm needs to cover this new requirement.

References

1. Alec Sharp & Patrick McDermott, Workflow Modeling: Tools for Process Improvement and Application Development, Artech House, February 2001.
2. Alan Mainwaring, Joseph Polastre, Robert Szewczyk, and David Culler, Wireless Sensor Networks for Habit Monitoring, ACM Sensor Networks and Applications, September, pp. 88–97, 2002.

3. Andrezei Cichocki, Abdelsalam Helal, and Marek Rusinkiewicz, Darrell Woelk, Workflow Process Automation, Kluwer Academic Publishers, 1998.
4. EPCglobal, EPC Information Services (EPCIS) Version 1.0 Specification, Workinf Draft, October 2004.
5. Gary Poyssick and Steve Hannaford, Workflow Reengineering, Adobe Press, 1996.
6. Roy Want, Enabling Ubiquitous Sensing with RFID, Computer, Vol. 37, April 2004.
7. Thomas M. Koulopoulos, The Workflow Imperative, John Wiley & Sons, Inc., 1995.
8. WfMC, The Workflow Reference Model, DN TC00-1003, 19-Jan-95.

Chapter 133
Visuo-Spatial Attention Frame Recognition for Brain-Computer Interfaces

Ferran Galán, Julie Palix, Ricardo Chavarriaga, Pierre W. Ferrez, Eileen Lew, Claude-Alain Hauert and José del R. Millán

Abstract *Objective:* To assess the feasibility of recognizing visual spatial attention frames for brain-computer interfaces (BCI) applications. *Methods:* EEG data was recorded with 64 electrodes from two subjects executing a visuo-spatial attention task indicating two target locations. Continuous Morlet wavelet coefficients were estimated on 18 frequency components and 16 preselected electrodes in trials of 600 ms. The spatial patterns of the 16 frequency components frames were simultaneously detected and classified (between the two targets). The classification accuracy was assessed using 20-fold cross-validation. *Results:* The maximum frames average classification accuracies are 80.64% and 87.31% for subject 1 and 2 respectively, both utilizing frequency components located in gamma band.

Introduction

Asynchronous EEG-based brain-computer interfaces (BCI) [1] allow subjects to control devices spontaneously and at their own pace, contrarily to synchronous BCI systems [2], and without requiring external cues such as in the case of relying on evoked potentials [3]. To this end, people learn how to voluntary modulate different oscillatory EEG rhythms by the execution of different mental tasks. A limitation of using mental tasks as control commands (e.g., imagining movements or doing arithmetics) is that subjects need to keep performing those mental tasks during the whole interaction, what can be exhausting, especially for novel users. An alternative is to exploit conscious behaviors that do not require sustained attention. Recent studies have demonstrated the possibility to modulate EEG alpha band by orienting visuo-spatial attention [4]. In an ideal case, BCI users could make a wheelchair *turn left* just by orienting their attention (without any eye movement) to some location in the left visual field, what is more natural than, for instance, imagining a left hand movement. Moreover, once the wheelchair just turn left, users will simply stop

F. Galán
IDIAP Research Institute, Martigny, Switzerland
e-mail: Ferran.Galan@idiap.ch

R. Wang et al. (eds.), *Advances in Cognitive Neurodynamics*,

attending to any particular spot of their visual field and the wheelchair, endowed with an intelligent controller [1], will move forward.

In this paper we assess the feasibility of recognizing user's voluntary modulation of EEG rhythms associated to visuo-spatial attention in an experimental setup close to the ecological conditions of asynchronous EEG-based BCIs. To this end, we compare both, a *traditional BCI approach* and a *frames approach*. These frames, as described by Freeman [5], correspond to active intermittent induced spatial patterns of amplitude modulation of beta-gama oscillations in response to conditioned stimuli. Based on those findings we address the following questions: *(i)* Does this discontinuous mode of function (i.e., frames) also appear in response to voluntary modulation of EEG rhythms? *(ii)* In this case, is it possible to classify these frames with respect to the attended location? *(iii)* Which frequency ranges yields better classification accuracy? *(iv)* Can this approach improve BCI performance? We hypothesize that *traditional approaches* (assuming sustained modulation of EEG rhythms over time) would face methodological problems: they will label (for training purposes) and classify samples extracted from periods of time where the underlying brain phenomena is either not present or is not salient enough. Then, a *frames approach* (which only classifies those samples where the induced episodic frames are detected) would be more appropriate. This paper addresses these questions and presents some hints for future work.

Methods

Data were recorded from two subjects with a portable Biosemi acquisition system using 64 channels sampled at 512 Hz and high-pass filtered at 1 Hz. The sampling rate was fixed at 512 Hz to ensure a good estimation of the highest frequency component under analysis. The subjects were sitting in a chair looking at a fixation cross placed at the center of a monitor. The subjects were instructed to covertly attend to one of two possible target locations (lower-left and lower-right monitor's corners). The target location was specified by the operator in a pseudo-random balanced order. The subjects specified when they started to shift their attention. Each subject participated in 10 sessions composed by four trials each, two trials for each target. The duration of each trial was 7 s but only the first 600 ms were utilized in this study.

The signal was spatially filtered using common average reference (CAR) previous to estimate the continuous Morlet wavelet coefficients on 18 frequency components (7, 8, 9, 10, 11, 12, 28, 32, 36, 40, 44, 48, 56, 64, 72, 80, 88, and 96 Hz) and 16 electrodes (F5, FC5, C5, CP5, P5, AFz, Fz, FCz, Cz, PCz, Pz, F6, FC6, C6, CP6, P6). The selection of electrodes was based on preliminary analysis of continuous Morlet wavelet coefficients scalp topography. Thus, each trial is composed by 512×0.6 samples and 18×16 features. The analysis carried on aims to compare the recognition rates over the different frequency components using two different approaches, namely the *traditional BCI approach* and the *frames approach*. The process was structured in two steps:

1. One canonical space was built per each frequency component (18 canonical spaces) [6] using 16-dimensional vectors (estimated wavelet coefficients at 16 electrodes). Since it is a two-class problem, canonical spaces are defined by one canonical function.
2. A linear discriminant classifier (LDA) was built following two different approaches:

   (a) *Traditional BCI approach*: using all the training projected samples on the canonical space and classifying all the test projected samples.
   (b) *Frames approach*: only a subset of the projected samples (i.e. frames) are used for training and classification. A sample was considered as a frame if its projection on the training canonical space was located on the opposite tails of each class distribution. Eight percentiles were utilized as thresholds: P_{40}, P_{35}, P_{30}, P_{25}, P_{20}, P_{15}, P_{10} and P_5. Thus, a sample was identified as a frame either its projection was below a given percentile (i.e: P_5) of class 1 or above the opposite percentile (i.e: P_{95}) of class 2. From now, the reference to one percentile also includes its opposite.

Both approaches were assessed using k-fold crossvalidation, $k = 20$. Each fold was integrated per one trial of each condition respecting the timing when they were recorded.

Results and Conclusions

The average LDA classification accuracy is higher utilizing the frames approach. For both subjects, the maximum classification accuracy is reached utilizing P_5. We report on detail the results obtained on this percentile. The maximum average classification accuracy classifying all the samples (i.e. traditional approach) is 58.41% at 10 Hz and 63.08% at 12 Hz for subject 1 and 2 respectively (see Fig. 133.1 *left*), both in the alpha range. Utilizing frames approach, the maximum average classification accuracies are 80.64% at 72 Hz, and 87.31% at 32 Hz for subject 1 and 2 respectively (Fig. 133.1 *center*), both in the gamma range. It represents an absolute increase of 22.23% and 27.13% for subject 1 and 2 respectively. Notice that these classification accuracies are computed only on those samples identified as frames. The average percentage of samples identified as frames out of the total of samples of a trial is 5.85% for subject 1 and 5.92% for subject 2 (see Fig. 133.1 *right*) at 72 Hz and 32 Hz respectively. In case of subject 1, only in one-fold out of 20 it was not possible to identify any frame. In case of subject 2, it was not possible in 4 out of 20 folds. To understand the implication of these results in a real BCI application, each trial has been labelled according to the class maximum recognized by the classifier, using all the samples in case of traditional approach, and using only frames in case of frames approach. In the first case, the trial classification accuracies are 60.00% and 57.50% for subjects 1 and 2 respectively, what implies that channels capacities are 0.05 b/s and 0.03 /s (using estimator proposed in [1]). Using frames approach,

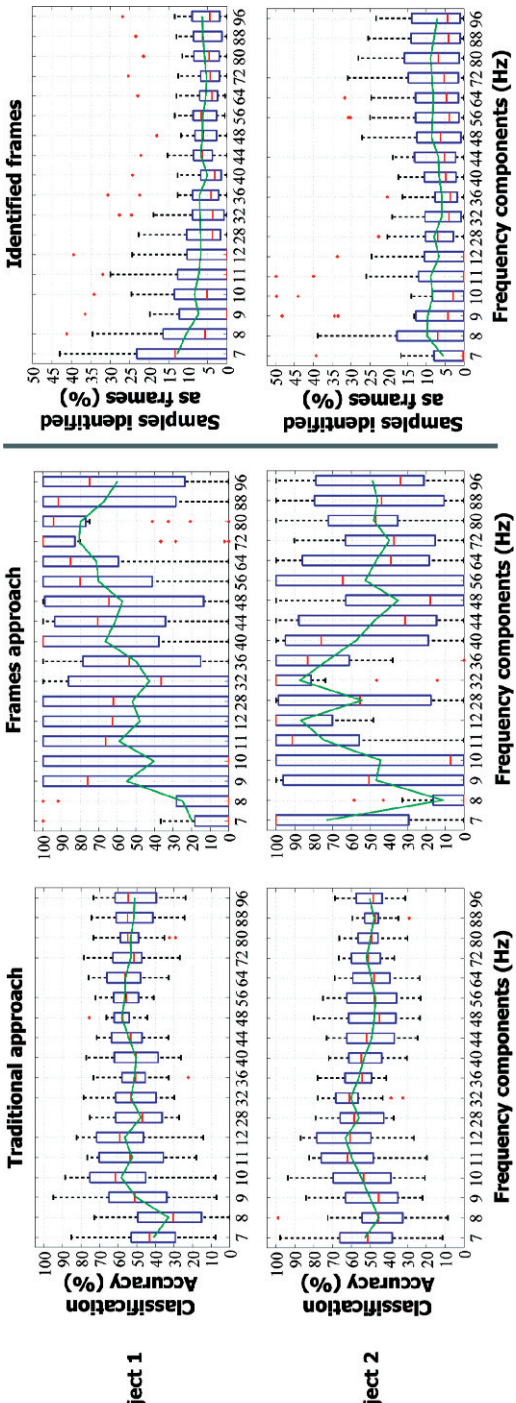

Fig. 133.1 Classification results using 20-fold crossvalidation over the 18 frequency components. Solid line represents the mean. LDA classification accuracy distributions utilizing traditional approach (*left*) and frames approach (*center*). *Right*, percentage of the total trial samples identified as frames

the trial classification accuracies are 60.00% and 47.50%, but with only 12.50% of error recognition in both cases, what implies that channels capacities are 0.55 b/s and 0.46 b/s. Using frames approach the BCI theoretical channel capacity is boosted by 10.

This preliminary study on visuo-spatial attention frame recognition for BCI provides relevant hints for further research. First, it is possible to voluntary modulate EEG rhythms by orienting visuo-spatial attention in order to use asynchronous non-invasive EEG-based BCI's. Second, the intensity of this modulation is not sustained over time. This fact can be related to the active intermittent induced spatial patterns of amplitude modulation (frames) in response to conditioned stimuli described by Freeman [5]. In this case these patterns are voluntary driven by the subject. Third, it is possible to classify the frames generated by orienting the attention to different visual locations with high classification accuracies (above 80%). Fourth, these classification accuracies are maximum in gamma band (>30 Hz), corresponding to endogenous shifts of attention effects [7]. Fifth, classification accuracies utilizing a traditional approach, i.e. assuming modulations sustained over time, are around the chance level. It suggests that this approach is not optimal to recognize induced EEG phenomena, what is confirmed comparing the BCI theoretical channel capacity achieved using both approaches. Using frames approach the BCI theoretical channel capacity is drastically increased.

Acknowledgements We thank Drs. S. Gonzalez and R. Grave, Geneva Univ. Hospital, for suggesting the use of visuo-spatial attention in BCI. This work was supported in part by the Swiss National Science Foundation through the NCCR 'IM2' and by the European IST Programme, Projects FP6-003758 and FP6-IST-027140. This paper only reflects the authors' views and funding agencies are not liable for any use that may be made of the information contained herein.

References

1. Millán, J. del R., Renkens, F., Mouriño, J., Gerstner, W.: Noninvasive brain-actuated control of a mobile robot by human EEG. IEEE Trans. Biomed. Eng. **51** (2004) 1026–1033.
2. Birbaumer, N., Ghanayim, N., Hinterberger, T., Iversen, I., Kotchoubey, B., Kübler, A., Perelmouter, J., Taub, E., Flor, H.: A spelling device for the paralysed. Nature **398** (1999) 297–298.
3. Kelly, S. P., Lalor, E. C., Reilly, R. B., Foxe, J. J.: Visual spatial attention tracking using high-density SSVEP data for independent brain-computer communication. IEEE Trans. Neural Sys. Rehab. Eng. **13** (2005) 172–178.
4. Thut, G., Nietzel, A., Brandt, S., Pascual-Leone, A.: Alpha-band electroencephalographic activity over occipital cortex indexes visuospatial attention bias and predicts visual target detection. J. Neurosci. **26** (2006) 9494–9502.
5. Freeman, W. J.: Origin, structure, and role of background EEG activity. Part 3. Neural frame classification. Clin. Neurophysiol. **116** (2005) 1118–1129.
6. Galán, F., Ferrez, P. W., Oliva, F., Guárdia, J., Millán, J. del R.: Feature extraction for multi-class BCI using canonical variates analysis. In: Proceedings of the 2007 IEEE Int. Symp. Intell. Signal Process (WISP 2007). Alcaláde Henares, Spain, (2007).
7. Palix, J., Hauert, C. A., Leonards, U.: Brain oscillations: Indicators for serial processing in inefficient visual search? Perception **35** (2006) 234.

Chapter 134
To Err is Human: Learning from Error Potentials in Brain-Computer Interfaces

Ricardo Chavarriaga*, **Pierre W. Ferrez and José del R. Millán**

Abstract Several studies describe evoked EEG potentials elicited when a subject is aware of an erroneous decision either taken by him or by an external interface. This paper studies *Error-related potentials* (ErrP) elicited when a human user monitors an external system upon which he has no control whatsoever. In addition, the possibility of using the ErrPs as a learning signals to infer the user's intended strategy is also addressed. Experimental results show that single-trial recognition of correct and error trials can be achieved, allowing the fast learning of the user's strategy. These results may constitute the basis of a new kind of human-computer interaction where the former provides monitoring signals that can be used to modify the performance of the latter.

Introduction

The error monitoring process is crucial to improve performance for both humans and artificial cognitive systems. Upon identification of erroneous decisions, the likelihood of repeating such actions in the same context should be decreased in order to improve the performance. This mechanism is the base of the reinforcement learning theory [1]. Several studies on human EEG have identified event-related potentials elicited by erroneous decisions or error feedback; i.e. *error-related negativity* (ERN) and *feedback-related negativity* (FRN), respectively [2]. These potentials are characterized by a midline frontal negative deflection of the EEG around 80 ms and 250 ms, respectively. Moreover, evoked potentials have also been described when errors are generated by a human-computer interface and not by the user himself – e.g. keyboard or brain-computer interfaces (BCI) [3].

R. Chavarriaga
IDIAP Research Institute, Martigny, Switzerland
e-mail: rchava@idiap.ch

* This work has been supported by the Swiss National Science Foundation NCCR-IM2 and by the EC-contract number BACS FP6-IST-027 140. This paper only reflects the authors' views and funding agencies are not liable for any use that may be made of the information contained herein.

R. Wang et al. (eds.), *Advances in Cognitive Neurodynamics*,

Although these signals convey valuable information about the user's evaluation of performance, they have seldom been used in the field of non-invasive BCIs. Parra and colleagues have proposed the use of ERNs to correct user's erroneous decisions on speed response tasks [4], while Ferrez et al. use *error-related potentials* (ErrP) to improve the information transfer rate of a BCI system [3]. However, these studies use ErrPs only to correct the response that generated the error, but they do not include a learning mechanism to prevent that error to be repeated in the future.

This paper addresses this issue by testing the use of error-related potentials as a teaching signal to learn the user's strategy when solving a simple task. In particular, *(i)* we test whether these potentials can be detected on single trial when a human subject monitors the performance of an external system upon which he has no control whatsoever; and *(ii)* we assess the feasibility of using such signals to learn the user's intention, i.e. the strategy the user expects the system to perform.

Experimental Protocol

Subjects seat in front of a computer screen where a moving cursor (a green square) is displayed. A red square at either the left or right of the cursor signals the target location, as shown in Fig. 134.1a. At each time step the cursor moves horizontally depending on the location of the target. The user has no control over the cursor's movement and is asked only to monitor the performance of the system, knowing that the goal is to reach the red target. Cursor movement law is defined in a suboptimal way in order to study signals elicited by the system's errors. Specifically, at each

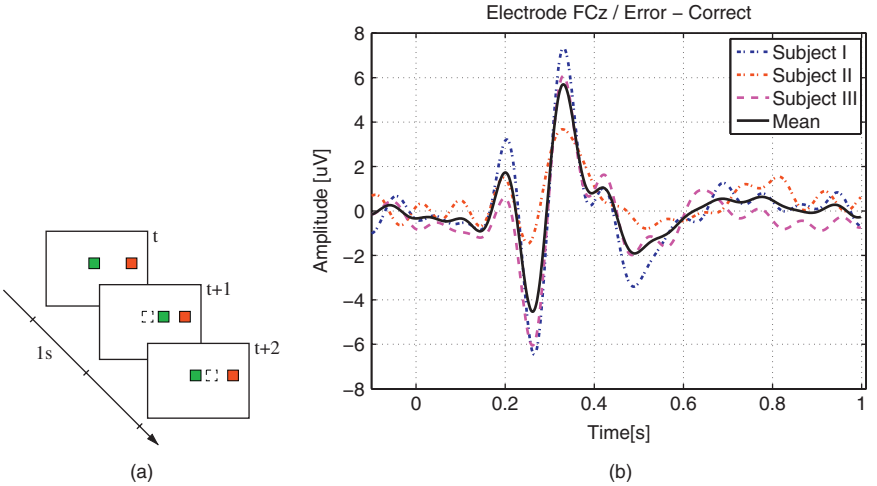

Fig. 134.1 (a) Experimental protocol. *Green square*, moving cursor. *Red square*, target location. *Dotted square*, cursor location at the previous time step. Correct and erroneous movements are shown at times $t+1$ and $t+2$ respectively. (b) Grand average error related potential—Error minus Correct condition—on the FCz electrode (feedback is given at time t = 0)

time step there is a probability of 80% for the cursor to move towards the target. One experimental session consists of 10 blocks of 3 min each (approx. 75 trials per block).

Three healthy male subjects performed two sessions of the experiment. Data from the first session was used to characterize the evoked potentials for both error and correct trials and to train the classifier parameters (see Section 3 below). The second session, recorded seven weeks after the first one, was used to test ErrP single-trial classification. EEG was recorded for all subjects with a sampling rate of 512 Hz using 64 electrodes according to the standard 10/20 International system. Data was re-referenced to the common average reference (CAR) and a 1–10 Hz band-pass filter was applied. The average feedback-locked potential at channel FCz—difference between error and correct grand averages—for the three subjects is shown in Fig. 134.1b.

To emulate experimental conditions of a BCI application, no artifact rejection was applied and all trials were used in the analysis. Moreover classification accuracy was assessed on a single-trial basis, as opposite to batch performance evaluation techniques such as cross-validation.

Single-Trial Classification

Following previous studies, we classify the signals using a Gaussian classifier [3]. The activity on the FCz and Cz electrodes on the [200 ms, 450 ms] time window after the feedback presentation was used as input to the classifier. The statistical classifier estimates the posterior probability of a single trial corresponding to each of the two classes *error*, and *correct*. Classifier parameters were tuned using a stochastic gradient descent on the mean square error.

Table 134.1 shows the recognition rates on single-trial for the three subjects. The same classifier parameters were used in all cases. Learning rates were 10^{-2} and 10^{-4} for the center and covariances of the Gaussian prototypes. A total of 6 prototypes were used for each class. These results show classification above chance for both correct and error trials, with higher recognition rates for the correct trials.

Table 134.1 Single trial recognition rates (%) for the three subjects on the test set (i.e. session 2)

	Subject I		Subject II		Subject III	
	Correct	Error	Correct	Error	Correct	Error
Correct	92.01	7.99	83.82	16.18	86.86	13.14
Error	26.50	73.50	41.08	58.91	33.71	66.29

Learning from Error-Related Potentials

We test then whether the detection of ErrPs can be used as to infer what the optimal behavior should be. The rationale of this approach is that, given the system decisions

and the user's evaluation of such decisions – indicated by the presence or not of ErrPs –, it is possible to infer what strategy is considered as correct by the human user.

Considering the experiment described above, the optimal strategy is to move the cursor towards the target. Let define $T_t, A_t \in [L, R]$ the target location and the cursor's direction of movement at time t, where $[L, R]$, stand for left and right respectively. Let $P_{A,T}$ be the probability of taking action A given the target location T, and a strategy Π, i.e. $P_{A_t,T_t} = P(Action = A_t|Target = T_t, \Pi)$. The optimal strategy Π^* can be expressed in terms of probabilities $P^*_{L,L} = P^*_{R,R} = 1$; respectively, $P^*_{L,R} = P^*_{R,L} = 0$.

Alike to reward signals in reinforcement learning, ErrP detection can be used to decrease the likelihood of performing actions considered as erroneous and, in the opposite case, to encourage correct actions. Let define $\Pi^t = \{P^t_{L,L}, P^t_{L,R}, P^t_{R,L}, P^t_{R,R}\}$ the strategy at time t, if an ErrP is detected, the probability of repeating the action A_t given the target location T_t must be decreased, i.e. $P^{t+1}_{A_t,T_t} = P^t_{A_t,T_t} - \Delta P^t_{A_t,T_t}$. Conversely, if the trial is considered as correct, $P^t_{A_t,T_t}$ is increased for the next time step. The probabilities of other actions given T_t are updated so that $\sum_i P_{A_i,T_t} = 1$. Note that we keep separate models for each possible target location.

We choose a variable step size $\Delta P^t_{A_t,T_t}$ such that probabilities close to chance level are penalized (i.e. $P^t_{A_t,T_t} = 0.5$, for two-action problems). In the current implementation $\Delta P^t_{A_t,T_t} = \eta H(P^t_{A_t,T_t})$, where $\eta = 0.3$ is a constant scaling factor, and $H(x) = -\sum_i^n P(x_i) log_2 P(x_i)$ is the binary entropy function.

Figure 134.2 shows how the optimal strategy is learned using error related potentials. For the three subjects, based on the recognition of error and correct trials the probability of performing the correct action increases for both possible target locations. On average, the optimal strategy Π^* is acquired in about 40 trials.

Conclusions

This study shows a novel use of error-related potentials in the frame of brain-computer interfaces. In the proposed approach, the human user acts as a critic who observes the behavior of an acting agent and emits monitoring signals about its performance. Successful learning of the optimal strategy is achieved by *(i)* single trial recognition of ErrPs as monitoring signals (c.f. Table 134.1), as well as *(ii)* an efficient strategy update mechanism based on these signals (c.f. Fig. 134.2).

Recent studies have linked ErrPs to the theory of reinforcement learning in humans [5]. Similarly, this study exploits ErrPs as a reinforcement signal for an external system to learn the user's intended strategy. Notice that we have reported results on the off-line learning of the optimal strategy. New experiments are currently undergoing to test this approach when the ErrP signals modify the performance of the actual system being monitored.

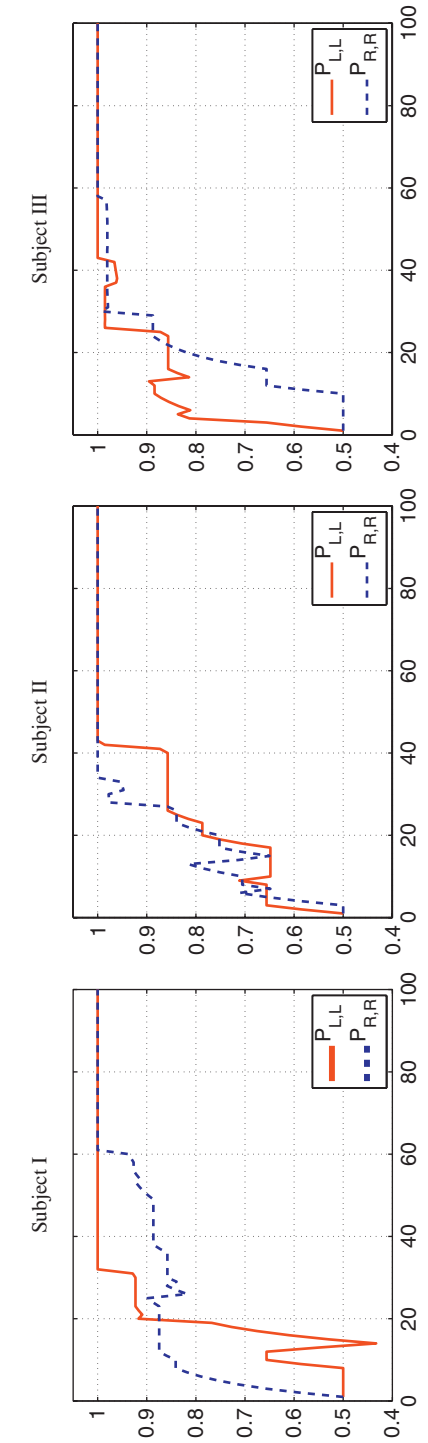

Fig. 134.2 ErrP-based learning of the user's intended strategy for the three subjects. The X-axis represents the time steps and the Y-axis represents the probability of performing the correct action given the current strategy (i.e. $\Pi^t = \{P^t_{L,L}, P^t_{R,R}\}$)

References

1. Sutton, R., Barto, A.G.: Reinforcement Learning – An Introduction. MIT Press, Cambridge, MA, USA (1998).
2. Falkenstein, M., Hoormann, J., Christ, S., Hohnsbein, J.: ERP components on reaction errors and their functional significance: A tutorial. Biol Psychol **51**, (2000) 87–107.
3. Ferrez, P.W., Millán, J.d.R.: You are wrong! – Automatic detection of interaction errors from brain waves. In: Proceedings of the 19th International Joint Conference on Artificial Intelligence, Edinburgh, UK (2005).
4. Parra, L.C., Spence, C.D., Gerson, A.D., Sajda, P.: Response error correction – A demonstration of improved human-machine performance using real-time *EEG* monitoring. IEEE Trans Neural Syst Rehabil Eng **11**, (2003) 173–177.
5. Holroyd, C.B., Coles, M.G.H.: The neural basis of human error processing: Reinforcement learning, dopamine, and the error-related negativity. Psychol Rev **109**, (2002) 679–709.

Chapter 135
Multi-Command Real-Time Brain Machine Interface Using SSVEP: Feasibility Study for Occipital and Forehead Sensor Locations

Pablo Martinez, Hovagim Bakardjian and Andrzej Cichocki

Abstract We propose a new multi-stage procedure for a real time brain machine/computer interface (BMI) based on the Steady State Visual Evoked Potentials (SSVEP) paradigm. The developed system allows a BMI user to navigate a small car (or any other object) on the computer screen in near real time, in any of the four directions. Extensive experiments with 4 young healthy subjects for two different electrode configurations (Occipital/Forehead), confirmed the high performance of the proposed on-line BMI system.

Introduction

A brain-machine interface (BMI) is a system that acquires and analyzes brain signals to create a new communication channel in real-time between the human brain and a computer or a machine [1]. We present a flexible and extendable BMI platform with an application based on the SSVEP paradigm. Although some aspects of the SSVEP BMI paradigm have been already exploited in a number of studies [2, 3, 4], our design is innovative, suitable for real-time applications and more robust to artifacts allowing us to place the electrodes on other areas than the occipital area, as an example forehead locations, for easier sensor application.

Methods

Our BMI system consists on a visual stimulation unit designed as a multiple choice table in the form of an array of four small checkerboard images flickering with different frequencies and moving continuously along with the controlled object,

P. Martinez
Laboratory for Advanced Brain Signal Processing, RIKEN Brain Science Institute 2-1, Hirosawa, Wako-shi Saitama, Japan
e-mail: pablo.martinez@brain.riken.jp

R. Wang et al. (eds.), *Advances in Cognitive Neurodynamics*,

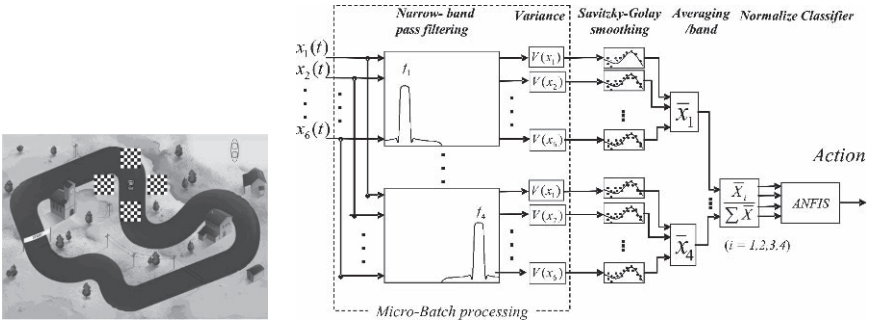

Fig. 135.1 (a) Stimulation unit layout. Four small checkerboards flickering at different but fixed frequencies move relatively slowly along with a navigated car. The subject is able to control the direction of movement of the car by focusing her/his attention on a specific checkerboard. (b) The conceptual block diagram of the developed BMI-platform

Fig. 135.1.a. The BMI analysis unit consist of the following functional blocks: (1) A data acquisition an module, recoding six EEG channels sampled at 256 Hz pre-filtered by means of a high pass filter with a cutoff frequency of 2 Hz. (2) A second Order Blind Source Separation algorithm AMUSE [5] applied for artifact rejection. As AMUSE ranks automatically the EEG components, the undesired components corresponding to artifacts were removed for each time sub-window, by canceling the first and last components and back-projecting the other components to the scalp level [5]. (3) A bank of IIR (Infinite Impulse Response) narrow elliptic band-pass filters of third-order with bandwidth 0.5 Hz and centered at each corresponding flickering frequencies of the four checkerboards, see bellow; (4) The Variance of the filtered signals per each band over time were subsequently smoothed by means of (5) A Savitzky-Golay (S-G) smoothing filter [6]. (6) The mean values for all the channels and a normalization per each band generated a time series of 4 values describing the percentage of energy per each band on the EEG. See Fig. 135.2.b, for an example of the normalized power values per band for one of the subjects in the forehead configuration. (7) The standard Adaptive Network Based Fuzzy Inference System (ANFIS) was used as a classifier [7]. See [8], for a detailed description of the algorithm, Fig. 135.1.b.

We tested our SSVEP-based BMI system for four healthy subjects and for two different ranges/sets of flicker frequencies: Low-Frequency (LF) range -{5,6,7,8 Hz} and Medium-Frequency (MF) range -{12, 13.3, 15, 17 Hz}. For each of these stimulation frequency ranges, we performed experiments for two sets of electrode configurations: (1) Occipital configuration: {CPz, Pz, POz, P1, P2, Fz}. (2) Forehead configuration: six electrodes distributed on the forehead, see Fig. 135.2.a.

Results

Subjects sat on a chair at a distance of 80–100 cm from the center of a 21-inch CRT monitor screen using a refresh rate of 120 Hz. After a short training period, we asked all subjects first to move the car freely to confirm that they had full control of

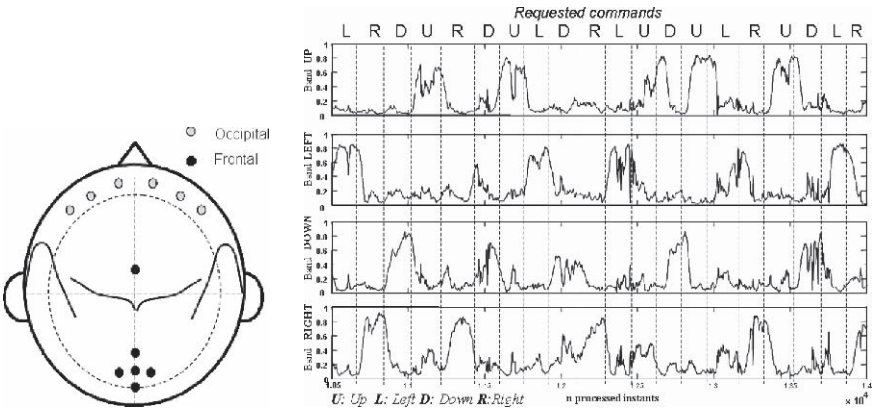

Fig. 135.2 (a) Electrode layouts (b) Normalized multi-band variance evolution during evaluation -a performance example case for one subject with forehead electrode configuration and for MF band pattern flicker

Table 135.1 Experimental results for the Occipital and Forehead configuration for four subjects. Mean values

	LF (5–8 Hz)		MF (12–17 Hz)	
	Occipital	Forehead	Occipital	Forehead
Success rate (%)	93	72	96.5	78
Execution Time [s]	3.5 ± 1.0	4.8 ± 2.0	3.5 ± 1.0	4.5 ± 1.2
Bit rate (bit/min)	26	8.7	30	11.9

the object. To evaluate the performance the computer generated randomly requests for movement in each direction using voice messages. The subject was requested to move the car in one of the four directions at intervals of 9 s in 36 trials (eight trials per direction).

As expected, a better performance has been achieved using the Occipital electrode configuration, with higher transfer rates with lower time delays. For the forehead configuration the subjects' performance was more volatile and time-dependent, although we found that it is possible to achieve promising.However, in the such case it is necessary to apply more advanced signal processing and machine learning tools in order to enhance SSVEP and to reduce influence of artifacts.

Table 135.1 illustrates that for both electrode configurations of electrodes, the best performance was achieved using frequencies in the MF range, i.e. 12–17 Hz.

Conclusions

The occipital configuration allowed the subject to move the any target on the screen with a high degree of control (93%/96.5%), in terms of reliability and speed, while forehead sensor layouts were shown to be also feasible and realistic (72%/78%) although in needs more sophisticated and advanced adaptive signal processing tools

in order to achieve similar performance. Although the SSVEP paradigm has been well known in the BMI community since the studies performed by several research groups [2, 3, 4],we believe that our online BMI system offers several novel points for improved usability and efficiency, such as the integrated moving checkerboards patterns to maximize selective attention and to minimize eye movements respect to the target, as well as an online BSS module to reduce automatically artifacts and noise, improved feature selection algorithm with efficient smoothing and filtering and an adaptive fuzzy neural network classifier ANFIS. In summary, we have shown in this study that it is possible to extract SSVEP responses for BMI by locating the electrodes only in the forehead and possibly another areas which are relatively far from the visual cortex. Such electrode placement design is unusual but much more convenient, although the overall performance may depend increasingly on the subject's state of concentration and attention, thus may lead to a slightly less robust performance than placing the electrodes over the occipital brain area. We believe that the approach described in this study holds a promise for the future application of a substantially increased number of BMI commands with acceptably high reliability and speed, and including also EEG sensors easily placeable on hairless head locations such as the forehead.

References

1. Wolpaw J., Birmbaumer N., McFarland D., and Pfurtscheller G., Vaughan T. *Braincomputer interfaces for communication and control*, Clinical Neurophysiology, 113 (6), 767–791, 2002.
2. Trejo L.J., Rosipal R., and Matthews B. *Brain-computer interfaces for 1-D and 2-D cursor control: Designs using volitional control of the EEG spectrum or steady-state visual evoked potentials*, IEEE Transactions of Neural Systems and Rehabilitation Engineering, 14(2), 225–229, 2006.
3. Middendorf M., McMillan G.R., Calhoun G.L., and Jones K.S. *Brain-computer interfaces based on the steady-state visual-evoked response.* IEEE Transactions on Neural Systems and Rehabilitation Engineering, 8(2), 211–214, 2000.
4. Wang Y., Wang R., Gao X., Hong B., and Gao S. *A practical VEP-based brain-computer interface*, Neural Systems and Rehabilitation Engineering, 14(2), 234–240, 2006.
5. Cichocki A., and S. Amari S. *Adaptive blind signal and image processing: Learning algorithms and applications*, West Sussex: John Wiley & Sons, 2003.
6. Savitzky A., and Golay Marcel J.E. *Smoothing and differentiation of data by simplified least squares procedures*. Analytical Chemistry, 36(8), 1627–1639, 1964.
7. Jang J. *ANFIS: adaptive-network-based fuzzy inference systems*, IEEE Transactions on Systems, Man, and Cybernetics, 23(3), 665–685, 1993.
8. Martinez P., Bakardjian H., and Cichocki A. *Fully-online, multi-command brain computer interface with visual neurofeedback using SSVEP paradigm*, computational intelligence and neurocience (CIN) open issue on brain-computer interfaces (2007).

Chapter 136
Towards Learning Retina Implants: How to Induce Visual Percepts with Electrical Stimulation Patterns

Rolf Eckmiller, Oliver Baruth and Stefan Borbe

Abstract We studied the conditions for joint information processing of a learning retina implant and central visual system in humans with normal vision in preparation of future retina implant applications in the blind. The visual system was modeled by a retina module (RM) as a learning Retina Encoder (RE) with spatio-temporal (ST) filters and a central visual system module (VM). RE performs a mapping of an optical pattern P1 from the physical- onto a neural domain, whereas VM performs a mapping from the neural- onto the perceptual domain and yields a visual percept P2. Our simulation results suggest that the elicitation of 'Gestalt' percepts may be improved by dialog-based RE tuning with evolutionary algorithms and by simulated miniature eye movements. However, considerable efforts in neuroinformatics are still needed to elucidate not only the algorithmic representation of data in the neural domain but also its enigmatic mapping onto the perceptual domain.

Keywords Visual prosthesis · perception · retina · neural processing

Neural Computations of the Visual System in Humans

We recently proposed [1] a model of the human visual system as a sequence of a retina module (RM) and a central visual system module (VM) This model is now being extended by means of oculomotor feedback to provide both miniature eye movements upon request by the central visual system (Fig. 136.1). RM consists of an ensemble of ST filters [2], which mimic the receptive field properties of retinal ganglion cells. RM performs a mapping of an optical pattern P1 in the physical domain onto a neural domain as parallel data stream of neural activity at the retinal output, whereas VM performs another mapping from the neural domain onto a visual percept P2 in the perceptual domain. The two rhombic dotted frames in Fig. 136.1 depict time frames of the parallel data stream of neural impulse activity

R. Eckmiller
Division of Neural Computation, Department of Computer Science, University of Bonn, 53117 Bonn, Germany
e-mail: eckmiller@nero.uni-bonn.de

R. Wang et al. (eds.), *Advances in Cognitive Neurodynamics*,

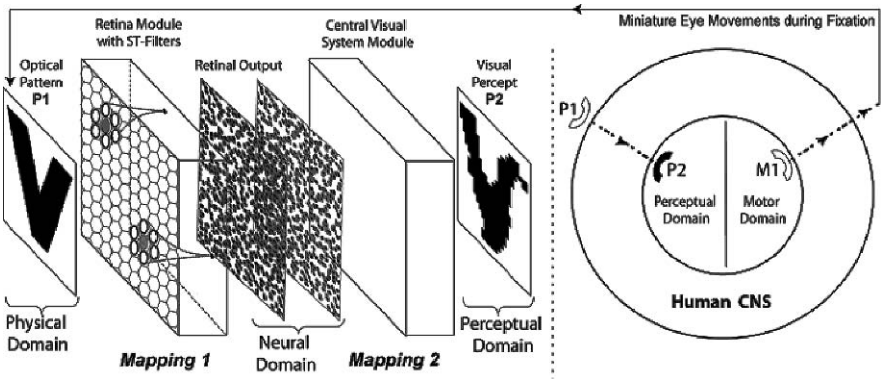

Fig. 136.1 Left: Schema of the primate visual system as sequence of two mapping operations and oculomotor feedback. Retina Module (RM) represents the retina with an array of spatio-temporal ST filters for mapping 1. Central Visual System Module (VM) represents visual and oculomotor brain structures for mapping 2. Right: abstract schema of the central nervous system (CNS) with the physical domain outside, the neural domain, and the perceptual domain as well as motor domain (inside the inner ring). A motor system M1 for extraocular eye movements represents connections from the neural domain back to the physical domain

of all retinal ganglion cells. VM was simulated in our studies by an inverter module, which provided the exact inverse mapping of a selected reference RM [1]. The right side of Fig. 136.1 depicts an abstract schema of the human central nervous system (CNS as ring structure) with the physical domain on the outside, the neural domain between outer and inner ring, and both perceptual domain and motor domain inside the inner ring. A motor system M1 for extraocular eye movements represents connections from the neural domain back to the physical domain.

Psychophysical Requirements for Implant-Induced Vision

Human visual perception transcends neuroscience and biophysics [3, 4]. Humans base their interaction with the physical domain on the assumption that the corresponding visual percepts (in the perceptual domain) are reliable and 'real' optical images. However, another hypothesis says that the function of the central visual system forms an unknown kind of 'gateway' into the perceptual domain. This 'gateway' may be closed unless the neural data stream at its input contains sufficient information and can be disambiguated. Neurophysiological and behavioral data support our hypothesis (Fig. 136.1), that the visual processes use eye movements [5, 6, 7] based on the respec-tive requirements of VM. This hypothesis suggests that visual perception typically re-quires and is achieved by means of perception-specific sensory motor feedback loop sequences.

The principle task of VM (Fig. 136.1) is to elicit a visual percept P2 "corresponding" to P1 in the entirely subjective perceptual domain of a given human. It is postulated here that VM, which receives a pulse-coded signal data stream of the

ensemble of retinal ganglion cells, generates visual percepts only if the corresponding data stream is properly encoded and can be disambiguated.

Implementation of Learning Retina Encoder Features

So far, chronically implanted retina implant models for blind humans with retinal degenerative dysfunctions lack a retina encoder and yield only very basic stimulationinduced visual phosphene sensations rather than 'Gestalt' perception. For our study in humans with normal vision, we assumed the availability of a multielectrode neural interface at the retinal output and explored the conditions for successful joint information processing of both retinal prosthesis and the central visual system. RE performed a first mapping of an optical pattern P1 in the physical domain onto a parallel neural data stream in a neural domain at the retinal output, whereas the simulated VM [1] performed a second mapping of the optic nerve activity from neural domain onto a visual percept P2 in the perceptual domain.

The learning RE dialog module in Fig. 136.2 was implemented with learning algorithms. The subject suggested changes of the RE function in order to optimize the perceptual result, P2. For this purpose, the dialog module generated a set of six

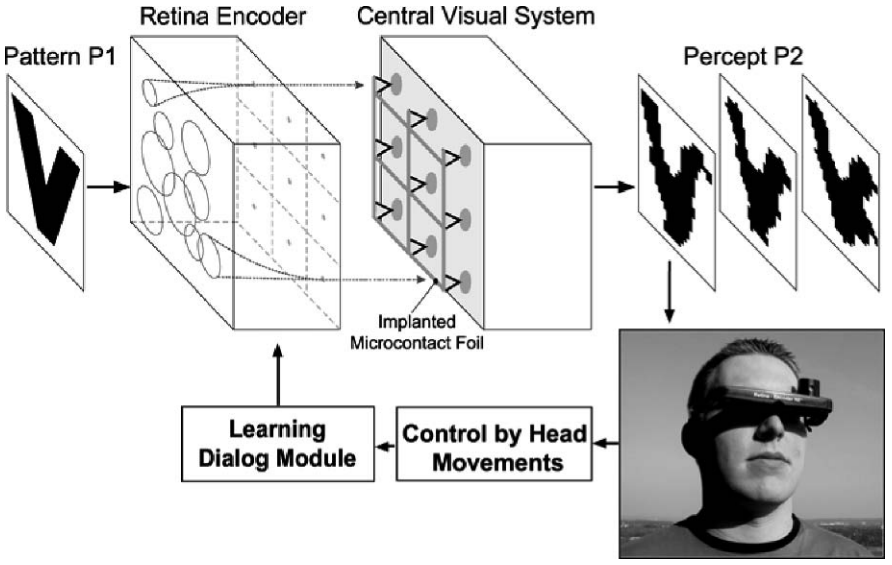

Fig. 136.2 Dialog-based Retina Encoder (RE) learning schema for normally sighted or blind (central visual system (VM)) subjects. Retina encoder output signals reach the simulated VM (forsubjects with normal vision) or, in the future, in blind subjects the electrode array of an implanted microcontact foil (gray rhombic structure with open ellipses as microcontacts). Subject compares visual percept P2 with input pattern P1. Bottom right: normally sighted subject with a portable display with connected acceleration sensors

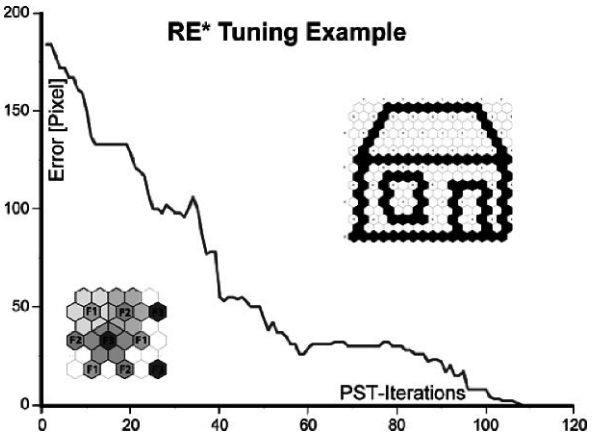

Fig. 136.3 Example for dialog-based tuning of RE* with a selected ST filter configuration (inset in lower left) with three partly overlapping filter types: F1, F2, and F3 on a hexagonal pixel grid. P1: house image. Learning used a position-sensitive tuning (PST) algorithm [9]

RE parameter vectors, which led to six different percepts P2. The subject selected the three "best matching" out of six percepts and signaled the choices to the dialog module, which then generated another six percepts by means of an evolutionary algorithm. As depicted in Fig. 136.2, we are currently working with a portable retina encoder, which provides perceptual feedback signals to the dialog module by means of a set of small head movement signals via a set of head-mounted acceleration sensors [8].

Figure 136.3 gives an example for the dialog-based tuning of RE* [1], which considers both ambiguity removal and simulated miniature eye movements. P1 and P2 on a hexagonal grid consisted of 16 $\times$ 16 pixels. RE* contained 10 $\times$ 10 individually tunable ST filters. The simulation results in Fig. 136.3 indicate that the error between P1 and P2 could be reduced to zero within about 100 position-sensitive tuning (PST) iterations [9]. Finally, the simulation of P2 became identical to P1.

Conclusions

The combination of tunable spatio-temporal filters for a functional simulation of parts of the human retina and of dialog-based learning algorithms provides a powerful technology for visual prostheses. Major research efforts in neuroinformatics, computer science, psychophysics, and ophthalmology are still required to decide, if and to what extent 'Gestalt' perception can be re-gained in the blind by retina implants.

References

1. Eckmiller, R., Neumann, D., Baruth, O.: Tunable retina encoders for retina implants: why and how. J. Neural Eng. **2** (2005) 91–104.
2. Eckmiller, R., Hünermann, R., Becker, M.: Exploration of a dialog-based tunable retina encoder for retina implants. Neurocomputing **26–27** (1999) 1005–1011.
3. Noe, A.: Action in Perception. 2004 (Cambridge: MIT Press).
4. O'Regan, J. K.: Solving the "real" mysteries of visual perception: the world as an outside memory. Can. J. Psychol. **46** (1992) 461–488.
5. Chalupa, L. M., Werner, J. S.: The Visual Neurosciences Vol.1+2. 2004 (Cambridge: MIT Press).
6. Martinez-Conde, S., Macknik, S. L., Hubel, D. H.: The role of fixational eye movements in visual perception. Nature Rev. Neurosci. **5** (2004) 229–240.
7. Rucci, M. Desbordes, G.: Contributions of fixational eye movements to the discrimination of briefly presented stimuli. J. Vision **3** (2003) 852–864.
8. Eckmiller, R., Schatten, R., Baruth, O.: Portable learning retina encoder RE-2 with image segment tuning and head movement control. ARVO Invest. Opththal. & Vis. Sci. **48** (2007) E-Abstract # 654.
9. Baruth, O.: Zur Invertierbarkeit von durch spatio-temporale Filter erzeugten Abbildungen mit besonderem Bezug zur Entwicklung einer lernfähigen Sehprothese. 2007 (PhD thesis, Bonn, in preparation).

Chapter 137
The Effects of Speed Steps on Brain Cognitive Processing: An ERP Study

Lin-Jie Wang, Jin-He Wei, Dan Zhang, Wei-Jun Dong, Jian-Ping Guo and Mao-Qi Hu

Abstract Speed steps were used to elicit cognitive processing variations in order to explore the role of vestibular speed information in cortical level. Constant 30°/s, 60°/s, 90°/s and 120°/s rotation were given as speed steps. During rotation the subjects were asked to perform auditory selective attention task, that is prerecorded Chinese numbers 2–9 with a random interval around 1 s. Subjects were asked to respond to the odd number (target signal, T) by pressing a button and withhold to the even number (non-target signal, NT). It was found that during 30°/s rotation the P3 latencies induced by non-target signal were the shortest and during 120°/s rotation it was the slowest. Non-target P3 latency and speed steps showed significant linear correlation. It was suggested that although in vestibular physiology concept the angular velocity responses have nothing special compared to control, the automatic non-target processes were influenced by the increasing of speed step.

Keywords Speed steps · event-related potentials · P3

Introduction

Ethological studies performed on vestibular disorder patients and healthy adults accumulated to suggest that cognitive function was involved in the vestibular and ocular motor processing [1]. But the concept of the constant velocity's physiological response still remains in its original level. As far as we known, during rotation at a constant velocity, after about 20 s viscous drag of the endolymph causes the endolymph to rotate at the same rate as the semicircular canal, and the cupula restored to its rest position [2]. It seems that the angular velocity value during the constant velocity rotation has nothing to do with its responses, but the results from psychophysical and neurophysiological experiments gave another answer. Loose R and Probst T had verified that it was the achieved angular velocity not acceleration

L.-J. Wang
Laboratory of Gravitational Physiology, Institute of Space Medico-Engineering, Beijing, P.R. China, 100094
e-mail: wlj823@sina.com

R. Wang et al. (eds.), *Advances in Cognitive Neurodynamics*,

that predominated on the perception of visual motion direction during vestibular stimuli [3]. Psychophysical studies showed that our speed sensitivity was better than our acceleration sensitivity [4]. Price NSC et al studied the physiology and modeling of acceleration and speed tuning in Macaque MT (cortical middle temporal area) [5]. And they found that the detection of velocity modulations was not directly based on an acceleration signal, but was generated from the velocity signal. The next step they predicted was to measure responses to speed steps and ramps in brain stem regions and higher level cortical areas. Our previous works have explored the psycho-physiological responses of vestibular stimuli that were angular accelerations and constant 10°/s rotation. And it was found that constant 10°/s rotation had an activating effect on the late attention selection process and constant angular acceleration had an inhibition effect on the cognitive processes [6]. In this paper the psychophysical response of constant velocity ramps on cognitive processing were studied and it was demonstrated that increasing speed step affected the brain autonomic non-target processing.

Materials and Methods

Participants

Thirty students (male 16 and female 14, aged 19–25, with a mean age of 20.4) participated in this experiment.

Task

The go/no-go auditory stimulus was one-digit Arabian number 2–9 in Chinese pronunciation with about 1000 ms interval that pre-recorded on a Sony MD-N1. The subjects were asked to press the button as soon as possible after hearing the odd numbers (Target signal, T) and withhold to the even numbers (Non-target signal, NT).

Vestibular Stimuli

The constant angular velocity rotation was performed by the Nystagliner PRO rotary chair (Toennies, JAEGER, Germany). The chair was accelerated at $10°/s^2$ to the constant angular velocity, that is 30°/s, 60°/s, 90°/s and 120°/s respectively, and rotated at the speed for 5 min then decelerated at $10°/s^2$ to stop.

Each subject had four constant velocity rotation trials with different angular velocity. During each vestibular stimulus trial, subject performed two sets of 150 s auditory tasks with 10 s interval. The rotating direction (i.e. counter clockwise or clockwise) and angular velocity value of each vestibular stimulus trial were

randomly counter balanced. Subjects were permitted to rest for 2 min after each rotation.

Electroencephalogram Recording

EEG Holter system (Medilog95, Oxford, Great Britain) was used to record all EEG activities, eye movement, the auditory task signals and the button press signals. The scalp potentials were recorded using a 12 channel electrode cap and recording locations were in compliance with the recognized Standard International 10–20 system sites – F_3, F_4, F_z, C_3, C_4, C_z, P_3, P_4, P_z, T_3, T_4 and O_z. All scalp channels were referred to the linked mastoids. The central prefrontal electrode was used as ground. The two vertical EOG electrodes were placed above and below the left eye. The two horizontal EOG electrodes were placed at the external canthus of each eye.

All electrode impedances were maintained below 5 kΩ. EEG signals were amplified and filtered with a frequency range of 0.05–70 Hz. The amplified signals were sampled at a rate of 256 Hz. Sampled data were stored on PC card with a storage capacity of 260 MB.

Analysis

The EEG data sections with obvious artefacts were excluded, and eye movement was corrected by least square linear regression in terms of EOG signals The ERPs were computed separately using the EEG epochs that began 200 ms before and ended 720 ms after the onset of each category auditory stimulus. The first 200 ms were used to compute the baseline.

The P3 peak mean amplitudes and latencies, within 290–700 ms respectively, were measured from the ERPs elicited by target and non-target auditory signal and submitted to three-way ANOVAs, with the stimulus type (target or non-target), electrode location (F_3, F_4, F_z, C_3, C_4, C_z, P_3, P_4, P_z, T_3, T_4 and O_z) and constant angular velocity (30°/s, 60°/s, 90°/s and 120°/s). Least Significant Difference test was used for multiple comparisons.

Results

Reaction Times and Accuracy

The accuracy and reaction times (RT) exhibited similar values irrespective of the different constant velocity rotation. The control condition exhibited a relative shorter reaction time (control: 458 ± 59 ms, 90 ± 6%; 30°/s: 466 ± 59 ms, 91 ± 6%; 60°/s: 466 ± 70 ms, 90 ± 6%; 90°/s: 470 ± 61 ms, 90 ± 6%; 120°/s: 472 ± 60 ms, 91 ± 7%). No significant difference was found among different vestibular stimuli in terms of the averages of the RT and accuracies.

Amplitudes of P3 Components

P3 amplitudes showed a significant main effect of electrode sites [$F_{(11,119)} = 23.615$; $p < 0.001$] with largest amplitudes at P_z electrode. There was also a significant angular velocity effect for P3 amplitudes [$F_{(4,119)} = 16.602$; $p < 0.001$]. The P3 amplitudes in control and constant 120°/s rotation were significantly larger than that in constant 30°/s, 60°/s and 90°/s rotation ($p < 0.05$). The P3 amplitudes in constant 30°/s rotation were significantly lower than that in control, constant 60°/s, and 120°/s rotation ($p < 0.05$). A significant effect of signal type [$F_{(1,119)} = 209.013$; $p < 0.001$] indicated P3 amplitudes of target signal ERPs were larger than that of non-target signal ERPs. The signal type × electrode interaction [$F_{(4,119)} = 6.573$; $p < 0.001$] was also of significant changes.

Latency of P3 Components

P3 latencies showed a significant electrode sites effect [$F_{(11,119)} = 23.948$; $p < 0.0001$] with shortest latencies at P_3. A significant signal type × angular velocity interaction [$F_{(4,119)} = 2.800$; $p < 0.025$] with significant difference in non-target ERPs [$F_{(4,4)} = 2.599$; $p < 0.035$]. And non-target ERPs P3 latency in constant 30°/s rotation was significantly shorter than that in constant 90°/s and 120°/s rotation ($p < 0.03$). The non-target P3 latency emerged a slowly increasing trend with the increasing of angular velocity. Figure 137.2 showed the regression result between angular velocity and non-target ERPs P3 latency and gave the linear function.

$$Y = 523.7 + 0.2786678^{*}X \tag{137.1}$$

In function 136.1, Y represented P3 latencies of non-target ERPs and X was angular velocity.

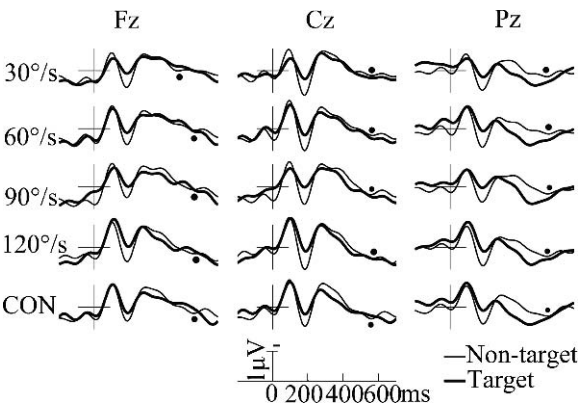

Fig. 137.1 Grand average ERPs of target and non-target signal ($n = 30$) (Filled circles represent the P3 component of Non-target ERPs)

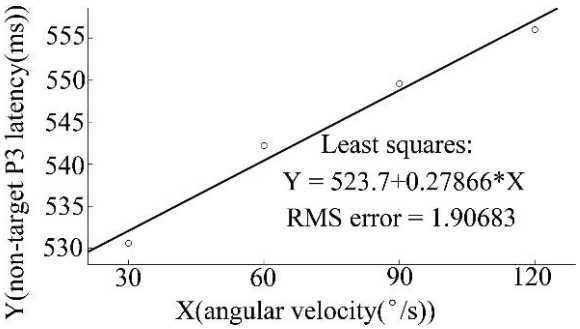

Fig. 137.2 The least square regression between angular velocity and the P3 latency of Non-target ERPs

Discussion

In present study the explicit role of speed steps on cognitive processing were depicted.

On the one hand, the reaction times and accuracies of different constant velocity rotation had no significant change compared with control. Another time these results gave the evidences that the behavioral responses to constant velocity rotation were nearly the same. At least work efficiency did not vary with different constant rotation speed.

On the other hand, P3 amplitude was lowest in $30^\circ/s^2$ and largest in control and $120^\circ/s^2$ and the regression between non-target P3 latency and velocity present significant linear correlation. As P3 amplitude reflects demands on "perceptual-central" resources [7], it may demonstrated the little cognitive resources needed in the low velocity and higher brain resources expended in high speed. Kayatama J et al suggested that the P3 from non-target stimuli may be a useful parameter to distinguish automatic processes among various clinical populations [8]. Salisbury DF et al had found that the increased frontal P3 in no-go tasks not only attributed to a positive-going inhibitory process and memory-related process, it may also reflect negative voltage response execution processes on go trials [9]. Ford argued that P3 latency reflected the depth of processing [10], and thus the linear non-target P3 latency variations with the angular velocity value may reflect the automatic non-target processes were influenced during different constant velocity rotation. And with the increasing speed step the less extensive processing of non-target stimuli, the increase difficulty of inhibition response and the prolongation of memory-related process were successively occurred.

Acknowledgements This work was supported by Experimental Technique Grant from Ministry General Equipment (No. 01101307) and National Science Foundation Grant (No. 30670715).

References

1. Talkowski ME, Redfern MS, Jennings JR, Furman JM: Cognitive requirements for vestibular and ocular motor processing in healthy adults and patients with unilateral vestibular lesions. J. Cogn. Neurosci. 17 (2005) 1432–1441.

2. Robert WB, Vicete H: Clinical neurophysiology of the vestibular system (Edition 2) contemporary neurology series. F.A. Davis Company, Philadephia (1990).
3. Loose R, Probst T: Velocity not acceleration of self-motion mediates vestibular-visual interaction. Perception 30 (2001) 511–518.
4. Yakushin SB, Raphan T, Cohen B.: Spatial properties of central vestibular neurons. J. Neurophysiol. 95 (2006) 464–478.
5. Price NSC, Ono S, Mustari MJ, Ibbotson MR.: Comparing acceleration and speed tuning in macaque MT: physiology and modeling. J. Neurophysiol. 94 (2005) 3451–3464.
6. Wang LJ, Wei JH, Zhang D, Dong WJ, Guo JP, Hu MQ.: The effects of vestibular stimuli on brain cognitive processing: an ERP study. Neuroreport 15 (2004) 2757–2760.
7. Kok A.: On the utility of P3 amplitude as a measure of processing capacity. Psychophysiology 38 (2001) 557–544.
8. Kayatama J and Polich J.: Auditory and visual P3 topography from a 3 stimulus paradigm. Clin. Neurophysiol. 110 (1999) 463–468.
9. Salibury DF, Griggs CB, Shenton ME, McCarely RW.: The NoGO P3 ‘anteriorization’ effect and response inhibition. Clin. Neurophysiol. 115 (2004) 1550–1558.
10. Ford J, Pfefferbaum A, Tinklenberg J, Kopell B.: Effects of perceptual and cognitive difficulty on P3 and RT in young and old adults. Electroencephalogr. Clin. Neurophysiol. 54 (1982) 311–321.

Chapter 138
Design and Implementation of the Adaptive Teachable Agent

SungHyun Yun, DongSeong Choi and SungIl Kim

Abstract Traditionally intelligent tutoring system (ITS) uses expert model to deliver knowledge and train skills to users. According to the theories of leaning, learning by teaching method is more efficient for enhancing motivation to learn and cognitive ability than learning by listening or learning by reading. For the purpose of developing an intelligent agent to enhance the motivation to learn, the new type of teachable agent were designed and implemented, in which the user plays a role of a tutor by teaching the agent. In addition, we provide adaptive user interface where each user plays his/her own scenario according to level of interests and motivation. We design the program to teach the agent about 'rock cycle'. The program consists of four modules: teach module, Q&A module, test module, and network module. In teach module, the user teaches the agent and the agent's knowledge is structured and organized. In Q&A module, the user answer the question through an interactive window. In network module, the database server gathers log data of users to measure users' interest and motivation about TA. It is expected that providing the user with the active role of teaching the agent enhance the motivation to learn and the positive attitude toward the subject matter as well as cognition.

Keywords TA (teachable agent) · intelligent tutoring system · learning by teaching · concept map · motivation to learn · inference engine · knowledge representation

Introduction

The traditional intelligent tutoring system (ITS) provides the learning materials and practice drills repetitiously to train the students and the level of student's learning is evaluated by the computer. The ITS has received the criticism that the iterative nature of learning and the passive role of the learner does not enhance the learner's motivation and cognition [1, 2, 3]. To overcome this limitation of ITS, the system should provide the learners with a chance for deep learning and allow them to play

S. Yun
Division of Information and Communication Engineering, Baekseok University, Cheonan, Korea
e-mail: shyoon@bu.ac.kr

R. Wang et al. (eds.), *Advances in Cognitive Neurodynamics*,

an active role in the process of learning. One way of providing an active role for the learners is to give them an opportunity to teach. The researchers in the field of cognitive science and learning science suggest that the teaching activity induce the elaborative and meaningful learning. A lot of research findings have shown the beneficial effect of learning by teaching [1, 4, 5].

This study introduces the design of the new type of intelligent teachable agent system, called KORI (KOREa university Intelligent agent), for maximizing the motivation to learn and enhancing cognitive ability based on concept of 'learning by teaching'. For the KORI as a student, it is necessary to use AI (Artificial Intelligence) algorithm to construct the knowledge-based of the KORI. The concept map is used to teach the learning material and the inference engine is used to create the new knowledge.

The KORI consists of four independent modules: teach module, Q&A module, test module, and resource module. In teach module, the users teach KORI by drawing a concept map. In Q&A module, both the users and KORI ask questions and answer each other through an interactive window. To assess KORI's knowledge and provide feedback to the users, the test module consists of a set of predetermined questions that KORI should pass. In the resource module, the users can refer to the basic concepts to teach or explore the additional expanded information whenever they want in order to teach, ask questions, and provide feedbacks.

The KORI's brain can represent the knowledge based on the concept map and make new knowledge through the inference engine and it becomes more intelligent by the student tutor.

In the section 'Teachable Agent', the Teachable Agent (TA) and our motivation to implement KORI are introduced. In the section 'The Architecture of the KORI's brain and Implementation Details', the structure of the KORI's brain and the implementation details are discussed. In the section 'Conclusion', the conclusion and the implications for the future work are described.

Teachable Agent

The fact that the active and meaningful learning occurs through the teaching process is reported consistently in the research area of learning science [1]. [1] showed that students who studied for the purpose of teaching other students understood the article better than those who studied for the qualifying examination. In addition, there are many variations of the instructional methods based on the concept of 'learning by teaching', such as reciprocal teaching, peer tutoring, or self-explanation [2, 3]. TA is a computer program where students teach the computer agent to maximize their motivation to learn and to enhance the cognitive ability [5, 6]. TA provides the student tutors with an active role so that they can have a positive attitude toward the subject matter. Teaching activity consisted of sub-activities such as memorization and comprehension, knowledge reorganization, explanation, demonstration, questioning, answering, and evaluation, and so on. These sub-activities lead

to elaboration, organization, inference, and metacognition. In terms of motivational aspects, allowing the learner to play a tutor role can enhance the learners' motivation, which instills a sense of responsibility and increases a feeling of engagement, self-relevance, and situational interests to persist in learning [5].

The Architecture of the KORI's Brain and Implementation Details

Students teach the KORI by drawing a concept map and then the KORI creates its own knowledge through the inference engine, and updates it through the feedback mechanism. Figure 138.1 shows the schematic representation of the interface between KORI and the user to construct the KORI knowledge.

The following modules are used to design and implement the KORI's brain.

Concept map - to construct the KORI's knowledge
Knowledge inference engine - to make inferences and decisions
Search engine - to make, modify and search link paths between objects in the concept map

Knowledge Representation Based on the Concept Map

Concept map is used to structure and organize knowledge into objects and relations [7, 8]. In KORI system, the objects are represented by the boxes and the relations between objects are represented by the arrows with the specific description of the relation. KORI also can represent the inheritance between objects as in semantic network.

The user can put the concepts whatever he/she want and draw arrows between concepts to indicate their relations. In the main window of the screen, the user types

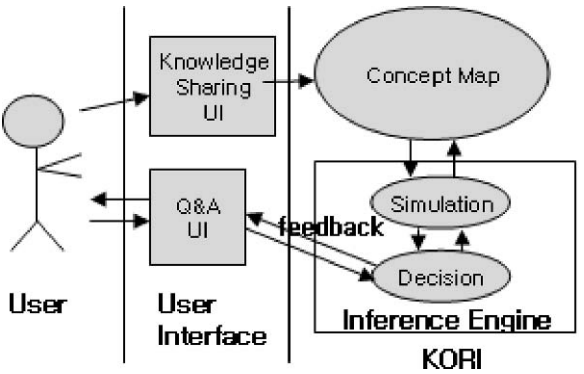

Fig. 138.1 Knowledge construction interface between the user and KORI

Fig. 138.2 Representation of objects and their relations

the name of rock in the box and represents the transformation between rocks with the arrow.

Figure 138.2 shows an example of the concept map construction. In this study, the learning material is about the 'rock cycle'. The object 'sedimentary rock' has a relation with the object 'deposit'. To represent the relation between these two objects, an arrow is used with the specific description of 'be weathered'. In this example, each object has a transitive relation. The users can deliver their knowledge on the rock cycle through the concept map.

Knowledge Inference Engine

Using the forward and backward reasoning on objects, the KORI's knowledge inference engine makes new relations between objects that are not represented in the concept map. In KORI, the reasoning process occurs when the user asks the specific type of questions to the KORI. With the structured input interface where all objects and relations are displayed in pull-down menu, and the user can generate questions by selecting them.

Figure 138.3 shows an example of reasoning process through the knowledge inference engine. The user defines the 'sedimentary rock' object and the 'deposit' object. He/she specifies the relationship between these two objects by drawing an arrow with the description of 'be weathered'. Then, the user also defines the 'soil' object and draws an arrow with the 'be weathered' label from the 'deposit' object to the 'soil' object. After the user has finished drawing the concept map, the KORI activates inference engine with the predetermined rules that find a new relations between the 'sedimentary rock' and the 'soil'. The dotted arrow with 'be weathered' label shows the result of this reasoning processing. Using these two diagrams, the KORI represents its own knowledge and generate answers to students' questions.

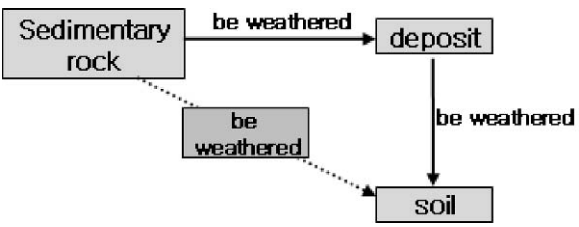

Fig. 138.3 New knowledge construction through the inference engine

Conclusion

In this study, the design and implementation of the teachable agent KORI was introduced, which is a modified version of traditional intelligent tutoring system that assigns the user for the tutor role to teach the agent to enhance motivation to learn and cognition ability. The KORI's knowledge is constructed and organized through the concept map and KORI makes new knowledge from it through the inference engine. The user interface of KORI consists of the teach module, the Q&A module, the test module, and the resource module. It is expected that teaching KORI would not only maximize the users' motivation and cognition, but also increase their self-efficacy and responsibility through various interactions and an immediate feedback.

Future research in the field of the intelligent tutoring agent should focus on the learners' motivation. The new generation of teachable agent should be able to reflect the individual differences in cognitive abilities, interest and motivation, and ongoing changes of the interest level. In addition, the dialog based query input interface to increase the interactivity and the learner control would make the teachable agent more interesting and efficient. To enhance the intelligence of teachable agent, various ways of knowledge construction should be developed and the collaborative learning system, in which multi-user can teach the agent by sharing knowledge, should be implemented.

References

1. Bargh, J.A. & Schul, Y, "On the cognitive benefits of teaching," Journal of Educational Psychology, 72, pp. 593–604, 1980.
2. Chi, M.T.H., Siler, S.A., Jeong, H., Yamauchi, T., & Hausmann, R.G., "Learning from human tutoring," Cognitive Science, 25(4), pp. 471–533, 2001.
3. Graesser, A.C., Person, N., & Magliano, J., "Collaborative dialog patterns in naturalistic one-on-one tutoring," Applied Cognitive Psychologist, 9, pp. 359–387, 1995.
4. Biswas, G., Schwartz, D., Bransford, J. & TAG-V, "Technology support for complex problem solving: From SAD environments to AI," In Forbus and Feltovich, (Eds.), Smart Machines in Education (pp. 71–98). Menlo Park, CA: AAAI Press, 2001.
5. Kim. S., Kim, W.S., Yoon, M.S., So, Y.H., Kwon, E.J., Choi, J.S., Kim, M.S. Lee, M.J., & Park, T.J., "Understanding and designing teachable agent," Journal of Korea Cognitive Science, 14(3), pp. 13–21, 2003.
6. Brophy, S., Biswas, G., Kaltzberger, T., Bransford, J., & Schwartz, D., "Teachable agent: Combining insights from learning theory and computer science," Vandervielt, LTC, 1999.
7. Novak, J.D., "Concept mapping as a tool for improving science teaching and learning," In: D.F. Treagust; R. Duit; and B.J. Fraser (Eds), Improving Teachable and Learning in Sceince and Mathematics (pp. 32–43). London: Teachers College Press, 1996.
8. Stoyanov, S., & Kommers, P, "Agent-support for problem solving through concept-mapping," Journal of Interative Learning Research, 10 (3/4), pp. 401–442, 1999.

Chapter 139
The Convertible Undeniable Multi-Signature Scheme

SungHyun Yun, Hyung-Woo Lee and MyungHo Lee

Abstract In the convertible undeniable multi-signature scheme, signers can convert undeniable multi-signature to the ordinary one. The authenticity of confidential document signed by undeniable multi-signature scheme can only be verified with co-operation of all signers. If the document is no longer confidential, it can be opened to public use by converting the undeniable multi-signature to the ordinary one. In this study, the efficient multipurpose convertible undeniable multi-signature scheme is proposed. The proposed scheme satisfies undeniable property and can be used to protect ownership of multimedia contents made by many authors.

Introduction

By using an undeniable multi-signature scheme, signers can make a multi-signature on the document. However, the multi-signature on the document has no self verification property which is available in ordinary multi-signature scheme. To verify the authenticity of the undeniable multi-signature, all signers must participate in the signature verification stage. A signed confidential document of a company can be copied and delivered to a rival company. If a conventional multi-signature scheme is used to sign the document, it can be confirmed as authentic by verifying the signature without signers' cooperation. However, if the company doesn't want the document to be verified as authentic by the rival company, it is recommended to use the undeniable multi-signature scheme [1].

Convertible undeniable multi-signature scheme has additional property that undeniable multi-signature can be converted to the ordinary multi-signature by releasing partial secret information. The document signed by undeniable multi-signature scheme that is no longer confidential can be opened to public use by converting the undeniable multi-signature to the ordinary multi-signature.It has many applications where an ordinary digital multi-signature scheme can not be applied to.

S. Yun
Division of Information and Communication Engineering, Baekseok University, Anseo-dong, Cheonan, 330-704, Korea
e-mail: shyoon@bu.ac.kr

R. Wang et al. (eds.), *Advances in Cognitive Neurodynamics*,

In general, a digital audio/viedo multimedia contents is made through cooperation of many authors. In this case, authors of the digital contents want to know whether a distributor sells the contents to customers fairly. Authors can satisfy online sales model if the model provides the mechanism that the customer can not buy the digital contents without help of the authors. The digital copyright generated by undeniable multi-signature scheme differs from the ordinary copyright in that the customer can not distinguish between valid and invalid copyright without help of copyright owners. Only the original owners can confirm this copyright as authentic to the customer [1].

However, in customers' position, they want to verify the signature on the digital contents by themselves after purchasing the contents. In this case, customers can satisfy if the copyright owners make the undeniable multi-signature on the contents to the ordinary one. Convertible undeniable multi-signature scheme can be used to solve these problems.

In the section, 'The Proposed Scheme', the proposed convertible undeniable multi-signature scheme is presented. Conclusion and application of our scheme are discussed in the section 'Conclusion and Application of the Proposed Scheme'.

The Proposed Scheme

To make the proposed scheme, we modify the El-Gamal signature equation [2], let $k(m_h + s) \equiv xr \ (mod\ p-1)$, and extends it to accept undeniable properties of D.Chaum's scheme [3] and multi-signature properties [4, 5]. The proposed scheme consists of multi-signature generation, multi-signature confirmation, disavowal and conversion protocols. The following parameters are used in the proposed scheme.

Authors: $u_1, u_2, \ldots, u_n$, Message: $m \in Z_{p-1}$ Author i's Private Key: $x_i \in Z_{p-1}$, Author i's Public Key: $y_i \equiv g^{x_i} \ (mod\ p)$

Multi-Signature Generation Protocol

The message drafter computes the undeniable multi-signature as follows.

Step 1: The message drafter generates hash value $m_h = h(m, hpr)$ and sends (m, hpr) to the first signer u_1.

Step 2: The first signer u_1 let $Y_1 = y_1$. The u_1 chooses a random number k_1 which is relatively prime to $p-1$. The u_1 computes $r_1 \equiv {m_h}^{k_1} \ (mod\ p)$ and sends it to the second signer u_2.

Step 3: The intermediate signer u_i $(2 \le i \le n)$ receives (r_{i-1}, Y_{i-1}) from the u_{i-1}. The u_i chooses a random number k_i which is relatively prime to $p-1$ and computes $r_i \equiv r_{i-1}^{k_i} \equiv m_h^{\prod_{j=1}^{i} k_j} \ (mod\ p)$, $Y_i \equiv Y_{i-1}^{x_i} \equiv g^{\prod_{j=1}^{i} x_j} \ (mod\ p)$. The u_i sends (r_i, Y_i) to the next signer u_{i+1}. If u_i is the last signer, the u_i computes $R \equiv r_{n-1}^{k_n} \equiv {m_h}^{\prod_{j=1}^{n} k_j} \ (mod\ p)$, $Y \equiv Y_{n-1}^{x_n} \equiv g^{\prod_{j=1}^{n} x_j} \ (mod\ p)$ and sends it to all signers as well as the message drafter.

Step 4: Each signer u_i $(1 \leq i \leq n)$ computes the undeniable signature s_i and sends it to the message drafter. Since k_i and $p-1$ are relatively prime integers, there exists s_i satisfying the following equation, $k_i \cdot s_i \equiv x_i \cdot R - k_i \cdot m_h \ (mod\ p-1)$.

Step 5: The message drafter computes the undeniable multi-signature $S \equiv \prod_{j=1}^{n}(m_h + s_j)\ (mod\ p)$.

Multi-Signature Confirmation Protocol

Step 1: The verifier chooses two random numbers (a, b) and computes the challenge $ch \equiv R^{S \cdot a} \cdot Y^{R^n \cdot b}\ (mod\ p)$. The challenge ch is delivered to the first signer u_1.

Step 2: The u_1 computes the response $rsp_1 \equiv ch^{x_1^{-1}}\ (mod\ p)$ and sends it to the second signer u_2.

Step 3: The intermediate signer u_i $(2 \leq i \leq n)$ receives the response rsp_{i-1} from the u_{i-1}. Then the u_i computes the response $rsp_i \equiv rsp_{i-1}^{x_i^{-1}}\ (mod\ p)$ and sends it to the next signer u_{i+1}. If the u_i is the last signer, the response rsp_n is delivered to the verifier.

Step 4: If the equation $rsp_n \equiv m_h^{R^n \cdot a} \cdot g^{R^n \cdot b}\ (mod\ p)$ holds, the verifier ensures that multi-signature is valid. Otherwise, the disavowal protocol is launched to identify whether multi-signature is invalid or some signers have cheated.

Disavowal Protocol

The verifier chooses two random numbers (c, d) and computes the second challenge $ch' \equiv R^{S \cdot c} \cdot Y^{R^n \cdot d}\ (mod\ p)$, $a \cdot d \neq b \cdot c\ (mod\ p-1)$. If the second response rsp'_n is not equal to $m_h^{R^n \cdot c} \cdot g^{R^n \cdot d}\ (mod\ p)$, additional step 5 is required.

Step 5: The verifier makes the discrimination equations. If $R_1 \equiv (rsp_n \cdot g^{-R^n \cdot b})^c\ (mod\ p)$ equals to $R_2 \equiv (rsp'_n \cdot g^{-R^n \cdot d})^a\ (mod\ p)$, the verifier confirms that multi-signature is invalid. Otherwise, some signers have cheated on valid multi-signature.

Conversion Protocol

To convert the undeniable multi-signature to the ordinary one, the first signer generates $g^{k_1}\ (mod\ p)$ and sends it to the second signer. The intermediate signer u_i $(2 \leq i \leq n)$ receives $g^{K_{i-1}}\ (mod\ p)$, $K_{i-1} = \prod_{j=1}^{i-1} k_j$. Then the signer u_i computes $g^{K_i} \equiv (g^{K_{i-1}})^{k_i}\ (mod\ p)$ by using k_i. The last signer sends $g^{K_n}(mod\ p)$ to the message drafter. By releasing the $g^{K_n}(mod\ p)$, the undeniable multi-signature can be converted to the ordinary one as follows. The following equation shows that the multi-signature can be verified without help of all signers.

$$x_i \cdot R \equiv k_i(s_i + m_h) \ (mod\ p-1), 1 \leq i \leq n$$

$$Y \equiv g^{\prod_{j=1}^{n} x_j} \ (mod\ p), \quad S \equiv \prod_{j=1}^{n}(m_h + s_j) \ (mod\ p)$$

• multi-signature verification: $(g^{K_n})^S \equiv Y^{R^n} \ (mod\ p)$

Conclusion and Application of the Proposed Scheme

In this paper, we propose the convertible undeniable multi-signature scheme. It satisfies undeniable property and can convert undeniable multi-signature to the ordinary one. We discuss how the proposed scheme is used to protect DRM application in on-line and off-line environment. In general, many authors participate jointly in authoring of digital multimedia contents. In this case, the copyright of the digital contents must be shared by all authors. The joint-copyright on the multimedia contents is created through the multi-signature generation protocol. Each author computes the undeniable signature on the contents and sends it to the copyright maker. Then the copyright maker computes the undeniable multi-signature and watermarks it on the digital contents. A distributor sells the digital contents to a customer by on-line. The customer can buy it by launching multi-signature confirmation protocol. Especially, in case of dispute between authors, the disavowal protocol can discriminate whether authors have cheated or the multi-signature is invalid. The customer can not activate digital contents without help of all authors. After purchasing the digital contents, the customer may want to activate the digital contents in off-line environment as well. If the customer request capability of activation on digital contents by himself, the undeniable multi-signature can be converted to the ordinary one by using the proposed conversion protocol with co-operation of all authors.

Acknowledgements This work was supported by the Korea Research Foundation Grant funded by the Korean Government(MOEHRD)(KRF-2006-521-D00464)

References

1. S.H. Yun, H.W. Lee.: The Undeniable Multi-signature Scheme Suitable for Joint Copyright Protection on Digital Contents. LNCS 3333. Springer-Verlag. (2004) 402–409.
2. T. Elgamal.: A Public Key Cryptosystem and a Signature Scheme Based on Discrete Logarithms. IEEE Transactions on Information Theory. Vol IT-31. No 4. (1985) 469–472.
3. D. Chaum.: Undeniable Signatures. Proceedings of CRYPTO'89. Springer-Verlag. (1990) 212–216.
4. L. Harn.: (t,n) Threshold Signature and Digital Multisignature. Workshop on Cryptography & Data Security. (1993) 61–73.
5. S.H. Yun, T.Y. Kim.: A Digital Multisignature Scheme Suitable for EDI Message. Proceedings of 11th International Conference on Information Networking. (1997) 9B3.1–9B3.6.

Chapter 140
A Cognitive-Neuro Computational Lexical Acquisition Model

Heui Seok Lim, Kichun Nam, SeongBom Pyun, ChangWhan Lee and Kunhee Han

Abstract This paper proposes an automatic lexical acquisition model which reflects the characteristics of human language acquisition. The proposed system automatically builds two kinds of lexicon, full-form lexicon and morpheme lexicon by using large corpus as its input. The model is independent of language from which it acquires the lexical knowledge. As experimental results using Korean Sejeong corpus of which size is 10 million Eojeols, the proposed system acquired 2,097 full-form Eojeols and 3488 morphemes. The accumulated frequency of the acquired full-form Eojeols covers the 38.63% of the input corpus and accuracy of morpheme acquisition is 99.87%.

Introduction

The advantages of cognitive neuro model of lexical acquisition are as follows. Frist, the model provides us with a simulator of language acquisition process in brain. Understanding mechanism involved with lexical acquisition contributes to understanding of human lexical processing. Second, understanding of lexical acquisition in human brain plays an important role in understand of representation of mental lexicon. Third, computational model may suggest fruitful areas for experimentalists to investigate. Finally, the intensional lesion study using the computational model is possible which is never possible with human subjects.

Representation of mental lexicon is related with the way of organizing and storing of lexical entries in human brain. Because the organization and representation of mental lexicon result from natural language experiences of people, the characteristics involved in lexical acquisition have influence on the representation of mental lexicon. For this reason, the automatic lexical acquisition system should be designed to reflect the characteristics of mental lexicon.

H.S. Lim
Division of Computer Engineering, Hanshin University, Korea
e-mail: limhs@hs.ac.kr

R. Wang et al. (eds.), *Advances in Cognitive Neurodynamics*,

The recent models of the lexical representation of the morphologically complex words can be divided into three types: the full-list representation model, the decomposition representation model, and the hybrid representation model. The supporters of the full-list model propose that full forms are stored separately in mental lexicon and these full forms are linked together with the related forms [1, 2]. On the other hand, in the decomposition model, the stored representations are composed of roots or stems and affixes, and these morpheme representations are combined to make an inflected word and a derivation word [3, 4]. In the decomposition model, there should be decomposition of the morphologically complex words into the component morphemes before the lexical access and there should be morpheme-based lexical access. The hybrid model proposes that some word representations are stored in the full form and others in the decomposition form [5, 6, 7]. For example, the high frequency words are stored in the full form, while the low frequency words stored in the decomposition form. And the inflected words are accessed in the decomposition form, but the derivation words are accessed in the full form [8].

This paper proposes a cognitive neuro computational model of automatic lexical acquisition and describes results of its application to Korean lexical acquisition.

The Automatic Lexical Acquisition Model

The proposed model is based on the hybrid model of mental lexicon , which builds full-form (Eojeol) dictionary and morpheme dictionary using corpus as its input. Size of the input corpus decides the language experience of the automatic lexical acquisition model. There are three basic assumptions on which the proposed model is based to acquire Eojeols and morphemes.

(1) A high frequent Eojeol is stored as a full-form in mental lexicon so that the Eojeol can be recognized and produced rapidly and efficiently.
(2) An Eojeol which are highly repeated in a fixed context is stored as a full-form in mental lexicon.
(3) A high frequent string in Eojeols which has high productivity of Eojeols by combining with other strings is stored as a morpheme.

Figure 140.1 shows an overall architecture of the proposed model. It consists of three main modules: frequency module, recency module, and morpheme extractor modules. In the frequency module and the recency module, Eojeols are acquired and stored in full-form dictionary based on our basic assumptions (1) and (2). Two kinds of morphemes, head morpheme and tail morpheme are acquired in the morpheme extractor modules. The head morphemes is defined as concatenated form of more than one lexical morpheme and optional grammatical morphemes. The tail morpheme is defined as concatenated form of more than one grammatical morpheme and optional lexical morphemes.

A substring in an Eojeol is decided as morpheme by using entropy value of the every successive syllables which occurred right after the substring in Eojeols. If the

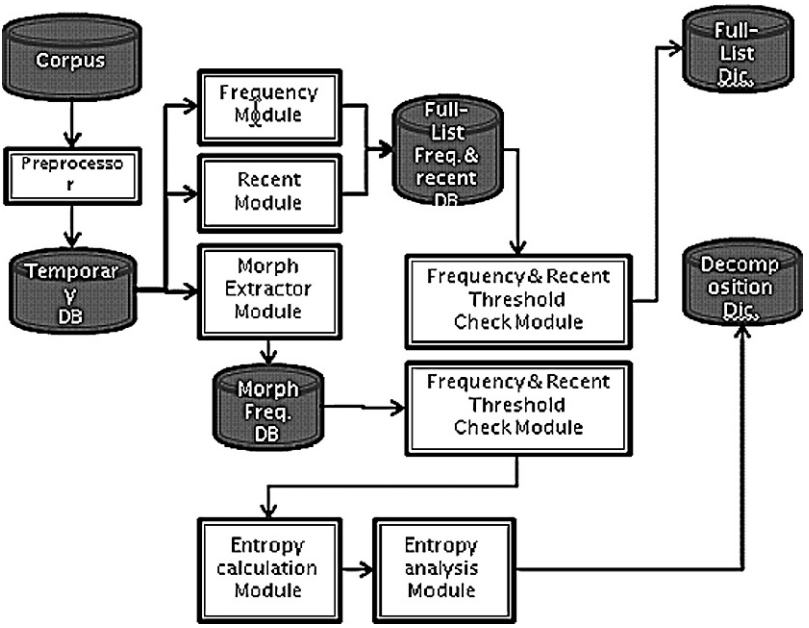

Fig. 140.1 The overall architecture of the model

entropy is high, the substring is likely to be a morpheme. It is because many kinds morphemes which start with different syllables can be combined with the a lexical morpheme or a grammatical morpheme. The entropy of a substring is calculated as Eq. 140.1. $Freq(s, c_i)$ indicate frequency of concatenated string of s and syllable c_i.

$$Entropy(s) = -\sum p_i \, log \, p_i, \; where \; p_i = \frac{Freq(s, c_i)}{Freq(s)} \tag{140.1}$$

There are many different morphemes which have same substring but which is not a morpheme. In this case, the entropy of a substring, may be high, and the substring can be misclassified as a morpheme. To reduce the problem of misclasifying the substring, we double-check whether the substring can a morpheme by using bidirectional entropy verification. If a substring, str is a head morpheme, the rest subtring of the input Eojeol must be a tail morpheme. So, if backward entropy of the rest substring does not exceed the threshold, the str can not be classified as a head morpheme.

Experimental Results

We implemented the model and experimented the system by using Korean Sejong corpus of which size is 10 million Eojeol. The model needs two threshold parameters: ft and rt. The ft is threshold to verify whether an Eojeol is highly frequent or not.

The rt is threshold to verify the recency frequency of an Eojeol. We used 500 and 200 as the ft and the rt threshold. As experimental results, the system acquires 2097 Eojeols in full-form dictionary. The ratio of occurrences of the the acquired Eojeols is 38.63% of the whole corpus. The system acquired 3488 morphemes with accuracy of 99.87%. We decide that the system acquire a correct morpheme if the morpheme is valid in terms of definitions of the head morpheme and the tail morpheme. The accuracy of morpheme acquisition is calculated as in Eq. 140.2.

$$\frac{\textit{The number of morphemes correctly acquired}}{\textit{The number of morphemes acquired}} \tag{140.2}$$

Conclusion

This paper proposes an congnitive neuro computational lexical acquisition model and describes the performance results of the model by using 10 million Korean Eojeol size corpus. The implemented system acquired 2097 highly frequent Eojeols with accuracy of 100% and 3488 morphemes with accuracy of 99.87. To build a computational lexicon, lexical knowledge such as POS information and semantic information is needed. Currently, we are now studying how to acquire such lexical knowledge as well as lexical entries. Also, we are experimenting the model with other foreign corpus as the proposed model is language independent and universal lexical acquisition model. Furthermore, we plan to make integrated lexical processing model which consists of the automatic lexical acquisition model and a lexical analysis model.

Acknowledgements This work was supported by the Korea Science and Engineering Foundation (KOSEF) grant funded by the Korea government(MOST) (No. M10644000033-06N4400-03310).

References

1. Bradley, A. D., Lexical representation of derivational relation. In M. Aronoff, M. L. Kean (Eds.), Juncture, 37–55. Cambridge, MA: MIT Press, (1980).
2. Butterworth, B., Lexical representation. In B. Butterworth (Ed.), Language Produciton, 257–294. San Diego, CA: Academic Press, (1983).
3. Caramazza A., Laudanna, A., Romani, C., Lexical access and inflectional morphology. Cognition, 28, (1988), 207–332.
4. Taft, M., Zhu, X., The representation of bound morphemes in the lexicon : A Chinese study. In L. Feldman (Eds.), Morphological Aspects of Language Processing. Hillsdale, NJ: Erlbaum, (1995), 293–316 .
5. Cole, P., Segui, J. Taft, M., Words and morphemes as units for lexical access. Journal of Memory and Language, 37, (1997), 312–330.
6. Marslen-Wilson, W., Tyler, L. K., Waksler, R., Older, L., Morphology and meaning in the English mental lexicon. Psychological Review, 101, (1994), 3–33.
7. Jung, J., Kim, M., Kim, T., Chae, S., Nam, K., Morphological processing in Broca's Aphasia. The Proceedings of conference of Korean Society of Cognitive Science. (1999), 15–21.
8. Stemberger, J., MacWhinney, B., Frequency and the lexical storage of regularly inflected forms. Memory and Cognition, 14, (1986), 17–26.

Chapter 141
Brain Activation Connected with Visual Word Processing in Korean Language

Hyojeong Sohn, Sung Bum Pyun, Jaebum Jung, Hui-jin Song, Yongmin Chang, Hui Seok Lim and Kichun Nam

Abstract This present study was carried out to investigate the functional role of midfusiform gyrus known as "VWFA (visual word form area)" in visual word processing. In experiment 1, we conducted an fMRI for two dyslexic patients. The results showed that letter-by-letter reading (in fact, syllable-by-syllable reading in Korean) patient has more activation of right fusiform gyrus than global alexic patient in word reading. In experiment 2, volunteers performed word and nonword reading during fMRI scanning. The results showed that the activation area of the left fusiform gyrus was modulated by lexicality and word frequency, whereas the activation of the right fusiform gyrus varied by the word difficulty and nonword reading.

Keywords Dyslexia · visual word · fusiform gyrus

Introduction

It is well known that fusiform gyrus in the left and right hemispheres are responsible for visual word identification and visual object recognition. Recently, the locus of visual word form area and the different role of the left and the right fusiform gyrus in recognizing visual words have been the issue of the lexical identification. Cohen and his colleagues proposed that there is an area specialized for visual word identification in the left hemisphere [1, 2, 3, 4, 5]. They reported several research results to support their assertion. First, the correlation in patients showing pure alexia was presented. Second, they reported neuroimaging results to pin point the visual word form area (TC − 43, −54, −12). However, Price and his co-researchers argued against the above observations [6, 7, 8]. Firstly, Price and Devlin pointed out that the visual word form area is not activated only by the visual word reading but also by naming colors, naming pictures, reading Braille, repeating auditory words, and motoric responses. That is, the visual word from area proposed by Cohen and his

H. Sohn
Department of Psychology, Korea University, Korea
e-mail: Hyojeong.sohn@gmail.com

R. Wang et al. (eds.), *Advances in Cognitive Neurodynamics*,

colleagues is not specific to visual words. In the second argument, they were no cases of pure alexia who had been injured only in the visual word from area. In considering two camps on this issue, each position has its own reason and reasonable argument. Thus, by adopting new method and different orthographies, it is necessary to do new research to see which position is correct. The purpose of the current research is to resolve the controversy between Cohen's and Prices arguments by using the Korean scripts and to decide the role of the right fusiform region in visual word reading.

Method

Subjects

In experiment 1, two patients with alexia after left OT cortex lesion participated. MJ was a 59-year-old right-handed woman and she had developed global alexia after left posterior cerebral artery infarction. She participated in this study 1 month after the onset and was followed up 5 months later. HO was a 56-year-old right handed woman and she had developed intracerebral hemorrhage involving left temporoparietal area. She had revealed characteristic letter-by-letter (LBL) reading and she participated in this study 1 month after the onset and was followed up 7 months later.

In experiment 2, nine right-handed Korean-speaking males (mean age $= 24$, SD $= 5$) participated in current study. They had no history of neurological or psychiatric disorders.

Experimental Design

We acquired fMRI scans at 1 month after the onset of stroke in two patients and followed up 5 months (MJ) and 7 months (HO) later. fMRI was performed during three tasks as picture naming, word reading and pronouncable nonword reading.

Volunteers performed the task including each six blocks of high frequency words, low frequency words, pronounceable nonword, consonants string, checker board and fixation. Two patients and volunteers were trained prior to being in the fMRI scanner with trials similar to those used in the experimental conditions and were instructed to read covertly.

Results

Experiment 1: Patients

Results of word reading task showed remarkable changes in two patients. At follow-up results of MJ, fusiform gyrus or language area were not activated. Whereas right

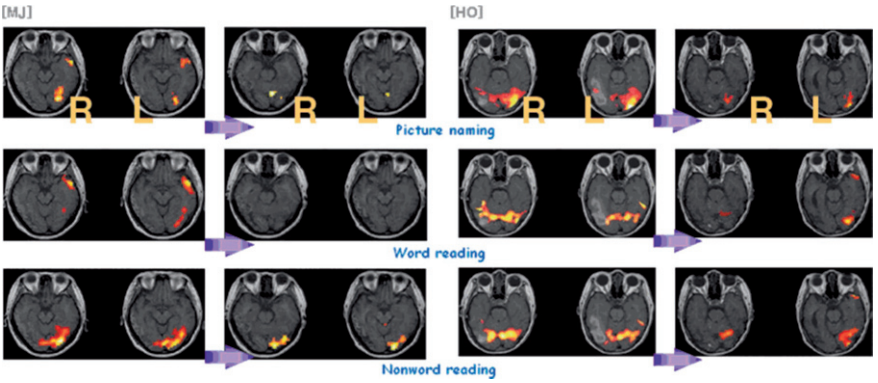

Fig. 141.1 fMRI results of two dyslexic patients. Left two columns: initial and follow-up results of MJ, global alexia. Right two columns: initial and follow-up results of HO, letter-by-letter reader. Top: picture naming task, middle: word reading, bottom: nonword reading. Uncorrected $p < 0.0001$ at a single voxel

fusiform gyrus activated at follow-up results of HO. In other words, letter-by-letter reading patient has more activation of right fusiform gyrus than global alexic patient in word reading (Fig. 141.1).

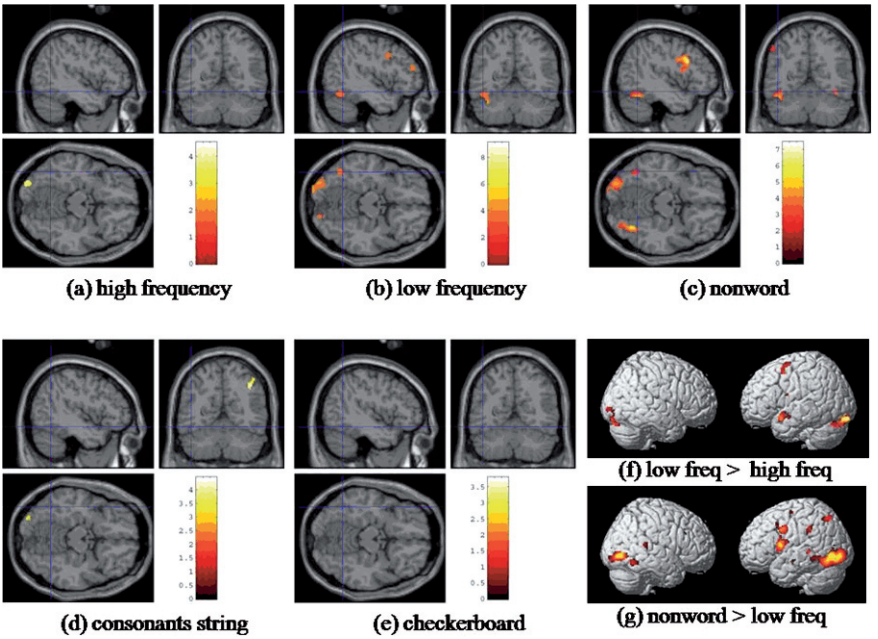

Fig. 141.2 fMRI results of volunteers. The activation in each condition, (**a**)∼(**e**), is the relative value of each task minus baseline(fixation). Uncorrected $p < 0.01$ at a single voxel

Experiment 2: Volunteers

In low frequency word reading and nonword reading, left visual word form area (TC −43, −54, −12) significantly activated. Interestingly, the opposite side of left VWFA at right fusiform gyrus activated in nonword reading task.

The results of Experiment showed that the activation area of the left fusiform gyrus was modulated by lexicality and word frequency, whereas the activation of the right fusiform gyrus varied by the word difficulty and nonword reading.

In conclusion, the specialized area of the left fusiform gyrus manages the normal word reading, and in contrast, the corresponding right area is responsible for the compensatory syllable-by-syllable reading (Fig. 141.2).

Acknowledgements This work was supported by the Korea Science and Engineering Foundation(KOSEF) grant funded by the Korea government(MOST)(No. M10644000033-06N4400-03310).

References

1. Cohen, L., Lehericy, S., Henry, C., Bourgeois, M., Larroque, C., Sainte-Rose, C., Dehaene, S., and Hertz-Pannier, L. (2004) Learning to read without a left occipital lobe: right-hemispheric shift of visual word form area. Annals of Neurology, 56, 890–894.
2. Cohen, L., and Dehaene, S. (2004) Specialization within the ventral stream: the case for the visual word form area. NeuroImage, 22, 466–476.
3. Cohen, L., Henry, C., Dehaene, S., Martinaud, O., Lehericy, S., Lemer, C., and Ferrieux, S. (2004) The pathophysiology of letter-by-letter reading. Neuropsychologia, 42, 1768–1780.
4. Cohen, L., Lehericy, S., Chochon, F., Lemer, C., Rivaud, S., Dehaene, S. (2002) Language-specific tuning of visual cortex? functional properties of the visual word form area. Brain, 125, 1054–1069.
5. McCandliss, B.D., Cohen, L., and Dehaene, S. (2003) The visual word form area: expertise for reading in the fusiform gyrus. TRENDS in Cognitive Science, 7:7, 293–299.
6. Price, C.J., and Devlin, J.T., (2003) The myth of the visual word form area. NeuroImage, 19, 473–481.
7. Price, C.J., Wise, R.J., Warburton, E.A., Moore, C.J., Howard, D., Patterson, K., et al., (1996) Hearing and saying. The functional neuroanatomy of auditory word processing. Brain, 119, 919–931.
8. Price, C.J., Winterburton, D., and Giraud, A.L. (2003) Cortical localization nof the visual and auditory word form areas: a reconsideration of the evidence. Brain and Language, 86, 272–286.

Chapter 142
A GJK Based Real-Time Collision Detection Algorithm for Moving Objects

Sangyoung Oh and Seonmin Hwang

Abstract This paper studies a collision detection technique to dealing with moving polyhedra. Even though the problem is well-studied in computer graphics, the existing methods are inapplicable to highly dynamic environments. We use the GJK algorithm to determine collisions between convex objects. Also, our method is applied for moving objects.

Keywords Collision detection · real-time animation · GJK algorithm · robotics · virtual reality · rigid body

Introduction

Collision detection has received attention in computer graphics, virtual reality, physical simulation, and haptic. The existing work on collision detection can be classified based on the types of models handled: polyhedral models, polygon soups, curved surfaces, etc. [1]. In this paper, we focus on collision detection for polyhedral models.

Hybrid collision detection [2] refers to the algorithm as the broad phase and the narrow phase. The former is approximate intersection tests, the latter is exact collision detection.

The separation distance between two polyhedra P and Q is equal to the distance from the origin to the Minkowski sum of P and −Q [3]. This property was exploited by Gilbert et al. [4] in order to design a convex optimization algorithm (known as GJK). GJK algorithm is one of the most effective methods for determining collision detection between two polyhedra. As originally described, GJK is an efficient and reliable algorithm for computing the Euclidean distance between a pair of convex sets in R^n. The GJK algorithm can also be applied to arbitrary convex points sets,

S. Oh
Division of Business Management, College of Economics and Business Administration, Cheongju University, Korea
e-mail: culture@cju.ac.kr

R. Wang et al. (eds.), *Advances in Cognitive Neurodynamics*,

not just polyhedra [5, 6]. The algorithms depend on the object being rigid, and are hence unsuitable for collision detection between deformable objects.

The algorithms for collision detection between convex polyhedra are not applicable to models described as polygon soups. Bounding volume hierarchies (BVH) have proved successful collision detection for rigid bodies. One determining factor in the design of a BVH is the selection of the type of BV. Some of the common BVs are: spheres [7], axis-aligned bounding boxes (AABB) [8], oriented bounding boxes (OBB) [9], and k-discrete-orientation polytopes (k-DOP) [10]. With deformable objects, the hierarchical approximation must be updated at each frame and hence, computational process is very expensive.

Minkowski Sums and Differences

GJK algorithm does not operate on the two objects, but on the Minkowski difference between the objects. We use $x \cdot y$ for the inner product of $x, y \in R^{\mathrm{m}}$ and $|x|^2 = x \cdot x$. For $X_1, X_2 \subset R^m$, $X_1 \pm X_2 = \{x_1 \pm x_2 : x_1 \in X_1, x_2 \in X_2\}$ denotes the Minkowski set sum or diffenence.

The Minkowski sum can be seen as the region swept by X translated to every point in Y. The Minkowski difference is presented by adding X to the reflection of Y about the origin, that is $X - Y = X + (-Y)$ (Fig. 142.1). If Minkowski difference Z, $Z = X - Y$, contains the origin (Fig. 142.1). Clearly,

$$\begin{aligned} d(X, Y) &= \min\{|x - y| : x \in X, y \in Y\} \\ &= \min\{|z| : z \in X - Y\} \end{aligned}$$

Sweeping Intersection

One approach to dealing with moving polyhedra is presented in Xavier [11]. Consider two polyhedra P and Q, with movements given by the vectors $\mathbf{t}_1$ and $\mathbf{t}_2$, respectively. To simplify the collision test, the problem is recast so Q is stationary. The

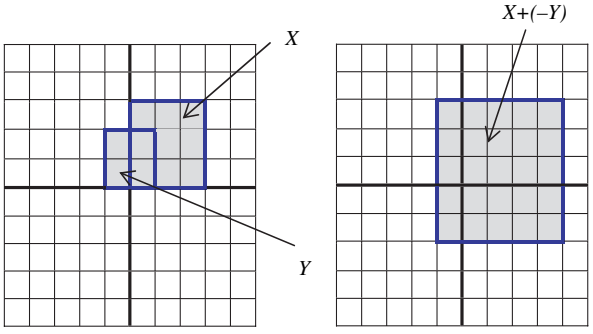

Fig. 142.1 The origin must be contained in their Minkowski difference

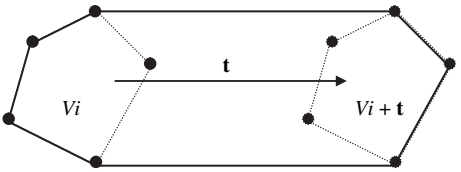

Fig. 142.2 For a convex polyhedron under a translational movement *t*

vector of P is given by $\mathbf{t} = \mathbf{t}_1 - \mathbf{t}_2$. Let Vi be the vertices of P in its initial position. $Vi + \mathbf{t}$ describes the location of the vertices of P at the end of its translational motion. If P moves from start to end over its range of motion, the volume swept out by P corresponds to the convex hull of its vertices at their initial and final positions (Fig. 142.2).

Multi-Level Collision Detection

Multi-level collision detection is able to divide into two phases. In the first phase, we use a fast and rough algorithm likely AABB. In the second phase, we apply the method based on the distance to decide if the moving polyhedra will collide or not.

Our approach decreases the operation by reducing the sweeping test. Sweeping intersection tests detect the intersection between the sweeping volumes of objects over time, or an approximation thereof [12]. However, these tests conservatively report false alarms that never actually occur, because they do not account for the displacement of objects as they move.

Our algorithm proceeds in two phases, as shown in Fig. 142.3. We first use an AABB based culling approach. Next, we perform GJK algorithm based on the distance.

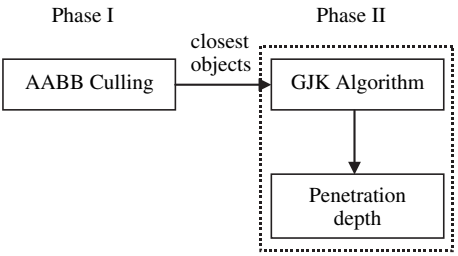

Fig. 142.3 Our multi-level collision detection algorithm proceeds in two phases

Conclusions and Future Work

We have presented in this paper a hybrid method that allows real-time collision detection in complex environments composed of moving objects. We use AABB and GJK algorithm to perform collision detection. Our approach is very fast and can be adopted in a variety of environments. We would like to use our method for other environments such as deformable objects.

References

1. Miguel, A., Otaduy, M., Lin, C.: Introduction to haptic rendering. International Conference on Computer Graphics and Interactive Techniques archive ACM SIGGRAPH 2005 Courses (2005) 11–14.
2. Kitamura, Y., Takemura, H., Ahuja, N., Kishino, F.: Efficient collision detection among objects in arbitrary motion using multiple shape representations. Conference A: Computer Vision & Image Processing, Vol. 1 (1994) 390–396.
3. Cameron, S., Culley, R.K.: Determining the minimum translational distance between two convex polyhedra. Proceedings of International Conference on Robotics and Automation, (1986) 591–596.
4. Gilbert, E., Johnson, D., Keerthi D.: A Fast procedure for computing the distance between objects in three-dimensional space. IEEE Journal on Robotics and Automatin, Vol. 4 (1988) 193–203.
5. Gilbert, E., Chek-Peng, F.: Computing the distance between general convex objects in three-dimensional space. IEEE Transactions on Robotics and Automation, 6 (1990) 53–61.
6. Sunil, H., Dave, E., Pascal, V., Lin, M.C., Stephane, R., Christer, E.: Collision detection and proximity queries. International Conference on Computer Graphics and Interactive Techniques ACM SIGGRAPH 2004 Course Notes (2004).
7. Hubbard, P.: Collision Detection for Interactive Graphics Applications. PhD thesis, Brown University (1994).
8. Beckmann, N., Kriegel, H., Schneider, R., Seeger, B.: The r*-tree: An efficient and robust access method for points and rectangles. Proceedings of SIGMOD Conference on Management of Data, Vol. 19 (1990) 322–331.
9. Gottschalk, S., Lin, M., Manocha, D.: OBB-Tree: A hierarchical structure for rapid interference detection. Proc. of ACM Siggraph'96 (1996) 171–180.
10. Klosowski, J., Held, M., Mitchell, J., Sowizral, H., Zikan, K.: Efficient collision detection using bounding volume hierarchies of k-dops. IEEE Transactions on Visualization and Computer Graphics 4, 1 (1998) 21–37.
11. Xavier, P.: Fast swept-volume distance for robust collision detection. Proceedings of the 1997 IEEE International Conference on Robotics and Automation, Albuquerque, NM, April (1997) 1162–1169.
12. Vlack, K., Susumu, T.: Fast and accurate spacio-temporal intersection detection with the GJK algorithm. Proceedings of the International Conference on Artificial Reality and Telexistence (ICAT) (2001) 79–84.

Chapter 143
Neural Information Encoding Based on a Bifurcation Machinery

Wei Ren, Huaguang Gu, Minghao Yang, Zhiqiang Liu, Li Li, Yulin Xu and Hongjv Liu

Abstract Neural information encoding mechanism based on a bifurcation machinery was proposed based on the results on two experimental models and theoretical models. The framework structures of bifurcation scenarios of neuronal firing pattern were acquired in the experimental neural pacemaker. The dynamics of dynamic neural firing pattern and the neural information encoding of firing patterns were elucidated in the experiment on rabbit depressor nerve, based on the bifurcation structure of firing patterns, and the mean level and temporal procedure of blood pressure.

Keywords Neural information encoding · bifurcation · neural firing · Chaos

Introduction

The rhythm of neuronal firing is central to the information processing in the nervous system. In the working brain, each neuron receives diverse inputs, and outputs the integrated information in the form of firing trains. Since the waveform of each firing spike is identical, the output information from each single neuron is believed encoded in the temporal pattern of its firing trains. Although the physiological significance of neuronal firing rhythm was recognized very long ago, identification of various rhythm patterns and investigation of their mechanisms had been almost impossible for a quite long period of time. There was a lack of high speed data acquisition techniques, and more importantly the fundamental scientific concept describing the complex and usually irregular physiological rhythms was unavailable. In the physiological study of last century, the problem of neuronal encoding by firing trains became an empirical association of the stimulus intensity with the firing rate of the considered neuron.

A large advances in the field of nonlinear science has provided necessary theoretical concepts and a series of powerful tools for a deeper understanding of this

W. Ren
College of Life Science, Shaanxi Normal University, Xian, Shaanxi 710062, China
e-mail: renwei1964@vip.sina.com

R. Wang et al. (eds.), *Advances in Cognitive Neurodynamics*,

physiological problem [1]. In early 1980s, the pioneering research gave a great example for the study of complex (chaotic) firing patterns [2, 3]. Since 1990s, various neuronal firing patterns have been rigorously defined according to the quality of the motions of theoretical neuronal models. In these works, the transitions among different firing patterns have been elucidated by means of bifurcation theories [4, 5]. A further understanding of the rhythmogenesis and its neurophysiological significance requires an approach that integrates nonlinear dynamics and neurophysiology.

Following this approach, our laboratory aims at the basic principles of neuronal firing rhythm transitions and information encoding based on such principles [6, 7, 8, 9, 10, 11, 12]. Neuron is regarded as a neuronal dynamic system capable of qualitatively different firing rhythms. The information input to the neuron affects its corresponding physiological parameters and therefore changes its output firing rhythms. The input effect is then represented in the output changing rhythms via mediate coding dynamic machinery. Since the firing rhythm changes under the driven of physiological parameters through a series of bifurcation processes, the relevant bifurcation scenarios is of key importance in this encoding machinery. A systematic knowledge of firing rhythm bifurcation scenarios will provide a theoretical framework for a further understanding of neuronal information encoding. Over the years, this theme has provided a central rationale for our research.

Experimental Model

Experimental pacemakers are formed at the injured site of rat sciatic nerve subjected to chronic ligature. Surgical operation is performed to produce the pacemaker using adult male SD rats. After a survival time of 8–12 days, the previously injured site is exposed and is perfused continuously with 34 Kreb's solution. The spontaneous spike trains of individual fibers ending at the injured site are recorded with a Maclab system (Australia) with sampling frequency being 10.0 kHz. Meanwhile the spike trains are monitored with the Maclab system during the whole experiment to make sure that the recording is of a single unit. The time intervals between the maximal values of the successive spikes are recorded seriatim as ISI series [6, 7, 8, 9, 10, 11, 12].

Adult male New Zealand rabbit, was anesthetized with urethane intravenously. The trachea was cannulated. Arterial blood pressure was recorded with a cannula pressure transducer connected to an ML221 amplifier from arteria carotis. The depressor nerve was isolated and marinated in an oil pool. A thin bundle of depressor fibers was separated, and its afferent firing trains were induced by means of a fine platinum electrode with a nearby reference and connected to a bioelectrical amplifier. Blood pressure and spike trains of individual fibers were recorded simultaneously with a Powerlab system (Australia) with a sampling frequency of 10.0 kHz and monitored to make sure that the recording was of a single unit during the experiment. The time intervals between the maximal values of the successive spikes were recorded seriatim as interspike interval series. The overall blood pressure level was elevated by intravenous administration of norepinephrine (NE).

Results

We studied the diversity of firing rhythms and the underlying dynamic mechanisms [6, 7, 8, 9, 10, 11, 12]. A variety of spontaneous firing patterns were stably recorded, as environmental parameters were maintained at as constant a level as possible and no perturbing influences could be identified. The rhythms of the observed firing patterns were defined according to the dynamic quality of the firing trains. The observed various periodic rhythms and different chaotic rhythms were identified using nonlinear time series analysis methods and simulated using deterministic and stochastic mathematical neuronal models. Mathematical models based on ionic channels are capable of giving qualitative and sometime quantitative agreements with observed oscillatory behavior. The periodic rhythms were related to the dynamics of limit cycle, and the chaotic rhythms to the strange attractors [6, 7, 8]. Theoretical bifurcation analysis revealed that there were remarkable dynamic differences between the observed spiking and bursting rhythms. It also revealed the 'fast-slow' dynamics of the complex rhythmogenesis. In addition, we observed a number of different 'integer multiple rhythms' and elucidated their stochastic alternating mechanism by adding white noise into the model [9, 10, 11]. The integer multiple rhythms are resulted from the interplay between the inherent fluctuations in real neuron and the fundamental neuronal excitation dynamics. They arose from a stochastic alternation or 'jump' between two neighboring trajectories.

In experiment, a series of bifurcation scenarios among the neuronal rhythms were discovered by adjusting g_{kc}, a physiological 'driving' parameter [7]. Maintaining a 'conditional' physiological parameter, g_{kv}, at different levels, and adjusting the 'driving' parameter under each of the 'conditional' parameter level, the relations among the various bifurcation scenarios in parameter space were analyzed both in experiment and simulation. We found that the global changing patterns of the firing rhythms driven by adjusting specific parameters fallen into a series related categories of bifurcation scenarios. In each of those scenarios, the behavior of the nerve changed from a polarized resting state into firing state, experienced complex firing pattern transitions, and then move into a depolarized resting state. In the observed most complex scenario, the behavior of the nerve was driven from a polarized resting state to period one bursting rhythm via a Hopf bifurcation, then into complex bursting pattern transitions via period doubling bifurcation or period-adding bifurcations with or without chaos, and then from 'crisis' and spiking chaos to a fast period one spiking rhythm via a revise period doubling bifurcation, and finally into a polarized resting state via another Hopf bifurcation. The complete bifurcation structure of the firing state in ISI was located in a limited subspace of the two dimensional parameter space and was surrounded by resting states. The dynamic effects of noise and perturbations near a number of bifurcation points were studied and their stochastic resonance mechanisms were analyzed.

Then, employing an experiment model of blood pressure sensory nerve, the dynamically changing firing patterns under the continuous driven of blood pressure input were recorded from rabbit depression nerve. In this part of experiment and relevant simulation, we studied the information encoding process of a sensory

terminal. The result confirmed the theme that neuronal encoding was based on the bifurcation scenarios of its firing rhythm. The importance of the result is that it appears to typify the general neural dynamic mechanism of information encoding at the sensory terminals. The rich and changing rhythm, which is representing neural information, results from the dynamic perturbation, in 'noisy' physiological context, of the parameters by physiological signals and modulations. The rhythmogenesis is the complex 'evolving' behavior of the neuronal system on the global bifurcation structure driven by the input signals [12].

Discussion and Conclusion

With rigorous identifications of the firing patterns and firing pattern transitions, aided by dynamic system theory, neuronal coding machinery now can be studied as an object of 'exact' science. A systematic investigation of the 'global' bifurcation structures controlled by the biologically significant parameters could provide a basic guiding framework of knowledge to the understanding of neuronal encoding. The encoding process of a neuron is actually its rhythms changing response to the dynamic modulations on its parameters, in the thermal fluctuating and synaptic noisy environment, on the basis of such bifurcation structures. The dynamic temporal relations between the input modulations and the output changing rhythms in the working brain are to be eventually illuminated by the underlying dynamic and stochastic bifurcation machinery.

This work was supported by the NNSF of China under Grant Nos. 30270432, 30300107 and 10432010.

References

1. Izhikevich, E.M.: Neural excitability, spiking and bursting. Int J Bifurcat Chaos 10 (2000) 1171–1266.
2. Hayashi, H., Ishzuka, S., Ohta, M.: Chaotic behavior in the onchidium giant neuron. Phys Lett A 88(8–9) (1982) 435–438.
3. Aihara, K., Matsumoto, G., Ichikawa, M.: An alternating periodic-chaotic sequence observed in neural oscillators. Phys Lett A 111(5) (1985) 435–438.
4. Chay, T.R.: Bursting, spiking, chaos, fractals, and universality in biological rhythms. Int J Bifurcat Chaos 5(3) (1995) 595–635.
5. Holden, A.V., Fan, Y.S.: From simple to simple bursting oscillatory behavior via chaos in the Rose-Hindmarsh model for neuronal activity. Chaos Solitons Fractal 2 (1992) 221–236.
6. Ren, W., Hu, S.J., Zhang, B.J.: Period-adding bifurcation with chaos in the interspike intervals generated by an experimental neural pacemaker. Int J Bifurcat Chaos 7 (1997) 1867–1872.
7. Li, L., Gu, G.H., Yang, M.H.: A series of bifurcation scenarios in the firing transitions in an experimental neural pacemaker. Int J Bifurcat Chaos 14(5) (2004) 1813–1817.
8. Ren, W., Gu, H.G., Jian, Z.: Different classification of UPOs in the parametrically different chaotic ISI series. NeuroReport 12 (2001) 2121–2124.
9. Gu, H.G., Ren, W., Lu, Q.S.: Integer multiple spiking in the neuronal pacemaker without periodic stimulation. Phys Lett A 285 (2001) 63–68.

10. Gu, H.G., Ren, W., Yang, M.H.: Experimental observation of stochastic bursting caused by coherence resonance in experimental neural pacemaker. NeuroReport 13(13) (2002) 1657–1660.
11. Gu, H.G., Yang, M.H., Li, L.: Dynamics of autonomous stochastic resonance in neural period adding bifurcation scenarios. Phys Lett A 319(1–2) (2003) 89–96.
12. Yang, M.H., An, S.C., Gu, H.G., Liu, Z.Q., Ren, W.,: Understanding of physiological neural firing through dynamical bifurcation machineries. NeuroReport 17(10) (2006) 995–999.

Chapter 144
Identify Stochastic Bursting from Chaotic Bursting Generated in an Experimental Neural Pacemaker

Huaguang Gu and Qishao Lu

Abstract The stochastic and chaotic bursting lying between period k and period $k + 1$ bursting ($k = 2, 3$) exhibit similar characteristics such as positive Lyapunov exponent, non-periodic spike trains and deterministic structures such as periodic orbit. The distinctions are identified as different evolutions of the periodic orbit and multi-peaked histogram exhibited in stochastic bursting. The results give practical indicators to distinguish the chaotic bursting and stochastic bursting.

Keywords Chaotic bursting · stochastic bursting · period adding bifurcation · periodic orbit · lyaponov exponent

Introduction

The dynamics of neural firing patterns and firing pattern transition were fundamental to the elucidation of neural encoding mechanism [1]. In the last two decades, various firing patterns and firing pattern transition regularities were simulated in the theoretical neuronal models [2, 3] and discovered in the experiments [4, 5, 6, 7, 8]. Chaotic bursting lying in a period adding bifurcation scenario were discovered in experimental neural pacemaker and were analyzed by nonlinear time series analysis method [4, 5]. In our recent studies, stochastic burstings lying in a period adding bifurcation scenario were also discovered in the experimental neural pacemaker and was verified to be caused by autonomous stochastic resonance (ASR) [6, 7, 8].

The aforementioned chaotic [4, 5] and stochastic bursting [6, 7, 8] lying in period adding bifurcation scenario discovered in the experiment were studied independently. The similarity and distinction between the stochastic and chaotic bursting were seldom studied and remained unclear, and will be studied in this Letter.

H. Gu
School of science, Beihang University, Beijing 100083, China
e-mail: guhuaguang@263.net

R. Wang et al. (eds.), *Advances in Cognitive Neurodynamics*,

Experimental Model and Nonlinear Time Series Analysis Method

Experimental model Experimental pacemakers are formed at the injured site of rat sciatic nerve subjected to chronic ligature. Surgical operation is performed to produce the pacemaker using adult male SD rats. After a survival time of 8–12 days, the previously injured site is exposed. The spontaneous spike trains of individual fibers ending at the injured site are recorded with a Maclab system (Australia) with sampling frequency being 10.0 kHz. Meanwhile the spike trains are monitored with the Maclab system during the whole experiment to make sure that the recording is of a single unit. The time intervals between the maximal values of the successive spikes are recorded seriatim as ISI series [4, 5, 6, 7, 8]. The extra-cellular calcium concentration ($[Ca^{++}]_o$) is taken as the bifurcation parameter.

Method to detect periodic orbit Detection of periodic orbit (PO) is a common method to characterize many dynamics such as deterministic mechanisms of chaotic bursting [4]. In this Letter, method proposed by So et al. [9] is employed to detect period orbits embedded in ISI series of the firing from experiment.

Calculation of Lyapunov exponent A positive maximal Lyapunov exponent is a strong signature of chaos to characterize the sensitivity to initial value. In this Letter, the method proposed by Kantz [10] is employed.

Results

Chaotic and stochastic bursting When $[Ca^{++}]_o$ is decreased, the period 2 bursting was changed to chaotic bursting, to period 3 bursting, to chaotic bursting, to period 4 bursting in some pacemaker, while period 2 bursting could also be changed to stochastic bursting, to period 3 bursting, to stochastic bursting, to period 4 bursting in other pacemakers. The spike trains of the stochastic bursting pattern lying between period k bursting and period $k + 1$ ($k = 2, 3$) bursting is stochastic transition between period k burst and period $k + 1$ burst, as shown in Fig. 144.1a. The spike

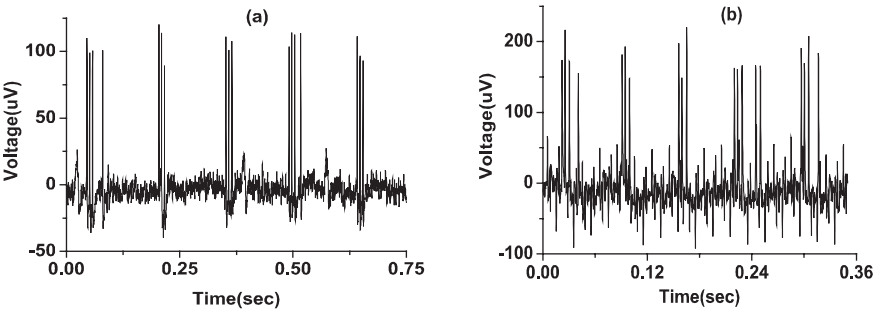

Fig. 144.1 Spike trains of firing lying between period 3 and period 4 bursting. (**a**) stochastic bursting, (**b**) Chaotic bursting

trains of the chaotic bursting contains not only period k and $k + 1$ burst, but also other kinds of burst, as shown in Fig. 144.1b.

Lyapunov exponent The Lyapunov exponent of the ISI series are about 1.263 ± 0.098 and 1.073 ± 0.027, respectively for the chaotic and stochastic bursting lying between period 3 bursting and period 4 bursting, are about 1.273 ± 0.103 and 1.035 ± 0.094 for the chaotic and stochastic bursting lying between period 2 bursting and period 3 bursting are about, respectively. Little difference is exhibited between the values of Lyapunov exponent.

PO in the ISI of bursting lying between period 3 and 4 bursting For the chaotic bursting, only a single deterministic period 3 orbit can be detected in ISI series of near period 3 bursting and only a single deterministic period 4 orbit can be detected in ISI series near the period 4 bursting. The periodic 3 orbit and period 4 orbit are identified to be (0.0033, 0.0054, 0.0507) s and (0.0040, 0.0090, 0.0480, 0.0500) s respectively, as shown in Fig. 144.2a and Fig. 144.2b, similar to those of period 3 bursting and period 4 bursting respectively. For the stochastic bursting, both a single period 3 orbit and a single period 4 orbit can be detected in the stochastic bursting, whether near period 3 bursting or near period 4 bursting, are identified to be (0.0064, 0.0088, 0.1260) s and (0.0059, 0.0076, 0.0104, 0.1271) s respectively, similar to those of period 3 bursting and period 4 bursting respectively.

PO in ISIs of firing lying between period 2 and period 3 bursting For the stochastic bursting, both a single deterministic period 2 orbit and a single deterministic period 3 orbit can be detected in ISI series of the stochastic bursting, whether near period 2 bursting or near period 3 bursting. The locations of period 2 orbit in firing near period 2 bursting are (0.0088, 0.1264) s, similar to those of period 2 bursting. The locations of period 3 orbit in firing near period 2 bursting are (0.0080, 0.0148, 0.1112) s, similar to those of period 3 bursting. For the chaotic ISI series, only a single deterministic period 2 orbit can be detected in the chaotic ISI series near period 2 bursting, while both a single deterministic period 2 orbit and a single period 3 orbit can be detected in near period 3 bursting, as shown in our previous study [5].

Histogram with multi-peaks in the stochastic bursting For the stochastic bursting lying between period k and period $k + 1$ ($k = 2, 3$) bursting, Inter-event interval

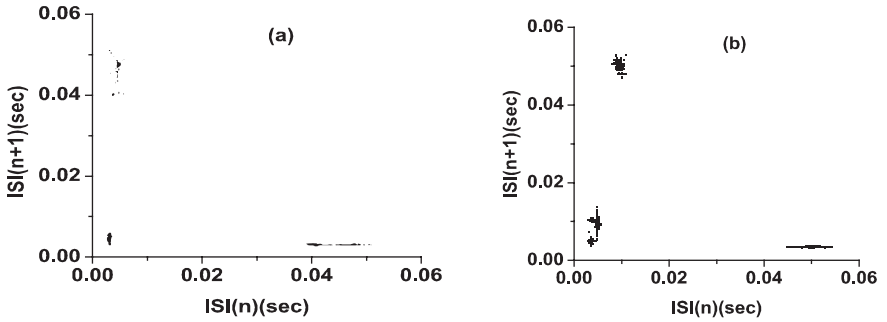

Fig. 144.2 First return map of period orbit detected in the ISI series of chaotic bursting lying between period 3 and period 4 bursting. (**a**) Period 3 orbit, (**b**) Period 4 orbit

(IEI) histogram exhibits multi-peaks, being the signature of the ASR in neural firing [6, 7, 8] when period k burst is defined as an event. The chaotic bursting does not exhibit multi-peaks characteristics.

Discussion and Conclusion

The common and important indicators to characterize chaos, such as the Lyapunov exponent and deterministic structures, can be exhibited in both chaotic and stochastic bursting lying in period adding bifurcation scenario. Two practical indictors to distinguish two kinds of bursting are also identified. The first is IEI histogram with multi-peaks in stochastic bursting. The second is that the evolutions of period orbit with respect to the bifurcation parameter are different. In addition, the dynamics of two kinds of period adding bifurcation scenario are further analyzed.

Acknowledgements This work was supported by NSFC under Grant No. 10432010, 30300107 and 30270432.

References

1. Yang, M.H., An, S.C., Gu, H.G., Liu, Z.Q., Ren, W. Understanding of physiological neural firing through dynamical bifurcation machineries. NeuroReport 17 (2006) 995–999.
2. Fan, Y.S., Holden, A.V. Bifurcations, burstings, chaos and crises in the Rose-Hindmarsh model for neuronal activity. Chaos, Solitons, Fractals 3 (1993) 439–449.
3. Fan, Y.S., Chay, T.R. Generation of periodic and chaotic bursting in an excitable cell model. Biol. Cybern. 71 (1994) 417–431.
4. Ren, W., Hu, S.J., Zhang, B.J., Wang, F.Z. Periodadding bifurcation with chaos in the interspike intervals generated by an experimental neural pacemaker. Int. J. Bifurcat. Chaos. 7 (1997) 1867–1872.
5. Ren, W., Gu, H.G., Jian, Z., Lu, Q.S., Yang, M.H. Different classification of UPOs in the parametrically different chaotic ISI series. NeuroReport 12 (2001) 2121–2124.
6. Gu, H.G., Yang, M.H., Li, L., Liu, Z.Q., Ren, W. Dynamics of autonomous stochastic resonance in neural period adding bifurcation scenarios. Phys. Lett. A 319 (2003) 89–96.
7. Yang, M.H., Gu, H.G., Li, L., Liu, Z.Q., Ren, W. Characteristics of period adding bifurcation without chaos in firing pattern transitions in an experimental neural pacemaker. NeuroReport 14 (2003) 2153–2157.
8. Gu, H.G., Ren, W., Lu, Q.S., Yang, M.H., Chen, W.J. Integer multiple spiking in neural pacemakers without external periodic stimulation. Phys. Lett. A. 285 (2001) 63–68.
9. So, P., Francis, J.T., Netoff, T.I., Gluckman, B.J., Schiff, S.J. Periodic orbits: a new language for neuronal dynamics, Biophys. J. 74 (1998) 2776–2785.
10. Kantz, H. A robust method to estimate the maximal Lyapunov exponent of a time series. Phys. Lett. A 185 (1994) 77–87.

Chapter 145
Ocular Artifacts Removal from EEG Using EMD

David Looney, Ling Li, Tomasz M. Rutkowski, Danilo P. Mandic and Andrzej Cichocki

Abstract Electroencephalogram (EEG) provides a non-invasive way to analyze brain activity. Blinking and movement of the eyes causes a strong electrical activity that can contaminate EEG recordings, particularly around the forehead but also as far as in occipital areas. Removal of such ocular artifacts is a considerable signal processing problem, since those artifacts overlap in frequency domain with EEG. In this paper we propose a signal reconstruction method based on a time frequency analysis tool known as the Hilbert-Huang spectrum. We demonstrate how our reconstruction scheme can be successfully applied to contaminated EEG data for the purposes of removing unwanted ocular artifacts.

Introduction

EEG is becoming a very popular brain activity analysis tool due to the low cost and easy application. Longer EEG recording experiments usually suffer from strong artifacts coming from muscle activity of which ocular artifacts, often recorded as reference in the form of electro-oculorgrams (EOG), are the most common. The problem of ocular interference cannot be simply removed with conventional filtering methods due to frequency overlapping between ocular activity and EEG, and also due to the nonlinear nature of the interference. We propose an adaptive approach based on the empirical mode decomposition (EMD), first introduced in [1], which is a fully data driven method for decomposing multi-component signals into a set of amplitude & frequency modulated (AM/FM) components known as intrinsic mode functions (IMFs). The IMFs act as locally orthogonal "basis functions" for the data, unlike other signal decomposition techniques that map the signal space onto a space spanned by a predefined basis. EMD has demonstrated considerable success in removing complex nonlinear disturbances from non-stationary biomedical signals [2]. By definition, an IMF is a function for which the number of extrema and the

D. Looney
Communications and Signal Processing Group Department of Electrical and Electronic Engineering, Imperial College, London, UK
e-mail: david.looney06@imperial.ac.uk

R. Wang et al. (eds.), *Advances in Cognitive Neurodynamics*,

number of zero crossings differ by at most one, and the mean of the two envelopes associated with the local maxima and local minima is approximately zero. The decomposition of a signal x(k)is given by

$$x(k) = \sum_{i=1}^{N} c_i(k) + r(k) \tag{145.1}$$

where $c_i(k)_{i=1}^{N}$ is the set of IMFs and $r(k)$ is the residual. The first IMF is obtained as follows [1]: (i) Let $\tilde{x}(k) = x(k)$; (ii) Identify all local maxima and minima of $\tilde{x}(k)$; (iii) Find an "envelope," $e_{\min}(k)$ that interpolates all local minima($e_{\max}(k)$ maxima respectively); (iv) Extract the "detail," $c(k) = x(k) - (1/2)(e_{\min}(k) + e_{\max}(k))$; (v) Let $\tilde{x}(k) = c(k)$ and go to step (2); repeat until $c(k)$ becomes an IMF. Once the first IMF is obtained, the procedure is applied to the residual $r(k) = x(k) - c(k)$ to obtain the second IMF. In this way, the procedure is applied recursively to obtain all the IMFs. By definition, the IMFs are mono component signals and their instantaneous frequency can therefore be determined as defined by the Hilbert spectrum. Combining the instantaneous frequencies and corresponding instantaneous amplitudes of the IMFs, a time-frequency distribution known as the Hilbert-Huang spectrum can be constructed.

Hilbert-Huang Reconstruction

We now consider a unique reconstruction method based on the Hilbert-Huang spectrum which we refer to as Hilbert-Huang (HH) reconstruction. Given a signal d(k), we propose to remove any unwanted frequency information and construct a signal, $\hat{\mathrm{d}}(k)$,that retains only desired frequency characteristics from d(k).This is achieved by first decomposing d(k) into a set of N IMFs, $\mathrm{c_i}(k)$, and determining the instantaneous frequencies. $\mathrm{f_i(k)}$ denotes the instantaneous frequency of the ith IMF at time instant k. Given the scenario where it is required to retain frequencies greater that f_{low} and lower than f_{high}, we have

$$\tilde{c}_i(k), = \begin{cases} c_i(k), & \text{if } f_{low} < f_i(k) < f_{high} \\ 0 & \text{otherwise} \end{cases} \tag{145.2}$$

Essentially all values of $c_{\mathrm{i}}(k)$that do not fall within the desired frequency range are set to zero. We can construct $\hat{\mathrm{d}}(k)$ by summation of the IMF values that fall within the desired frequency range, to obtain

$$\tilde{d}(k) = \sum_{i=1}^{N} \tilde{c}_i(k) \tag{145.3}$$

However, $\hat{\mathrm{d}}(k)$ is not a suitable solution on its own. Often it is the case that the instantaneous frequency of a particular IMF may intermittently become located within the desired frequency range. This has the effect of introducing unwanted discontinuities in $\hat{\mathrm{d}}(k)$ as certain IMFs are sparsely included in the summation process described above (145.3). These discontinuities have the potential to undo the goal of this report as their existence can reintroduce spurious frequency components in the data. To cater for this problem, we propose to determine the best approximation to $\hat{\mathrm{d}}(k)$ using the block based solution presented in [3]. The approximation, $\hat{\mathrm{d}}(k)$, is achieved by linear summation of the original set of IMFs and residue using an optimally defined $(N + 1) \times 1$ weight vector, w, given by

$$\hat{\mathrm{d}} = \mathrm{w}^T \mathbf{I} \tag{145.4}$$

where $\{\cdot\}^{\mathrm{T}}$ denotes the vector transpose and matrix I contains the original IMFs and the residue (5).

$$\mathbf{I} = \begin{pmatrix} c_1(1) & c_1(2) & \dots & c_1(M) \\ c_2(1) & c_2(2) & \dots & c_2(M) \\ \vdots & \vdots & & \vdots \\ c_N(1) & c_N(2) & \dots & c_N(M) \\ r(1) & r(2) & \dots & r(M) \end{pmatrix} \tag{145.5}$$

Letting $D = \mathrm{I}\,\mathrm{I}^{\mathrm{T}}$, we can determine the optimal weight vector by the following

$$\mathrm{w} = \mathrm{D}^{-1}\mathrm{I}\tilde{\mathrm{d}}^T \tag{145.6}$$

Results and Conclusions

We applied the HH reconstruction algorithm described above to several sets of EEG data contaminated by ocular artifacts. Since ocular artifacts occupy the critical low frequency band of EEG in a range 0–13 Hz [4] we proposed the carefully designed algorithm to retain the EEG important information within the above mentioned range while removing the ocular artifacts. The EEG data used was sampled at a rate of 512 Hz and recorded from electrodes Fp1, Fp2, C6, C5, O1, O2 with ground placed over Cz and additional bipolar channels vEOG, hEOG as in standard extended 10/20 EEG system. The results are displayed in Figs. 145.1 and 145.2, respectively.

To demonstrate how the algorithm retains EEG information within the frequency range originally contaminated by ocular interference we present time-frequency representations in the form of a Morlet spectrogram in Fig. 145.2.

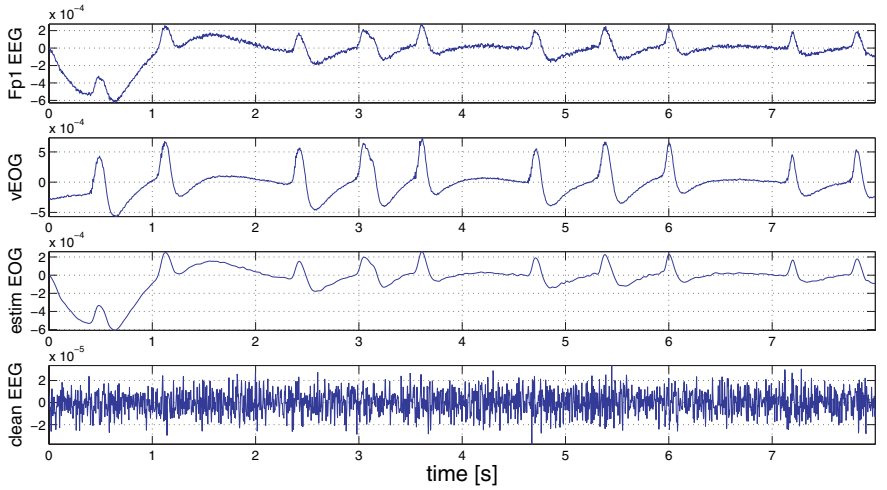

Fig. 145.1 The results of the proposed approach to remove ocular artifacts. The top panel presents the recorded EEG at Fp1 electrode with very strong ocular artifacts which is also presented as vEOG channel in second from the top panel. The third from the top panel present sestimated ocular interference. The resulting and cleaned EEG is depicted in bottom panel, where no remains of ocular artifacts can be spotted

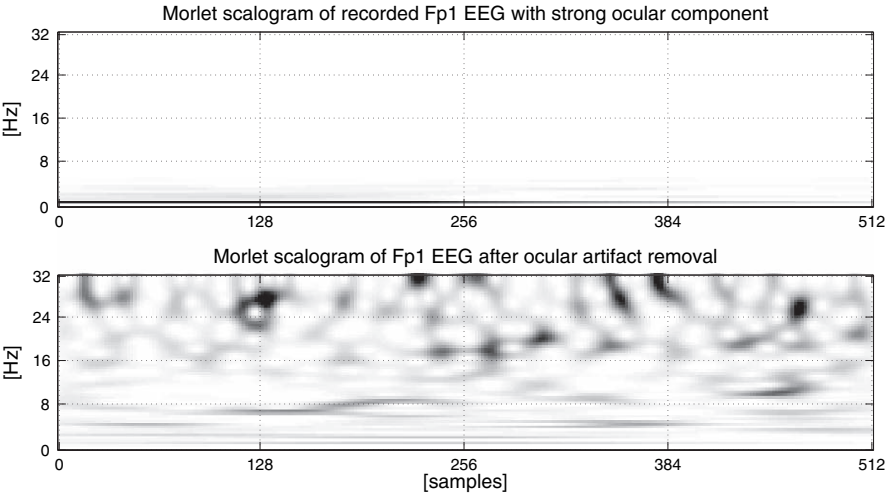

Fig. 145.2 Morlet spectrogram of the contaminated EEG from the electrode Fp1 is shown in top panel. The very strong low frequency artifact from ocular activity is visible only around 0 Hz and the rest of the spectrum is useless for analysis. The bottom panel presents the cleaned EEG showing a very rich activity across the whole frequency range

References

1. Huang, N., Shen, Z., Long, S., Wu, M., Shih, H., Zheng, Q., Yen, N.C., Tung, C., Liu, H.: The empiric almode decomposition and the hilbert spectrum for nonlin-ear and non-stationary time series analysis. Proceedings of the Royal Society A: Mathematical, Physical and Engineering Sciences 454 (1971) (March 1998) 903–995.
2. Souretis, G., Mandic, D.P., Griselli, M., Tanaka, T., Hulle, M.M.V.: Blood volume signal analysis with empirical mode decomposition. In: Proceedings of the 15th International DSP Conference. (2007) 147–150.
3. Weng, B., Barner, K.E.: Optimal and bidirectional optimal empirical mode decomposition. In: Proceedings of the 2007 IEEE International Conference on Acoustics, Speech, and Signal Processing.Volume III., Honolulu, Hawaii, U.S.A. (April1 5–20, 2007) 1501–1504.
4. Gasser, T., Sroka, L., Mocks, J.: The transfer of EOG activity into the EEG for eyesopen and closed. Electroencephalography and Clinical Neurophysiology 61(2) (1985) 181–193.

Chapter 146
Quasi-Brain-Death EEG Data Analysis by Empirical Mode Decomposition

Yuki Saito, Toshihisa Tanaka, Jianting Cao and Danilo P. Mandic

Abstract A practical and understandable method analyzing the Electroencephalogram (EEG) data of quasi-brain-death patients by using the empirical mode decomposition (EMD) is proposed. A brain-death diagnosis is made by well-defined process and some precise criteria. The process takes a long time and involves risky tests. As a preliminary EEG test, the proposed method can be easily applied in the bedside of a patient using small number of electrodes. In this method, the amplitude variation of the Hilbert–Huang spectrum (HHS) with respect to a frequency range of interest is extracted, then the amplitude variations in neighboring channels are compared. Experimental results show that the EMD-based method works well in extracting a signal which represents brain activity.

Introduction

A brain-death diagnosis is quite crucial in particular, in the case of organ transplants. The brain-death is defined as the cession and irreversibility of all brain and brain-stem function. The brain-death diagnosis must be made by the following time-consuming and risky tests: EEG confirmatory test, which takes 30 min twice (6-h interval), and apnea test, in which the breath machine is shortly removed.

To avoid the risks, it has been proposed [1] to conduct a simple preliminary EEG test detecting the brain activities in the forehead. In this preliminary test, independent component analysis (ICA) is applied for EEG data of small number of channels recorded in the bedside of a patient. However, standard ICA presumes the same number of sources as the number of channels. Therefore, it is unclear if the extracted signals by ICA represents brain activity itself.

Y. Saito
Tokyo University of Agriculture and Technology, Tokyo, Japan
e-mail: saito@sip.tuat.ac.jp

R. Wang et al. (eds.), *Advances in Cognitive Neurodynamics*,

In this paper, we propose an analysis method as preliminary EEG test of brain-death diagnosis using Hilbert–Huang spectrum (HHS) obtained by empirical mode decomposition (EMD) [2, 3]. In this method, we apply the EMD to the EEG raw data to obtain its HHS, and extract the amplitude variation of the signal of interest on time. As proposed in [1], only the electrodes of the forehead is chosen for its facility to apply this method to quasi-brain-death patient. By comparing it in different channels, we examine the existence of a signal which represents brain activity. The experimental results illustrate the proposed method is effective to extract a signal generated by brain activity from quasi-brain-death EEG data.

Method of EEG Data Analysis

It is well-known that the brain activity generates some characteristic signals such as alpha wave, beta wave, theta wave and so forth. If the amplitude variations of such characteristic signals are very similar between the neighboring electrodes, a common signal exists in the EEG data; therefore there is the brain activity. Then we detect a brain activity by extracting a common characteristic signal. We propose to extract the amplitude variation of such signals by using EMD. The EMD is a time–frequency analysis tool for non-stationary and non-linear signals. The EMD decomposes a signal into a collection of oscillatory modes, called intrinsic mode functions (IMF). The local energy and the instantaneous frequency is derived from IMFs, and we can obtain the result as a time-frequency spectrum called HHS.

More specifically, we first apply the EMD to the EEG signal $x(t)$ to represent the signal as a summation of m IMFs, $c_k(t), k = 1, \ldots, m$, and residue $r_m(t)$: $x(t) = \sum_{k=1}^{m} c_k(t) + r_m(t)$. Repeat this operations in all n channels. Then the collection of IMFs is mapped to HHS, where IMFs are converted to analytic signals for taking account of the phase difference between IMFs, and instantaneous frequency and amplitude at time instance t are obtained [2]. We denote HHS of channel i by $H_i(\omega, t)$, where ω and t are angular frequency and time respectively.

The variation of the amplitude in frequency band of interest is obtained from $H_i(\omega, t)$ in the following manner. Let b be the central frequency and let α be the half bandwidth of the subband of our interest, i.e. the subband is of the range $\omega \in [b - \alpha, b + \alpha]$. Then we obtain the variation in the i-th channel, $v_i(t)$: $v_i(t) = \int_{b-\alpha}^{b+\alpha} H_i(\omega, t)d\omega$, and normalized variation $v_i{}^*(t)$ is defined as follows: $v_i{}^*(t) = v_i(t)/\int H_i(\omega, t)d\omega$. By definition, HHS is very sparse and in the discrete signal case includes many discontinuous points. As a result, $v_i^*(t)$ can contain "noise," which is removed in the following way. We consider a part of $v_i^*(t)$ being noise set it to zero unless it continuously has non-zero values for period T. T should be the shortest period corresponding to the frequency band, $T = \dfrac{2\pi}{b+\alpha}$. Furthermore, we smooth $v_i^*(t)$ by an averaging filter.

Experimental Condition and Results

In this experiment, we focused on two typical cases of quasi-brain-death patients and tried to extract the amplitude variation of alpha wave, periodic signal with frequency component of 8–13 Hz as a simple example. Note that since in this method, arbitrary frequency ranges can be chosen. The both of patients were in a deep-coma state at first. One patient (Patient 1) was going to awake after the treatment, and the other (Patient 2) was going to brain-death. See [1] for details on the patients. Note that the EEG data used in this experiment was directly recorded in the bedside of patient where environmental noise incorporates into the data easily. The number of channel was six illustrated in Fig. 146.1, and the sampling rate of EEG data was 1 kHz.

Patient 1

The resulting variation of the i-th channel denoted by $v_i{}^*(t)$, which is derived from EMD and HHS, is illustrated in Fig. 146.2a. For comparison, the result by Fourier method, extracting the amplitude variation using the spectrogram $S(\omega, t)$ by short-time Fourier Transform instead of HHS, is shown in Fig. 146.2b. In Fig. 146.2a, very similar amplitude variations between neighboring channels are obtained, whereas it is difficult in the result by the Fourier method to see the similarity between the variations. A result similar to this example was obtained in other time windows. This result indicates that the patient had physiological brain activity which we could not estimate from the symptom.

Patient 2

In a fashion similar to Patient 1, the variation by the EMD, and the one by the Fourier method are respectively shown in Figs. 146.3a,b. In Fig. 146.3a, we find that there

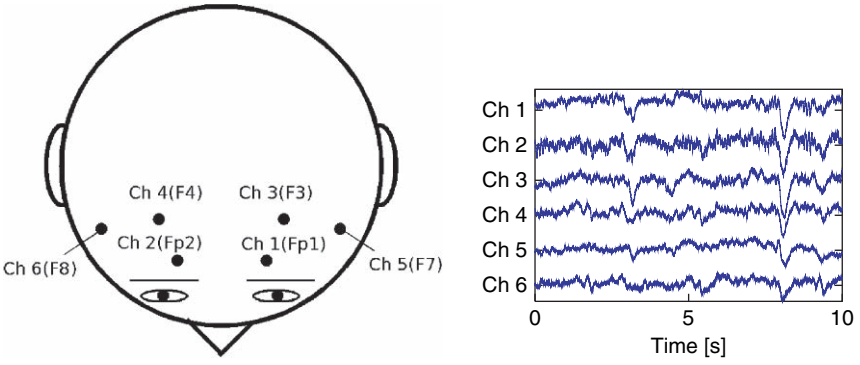

Fig. 146.1 Left: the electrode layout. Right: the recorded EEG (Patient 1)

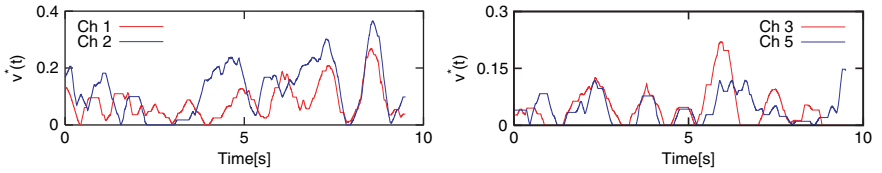

(a) Amplitude variations by the EMD method

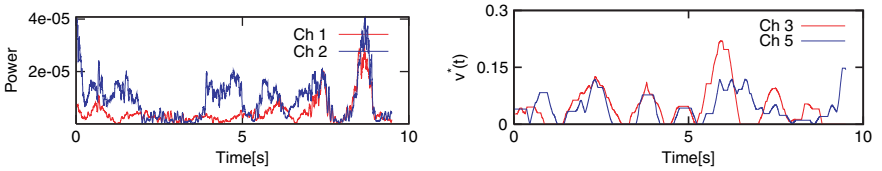

(b) Amplitude variations by the Fourier method

Fig. 146.2 Recorded EEG data from Patient 1 and the analyzed results

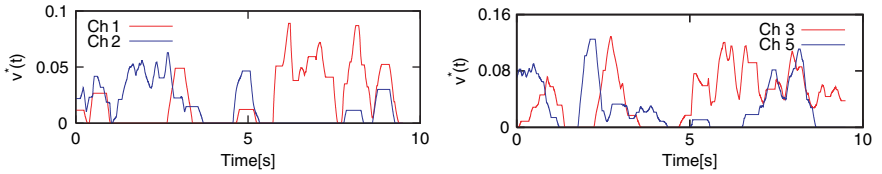

(a) Amplitude variations by the EMD method

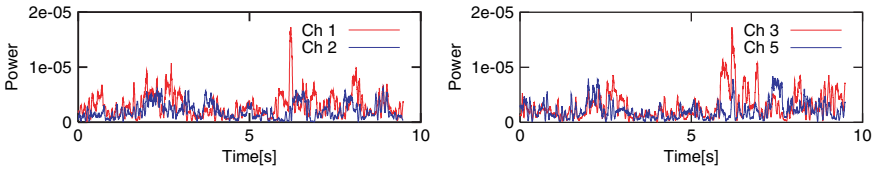

(b) Amplitude variations by the Fourier method

Fig. 146.3 Recorded EEG data from Patient 2 and the analyzed result

is no relationship between the variations. This means that the extracted amplitude variations may not be alpha wave but only noise component, and we cannot detect the brain activity. By comparison between Figs. 146.2b and 146.3b, we also find that there is no obvious difference in the results by the Fourier method.

Conclusion

We have proposed a practical method using the EMD and HHS for a preliminary EEG test. The analysis illustrates that there exists the brain activity. Since we can

apply this method to real-time measured data, the burden of a patient and a doctor will be reduced and the diagnosis will be able to be more precise with this method.

Acknowledgements The authors would like to thank Dr. Zhen Hong, Dr. Guoxian Zhu and Yue Zhang at the Shanghai Huashan Hospital, Prof. Yang Cao and Prof. Fanji Gu at the Fudan University, China for the EEG recordings. This work was supported in part by JSPS and Royal Society under the Japan–UK Research Cooperative Program, 2007.

References

1. Cao, J.: Analysis of the quasi-brain-death EEG data based on a robust ICA approach. Lect. Notes Artif. Intell. **3973** (2006) 1240–1247.
2. Huang, E. N., et al.: The empirical mode decomposition and the Hilbert spectrum for nonlinear and nonstationary time series analysis. Proc. Roy. Soc. London A **454** (1998) 903–995.
3. Tanaka, T., Mandic, P. D.: Complex empirical mode decomposition. IEEE Sig. Proc. Lett. **14** (2007) 101–104.

Chapter 147
Synchronization Between Two Coupled Networks of Discrete-Time Systems

Congxiang Xu, Weigang Sun and Changpin Li

Abstract Synchronization between two discrete-time dynamical networks is studied in this paper, this is a substantial generalization of a lot of recent works on synchronization inside a network. We mainly study the case that both networks are of the same topological connectivity, a criterion is derived which guarantees the synchronization. Linearization approach was applied in the analysis process. Simple numerical example is presented to illustrate the conclusion in the end.

Introduction

Networks have been studied extensively since the creative works which revealed the small-world [1] effect and scale-free [2] property. Recent years have witnessed a great progress in the network research, with the focus shifting away from the analysis of single small graphs and the properties to the consideration of large-scale statistical properties of graphs.

Synchronization is a ubiquitous phenomenon in the physical world, and it has become a hot topic studied in complex networks. Chaos is well-known for its sensitivity to initial values, it is an intrinsic characteristic in nonlinear dynamical systems. Likewise, chaos exists universally. Synchronization of chaotic systems has been studied widely since the drive-response approach put forward by Pecora and Carroll.

Studies on individual node behavior, dynamical analysis and statistical properties were mainly focused within a network, which have attracted much attention. There are a lot of papers, such as [3] concerning the synchronization inside a network, which reveals the relations between network topology and network dynamics. However synchronization between two coupled networks is more common in nature, yet

C. Xu
Department of Mathematics, Shanghai University, Shanghai 200444, China
e-mail: xcx19831005@yahoo.com.cn

R. Wang et al. (eds.), *Advances in Cognitive Neurodynamics*,

more difficult because these two networks are highly dimensional and of several parameters.

In the present paper, we consider this interesting topic. The rest of this paper is organized as follows. In Section 'Model Presentation and Synchronization Analysis', the model presentation and synchronization analysis is given, numerical example is shown in Section 'Numerical Examples', finally the conclusion is presented.

Model Presentation and Synchronization Analysis

Let us consider the following drive-response system, taking the driving network in the following form

$$x_i(t+1) = f(x_i(t)) + c\sum_{j=1}^{N} a_{ij}\Gamma x_j(t), \quad i = 1, 2, \cdots, N, \tag{147.1}$$

and the response network as

$$y_i(t+1) = f\big(y_i(t)\big) + \left(H - \frac{\partial f(x_i)}{\partial x_i}\right)\big(y_i(t) - x_i(t)\big) + c\sum_{j=1}^{N} b_{ij}\Gamma y_j(t), \quad i = 1, 2, \cdots, N, \tag{147.2}$$

where f mentioned here is a continuously differentiable map from $\mathbb{R}^n$ to itself, $x_i = (x_{i1}, x_{i2}, \cdots, x_{in})^T \in \mathbb{R}^n$ are the state variables of node i, N is the total number of nodes, $c > 0$ is a coupling strength, and $\Gamma \in \mathbb{R}^{n\times n}$ is a constant $0-1$ matrix linking coupled variables. $A = (a_{ij})_{N\times N}$, $B = (b_{ij})_{N\times N}$ represent the coupling configuration of the two networks, whose entries a_{ij}, b_{ij} are defined as follows: if there is a connection between node i and node j ($j \neq i$), then set $a_{ij}, b_{ij} = 1$, otherwise $a_{ij}, b_{ij} = 0$ ($j \neq i$); the diagonal elements of A, B are defined as $a(b)_{ii} = -\sum_{j=1, j\neq i}^{N} a(b)_{ij}$, for $i = 1, 2, \cdots, N$. $H \in \mathbb{R}^{n\times n}$ is a matrix to be set.

Hereafter, synchronization between these two networks is achieved if

$$\lim_{t\to+\infty} \|y_i(t) - x_i(t)\| = 0, \quad i = 1, 2, \cdots, N. \tag{147.3}$$

We study the synchronization between system (1) and system (2), where both of them have same topological structure, i.e. $A = B$. Letting $e_i = y_i - x_i$, and by linearizing the error system around x_i, we get

$$e(t+1) = He(t) + c\Gamma e(t)A^T, \tag{147.4}$$

where $e = [e_1, e_2, \cdots, e_N] \in \Re^{n\times N}$ and A^T denote the transpose of matrix A. As we know that the coupling matrix can be decomposed into $A^T = SJS^{-1}$, where J

is a Jordan form with complex eigenvalues $\lambda \in \mathcal{C}$ and S contains the corresponding eigenvectors s. Denoting $\eta = eS$, we get

$$\eta(t+1) = H\eta(t) + c\Gamma\eta(t)J, \tag{147.5}$$

where J is a block diagonal matrix, $\begin{bmatrix} J_1 & & \\ & \ddots & \\ & & J_h \end{bmatrix}$ and J_k is a block corresponding to the m_k multiple eigenvalue λ_k of A.

Let $\eta = [\eta_1, \eta_2, \cdots, \eta_h]$ and $\eta_k = [\eta_{k,1}, \eta_{k,2}, \cdots, \eta_{k,m_k}]$. Due to the fact that the sum of every line of the matrix A is zero, we can assume $\lambda_1 = 0$, and J_1 is a 1×1 matrix. If $\lambda_1 = 0$, we get $\eta_1(t+1) = H\eta_1(t)$. If the zero solution $\eta_1 = \mathbf{0}$ is asymptotically stable, then the condition $\|H\|_2 < 1$ must be satisfied. Next, we discuss the cases $k = 2, 3, \cdots, h$. We can rewrite Eq. (147.5) in component form.

$$\begin{cases} \eta_{k,1}(t+1) = (H + c\lambda_k\Gamma)\eta_{k,1}(t), \\ \eta_{k,p+1}(t+1) = (H + c\lambda_k\Gamma)\eta_{k,p+1}(t) + c\Gamma\eta_{k,p}(t), \ 1 \le p \le m_k - 1\ . \end{cases} \tag{147.6}$$

where $k = 2, 3, \cdots, h$.

Theorem 1. *Assume $A = B$ and $\|H\|_2 < 1$. Consider the network model (1) and (2). Let $\lambda_k = \alpha_k + j\beta_k$ be the eigenvalues of the coupling matrix, where j is an imaginary unit. If there exist constants $0 < \gamma_0 < \gamma < 1$ and $t_0 > 0$ such that*

$$\|H\|_2 + c|\lambda_k| \cdot \|\Gamma\|_2 \le \gamma_0, \tag{147.7}$$

then synchronization between the drive system (1) and the response one (2) can be achieved.

Proof. To begin, we consider the first equation of Eq. (147.6). Let $\eta_{k,1} = \xi + j\zeta$, where ξ and ζ are both real vectors, $\|\eta_{k,1}\|_2 = \xi^T\xi + \zeta^T\zeta$, then

$$\|\eta_{k,1}(t+1)\|_2 \le \|H + c\lambda_k\Gamma\|_2\|\eta_{k,1}(t)\|_2 \le \gamma_0\|\eta_{k,1}(t)\|_2, \tag{147.8}$$

for all $t \ge t_0$. Therefore there exists a constant $M > 0$ such that

$$\|\eta_{k,1}(t)\|_2 \le M\gamma_0^t, \text{ for } t \ge t_0, \text{ and } k = 2, 3, \cdots, h. \tag{147.9}$$

Next we consider the second equation of Eq. (147.6). Without loss of generality, let $p = 1$ and $v(t) = \|\eta_{k,2}(t)\|_2\gamma^{-t}$, then

$$
\begin{aligned}
v(t+1) &= \|\eta_{k,2}(t+1)\|_2 \gamma^{-t-1} \\
&\le \|H + c\lambda_k \Gamma\|_2 \|\eta_{k,2}(t)\|_2 \gamma^{-t-1} + c\|\Gamma\|_2 \|\eta_{k,1}(t)\|_2 \gamma^{-t-1} \\
&\le \frac{\gamma_0}{\gamma} v(t) + c\|\Gamma\|_2 \frac{M}{\gamma} \left(\frac{\gamma_0}{\gamma}\right)^t \\
&\le \left(\frac{\gamma_0}{\gamma}\right)^{t+1-T} v(T) + c\|\Gamma\|_2 (t+1-T) \frac{M}{\gamma} \left(\frac{\gamma_0}{\gamma}\right)^t \\
&< +\infty \quad \text{for all } t \ge t_0
\end{aligned}
\tag{147.10}
$$

thus $v(t)$ is bounded which implies that $\eta_{k,2}(t) = O(\gamma^t)$ for all $k = 2, 3, \cdots, h$, then synchronization between the drive system (1) and the response one (2) can be achieved.

Numerical Examples

In the networks considered below, the dynamics at every node follows the Logistic map $f(x) = \mu x(1-x)$ where μ is an adjustable parameter.

The topological structures in two networks we considered in this section are of the same. Firstly we consider the subcase that the coupling matrix is symmetric, suppose $A = B = A_1$, where A_1 is a 100-dimensional matrix with small-world network connection which can be constructed by an algorithm [1]; next we consider the second subcase that the coupling matrix is asymmetric, suppose $A = B = A_2$, where A_2 is a 100-dimensional matrix with random network connection, and Γ is an unit matrix.

From the theoretical analysis, if H is chosen from $(-1, 1)$, μ is in $(0, 4)$, we can adjust the coupling strength to synchronize the two networks, the maximum threshold value of c is 0.008 for small-world connection, for random connection the threshold value is 0.001. Let $e(t) = \max_{1 \le i \le 100} |y_i(t) - x_i(t)|$. Figure 147.1 plots the synchronization errors for two values of H.

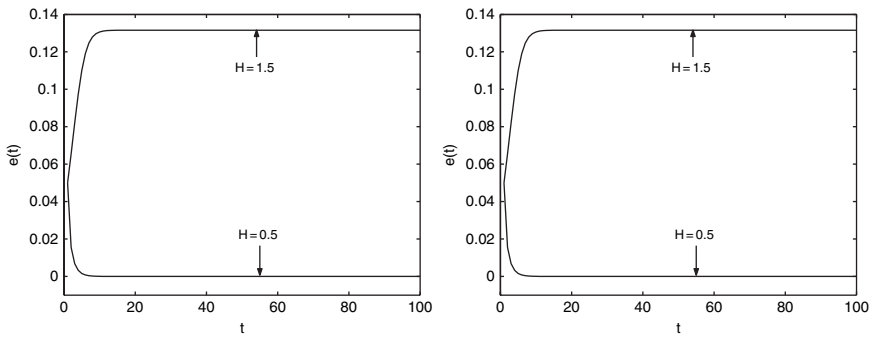

Fig. 147.1 Synchronization errors between network (1) and network (2) for two values of H with $\mu = 3.9$, $A = B = A_1$, $c = 0.003$ and $A = B = A_2$, $c = 0.001$

Conclusion

In this paper, synchronization between two coupled complex networks but not that inside one network is studied. We theoretically and numerically show that when driving-response networks have identical connection topologies, then synchronization between them can be achieved. The scales of networks and the connection topology might influence the synchronization between them.

References

1. Watts, D.J., Strogatz, S.H.: Collective dynamics of small-world networks. Nature **393** (1998) 440–442.
2. Barabási, A.L., Albert, R.: Emergence of scaling in random networks. Science **286** (1999) 509–512.
3. Li, C.P., Sun, W.G., Kurths, J.: Synchronization between two coupled complex networks. Phys. Rev. E **76** (2007) 046204.

Chapter 148
Walk-Aided System with Wearable Lower Extremity Exoskeleton for Brain-Machine Engineering

Heng Cao, Yuhai Yin, Zhengyang Ling, Wenjin Gu, Zhiyong and Yang Di Cao

Abstract Walk-aided system is to assist the motion of the disabled, injured, elderly people and soldiers. The ultimate goal of this project is to apply the system to brain-machine engineering as terminal actuator. Mechanical design, actuator modeling, and force feedback control algorithm based on neuron are discussed. A co-simulation with Matlab and Adams is used to analyze the performance of system. This human-machine interaction control scheme can be applied to test platform of brain-machine in the future.

Keywords Walk-aided system · neuron · co-simulation · BMI · exoskeleton

Introduction

In recent years, the research of walk-aided robot (also called exoskeleton) has become more and more popular [1]. According to different applications, it is mainly used in two areas. One is to help old or disabled person to walk, the other is to help those who have to carry heavy objects long distances. Compared with other intelligent robots, walk aided robot does not need vision signal or gait configuration. The principal control feature is its human-machine interaction.

Nowadays, the most successful example of exoskeleton used as a walking aided device for gait disorder persons is the Hybrid Assistive Leg (HAL) developed by Yoshiyuki Sankai [2]. EMG (ElectroMyoGram) sensors and floor reaction force sensors are adopted in order to obtain the conditions of the HAL and the operator [3]. Bleex (Berkeley lower Extremity Exoskeleton) is a latest research result in this field, which has been designed by Human Engineering Laboratory of UC Berkeley since the year 2000 [4]. A novel control scheme was applied that does not require sensor interfaces between the human and machine.

H. Cao
East China University of Science and Technology, School of Mechanical and Power Engi-neering, Postbox 401, Postcode 200237, Shanghai, China
e-mail: hengcao@ecust.edu.cn

R. Wang et al. (eds.), *Advances in Cognitive Neurodynamics*,

At present, the development of brain-machine interface (BMI) technology continues to attract researchers with a wide range of backgrounds and expertise. The medical machine based on BMI technology should provide the disabled with a new method. It could also be applied in walk-aided system as a control method.

In this paper, mechanical structure, hydraulic driver, intelligence control algorithm based on single neuron, and co-simulation will be discussed. We also planed to apply the BMI technology to this system in the near future.

Mechanical Structure

The intelligent walk aid robot could provide extra muscle ability for people carrying heavy loads through its mechanical power installment. And it moves in concert with the body's lower extremity without influencing the flexibility of human body action. The design of walk aided system has to follow the following principles [3, 5]:

1. The structure which is required to guarantee the maximum flexibility of the wearer's movement should be designed to imitate human being.
2. The system can provide the continuous power for at least 35kg load and it can last 12 h. Its gross weight is 25 kg.
3. The structure strength must sufficiently deal with the impact load brought by any body movement.
4. The control system should be able to recognize the movement tendency and study on its own.

Above all, the walk aided robot (shown as Fig. 148.1) includes several parts independently and connectedly as following:

1. The back-frame system and lower extremity connection part

The back-frame system includes the setting positions of the energy storage, the power supply, the control system and so on. It transfers the load weight to the ground (not to the wearer's ankle) through exoskeleton. At the same time, the exoskeleton should fit the user and guarantee the reliability of action. The objective is to make user realize the existence of exoskeleton other than the load.

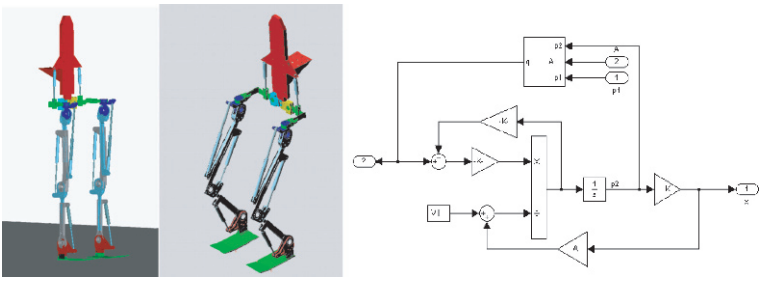

Fig. 148.1 The 3D model of exoskeleton and the model of the throttle valve speed control loop circuit

2. The dynamic output installment

The dynamic installment on the exoskeleton can output power linearly and nonlinearly according to the control system demand. It replaces the human body lower extremity muscle to supply the movement power for load. It is an essential part of independent combat system. The single-action spring reposition cylinder is chosed in this paper. The model of the throttle valve speed control loop circuit made in Matlab is shown in Fig. 148.1

3. Sensor and control system

The proper installment of sensors is the precondition which is to guarantee exoskeleton to react quickly to the body movement. It can not only control the process of exoskeleton according to the programmed setting parameters, but also modify the control system to well suit the environment changes as well as the changes of the user's physical condition.

The Research of Intelligent Control Algorithm

In the case of an aided system, the force between the operator and the machine should be controlled through force-feedback control, which made the operator cannot feel the machine and load [6, 7], and single neuron self-adaptive PID control algorithm is applied.

The Actuator Control Scheme Based on Force Feedback

When the operator who wears the exoskeleton starts to move, his joints circumrotate and send signals to exoskeleton. Sensors such as angle sensors and force sensors are adopted in order to monitor the dimensional position of the operator. Then each joint of the exoskeleton should rotate to a certain angle to avoid interference between human and machine. At the same time, a magnitude of force is created by the feedback block, which will be used to compensate for the consumed energy of the operator. This process also needs a controller that can calculate inverse mathematic model and transfer a magnitude of force to the displacement of the hydraulic cylinder. Through this control process, it provides extra muscle ability for people carrying a heavy load. And it is consistent with the body's lower extremity movement without influencing the flexibility of human body action. Figure 148.2 illustrates the

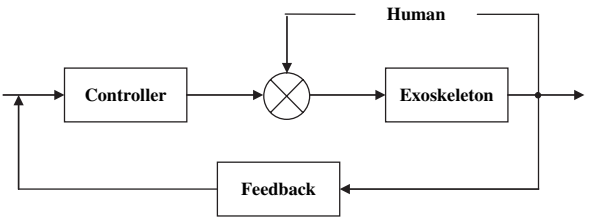

Fig. 148.2 Block of force feedback control scheme

force-feedback control scheme for the case in which all forces between the human and the machine occur through a sensing interface.

Application of Single Neuron Self-adaptive PID Control Algorithm

The aid system is a complex and nonlinear system, which cannot be built as a math model accurately. The normal PID controller can't feed the demand of real time control. Neuron has a great ability of information integration, memorization, self-learning and self-adaption, which can deal with those complex processes. In this paper, neuron and PID are combined to control the hydraulic actuator. The PID parameters can be adjusted online to make the system be robustness [8, 9].

The configuration of single neuron self-adaptive PID control system is shown as Fig. 148.3. The input of trans-block is the control setting, $r(k)$ is input, $y(k)$ is output, $x_1(k)$, $x_2(k)$, $x_3(k)$; $x_1(k) = e(k)$, $x_2(k) = e(k) - e(k-1)$, $x_3(k) = e(k) - 2e(k-1) + e(k-2)$ can be obtained which are necessary for single neuron learning; $w_i(k)$ is the weight coefficient of $x_i(k)$; K is the neuron scale coefficient, $K > 0$. η is learning speed, $\eta > 0$; the learning algorithm based on single neuron self-adaptive PID can be standardized as:

$$u(k) = u(k-1) + K \sum_{i=1}^{3} \omega_i'(k) x_i(k) \tag{148.1}$$

$$\omega_i'(k) = \frac{\omega_i(k)}{\sum_{i=1}^{3} |\omega_i(k)|} \tag{148.2}$$

$$\omega_1(k+1) = \omega_1 + \eta_i z(k) u(k)[e(k) + \Delta e(k)] \tag{148.3}$$

$$\omega_2(k+1) = \omega_2 + \eta_p z(k) u(k)[e(k) + \Delta e(k)] \tag{148.4}$$

$$\omega_3(k+1) = \omega_3 + \eta_D z(k) u(k)[e(k) + \Delta e(k)] \tag{148.5}$$

$$x_1(k) = e(k) \tag{148.6}$$

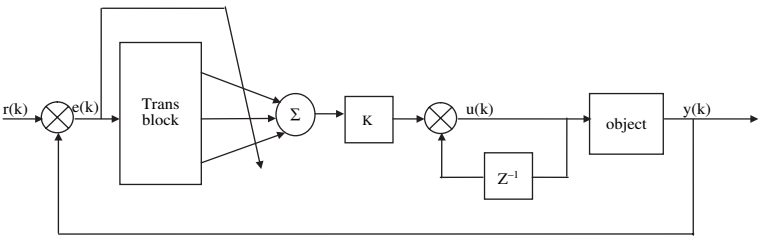

Fig. 148.3 Block diagram of single neuron self-adaptive PID control system

$$x_2(k) = e(k) - e(k-1) \tag{148.7}$$

$$x_3(k) = e(k) - 2e(k-1) + e(k-2) \tag{148.8}$$

$$z(k) = e(k) \tag{148.9}$$

Co-simulation with Matlab and Adams

An analysis method of co-simulation in Matlab and Adams has been used in this paper. For 1 DOF of a single leg, simulation of hydraulic drive instrument has been made based on force feedback control. Matlab is used to build the whole system control modules, which include hydraulic servo drive module, force feedback module, and single neuron PID control module. The input of system is an angle of joint, and the output is the displacement of piston. Meanwhile, rigid model of a single leg is set up with Adams as shown in Fig. 148.4.

At present, it is difficult to build a perfect human model by computer. In this paper, five joint degrees are recognized as simulation input. Through the sensor module S, electrical current i is used to control the hydraulic servo valve module, and the open or close of valve controlls the cylinder's flow, and finally controls the displacement of the piston. The displacement is sent to Adams module as the input in order to realize the change of joint angle. In simulation, inverse block module is used to compute the angle value by the piston displacement; the controller module is a single neuron self-adaptive PID controller which is used to improve the system control performance and robustness. The diagram of Matlab control system is shown in Fig. 148.4.

Under the same condition, simulations based on traditional PID control and single neuron self-adaptive PID control are made separately. Comparing the results (shown as Fig. 147.5), it has been found that single neuron self-adaptive PID control has better performance, such as rise time, excessive adjustment value, response time and steady error. The 0.2 s response time fits the demand of system fast response.

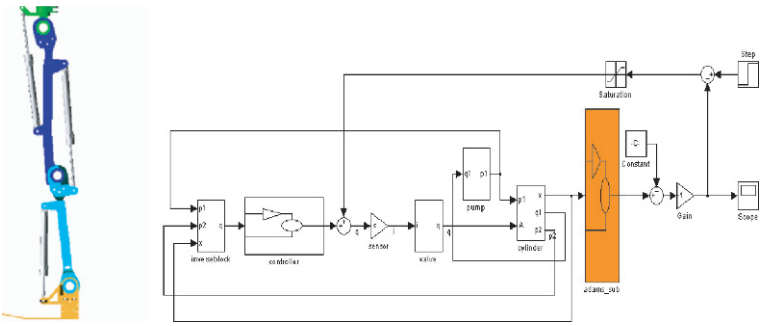

Fig. 148.4 The rigid model of single leg made by Adams and block of Matlab control system

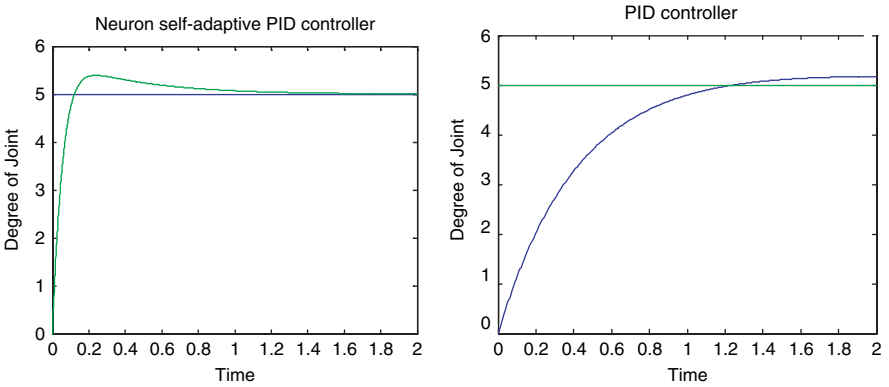

Fig. 148.5 Step responses of neuron self-adaptive PID controller (right) and the characteristic of PID controller (left)

Conclusion

In the preliminary research of Human-Machine Intelligent Walking Aid, structure of the walk aid system is designed which include a mathematic model of hydraulic actuator, and the method of force feedback which adopts the algorithm of nerve control is discussed. At last, the method based on the co-simulation of multi-software is applied to the model.

In the future work, the main research task is to make a further optimization of the mechanism. More practical experimental data by building the entity simulation will be obtained; the feasibility of control method need to be proved; the design of practical control system according to the mechanical dimension of the computer simulation model will also be started.

We believe that the Walk-Aid System has a prosperous future for both the civilian and military use. This equipment has a very bright application prospect and will also encounter many challenges at the same time.

References

1. J. Pratt, B. Krupp, C. Morse, S. Collins.: The RoboKnee: An Exoskeleton for Enhancing Strength and Endurance during Walking. Proceedings of the IEEE International Conference on Robotics and Automation (ICRA), Vol. 3, (2004) 2430–2435.
2. H. Kawamoto, Y. Sankai.: Power Assist System HAL-3 for Gait Disorder Person. Lecture Notes in Computer Science (LNCS), Vol. 2398, Proceedings of the Eighth International Conference on Computers Helping People with Special Needs (ICCHP), Germany, (2002).
3. A. Chu, H. Kazerooni, A. Zoss.: On the Biomimetic Design of the Berkeley Lower Extremity Exoskeleton (BLEEX). IEEE International Conference on Robotics and Automation, (2005) 4345–4352.
4. H. Kazerooni.: The Human Power Amplifier Technology at the University of California, Berkeley. Journal of Robotics and Autonomous Systems, Elsevier, Vol. 19, (1996) 179–187.

5. K. Naruse, S. Kawai, H. Yokoi, Y. Kakazu.: Design of Compact and Lightweight Wearable Power Assist Device. Proceedings of ASME International Mechanical Engineering Congress and Exposition (IMECE), Washington D.C., (2003).
6. Kazerooni, H., Snyder, T.: A Case Study on Dynamics of Haptic Devices: Human Induced Instability in Powered Hand Controllers. AIAA Journal of Guidance, Control, and Dynamics, Vol. 18, (1995) 108–113.
7. H. Kazerooni, L. Huang, R. Steger.: On the Control of the Berkeley Lower Extremity Exoskeleton (BLEEX). IEEE International Conference on Robotics and Automation, Barcelona, (2005).
8. H. Cao, Y. Yin, D. Du.: Neural-Network Inverse Dynamic Online Learning Control on Physical Exoskeleton. Lecture Notes in Computer Science. 13th International Conference of Neural Information Processing, ICONIP 2006, Hong Kong. Part III, LNCS 4234, (2006) 702–710.
9. S. Hesse, H. Schmidt, C. Werner, A. Bardeleben.: Upper and Lower Extremity Robotic Devices for Rehabilitation and for Studying Motor Control. Current Opinion in Neurology, V16, (2003) 705–710.

Chapter 149
A Study on the Filter Effect for Calculating the Mass Center of the Traveling Alpha Waves

Hongchuan Xiong, Gang Yin,Yin Tian, Yongxiu Lai and Dezhong Yao

Abstract Calculating the mass center of alpha rhythm is an important way to explore the brain function. In this work, instead of using the raw data or common alpha band (8–13 Hz) for the calculation of the mass center of the traveling alpha waves, the individual alpha center frequency was identified firstly, then a 5 Hz band was utilized to calculate the mass center (MC), the statistic difference of some properties such as the trajectory, the velocity, and the fractal dimension are evaluated after they are calculated from the raw data and the data preprocessed with the personally identified filter, the results show that the result with filter is more regular and explainable.

Keywords Electroencephalogram · traveling alpha wave · mass center · filter · velocity · fractal dimension

Introduction

The electroencephalogram (EEG) represents the spatial-temporal characters of collective electrical response of neuronal population [1, 2]. The neural activities in various brain areas are influenced by many inside and outside factors, such as the application of periodic sensory stimuli, or the different stages of sleep and wakefulness [3, 4, 5]. For example, in a wakeful rest state, the EEG alpha waves are most prominent over parietal and occipital regions, which are usually called α rhythm and μ rhythm [3, 6]. To understand the dynamic mechanism, it is important to investigate the signal propagation routine of the alpha wave on the scalp surface.

As for the propagation and distribution of alpha wave, various methods have been adopted to study, such as scalp potential topography, signal phase mapping, etc. Recently, Manjarrez et al. calculated the mass center (MC) of the traveling alpha waves [4]. However, their calculation was based on the raw EEG which included the whole frequency band of the electric activations of the human brain, and this

H. Xiong
Center of NeuroInformatics, School of Life Science and Technology, University of Electronic Science and Technology of China, Chengdu 610054, China
e-mail: hchxiong@126.com

R. Wang et al. (eds.), *Advances in Cognitive Neurodynamics*,

would bring on obvious bias, especially the low frequency band may have a strong effect on the result.

Usually, alpha rhythm is treated as an oscillation with 3–5 Hz bandwidth, e.g. 8–13 Hz or 9–12 Hz. Therefore, researchers usually assumed the alpha rhythm is of a fixed center frequency: 10.5 Hz. In fact, the center frequency of alpha rhythm is an individually variable value. If we need to get the exact information of an individual alpha rhythm, the different filter range should be adopted. In this paper, we adopted a different procedure from that adopted by Manjarez et al. [4] to investigate the propagation and distribution of alpha wave. The procedure includes: identifying the individual alpha spectra peak, adopting a band pass filter around the alpha peak, calculating MC. Finally, the differences of the two strategies were compared.

Materials and Methods

Subjects

The EEG data were recorded from 12 subjects during eyes-closed wakeful rest state, they are healthy right-handed volunteers of both sexes with written informed consent, age 20–24 years, the instrument is an EGI System 200 EEG amplifier (EGI, Inc.) the sampling rate is 500 Hz (0.1 $\sim$ 49 Hz band-pass filter). The normalized electrodes coordinates are illustrated Fig. 149.1. And the data were re-referenced to the infinity (zero reference) by the reference electrode standardization technique (REST) [7].

Data Preprocessing

Data were preprocessed before calculating MC. First, calculate the power spectral density of each subject respectively, an example is shown in Fig. 149.2. Second, identify the peak of the alpha band, and it is 9.766 Hz in Fig. 149.2. Third, filter the data with a band-pass filter centered at the central frequency with a 5 Hz bandwidth.

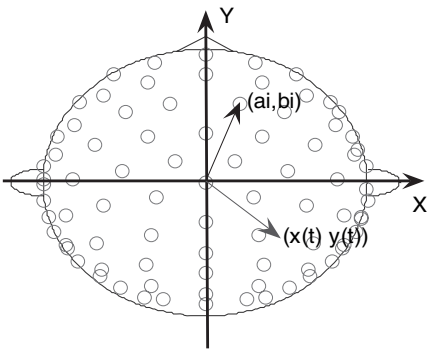

Fig. 149.1 The distribution of selected electrodes

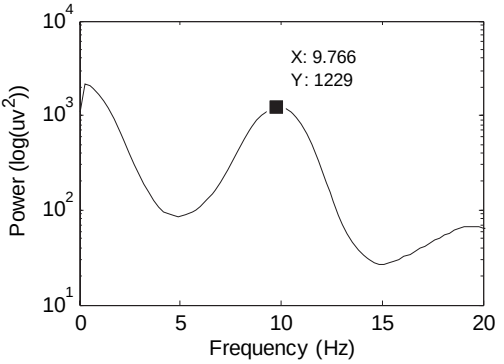

Fig. 149.2 The raw EEG data's power spectral density.
2.3 Algorithms

After data preprocessing, we calculated the coordinates of the mass center of the electrical activity recorded on the scalp with the following Eq. (148.4), the length of data is 2000 time points (4 s):

$$X(t) = \frac{\sum a_i m_i(t)}{\sum m_i(t)} \qquad (149.1)$$

$$Y(t) = \frac{\sum b_i m_i(t)}{\sum m_i(t)}$$

where $X(t)$, $Y(t)$ are the coordinates of the mass center, a_i, b_i are the coordinates of electrodes, and $m_i(t)$ is the value at the ith electrode at time point t, the sum is operated on the channels with $m_i(t) > 0$. At each time point, a two dimensional position (X, Y) is obtained, and this position is just the mass center of the individually identified traveling alpha waves, along with the time evolution, the mass center shows a trajectory.

For each data, we calculated the trajectory two times: using the raw data and the data after filtering, respectively. Figure 149.3 shows an alpha burst, top: the raw data of one channel (O1), bottom: the same data after filtering. The data length is 1 s (500 time points). Figure 149.4 shows the trajectories of the MC calculated from the data in Fig. 149.3.

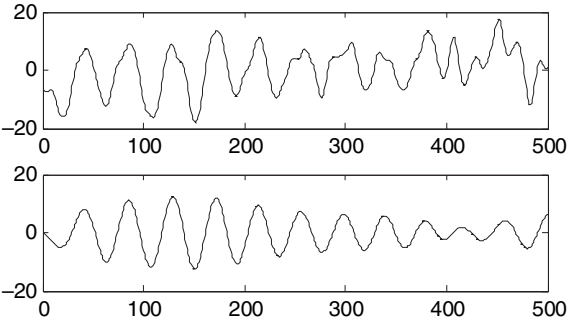

Fig. 149.3 EEG data of one channel (O1). Top: the raw data, bottom: the same channel's data after filter in same time epoch

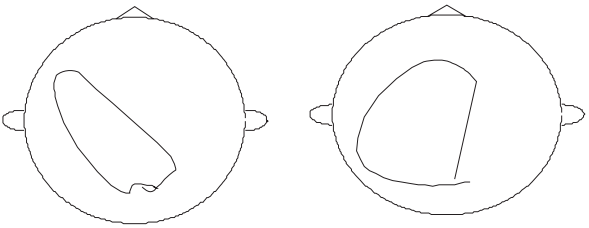

Fig. 149.4 Trajectory of 0.1 s data (50 time points) alpha burst. left: the raw data directly, right: the same time epoch data after filtering

Result and Discussion

Figures 149.4 and 149.5 show that there exist obvious differences between the two conditions. According to Fig. 149.5, the filtered trajectory [Fig. 149.5 (right)] is more regular than the raw data one [Fig. 149.5 (right)]. Currently, more and more evidences show that the alpha rhythm state is not a simple rest state. It belongs to some specific functional brain states. For example, the traveling alpha wave was assumed being a phenomenon of an un-detailed underlying scanning mechanism [8], so the trajectory distribution of the traveling wave shouldn't be a purely stochastic.

Based on Fig. 149.5, the average velocity [4] and fractal dimensions [9] of the velocity and trajectory were calculated over the 12 subjects, the results are shown in Table 149.1. The fractal dimension of the velocity and trajectory are significantly smaller after filtering than the raw data. For the mean velocity, there is no significant difference but the standard deviation is smaller after filtering. All these results indicate that the filtered one is more regular that is more possible to take responsibility for a meaningful brain function.

As shown by Fig. 149.2, though the power of the alpha rhythm is big for an alpha burst, the power of the low frequency band is large too. In fact, the low frequency band is the more basic background of the raw EEG. According to this phenomenon, when we explore the behaviors of a specific high frequency band, a band filter should be adopted to reduce the influence came from the low frequency.

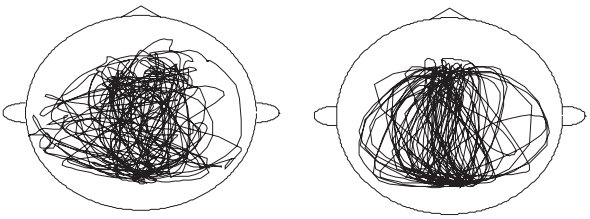

Fig. 149.5 Trajectories of 4 s data (2000 time points). Left: the raw data directly, right: the same time epoch data after filtering

Table 149.1 Velocity and fractal dimension of the trajectory

	Mean velocity (m/s)	Fractal dimension of velocity	Fractal dimension of trajectory
Unfiltered	3.562 ± 0.96	1.574 ± 0.022	1.706 ± 0.044
Filtered	3.436 ± 0.33	1.507 ± 0.017	1.557 ± 0.140
Statistics test	$F = 0.03$, $P = 0.8735$	$F = 67.57$, $P < 0.001$	$F = 12.34$, $P < 0.002$

Commonly, when calculating the alpha rhythm, the band pass filter 8–13 Hz was adopted. However, for each individual, the actual alpha rhythm band was different. If we treat the alpha band of every body as the same, the genuine alpha information might be missed. In this work, to avoid the bias coming from calculating, individual alpha band filter was adopted in studying the mass center of alpha waves. The above primary results indicate that the band filter may help us to get a more regular and meaningful result.

Acknowledgements This work is supported by NSFC 60571019. The authors would like to thank Gao Tingting for her assisting in collecting the raw EEG data.

References

1. Nunez, P.L., Wingeier, B.M., Silberstein, R.B.: Spatialtemporal structures of human alpha rhythms: theory, microcurrent sources, multiscale measurements, and global binding of local networks. Hum. Brain Mapp. 13 (2001) 125–164.
2. Lopes da Silva, F.H., Storm van Leeuwen, L.W.: The cortical source of alpha rhythm. Neurosci. Lett. 6 (1977) 237–241.
3. Hughes, S.W., Crunelli, V.: Thalamic mechanisms of EEG alpha rhythms and their pathological implications. Neuroscientist 11 (2005) 357–372.
4. Manjarrez, E., Vázquez, M., Flores A.: Computing the center of mass for traveling alpha waves in the human brain. Brain Res. 1145 (2007) 239–247.
5. Xiong, H., Yao, D.: A study of power density spectra of split-alpha rhythm. ACTA Biophys. Sin. 21(4) (2005) 301–306.
6. Yao, D., Wang, L., Nielsen, K.D., Arendt-Nielsen, L., Chen, C.A.N.: Cortical mapping of EEG alpha power using a charge layer model. Brain Topogr. 17(2) (2004) 65–71.
7. Yao, D.: A method to standardize a reference of scalp EEG recordings to a point at infinity. Physiol. Meas. 22 (2001) 693–711.
8. Pitts, W., McCulloch, W.S.: How we know universals. The perception of auditory and visual forms. Bull. Math. Biophys. 9 (1947) 127–147.
9. King, C.C.: Fractal and chaotic dynamics in nervous systems. Prog Neurobiol 36 (1991) 279–308.

Chapter 150
Differentiate Negative and Positive Schizophrenia Using Support Vector Machine

Ming Ke, Hui Shen, Baojuan Li, Zongtan Zhou and Dewen Hu

Abstract In the present study, we identified the correlative pattern of gray matter distribution that best discriminates between positive and negative schizophrenia patients, which might provide additional information to psychiatric diagnostic system for mental disorders. First, we applied the voxel-based morphometry (VBM) to compare the gray matter distribution between negative and positive schizophrenia patients. Second, we trained the support vector machine (SVM) to obtain a classification model that classified 20 positive and 11 negative schizophrenic patients. The results showed that 84% subjects were correctly classified. We demonstrated that the united method of VBM and SVM would provide a useful tool for clinical diagnostic systems.

Keywords Positive schizophrenia · negative schizophrenia · support vector machine · classifiers · voxel-based morphometry

Introduction

Although almost one century's efforts to understand the neuropsychology and etiology of schizophrenia have produced exciting results, current operational diagnostic systems for the disease are based solely on clinical manifestations. In recent years, many neuroimaging studies have suggested that significant structure changes in some brain regions in schizophrenia may provide additional information for clinic diagnostic systems as an assistant and comparatively stable diagnostic tool. Moreover, the discriminating experiments based on the spatial pattern of gay matter distribution enable higher correct classification rate than that only based on morphological parameters [1].

In the present work, we hypothesized that the characteristic distribution of regional brain tissue change in schizophrenia patients would contribute to discriminate

D. Hu
Department of Automatic Control, College of Mechatronics and Automation, National University of Defense Technology, Changsha, Hunan, 410073, P.R. China
e-mail: dwhu@nudt.edu.cn

R. Wang et al. (eds.), *Advances in Cognitive Neurodynamics*,

them. Application of VBM would capture the spatial pattern of tissue distribution in feature selection step. Then we used SVM to categorize the two distinct symptoms in classification procedure.

Method and Materials

Subjects

Twenty-eight right-handedness positive schizophrenic patients and nineteen right-handedness negative schizophrenic patients participated in this study. All the subjects were randomly assigned to two independent groups. The first group included eight positive patients and eight negative patients, which would use for training set. The second group included 20 positive patients and 11 negative patients, which would use for testing set.

MRI Acquisition and Preprocessing

All the MRI measurements were performed with a 1.5T GE Signa System (GE Signa, Milwaukee, Wisconsin, USA). The images were acquired with the parameters: TR= 12 s, TE= 4.2 ms, FOV= 24 cm, FA= 15°, matrix = 256 × 256 × 172, slice thickness= 1.8 mm, no gap.

The obtained images were preprocessed with the standard VBM [2] in the statistical parametric mapping software package (SPM2, `http://www.fil.ion.ucl.ac.uk/spm`). The whole brain images of every subject were normalized to the standard T1 template in MNI space and segmented into gray matter, white matter and cerebrospinal fluid. The gray matter images then were spatially smoothed with an 6*mm* FWHM Gaussian kernel.

Statistical Analysis

The gray matter images in the first groups were submitted to a second-level random-effect two-sample *t*-test framework. The statistical significance was evaluated between positive schizophrenics and negative schizophrenics in the first groups.

Classification Analysis for Two Subtypes by Using SVM

Here, we addressed classification of subjects between positive and negative patients by a general methodology which took two steps, as follows:

In the feature selection step, we firstly created a mask from t-statistical contrast map in the previous statistical analysis. In this contrast map, a single voxel, which was exceed the threshold based upon a $P = 0.001$ (uncorrected) level of significance, would be set 1 instead of the original t value. The remains would set 0.

Then, every subject GM image in the first group was processed by the mask obtained just now and the eigenimage of each subject in the first group was get.

Next, the support vector machines (SVM) using libsvm software (`http://www.csie.ntu.edu.tw/~cjlin/libsvm`) [3] was applied to the first group (the training set) and the second group (the testing set). The detailed description of SVM can be found in [4].

The choice of kernel and the parameter C is most important in SVM. We found the optional parameters by using grid search (GS) and selected Gaussian radial basis (RBF) kernels for statistical analysis. A measure to validate the generalization capability of the discrimination method would be achieved by using five-fold cross-validation approach.

Results

The results of group comparison between the positive and negative schizophrenics revealed that lower gray matter concentrations included the bilateral frontal regions, left temporal region, left occipital region, and bilateral cerebellum. While there were no significant increase gray matter concentrations in negative patients. Fig. 150.1 show the statistical parametric map in maximal projections and the coordinate locations.

As show in Fig. 150.2, 84% subjects were correctly classified, of which 17 of the 20 positive schizophrenia patients and 9 of the 11 negative schizophrenia patients, respectively.

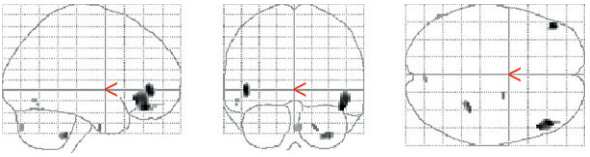

Fig. 150.1 SPM{t} statistically significant voxels with decrease gray matter concentrations in positive schizophrenics compared with negative schizophrenics

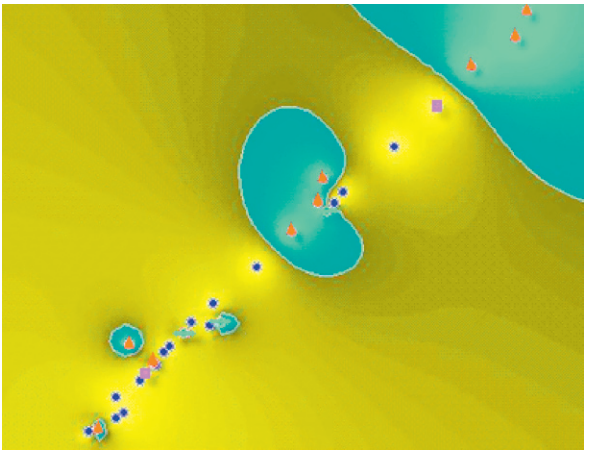

Fig. 150.2 The results of classification for contrasts between positive and negative schizophrenics. The blue dots present the correct samples of positive schizophrenics. The red triangles present the correct samples of negative schizophrenics. The green short lines present the false samples of positive schizophrenics. The magenta rectangles present the false samples of negative schizophrenics

Discussion

Our data-driven analysis using the VBM and SVM method effectively specified the discrimination between positive and negative schizophrenic patients. This is the first application on classifying the two subtypes of schizophrenia patients. In our study, eigenimage from the results of VBM reflected significant morphological differences between two subtype patients. The group from our results comparisons between two subtypes schizophrenia are in accordance with these earlier reports [5].

The favorable classification of the positive and negative patients by using SVM appeared useful for overcoming the limitations of the previous studies. Moreover, The approach of K-fold cross-validation [6] has an advantage of using as much data as possible and covering effectively the entire data set. Five-fold cross-validation was applied in this study and the accuracy of generalization achieved 80% by using all the data.

In summary, we provided a united method of VBM and SVM for classifying favorably the positive schizophrenic patients from the negative schizophrenic patients. Further study would be focused on application of the present method as an assistant and comparatively stable diagnostic tool.

Acknowledgements This work is supported by the State Key Development Program for Basic Research of China (973 Program), Grant No. 2003CB716104.

References

1. Kawasaki, Y., Suzuki, M., Kherif, F., Takahashi, T., Zhou, S., Nakamura, K., Matsui, M., Sumioshi, T., Seto, H., Kurachi, M.: Multivariate voxel-based morphometry successfully differentiates schizophrenia patients from healthy controls. Neuroimage 34 (2007) 235–242.
2. Ashburner, J., Friston, K.J.: Voxel-based morphometry-the methods. Neuroimage 11 (2000) 805–821.
3. Chang, C., Lin, C.: LIBSVM: a library for support vector machines (2001).
4. Burges, C.J.C.: A Tutorial on Support Vector Machines for Pattern Recognition. Data Min. Knowl. Discov. 2 (1998) 121–167.
5. Shenton, M.E., Dickey, C.C., frumin, M., McCarley, R.W.: A review of MRI findings in schizophrenia. Schizophr. Res. 49 (2001) 1–52.
6. Shawe-Taylor, J., Cristianini, N.: Kernel Methods for Pattern Analysis. Cambridge University Press, Cambridge, England (2004).

Chapter 151
Detecting Nonlinearity in Wrist Pulse Using Delay Vector Variance Method

Jianjun Yan, Yiqin Wang, Chunming Xia, Fufeng Li and Rui Guo

Abstract The cardiovascular system is known theoretically to contain many nonlinearities. Delay Vector Variance method is a novel method for detecting nonlinearity of time series, which can detect the nonlinearity of the original time series comparing test data to surrogate data. This method provides a new approach for wrist pulse analysis based on the local predictability in phase space. In this paper the wrist pulse signals of healthy group and coronary heart disease group are analyzed and studied with the Delay Vector Variance method, the results indicated that there is distinct difference between two groups of wrist pulse signals from DVV plots and test statistics, most of the wrist pulse signals of the coronary heart disease group are nonlinear, while the wrist pulse signals of the healthy group are commonly linear.

Keywords Wrist pulse · delay vector variance · surrogate data · nonlinear · coronary heart disease

Introduction

The blood forced in the aorta during systole not only moves the blood in the vessels forward but also sets up a pressure wave that travels along the arteries. The pressure wave expands the arterial walls as it travels, and the expansion is palpable as the pulse. Pulse amplitude and waveform morphology contain important physiological information reflecting the status of the heart and the vascular system.

The mechanisms regulating the cardiovascular system are known theoretically to contain many nonlinearities [1]. Yet the dominant techniques for analyzing time series – for example, spectral analysis – are based on the assumptions of linear dynamics. The ultimate resolution to this dilemma may come in the form of improved time series analysis techniques that can cope optimally with nonlinearities. Linear analysis techniques are not capturing all of the information in the time series.

J. Yan
Center for Mechatronics Engineering, East China University of Science and Technology, Shanghai 200237, P. R. China
e-mail: jjyan@eucst.edu.cn

R. Wang et al. (eds.), *Advances in Cognitive Neurodynamics*,

The Delay Vector Variance method is a novel method for detecting the nonlinearity of the time series. In this paper the wrist pulse signals of two group people are analyzed and studied with the Delay Vector Variance method, and the results are discussed.

Delay Vector Variance

The Delay Vector Variance method is a novel analysis of a time series which examines the predictability of a time series by virtue of the observation of the variability of the targets. The approach is somewhat related to the false nearest neighbors [2] and the $\delta - \varepsilon$ methods. For a given embedding dimension m, the mean target variance, σ^{*2}, is computed over all sets Ω_k. A set Ω_k is generated by grouping those DVs that are within a certain distance to x(k), which is varied in a manner standardized with respect to the distribution of pairwise distances between DVs. In this way, the threshold scales automatically with the embedding dimension m, as well as with the dynamical range of the time series at hand, and thus, the complete range of pairwise distances is examined. For a given embedding dimension m, the DVV algorithm can be summarized as follows:

1. Map the original time series from time domain to a set of delay vectors (DVs) in phase space, $\mathbf{x}(k) = [x_{k-\tau m}, \ldots, x_{k-\tau}]^T, k = 1, \ldots, N - m + 1$, where N denotes the length of the time series and τ denotes the time lag which for convenience is set to unity in all the simulations and the corresponding target x_k;
2. The mean μ_d and standard deviation σ_d are computed over all pairwise Euclidean distances between DVs, $||x(i) - x(j)||(i \neq j)$;
3. The sets $\Omega_k(r_d)$ are generated such that $\Omega_k(r_d) = \{x(i)||x(k) - x(i)|| \leq r_d\}$, i.e., consisting of all DVs that lie closer to $x(k)$ than a certain distance

$$r_d(n) = \mu_d - n_d\sigma_d + (n-1)\frac{2n_d\sigma_d}{N_{tv} - 1}; n = 1 : \cdots : N_{tv}. \tag{151.1}$$

   where N_{tv} denotes how fine the standardized distance is uniformly spaced, and n_d is a parameter controlling the span over which to perform the DVV analysis;
4. For every set $\Omega_k(r_d)$, the variance of the corresponding targets, $\sigma_k^2(r_d)$, is computed. The average over all sets $\Omega_k(r_d)$, normalized by the variance of the time series, σ_x^2, yields the 'target variance', $\sigma^{*2}(r_d)$:

$$\sigma^{*2}(r_d) = \frac{\frac{1}{N}\sum_{k-1}^{N}\sigma_k^2(r_d)}{\sigma_x^2} \tag{151.2}$$

Only consider a variance measurement valid, if the set $\Omega_k(r_d)$ contains at least $N_0 = 30$ DVs, since too few points for computing a sample variance yields unreliable estimates of the true variance.

The idea behind the DVV method is that if two DVs of a predictable signal lie close to one another in terms of their Euclidean distance, they should also have similar targets. The smaller the Euclidean distance between them, the more similar targets they have. Therefore, the presence of a strong deterministic component within a signal will lead to small target variances for small spans rd. The minimal target variance, $\sigma^{*2}_{\min} = \min_{rd}[\sigma^{*2}(r_d)]$, is a measure for the amount of noise present within the time series. Besides, the target variance $\sigma^{*2}_{\min}$ has an upper bound which is unity. This is because, when rd becomes large enough, all DVs belong to the same set $\Omega_k(r_d)$. Thus, the variance of the corresponding target of those DVs will be almost identical to that of the original time series.

As a result of the standardisation of the distance axis, the resulting 'DVV plots' are easy to interpret. The presence of a strong deterministic component will lead to small target variances for small spans. At the extreme right, the DVV plots smoothly converge to unity, since for maximum spans, all DVs belong to the same set, and the variance of the targets is equal to the variance of the time series. If this is not the case, the span parameter, n_d, should be increased [3].

In the following step, the linear or nonlinear nature of the time series is examined by performing DVV analyses on both the original and a number of surrogate time series, using the optimal embedding dimension of the original time series. Due to the standardisation of the distance axis, these plots can be conveniently combined in a scatter diagram, where the horizontal axis corresponds to the DVV plot of the original time series, and the vertical to that of the surrogate time series. If the surrogate time series yield DVV plots similar to that of the original time series, the 'DVV scatter diagram' coincides with the bisector line, and the original time series is likely to be linear. The deviation from the bisector line is, thus, an indication of nonlinearity, and can be quantified by the root mean squared error (RMSE) between the $\sigma^{*2}s$ of the original time series and the $\sigma^{*2}s$ averaged over the DVV plots of the surrogate time series. In this way, a single test statistic tDVV is obtained [3]:

$$t^{DVV} = \sqrt{\left\langle \left(\sigma^{*2}(r_d) - \frac{\sum_{i=1}^{N_s} \sigma^{*2}_{s,i}(r_d)}{N_s} \right)^2 \right\rangle_{valid_{rd}}} \tag{151.3}$$

where $\sigma^{*2}_{s,i}(r_d)$ is the target variance at span rd for the ith surrogate, and the average is taken over all spans rd that are valid in all surrogate and original DVV plots.

Detection of Nonlinearity of Wrist Pulse with Delay Vector Variance

In order to examine the nonlinearity of wrist pulse signals of healthy group, 29 sets of wrist pulse in the healthy group and 59 sets of wrist pulse in the coronary heart

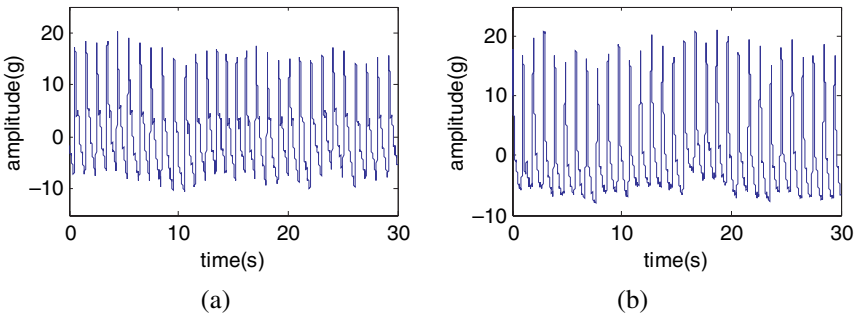

Fig. 151.1 Wrist pulse wave of: (**a**) a healthy person; (**b**) a patient with coronary heart disease

disease group are analyzed with Delay Vector Variance, and the statistical results of the samples are obtained. Typical wrist pulses in the two groups are shown as Fig. 151.1.

Figure 151.2 illustrates the signal nature of these wrist pulse signals. The diagram is DVV plots, which are obtained by plotting the target variance as a function of standardised distance. The diagram in Fig. 151.3 represents DVV scatter diagram, obtained by plotting the target variance of the original data against the mean of the target variances of the surrogate data where error bars denote the standard deviation of the target variance of surrogate data. From the Fig. 151.3a, the DVV scatter diagram for a wrist pulse signal in the healthy group lies on the bisector line, indicating its linear nature; while for a pulse wave signal of the coronary heart disease it deviates from the bisector line in Fig. 151.3b, indicating its nonlinear nature.

In healthy group, there are 76% of sets with tDVV less than 0.04; it indicates that a majority of the wrist pulse signals of healthy group are linear. In the coronary heart disease group, there are 80% of sets with tDVV greater than 0.04, it indicates that most of the wrist pulse signals of coronary heart disease group are nonlinear.

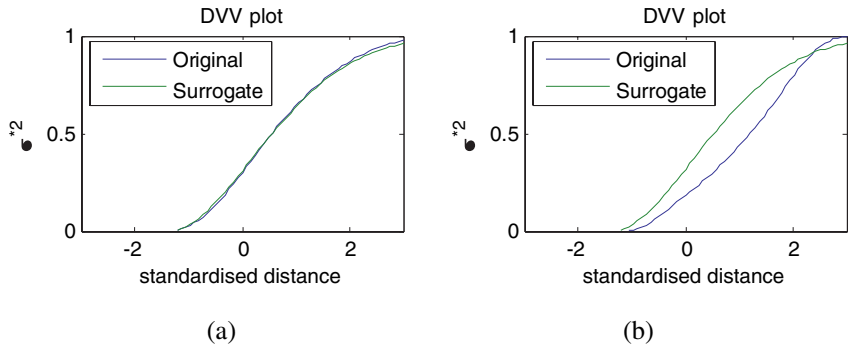

Fig. 151.2 DVV plot of the wrist pulse of: (**a**) a healthy person; (**b**) a patient with coronary heart disease

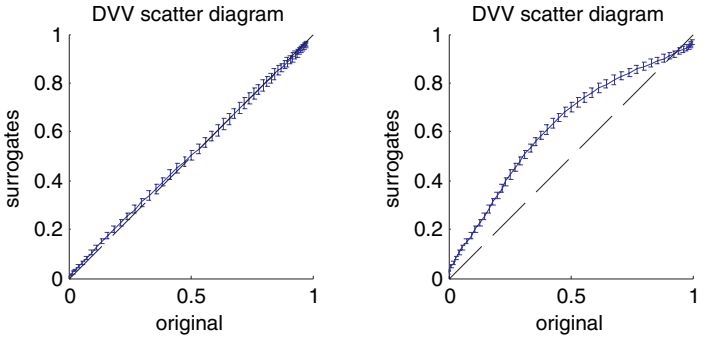

Fig. 151.3 DVV scatter diagram of the wrist pulse of: (**a**) a healthy person; (**b**) a patient with coronary heart disease

Summary

The cardiovascular system is known theoretically to contain many nonlinearities. Delay Vector Variance method is a novel method for detecting nonlinearity of time series, it can be estimated whether the original time series is nonlinear with comparing test data to surrogate data. This method provides a new approach for pulse wave analysis based on the local predictability in phase space. In this paper the pulse wave signals of two group people are analyzed and studied with the Delay Vector Variance method, the results indicated that there is distinct difference between two group of wrist pulse signals from DVV plot and test statistics, most of the wrist pulse signals of the coronary heart disease group are nonlinear, while the wrist pulse signals of the healthy group are commonly linear. Kaplan mentioned in [1] that the interaction of many cardiovascular feedback loops, together with random environmental influences, may eliminate detectable traces of nonlinearity from the time series, even though the time series is caused by nonlinear mechanisms. But the mechanism of difference of wrist pulse's nonlinearity between healthy persons and coronary heart disease patients need further study.

Acknowledgements This work was supported by the National Science & Technology Pillar Program in the Eleventh Five-year Plan Period (No. 2006BAI08B01-04). The test data was provided by School Basic Medicine of Shanghai University of TCM.

References

1. Kaplan, D.T.: Nonlinearity and nonstationarity: the use of surrogate data in interpreting fluctuations. In: Rienzo, M. Di, Mancia, G., Parati, G., Pedotti, A., Zanchetti, A. (eds.): Frontiers of Blood Pressure and Heart Rate Analysis. IOS Press, Amsterdam (1997).
2. Gautama, T., Mandic, D.P., Van Hulle, M.M.: The delay vector variance method for detecting determinism and nonlinearity in time series. Physica D, Vol. 190 3–4 (2004) 167–176.
3. Gautama, T., Mandic, D.P., Van Hulle, M.M.: Indications of nonlinear structures in brain electrical activity. Phys. Rev. E, Vol. 67 4 (2003) 046204.

Chapter 152
Orthogonal Filter-Based Networks for Learning

Wieslaw Sienko and Wieslaw Citko

Abstract Design of mappings considered in this paper rely on multivariate function approximations with skew-symmetric kernels and, due to regularization, can be implemented for any number of training patterns. Such kernels are implemented by using HNN-based orthogonal filters, specifically by using 8-dim building blocks (design with best adapted basis).

Keywords Supervised learning · mapping approximations · hamiltonian neural networks · orthogonal filters

Introduction

The problem of learning represents a gateway to understanding intelligence in both brains and machines. Many believe that supervised learning will become a key technology for extracting and classifying information from the data around us. Supervised learning techniques, i.e. the learning from examples, can be implemented as mappings $\mathbf{y} = \mathbf{F}(\mathbf{x})$ relying on the fitting of experimental data pairs $\{\mathbf{x}_k, \mathbf{y}_k\}$. A number of models in the form of networks for learning, implementing the supervised learning techniques, have been proposed in literature. Recently, some general learning techniques relying on multivariate function approximation have been proposed [1]. Regularization theory has been introduced as a natural framework for solving ill-posed problems of approximation. Relying on the Regularized Least Squares Classification (RLSC) concept, some novel structures of networks for learning have been considered [2, 3]. These structures are specific to using the Hamiltonian Neural Networks (HNN) based spectrum analysis, recognition and memorization, giving rise to mapping implementations with skew-symmetric kernels. The purpose of this paper is to present, how very large scale networks for learning can be designed

W. Sienko
Department of Electrical Engineering, Gdynia Maritime University, ul. Morska 83, 81-225 Gdynia, Poland
e-mail: sienko@am.gdynia.pl

R. Wang et al. (eds.), *Advances in Cognitive Neurodynamics*,

by using HNN-based orthogonal filters, and, specifically, by using 8-dimensional building blocks.

RLSC Basics

Learning issues can be seen as a special problem in multivariate approximations. Specifically, starting with training data $(x_i, y_i)_i^m = 1$, where input vectors $\mathbf{x}_i \in X \subset R^n$ and $y_i \in Y \subset R$, one synthesizes a function which best represents relation between the input $\mathbf{x}_i$ and y_i. According to [1] the most general approximation algorithm (RLSC) in learning theory can be formulated by the following equation:

Define f: $X \rightarrow Y$ by

$$f(\mathbf{x}) = \sum_{i=1}^{m} c_i \mathbf{K}_{\mathbf{x}i}(\mathbf{x}) \tag{152.1}$$

where: $\mathbf{c} = [c_1, c_2, \ldots, c_m]^T$, $c_i \in R$ and kernels $K_{Xi}(\mathbf{x})$ are definite functions continuous on $X \times X$.

Our purpose here is to show, how a mapping (or classifier) can be implemented in the form of a composition of HNN based spectrum analysis. Spectrum analysis can be treated as a transform from input signal space into a feature space. We propose to define the following kernel $K_{\mathbf{x}_i}(\mathbf{x})$[2]:

$$K_{\mathbf{x}_i}(\mathbf{x}) = \Theta(\mathbf{x}_i^T \mathbf{H}_n \mathbf{x}) \tag{152.2}$$

where: $\mathbf{x}_i^T = [x_1, \ldots, x_n]$, $x_i \in \Re^n$ is i-th training vector, $\mathbf{H}_n$ is orthogonal and skew-symmetric (Hurwitz-Radon matrices) i.e.:

$$\mathbf{x}_i^T \mathbf{H}_n \mathbf{x}_i = 0, \quad \mathbf{x}_i^T \mathbf{H}_n \mathbf{x}_j = -\mathbf{x}_j^T \mathbf{H}_n \mathbf{x}_i \tag{152.3}$$

$\Theta(\cdot)$ is an odd function. Thus, the matrix $\mathbf{K} = \{K_{i,j}\} = \{K_{\mathbf{x}_i}(\mathbf{x}_j)\}$ is skew-symmetric.

One of the possible architectures, implementing Eq. (152.1) with kernels Eq. (152.2), forms a set of perceptrons, memorizing training vectors $\mathbf{x}_i$, as shown in Fig. 152.1, where output $\mathbf{u}$ denotes Haar spectrum of input vector $\mathbf{x}$ and block $\mathbf{H}_n$ denotes the HNN based spectrum analyzer. Moreover, $\mathbf{x}$ and $\mathbf{u}$ are orthogonal, i.e. $(\mathbf{x}, \mathbf{u}) = 0$.

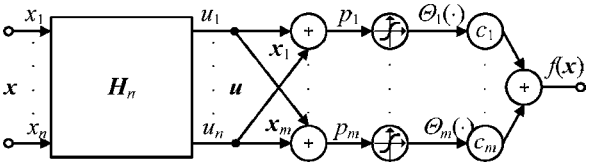

Fig. 152.1 Structure of function approximator (network for learning)

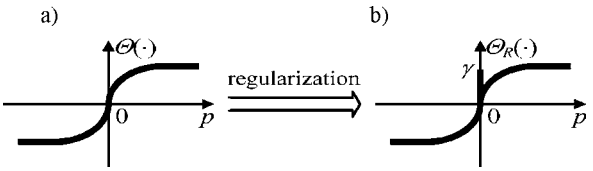

Fig. 152.2 Activation functions of perceptron

Thus, in the case of a kernel given by Eq. (152.2), Eq. (152.1) approximates the unknown function by a superposition of perceptrons, each designed at the location $\mathbf{x}_i$ of one of the m training points, for any m. The key problem in design of the approximator is the solvability of equation:

$$\mathbf{K}\,\mathbf{c} = \mathbf{y} \tag{152.4}$$

where: $\mathbf{y}$ is the vector with y_i coordinates.

It is well known that, since $\mathbf{K}$ is skew-symmetric, the design Eq. (152.4) can be ill-posed.

Hence, we propose the following regularization of matrix $\mathbf{K}$:

$$\mathbf{K}_R = (\gamma \mathbf{1} + \mathbf{K}) \tag{152.5}$$

where: $\gamma \neq 0$ for odd m, $\gamma \in \Re$ for even m.

Then, assuming $\gamma \neq 0$, the following equation is well-posed for any m and strictly well-posed for even m:

$$\mathbf{K}_R\mathbf{c} = \mathbf{y}; \quad \mathbf{c} = \mathbf{K}_R^{-1}\mathbf{y} \tag{152.6}$$

It is easy to see that, for error free approximation, the activation functions $\Theta(\cdot)$ of perceptrons should be endowed with a "superconducting impulse" γ as shown in Fig. 152.2b.

Due to the properties of the matrix $\mathbf{K}_R$, a solution of key Eq. (152.6) exists for any m (number of training points or patterns).

Design with Best Adapted Basis

The function approximator (network for learning) from Fig. 152.1, based on spectrum analysis and pattern memorization, is generally valid for even dimension *n* and any number of patterns m. Due to losslessness of block H_n (HNN) in Fig. 152.1 this structure should be rather treated as pictorial representation of an algebraic algorithm. Hence, it gives rise to questions about how such a structure could be seen as biologically inspired and implementable by stable, dynamical systems in the form of neural networks. We propose the following solution: For physical realizability of HNN one should rely on HNN-based orthogonal filters, as shown in Fig. 152.3,

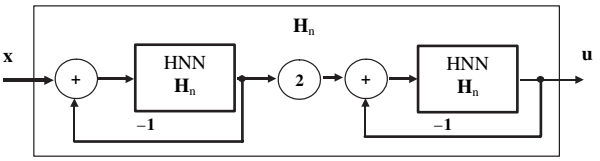

Fig. 152.3 Haar spectrum analyzer by using two orthogonal filters

where implementation of block H_n through cascade connection of two orthogonal filters, is presented, as well.

Moreover, we propose here to implement HNN-based orthogonal filters by compatible connection of 8-dimensional building blocks. The state space equation of such a building block (i.e. 8-dim HNN-based orthogonal filter) is given by:

$$\dot{\mathbf{z}} = \mathbf{W}\Theta(\mathbf{z}) + \mathbf{x} \tag{152.7}$$

where: weight matrix $\mathbf{W}$ fulfils:

$$\mathbf{W} = \mathbf{H}_8 - \mathrm{h}_0\mathbf{1}; \mathbf{H}_8{}^2 = -\mathbf{1}, \quad \mathrm{h}_0 > 0 \tag{152.8}$$

It easy to see that such an orthogonal filter sets up the following orthogonal transformation:

$$\mathbf{y} = \Theta(\mathbf{z}) = \frac{1}{1 + \mathrm{h}_0^2}(\mathbf{H}_8 + \mathrm{h}_0\mathbf{1})\mathbf{x} \tag{152.9}$$

and due to the structure of $\mathbf{H}_8$:

$$\mathbf{H}_8 = \begin{bmatrix} 0 & \mathrm{h}_1 & \mathrm{h}_2 & \mathrm{h}_3 & \mathrm{h}_4 & \mathrm{h}_5 & \mathrm{h}_6 & \mathrm{h}_7 \\ -\mathrm{h}_1 & 0 & \mathrm{h}_3 & -\mathrm{h}_2 & \mathrm{h}_5 & -\mathrm{h}_4 & -\mathrm{h}_7 & \mathrm{h}_6 \\ -\mathrm{h}_2 & -\mathrm{h}_3 & 0 & \mathrm{h}_1 & \mathrm{h}_6 & \mathrm{h}_7 & -\mathrm{h}_4 & -\mathrm{h}_5 \\ -\mathrm{h}_3 & \mathrm{h}_2 & -\mathrm{h}_1 & 0 & \mathrm{h}_7 & -\mathrm{h}_6 & \mathrm{h}_5 & -\mathrm{h}_4 \\ -\mathrm{h}_4 & -\mathrm{h}_5 & -\mathrm{h}_6 & -\mathrm{h}_7 & 0 & \mathrm{h}_1 & \mathrm{h}_2 & \mathrm{h}_3 \\ -\mathrm{h}_5 & \mathrm{h}_4 & -\mathrm{h}_7 & \mathrm{h}_6 & -\mathrm{h}_1 & 0 & -\mathrm{h}_3 & \mathrm{h}_2 \\ -\mathrm{h}_6 & \mathrm{h}_7 & \mathrm{h}_4 & -\mathrm{h}_5 & -\mathrm{h}_2 & \mathrm{h}_3 & 0 & -\mathrm{h}_1 \\ -\mathrm{h}_7 & -\mathrm{h}_6 & \mathrm{h}_5 & \mathrm{h}_4 & -\mathrm{h}_3 & -\mathrm{h}_2 & \mathrm{h}_1 & 0 \end{bmatrix} \tag{152.10}$$

the columns (and rows) constitute the orthogonal basis, i.e. the output vector $\mathbf{y} = \Theta(\mathbf{z})$ gives the Haar spectrum of $\mathbf{x}$. Moreover, for given $\mathbf{x}_0 = [x_1, \ldots, x_8]^{\mathrm{T}}$ and $\mathbf{y}_0 = [y_1, \ldots, y_8]^{\mathrm{T}}$ one sets up so called best adapted basis:

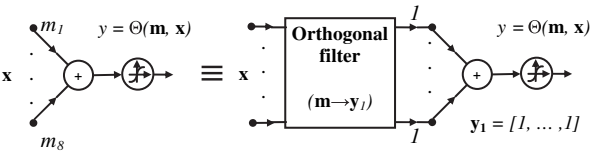

Fig. 152.4 Implementation of perceptron by orthogonal filters

$$\begin{bmatrix} h_0 \\ h_1 \\ h_2 \\ h_3 \\ h_4 \\ h_5 \\ h_6 \\ h_7 \end{bmatrix} = \frac{1}{\sum_{i=1}^{8} x_i^2} \begin{bmatrix} y_1 & y_2 & y_3 & y_4 & y_5 & y_6 & y_7 & y_8 \\ -y_2 & y_1 & -y_4 & y_3 & -y_6 & y_5 & y_8 & -y_7 \\ -y_3 & y_4 & y_1 & -y_2 & -y_7 & -y_8 & y_5 & y_6 \\ -y_4 & -y_3 & y_2 & y_1 & -y_8 & y_7 & -y_6 & y_5 \\ -y_5 & y_6 & y_7 & y_8 & y_1 & -y_2 & -y_3 & -y_4 \\ -y_6 & -y_5 & y_8 & -y_7 & y_2 & y_1 & y_4 & -y_3 \\ -y_7 & -y_8 & -y_5 & y_6 & y_3 & -y_4 & y_1 & y_2 \\ -y_8 & y_7 & -y_6 & -y_5 & y_4 & y_3 & -y_2 & y_1 \end{bmatrix} \begin{bmatrix} x_1 \\ x_2 \\ x_3 \\ x_4 \\ x_5 \\ x_6 \\ x_7 \\ x_8 \end{bmatrix} \tag{152.11}$$

It means that given $\mathbf{x}_0$ is transformed into given $\mathbf{y}_0(\mathbf{x}_0 \rightarrow \mathbf{y}_0)$ by the orthogonal filter with weight matrix given by Eq. (152.11). Thus, a classical perceptron performing a scalar product can be implemented by orthogonal filter with best adapted basis ($\mathbf{x}_0 \rightarrow \mathbf{y}_0$), as shown in Fig. 152.4:

It is worth noting, that the implementation in Fig. 152.4 relies on a linear summing of the output spectrum of the orthogonal filter. Thus, structure of network from Fig. 152.1 can be implemented by compatible connection of 8-dim orthogonal filters.

Conclusion

The main issue considered in this paper is the design of mappings. Mappings designed here rely on multivariate function approximations with skew-symmetric kernels, giving rise to very large scale networks for learning. Kernels utilized in function and mapping approximation are implemented by using HNN-based orthogonal filters and, specifically. by using 8-dim building blocks (design with best adapted basis). Thus, a network for learning, here designed, can exist as numerically stable algorithms or physical devices, performing their functions in real-time. Moreover, integrator implementations, as proposed here, can be transformed one-to-one, to phase-locked loops (PLL) structures [3]. To our knowledge, orthogonal filter-based information processing can be considered as inspired by biological systems [4].

References

1. Poggio T., Smale S.: The Mathematics of Learning: Dealing with Data, Notices of the AMS, vol. 50, no. 5, pp. 537–544, 2003.
2. Sienko W., Zamojski D.: Hamiltonian Neural Networks Based Classifiers and Mappings, Proceedings of the IEEE International Joint Conference on Neural Networks, pp. 1773–1777, Vancouver, Canada, 2006.

3. Sienko W., Citko W.: Orthogonal Filters Based Classifiers and Associative Memories, Proceedings of the IEEE International Joint Conference on Neural Networks, pp. 2823–2828, Orlando, Florida, 2007.
4. Kohonen T.: Self Organizing Maps, Springer Series in Information Sciences, Vol. 30, Springer, Berlin, Heidelberg, New York, 1995, 1997, 2001.

Chapter 153
Modeling and Simulation of Foreign Body Reactions to Neural Implants

Jianzhong Su, Humberto Perez Gonzales and Liping Tang

Abstract The fibrotic capsulations to neural implant within brains are found to substantially reduce the effectiveness of the devices. While in vitro and in vivo experiments can single out each of the steps in foreign body reaction process leading to the formation of fibrotic tissue surrounding implants, we need the predictive power to analyze the outcome of multiple interactive complex kinetics of various factors and processes and to understand its dynamical behavior during the entire period (up to several months). A mathematical model is constructed to facilitate such a need and to complement experimental work. We report that preliminary simulation results have been consistent with experimental data and the model can provide useful information for future design of implant device.

Keywords Mathematical model · fibrosis · medical implants · foreign body reactions

Introduction

Mathematical modeling and simulation have been increasingly recognized as a powerful tool for studying signal transduction mechanism and related system biology, by utilizing the large volume of experimental data. In devising novel application of human implants, solely identifying one or one group molecular targets among the complex signaling machinery is not enough. Further, the timing and strength of the signals that carry their information contents need to be assessed quantitatively [1]. The models that we are presenting, can reveal information content that resides within the signals' dynamics, i.e. the transient interactions rather than simple steady states relations. As an application, the predictive power can determine quantitatively how to influence adherent monocytes, macrophages, and foreign body giant cells to minimize the recruitment of fibroblasts and/or produce matrix metalloproteinases to degrade the fibrotic capsules on the implants.

J. Su
Department of Mathematics, University of Texas at Arlington, Arlington, Texas 76019, USA
e-mail: Su@uta.edu

R. Wang et al. (eds.), *Advances in Cognitive Neurodynamics*,

Despite of the numerous studies in the subject area, there are few realistic and kinetics-based mathematical models. Previous studies had developed models to investigate cell-cell adhesion, the spatial interactions between tumor-associated macrophages, tumor cells, and normal tissue cells, and the role of macrophages in angiogenesis ([2] and references therein). To fully account for the network effects of the coagulation and collagen formation, a detailed system consisting of kinetics of all major growth factors, platelet and others were modeled by Kuharsky and Fogelson [3], and others. The basic reactions of collagen formations were considered in previous modeling study [4, 5] and their corresponding kinetics were based on a logistics equation for fibroblast proliferation. Their reaction equations were simplified in a certain way that activations rate were linear function. To modify the specific behavior of the phosphoinositide (PI) 3-kinase pathway, Haugh et al. [6] and others had modeled a more realistic activation and proliferation of fibroblast.

Our model will follow the work of Kuharsky and Fogelson [3] and that of Dale et al. [4] not only to be inclusive of various growth factors and adherent cells, but also to be realistic in terms of activations and proliferation and migration of cells, similar to Haugh [6].

Physical Background of Model

We have selected our mathematical model based on the previous modeling work of Dale et al. [4], Kuharsky et al. [3] and Haugh [6]. The basic principles of the system are the chemical kinetic equations of the protein-cell and cell-cell reactions. The implant site contains enzymes which activate latent growth factors and also initiate the stabilization of collagen precursors [7]. Similar to other collagen formation such as dermal wound healing, collagenase is synthesized and secreted by fibroblasts as a 'zymogen' [8], but collagen degradation cannot occur until the zymogen is activated. These basic reactions were considered in previous study [4, 5] and their corresponding kinetics is incorporated in our modeling.

We show below several representative equations of a large system of 69 equations. The active forms of TGFβ isoform 1 and isoform 3 $\beta_1(t), \beta_3(t)$ undergo rapid decay and they are also transformed from inactive forms of TGFβ, namely $l_1(t), l_3(t)$ under the activation of specific enzyme $e_1(t)$. Use the law of mass action, their relations are:

$$\frac{\partial \beta_1}{\partial t} = k_{12} e_1 l_1 - k_{13} \beta_1 \tag{153.1}$$

$$\frac{\partial \beta_3}{\partial t} = k_{14} e_1 l_3 - k_{15} \beta_3. \tag{153.2}$$

Now these enzymes $e_1(t), e_2(t), e_3(t)$ are activated by latent forms of TGFβ : $l_1(t)$ and $l_3(t)$, latent forms of collagens (i.e. procollagens) $p_1(t)$ and $p_3(t)$ and collagenases $z_1(t)$ and $z_3(t)$ respectively and satisfy their corresponding kinetics equations. Eventually collagens 1 and collagen 3 fibers are transformed from procollagen 1 and procollagen 3 fibers ($p_1(t)$ and $p_3(t)$ respectively), under the actions of enzymes

$e_2(t)$. Collagenases ($s_1(t)$ and $s_3(t)$ respectively) gradually degrade collagen 1 and collagen 3. We use law of mass-action to describe the kinetics

$$\frac{\partial c_1}{\partial t} = k_{28} p_1 e_2 - k_{29} s_1 c_1 \tag{153.3}$$

$$\frac{\partial c_3}{\partial t} = k_{30} p_3 e_2 - k_{31} s_3 c_3; \tag{153.4}$$

Some specific modifications have been made for foreign body reaction process. For example, the activation rate of fibroblast $r = (k_1 + k_2\beta_1 + k_3\beta_3)$ was a simple linear function of $\beta_1(t)$, $\beta_3(t)$ in previous studies [4]. We have modified fibroblast kinetics according to the limiting activation [6] so that

$$\frac{\partial u}{\partial t} = \frac{c_1(k_1 + k_2\beta_1 + k_3\beta_3)^2}{1 + k_1 + k_2\beta_1 + k_3\beta_3 + (k_1 + k_2\beta_1 + k_3\beta_3)^2} u \left(1 - \frac{u}{k_0}\right) - A_4 u. \tag{153.5}$$

Shown below are the major components of the kinetics model.

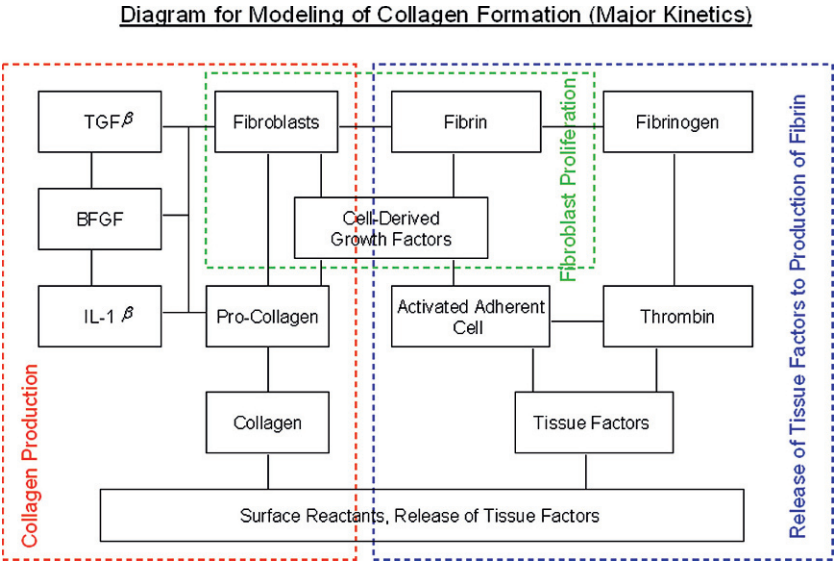

Simulated Collagen Formation Kinetics

The majority of reaction parameters is obtained from literatures (for example, the earlier models by Dale et al. [4], Kuharsky and Fogelson [3] and Haugh [6], respectively) and some parameter are determined by simulating the systems and comparing with the experiments results.

The numerical code, based on Matlab, can simulate the entire system reactions up to several months. The calculation time is about 2 min. We demonstrate the simulated

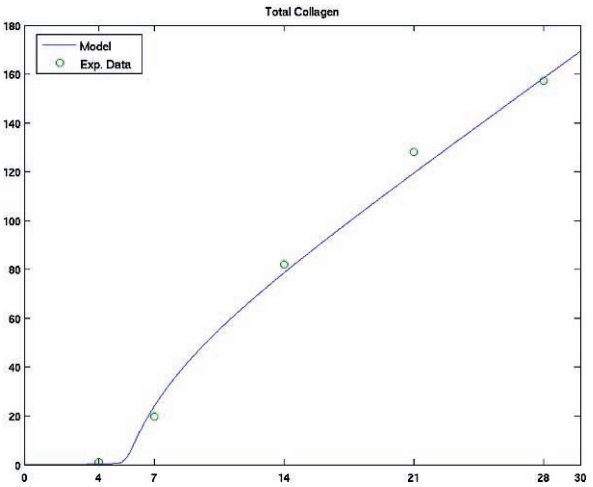

Fig. 153.1 The comparison of collagen of experimental data (the average value of two samples during a 28-day period, unit: up/cm^2) with a simulated data from the mathematical model

kinetics dynamics of collagen formation process in Figures inserted. We compare the collagen measurements with simulated data from our model for first 30 days in Fig. 153.1. In Fig. 153.2, we depict the kinetics dynamics of various variables in collagens, procollagens, collageneses, active and latent isoforms of TGFβ etc.

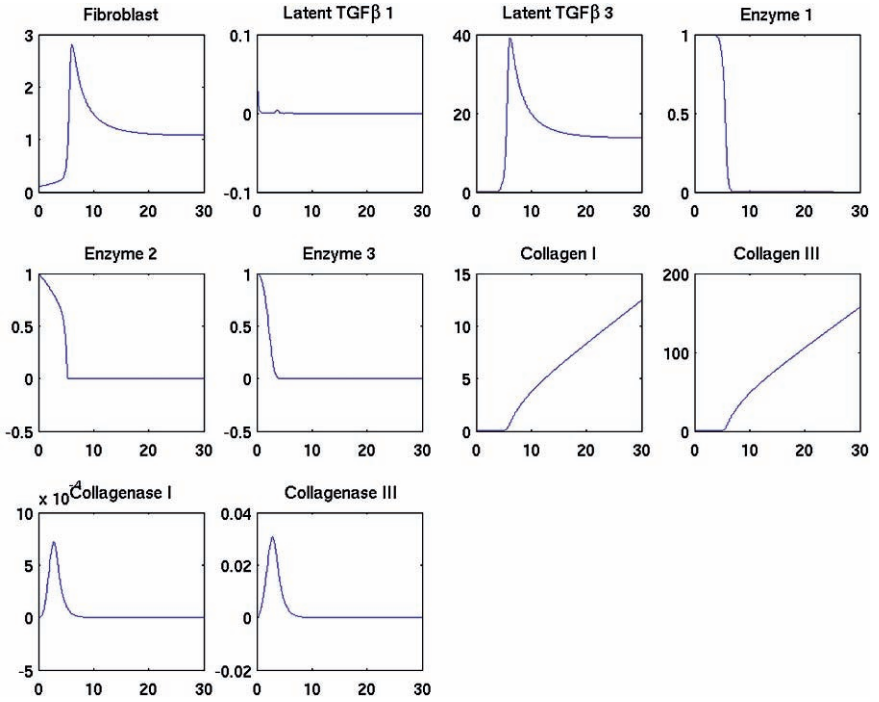

Fig. 153.2 The simulated kinetics dynamics of various variables in collagens, procollagens, collageneses, active and latent isoforms of TGFβ etc., during first 30 days

The code is also capable to systematically test all combinations of parameter values and to find the correct parameters to fit the experimental data. This code can help to find multiple pathways for activate fibroblast proliferation and the collagen formation. Our preliminary date presented here showed the feasibility of our model as a predictive tool for the purpose of studying collagen formation/or fibrotic reactions to implants.

References

1. Asthagiri, A.R., Lauffenburger, D.A.: Bioengineering models of cell signaling, Annu. Rev. Biomed. Eng. 2 (2000), 31–53.
2. Jones, J.A.: Biomaterials and the foreign body reaction:surface chemistry dependent macrophage adhesion, fusion, apoptosis, and cytokine production, Ph.D. dissertation, Case Western Reserve University, 1–241 (2007).
3. Kuharsky, A.L., Fogelson, A.L.: Surface-mediated control of blood coagulation: the role of binding site densities and platelet deposition, Biophys. J. 80 (3) (2001), 1050–1074.
4. Dale, P.D., Sherratt, J.A., Maini, P.K.: A mathematical model for collagen fibre formation during foetal and adult dermal wound healing, Proc. R. Soc. Lond. B, 263 (1996), 653–660.
5. Dallon, J.C., Sherratt, J.A., Maini, P.K.: Modeling the effects of transforming growth factor-β on extracellular matrix alignment in dermal wound repair, Wound Repair Regen. 9 (2001), 278–286.
6. Haugh, J.M.: Deterministic model of dermal wound invasion incorporating receptor-mediated signal transduction and spatial gradient sensing. Biophys. J. 90 (2006), 2297–2308.
7. Miller, G.J., Gay, S.: Collagen structure and function. In wound healing: Biochemical and Clinical aspects (ed I.K. Cohen, R.F. Diegelmann and W.J. Lindablad), Philadelphia: W.B. Saunders Co (1992), 63–76.
8. Stricklin, G.P., Bauer, E.A., Jeffery, J.J. Human skin collagenase: chemical properties of precusor and active forms: Biochemistry 17(1978), 2331–2337.

Chapter 154
Transiently Chaotic Neural Network with Variable Thresholds for the Frequency Assignment Problem in Satellite Communications

Wen Liu, Haixiang Shi and Lipo Wang

Abstract We proposed a transiently chaotic neural network with variable thresholds (TCNN-VT) by mapping the optimization problem onto the thresholds in the self-feedback terms of the neural network. This TCNN-VT model consists of $N \times M$ noisy chaotic neurons for an N-carrier-M-segment frequency assignment problem (FAP). The application of this new model on the FAP in satellite communications shows better performance compared with existing techniques, especially in large-scale problem.

Introduction

For the frequency assignment problem (FAP) in satellite communications, Mizuike and Ito [1] divided the carrier to consecutive unit segments and proposed segmentation of frequency band. Funabiki and Nishikawa [2] solved the FAP with a gradual neural network (GNN), where cost optimization is achieved by a gradual expansion scheme and a binary neural network is in charge of the satisfaction of constraints. Salcedo-Sanz *et al.* combined the Hopfield network with simulated annealing (HopSA) [3] and the genetic algorithm (NG) [4] for the FAP. However, as a kind of hybrid algorithms, the computational cost of the HopSA and the NG are increased compared with the GNN [2, 3].

Chen and Aihara [5] proposed a transiently chaotic neural network (TCNN) by introducing transiently chaotic dynamics into the Hopfield neural network (HNN) [6]. With decaying of the self-feedback connection, TCNNs are more effective in solving combinatorial optimization problems compared to the HNN [7]. We further develop the TCNN by proposing a transiently chaotic neural network with variable thresholds (TCNN-VT). The thresholds are designed to minimize the largest interference after frequency rearrangements.

This paper is organized as follows. We propose the TCNN-VT and described the formulation of the TCNN-VT on the FAP in Section "Transiently Chaotic

W. Liu
College of Information Engineering, Xiangtan University, Xiangtan, Hunan, China
e-mail: liuw0004@ntu.edu.sg

R. Wang et al. (eds.), *Advances in Cognitive Neurodynamics*,

Neural Networks with Variable Thresholds.". Simulation results are presented in Section "Simulation Results and Discussion". Finally, we conclude this paper in Section "Conclusion".

Transiently Chaotic Neural Networks with Variable Thresholds

In the self-feedback term of the TCNN [5], the threshold I_0 is constant positive. We propose the TCNN-VT by varying the threshold with the interference of the assignment which firing of the neuron represents and denote it as $I_{ij}^{(0)}$:

$$I_{ij}^{(0)} = 1 - \frac{d_{ij}}{d_{i,max}} \tag{154.1}$$

where d_{ij} is the element on row i column j of the cost matrix D, and $d_{i,max}$ is the maximum value in row i. Cost matrix $D = (d_{ij}, i = 1, \ldots, N; j = 1, \ldots, M)$ is obtained from the interference matrix $E^{(I)}$ [2].
Hence, the new TCNN-VT model is described as:

$$x_{ij}(t) = \frac{1}{1 + e^{-y_{ij}(t)/\varepsilon}} \tag{154.2}$$

$$y_{ij}(t+1) = k y_{ij}(t) + \alpha \left(\sum_{p=1,\, p\neq i}^{N} \sum_{q=1,\, q\neq j}^{M} w_{ijpq} x_{pq}(t) + I \right) - z(t) \left[x_{ij}(t) - I_{ij}^{(0)} \right] \tag{154.3}$$

where x_{ij} and y_{ij} is the output and the internal state of neuron ij, respectively. ε is the steepness parameter of the neuron activity function ($\varepsilon > 0$). k is the damping factor of the nerve membrane ($0 \leq k \leq 1$). w_{ijpq} is the connection weight from neuron ij to neuron pq and is determined [8] by the energy function (154.4). Furthermore, α is the positive scaling parameter for inputs. $z(t)$ is the self-feedback neuronal connection weight ($z(t) \geq 0$), $z(t+1) = (1-\beta)z(t)$. β is the damping factor ($0 \leq \beta \leq 1$). I is a positive input bias.

The objective of the FAP includes two part, i.e., minimization of the largest interference after reassignment and minimization of the total accumulated interference between systems [1, 2, 3]. According to [1, 2, 9], the energy function for the TCNN-VT of the FAP is defined as:

$$\begin{aligned} E = {} & \frac{W_1}{2} \sum_{i=1}^{N} \left(\sum_{j=1}^{M} x_{ij} - 1 \right)^2 + \frac{W_2}{2} \sum_{i=1}^{N} \sum_{j=1}^{M} \sum_{\substack{p=1 \\ p\neq i}}^{N} \sum_{q=max(j-c_p+1,1)}^{min(j+c_i-1,M)} x_{ij} x_{pq} \\ & + \frac{W_3}{2} \sum_{i=1}^{N} \sum_{j=1}^{M} x_{ij}(1 - x_{ij}) + \frac{W_4}{2} \sum_{i=1}^{N} \sum_{j=1}^{M} d_{ij} x_{ij} \end{aligned} \tag{154.4}$$

where $W_i, i = 1, \ldots, 4$ are weighting coefficients. The W_1 term forces that every segment in system 2 is assigned to one and at most one segment in system 1. The W_2 term guarantees that all the segments of one carrier in system 2 are assigned to consecutive segments in system 1 in the same order [2]. The W_3 term is used to force neuron outputs to approach 0 or 1 [9]. The W_4 term is needed to optimize the total interference. We convert the continuous output x_{ij} to discrete neuron output x_{ij}^b according to the average value of neuron outputs. If the neuron output x_{ij}^b is 1 at the end of the neuron update, then carrier i is assigned to segment j, and no assignments are made if $x_{ij}^b = 0$.

Simulation Results and Discussions

An iteration is terminated once a feasible assignment is obtained or the number of iteration steps exceeds 15,000. The specifications of the five instances from [2] are listed in Table 154.1.

The choices of these parameters are similar to those used in other optimization problems [5, 7] as follows: $\varepsilon = 0.004$, $k = 0.99$, $\alpha = 0.0015$, $\beta = 0.001$, and $z(0) = 0.1$. Initial inputs $y_{ij}(0)$ are randomly generated from $[-1, 1]$. Values for the weighting coefficients are chosen as follows: $W_1 = 1.0$, $W_2 = 1.0$, $W_3 = 0.7$, $W_4 = 0.00015$. The tuning of these weight coefficients is necessary to obtain better performance.

We run the TCNN-VT on each instance 1, 000 times with different randomly generated initial neuron states. Table 154.2 shows results for every instance, including the largest interference, the total interference, and the convergence rate. The convergence rate is the ratio at which the neural network finds a feasible solution in 1,000 runs. The average iteration steps T and standard deviations are also shown in this Table. The results show that the TCNN-VT is effective in reducing the largest interference and total interference by rearranging the frequency assignment.

Table 154.3 shows and the comparison of the TCNN-VT with the GNN [2] and the HopSA [3]. We show that the TCNN-VT is comparable with the GNN in terms of the largest interference and outperforms the GNN in terms of the total interference. Compared with the HopSA, the TCNN-VT is more efficient.

Table 154.1 Specifications of the FAP instances used in the simulation

Instance	Number of carriers N	Number of segments M	Range of carrier length	Range of interference
1	4	6	1–2	5–55
2	4	6	1–2	1–9
3	10	32	1–8	1–10
4	10	32	1–8	1–100
5	10	32	1–8	1–1000

Table 154.2 The performance of the TCNN-VT on five instances. The interference is shown as the best and average values (Best/ Ave). T is the average number of iteration steps. The convergence rate is the ratio at which the neural network finds a feasible solution in 1,000 runs. "SD" stands for "standard deviation"

Instance	Largest Interference (Best/ Ave)	Total Interference (Best/ Ave)	T mean±SD	Convergence Rate (%)
1	30/ 35.4	100/ 112.6	1191 ± 273	100
2	4/ 4.8	13/ 15.4	1799 ± 317	100
3	7/ 8.4	96/ 130.6	2904 ± 96.5	92.4
4	70/ 94.1	828/ 1145	2716 ± 172.8	89.1
5	661/ 849	6910/ 9527	3075 ± 268	86.6

Table 154.3 Comparison of simulation results (largest interference and total interference) obtained by the TCNN-VT, GNN and HopSA for instances 1 to 5

Instance	GNN [2]		HopSA [3]		TCNN-VT	
	Largest	Total	Largest	Total	Largest	Total
1	30	100	30	100	30	100
2	4	13	4	13	4	13
3	7	85	7	85	7	96
4	64	880	84	886	70	828
5	640	8693	817	6851	661	6910

Conclusions

We proposed a novel approach, i.e., the transiently chaotic neural network with variable thresholds, to solve the FAP in satellite communications. The novel aspect of the TCNN-VT is that the threshold in the self-feedback term of every neuron is dependent on the interference of the frequency assignment which the neuron represents. Compared with other techniques, i.e. the GNN [2] and the HopSA [3], the TCNN-VT is more efficient for the FAP in satellite communications, especially in large-scale problem.

References

1. Mizuike, T., Ito, Y.: Optimization of frequency assignment. IEEE Trans. Commun. **37**(10) (1989) 1031–1041.
2. Funabiki, N., Nishikawa, S.: A gradual neural-network approach for frequency assignment in satellite communication systems. IEEE Trans. Neural Netw. **8**(6) (1997) 1359–1370.
3. Salcedo-Sanz, S., Santiago-Mozos, R., B-Calzón, C.: A hybrid hopfield network-simulated annealing approach for frequency assignment in satellite communications systems. IEEE Trans. Syst. Man Cybern. B **34**(2) (2004) 1108–1116.
4. Salcedo-Sanz, S., B-Calzón, C.: A hybrid neural-genetic algorithm for the frequency assignment problem in satellite communications. Appl. Intell. **22**(3) (2005) 207–217.
5. Chen, L.N., Aihara, K.: Chaotic simulated annealing by a neural network model with transient chaos. Neural Netw. **8**(6) (1995) 915–930.

6. Hopfield, J.J.: Neural networks and physical systems with emergent collective computational abilities. Proc. Natl. Acad. Sci. USA **79** (8) (1982) 2554–2558.
7. Wang, L.P., Smith, K.: On chaotic simulated annealing. IEEE Trans. Neural Netw. **9**(4) (1998) 716–718.
8. Wang, L.P.: Discrete-time convergence theory and updating rules for neural networks with energy functions. IEEE Trans Neural Netw. **8**(2) (1997) 445–447.
9. Rauch, H.E., Winarske, T.: Neural networks for routing communication traffic. IEEE Control Syst. Mag. **8**(2) (1988) 26–31.

Chapter 155
Sparse Coding of Visual Context

Jun Miao, Laiyun Qing, Lijuan Duan, Xilin Chen and Wen Gao

Abstract In the field of visual object search, most of past work is focused on object-centered detection. A probable reason for seldom trying to use context is that learning spatial relationship usually needs such a large memory that a practical system generally cannot afford. This paper gives a discussion on sparse winner-take-all coding of visual context between feature positions by a neural architecture for object position perception. Some sparse features, such as extended Haar-like and extended LBP (Local Binary Pattern) features, are explored for the visual context coding for accuracy and speed. A group of experiments on the efficiency of the coding are analyzed and discussed.

Keywords Sparse coding · visual context · object search · perception · cognition

Introduction

A lot of psychological experiments [1] support the theory that context is the way that humans cognize the world. Furthermore, when humans perceive an image, e.g. a human face image, only a few neurons in his visual cortex respond [2]. This is the strategy of sparse coding for human's visual neural system. Quit a few approaches have been proposed for finding such sparse bases [3]. Some research work [4, 5] have utilized context for object search. However, seldom has research work been found to implement sparse winner-take-all coding of visual context in the form of neuronal architecture. This paper tries to make some discussions on several questions: (1) properties of some typical sparse coding features (2) structure of sparse coding for visual context; (3) performance of coding on spatial relationship between initial positions and object position. The experiments on a real image database are described and the global discussions are given in the last section.

J. Miao
Institute of Computing Technology, Chinese Academy of Sciences, Beijing 100080, China
e-mail: jmiao@ict.ac.cn

R. Wang et al. (eds.), *Advances in Cognitive Neurodynamics*,

Sparse Coding Features

Bell and Sejnowski proved that independent components of natural scenes are edge filters [6], which can be viewed as a kind of sparse bases for images. A set of features called local binary patterns (LBP) [7] is also a type of sparse coding. We designed two groups of features that are extended from the widely used features: Haar-like features and LBP features (Fig. 155.1a,b).

Figure 155.1a shows a set of extended Haar-like features for receptive field $=$ 2×2 pixels. Two types of features are given: brightness (f_0) and contrast ($f_1 \sim f_{14}$). Among them, the 14 contrast features are actually representing three kinds of geometrical features, which are points, line segments and arcs with different positions or orientations. A gray small box in the feature patterns in Fig. 155.1 represents excitatory input with a positive weight and a black box represents inhibitive input with a negative weight.

A set of extended LBP features are illustrated in Fig. 155.1b. Basic LBP is a kind of binary code for representing one of 256 patterns for image blocks of 3×3 pixels. Original LBP only output a discrete number from $0 \sim 255$ to encoding an image block pattern instead of producing a continuous comparable value for local image pattern. We extend LBP features by assigning them continuous output with the following definition:

$$f_k(\vec{x}_i) \approx \sum_{j=1}^{8} \left| x_{ij} - x_{i9} \right|$$

where vector $\vec{x}_i = (x_{i1}, x_{i2}, \ldots, x_{i9})$ represent the i-th image block of 3×3 pixels, k is a discrete number among $0 \sim 255$, which responds to a 8-bit binary code $\mathrm{LBP}_k(\vec{x}_i) = (b_{i1} b_{i2} \ldots b_{ij} \ldots b_{i8})$, where

$$b_{ij} = \begin{cases} 1 & \text{if } (x_{ij} - x_{i9}) > 0 \\ 0 & \text{otherwise} \end{cases}$$

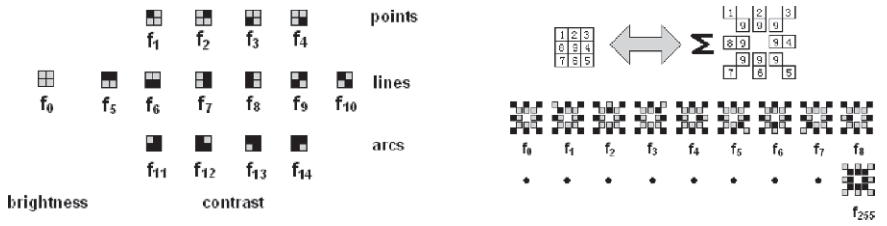

a. Extended Haar-like features (receptive field=2×2 pixels)

b. Extended LBP features (receptive field=3×3 pixels)

Fig. 155.1 Two sets of features that are extended from the widely used ones

Sparse Coding Architecture for Visual Context

Visual context consists of two aspects: image objects and their spatial relationship. So visual context coding means coding of image content and spatial relationship. To reach this goal, a neural architecture for coding the visual context is constructed, which is illustrated in Fig. 155.2a. The suggested coding framework consists of two parts. One is image content coding, which inputs a local image from a group of visual fields at different resolutions and coding the current local image with sparse features. The second part is spatial relation coding, in which winner-take-all neurons in the third layers memorize spatial relations between objects and their environments in terms of horizontal and vertical shift distances (Δx, Δy) from the center position (x, y) in a current visual field. All the coding information is stored in the connecting weights between neurons in different layers, which are learned with the Hebbian rule. The two parts naturally incorporate into an entire one and cooperate to code image content and spatial relationship in a repeated mode. Fig. 155.2b describes the object search procedure using the visual context coding memory. The two parts of the system cooperate to perceive and move gaze in a repeated mode until the system acquires the full perception of the object with 0 shift distances ($\Delta x = 0$, $\Delta y = 0$).

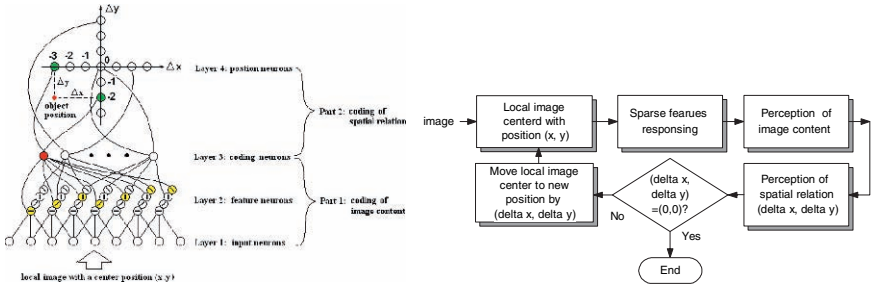

a. Visual context sparse coding architecture b. Object position perception procedure

Fig. 155.2 Sparse coding of visual context and object position perception

Experiments

To study the efficiency and performance of visual context coding and object position perception, two experiments on two systems (using extended Haar-like and LBP features respectively) for searching and locating left eye centers are carried on the still face image database of the University of Bern, which has totally 300 images (320 × 214 pixels) with 30 people (10 images each person) in ten different poses.

As illustrated in Figs. 155.3 and 155.4, coding was with a group of initial points in even distribution while testing was with a group of initial points in random distribution. Given an initial position, the system was trained or tested to codes or

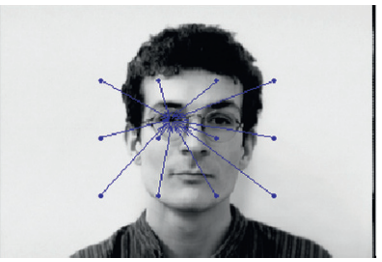

Fig. 155.3 Training for coding visual context between eye center and a group of initial positions in even distribution

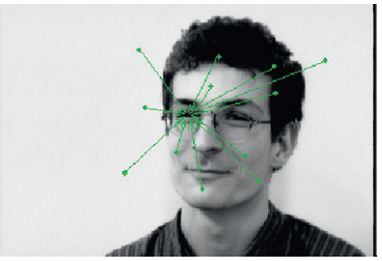

Fig. 155.4 Testing for inferring eye center positions from a group of initial positions in random distribution

Table 155.1 Performances of two systems (M: million)

Systems (sparse feature used)	Number of feature neurons	Number of coding neurons		Number of connections between feature neurons and coding neurons (M)		Average locating error (pixels)	
		#1	#2	#1	#2	#1	#2
Extended Haar-like	2250	6026	18,988	13.5585	42.723	5.47	8.25
Extended LBP	980	3397	10,511	3.32906	10.30078	8.23	10.46

search the eye centers. In the first experiment (#1) for each system, 30 images of 30 people (one frontal image each person) were recorded with 368 initial gaze positions on each image, and the rest of 270 images were tested at 48 random initial gaze positions on each image. In the second experiment (#2) for each system, 90 images of nine people (10 images each one) were recorded with 368 initial gaze positions on each image, and the rest of 210 images were tested at 48 random initial gaze positions on each image. The number of feature neurons in the second layer, the number of coding neurons in the third layer, the number of connections between feature neurons and coding neurons and the average locating error are listed in the Table 155.1.

Discussion

In the 1st experiment in section 'Experiments', the two systems learned 6026 and 3397 local image object categories with about 13 and 3 million connections, which seems quit large for the images with some human heads in the blank backgrounds. Similar results can be found in the 2nd experiment. Visual context coding seems a challenge in simulating the human vision system. To compare the winner-take-all

coding mechanism introduced in this paper, population coding of visual context will be studied and implemented in the future research.

Acknowledgements This research is partially sponsored by NSFC (No.60673091, No.60702031, No.60332010, and No.60473043), Hi-Tech R&D Program of China (No.2006AA01Z122, No.2007AA01Z163), Natural Science Foundation of Beijing (No.4061001, No.4072023), Beijing Municipal Education Committee (No.KM200610005012), "100 Talents Program" of CAS, Program for New Century Excellent Talents in University (NCET-04-0320), and ISVISION Technologies Co., Ltd.

References

1. M.M. Chun, and Y. Jiang, Contextual cueing: implicit learning and memory of visual context guides spatial attention. Cognitive Psychology, vol. 36, pp. 28–71, 1998.
2. M.P. Yong, and S. Yamane, Sparse population coding of faces in the inferotemporal cortex. Science, vol. 256(1), pp. 1327–1330, 1992.
3. B.A. Olshausen, and D.J. Field, Sparse coding with an overcomplete basis set: a strategy employed by V1?, Vision Research, vol. 37, pp. 3313–3325, 1997.
4. I.A. Rybak, V.I. Gusakova and et.al., A model of attention-guided visual perception and recognition, Vision Research, vol. 8, pp. 2387–2400, 1998.
5. A.B. Torralba, K.P. Murphy and W.T. Freeman, Contextual models for object detection using boosted random fields. Advance in Neural Information Processing Systems, Vancouver, British Columbia, Canada, 2004.
6. J. Bell, and T.J. Sejnowski, The independent components of natural scenes are edge filters, Vision Research, vol. 37(23), pp. 3327–3338, 1997.
7. T. Ojala, M. Pietikainen, D. Harwood, A comparative study of texture measures with classification based on featured distribution. Pattern Recognition, vol. 29(1), 51–59, 1996.

Chapter 156
Mark Design and Recognition in Blind-Guiding System

Jihong Liu, Guannan Shao, Xinhe Xu and Soo-Young Lee

Abstract For convenience of the blind or asthenopia people visiting all kinds of works in the museums or exhibitions, we design a blind-guiding system, and propose a novel artificial guiding mark. The method of new guiding mark's design and recognition is discussed. In order to use artificial vision to compensate blind people's vision, we make use of the cross-ratio invariance and the character of the seven-segment number, to design an artificial guiding mark. It consists of six rectangles, a letter and a couple of seven-segment number, the six rectangles is used to construct cross ratio detecting guiding mark, the letter and the seven-segment number stand for the work's code in the museum. In the process of camera imaging, the cross ratio invariance ensures the reliability of the mark's detection. The experiment shows that the proposed method can be applied in the blind guiding system efficiently.

Keywords Invariance · cross ratio · artificial guiding mark

Introduction

There are millions of blind or asthenopia people all over the world. In order to improve blind people's life quality and enhance the ability of getting information from the environment, all counties in the world have been studying the blind-guiding system. The purpose of studying and exploring blind's system is to apply the convenient, real time, high intelligent devices. The research in this field has great significance, no matter in our society or future technology. With the improvement of high-performance computer and high-precision optical appliance, vision guiding becomes an advanced location and guiding technic in recent years. By contrast, the artificial landmark-based guiding system with low-expense, easy-recognize, flexibility, is focused by scholars all over the world [1].

J. Liu
College of Information Science and Engineering, Northeastern University, Shenyang, 110004 Liaoning, China
e-mail: liujihong@ise.neu.edu.cn

R. Wang et al. (eds.), *Advances in Cognitive Neurodynamics*,

Various natures of invariants play an important role in pattern recognition of computer vision. Cross ratio invariant is the most applicable invariants in all proposed geometric invariants. Cross-ratio invariant has been applied to pattern recognition on computer vision for a long time as the most fundamental projective invariant [2, 3], but few apply this invariant to design landmark pattern.

For the purpose of helping blind or asthenopia people conveniently visiting in all kinds of exhibition, we design this blind guiding system. In this system, the CCD camera captures the front image of the blind people, the image-processing model recognize the guiding mark designed by the certain rules, then identify the character in the landmark, finally, the system broadcast the corresponding speech to explain the work for the blind in their earphone. The paper will mainly introduce the guiding mark's design and recognition. The artificial guiding mark proposed in this paper makes use of cross ratio invariants' characteristic, and the recognition processing is simulated in matlab 7.4.0 platform.

Cross Ratio Invariants Theory

The cross-ratio of four collinear points is invariable during the process of projective mapping [4, 5]. And cross ratio value is preserved after the projection mapping, linear scaling, rotation and transformation [6]. Figure 156.1a shows that A, B, C, D is four collinear points in projection plane Ω_0, A and B are general points, C and D are general points or infinite far points. The definition of the four collinear points A, B, C, D cross ratio is $\frac{\frac{AC}{CB}}{\frac{AD}{DB}}$, that is $l = (A, B; C, D) = \frac{\frac{AC}{CB}}{\frac{AD}{DB}}$. When the line L is central-projected after O-centre projection, it is transformed into another line L' in the projection plane Ω_1; At the same time, the four points in line L is transformed into A', B', C', D' in line L'. The cross-ratio invariance of four collinear points mean $\frac{\frac{AC}{CB}}{\frac{AD}{DB}} = \frac{\frac{A'C'}{C'B'}}{\frac{A'D'}{D'B'}}$, or $(A, B; C, D) = (A', B'; C', D')$.

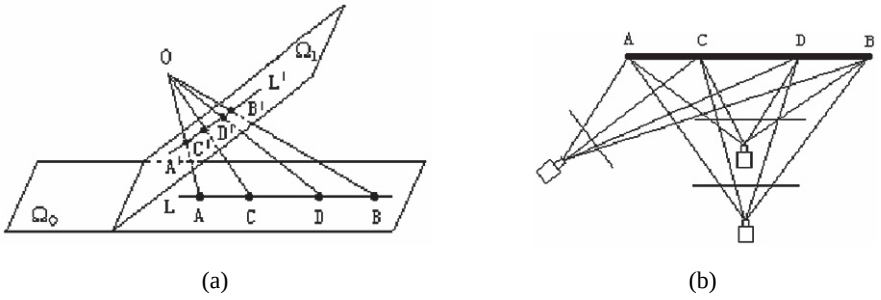

(a) (b)

Fig. 156.1 (**a**) The cross-ratio of four collinear points. (**b**) Cross-ratio value is unchanged in different perspectives

The distance between A', B', C', D' is quite different from the distance between A, B, C, D but the line is invariable, O-centre, A, B, C, D determine four lines are the same with O-centre, A', B', C', D' determine four lines. While the four lines can be determined by their cross angles, so the cross ratio of four co-point lines can be defined as Eq. (156.1).

$$(OA, OB; OC, OD) = \frac{\sin \angle AOC / \sin \angle BOC}{\sin \angle AOD / \sin \angle BOD} \tag{156.1}$$

It is showed above that the cross-ratio of four collinear points and the cross-ratio of four co-point lines are preserved after central projection [5].

Design and Recognition of Guiding Mark

In general, a landmark should be designed with three key functions [7] which are detection, localization and recognition. In order to detect and recognize the landmark in the cluttered scene robustly, the landmark pattern should show invariant characteristics under various viewing angles (e.g. front-glance, side-glance, near-glance, far-glance), as Fig. 156.1b shows. Four collinear points in the pixel plane, preserve the collinear and position relations, and another important aspect is the cross-ratio value is unchanged, namely, the cross ratio in pixel plane is equal to in the space, that is the main basic theory in constructing landmark [8]. Moreover, the quantity of landmark model should be enough and different landmark should be encoded unique information. The guiding mark model designed in this paper is showed in Fig. 156.2a.

It consists of three parts: two vertical and the same wideness black bars; four horizontal and the same wideness black bars; a letter, a couple of seven-segment numbers. In order to distinguish two numbers, the letter in this paper chooses six differentiable letters: E,F,H,C,P,U. To different landmarks, the six black bars is unchangeable no matter the size or the position, they are used for detecting landmarks; and the difference of the letter and the seven-segment number are used for

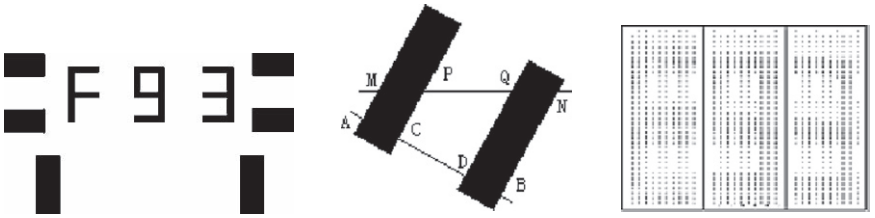

(a) (b) (c)

Fig. 156.2 (**a**) The artificial landmark model. (**b**) Declining black bars makes the cross ratio unchangeable. (**c**) The letter and number region under side glance

distinguish different landmarks. Another merit to use black bars constructing cross ratio, shows in Fig. 156.2b, is proved that in the declining state, the cross-ratio value is unchanged, that is as Eq. (156.2).

$$l = \frac{\frac{AC}{CB}}{\frac{AD}{DB}} = \frac{\frac{MP}{PN}}{\frac{MQ}{QN}} \tag{156.2}$$

It ensures that once the landmark is put declining, as long as λ does not change, it can also detect and recognize landmark successfully, greatly increase the stability of landmark detection. The two vertical rectangles construct horizontal cross ratio and left or right two row rectangles construct vertical cross ratio, During the process of designing landmark, two directions of cross-ratio values are pre-counted, when detecting, once determine a landmark in the image using the two-directional cross-ratio values, a small rectangle including a letter and a couple of seven-segment numbers are get by six rectangles' edge information, then recognize the letter and seven-segment number in this small rectangle, that is recognition of different landmarks.

Experiment Results

The algorithm is programmed in matlab, detecting and recognizing. The results are shown in the Table 156.1. The side glance running result in matlab is shown in Fig. 156.2c, the letter and number parts are 0, and others are 1 from Fig. 156.2c.

Table 156.1 Data comparison in several situation of image processing

Comparison	Horizontal cross-ratio value	Vertical cross-ratio value	Size of segment region
Front glance	0.0129	0.1660	39 × 85
Side glance	0.0121	0.1543	36 × 63
Declining glance	0.0019	0.1674	29 × 68

Conclusion

In order to compensate blind people's vision using artificial vision, an artificial guiding mark is designed in this paper, which is based on the cross ratio invariance and seven-segment number's characteristic. We conduct the experiment from front glance, side glance, declining perspectives detecting and segmenting the same landmark. The result shows that the guiding mark is robust, and this method can be reliably applied in the blind-guiding system.

References

1. Li-Chun L., et al.: Self-Localization of Mobile Robots Based on Visual Information. IEEE Conference on Industrial Electronics and Applications (2006) 1–6.
2. Bruno M., et al.: Localisation Based on Invariant-Models Recognition By SYCLOP. Proceedings of the International Conference on Intelligent Robots and Systems, vol. 2. (1999) 793–798.
3. Vassilios S. Tsonis, et al.: Landmark-based Navigation Using Projective Invariants. Proceedings of the International Conference on Intelligent Robots and Systems (1998) 342–347.
4. Mohr R., Morin L.: Relative Positioning from Geometric Invariants. Proceedings of the Conference on Computer Vision and Pattern Recognition (1991) 139–144.
5. Dezhi F., Yipei C.: Projective Geometry. Beijing: Higher Education Publishing Company (1983) 109–113.
6. Natapon Pantuwong, Nopporn Chotikakamthorn: Comparative Study of Two Projective-Invariant Digital Watermarking Methods Using Cross-Ratios and Line Intersections. The Fifth International Conference on Computer and Information Technology (2005) 543–547.
7. Becker J., Salas K., Tokusei J.-C. Latombe: Reliable Navigation Using Landmarks. IEEE International Conference on Robotics and Automation, vol. 1 (1995) 401–406.
8. Yang G.: Research on the Problems Concerning Based on New Artificial Landmark based-single-view Navigation of Autonomous Mobile Robot. Shenyang: Northeastern University (2006).

Chapter 157
An Animal Model of Alzheimer's Disease Highlighting Targets for Computational Modeling

Diana S. Woodruff-Pak, Alexis Agelan, Luis Del Valle and Mohan Achary

Abstract Having demonstrated that eyeblink classical conditioning is severely impaired in Alzheimer's disease (AD), we are modeling AD in rabbits and evaluating outcomes in the context of empirical data and computational models. Results indicate that: (a) computational models of the essential role of cerebellar cortical LTD in delay conditioning could amplify upon new empirical data; (b) computational models of the length of the trace interval that makes the paradigm hippocampus-dependent could elucidate species differences in the critical trace interval; and (c) computational models of cortical-hippocampal-cerebellar inter-actions in trace conditioning could magnify knowledge about the neurodynamics of associative learning and memory.

Introduction

Computational modeling of eyeblink classical conditioning has taken advantage of the extensive knowledge base on the behavioral parameters and neural substrates of this form of associative learning. Rescorla and Wagner [1] used behavioral eyeblink conditioning data to formulate a mathematical model that predicted changes in the strength of association between the conditioned stimulus (CS) and the unconditioned stimulus (US). More recently, the Rescorla-Wagner model was mapped to the cerebellum, the essential substrate of eyeblink classical conditioning [2]. This model predicted activity of cerebellar cortical Purkinje neurons during phases of acquisition.

Another brain structure that is normally engaged in eyeblink classical conditioning is the hippocampus. Models of hippocampal function in delay eyeblink conditioning in which the CS and US overlap and coterminate [3] and of trace eyeblink conditioning in which the CS onsets and then turns off before US onset made successful predictions at the cellular level [4]. Computational models of the

D.S. Woodruff-Pak
Department of Psychology, Temple University, Philadelphia, PA 19122, USA
e-mail: pak@temple.edu

R. Wang et al. (eds.), *Advances in Cognitive Neurodynamics*,

empirical observation that disruption of the septo-hippocampal cholinergic system impairs acquisition in delay eyeblink conditioning have also been successful [5]. Disruption of the septo-hippocampal cholinergic system and impaired acquisition in animals led us to predict that delay eyeblink conditioning would be impaired in patients with Alzheimer's disease (AD) [6]. Now we are modeling AD in rabbits and evaluating neurobiological, cognitive, and therapeutic outcomes in the context of empirical and computational models.

An Animal Model of Alzheimer's Disease

Normal brain function involves the use of cholesterol and metals such as copper, but recent evidence indicates that both may be involved in the etiology of AD. Research in domains as divergent as epidemiology, cell biology, and genetics has converged to indicate that cholesterol plays a central role in the biology of amyloid precursor protein (APP) and its proteolytic product, β-amyloid. Mounting evidence demonstrates roles for APP and β-amyloid in metal homeostasis. Cholesterol-fed rabbits develop a number of pathological indices of AD that are accelerated when a trace amount of copper is added to the drinking water [7]. In our laboratory, when young male rabbits were treated with 2% cholesterol added to their normal diet and 0.12 mg/l copper added to their distilled drinking water, they developed AD neuropathology within eight weeks [8]. At molecular and neuropathological levels, the brains of AD model rabbits have at least a dozen features similar to the pathology observed in the AD brain. AD model rabbits also have impairment in learning and memory in eyeblink classical conditioning that parallels impairment observed in human AD [8, 9].

Cognition: Impaired Eyeblink Conditioning in Alzheimer's Disease

Severe memory loss is the most prominent clinical symptom of AD, and this memory impairment has long been associated with impairment in acetylcholine neurotransmission. Eyeblink conditioning impairment in AD may reflect cholinergic dysfunction in the brain that occurs early in disease progression. In addition to being impaired in AD, eyeblink conditioning was severely impaired in adults over the age of 35 with Down's syndrome and associated AD neuropathology. Eyeblink conditioning in patients with other neurodegenerative diseases such as Huntington's disease and Parkinson's disease was relatively normal and clearly differentiated from eyeblink conditioning in AD [10].

Neuropathology and Cognition in the AD Rabbit Model

Adding 2% cholesterol to the diet and a trace amount of copper to the drinking water for 8–10 weeks creates neuropathology in young adult male rabbits that resembles AD neuropathology. Rabbits treated in this manner were impaired in trace eyeblink classical conditioning but not short-delay eyeblink conditioning [9]. We replicated

these results with trace conditioning and extended them by demonstrating that long-delay eyeblink conditioning was also impaired. A novel feature of our study was the treatment with 3.0 mg/kg galantamine (Razadyne™), a drug approved by the FDA to treat mild to moderate AD. Galantamine is a mild acetylcholinesterase (AChE) inhibitor and an allosteric modulator of nicotinic acetylcholine receptors (nAChRs). Treatment with galantamine ameliorated impaired eyeblink classical conditioning in this rabbit model of AD in both the trace and long-delay paradigms [8].

Abnormal neurons, tau, and β-amyloid immunoreactivity were found in the hippocampus of AD model rabbits, and in the cerebellum there was also tau and β-amyloid immunoreactivity as well as substantial Purkinje neuron loss in cerebellar cortex [8]. A biological model of AD induced by dietary means in rabbits impairs both delay and trace eyeblink classical conditioning. Behavioral results, neuropathology, and therapeutic outcome are consistent with empirical data and computational models of eyeblink classical conditioning.

Cerebellum and Deep Cerebellar Nuclei

The deep cerebellar nuclei of AD model rabbits were intact as confirmed with histology. Also, rabbits showed significant acquisition of CRs in delay and trace eyeblink conditioning [8]. Lesions to deep cerebellar nuclei abolish CRs.

Cerebellum, Purkinje Neuron Loss, and Acquisition

The rabbit model of AD has substantial loss of cerebellar cortical Purkinje neurons and impaired delay eyeblink conditioning [8]. Cerebellar cortical Purkinje neurons affect function in neurons in the interpositus nucleus, as Purkinje neurons are the only efferents to cerebellar deep nuclei. Purkinje neuron number is associated with the rate of acquisition of CRs in the delay paradigm in rabbits, rats, and mice [11]. Purkinje cell deterioration (*pcd*) mutant mice that lose all Purkinje neurons by four weeks of age were dramatically impaired in delay eyeblink conditioning [12]. Transgenic mice with intact Purkinje neurons that had a functional lesion, knock-out of the Purkinje neuron *Scn8a* sodium channel, were impaired in delay eyeblink conditioning [13].

Purkinje neurons are central components of a mechanism for information storage in the cerebellum called long-term depression (LTD). In this model, coactivation of climbing fiber and parallel fiber inputs to a Purkinje cell induces a persistent, input-specific depression of the parallel fiber-Purkinje cell synapse. When LTD is impaired in cerebellar cortex, delay (but not trace) eyeblink classical conditioning is impaired.

Hippocampus and Trace Conditioning

The hippocampus of AD model rabbits had positive immunostaining for tau and β-amyloid. In CA1 and CA3, where pyramidal neurons are normally engaged in

eyeblink conditioning, there was neuron loss and apparent synaptic disruption [8]. These impairments likely contributed to impaired trace conditioning. The hippocampus is normally engaged in delay eyeblink conditioning, and in trace eyeblink conditioning an intact hippocampus and medial prefrontal cortex are essential. The trace interval requiring essential involvement of cortical structures varies among different mammalian species. That critical trace interval is 250 ms in mice and rats, over 300 ms in rabbits, and 1000 ms in humans [11].

Galantamine and Cholinergic Facilitation of Learning

Acetylcholine neurotransmission plays a crucial role in learning and memory. Disruption of acetylcholine neurotransmission in the septohippocampal system impairs learning of the conditioned eyeblink response in rabbits. Pharmacologic therapies to preserve the action of a dwindling acetylcholine pool in the AD brain have focused on prolonging its presence at the synapse. Galantamine is a relatively mild AChE inhibitor. For an equivalent magnitude of AChE inhibition to donepezil, 3 to 15 times as much galantamine must be administered. At equal levels of AChE inhibition, only galantamine improves eyeblink classical conditioning, suggesting that allosteric modulation of nAChRs is an additional effective mechanism of action [14].

Future Directions for Computational and Empirical Work

Computational models have predicted rate and qualitative features of Purkinje neuron activity during acquisition of delay eyeblink conditioning [2]. More recently, empirical data have demonstrated that disruption of LTD in cerebellar cortex disrupts delay but not trace eyeblink conditioning [11]. Computational models of the essential role of cerebellar cortical LTD in delay conditioning would amplify upon the empirical demonstrations.

Progress in computational modeling of the hippocampus in trace conditioning was made with a model focusing on neurons in the CA1 and CA3 regions [4]. Computational modeling might elucidate substrates of the species difference in the length of the trace interval that makes the paradigm hippocampus dependent. Prefrontal cortex is also essential in trace eyeblink conditioning, and the role of cerebral cortex in eyeblink conditioning requires additional modeling.

Finally, why and how does cerebellar cortex get bypassed in trace eyeblink conditioning? The essential involvement of hippocampus, medial prefrontal cortex and other forebrain regions in trace eyeblink conditioning may eliminate or supersede the role that cerebellar cortex plays in delay eyeblink conditioning. Forebrain regions may act to bridge the trace interval between the CS and US in trace conditioning [11]. Computational modeling of cortical-hippocampal-cerebellar interactions in trace conditioning would amplify knowledge about cognitive neurodynamics.

Acknowledgements Supported by grants from NIH (NIA) 1 R01 AG021925 and 1 R01 AG023742 and from the Alzheimer's Association to DSW-P.

References

1. Rescorla, R., Wagner, A.: A theory of Pavlovian conditioning: Variations on the effectiveness of reinforcement and non-reinforcement. In: Black, A., Prokasy, W. (eds.): Classical Conditioning II: Current Research and Theory. Appleton-Century-Crofts, New York (1972) 64–99.
2. Gluck, M.A., Myers, C.E., Thompson, R.F.: A computational model of the cerebellum and motor-reflex conditioning. In: Zornetzer, S.F., McKenna, T.M., Lau, C., Davis, J.L. (eds.): An Introduction to Neural and Electronic Networks, 2nd edn. Academic Press, New York (1995) 91–98.
3. Gluck, M.A., Myers, C.E.: Hippocampal mediation of stimulus representation: A computational theory. Hippocampus, 3 (1993) 491–516.
4. Yamazsaki, T., Tanaka, S.: A neural network model for trace conditioning. Int J Neural Syst, 15 (2005) 23–30.
5. Rokers, B., Mercado, E., Allen, M.T., Myers, C.E., Gluck, M.A.: A connectionist model of septohippocampal dynamics during conditioning: closing the loop. Behav Neurosci 116 (2002) 48–62.
6. Woodruff-Pak, D.S., Finkbiner, R.G., Sasse, D.K.: Eyeblink conditioning discriminates Alzheimer's patients from non-demented aged. NeuroReport 1 (1990) 45–48.
7. Sparks, D.L.: Cholesterol, copper, and accumulation of thioflavine S-reactive Alzheimer's-like amyloid β in rabbit brain. J Mol Neurosci 24 (2004) 97–104.
8. Woodruff-Pak, D.S., Agelan, A., del Valle, L.: A rabbit model of Alzheimer's disease: Valid at neuropathological, cognitive, and therapeutic levels. J Alzheimer's Dis 11 (2001) 371–383.
9. Sparks, D.L., Schreurs, B.: Trace amounts of copper in water induce beta-amyloid plaques and learning deficits in a rabbit model of Alzheimer's disease, PNAS 100 (2003) 11065–11069.
10. Woodruff-Pak, D.S.: Insights about learning in Alzheimer's disease from the animal model. In: Carroll, M.E., Overmier, J.B. (eds.): Linking Animal Research and Human Psychological Health. American Psychological Association, Washington D.C. (2001) 323–336.
11. Woodruff-Pak, D.S., Disterhoft, J.F.: Where is the trace in trace conditioning? TINS 31 (2008) 105–112.
12. Chen, L., Bao, S., Lockard, J.M., Kim, J..J., Thompson, R.F.: Impaired classical eyeblink conditioning in cerebellar lesioned and Purkinje cell degeneration (*pcd*) mutant mice. J Neurosci 16 (1996) 2829–2838.
13. Woodruff-Pak, D.S., Green, J.T., Levin, S.I., Meisler, M.H.: Inactivation of sodium channel Scn8A (NaV1.6) in Purkinje neurons impairs learning in Morris water maze and delay but not trace eyeblink classical conditioning. Behav Neurosci 120 (2006) 229–240.
14. Woodruff-Pak, D.S., Tobia, M.J., Jiao, X., Beck, K.D., Servatius, R.J.: Preclinical investigation of the functional effects of memantine and memantine combined with galantamine or donepezil. Neuropsychopharmacologia 32 (2007) 1284–1294.

Chapter 158
An Improved Transiently Chaotic Neural Network Approach for Identical Parallel Machine Scheduling

Aiqing Yu and Xingsheng Gu

Abstract Identical parallel machine scheduling problems (IPMSP) have been intensively studied for its universality in real life. A transiently chaotic neural network is improved by introducing a time-dependent parameter and it is applied to solve IPMSP. To overcome the tradeoff problem existing among the penalty terms, time-varying penalty parameters are used in the energy function. The simulation results tested on three different problems with 100 random initial conditions show that this approach solves problems in reasonable time.

Keywords Scheduling · identical parallel machines · transiently chaotic neural network · time-varying penalty coefficients

Introduction

There have been many studies on conventional and intelligent techniques for parallel machine scheduling problems [1]. However, not much progress has been made for the exploration of the use of Neural Networks in solving this problem. Akyol and Bayhan proposed a Hopfield type dynamical neural network for solving IPMSP [2]. Unlike conventional neural networks only with point attractors, transiently chaotic neural network (TCNN) proposed by Chen and Aihara [3] has richer and more flexible dynamics, so that it can be expected to have higher ability of searching for global optimal or near-optimal solutions. In this paper we propose an improved TCNN model and present the architecture including neural network energy function as an innovative, alternative approach for solving IPMSP to minimize the makespan.

A. Yu
Research Institute of Automation, East China University of Science and Technology, 200237 Shanghai, China
e-mail: yuaiqing@mail.ecust.edu.cn

R. Wang et al. (eds.), *Advances in Cognitive Neurodynamics*,

An Improved TCNN Model for IPMSP

An Improved Transiently Chaotic Neural Network Model

In [3], Chen et al. showed that both the parameter α could affect the neurodynamics and parameter β governed the bifurcation speed of the transient chaos. In order to improve the convergence speed and search ability of TCNN, we replace α with a time variable $\alpha(t)$, defined as follows.

$$\alpha(t+1) = \begin{cases} (1+\lambda)\alpha(t) & \text{if } \Delta E > \eta E_0 \\ \alpha(t) & \text{otherwise} \end{cases} \tag{158.1}$$

where λ, η are small positive constants (selected empirically) and E_0 is the energy of the previous generation, and ΔE is the energy gap. Initially, α_0 is set to a small values and the influence of the energy function is still weak enough to allow transient chaos to be generated. Gradually, $\alpha(t)$ will be increased to strengthen the influence of the energy function when the energy gap is greater than E_0.

The Energy Function of TCNN for IPMSP

Assume Vx_{ij} to be the neuron output representing whether job j ($j = 1, 2, \cdots, n$) is assigned to machine i ($i = 1, 2, \cdots, m$) or not.

The global energy function for this network consisting of the objective C max and these constraints of IPMSP can be defined as:

$$\begin{aligned} E = {} & \mathrm{A}VC\max + \mathrm{B}\sum_{i=1}^{m} v\left(\sum_{j=1}^{n} p_j Vx_{ij} - VC\max\right) \\ & + \mathrm{C}\sum_{j=1}^{n}\sum_{i=1}^{m}\sum_{k=1,k\neq i}^{m} Vx_{ij}Vx_{kj} + \mathrm{D}\left(\sum_{i=1}^{m}\sum_{j=1}^{n} Vx_{ij} - n\right)^2 \end{aligned} \tag{158.2}$$

where A, B, C and D are positive penalty parameters for the objective, makespan constraints, column constraints and global constraints respectively, besides v represents the penalty function [4] and p_j is processing time of job j.

$$v(\varepsilon) = \begin{cases} \varepsilon^2 & \varepsilon > 0 \\ 0 & \varepsilon \leq 0 \end{cases} \tag{158.3}$$

The difference equations describing the network dynamics of TCNN for Identical parallel machine scheduling problem (IPMSP) are obtained as follows:

$$UC\max(t+1) = kUC\max(t) + \alpha(t)\left(-\frac{\partial E}{\partial VC\max}\right) - z(t)(VC\max(t) - I_0) \tag{158.4}$$

$$Ux_{ij}(t+1) = kUx_{ij}(t) + \alpha(t)\left(-\frac{\partial E}{\partial Vx_{ij}}\right) - z(t)\left(Vx_{ij}(t) - I_0\right) \tag{158.5}$$

$$\frac{\partial E}{\partial VC\max} = \mathrm{A} + \mathrm{B}\cdot(-1)\cdot\sum_{i=1}^{m} v'\left(\sum_{j=1}^{n} p_j Vx_{ij} - VC\max\right) \tag{158.6}$$

$$\frac{\partial E}{\partial Vx_{ij}} = \mathrm{B}\cdot p_j\cdot v'\left(\sum_{l=1}^{n} p_l Vx_{il} - VC\max\right) + \mathrm{C}\cdot 2\cdot\sum_{k=1,k\neq i}^{m} Vx_{kj} + \mathrm{D}\cdot 2\cdot\left(\sum_{k=1}^{m}\sum_{l=1}^{n} Vx_{kl} - n\right) \tag{158.7}$$

$$VC\max = \begin{cases} UC\max & UC\max \geq 0 \\ 0 & \text{otherwise} \end{cases}, \quad Vx_{ij}(t) = \frac{1}{1+e^{-Ux_{ij}(t)/\varepsilon}} \tag{158.8}$$

Time-Varying Penalty Parameters

Because there is no theoretically established method for choosing the values of the penalty coefficients for an arbitrary optimization problem, the appropriate values for these coefficients can be determined by empirically running simulations [5]. Recently, time based penalty parameters are proposed to overcome the tradeoff [4]. In this paper, we make penalty parameters time variables, starting with small values and continuously increasing them when their corresponding constraints are not satisfied.

Simulation Analysis

To evaluate performance of the proposed TCNN algorithm, computational experiments were performed on randomly generated test problem of three different sizes. The processing time was generated from the uniform distribution over the interval [1, 50]. Considering the solution quality depending highly on initial conditions, all the solutions were obtained by simulations with 100 random initial conditions.

TCNN parameters for test problems were determined by trial and error as shown in Table 158.1. In Table 158.2, the results are compared with those of Hopfield-like dynamic neural network (HDNN) proposed in [2] and the original TCNN proposed

Table 158.1 TCNN parameters for test problems

Problem size (m*n)	κ	α_0	λ	η	β	I_0	ε	$z(0)$
3*10	0.997	0.008	0.005	0.05	0.001	0.65	0.008	0.08
3*20	0.997	0.010	0.005	0.05	0.001	0.65	0.008	0.08
3*50	0.998	0.015	0.005	0.15	0.0005	0.5	0.008	0.1

Table 158.2 Results of 100 different initial conditions over three problems

	Proposed			TCNN			HDNN		
Problem size(m*n)	Best Cmax	Avg. Cmax	PFS	Best Cmax	Avg. Cmax	PFS	Best Cmax	Avg. Cmax	PFS
3*10	76.56	90.21	100%	79.65	99.55	100%	95.31	115.42	90%
3*20	163.99	194.43	100%	171.44	197.25	98%	180.24	215.89	85%
3*50	352.31	388.38	100%	368.78	399.37	86%	389.03	440.13	68%

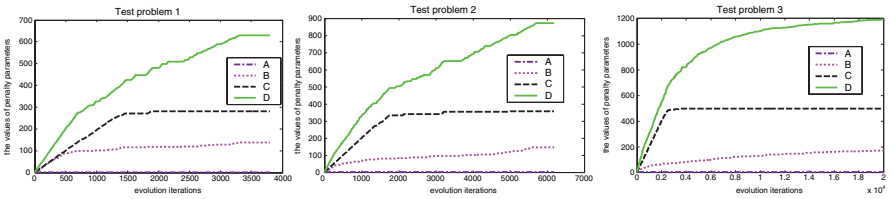

Fig. 158.1 Time varying penalty parameters of the best solutions over three problems

in [3] in terms of Best Cmax, Average Cmax and Percent Feasibility of the Solutions (PFS). The results show that along with the increase of the test problem size, the percent feasibility of solutions decreased and the network were trapped into local minima more easily. Compared to HDNN and original TCNN, this improved TCNN model can find better solution of Cmax.

Figure 158.1 shows the time varying penalty parameters of the best solutions over three different problems. The coefficient B of the inequality constraint and coefficient D of the global constraint were higher than parameter C of the column constraint during the evolution process. Along with the increase of the test problem size, evolution iterations aggrandized correspondingly.

Conclusion

In this paper, we just construct the network model for the basic identical parallel machines scheduling problem. Other models which setup times, job splitting are considered can be further research directions. Besides, architecture of the neural network, selection of penalty parameters and construction of energy function also may be research topics.

Acknowledgements This work is supported by National Natural Science Foundation of China under Grant No. 60674075

References

1. Mokotoff, E.: Paralel machine scheduling problems: A survey. Asia-Pacific Journal of Operational Research. 18 (2001) 193–242.
2. Akyol, D. E., Bayhan, G.: Minimizing makespan on identical parallel machines using neural networks. Proceedings of ICONIP 2006, Part III, 553–562.
3. Chen, L., Aihara, K.: Chaotic simulated annealing by a neural network model with transient chaos. Neural Networks, 8 (1995) 915–930.
4. Wang, J.: A Time-varying recurrent neural system for convex programming. Proceedings of IJCNN-91-Seattle International Joint Conference on Neural Networks. 1 (1991) 147–152.
5. Watta, P.B., Hassoun, M.H.: A coupled gradient network approach for static and temporal mixed-integer optimization. IEEE Transactions on Neural Networks. 7 (1996) 78–593.

Chapter 159
Support Vector Machine on Functional MRI

Ling Zeng, Qingwei Liu, Huiling Xiao and Huafu Chen

Abstract In the present study, the Support Vector Machine (SVM) algorithm are introduce to detect activity region of brain function from whole function volume. Firstly, temporal compression (averaging across multiple scans) is implemented by using single value decomposition (SVD) to functional magnetic resonance imaging (fMRI) data. Then SVM algorithm is used to separate different brain functional activation pattern in different task state. Subjects are request to finish fMRI experimental in three conditions: rest state, right hand movement and left hand movement. fMRI imaging result demonstrate that the SVM method can exactly detect the activity region of brain function in the spatial maps of discriminating volume which contains the most discriminating regions in the voxels space.

Introduction

Function Magnetic Resonance Imaging (fMRI) provided in the early 1990s is a revolution tool for Neuroinformatics. A number of fMRI experiments have been used to investigate activated regions of brain corresponding certain cognitive and psychological states [1]. Univariate statistical analysis methods such as general linear model (GLM) are commonly applied to the time series at each voxel [2].

Recently, support vector machine (SVM) method first proposed by Vapnik [3] has been used in the pattern classification and the non-linear return.

In this paper, SVM method is introduced to detect brain functional activation pattern in different task state. The fMRI data dimension is reduced by principal component analysis(PCA)/single value decomposition(SVD), then SVM approach is applied to detect brain functional activation.

SVM method' aim is to find a decision function or the optimal separation hyperplane which can solates two states [4] with the maximization edge. The essence is to solve a quadratic programming problem.

L. Zeng
School of Life Science and Technology, University of Electronic Science and Technology of China, Chengdu 610054, China
e-mail: chenhf@uestc.edn.cn

R. Wang et al. (eds.), *Advances in Cognitive Neurodynamics*,

we use the kernel function $\phi(x_)$ which can project voxel space into high dimensionality. The optimal separation hyperplane is:

$$H : w^T \phi(x) + b = 0 \tag{159.1}$$

The w is a linear weight vector, b an offset and $\phi(x)$ convex function of w. we need solve its restraint dual question:

$$\begin{aligned} &\min\{\mathrm{w}(\alpha) = \tfrac{1}{2}\alpha^{\mathrm{T}}\mathrm{Q}\alpha - \mathrm{e}^{\mathrm{T}}\alpha\} \\ &\text{subject to } \mathrm{y}^{\mathrm{T}}\alpha = 0, 0 \le \alpha_{\mathrm{i}} \le \mathrm{C}, \mathrm{i} = 1, \ldots, \mathrm{l}. \end{aligned} \tag{159.2}$$

The solution w is given by

$$\mathrm{w} = \sum_{\mathrm{i}=1}^{\mathrm{l}} \alpha_{\mathrm{i}} \mathrm{y}_{\mathrm{i}} \phi(\mathrm{x}_{\mathrm{i}}) \tag{159.3}$$

Methods

Data Acquisition

The data were acquired with a 1.5 T siements Vision scanner. The imaging sequence was an echo planar sequence (slice thickness = 6 mm, gap between slices = 1 mm; repetition time (TR) = 2 s; echo time (TE) = 60 ms; matrix, 64×64; voxel dimensions, $4 \times 4 \times 6$ mm). In each run, 164 function volumes were acquired.

Stimuli and Tasks

The stimuli were presented in a block fashion. There were three different experimental conditions: rest contrast; right-hand movement task; left-hand movement task. In each run, there were 16 blocks(eight rest blocks, four right-hand movement blocks, four left-hand movement blocks), they were presented in the order control block; right-hand movement block; control block; left-hand movement block. each block consisted 10 imaging volumes [5].

Pre-processing

We deleted the first four volumes. The remaining data were preprocessed using SPM2, the data were realigned to remove residual motion effects and then were

corrected for the timing differences between each slice using Fourier interpolation [6], at last were spatially smoothed using an 8-mm Gaussion filter (FWHM).

Temporal Compression

The temporal compression [6] can increase the accuracy of classification trained on single subject data. we subtracted the mean volume of the previous and posterior control blocks from the mean volume of the blocks.

Dimensionality Reduction

we can use PCA/SVD formulation methods [7] to reduce the data dimensionality in neuroimaging field.

The voxels space data is $D_{m\times n}$ with one volume per column and one voxel per row. The SVD of D is :

$$D = USV^T \tag{159.4}$$

Where the U is the matrix of eigenvectors of D, so the principal components was carried out as:

$$D^p = U^T D \tag{159.5}$$

Result

Brain Activation Map

The result show the SVM presents a good classifiers' performance. Figure 159.1 show that left and right brain control the right and left hand movement respectively, In the discriminating volume(w), the value of each voxel indicates the importance of such voxel in differentiating between two brain states, the value at each voxel is a function of the difference in activation in the voxel between the tasks.

Conclusion

In this paper, we proposed SVM approach to detect brain functional activation (Fig. 159.1). fMRI results show that SVM is useful method to detect the different brain functional pattern in left and right hand movement.

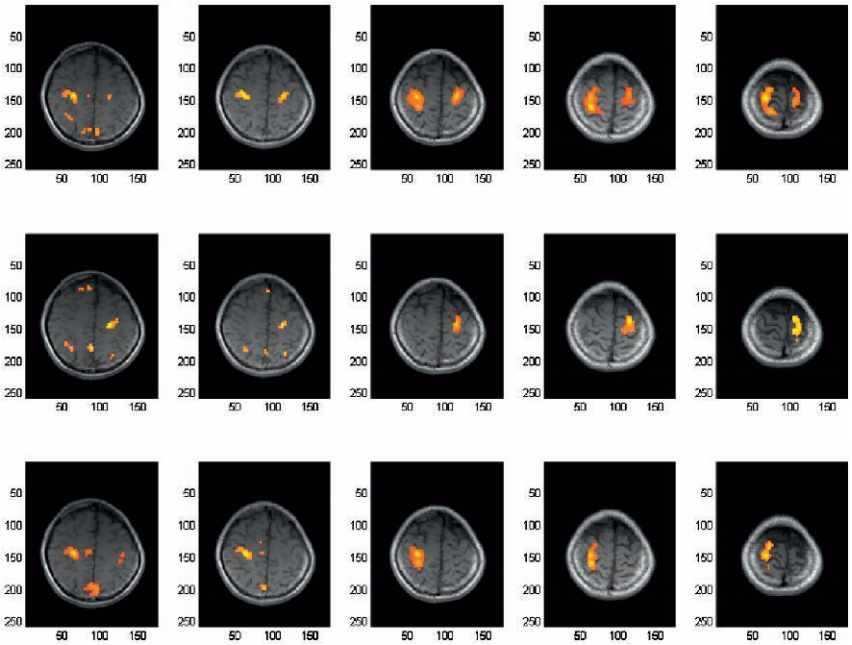

Fig. 159.1 The first five maps are right-left hand movement's activation map; the second five maps are left-hand movement's activation maps; and the last five maps are right-hand movement's activation maps

Acknowledgements Supported in NSFC# 30570507, New Century Excellent Talents in University (NECT-05-0809). Key research project of science and technology of MOE (107097).

References

1. Mandeville, J.B., Marota, J.J.A., Ayata, C., Zaharchuk, G., Moskowitz, M.A., Rosen, B.R., and Weisskoff, R.M.: Evidence of Cerebrovascular Postarteriole Windkessel with Delayed Compliance. J. Cereb. Blood Flow Metab. 19 (1999), 679–689.
2. Friston, K.J.: Statistical parametric maps in functional imaging:a general linear approach. Hum. Brain Map. 2 (1995), 189–210.
3. Vapnik, V.: The Nature of Statistical Learning Theory. Springer Verlag, New York, (1995).
4. LaConte, S., Strother, S., Cherkassky, V., Hu, X., Predicting motor tasks in fmri data with support vector machines. Proceedings of the 11th Science Meeting of the International Society for Magnetic Resonance in Medicine, July 10–16.Toronto,Canada (2003), p.494.
5. LaConte S.: Support vector machines for temporal classification of block design fmri data. NeuroImage 26 (2005), 317–329.
6. J. Mourao-Miranda, E. Reynaud, F. McGlone: The impact of temporal compression and space selection on SVM analysis of single-subject and multi-subject fmri data: NeuroImage. 33 (2006), 1055–1065.
7. Chen H., Yao D., Liu z.: Analysis of the fMRI BOLD Response of Spatial Visual by Analysis of the fMRI BOLD Response. Brain Topography. 17 (2004), 39–46.

Part V
Methods and Technics

Chapter 160
Face Detection Using Multi-Feature

Huaiyi Zhu, Liqing Zhang, He Sun and Rong Xiao

Abstract In this paper, we propose a novel method called Multi-Feature Soft Cascade Learning for improving the performance of face detection. The main contribution of this paper consists of the following two aspects. The first is the use of Multi-Feature in AdaBoost, resulting in a more stable boost classifier with fewer features compared with using only single features as well as the improvement of the detection performance. The second is the new soft cascade algorithm for the Multi-Feature training, which works together with the Multi-Feature selection criterion. Experiment results show the improvement by using Multi-Feature compared with single feature. We also find that the candidate feature set is another important factor to improve the face detection performance.

Introduction

Face detection is a challenging problem in computer vision. The trade-off between accuracy and speed is the main problem of face detection in images. Schneiderman [1] developed a highly accurate detector based on a restricted Bayesian Network but with huge computational cost while detecting. Viola and Jones [2] proposed a framework of cascade boosting using haar-like features, resulting in the first highly accurate real time face detector. However, the detection problem under different light, illumination conditions and large pose, expression variations remains a big challenge. Since haar-like feature in [2] is less discriminative for describing high frequency texture information, different types of features are used for feature selection. For example, Huang *et al*. [3] used Gabor filter features in face detection. Jin *et al*. [4] proposed improved Local Binary Pattern(LBP). Levi and Weiss [5] proposed a set of features based on local edge orientation histograms(EOH). According to their

H. Sun
Department of Computer Science and Engineering, Shanghai Jiao Tong University, Shanghai 200240, China
e-mail: hesun_830110@sjtu.edu.cn

R. Wang et al. (eds.), *Advances in Cognitive Neurodynamics*,

experiment, these feature sets can significantly improve the detection performance. Xiao *et al*. [6] proposed a three-stage framework with different features in different stages to do face detection. Their studies shows that a type of features may perform excellent in earlier stages but poor in later stages, then other types of features are needed to obtain a better performance. Since different features might complement in their characteristics, the combination use of these features seems to be perform better in face detection than with single feature. Hence, an algorithm that can achieve better performance with multiple complement features under viola's framework is needed.

Variations of cascade frames have been studied to achieve better performance. Xiao *et al*. [7] proposed a framework called "Boosting Chain", which combines the earlier stage classification confidence into the later cascade stage and achieved a better performance. Then a new method called SoftCascade [8] provided by Bourdev and Brandt considers each weak learner as a cascade layer and results in a detection rate and speed comparable to that of the best published detectors. Besides, it results in easier training and a detector with fewer features.

In this paper, a new method, called Multi-Feature Soft Cascade Learning, is proposed to learn robust face detector using multiple features. Different types of features, such as haar-like [2], EOH [5], Gabor [3], will be used together for detector training under a certain criterion. Meanwhile, to use Multi-Feature in face detection training, a method based on soft cascade [8] will be used as part of the criterion of selecting weak learner while boosting.

Multi-Feature for Face Detection

When Multi-Feature is used in AdaBoost, two key issues are needed to be resolved: when to use Multi-Feature and how to use Multi-Feature. For the sake of detection speed, we use haar-like feature at the beginning stages, which can decrease the false alarm rate severely in very few detection time. When the false alarm rate reaches a certain value (such as 10^{-5}), multi-feature can be used to achieve a better performance.

To use Multi-Feature in AdaBoost learning, a new method based on Soft Cascade [8] is provided. We need to take each weak learner as a cascade layer and aggressively find the weak learner that can best separate the negative from positive samples for a boosting iteration. The procedure of the new Soft Cascade learning is illustrated in Fig. 160.1.

Multi-Feature selection criterion can be used under the framework of new Soft Cascade algorithm. We treat different types of features separately. For each kind of features, we use AdaBoost to train a weak classifier. Then we compare the performance of the selected K classifiers by the false alarm rate they evaluated in training set. The one with the minimal false alarm rate is selected as the final weak classifier in current stage, which means it separate the negative and positive samples the best. The algorithm for Multi-Feature selection is shown in Fig. 160.2.

1. For stage iteration t = 1, 2, . . . , T:
   - learn a weak classifier h_t, and the threshold b_t that can best separate positive and negative samples for current strong classifier $H_t(x) = \sum_{i=1}^{t} h_i(x) - b_t$.
   - Update training data, remove positive samples that is misclassified by the classifier H_t and negative samples that is correctly classified by the classifier H_t.
   - Do bootstrap for training data if needed.
2. Output final classifier

$$H(x) = \begin{cases} 1 & \forall \hat{t},\ H_{\hat{t}}(x) \geq 0 \\ 0 & \text{otherwise.} \end{cases} \tag{160.1}$$

Fig. 160.1 New Soft Cascade learning

1. Initialize weights for all N samples as in [2]
2. Repeat for stage iteration t = 1, 2, . . . , T:
   (a) For each type of features, $k = 1, \ldots, K$.
   - For $F_k = \{Feature_{kj}\}$, select a weak classifier h_{tk} with minimal cost as in [2]
   - For current classifier of this feature type, find threshold $b_{tk} = \arg\min_{b_{kj}} \{FA_{tkj}\}$ for $H_{tk}(x) = sign\left[\sum_{i=1}^{t-1} \alpha_i h_i(x) + \alpha_{tk} h_{tk}(x) - b_{tk}\right]$, in constrain of $\sum_{i=1}^{n} H_{tk}(x_i) \geq Re_t * N$. Get FA_{tk} for threshold b_{tk}, where FA_t is the false alarm rate of the current classifier, Re_t is the recall for the stage t.

   (b) Select $k^* = \arg\min_k \{FA_{tk}\}$, set $FA_t = FA_{tk^*}$, $h_t = h_{tk^*}$, $b_t = b_{tk^*}$, and the classifier for stage t, $H_t(x) = sign\left[\sum_{i=1}^{t} \alpha_i h_i(x) - b_t\right]$.
   (c) Update weights as in [2]
3. Output classifier in Eq. 160.1

Fig. 160.2 Multi-Feature Soft Cascade learning

Experiments and Results

More than 6,000 non-face Images are collected from the Internet. Among them, more than 40 million 24 × 24 window samples are cropped as the first trained non-face samples. Other negative samples will be generated while doing bootstrap. 20,000 faces are cropped as positive samples. Three features, Haar-like [2], EOH [5], Gabor [3], are used for training. Among them, Haar-like feature is used not only in Multi-feature training procedure, but also in the early stage training. Other features are used only in Multi-feature Soft Cascade training procedure. In our experiments, 209 haar-like features are used in early stage, while the false alarm rate reaches 1.8×10^{-6}. All trained detectors will be tested under CMU+MIT face lib.

The ROC curves for different types of feature used in face detection on CMU+MIT face lib is in Fig. 160.3. EOH, Gabor, Haar-like features are trained for

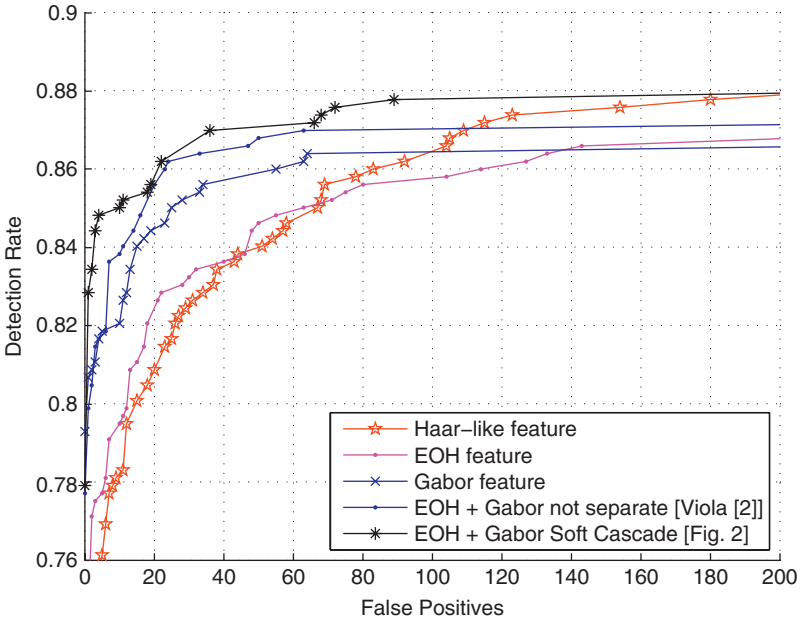

Fig. 160.3 ROC curves for different feature used in face detector on CMU+MIT face lib

face detector, respectively. And their combination for face detector training on Multi-Feature Soft Cascade algorithm are also provided. We can see that the performance of the face detector trained with multi-feature is better than that with single feature. For example, when false positives is 36, the detection rate is 87% for the EOH+Gabor features, 85.5% for Gabor features and 83.5% for EOH features. Besides, the face detector trained with Multi-feature selection criterion (Fig. 160.2) is better than that is selected by the original AdaBoost algorithms [2].

Conclusions and Discussions

In this paper, we propose a novel method called Multi-feature Soft Cascade Learning which use multiple feature combination for face detection. The experiment results show the improvement of using Multi-feature selection criterion with new Soft Cascade Learning compared with single feature learning. Also, it is proved that Multi-Feature selection criterion is better than that treats multiple features as a uniform type.

The criterion of multi-feature selection is the key point for Multi-Feature usage in face detection. Further work is to find a more effective way that not only decrease the training set false alarm rate, but also make higher detection rate.

Acknowledgements The work was supported by the National Basic Research Program of China (Grant No. 2005CB724301) and the National High-Tech Research Program of China (Grant No. 2006AA01Z125).

References

1. Schneiderman, H.: Learning a restricted bayesian network for object detection. In: Computer Vision and Pattern Recognition. Volume 2. (2004) 639–636.
2. Viola, P., Jones, M.: Rapid object detection using a boosted cascade of simple features. In: Computer Vision and Pattern Recognition. Volume 1. (2001) 511–518.
3. Huang, L.L., Shimizu, A., Kobatake, H.: Classification-based face detection using gabor filter features. In: Automatic Face and Gesture Recognition. Proceedings of Sixth IEEE International Conference (2004) 397–402.
4. Jin, H., Liu, Q., Lu, H., Tong, X.: Face detection using improved lbp under Bayesian framework. In: International Conference on Image and Graphics. Proceedings of Third International Conference (2004) 306–309.
5. Levi, K., Weiss, Y.: Learning object detection from a small number of examples: the importance of good features. In: Computer Vision and Pattern Recognition. Volume 2. (2002) 53–60.
6. Xiao, R., Li, M.J., Zhang, H.J.: Robust multipose face detection in images. Circuits and Systems for Video Technology. Volume 14. (2004) 31–41.
7. Xiao, R., Zhu, L., Zhang, H.J.: Boosting chain learning for object detection. In: International Conference on Computer Vision. Volume 1. (2003) 709–715.
8. Bourdev, L., Brandt, J.: Robust object detection via soft cascade. In: Computer Vision and Pattern Recognition. Volume 2 (2005) 236–243.

Chapter 161
A Text Classification Method Based on Cascade

Hui Li, Qi Zhang, Huchuan Lu and Deli Yang

Abstract Text categorization is an important research area in many Information Retrieval applications. Based on the research of text classification technology, a new bi-class text categorization method, which uses a cascade of AdaBoost classifiers, is proposed. Experiment on Fudan University data set shows that this method has a good classify performance at 92.167%. Compared with other classification methods, it has a lower storage space, smaller computation time and is suitable for different situations.

Keywords Text classification · AdaBoost · cascade

Introduction

Most of the explicit knowledge assets of today's organizations consist of unstructured textual information in electronic form. Users are facing the challenge of organizing, analyzing and searching the ever-growing amounts of documents. Systems that automatically classify text documents into predefined thematic classes and thereby contextualize information offer a promising approach to tackle this complexity.

During the last decades, a large number of machine learning methods have been proposed for text classification tasks, such as K-Nearest Neighbor (KNN), Centroid Classifier, Rocchio, Naïve Bayes, Winnow, Support Vector Machines (SVM) and Boosting Algorithms. The overview of Sebastiani [1] discusses the main approaches to text classification.

Paul Viola and Michael J. Jones had proposed an object detection framework which consist of a cascade of AdaBoost classifiers. This method has been proved to be efficient by the frontal face detection. In this paper, we apply this classifier framework to text classification by representing the documents to VSM (Vector

H. Li
School of Management, Dalian University of Technology, 116024 Dalian, China
e-mail: inkoil2001@163.com

R. Wang et al. (eds.), *Advances in Cognitive Neurodynamics*,

Space Model). The main idea behind our strategy is to take advantage of the high precision of the classifier to successively refine the information that the users need.

The remainder of this paper is organized as follows: In section 'The Cascade of AdaBoost Classifiers', we describe the classifier framework, "cascade". In section 'Experiment', we present an extensive experimental evaluation of our classifier. Finally, section 'Conclusion' we present our summary, concluding remarks and directions of our future work.

The Cascade of AdaBoost Classifiers

The classification framework is to view it as a classic pattern recognition process including text representation, classifier training and using, and performance evaluation. All the texts should be represented as VSM after preprocessing, feature reduction and Weight Computation.

After the steps in section 'The Cascade of AdaBoost Classifiers', the documents are changed to the vectors that can be used by classifiers. In the bi-class text classification, only two categories need to be classified—positive and negative, represented the texts that user needs and the texts that user doesn't need. In our system, a variant of AdaBoost is used to select the training feature and to train the classifier [2, 3]. In its original form, the AdaBoost learning algorithm is used to boost the classification performance of a simple learning algorithm. It does this by combining a collection of weak classification functions to form a stronger classifier. The final strong classifier takes the form of a perceptron, a weighted combination of weak classifiers followed by a threshold.

One AdaBoost classifier can get good performance, but the most straightforward technique for improving the classification performance, adding features to the classifier, directly increases the computation time. P. Viola [4] has presented an algorithm for constructing a cascaded of classifiers which achieves increased accuracy performance while radically reducing computation time. The key insight is that smaller, and therefore more efficient, boosted classifiers can be constructed which rejects many of the negative samples while detecting almost all positive instances. Simpler classifiers are used to reject the majority of samples before more complex classifiers are called upon to achieve low false positive rates.

An effective text classifier can be obtained by adjusting the strong classifier threshold to minimize false negatives rates. The initial AdaBoost threshold is designed to yield a low error rate on the training data. A lower threshold yields higher accuracy and higher false positive rates.

The accuracy performance of the initial AdaBoost classifier is far from acceptable as a text classification system. Nevertheless the classifier can significantly reduce the number of dimensions that need further processing with very few operations.

The overall form of the detection process is that of a degenerate decision tree, what is called as a "cascade". A positive result from the first classifier triggers the

evaluation of a second classifier which has also been adjusted to achieve very high detection rates. A positive result from the second classifier triggers a third classifier, and so on. A negative outcome at any point leads to the immediate rejection of the text vector.

In the classification system, positive samples must be correctly recognized and negative samples should be recognized as many as possible. As such, the cascade attempts to reject as many negatives as possible at the earliest stage. While a positive instance will trigger the evaluation of every classifier in the cascade, this is an exceedingly rare event.

Much like a decision tree, subsequent classifiers are trained using those examples which pass through all the previous stages. As a result, the second classifier faces a more difficult task than the first. The examples that make it through the first stage are "harder" than typical examples. The more difficult examples faced by deeper classifiers push the entire receiver operating characteristic (ROC) curve downward. At a given accuracy, deeper classifiers have correspondingly higher false positive rates.

Experiment

The corpus used for training and testing is from Fudan University. It consists of 20 categories, 8503 for training documents and 8982 for testing documents. We construct the bi-class training data set by combining other 19 categories except the "Economy" category.

Evaluation on Feature Selection

Result

Table 161.1 summarizes the results of the experiments for different feature selection. The relative gains on the F1 value, which is in influenced both by precision and recall, show that all the three feature selection methods have no less than 87.43%. The X2 has the highest F1 at 92.27% by using 2000 features.

The result of the significance tests allow us to conclude that this "cascade" framework of classifiers is suitable for different feature selection methods and different

Table 161.1 Result on different feature selection methods and different dimensions

	1000 dimensions			2000 dimensions			3000 dimensions		
	Precision (%)	Recall (%)	F1 (%)	Precision (%)	Recall (%)	F1 (%)	Precision (%)	Recall (%)	F1 (%)
DF	92.44	90.41	91.41	92.76	90.48	91.61	90.44	84.62	87.43
IG	91.54	88.01	89.74	92.72	90.40	91.55	90.51	86.79	88.61
X2	92.78	91.18	91.97	93.03	91.52	92.27	90.13	85.86	87.94

Table 161.2 Result on different classifiers

	Precision (%)	Recall (%)	F1 (%)	Time
NB	85.40	82.25	83.80	73 s
Cascade	93.03	91.52	92.27	69 s
KNN($k = 19$)	93.88	91.86	92.86	48 m 27 s
AdaBoost	92.23	87.99	90.06	65 s

numbers of features. In general, the classifier that we presented in this paper is robust to different feature selection methods. Because of the highest F1 in X2, X2 is chosen to be the feature selection method in the second section of experiment and the feature number is 2000.

Evaluation on Classifiers

A second series of experiment was conducted on different Classifiers. All the training documents were processed by the stages described in section 'The Cascade of AdaBoost Classifiers'. Information gain (IG) was chosen to feature selection.

Result

The "cascade" framework also has a good performance. In the KNN classification section, K was set from 1 to 100. When $K = 19$, KNN has the best F1 score at 92.86% which is better than the cascade by 0.6%. But the classification time shows that KNN has the longest runtime nearly 50 min. Because KNN classifier need to compute every Euclidean distances between the training samples and test samples. When the data set is very large just like this experiment the computation time is extremely huge. Compare with the KNN, the "cascade" only uses 69 s.

The AdaBoost classifier that chooses 300 features to classify is just like one layer of the cascade classifier. The cascade classifier only chooses eight features in the first layer and a total of 65 features. Though the AdaBoost has the lowest computation time, the F1 score is lower than the cascade. This result concludes that one strong classifier is not better that the combination of weak classifiers.

Conclusion

In this paper, we present a new bi-class text classification system based on a cascade of AdaBoost classifiers. Different feature selection methods were proposed to perform the classification. At the same time, different kinds of classifiers were chosen to compare with the cascade of AdaBoost classifiers.

The experiment result on different feature selection methods shows that the cascade framework is robust to different kinds of feature selection methods. It can be applied to different field. The second experiment shows that this classification

method has a better performance than other classifiers not only on the F1 score but on the classification time. So it can be easily used as a real-time system, such as mobile phone and PDA.

There is another advantage of this cascade framework. The training parameter can be updated easily by adding another layer of the classifier. The pervious layer parameters do not need to change.

References

1. F. Sebastiani: Machine Learning in Automated Text Categorization. ACM Computing Surveys. 34(2002) 1–47.
2. R.E. Schapire and Y. Singer: BoosTexter: A Boosting-based System for Text Categorization. Machine Learning, 39(2000) 135–168.
3. Y. Freund and R.E. Schapire: A Decision-Theoretic Generalization of Online Learning and an Application to Boosting. In Computational Learning Theory: Eurocolt '95, Springer-Verlag, Berlin, (1995) 23–37.
4. P. Viola and M. Jones: Robust Real-time Object Detection[J]. International Journal of Computer Vision, 57(2004) 137–154.

Chapter 162
A PCNN Based Approach to Image Segmentation Using Size-Adaptive Texture Features

Lijuan Duan, Jun Miao, Can Liu, Yunfeng Lu, Yuanhua Qiao and Baixian Zou

Abstract Pulse Coupled Neural Network (PCNN) and its modified forms are widely applied to image segmentation. However, most PCNN based methods are difficult in segmentation of the regions that contain rich texture information in a complex image. This paper proposes an improved approach to image segmentation based on simplified region growing PCNN with adaptive texture features input. It shows promising results to process regions with complex texture.

Keywords Image segmentation · texture features · pulse coupled neural network (PCNN) · simplified region growing PCNN (SRG-PCNN)

Introduction

In 1990, Eckhorn presented the linking field network [1]. It is based on the phenomena of synchronous pulse firing in the cat's visual cortex. Some researchers modified the linking field network, and then it became the pulse coupled neural network (PCNN) [2, 3]. Figures 162.1 and 162.2 show a basic PCNN neuron model and a PCNN structure respectively.

The PCNN model can be described by a group of equations [2].

$$F_i = \sum_j M_{ji} Y_j(t) \otimes \phi_{ji}(t) + I_i \tag{162.1}$$

$$L_i = \sum_k W_{ki} Y_k(t) \otimes \phi_{ki}(t) + J_i \tag{162.2}$$

$$U_i = F_i(1 + \beta_i L_i) \tag{162.3}$$

L. Duan
College of Computer Science and Technology, Beijing University of Technology, Beijing 100022, China
e-mail: ljduan@bjut.edu.cn

R. Wang et al. (eds.), *Advances in Cognitive Neurodynamics*,

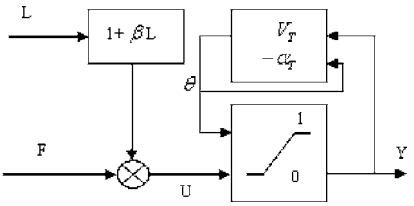

Fig. 162.1 A PCNN neuron model

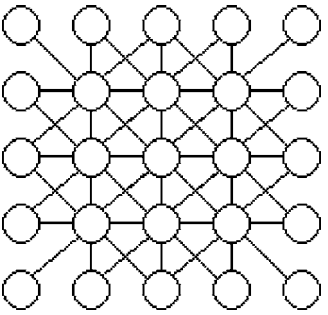

Fig. 162.2 A PCNN structure

$$Y_i(t) = Step(U_i - \Theta_i) \tag{162.4}$$

$$\Theta_i = -\alpha_T \Theta_i + V_T Y_i(t) \tag{162.5}$$

The pulse output will be delivered to the adjacent neurons. If the adjacent neurons have the similar intensity with the neuron i, they will fire too because of pulse coupled action [3]. In this case, the neuron i and the similar adjacent neurons will emit synchronous pulses. This is the theoretical foundation of PCNN for image segmentation.

As a result of the biological background, PCNN has a great difference with the traditional neural networks and has proven to be highly effective in some applications, such as image de-noise, enhancement and segmentation. Usually, when using PCNN to segment images, a single layer two-dimensional network is designed (Fig. 162.2). In the network, generally the neurons and the pixels (or response input) are in one to one correspondence.

In 2002, Stewart combined PCNN with region growing algorithm (RG-PCNN) to segment images [4]. RG-PCNN is efficient in multi-value image segmentation, but it cannot process edge pixels very well. Ma et al. [5] proposed to compensate the edge pixels. Reference [2] pointed out that "a significantly more uniform segmentation is obtained when the linking modulation is more uniform in its value," which is proved by Gu et al. [6]. According to these results, Lu et al. [7] brought forward a simplified region growing PCNN (SRG-PCNN) to overcome the disadvantage of RG-PCNN by modifying the linking function to a uniform one.

However, either RG-PCNN or SRG-PCNN is difficult in segmentation of regions that contains rich texture information in a complex image. This paper proposed an

improved approach to image segmentation based on SRG-PCNN, which use a kind of size-adaptive texture features as input to the PCNN neurons instead of original gray responses. It has shown promising results to process regions with complex texture.

Size-Adaptive Texture Features

In order to resolve the problem that RG-PCNN and SRG-PCNN can not segment region with rich texture from other regions, instead of directly inputting the original gray responses to PCNN, our method extracts a kind of size-adaptive texture features and input these features to SRG-PCNN [7] for image segmentation. The goal of this manipulation is to make the region with rich texture become uniform and simultaneously keeps borders between regions as clear as possible. Figure 162.3 show the designed texture features and corresponding image transforming, in which the size of windows for extracting texture features is adaptive. The adaptive mechanism is: if the average texture feature response of an initial window is smaller than a threshold, then decrease the size of the window to a certain degree and uses the new average texture feature response to replace the original response of the center pixel of the image window.

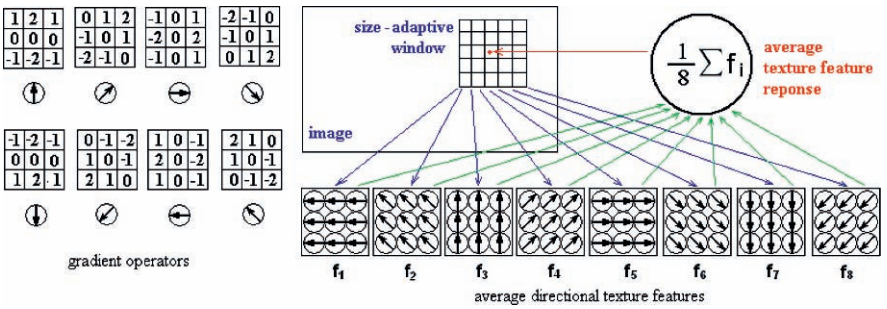

Fig. 162.3 Size-adaptive texture feature extracting

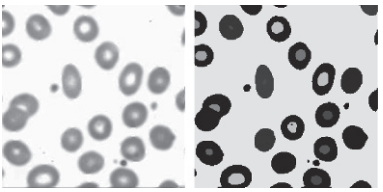

a. Original image b. Our method

Fig. 162.4 Experiment 1

Experiments

Three experiments are carried out on several images that have different texture information. The first is on a cell image in which regions contains little texture. The result is shown in Fig. 162.4, from which we can see the clear segmentation. The second is on a constructed picture which consists of three interlaced regions containing rich or no texture information. From the result shown in Fig. 162.5, we can also see a clear segmentation except for few isolated points.

In order to sufficiently demonstrate the advantage of the proposed approach, we make a comparison with RG-PCNN and SRG-PCNN. Figure 162.6a is the 256-level original gray image which contains complex regions containing various textures. Figure 162.6b–d are the segmentation results using RG-PCNN [4], SRG-PCNN [7] and our method respectively. Form Fig. 162.6, we can see that SRG-PCNN can resolve the problem of non-smooth borders between two segmented regions from RG-PCNN, and our method can overcome the disadvantage of SRG-PCNN, which can not segment regions containing rich texture from other regions. For example, the pelage region of the hat and the hair region in Fig. 162.6a are always difficult to be segmented into several or one uniform region(s) by RG-PCNN and SRG-PCNN, but the segmentation result in Fig. 162.6d shows our approach can process the region containing rich texture information efficiently. At the same time, a small part of the hat brim in Fig. 162.6a is mistakenly segmented into a pelage region, which is shown in Fig. 162.6d. Besides, there are some sparse points to the left of the hat is more obvious than those in Fig. 162.6b,c, which is leaded by texture features extracting from non-suitable size windows.

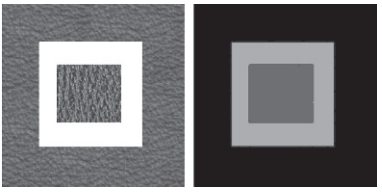

a. Original image b. Our method

Fig. 162.5 Experiment 2

a. Original image b. RG-PCNN c. SRG-PCNN d. Our method

Fig. 162.6 Experiment 3

Conclusion

Most PCNN based method, including RG-PCNN and SRG-PCNN, keep original gray response as direct input into the PCNN. They are usually difficult in segmenting regions that contain rich texture from other regions that contain little texture. This paper proposed an improved approach to solve this problem. Instead of directly inputting original gray responses to PCNN, our method extracted a kind of size-adaptive texture features and input these features to SRG-PCNN for image segmentation. This manipulation makes the regions with rich texture become uniform to a certain extent and simultaneously keeps the borders between regions as clear as possible. Up to now, our method does not well in segmentation between two adjacent regions that have the same complexity of texture information, which is the next topic in the future research.

Acknowledgements This research is partially sponsored by NSFC (No.60673091, No.60702031, No.60332010, No.60473043), Hi-Tech R&D Program of China(No.2006AA01Z122, No.2007AA 01Z163), Natural Science Foundation of Beijing (No.4072023), Beijing Municipal Education Committee (No.KM200610005012), Beijing Municipal Elitist foundation (No. 20061D0501 500211), "100 Talents Program" of CAS, and Program for New Century Excellent Talents in University (NCET-04-0320).

References

1. R. Eckhorn, H.J. Reitboeck, M. Arndt and P.W. Dicke.: Feature Linking via Synchronization among Distributed Assemblies: Simulation of Results from Cat Cortex. Neural Computation Vol. 2 (1990) 293–307.
2. J.L. Johnson and M.L. Padgett.: PCNN Models and Applications. IEEE Transactions on Neural Networks Vol. 10(3) (1999) 480–498.
3. G. Kuntimad and H.S. Ranganath.: Perfect Image Segmentation Using Pulse Coupled Neural Networks. IEEE Transactions on Neural Networks Vol. 10 (1999) 591–598.
4. R.D. Stewart, I. Fermin and M. Opper.: Region Growing With Pulse-Coupled Neural Networks: An Alternative to Seeded Region Growing. IEEE Transactions on Neural Networks Vol. 13(6) (2002) 1557–1662.
5. Y. Ma, L. Li, Y. Wang and R. Dai.: Principles and Applications of PCNN. Science Publishing Company, Beijing (2006) 69–80.
6. X. Gu, S. Guo and D. Yu.: A New Approach for Automated Image Segmentation Based on Unit-Linking PCNN. Proc. the First International Conference on Machine Learning and Cybernetics (2002) 175–177.
7. Y. Lu, J. Miao, L. Duan, et al.: A New Approach to Image Segmentation Based on Simplified Region Growing PCNN. 2007 International Conference on Intelligent Computing (accepted).

Chapter 163
Entropy-Partition of Complex Systems and Emergence of Human Brain's Consciousness

Guangcheng Xi

Abstract Consciousness is discussed from viewpoint of theory of Entropy-partition of complex system. Human brain's system self-organizably and adaptively implements partition, aggregation and integration, and consciousness emerges. We use mutual information to define correlative measure between (among) variables or subsystems of complex system. In order to make good use of the correlative measure in infinite-dimensional space, proof of countable superadditivity and uniqueness of the correlative measure is given. Emergence of consciousness is mathematically (some approaches in probability theory and information theory) formulated in this paper.

Keywords Human brain's system · entropy-partition (aggregation) · integration · consciousness

Introduction

In article of Giulio Tononi and G.M. Edelman [1], studying of consciousness is concentrated on description of kinds of neural processes which can account for key properties of conscious experience. They have emphasized two key properties of consciousness: conscious experience is integrated (each conscious scene is unified) and at the same time it is highly differentiated (within a short time, one can experience any of a huge number of different conscious states), and have proposed notions so-called functional clustering, neural complexity and dynamical core hypothesis. Those researching methods and train of thought to problem of consciousness agree to a certain extent, with theory and method of Entropy-partition of Complex System I proposed 23 years ago [2]. At that time related specialists (appraising group of achievements in scientific research) ever have pointed out: theory of Entropy-partition (Aggregation) of complex system not only has been applied to Ecologico-Economical regionalization [3] of Ecologico-Economico-social complex system but also will certainly be applied to researching of human Brain's neural

G. Xi
Institute of Automation, Chinese Academy of Science, Beijing 100080, P.R. China
e-mail: guangcheng.xi@ia.ac.cn

R. Wang et al. (eds.), *Advances in Cognitive Neurodynamics*,

system. Therefore having read the article of G. Tononi and G.M. Edelman, I have much sensation seem to have met before, and excited feeling arises spontaneously. Though such, we strongly have felt it still necessary to discuss problem of consciousness from viewpoint of theory of entropy-partition (aggregation) of complex system.

Entropy-Partition (Aggregation) of Neural System X

Suppose neural system $X = (X_1, X_2, \cdots, X_a, \cdots, X_p)^T$ is consisted of p neuron, $p \in N(N$ set of natural number), where $X_a = (X_{a_i})$, $a = 1, 2, \cdots, p$; $i = 1, 2, \cdots, q$. Let $C_a(a = 1, \cdots, p)$ be set of classification of X_a, $C_{a_i} = i$ be i-th element of C_a, then we have $C_a = \{1, 2, \cdots, i \cdots, k\}$, $k \leq q$, and let n_i be quantity for X_a belong to i-th class, then entropy of X_a is defined as

$$H(X_a) = -\sum_{i=1}^{k} n_i/q \log n_i/q \tag{163.1}$$

joint entropy of X_a, X_b is similarly defined as

$$H(X_a \cup X_b) = -\sum_{i}\sum_{j} n_{ij}/q \log n_{ij}/q \tag{163.2}$$

where n_{ij} is quantity for X_a belong to i-th class of C_a simultaneously X_b belong to j-th class of C_b. For the convenience of application, expressions (163.1) and (163.2) can respectively be represented as

$$H(X_a) = \log q - \frac{1}{q}\sum_{i=1}^{k} n_i \log n_i \tag{163.1$'$}$$

$$H(X_a \cup X_b) = \log q - \frac{1}{q}\sum_{i}\sum_{j} n_{ij} \log n_{ij} \tag{163.2$'$}$$

Having had above-mentioned definition of entropy, in what follows, correlative measure by which statistical dependence between the X_a and the X_b is denoted is defined by their mutual information.

Definition 1. *Suppose $X_a \cap X_b = \phi$, then entropy*

$$H(X_a, X_b) = H(X_a) + H(X_b) - H(X_a \cup X_b) \tag{163.3}$$

is called correlative measure $\mu(X_a, X_b)$ between the X_a and the X_b.

Definition 2. *Suppose* $X_a \cap X_b = \phi$ *for arbitrary* $a, b(a \neq b)$*, then*

$$\mu(X_1, X_2, \cdots, X_p) \stackrel{\Delta}{=} \sum_{a=1}^{p} H(X_a) - H\left(\sum_{a=1}^{p} X_a\right) \tag{163.4}$$

is called correlative measure among $X_1, X_2, \ldots$, and X_p.

Definition 2′. *Suppose system* X *be partitioned into* m *subsystems* $s_1, s_2, \cdots, s_m$*, for arbitrary* i, j $(i \neq j)$*,* $s_i \cap s_j = \phi$*,* $X = \sum_{i=1}^{m} s_i$*, then*

$$\mu(s_1, s_2, \cdots, s_m) \stackrel{\Delta}{=} \sum_{i=1}^{m} H(s_i) - H\left(\sum_{i=1}^{m} s_i\right) \tag{163.5}$$

is called correlative measure among $s_1, s_2, \cdots, s_m$.

Let us consider nonempty finite set $\boldsymbol{X}$ and set-family $E(\boldsymbol{X})$ consisted of its subset, P_e a set-function defined on $E(\boldsymbol{X})$ with properties

(i) $P_e(A) \geq 0, \forall A \in E(\boldsymbol{X})$,
(ii) $P_e(\phi) = 0$

Definition 3. *If for arbitrary nonempty finite set* $S_i \in E(\boldsymbol{X})$*,* $S_j \in E(\boldsymbol{X})$*,* $i \neq j$*,* $S_i \cap S_j = \phi$*, have*

$$P_e(S_i \cup S_j) \geq P_e(S_i) + P_e(S_j) \tag{163.6}$$

then, set-function P_e satisfied conditions (i), (ii) is called superadditive.

Although finite superadditivities of mutual information or the so-called measure of cohesion of the components of the set of entities is well known result, it is not still unnecessary to write down our proof about finite superadditivity of the correlative measure among some subsystems of the system X which is given.

Theorem [2]. *Correlative measure* $\mu(s_1, s_2, \cdots, s_m)$ *is finitely superadditive, countably superadditive and unique.*

Proof. Finite superadditivity.

Suppose system X is partitioned into m subsystems $s_1, s_2, \ldots, s_m$, and that $s_i \in R, s_i \neq \emptyset; s_j \in R, s_j \neq \emptyset; s_i \cap s_j = \emptyset, X = \sum_{j=1}^{m} s_j \in R$, for any $i, j(i \neq j)$, where R is a algebra on set X which is given. By definition of the correlative measure, we have

$$\mu(S) = \mu\left(\sum_{j=1}^{m} s_j\right) = \mu\left(\mathrm{s}_1, \mathrm{s}_2, \ldots\ldots, \mathrm{s}_\mathrm{m}\right) = \mu\left(X_1, X_{2,}\ldots\ldots X_p\right)$$

$$= \sum_{i=1}^{p} H(X_i) - H\left(\sum_{i=1}^{p} X_i\right) \tag{163.7}$$

$$\sum_{s_j \in S} \mu(s_j) = \sum_{s_j \in S}\left(\sum_{X_j \in s_j} H(X_j) - H\left(\sum_{X_j \in s_j} X_j\right)\right)$$

$$= \sum_{i=1}^{p} H(X_i) - \sum_{s_j \in S} H(s_j)$$

$$= \sum_{i=1}^{p} H(X_i) - \sum_{j=1}^{m} H(s_j) \tag{163.8}$$

Subtracting (163.8) from (163.7) leads to

$$\mu\left(\sum_{j=1}^{m} s_j\right) - \sum_{j=1}^{m} \mu(s_j) = \sum_{j=1}^{m} H(s_j) - H\left(\sum_{i=1}^{p} X_i\right)$$

$$= \sum_{j=1}^{m} H(s_j) - H\left(\sum_{j=1}^{m} s_j\right) \geq 0 \tag{163.9}$$

Countable superadditivity and uniqueness:

Suppose system X is partitioned into a sequence of subsystems $s_1, s_2, \cdots, s_n \cdots$, $s_n \in R$ -algebra on $X, s_n \in R, s_n \neq \emptyset; s_m \in R, s_m \neq \emptyset; s_n \cap s_m = \emptyset, X = \sum_{n=1}^{\infty} s_n \in R$, for any $n, m(n \neq m)$.

Let $E_k = \sum_{n=1}^{k} s_n$, obviously, we have

$$E_1 \subset E_2 \subset \cdots \subset E_k \cdots, E_k \in R, \lim_{k \to \infty} E_k = \sum_{n=1}^{\infty} s_n \in R \tag{163.10}$$

From non-negativity and monotonicity of μ, we have

$$\mu(E_1) \leq \mu(E_2) \leq \cdots \leq \mu(E_k) \leq \cdots \leq \mu\left(\sum_{n=1}^{\infty} s_n\right) \tag{163.11}$$

If $\lim_{k\to\infty} \mu(E_k) \to \infty$, from monotonicity of μ, then inevitably we have

$$\mu\left(\sum_{n=1}^{\infty} s_n\right) = \infty$$

Hence by using finite superadditivity, we have

$$\mu\left(\sum_{n=1}^{\infty} s_n\right) = \infty = \lim_{k\to\infty} \mu(E_k) = \lim_{k\to\infty} \mu\left(\sum_{n=1}^{k} s_n\right) \geq \lim_{k\to\infty} \sum_{n=1}^{k} \mu(s_n) = \sum_{n=1}^{\infty} \mu(s_n)$$

If $\lim_{k\to\infty} \mu(E_k) = c < \infty$, above-mentioned process of proof is understood easily. And either of the $\lim_{k\to\infty} \mu(E_k) = c < \infty$ and $\lim_{k\to\infty} \mu(E_k) = \infty$ makes uniqueness of the limit to hold still, i.e. $\lim_{k\to\infty} \mu(E_k) = \lim_{k\to\infty} \mu\left(\sum_{n=1}^{k} s_n\right)$ is unique. Up to this point, proof of the theorem is completed.

From above-mentioned property of correlative measure, criterion by which lowest requirement of ideal partition is presented should be

(i) $\mu(s_i) > \mu(s_i, s_j), \mu(s_j) > \mu(s_i, s_j)$
(ii) $\mu(s_i) > \mu(s_{i_1}) + \mu(s_{i_2}), \mu(s_j) > \mu(s_{j_1}) + \mu(s_{j_2})$.
for any $i, j(i \neq j), s_i \cap s_j = \phi$

Here $s_{i_l}, s_{j_l}(l = 1, 2)$ denotes partition of s_i and s_j, respectively. (i) denotes that correlative measure of any subsystem itself which is obtained by partition is larger than correlative measure between it and any subsystem. (ii) denotes that correlative measure of any subsystem which is obtained by partition possesses strictly superadditivity.

When number of characteristic variable of system X is very large, comprehensive observation for data is impossible. Even though the observation is possible, as obtaining complete data spends very long time and for other reason such that obtained data loses its available value. At this time, statistical method and theory can be applied to obtaining data and to analyzing problem.

Suppose $\boldsymbol{x}_a = (x_{a_1}, x_{a_2}, \cdots, x_{a_N})$ be index of quantity of characteristic variable X_a of the complex system X, data obtained by mean of random sampling is $\bar{\boldsymbol{x}}_a = (x_{a_1}, x_{a_2}, \cdots, x_{a_q})$, $\bar{\boldsymbol{x}}_a$ be a random sample from population X_a. Obviously any x_{a_i} necessarily is equal to some $x_{a_{\theta_i}}$, here $\theta_i \quad (i = 1, 2, \cdots, q)$ is number of i-th individual of $\boldsymbol{x}_a$. For any θ_i, we have probability

$$p\left\{x_{a_1} = x_{a_{\theta_1}}, x_{a_2} = x_{a_{\theta_2}}, \cdots, x_{a_q} = x_{a_{\theta_q}}\right\} = (N-q)!/N! \tag{163.12}$$

Corresponding to expressions (163.1′) and (163.2′), we have

$$H(\bar{\boldsymbol{x}}_a) = \frac{(n-q)!}{n!}\left[\log(n!q) - \log(n-q)! - \frac{1}{q}\sum_i n_i \log n_i\right] \tag{163.13}$$

$$H(\bar{\boldsymbol{x}}_a \cup \bar{\boldsymbol{x}}_b) = \frac{(N-q)!}{N!}\left[\log(N!q) - \log(N-q)! - \frac{1}{q}\sum_i \sum_j n_{ij} \log n_{ij}\right] \tag{163.14}$$

At this time, correlative measure of the system X is defined by way similar to the above-mentioned method. Actually, in order to obtain the partition of the complex system X, we often introduce coefficient of correlative measure $\mu_{ab} = \mu(X_a, X_b)/H(X_b)(\mu_{ij} = \mu(s_i, s_j)/H(s_j)$, obviously, $\mu(a, b)(\mu_{ij})$ is between 0 and 1. Having computed μ_{ab} for all a, b, those X_a, X_b whose correlative measure is larger than other $\mu(a, l)$, $l \neq b$ or $\mu(r, b)$, $r \neq a$, are combined so as to accord with the preceding criterion (i̇), (2̇). Hence some corresponding subsystems s_i, $i = 1, \cdots, m$, i.e. some neural functional units are obtained.

From neurophysiological studies, elementary unit representing information in human brain is mutually coordinated clique of neuron; by combining mutual function, neurons with different properties carry out correlative activity, form various dynamic neural networks which correspond to various function of information.

Above-mentioned partition or aggregation of neurons is carried out in self-organizable and adaptive form; the partition or aggregation of neurons makes human brain emerge intelligence.

Emergence of Consciousness

Suppose system X self-organizably and adaptively is partitioned into m subsystem. Correspondingly, there are m subspace $(\Omega_i, \Im_i, P_i)$, $i = 1, \cdots, m$, of probability-space $(\Omega, \Im, P)$, where Ω is space of configuration of system X. Let $(\Omega, \Im, P)$ be Radon measurable space, then for any $\Im_i$ there exists regular conditional probability $P(\cdot|\Im_i)$, obviously, $P(\cdot|\Im_i) = P(\cdot|\Im(s_i)) = P(\cdot|s_i) \overset{\Delta}{=} \mu(\cdot|s_i)$. Hence, for any $A \in \Im$

$$\mu(A) = \int_{X|\boldsymbol{s}} \mu(\cdot|s_i) d\mu(s_i) \tag{163.15}$$

and for any random variable η

$$E\eta = \int_{X|\boldsymbol{s}} E(\eta|s_i) d\mu(s_i) \tag{163.16}$$

where $X|\boldsymbol{s}$ is quotient space.

Let us define following two functions,

$$f_{\varepsilon}^{(1)}(t) = \begin{cases} \dfrac{\mu(A)}{\varepsilon}, & 0 \le t \le \varepsilon \\ 0, & \varepsilon < t \end{cases} \tag{163.17}$$

$$f_{\varepsilon}^{(2)}(t) = \begin{cases} \dfrac{E\eta}{\varepsilon}, & 0 \le t \le \varepsilon \\ 0, & \varepsilon < t \end{cases} \tag{163.18}$$

where ε is arbitrary positive number, t is time.

To be this, we eventually have conscious experience, that is $\mu(A)$ or $E(\eta)$ under some situations or $\lim\limits_{\varepsilon \downarrow 0} f_{\varepsilon}^{(i)}(t)$, $i = 1, 2$, under other situations.

When A or η comes from outside of X, or when A or η is caused by "gene" or "experience" which is in inside of X, all will emerge consciousness, and is emerged by system X self-organizably and adaptively to be partitioned (aggregated), then to be integrated in hundreds of milliseconds. $\mu(A)$ or $E\eta$ is the integrated process.

If there exists sequences of mutual information between any appointed two neurons and between any appointed two subsystems, and the sequences of the mutual information have nice asymptotical properties, that is, if there exists ergodic superadditive process for the sequence of mutual information in neural system X, then the system can implement self-organization and self-adaptation.

Remarks

(1) That the neural system X is self-organizably and adaptively partitioned into some subsystems is implemented by means of the correlative measure, i.e. mutual information, which does not touch upon change of location of space of neurons or subsystems. This is a "Internet" in the neural System X. The some subsystems form large-scale hierarchical intelligent system. On the hierarchical intelligent system, basic principle of hierarchical intelligent system IPDI (Increasing precision with decreasing intelligence) holds [4, 5]. The layer with high intelligence is dynamic core of the neural system X.
(2) Consciousness is some memory.
(3) Unconsciousness is also consciousness.
(4) Consciousness is conscious of consciousness.
(5) Nearly 3000 years ago, Chinese ancient learned men said consciousness is that Saint hears at silence, looks at immateriality, and firmly believed memory all is in brain.
(6) Oneself-consciousness can only be experienced; it forever cannot be captured by oneself.

Acknowledgements This work was partly supported by the National 973 Project No. 2003CB517106, China and the NSFC Projects under Grant No. 60621001, China.

References

1. Giulio Tonoi and Gerald M. Edelman: Consciousness and Complexity. Science 828 (1998) 1846–1851.
2. Xi Guangcheng: Entropy-method of Partition of Complex System. ACTA AUTOMATICA SINICA 13(3) (in Chinese 1987) 216–220.
3. Xi Guangcheng: The Entropy-Method of Eologico-Economical Regionalization. ACTA AUTOMATICA SINICA 16(2) (in Chinese 1990) 170–173.
4. Xi Guangcheng: Intelligent Control with Relative Entropy Minimizing. Control Theory and Applications 16(1) (in Chinese 1999) 27–31.
5. Saridis G. N.: Analytic Formulation of the Principle of Increasing Precision with Decreasing Intelligence for Intelligent Machine. Automatica 25(3) (1989) 461–467.

Chapter 164
Multi-Qubit State Teleportation via Multiparty-Controlled Entanglement

Ying Guo and Guihua Zeng

Abstract Conditioned teleportation plays important roles in the quantum communication and quantum information processing. In this paper the conditioned teleportation schemes of N-qubit state with M-agent have been investigated, where N, M are integers and N, $M \geq 1$. Since absence of any agents will lead impossibility of restoring the teleported N-qubit state, the proposed schemes may be employed in the quantum secret sharing and the distributed quantum computation.

Introduction

Physically, quantum teleportation, a disembodied transport of quantum information between subsystems through a classical communication channel requiring the shared resource of entanglement, is one of most striking features emerging from quantum mechanics. Entangled systems divided into two subsystems enable the transfer of quantum state to the remote place while the original state is destroyed without any useful information on the original state revealed. Since the pioneer work presented in [1] for teleportation of arbitrary single-qubit quantum state, the quantum teleportation has been developed rapidly in theoretics [2, 3, 4, 5, 6, 7, 8, 9, 10, 11] and experiments [12, 13, 14, 15].

To teleport an arbitrary single-qubit state to one of two receivers conditioned on the measurement outcome of the other, Karlsson and Bourennane [16] generalized the idea of quantum teleportation [1] making use of the three-qubit entangled Greenberger-Horne-Zeilinger (GHZ) state instead of the two-qubit Einstein-Podolsky-Rosen state (EPR). After that, the controlled teleportation for multi-qubit state has been proposed [3, 17]. In those protocols, the initial state can be restored by one of the receivers with assistance of the others. This characteristic leads that

Y. Guo
Department of Electronic Engineering, Shanghai Jiaotong University, Shanghai 200030, China
e-mail: yingguo1001@sjtu.edu.cn

R. Wang et al. (eds.), *Advances in Cognitive Neurodynamics*,

the conditioned teleportation scheme may be employed for spitting a quantum secret in the quantum secret scheme [18, 19, 20, 21, 22, 23, 24], and splitting a message into several parts so that no subset of parts is sufficient to read the message but the entire is.

In this paper, we propose several new schemes which teleports multi-qubit state from a sender (Alice) to a distant receiver (Charlie) via controls of many agents ($\text{Bob}_1, \text{Bob}_2, \cdots, \text{Bob}_n$). Charlie may reconstruct the initial state conditioned on the measurement outcome of all of other participants (the n agents plus Alice) through local operations and classical communications. However, even if one participant does not cooperate, Charlie can not restore the initial state. It has advantage of transferring the secret state via cooperations of all participants. Subsequently, the proposed controlled teleportation schemes may be useful in networked quantum information processing.

Teleportation of Single-Qubit State via Controlled Participants

In the original teleportation scheme [1] for teleporting single qubit state $|\phi_m\rangle = a|0_m\rangle + b|1_m\rangle$ carried by particle p_m, Alice and Bob initially share a maximally two-qubit entangled state $|\Psi^-\rangle_{AB} = \frac{1}{\sqrt{2}}(|0_A 1_B\rangle - |1_A 0_B\rangle)$ with two particles denoted by p_A and p_B. The joint system of the teleported state and EPR state before Alice's measurement can be written as

$$\begin{aligned}
|\Theta\rangle_{AB} &= |\phi_m\rangle \otimes |\Psi^-\rangle_{AB} \\
&= \frac{a}{\sqrt{2}}(|0_m 0_A 1_B\rangle - 0_m 1_A 0_B) + \frac{b}{\sqrt{2}}(|1_m 0_A 1_B\rangle - 1_m 1_A 0_B) \\
&= \frac{1}{2}[|\Psi^-\rangle(-a|0_B\rangle - b|1_B\rangle) + |\Psi^+\rangle(-a|0_B\rangle + b|1_B\rangle) \\
&\quad + |\Phi^-\rangle(a|1_B\rangle + b|0_B\rangle) + |\Phi^+\rangle(a|1_B\rangle - b|0_B\rangle)], \qquad (164.1)
\end{aligned}$$

where $|\Psi^\pm\rangle = \frac{1}{\sqrt{2}}(|0_m 1_A\rangle \pm |1_m 0_A\rangle)$ and $|\Phi^\pm\rangle = \frac{1}{\sqrt{2}}(|0_m 1_A\rangle \pm |1_m 0_A\rangle)$. Alice makes a Bell measurement on the particles in her hand and classically communicates the result to Bob, who can get the state $|\phi_B\rangle = a|0_B\rangle + b|1_B\rangle$ by applying an appropriate unitary operation.

Now we consider a new scheme which employs multipartite entanglement with three participants. Without loss of generality, assume that Alice teleports the state $|\phi_m\rangle$ to Charlie with Bob's assistance. Before communication of three participants, the shared two EPR states are denoted by $|\Psi^-\rangle_{AB}$ with the particles denoted by p_A and p_B (held by Alice and Bob) and $|\Psi^-\rangle_{BC}$ with the particles denoted by p_B and p_C (held by Bob and Charlie), respectively. The joint system of the teleported state and two EPR states before Alice's and Bob's measurement may be written as

$$
\begin{aligned}
|\Theta\rangle_{ABC} &= |\phi_m\rangle \otimes |\Psi^-\rangle_{AB} \otimes |\Psi^-\rangle_{BC} \\
&= \frac{1}{4}\{|\Psi^-\rangle[|\Psi^-\rangle(a|0\rangle + b|1\rangle) + |\Psi^+\rangle(a|0\rangle - b|1\rangle) + |\Phi^-\rangle(-a|1\rangle - b|0\rangle) \\
&\quad + |\Phi^+\rangle(-a|1\rangle + b|0\rangle)] + |\Psi^+\rangle[|\Psi^-\rangle(a|0\rangle - b|1\rangle) \\
&\quad + |\Psi^+\rangle(a|0\rangle + b|1\rangle) + |\Phi^-\rangle(-a|1\rangle + b|0\rangle) + |\Phi^+\rangle(-a|1\rangle - b|0\rangle)] \\
&\quad + |\Phi^-\rangle[|\Psi^-\rangle(-a|0\rangle - b|1\rangle) + |\Psi^+\rangle(-a|0\rangle + b|1\rangle) \\
&\quad + |\Phi^-\rangle(a|1\rangle + b|0\rangle) + |\Phi^+\rangle(a|1\rangle - b|1\rangle)] + |\Phi^+\rangle[|\Psi^-\rangle(-a|0\rangle + b|1\rangle) \\
&\quad + |\Psi^+\rangle(-a|0\rangle - b|1\rangle) + |\Phi^-\rangle(a|1\rangle - b|0\rangle) + |\Phi^+\rangle(a|1\rangle + b|0\rangle)]\},
\end{aligned}
\tag{164.2}
$$

where the subscripts m, A, B and C are omitted for simplicity. After Alice makes a Bell measurement on the first two particles and Bob makes a Bell measurement on the next two particles in their hands, they classically communicate results to Charlie. Finally, Charlie obtains the teleported state by applying an appropriate unitary operation. The details are presented in Table 164.1.

We note that after Alice's Bell-state measurement, Bob and Charlie are left sharing a three-qubit state of the form $\{(-1)^i[|\Psi^-\rangle(a|0\rangle \pm b|1\rangle) + |\Psi^+\rangle(a|0\rangle) \mp b|1\rangle) + |\Phi^-\rangle(-a|1\rangle) \mp b|0\rangle) + |\Phi^+\rangle(-a|1\rangle \pm b|0\rangle)] : i = 1, 2\}$. If Bob does not cooperate with Charlie, the resulting density operator of Charlie would become $\rho_c = |a|^2|0\rangle\langle 0| + |b|^2|1\rangle\langle 1|$ or $|a|^2|1\rangle\langle 1| + |b|^2|0\rangle\langle 0|$. It implies that Charlie has amplitude information on Alice's message but knows nothing on its phase. Subsequently, Charlie can not recover Alice's initial state without Bob's participation.

The proposed protocol may be generalized to teleport a single-qubit state with assistances of multi-agents, i.e., $\text{Bob}_1, \text{Bob}_2, \cdots, \text{Bob}_N$. This is useful for multiparty quantum secret sharing. In this case, the participants should preshare $N + 1$ EPR states denoted by $|\Psi^-\rangle_{AB_1}, |\Psi^-\rangle_{B_1B_2}, \cdots, |\Psi^-\rangle_{B_{N+1}}C$. Then the joint system of the teleported state $|\phi_m\rangle$ and $N+1$ EPR states before Alice's, Bob_i's ($i = 1, 2, \cdots, N$) measurement may be written as $|\Theta\rangle_{AB_1B_2\cdots C} = |\phi_m\rangle \otimes |\Psi^-\rangle_{AB_1} \otimes |\Psi^-\rangle_{AB_2} \otimes \cdots \otimes |\Psi^-\rangle_{B_{N+1}C}$. After Alice makes a Bell measurement on the first-two particles and Bob_i makes a Bell measurement on the $(i+1)^{th}$-two particles in their hands, they classically communicate results to Charlie which bases have been used for the measurements. Finally, Charlie obtains the teleported state by applying appropriate unitary operations.

Table 164.1 The unitary transformations Charlie must perform on his qubit, conditioned to Alice's measurement result, to complete the teleportation protocol. I is the identity operator, σ_x and σ_z are the usual Pauli operators

Alice's result	Bob's result	Charlie's operation	Charlie's qubit
$\|\Psi^-\rangle$	$\|\Psi^-\rangle(\|\Psi^+\rangle, \|\Phi^-\rangle, \|\Phi^+\rangle)$	$I(\sigma_z, \sigma_x, \sigma_z\sigma_x)$	$\|\phi\rangle(\|\phi\rangle, -\|\phi\rangle, -\|\phi\rangle)$
$\|\Psi^+\rangle$	$\|\Psi^-\rangle(\|\Psi^+\rangle, \|\Phi^-\rangle, \|\Phi^+\rangle)$	$\sigma_z(I, \sigma_z\sigma_x, \sigma_x)$	$\|\phi\rangle(\|\phi\rangle, -\|\phi\rangle, -\|\phi\rangle)$
$\|\Phi^-\rangle$	$\|\Psi^-\rangle(\|\Psi^+\rangle, \|\Phi^-\rangle, \|\Phi^+\rangle)$	$I(\sigma_z, \sigma_x, \sigma_z\sigma_x)$	$-\|\phi C\rangle(-\|\phi\rangle, \|\phi\rangle, \|\phi\rangle)$
$\|\Phi^+\rangle$	$\|\Psi^-\rangle(\|\Psi^+\rangle, \|\Phi^-\rangle, \|\Phi^+\rangle)$	$\sigma_z(I, \sigma_z\sigma_x, \sigma_x)$	$-\|\phi\rangle(-\|\phi\rangle, \|\phi\rangle, \|\phi\rangle)$

Teleportation of Multi-Qubit State via Controlled Participants

To teleport a multi-qubit state, e.g., a two-qubit state $|\phi\rangle_{m_1m_2}$ with two particles p_{m_1} and p_{m_2}, to Charlie with Bob's assistances, two four-qubit states $|G^{00}_{A_1A_2B_1B_2}\rangle$ of the particles $\{pA_1, pA_2, pB_1, pB_2\}$ and $|G^{00}_{B_3B_4C_1C_2}\rangle$ of the particles $\{pB_3, pB_4, pC_1, pC_2\}$ should be initially shared among three participants, i.e.,

$$|G^{00}\rangle_{A_1A_2B_1B_2} = \frac{1}{2}\sum_{j=1}^{4}(|\Psi_j\rangle_{A_1A_2} \otimes |\Psi'_j\rangle_{B_1B_2}),$$
$$|G^{00}\rangle_{B_3B_4C_1C_2} = \frac{1}{2}\sum_{j=1}^{4}(|\Psi_j\rangle_{B_3B_4} \otimes |\Psi'_j\rangle_{C_1C_2}), \tag{164.3}$$

where $|\Psi_1\rangle = \cos\alpha|00\rangle + \sin\alpha|11\rangle$, $|\Psi_2\rangle = \cos\beta|01\rangle + \sin\beta|10\rangle$, $|\Psi_3\rangle = -\sin\beta|01\rangle + \cos\beta|10\rangle$, $|\Psi_4\rangle = -\sin\alpha|00\rangle + \cos\alpha|11\rangle$, $|\Psi'_1\rangle = \cos\theta|00\rangle + \sin\theta|11\rangle$, $|\Psi'_2\rangle = \sin\varphi|01\rangle + \cos\varphi|10\rangle$, $|\Psi'_3\rangle = \cos\varphi|01\rangle + \sin\varphi|10\rangle$, $|\Psi'_4\rangle = -\sin\theta|00\rangle + \cos\theta|11\rangle$ with $0 < \alpha, \beta, \theta, \varphi < \pi/2$ for $\alpha \neq \theta$ and $\beta \neq \varphi$. It can be proved that $\{|\Psi_i\rangle : i = 1, 2, 3, 4\}$ or $\{|\Psi'_i\rangle : i = 1, 2, 3, 4\}$ constitutes an orthogonal basis of the two-qubit state space. Thus, the teleported state can be denoted by $|\phi\rangle_{m_1m_2} = \sum_{i=1}^{4} a_i|\Psi'_i\rangle_{m_1m_2}$ with $\sum_{i=1}^{4}|a_i|^2 = 1$. After applying the operation $\mu \otimes \nu$ onto the first two qubits of $|G^{00}\rangle$, we may obtain sixteen orthogonal states denoted by $\{|G^{\mu\nu}\rangle : \mu \otimes \nu \otimes I \otimes I|G^{00}\rangle\}$, where $\mu, \nu \in \{I, \sigma_x, \sigma_z, \sigma_x\sigma_z\}$. Thus, the partial trace over Alice's and Bob's (or Bob's and Charlie's) subsystem can be calculated as

$$Tr_{B(A)}(|G^{00}\rangle_{A_1A_2B_1B_2}\langle G^{00}|) = \frac{1}{4}\mathcal{I}_{A(B)} \tag{164.4}$$

or

$$Tr_{B(C)}(|G^{00}\rangle_{B_1B_2C_1C_2}\langle G^{00}|) = \frac{1}{4}\mathcal{I}_{C(B)}, \tag{164.5}$$

where $\mathcal{I}$ is an identity operator. It implies that all of the states $|G^{\mu\nu}\rangle$ are maximally entangled states similar to EPR states $|\Psi^{\pm}\rangle$ and $|\Phi^{\pm}\rangle$. Thus, the joint system of the teleported state $|\phi\rangle_{m_1m_2}$, $|G^{00}\rangle_{A_1A_2B_1B_2}$ and $|G^{00}\rangle_{B_3B_4C_1C_2}$ before Alice and Bob's measurement can be written as

$$|\Omega\rangle_{ABC} = |\phi\rangle_{m_1m_2} \otimes |G^{00}\rangle_{A_1A_2B_1B_2} \otimes |G^{00}\rangle_{B_3B_4C_1C_2}. \tag{164.6}$$

If Alice and Bob apply jointly the complete projective measurements on $\{p_{m_1}, p_{m_2}, p_{A_1}, p_{A_2}\}$ and $\{p_{B_1}, p_{B_2}, p_{B_3}, p_{B_4}\}$ in the basis $\{|G^{\mu\nu}\rangle\}$ with the respective measurement outcomes $\mu\nu$ and $\mu'\nu'$, Charlie's state of particles p_{C_1} and p_{C_2} becomes

$$
\begin{aligned}
|M\rangle_{C_1C_2} &= \frac{1}{\sqrt{p}}\langle G^{\mu'\nu'}_{B_1B_2B_3B_4}| \otimes \langle G^{\mu\nu}_{m_1m_2A_1A_2}|\phi\rangle_{m_1m_2} \otimes |G^{00}\rangle_{A_1A_2B_1B_2} \\
&\quad \otimes |G^{00}\rangle_{B_3B_4C_1C_2}, \\
&= \frac{1}{\sqrt{p}}\langle G^{\mu'\nu'}_{B_1B_2B_3B_4}| \otimes \langle G^{00}_{m_1m_2A_1A_2}|[(\mu_{m_1} \otimes \nu_{m_2})|\phi\rangle_{m_1m_2} \\
&\quad \otimes |G^{00}\rangle_{A_1A_2B_1B_2}] \otimes |G^{00}\rangle_{B_3B_4C_1C_2} \\
&= \frac{1}{4\sqrt{p}}\langle G^{00}_{B_1B_2B_3B_4}|[(\mu'_{B_1}\mu_{B_1} \otimes \nu'_{B_2}\nu_{B_2})|\phi\rangle_{B_1B_2}] \otimes |G^{00}\rangle_{B_3B_4C_1C_2} \\
&= \frac{1}{16\sqrt{p}}(\mu'_{C_1}\mu_{C_1} \otimes \nu'_{C_2}\nu_{C_2})|\phi\rangle_{C_1C_2} \qquad (164.7)
\end{aligned}
$$

The success of the present protocol is guaranteed by the equation ${}_{m_1m_2A_1A_2}\langle G^{00}| \otimes_{B_1B_2B_3B_4} \langle G^{00}|G^{00}\rangle_{A_1A_2B_1B_2} \otimes |G^{00}\rangle_{B_3B_4C_1C_2} = \frac{1}{16}\sum_{i=1}^{4} |\Psi'_i\rangle_{C_1C_2} \times_{m_1m_2} \langle\Psi'_i|$. Thus, one may obtain $p = \frac{1}{256}$ which implies that Charlie can always succeed in restoring the original state $|\phi\rangle_{m_1m_2}$ as long as Charlie receives Alice's and Bob's classical information on the measurement results.

Generally, the present protocol can be used for the teleportation of the three-qubit state with the agent Bob. Assume that the initial three-qubit message state is denoted by $|\phi\rangle_{m_1m_2m_3}$ and two shared six-qubit states between three participants are denoted respectively by

$$
\begin{aligned}
|G^{000}\rangle_{A_1A_2A_3B_1B_2B_3} &= \frac{1}{2}\sum_{j=1}^{8}(|\Psi_j\rangle_{A_1A_2A_3} \otimes |\Psi'_j\rangle_{B_1B_2B_3}), \\
|G^{000}\rangle_{B_4B_5B_6C_1C_2C_3} &= \frac{1}{2}\sum_{j=1}^{8}(|\Psi_j\rangle_{B_4B_5B_6} \otimes |\Psi'_j\rangle_{C_1C_2C_3}), \qquad (164.8)
\end{aligned}
$$

Where $|\Psi_1\rangle = \cos\alpha_1|000\rangle + \sin\alpha_1|111\rangle$, $|\Psi_2\rangle = \cos\beta_1|001\rangle + \sin\beta_1|110\rangle$, $|\Psi_3\rangle = \cos\gamma_1|010\rangle + \sin\gamma_1|101\rangle$, $|\Psi_4\rangle = \cos\delta_1|011\rangle + \sin\delta_1|100\rangle$, $|\Psi_5\rangle = -\sin\alpha_1|000\rangle + \cos\alpha_1|111\rangle$, $|\Psi_6\rangle = -\sin\beta_1|001\rangle + \cos\beta_1|110\rangle$, $|\Psi_7\rangle = -\sin\gamma_1|010\rangle + \cos\gamma_1|101\rangle$, $|\Psi_8\rangle = -\sin\delta_1|011\rangle + \cos\delta_1|100\rangle$, and $|\Psi'_1\rangle = \cos\alpha_2|000\rangle + \sin\alpha_2|111\rangle$, $|\Psi'_2\rangle = \cos\beta_2|001\rangle + \sin\beta_2|110\rangle$, $|\Psi'_3\rangle = \sin\gamma_2|010\rangle + \cos\gamma_2|101\rangle$, $|\Psi'_4\rangle = \sin\delta_2|011\rangle + \cos\delta_2|100\rangle$, $|\Psi'_5\rangle = -\sin\alpha_2|000\rangle + \cos\alpha_2|111\rangle$, $|\Psi'_6\rangle = -\sin\beta_2|001\rangle + \cos\beta_2|110\rangle$, $|\Psi'_7\rangle = \cos\gamma_2|010\rangle - \sin\gamma_2|101\rangle$, $|\Psi'_8\rangle = \cos\delta_2|011\rangle - \sin\delta_2|100\rangle$, with $0 < \alpha_i, \beta_i, \gamma_i, \delta_i < \pi/2 (i = 1, 2)$ for $\alpha_1 \neq \alpha_2$, $\beta_1 \neq \beta_2$, $\gamma_1 \neq \gamma_2$ and $\delta_1 \neq \delta_2$. It can be proved that both $\{|\Psi_i\rangle : 1 = 1, 2, \ldots, 8\}$ and $\{|\Psi'_i\rangle : 1 = 1, 2, \ldots, 8\}$ can constitute respectively an orthogonal basis of three qubit state space. So the initial state $|\phi\rangle_{m_1m_2m_3}$ can be repressed as $|\phi\rangle_{m_1m_2m_3} = \sum_{i=1}^{8} a_i|\Psi'_i\rangle$ with $\sum_{i=1}^{8}|a_i|^2 = 1$. After applying the operation $\mu \otimes \nu \otimes \omega$ onto the first three qubits of $|G^{000}\rangle$, we may obtain forty-eight orthogonal states denoted by $\{|G^{\mu\nu\omega}\rangle : \mu \otimes \nu \otimes \omega \otimes I \otimes I \otimes I|G^{000}\rangle\}$, where $\mu, \nu, \omega \in \{I, \sigma_x, \sigma_z, \sigma_x\sigma_z\}$. Thus, the joint system of the teleported state $|\phi\rangle_{m_1m_2m_3}$, $|G^{000}\rangle_{A_1A_2A_3B_1B_2B_3}$ and

$|G^{000}\rangle_{B_4B_5B_6C_1C_2C_3}$ before Alice and Bob's measurement can be written as $|\Upsilon\rangle_{ABC} = |\phi\rangle_{m_1m_2m_3} \otimes |G^{000}\rangle_{A_1A_2A_3B_1B_2B_3} \otimes |G^{000}\rangle_{B_4B_5B_6C_1C_2C_3}$. If Alice and Bob apply the complete projective measurements jointly on $\{p_{m_1}, p_{m_2}, p_{m_3}, p_{A_1}, p_{A_2}, p_{A_3}\}$ and $\{p_{B_1}, p_{B_2}, p_{B_3}, p_{B_4}, p_{B_5}, p_{B_6}\}$ in the basis $\{|G^{\mu\nu\omega}\rangle\}$ with the respective measurement out-comes $\mu\nu\omega$ and $\mu'\nu'\omega'$, Charlie can obtain the three-qubit state

$$|M\rangle_{C_1C_2C_3} = \frac{1}{256}\mu'_{C_1}\mu_{C_1} \otimes \nu'_{C_2}\nu_{C_2} \otimes \omega'_{C_3}\omega_{C_3}|\phi\rangle_{C_1C_2C_3}. \tag{164.9}$$

Thus, Charlie can gain the initial three-qubit state conditioned on Alice's and Bob's measurement outcomes $\mu\nu\omega$ and $\mu'\nu'\omega'$.

Discussion and Conclusions

The proposed schemes are probably secure according to the following reasons. Firstly, the eavesdropping by entangling ancillary qubit with the participants' qubits can be revealed by comparing a subset of the states Charlie received to those Alice sent via a quantum one way map. Secondly, the qubits Alice sends to Charlie are basically useless without the classical information possessed by all participants including Alice, $\text{Bob}_1, \ldots, \text{Bob}_n$. Hence, even if the eavesdropper were to intercept the qubits intended for Charlie and replace them with fakes and the classical communication channel for the participant's measurement outcomes, she could not restore the initial state without Alice's measurement outcomes conditioned on that Alice sends her classical information via the standard method implemented in references [18, 19, 20]. Actually, the security of the present schemes can be proved in essence in the same way as those in references [1, 2, 3].

In summary, we present a method for the multiparty-controlled teleportation of an arbitrary m-qubit entangled state with n $2m$-qubit states shared by all of the participants. Any one (say Bob_i) of the agents can reconstruct the initial state conditioned on the measurement outcomes of Alice and the previous agents $\text{Bob}_1, \ldots, \text{Bob}_{i-1}$. This method may be useful in the networked quantum information processing. Also, it can be used to share the classical message or the multi-qubit state with just a few modifications.

References

1. C. H. Bennett, G. Brassard, C. Crépeau, *et al.*, Phys. Rev. Lett. 70, 1985 (1993).
2. Y. Yeo and W. K. Chua, Phys. Rev. Lett. 96, 060502 (2006).
3. F. G. Deng, C. Y. Li, Y. S. Li, H. Y. Zhou and Y. Wang, Phys. Rev. A 72, 022338 (2005).
4. M. Zukowski, A. Zeilinger, M. A. Home and A. K. Ekert, Phys. Rev. Lett. 71, 4287 (1993).
5. J. Fang, Y. Lin, S. Zhu, and X. Chen, Phys. Rev. A 67, 014305 (2003).
6. W. Son, J. Lee, M. S. Kim, and Y.-J. Park, Phys. Rev. A 64, 064304 (2001).
7. E. F. Galvao and L. Hardy, Phys. Rev. A 62, 012309 (2000).
8. M. Fujii, Phys. Rev. A 68, 050302 (2003).

9. N. Ba An, Phys. Rev. A 68, 022321 (2003).
10. W. P. Bowen, N. Treps, B. C. Buchler, *et al.*, Phys. Rev. A 67, 032302 (2003).
11. T. J. Johnson, S. D. Bartlett, and B. C. Sanders, Phys. Rev. A 66, 042326 (2002).
12. D. Bouwmeester, J. W. Pan, K. Mattle, *et al.*, Nature (London) 390, 575 (1997).
13. A. Furusawa, J. L. Soensen, S. L. Braunstein, *et al.*, Science 282, 706 (1998).
14. M. A. Nielsen, E. Knill, and R. Laflamme, Nature (London) 396, 52 (1998).
15. G. Y. Xiang, J. Li and G. C. Guo, Phys. Rev. A 71, 044304 (2005).
16. A. Karlsson and M. Bourennane, Phys. Rev. A 58, 4394 (1998).
17. C. P. Yang, S. I. Chu and S. Han, Phys. Rev. A 70, 022329 (2005).
18. M. Hillery, V. Buzek, and A. Berthiaume, Phys. Rev. A 59, 1829 (1999).
19. R. Cleve, D. Gottesman, and H. K. Lo, Phys. Rev. Lett. 83, 648 (1999).
20. S. Bandyopadhyay, Phys. Rev. A 62, 012308 (2000).
21. Li-Yi Hsu, Phys. Rev. A 68, 022306 (2003).
22. A. C. A. Nascimento, J. M. Quade, and H. Imai, Phys. Rev. A 64, 042311 (2001).
23. A. Zhang, Y. Li and Z. Man, Phys. Rev. A 71, 044301 (2005).
24. T. Ogawa, A. Sasaki, M. Iwamoto and H. Yamamoto, Phys. Rev. A 72, 032318 (2005).

Chapter 165
New Multiobjective PSO Algorithm for Nonlinear Constrained Programming Problems

Chun-An Liu

Abstract A new approach is presented to solve nonlinear constrained programming problems (NLCPs) by using particle swarm algorithm (PSO). It neither uses any penalty functions, nor distinguish the feasible solutions and the infeasible solutions including swarm. The new technique treats the NLCPs as a bi-objective optimization problem, one objective is the original objective of NLCPs, and the other is the degree violation of constraints. As we prefer to keep the ratio of infeasible solutions so as to increase the diversity of swarm and avoid the defect of conventional over-penalization, a new fitness function is designed based on the second objective. In order to make the PSO escape from the local optimum easily, we also design a adaptively dynamically changing inertia weight. The numerical experiment shows that the algorithm is effective.

Introduction

Nonlinear constrained programming problems (NLCPs) are encountered in numerous applications. Structural optimization, engineering design, economic, allocation and location problems are just a few of the scientific fields in which NLCPs are frequently met. The key point in the NLCPs process is how to deal with the constraints. The traditional methods usually convert the problem into non-constrained problem to solve, such as [1, 2, 3]. However, these methods demand the high quality of the function, and they can only solve those better quality functions.

Particle swarm algorithms (PSO) [4] originally developed by Kennedy and Eberhart is a swarm based algorithm. PSO is initialized with a swarm of candidate solutions, each candidate solution is called particle and move according the velocity-location equation. PSO have been found to be fast in solving nonlinear, non-differentiable and multi-modal optimization problems. In the last years, several

C.-A. Liu
Department of Mathematics, Baoji University of Arts and Sciences, Baoji 721013, China
e-mail: liu2006@126.com

R. Wang et al. (eds.), *Advances in Cognitive Neurodynamics*,

important effort has been reported in the literatures. Coath and Halgamuge [5] proposed the feasible solutions method(FSM) and the penalty function method(PFM) to handle constraints in PSO. however, both of the two method have disadvantages. FSM demands all particles must be include in the feasible region, and the PFM required careful fine tuning of the penalty function parameters.

Recently, some genetic algorithm based on the multiobjective optimization concepts have been proposed to handle constraints [6, 7]. Its main ideal is consider each constraints as an objective function, and transform the NLCPs into multiobjective optimization problem with $m + 1$ objectives, where m is the number of the constraints of NLCPs. Then using the Pareto dominance concepts of multiobjective optimization or Pareto ranking to select the candidates individuals and consist the next swarm. However, this method has a serious drawback according to the following two case if all objectives are considered as the same importance. one case is that an feasible solution which is seen to the true optimal solution of the NLCPs, but it has a small fitness and be seen as a bad solution to delate according to the the Pareto dominance or Pareto rank. However, this solution should survive in the next generation. The other case is that one infeasible solution which is far away from the true optimal solution of the NLCPs or the boundary of constraints, maybe its has a very big fitness value to survive according to the Pareto dominance or Pareto rank. However, this solution should keep away from the next generation.

In this paper, the constraints of NLCPs are firstly transformed into a degree violation and thus the NLCPs is transformed into a bi-objective problem. In order to increase the diversity of population and avoid the defect of conventional overpenalization, a new fitness function is designed based on the degree violation. and in order to make the PSO escape from the local optimum easily, we also design a adaptively dynamically changing inertia weight. The numerical experiment shows that the algorithm is effective.

Transformation of NLCPs

Consider the following nonlinear constrained programming problems (165.1):

$$\begin{cases} \min\limits_{x \in D \subset [L,U]} f(x) \\ s.t. \quad g_i(x) \leq 0 \; i = 1 \sim m \end{cases} \tag{165.1}$$

Where $[L, U] = \{x = (x_1, x_2, \cdots, x_n) | l_i \leq x_i \leq u_i, i = 1 \sim n\} \subset R^n$. $D = \{x | x \in [L, U], g_i(x) \leq 0, i = 1 \sim m\}$ is called feasible region and each point is called a feasible point.

For the problem (165.1), it can be transformed into the following bi-objective optimization problem (165.2):

$$\min F(x) = (f_1(x), f_2(x)) \tag{165.2}$$

Where $f_1(x)$ is objective function of the original optimization problem (165.1), $f_2(x) = \frac{1}{m}\sum_{i=1}^{m}\frac{c_i(x)}{c(x)+\varepsilon}$, $c_i(x) = \max\{0, g_i(x)\}$, $i = 1 \sim m$, $c(x) = \max\limits_{1\le i\le m}\{c_i(x)\}$, $\varepsilon > 0$. It is obvious that to minimize the first objective function of optimization problem (165.2) means to find a point x^* so as to obtain the optimal value of the problem (165.1). Since the second objective function of problem (165.2) is defined as the function of degree violation of constraints. Thus, to minimize $f_2(x)$ means to search the point x^* in order to meet all the constraints. Therefore, to minimize the two objectives of problem (165.2) simultaneously means to search for the point so as to meet all the constraints and make the first objective $f_1(x)$ minimize.

New Multiobjective PSO Algorithm

PSO Algorithm

PSO was initially proposed by Kennedy and Eberhart [4]. It is a population evolution based optimization method inspired by the behavior of bird flocks, which employs a swarm of particles to probe the search space. In PSO, each individual (called particle) is described by three main concepts: its current location in the search space, a memory of its best previous location and information regarding the best location and information regarding the best location ever attained by a topological neighborhood of it. Suppose that $X_{id}(t)$ is the present position of i-th particle (termed as same as its present location $X_{id}(t)$) in generation t, $P_{id}(t)$ be its own best previous position, and $P_{gd}(t)$ be the best position ever attained by the swarm. Then, the particle $X_{id}(t)$ is manipulated according to the following velocity-location equations:

$$V_{id}(t+1) = \omega \cdot V_{id}(t) + c_1 \cdot r_1(P_{id}(t) - X_{id}(t)) + c_2 \cdot r_2(P_{gd}(t) - X_{id}(t)) \tag{165.3}$$

$$X_{id}(t+1) = X_{id}(t) + V_{id}(t+1), i = 1 \sim N \tag{165.4}$$

Where $V_{id}(t)$ is the previous velocity, $V_{id}(t+1)$ is the present velocity, $X_{id}(t+1)$ is the new position, c_1, c_2 are realizations of uniformly distributed random variables in [0,1]. The parameters c_1 and c_2 are called cognitive and social parameters. The parameter ω is called inertia weight and it is used to control the trade-off between the global exploration and the local exploitation ability of the swarm.

Selection Operator

For particle x, we defined the new fitness function as following:

$$F(x) = \begin{cases} f_1(x) & x \in D \\ \max(\frac{p}{N} \cdot f_1^{min} + \frac{N-p}{N} \cdot f_1^{max}, f_1(x)) + f_2(x) & x \notin D \end{cases} \tag{165.5}$$

Where N is the particle swarm size, p is the number of feasible particles of current generation. f_1^{min} and f_1^{max} is the smallest value and the biggest value of feasible particles of current generation, respectively. for any two particles, we can see from the fitness function (165.5):

1. If the two particles are both feasible, then the particle with a minimum value of the first objective function of problem (165.2) wins.
2. If both of the particles are infeasible, the particle with a minimum value of the second objective function of problem (165.2) wins.
3. If one is infeasible, the other is feasible. then compare the deviation degree of The two particle far away from the f_1^{min}, when the bigger of the proportion of feasible particle, the bigger of the probability to choice the infeasible in current particle swarm. On the contrary, the bigger of the proportion of infeasible particle in current particle swarm, the bigger of the probability to choice the feasible.

Self-adaptive Variation of ω

From (165.3), It's obvious that a large inertia weight can make the PSO to explore the search space of problem, while a small one tends to facilitates exploitation. Hence, the inertia weight is a very important parameter to balance the global and local search. To evaluate the diversity of the swarm, we defined a diversity measure as follows:

$$\lambda(t) = \frac{\sum_{i=1}^{N} \left(f_i^t - \frac{(\sum_{i=1}^{N} f_i^t)}{N} \right)^2}{N \cdot \max\limits_{k \in \{1,2,\cdots,t\}} \left\{ \sum_{i=1}^{N} \left(f_i^k - \frac{(\sum_{i=1}^{N} f_i^k)}{N} \right)^2 \right\}} \tag{165.6}$$

where f_i^t present the fitness value of the i-th paticle in t-th generation. The bigger the value of $\lambda(t)$, the better the diversity of the swarm is. the smaller the value of $\lambda(t)$, the more crowded the swarm is. When the swarm become very crowded, it is difficult for the algorithm to jump out from the local optimal solution. Thus, we can define the self-adaptive variation inertia weight based on the dynamic parameter $\lambda(t)$ as $\omega(t) = \frac{g_{size}^{-t}}{(\lambda(t)+\in)\cdot(g_{size}+0.4)}$, where g_{size} be the maximum generation of swarm, t be the current generation. $\in$ is a very small positive number, It can be seen from the $\omega(t)$ that when paticle are crowded, that's to say $\lambda(t)$ is small, $\omega(t)$ will become big in order to enhance the ability of global search of the algorithm.

The Multiobjective PSO Algorithm

Step 1. (Initialization) Given the particle swarm size N, randomly generate initial swarm $p(0)$ in $[L, U]$, and let $t = 0$.

Step 2. (Update velocity and position)For each of the particle in $p(t)$, it was manipulated to find its good position and velocity based on the new selection operator in current generation. Then update each particle's velocity and position according to the velocity-position equation and constitute a temporary particle swarm $c(t)$.

Step 3. Utilize the crossover operator proposed in [6] to generate the offspring of the particles in $c(t)$.

Step 4. (Crossover)Select N individuals by the selection operator from $p(t) \cup c(t)$ and constitute the next particle swarm $p(t+1)$, and use the best solution $x_t' = \arg \min_{x \in D \cap p(t)} f_1(x)$ to replace the particle which its fitness value is biggest in the $p(t+1)$, let $t = t+1$.

Step 5. (Stop criterion)If $t = T$, the best particle in $p(t)$ is as the optimal and the algorithm is stopped; otherwise, go to Step 2.

Simulation Results

Test Functions

Test Problem *F*1([8])

$$\min f(x) = (x_1 - 10)^2 + (x_2 - 20)^2,$$

subject to: $g_1(x) = (x_1 - 5)^2 + (x_2 - 5)^2 - 100 \geq 0$, $g_2(x) = (x_1 - 6)^2 + (x_2 - 5)^2 - 82.81 \leq 0, 13 \leq x_1 \leq 100, 0 \leq x_2 \leq 100$. The best known solution is $f^* = -6961.814$.

Test Problem *F*2([8])

$\min f(x) = (x_1-10)^2+5(x_2-12)^2+x_3^4+3(x_4-11)^2+7x_6^2+x_7^4-4x_6x_7-10x_6-8x_7$, subject to: $g_1(x) = 127 - 2x_1^2 - 3x_2^4 - x_3 - 4x_4^2 - 5x_3 \geq 0$, $g_2(x) = 196 - 23x_1 - 3x_2^2 - 6x_6^2 - 8x_7 \geq 0$, $g_3(x) = 282 - 7x_1 - 3x_2 - 10x_3^2 - x_4 + x_5 \geq 0$, $g_4(x) = -4x_1^2 - x_2^2 + 3x_1x_2 - 5x_6 + 11x_7 \geq 0, -10 \leq x_i \leq 10, i = 1, 2, \cdots, 7$. The best known solution is $f^* = 680.630$.

The Problem *F*3([9])

$$\max f(x) = \left| \frac{\sum_{i=1}^{n} cos^4(x_i) - 2\prod_{i=1}^{n} \cos^2(x_i)}{\sqrt{\sum_{i=1}^{n} i x_i^2}} \right|,$$

subject to: $g_1(x) = 0.75 - \prod_{i=1}^{n} \leq 0$, $g_2(x) = \sum_{i=1}^{n} x_i - 0.75n \leq 0$, n $= 20, 0 \leq x_i \leq 10(i = 1, 2, \cdots, n)$. The global maximum is unknown; the best reported solution [10] is $f^* = -0.803619$. Constraint g_1 is close to being active ($g_1 = -10^{-8}$).

Test Problem *F*4([9])

$$\max f(x) = \frac{\sin^3(2\pi x_1) sin(2\pi x_2)}{x_1^3(x_1 + x_2)},$$

subject to: $g_1(x) = x_1^2 - x_2 + 1 \leq 0$, $g_2(x) = 1 - x_1 + (x_2 - 4)^2 \leq 0, 0 \leq x_1, x_2 \leq 10$. the best reported solution is $f^* = -0.095825$.

Test Problem *F*5([8])

$$\min f(x) = e^{x_1 x_2 x_3 x_4},$$

subject to: $6x_1^2 + x_2^2 + x_3^2 + x_4^2 + x_5^2 - 10 = 0$, $x_2 x_3 - 5x_4 x_5 = 0$, $x_1^3 + x2^3 + 1 = 0, -2.3 \leq x_i \leq 2.3, i = 1, 2, -3.2 \leq x_i \geq 3.2(i = 3, 4, 5)$. the best reported solution is $f^* = 0.0539498$.

Result and Comparison

In the simulation, we termed our approach as MOPSO, The particle swarm size $N = 200, c_1 = c_2 = 0.5, r_1, r_2 \in rand[0, 1]$. For each problems, the best result, the mean and the worst result obtained by MOPSO in all 20 runs were recorded. All the result obtainted by MOPSO was compared with the existing ones obtainted from the reference [7, 8, 9, 10] in Table 165.1.

Table 165.1 Comparison of the best, mean and worst results among MOPSO and other algorithms in reference [7, 8, 9, 10] for each test problems,N.A. represents the coresponding result is not available.

It can be seen from Table 165.1, for $F1$, $F3$ and $F5$, the best solutions found are better than the optimal one. For $F2$, the solution found by MOPSO is equal to the optimal and these solutions found by other algorithms in reference [7, 8, 9], but the mean and worst solution found by MOPSO is better than these algorithms in difference references [7, 8, 9]. For $F4$, the results obtained by MOPSO are same as these results obtained by each algorithm in reference [8, 9, 10]. Thus, these results indicates MOPSO is effective to solve nonlinear constrained programming problems.

Table 165.1 Result comparison

Problem	Optimal	Method	Best result	Mean	Worst result
		MOPSO	−6961.820	−6961.818	−6961.813
		Reference[7]	−6961.817	−6960.942	−6960.456
$F1$	−6961.814	Reference[8]	−6961.814	−6875.940	−6850.262
		Reference[9]	−6961.814	−6961.813	−6961.810
		Reference[10]	N.A.	N.A.	N.A.
		MOPSO	680.630	680.631	680.632
		Reference[7]	680.630	680.683	680.876
$F2$	680.630	Reference[8]	680.630	680.656	680.763
		Reference[9]	680.630	680.633	680.634
		Reference[10]	N.A.	N.A.	N.A.
		MOPSO	−0.803614	−0.804115	−0.805298
		Reference[7]	N.A.	N.A.	N.A.
$F3$	−0.803619	Reference[8]	−0.803616	−0.804975	−0.806288
		Reference[9]	−0.803619	−0.805281	−0.809291
		Reference[10]	−0.803933	−0.806301	−0.809747
		MOPSO	−0.095825	−0.095825	−0.095825
		Reference[7]	N.A.	N.A.	N.A.
$F4$	−0.095825	Reference[8]	−0.095825	−0.095825	−0.095825
		Reference[9]	−0.095825	−0.095825	−0.095825
		Reference[10]	−0.095825	−0.095825	−0.095825
		MOPSO	0.0539492	0.0541245	0.0559764
		Reference[7]	N.A.	N.A.	N.A.
$F5$	0.0539498	Reference[8]	0.0539498	0.0541795	0.0562234
		Reference[9]	N.A.	N.A.	N.A.
		Reference[10]	N.A.	N.A.	N.A.

Conclusions

In this paper, we first transform the nonlinear constrained programming problem into a bi-objective optimization problem, and then a new multiobjective PSO algorithm which dose not requires the use of a penalty function is proposed. The numerical simulations on five test problems also indicate the effectiveness of the proposed algorithm.

Acknowledgements This work was jointly supported by the National Natural Science Foundation of China (60374063) and the Natural Science Foundation of Shaaxi Province of China (2006A12).

References

1. K. Deb, S. A. Agrawal. Niched-penalty approach for constraint handing in genetic algorithms. Artificial Neural Nets and Genetic Algorithms, Proceedings of the International Conference In Portoroz Slovenia, 1999, Andrej, Dobnikar Eds. Springer Verlag, Wien, New York, (1999)235–243.
2. K. Deb. An efficient constraint handing method for genetic algorithms. Comput. Methods Appl. Mech. Eng., 186 (2000)311–338.

3. R. Farmani, J. Wright. Self-adaptive fitness formulation for constrained optimization. IEEE Trans. Evol. Comput., 7 (2003)445–455.
4. J. Kennedy, R. Eberhart. Particle Swarm Optimization. IEEE International 1 Conference on Neural Networks, Perth, Australia, Carlos A, Coello, Eds. Springer Verlag (1995)678–682.
5. A. Hernandez-Aguirre, C. Coello. Passss: An Implementation of a Novel Diversity Strategy to Handle Constraints. In Proceeding of the 2004 Congress on Evolutionary Computation CEC-2004, IEEE Press. Vol. 1 (2004)503–410.
6. S. Tsutsui, M. Yamamura. Multi-parent recombination with simplex crossover in real coded genetic algorithms, In Banzhaf W, Daida J, Eiben E, Eds. GECCO'99: Proceeding of the Genetic and Evolutionary Computation Conference. San Mateo, Morgan Kaufmann Publishers, (1999)57–664.
7. K. E. Parsopoulos, M. N. Vrahatis. Particle swarm optimization method for constrained optimization problems. In Proceedings of the 5th Conference on Parallel Problems solving from Nature, Springer Verlag, Wien, Koziel, Mich alewics, (1999)254–259.
8. T. P. Runarsson, X. Yao. Stockastic ranking for constrained evolutionary optimization. IEEE Trans. Evolut. Comput., 4 (2000)284–294.
9. Arturo Hernandez Aguirre, Salvador Botello Rionda, Salvador, Carlos A, Coello. Coello. IS-PAES: A Constraints handling Technique Based on Multi-objective Concepts. C.M. Fonseca et al., Eds. EMO2003, LNCS 2632 (2003)73–87.
10. Carlos A, Coello. Coello. Efrén Mezura-Montes. Handleing constrains in genetic algorithm using dominace-based tournaments [C]. In Proceedings of the 5th Conference on Computational Intelligence and Multimedia Applications (ICCIMA'03), Springer Verlag, Wien, New York, (2003) 236–239.

Chapter 166
Binary Kernel in Morphological Associative Memory

Wei-Chen Cheng and Cheng-Yuan Liou

Abstract This work presents a binary implementation of the internal representation kernel in morphological associative memory (MAM) [IEEE International Conference on System, Man, and Cybermetics 4: 3570–3575, 1997]. This kernel was proposed by Ritter *et al*. [IEEE International Conference on System, Man, and Cybermetics 4: 3570–3575, 1997] and further solved by Hattori *et al*. [Proceedings of the 9th International Conference on Neural Information Processing 2:1058–1063, 2002]. Ritter used a trial and error method to search for a suitable kernel Z for MAM and attempted to work out a theoretical way to estimate the kernel. Hattori proposed a fast solution for finding this kernel. This work shows that in binary cases, when solving the kernel, only those bits satisfying certain specific conditions need to be checked. This can speed the checking procedure in large scale data processing.

Keywords Pattern recognition · pattern classification · image algebra · image recognition · morphological associative memory · morphological kernel

Introduction

Ritter applys the lattice-based matrix operation to image processing and transforms the mathematical structures of image algebra to the structures of neural networks [1, 2]. A single layer morphological perceptron [3, 4] has been designed to perform pattern classification tasks. A morphological associative memory (MAM) [5, 6] has been constructed with a similar structure as that of Hopfield model. The MAM employs two weight matrices, W and M, to tolerate two kinds of noisy patterns [5, 6] separately where W can tolerate erosive damaged patterns and M can tolerate dilative damaged patterns. These two matrices are useless in the presence of noisy

C.-Y. Liou
Department of Computer Science and Information Engineering, National Taiwan University, Republic of China, Supported by National Science Council and NTU College of EECS 95R0036-07
e-mail: cyliou@csie.ntu.edu.tw

R. Wang et al. (eds.), *Advances in Cognitive Neurodynamics*,

patterns consisting of mixed erosive and dilative damages. To recover such damages, Ritter *et al*. proposed to develop an internal representation kernel to recall patterns with mixed damages [5]. A kernel pattern is a severe eroded pattern of a stored pattern. In other words, the kernel pattern is a sparse version of the stored pattern. This means that there are a small number of key feature bits saved in the kernel pattern. Since the kernel pattern contains much fewer bits than those stored pattern contains, the kernel pattern suffer little under noise damaging. Ritter defines that a kernel pattern should not mix with any other stored pattern. He further suggests that kernel patterns can not have a common bit. He determines the kernel pattern by randomly flipping bits in a trial-and-error way. Hattori discards the condition that kernel patterns can not have a common bit and constructs an efficient algorithm to resolve the kernel [7, 8].

This paper presents several useful observations. These observations can save the computations to one third of that of Hattori's algorithm. This work reveals insights on the lattice-based memory.

Review MAM

The MAM is based on the algebraic structure $(\mathbb{R}, \vee, \wedge, +)$, where $\vee$ is the binary maximum operation, $\wedge$ is the binary minimum operation, $\mathbb{R}$ denotes real number and $+$ is the addition. p denotes the total number of stored patterns and n denotes the dimension of stored patterns. Matrices are column-based. Each column represents a vector of the stored pattern, $\mathbf{x}^\gamma$. We arrange X to an $n \times p$ matrix. x_i^γ denotes the ith bit of the γ th pattern. x_i^γ is the same as $x_{i\gamma}$. For $A \in \mathbb{R}^{n\times p}$, $B \in \mathbb{R}^{p\times n}$ and $C \in \mathbb{R}^{n\times n}$, the matrix operation of max product, $\boxtriangledown$, and min product, $\boxtriangle$, is defined by

$$\begin{aligned} C = A \boxtriangledown B \Leftrightarrow c_{ij} &= \bigvee_{k=1}^{p} \left(a_{ik} + b_{kj}\right) \quad \text{and} \\ C = A \boxtriangle B \Leftrightarrow c_{ij} &= \bigwedge_{k=1}^{p} \left(a_{ik} + b_{kj}\right) \end{aligned} \tag{166.1}$$

The two weight matrices of MAM, W and M, are defined as

$$W_{XY} = \bigwedge_{\xi=1}^{p} \left(\mathbf{y}^\xi \boxtriangledown \left(-\mathbf{x}^\xi\right)^T\right) \quad \text{and} \quad M_{XY} = \bigvee_{\xi=1}^{p} \left(\mathbf{y}^\xi \boxtriangledown \left(-\mathbf{x}^\xi\right)^T\right). \tag{166.2}$$

where $\mathbf{x}^T$ means the transpose of $\mathbf{x}$ and the suffix XY of W means X is the input matrix and Y is the output matrix.

Mathematical Explanation and Improvement

We now discuss the binary kernel implementation [7, 8]. The kernel method is a two-step process, the first step is to compute the generated internal representation, $M_{ZZ}\boxtriangle X = Z$, and the second is to compute the output of the $\boxtriangledown$-product from the internal representation, $W_{ZX}\boxtriangledown Z$. A competent kernel Z should satisfy that each bit in Z must be less or equal to the corresponding bit in X and

$$X = W_{ZX}\boxtriangledown(M_{ZZ}\boxtriangle X) = \left(X\boxtriangle - Z^T\right)\boxtriangledown\left(\left(Z\boxtriangledown - Z^T\right)\boxtriangle X\right). \tag{166.3}$$

Equation (166.3) can be expanded as

$$\bigvee_{s=1}^{n}\left(\bigwedge_{q=1}^{p}\left(x_{iq} - z_{sq}\right) + \bigwedge_{u=1}^{n}\bigvee_{k=1}^{p} z_{sk} - z_{uk} + x_{u\gamma}\right) = x_{i\gamma}. \tag{166.4}$$

Equation (166.4) has two meanings. One is the recall of the internal representation Z, $Z = M_{ZZ}\boxtriangle X$, and the other is the output of the $\boxtriangledown$-product W_{ZX} with the representation Z. With the assumption that $\{x_{i\gamma} = 0 \text{ and } z_i^{\gamma} = 1\}$ won't happen, when $\{x_{i\gamma} = 1 \text{ and } z_i^{\gamma} = 1\}$, then

$$\begin{aligned}
&\bigwedge_{u=1}^{n}\bigvee_{k=1}^{p} z_{ik} - z_{uk} + x_{u\gamma} = \bigwedge_{u\neq i}\bigvee_{k=1}^{p} z_{ik} - z_{uk} + x_{u\gamma} \\
&= \bigwedge_{u\neq i}\left(\left(z_{i\gamma} - z_{u\gamma} + x_{u\gamma}\right) \vee \bigvee_{k\neq\gamma}\left(z_{ik} - z_{uk} + x_{u\gamma}\right)\right) \\
&= \bigwedge_{u\neq i}\left(\left(1 - z_{u\gamma} + x_{u\gamma}\right) \vee \bigvee_{k\neq\gamma}\left(z_{ik} - z_{uk} + x_{u\gamma}\right)\right) \geq 1.
\end{aligned} \tag{166.5}$$

Therefore the result of the ith bit of pattern γ is always 1. For another case $x_{i\gamma} = 0,\ z_i^{\gamma} = 0$, the calculation result is always 0 by the same derivation. We have derived equations for correct recall of Z, and the next step is to derive equations of correctly recalling X from Z. Start from $W_{ZX}\boxtriangledown Z = X$. If $x_{i\gamma} = 0$ and $z_{i\gamma} = 0$, then we have

$$\begin{aligned}
&\bigvee_{s=1}^{n}\bigwedge_{q=1}^{p} x_{iq} - z_{sq} + z_{s\gamma} \\
&= \left(0 \wedge \bigwedge_{q\neq\gamma}\left(x_{iq} - z_{iq} + 0\right)\right) \vee \bigvee_{s\neq i}\left(0 \wedge \bigwedge_{q\neq\gamma}\left(x_{iq} - z_{sq} + z_{s\gamma}\right)\right) = 0.
\end{aligned} \tag{166.6}$$

Therefore the calculation result is always correct. From the same derivation, the calculation result of $x_{i\gamma} = 1$, $z_{i\gamma} = 1$ is also guaranteed to be correct. Based on this, some computations can be saved. In calculating the first step process of MAM, $M_{ZZ}\boxtimes X = Z'$, $z'_{i\gamma}$ needs to be calculated only when $x_{i\gamma} = 1$ and $z_{i\gamma} = 0$. Z' means the result of first step process of MAM. For other cases, $z'_{i\gamma} = z_{i\gamma}$ is automatically satisfied. Note that when the elements in Z' are not totally equal to those in Z, we show how to check $W_{ZX}\boxtimes Z' = X$ to save computations.

$$x_{i\gamma} = \bigvee_{s=1}^{n}\left(\bigwedge_{q=1}^{p} x_{iq} - z_{sq} + z'_{s\gamma}\right) = \bigvee_{s=1}^{n}\left(\left(x_{i\gamma} - z_{s\gamma} + z'_{s\gamma}\right) \wedge \bigwedge_{q\neq\gamma}\left(x_{iq} - z_{sq} + z'_{s\gamma}\right)\right)$$
$$= \left(\left(x_{i\gamma} - z_{i\gamma} + z'_{i\gamma}\right) \wedge \bigwedge_{q\neq\gamma}\left(x_{iq} - z_{iq} + z'_{i\gamma}\right)\right)$$
$$\vee \bigvee_{s\neq i}\left(\left(x_{i\gamma} - z_{s\gamma} + z'_{s\gamma}\right) \wedge \bigwedge_{q\neq\gamma}\left(x_{iq} - z_{sq} + z'_{s\gamma}\right)\right). \tag{166.7}$$

For $x_{i\gamma} = 1$ and $z'_{i\gamma} = 1$, the term $\left(x_{i\gamma} - z_{i\gamma} + z'_{i\gamma}\right) \wedge \bigwedge_{q\neq\gamma}\left(x_{iq} - z_{iq} + z'_{i\gamma}\right)$ equals $\left(1 - z_{i\gamma} + 1\right) \wedge \bigwedge_{q\neq\gamma}\left(x_{iq} - z_{iq} + 1\right)$. It is rare that this term will have a value equal to 2. Also, it is rare that the term in (166.7), $\left(x_{i\gamma} - z_{s\gamma} + z'_{s\gamma}\right) \wedge \bigwedge_{q\neq\gamma}\left(x_{iq} - z_{sq} + z'_{s\gamma}\right)$, will have a value equal to 2. We need to check whether $W_{ZX}\boxtimes Z'$ equals X only when $z'_{i\gamma} = 0$. We compute and compare the ratio of omitted calculations in the two cases $\{M_{ZZ}\boxtimes X = Z',\ W_{ZX}\boxtimes Z' = X\}$ and $\{M_{ZZ}\boxtimes X = Z',\ W_{ZX}\boxtimes Z' = X\}$. In Fig. 166.1, the solid line net shows the ratio of omitted calculations in case $\{M_{ZZ}\boxtimes X = Z',\ W_{ZX}\boxtimes Z' = X\}$. The dotted line net shows the ratio of omitted calculations in case $\{M_{ZZ}\boxtimes X = Z',\ W_{ZX}\boxtimes Z' = X\}$.

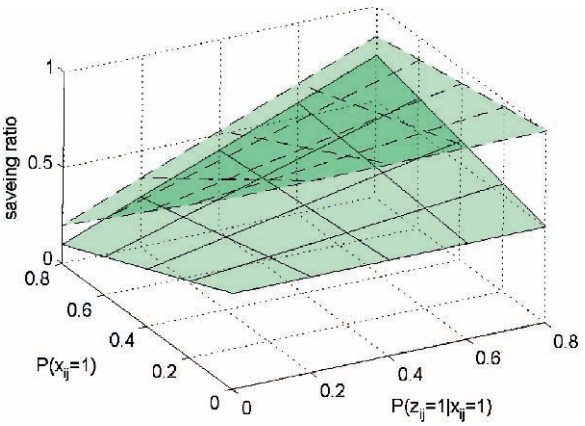

Fig. 166.1 The 25 saving ratios. $P\left(x_{ij} = 1\right)$ denotes the probability of a bit in X to be one. $P\left(z_{ij} = 1 | x_{ij} = 1\right)$ means the conditional probability that given $x_{ij} = 1$ the probability of $z_{ij} = 1$. The parameters $n = 300$, $p = 500$

Table 166.1 Learning time(secs) comparison between [8] and current method

	$n = 50$	$n = 75$	$n = 100$	$n = 125$	$n = 150$
Hattori [8]	23.67	71.09	178.71	301.28	186.76
Proposed method	7.83	22.28	52.68	40.88	58.18

$p = 75, \#times = 10, P\left(x_{ij} = 1\right) = 0.6.$

We applied this computation improvement to Hattori's algorithm [7]. In Table 166.1, $\#times$ denotes the total number of times the experiment has been run. The results are averaged by the number of experiments, $\#times$. From Table. 166.1, it shows that the speed of the proposed method is triple of that of the method in [8].

Summary

We find that when calculating $M_{ZZ}\boxtriangle X$, only those bits that $x_i^\gamma = 1$ and $z_i^\gamma = 0$ need to be checked. The rest are set to z_i^γ. The mathematical expression is

$$\left(M_{ZZ}\boxtriangle \mathbf{x}^\gamma\right)_i = \begin{cases} \bigwedge_{u\neq i} \bigvee_{k=1}^{p} z_{ik} - z_{uk} + x_{u\gamma} & \text{if } x_i^\gamma = 1 \text{ and } z_i^\gamma = 0 \\ z_i^\gamma & \text{otherwise} \end{cases}.$$

We also show that when calculating $W_{ZX}\boxtriangledown Z'$ (where $Z' = M_{ZZ}\boxtriangle X$), we only calculate those bits which satisfy $z_i^\gamma = 0$. The mathematical expression is

$$\left(W_{ZX}\boxtriangledown \mathbf{z}'^\gamma\right)_i = \begin{cases} \bigvee_{s=1}^{n} \bigwedge_{q=1}^{p} x_{iq} - z_{sq} + z'_{s\gamma} & \text{if } z_i'^\gamma = 0 \\ x_i^\gamma & \text{otherwise} \end{cases}.$$

We exploited the detailed relations between stored patterns and kernel patterns, and did experiments to show that these details can save the computations to one third of Hattori's algorithm. This can benefit the application of MAM in large scale data processing.

References

1. Davidson, J.L., Ritter, G.X.: Theory of morphological neural networks. Proceedings of SPIE–the International Society for Optical Engineering **1215** (1990) 378–388.
2. Ritter, G.X., Li, D., Wilson, J. N.: Image algebra and its relationship to neural networks. Technical Symposium Southeast on Optics, Electro-optics, and Sensors, Proceedings of SPIE, Orlando **1098** (1989) 90.
3. Ritter, G.X., Sussner, P.: An Introduction to Morphological Neural Networks. Proceedings of 13th International Conference on Pattern Recognition (ICPR'96) **4** (1996) 709–717.
4. Ritter, G.X., Iancu, L., Urcid, G.: Morphological perceptrons with dendritic structure. The 12th IEEE International Conference on Fuzzy Systems **2** (2003) 1296–1301.
5. Ritter, G.X., Sussner, P.: Associative memories based on lattice algebra. IEEE International Conference on Systems, Man, and Cybernetics **4** (1997) 3570–3575.

6. Ritter, G.X., Sussner, P., Diza-de-Leon, J.L.: Morphological associative memories. IEEE Transactions on Neural Networks **9** (1998) 281–293.
7. Hattori, M., Fukui, A., Ito, H.: A fast method of constructing kernel patterns for morphological associative memory. Proceedings of the 9th International Conference on Neural Information Processing **2** (2002) 1058–1063.
8. Hattori, M., Hashiguchi., H.: Improvement of Noise Reduction Effect for Morphological Associative Memories. Proceedings of the 12th International Conference on Neural Information Processing (2005) 400–403.

Chapter 167
Intrusion Detection Classifier Based on Dynamic SOM and Swarm Intelligence Clustering

Yong Feng, Jiang Zhong, Zhong-yang Xiong, Chun-xiao Ye and Kai-gui Wu

Abstract A clustering analysis model based on dynamic self-organizing maps (DSOM) and swarm intelligence (SI) is systematically proposed for intrusion detection system. The basic idea of the model is to produce the cluster by DSOM and SI. With the classified data instances, the detection classifier can be established. And then the detection classifier can be used in real intrusion detection. Experimental results show that our detection classifier maintained a higher performance than SVM, LGP, DT and K-NN.

Keywords Intrusion detection · classifier · dsom · swarm intelligence · clustering

Introduction

Precisely on the context of adopting complex adaptive systems into ID systems [1, 2, 3]. The present work introduces a clustering model based on DSOM and swarm intelligence to detect intrusions and compares its performance with Linear Genetic Programming (LGP), Support Vector Machines (SVM), K-NN and Decision Trees (DT).

The rest of the paper is organized as follows. Section 'Clustering Model Based on DSOM and SI' presents our clustering model based on DSOM and swarm intelligence. Establishment of the detection classifier is reported in section 'Establishing Detection Classifier'. Experiment results are presented in Section 'Experiment' and some conclusions are also provided towards the end.

Clustering Model Based on DSOM and SI

The DSOM is initialized with four nodes [4]. The weight values of the nodes are self-organized according to a similar method as the SOM.

Y. Feng
College of Computer Science, Chongqing University, Chongqing 400030, China
e-mail: fengyong@cqu.edu.cn

R. Wang et al. (eds.), *Advances in Cognitive Neurodynamics*,

Definition 1. *E is the error distance between b and v, E is defined as:* $E = \sum_{j=1}^{d} (v_j - w_{b,j})^2$, *where d is dimension of the vector v.*

Definition 2. *GT is the growth threshold of DSOM. For the node i to grow a new node, it is required that* $E \geq GT$. *It can be deduced from E,* $0 \leq v_j, w_{b,j} \leq 1$ *and* $0 \leq E \leq d$ *that* $0 \leq GT < d$. *The spread factor SF can be used to control and calculate the GT for DSOM. The GT can be defined as:* $GT = d \times f(SF)$, *where* $SF \in R, 0 \leq SF \leq 1$, *and f (SF) is a function of SF.*

Definition 3. *f (SF) is defined as:* $f(SF) = Sigmoid_{n(t)}(1 - SF) = \frac{1-e^{-n(t)*(1-SF)}}{1+e^{-n(t)*(1-SF)}}$, *where n(t) is the total number of nodes at* t^{th} *iteration. f (SF) gradually saturated with the increase of network training that GT is stable, and DSOM algorithm is reaching convergence.*

SI clustering has two main phases. First, each ant chooses the object at random, and picks up or moves or drops down the object according to picking-up or dropping probability in the output layer of DSOM. Second, clusters are collected from the output layer of DSOM. The details of SI clustering algorithm could be found in our previous work [5].

Establishing Detection Classifier

The maximum quantitative difference D_i and the labeling clusters threshold N are defined to label the clusters. The D_i and N can be defined as: $D_i = (Q_i - Q_{min})^2/(Q_{max} - Q_{min})^2$, $N = SF/(1 + 1/S)$, where $0 \leq D_i \leq 1, 0 < N < 1$. Q_i is the number of instances in C_i, $1 \leq i \leq S$. Q_{max} is the maximum of $\{Q_i\}$. Q_{min} is the minimum of $\{Q_i\}$. S is the number of the clusters. If $D_i > N$, then C_i is labeled as the 'normal' cluster, or C_i is labeled as the 'anomalous' cluster.

Accuracy of DSOM and SI clustering is depend on SF and α to some extent. In order to obtain precision intrusion detection, we need to determine stable SF and α. DSOM and SI-based detection classifier can help us to balance the contradiction between the clustering results and the apriori knowledge, and stable value of SF and α can also be determined by it. Figure 167.1 shows the DSOM and SI-based detection classifier, where $d(O_i, x)$is Euclidean distance between x and $\{O_1, O_2, \ldots, O_S\}$.

Experiment

The data for our experiments was prepared by the 1998 DARPA intrusion detection evaluation program by MIT Lincoln Labs [6]. The dataset has 41 attributes or features for each connection record plus one class label. Our experiments had two conventional phases namely training phase and testing phase.

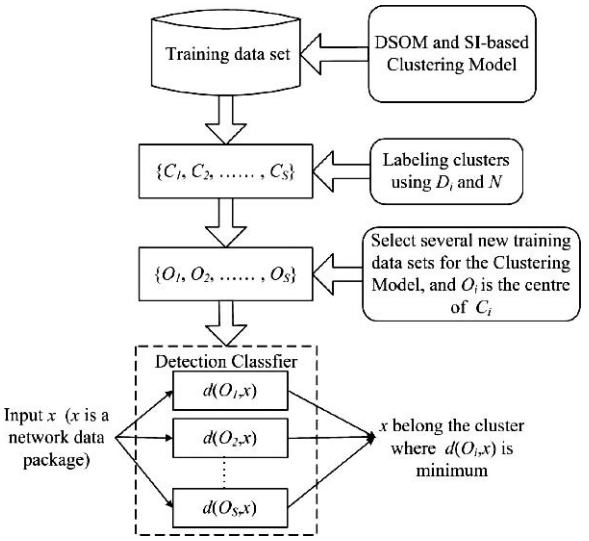

Fig. 167.1 DSOM and SI-based detection classifier principles

Training Phase

According to the first assumption of the unsupervised intrusion detection algorithms (UADA), we need to generate the training data set D from DARPA reduced data sets by filtering it for attacks. D consisted of 1–1.5% intrusion instances and 98.5–99% normal instances. To evaluate the algorithm we are interested in three major indicators of performance: DR (Detection Rate), FPR (False Positive Rate) and FNR (False Negative Rate). In the training phase, we adopt four training data sets from D: DS1, DS2, DS3 and DS4. Each data set contains 1000 instances, we adjust SF from 0.3 to 0.8 (interval is 0.1) and α from 0.85 to 0.2 (interval is 0.05). The other parameters are set as follows: $ant-number = 10, r = 12, k = 10, n = 60 \times 1000$. The training experiment results are reported in Figs. 167.2–167.5.

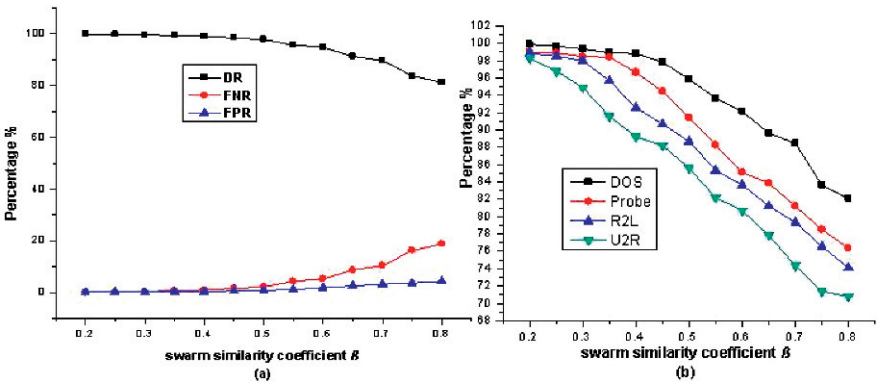

Fig. 167.2 Training results on DS1

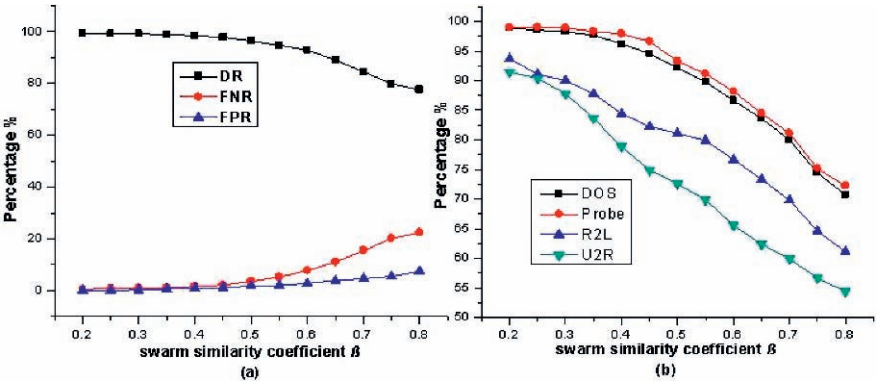

Fig. 167.3 Training results on DS2

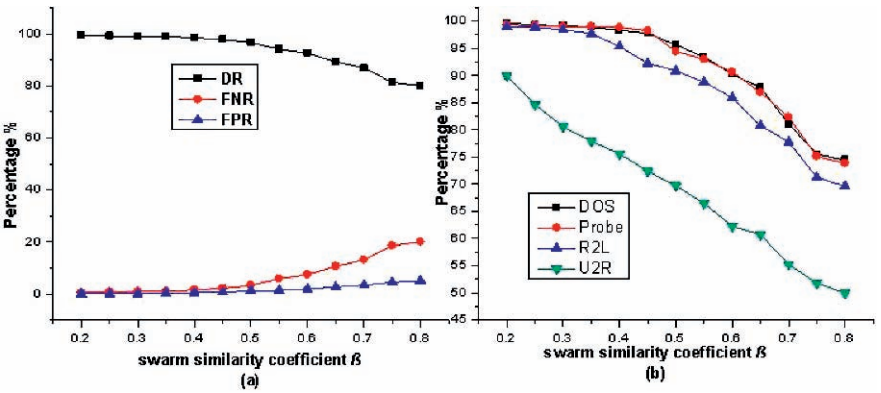

Fig. 167.4 Training results on DS3

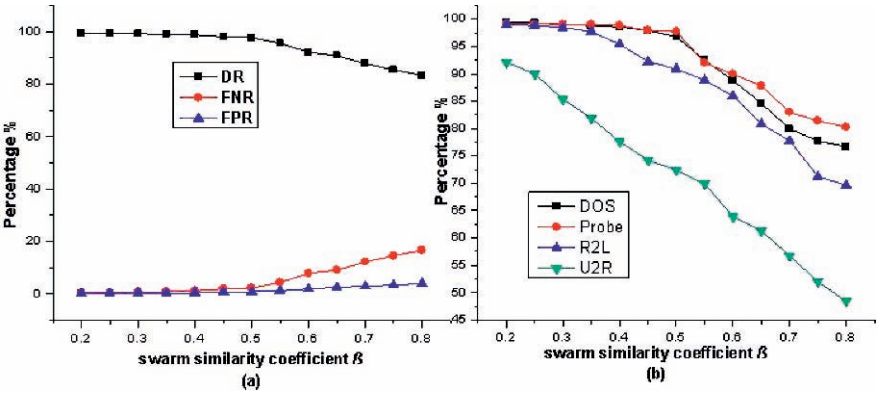

Fig. 167.5 Training results on DS4

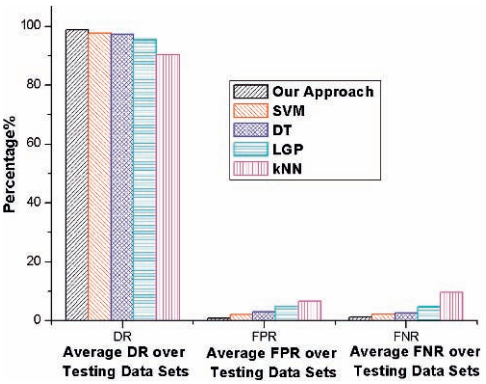

Fig. 167.6 Average performance comparing

We can decide the best value of SF is 0.7 and α is 0.25 by the training experiment results.

Testing Phase

The classifier is produced by the training experiment. In testing experiment, we use always the full training data sets (5000 training samples) plus only a part of new data sets (1000 samples each time). That is, we made five testing data sets with 5000 training samples and 1000 new samples for our testing experiment, we set $SF = 0.7$ and $\alpha = 0.25$, the other parameters are same as the training experiment. The average performance comparing between our classifier and the other detection classifiers over the five same testing data sets is presented in Fig. 167.6.

Conclusions

Our detection classifier overcomes the contradiction between the clustering results and the apriori knowledge to some extent, and the accuracy and the efficiency are improved. Experimental results show that our approach maintained a higher performance than SVM, LGP, DT and K-NN.

Acknowledgements This work is supported by the Graduate Student Innovation Foundation of Chongqing University of China (Grant No. 200506Y1A0230130).

References

1. N. Foukia, S. Hassas, S. Fene: An Intrusion Response Scheme: Tracking the Source Using the Stigmergy Paradigm. In Proc. of Security of Mobile Multi-agent Systems Workshop (SEMAS-2002), Bologna, Italy (2002) 18–26.

2. V. Ramos, J. J. Merelo: Self-Organized Stigmergic Document Maps: Environment as a Mechanism for Context Learning. In Procs. of AEB'02 – 1st Spanish Conf. on Evolutionary and Bio-Inspired Algorithms, Merida Univ., Spain (2002) 284–293.
3. N. Foukia, S. Hassas, S. Fenet: Combining Immune Systems and Social Insect Metaphors: A Paradigm for Distributed Intrusion Detection and Response System. In Proc. of Mobile Agents for Telecommunication Applications, Marrakech, Morocco (2003) 251–264.
4. Y. Feng, J. Zhong, Z. Y. Xiong, C. X. Ye, K. G. Wu: Network Anomaly Detection Based on DSOM and ACO Clustering. Lecture Notes in Computer Science, LNCS 4492, Part 2 (2007) 947–955.
5. Y. Feng, Z. F. Wu, K. G. Wu: An unsupervised anomaly intrusion detection algorithm based on swarm intelligence. 2005 International Conference on Machine Learning and Cybernetics, ICMLC 2005, Chongqing (2005) 3965–3969.
6. MIT Lincoln Laboratory: http://www.ll.mit.edu/IST/ (1998).

Chapter 168
New Evolutionary Algorithm to Solve Dynamic Constrained Optimization

Chun-An Liu and Yuping Wang

Abstract In this paper, a new multiobjective evolutionary algorithm for dynamic nonlinear constrained optimization problems (DNCOPs) is proposed. First, the time period is divided into several equal subperiods. In each subperiod, the DNCOPs is approximated by a static nonlinear constrained optimization problem (SNCOPs). Second, for the SNCOPs, inspired from the ideal of multiobjective optimization, it is transformed into a static bi-objective optimization problem. Third, a new multi-objective evolutionary algorithm (DMEA) for DNCOPs is proposed and the simulation results indicate the proposed algorithm is effectiveness for dynamic nonlinear constrained optimization problems.

Introduction

Many real-world problems naturally fall within the purview of optimization problems, in which the objective functions are not only decided by the decision variables but also varies with the time (or termed as environment). Thus, the optimal solutions also varies with the environment changing. This kind of optimization problem is called dynamic optimization problems (DOPs) [1]. DOPs include dynamic simple-objective optimization problems (DSOPs) and dynamic multi-objective optimization problems (DMOPs) [2, 3, 4, 5]. When DSOPs is considered, several studies for dynamic nonlinear unconstrained optimization problems (DNUCOPs) are available in the literature [1, 2, 3]. However, when dynamic nonlinear constrained optimization problems (DNCOPs) is concerned, very few studies are available in the literature. In this paper, we divide the time period of DNCOPs into several smallest equal subperiods. In each subperiod, the DNCOPs is approximated by a static bi-objective optimization problem, one objective is the original objective of DNCOPs, and the

C.-A. Liu
Department of Mathematics, Baoji University of Arts and Sciences Baoji, Shaanxi, 721013, People's Republic of China
e-mail: liu2006@126.com

R. Wang et al. (eds.), *Advances in Cognitive Neurodynamics*,

other is the degree violation of constraints on the fixed time (environment). Thus, the DNCOPs is approximately transformed into several static bi-objective optimization problems defined in different subperiods and a new multiobjective evolutionary for DNCOPs is also proposed. The numerical experiments verified the feasibility and effectiveness of the algorithm.

Transformation of DNCOPs

Considering the DNCOPs as follows:

$$\begin{cases} \min\limits_{x\in\Omega(t)\subset[L,U]_t} & f(x,t) \\ s.t. & g_i(x,t)\le 0 i=1\sim m \end{cases} \tag{168.1}$$

Where $t \in [a,b] \subset R$, $x = (x_1, x_2, \cdots, x_n)$ is n dimension decision vector, $g_i(x,t)(i = 1,2,\cdots,m)$ are constraint conditions depending on time variable t $\Omega(t) = \{x|g_i(x,t) \le 0, i = 1,2,\cdots,m\}$ is called feasible region and $[L,U]_t = \{x = (x_1, x_2, \cdots, x_n)|l_i(t) \le x_i \le u_i(t), i = 1,2,\cdots,n\}$ is called search space.

Continuous Time Variable Discretization

For the DNCOPs (1), we chose several points $a = t_0 < t_1 < t_2 < \cdots < t_{n-1} < t_n = b$ and insert those points into the time period $[a,b]$. Thus, the time period $[a,b]$ is divided into n equal disintersection subperiods $[t_{i-1}, t_i], i = 1,2,\cdots,n$. Might as well denote $[a,b] = \biguplus_{i=1}^{n}[t_{i-1}, t_i]$ and $\forall i$, $[t_{i-1}, t_i]\bigcap[t_i, t_{i+1}] = \emptyset$. For $\Delta t_i = t_i - t_{i-1}(i = 1,2,\cdots,n)$, when $\Delta t_i \to 0$, we approximately regard the dynamic nonlinear constrained optimization problem defined on each subperiod as a static nonlinear constrained optimization problem defined on fixed instant(environment) ξ_i. When the number of points inserted into the time period $[a,b]$ increased infinitely, the optimal solutions of the problem (168.1) can be approximately regard those optimal solutions superimposition of several static nonlinear constrained optimization problems defined on those different fixed environments ξ_i.

New Model of DNCOPs

Giving a division of time period $[a,b]$ according to 2.1, for fixed environment t, defined functions

$$f_1(x,t) = f(x,t) \tag{168.2}$$

and

$$f_2(x,t) = \max\{0, g_i(x,t)\}, i = 1, 2, \cdots, m \tag{168.3}$$

Obviously, for $\forall x \in [L,U]_t$, we have $f_2(x,t) > 0$ and $f_2(x,t) = 0$ if and only if $\forall x \in \Omega(t)$. Thus $f_2(x,t)$ attains the minimum value at x if and only if $x \in \Omega(t)$. Therefore, in the fixed environment t, problem (168.1) can be transformed into the following several two objective optimization problem (168.4):

$$f(x,t) = \min(f_1(x,t), f_2(x,t)) \tag{168.4}$$

It is obvious that, in the fixed environment t, to minimize $f_1(x,t)$ means searching optimal solution for problem (168.1), and optimize $f_2(x,t)$ means searching for the feasible solution for problem (168.1). Thus simultaneously optimizing both $f_1(x,t)$ and $f_2(x,t)$ means looking for not only a feasible solution for problem (168.1), but also a solution minimize the objective function of problem (168.1), i.e., an optimal solution of problem (168.1) in the fixed environment t. Therefore, when the problem (168.1) changed from one environment to another new environment, the optimal solution obtained in different fixed environment can be approximately regard as the optimal solutions of problem (168.1).

New Multiobjective Evolutionary Algorithm

1. Divide the time period $[a,b]$ of problem (168.1) into several smallest equal subperiods according to 2.1. Suppose that different environment $t_0, t_1, \cdots, t_s$ are obtained, let $i = 0$.
2. For environment t_i, generate initial population $p^0(t_i)$in $[L,U]_t$ and let the number of generation $k = 0$.
3. Select a pair of parents $x_i^k(t_i), x_j^k(t_i)$ from $p^k(t_i)$, adopt the arithmetic crossover operator to generate two offsprings. All the offsprings are kept in the set $c^k(t_i)$.
4. Select a parent from $c^k(t_i)$ and utilize the mutation operator [3] to generate an offspring. The set of all these offsprings is denoted as $\bar{p}^k(t_i)$.
5. Select the next population $p^{k+1}(t_i)$ among $p^k(t_i) \bigcup c^k(t_i) \bigcup p^k(t_i)$ by selection operator [6].
6. If $k = K$, go to step 7; otherwise, go to step 3.
7. If $i = s$, stop, otherwise, let $i = i + 1$, go to step 2.

Simulation Results

Test Problems

To evaluate the efficiency of DMEA, we choose two dynamic nonlinear constrained optimization functions. $G1$ is borrowed from [5]. $G2$ is structured by ourselves utilizing the nonlinear constrained test problem appeared in [7].

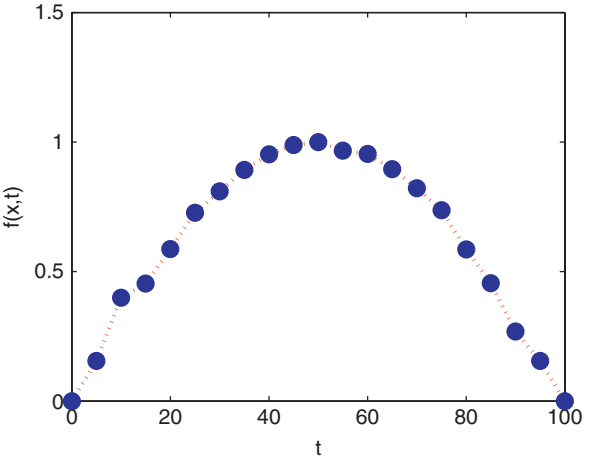

Fig. 168.1 The optimal solutions obtained by DMEA in different environment for $G1$

$$G1 : \min f(x,t) = (1 - 0.01t)\sum_{i=1}^{n} x_i^2 + 0.01t\sum_{i=1}^{n}(x_i - 2)^2, s.t : -2 \le x_1, x_2 \le 2; 0 \le t \le 100; n = 2.$$

$$G2 : \begin{cases} \min f(x,t) = t(x_1 - 10)^2 + (1-t)(x_2 - 20)^2, s.t : \\ g_1(x,t) = (1 - 0.2t)(x_1 - 5)^2 + 0.2t(x_2 - 5)^2 - 100 \ge 0 \\ g_2(x,t) = 0.2t(x_1 - 6)^2 + (1 - 0.2t)(x_2 - 5)^2 - 82.81 \le 0 \\ 13 \le x_1 \le 100; 0 \le x_2 \le 100; t \in [0, 1]. \end{cases}$$

In the simulations, the population size $N = 200$, crossover probability $p_c = 0.9$, mutation probability $p_m = 0.05$, $K = 1000$. For $G1 \sim G2$, we divide the time period into several equal subperiods(seeing in Fig. 171.1 and Fig. 171.2).

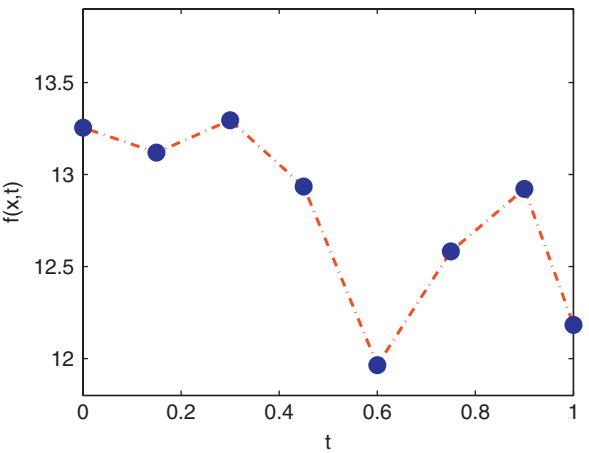

Fig. 168.2 The optimal solutions obtained by DMEA in different environment for $G2$

In Figs. 171.1 and 171.2, the optimal solutions achieved by DMEA for $G1$ and $G2$ under different fixed environment are visualized. From these two figures, it obviously that the DMEA can find the optimal solutions of DNCOPs in the changing environment.

Acknowledgements This work was jointly supported by the Natural nature Science Foundation of China (60374063), the Natural Science Foundation of Shaanxi Province (2006A12), the Science and Technology Research Project of the Educational Department of Shaanxi Province of China (No.07JK180) and the Emphasis Research Plan Project of Baoji University of Arts and Sciences (No.ZK0619).

References

1. C. Ronnewinkel, C. O. Wilke, T. Martinetz. Genetic algorithms in time-dependent environments[C]. In Theoretical Aspects of Evolutionary Computing, L. Kallel, B. Naudts, and A. Rogers, Eds. Berlin, Germany: Springer-Verlag, 2000 263–288.
2. T. Blankwell, J. Brank. Multi-swarm optimization in dynamic environments[C]. In Proceedings of Applications of Ecolutionary Computing, Volume 3005 of Lecture Notes in Computer Science, T. Blackwell, M. Zhang, A. M. Tyrrell, and L. Ballerini, Eds. Coimbra, Portugal: Springer-Verlag, 2004 489–500.
3. K. E. Parsopoulos, M. N. Vrahatis. Unified Particle Swarm Optimization in Dynamic Environments[C]. In Proceedings Evo Workshops 2005, LNCS3449, F. Rothlauf et al. Eds. Berlin, Germany: Springer-Verlag, 2005, 590–599.
4. M. Farina, K. Deb, P. Amato. Dynamic Multiobjective Optimization Problems: Test Cases, Approximations, and Applications[J]. IEEE Transactions on Evolutionary Computation, 2004, 8, 425–442.
5. Y. Jin, B. Sendhoff. constructing dynamic optimization test problems using the multiobjective optimization concept[C]. In Proceedings Evo Workshops 2004, LNCS3005, G. R. Raidl et al. Eds. Berlin, Germany: Springer-Verlag, 2004 525–536.
6. G. G. Yen, H. Lu. Dynamic Multi-objective evolutionary algorithm: adaptive cell-based rank and density estimation[J]. IEEE Transactions on Evolutionary Computation, 2003, l7, 253–274.
7. Carlos A, Coello. Coello. Treating constrains as objective for single-objective evolutionary optimization[J]. Engineering Optimization, 2000, 32, 275–308.

Chapter 169
Effects of 3D Co-Occurrence Features on Terrain Classification

Dong-Min Woo, Dong-Chul Park, Quoc-Dat Nguyen, Young-Soo Song and Quang-Dung Nguyen Tran

Abstract This paper suggests 3D co-occurrence texture features by extending the concept of co-occurrence feature to the 3D world. The suggested 3D features are described as a 3D co-occurrence matrix by using a co-occurrence histogram of digital elevations at two contiguous positions. With the addition of 3D co-occurrence features, we encounter the high dimensionality problem in the classification process. In this context, FCM (Fuzzy C-mean) clustering algorithm is employed to implement the terrain classifier, since this ANN (Artificial Neural Networks) clustering algorithms is known as robust in this particular situation. Experimental results show that the classification accuracy with the addition of 3D co-occurrence features is significantly improved over the conventional classification method only with 2D features.

Keywords Texture · terrain · co-occurrence · clustering · 3D feature

Introduction

The selection of features is very important in terrain classification. 2D texture features [1, 2, 3] are conventionally utilized in this application. Among the various 2D texture features, co-occurrence feature has been reported to be the most effective for terrain classification [4].

3D texture introduced by Dana et al. [5] and Wang et al. [6] considers the physical characteristics of an object surface in the real world. The addition of 3D texture features can thus improve the accuracy of terrain classification. However, these early 3D features do not directly reflect 3D texture from the physical appearance of the surface. In this paper, we propose a new 3D co-occurrence feature, which directly and systematically defines 3D texture from a DEM (Digital Elevation Map).

A quantization scheme such as histogram equalization with several levels can preserve texture information in 2D image. In a DEM, however, the dynamic range of

D.-M. Woo
Department of Information Engineering, Myong Ji University, Gyeonggido, Korea 449-728
e-mail: dmwoo@mju.ac.kr

R. Wang et al. (eds.), *Advances in Cognitive Neurodynamics*,

elevation change is so wide that it is not possible to obtain texture information from the elevation quantized in a general way. In the present paper, in order to preserve the texture information of quantized elevation, we employ a local quantization scheme. Since quantization is carried out locally, we can obtain the texture information with only a few quantization levels. To resolve high dimensionality problem, FCM is employed for the implementation of the terrain classifier.

ANN Clustering Algorithms

FCM Algorithm

The objective of clustering algorithms is to group of similar objects and separate dissimilar ones. For FCM, the objective function is defined as:

$$J_m(U, v) = \sum_{k=1}^{n} \sum_{i=1}^{c} (\mu_{ki})^m (d_i(x_k))^2 \tag{169.1}$$

where $d_i(x_k)$ denotes the distance from the input data x_k to v_i, the center of the cluster i, μ_{ki} is the membership value of the data to the cluster i, and m is the weighting exponent, $m \in 1, \cdots, \infty$ while n and c are the number of input data and clusters, respectively.

Bezdek defined a condition for minimizing the objective function with the following two equations [7]:

$$\mu_{ki} = \frac{1}{\sum_{j=1}^{c} \left(\frac{d_i(x_k)}{d_j(x_k)} \right)^{\frac{2}{m-1}}} \tag{169.2}$$

$$v_i = \frac{\sum_{k=1}^{n} (\mu_{ki})^m x_k}{\sum_{k=1}^{n} (\mu_{ki})^m} \tag{169.3}$$

Experimental Results

The experimental environment was set up so as to classify aerial image data into 4 classes: foliage, grass-covered ground, bare ground, and shadow. Four feature sets are used for the experiments. Feature set A includes only 2D co-occurrence features, and feature set B includes image intensity and 2D co-occurrence features. Feature sets C and D are produced by the addition of 3D co-occurrence features to feature sets A and B, respectively.

The ground truth is shown in Fig. 169.1a, where the white area represents bare ground such as roads, the light gray area is for foliage, the dark gray area is

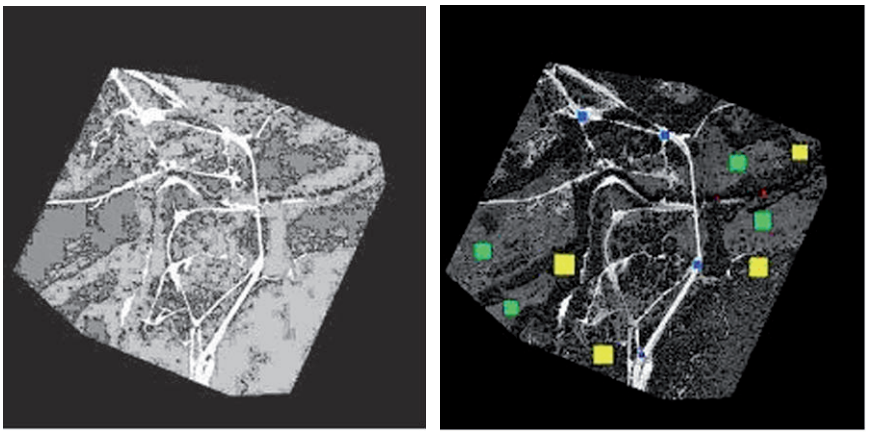

(a) Ground truth (b) Training data

Fig. 169.1 Ground truth of experimental terrain and its training data

for grass-covered ground, and the black area represents shadows. We randomly selected the training area, which is 1% of each class, shown in small windows as in Fig. 169.1b.

To calculate 3D co-occurrence features, first the 3D co-occurrence matrix is established by carrying out local quantization with eight quantization levels, which yields an 8×8 3D co-occurrence matrix. Since we use three types of co-occurrence features – ASM, CON, ENT – for four angular directions, 12 3D co-occurrence features are calculated.

For 2D co-occurrence features, an ortho-image with eight gray levels is needed to construct an 8×8 2D co-occurrence matrix. Histogram equalization was carried out to obtain this image. Figure 169.2 show ASM, CON and ENT features with $\theta = 0^o$ in gray scale for 2D co-occurrence and 3D co-occurrence. To carry out the classification experiments based on feature sets A, B, C and D, we implemented four ANN-based classifiers. Table 169.1 presents the classification results using FCM where the bold number indicates the number of correctly classified pixels for each class.

In comparison with feature set A, feature set D with the addition of 3D co-occurrence features improves the classification accuracy. In particular, the classification of road and foliage is significantly improved. This is due to the use of the physical surface characteristics of the real world, thus indicating that the suggested 3D co-occurrence features can be utilized very efficiently in terrain classification applications.

Figure 169.3a shows the classification result 2D co-occurrence features (feature set A), and Fig. 169.3b shows the classification result using pixel intensity, 2D co-occurrence features and 3D co-occurrence features (feature set D). In comparison with the ground truth as in Fig. 169.1, we find that the addition of 3D co-occurrence features improves overall classification accuracy.

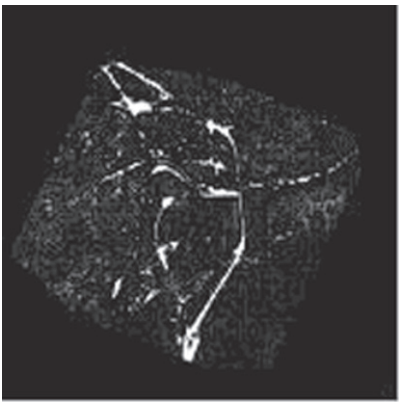

(a) 2D ASM

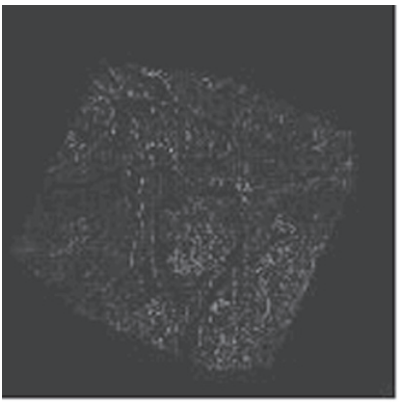

(b) 2D CON

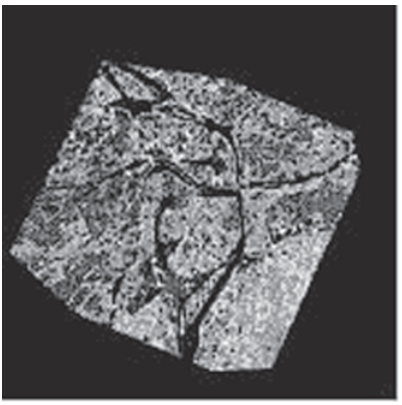

(c) 2D ENT

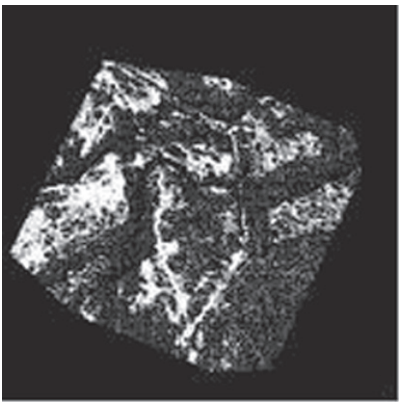

(d) 3D ASM

(e) 3D CON

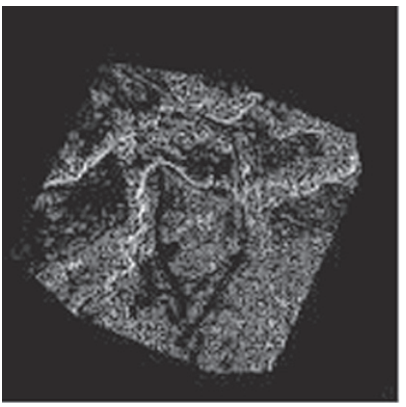

(e) 3D ENT

Fig. 169.2 2D and 3D co-occurrence features

Table 169.1 Classification result using FCM. (unit: 1,000 pixels)

Ground truth	Feature Set A				Feature Set D			
	Shadow	Grass	Foliage	Road	Shadow	Grass	Foliage	Road
shadow (41.8)	**8.243**	7.019	2.14	26.336	**37.246**	1.892	57.688	0.058
grass (683.0)	23.224	**346.326**	164.73	61.816	0.151	**543.534**	65.705	30.394
foliage (1018.6)	4.276	324.38	**851.15**	25.969	.42	123.374	**888.129**	5.873
road (193.4)	6.074	5.281	0.543	**79.282**	0	14.206	7.041	**157.078**
total (1936.8)	41.817	683.006	1018.563	193.403	41.817	683.006	1018.563	193.403
	Correctly classified: 1285.001 (66.35%)				Correctly classified: 1625.987 (83.95%)			

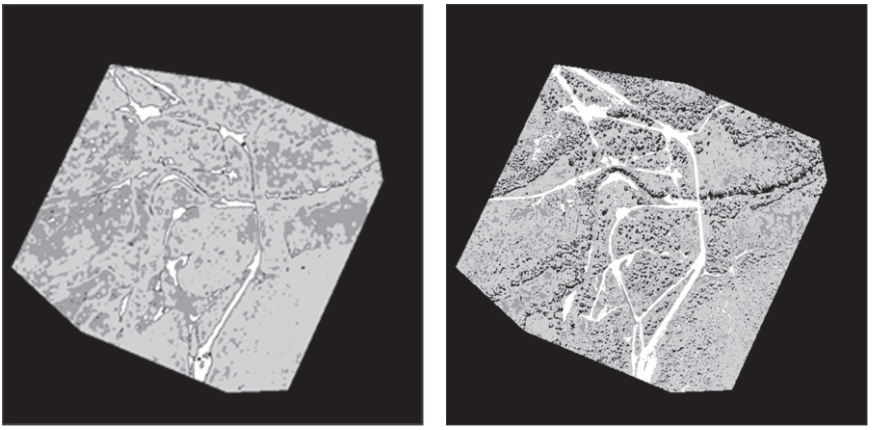

(a) Feature set A (b) Feature set D

Fig. 169.3 Classification results using FCM

Conclusions

In this paper we have proposed the use of 3D co-occurrence features, which can effectively reflect physical surface characteristics in the real world in a direct fashion, for the purpose of terrain classification. Experimental results show that the addition of 3D co-occurrence features significantly improves classification accuracy. However, since classified ground truth is relatively scarce, experiments were carried on a single aerial image set. In this context, extensive experiments involving various sites with classified ground truths, in conjunction with intensive analyses of the effects of 3D co-occurrence features should be carried out in future work.

References

1. Tamura, H., Mori, S., Yamawaki, T.: Textural features corresponding to visual perception. IEEE Transactions on Systems, Man, and Cybernetics, Vol. 8 (1978) 460–473.
2. Haralick, R., Shanmugam, K., Dinstein, I.: Texture features for image classification. IEEE Transactions on Systems, Man, and Cybernetics, Vol. 3 (1973) 610–621.
3. Dubes, R., Jain, A.: Random field models in image analysis. Journal of Applied Statistics, Vol. 16 (1989) 131–164.
4. Ohanian, P., Dubes, R.: Performance evaluation for four classes of textural features. Pattern Recognition, Vol. 25 (1992) 819–833.
5. Dana, K., Nayar, S., Van Ginneken, B., Koenderink, J.: Reflectance and texture of real-world surfaces. IEEE Computer Society Conference on Computer Vision and Pattern Recognition, (1997) 151–157.
6. Wang, X., Stolle, F., Schultz, H., Riseman, E., Hanson, A.: Using three-dimensional features to improve terrain classification. IEEE Computer Society Conference on Computer Vision and Pattern Recognition, (1997) 915–920.
7. Bezdek, J.C.: Pattern Recognition with Fuzzy Objective Function Algorithms, New York: Plenum, (1981).

Chapter 170
New Heuristic of Self Organizing Map Using Updating Distribution

Sung-Hae Jun

Abstract Self organizing map (SOM) is a special type of artificial neural networks for unsupervised learning. SOM has been used as a good tool of clustering. Generally the weights of SOM are updated by a learning process which is depended on not distributions but values. After complete updating process, the final weights are determined by fixed values. So, the clustering result from a complete updating is only outcome. But, for example, the cognitive behaviors of human being are shown different results from the given experience. In this paper, we propose a new heuristic of SOM (NHSOM) using updating distributions. NHSOM is able to provide diverse results from the weight distributions. In our experimental results, we verify efficient and improved performances of NHSOM to compare other competitive algorithms using the data sets from UCI machine learning repository and synthesis.

Introduction

SOM has been used as a valuable tool in diverse mining fields such as clustering, text mining, customer relationship management, and so forth. The synaptic weight vector of feature map is updated by a learning process which is depended on training data set. Also, the final weights are determined by fixed values after complete updating. So, the clustering result from the last updating is only result. But, the cognitive behaviors of human being may be shown different results from the given experience. In this paper, we propose a new heuristics of SOM (NHSOM) by updating distributions. Our NHSOM is able to provide diverse outcomes after final updating weights by repeated random samplings. In our experimental results, we verify improved performances of our model to compare other learning algorithms using data sets from UCI machine learning repository and synthesis.

S.-H. Jun
Department of Bioinformatics & Statistics, Cheongju University, Chungbuk, Korea
e-mail: shjun@cju.ac.kr

R. Wang et al. (eds.), *Advances in Cognitive Neurodynamics*,

New Heuristic of SOM

In this paper, we use Bayesian learning for updating the weight distributions of NHSOM as the following expression [1].

$$P(X) = \int P(X, \theta) d\theta = \int P(\theta) P(X|\theta) d\theta \tag{170.1}$$

where, θ is parameterized model and X is data. Generally each node of the feature map achieves clustering by competitive learning from training data. Each point crisply belongs to only one exclusive cluster after the last training. The clustering result is one type because the weights are fixed values in nodes after complete training. This result may not be optimal [2, 3, 4, 5]. In this paper, we are able to get a probability distribution for a heuristic to determine optimal number of clusters. NHSOM updates parameters of probability distribution without having the fixed values of weights on each node of feature map. This strategy makes it possible to converge to optimal number of clusters by performing repeated experiments with same data to get different results. NHSOM is summarized in the following.

Step 1: *Initialize (n: data size, p: the dimension of input vectors)*

1.1 Normalization of input vector, $x_i = (x_{i1}, \cdots, x_{ip})$ represents the ith input pattern

$$x_i^{normal} = \left(\frac{x_{i1} - \mu_1}{\sigma_1}, \cdots, \frac{x_{ip} - \mu_{1p}}{\sigma_p} \right) = \left(x_{i1}^{normal}, \ldots, x_{ip}^{normal} \right)$$
$$x_i^{normal} \sim N(0, 1), \ (i = 1, \ldots n); \text{ Likelihood}$$

1.2 Initialize the weights vectors: Prior of weights, determine the distribution type of $f(\cdot)$

$f(\cdot)$ is any probability density function (pdf)
$w \sim f(\theta)$, optionally, $\theta \sim g(\varphi)$: φ is the hyper-parameter of θ, $g(\cdot)$ is also pdf

Step 2: *Determine winner node (m: feature map dimension)*

2.1 Weights sampling from current prior
2.2 Compute the $dist(x_i^{normal}, w_j)$ (Euclidean distance of x_i^{normal} and w_j)

$$dist(x_i^{normal}, w_j) = \sqrt{\left(x_{i1}^{normal} - w_{j1}\right)^2 + \cdots + \left(x_{ip}^{normal} - w_{jp}\right)^2}, \quad (i = 1, \ldots, n, \ j = 1, \ldots, m^2)$$

2.3 Determine winner node, w_k is winner node if $dist(x, w_k) < dist(x, w_j)$, $j = 1, \ldots, m^2$

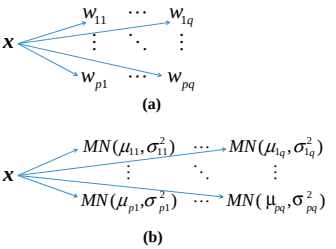

Fig. 170.1 Feature maps of SOM (**a**) and NHSOM (**b**)

$$\text{i.e., } w_k = \arg\min_j \{dist(x, w_j)\}$$

Step 3: *Update distribution of weights*
Compute posterior of winner node and replace current posterior by new prior

Repeat step 2 and step 3 until given conditions are satisfied

After complete learning of NHSOM, we get multivariate normal(*MN*) distribution based feature map in (b) of the Fig. 170.1.

Figure 170.1a is a feature map of traditional SOM which has fixed value as updated weights. But, the weights of NHSOM have their updated distribution.

NHSOM Design and Experimental Results

In this paper, we design the distribution of weights of NHSOM feature maps. Using Gaussian distribution with mean and variance, the weight value of each feature node is generated from this distribution. Using Gaussian prior and Gaussian likelihood, we compute a posterior probability distribution. Current posterior distribution is used for the next prior distribution. In NHSOM training we find the weight value of output node is generated from this prior probability distribution. This updating continues until satisfying stopping conditions. When noticeable change of feature map is not occurred, our NHSOM training is stopped. Also, it stops according to predefined iteration size. In this paper, to evaluate clustering results, we show a measure based on variance criteria in the following.

$$f_{eval}\left(x; \overline{v}_i, \overline{V}_M, M\right) = \frac{1}{M}\sum_{i=1}^{M}\overline{v}_i + \frac{1}{\overline{V}_M}M \tag{170.2}$$

Where, x is input vector. Also, M is the number of clusters and $\overline{v}_i$ is the average of variances of points in the ith cluster. $\overline{V}_M$ is the variance of M clusters. The smaller $f_{eval}(M)$ is, the better the result of clustering is. $f_{eval}(M)$ is the concept of the within variance of cluster. That is, the similarities among objects in each cluster are high when $f_{eval}(M)$ is small. To verify improved performance of our NHSOM, we make experiments using data sets from UCI machine learning repository [6] and

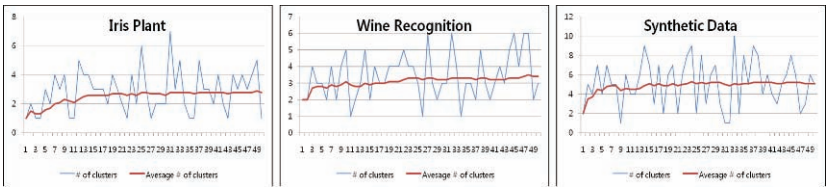

Fig. 170.2 NHSOM results of Iris plant, wine recognition, and synthetic data sets (x axis: # of samples, y axis: # of clusters)

synthesis. The number of classes of target variables in Iris plant, Wine recognition and synthetic data sets are 3, 3, and 5, respectively. For usage of synthetic data sets, we generate multivariate random data from finite mixture density [7]. We generate data set which has 1000 data points randomly from the multivariate normal distribution with each covariance matrix. First of all, we make an experiment on optimal determination of the number of clusters with our NHSOM. Using the weight distributions of feature nodes, we are able to generate random vector of the nodes of the feature map. So, we perform NHSOM by repeated random sampling from the weight distributions. We show the results of NHSOM which determines the number of clusters in the following figures. NHSOM results of Iris plant, Wine recognition, and synthetic data are shown in Fig. 170.2. In the experiments, we use 50 repeated random samplings.

In Fig. 170.2, the line of # of the clusters represents each result of a random sample from the weight distributions. Heuristic result of NHSOM is shown by the bold line of average # of clusters. In this line, the value of each step from 1 to 50 is computed by averaging previous values. From above results, we find the numbers of clusters of Iris plant, Wine recognition, and synthetic data sets are 3, 3, and 5, respectively. These are equal to the numbers of classes of the target variables in Iris plant, Wine recognition, and synthetic data sets. Therefore, we are able to verify the improved performance of NHSOM. Next, to verify the improved performance of our NHSOM, we compare NHSOM with competitive algorithms which are SOM, support vector clustering(SVC), K-means clustering, and hierarchical clustering algorithms [8, 9].

The result shows the misclassification rates of NHSOM are better than others. The misclassification rate of SVC in synthetic data is smaller than the value of NHSOM. But, the difference between SVC and NHSOM is very small. So, we are able to confirm improved performance of NHSOM.

Table 170.1 Competitive algorithms evaluation

	SOM	SVC	K-means	Hierarchical	NHSOM
Iris	0.02	0.02	0.08	0.13	0.01
Wine	0.12	0.17	0.21	0.25	0.09
Synthesis	0.20	0.18	0.31	0.38	0.19

Conclusions

In this paper, we proposed NHSOM for a heuristic for optimal clustering. NHSOM is a new heuristic of SOM. We were able to determine optimal number of clusters using NHSOM. Also, we verified improved performances of NHSOM compared with other learning algorithms using data sets from UCI machine learning repository and synthesis.

References

1. Neal, R. M.: Bayesian Learning for Neural Networks, Springer, (1996).
2. Bishop, C. M., Svensen, M., Williams, C. K. I.: GTM: A principled alternative to the self organizing map, ICANN 96, Bochum, Germany, 1112, pp. 165–170, (1996).
3. Stacey, D. A., Farshad, R.: A probabilistic self-organizing classification neural network architecture, Proceedings of International Joint Conference on Neural Networks, 6, 4059–4063, (1999).
4. Utsugi, A.: Topology Selection for Self-organizing Maps, Network: Computation in Neural Systems, 7, 727–740, (1996).
5. Utsugi, A.: Hyperparameter Selection for Self-organizing Maps, Neural Computation, 9, 623–635, (1997).
6. UCI Machine Learning Repository, http://www1.ics.uci.edu/∼mlearn.
7. Everitt, B. S., Landau, S., Leese, M.: Cluster Analysis, Arnold, Replika Press, Kundli, India, (2001).
8. Han, J., Kamber, M.: Data Mining Concepts and Techniques, Second Edition, Morgan Kaufmann, (2001).
9. Haykin, S.: Neural Networks A Comprehensive Foundation, Prentice Hall, 842 pp, (1999).

Chapter 171
Regression ICA Algorithm for Image Denoising

Shangming Yang, Zhang Yi and Guisong Liu

Abstract In this paper, regression ICA is employed to construct a new algorithm for image denoising. In this algorithm, we first predict the missing observations and then estimate all the independent components based on the previous observations and the predictions. Experiments show that the proposed algorithms are efficient for extracting useful data from multiple high level noise mixed sources.

Introduction

The problem of independent component analysis (ICA) for blind source separation (BSS) has been studied by many authors in recent years. The goal of ICA is to recover independent sources with sensor observations that are unknown linear mixtures of the original independent source signals [1, 2, 3]. For the overcomplete ICA, it requires the number of the observations to be less than that of the original signals. Up to now, many important algorithms for different types of ICA model have been achieved. Lewicki and Sejnowski in [4] derived a gradient-based method called learning overcomplete representations of the data that allowed for more basis vectors than dimensions in the inputs, and this algorithm had a requirement for the assumption of a low level of noise. Li et al. [5] presented a sparse decomposition approach of observed data matrix which was used in BSS with less sensors than sources. For the noise ICA model, by employing bias removal algorithm, Cichocki et al. [6] proposed a modified ICA adaptive algorithm, which can reduce the noise to very low level. Cao et al. [7] proposed an approach to high level noisy ICA which can separate the mixtures of sub-Gaussian and super-Gaussian source components. In this paper, we will propose a very efficient overcomplete ICA algorithm for image denoising.

S. Yang
Computational Intelligence Laboratory, School of Computer Science and Engineering, University of Electronic Science and Technology of China, Chengdu 610054, China
e-mail: minn003@163.com

R. Wang et al. (eds.), *Advances in Cognitive Neurodynamics*,

ICA Regression for the Prediction of Noisy Observations

Regression ICA is one of the most important algorithms in supervised learning. In this model, the number of observations m is less than that of the original signals n. For simplicity, we assume the first m variables form the vector of the observed variables $\mathbf{x}_o = (x_1, x_2, ..., x_m)^T$, and the other n-m variables form the vector of the missing variables $\mathbf{x}_m = (x_{m+1}, x_{m+2}, ..., x_n)^T$. The model can be written as:

$$\begin{bmatrix} \mathbf{x}_0 \\ \mathbf{x}_m \end{bmatrix} = \begin{bmatrix} \mathbf{A}_0 \\ \mathbf{A}_m \end{bmatrix} \mathbf{s}. \tag{171.1}$$

For the given observation $\mathbf{x}_o$, the problem is how to predict $\mathbf{x}_m$. To do this, the estimation of $\mathbf{x}_m$ is defined as its conditional expectation [8]:

$$\mathbf{x}_m = E\{\mathbf{x}_m|\mathbf{x}_o\} \approx \mathbf{A}_m \tilde{g}(\mathbf{A}_o^T \mathbf{x}_o). \tag{171.2}$$

where the vector $\mathbf{A}_o^T \mathbf{x}_o$ can be considered as an initial linear estimate of $\mathbf{s}$, the probability density of each s_i is p_i, and $\tilde{g}_i(u) = p_i'(u)/p_i(u) + cu$ for all i. Here p_i'/p_i is called a negative score function of the probability density of variable s_i and cu is called a linear term. To make this approximation simpler, one way is to consider the mildly super-Gaussian densities with $\tilde{g}_i(u) = -tanh(u) + u$ for all i, but in most situations, we can use the generalized Gaussian distribution and its negative score function for the estimation.

For the overcomplete ICA, it has the following model:

$$\mathbf{x}_o = \mathbf{A}_o \mathbf{s} = (a_{ij})_{m \times n} (s_1, s_2, ...s_n)^T, \tag{171.3}$$

where the number of independent components is larger than the number of observed variables(n>m). For this model, we denote the m observation components vector to be $\mathbf{x}_o$. If we can find a way to estimate the another n-m component vector $\mathbf{x}_m$ first, then the problem will be expanded to standard ICA so that we can estimate all the original sources and we will call this algorithm the regression ICA based overcomplete ICA algorithm. The Eq. (171.3) now becomes the same expression to Eq. (171.1).

Using the regression ICA method in Eq. (171.2), we can predict the last $n - m$ components in vector $\mathbf{x} = (x_1, x_2, ..., x_n)$ which are $\mathbf{x}_m = (x_{m+1}, x_{m+2}, ..., x_n)$ as follows:

$$\mathbf{x}_m = \mathbf{A}_m \hat{\mathbf{s}} = \mathbf{A}_m \tilde{g}(\mathbf{A}_o^T \mathbf{x}_o). \tag{171.4}$$

To find a right expression for $\tilde{g}_i(u)$(the ith component of $\tilde{g}(\mathbf{u})$), we introduce the generalized Gaussian distribution:

$$p(\mathbf{y}) = \frac{\alpha\lambda_\alpha}{2\Gamma(\frac{1}{\alpha})} exp(-|\lambda_\alpha \mathbf{y}|^\alpha), \tag{171.5}$$

where Gamma function is defined by $\Gamma(x) = \int_0^\infty t^{x-1} exp(-t)dt$ and λ_α is a scaling factor which depends on the expectation and variance of the variables. α is also called a shape parameter. When $\alpha = 2$, Eq. (171.5) is the pdf of Gaussian distribution, $\alpha < 2$ the super-Gaussian and $\alpha > 2$ the sub-Gaussian. The corresponding negative score function plus linear term will be

$$\tilde{g}(\mathbf{y}) = p'(\mathbf{y})/p(\mathbf{y}) + c\mathbf{y} = -|\mathbf{y}|^{\alpha-1} sign(\mathbf{y}) + c\mathbf{y}. \tag{171.6}$$

If we consider noisy variables to be part of the independent components, from [6], the correlation matrix of vector is

$$\mathbf{R}_{vv} = \mathbf{R}_n = \mathbf{E}\{\mathbf{n}\mathbf{n}^T\} = \mathbf{E}\{\mathbf{A}_{m\times(n-m)}\mathbf{s}_{n-m}\mathbf{s}_{n-m}^T\mathbf{A}_{m\times(n-m)}^T\}. \tag{171.7}$$

Since the *n-m* components are mutually independent, if the ith component has variances σ_i^2, then Eq. (171.7) becomes

$$\mathbf{R}_{vv} = \mathbf{A}_{m\times(n-m)}(\mathbf{I}_{(n-m)})\mathbf{A}_{m\times(n-m)}^T. \tag{171.8}$$

where $I_{n-m} = diag(\sigma_1^2, \sigma_2^2, ...\sigma_{n-m}^2)$. The bias removal algorithm [6] for the noisy ICA is usable only when the noisy variables have identical distribution. If there are two more types of noise, the regression ICA based algorithm can be used, in which the noisy observations can be considered as missing variables. Therefore, this is also an overcomplete ICA problem.

Simulations and Discussions

To test the ability of image denoising of the proposed algorithm, different types of noise can be added to a picture which means we only have one observation (Fig. 171.1 right) for these original sources. In this experiment, Gaussian and uniform noise are added to an 128 × 128 color picture and then be removed, in which

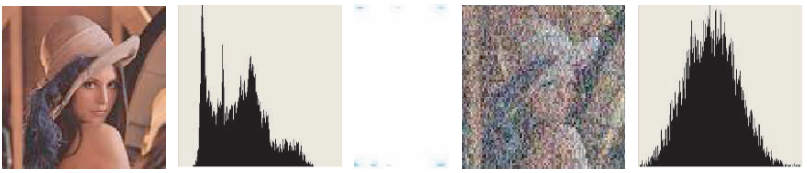

Fig. 171.1 The original image and its histogram (left two pictures) and the observed mixture and its histogram (right two pictures)

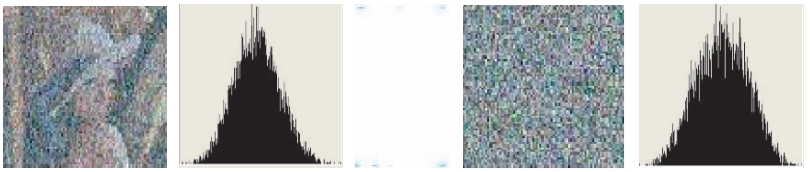

Fig. 171.2 The predicted observation of Gaussian noise image and its histogram (left two pictures) and the predicted observation of uniform noise image and its histogram (right two pictures)

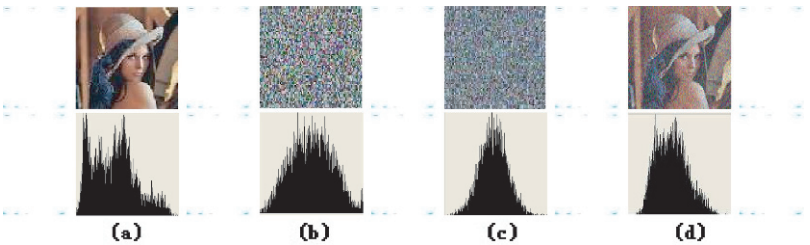

Fig. 171.3 The proposed algorithm estimated images and their histograms (a), (b), (c) and the bias removal algorithm estimated image and its histogram (d)

the signal to noise ratio of these two noisy sources is high up to SNR $= 5$ dB, the standard deviation σ of Gaussian noise is 18.74 and the uniform noise is 49.42. The picture is selected from: The NMFLAB Package: for Image Processing [9]. The traditional noisy ICA algorithm is not working well for this type of image denoising. Fig. 171.3d shows the result of the bias removal algorithm denoised image which is still with high level noise. We use the regression ICA to predict the noisy observations. Fig. 171.2 shows the predicted observations and their histograms. Figure 171.3a–c shows the proposed algorithm restored image and the two noisy signals and their corresponding histograms respectively. Comparing with the original image in Fig. 171.1 (left), the estimations (Fig. 171.3a) still have some errors, but it is obviously better than that in Fig. 171.3d. The errors indicate that the prediction algorithm still can not achieve the best estimations of the original image, but the major advantage of this algorithm is its ability of removing multiple high level noisy sources in a picture.

References

1. J. F. Cardoso: Blind signal separation: statistical principles, Proc. IEEE, 86 (1998) 2009–2025.
2. T. W. Lee: Independent Component Analysis: Theory and Applications (1998) Kluwer, Boston, MA.
3. S. I. Amari, A. Cichocki, H. Yang: A new learning algorithm for blind source separation, advances in neural information processing system, Vol. 8. MIT Press, Cambridge, MA, (1996) 757–763.
4. M. S. Lewicki, T. J. Sejnowski: Learning overcomplete representations. Neural Comput. 12 (2000) 337–365.

5. Y. Li, A. Cichocki, S. Amari: Sparse component analysis for blind source separation with less sensors than sources. Fourth international symposium on independent component analysis and blind signal separation (ICA2003) Japan, pp. 89–94.
6. A. Cichocki, S. C. Douglas, S. Amari: Robust techniques for independent component analysis (ICA) with noisy data. Neurocomputing 22 (1998) 113–129.
7. J. Cao, N. Murata, S. Amari, A. Cichocki, T. Takeda.: A robust approach to independent component analysis of signals with high-level noise measurements. IEEE Trans. Neural Netw., 14 (2003) 631–645.
8. A. Hyvärinen, E. Bingham.: Connection between multilayer perceptrons and regression using independent component analysis. Neurocomputing 50 (2003) 211–222.
9. A. Cichocki, R. Zdunek: The NMFLAB Package: for Image Processing, Version 1 (2006) RIKEN Brain Science Institute, Wako shi, Saitama, Japan.

Chapter 172
Thumbnail Generation Based on Global Saliency

Xiaodi Hou and Liqing Zhang

Abstract In this paper, we present a novel approach to generate thumbnail images. Our method crops an image into a smaller but more informative region in the thumbnail representation. From the perspective of information theory, we propose a novel approach to generate bottom-up saliency in a global manner. In our method, we evaluate the statistical distribution of feature maps, and use its *coding length* as a measurement for image cropping. The experimental results offer viewers a more effective representation of images.

Introduction

Thumbnail image is an effective way visual information representation. The thumbnail image is widely used in representing collections of images, or displaying images on hand-held devices with limited screen size or limited bandwidth.

Corresponding to the growing varieties of applications of thumbnail images, several methods of generating effective thumbnails are proposed in literature [1, 2]. Many of these methods first evaluate the image based on the importance of its content, and then crop and resize to display only part (such as the face in a portrait) of the image in the thumbnail.

In order to define "important regions" in a general sense, attention models [3] of computer vision are adopted. However, most of attention models are based on local saliency: they are apt in finding key-points such as corners, edges or other local patterns [4], but given the task to crop important regions in an image instead, these local features often fail to capture the global structure of the image.

This paper presents a global method to detect salient regions. In our framework, the optimal thumbnail image should represent regions that contains richest information. Based on information theory, we consider the global distribution of

X. Hou
Department of Computer Science and Engineering, Shanghai Jiao Tong University, Shanghai, China 200240
e-mail: filestorm@sjtu.edu.cn

R. Wang et al. (eds.), *Advances in Cognitive Neurodynamics*,

features in an image, and quantify the "richness of information" by evaluating the optimal coding length of the region. Computer simulations indicate that the novel thumbnail representation captures the important regions of the image.

Assessing the Information of an Image

It has been widely acknowledged that the detection of saliency in human visual system is achieved by the cooperation of low-level visual features such as colors and textures. In our models, different local features are extracted by *descriptors*. Details of descriptor selection of our model will be discussed in section "Implementation". By gathering the responses of descriptor of a certain feature, the *feature map* of the image is generated.

Former methods rely on the assumption that the salient regions are usually related with high values in the feature map. Most algorithms link responses of local salient features such as edge, border, or blob descriptors directly with the visual salient regions [3, 5].

In this paper, we propose that the saliency is dependent on the global distribution of the feature map. According to Kadir and Brady [5], saliency implies rarity. To quantify the rarity of a feature, we introduce the *optimal coding length* of a pattern. Suppose we have a feature map $\mathbf{X}$ whose possible value is in the alphabet $\mathcal{X}$. The probability density function $p(x)$ can be estimated by taking the histogram of the feature map. According to Shannon's information theory, the optimal coding length $L(x)$ of a feature $x \in \mathcal{X}$ is:

$$L(x) = -\log_2(p(x)). \tag{172.1}$$

According to Eq. 172.1, a *coding length map* $\mathbf{L}$ can be constructed by assigning $\mathbf{L}_{ij} = L(\mathbf{X}_{ij})$. The coding length map measures the rarity of values presented in the feature map. It worths noting that the spatial information of the image is preserved in $\mathbf{X}$ and $\mathbf{L}$, so that the regional summation of the coding length map reflects the global rarity of that region.

Particularly, the sum of the coding length map equals the entropy of the feature map $H(\mathbf{X})$:

$$\begin{aligned} H(\mathbf{X}) &= -\sum_{x\in\mathcal{X}} p(x)\log_2(p(x)) \\ &= \sum_{x\in\mathcal{X}} p(x)L(x) = \sum_{i,j} \mathbf{L}_{ij}. \end{aligned} \tag{172.2}$$

The optimal coding length bridges the spatial location and statistical distribution of a descriptor's response. A region will be considered rare only when the statistical minority clusters at certain regions become regional majority.

Implementation

In this paper, a feature descriptor computes certain statistics of a $10px \times 10px$ non-overlapping patch. We consider two kinds of statistics: color and texture. More features are not adopted because the computational resource required in generating a thumbnail must be parsimoniously controlled. However, the architecture of our method is readily to incorporate new features.

For efficiency, the image is down-sampled before processing. We shrink each input image to size $\min(height, width) = 256$. Also, the final output of the thumbnail should be square image to guarantee maximal screen space usage when multiple thumbnails are displayed simultaneously.

Color Feature Map

We convert the input RGB image into HSV color space, and use the hue value as our primary indicator of color property. That is:

$$\mathbf{C}_i = \frac{1}{100} \sum_{x,y} h_i. \tag{172.3}$$

Since low saturation or lightness will affect the perception of chromaticity, a weighting method is applied in estimating color feature distribution:

$$p(k) = \frac{\sum_{h_i=k} s_i \cdot v_i}{\sum s_i \cdot v_i}, \tag{172.4}$$

where h_i, s_i and v_i are the mean hue, saturation and gray-scale value of the i^{th} patch, separately.

Texture Feature Map

Here we refer the term "texture" in a general sense. Shape, border, contrast, intensity, and other characteristics reflected in a gray-scale image may have influences on the texture feature value. This descriptor supplements many structural information that is neglected by color channel.

We use standard deviation of the gray image to capitulate texture property of a patch. Different from previous literature [4], we do not put much efforts in the selection of appropriate descriptors, since the degree of saliency is not directly linked with texture value T_i of the ith patch in our framework. Specifically, we have:

$$\mathbf{T}_i = \frac{1}{100} \sum_{x,y} \left\{ v_{xy} - \frac{1}{100} \sum_{x,y} (v_{xy}) \right\}^2. \tag{172.5}$$

Cropping

Since the measurement for coding length maps is *bits*, maps corresponding to different features can be added up. Given the combined coding length map $\mathbf{L}$ of an image, the optimal cropping selects a square area that is most informative. It is easy to see that $\mathbf{L}$ is non-negative. Therefore, the cropping is a trade-off between the inclusion of more information and the average intensity of included information. Our method solves this problem by introducing a variable λ. For an $a \times a$ square area A, the degree of informative $\mathbf{I}_A$ is:

$$\mathbf{I}_A = \frac{1}{a^\lambda} \cdot \sum_{i \in A} \mathbf{L}_i \quad (0 \leq \lambda \leq 2), \tag{172.6}$$

empirically, we choose $\lambda = 1.5$.

Figure 172.1 compares traditional thumbnails and thumbnails generated by our method. These results indicate that our algorithm has accomplished a reasonable estimation to human visual attention. The cropped thumbnails focus primarily on the most informative regions of the original images.

Fig. 172.1 Examples results. Left: the input image. Upper-right: traditional thumbnail. Lower-right: thumbnail generated by our method

Conclusion

In this paper, we have proposed a novel approach of saliency detection, and use it to generate thumbnails. Within the framework of information theory, we interpreted the relation between saliency and the amount of information. We also provide an application of the proposed method. Experiment results indicate that our thumbnails capture the central objects in the pictures.

Acknowledgements The work was supported by the National High-Tech Research Program of China (Grant No. 2006AA01Z125) and the National Basic Research Program of China (Grant No. 2005CB724301).

References

1. Suh, B., Ling, H., Bederson, B., and Jacobs, D.: Automatic thumbnail cropping and its effectiveness. ACM-UIST, (2003) 95–104.
2. Liu, F., and Gleicher, M.: Automatic image retargeting with fisheye-view warping. ACM-UIST, (2005) 153–162.
3. Itti, L., Koch, C., and Niebur, E.: A model of saliency-based visual attention for rapid scene analysis. IEEE-TPAMI, **20 (11)** (1998) 1254–1259.
4. Lowe, D.: Distinctive image features from scaleinvariant keypoint. Int. J. Comput. Vis., **60 (2)** (2004) 91–110.
5. Kadir, T. and Brady, M.: Saliency, scale and image description. Int. J. Comput. Vis., **45 (2)** (2001) 83–105.

Chapter 173
Exponential Stability of Delayed Hopfield Neural Networks by Using Comparison Method

Wudai Liao and Yuguo Chen

Abstract The exponential stability of delayed Hopfield neural networks is studied by comparison principle. Hopfield neural networks can be regarded as a linear system perturbed by the exterior input. Based on this view of point, the method of variation of coefficient is used to solve the system's solutions, which are estimated by its comparison system. By this comparison system, which is a linear differential difference equation, and by using theory of linear functional differential equation, some stability criteria are obtained, which is very simple to verified. An examples are given to show the efficiency of the results in this paper.

Introduction

The stability problem on Hopfield neural networks is widely studied from origin to now, including the original work [1, 2], delayed cases [3, 4, 5, 6] and other studies. The methods used in these papers are mainly Lyapunov direct approaches, that is, all results obtained in these papers depend on the selection of appropriate Lyapunov functions.

In this paper, we are going to consider the following delayed Hopfield neural networks

$$\begin{aligned} \frac{\mathrm{d}u_i(t)}{\mathrm{d}t} &= -b_i u_i(t) + \sum_{j=1}^{n} T_{ij} v_j(t)\,, i = 1, 2, \cdots, n \ , \\ v_j(t) &= f_j(u_j(t - \tau_j))\,, j = 1, 2, \cdots, n \ . \end{aligned} \tag{173.1}$$

Where, $u_i(t)$ is the state of neuron i at time t, $b_i > 0$ is the time constant, T_{ij} is the connection weight from neuron j to neuron i, $v_j(t)$ is the output of neuron j at time

W. Liao
School of Electrical and Information Engineering, Zhongyuan University of Technology, 450007 Zhengzhou, Henan, China.
e-mail: wdliao@zzti.edu.cn, cygzzti@163.com

R. Wang et al. (eds.), *Advances in Cognitive Neurodynamics*,

t, $f_j(\cdot)$ is the amplifier or output function, which satisfies $|f_j(u)| \le \beta_i |u|$, $\beta_i > 0$ is a constant, $\tau_j \ge 0$ is the time delay of the amplifier j, $\tau = \max_{0\le j\le n}\{\tau_j\}$.

In fact, we can treat (173.1) as a linear power system perturbed by the exterior input [7]. So, we can use the method of variation of coefficient to compute the solution of the system's equation, which don't depend on the selection of Lyapunov functions. Based on this system's expression, we use some skills of matrix norm and theory of functional differential equations to study the exponential stability problem. Some stability criteria are obtained which are very simple to verify and are convenience to test for system's design.

In the following of this section, we will give some notations and some lemma, which will be used later in this paper.

For any $t \ge 0$, the continuous vector function $x_t \in C\big([-\tau, 0]; \mathbb{R}^n\big)$ means

$$x_t(\theta) = x(t+\theta), \quad \theta \in [-\tau, 0] \ .$$

Consider the linear differential difference equations

$$\dot{x}(t) = Ax(t) + Bx(t-\tau) \ , \tag{173.2}$$

where $x \in \mathbb{R}^n$, $A, B \in \mathbb{R}^{n\times n}$, $x(t-\tau) = (x_1(t-\tau_1), \cdots, x_n(t-\tau_n))^T$.

The characteristic polynomial of Eq. (173.2) is defined as

$$f(\lambda, \tau) = \det\big(\lambda E - A - B \cdot \mathrm{diag}(e^{-\lambda\tau_1}, e^{-\lambda\tau_2}, \cdots, e^{-\lambda\tau_n})\big) \ , \tag{173.3}$$

where E denotes $n \times n$ unit matrix.

Lemma 1. *The equilibrium $x = 0$ of Eq. (173.2) is delay-independent asymptotic stability if and only if*

1) Each eigenvalue of character equation $f(\lambda, 0) = 0$ has negative real part;

2) For any $\omega \in \mathbb{R}$ and any $\tau \ge 0$, $f(J\omega, \tau) \ne 0$, where J is the imaginary unit.

Main Results

Theorem 1. *For System (173.1), if $b_i > \sum_{j=1}^n |T_{ij}|\beta_j \ , i = 1, 2, \cdots, n$, then the trivial equilibrium $u = 0$ is globally exponential stability.*

Proof. According to the variation of coefficient of liner differential equations, for any initial function $u_{0i} \in C\big([-\tau, 0]; \mathbb{R}\big)$, the solution of System (173.1) is

$$u_i(t) = e^{-b_i t}u_{0i}(0) + \int_0^t e^{-b_i(t-s)} \sum_{j=1}^n T_{ij} v_j(s)\mathrm{d}s, \ \ i = 1, 2, \cdots, n \ .$$

By using the property of output functions: $|f_j(u)| \le \beta_i|u|$, we have

$$|u_i(t)| \le e^{-b_i t}|u_{0i}(0)| + \int_0^t e^{-b_i(t-s)} \sum_{j=1}^n |T_{ij}||v_j(s)|\mathrm{d}s$$
$$\le e^{-b_i t}|u_{0i}(0)| + \int_0^t e^{-b_i(t-s)} \sum_{j=1}^n |T_{ij}|\beta_j|u_j(s-\tau_j)|\mathrm{d}s := y_i(t) \ .$$

This implies $|u_i(t)| \le y_i(t)$ for any $t \ge 0$ and choose the initial conditions $y_{0i} = |u_{0i}| \in C\big([-\tau, 0]; \mathbb{R}\big)$, we have

$$\frac{\mathrm{d}y_i(t)}{\mathrm{d}t} \le -b_i y_i(t) + \sum_{j=1}^n |T_{ij}|\beta_j|y_j(t-\tau_j)| \ .$$

Its comparison equation is (initial conditions $z_{0i} = |u_{0i}|$)

$$\frac{\mathrm{d}z_i(t)}{\mathrm{d}t} = -b_i z_i(t) + \sum_{j=1}^n |T_{ij}|\beta_j|z_j(t-\tau_j)| \ .$$

By using the condition of this theorem, $b_i > \sum_{j=1}^n |T_{ij}|\beta_j$, we can choose a constant $\alpha_i > 0$ such that $b_i - \alpha_i > \sum_{j=1}^n |T_{ij}|\beta_j$, and take the transform:

$$z_{ti} = e^{-\alpha_i t}\eta_{ti} \in C\big([-\tau, 0]; \mathbb{R}\big) \ , \forall t \ge 0 \ .$$

That is, $z_i(t) = e^{-\alpha_i t}\eta_i(t)$, $z_i(t-\tau_i) = e^{-\alpha_i t}\eta_i(t-\tau_i)$, $i = 1, 2, \cdots, n$. So, the comparison system (173.4) has the following form (initial conditions $\eta_{0i} = |u_{0i}|$):

$$\frac{\mathrm{d}\eta_i(t)}{\mathrm{d}t} = -(b_i - \alpha_i)\eta_i(t) + \sum_{j=1}^n |T_{ij}|\beta_j|\eta_j(t-\tau_j)| \ . \tag{173.4}$$

Its eigenvalue polynomial is

$$f(\lambda, \tau) = \det\big([\lambda + (b_i - \alpha_i)]\delta_{ij} - |T_{ij}|\beta_j e^{-\lambda\tau_j}\big)_{n\times n} \ ,$$

where

$$\delta_{ij} = \begin{cases} 1, \text{ if } i = j \\ 0, \text{ if } i \ne j \end{cases} \ .$$

All eigenvalues of $f(\lambda, 0) = 0$ satisfy one of the following conditions:

$$|\lambda - (-b_i + \alpha_i + |T_{ii}|\beta_i)| \leq \sum_{j=1 j\neq i}^{n} |T_{ij}|\beta_j \ ,$$

and by the selection of α_i, we have

$$b_i - \alpha_i - |T_{ii}|\beta_i > \sum_{j=1, j\neq i}^{n} |T_{ij}|\beta_j \ ,$$

this shows that all eigenvalues of $f(\lambda, 0) = 0$ are of negative real parts, which satisfy condition 1) in Lemma 1.

For the same reason, for the imaginary unit J, the matrix

$$\left([J\omega + (b_i - \alpha_i)]\delta_{ij} - |T_{ij}|\beta_j e^{-J\omega\tau_j}\right)_{n\times n}$$

is diagonal dominated, and therefore, its determinant $f(J\omega, \tau) \neq 0$, which satisfies condition 2) in Lemma 1.

By Lemma 1, the trivial equilibrium $\eta = 0$ of Eq. (173.4) is asymptotical stability.

By comparison principle, we have

$$|u_i(t)| \leq y_i(t) \leq z_i(t) = e^{-\alpha_i t}\eta_i(t) \ ,$$

so, the trivial equilibrium $u = 0$ of System (173.1) is globally exponential stability. The proof is complete.

Corollary 1. *If all the output functions in System (173.1) are the same and $b > \beta\|T\|_\infty$, then, the trivial equilibrium $u = 0$ of System (173.1) is globally exponential stability, where $b = \min\{b_i\}$, $\beta = \beta_i$, $i = 1, 2, \cdots, n$.*

Proof. For any $i = 1, 2, \cdots, n$, we have $b_i \geq b > \beta\|T\|_\infty \geq \beta\sum_{j=1}^{n} |T_{ij}|$, by using Theorem 1, the corollary is true. The proof is complete.

Examples

Example 1. Consider the 2-dimensional delayed Hopfield neural networks:

$$\begin{aligned}
\frac{\mathrm{d}u_1(t)}{\mathrm{d}t} &= -u_1(t) - 0.5s(u_1(t-\tau_1)) + 2s(u_2(t-\tau_2)) \\
\frac{\mathrm{d}u_2(t)}{\mathrm{d}t} &= -u_2(t) + s(u_1(t-\tau_1)) + 1.5s(u_2(t-\tau_2)) \ .
\end{aligned}$$

Where, the output function is $s(u) = 1/(1 + e^{-u})$.

Here, $b = 1$, $\beta = 0.25$, $\|T\|_\infty = 2.5$, and $b > \beta\|T\|_\infty$, so, the trivial equilibrium $u_1 = u_2 = 0$ is globally exponential stability (by using Corollary 1).

Acknowledgements The work is supported by National Natural Science Foundation of China (60474001) and Natural Science Foundation of Henan Province of China (0611054500).

References

1. Hopfield, J.J.: Neural Networks and Physical Systems with Emergent Collective Computational Abilities. Proc. Natl. Acad. Sci. USA, 79 (1982) 2554–2558
2. Hopfield, J.J.: Neurons with Graded Response have Collective Computational Properties Like Those of Two-state Neurons. Proc. Natl. Acad. Sci. USA, 81 (1984) 3088–3092
3. Liao, W., Liao, X.: Robust Stability of Time-Delayed Interval CNN in Noisy Environment. Acta Automat Sin, 30(2)(2004) 300–305
4. Zeng, Z., Wang, J., Liao, X.: Global Asymptotic Stability and Global Exponential Stability of Neural Networks with Unbounded Time-varying Delays. IEEE Trans. Circuits Systs, 52 (2005) 168–173
5. Shen, Y., Liao, X.: Exponential Stability of Delayed Hopfield Neural Networks. Acta Mathematica Sci, 19 (1999) 211–218
6. Zeng, Z. , Wang, J., Liao, X.: Global exponential stability of neural networks with time-varying delays. IEEE Trans. Circuits Sys: 50 (2003) 1353–1358
7. Liao, X.: Studies on Mathematic Meaning of Phisic Parameters in Hopfield Neural Networks. Science in China (Series E), 33 (2003) 127–136

Chapter 174
Adaptive Fuzzy Clustering Neural Network

Fang Bao, Yonghui Pan and Wenbo Xu

Abstract Due to the localization of the objective function of traditional fuzzy clustering algorithm, a novel adaptive objective function of fuzzy clustering is proposed, the new objective function integrates the clustering characteristic of input space and the real time approximate characteristic of output space. The extraordinary neural network to handle the fuzzy clustering algorithm is also proposed. The experimental results show that the new algorithm has better performance in stable convergent rate, convergent speed, and the initial condition sensitivity compared with traditional fuzzy clustering algorithm. The result illuminates the rationality of importing felicitous adaptive feedback factors into the objective function.

Keywords Fuzzy clustering · neural network · objective function · adaptive

Introduction

Fuzzy clustering finds out the uncertainty of class attribute each individual belongs to, delivers the probability deflection of it. Now, in different apply domains, based on different techniques, many fuzzy clustering algorithm have been proposed.

Objective function-based Fuzzy clustering algorithm constructs an objective function via the distance between the initial cluster set and the prototypes of each cluster, achieves the optimized fuzzy c-means results by optimizing such nonlinear programming question.

But, the commonly used objective functions are often the minimization of internal squared error in the initial input space, namely the Euclidean distance between the initial cluster set and the prototypes of each cluster. Unsupervised learning based on such distance function has good learning speed, but have many limitations, for example, convergent to wrong cluster center because of the high initial condition

F. Bao
School of Information Technology, Jiangnan University No. 1800, Lihudadao, Wuxi Jiangsu, China 214122
e-mail: baofang@mail.jypc.org

R. Wang et al. (eds.), *Advances in Cognitive Neurodynamics*,

sensitivity, depend on the characteristic of clustering set because the inflexible attracting domain [1].

The challenges are, what is the guideline of proper distance? Could a fuzzy clustering algorithm not depend on the predefined distance been constructed? Can we supervise the clustering process [2]?

The paper proposed an adaptive objective function via integrates the clustering characteristic of input space and the real time approximate characteristic of output space. The objective function represents the internal squared error in the initial input space as well as the real time approximate squared error in the output space, equivalent to that we supervise the clustering process using the real time output of the system, and the adaptive feedback control to the clustering process is achieved. The extraordinary neural network to handle the fuzzy clustering algorithm is also proposed, we call it adaptive fuzzy clustering neural network (AFCNN). The experimental results shows that the new algorithm has better performance in stable convergent rate, convergent speed, and the initial condition sensitivity.

The remaining of the paper is organized as follows: section 'Construct the Adaptive Objective Function' illustrates construction of the adaptive objective function, section 'Construct the Adaptive Fuzzy Clustering Neural Network' focus on the design of the adaptive fuzzy neural network that handling the algorithm and the corresponding fuzzy clustering algorithm, section 'Experimental Results' presents the experiment evaluation of the proposed algorithm, finally, we provide concluding comments.

Construct the Adaptive Objective Function

Construction of Adaptive Objective Function

For the sake of constructing a proper objective function that not depend on the predefined distance, according to the supervised learning principle of the ellipse fuzzy system [3], we make the new objective function represents the internal squared error in the initial input space as well as the real time approximate squared error in the output space. Further more, using neural network as the instrument to handle the clustering algorithm, we can optimize the input-output joint space more conveniently.

According to the fuzzy add-up principle, a big enough add-up fuzzy system could approximate any limited measurable function. So we construct a local linear regression function in the input-output joint space to simulate one clustering pattern, thus, the sum of all the local linear regression functions becomes the global regression model of the whole system. We define the distance between current real system output and the current global approximate of the system be the current approximate characteristic of the output space. Namely, we supervise the clustering process using current output approximate situation, the proposed clustering process is self-adaptive.

So, besides the intrinsic internal squared error in the initial input space, we add the distance between current real system output and the current global approximate of the system to the new objective function. Thus, the objective function represents the internal squared error in the initial input space as well as the real time approximate squared error in the output space.

Let's start constructing the adaptive objective function.

Given the initial input pattern $X = \{x_1, x_2, \ldots, x_N\}$, suppose to organize the data in C clusters.

Let vi and zi are the cluster center of the input and output space respectively, αi is the local linear smoothness parameter of the ith local model, which will be optimized step by step during the training process. Define the local linear regression model for each cluster as:

$$\hat{y}_i - z_i = \alpha_i(x_k - v_i), k = 1, 2, \ldots, N, i = 1, 2, \ldots C \tag{174.1}$$

Based on it, the global regression model is:

$$\hat{y}_k = \sum_{i=1}^{c} \alpha_i(x_k - v_i) + z_i, k = 1, 2, \ldots, N \tag{174.2}$$

Suppose Wi is the backward parameter matrix of the ith fuzzy rule, then the current real fuzzy output of the system is:

$$y_k = w_i x_k \tag{174.3}$$

In order to represent the internal squared error and the real time approximate squared error simultaneously, the adaptive objective function is defined as:

$$J = \sum_{i=1}^{c} \sum_{k=1}^{N} {u_{ik}}^m (\|x_k - v_i\|^2 + \|y_k - \hat{y}_k\|^2) \tag{174.4}$$

Having the definition of the objective function, follow FCM algorithm, by applying the Lagrange multipliers technique to J in (8), we derive the necessary conditions for the partition matrix:

$$u_{ik} = \frac{1}{\sum_{j=1}^{c} \left(\frac{\|x_k - v_i\|^2 + \|y_k - \hat{y}_k\|^2}{\|x_k - v_j\|^2 + \|y_k - \hat{y}_k\|^2} \right)^{1/(m-1)}}, 1 \le k \le N, 1 \le i \le c \tag{174.5}$$

Construct the Adaptive Fuzzy Clustering Neural Network

As described before, according to the proposed objective function, we design a BP neural network to handle the new algorithm. The whole neural network system consist of three major parts, the first part is a neural network fuzzy cluster, the second one is a fuzzy output controller, last one is the system synthesizer.

Neural Network Fuzzy Cluster

The neural network fuzzy cluster is a 4-layers BP neural networks. The input layer have P neurons, represent the p dimensions of the input vector. Two hidden layers and the output layer all have C neurons.

The transfer function between the input and the first hidden layer is $D_{ik} = \|x_k - v_i\|^2$, which represents the distance between the input vector and the ith cluster center, the connect weight form the input layer to the first hidden layer is the ith cluster center vi,.

The neurons in the second hidden layer is calculated by the function in (2), represent the currently global regression model of the system. The connect weight from the first hidden layer to the second hidden layer defined as the local linear smoothness parameterαi. The output of the second hidden layer connect to the output layer without connect weight, along with the output of the fuzzy output controller, make up the input of the output layer.

The output layer get the partition matrix which represent the class attributes of the input vector to the certain cluster model, the transfer function is in (4).

Fuzzy Output Controller

The fuzzy output controller consists of C sub neural networks, each neural network is a 2-layers network, calculates the current real fuzzy output of the system. Wi is the backward parameter matrix of the ith fuzzy rule, the output of each network is $y_k = w_i x_k$.

System Synthesizer

Having gain the partition matrix via neural network fuzzy cluster and fuzzy output of the system via fuzzy output controller, the final output of the whole system is synthesized as:

$$o_k = \sum_{i=1}^{c} u_{ik} y_{ki} \tag{174.6}$$

The Training Algorithm of the Adaptive Fuzzy Clustering Neural Network

According to the principle of uniting the supervised learning and unsupervised learning together for discovering the ellipse fuzzy rule [3], we gain the primary rough result set by the unsupervised learning, and optimize the rough set to more precise one by supervised learning.

We can conclude from the proposed objective function and the neural network structure that the parameter needs to be optimized include the cluster center vi, the local linear smoothness parameterαi, and the backward parameter matrix of the ith fuzzy rule wi.

So we define the training algorithm of the adaptive fuzzy clustering neural network as follows.

let T = {t1, t2, . . ., tN} be the desired output values of the whole system, and O = {o1, o2, . . ., oN} be the actual output of the whole system, calculated in (6).

The error function of the neural network is:

$$E_k = \frac{1}{2}\sum_{k=1}^{N} \|t_k - o_k\|^2 \tag{174.7}$$

Step. 1 Expand the input space to input-output joint space, perform FCM on the joint space, vi0,zi are the result prototypes in the input and output space respectively, note vi0 is the primary rough cluster center of the input space, it will be optimized during the training process, while zi is the cluster center of the output space,and is calculated only in this step.

Step. 2 Initialize the local linear smoothness parameterαi, and the backward parameter matrix of the ith fuzzy rule wi.

Step.3 According to the error function in (7), using grads descend training method with impulse item, repeatedly updates the cluster center vi, the local linear smoothness parameterαi, and the backward parameter matrix of the ith fuzzy rule wi.

Step. 4 With vi, wi, αi, calculate the uik using functions in (5).

Step. 5 Repeat step 3, 4 until the error function of the neural network is smaller than the predefined threshold value.

Experimental Results

The experiment dataset is a standard dataset of address selection information, the dataset have 20 groups of different address selection scheme, each scheme have eight key factors that deciding the address selection and expert's grade for this scheme. All the scheme is divided into three categories depend on the expert's experience.

Table 174.1 Rational convergent rate

	Rational convergent rate (%)
AFCNN	98.2
FCNN (FCM)	88.5

Table 174.2 Summarize the performance parameter when AFCNN and fcnn(FCM) could achieve rational convergence

	Overlap steps	Initial error range
AFCNN	100	0.7–2.5
FCNN (FCM)	1000	0.2–0.8

Made the dataset be the training dataset of both the adaptive objective function based fuzzy clustering neural network(AFCNN) and traditional fuzzy c-means objective function based fuzzy clustering neural network(FCNN(FCM)), both use the same neural network training mentioned above. Here, input space are the eight key factors, output space is the expert's grade.

Table 174.1 represents the rational convergent rate under all initial condition of two algorithms contrastively.

We can see that the AFCNN algorithm could achieve fine convergence and approximation after 100 times of overlaps, and the convergence could be achieved under wider initial error range, namely, the algorithm is less sensitive to the initial condition. While the FCM objective based fuzzy clustering algorithm, FCNN(FCM), shall achieve convergence after about 1000 times of overlap, and the rational convergence could be achieved under much narrow initial error range, meanly, the algorithm is quite sensitive to the initial condition.

So, we can conclude that the propose AFCNN algorithm has made improvement on stable convergent rate, convergent speed, and the initial condition sensitivity compared with traditional objective function based fuzzy clustering algorithm.

Conclusions

By adding the distance between current real system output and the current global approximate of the system to the new objective function, we proposed a new objective function that integrates the clustering characteristic of input space and the real time approximate characteristic of output space, and we construct an effective neural network to handle the fuzzy clustering algorithm. The experimental results show that the new algorithm has better performance in stable convergent rate, convergent speed, and the initial condition sensitivity compared with traditional fuzzy clustering algorithm. The result illuminates the rationality of importing felicitous adaptive feedback factors into the objective function. The algorithm is effective to all machine-learning situation that have teacher data, and is provided with stable practical action.

References

1. H. Pilian, H. Yuexian. An Asynmmetric Robust Learnning Algorithm of Fuzzy Clustering Neural Network. Journal of Computer Research and Development. (2001) 38, 296–301.
2. A. Staiano, R. Tagliaferri, W. Pedrycz. Improving RBF Networks Performance in Regression Tasks by Means of a Supervised Fuzzy Clustering. Neurocomputing. (2006) 69, 1570–1581.
3. B. Kosko. Fuzzy Engineering. Publish of Xi'an Jiaotong University, Prentice-Hall, Englewood Cliffs, NJ (1996) 118–126, 60–72.
4. W. Pedrycz, G. Vukovich. Logic-oriented Fuzzy Clustering. Pattern Recognition Letters. (2002) 23, 1515–1527.

Chapter 175
Compound Attack on Synchronization Based Neural Cryptography

Ping Li and Zhang Yi

Abstract In this paper we present a new and effective attack strategy on neural cryptography. The neural cryptosystem has been recently shown to be secure under some different attack strategies. But all these attack strategies aim at the mechanism of the secret key generated by the global dynamics of two interacting neural networks. The strategy we propose focuses on the authentication which the neural cryptosystem takes little account of. The proposed authenticated key exchange mechanisms are analyzed and convinced to be hardly applicable.

Introduction

Recent studies show that interacting neural networks can exhibit many interesting phenomena as described in [1]. The pioneer work was done by the physicists Kanter, Kinzel and Kanter [2] in 2002. They presented a new symmetric key exchange protocol which is based on the fast synchronization of two identically structured Tree Parity Machines (TPMs) [3]. The exchange protocol which is called as KKK schema is realized by a mutual adaptation process between two partners A and B, not involving large numbers and methods from number theory. The protocol is very simple to use [4] but effective in comparison with other commonly used cryptosystem, e.g. DES and RSA.

Unfortunately, there is no entity authentication in the neural cryptosystem. In the area of cryptography, authentication is an important step still before key exchange or even the encryption/decryption of information with an exchanged secret key [6]. In the original key exchange protocol, the structure of the network, the involved computations producing the output $O^A(t)/O^B(t)$, the adaptation-rule and especially the common inputs $\mathbf{x}_{kj}(t)$ are public. The only secrets involved are the different initial weights $\mathbf{w}^A_{kj}(t_0)/\mathbf{w}^B_{kj}(t_0)$ of the two parties. If they were not secret,

P. Li
Computational Intelligence Laboratory, School of Computer Science and Engineering, University of Electronic Science and Technology of China, Chengdu 610054, P.R. China
e-mail: tuxedolee21@hotmail.com

R. Wang et al. (eds.), *Advances in Cognitive Neurodynamics*,

the resulting keys could simply be calculated by an adversary, because all further computations are completely deterministic [7]. Markus etc. proposed two solutions [7] to the above problems: Authentication through secret common inputs and Embedding a Zero-Knowledge protocol. The basic idea of the two solutions is that they keep the common inputs $\mathbf{x}^A(t)/\mathbf{x}^B(t)$ secret between the two parties in addition to their individual secret (random) initial weights $\mathbf{w}^A(t_0)/\mathbf{w}^B(t_0)$. But it would conflict with the purpose of neural synchronization which is to generate symmetric secret key in public channel.

In this paper we propose a new attack strategy named as "Compound Attack" on TPMs which focuses on attack on entity authentication. The strategy incorporated with Denial of Service(DoS), Spoofing, Man-in-the-Middle(MitM) and Replay attack. In the following, we introduce the neural network structure and a learning algorithm in the section 'Neural Cryptography', then we propose the new attack strategy-Compound Attack in the section 'Compound Attack'. We give thorough explanation about Compound Attack. The letter concludes with a short summary in the section 'Conclusion'.

Neural Cryptography

We first briefly summarize the parallel-weights version of interacting neural networks. The anti-parallel-weights version, using anti-hebbian learning and leading to inverted weights at the other party, can be considered for our purpose as well but is omitted for brevity. The notation A/B denotes equivalent operations for the partners A and B. A single A or B denotes an operation which is specific to one of the parts. The TPM consists of K hidden units in a single hidden layer with non-overlapping inputs and a single unit in the output-layer. The particular tree structure has binary inputs, discrete weights and a single binary output. A TPM which consists of K hidden units σ_k with weight vectors $\mathbf{w}_k$ and input vectors $\mathbf{x}_k$ works like perceptron. The components of the input vectors are binary and the weights are discrete numbers with depths L, $x_{kj} \in \{-1, +1\}$, $w_{kj} \in \{-L, -L+1, \cdots, L-1, L\}$, where the index $j = 1, \cdots, N$ denotes the elements of each vector and $k = 1, \cdots, K$ the hidden units. The outputs of these neurons are defined by the scalar product of inputs and weights: $\sigma_k = sign(\mathbf{w}_k \cdot \mathbf{x}_k)$. The final output bit of each TPM is defined by the product of the hidden units: $O = \prod_{k=1}^{K} \sigma_k$. Both partners A and B initialize their weight vectors by means of random numbers before the training period starts. At each time step t a public input vector is generated and the bits O_A and O_B are exchanged over the public channel. In the case of identical output bits, that is, $O_A = O_B$. each TPM adjusts those of its weights for which the hidden unit is identical to the output,$\sigma_k^{A/B} = \tau^{A/B}$. These weights are adjusted according to a given learning rule. Here we consider the Hebbian rule: $\mathbf{w}_k^{A/B}(t+1) = \mathbf{w}_k^{A/B}(t) + O^{A/B}\mathbf{x}_k$. After some time t_{sync}, the two partners are synchronized, i.e. $\mathbf{w}_k^A(t) = \mathbf{w}_k^B(t)$, and the communication is stopped. Then the common weight vector is used as a key to encrypt secret messages.

Note that any possible attacker E knows as much about the process as A knows about B and vice versa. But E has some disadvantage with respect to A and B: it can only listen to the communication and cannot influence the dynamics of the weights in A's and B's neural networks. It turns out that this difference determines the security of the cryptosystem.

Compound Attack

In this part, we mainly analyze the new attack strategy named as "Compound Attack" which is different from the existing methods. It is well known that computer networks are vulnerable to DoS attacks [8] launched through compromised nodes or intruders. For the sake of destroying the neural cryptography, we also can consider attacking the communication between the partners A and B in public channel, besides those attacks which mimics the synchronization process of the coupled neural networks. We can easily make node A breakdown by means of DoS. Then we let node E just pretends as A, because there is no entity authentication in original neural cryptography, and we prove that there is no realizable authentication mechanism as mentioned above. So E could easily spoof node B into regarding E as A. Then E and B form a new neural cryptosystem and generate a shared secret key K_{EB} with neural synchronization method introduced above. For B, it still thinks that it has got a secret key with A (in fact it is E) and will use it consequently. We could get another secret key K_{EA} between E and A in the same way. Attacker E has the ability to position himself in the communication path of A and B. E spoofs the other part to each of the parts involved. Actually E can use MitM attack to capture all the communications between A and B. E captures and decrypts the message encrypted by A with K_{EA} and then encrypts the message just K_{EB} decrypted with and send the encrypted message to B. So there is no any confidentiality between A and B. Hence E could use other attacks such as replay attack to compromise A/B, i.e. E could store the messages from A to B, after a random time E could send them to B again. The replayed message will have unexpected effect on B. The compound attack proceeds as follows as a whole:

1. E makes node A breakdown by means of DoS;
2. E pretends as A and get shared secret key between E and B;
3. E makes node B breakdown by means of DoS;
4. E pretends as B and get shared secret key between E and A;
5. the MitM unwraps the messages received from A and forwards them to B after encryting them).

Let $EN_A(M)$ be that message M is encrypted by the key A using the encryption function $EN(\cdot)$ which is of one specific cryptosystem and $DE_A(M)$ be that message M is decrypted by the key A using the decryption function $DE(\cdot)$. We could present another attack scenario:

1. E makes node A breakdown by means of DoS;
2. E pretends as A and get shared secret key between E and B;
3. E could now fool B into doing something E'd like to do;

The key point that compound attack would succeed is that there is no entity authentication between A and B. So it is very easy to prevent such kind of attack conceptually. But just as we have mentioned before, entity authentication need another new secret key. This authentication which introduces a new second shared key will conflict with the purpose of neural cryptography. The purpose of neural synchronization is just to generate a shared secret key between A and B. It has to rely on the traditional cryptosystem to get the key required in the process of entity authentication.

We could see from above analysis:

– Neural cryptography without authentication is prone to be attacked;
– Entity authentication in neural cryptosystem is poorly implemented without the help of traditional cryptosystem;

In a word, it is very hard to get a shared secret key between two nodes securely according to our analysis and experiments. So the security of neural cryptography are in discuss and are expected to be improved. Due to this, its application is limited, although its advantages are remarkable.

Conclusion

In this paper, we present a new attack approach, which shows the TPM cryptosystem is not secure. This attack is focused on the entity authentication. The solution to this attack where another secret key is required is not applicable now. The question is whether we could create a more sophisticated system that will be secure under the attack we present. The secure system will provide a simple authentication scheme which is effective but no additional shared secret key required integrated into neural synchronization. Constructing such a system is still under our consideration. It is very challenging and valuable.

References

1. Metzler, R., Kinzel, W., and Kanter, I.: Interacting neural networks. Phys. Rev. E 62 (2000) 2555–2561.
2. Kanter, I., Kinzel, W. and Kanter, E.: Secure exchange of information by synchronization of neural networks. Europhys. Lett. 57 (2002) 141–147.
3. Volkmer, M. and Wallner, S.: Tree Parity Machine Rekeying Architectures. Proceeding of the 1st International Workshop on Secure and Ubiquitous Networks, SUN'05 (2005) 241–245.

4. Volkmer, M. and Wallner, S.: A Low-Cost Solution for Frequent Symmetric Key Exchange in Ad-hoc Networks. Proceedings of the 2nd German Workshop on Mobile Ad-hoc Networks, WMAN (2004) 128–137.
5. Ruttor, A., Kinzel, W. and Kanter, I.: Neural cryptography with queries. arXiv:cond-mat/0411374 v2 1 (2005).
6. Menezes, A. J., van Oorschot, P. C., and Vanstone, S. A.: Handbook of Applied Cryptography. CRC Press, 5th edition (2001).
7. Volkmer, M. and Wallner, S.: Authenticated tree parity machine key exchange. Preprint cs.CR/0408046 (2004).
8. Cheng, C., Kung, H. and Tan K.: Using of spectral analysis in defense against DoS attacks. Proceedings of IEEE GLOBECOM. Taipei (2002) 10–15.

Chapter 176
Two-Dimension Mass-Moment Control Based on the Fuzzy Neural Networks Variable Structure Control

Zhiqin Qian, Heng Cao, Ding Du, Zhengyang Ling, Di Cao and Yongbo Long

Abstract A new model with variable structure method is proposed to diminish chattering and to achieve accurate tracking for a class of nonlinear systems in the presence of disturbances and parameter variations. Compares to the common variable structure control, the new method can eliminate the chattering phenomenon efficiently and has more robustness while the bounds of the uncertainties and disturbances are not know in the controller design. Simulation results demonstrate the effectiveness of the method.

Keywords Multi-DOF · mass-moment · variable structure control · fuzzy · neural networks

Introduction

The variable structure control has the characteristics of fast response speed, low over shoot, high control accuracy and simple fabric. Compares to other control method, it has the extrude advance, especially the existence of sliding mode which provides more robustness while bounds of the uncertainties and disturbances are not know. Thus, the variable structure control system has broad applications in uncertain and time-variable nonlinear system.

A desirable variable structure control shall contain desirable switching mode. However, due to the impacts of inertia, time lag, delay in practical system, it is impossible to get the infinite switch frequency to perform ideal variable structure control in any practical systems. Besides, it will cause chattering dither.

Chattering dither is a big deficiency in the application of variable structure control, it degrades the quality performance. Moreover, it is easy to initiate the higher-order oscillation of model, at the same time it increases the consumption of

Z. Qian
East China University of Science and Technology, School of Mechanical and Power Engineering, Postbox 401, Postcode 200237 Shanghai, China
e-mail: qzq@ecust.edu.cn

R. Wang et al. (eds.), *Advances in Cognitive Neurodynamics*,

energy, even generates the devastating effects for systems, especially for mechanical systems.

At present, a two-dimension mass-moment experimental facility is used, when anti-ship missile space attitude control mode is investigated in the lab where the authors work. A kind of Fuzzy neural networks variable structure controllers are used to control the space attitude of two-dimension mass-moment.

Experiment System and Mathematical Model

The Hardware of Two-dimension Mass-Moment Experiment System

The system consists of a couple of I metal beams, the conjoint point of the two beams locates on their center, and the two beams perpendicular to each other. To locate the centre of gravity of the beams on the bracket to achieve the goal to balance, through assign the mass of beams properly.

Using three gyros to measure the angle of pitching, yaw angle and angle of bank of two-dimension mass-moment control experiment system.

The Mathematical Model of the Two-Dimension Mass-Moment

To establish the mathematical model of the system, the friction between beams and bracket and the air resistance of beams' movement need to be considered [1, 2, 3].

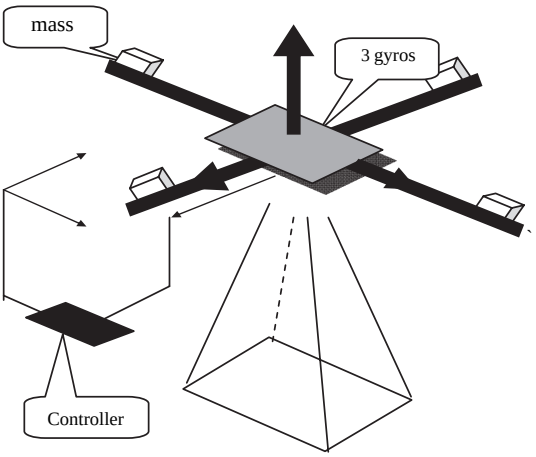

Fig. 176.1 Diagram of two-dimension mass moment control experiment system

Fig. 176.2 Photo of two-dimension mass moment

The Dynamics Equation of Beams Rotation

As shown in Fig. 176.1, It is supposed that the $ox_1y_1z_1$ is the set of coordinates of beams, where the two beams are matched with x_1 axis and x_2 axis respectively. Zero is on the pivot point. The $oxyz$ is the ground set of coordinates. These two coordinates match together before motion.

Because of the beams' symmetrical characteristic, the moment of inertia is $J_{x1} = J_{z1}$, and the product of the moment of inertia is: $J_{x1y1} = J_{y1z1} = J_{x1z1}$.

$$\begin{cases} \dot{\omega}_{x1} = \left[M_{x1} - (J_{z1} - J_{y1})\omega_{z1}\omega_{y1}\right]/J_{x1} \\ \dot{\omega}_{y1} = M_{y1}/J_{y1} \\ \dot{\omega}_{z1} = \left[M_{z1} - (J_{y1} - J_{x1})\omega_{y1}\omega_{x1}\right]/J_{x1} \end{cases} \tag{176.1}$$

Where $\omega_{x1}\omega_{y1}\omega_{z1}$ are the components of rotational speed on each axis of beam coordinates; J_{x1}, J_{y1}, J_{z1} are the moment of inertia on each axis of beam coordinate; M_{x1}, M_{y1}, M_{z1} are the components of resultant moment which are the beams act on each axis of coordinates.

The Kinematics Equation of Beams Rotation

There will be three attitude angles, while the beams rotate around the barycenter. There are pitch angle θ, yaw angle ψ and angle of bank γ, motion equations of correspondence is:

$$\begin{cases} \dot{\theta} = \omega_{y1}\sin\gamma + \omega_{x1}\cos\gamma \\ \dot{\psi} = (\omega_{y1}\cos\gamma - \omega_{x1}\sin\gamma)/\cos\theta \\ \dot{\gamma} = \omega_{x1} - tg\theta(\omega_{y1}\cos\gamma - \omega_{x1}\sin\gamma) \end{cases} \tag{176.2}$$

c. Aerodynamic force F_{x1}, F_{y1}, F_{z1}, and moment of composite $M_{x1}M_{y1}M_{z1}$:

$$\begin{cases} F_{x1} = K_{x1}(\gamma^* - \gamma) \\ F_{y1} = K_{y1}(\psi^* - \psi) \\ F_{z1} = K_{z1}(\theta^* - \theta) \end{cases} \tag{176.3}$$

$$\begin{cases} M_{x1} = K_{x1}l - f_{x1}\dot{\gamma} \\ M_{y1} = K_{y1}l - f_{y1}\dot{\psi} \\ M_{z1} = K_{z1}l - f_{x1}\dot{\theta} \end{cases} \tag{176.4}$$

Where F_{x1}, F_{y1}, F_{z1} are the beams' aerodynamic force rolling motion, yawing, and pitching; γ^*, ψ^*, θ^* are the ideal pitch angle, yaw angle and angle of bank; f_{x1}, f_{y1}, f_{z1} are the damp coefficient; l is the length of beam; K_{x1}, K_{y1}, K_{z1} are three pathways of gyro's gain.

Fuzzy Neural Network's Variable Structure Controller

Variable Structure Design

The system as described in preamble:

$$\begin{cases} x_i(t) = x_{i+1}(t) \\ \dot{x}_n(t) = f[X(t)] + g[X(t)]u(t) \\ i = 1, \ldots, n \end{cases} \tag{176.5}$$

Where $X(t) = [x_1, \ldots, x_n]$ is the determinable state variable, $f[X(t)]$, $g[X(t)]$ is the glossy indeterminacy function, which have unique solution. Choose a kind of variable structure model (manifold):

$$S[X(t)] = x_n(t) + \sum_{i=1}^{n-1} c_i x_i(t) = 0 \tag{176.6}$$

Where c_i is positive constant ($i = 1, \ldots,$ n), we can get the proper polynomial $P(z) = z_n + c_n z^{n-1} + \ldots + c_1$, its root has minus real part.

Where the single-order and second-order derivative of $S[X(t)]$ are:

$$\dot{S}[X(t)] = \dot{x}_n(t) + \sum_{i=1}^{n-1} c_i \dot{x}_i(t) = f[X(t)] + g[X(t)]u(t) + \sum_{i=1}^{n-1} c_i x_{i+1}(t) \quad (176.7)$$

$$\begin{aligned}\ddot{S}[X(t)] &= \frac{d}{dt} f[X(t)] + \frac{d}{dt} g[X(t)]u(t) + \sum_{i=1}^{n-2} c_i x_{i+2}(t) \\ &\quad + c_{n+1}[f[X(t)] + g[X(t)]u(t)] + g[X(t)]\dot{u}(t) \\ &= f[X(t), u(t)] + g[X(t)]\dot{u}(t) \end{aligned} \quad (176.8)$$

Suppose the input of the system is r, the system error is e_r and then the system equations is:

$$e_r = r - x_1; \quad \dot{e}_r = \dot{r} - \dot{x}_1 \quad (176.9)$$

Where r, $\dot{r}$(Suppose $\dot{r} = 0$) is expectation value.

Design of Fuzzy Neural Networks Variable Structure Controller

T-S fuzzy neural networks (FNN) (as shown in Fig. 176.3) instead of the uncertain dynamic characteristics f(*) and g(*). And then build- up the control rules according to generality variable structure control [4, 5].

Apply $(s, \dot{s})$ to the upper bound of standard FNN real time system input.

Establish two FNN, one FNN $(e, \dot{e})$ as controller, another as an identifier of object model. Its parameter is regulated by the error of object real output. During the procedure of controlling, check up if the condition of variable structure control has

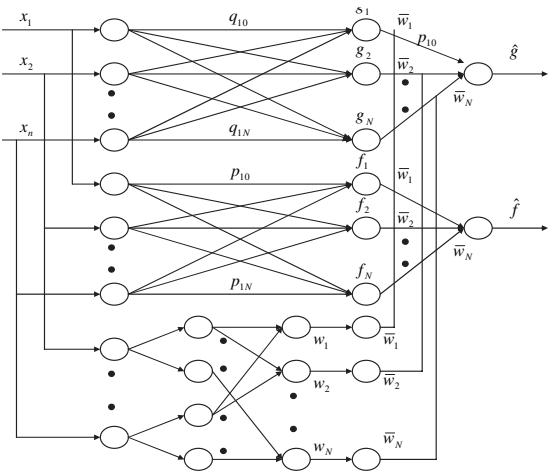

Fig. 176.3 T-S fuzzy neural networks

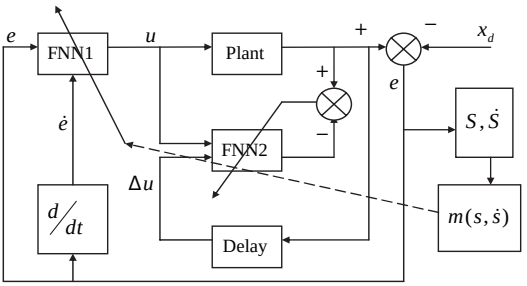

Fig. 176.4 A VSC (variable structure control) scheme based on fuzzy neural networks

been satisfied after gain the change of variable structure control function. Hereby, gain the symbol correction function m(s). And then the object identifier and m(s) result the control gain Δu. We use Δu to regulate the parameter of FNN(e, $\dot{e}$). The whole control flow chart is as shown in Fig. 176.4.

Simulation

Take the pitch pathway for example to process simulation research.

Let the simulation parameter: $c_a = 70$, $c_b = 6.66$, $k = 70$, $\psi = 0.09$, $K_f = 1.96$, $K_G = 0.5$, $a_2 = 3.5037$, $b = 2.3518$, $\theta^* = 2^\circ$, $\tau = 0.0015$ s, l = 1 m, $f_{x1} = 1.46 N^*$ m* s, $J_{x1} = 0.4167$ kg* m^2.

The result of simulation is shown below:

Figure 176.5 shows that tracking error of FNN with VSC (variable structure control) is closer to zero than Fig. 176.6. And the characteristic of FNN with variable structure control in Fig. 176.7 is much less disturbances than Fig. 176.8. Therefore the fuzzy neural networks variable structure control can eliminate the chattering phenomenon efficiently and has more robustness.

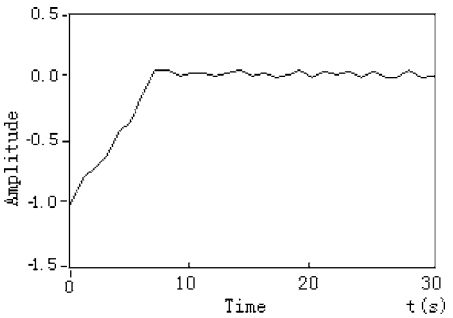

Fig. 176.5 Tracking error of FNN with VSC

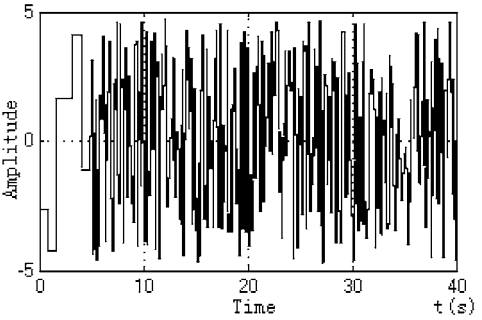

Fig. 176.6 Tracking error of VSC

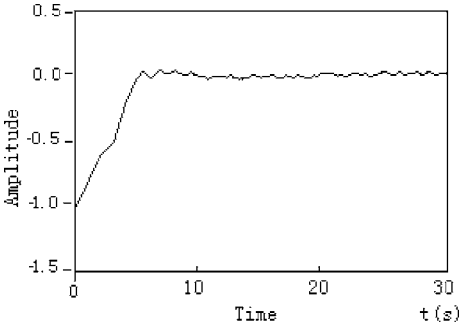

Fig. 176.7 Characteristic of FNN with VSC

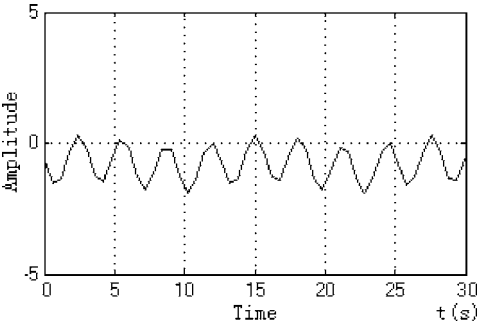

Fig. 176.8 Characteristic of VSC

Conclusion

The structure and operation of FNN variable structure control is simple, combine the characteristics of FNN independence to the model and robustness of variable structure control. To switch the control goal according to the principle of variable structure control. This method has desirable control effect, strong robustness and is easy to implement.

References

1. K.K. Shyu, Y.W. Tsai, C.K. Lai: A dynamic output feedback controller for mismatched uncertain variable structure systems. Automatica, 37, (2001) 775–779.
2. Z. Jiang, Y. Wang: Input-to-state stability for discrete-time nonlinear systems. Automatica, 37, (2001) 857–869.
3. R. Ordonez, K.M. Passmo: Control of discrete time nonlinear systems with a time-varying structure. Automatica, 39, (2003) 463–470.
4. S. Tong, T. Wang, H. Li: Fuzzy robust tracking control for uncertain nonlinear systems. International Journal of Approximate Reasoning, 30, (2002) 73–90.
5. Y.W. Cho, C.W. Park, M. Park: An indirect model reference adaptive fuzzy control for SISO Takagi-Sugeno model. Fuzzy Sets and Systems, 131, (2002) 197–215.

Chapter 177
Constructive Approximation Method of Polynomial by Neural Networks

Jianjun Wang, Zongben Xu and Jia Jing

Abstract This paper investigates that for a given polynomial with r order, a three-layer feedforward neural networks with determinate weights and the number of hidden-layer nodes can be established by a constructive method to approximate the polynomial to any degree of accuracy. And we give algorithmic examples, where the networks constructed can very efficiently approximate polynomial. Specifically, the network constructed and the realization of algorithm obtained are simpler and more efficient than those of the reference [Chinese Journal of computers 26: 906–912, 2003].

Keywords Approximation · feedforward neural networks · polynomial

Introduction

In the recent years, many researchers have done many researches on the problems in the artificial neural networks and gain a series of results. Nowadays, the artificial neural networks have widely been involved in studying problems in a variety of field, such as biology, mechanical engineering, electrical and computer engineering, computer science, and physics, etc. Why is so is mainly because the feedforward neural networks (FNNs) have the universal approximation capability [1, 2, 3]. A typical example of such universal approximation assertions states that for any given continuous function defined on a compact set $\mathbf{K}$ of $\mathcal{R}^d$, there exists a three-layer of FNNs so that it can approximate the function arbitrarily well. A three-layer of FNNs with one hidden layer, d inputs and one output can be mathematically expressed as

$$\mathcal{N}(x) = \sum_{i=1}^{m} c_i \phi \left(\sum_{j=1}^{d} w_{ij} x_j + \theta_i \right), \quad \mathbf{x} \in \mathcal{R}^d, \ \ d \geq 1. \tag{177.1}$$

J. Wang
The School of Mathematics & Statistics, Southwest University, Chongqing 400715, P.R. China
e-mail: wjj@swu.edu.cn

R. Wang et al. (eds.), *Advances in Cognitive Neurodynamics*,

Here $1 \le i \le m$, $\theta_i \in \mathcal{R}$ are the thresholds, $w_i = (w_{i1}, w_{i2}, \ldots, w_{id})^T \in \mathcal{R}^d$ are connection weights of neuron i in the hidden layer with the input neurons, $c_i \in \mathcal{R}$ are the connection strength of neuron i with the output neuron, and ϕ is the activation function used in the network. As we known, how to design the structure of FNNs make that it has capability of learning a given function, which is a important and fundamental question. The polynomial is the most simple and elementary function. In the past a few years, the question of approximating algebraic polynomial by FNNs had some works (see [4, 5]), here we will adopt a new,simple and constructive method different the past method to prove approximation of univariate polynomials by FNNs, and the networks constructed can very efficiently approximate polynomial.

Main Result

Let r be a fixed integer and

$$\mathcal{P}_r(x) = a_0 + a_1 x + \cdots + a_r x^r, \quad x \in \mathcal{R} \tag{177.2}$$

be a univariate polynomial of degree r defined on [a,b]. We will consider neural networks approximation problem in this paper confined to a special type of neural activation functions Υ_M of which each function $\phi : R \to [0, 1]$ has up to $M+1$ order continuous derivatives ϕ^k, $k = 1, 2, \ldots, M+1$, the derivative functions ϕ^k all have bounded range, and there is a common point, say $\theta_0 \in R$, such that $\phi^k(\theta_0) \neq 0$ for all $1 \le k \le M+1$. Such neural activation functions are abundant, as substantiated by the normal sigmoidal functions $\phi(x) = (1 + e^{\alpha x})^{-1}$ with any $\alpha > 0$ (see [6]). For $p \ge 1$, we denote by $L^p_{2\pi}([a, b])$ the space of pth-order Lebesgue integrable functions on $[a, b]$ to R with $\|f\|_p = \{\int_a^b |f(x)|^p dx\}^{1/p}$ and by $C_{[a,b]}$ the space of continuous functions on $[a, b]$ to R with $\|f\|_\infty = \sup_{x\in[a,b]} |f(x)|$. For convenience, we denote by $L^\infty([a, b])$ the space $C_{[a,b]}$. The main result is the following Theorem.

Theorem. *Let $\phi \in \Upsilon_M$ a neural activation function and $\mathcal{P}_r(x)$ a univariate polynomial of the form (2). Then for any $1 \le p \le \infty$ and $\varepsilon > 0$, there is a neural network of the form (177.1) the number of whose hidden units is not less than $\sum_{0\le j\le r} (j + 1) = (r + 1)(r + 2)/2$(independent of ε), such that*

$$\|\mathcal{N}_n - \mathcal{P}_r\|_p < \varepsilon, \tag{177.3}$$

where

$$N_n(x) = \sum_{0\le j\le r} \sum_{0\le i\le j} c_{i,j}\phi(wx + \theta), \tag{177.4}$$

$$w = h(2i - j), \quad c_{i,j} = a_j \frac{1}{\phi^{(|j|)}(\theta)}(2h)^{-j}(-1)^i \binom{j}{i}.$$

Proof. First we prove the Eq. (177.3) for $p = \infty$ in [a,b]. Let $M_1 = \max\{|a|, |b|\}$, Since $\phi^{(j)}(wx+\theta) \doteq \frac{\partial^{|j|}}{\partial\omega^{|j|}}[\phi(wx+\theta)] = x^j\phi^{(|j|)}(wx+\theta)$, so we have $\phi_{j,x}(\theta) \doteq \phi^{(j)}(\omega x+\theta)|_{\omega=0} = x^j\phi^{(|j|)}(\theta)$, hence $x^j = \frac{\phi_{j,x}(\theta)}{\phi^{(|j|)}(\theta)}$. Then we have $p_r(x) = \sum_{0\le j\le r} a_j \frac{\phi_{j,x}(\theta)}{\phi^{(|j|)}(\theta)}$. For any fixed $\theta \in R$, we consider the following finite j-th order difference, $\triangle^j_{h,x}\phi(\theta) = \sum_{0\le i\le j}(-1)^i\binom{j}{i}\phi(h(2i-j)x+\theta)$. By using of the triangle inequalities and the representation of difference, we have

$$\begin{aligned}
&\left|p_r(x) - \sum_{0\le j\le r} a_j \frac{1}{\phi^{(|j|)}(\theta)}(2h)^{-j}\triangle^j_{h,x}\phi(\theta)\right| \\
&\quad\le \sum_{0\le j\le r}|a_j|\frac{1}{|\phi^{(|j|)}(\theta)|}\left|\phi_{j,x}(\theta) - (2h)^{-|j|}\triangle^j_{h,x}\phi(\theta)\right| \\
&\quad= \sum_{0\le j\le r}|a_j|\frac{1}{|\phi^{(|j|)}(\theta)|}x^j\left|(2h)^{-j}\int_{-h}^{h}\int_{-h}^{h}\cdots\int_{-h}^{h}\phi^{(|j|)}(\theta)d\tau_1 d\tau_2\cdots d\tau_j\right. \\
&\qquad\left. - (2h)^{-j}\int_{-h}^{h}\int_{-h}^{h}\cdots\int_{-h}^{h}\phi^{(|j|)}(\theta+(\tau_1+\tau_2+\cdots+\tau_j)x)d\tau_1 d\tau_2\cdots d\tau_j\right| \\
&\quad\le \sum_{0\le j\le r}|a_j|\frac{1}{|\phi^{(|j|)}(\theta)|}x^j L(\phi^{(|j|}, 2M_1 jh) \le 2M_1 h\sum_{0\le j\le r}|a_j|jM_1^j\frac{\|\phi^{(|j|+1)}\|_\infty}{|\phi^{(|j|)}(\theta)|}.
\end{aligned} \tag{177.5}$$

Here $L(\phi,\delta) = \sup_{|t-x|<\delta}\left|\phi(x)-\phi(t)\right|$(see [7]) is continuous modulus of function ϕ, and when the function ϕ has continuous derivative, we have $L(\phi,\delta)\le\delta|\phi'|_\infty$.

Let $M_0 = \max\left\{|\phi^{(i)}(\theta)|, i = 0,1,\cdots,r+1\right\}$, we have

$$\left|p_r(x) - \sum_{0\le j\le r} a_j \frac{1}{\phi^{(|j|)}(\theta)}(2h)^{-j}\triangle^j_{h,x}\phi(\theta)\right| \le Mh \tag{177.6}$$

where $M = 2M_1M_0\sum_{0\le j\le r}\frac{|a_j|j}{|\phi^{(|j|)}(\theta)|}M_1^j$. By using of the Eqs. (177.5) and (177.6), we can construct neural networks (4). From the Eq. (177.6), we get $\left|p_{\mathbf{r}}(\mathbf{x}) - N_n(\mathbf{x})\right| \le Mh$, and set $h < \frac{\varepsilon}{M}$, then $\left|p_{\mathbf{r}}(\mathbf{x}) - N_n(\mathbf{x})\right| < \epsilon$. That is (3) is valid for $p = \infty$.

For $1 \le p < \infty$, from the conclusion of $p = \infty$, we can easily prove it. As for the number of hidden units of the networks constructed, we can easily obtain that is $\sum_{0\le j\le r}(j+1) = \frac{(r+1)(r+2)}{2}$ from (4).

Example

In this section show two examples of the networks approximation method proposed in the paper. we take two polynomial functions $f = 1-3x$ and $g = 1/2 + 3/4x^3 + 1/2x^4$ to testify our results. A plot of the error function $|N-f|$ is shown in Fig. 177.1a, in addition, we give the error function of the reference [5]

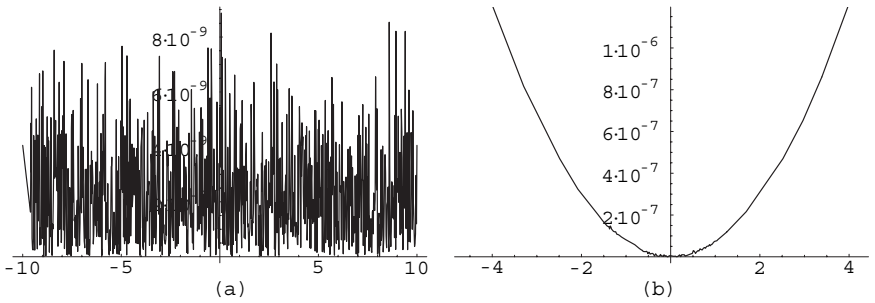

Fig. 177.1 (a) Error function between the function $1 - 3x$ and the networks $N_3(x)$ we constructed($h = 10^{-7}$); (b) Error function between the function $1 - 3x$ and the networks $N(x)$ in [5] ($h = 10^{-7}$)

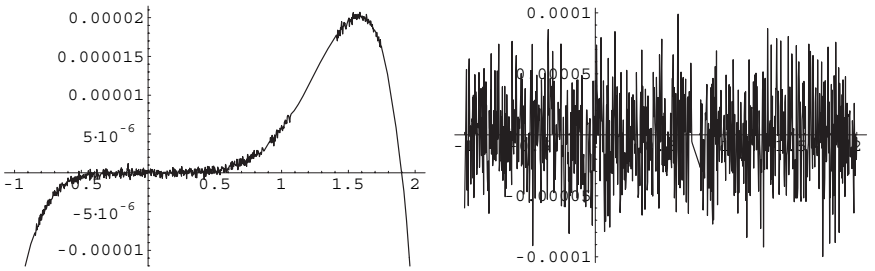

Fig. 177.2 Error between the function $1/2 + 3/4x^3 + 1/2x^4$ and the networks $N_{10}(x)$ we constructed in$[-1,2]$ when $h = 10^{-2.5}$ and $h = 10^{-3}$, respectively

in Fig. 177.1b. Obvious, our results is better than that of [5]. Figure 177.2 show that the error between the polynomial $1/2 + 3/4x^3 + 1/2x^4$ defined on $[-1, 2]$ and the networks we proposed in the condition of $h = 10^{-2.5}$ and $h = 10^{-3}$.

Acknowledgements This work was supported by Southwest University (China) Doctor Foundation (SWUB2007006).

References

1. Cybenko, G.: Approximation by superpositions of a sigmoidal function. Math. Contr. Signals Syst. 2(1989) 303–314.
2. Chen, T.P., Chen, H.: Universal approximation to nonlinear operators by neural networks with arbitrary activation functions and its application to a dynamic system. IEEE Trans. Neural Netw. 6(1995) 911–917.
3. Chen, T.P.: Approximation problems in system identification with neural networks. Science in China, Series A 24(1)(1994) 1–7.
4. Attali, J.G., Pages, G.: Approximation of functions by a multilayer perceptron: a new approach. Neural Netw. 10(1997) 1069–1081.

5. Cao, F.L., Xu Z.B., Liang J.Y.: Approximation of ploynomial functions by neural networks: construction of network and algorithm of approximation. Chinese Journal of Computers 26(8)(2003) 906–912.
6. Xu Z.B., Cao, F.L.: Simultaneous L^p-Approximation order for neural networks. Neural Netw. 18(2005) 914–923.
7. Timan, A.F.: Theory of approximation of functions of a real variable. New York: Macmillan (1963).

Chapter 178
Fault Pattern Recognition Based on Improved Wavelet Neural Network

Deng-Chao Feng, Zhao-Xuan Yang and Zeng-Min Wang

Abstract The basic principle of wavelet neural network is analyzed and the learning algorithm is improved as well. Correspondingly, fault pattern recognition model is constructed based on improved wavelet neural network. Simulation experiment shows that improved wavelet neural network has good fault-tolerant capacity and global convergence. However, how to establish an objective criterion of parameter settings and enhance the real time capability of fault pattern recognition still need further research.

Introduction

With the development of the industrial processes, the problems on security and reliability are getting more and more serious. Accordingly, the research and application of intelligent fault diagnosis algorithm has positive significance. Due to the capability of simulating arbitrary nonlinear continuous function and self-learning capability, artificial neural network [1] has been widely used in fault diagnosis field. However, the initialization of network parameters and the construction of neural network lack of effective theory guidance in actual operation. WNN (Wavelet neural network) introduced by Zhang Qinghua [2] is a new feedforeward neural network with strong non-linear approach capability and fault-tolerant capability [3].

On the basis of traditional WNN, improved wavelet neural network based on ant colony algorithm [4] is constructed in the paper and applied in fault pattern recognition. The simulation experiment shows the validity of the algorithm.

D.-C. Feng
Institute of Electronic and Information Engineering, Tianjin University, Tianjin 300072, P.R. China
e-mail: tyfdc001@163.com

R. Wang et al. (eds.), *Advances in Cognitive Neurodynamics*,

Improved Wavelet Neural Network

As a new feedforward neural network, wavelet neural network (WNN) can be classified into relax-type and close-type [5]. The close-type WNN is constructed in the paper and the corresponding formula is as follows:

$$y_i(t) = f\left(\sum_{j=0}^{n} w_{ij}\psi_{a,b}\left(\sum_{k=0}^{m} w_{ik}x(t)\right)\right) \quad (i = 1, 2, \ldots, N) \tag{178.1}$$

where, $f(.)$ is the linear function of output layer, x_k is the kth input sample, y_i is the ith output value of output layer, w_{ij} is the weight between output layer unit i and hidden layer unit j, w_{jk} is the weight between hidden layer unit j and input layer unit k, $N(i = 1, 2, \ldots, N)$ is the output layer number, $\psi_{a,b}$ is the wavelet function, a_j and b_j are the scale coefficient and translation coefficient in the jth hidden layer unit respectively. The minimum value of the error energy function can be obtained through adjustment of network parameters.

The gradient descent method is often adopted to optimize network parameters. However, a local minimization problem is easily to occur as well [5]. The combination of ant colony algorithm and WNN has a good learning character by virtue of the good property of time-frequency localization of wavelet transform, self-learning function of neural network and the heuristic study of ant colony algorithm. Therefore, improved ant colony algorithm is proposed to train WNN in the paper.

The optimization learning process is as follows. Firstly, the parameters of WNN, namely w_{jk}, w_{ij}, a_j, b_j, will be transformed to the city matrix in TSP problem [6]. According to the selection rules of the shortest path, the parameters of WNN can be transformed to column vector. Then, a random column vector will be produced by virtue of Matlab function. The coordinate matrix C in TSP problem is produced by the above two column vector. Finally, the optimization of network parameters can be realized by virtue of the similar algorithm of solving TSP problem. In pheromone update stage, accumulated error σ_{n} is used to update the pheromone and the corresponding formula of it is as follows:

$$\sigma_n = \sqrt{\sum_{i=1}^{m} (e_i - \overline{e})^2 / m} \tag{178.2}$$

where m is the number of sample data, e_i is the absolute error and $\overline{e}$ is the mean absolute error. Correspondingly, the pheromone increment at route (i, j) is as follows:

$$\Delta\tau_{ij}(C_i)(n) = \sum_{k=1}^{m} \Delta\tau_{ij}^{k}(C_i)(n) = \begin{cases} Q/\sigma_n & \text{if } C_i \text{ is selected} \\ 0 & \text{otherwise} \end{cases} \tag{178.3}$$

However, when the scale of problem is large enough, the optimization learning algorithm based on ant colony algorithm will inevitably effect the global search capability by pheromone volatilization factor ρ [7]. Therefore, the adaptive selection algorithm for ρ is adopted as follows:

$$\rho(t) = \begin{cases} 0.95\rho(t-1) & 0.95\rho(t-1) \geq \rho_{\min} \\ \rho_{\min} & \text{otherwise} \end{cases} \tag{178.4}$$

When all ants finish the optimization of the shortest path, the parameters of wavelet neural network w_{jk}, w_{ij}, a_j, b_j can be selected from the first column vector according to the principle of dimension matching.

Construction of Fault Pattern Recognition

The essence of fault pattern recognition is to find the hidden order in fault space and to execute the discrimination and prediction for mechanical running condition, namely to realize the data mapping from fault eigenvector to fault state. The improved WNN with adaptive learning mechanism has better robustness for uncertainty factor, noise and imperfection of input. Therefore, it can be used in the construction of fault pattern recognition.

As shown in Fig. 178.1, the fault pattern recognition model can be constructed by the improved WNN. The input layer code corresponds to fault symptom, the hidden layer takes wavelet function as activation function, and the output layer node

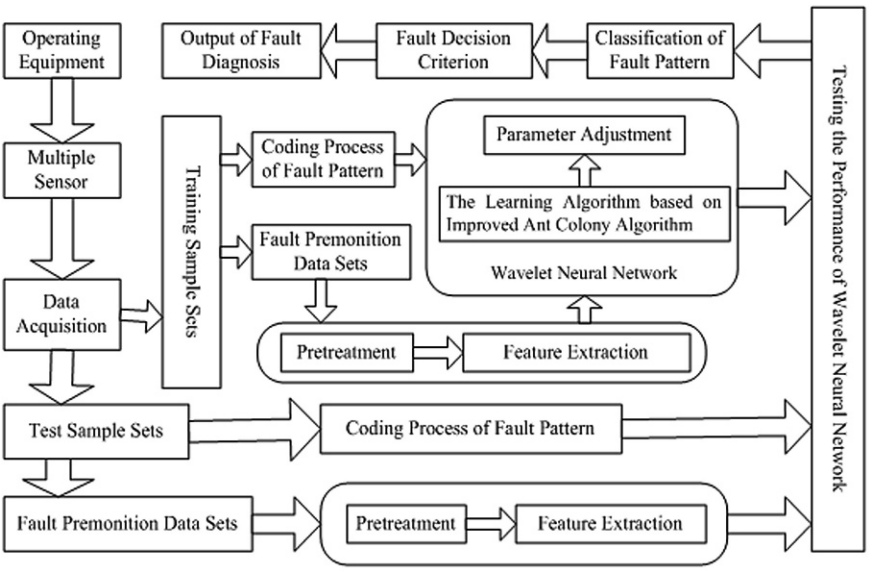

Fig. 178.1 Construction of fault pattern recognition based on improved WNN

corresponds to fault reason. Firstly, a group of fault data is trained in improved WNN by the learning algorithm based on ant colony algorithm to obtain the expected neural network. The wavelet network parameters can be obtained after training. Then, a group of new fault symptom data is given to realize the nonlinear mapping from fault symptom sets to fault classification sets. The training results by network testing will be saved in the knowledge base of fault classification. In order to offer proper input and training sample of fault classification, the original data and training sample data will be processed properly before learning and classification. The process includes data preprocessing and feature extraction. Finally, the testing sets will be adopted to monitor the training effect and generalization capability of fault classification model.

Results and Analysis of Simulation Experiment

In simulation experiment, fault data is adopted by reference [8]. In order to verify the robustness of the algorithm, BP network, traditional WNN and improved WNN proposed in the paper are adopted respectively in fault pattern recognition under the circumstance of MATLAB7.0. Statistical results for original eigenvector are shown in Table 178.1

In order to improve the recognition precision, Z-score [9] is adopted to transform the original eigenvector to the normalization and standardization of scores. The Z-score for original fault eigenvector are shown in Fig. 178.2.

In fault pattern recognition model, fault space includes five kinds of fault state, namely normal state, fault state 1, fault state 2, fault state 3 and fault state 4. Correspondingly, the fault code is $\{0, 0, 0, 0\}$, $\{1, 0, 0, 0\}$, $\{0, 1, 0, 0\}$, $\{0, 0, 1, 0\}$ and $\{0, 0, 0, 1\}$, respectively. In BP neural network, the structure of network is 5-11-4, and the leaning algorithm is gradient descent method based on momentum. S-type tangent function and logarithm function are selected as activation functions of the hidden layer and output layer respectively. The maximum training time is 1000, the learning rate is 0.01 and the error precision is 0.01. In traditional WNN, morlet wavelet function is adopted in hidden layer, and other parameters are the same with those of BP network. In improved WNN, the structure is the same as WNN, while the learning algorithm adopted is ant colony algorithm. The number of ant is 120, $a = 1, \beta = 5, \rho_0 = 0.1$, Q $= 100$, the maximum cycle iteration is 1000. The original values of weight, translation factor and scale factor are adopted by random function.

Table 178.1 Descriptive statistics for fault sample data

Eigenvector	*N*	Minimum	Maximum	Mean	SD
Peak index	20	4.19	12.45	8.2325	2.84235
Waveform index	20	1.23	2.16	1.5765	0.31749
Pulsed index	20	5.63	25.60	13.0485	7.13944
Margin index	20	6.58	36.75	17.7690	10.71371
Kurtosis index	20	3.01	9.71	5.8350	2.68306
Valid *N* (listwise)	20				

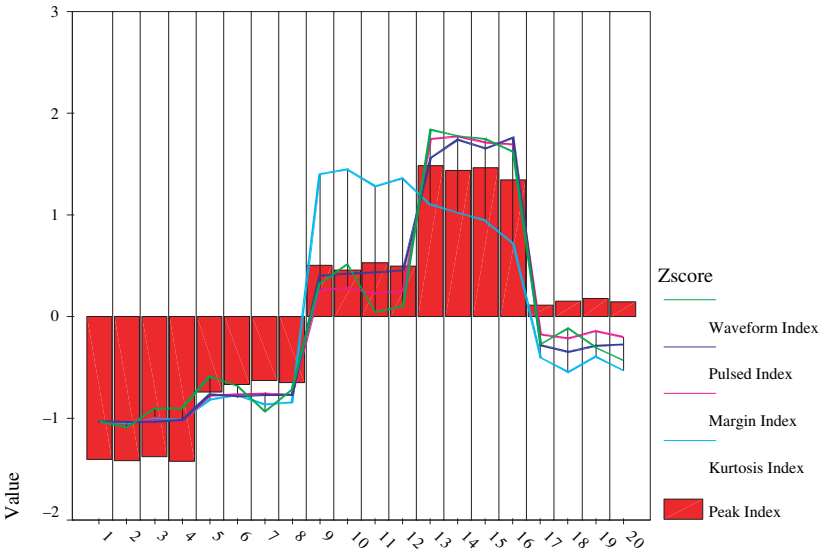

Fig. 178.2 Z-Score of original fault eigenvector

In simulation experiment, the above three kinds of neural network are applied in fault pattern recognition, where original fault eigenvector and Z-score eigenvector are adopted as input vector respectively. Due to the random selection of network parameters, the output vector and iteration number in network performance are different each time. Although all the above neural network can realize fault pattern recognition, the output errors are different as well. After running for many times, the performance evaluation of fault pattern recognition were done in these different network. According to Euclid norm theory [9], output errors can be obtained and the corresponding statistic analysis for them is shown in Fig. 178.3.

The statistical analysis of output error shows the small range and standard deviation can be obtained with Z-score method, which means the less data fluctuation. Comparison of the above three algorithm, the minimum value of range and standard deviation was obtained by improved WNN respectively, which means the smallest data fluctuation and the maximum approaching probability.

The above simulation experiment results show that, the fault diagnosis model constructed by BP network could easily cause slow convergence speed and local minimum problem. Training results also show that, it is sensitive to initial value and could easily cause the oscillation phenomenon. Compared with BP network, the convergence speed of traditional WNN is faster, but it still has some similar problems with those in BP network. The algorithm proposed in the paper effectively overcomes the local minimum problem and improves the fault classification precision. However, the parameter selection of improved WNN is still based primarily on knowledge gained from experiences. Therefore, how to establish an objective criterion of parameter settings is still an urgent problem waiting to be solved effectively.

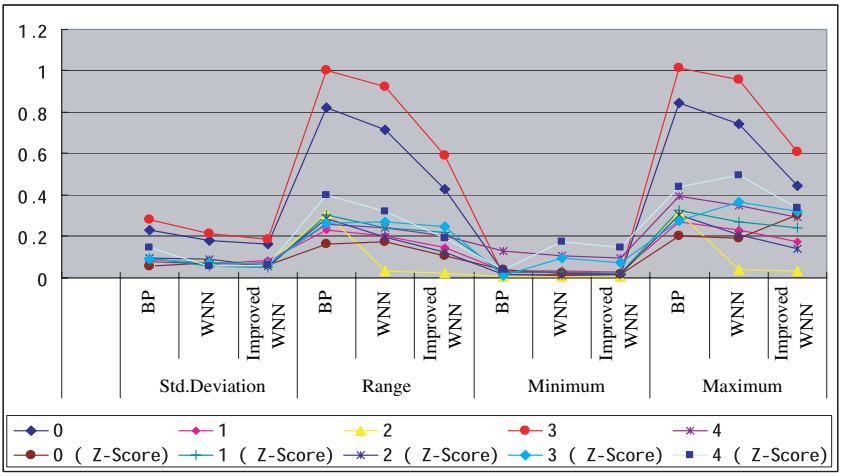

Fig. 178.3 Statistics results of output error

Conclusion

The application of fault pattern recognition technique can avoid equipment failure and reduce the maintenance cost in automatic production line. Improved wavelet neural network proposed in the paper has dual characteristics of ant colony algorithm and wavelet neural network, so, it has a great application prospect in fault pattern recognition. However, how to establish an objective criterion of parameter settings and choose the best combination point between the fault classification precision and running time in order to enhance the real time capability of the network still need further research.

Acknowledgements This work was supported by the Major Project of Tianjin Natural Science Fund under Grant No. 07JCZDJC05800.

References

1. Yan, P.-F., Zhang, C.-S.: Artificial Neural Networks and Evolutionary Computing. 2nd edn. Tsing Hua University Press, Beijing (2005).
2. Zhang, Q.-H., Benveniste, A.: Wavelet Networks. IEEE Transactions on Neural Networks 3(6) (1992) 889–898.
3. Zhang, H., Wu, B.: Research and Prospects of Wavelet Neural Networks. Journal of Southwest China Institute of Technology 17(1) (2002) 10–12.
4. Dorigo, M., Maniezzo, V., Colorni, A.: Ant System: Optimization by A Colony of Cooperating Agent. IEEE Transactions on Systems, Man, and Cybernetics 26(1) (1996) 29–41.
5. Feng, D.-C., Yang, Z.-X., Qiao, X.-J.: The Application of Wavelet Neural Network with Orthonormal Bases in Digital Image Denoising. In: Wang, J., et al. (eds.): ISNN2006. Lecture Notes in Computer Science, **3972**. Springer-Verlag, Berlin Heidelberg New York (2006) 539–544.

6. Dorigo, M., Gambardella, L.M.: Ant Colony System: A Cooperative Learning Approach to The Traveling Salesman Problem. IEEE Transactions on Evolutionary Computation 1(1) (1997) 53–66.
7. Duan, H.-B.: Ant Colony Algorithms: Theory and Applications. 1st edn. Science Publishing House, Beijing (2005) 33–36.
8. Zhang, J., Lu, S.-L., He, W.-X., et al.: Vibrating Diagnosis of Rolling Bearings Based on Back-propagation Neural Network. Light Industry Machinery 25(2) (2007) 90–92.
9. Jia, J.-P., He, X.-Q., Jin, Y.-J.: Statistics. 3rd edn. Renmin University of China Press, Beijing (2007).

Chapter 179
Estimation of the Flooded Volume in *Ad Hoc* Networks Using Evolving Networking Theory

Demin Li, Jie Zhou and Jiacun Wang

Abstract Since mobile nodes in mobile ad hoc network may spread in an arbitrary manner, one of the fundamental issues is how to enhance flooded volume in a mobile ad hoc network. In this paper, we model the flooded volume in mobile ad hoc network using Watts–Strogatz (W–S) evolving networking theory, and get the result that if some conditions for observer gain constant are satisfied, the total volume of the flooded nodes can be estimated.

Keywords Watts-Strogatz evolving model · flooded volume · flooded node · mobile *ad hoc* network

Introduction

Mobile ad hoc networks (MANET) are decentralizing, self-organizing, and highly dynamic networks formed by a set of mobile hosts connected through wireless links, without requiring any fixed infrastructure. If the destination node is not within the transmission range of the source node, the source node takes help of the intermediate nodes or routers to communicate with the destination node. Civilian applications include peer-to-peer computing and file sharing, collaborated computing, and searching rescue operations. Military applications include battle-fields among a fleet of ships, a group of armored vehicles or a large of military aircraft. With the rapid progress of wireless ad hoc networks and embedded micro-sensing technologies, those applications make possible and wide.

Since mobile nodes may spread in an arbitrary manner, one of the fundamental issues is how to enhance flooded volume in a mobile ad hoc network. Watts and Strogatz [1] described a basic evolving mechanism for collective dynamics of small world network. The discoveries of small-world phenomena in many complex networks have led to a fascinating set of common problems [2, 3]. After proposing a

Demin Li
College of Information Science and Technology, Donghua University, Songjiang District, Shanghai 201620, China
e-mail: deminli@dhu.edu.cn

R. Wang et al. (eds.), *Advances in Cognitive Neurodynamics*,

novel Watts–Strogatz spreading model, which captures the general spreading mechanism in small-world networks [4], investigated the stability and Hopf bifurcations of delay-controlled spreading models with linear and nonlinear feedback controllers, where parameters of small-world rewiring probability, feedback control gain, and time delay are analyzed for the oscillating behaviors. But to best our knowledge, we can not find any results to estimate the flooded volume in ad hoc networks using evolving networking theory.

The remainder of the present paper is arranged as follows. The basic model is formulated in section 'Problem Formulation and Basic Model' for ad hoc network flooded volume. In section 'Main Results', main results for constant delay time-varying delay are given. Finally, some concluding remarks are drawn in section 'Conclusions'.

Problem Formulation and Basic Model

The random rewiring in the W–S model for the propagation process means that, each time the infective node spreading through the forthcoming edge in the nearest-neighbor ring may be linked with another node through the rewired long-range connection with probability $0 \leq p \leq 1$. Therefore, the total volume of infected individuals $V(t)$ in a d-dimensional W–S evolving network grows as a sphere of radius time t and surface $(1-p)\Gamma_d t^{d-1}$. At the same time, the primary sphere (sphere from the infective individual) hits the end of a rewired long-range edge with probability $p\Gamma_d t^{d-1}$ per unit time, which is assumed to start with a time delay $\delta > 0$ due to the long-range spatial distance [4, 5]. Finally, the total infected volume $V(t)$is the sum of the primary volume $(1-p)\Gamma_d t^{d-1}$ plus a contribution $V(\tau-\delta)$, for each new sphere at time τ, satisfying

$$V(t) = \Gamma_d \int_0^t \tau^{d-1}[1-p+pV(\tau-\delta)]d\tau$$

Consider one–dimension W–S evolving network, $d = 1$,

$$x(t) = \Gamma_1 \int_0^t [1-p+px(\tau-\delta)]d\tau \tag{179.1}$$

And differentiating (179.1), we have the spreading model

$$\dot{x}(t) = \Gamma_1[1-p+px(t-\delta)] = \Gamma_1 px(t-\delta) + \Gamma_1(1-p) \tag{179.2}$$

Let $a = \Gamma_1 p > 0$, $b = \Gamma_1(1-p) > 0$, we have

$$\dot{x}(t) = ax(t-\delta) + b \tag{179.3}$$

The equation is a one-dimension, time-invariable parameter equation with time delay. We may only care about the volume of the flooded nodes in some directions, and then volume output equation followed

$$y(t) = cx(t) \tag{179.4}$$

Where $c > 0$ is constant or direction throughput factor.

Main Results

The observer for (179.3) is constructed as follows:

$$\dot{\hat{x}}(t) = a\hat{x}(t-\delta) + b + k[y(t) - c\hat{x}(t)] \tag{179.5}$$

where k is a observer gain constant and $\hat{x}(t)$ is a estimator for $x(t)$

Theorem 1. *Let $\delta > 0$ be a constant and the condition $k > a/c$ holds, then $\hat{x}(t)$ in (179.5) can globally approach to the $x(t)$ in (179.3)*

Proof. let $e(t) = x(t) - \hat{x}(t)$

$$\dot{e}(t) = \dot{x}(t) - \dot{\hat{x}}(t) = ae(t-\delta) - kce(t) \tag{179.6}$$

Consider the following Lyapunov function candidate:

$$V(e(t), \delta) = e^2(t) + a\int_{t-\delta}^{t} e^2(\tau)d\tau \geq 0 \tag{179.7}$$

differentiating $V(e(t), \delta)$and substitute (179.6) we get

$$\begin{aligned} \dot{V}(e(t), \delta) &= 2e(t)\dot{e}(t) + ae^2(t) - pae^2(t-\delta) \\ &= 2e(t)[ae(t-\delta) - kce(t)] + ae^2(t) - ae^2(t-\delta) \\ &= [a - 2kc]e^2(t) + 2ae(t)e(t-\delta) - ae^2(t-\delta) \end{aligned} \tag{179.8}$$

consider

$$2e(t)e(t-\delta) \leq e^2(t) + e^2(t-\delta)$$

from (179.8), we get

$$\begin{aligned} \dot{V}(e(t), \delta) &= [a - 2kc]e^2(t) + 2ae(t)e(t-\delta) - ae^2(t-\delta) \\ &\leq [2a - 2kc]e^2(t) \\ &\quad \text{If } k > a/c, \quad \dot{V}(e(t), \delta) < 0 \end{aligned}$$

From the Lyapunov stability theory, the theorem 1 is proofed.

Remark 1. For constant time delay, the total volume of the flooded nodes approach to an estimator when Kalman gain constant satisfies $k > a/c$. In other words, if the Kalman gain satisfies the condition, the total volume of the flooded nodes can be estimated.

Theorem 2. *If $\delta(t)$ is time varying bounded state delay satisfying $0 < \delta(t) < +\infty$, $\dot{\delta}(t) < 0$ and the condition $k > a/c$ holds, then $\hat{x}(t)$ in (179.5) can globally approach to the $x(t)$ in (179.3)*

Proof. Consider the following Lyapunov function candidate similar to (179.7):

$$V(e(t), \delta) = e^2(t) + a \int_{t-\delta(t)}^{t} e^2(\tau) d\tau \geq 0 \tag{179.9}$$

differentiating $V(e(t), \delta(t))$ in (179.9), we get

$$\begin{aligned} \dot{V}(e(t), \delta(t)) &= 2e(t)\dot{e}(t) + ae^2(t) - a[1 - \dot{\delta}(t)]e^2(t - \delta(t)) \\ &= 2e(t)[ae(t - \delta(t)) - kce(t)] + ae^2(t) - a[1 - \dot{\delta}(t)]e^2(t - \delta(t)) \\ &= [a - 2kc]e^2(t) + 2ae(t)e(t - \delta(t)) - a[1 - \dot{\delta}(t)]e^2(t - \delta(t)) \end{aligned} \tag{179.10}$$

consider

$$2e(t)e(t - \delta) \leq e^2(t) + e^2(t - \delta)$$

from (179.10), we get

$$\begin{aligned} \dot{V}(e(t), \delta(t)) &= [a - 2kc]e^2(t) + a[e^2(t) + e^2(t - \delta)] - a[1 - \dot{\delta}(t)]e^2(t - \delta(t)) \\ &\leq [2a - 2kc]e^2(t) + a\dot{\delta}(t)e^2(t - \delta(t)) \end{aligned} \tag{179.11}$$

Consider $\dot{\delta}(t) < 0$, $a = \Gamma_1 p > 0$ and $k > a/c$, from (179.11) we get $\dot{V}(e(t), \delta(t)) < 0$

From the Lyapunov stability theory, the theorem 2 is proofed.

Remark 2. For time-varying bounded state delay, the total volume of the flooded nodes approach to an estimator when Kalman gain constant satisfies $k > a/c$. In other words, if the Kalman gain satisfies the condition, and time-varying delay is decreasing with time, the total volume of the flooded or infected nodes can be estimated.

Conclusions

In this paper, we model the flooded volume in mobile ad hoc network using Watts–Strogatz (W–S) evolving networking theory, and get the result that if some conditions for observer gain constant are satisfied, the total volume of the flooded can be estimated. In other words, no matter time delay is constant or not, if the Kalman gain satisfies the condition $k > a/c$, the total volume of the flooded nodes can be estimated. It is a challenge to model the flooded volume in ad hoc network, especially in multi-dimensional situations. We are managing to do this work in ad hoc networks.

Acknowledgements This work is partially supported by NSFC under granted number 70271001, China Postdoctoral Fund under granted number 200203271.

References

1. Watts D. J., and Strogatz S. H.: Collective dynamics of small-world networks. Nature 393 (1998) 440–442.
2. Wang X. F., and Chen G.: Synchronization in small-world dynamical networks. Int. J. Bifurcation Chaos 12(1) (2002) 187–192.
3. Li C. G., and Chen G., Synchronization in general complex dynamical networks with coupling delays. Physica A. 343 (2004) 267–278.
4. Li X., and Wang X., Controlling the spreading in small-world evolving networks: stability, oscillation, and topology. IEEE Transactions on Automatic Control 51(3) (2006) 534–540.
5. Yang X. S., Chaos in small-world networks. Phys. Rev. E 63 (2001) 046206.

Chapter 180
A Plausible Modeling for Cellular Responding DNA Damage Under Radiotherapy

Jinpeng Qi, Shihuang Shao, Xiaojing Gu and Guangzhu Yu

Abstract P53, a vital anticancer gene, acts important role in controlling cell cycle arrest and cell apoptosis by regulating the downstream genes and their complicated signal pathways. Under radiotherapy, cell can trigger internal self-defense mechanisms in fighting against genome stresses induced by acute ion radiation (IR). To simulate the cellular responding DNA damage at single cell level, a model for P53 gene networks is proposed under radiotherapy. The model can be used to present the dynamic processes of the double-strand breaks (DSBs) generation and repair, ataxia telangiectasia mutated (ATM) and ARF activation, as well as the oscillations of P53-MDM2 feedback loop in response to acute IR. Especially, the model can predict the plausible outcomes of cellular responding DNA damage versus continuous radiation time.

Keywords P53 · DNA damage · IR · oscillations · modeling · radiotherapy

Introduction

Radiotherapy, one of the main tumor therapies, acts through the induction of DSBs to DNA, triggering the cellular self-defense mechanisms to induce apoptosis of cancerous cells via programmed apoptosis [1]. As an important transcription factor within nuclear, P53 can be activated by DNA damage transferring through ATM activation [2, 3]. By regulating downstream genes and their signal pathways, the activated P53 control the process of cell cycle arrest to repair DNA damage and cell apoptosis to eliminate the abnormal cells with genome damage or deregulated proliferation further [4, 5]. Recently, some models have been proposed to simulate the kinetics of tumor therapy and explain the damped oscillations of P53 in cell populations at cellular level [6, 7, 8, 8, 10]. To simulate the investigations of the cellular responding genome stresses and the complicated regulations among vital

Jinpeng Qi
College of Information Sciences and Technology, Donghua University, Shanghai 201620, P.R. China
e-mail: qipengkai@mail.dhu.edu.cn

R. Wang et al. (eds.), *Advances in Cognitive Neurodynamics*,

genes further, a model of P53 gene networks is proposed under radiotherapy. The dynamic interactions among vital components are presented in response to continuous effect of different IR dose. Meanwhile, the time threshold of ATM activation, and dynamic oscillations between P53 and MDM2, as well as the vital role of P53 in toxins eliminating are analyzed.

Methods

The scheme of the integrated model is given in Fig. 180.1. Compared with the former models [7, 8, 9, 10], more vital components are involved, such as oncogenes, ARF etc. As acute IR is applied, the resulting DSBs form the DSB–protein complexes (DSBCs) at damage sites after interacting with the DNA repair proteins [5, 11]. The cooperation of active ATM (ATM*) and active ARF (ARF*) switches on or off the P53-Mdm2 feedback loop to control the cell cycle arrest and the cell apoptosis further [1, 11]. The implementation of the model is described in the following paragraphs, and the detailed formulations can be found in [7, 8, 9, 10].

DSBs Generation and Repair

As shown in Fig. 180.2, this module contains both a fast and a slow kinetics, each of which is composed of a reversible binding of repair proteins and DSB lesions into DSBCs, and an irreversible process from the DSBCs to the fixed DSBs [10, 11]. In our model, DSBCs and repair proteins (RP) are treated as the dynamic variables [7, 8, 9], and the correct repair part of DSBs (F_r) and F_w are distinguished due to the profound consequences of the misrepair part of DSBs (F_w) on the subsequent cellular viability [9, 10, 11].

ATM and ARF Activation

The module scheme is shown in Fig. 180.3, ARF, oncogenes are involved in this module [5, 11]. Shown in Fig. 180.3a is the scheme of ATM activation, we deal that DSBCs is the main signal transduction from DSBs to P53-MDM2 feedback

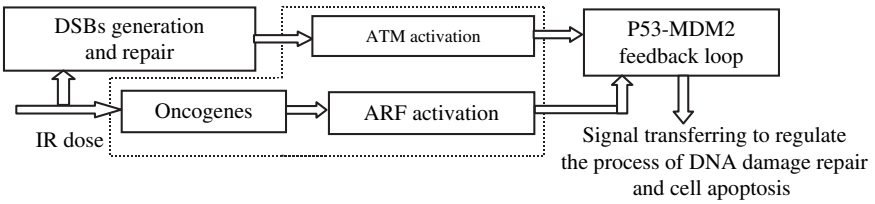

Fig. 180.1 The scheme of P53 gene networks under radiotherapy. It includes the modules of DSBs generation and their repair, ATM and ARF activation, as well as P53-MDM2 feedback loop

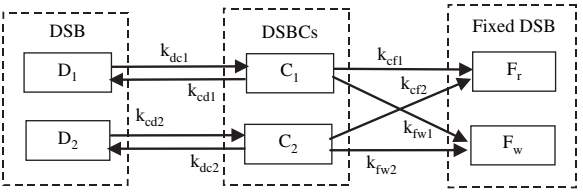

Fig. 180.2 The scheme of DSBs repair process. It includes both a fast repair pathway and a slow one. DSB can be in one of four states: intact DSB (DSB), DBSC, F_r and F_w

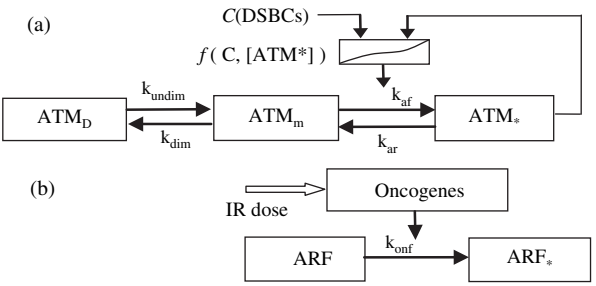

Fig. 180.3 The module scheme of ATM and ARF activation in response to acute IR

loop through ATM activation, and the rate of ATM activation is a function of the amount of DSBCs and the self-feedback of ATM* [7, 8, 9]. Meanwhile, shown in Fig. 180.3b is the scheme of ARF activation, ARF is activated by over-expression of oncogenes induced by acute IR, and subsequently increases the regulating effect of P53 by inhibiting Mdm2 expression and preventing P53 degradation [5, 11].

Regulations of P53-MDM2 Feedback Loop

P53-MDM2 feedback loop is the core part in the integrated networks [7, 8, 9, 10]. As shown in Fig. 180.4, P53 and its principal antagonist, Mdm2 acts essential roles in response to genome stresses [4, 5]. With the cooperation of both ATM and ARF, this negative feedback loop can produce oscillations in response to the sufficiently strong IR dose [5, 11].

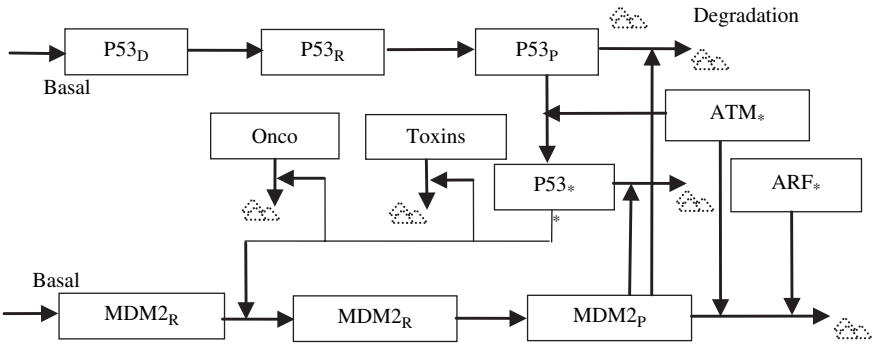

Fig. 180.4 The scheme of P53-MDM2 feedback loop. ATM* and ARF* stimulate the degradation of Mdm2, and further increase the regulatory activation of P53*

Results

In our simulations, the continuous 1, 3, 6Gy IR are applied into a cell, respectively. As shown in Fig. 180.5a, followed IR dose increasing, the rate of DSBCs synthesizing speed up due to the RP available around increasing damage sites. The kinetics shown in Fig. 180.5b indicate that ATM* switch to "on" state and trend to saturation versus continuous radiation time. Meanwhile, without the degradation

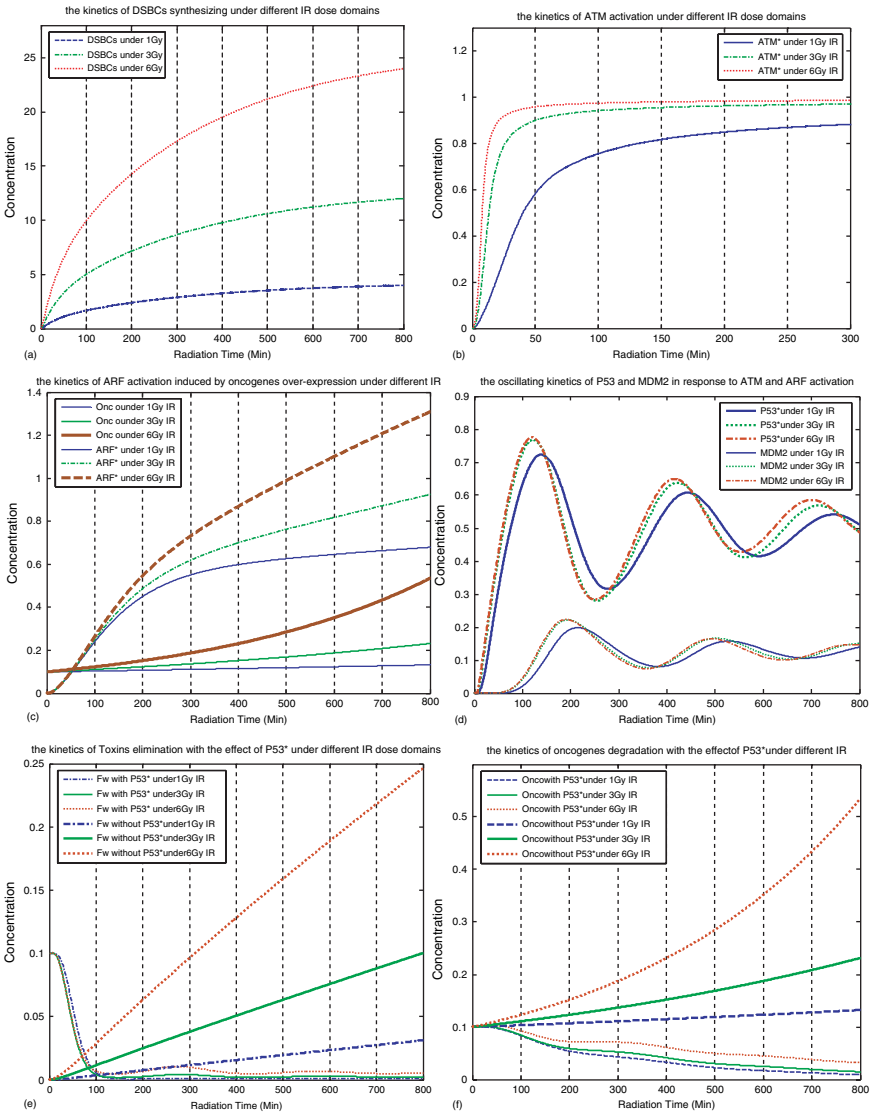

Fig. 180.5 The kinetics of integrated model in response to continuous 1,3,6Gy IR, respectively

functions of P53*, the oncogenes keep increasing versus radiation time. Subsequently, as shown in Fig. 180.5c, ARF is activated with respective rate in response to the over-expression of oncogenes under different IR dose domains.

Shown in Fig. 180.5d are the oscillations of P53* and MDM2 in response to continuous 1, 3, 6Gy IR. Followed IR dose increasing, the strength of these oscillations keep increasing, and trendind to a new equilibrium versus radiation time [7, 8, 9, 10]. Based on the assumption that F_w and oncogenes can be degraded directly by the eliminating effect of P53*, as shown in Fig. 180.5e, F_w decrease dramatically from initial value and trend to zero due to the eliminating functions of P53*. In addition, as shown in Fig. 180.5f, with the degradation effect of P53*, the expression of oncogenes keeps relatively lower with some oscillations. These simulations above suggest that P53* indeed act an important role in cellular response to genome stresses.

Conclusion

We proposed a plausible model of P53 gene network under radiotherapy by using a set of differential equations. In our simulations, ATM and ARF exhibit a strong sensitivity behavior in response to continuous IR, and further trigger the oscillations of P53-MDM2 feedback loop. The degradations of toxins and oncogenes prompted by the regulating functions of P53* can quantitatively present the outcomes of cellular responding DNA damage. Our mode provides a framework for the theoretical analysis of the self-defense mechanisms of cellular responding DNA damage under radiotherapy.

References

1. C. Perez and L. Brady, Principles and Practice of Radiation Oncology. Philadelphia, PA: Lippincott-Raven, (1998) 784–785.
2. M. Oren, "Decision making by P53: life, death and cancer," Cell Death and Differentiation, (2003) 10, 431–442.
3. B. Vogelstein, D. Lane and A.J. Levine, "Surfing the P53 network," Nature, (2000) 8307–8310.
4. M.A. Ritter, K.W. Gilchrist, et al., "The role of P53 in radiation therapy outcomes for favorable-to-intermediate-risk prostate cancer T," International Journal of Radiation Oncology, Biology, Physics, (2002) 53, 574–580.
5. K.W. Kohn and Y. Pommier, "Molecular interaction map of the P53 and Mdm2 logic elements, which control the Off-On switch of P53 in response to DNA damage", Biochemical and Biophysical Research Communications, (2005) 331, 816–827.
6. L.D. Ding, D. Matthew et al., Mathematical modeling of cancer radiovirotherapy. Mathematical Biosciences, (2006) 199, 80–103.
7. J.P. Qi, S.H. Shao and Y. Zhu, "Mathematical modeling of P53 gene regulatory network," Dynamics of Continuous Discrete and Impulsive Systems-Series B-Applications and Algorithms, (2006) 13, 11–15.
8. J.-P. Qi, S.-H. Shao, D.-D. Li and G.-P. Zhou, "A dynamic model for the P53 stress response networks under ion radiation," Amino Acids, (2007) 33, 75–83.

9. J.P. Qi, S.H. Shao, Y. Zhu and G.Z. Yu, "A mathematical model of P53 gene regulatory networks under radiotherapy," BioSystems, 2007, 90, 698–706. E pub 2007 Mar 6 doi:10.1016/j.biosystems.2007.02.007.
10. L. Ma, J. Wagner et al., "A plausible model for the digital response of P53 to DNA damage," PNAS, (2005) 2, 14266–14271.
11. L. Li, M. Story, R. Legerski, "Cellular responses to ionizing radiation damage," International Journal of Radiation Oncology, Biology, Physics, (2001) 49, 1157–1162.

Chapter 181
An Improvement of Sequential Minimum Optimization Algorithm

Jian Zhang, Jun-zhong Zou, Xing-yu Wang and Lan-lan Chen

Abstract Sequential Minimum Optimization (SMO) algorithm is a good method to solve Support Vector Machine (SVM) problem. One-dimensional cache strategy is proposed to speed up SMO algorithm. Experiments have been conducted to show that the proposed method is effective. Comparing with two-dimensional array, this cache strategy has some advantages: (1) To utilize the memory by the greatest degree; (2) The size of cache is not restrained. The training process will be speed up with the growth of cache; (3) The cost of maintain work is almost zero in contrast.

Keywords Machine learning · support vector machine · sequential minimum optimization · kernel caching

Introduction

Support vector machine was proposed by Vapnik in the middle of 1990s [1]. It can be taken as a general learning machine based on limited samples theory. SVM is an effective method to avoid the local minimum and over-fitting problems that occur in conventional classification methods. Besides, it resolved the dimension disaster effectively by introducing kernel function, which made it feasible to analyze the nonlinear relationship in a higher dimensional space.

Let training sample set $T = \left\{\left(x_1, \mathrm{y}_1\right), \cdots, \left(x_\mathrm{m}, \mathrm{y}_\mathrm{m}\right)\right\} \in (\mathrm{X} \times \mathrm{Y})^\mathrm{m}$, where $x_\mathrm{i} \in \mathrm{R}^\mathrm{n}$, $y_i \in \{1, -1\}$, $\mathrm{i} = 1, \cdots, \mathrm{m}$.

By introducing maximal interval method, an optimization problem is formed as follows:

$$\min_{\boldsymbol{\alpha}} \frac{1}{2} \sum_{i=1}^{m} \sum_{j=1}^{m} y_i y_j \alpha_i \alpha_j \kappa\left(\boldsymbol{x}_i, \boldsymbol{x}_j\right) - \sum_{j=1}^{m} \alpha_j = \min_{\boldsymbol{\alpha}} \frac{1}{2} \boldsymbol{\alpha}^T \boldsymbol{Q} \boldsymbol{\alpha} - \boldsymbol{e}^T \boldsymbol{\alpha} \qquad (181.1)$$

J. Zhang
School of Information Science and Engineering, East China University of Science and Technology, Box 579, 130 Meilong Road, Shanghai 200237, China
e-mail: zhjmaster@sina.com

R. Wang et al. (eds.), *Advances in Cognitive Neurodynamics*,

$$s.t. \quad \sum_{i=1}^{m} y_i \alpha_i = 0, \tag{181.2}$$

$$0 \le \alpha_i \le \mathrm{C}, \quad \mathrm{i} = 1, \cdots, \mathrm{m}. \tag{181.3}$$

where $Q_{\mathrm{ij}} = \mathrm{y_i y_j} \kappa\left(x_{\mathrm{i}}, x_{\mathrm{j}}\right)$ is the kernel matrix; $e = (1, 1, \cdots, 1)^{\mathrm{T}}$; C is a regularization parameter. There are two common kernel functions: polynomial kernel function on $\kappa_{ij} = \left[\left(x_{\mathrm{i}}^{\mathrm{T}} x_{\mathrm{j}}\right) + 1\right]^{\mathrm{d}}$ and gaussian kernel function $\kappa_{ij} = \exp\left(-\left\|x_{\mathrm{i}} - x_{\mathrm{j}}\right\| / 2\sigma^2\right)$. After resolving this optimization problem, we get the optimization resolution $\alpha^* = \left(\alpha_1^*, \cdots \alpha_{\mathrm{m}}^*\right)^{\mathrm{T}}$. One component from α^* is chosen and denoted as $0 < \alpha_{\mathrm{j}}^* < \mathrm{C}$. Then a threshold value is calculated as $\mathrm{f}(x) = \mathrm{sgn}\left(\sum_{\mathrm{i}=1}^{\mathrm{m}} \alpha_{\mathrm{i}}^* \mathrm{y_i} \kappa\left(x, x_{\mathrm{i}}\right) + \mathrm{b}^*\right)$. Finally, we get the decision function: $\mathrm{f}(x) = \mathrm{sgn}\left(\sum_{\mathrm{i}=1}^{m} \alpha_{\mathrm{i}}^* \mathrm{y_i} \kappa\left(x, x_{\mathrm{i}}\right) + \mathrm{b}^*\right)$.

Conventional convex quadratic programming problems need storage kernel matrix Q. This matrix is a two-dimensional m × m array. The scale of matrix Q will grow quickly with the increase of the sample size m. The matrix should occupy very large memory space in computer when the sample size is large. Besides, a large amount of matrix operation will take a lot of training time. Ossuna took the lead in proposing the decomposition strategy and proved its convergence. Platt introduced SMO Algorithm which was a particular case of decomposition strategy when the size of work sets is two [2]. Based on SMO algorithm, Keerthi modified the Karush-Kuhn-Tucker (KKT) conditions and proposed two modified algorithms (referred to as KSMO1 and KSMO2) [3]. The convergence for both algorithms has been proved [4]. Chang et al. pointed out that KSMO2 was a particular case of feasible direction strategy when the size of working sets is two [5].

In KSMO2 algorithm, it is optimized by i_{low} and i_{up} directly in inbound iteration [3]. This paper is based on KSMO2 algorithm.

This paper is organized as follows: Firstly, one dimensional kernel caching strategy was proposed in detail. Secondly, some experiments were conducted to indicate the new strategy can improve the training speed significantly with the growth of C/σ^2 ratio. Finally, the advantages were summarized.

Improvements on Inbound Iteration

When parameter C is very large relative to σ^2, the computation quantity will increase obviously in inbound iteration. Comparatively, the computation quantity of full iteration is very small. Take the data set pima-indians-diabetes for example. This data set contains 768 samples and 8 characters altogether. 575 samples were chosen randomly to form a training set which contained 200 positive samples and 375 negative samples; the other 193 samples were left to form a test set. Firstly, the data set was standardized by $x_{ij} = (x_{ij} - x_j)/s_j$, where x_{ij} is the jth character of the ith sample, x_j is the mean of the jth character, s_j is the standard deviation of the jth character. Gaussian kernel function was adopted. The optimum parameters were set as: $C = 500$, $\sigma^2 = 40$. The training correct rate is 85.22%, the testing correct

rate is 83.94%. During the training process, the number of kernel evaluations was statistically analyzed. In inbound iteration process, the number is 51,912,480; in full iteration process, the number is 10,00,061. It was found that the inbound iteration took up 98% of the computing work. Therefore, the improvements on inbound iteration process could improve the computing speed effectively.

One-Dimensional Kernel Caching Strategy

During the process of inbound iteration, it was observed that: if the update frequency of some Lagrange multiplier α_i is higher, then the update frequency will be still higher in successive inbound iterations. The corresponding kernel should be cached with higher priority. According to this regularity, a flowchart has been designed in Fig. 181.1. The variable Count specifies the total optimize number. The cache structure is described in Fig. 181.2.

In inbound iteration, for example, only four Non-Bound Support Vectors (NBSV) left. If enough space can be allocated, Cache (1) means to put the value of $\kappa_{11}, \kappa_{12}, \kappa_{13}, \kappa_{14}$ into one-dimensional array together because they will be used to update $F_i (i = 1, 2, 3, 4)$ [3]. Remove (1) means that these four variables should be covered with the other variables. κ_{ij} is saved in the fixed linear address computed by the following formula:

$$A_{ij} = (i-1) \times (T-1) - (i-1)^*(i-2)/2 + (j-1). \quad (i < j) \qquad (181.4)$$

where T is the total number of NBSV. It equals to four in this example. Besides, a reverse index table S is maintained to track the index in the training date set such as $S = (128, 2, 59, 575)$.

Experiment and Result Analysis

Both KSMO2 algorithm and our improved algorithm were realized under P4 2.4GHz, Windows2000, VC^{++} 6.0 environment. In order to distinguish these two algorithms, no other optimization methods have been applied. The data set pima-indians-diabetes was chosen for analysis. During the analysis, the parameter σ^2 is set to different values when C was fixed. In the improved algorithm, the size of cache was set to 50,000 * size (float) = 200, 000 Bytes. The comparison between the improved algorithm and KSMO2 algorithm was as follows.

From the comparison in Table 181.1, we found that computing time in improved algorithm was changing smoothly with the increase of C/σ^2 ratio. The computing

κ_{11}	κ_{12}	κ_{13}	κ_{14}	κ_{22}	κ_{23}	κ_{24}	κ_{33}	κ_{34}	κ_{44}	$\cdots$

Fig. 181.1 Flowchart corresponding to the inbound iteration of SMO algorithm

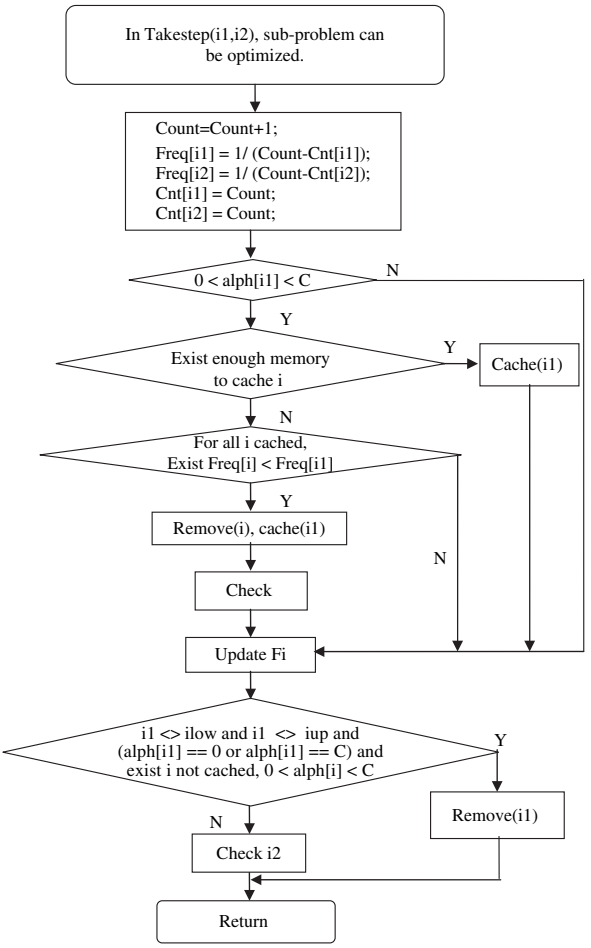

Fig. 181.2 One-dimensional cache structure

Table 181.1 Training time comparison ($C = 500$)

σ^2	10	20	30	40	50	60	70	80	90	100
Improved method/s	4.6	5.9	6.4	5.6	5.6	4.7	4.2	4.4	4.6	3.4
KSMO2/s	32.2	35.6	34.2	27.8	25.6	20.4	18.0	17.2	17.6	11.7

speed was 3–7 times higher than KSMO2. One-dimensional cache structure has some advantages below:

1. To utilize the memory by the greatest degree;
2. The size of cache is not restrained. The training process will be speed up with the growth of cache;
3. The cost of maintain work is almost zero in contrast.

Conclusion

One-dimensional cache strategy is proposed to speed up Keerthi et al.'s improved algorithm. Experiments have been conducted to show that the proposed method is effective when C is larger than. Comparing with two-dimensional array, this cache strategy has many advantages. Our future work is to extend this strategy to full iteration and replace array with chained list.

References

1. Vapnik V. N. Statistical Learning Theory. New York: Wiley, (1995).
2. Platt J. Fast Training of Support Vector Machines Using Sequential Minimal Optimization. Advances in Kernel Methods – Support Vector Learning. Cambridge, MA: MIT Press, (1999) 185–208.
3. Keerthi S, Shevade S, Bhattcharyya C, et a1. Improvements to Platt's SMO Algorithm for SVM Classifier Design. Neural Computation, (2001), 13: 637–649.
4. Keerthi S, Gilbert E. Convergence of a generalized SMO algorithm for SVM classifier design. Machine Learning, (2002), 46: 351–360.
5. Chang CC, Lin, CJ. LIBSVM: A library for support vector machines (Version 2.3). http://www.csie.ntu.edu.tw/∼cjlin/papers/libsvm.pdf, (2001).

Index